Tampereen yliopisto - Tampere University

PROCEEDINGS

The Sixteenth Scandinavian International Conference on Fluid Power, SICFP19

May 22 - 24, 2019
Tampere, Finland

Editors:
Kalevi Huhtala,
Seppo Tikkanen,
Janne Uusi-Heikkilä

Tampere University
Faculty of Engineering and Natural Sciences
Automation Technology and Mechanical Engineering
Tampere 2019

ISBN 978-952-03-1125-4 (Book of Abstracts, print)
ISBN 978-952-03-1126-1 (Proceedings, USB)
ISBN 978-952-03-1302-9 (Proceedings, pdf)
ISSN 2342-2726

PREFACE

The first international conference on fluid power in Tampere was held in 1987. That was the start of the series of Scandinavian fluid power conferences. In 1993 the conference was named as Scandinavian International Conference on Fluid Power and it was decided to hold the conference every second year alternately in Tampere and Linköping. So, we have already over 30 years' tradition.

The 16th Scandinavian International Conference on Fluid Power conference is organized by Innovative Hydraulics and Automation (IHA) at Tampere University (TAU) together with network of Global Fluid Power Society (GFPS).

At this time the conference includes various themes robotics, drives, digital hydraulics and pneumatics. Special attention in the program is given for energy efficiency and IoT in Fluid Power solutions.

We received interesting and high-level abstract proposals. In addition to two invited speakers and 6 plenary presentations, 44 papers were selected for the final programme. This year for the second time in the SICFP conference also peer-review of papers was available for those who asked it and 30 papers passed the evaluation. GFPS will give the best paper award to one of the presented publication. We appreciate the work what the reviewers have been done. We believe that the conference will give the participants fine opportunities to listen interesting presentations, to exchange opinions and strengthen of old contacts and to establish new ones.

This time the conference proceeding will be published as a printed abstract book and as a USB memory stick and the papers will be publicly available later 2019. We hope that this proceeding will serve you well during the conference but also far in the future as a source of reference.

We would like to express our sincere appreciation to everybody who has contributed to the success of the conference.

Tampere, 8th May, 2019

Kalevi Huhtala
Professor, Conference Chairman

SCIENTIFIC COMMITTEE

- Professor Matti Vilenius, Finland, Honorary Chair
- Professor Kalevi Huhtala, Finland, Chair
- Dr. Peter Achten, Netherlands
- Professor Ludger Frerichs, Germany
- Professor Marcus Geimer, Germany
- Professor Heikki Handroos, Finland
- Professor Petter Krus, Sweden
- Professor Jouni Mattila, Finland
- Professor Andrew Plummer, UK
- Professor Kazushi Sanada, Japan
- Professor Rudolf Scheidl, Austria
- Professor Katharina Schmitz, Germany
- Professor Kim Stelson, USA
- Professor Seppo Tikkanen, Finland
- Professor Jürgen Weber, Germany
- Professor Huayong Yang, China

REVIEWERS

- Dr. Peter Achten, Innas
- Prof. Torben Andersen, Aalborg University
- Prof. Eric Bideaux, INSA Lyon
- Dr. Liselott Ericson, Linköping University
- Prof. Ludger Frerichs, Technische Universität Braunschweig
- Prof. Marcus Geimer, Karlsruhe Institute of Technology
- Prof. Reza Ghabcheloo, Tampere University
- Prof. Heikki Handroos, LUT University
- Prof. Kalevi Huhtala, Tampere University
- Dr. Mikko Huova, Tampere University
- Dr. Juha Inberg, Ponsse Oyj
- Dr. Nigel Johnston, University of Bath
- Dr. Tomi Krogerus, Cargotec Finland Oy
- Prof. Petter Krus, Linköping University
- Dr. Arto Laamanen, Hydac Oy
- Dr. Matti Linjama, Tampere University
- Dr. Tatiana Minav, Aalto University
- Dr. Petteri Multanen, Tampere University
- Dr. Marko Paakkunainen, John Deere Forestry Oy
- Prof. Matti Pietola, Aalto University
- Prof. Andrew Plummer, University of Bath
- Prof. Kazushi Sanada, Yokohama National University
- Prof. Rudolf Scheidl, Johannes Kepler University Linz
- Prof. Katharina Schmitz, RWTH Aachen University
- Prof. Seppo Tikkanen, Tampere University
- Prof. Andrea Vacca, Purdue University
- Prof. Jürgen Weber, Technische Universität Dresden
- Prof. Huayong Yang, Zhejiang University

ORGANIZING COMMITTEE

- Kalevi Huhtala, Tampere University, Chairman
- Kari Aaltonen, Agco Power
- Liisa Aha, Tampere University
- Petri Hannukainen, Valtra
- Juha Inberg, Ponsse
- Arto Laamanen, Hydac
- Tapio Lehti, Parker Hannifin
- Juha Leppänen, Hermia Group
- Marko Paakkunainen, John Deere
- Seppo Tikkanen, Tampere University
- Arto Timperi, Comatec
- Kalle Tuohimaa, Bosch Rexroth
- Pasi Tuominen, Wapice
- Janne Uusi-Heikkilä, Tampere University
- Jani Vilenius, Sandvik Mining and Construction

SICFP19 Exhibitors / Sponsors

Programme

WEDNESDAY, MAY 22

8:30	Registration & Coffee
9:30 - 11:30	OI: Opening and Invited Speakers
11:45 - 12:30	P1: Plenary 1
12:30	Lunch
13:30 - 15:00	A1: Mobile Machines 1
13:30 - 15:00	B1: Digital Hydraulics
15:00	Coffee
15:30 - 16:30	A2: Hydraulic Pumps 1
15:30 - 16:30	B2: Pneumatics
19:00 -	**Reception by the City of Tampere, Tampere City Hall**

THURSDAY, MAY 23

8:30 - 10:30	P2: Plenary 2 - IoT
10:30	Coffee
11:00 - 12:00	A3: Auxiliary Systems
11:00 - 12:00	B3: Water Hydraulics
12:00	Lunch
13:00 - 14:30	A4: Valves
13:00 - 14:30	B4: Hydraulic Pumps 2
14:30	Coffee
15:00 - 16:30	A5: Fundamentals
15:00 - 16:30	B5: Mobile Machines 2
19:00-	**Gala Dinner, Tampere Hall, Park Hall**

FRIDAY, MAY 24

9:30 - 10:30	P3: Plenary 3
10:30	Coffee
11:00 - 12:30	A6: Energy Efficiency
11:00 - 12:30	B6: Robotics and Control
12:30	Lunch
13:30 - 15:30	L: Laboratory Tour

Peer-reviewed papers are marked with (peer review) text after title in abstracts section.

Wednesday, May 22, 2019

8:30	**Registration & Coffee**	
9:30 - 11:30	**OI: Opening and Invited Speakers, Maestro** *Session Chair: Kalevi Huhtala, Tampere University* **Thermal Aspects in Fluid Power Systems** Jürgen Weber, Technische Universität Dresden, Germany **Fluid Power Memes and Genes: About Sharks, Mice and a Poor Albatross Chick** Peter Achten, Innas BV, Netherlands	
11:45 - 12:30	**P1: Plenary 1, Maestro** *Session Chair: Kalevi Huhtala, Tampere University* **Sandvik company presentation** Jussi Puura, Sandvik Mining and Construction, Finland	
12:30	**Lunch**	
13:30 - 15:00	**A1: Mobile Machines 1, Maestro** *Session Chair: Matti Pietola, Aalto University* **Drive Cycle Generation for a Hydraulic Loader Crane** Amy Rankka, Linköping University, Sweden; Hiab AB, Sweden **Multi-Pressure Actuator in Enhancing Energy Balance of Micro-Excavator** Husnain Ahmed, Tampere University, Finland **Phlegmatization of a Combustion Engine for Reduction of Transient Emissions** Felix Pult, Karlsruhe Institute of Technology, Germany **Sustainable Logging Process by a Forwarder with an Innovative Hydro-Pneumatic Suspension** Chris Patrick Geiger, Karlsruhe Institute of Technology, Germany	**B1: Digital Hydraulics, Duetto 1** *Session Chair: Rudolf Scheidl, Johannes Kepler University Linz* **Linear Hybrid Dynamical Control of Digital Displacement Units** Niels Pedersen, Aalborg University, Denmark **Investigation of the Fault Tolerance of Digital Hydraulic Cylinders** Viktor Hristov Donkov, Aalborg University, Denmark **As Simple as Imaginable - an Analysis of Novel Digital Pump Concepts** Karl Samuel Kärnell, Linköping University, Sweden **Digital Hydraulic IMV System in an Excavator – First Results** Matti Linjama, Tampere University, Finland

15:00	**Coffee**	
15:30 - 16:30	**A2: Hydraulic Pumps 1, Maestro** *Session Chair: Jürgen Weber, Technische Universität Dresden* **Experimental Investigation of Churning Losses in a High-Speed Axial Piston Pump** Junhui Zhang, State Key Laboratory of Fluid Power and Mechatronic Systems, Zhejiang University, People's Republic of China **Swashplate Plate Type Axial Piston Pump Noise Diagnostics for Design** Paul Kalbfleisch, Purdue Univeristy, United States of America **Power Density Increase in Axial Piston Pumps by Use of Numerical Design of Experiments** Franck Maurice, Université de Technologie de Compiègne, France; HYDRO LEDUC, France	**B2: Pneumatics, Duetto 1** *Session Chair: Liselott Ericson, Linköping University* **A Novel Exergy Efficient Pneumatic Vacuum Pump** Olivier Reinertz, Institute for Fluid Power Drives and Systems (IFAS), RWTH Aachen University, Germany **Research on Dynamic Characteristics of a Suction Cantilever Valve in Miniature High Pressure Compressor Based on Equivalent Model** Yipan Deng, Huazhong University of Science & Technology, People's Republic of China **Mathematical Modeling of Pneumatic Steady Flow Through Tubes with Heat Transfer in Matlab/Simulink and its Experimental Verification** Riku Ito, Shibaura Institute of Technology, Japan

Thursday, May 23, 2019

8:30 - 10:30	**P2: Plenary 2 - IoT, Maestro** *Session Chair: Peter Achten, Innas BV BV* **Automation for the Factory of the Future** Hans Michael Krause, Bosch Rexroth AG, Germany **Smart Factory Concepts: Cyber-Physical Systems and Integrated Solutions** Eberhard Klotz, Festo, Germany **Integration of Customized IoT Solutions with Mobile Working Machines** Arto Orava, Epec Oy, Finland	
10:30	**Coffee**	
11:00 - 12:00	**A3: Auxiliary Systems, Maestro** *Session Chair: Petter Krus, Linköping University* **Data Correlation Model for Hydraulic Fluid Filter Condition Monitoring** Anton Jokinen, Aalto University, Finland **Coupled Fluid-Thermal-Structural Analysis of Two-Phase Flow in a Hydraulic Tank** Jaganmohan Rao Gorle, Parker Hannifin, Finland **Lightweight Piston Accumulator for Hydraulic Hybrid Drive Systems** Thorsten Hillesheim, Freudenberg Sealing Technologies, Germany	**B3: Water Hydraulics, Duetto 1** *Session Chair: Kazuhisa Ito, Shibaura Institute of Technology* **Methods for Determination of the Gap Height in Water-Lubricated Contacts** Florian Schoemacker, Institute for Fluid Power Drives and Systems (IFAS), RWTH Aachen University, Germany **Optimization of Silencing Groove for Port Plate of Water Hydraulic Axial Piston Pump** Hao Pang, Huazhong University of Science and Technology, People's Republic of China **Adaptive Model Predictive Tracking Control of Tap-Water Driven Muscle Using Hysteresis Compensation with Bouc-Wen Model** Ryo Inada, Shibaura Institute of Technology, Japan

12:00	**Lunch**	
13:00 - 14:30	**A4: Valves, Maestro** *Session Chair: Torben Andersen, Aalborg University* **The Effects of Bulk Modulus on the Dynamics of Controlled Independent Metering System** Goran Stojanoski, University of Leoben, Chair of Automation, Leoben, Austria **Analysis and Test of Model-Based Fault Detection Methods for Mobile Machinery Using Independent Metering Systems** Benjamin Beck, TU Dresden, Germany **Simulation Research on Temperature Rise Characteristics of Permanent Magnet Spring Overflow Valve** Lianming Su, Beihang University, People's Republic of China **Electro-Hydraulic Proportional Pressure Reducing Valve for Independent Metering Valve with a Spool-Poppet Hybrid Actuator** So-Nam Yun, Korea Institute of Machinery & Materials, Republic of Korea (South Korea)	**B4: Hydraulic Pumps 2, Duetto 1** *Session Chair: Andrea Vacca, Purdue University* **Analytical Approach to Calculate the Rotation Angle-Dependent Compensation Ratio of the Cylinder Block – Valve Plate Contact in Axial Piston Machines** Seong-Ryeol Lee, Institute for Fluid Power Drives and Systems (IFAS), Aachen, Germany **Fluid Dynamic Simulation of Hydraulic Orbital Motors** Venkata Harish Babu Manne, Maha Fluid Power Research Center, Purdue University, Lafayette, Indiana, USA **Double-Pump (R)Evolution – Higher Efficiency and Lower Noise Level for Variable Speed Pump Drives** Tobias Speicher, Hochschule für Technik und Wirtschaft des Saarlandes, Germany **Multi-Disciplinary Model for Preliminary Design of Electro-Mechanical Servo Pump** Tatiana Minav, Aalto University, Finland
14:30	**Coffee**	

15:00 - 16:30	**A5: Fundamentals, Maestro** *Session Chair: Andrew Plummer, Professor* **On the Saturation Dynamics of the Oil Film on a Hydraulic Cylinder Rod During Extension** Tobias Mielke, Institute for Fluid Power Drives and Systems (IFAS), RWTH Aachen University, Germany **Stick Slip Prevention of Hydraulic Rod and Piston Seals in the Boundary Condition** Mandy Wilke, Trelleborg Sealing Solutions Germany GmbH, Germany **Experimental Investigation of the Hard-Hard Contact in Seat Valves** Tobias Mielke, Institute for Fluid Power Drives and Systems (IFAS), RWTH Aachen University, Germany **Improved Performance on Reciprocating Seals due to Optimized Lubrication in the Sealing System** Mandy Wilke, Trelleborg Sealing Solutions Germany GmbH, Germany	**B5: Mobile Machines 2, Duetto 1** *Session Chair: Seppo Tikkanen, Tampere University* **Classification of Machine Functions: A Hydraulic Excavator Case Study** Nathan Keller, Purdue University, United States of America; Maha Fluid Power Lab, United States of America **Hydraulic Hybrid Working Machines Project - Lessons Learned** Matti Linjama, Tampere University, Finland **Energy Efficiency Optimization of Electric Powertrain of Underground Load-Haul-Dump Mining Loader by Means of Dynamic Programming** Marius Baranauskas, Aalto University, Finland **Automatic process pattern recognition for mobile machinery** Martin Starke, Technische Universität Dresden, Germany

Friday, May 24, 2019

9:30 - 10:30	**P3: Plenary 3, Maestro** *Session Chair: Marcus Geimer, Karlsruhe Institute of Technology* **A multi pressure network system for mobile applications** Edwin Heemskerk, Bosch Rexroth AG, Germany **Design, Process, and Performance of Hydraulic Components using Additive Manufacturing** Huayong Yang, Zhejiang University, People's Republic of China	
10:30	Coffee	
11:00 - 12:30	**A6: Energy Efficiency, Maestro** *Session Chair: Marko Paakkunainen, John Deere Forestry Oy* **Carbon Footprint Determination of an Electro-Hydraulic Compact Axle (EHA) Based on DIN EN ISO 14067** Maximilian Waerder, Institute for Fluid Power Drives and Systems (IFAS), RWTH Aachen University, Germany **Energy Efficiency Analysis of a Novel Hydro-Electric Hybrid Driving System for Hydraulic Excavator Boom** Yunxiao Hao, Key Lab of Advanced Transducers and Intelligent Control System of Ministry of Education and Shanxi Province, Taiyuan University of Technology, People's Republic of China **Theoretical Study on the Energy Regeneration Mechanism of a Switched Inertance Hydraulic System with Cylinder and Load** Satoshi Maekawa, Kobe Steel, Japan **Servo Hydraulic Axis (SHA)** Thomas Gellner, Bosch Rexroth AG, Germany	**B6: Robotics and Control, Duetto 1** *Session Chair: Jouni Mattila, Tampere University* **Simulation of a Hydraulic Direct-Drive System for a Biped Walking Robot** Juri Shimizu, Hitachi, Ltd., Japan; Waseda University, Japan **Model Predictive Path Tracking Control with Off-Axle Reference Point for Car-Like Robots** Ilja Stasewitsch, Technische Universität Braunschweig, Germany **Design and Implementation of Pressure Feedback for Load-Carrying Applications with Position Control** Daniel Hagen, University of Agder, Norway **Experimental Analysis of an Electro-Hydraulic Drive for an Elbow Support Exoskeleton** Rudolf Scheidl, Johannes Kepler University Linz, Austria
12:30	**Lunch**	
13:30 - 15:30	**L: Laboratory Tour**	

Wednesday A1: Mobile Machines 1, Maestro, 13:30 - 15:00

Session Chair: Matti Pietola, Aalto University

Title	**Drive Cycle Generation for a Hydraulic Loader Crane** (peer reviewed)
Presenting author	Amy Rankka, Linköping University, Sweden; Hiab AB, Sweden
Electrification of hydraulic systems has become an important research topic. The cost of the electric energy storage is high and drives the development of new efficient solutions for the system to be of commercial interest. This study is part of a project where the electrification of a loader crane is the main focus. The crane is a versatile machine and the energy efficiency of the hydraulic system is strongly dependent on the working envelope. A representative envelope can be called a drive cycle and is necessary to evaluate new solutions. This paper describes the method of producing such a cycle. A large amount of data from a field crane has been recorded for several weeks. A pattern of movement is found and used to define parameters of the drive cycle. To extract combinations of the parameters that form a good representation of the measurement data a principal component analysis is carried out. Finally, the drive cycle is defined as a sequence of trajectories with different payloads, corner points and actuator commands for movements between corner points. The drive cycle is tested and verified on a crane of the same model as the field crane in a laboratory environment. The methodology is found to produce a drive cycle with good variation and representation of geometrical parameters.	

Title	**Multi-Pressure Actuator in Enhancing Energy Balance of Micro-Excavator** (peer reviewed)
Presenting author	Husnain Ahmed, Tampere University, Finland
This paper presents results of an experimental study conducted with an electrified small sized excavator, whose boom swing function is equipped with digital hydraulic multi-pressure actuator. Highlighted and discussed are the performance, energy efficiency and controllability of the function in varying inertia loads. In addition, component wise energy losses are analyzed. This data is compared with the results gained with the excavator's original control arrangement, a load-sensing system based on pressure adjustment valve. Results manifest high energy saving potential of the multi-pressure system in mobile machinery.	

Title	**Phlegmatization of a Combustion Engine for Reduction of Transient Emissions** (peer reviewed)
Presenting author	Felix Pult, Karlsruhe Institute of Technology, Germany
The main topic of this paper is the reduction of transient engine-out emissions ejected by diesel engines through phlegmatization. This phlegmatization is supported by a hydraulic hybrid module to prevent system dynamics from dropping. In order to design the hybrid module according to its size and an optimal reduction of transient engine-out emissions, a design tool will be developed. In addition, the structure of a simulation model is presented, which serves to test different hybrid module concepts and creates the data basis for the design tool.	

Title	**Sustainable Logging Process by a Forwarder with an Innovative Hydro-Pneumatic Suspension** (peer reviewed)
Presenting author	Chris Patrick Geiger, Karlsruhe Institute of Technology, Germany
Forest machines enable a fast and save way to harvest the sustainable product wood. Especially forwarders have a huge impact on the forest site, as they have high wheel loads combined with frequent crossings. To enable a sustainable logging process, a new hydro-pneumatic suspended bogie axle is developed. In this paper, the suspended axle is evaluated and compared simulative to a standard in-market bogie axle without any suspension. Therefore, a simulation model of a forwarder with suspended bogie axles was built based on a validated model of an in-market forwarder. Both simulation models were driven over a skid road and a forest road. Dynamic wheel forces can be reduced with the suspended system up to 40 %. The maximum amplitude of vertical accelerations is reduced significantly with the hydro-pneumatic suspension up to one-third of the standard bogie. Furthermore, there is no significant Eigen frequency of the developed system compared to the reference system. As a result, not only soil damage can be reduced but also the working conditions of the operator can be improved with hydro-pneumatic suspended bogie axles.	

B1: Digital Hydraulics, Duetto 1, 13:30 - 15:00

Session Chair: Rudolf Scheidl, Johannes Kepler University Linz

Title	**Linear Hybrid Dynamical Control of Digital Displacement Units** (peer reviewed)
Presenting author	Niels Pedersen, Aalborg University, Denmark

This paper concerns development of control strategies for energy efficient fluid power digital displacement machines (DDM). The DDM technology yields an efficient reduction in displacement levels by deactivating independently cylinder pressure chambers by electromagnetically controlled on-off valves. Since the continuous dynamics of each pressure chamber is activated/deactivated discretely at fixed shaft positions, the DDM dynamics belongs to the class of hybrid dynamical systems. However, control development for hybrid system is in general very complex due to the use of Lyapunov stability theory for both continuous and discrete systems. This paper shows stability based on hybrid dynamical theory for a linear continuous plant actuated by a DDM, which dynamics has been approximated by a linear discrete model. It is shown that the control design problem is identically to that of a fully discrete description of the system based on a zero-order-hold approximation of the continuous design. Furthermore, the problem of having a nonlinear plant, multiple DDMs or an angle dependent asynchronous control update rate for a variable speed DDM is addressed, where measures of stability analysis is discussed.

Title	**Investigation of the Fault Tolerance of Digital Hydraulic Cylinders** (peer reviewed)
Presenting author	Viktor Hristov Donkov, Aalborg University, Denmark

This paper investigates the fault tolerance of Discrete Displacement Cylinders (DDCs) controlled with a Model Predictive Controller (MPC). Due to the nature of DDCs there are multiple components such as several pressure chambers, constant pressure rails, and on/off valves, which operate in parallel. Some of these components do similar jobs, i.e. more than one cylinder chamber provides a positive force when pressurized. This modularity in design is an often stated benefit of digital hydraulics because failed components have less influence on the behaviour of the whole system. The exact influence of faults in the components, when the fault is detected and when it is not, is shown through a sensitivity study. Certain faults are tested in a laboratory setting to verify the simulation results. The results show that different component failures lead to different types of loss of capability of the system because the components are not equivalent in size. Furthermore the results show that the performance of the system is better when the fault is detected and the controller is able to take appropriate action.

Title	**As Simple as Imaginable - an Analysis of Novel Digital Pump Concepts** (peer reviewed)
Presenting author	Karl Samuel Kärnell, Linköping University, Sweden

This paper focuses on how digital displacement can be achieved in a wobble plate pump by connecting the cylinders in the pump to different groups and using by-pass valves to control the flow from each group. The idea is to make a simple and inexpensive electronically controlled pump. The paper deals with two main aspects, the cylinder configuration and the valve configuration. The cylinder configuration refers to how the cylinders in the pump can be grouped and how different groupings will affect the flow pulsations. The valve configuration refers to the by-pass solution. Two principally different solutions are analysed: one that uses 3-way by-pass valves and one that makes use of check valves in combination with 2-way on/off-valves. A comprehensive simulation model has been used as a tool for analysing flow pulsations for the different design configurations. The results show that a cylinder configuration with 3+6 cylinders delivers low flow pulsations for all three displacement settings. However, if more displacement settings are desired, an interesting finding is that a configuration with 3+6+12 cylinders is only slightly better than a configuration with 2+4+8 cylinders, from a pulsation amplitude point of view. This is due to the pre-compression in the cylinders. Regarding the valve configuration, it has been shown that both of the analysed configurations might suffer from problems during switching, especially if the valves are slow.

Title	**Digital Hydraulic IMV System in an Excavator – First Results**
Presenting author	Matti Linjama, Tampere University, Finland

This study presents the conversion process of the working hydraulics on a 20 ton wheeled excavator from a load sensing system into a digital hydraulic independent metering valve system. Independent metering valves enable better energy efficiency by allowing reduction of throttling losses and by allowing energy recuperation and harvesting with different control modes. Digital hydraulics with parallel connected on/off valves offers robustness, more deterministic valve opening and improved durability compared to analogue IMV systems realised with proportional valves. The paper studies the feasibility of a digital hydraulic valve system in a high flow rate construction machine with multiple actuators operating simultaneously with a single electronically pressure controlled pump. Paper includes the process steps of design, feasibility analysis, building of the machine and the first measurements to validate the system operation and to show the performance compared to the original load-sensing system.

A2: Hydraulic Pumps 1, Maestro, 15:30 - 16:30

Session Chair: Jürgen Weber, Technische Universität Dresden

Title	**Experimental Investigation of Churning Losses in a High-Speed Axial Piston Pump**
Presenting author	Junhui Zhang, State Key Laboratory of Fluid Power and Mechatronic Systems, Zhejiang University, People's Republic of China
Churning loss has a significant influence on the mechanical efficiency in axial piston pumps. This paper focuses on experimental investigations on the churning losses and introduces a test rig to measure the influence of various parts on churning loss in an axial piston pump. The description of the test method is presented in detail, followed by sample results of the churning losses measurement. According to the measuring results under test conditions, it is found that the churning loss is mainly related to cylinder block and pistons, and has little relation with swash plate and variable mechanism.	

Title	**Swashplate Plate Type Axial Piston Pump Noise Diagnostics for Design** (peer reviewed)
Presenting author	Paul Kalbfleisch, Purdue Univeristy, United States of America
The characterization of the noise admitted by positive displacement machine is an important metric in designing positive displacement machines and their corresponding systems. Many companies in industry design their pumps noise based on traditions of trial and error verified by simple measurements of sound pressure level. A research initiative between Parker Hannifin and Maha Fluid Power Research Center at Purdue University will introduce a new methodology for diagnosing for designing existing pumps to reduce noise. This paper will provide a high-level overview of the proposed methodology. The methodology consists of organizing the unit’s oscillatory energy into five stages of the structural acoustic process, where each stage can be independently characterized using various experimental and empirical modeling methods.	

Title	**Power Density Increase in Axial Piston Pumps by Use of Numerical Design of Experiments** (peer reviewed)
Presenting author	Franck Maurice, Université de Technologie de Compiègne, France; HYDRO LEDUC, France

This paper deals with the increase in power density of an axial piston pump using numerical Design of Experiments (DoE). Piston pumps are an important source of fluid power in hydraulic systems. The strength of these technologies, whether radial, bent axis, or axial, relies on their high power density. Increasing the overall efficiency and making products reliable in terms of lifetime for high-pressure uses are the main concern of hydraulic components manufacturers. Our work focuses on a HYDRO LEDUC pump type “TXV indexable”. An optimisation strategy using 1D and 3D simulations relying on Design of Experiments will be described. The pump is characterised on a test rig to get a set of experimental data. A numerical model of the pump is then built on the Amesim® software and represents a virtual test rig. To improve the power density of the pump, the Design of Experiments methodology is applied to the valve plate, with the aim of finding a satisfying geometry which allows to meet the desired fatigue life requirements as well. Using response surface optimisation methodology, a new optimal geometry is implemented into the Amesim® model to validate the gain in power density of the pump. From the results of the simulations performed on the Amesim ® virtual test rig, the new design of the valve plate is validated. The power density of the pump equipped with the new valve plate has increased by 7%.

B2: Pneumatics, Duetto 1, 15:30 - 16:30

Session Chair: Liselott Ericson, Linköping University

Title	**A Novel Exergy Efficient Pneumatic Vacuum Pump** (peer reviewed)
Presenting author	Olivier Reinertz, Institute for Fluid Power Drives and Systems (IFAS), RWTH Aachen University, Germany
The usage of wasted exergy of pneumatic pressure regulators to deliver a sufficient vacuum pressure for adjacent gripping systems carries significant energy and cost saving potentials. Unfortunately, nowadays pneumatic vacuum generators are unable to fulfil the resulting demands. Therefore, a novel suitable pneumatic membrane vacuum generator is introduced. At first, the underlying thermo-dynamical effects during vacuum generation and pressure reduction in pneumatic systems are analytically investigated to highlight the existing optimization potentials. Thereof, the underlying principles of the novel component are deduced, the modelling of the device is described and geometrical parameters are analytically defined. Furthermore, a corresponding energy efficient control algorithm is presented. Finally, the behaviour of the device in typical load cases is assessed by dynamic multi-domain simulation in DSHplus. The results show broad applicability of the device in relevant applications and significant energy saving potentials compared to state of the art products.	

Title	**Research on Dynamic Characteristics of a Suction Cantilever Valve in Miniature High Pressure Compressor Based on Equivalent Model** (peer reviewed)
Presenting author	Yipan Deng, Huazhong University of Science & Technology, People's Republic of China
In this paper, a cantilever valve for miniature high-pressure compressor is proposed. An equivalent model of cantilever valve has been presented to obtain the equivalent stiffness and equivalent mass for the valve motion equation. Based on the equivalent model and thermodynamic process in the cylinder, A theoretical analysis has been constructed to reveal the dynamic characteristics of the suction valve. Crucial parameters such as reed thickness and valve lift are analysed to reveal their effects on the performance of suction valve, as well as the miniature high pressure compressor. It can be found that both reed thickness and valve lift exert an more obvious effect on closing process of suction valve comparing to opening process. Volumetric efficiency can be improved by reducing valve lift. Based on the numerical investigation, the optimized parameters can be obtained for reliable performance of the miniature high pressure compressor.	

Title	**Mathematical Modeling of Pneumatic Steady Flow Through Tubes with Heat Transfer in Matlab/Simulink and its Experimental Verification** (peer reviewed)
Presenting author	Riku Ito, Shibaura Institute of Technology, Japan

The purpose of this research is the development of simulation models of pneumatic steady flow through tubes with wall friction and external heat transfer by making use of MATLAB/Simulink® for system engineers. We considered straight uniform tubes which were heated or cooled to maintain the wall temperature at certain constants. The developed model consists of the thermal entry region model and the Fanno region model, which is connected in series to the former model. The heat transfer effects through walls are modelled by utilizing the Chilton-Colburn analogy in the thermal entry region model. On the other hand, adiabatic tube-walls are assumed in the Fanno region model, because of the small temperature difference between the walls and internal air. In the experiment, compressed air was supplied from a constant temperature tank to a copper tube set in a water jacket to adjust the wall temperature. The pressure at both ends of the tube and the mass flow rate were measured. The usefulness of the newly developed models was verified by comparing the simulation results with the experimental results.

A3: Auxiliary Systems, Maestro, 11:00 - 12:00

Session Chair: Petter Krus, Linköping University

Title	**Data Correlation Models for Hydraulic Fluid Filter Condition Monitoring** (peer reviewed)
Presenting author	Anton Jokinen, Aalto University, Finland

In fluid power systems, one of the most common causes of failure is contamination of the hydraulic fluid. Without filtering the fluid gets contaminated with harmful particles over time, which will cause excessive wear of components or even block motion of parts in flow control valves. In order to avoid machine downtime, it is important to monitor that adequate technical performance level of the fluid is maintained at all times.

This study contributes to condition-based maintenance of hydraulic fluid filter units by establishing a correlation equation, based on comprehensive laboratory tests and incorporated in a simulation model, relating the pressure drop over the filter unit with the main variables describing the operating conditions of the fluid system as well as with filter operating time.

The paper describes how the correlation equation and the simulation model was constructed. The results indicate that good correlation was obtained (R-square value 0.98) with the constructed equation between the physical variables and the temporal development of the pressure drop over the filter. The model can be used as a building block for a smart filter unit that can predict its lifetime.

Title	**Coupled Fluid-Thermal-Structural Analysis of Two-Phase Flow in a Hydraulic Tank** (peer reviewed)
Presenting author	Jaganmohan Rao Gorle, Parker Hannifin, Finland

In addition to storing the hydraulic oil, the hydraulic tanks are expected to cool the fluid, eliminate the air and water content, and avoid condensation and solid deposition. Besides these functional capabilities, the optimum use of internal volume is desired, which ensures better vorticity distribution in the tank. Being the reservoir and supplier of preconditioned oil, a typical tank design should meet certain standards as oil cleanliness is concerned. On the other hand, the design of a hydraulic tank is often subject to space management and hence enormous design complexity. In this context, virtual engineering practices for flow and structural analysis during designing and redesigning phases of the tank's development process have become decisive in reaching the final outcome.

In this study, a coupled-field investigation, using Computational fluid and solid dynamics, has been performed for flow and structural mechanics of a hydraulic oil reservoir. The size of the tank is approx. 0.047 m3 and the return line steadily supplies the oil at 1.96 kg/s. First, the thermofluid flow analysis, with initial volumes of oil and air, was performed using Volume of Fluid (VOF) model with second order solution accuracy. The flow and heat transfer characteristics were studied in detail. The resulting thermal and pressure loads on the tank walls were obtained by exporting the CFD solution to CSD solver. The coupled field was then analysed for stresses in the tank's structure. This simulation-driven product design provides a useful knowledge base for further exploration of complex structured hydraulic tanks.

Title	**Lightweight Piston Accumulator for Hydraulic Hybrid Drive Systems**
Presenting author	Thorsten Hillesheim, Freudenberg Sealing Technologies, Germany

Freudenberg Sealing Technologies (FST) has developed innovative solutions for high and low pressure accumulators for hydraulic hybrid energy storage systems. These systems support demand for more energy efficient and fuel saving solutions. For vehicles with heavy stop and go duty cycles, a hybrid accumulator system can be an optimal choice to recover brake energy and reduce overall fuel consumption. During braking, the kinetic energy is converted to stored energy via a gas-filled accumulator system. This stored energy is then available when needed for accelerating the vehicle from a stopped position. This makes a significant contribution to reduced fuel consumption, lower CO2 emissions and also enables downsizing of other vehicle system components. In addition, wear on braking systems is significantly reduced, contributing to an overall improvement in total cost of ownership. Hydraulic hybrid accumulator systems can be used in cars and mobile applications, including smaller delivery vans, refuse trucks, and other vocational vehicles with high stop and go duty cycles. FST has now succeeded in reducing the weight of the storage system (consisting of a high pressure and low pressure piston accumulator), thus making its application even more attractive for mobile use. Hydraulic Hybrid Accumulator systems are also an alternative to electric hybrid solutions for smaller vehicles.

B3: Water Hydraulics, Duetto 1, 11:00 - 12:00

Session Chair: Kazuhisa Ito, Shibaura Institute of Technology

Title	**Methods for Determination of the Gap Height in Water-Lubricated Contacts** (peer reviewed)
Presenting author	Florian Schoemacker, Institute for Fluid Power Drives and Systems (IFAS), RWTH Aachen University, Germany
Applications, which require the pressure fluid to be environmentally safe, often use water hydraulics as motion technology. If the tribological contacts of the components are chosen to be lubricated with water as well, the gap height is reduced compared to oil lubrication due to the lower viscosity of water compared to oil. Because of occurring wear and increased leakage the pressure load of the components is limited. This limitation is investigated for the purpose of the piston slipper / swash plate contact of an axial piston pump. This research is based upon simulation using a model containing the Reynolds-Equation and a solid contact model. Furthermore deformation of the slipper surface is considered.	

Title	**Optimization of Silencing Groove for Port Plate of Water Hydraulic Axial Piston Pump** (peer reviewed)
Presenting author	Hao Pang, Huazhong University of Science and Technology, People's Republic of China
Water hydraulic axial piston pump is a key component in water hydraulic system. One of the most important drawbacks of water hydraulic system is noise and vibration, which mainly originate from the water hydraulic pump. And the noise and vibration mainly caused by pressure and flow ripple of pump. So there are great number of researches to reduce pressure and flow ripple, for example, the silencing groove of port plate. In this paper, the port plate of a water hydraulic axial piston pump with U-shaped silencing groove is investigated. Through establishing the pressure and flow mathematical model of a water hydraulic pump considering the silencing groove, the silencing groove of port plate is optimized. The simulation results show that the pressure and flow ripple with optimized port plate is decreased. Then the experiment verifies that the optimized silencing groove can be to reduce the pressure ripple.	

Title	**Adaptive Model Predictive Tracking Control of Tap-Water Driven Muscle Using Hysteresis Compensation with Bouc-Wen Model** (peer reviewed)
Presenting author	Ryo Inada, Shibaura Institute of Technology, Japan

Recently, high-precision displacement control of McKibben type artificial muscles driven by tap water has attracted attention because the muscle exhibits a few advantages including high flexibility, low cost, light weight, and high-power density and is promising in terms of industrial applications that necessitate high cleanliness. However, the muscle generally has hysteresis characteristics, and the characteristics depend on the load. Therefore, it is difficult to obtain high-precision displacement control. The authors introduce the Bouc–Wen model to obtain a model that describes hysteresis characteristics, and propose a linearization technique by using the inverse of the model. Furthermore, in order to obtain robustness for load and high control performance, we apply an adaptive model predictive control with a servo mechanism by using its linearization technique to the muscle. The experimental results indicate that the proposed method improved control performance by 66% when compared to that of the conventional method under different load conditions.

A4: Valves, Maestro, 13:00 - 14:30

Session Chair: Torben Andersen, Aalborg University

Title	**The Effects of Bulk Modulus on the Dynamics of Controlled Independent Metering System** (peer reviewed)
Presenting author	Goran Stojanoski, University of Leoben, Chair of Automation, Leoben, Austria

The bulk modulus significantly affects the dynamics of hydraulic systems. In this paper, various known approaches for modelling the bulk modulus are investigated and tested. The models include: volumetric compression, solubility of air in oil and oil temperature. These models have been modified here to enable their use in a simulation environment which includes position controlled hydraulics. The results confirm, that air content in and the temperature of the oil can considerably lower the bulk modulus and the overall stiffness of the hydraulic system. This paper shows the different impacts that the low bulk modulus has on pressure and flow controllers as part of the independent metering control strategy. Additionally, the contributions of the pressure and flow controlled cylinder sides on the overall stiffness of the system are analysed and demonstrated. To minimize these effects, a new approach, which pre-pressurizes the rod side of the hydraulic cylinder according to the stiffness of the piston side is proposed. This approach alleviates the shortcomings of previous scientific research and improves the energy efficiency of the system. Furthermore, the results of the new approach are compared with already existing methods, where the set value for the pressure on the rod side is pre-set to a constant value. Depending on the pressure region in which the system operates and the speed of position change this new approach can increase the energy efficiency by 5-15%.

Title	**Analysis and Test of Model-Based Fault Detection Methods for Mobile Machinery Using Independent Metering Systems** (peer reviewed)
Presenting author	Benjamin Beck, TU Dresden, Germany

Based on an analysis of suitable model-based fault detection methods, the contribution deals with parity equations. After a detailed description of the system, test rig, testing cycle and safety-critical-faults, the development of the parity equations using different sensor information will be illustrated. The goal is to get a zero residuum between the sensor signal and the parity equation output during normal system behaviour and a significant change of the residuum in case of a failure. This allows fault detection by limit checking on the residuum. Software-in-the-Loop (SiL) simulation is used to analyse the quality of the different parity equations by using two modelling approaches for the valve's flow characteristic. Dependent on the model output the residuum drifts apart from zero over time during fault-free system behaviour and would therefore cause fault alarms. One countermeasure is an observer approach (closed-loop approach) by introducing a model-feedback, which will be analysed and designed. Additionally, the influence of the type of the numerical solver and its time-step on the results in combination with aspects of numerical stability will be discussed. Finally, the model-based approach will be tested on an excavator test rig with an independent metering system and a typical mobile control unit.

Title	**Simulation Research on Temperature Rise Characteristics of Permanent Magnet Spring Overflow Valve** (peer reviewed)
Presenting author	Lianming Su, Beihang University, People's Republic of China

Aiming at the characteristics of high-pressure and large-flow of aerospace servo system, a permanent magnet spring relief valve is designed. The permanent magnet spring of the valve was designed by means of analytical calculation and experimental validation. Because of taking the advantage of magnetic force characteristics, the magnet spring is superior to coil spring. Therefore, the permanent magnet spring relief valve has higher reliability, pressure regulation accuracy and thrust-weight ratio. However the permanent magnet spool is sensitive to temperature, if the temperature of the spool is too high in the working condition, the magnetism of the permanent magnet will be weakened, which will affect the stability of the relief valve. Therefore, in order to verify whether the temperature rise generated under rated condition will affect the magnetic properties of the permanent magnet spool, the temperature rise of the relief valve under rated condition is theoretically analysed first, and the source of heat and the way of loss are clarified. Secondly, the heat generated in the relief valve is calculated by the finite element simulation in COMSOL, and the temperature of the relief valve is observed. The results show that the temperature rise of the relief valve under rated condition does not affect the magnetic properties of the permanent magnet spool, which ensures the stability of the permanent magnet spring relief valve under rated conditions.

Title	**Electro-Hydraulic Proportional Pressure Reducing Valve for Independent Metering Valve with a Spool-Poppet Hybrid Actuator**
Presenting author	So-Nam Yun, Korea Institute of Machinery & Materials, Republic of Korea (South Korea)

This study is related to Independent Metering Valve (hereinafter IMV) which is a hot area of excavator research because of having increased energy saving operation and better controllability. An IMV is a combination of two valves; one is main valve (containing spool or poppet) and the other is a pilot valve. The flow rate is controlled by the movement of spool or poppet in the main valve while the movement of the spool or poppet is controlled by pilot pressure provided by the pilot valve. In this study, the pilot valve was chosen to be electro-hydraulic proportional pressure reducing valve (hereinafter EPPR valve). An IMV circuit for excavator was suggested and a model for the EPPR valve was built and analysed. Finally proportional characteristics of solenoid actuator of EPPR valve from the analysis results were derived and the endurance test was carried out for 18 million cycles.

B4: Hydraulic Pumps 2, Duetto 1, 13:00 - 14:30

Session Chair: Andrea Vacca, Purdue University

Title	**Analytical Approach to Calculate the Rotation Angle-Dependent Compensation Ratio of the Cylinder Block – Valve Plate Contact in Axial Piston Machines** (peer reviewed)
Presenting author	Seong-Ryeol Lee, Institute for Fluid Power Drives and Systems (IFAS), Aachen, Germany

Hydraulic piston machines are commonly used in many industry fields because of their high power density and high efficiency. One of the most important components in axial piston machines that determines the efficiency is the valve plate, which is in lubricated contact with the rotating cylinder block. The fluid force, generated by the fluid film and acting against the load force, lifts the cylinder block to reduce the solid friction with the valve plate. The ratio of the fluid and load force, called compensation ratio or balance ratio, is used in the industry as design parameter in terms of losses. To calculate the compensation ratio, many analytical calculations have been introduced on a fixed position. In practice, however, the effective pressurized area varies depending on the rotation angle, therefore changing the fluid force. Thus, the calculation method has an inconsistent accuracy over one revolution, depending on the valve plate shape.

This paper discusses an analytical approach to calculate the rotation angle-dependent compensation ratio of the cylinder block and valve plate. A proposed calculation method differs from the conventional method in that it can calculate the rotation angle dependent compensation ratio. In order to check the accuracy of the proposed method, the analytical results are compared to simulation results using a verified EHD (Elasto-Hydrodynamic) simulation under the same operating conditions. The comparison shows that the maximum error is less than 2%. Moreover, the relation of the compensation ratio and the design parameters is analyzed.

Title	**Fluid Dynamic Simulation of Hydraulic Orbital Motors** (peer reviewed)
Presenting author	Venkata Harish Babu Manne, Maha Fluid Power Research Center, Purdue University, Lafayette, Indiana, USA

This paper presents an approach for the simulation of the fluid displacing action realized by Orbit Gerotor Motors. The goal of the proposed approach is to achieve a correct simulation of the internal flow features of the motor, of the port flow fluctuations as well as to predict the volumetric efficiency, for various operating conditions, in terms of shaft speed and port pressures. The simulation tool is based on coupling of different models: a geometric tool to estimate the instantaneous chamber volumes and port areas, a lumped parameter model that simulates the fluid dynamics of the motor and a 2D-CFD model to simulate the leakage flows. The geometric tool considers the measured CAD profiles of the gear geometry inclusive of the machining tolerance data as input, and it provides as output the information needed by the following fluid dynamic models, such as the instantaneous volume of each internal chamber, the connecting areas realized by the commutator and the internal timing slots. A lumped parameter model implemented in AMESim permits the evaluation of the main flow features, including the instantaneous chambers' pressures and the port flows. A 2D-CFD model complements the main flow simulation by simulating the internal lubricating gaps. The most significant results of the model are illustrated in the paper, taking as reference a commercial unit produced by Parker Hannifin Corp. The model validation is also provided, by comparing the predicted volumetric efficiency map with the one derived from a test campaign obtained on a series of production units.

Title	**Double-Pump (R)Evolution – Higher Efficiency and Lower Noise Level for Variable Speed Pump Drives** (peer reviewed)
Presenting author	Tobias Speicher, Hochschule für Technik und Wirtschaft des Saarlandes, Germany

Regarding the trend of optimizing energy efficiency and meeting upcoming regulations of energy consumption, there are many ways to refine existing hydraulic drive systems. Based on the energy-on-demand strategy, one important way towards more efficient systems are variable speed driven systems that can save up to 80% energy. This work focuses on variable speed driven systems with double pumps consisting of a small high pressure stage and a large stage for low pressure but high flow levels. Compared to a system with a large single pump, these systems reduce the torque level needed at the drive shaft and therefore allow a smaller motor, reducing initial costs and increasing the efficiency. A new double pump concept using different pump principles for high and low pressure stage is introduced. It is shown that, compared to existing systems, the new design is superior in energy efficiency and fluid born noise. Also its behavior in one of the most challenging operational points, holding high pressure with small or even no flow at all, is thermally stable.

Title	**Multi-Disciplinary Model for Preliminary Design of Electro-Mechanical Servo Pump** (peer reviewed)
Presenting author	Tatiana Minav, Aalto University, Finland

A new electro-mechanical servo pump (EMSP) is proposed for high-power variable pump fixed motor electro-hydrostatic actuator for heavy-duty vehicle application. The EMSP has a highly integrated structure with the displacement regulating unit inside the same shell. This results in more challenges for sizing during design stage. Therefore, a dedicated multidisciplinary model for the EMSP preliminary design is presented in this paper. Initially model parameters are analysed and classified into different categories. As a result, only a fraction of parameters such as pump displacement, motor nominal torque, etc. was employed for active EMSP sizing to achieve more effective trade off and optimization. Rest of parameters were generated automatically with various methods such as scaling laws, product database, and empirical equations. Next, the hydraulic, electrical and thermal dynamic characteristics were investigated in the model. Finally, a multidisciplinary model equipped with the parameter generation tools was proposed as a practical tool for the EMSP preliminary design. At last, dynamic simulation results of hydraulic, electrical and thermal under typical cycles were utilised to verify the model functionality. The performance of the given EMSP design option can be evaluated by the proposed model, which makes the preliminary design and optimization feasible.

A5: Fundamentals, Maestro, 15:00 - 16:30

Session Chair: Andrew Plummer, University of Bath

Title	**On the Saturation Dynamics of the Oil Film on a Hydraulic Cylinder Rod During Extension** (peer reviewed)
Presenting author	Tobias Mielke, Institute for Fluid Power Drives and Systems (IFAS), RWTH Aachen University, Germany

Water can be dissolved into conventional pressure fluids, based on mineral oil, to a certain extend. Unknown in this matter is the dynamics of the absorption process.

In this work, the saturation dynamics of water into a thin oil film on the rod of a hydraulic cylinder is investigated. A physically motivated model is derived to describe the processes. He model is able to describe any saturation process of water in oil and is therefore independent of the oil mass or volume. Furthermore absorption experiments were carried out on a large oil volume compared to lubrication layers. The gained data was used to parameterize the model. Finally the findings were transferred to the dimension of the oil layer on the rod.

Title	**Stick Slip Prevention of Hydraulic Rod and Piston Seals in the Boundary Condition**
Presenting author	Mandy Wilke, Trelleborg Sealing Solutions Germany GmbH, Germany

Continuous trends in the hydraulic world lead to increasing power and efficiency. Weight is a driver for that and therefore hydraulic systems also are under the view of light weight constructions. The all known Stick Slip Effect then can easier occur in terms of vibration and noise creation in such an application.

With sealing elements, the respective choice of different materials and or design variations the engineering normally looks into possible solutions to overcome the problem. As the tribological system is somehow sensitive and some application related variations such as speed or pressure fluid viscosity again can bring a solution to limits. The paper presents a new sealing solution, which now allows to eliminate stick slip due to an intelligent combination of materials.

In the situation of stick slip at a sealing contact area some micro movements can be damped by using the dampening character of an elastomeric material to eliminate vibration and noise.

Title	**Experimental Investigation of the Hard-Hard Contact in Seat Valves** (peer reviewed)
Presenting author	Tobias Mielke, Institute for Fluid Power Drives and Systems (IFAS), RWTH Aachen University, Germany

Static sealing valves are machine elements of critical importance in various fluid power applications. Their main task is the prevention of leakage and thus the upholding of a pressure difference. Seals with metallic contacts are used, among other things, for seat valves. Despite the seemingly simple design, it is still not possible to correctly predict the leakage depending on their mechanical properties, design and operating parameters. Therefore, efforts are carried out to increase the knowledge on the mechanisms involved in the hard-sealing contact to be able to predict the leakage based on a physical model which also aids in potential optimization. [1] In this paper, the critical contact area of the sealing parts is investigated. To do so a test rig is built up. The sealing parts, consisting of a ball and a seat, are exposed to different loads. The resulting malleable deformation is measured and compared. Finally, the results are compared with finite element calculations.

Title	**Improved Performance on Reciprocating Seals due to Optimized Lubrication in the Sealing System**
Presenting author	Mandy Wilke, Trelleborg Sealing Solutions Germany GmbH, Germany

The performance requirements of multiple sealing systems for reciprocating movements are continuously increasing with friction, wear and service time being key performance criteria. The new concept, presented in this paper, is about adjusting lubrication conditions of all single sealing elements within a sealing system so the load on each element can be reduced and the performance in terms of friction-wear-lifetime can be optimized.

Best practice in demanding fluid power sealing applications is a primary and a secondary seal. The primary seal does the sealing job for as long as possible and the secondary seal is the redundancy, there when it is needed. The challenge for this secondary sealing element is length of life under dry running conditions. The more effective the primary seal in sealing in lubricant to the hydraulic system, the drier the running conditions of the secondary seal. Starvation of lubrication can lead to wear issues that come in to play in the case of a needed redundancy. The paper describes the dilemma in terms of optimizing the performance of the primary and secondary seal and brings up a new seal concept, where the risk of leakage of lubricant is balanced to ensuring performance of the primary seal and the extended life of the secondary seal. This is achieved by allowing a better, thicker oil film under the most pressure loaded first sealing element to reduce the load on that seal.

B5: Mobile Machines 2, Duetto 1, 15:00 - 16:30

Session Chair: Seppo Tikkanen, Tampere University

Title	**Classification of Machine Functions: A Hydraulic Excavator Case Study** (peer reviewed)
Presenting author	Nathan Keller, Purdue University, United States of America; Maha Fluid Power Lab, United States of America

The goal of this research is to successfully classify the machine functions on a hydraulically driven mini-excavator. Machine function classifications can provide points of reference for future online condition monitoring techniques and algorithms. Therefore, this work will be used as a springboard into more traditional condition monitoring techniques to monitor the health of the hydraulic system on mobile equipment.

To accomplish the aforementioned goal it seemed important to first explore common types of classification algorithms available. Then, a displacement controlled mini-excavator was instrumented to record many different parameters during a typical truck loading cycle. Each data point was assigned a label that corresponds to the current function of the machine; travelling, unloading, swinging, digging, or idling. The data was then taken with the corresponding labels and trained in a decision tree learning algorithm. The algorithm was then tested to determine the accuracy of labelling unseen data.

This work focuses on the classification of the machine functions on a Bobcat 435 mini excavator that is equipped with a displacement controlled hydraulic system and is instrumented with various sensors. The data collected during a representative truck loading cycle is fed into a decision tree training algorithm to predict machine functions on unseen data.

Title	**Hydraulic Hybrid Working Machines Project - Lessons Learned**
Presenting author	Matti Linjama, Tampere University, Finland

A big research project was implemented in Finland in 2016-2018 to find economically and technologically feasible ways to improve fuel efficiency of hydraulic working machines. Two main approaches were hydraulic hybrids and independent metering. Objective was also to study experimentally the effect of Diesel engine loading profile on emissions. An analysis tool was developed to estimate the fuel consumption of working machines using measured load cycle data and dozens of solutions were analysed. This paper summarizes the main findings of the project. Important finding is that simple “accumulator + control valve” type hybrid is a low-cost and effective method to reduce fuel consumption. The second finding is that hybridization alone reduces fuel consumption by approximately 15 per cent in the machines studied quite independently on the hybridization solution. An exception is multi-pressure systems, which have potential for bigger fuel savings. The third finding is that independent metering is equally effective in the reduction of losses. The most effective solution is the combination of independent metering and hybridization where 28 per cent reduction in the fuel rate together with 12 per cent faster cycle time is demonstrated.

Title	**Energy Efficiency Optimization of Electric Powertrain of Underground Load-Haul-Dump Mining Loader by Means of Dynamic Programming** (peer reviewed)
Presenting author	Marius Baranauskas, Aalto University, Finland

The emissions of heavy-duty underground mobile machinery put the health of human workers at risk and increase the overall maintenance cost of the underground mine due to extra ventilation expenses. Besides, tightening emission standards for non-road vehicles are pushing towards greener solutions, hence fully electric powertrains are becoming a viable alternative to conventional solutions. A fully electric powertrain provides mechanical power with no local emissions and it is characterized by a superior energy efficiency compared to conventional diesel powered machines. This paper analyzes a case study of a real-size load-haul-dump mining loader equipped with a fully electric powertrain. An optimal speed profile is generated for the mining loader by means of Bellman’s dynamic programming algorithm in MatLab environment. The optimal speed profile demonstrated a 9.1% decrease in energy consumption comparing to a profile composed of constant speed and constant acceleration. As the traction motors are operated in the higher efficiency areas, they generate less heat prolonging the lifetime of the powertrain components.

Title	**Automatic process pattern recognition for mobile machinery**
Presenting author	Martin Starke, Technische Universität Dresden, Germany

In nowadays-used mobile construction machinery, the knowledge of the usage profiles is in fact not available. This lack causes a design phase, which is characterized by assumptions. This affects every development step in which the application has a significant influence on the design, what in nearly every section is the case (e.g. dimensioning of structural-mechanical part, drive system development, hydraulic structure construction). This paper presents the development of a process pattern recognition (PPR). Process patterns are from an engineering perspective a class of uniform or similar working cycles. The developed system will answer the question which working-cycles the machine executes during its lifetime.

A6: Energy Efficiency, Maestro, 11:00 - 12:30

Session Chair: Marko Paakkunainen, John Deere Forestry Oy

Title	**Carbon Footprint Determination of an Electro-Hydraulic Compact Axle (EHA) Based on DIN EN ISO 14067** (peer reviewed)
Presenting author	Maximilian Waerder, Institute for Fluid Power Drives and Systems (IFAS), RWTH Aachen University, Germany

This paper introduces the methodology of calculating the product carbon-footprint (PCF) of industrial linear actuators by the example of an electro-hydraulic compact axle (EHA). The EHA system design and the manufacturing process is highly complex since it contains many components of different domains (i.e., mechanical, hydraulic and electronic parts). Therefore, the system must be be virtually disassembled into its components to the extent that an individual determination of the PCFs is possible. For a straight understanding of the method, the paper is subdivided into three major topics: description of PCF determination method, exemplary calculation of an EHA PCF and, finally, its critical review. The PCF calculation is based on DIN EN ISO 14067 and, thus, classifies the ecological impact of the individual life cycle steps (i.e., material production, product development, commissioning, use and maintenance as well as the end-of-life) referring to the global warming potential (GWP). As a conclusion, this paper reveals the opportunities of analysing the ecological impact of industrial components (especially fluid power industry) and the current existing difficulties of implementation and objective interpretation of different results.

Title	**Energy Efficiency Analysis of a Novel Hydro-Electric Hybrid Driving System for Hydraulic Excavator Boom** (peer reviewed)
Presenting author	Yunxiao Hao, Key Lab of Advanced Transducers and Intelligent Control System of Ministry of Education and Shanxi Province, Taiyuan University of Technology, People's Republic of China

Energy recovery and reutilization is an important way to improve the energy efficiency of hydraulic excavators. In this paper, a novel electro-hydraulic hybrid driving system adopting hydraulic cylinder and electromechanical cylinder is proposed. The non-rod chamber of the hydraulic cylinder is connected to a hydraulic accumulator, which can realize the direct conversion of the potential energy and hydraulic energy. Due to the less energy conversion links, the recovery and reutilization rates of the potential energy are significantly improved. Adopting the electromechanical cylinder as the active actuator, the electric energy can be directly converted into working device’s potential energy. The energy transfer chain of the proposed system is shorter than other transmission systems, and the proposed system will have very high energy efficiency. The working principle is first introduced, a test rig and a co-simulation model are built to validate the feasibility and the energy-saving effect of the proposed system. The test results show that the proposed system has good operating characteristics; compared with a separate meter-in and meter-out system, the peak power of the boom system is reduced by 77.5% and the energy consumption by 71.7%.

Title	**Theoretical Study on the Energy Regeneration Mechanism of a Switched Inertance Hydraulic System with Cylinder and Load**
Presenting author	Satoshi Maekawa, Kobe Steel, Japan

The energy efficiency of the conventional flow control of hydraulic systems using the pressure loss of throttle valves, which are widely used in construction machinery, is very low. If a switched inertance hydraulic system (SIHS) is used, a significant improvement in the energy regeneration efficiency can be expected. This is a kind of PWM control system for switching between a high-pressure source and a low-pressure source at high speed. The purpose of this study was to propose a new analysis method which can consider the valve pressure loss, the elasticity of oil and the influence of the hydraulic cylinder mass and load in a typical hydraulic system. This method can help us understand the mechanism of energy regeneration and the effect of parameters on the energy regeneration efficiency. As a new analysis method, a flow response calculation method using modal analysis with approximate equations is proposed. This is performed by separation into the low-order modes affected by a hydraulic cylinder and the mass of the mechanical parts and the high-order modes affected by the elasticity of oil in the piping. Next, a new definition of the energy regeneration efficiency is proposed, expressed by the product of the average component and the vibration component. A method to grasp how the two types of mode components influence the energy regeneration efficiency by changing various parameters is proposed.

B6: Robotics and Control, Duetto 1, 11:00 - 12:30

Session Chair: Jouni Mattila, Tampere University

Title	**Simulation of a Hydraulic Direct-Drive System for a Biped Walking Robot** (peer reviewed)
Presenting author	Juri Shimizu, Hitachi, Ltd., Japan; Waseda University, Japan

A disadvantage of biped robots with electric motor-driven serial links is that a motor and transmission must be installed in each joint, causing the legs to become extremely heavy. Thus, a high-power motor is required at the root of each leg, i.e., at the hip joint. To this end, the use of a hydraulic system has been proposed. This system reduces the power required for the hip joint by installing pressure sources consisting of a heavy motor and a pump outside the legs and by placing only lightweight cylinders at each joint. Previously proposed robots with hydraulic systems have incorporated multiple actuators, where each was controlled by a dedicated proportional valve. However, for biped robots, highly responsive proportional valves are required to ensure that the posture of the robot remains stable. Furthermore, a high supply pressure is necessary for high responsiveness, and thus the energy losses are large. Hence, we propose the use of a hydraulic direct-drive system in which the pump controls the cylinder meter-in flow and a proportional valve controls the meter-out flow. A performance comparison with a conventional system shows that a good position-following capability is achieved, and the motor output can be reduced by 64.9% using the proposed system. A simulation was performed to evaluate whether walking would be possible using the proposed system, and it was found that the system realized walking using a proportional valve with a frequency response of only 20 Hz. These results prove that it is possible to construct a biped robot without incorporating highly responsive servo valves.

Title	**Model Predictive Path Tracking Control with Off-Axle Reference Point for Car-Like Robots** (peer reviewed)
Presenting author	Ilja Stasewitsch, Technische Universität Braunschweig, Germany

Two path tracking controls are presented for car-like robots with a reference point which is offside of the robot’s pivot point. This offset reference point is called as off-axle reference point. One control method is the linear model predictive path tracking control and the other one is the nonlinear model predictive path tracking control. These controls are implemented and tested in a simulation environment. The nonlinear model predictive control is validated at a test vehicle. In this system a tractor (Fendt 724) is coupling automatically to an implement by using the presented controls.

Title	**Design and Implementation of Pressure Feedback for Load-Carrying Applications with Position Control** (peer reviewed)
Presenting author	Daniel Hagen, University of Agder, Norway

This research paper presents the design and implementation of pressure feedback on a hydraulically actuated single-boom crane operated in closed-loop position control. It is well known that systems with pressure compensated proportional valves in combination with over-center valves tend to induce instability, especially when the external load is overrunning (e.g., while lowering a load). However, in some applications pressure oscillations arise also with resistant external loads (e.g., while lifting a load). Hence, a pressure feedback capable of stabilizing the system functioning in both operations using the pressures from both actuator chambers (i.e., piston-side and rod-side) is proposed and compared against the conventional solution using only the rod-side chamber pressure. The investigation demonstrates that the implementation of a proposed “inverse valve dynamic” algorithm is needed in order for the control valve to stabilize the system when introducing the piston-side pressure in the pressure feedback. With this new method, the experimental tests demonstrate a satisfactory reduction of the pressure fluctuations in closed-loop motion control and a good position tracking (the average position error while lowering the load is reduced by almost 90% compared to the original system without pressure feedback). Finally, simulated results show that the proposed pressure feedback allows for potential energy savings of about 50% when lowering the load.

Title	**Experimental Analysis of an Electro-Hydraulic Drive for an Elbow Support Exoskeleton** (peer reviewed)
Presenting author	Rudolf Scheidl, Johannes Kepler University Linz, Austria

The study object is a hydraulic drive at the elbow joint for supporting of a human in lifting weight by hand. The range of motion needed to support is flexion of 145°. The arm is connected to an exoskeleton in form of a lateral structure to enable the lifting process by force enhancement. The human controls the lifting motion with his/her arm and the drive supports the weight lifting process by an adjustable percentage. The controller takes the applied hand force from a sensor and adjusts the drive to achieve the desired force support, thereby correcting also the nonlinear kinematical characteristics of the arm structure.

The construction uses a four bar linkage connected to a hydraulic cylinder. The hydraulic cylinder is actuated by a closed circuit, combining a fixed displacement axial piston pump and a speed variable electric motor. This concept is a nowadays common technology for many industrial applications and is studied in this paper to have a benchmark technology for digital hydraulic concepts which the authors want to work on in the future.

The actuator selection focuses on the main performance criterion of exoskeleton drives, which are low weight and compactness. Drive efficiency is serving these to keep battery and motor small. Dynamic response has to fulfill the wearer's expectations for a convenient arm motion. As test rig an elbow support system is designed. It is linked to upper and lower arm and supports the flexional degree of freedom of the elbow joint. The performance of the drive system is measured and assessed with respect to the requirements on exoskeleton drives.

DRIVE CYCLE GENERATION FOR A HYDRAULIC LOADER CRANE

MSc Amy Rankka, PhD Alessandro Dell'Amico, Prof. Petter Krus
Linköping University
Department of Management and Engineering, Division of Fluid and Mechatronic Systems
SE-581 83 Linköping, Sweden
E-mail: amy.rankka@liu.se

ABSTRACT

Electrification of hydraulic systems has become an important research topic. The cost of the electric energy storage is high and drives the development of new efficient solutions for the system to be of commercial interest. This study is part of a project where the electrification of a loader crane is the main focus. The crane is a versatile machine and the energy efficiency of the hydraulic system is strongly dependent on the working envelope. A representative envelope can be called a drive cycle and is necessary to evaluate new solutions. This paper describes the method of producing such a cycle. A large amount of data from a field crane has been recorded for several weeks. A pattern of movement is found and used to define parameters of the drive cycle. To extract combinations of the parameters that form a good representation of the measurement data a principal component analysis is carried out. Finally, the drive cycle is defined as a sequence of trajectories with different payloads, corner points and cylinder speeds for movements between corner points. The drive cycle is tested and verified on a crane of the same model as the field crane in a laboratory environment. The methodology is found to produce a drive cycle with good variation and representation of geometrical parameters.

KEYWORDS: drive cycle, test cycle, loader crane, hydraulic crane

1 INTRODUCTION

In order to produce new energy efficient systems a proper methodology for conceptual comparison and a baseline must be defined. In the case of a loader crane the aim of the machine is to perform a series of lifting movements. If the average geometrical properties as well as the payload of these movements are known they can be defined as a drive cycle and different systems can be compared based on their results performing this cycle. The baseline can be set as the results from the conventional system. This study is part of the project STEALTH, a collaboration between Linköping University and the companies in the hydraulic cluster of Hudiksvall, including Hiab, Sunfab, Huddig, Oilquick and Tube Control. The aim of the project is to develop an efficient electrified hydraulic system for a loader crane, including the whole actuation system from battery to cylinders. This initial study focuses on finding a good representation of crane movements and forming a drive cycle that can be used in the project. A key question is to develop a method for drive cycle generation that finds the amount of information needed in the cycle to obtain a reasonable representation.

Some examples of methods for defining drive cycles used for forestry cranes, which are very similar to loader cranes, can be found in the literature. In one study [1], a general movement of loading and unloading a single load with a crane is defined based on the possible working range. The speed of the crane tip during

this movement is defined by a statistical analysis on the data gathered when letting a skilled driver perform the movement several times. A forestry crane is also studied in [2]. The cycle studied describes how the force on each cylinder varies with position during a typical log lift. The force is calculated based on pressure measurement on a real crane but the typical lift is pre-defined without taking variation in position or weight of the log into account. A somewhat more thorough example is a study of a forwarder crane [3] where cylinder positions and loads are recorded during real life operation of the machine. Different phases in the loading of logs are found and a general pattern of movement is defined as well as the average weight of a log. Skilled drivers are then set to perform this pattern of movement in a laboratory environment and the average cylinder movements of the 1st and 2nd boom from these tests are produced by the mean value of the uniformed scaling of the signals.

Ideas of methodology can also be taken from other hydraulic machines. A drive cycle based on measurement data has been produced for refuse vehicles and the method is described in [4]. Both operation of the vehicle and use of the hydraulic functions are taken into account. A method of producing distributions for different parameters, calculating statistical metrics for different segments of the operation and performing a cluster analysis on the metrics of each segment is used for the hydraulic operation. The hydraulic functions of the refuse collector are however only classified based on their pressure levels.

Drive cycles based on an extensive amount of measurement data can be found in the automotive industry. The procedure of making the ARTEMIS driving cycles are described in [5]. The cycles are made by collecting data from a large number of cars in the field. The data is then analyzed and divided into segments that can be compared with a distance function and classified by a cluster algorithm. The car cycles differ from what is needed for a loader crane in the sense that it is only the speed of one function, i.e. the propulsion system, that is taken into account.

A methodology for defining drive cycles for heavy equipment vehicles has been developed in [6]. Some parts of the methodology are applicable to cranes but there is still a need for a general method for defining cycles for the various work patterns of the cranes that will be addressed in this study. Ideas from the studies mentioned above are used as well as a deeper focus on basing the cycle on measurement data and include significant variation of the movements. The method will be directly applied to a crane suitable for the project. The crane is part of a larges series of cranes in the range 11-30 tonnemeters working with the same type of brick and block handling.

2 DEFINITION AND EVALUATION OF THE DRIVE CYCLE

A drive cycle is a trade off between a precise representation of the real working situation and the length of the cycle. The purpose of the drive cycle in this project is to evaluate new concepts and compare their performance with that of the conventional system. It should be representative enough to sort out the most promising new system for the application with regards to energy efficiency and will be used both at an early stage in simulations and later in the project when testing prototypes. To be of practical use during testing it is considered that the drive cycle should not be longer than approximately 15 minutes. It is not included in the scope to investigate if 15 minutes gives an optimal trade off.

To evaluate how representative the drive cycle is the average work performed during the cycle will be compared to the measurement data. The variation in crane tip position and payload will also be compared since some variation in crane movements is required to be able to distinguish different systems from each other. Precision and maximum speed will not be evaluated by the drive cycle since these properties are easily tested without any knowledge of the average working pattern.

Ideally, a set of trajectories for the crane tip, possibly with different loads in the hook, should define the drive cycle. The trajectory represents the work that the crane has to perform rather than how the different actuators

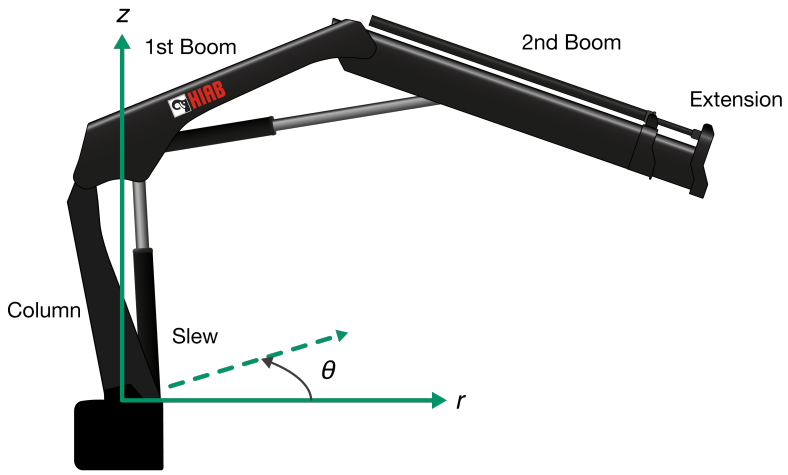

Figure 1: The crane with the cylindrical coordinate system with origin at the slew center and definition of the boom system.

of the crane should be used. In an autonomous system the usage of the different actuators could then be allowed to be optimized with regards to energy efficiency. It is assumed however, that systems developed in this project will be operated by human operators. How the different actuators of the crane are operated to make the crane perform the work task are therefore also of importance. The drive cycle will thus be compiled by a number of trajectories represented by a starting point, one or more intermediate points, an end point and actuator speed commands to complete the trajectory in a given time. Geometrical points will be defined in a cylindrical coordinate system with origin at the slew center at the crane base, see Figure 1. The crane has four actuators in the form of hydraulic cylinders; slew cylinder, first boom cylinder, second boom cylinder and extension cylinder.

3 METHOD FOR GENERATING THE DRIVE CYCLE

The method developed in this study includes five steps. First, data is gathered on a field crane. The mass of the payload of the crane cannot be measured and therefore the next step of the method is to find a load estimation procedure. Then, the parameters of the drive cycle are defined based on the patterns of the measured data. Average values of these parameters that give a good representation of the complete data set are found in the fourth step. Finally, the complete drive cycle is defined by setting the cylinder speeds that allow the crane tip to move between the positions from the parameter values.

3.1 Data Acquisition

One of the cranes from the selected series operating in the field is equipped with sensors for measuring position and power demand from the crane and an external device for logging and storing the data. All crane operation was recorded with at a sample rate of 20 Hz during a three month period. The following signals were recorded; 1st and 2nd boom angles, extension position, slew angle, cylinder pressures on rod and piston side, pump pressure and valve spool positions. The valve is a pressure compensated load-sensing valve which means that the flow to the different cylinders is proportional to the valve spool positions and can be estimated using the spool characteristics.

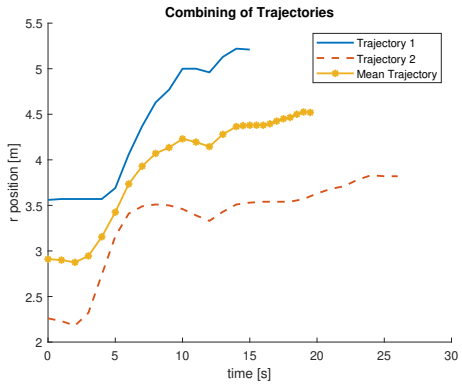

Figure 2: Example of two trajectories in the r dimension of different length but with a similar pattern being combined using DTW.

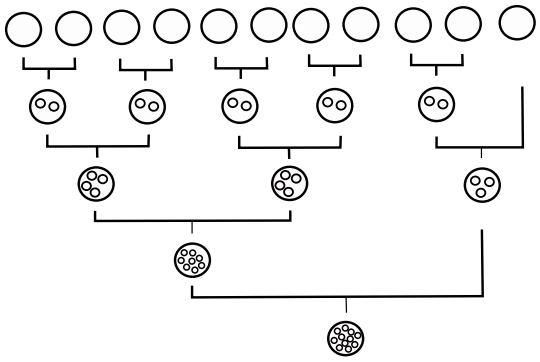

Figure 3: The trajectories are combined in a tree structure where the information about the number of original trajectories in each combined trajectory is kept to allow calculation of a combined mean.

3.2 Load Estimation

The weight of the payload in the hook is not measured and thus has to be estimated. Several loads are lifted during a work session. The moments when the load is lifted or put down are found by studying the pressure in the first boom cylinder. When the derivative of the pressure signal is higher than a threshold the payload is changed momentarily and these points are considered as breakpoints. The payload is assumed to be constant in between two breakpoints and can be calculated by comparing the moment from the dead weight of the boom system acting on the column-first boom joint, M_{dw}, to the lifting moment from the pressure in the first boom cylinder, M_{cyl}, see Equation 1. The payload leverage with regards to the column-first boom joint is a function of the boom angles and the extension position and denoted l_{pl}. The gravitational acceleration is denoted g. The load estimation of each segment is taken as the mean value of the calculated mass.

$$m_{pl} = \frac{M_{cyl} - M_{dw}}{g \cdot l_{pl}} \tag{1}$$

The segments always appear in pairs of one segment where the crane carries a load followed by a segment where the crane is unloaded. The movement of the crane tip during a segment is considered as a trajectory and the drive cycle will thus be compiled by a set of pairs of unloaded and loaded trajectories.

3.3 Definition of Drive Cycle Parameters

To simplify the analysis, the movement of the crane tip is studied in each dimension of the cylindrical coordinate system separately. The shape of average trajectories in each dimension are produced by a dynamic time warping algorithm (DTW) [7], [8]. DTW allows the trajectories to stretch in time so that similar patterns in the trajectories are found even if they occur at different time stamps. An example of two trajectories being combined is presented in Figure 2. DTW compares pairs of trajectories and to get the average of all measured trajectories, they are combined in pairs in a tree structure, see Figure 3. Every combined trajectory keeps the information about the number of original trajectories used to form it. This allows a combined mean value to be used when forming a new trajectory. The resulting trajectories from combining all the original trajectories are displayed in Figure 4. The trajectories in the r dimension are split based on their direction.

The shape of the trajectories in the r and θ directions are monotonic and the z trajectory has a clear peak. This corresponds well to the working situation of the crane where a set of pallets are unloaded from the truck. The

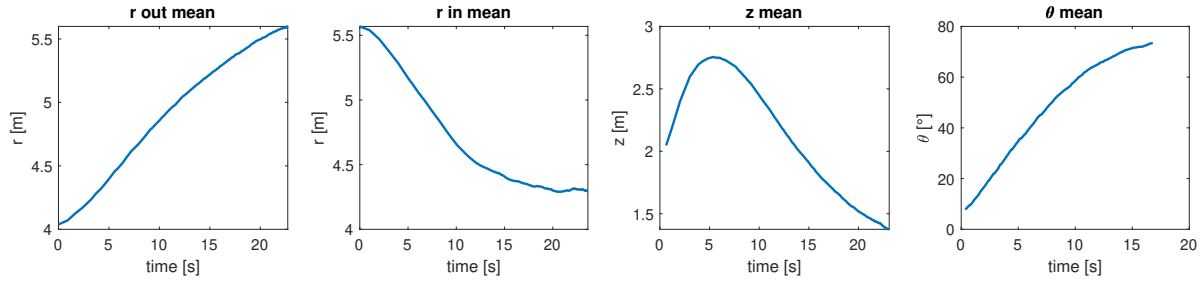

Figure 4: The resulting trajectories in each dimension. The trajectories in the r and θ dimensions are monotonic while the trajectory in the z dimension has a clear peak.

pallet must be lifted up from the flatbed and over other pallets but once the load is lifted the crane can slew and extend to the desired off-loading position. An approximation of a trajectory can thus be made up of three corner points, a starting point, an end point and an intermediate point with a peak z coordinate. The corner point parameters will be defined based on the following observations:

- The absolute position of the slew does not affect the energy consumption and the trajectories in the θ direction are normalized to always start at 0° and increase towards 360°, giving that the start position can be constant and the change, $\Delta\theta$, will be a parameter.
- There is a very small variation in the z start coordinate for loaded and end coordinate for unloaded trajectories and it will thus be assumed to be constant. Variations are taken into account by using the change in z, Δz, as a parameter. Δz is defined as the end position minus the start position. The peak position parameter, z_{peak}, is independent of Δz.
- A start and a change parameter, r_{start} and Δr, will be used in the r direction in order to avoid that hidden correlations between start and end positions result in unlikely small or large increments.

Further, the weight of the payload, m_{pl}, and the time to complete a lifting trajectory, t_{lift}, are included giving in total seven parameters.

3.4 Finding Average Trajectories

The next step of the method is to find a number of combinations of drive cycle parameter values that give a good representation of the measurement data. The distributions of values of the parameters from the measurement trajectories are studied to see whether any coarse clustering can be done directly. The following observations can be made:

- r trajectories are either increasing or decreasing in position. To avoid that the average change will be zero the data is split based on this parameter.
- There are two distinctive peaks in the distribution for the end coordinate for loaded and start coordinate for unloaded trajectories in the z dimension. The data is split based on this.
- To achieve as gaussian like distributions as possible some of the parameters that are limited to positive values are transformed to their logarithmic values.

The resulting grouping of the data is presented in Table 1. As an example, in loaded group 1, r trajectories increase with time and the z end position is greater than 1.14 m. 43 % of the loaded trajectories fall into this group making it the biggest loaded group. The distributions for the seven drive cycle parameters of the this group are displayed in Figure 5. The distributions for the other seven groups follow the same pattern.

Table 1: Grouping of the trajectories based on unloaded/loaded, on the r direction and on z start or end coordinate. The relative size of the groups within loaded/unloaded and the weighting of the PCA points is also presented.

	r direction	z start	z end	Relative size	w_{mean}	w_{std}
Unloaded group 1	Increasing	> 1.14	-	0.19	0.54	0.33
Unloaded group 2	Increasing	< 1.14	-	0.20	0.57	0.35
Unloaded group 3	Decreasing	> 1.14	-	0.25	0.71	0.43
Unloaded group 4	Decreasing	< 1.14	-	0.35	1.00	0.61
Loaded group 1	Increasing	-	> 1.14	0.43	1.00	0.61
Loaded group 2	Increasing	-	< 1.14	0.36	0.80	0.49
Loaded group 3	Decreasing	-	> 1.14	0.12	0.30	0.18
Loaded group 4	Decreasing	-	< 1.14	0.09	0.21	0.13

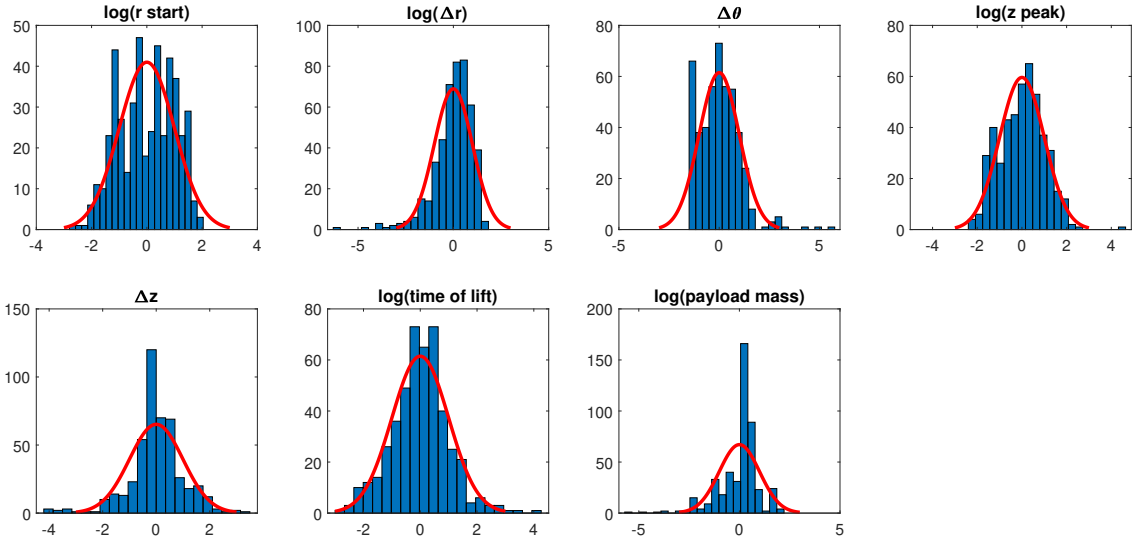

Figure 5: Centered and normalized (by the standard deviation) distributions of the drive cycle parameters for the first loaded group with fitted normal distributions.

The parameter data is now quite evenly distributed in each of the eight data groups and no more distinct patterns could be found although several clustering methods were applied. The mean parameter set of each group is a simple representation of the data but alone it would provide too little information to the drive cycle. A principal component analysis (PCA) [9] approach is therefore applied to the data. PCA is a structured way of extracting a small number of parameter sets that represent the original data set by taking into account the most significant variance and the correlation between the parameters.

The original data set, which can be seen as a number, m, of observations of the n different drive cycle parameters ($n = 7$ for loaded and $n = 6$ for unloaded groups), is pre-processed like in Figure 5, normalized and ordered in a matrix format, X, see Equation 2. Since the columns of X are centered, the principal components can be extracted as the column vectors of V from the singular value decomposition [10] of X according to Equation 3. The principal components are ordered by the magnitude of their singular values, which are the diagonal values of Σ, and most of the variance of the data is consequently found in the first few principal components. A point in the principal component dimension space, x_{pc}, can be defined by selecting values for the coordinates of the first d dimensions, $d \in [1, n]$, and setting the coordinates of the $n - d$ last dimensions to zero. Values for the n different parameters in the original dimension space are then obtained by transposing x_{pc} to x_{org} according to Equation 4.

$$X = \begin{bmatrix} [parameter_1(observation_1) & \dots & parameter_n(observation_1) \\ \vdots & \ddots & \\ parameter_1(observation_m) & & parameter_n(observation_m)] \end{bmatrix} \tag{2}$$

$$X = U\Sigma V^T \tag{3}$$

$$x_{org} = x_{pc}V^T \tag{4}$$

To keep the drive cycle within the time limit of 15 minutes, the number of trajectories is limited to 12 loaded and 12 unloaded in total. The mutual frequency of the number of original trajectories in each group is taken into account when selecting the 24 points from PCA. For the loaded data set the first two groups have approximately four times more members than the other two groups. Points offset by +/- one standard deviation in the first and second principal component direction are selected for the first two groups together with the mean point while only the mean point is selected for the other two groups. For the unloaded groups the mutual frequency is more equal and points offset by +/- one standard deviation in the first principal component direction are selected for all groups. Results from different trajectories of a drive cycle test will later be weighted based on the exact relative size on the corresponding group of measurement data, according to Table 1. The weight of the mean points, w_{mean}, is higher than the weight of points offset by +/- one standard deviation, w_{std}, according to the probability density function of a normal distribution. The average power consumption of the drive cycle will be calculated according to Equation 5 where both unloaded and loaded trajectories are included and the weighting of the trajectories originating from different PCA points is taken into account by w_i.

$$\overline{P}_{drivecycle} = \frac{\sum_{i=1}^{24} w_i P_i}{\sum_{i=1}^{24} w_i} \tag{5}$$

3.5 Defining Cylinder Speeds

The final stage of generating the drive cycle is to merge the parameter sets into continuous trajectories defined by the cylinder speeds. To achieve realistic trajectories for the different actuators and how they are used simultaneously a skilled crane operator is told to run a crane in a laboratory environment from each starting point of a drive cycle trajectory, over the peak height of the intermediate position and to stop when the end position of the trajectory is reached. The crane tip trajectory between the corner points does not have to be a straight line. Each trajectory of the drive cycle is run several times until the total time of completion correspond well to the parameter value. The cylinder speeds for this run are recorded and used in the definition of the drive cycle. The power consumption in the hydraulic system is also recorded during operation of the drive cycle and is later used in a comparison with the field measurement data.

4 RESULTS

A drive cycle has been produced by following the method described in Section 3. How well that cycle represent the measurement data from the field crane will be presented in this section. The validity of the load estimation will also be presented.

4.1 Load Estimation

Figure 6 shows an example of the estimated load on a number of segments from a work session. The algorithm detects, with a few exceptions, an unloaded segment after each loaded segment. The mean value of the payload mass estimation of all unloaded segments can be used as an indicator of the preciseness of the algorithm. The payload in the hook during unloading segments is only the weight of the brick stack grapple tool which is 365 kg. The mean value of the mass estimation is 347 kg. The error is 5 % which can be seen as the uncertainty of the estimate. Studying the distribution of the estimated mass in Figure 6, a sharp peak around 360 kg can be seen.

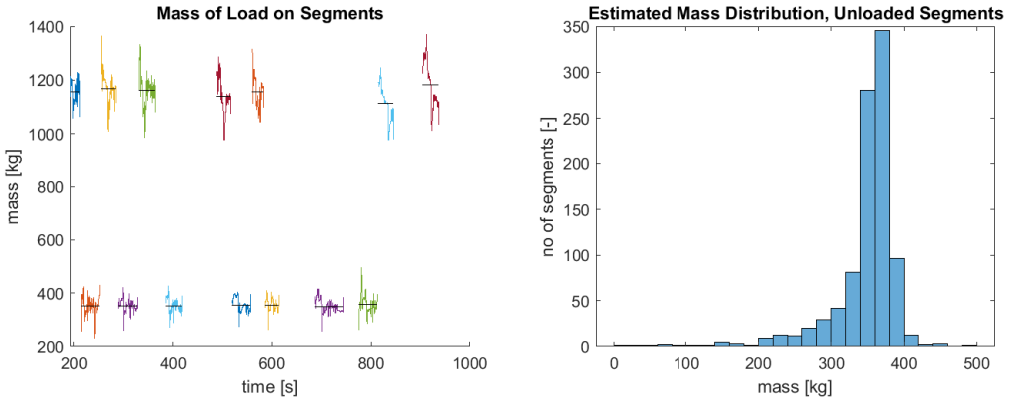

Figure 6: Mass estimation of a number of segments and distribution of estimated payload mass based on all unloaded segments. There is a sharp peak at 360 kg which corresponds well to the actual weight of 365 kg.

4.2 Generation of Drive Cycle

The projections back onto the original parameters of the 12 points selected for the loaded trajectories in the principal component space are displayed in Figure 7 on top of the distributions of the measurement data. No extreme values are captured but there is a spread around the mean value or, in the case of the z incremental parameter, around the mean of the two peaks of the data.

The combination of the parameter values in Figure 7 create the corner points for the crane tip trajectories. The fit of the drive cycle to the measurement data when both loaded and unloaded trajectories are included is 0.79. It is calculated as a root mean square (RMS) distance from a measured trajectory to its closest drive cycle trajectory according to Equations 6 - 7, where index i denotes the current data group, index m the current measurement trajectory and index n the current drive cycle trajectory. Further, k is the number of trajectories in each group, n_p is the number of drive cycle parameters ($n_p = 6$ for unloaded and $n_p = 7$ for loaded), x_{meas} is a measured trajectory represented as a point in the n_p dimensional PCA space and x_{dc} the drive cycle trajectory closest to x_{meas} represented in the same way.

$$RMS = \frac{\sum_{i=1}^{8} k_i RMS_i}{\sum_{i=1}^{8} k_i} \tag{6}$$

$$RMS_i = \frac{\sum_{m=1}^{k_i} \sqrt{\frac{\sum_{n=1}^{n_p} (x_{dc,i,n} - x_{meas,i,m,n})^2}{n_p}}}{k_i} \tag{7}$$

Together with the cylinder speeds defined by the tests of the drive cycle by a skilled operator complete trajectories are formed. An example of such a trajectory in three dimensions is presented in Figure 8. The trajectories have similar shapes as the average trajectories in Figure 4.

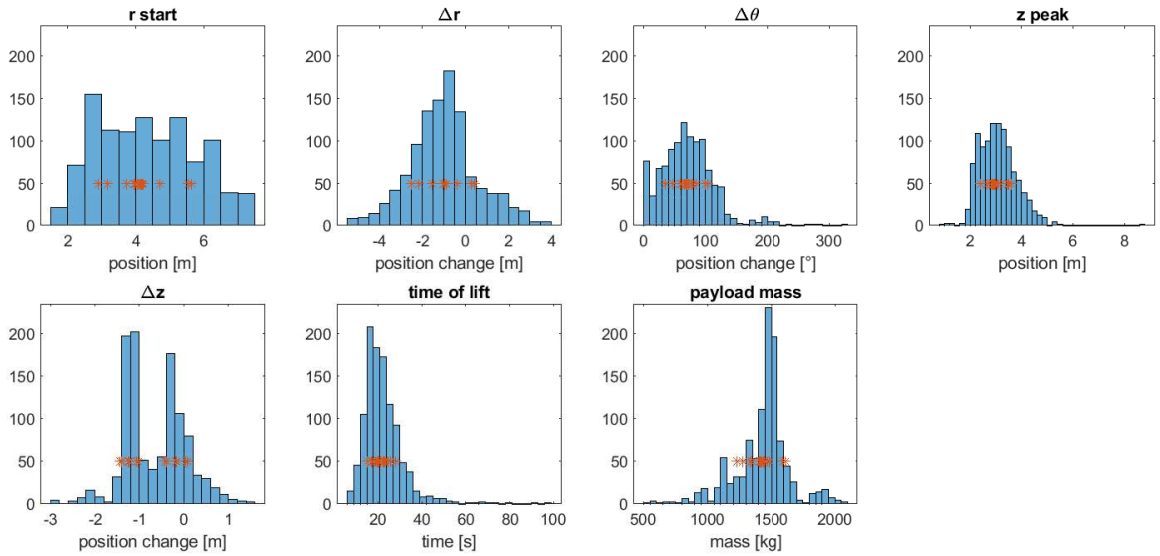

Figure 7: Distributions of the drive cycle parameters for the loaded data set together with the values obtained from the PCA (marked with '') for each parameter from the twelve loaded drive cycle trajectories. The drive cycle points are spread within the limits of the measurement data.*

The drive cycle should also be a good representation of the work that is performed by the hydraulic system to move the crane tip according to the geometrical parameters. A comparison between the drive cycle and the measurement data of total cylinder power, individual cylinder power and the usage, in percent of the total drive time, of the different cylinders is presented in Table 3. It can be noted that even though the total work performed by the cylinders to follow the drive cycle correspond to the measurement data, the individual power levels differs for the slew and 2nd boom cylinder. The usage of the different cylinders also impact the average total cylinder power as well as the pump power and it can be seen that the 1st and 2nd boom cylinder correspond well while there is a big difference in the usage time of the slew and the extension cylinders.

The average pump flow and pump pressure also correspond fairly good but the average input power to the hydraulic system is 18 % lower for the drive cycle than the measurements, see Table 3. This indicates that moments of high flow and high pressure occurs more often during the measurements and that the drive cycle only captures the more average working situations.

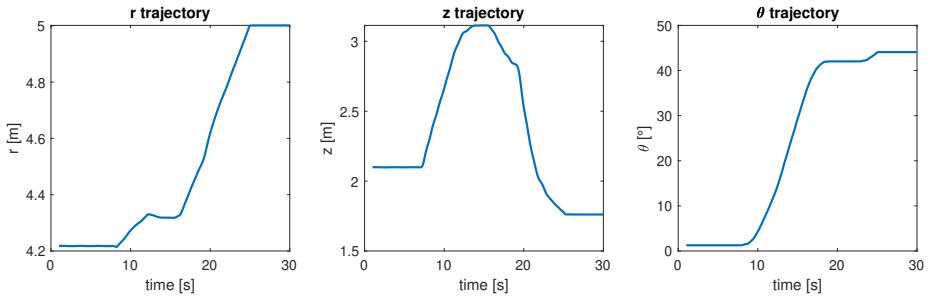

Figure 8: Crane tip trajectories in the three dimensions for one of the drive cycle trajectories. The trajectories are the result of the PCA and operation by a skilled operator.

Table 2: Comparison of different metrics from drive cycle tests and from measurement data. P_{cyl} is the sum of the individual cylinder powers P_{slew}, P_{ib}, P_{ob} and P_{ext}. u denotes the relative usage time of a cylinder. Note the good fit of the cylinder power and the poor fit of the pump power. Note also the good fit of the 1st boom and the poor fit of the slew.

	$\overline{P}_{pump}$ [kW]	$\overline{q}_{pump}$ [lpm]	$\overline{p}_{pump}$ [MPa]	$\overline{P}_{cyl}$ [kW]	$\overline{P}_{slew}$ [kW]	$\overline{P}_{1b}$ [kW]	$\overline{P}_{2b}$ [kW]	$\overline{P}_{ext}$ [kW]	u_{slew} [%]	u_{1b} [%]	u_{2b} [%]	u_{ext} [%]
Drive cycle	4.6	21	11.9	2.8	0.7	1.5	2.6	1.8	67	70	46	5
Measurements	5.6	24	11.4	2.8	1.4	1.5	1.6	1.6	48	70	46	24

5 DISCUSSION

The recording of cylinder pressures and valve positions during operation of the drive cycle shows that the average work performed by the hydraulic cylinders corresponds to that of the measurement data. A good fit of the individual actuators was more difficult to achieve with this method focused on the position of the crane tip. Even though the operator performing the drive cycle according to the parameters obtained from the PCA where given information about the average usage from the measurement and how that differed from his normal driving pattern, it was difficult to achieve a good fit of all four functions. This indicates that the total time of completing a lift might not be enough to define the time dimension of the cycle, the speed of the cylinders are also important parameters. The PCA method is, however, limited to work with scalar values and it would be too complex to include when and how much each cylinder should be actuated.

As mentioned earlier, it is however not necessary to include the actuator commands in the drive cycle. If a system with driver support or an autonomous system is developed the use of individual actuators can be optimized in order to perform the task of moving the crane tip in a trajectory with for example as low energy consumption as possible. What is most energy efficient will depend on the system design and to be able to decide on a suitable system concept for a human operator it is therefore of interest to know how the cylinders cooperate when a human is operating the crane. This study is however only based on the measurements from a single operator and a perfect fit to the movements of this specific operator is not important.

It is also important to consider that the selection of points to form the drive cycle in the principal component dimension space can be done in a number of different ways. The time limit of performing the drive cycle in real life sets the limit on the number of points but how these points should be selected is not optimized. There seems to be a good variance in the original parameters and a fit to the measurement data has been calculated that can be used to compare to other solutions but the drive cycle has not been optimized with regards to this. In future usage of the method proposed it could be useful to perform a sensitivity analysis on the parameters before doing the PCA. The objective of the analysis would be to extract the parameters with the variance that has the greatest impact on the efficiency and power demand of the drive cycle. That information could later be used to select suitable points during PCA.

Finally, it should be noted that the drive cycle only captures the average working situation, high power-demanding lifts are not included. In order to dimension components like electric motors and batteries the level, time duration and frequency of power peaks can be studied directly from the measurement data.

6 CONCLUSION

This study presents a method of defining a drive cycle based on measurement data for the operation of a hydraulic loader crane. The method is based on extracting average operating points from the data and can be an alternative to clustering methods when there are no clear patterns in the data. The difficulty with the method is to include sufficient information before extracting the average points. When applied to the crane of interest,

the method gives a good representation of the work performed at the crane tip. The energy consumption of a lifting movement is however also dependent on the actuation of the individual cylinders and how they cooperate to move the crane tip and that is dependent on the driving style of the operator and difficult to reproduce. Still, the drive cycle produced by the method is a reasonable example of human operation of the crane and will allow new concepts of the hydraulic system to be evaluated and compared based on real life data in an efficient way.

ACKNOWLEDGMENT

The authors would like to thank Hiab AB for their contribution to this paper. The work in this paper was sponsored by the Swedish Energy Agency and is part of STEALTH, Sustainable Electrified Load Handling, App. no 44427-1.

NOMENCLATURE

$\overline{X}$	Mean value of property X
g	Gravtiational acceleration
k	Number of measured trajectories
l_{pl}	Leverage of payload to 1st boom - column joint
M_{cyl}	Moment from 1st boom cylinder on 1st boom - column joint
M_{dw}	Moment from dead weight of boom system on 1st boom - column joint
m_{pl}	Payload mass
n_p	Number of drive cycle parameters
P	Hydraulic power
p	Hydraulic pressure
q	Hydraulic flow
u	Relative usage time of a cylinder
w	Weight constant for drive cycle trajectory
x	A 6 or 7 dimensional point defining the corner points of a trajectory

REFERENCES

[1] Sun Wei. 2004. *On Studies of Energy Regeneration System for Hydraulic Manipulators*. PhD thesis, Tampere University of Technology.

[2] Martin Scherer. 2015. *Beitrag zur Effizienzsteigerung mobiler Arbeitsmaschinen: Entwicklung einer elektrohydraulischen Bedarfsstromsteuerung mit aufgeprägtem Volumenstrom*. PhD thesis, Karlsruher Institut für Technologie.

[3] M Sc Chris Geiger and Prof Marcus Geimer. 2017. Efficiency Optimisation of a Forestry Crane by Implement Hydraulics with Energy Recovery. In *VDI-MEG - 75th International Conference on Agricultural Engineering - LAND.TECHNIK AgEng 2017 - The Forum for Agricultural Engineering Innovations, Hannover, 10.-11. November 2017*, pages 175–184.

[4] Nicholas Dembski, Giorgio Rizzoni, Ahmed Soliman, Jim Fravert, and Kenneth Kelly. 2005. Development of Refuse Vehicle Driving and Duty Cycles. In *SAE World Congress & Exhibition*, volume 2005, pages 1–16.

[5] Michel André. 2004. The ARTEMIS European driving cycles for measuring car pollutant emissions. *Science of the Total Environment*, 334-335:73–84.

[6] Philipp Scherer and Marcus Geimer. 2014. A Methodology for the Derivation of Movement-and Load Spectra for Energy-Efficiency Test Cycles of Heavy Equipment Vehicles. *SAE Technical Papers*, 2014-01-23.

[7] Neil Vaughan and Bogdan Gabrys. 2016. Comparing and combining time series trajectories using Dynamic Time Warping. *Procedia - Procedia Computer Science*, 96(September):465–474.

[8] Zahedeh Izakian, Saadi Mohammad Mesgari, and Ajith Abraham. 2016. Automated Clustering of Trajectory Data Using a Particle Swarm Optimization. *Computers Environment and Urban Systems*, (January).

[9] Jake Lever, Martin Krzywinski, and Naomi Altman. 2017. Points of Significance: Principal component analysis. *Nature Methods*, 14(7):641–642.

[10] Michael E. Wall, Andreas Rechtsteiner, and Luis M. Rocha. 2003. Singular value decomposition and principal component analysis. In *A Practical Approach to Microarray Data Analysis*, pages 91–109. Kluwer, Norwell, MA.

MULTI-PRESSURE ACTUATOR IN ENHANCING THE ENERGY BALANCE OF MICRO-EXCAVATOR

Husnain Ahmed[1], Otto Gottberg[2], Heikki Kauranne[3], Jyrki Kajaste[2], Olof Calonius[2], Mikko Huova[1], Matti Linjama[1], Juha Elonen[3], Pertti Kahra[3], Matti Pietola[2]
[1)]Tampere University of Technology, Automation and Hydraulic Engineering, Tampere, Finland;
[2)]Aalto University, Department of Mechanical Engineering, Espoo, Finland;
[3)]Fiellberg Oy, Vantaa, Finland;
jyrki.kajaste@aalto.fi

ABSTRACT

This paper presents results of an experimental study conducted with an electrified small sized excavator, whose boom swing function is equipped with digital hydraulic multi-pressure actuator. Highlighted and discussed are the performance, energy efficiency and controllability of the function in varying inertia loads. In addition, component-specific energy losses are analysed. This data is compared with the results gained with the excavator's original control arrangement, a load-sensing system based on pressure adjustment valve. Results manifest high energy saving potential of the multi-pressure system in mobile machinery.

KEYWORDS: digital multi-pressure actuator, micro-excavator, energy efficiency, control, experimental

1. INTRODUCTION

Tightening international legislation regarding the allowed NO_x and particle emissions of fossil fuel burning machines along with the rising fuel prices are directing the machine manufacturers to develop more environmentally friendly and energy efficient machines to keep their products both competitive and in accordance with the valid regulations.

When considering mobile work machinery, one of their most essential systems considering machine's performance and energy efficiency are their hydraulic systems that are used to operate various functions of the machine. If the drive transmission is left aside, the hydraulic systems, the work hydraulics, in these machines are typically realized as open circuit valve controlled central hydraulic systems. In these, the individually valve controlled actuators that operate the functions of the machine are connected in parallel and fed by a single pump or pump combination run by a combustion engine, typically a diesel-engine. Because of the direct interconnection between actuators and prime mover, the diesel-engine has to be dimensioned according to the combined maximum power required by the actuators at any instant. However, this maximum power may be required only at minor portion of the machine's work cycle, and most of the time the combined power requirement of the actuators can be significantly lower and have much variation. From the diesel-engine's point of view, this variation of power requirement means ever changing operating point and thus not constantly operating in the most energy-efficient one, which in turn significantly increases the fuel consumption and the emission of pollutants of the engine.

Feeding parallel connected and simultaneously operated actuators from a single supply line, as it is in the open circuit valve controlled central hydraulic systems, leads to a need to throttle the input and output flows of

at least one of the actuators if the ratios of the actuator sizes and loads between the simultaneously operated actuators are not identical. This throttling is required to produce pressure losses that balance the existing differences in supply line pressure and load pressures between the actuators, and is therefore required always regardless whether the pump of the system is of fixed delivery flow type or variable delivery flow type, e.g. a Load-Sensing (LS) pump. Although the valve actuated throttling allows for very accurate control of actuator velocity and position, it induces high pressure losses and therefore also high power losses leading to low energy efficiency of the system and because of this, typically a need for a cooling system that further reduces the energy efficiency of the system.

Since the energy-efficiency related weaknesses of open circuit valve controlled central hydraulic systems are due to incapability to match the prime mover produced power with the power requirements of parallel connected actuators without intentionally induced power losses, which in turn are due to the direct connection between the actuators and prime mover, the solution for higher system energy efficiency has to be sought by reducing or even totally removing both the interdependency between actuators and the direct connection between the prime mover and actuators. During recent years, some new system architectures have been proposed to reach these targets.

Of these, the quite widely studied electro-hydraulic actuators (EHAs), e.g. [1, 2, 3] are based on one motor – one pump – one actuator –principle, where the actuator is directly controlled by the pump without any valves. The control of the pump flow is typically implemented through the control of the rotational velocity of the motor running the pump, although pump displacement control or combined velocity-displacement control are also possible. Even though there is a direct interdependency between the prime mover and actuator, this solution enables very good matching of the actuator required power and the motor produced power and thus reaching high system efficiencies in absence of throttling losses. Another advantage is that from hydraulic point of view each actuator constitutes a self-sufficient power pack unit not dependent on the other actuators of the machine, and requires only the electric energy and control signal from outside of the pack. This autonomy enables the dimensioning of machine's each power pack according to the requirements of the function that they are intended to operate. It also enables their relatively easy adoption for various functions in different machines. The major disadvantage of this system structure is the relatively high commissioning price compared to traditional open circuit valve controlled central hydraulic systems, since each actuator requires its own pump, prime mover and control drive.

Some alternative solutions for reducing the interdependence both between system's actuators and between prime mover and actuators were presented in [4]. Amongst these was one, which was based on several pressure sources for each of the actuators of a hydraulic system. In following research works this concept was developed further and named digital hydraulic multi-pressure actuator (DHMPA). In this concept, each of the available pressure sources can be optionally connected to whichever actuator chamber. This enables a variety of actuator produced forces in both directions of movement and thus also actuator's adaptation to several operating points, the number of which naturally depends on the number of source pressures. The selectable pressures are generated through an actuator specific high-pressure accumulator and a set of pressure transformers between the accumulator and actuator, and the pressure sources to be connected to the actuator chambers are selected via a group of low pressure loss 2/2 on/off -valves, a detailed structure of the system is presented in Chapter 2. The charge of the high-pressure accumulator is maintained by a pump that is common to all of the digital hydraulic multi-pressure actuator units of the machine, Figure 1. Since the occasionally required actuator power peaks can be dealt with using the pressure transformers, this pump and its drive motor can be dimensioned according to lower power requirements. Despite of the common pump, each actuator can be operated without mutual dependence and the pressure transformers practically remove the direct connection between the actuators and the prime mover. This enables both reaching high energy-efficiency of the system and possibility to run the prime mover in its most energy-efficient operating point while charging the pressure accumulators. As a consequence, the energy (fuel) consumption and the pollution emissions of the machine are lowered compared to a machine with open circuit valve controlled central hydraulic systems.

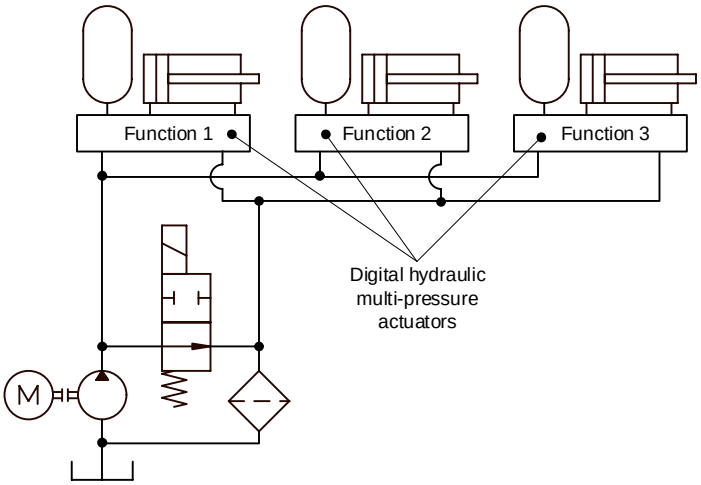

Figure 1. Circuit diagram of a system implemented with digital hydraulic multi-pressure actuators.

The digital hydraulic multi-pressure actuator was proven functional and energy-efficient already with the measurements with the first prototype in [5]. Later it has been tested with four different control strategies [6, 7] with promising results; the energy savings compared to traditional proportional valve based Load-Sensing (LS) system varied between 58–77 %, it has high dynamics, small position tracking error, but on the other hand, at slow actuator velocities the control resolution was found to require improvement to enable smooth tracking, accurate positioning and to avoid oscillations during stopping of the movement. Although the system efficiency was proven to be high, there is room for improvement considering the pressure losses of 2/2 on/off -valves, which were the highest in the system. The proof-of-concept prototype used in these measurements was constructed using separate components connected and by hoses, which highly likely had impact on the gained results.

In this study, the second prototype of the digital hydraulic multi-pressure actuator with more compact structure is presented and applied to operate the boom swing function of an electrically driven micro excavator. The challenge of this function is that the boom inertia is not constant, but changes depending on the position of the boom, i.e. how extended or folded the boom structure is, and also on the state of the boom bucket (empty-full). The effect of the changing inertia has to be taken into account in the control of the swing motion.

Focus of this study is in experimental research considering the energy efficiency, controllability, and performance of the multi-pressure actuator based system. The acquired results are compared to measurement results gained with the original control arrangement of the excavator, which consisted of fixed displacement pump running with constant velocity and a LS-system realized purely with valves. In addition, the component wise energy losses are analysed. The study ends with recommendations for further development and research.

2. METHODS

The methods used in this paper include experimental boom turning tests in an actual working machine, involving both the original pressure adjustment valve-operated LS-system and the digital hydraulic multi-pressure actuator system. Analytical power loss analyses of both systems have also been conducted in order to determine most important targets for energy saving.

2.1. Test rig

The digital hydraulic multi-pressure actuator was installed to drive the boom swing function of a small-sized working machine, a 1.1 tonne JCB Micro excavator. Originally the machine had been equipped with 13.6 kW diesel-engine, but in conducted electrification projects it had been replaced with a 10 kW variable speed electric motor and a battery pack. The work hydraulics for the four boom functions is a low cost Load-Sensing

(LS) system comprising of a fixed displacement pump and a pressure adjustment valve, which senses (using shuttle valves) the highest prevailing load pressure of the actuators and adjusts the system pressure such that it is approximately 20 bar higher than the highest load pressure. At the same time, it directs back to tank the portion of the fixed pump flow that is not needed in the actuators.

This system had been modified by replacing the original manually controlled proportional directional valves with electrically controlled valves, but otherwise the control structure remained as original. A simplified system schematics presenting only one function is shown in Figure 2, a more detailed description of this system structure with measured characteristics is presented in [8], although those measurements did not include the boom swing function, but these were conducted separately for this study for baseline reference. Despite of the possibility to vary the rotational velocity of the electric motor and thus also the pump outflow, in the measurements presented in this paper the motor was run with fixed speed, the purpose of this being to emulate a simple valve-based LS-system used typically in small work machines. Although not used in this study, it would be possible with this test rig to imitate the operation of a conventional LS-system by controlling the rotational speed of the electric motor.

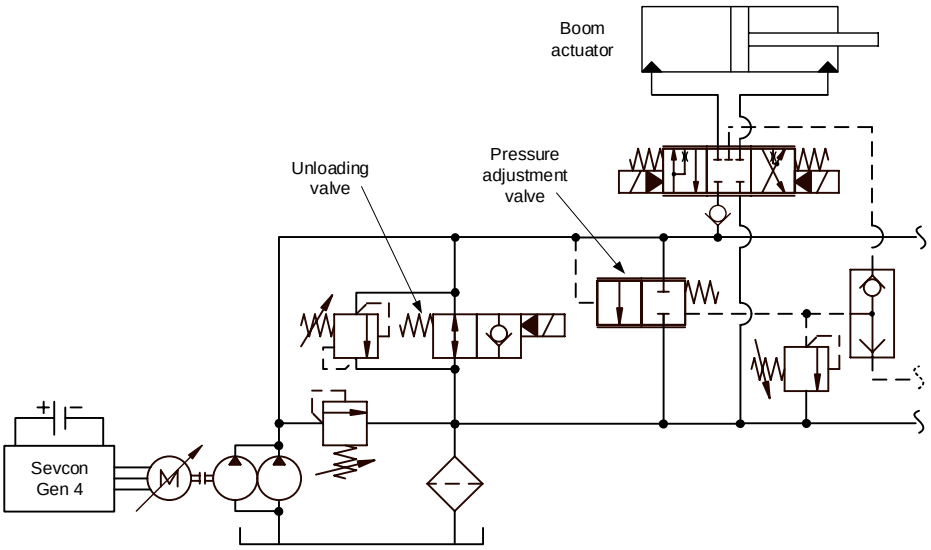

Figure 2. A section of the original valve-based LS-system of the excavator.

The excavator itself is presented in Figure 3. As the excavator is used as test rig in several studies, the individual boom functions are modified according to the need of the research. In the figure, the arm actuator is operated by an EHA unit attached to the boom, while the digital hydraulic multi-pressure unit used for the boom swing actuator is installed on the backside of the excavator and presented from above in the photo on the left.

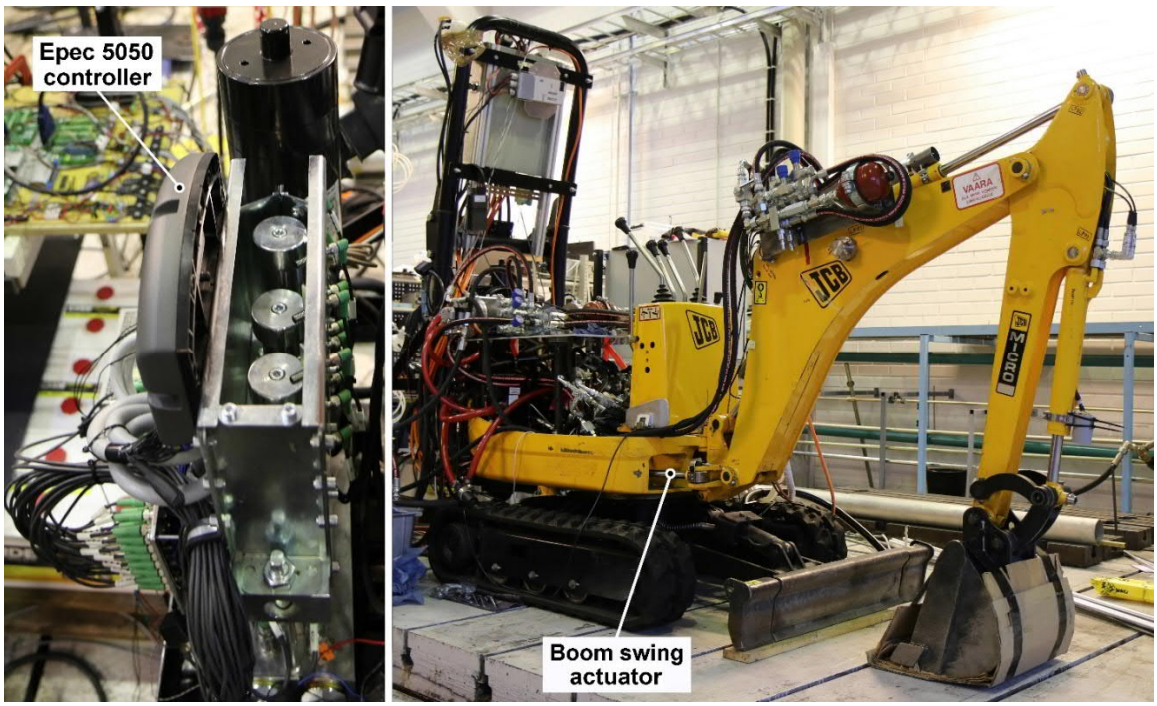

Figure 3. Digital hydraulic multi-pressure unit and excavator test rig.

The structure of the multi-pressure unit and its adaptation to boom swing function of the excavator is presented in Figure 4 with the main system components listed in Table 1. All the components of the multi-pressure unit are installed in a single manifold.

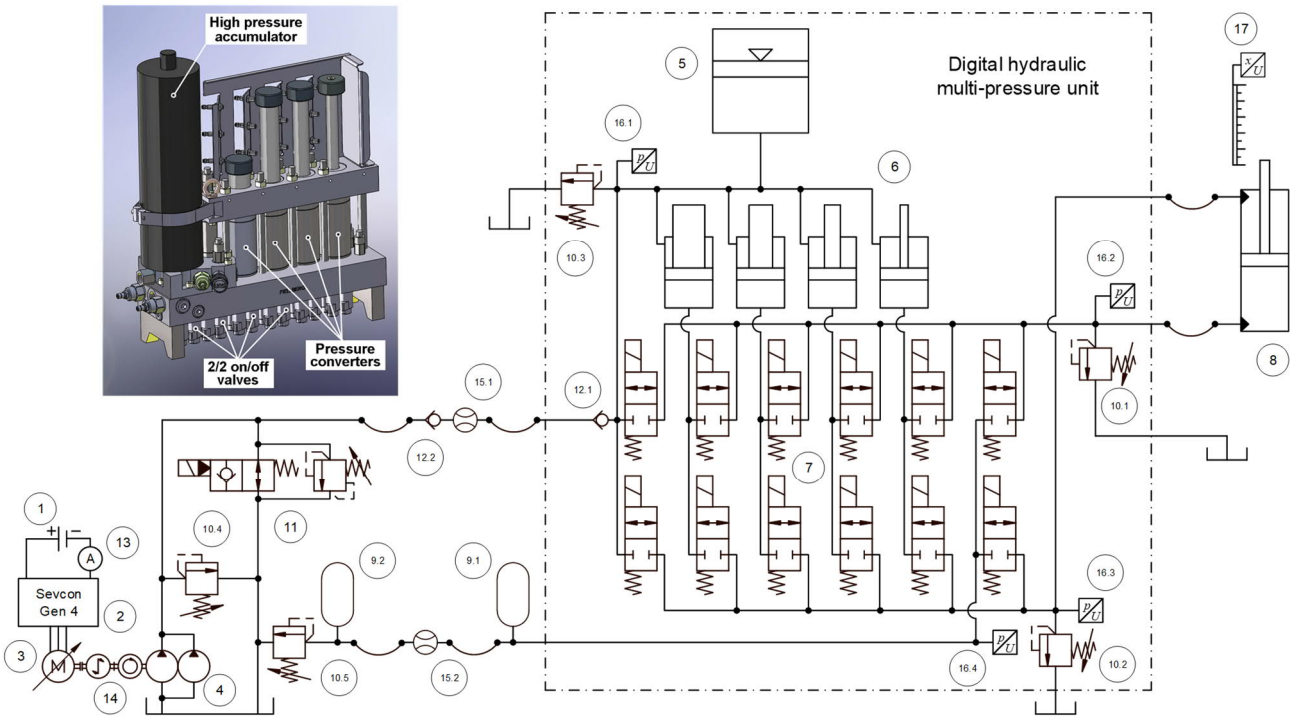

Figure 4. Digital hydraulic multi-pressure unit and its adaptation to boom swing function.

Table 1. Components of measurement system.

Nr	Description	Details
1	Battery pack	72 V Lead-acid
2	Motor controller	Sevcon Gen4
3	Electric motor	10 kW
4	Dual pump	Parker PGP511 (2* 6 cm^3/r)
5	High-pressure accumulator	2 litres
6	Pressure converters (piston Ø / piston rod Ø – stroke)	50/40-120 mm 50/36-120 mm 50/30-120 mm 50/22-120 mm
7	Doubled 2/2 on/off -valves	Bucher W22-D-5
8	Boom swing actuator (piston Ø / piston rod Ø – stroke)	52/25 - 293 mm
9.1 - 9.2	Low-pressure accumulator	1.0, 0.7 litre
10.1 - 10.5	Pressure relief valve	Rexroth VSC-30
11	Unloading valve	Rexroth VEI8A-VSBN-08A
12.1 - 12.2	Check valve	HBS ½" 0.5 bar
13	Current sensor	LEM DK 200
14	Torque and tachometer	Kistler 4502
15.1 - 15.2	Flow sensor	Kracht VC 0.4 - VC 1
16.1 - 16.4	Pressure sensor	Trafag NAH 8254
17	Position sensor	Siko SGH10

When started, the dual pump (4) driven by the speed-controlled electric motor (3) charges the high-pressure piston type accumulator (5) through check valves (12.1, 12.2) until the highest set charge pressure ~55 bar is reached, after which the controller of the multi-pressure unit shuts down the electric motor. As a result, there are six selectable pressures to connect to the boom swing actuator (8) chambers; the pressure prevailing in the high-pressure accumulator (5) directly, the four pressures generated by the accumulator and the four converter cylinders (6), and the pressure prevailing in the low-pressure accumulator (9.1) placed in the return line. When the boom swing actuator is given a command to move with certain velocity, the controller of the multi-pressure unit (Figure 5), which uses measured system pressures and actuator velocity as feedback signals, opens appropriate 2/2 on/off valves (7, representing six pairs of parallel connected valves) and connects pressures optimal to prevailing operating condition to the actuator chambers. The pressure relief valves (10) secure the system against excessive pressures, although the function of valve (10.5) is to maintain a back pressure of ~8 bar in tank line.

During the motion of the actuator, the controller keeps track of the positions of the converter cylinders and prevents them from running to their ends by changing the pressures connected to actuator chambers when necessary, i.e. when the required actuator movement requires more fluid volume than one converter cylinder can supply. The positions of the converter cylinders are maintained in acceptable regions by connecting their piston sides to appropriate pressure source when necessary. The control principle of the multi-pressure unit is described in detail in [5, 6, 7]. When the pressure of high-pressure accumulator decreases and reaches set minimum value of ~42 bar, the electric motor is started and the accumulator is charged again to its highest set pressure. In the measurements of this study, the electric motor was run with fixed rotational velocity, although the possibility to control the velocity could be utilized to increase the energy-efficiency of the accumulator charging process.

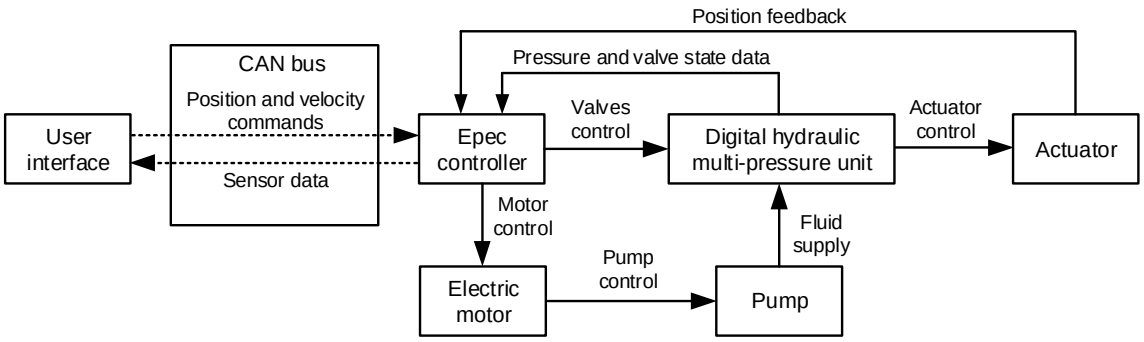

Figure 5. Control structure of the digital hydraulic multi-pressure system.

Control of the digital hydraulic multi-pressure actuator is built on Epec 5050 controller (see Fig. 3), which is able to control both all the 2/2 on/off -valves and the electric motor and thus also the pumps of the system, and in addition acquire sensor data and convey it to the user interface via CAN bus.

2.2. Experimental procedure

The characteristics and behavior of the digital hydraulic multi-pressure actuator were determined with measurements with excavator's boom swing function. Each single measurement consisted of velocity controlled boom deflection (i.e. swing actuator extension) from the excavator's centreline, followed by a short-timed immobility, after which the boom was returned (i.e. swing actuator retraction) to its starting position with controlled velocity. The loading of the system was varied by folding and extending the boom structure, two different positions were used. For comparison data, same measurements were repeated with a system that emulated the excavator's original valve-based LS-system.

During the measurements the following quantities were recorded; input current and voltage of the electric motor, output torque and rotational velocity of the electric motor, pump outlet flow rate and pressure, high-pressure accumulator's pressure, actuator chamber pressures, actuator position, low-pressure line pressure and flow rate. These were used in calculating the input and output powers and energies of system's components.

The positions of the pressure converter pistons and 2/2 on/off -valves were not recorded and are thus not presented here, but a description of their operation during actuator movements is explained in [6, 7].

3. RESULTS

This chapter presents the measurement results for both DHMPA and LS systems gained with low (folded boom) and high (extended boom) inertia, representing an inertia ratio of 1:10.

Figure 6 shows position trajectory command signals and actual actuator outputs for both directions of boom swing in the low and high inertia cases for both the digital hydraulic multi-pressure system and the LS-system.

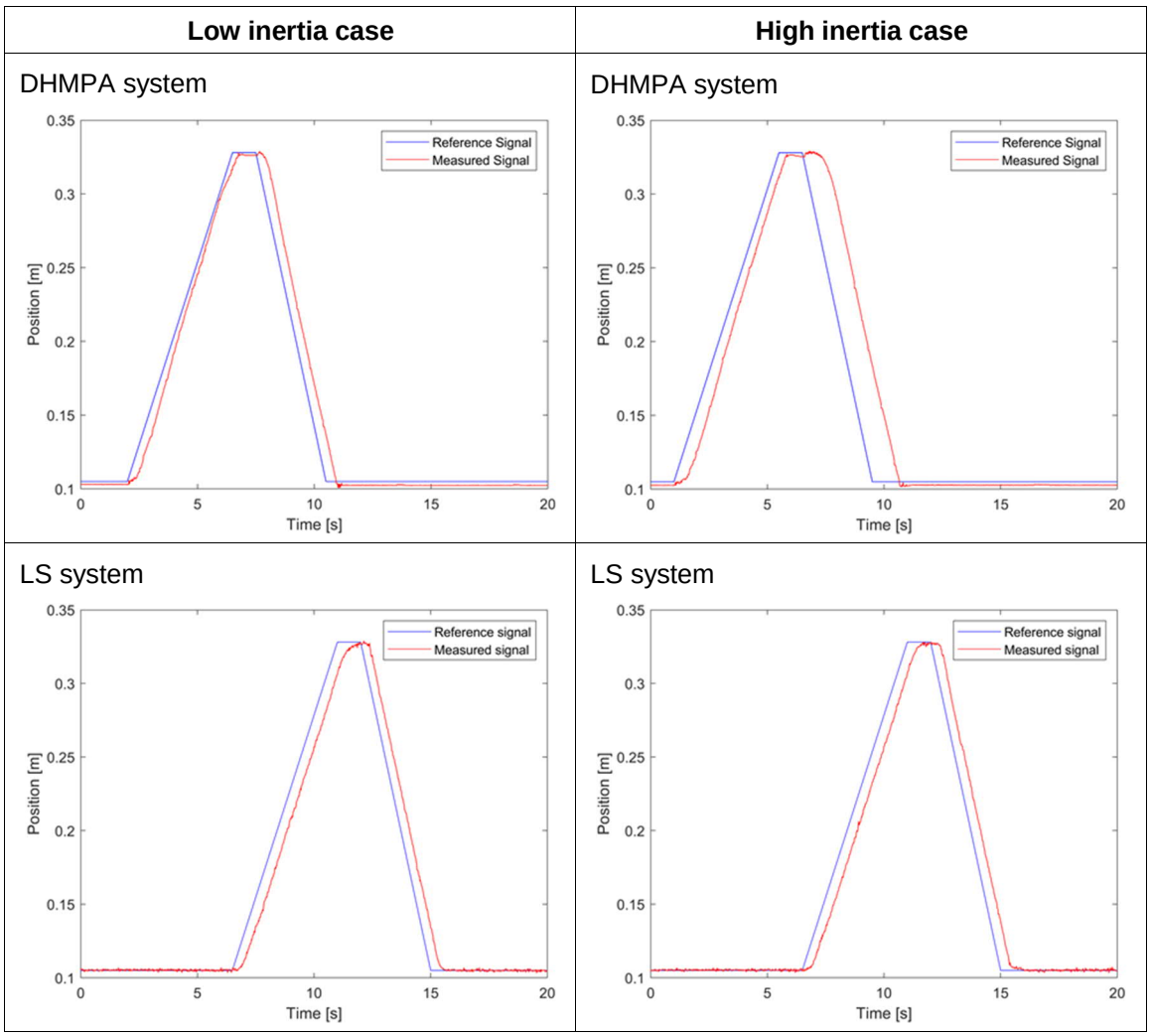

Figure 6. Position trajectories for the boom swing actuator with low and high boom inertia.

Figure 7 presents the multi-pressure system's high-pressure accumulator pressure, dual pump flow rate and boom swing actuator displacement during one work cycle. Accumulator charging control is based on pressostat (pressure switch) type of operation, the pump is turned on when the accumulator pressure reaches the minimum set pressure and it is turned off as the maximum set pressure is achieved. Only low inertia case is presented since differences between low and high inertia cases were negligible.

Figure 8 presents the power usage of the two studied systems in low and high inertia cases, i.e. with folded and extended boom structure. The plots include the input power of motor's inverter, the hydraulic pump's mechanical input power, and the pump's hydraulic output power. The electric motor had a tendency to creep with low velocity following the end of swing motion, i.e. during commanded immobility phase, which manifests itself in the measured electric input power. Since this unwanted phenomenon is later to be removed, the plots also present electric motor's input power calculated without this creeping.

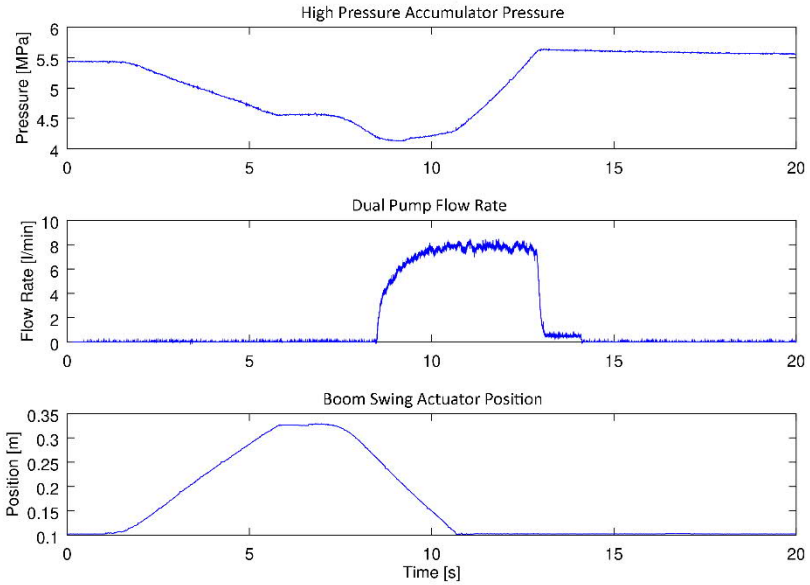

Figure 7. High-pressure accumulator pressure, dual pump flow rate and boom swing actuator position during work cycle, DHMPA system in low inertia case.

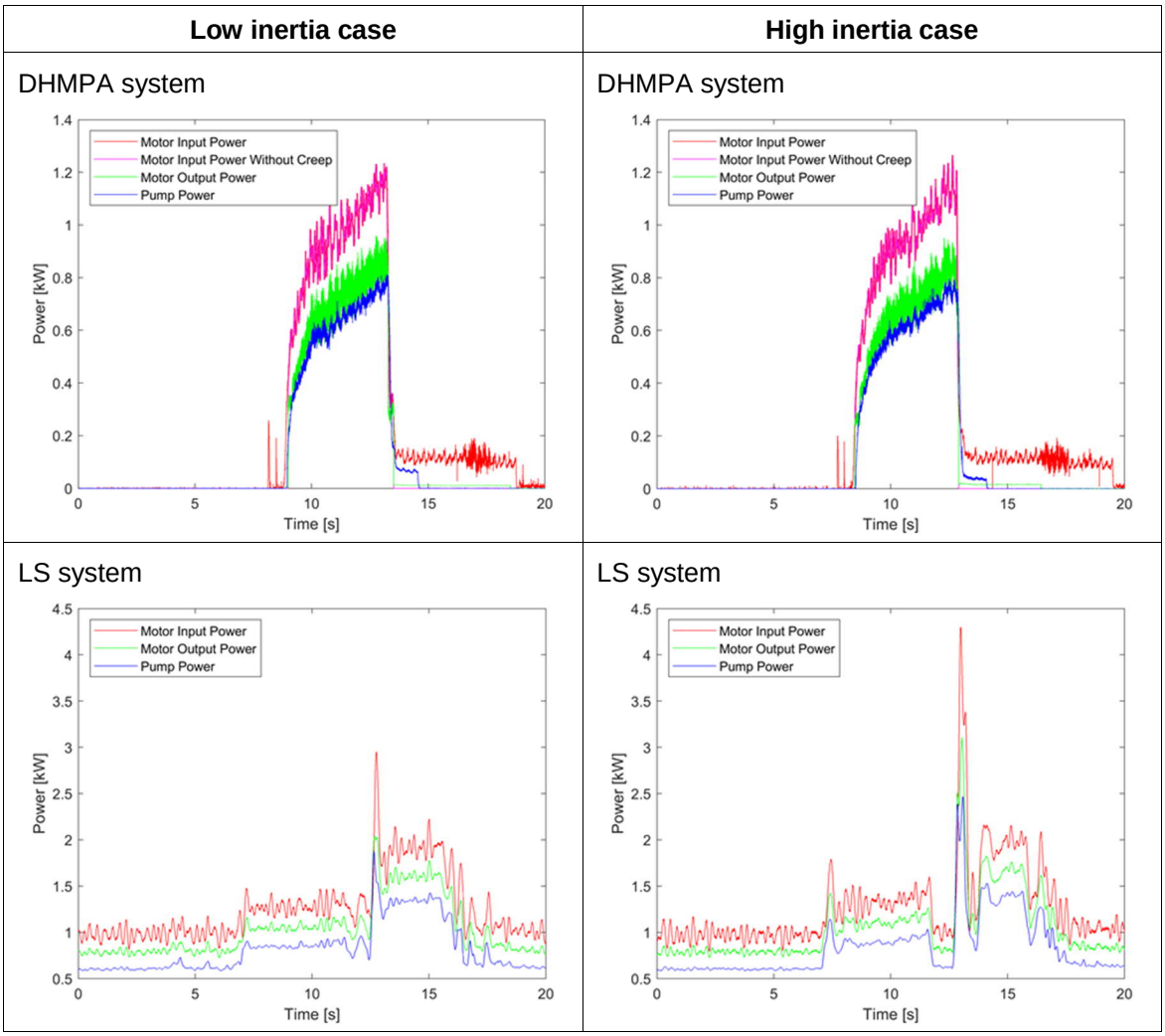

Figure 8. Power usage of studied systems during one work cycle with low and high boom inertia. Note the different power scales in upper and lower figures.

Figure 9 presents the cumulative energy consumption of the various sub-systems in low and high inertia cases. Electric motor's energy consumption is calculated both with the effect of creeping motion and without it.

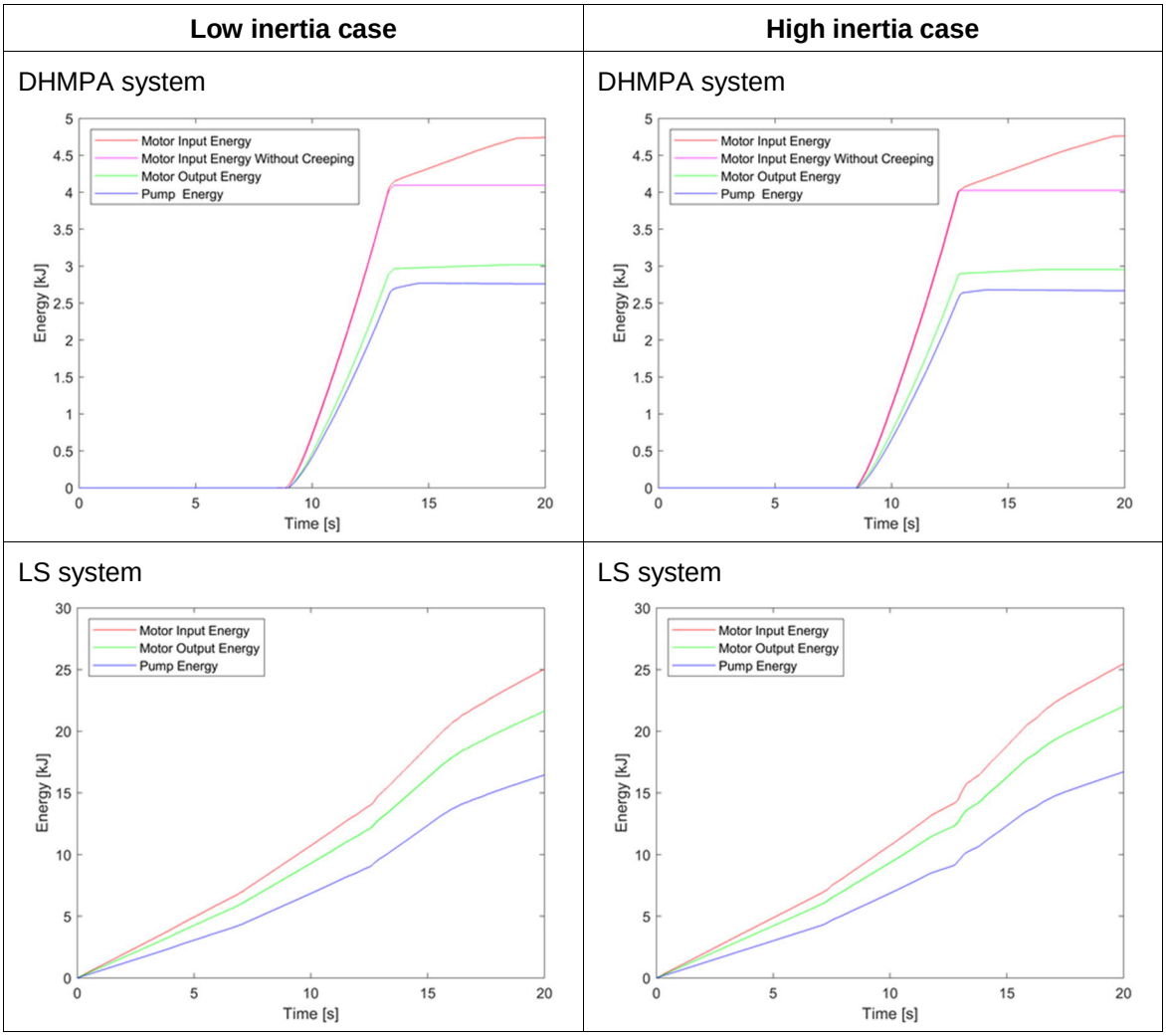

Figure 9. Cumulative energy consumption of studied systems during one work cycle with low and high boom inertia. Note the different energy scales in upper and lower figures.

Tables 2–4 present calculated peak powers, energy consumption and differences in efficiencies between digital hydraulic multi-pressure system and LS system.

Table 2. Peak powers of one back and forth swing motion in DHMPA and LS systems.

Power type	**Low inertia case**		**High inertia case**	
	DHMPA (kW)	**LS system** (kW)	**DHMPA** (kW)	**LS system** (kW)
Peak electric power	1.23	2.93	1.26	4.30
Peak mechanical power	0.95	2.03	0.95	3.10
Peak hydraulic power	0.81	1.85	0.79	2.46

Table 3. Energy consumption of one back and forth swing motion in DHMPA and LS systems.

Energy type	**Low inertia case**		**High inertia case**	
	DHMPA (kJ)	**LS system** (kJ)	**DHMPA** (kJ)	**LS system** (kJ)
Electric energy	4.09	14.92	4.01	15.43
Mechanical energy	3.01	12.91	2.95	13.33
Hydraulic energy	2.66	10.14	2.66	10.48

One reason for the substantial difference in power and energy consumptions between DHMPA and LS systems is that in order to be able to follow the position command, in LS system a pressure difference is needed across the proportional valve controlling the actuator. This necessitates that in the LS system the pump is constantly run at velocities that produce higher flow rate to the system than required by the actuator, whilst in DHMPA system, where there is no direct connection between pump and actuator, the pump is run only according to the real flow rate need of the accumulator. In LS system, the produced excess flow is directed back to tank through the pressure adjustment valve (see Fig. 2), whose setting value for the pressure difference between the pump and the actuator pressures is 20 bar. Despite of maintaining the system-specific pressure difference across the proportional valve, in the measurements the valve opening had to be kept close to its maximum value in order to achieve the demanded actuator velocities. For these reasons, a straight comparison of the net energy consumptions between the two systems can be misleading.

Table 4. Reduction of energy consumption with DHMPA compared to LS system.

Energy type	**Low inertia case** (%)	**High inertia case** (%)
Electric energy	72.6	74.0
Mechanical energy	76.7	77.9
Hydraulic energy	73.8	74.6

An analytical calculation of component-specific power losses were conducted for both systems to locate points of potential energy savings. In LS system, the losses caused by the mismatch in pump and actuator flow rates were excluded in this calculation. Thus the outcome of analysis are valid for both (ideal) pump and pressure adjustment valve operated LS-systems. The results related to the power consumptions for a one-directional boom swing motion (half cycle) are presented in Table 5. Table 6 presents the energy losses caused by charging of the high-pressure accumulator, which applies only to the DHMPA system.

Table 5. Estimated power consumption for one-directional swing motion.

Loss source	**DHMPA** (W)	**LS system** (W)
High-pressure accumulator seal friction	3.4	0.0
Pressure converter seal friction	5.8	0.0
Boom swing actuator (including cylinder seal)	220.0	220.0
2/2 on/off valves actuator inflow pressure loss	7.0	0.0
2/2 on/off valves actuator outflow pressure loss	3.2	0.0
Proportional valve actuator inflow pressure loss	0.0	233.0
Proportional valve actuator outflow pressure loss	0.0	180.0
Hose; actuator inflow pressure loss	26.8	26.8
Hose; actuator outflow pressure loss	15.8	15.8
Pressure relief valve pressure loss	71.8	0.0
Volume flow sensor (Kracht VC 1) pressure loss	4.5	4.5
Volume flow sensor (Kracht VC 0.4) pressure loss	0	8.2
Total power consumption in half cycle	**358.3**	**688.3**

Table 6. Estimated losses in high-pressure accumulator charging for one-directional swing motion.

Lost energy in accumulator charging	**DHMPA** (J)	**LS system** (J)
High-pressure accumulator thermal losses	56	0.0
High-pressure accumulator friction losses	7	0.0
Volume flow sensor (15.1 - Kracht VC 0.4) loss	29	0.0

The relatively low losses listed in Table 6 can be contrasted with the total energy consumption for the half cycle (obtained by time integration of the total power consumption and, for the DHMPA, by adding the high-pressure accumulator related losses): 1525 J for the DHMPA, and 2754 J for the LS system.

Note that if hose and volume flow sensor losses are omitted in both systems, the estimated energy consumption in DHMPA is circa 53% of the energy consumption in an LS system (with perfectly matched flow rate).

4. DISCUSSION

Both studied systems, LS and DHMPA, proved good trajectory following capability (Fig. 6), although in case of the latter system, the actuator load had greater impact on the tracking accuracy. The measurements with DHMPA were run with fixed control gains, and the noted dependency of accuracy on load could supposedly be answered by using load adaptive control gain.

The power and energy demands of the systems are clearly at different levels (Figs. 8 and 9; Tables 2 and 3). This is due both to the different operational principles of the systems and to the different magnitudes of systems' pressure losses. Since in DHMPA system there is no direct connection between the actuator and the pump, the latter is run only when the high-pressure accumulator requires charging and is shut down otherwise, whereas in LS system, where the direct connection exists, the pump runs constantly and thus also requires continuous, although not constant power input since the system pressure varies according to the operating situation. However, it must be noted, that the power and energy consumption of the DHMPA system during a boom swing motion depends on the dimensioning of the high pressure accumulator. The smaller the size the more frequent charging is required, and vice versa. Also if the load increases substantially, it leads to more frequent charging of the accumulator because of its fixed pressure and the fixed sized pressure converters. These differences in operational principles also give rise to the result that the magnitude of load inertia has negligible effect on the power and energy consumption of DHMPA system, but in LS system it has a major impact on these.

In LS system, the effect of increasing load force on energy consumption is due to the higher system pressure required, which increases both the power consumption of the fixed displacement – fixed speed pump and the pressure losses in the pressure adjustment valve of the studied one actuator LS system. In the studied case the high loads were predominantly associated with acceleration of the high inertia boom. In turn the deceleration of this boom structure would mean considerable energy losses since the braking mechanism in LS implementation is throttling by a proportional control valve. In DHMPA system the kinetic energy can be saved in the high-pressure accumulator and throttling losses are of minor importance, again.

In addition, in the studied system, the pump produced much higher flow rate than was needed by the boom swing actuator, which further increased the power losses in the pressure adjustment valve. In a multi-actuator system also the pressure losses of other actuators' control valves would change and probably contribute to the growth of power losses. On the other hand, if the pump could adapt to the changing need of flow rate (variable displacement pump or variable speed pump), then the effect of load on the power consumption of pump would be less. Also in DHMPA system, the magnitude of load naturally affects the power and energy need of the actuator, e.g. increasing load requires more power and energy, but this need is met internally

between the high-pressure accumulator and the actuator through the pressure converters, and the effect of loading is seen from the outside of the hydraulic system only when the high-pressure accumulator requires re-charging. This in turn depends on the dimensioning of the system components and on the velocity and frequency on which the actuator is operated. In the studied DHMPA system the accumulator was charged once per one back and forth boom swing motion (see Fig. 7). In continuous operation, the re-charging of high-pressure accumulator would be repeated similarly every time, and from an energy consumption point of view it would require the same amount of energy. The only energy losses that would depend on the operational conditions of the actuator are the system's seal frictions and pressure losses (see Table 5).

In LS system, where the control of actuator is actualized with flow throttling proportional valve, the valve pressure losses required by the control are of magnitude 15–20 bar, but in DHMPA system, where the 2/2 on/off-valves are used only to control the direction of flow between pressure converters and actuator, not the magnitude, the pressure losses of the actuator controlling valves are significantly lower. When using two parallel connected on/off-valves, the pressure losses of valves can be well below 1 bar in the studied case. In applications, where higher flow rates are required due to, e.g. larger actuator, the system can be implemented with higher numbers of parallel connected on/off-valves to keep the pressure losses moderate. This approach does not work for LS systems, since a certain pressure loss across the actuator controlling valve (LS pressure) has to be ascertained to ensure the functionality of the system and the accuracy and sensitivity of the control.

The operational environment, a micro excavator, where the DHMPA unit was tested, was not optimized for this unit, which had some impairing effects on the measurement results. The unit had to be placed further away from the actuator than the proportional valve of the LS system, which necessitated using very long hoses, which in addition were of only 6 mm inner diameter (i.e. the size of the excavator's original hoses). Although the flow velocities in hoses were moderate (circa 4 m/s), the relatively high fluid viscosity gave rise to pressure losses that were estimated to be four times the losses of the on/off-valves. In spite of being still much lower than the pressure losses of proportional valve in LS system, this elevated pressure loss had a significant effect on DHMPA system, which otherwise proved to be very energy efficient. The remedy for this is easy and affordable, since replacing the narrow hoses with 10 mm or 12 mm inner diameter hoses does not mean major investment, but has major impact on the pressure losses of hoses.

In addition to the above, also the power loss induced by the pressure relief valve placed in the low-pressure line of the DHMPA measurement system (10.5 in Fig. 4) has considerable influence on the energy efficiency of the system. Although being low in absolute value, the pressure loss in this valve is high in relation to the accumulator and system pressures, and therefore has a significant impairing effect on the energy efficiency. Paloniitty et al. have studied this problem and introduce several remedies [9]. Furthermore, the DHMPA measurement system was equipped with flow sensors, which are normally not included in similar systems. Like the other pressure loss sources, also these had some impairing effect on the energy efficiency.

When considering high-pressure accumulator, its observed pressure losses after charging were moderate indicating high thermal and overall efficiency of over 90 %. The peak pressures during charging were circa 56 bar and the steady state pressure after thermal stabilization was close to 54 bar. The limits set for accumulator's minimum and maximum pressures were close enough to each other to obtain moderate compression ratio and advantageous thermal efficiency. In addition, in the studied DHMPA system the accumulator fluid volume was high enough to enable the whole work cycle with only one recharge. Smaller sized accumulators would require more frequent re-charging whilst larger sized less frequent re-charging. Choosing a size is a question of optimizing the system's acquisition operation costs.

The fluid used in the measured systems was of viscosity class ISO VG 32. Even though it is a quite low class by nature, the fluid viscosity in DHMPA system remained at relatively high level because of the systems low general pressure losses, which in turn did not cause significant increase in systems temperature, but induced the above mentioned relatively high pressure losses in hoses. This is a phenomenon, which could be widely associated with new energy efficient fluid power systems. The power losses in these systems may be so low that the fluid either achieves balance temperature very slowly or the final temperature might remain close to the surrounding temperature. The fluid temperature was not continuously recorded during the measurements

presented in this paper, but it was monitored occasionally and remained at level 20–25 °C because of the short measurement runs.

Despite the above described shortcomings in the measurement system, the energy efficiency of DHMPA system was significantly higher than that of LS system, and the reduction of consumed electric energy was 72–74% depending on the loading of the measured systems. In the case where hose and volume flow sensor losses are omitted in both systems, the estimated energy consumption in DHMPA would still be only circa 53% of the energy consumption in an LS system with perfectly matched flow rate.

5. CONCLUSIONS

This study presents experimental results of digital hydraulic multi-pressure actuator (DMHPA) system and LS system applied to a boom swing function of 1.1 tonne JCB Micro excavator. In DHMPA system, the major sources of power losses were identified to be the pressure losses of on/off-valves controlling the flow between pressure converters and actuator, friction losses in pressure converters, friction and thermal losses in high-pressure accumulator, pressure losses in ducts, and pressure losses in the pressure relief valve of the low-pressure line. However, when compared to the pressure and power losses in LS system, these were minuscule both in absolute value and in relation to system's input power. The measurement results manifested a ~74% reduction in energy consumption when transferring from the valve-based LS system to DHMPA system.

The measurements were conducted with the second prototype of DHMPA and with original system architecture of the excavator, not optimized for the new control method. Therefore even higher system efficiencies are expected to be reached when the system components, mainly hoses and pipes, are dimensioned appropriately. In addition, if the charging process of the accumulator is also optimized to utilize the regions of highest efficiency of electric motor and pump, further enhancements in energy efficiency are expected. These remain to be studied in further research.

ACKNOWLEDGEMENTS

This research was enabled by the financial support of Business Finland (project HHYBRID), the Academy of Finland (project Digital Hydraulic Hybrid Actuators), and internal funding at the Department of Mechanical Engineering at Aalto University.

REFERENCES

[1] Helbig, A. & Boes, C. 2016. Electric hydrostatic actuation - modular building blocks for industrial applications. 10th International Fluid Power Conference, 10. IFK, March 8–10, 2016, Dresden, Germany.

[2] Willkomm, J., Wahler, M. & Weber, J. 2016. Potentials of speed and displacement variable pumps in hydraulic applications. 10th International Fluid Power Conference, 10. IFK, March 8–10, 2016, Dresden, Germany.

[3] Kauranne, H., Koitto, T., Calonius, O., Minav, T. & Pietola, M. 2018. Direct driven pump control of hydraulic cylinder for rapid vertical position control of heavy loads – Energy efficiency including effects of damping and load compensation. BATH/AASME 2018 Symposium on Fluid Power and Motion Control FPMC 2018, September 12–14, 2018, Bath, UK.

[4] Linjama, M., Huova, M., Pietola, M., Juhala, J. & Huhtala, K. 2016. Hydraulic hybrid actuator: Theoretical aspects and solution alternatives. 14th Scandinavian International Conference on Fluid Power, SICFP15, May 20–22, 2015, Tampere, Finland.

[5] Huova, M., Aalto, A., Linjama, M., Huhtala, K., Lantela, T. & Pietola, M. 2017. Digital hydraulic multi-pressure actuator – the concept, simulation study and first experimental results. International Journal of Fluid Power, 18(3), pp. 141–152.

[6] Huova, M., Aalto, A., Linjama, M. & Huhtala, K. 2017. Study of energy losses in digital hydraulic multi-pressure actuator. 15th Scandinavian International Conference on Fluid Power, SICFP'17, June 7–9, 2017, Linköping, Sweden, pp. 214–223.

[7] Linjama, M. & Huova, M. 2018. Model-based force and position tracking control of a multi-pressure hydraulic cylinder. Proceedings of the Institution of Mechanical Engineers, Part I: Journal of Systems and Control Engineering, 232(3), pp. 324–335.

[8] Gottberg, O., Kajaste, J., Minav, T., Kauranne, H., Calonius, O. & Pietola, M. 2018. Energy balance of electro-hydraulic powertrain in a micro excavator. 2018 IEEE Global Fluid Power Society PhD Symposium, GFPS2018, July 18–20, 2018, Samara, Russia.

[9] Paloniitty, M., Linjama, M. & Huova, M. Compact and Efficient Implementation of a Pressurized Tank Line. 2018. 4 p. White paper. Tampere University of Technology. Accessed 20 December 2018. https://tutcris.tut.fi/portal/en/publications/compact-and-efficient-implementation-of-a-pressurized-tank-line(7f0fb156-d5f2-49ea-a2b6-4ba03171f0c8).html.

PHLEGMATIZATION OF A COMBUSTION ENGINE FOR REDUCTION OF TRANSIENT EMISSIONS

MSc Felix Pult, Professor Marcus Geimer
Karlsruhe Institute of Technology
Institute Mobile Machines
Rintheimer Querallee 2, Building 70.04
76131 Karlsruhe, Germany
E-mail: felix.pult@kit.edu

ABSTRACT

The main topic of this paper is the reduction of transient engine-out emissions ejected by diesel engines through phlegmatization. This phlegmatization is supported by a hydraulic hybrid module to prevent system dynamics from dropping. In order to design the hybrid module according to its size and an optimal reduction of transient engine-out emissions, a design tool will be developed. In addition, the structure of a simulation model is presented, which serves to test different hybrid module concepts and creates the data basis for the design tool.

KEYWORDS: Diesel Engine, Phlegmatization, Transient Emission, Hydraulic Hybrid, Design Tool, Simulation

1. INTRODUCTION

Internal combustion engines with diesel direct injection, hereinafter referred to as ICE, are commonly charged by a turbocharger nowadays. This leads to higher specific work. Turbochargers are mainly applied because these use energy of the exhaust gas in contrast to compressors, which have to be powered with energy from the ICE. This results in a higher efficiency due to using the thermal and kinetic energy of exhaust gas mass flow. The turbocharger's boost pressure and due to that the amount of fresh air in the combustion chamber largely depends on the exhaust gas mass flow. This leads to the main problem of an ICE. At the beginning of transient load steps, when high torque is required, not enough exhaust gas mass flow is available. High torque implies a high mass of injected fuel and therefore a large amount of fresh air. Injecting this high mass of fuel is possible. But there is a delay until the exhaust gas flow is high enough to build up the turbocharger's boost pressure and to deliver the required amount of fresh air. This can be named as turbocharger delay or ramp-up time of the air path $\mathrm{T_{AP}}$. Because the ICE depends on the air path, $\mathrm{T_{AP}}$ can also be understood as ICE's ramp-up time. If during transient load steps $\mathrm{T_{AP}} = 0\ s$ applies, i.e. the ICE injects diesel directly, the air-fuel-ratio λ is not in the desired range which causes high transient engine-out emissions. For example nitrogen oxids $(\mathrm{NO_x})$ are 400 % higher and particulates are up to 1000 % higher than in steady state operating conditions . If T_{AP} rises by comparison, transient engine-out emissions will fall [1] [2] [3]. In summary it can be said that the transient behaviour of the turbocharger is the determining time constant when dealing with transient engine-out emissions. [4] [5]

[6] presents a method to reduce this transient emissions. If the ICE does not inject the whole required fuel at the beginning of the load step, but the ICE is given time to reach the load step ($T_{AP} > 0$ s), it will produce more exhaust gas mass flow. So the turbocharger has enough energy to build up the boost pressure for the current injected fuel and ergo λ and the transient emissions are in the desired range. The investigations of [1] confirm this approach. Reaching a load step slower will drop the dynamic of the machine which is not tolerable. To compensate this machine dynamic dropping a hybrid module will be used.

The operating principle of the hybrid module is shown in figure 1. In case of a positive load step (area I) the ICE has to build up the required torque M_{req}. But it can only provide a lower torque M_{ICE} within the ramp-up time T_{AP}. During this time the missing difference torque M_{hyb} will be provided by the hybrid module. This hybrid module can be charged during the negative load step (area II) by recuperation or by load point shift during partial load of the ICE. Together with an intelligent operating strategy, the hybrid module could thus be used for better λ-values into the combustion chamber and thus for lower transient engine-out emissions than in a conventional ICE. Moreover, lower fuel consumption compared to actively assisted turbochargers is possible.

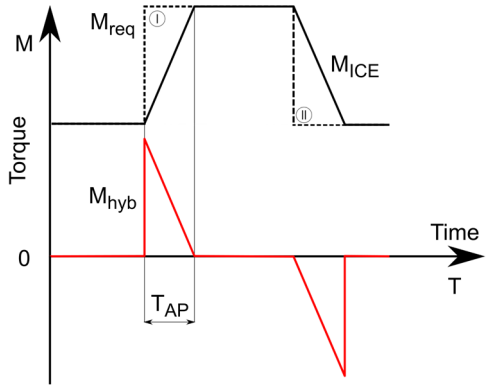

Figure 1. Operating principle of the hybrid module [6]

The presented concept decreases the ICE's dynamic which is called phlegmatization [7]. However, not to the extent that an ICE is operated at constant speed. Instead, only load peaks are buffered. Because of the short phlegmatizated durations of only a few seconds this concept has a low level of phlegmatization according to [7]. Aim of the presented investigations is to find the relationship between the size of the hybrid module and reduction of the ICE's transient engine-out emissions. This relationship should lead to a design tool that is valid for almost all machines and work cycles in the field of mobile machines.

2. HYBRID MODULE

In order to keep the required installation space of the hybrid module as small as possible, an accumulator of minimal size and capacity should be selected. This requires an intelligent operating strategy. Furthermore the hybrid module that is necessary to maintain machine dynamics will be located as close as possible by the ICE to influence its operating points as it will be proposed by [8]. In addition, it is planned to execute the hybrid module as an 'add-on'-solution which forms a unit out of the hybrid module and the ICE. Through this procedure the hybrid module can be defined as an 'emission control strategy' during the Non-Road Transient Cycle (NRTC) type approval which simplifies the compliance with the limits [9]. The NRTC is a cycle that composes several work cycles of different mobile machines. It is used in the EU and the USA for the approval of mobile machines with regard to its emissions [10].

When consulting the ragone plot in [6] it becomes obvious that hydraulic accumulators are the best choice for applications with high power density such as the presented one with a range of $T_{AP} = 0\,s$ to $T_{AP} = 6\,s$. In addition hydraulic accumulators are robust and machine operators and workshop staff are experienced with this technology. So the hybrid modules that are presented in figure 2 and figure 3 use a hydraulic accumulator to store the required energy during T_{AP}. The topology will not change for different ICEs, but depending on the ICE used in different mobile machines, the accumulator and the hydraulic unit will have a different size.

Concept 1 in figure 2 has the advantage that only the hydraulic unit and the accumulator are necessary. But due to the fixed mounting of the hydraulic unit on the crankshaft, the hydraulic unit always rotates with it and thus generates losses, even if the hydraulic unit is completely swivelled back.
In order to minimize the losses, concept 2 in figure 3 was developed. Due to the multi-disc clutch, which is connected to the crankshaft via a spur gear stage, the hydraulic unit only rotates during transient operating conditions. This reduces the losses of the system when the hydraulic unit is not active. Due to the transmission of the spur gear stage, a smaller hydraulic unit and thus a smaller accumulator is also conceivable.
Both presented concepts will be examined later, but concept 1 was chosen for the investigations in chapter 3 because of its simple structure. Further remarks on the concepts can be found in [6].

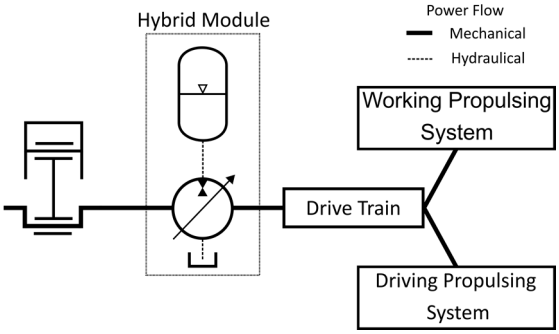

Figure 2. Hybrid module, concept 1

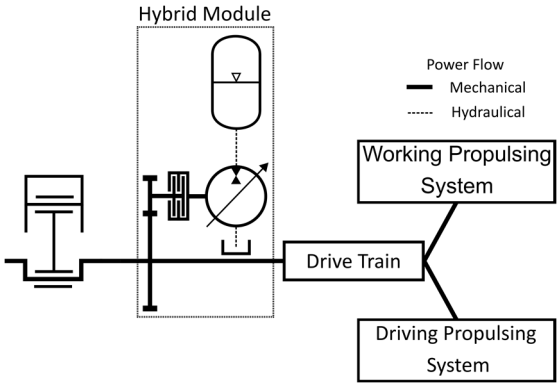

Figure 3. Hybrid module, concept 2

3. DESIGN TOOL

3.1. Concept

For different sizes of mobile machine's ICEs and the machine's work cycles the hybrid module needs to be sized suitable. To simplify the selection regarding size and design of the hybrid module for the manufacturer a design tool will be developed. In this tool the user puts in data as machine size, size of the ICE, work cycle and the desired amount of transient engine-out emissions. At present, the design is only carried out on the basis of particle emissions, since these have a significantly higher effect during transient operating conditions than NO_x emissions [1] [6]. As the first step of design, the size of the hydraulic unit is chosen according to the required torque in work cycle or load step. On base of the transient engine-out emissions to be reduced and other inputs the design tool then calculates the effective accumulator gas volume V_0 as a result. This V_0 can be seen as the equivalent value for the size of the accumulator. The design tool, in turn, is based on diagrams and its underlying data. How to determine this data and diagrams is explained in the following subchapter.

3.2. Preparation of the data basis for two ICEs as an example

For the investigated ICE in [1], which was loaded with a load step from 10 to 40 % maximum load at the considered engine speed, the required accumulator sizes can be determined for different T_{AP} as follows. With a larger T_{AP} the engine will reach the desired maximum load later due to later fuel injection. Accordingly, compared to the load step with $\mathrm{T}_{\mathrm{AP}} = 0\,\mathrm{s}$, a certain amount of injected fuel is missing to maintain the system dynamics. This missing amount of fuel is the energy that the hybrid module must provide. Therefore, the accumulator gas volume V_0 is then determined using a method of [11]. The whole procedure is described in more detail in [6]. In addition to V_0 which depends on T_{AP}, the reduction of transient engine-out emissions $\Delta\rho_{\mathrm{p,tra}}$ for each T_{AP} is given, compare figure 4. This $\Delta\rho_{\mathrm{p,tra}}$ for different T_{AP} are obtained by comparing the particle emissions of selected T_{AP} with the particle emissions for $\mathrm{T}_{\mathrm{AP}} = 0\,s$. This procedure is described in more

detail in [6] as well. Figure 5 results, if only the T_{AP} that creates a significant difference in $\Delta\rho_{p,tra}$ related to adjacent T_{AP} is considered for the ICE in [1]. In addition, a second ICE with a load step from 24 to 85 % maximum load at the considered engine speed is added [3]. More information about the investigated ICEs can be taken from table 1.

Table 1. Information about ICEs under investigation

	Measurements of [1]	Measurements of [3]
ICE's field of application	Commercial vehicles	Tractors
Number of cylinders	8	6
Considered engine speed $\boldsymbol{n_{ICE}}$	2000 rpm	1600 rpm
Displacement	6 l	6,8 l
Maximum torque	759 Nm at n_{ICE}	828 Nm at n_{ICE}
Load step	10 to 40 % maximum load at n_{ICE}	24 to 85 % maximum load at n_{ICE}

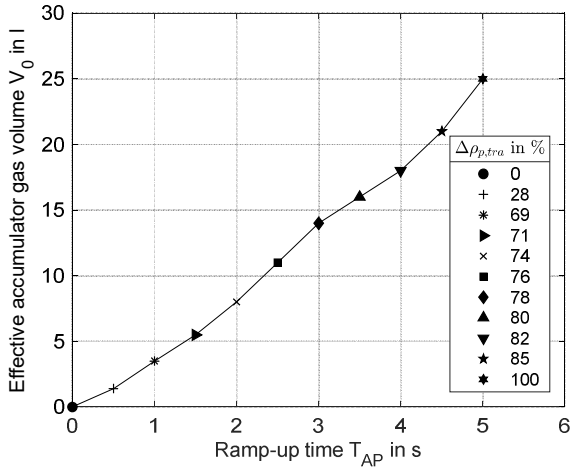

Figure 4. Effective accumulator gas volume for the ICE investigated in [1]

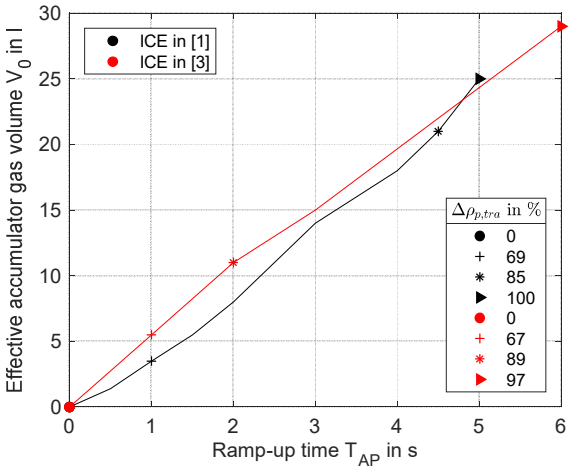

Figure 5. Effective accumulator gas volume for the ICEs investigated in [1] and [3]

In general figure 4 and figure 5 show that with higher T_{AP} and thus with more time for the turbocharger to accelerate, the reduction of the transient engine-out emissions increases as expected. In contrast figure 5 also shows low reduction potential for higher T_{AP}, when a certain T_{AP} has been reached. Here the turbocharger had enough time to accelerate and the combustion is mainly filled with the necessary amount of fresh air. If this certain T_{AP} is exceeded, a significant higher T_{AP} is necessary to reduce the transient engine-out emissions in a proper way and so the use of the hybrid module becomes ineffective.

Figure 5 shows that for the ICE in [1] for $T_{AP} = 1$ s the transient engine-out emissions can be reduced by 69 % and $T_{AP} = 1{,}5\,s$ allows to reduce the emissions by 71 %. A significant reduction of transient engine-out emissions with 85 % reduction only appears at $T_{AP} = 4{,}5$ s. The situation with the investigated ICE by [3] is very similar. At $T_{AP} = 1\,s$ the reduction of transient engine-out emissions is 67 %. The difference to the next considered $T_{AP} = 2$ s is clearly smaller. Thus it can be said that for both investigated ICEs $T_{AP} = 1$ s is decisive for the design of the hybrid module.

Generally it should be noted that the T_{AP} with the greatest difference in reduction of transient engine-out emissions to the previous T_{AP} and with the least difference in reduction of transient engine-out emissions to the following T_{AP} is the T_{AP} which is used as the basis of design. For this T_{AP} the accumulator's V_0 is then selected from the diagram in figure 5.

The comparison of the two ICEs regarding to their performance data in table 1 and to the correlation of V_0 and T_{AP} in figure 5 shows the following: On the one hand the two ICEs are quite similar in terms of their performance data but the ICE in [3] needs a slightly larger accumulator. This results from the significant larger load step that the ICE in [3] has to provide. Besides, the ICE in [3] has a slightly larger displacement and higher maximum torque. Hence a little more energy is needed during the ramp-up time T_{AP}.
On the other hand the ICE in [3] reduces the transient engine-out emissions more at $T_{AP} = 2\ s$ than the ICE in [1] at $T_{AP} = 4{,}5\ s$. This is because the ICE in [3] is under higher load from the beginning of the measurements, which leads to a higher basic quantity exhaust mass flow. As a result the ICE produces high exhaust mass flow faster which allows the turbocharger to deliver the right amount of fresh air into the combustion chamber more quickly. Thereby higher quantities of transient engine-out emissions can be reduced to a shorter T_{AP}.

The made investigations turn out that for different ICEs with different work cycles there are relationships between V_0, T_{AP} and the reduction of the transient engine-out emissions $\Delta\rho_{p,tra}$, which indicates characteristic curves of each ICE. But with the background that a general design tool has to be developed, the issue arises that from data of only two ICEs this design tool cannot be developed. How this can be done by using more data is explained in the next subchapter.

3.3. Preparation of the design tool

As explained in the subchapter before, a design tool, which should determine the right accumulator size to reduce transient engine-out emissions needs more than two measurements as data base. Especially for reaching universal validity in the field of mobile machines. So many different ICEs, mobile machines and their work cycles or load steps on this mobile machines have to be investigated. Each ICE has to perform the same load steps and additional work cycles matching the ICE. With this data it is possible to generate the relationships shown in figure 4 and figure 5 in a general way.
From the existing measurement data, characteristic curves for the investigated ICE need to be developed, which can be distinguished from each other by dividing the ICE into ICE class-specific key figures. This key figures can be calculated out of the machine data that are provided by the user via the input mask. Possible data as basis for the key figures can be the machine's work cycle or displacement and torque as discussed in subchapter 3.2 or the speed range, power or the mean effective pressure p_{me} which combines several of the machine data mentioned above. The valance of each machine data still needs to be determined, but subchapter 3.2 suggests that maximum torque and displacement definitely have an influence.

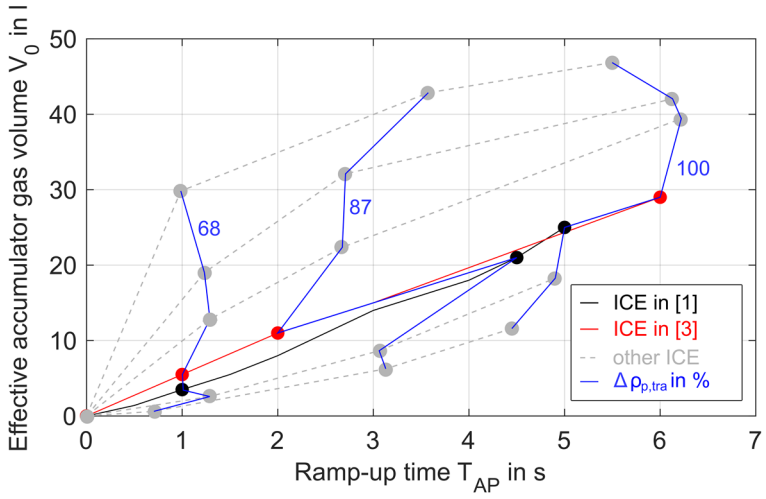

Figure 6. Scheme of the design tool

With the determined characteristic curves it is possible to develop the diagram shown in figure 6. In general, figure 6 is structured like figure 5. But in addition to the ICEs in [1] and [3], the characteristic curves of other fictitious ICEs were added in order to help explain the scheme of the design tool. These are represented by the grey dashed lines. If the characteristic curves are higher than those of the known ICEs, these are probably

larger ICEs with more torque. Conversely, the ICEs represented by the characteristic curves below those of the known ICEs have a lower torque. By interpolating between the points on each characteristic curve describing the same reduction of transient engine-out emissions, the blue lines appear. So figure 6 can be created out of the characteristic curves and the blue lines which represents a map.
In addition, it may be necessary to create several diagrams similar to figure 6 for different machine types or their work cycles. For the design process the design tool then selects at first the appropriate map for this work cycle based on the user's input regarding the work cycle. As a second step the appropriate characteristic curve regarding the investigated ICEs will be chosen by the design tool as it is described above. In this way, the relationship between effective accumulator gas volume V_0 and ramp-up time T_{AP}, i.e. reduction of transient engine-out emissions $\Delta\rho_{p,tra}$ for specific ICEs and mobile machines, can be established with the map.

The insight from chapter 3 is that the relationship between V_0 and $\Delta\rho_{p,tra}$ can be represented by the developed design tool. But at the same time this means a large amount of measurement data is required in order to create the data basis for the design tool. Due to the requirement to develop a generally valid design tool, a wide variety of ICE sizes and types that have been subjected to several load steps and work cycles that match the ICE needs to be examined. This is ineffective, which is why it is necessary to simulate the missing data basis.

4. SIMULATION MODEL

On the one hand the simulation model should be used to examine different types of hybrid modules and different operating strategies for their suitability in reducing the transient engine-out emissions. On the other hand, with the help of the simulation model and together with further measurements, the data basis for the preparation of the design tool is to be created, as already announced.
The main model will be built with the simulation environment Matlab Simulink from Mathworks. The ICE, as part of the whole model, will be built in the simulation environment Cruise M from AVL [12]. The simulation model's structure will be presented in the next subchapters.

4.1. Main model

The main simulation model consists of five main elements in summary. Due to the good ability to represent these elements in the blocks of Simulink, it is used to build up the main simulation model. The individual blocks represent functions and properties of the real components as followed: An input for load steps and work cycles. If a cycle with driving speeds of the real machine is entered to the input, the machine's drive train has to be considered. If the cycles are from an engine test bench the machine's drive train is not necessary, however the crankshaft is always part of the simulation model. So the second block represents the crankshaft, which is connected to the input, via the drive train if necessary. The next two blocks are the hybrid module and the ICE, connected and controlled by the fifth block, the machine control. Out of this five blocks the simulation model's structure is presented in figure 7.

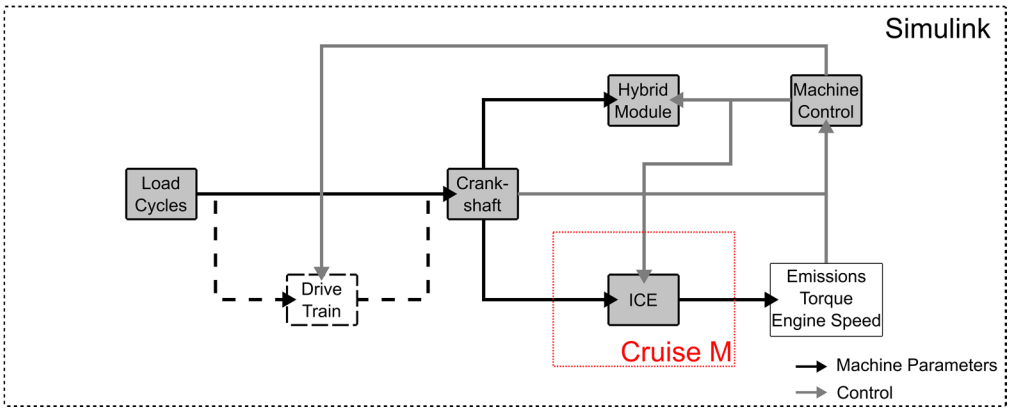

Figure 7. Structure of main simulation model

In order to better understand the power flows and the machine control within the simulation model, these are now briefly explained. The load, i.e. the torque, is applied to the flange of the crankshaft via load cycles. If necessary, torque and speed of the load cycle are transmitted to the torque and speed at the crankshaft via the drive train, equivalent to the real vehicle under investigation, as discussed above. This torque is then distributed by the machine control to the hybrid module and the ICE in such a way that the ICE generates less or no transient engine-out emissions during transient operating conditions. The machine control uses a control loop to check whether the ICE and hybrid module could provide the required torque and how good the reduction in transient engine-out emissions is. If the target values are not reached, operating parameters such as injection quantity, timing or the distribution of the torque demand to the hybrid module and ICE must be adjusted. In any case, the engine speed is determined from the comparison between the required and provided torque and returned to the crankshaft's flange.

4.2. Hybrid module

After the basic structure has been presented in chapter 2, the hybrid module is now explained in more detail. Currently, the introduced concepts are available for selection of the hybrid module, which are to be tested simulatively. As the structure of the concepts shows, the proportion of hydraulics within the simulation is very low. Therefore, the simulation of hydraulics in Simulink, executed by Simscape, should be sufficiently accurate and fast. However, the exact simulation of the individual components is not dealt with here. Instead, the interaction between the hybrid module and the machine controller is discussed. The hybrid module receives a signal from the machine control when and how much torque is needed for the drive. Accordingly, the hydraulic unit must swivel out and the accumulator is discharged. It is very important to ensure that the hydraulic accumulator is charged and discharged in such a way that there is always enough energy available to reduce transient engine-out emissions. For that an operating strategy must be developed and implemented in addition to the signals of the machine control.
There are two concepts for the hybrid module presented in chapter 2. In addition, further hybrid modules will be tested for their suitability. So standardized interfaces to the rest of the simulation model (control, torque, speed on crankshaft) must be defined in a way that the "exchange" of these hybrid modules in the simulation model is easy.

4.3. Internal combustion engine

In contrast to the hybrid module, a different simulation environment is chosen for the ICE simulation. This is Cruise M from AVL as it has been said above. However, the simulation within the ICE can be transferred to a block, which in turn can be integrated into Simulink, so that the structure explained in subchapter 4.1 remains the same. Cruise M has a similar structure to Simulink and it is particularly interesting for the system to be simulated because it contains a block called MoBEO. MoBEO simulates the cylinder and the combustion processes in it. For the simulation of these processes, information on the supply of fresh air and diesel to the cylinder as well as information about the environment in the form of inputs are required. Examples of these inputs are air mass flow, boost pressure, injection quantities, injection timing, ambient temperature and engine speed of the drive train. From this, MoBEO then determines torque, emissions and fuel consumption.

MoBEO is choosen here for the following reasons: As already mentioned, one of the tasks of the simulation model is to investigate several different hybrid modules with regard to their influence on the reduction of transient engine-out emissions. For this task, MoBEO has a relatively low computation time in relation to the accuracy because it is a semi-physical model, coupled to a 1D gas path [13]. Thus MoBEO is real-time capable and could be used for HiL applications [14]. Because the ICE requires information about the air path and injection to calculate the processes within the cylinder, these components must be parameterized accordingly for each ICE under investigation. However, this is relatively easy with parameterization tools using measurement data. The last reason that favoured the choice of Cruise M was already mentioned above: by converting the entire Cruise M model into a Simulink block, the integration into the simulation model in Simulink can be realised.

After the functionality of Cruise M and MoBEO and their needs for the simulation are explained, which led to the selection of this simulation environment, the simulation model of the ICE will now be presented. The air path can be divided into fresh air and exhaust gas. Both areas have contact points on the turbocharger, in the exhaust gas recirculation system (EGR) and in the cylinder itself. The fresh air path starts with the air filter, which in turn gets its information from a system boundary and is modelled as a restriction. The air filter is followed by the turbocharger, whose compressor is connected to the turbine via a shaft driven by the exhaust gas mass flow. Since the turbocharger has a decisive influence on the transient engine-out emissions, it must be modelled particularly carefully, among other things with the characteristic diagrams of the respective manufacturer. This is followed by the charge air cooler, which is modeled only as a restriction like the air filter for keeping the computing time to a minimum. The EGR, which combines fresh air and exhaust gas like the turbocharger, is represented by a valve. If required, this can add a desired amount of exhaust gas to the fresh air in order to reduce the oxygen content and thus the reactivity of the mixture. The fresh air then enters the cylinder, which is represented by the MoBEO block. The MoBEO block receives information from the engine control about the injection quantities, times, pressures and other parameters suitable for the load requirement. The given information are used to simulate torque, transient engine-out emissions and fuel consumption provided by the ICE. The torque is sent from the crankshaft to the Simulink model, where the load requirement comes from. The exhaust gas mass flow passes through the EGR and the turbocharger turbine to the exhaust gas flap. For simplicity's sake, this is modelled as a restriction again. This is where the exhaust gas mass flow and thus also the simulation model of the ICE end at another system boundary.
The engine control compares the required torque with the provided torque and adjusts the control signals for injection and air path accordingly in the sense of a PID controller. The resulting transient engine-out emissions also have an influence on the engine control. Its signals are also transferred to the higher-level machine control in Simulink to adjust the torque distribution between the ICE and the hybrid module.
All components and their described relations are shown in figure 8.

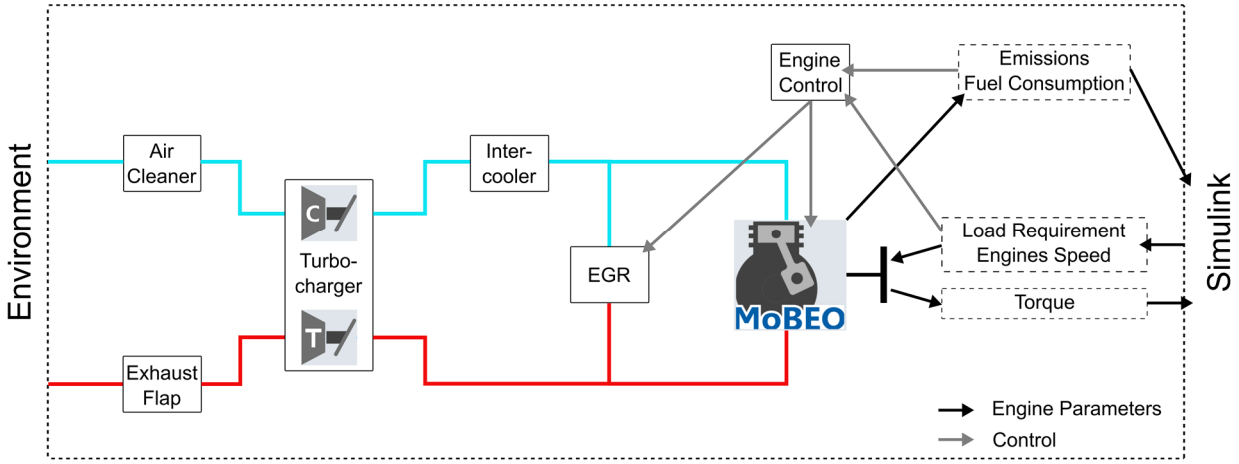

Figure 8. Structure of ICE's simulation model

5. CONCLUSION

A method was explained in which the internal combustion engine (ICE) is given more time to reach the required load level in order to reduce transient engine-out emissions. The resulting reduced dynamics of the ICE are to be provided by a hydraulic hybrid module so that the system dynamic does not drop. For this method two concepts for a hydraulic hybrid module were presented. The hybrid modules have to be designed accordingly for different ICEs, machines and work cycles, therefore the idea for a design tool was born. The idea for the design tool was tested for the measurement data of two ICEs. It was shown that the idea of the design tool is target-oriented. In addition, it became clear that each ICE class can be characterised by a certain key figure that still is to be determined. The maximum torque and displacement were determined as influencing variables. Many measurements would therefore be necessary to create the design tool. This does not make sense in

terms of time or cost. Therefore, the structure for a simulation model was presented, with which it is relatively easy to test different hybrid modules and operating strategies on different ICEs and for different work cycles using standardized interfaces. This simulation model is also used to create the data basis for the design tool.

6. OUTLOOK

This paper gives an outlook on a design tool and a simulation model for the reduction of transient engine-out emissions using a hydraulic hybrid module. Therefore, the next steps are the creation of the main simulation model as it is shown in figure 7 and the evaluation of its results. For this purpose, the hybrid modules and the periphery of the machine with the machine control and the integration of the load cycles must be created. On the other hand, the simulation model for the ICE in Cruise M must be parameterized for different ICEs. In order to achieve the goal of the smallest possible accumulator, operating strategies must also be developed and implemented in the simulation model.

In the introduction in chapter 1, it was pointed out that the entire investigations so far only apply to particulate emissions. The investigations must therefore be extended to NO_x emissions in order to be able to guarantee the universal validity of the design tool in the field of mobile machines.

In addition, measurement data or measurements of other ICEs are required for the parameterization of the ICE simulation model. With the corresponding simulation results and measurement data, the design tool for different ICEs and load cycles can then be created. In order to be able to distinguish individual ICE classes from each other in the design tool, it is necessary to define a characteristic ICE class key figure.

Ultimately, the design tool will be used to establish the general relationship between accumulator size and transient engine-out emission reduction and to design a hybrid module suitable for a particular machine. Thus it is possible to reduce the transient engine-out emissions of the machine by up to 100% by providing only a few details about the machine to be optimized. This reduction only requires a comparatively compact hybrid module, which in turn could make part of the exhaust aftertreatment system obsolete.

ACKNOWLEDGMENTS

The project is funded by the Deutsche Forschungsgemeinschaft (DFG, German Research Foundation) - GE 2022/14-1. Without this support the shown investigations would not be possible to do. In addition the authors want to express special thanks to the Anstalt für Verbernnungskraftmaschinen List GmbH (AVL) for providing the license for simulation tool Cruise M, including MoBEO.

REFERENCES

[1] Hagena J. R., Assanis D. N. & Filipi Z. S. 2011. Cycle-resolved measurements of in-cylinder constituents during diesel engine transients and insight into their impact on emissions. Proceedings of the Institution of Mechanical Engineers, Part D: Journal of Automobile Engineering, S. 1103–1117.

[2] Hagena J. R. Filipi Z. & Assanis D. N. 2006. Transient Diesel Emissions: Analysis of Engine Operation During a Tip-In. SAE Technical Paper 2006-01-1151.

[3] Engelsmann D. & Wachtmeister G. 2013. Untersuchung von Betriebsstrategien für einen elektrisch hybridisierten Traktor mittels einer multiphysikalischen Gesamtfahrzeugsimulation. 4. Fachtagung Hybridantriebe für mobile Arbeitsmaschinen, 20.02.2013, Karlsruhe, S. 1–11.

[4] Rakopoulos C. D. & Giakoumis E. G. 2009. Diesel engine transient operation. 1. edition. London. Springer.

[5] Lüddecke B. 2016. Stationäres und instationäres Betriebsverhalten von Abgasturboladern. Dissertation. Stuttgart. Technische Universität Stuttgart.

[6] Pult F., Engelmann D. & Geimer M. 2019. Hybridisierung einer Verbrennungskraftmaschine zur Emissionsreduktion. 7. Fachtagung Hybride und energieeffiziente Antriebe für mobile Arbeitsmaschinen, 20.02.2019, Karlsruhe, S. 95–115.

[7] Thiebes P. Hybridantriebe für mobile Arbeitsmaschinen. Dissertation. Karlsruhe. Karlsruher Institut für Technologie.

[8] Nagel P. 2016. Entwicklung einer Betriebsstrategie zur Energierückgewinnung in hybriden Mehrverbrauchersystemen. Dissertation. Karlsruhe. Karlsruher Institut für Technologie.

[9] Europäisches Parlament und europäischer Rat. Verordnung (EU) 2016/1628. https://eur-lex.europa.eu/legal-content/DE/TXT/?uri=CELEX%3A32016R1628 Last accessed on: 06.09.2018.

[10] Giakoumis E. G. 2017. Driving and Engine Cycles. 1. edition. Basel. Springer International Publishing.

[11] Korkmaz F. 1982. Hydrospeicher als Energiespeicher. Berlin, Heidelberg. Springer.

[12] AVL List GmbH. 2018. Cruise M release R2018a. https://www.avl.com/cruise-m.

[13] Rau, Nicolas. 2018. Accuracy of Cruise M and MoBEO. phone call with Pult F.

[14] AVL List GmbH. 2018. Cruise M - Software overview. Cruise M Training. Karlsruhe.

SUSTAINABLE LOGGING PROCESS BY A FORWARDER WITH AN INNOVATIVE HYDRO-PNEUMATIC SUSPENSION

M.Sc. Chris Geiger, M.Sc. Julius Happel, Prof. Dr.-Ing. Marcus Geimer
Karlsruhe Institute of Technology
Institute Mobile Machines
Rintheimer Querallee 2, Building 70.04
76131 Karlsruhe, Germany
E-mail: chris.geiger@kit.edu

ABSTRACT

Forest machines enable a fast and save way to harvest the sustainable product wood. Especially forwarders have a huge impact on the forest site, as they have high wheel loads combined with frequent crossings. To enable a sustainable logging process, a new hydro-pneumatic suspended bogie axle is developed. In this paper, the suspended axle is evaluated and compared simulative to a standard in-market bogie axle without any suspension. Therefore, a simulation model of a forwarder with suspended bogie axles was built based on a validated model of an in-market forwarder. Both simulation models were driven over a skid road and a forest road. Dynamic wheel forces can be reduced with the suspended system up to 40 %. The maximum amplitude of vertical accelerations is reduced significantly with the hydro-pneumatic suspension up to one-third of the standard bogie. Furthermore, there is no significant Eigen frequency of the developed system compared to the reference system. As a result, not only soil damage can be reduced but also the working conditions of the operator can be improved with hydro-pneumatic suspended bogie axles.

KEYWORDS: Suspended bogie axle, forwarder, logging, hydro-pneumatic, Forwarder2020

1. INTRODUCTION

For a sustainable logging process in a fully mechanized timber harvesting chain such as the cut-to-length (CTL) logging system soil damages, e.g. rut formation and soil compression caused by a forwarders wheel load, have to be minimized as much as possible [1; 2]. Equalizing dynamic wheel loads with a suspended bogie axle leads to more steady vertical wheel forces [3]. Hence, more drive torque can be applied to the track while concurrently slip decreases, resulting in a lower impact on forest soils. Reducing simultaneously carriage vibrations creates a higher productivity and healthier working environment for the machine operator [4–6].

At the current state of technology bogie axles have established themselves in forestry machines to run over harsh, uneven ground terrain. Nevertheless, several efforts were made to improve forwarders regarding soil protection by implementing different axles, e.g. machines with a crawler chassis or suspended pendulum arms [7; 8]. In the EU project ‘Forwarder2020’ a new hydro-pneumatic suspended bogie axle has been designed to reduce dynamic wheel loads and cabin vibrations [9]. In the following contribution, the development of simulation models with standard and suspended bogie axles including their functionality is described. Based on this models, the new concept of a hydro-pneumatic suspended bogie axle is compared to a standard bogie regarding wheel loads, vertical acceleration and roll angle speed of the front carriage.

2. SIMULATION MODEL OF A STANDARD BOGIE AXLE

An eight-wheeled forwarder is simulated and validated with the Simscape modules of MATLAB Simulink. A standard in-market vehicle is implemented to receive a reference simulation model to investigate and compare new suspension systems. The reference machine is simplified to six rigid bodies and eight tyre model components. Two of the bodies represent the front and the back carriage of the vehicle, which are connected to each other by one rotational joint in driving direction. Hence, an independent roll movement of the front and back carriage is ensured. The pitch angle degree of freedom between the front and back carriage is restricted, so these two bodies have the same pitch movement, as derived from forwarder kinematics. The further rigid bodies represent the four bogies, one at each side of the front and back carriage. These are jointed in transversal direction to allow a pitch movement of each bogie. Any bogie can move independently and is connected by a rotational joint at its middle point to the frame of the vehicle and at the front and back ends to a tyre model, implemented by the Hohenheim Tyre Model [10; 11]. The Hohenheim Tyre Model was developed to investigate wheel forces and wheel deformations of a tractor vehicle, while driving over obstacles. The model is performed by a spoke model to reach a high resoluted calculation of uneven ground terrain [11]. It has been validated at the University of Hohenheim based on measurement data of a tyre test bench [10; 11].

In the present simulation, any tyre model connects the wheel hub of the vehicle with the ground and calculates the relative wheel forces and torques, which are imprinted to the multi body system of the vehicle. The calculation circuit is closed, as the deformation of the tyre resulting from wheel forces and moments, is sent from the multi body to the tyre model. The spokes of the model are orientated in radial direction and allow through the modelling as a non-linear spring-damper-system a good approximation of a real tyre. The interradial elements effect a deformation of the adjacent spoke elements if one spoke is activated, so they have a major importance for the calculation of the wheel forces while driving over obstacles. The geometric tyre parameters are adapted from the forestry machine and the kinematic parameters taken over from the standard tyre model to use the validated parameters of the tyre model. [10; 11]

To validate the present model of the standard bogie system, measurement and simulation results of a previous publication by [12] are compared to the simulation in this paper. The geometry of the vehicle simulated in [12] is derived from a Komatsu forwarder with a maximum loading capacity of 12 tons. Its dimensions are taken over to the presented model of an in-market machine to simulate with the same vehicle parameters. As driving terrain the “Skogforsk” test track was implemented, which is a frequently used test track for forestry machines [12] This track includes a 28-meter track profile with triangular-shaped obstacles of three different heights from 150 mm to 350 mm. The simulation model can be calculated with a full loaded forwarder or an unloaded forwarder, to compare the different impacts on the dynamic wheel forces and the vibration of the vehicle. To keep a constant velocity, the vehicle speed is set a desired value and regulated by a PID-controller for the engine torque. This controller is necessary due to the obstacles, which cause a force against the driving movement of the vehicle, thus a non-regulated vehicle velocity would possibly end in stoppage. By using the described controller, the vehicle velocity oscillates for example in a range of 14 % around the demanded speed of 1.8 km/h, very well comparable with the measurement data in [12].

The rotational speed of any wheel is calculated by one equation of motion, which uses engine torque and rolling resistances of each wheel as input variables and wheel inertia as parameter. Hence, every wheel rotates with the same speed as derived from the real bogie axle systems. The inertia of the whole vehicle translation is calculated by the multi body system. With the velocity-controller there is a simple way to vary the velocity of the vehicle in a parameter study and guarantee a constant speed level.

The resulting bogie angles, exemplarily for the front carriage, are compared in Figure 1 for a validation of the built simulation model with a standard bogie axle. The figure shows an accurate accordance between the already validated simulations of [12], marked as Reference Model, and the results of this paper. The small deviations are considered due to the usage of different tyre models. Bogie angles, roll angles of front and back carriage and pitch angle rate fits as well as shown for the bogie angle of the front carriage.

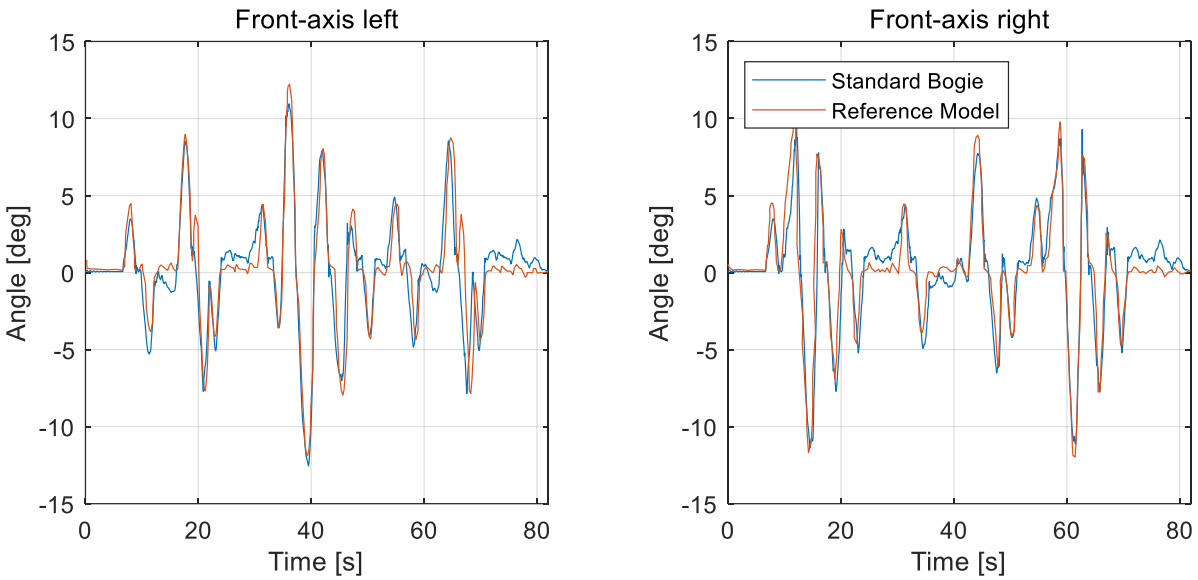

Figure 1. Bogie Angles at the front carriage at the Skogforsk test track driving with 1.8 km/h

With the validated simulation model including a standard bogie axle a possibility was created to implement new suspension systems and compare them to the standard system. Relevant values include for example the dynamic wheel forces or the vertical vibrations of the cabin in respect to the dynamic ground pressures and the driver's comfort. In the next chapter a new suspended bogie system is described and simulated to compare its advantages to the standard bogie.

3. FUNCTIONALITY OF A HYDRO-PNEUMATIC SUSPENDED BOGIE

To increase the productivity of forestry machines and to minimize ground pressure due to lower dynamic wheel forces, a new suspended bogie axle has been designed for a forwarder with a maximum load of 11 tons by the company HSM [9]. This new bogie axle, illustrated in Figure 2, allows the usual bogie motion but includes an additional suspension system. The suspension system is developed as a hydro-pneumatic unit. The expected main advantages of the suspended bogie are beside the decrease of the dynamic wheel forces, less vibrations of the vehicle and a smoother rolling movement of the front and back carriage compared to the standard bogie.

In the suspended bogie, each wheel is connected to its own bogie and is able to rotate individually. Preserving the bogie axle principle, both pendulum arms of each side are attached to each other through a hydraulic cylinder. By blocking this cylinder, the new system reacts nearly like a standard bogie axle. If the cylinders can move freely, a relative displacement between the pendulum arms is possible and a suspension and damping force is generated. Accordingly, the vehicle has four cylinders, while the hydraulic piston side of each cylinder is connected to a pneumatic accumulator, which is prestressed to a required pressure level to reach the desired height of the vehicle frame, compare Figure 3. At each carriage, the left and the right bogie system is connected by a cross circuit, so the piston side of the left cylinder with its accumulator is connected to the rod side of the right cylinder. This allows an increase of the rolling stability as already known e.g. from front axle suspension systems of tractors [3]. Between the piston side and the accumulator an orifice is constructively used as a hydraulic damper to decrease pressure-vibrations.

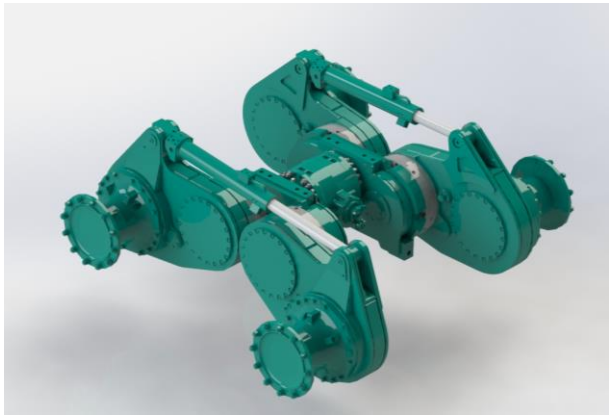

Figure 2. Suspended bogie axle © HSM [9]

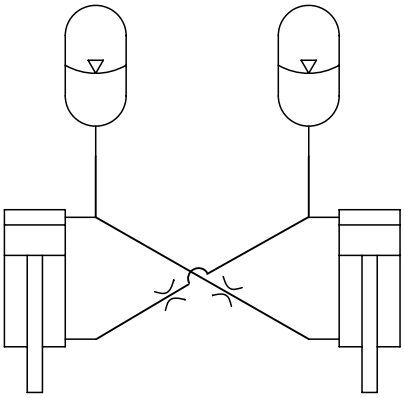

Figure 3: Hydraulic scheme of suspension [9]

To evaluate the advantages of this new system, a model of this suspended axle is implemented to the validated simulation model of the standard vehicle by replacing the standard bogie and keeping the vehicle dimensions of the Komatsu forwarder. The aim is to compare two equal vehicles with only different axle types. All parameters like vehicle mass and the velocity remain the same.

In Simulink the suspension system is build as a multibody and an additional hydraulic system. In contrast to the standard bogie, every wheel is connected to an own rigid body and can move independently, restricted by the connection of the bogie to the vehicle frame and the joint to the cylinder. The front and back carriage are connected as before and may only rotate in the rolling direction. The coupling between the hydraulic and the multi body model is implemented by a force-velocity coupling. The motion of the multi body is sent to the hydraulic system. The reaction force of the actuator is calculated in relation to the hydraulic pressure in cylinders and accumulators, which is given back to the linear joint in the multi body simulation. Figure 4 shows a possible installation situation in the forwarder. Both bogie axles are implement as hydro-pneumatic axles. The vehicle frame and dimensions can be retained with only minor changes.

Figure 4. Assembly situation in the forwarder © HSM [9]

The effects of the new suspension systems are discussed in the following chapter regarding the dynamic wheel forces, vibrations and accelerations of the vehicles front carriage. To give a conclusion and to ensure the comparability to the standard system, the results are always considered based on the validated simulation results of the standard bogie simulation.

4. EVALUATION OF THE SUSPENDED BOGIE

The suspended bogie axle was tested simulative under varying conditions regarding driving speed and road conditions.

4.1. Driving over the Skogforsk test track with 1.8 km/h

The main objectives of the hydro-pneumatic suspended bogie axle are to reduce dynamic wheel loads to improve soil protection as well as minimizing whole-body vibrations for healthier operator working conditions. Hence, in this section dynamic wheel loads, vertical accelerations and roll angles of the front carriage are evaluated to show the potential of a suspended bogie axle regarding the mentioned aims.

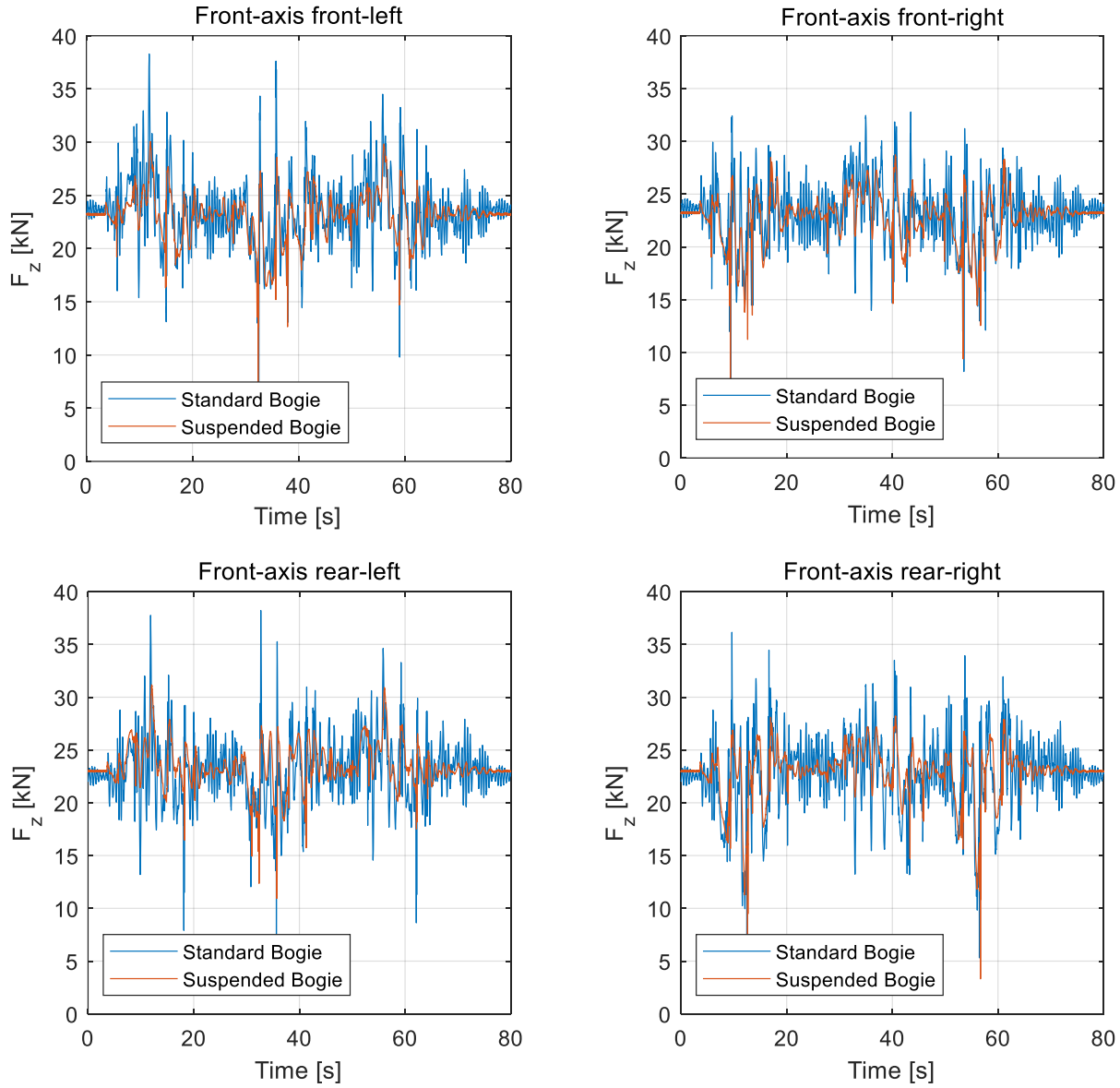

*Figure 5. Wheel forces at the Skogforsk test track driving with 1.8 km/*h

Both machines were driven simulative over the Skogforsk test track [12] with a vehicle velocity of 1.8 km/h. This represents a common driving speed at a skid trail. In Figure 5, wheel loads of the front carriage are displayed over time for the validated in-market machine and the suspended bogie axle while driving over the test track. With the suspended bogie, wheel load fluctuations are reduced significantly. Analysing exemplarily the front-left wheel of the front carriage, the maximum wheel load of the standard bogie is with 38.9 kN at

34.8 s about 62% higher than the static wheel load of 23.7 kN. With the suspended bogie, the maximum wheel load (29.7 kN at 55 s) is about 27 % higher than the static wheel load. Especially when driving over high obstacles (height of 0.35 m) for example between 31 s to 35 s, peak forces are minimized about 10 kN, which equals a reduction about 40 %. Driving fully loaded, this effect is magnified. The decreased fluctuation results also in less stresses for the chassis.

Another major improvement due to the suspended bogie can be seen in Figure 6, where the vertical accelerations of the front chassis are shown for the same passage of the test track. Relative vertical accelerations of the machine with the standard bogie varies between -1.9 m/s² and 2.4 m/s², shown via the blue graph. In comparison to this, the acceleration with a suspended bogie are in the range of -1 m/s² to 0.63 m/s². These describes a reduction to nearly one-third comparing the suspended bogie to a standard system. Same effect can be seen even better by transforming the accelerations from time domain into frequency domain via a standardized, discrete fast Fourier transformation, compare Figure 6. The main frequencies lay between 1.6 Hz and 2.4 Hz with the standard bogie, supplemented with two frequencies around 2.6 Hz and 2.9 Hz. In contrast, there are no main frequencies with the suspended bogie in this range. In general, the frequency spectrum is more distributed, with a minor shift to lower frequencies between 0.5 Hz and 1 Hz.

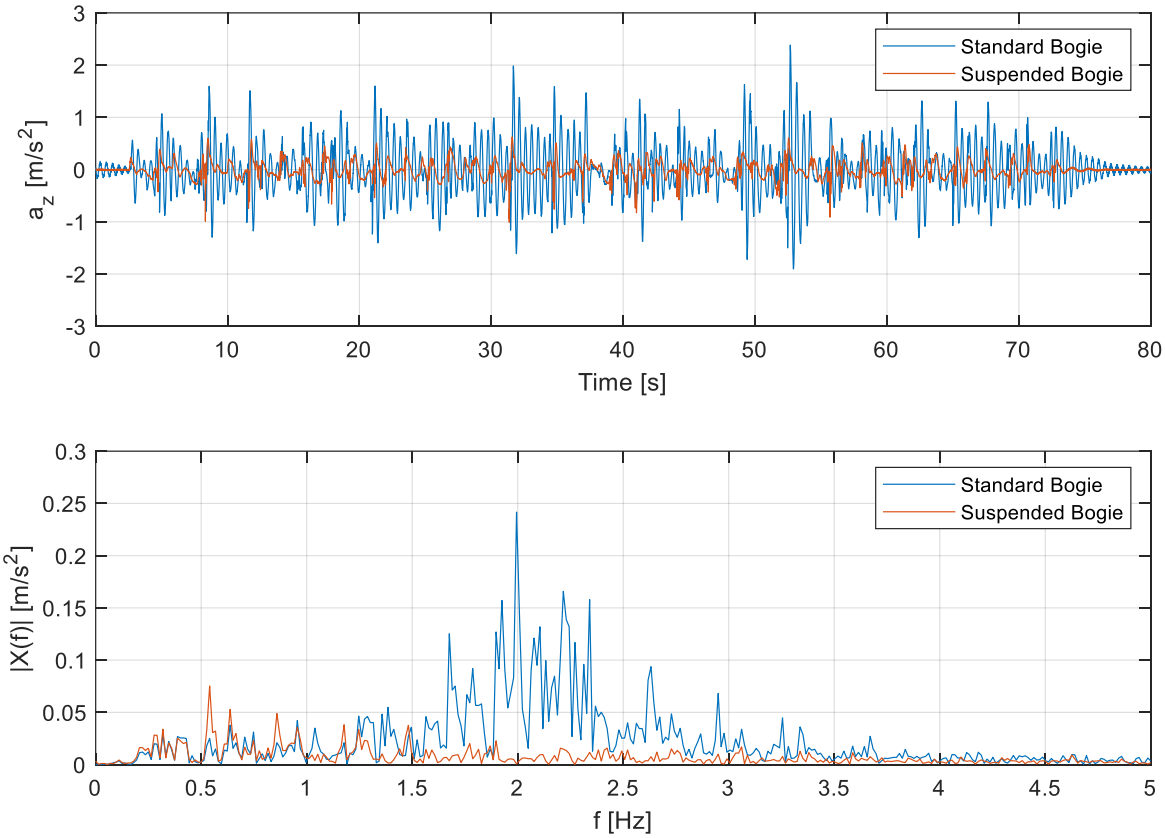

Figure 6. Vertical accelerations of the front carriage at the Skogforsk test track driving with 1.8 km/h

While driving a forwarder over rough terrain, especially rolling movements are uncomfortable for a driver. Evaluating this, the roll angle speed in time- and frequency-domain is chosen based on [12]. The suspended bogie with its used tuning of the hydraulic circuit shows almost the same behaviour as the standard system. During maximum peaks of roll angel speed, compare t = 12 s and t = 57 s at Figure 7, the suspended bogie system has a slightly higher speed, resulting in a minor increase in roll angle. Taking the frequency domain of the roll angle speed in account, see Figure 7, both systems have their main frequencies around 0.25 Hz and 0.7 Hz. Considering this, there is no improvement in roll angle speed with the suspended bogie axle at low frequencies, in contrast to an advantageous behaviour regarding vertical accelerations at higher frequencies. The effect is based on the cross-connection of the left and right hydraulic cylinder, compare Figure 3. If one

cylinder is moving at low speed, e.g. the left cylinder retracts, there is an oil-flow towards the rod chamber of the right cylinder, resulting in a retracting motion of the latter. These simulation results for the suspended bogie axle can be compared to a six-wheeled pendulum arm forwarder, which driving over the same test track at same speed [8]. With the concept presented in [8], maximum roll angle could be decreased only slightly, which is due to the low-frequency excitation.

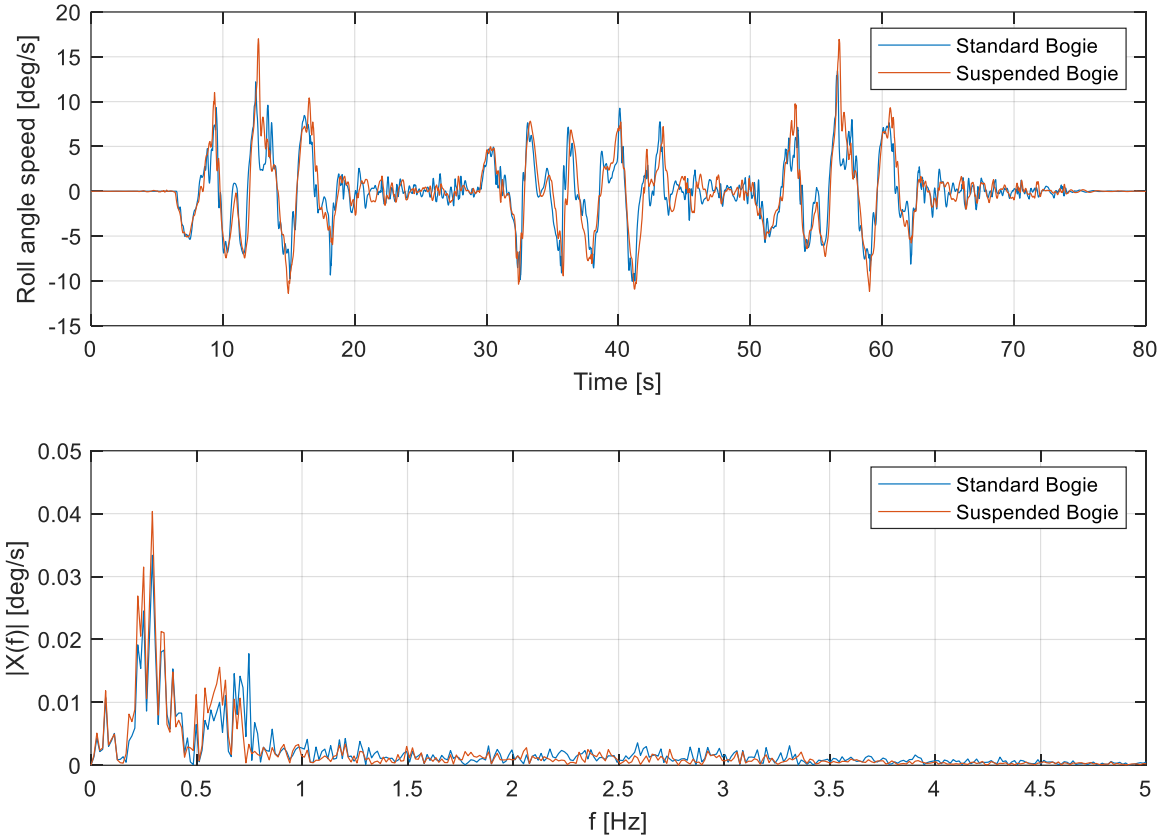

Figure 7. Roll angle speed at the Skogforsk test track driving with 1.8 km/h

4.2. Driving over a forest Road with 15 km/h

Driving loaded from the skid road to the landing area and unloaded reverse has a high proportion of time especially for long hauling distances. A test track which is supposed to be similar to a forest road is derived by downscaling the Skogforsk test track in vertical altitude with a factor of 6. This track is run over by both machine models at a vehicle velocity of 15 km/h. An advantage of the hydro-pneumatic suspended bogie axle while driving on forest roads with high speed is that wheel forces as well as vibrations are reduced.

As on the skid road, dynamic wheel forces are minimized significantly with the presented concept, compare Figure 8. Although only visualized for the front wheel of the front bogies in figure 8, the effect can be observed for each wheel. Another difference between both concepts is the varying damping behaviour after leaving the bumpy forest road, see the interval between 10 s to 14 s at Figure 8 and Figure 9. While the machine with standard bogie axles is still pitching and rolling, both motions are damped fast by the hydro-pneumatic suspension.

Furthermore, the amplitude of vertical accelerations is noticeable lower compared to a forwarder with standard bogie axles, see Figure 9. This results from the individual movement of each wheel, similar to a single-wheel suspension in the passenger vehicle sector. The frequency spectrum shows a clear peak at 2 Hz and a band between 2.3 Hz and 2.8 Hz for the standard bogie, whereby it has certain similarities with the frequency spectrum shown in Figure 6 for the Skogforsk test track. Nevertheless, a shift towards higher frequencies can be observed.

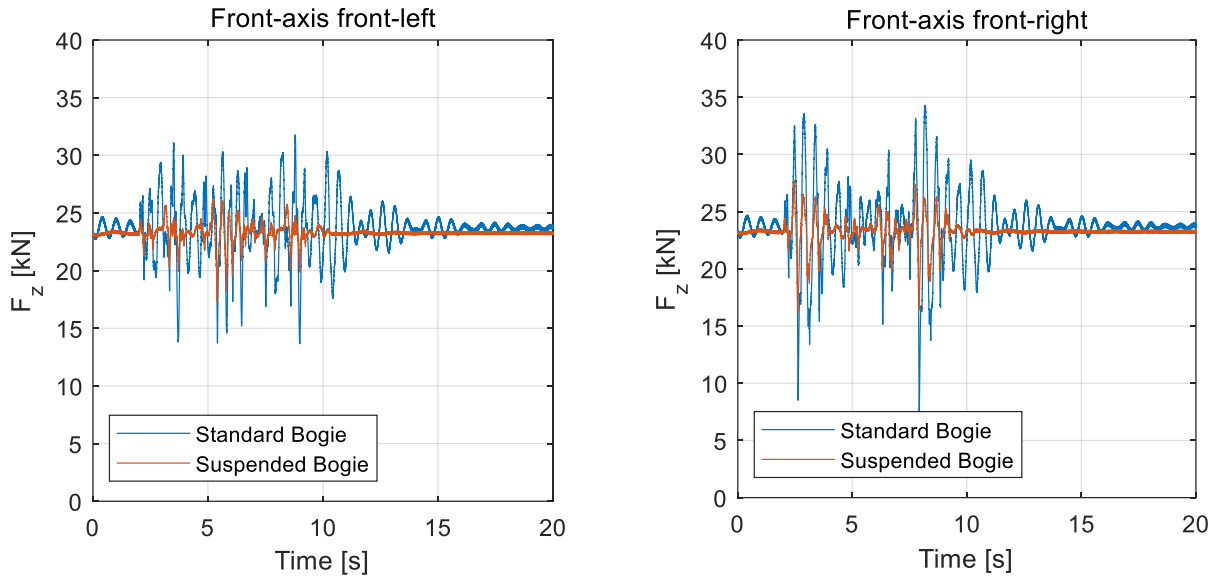

Figure 8. Wheel forces at a forest road driving with 15 km/h

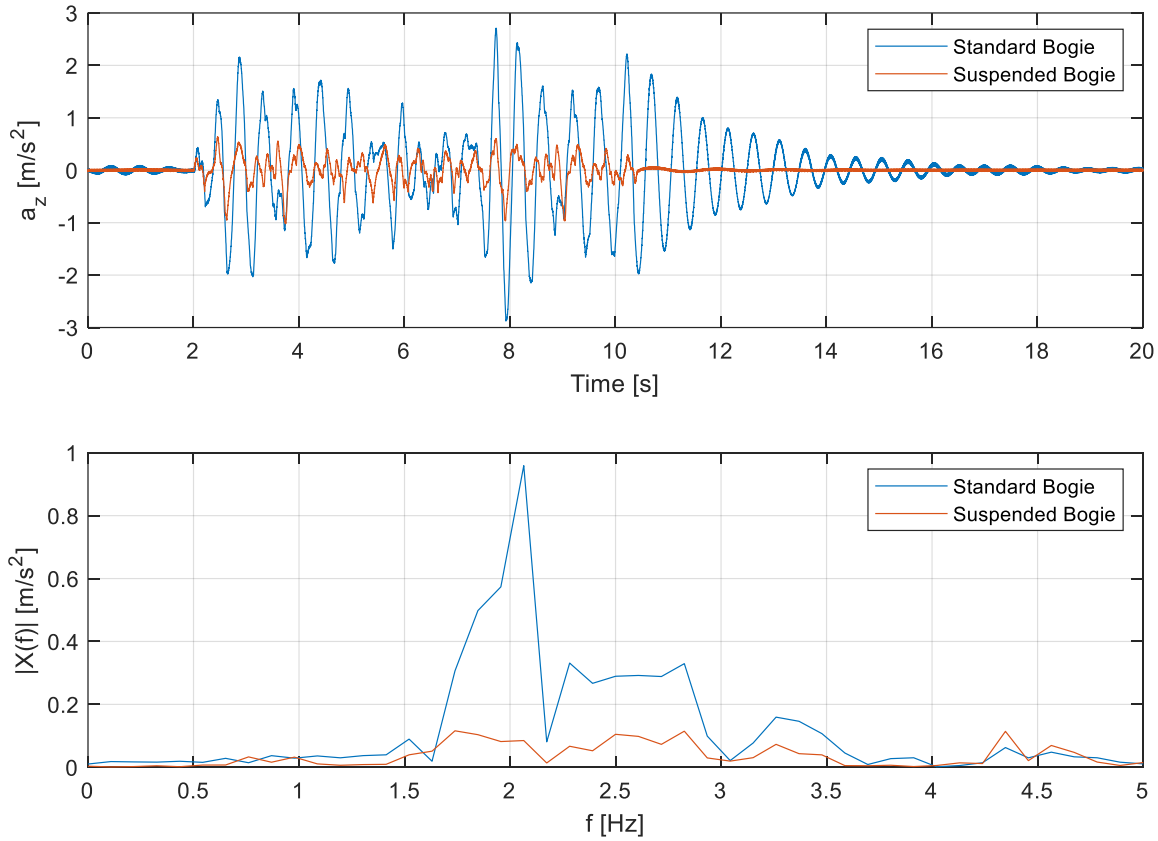

Figure 9. Vertical accelerations of the front carriage at a forest road driving with 15 km/h

In Figure 10, roll angle speed is compared. In difference to Figure 7, where the obstacles were higher, the maximum amplitude is obviously lower. While driving at the forest road, a suspended machine is rolling less then a standard forwarder, resulting in lower maximum amplitudes of the roll angle speed, compare Figure 10 for example at 3.2 s. In this case, main frequencies of roll angle speed varies in the range of 1.8 Hz to 3 Hz, significantly higher compared to the application scenario during driving on a skid road. Due to the higher vehicle

velocity, a transfer towards higher frequencies is logical. Under these driving conditions, a reduction of the maximal roll angle speeds up to 35 % is possible with suspended bogie axles. Obviously, suspension systems show higher effects when impinged with higher-frequency excitations.

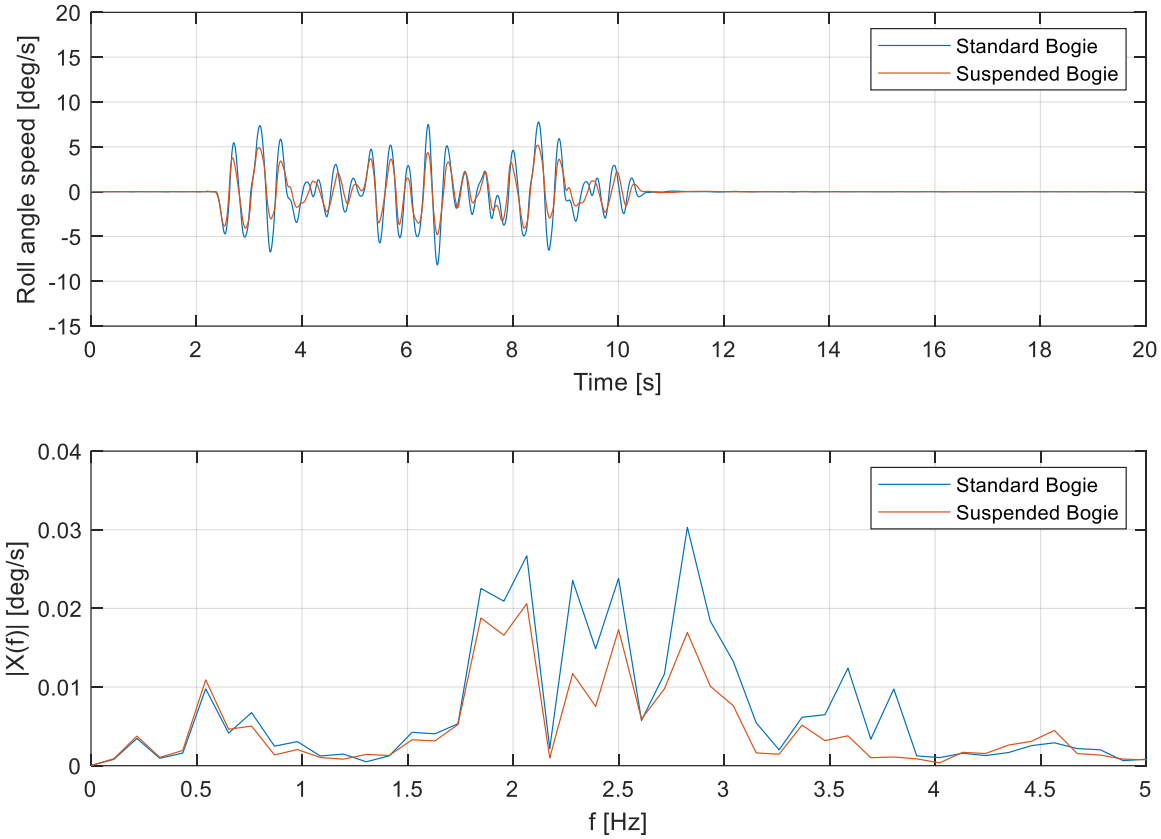

Figure 10. Roll angle speed a forest road driving with 15 km/h

5. CONCLUSION

Regarding the requirements of today's forestry machines, in this paper a hydro-pneumatic suspended bogie axle for a forwarder has been tested simulative and compared to a standard bogie axle for driving conditions on a skid road and a forest road. Therefore, a model of a forwarder with standard bogie axles was built and validated. Based on this, an additional model of a machine with hydro-pneumatic suspended bogie axles was set up and the functionality of the suspended system explained. Dynamic wheel loads can be decreased up to 40 % with the new concept in both cases. Furthermore, accelerations in vertical direction are reduced to one-third compared to an in-market machine. Evaluating this result not only in time domain but also in frequency domain shows no significant Eigen frequencies of a machine with suspended axles. Roll angle speed of a suspended machine is decreased while driving fast on a forest road.

Summarizing, a forwarder with hydro-pneumatic suspended bogie axles leads to a more sustainable logging process in relation to ground pressures, rut formation and driver's comfort. Especially the significantly reduced exposure of the machine operator to accelerations in a harmful frequency range improve working conditions.

6. OUTLOOK

A crucial advantage of the presented suspension system is, in contrast to other mentioned suspension possibilities, the option to use bogie tracks for wet surfaces. Blocking the hydraulic cylinder, the behaviour of

a standard bogie axle can be achieved. Therefore, a forwarder with this hydro-pneumatic suspension can be used under varying operational conditions.

The presented suspension system is a passive concept. With an active suspension, the ability to reduce accelerations and roll angle speed especially during low-frequent excitations can be improved. In addition, different test tracks can be investigated to evaluate the best parameter set for a specific machine and their working conditions. Furthermore, building-up a prototype machine with these hydro-pneumatic suspended axles would allow a validation of the expected effects shown with the simulation results.

7. ACKNOWLEDGEMENT

This project has received funding from the European Union's Horizon 2020 research and innovation programme under grant agreement No 727883.

REFERENCES

[1] Rieppo, K.; Kariniemi, A. und Haarlaa, R.: Possibilities to develop machinery for logging operations on sensitive forest sites. Helsinki: University of Helsinki 2002.

[2] Heubaum, F.: Bodenscherfestigkeit auf Rückegassen. In: Forst & Technik 8 / 2015.

[3] Bauer, W.: Hydropneumatische Federungssysteme. Berlin, Heidelberg: Springer-Verlag 2008.

[4] Burström, L.; Nilsson, T. und Wahlström, J.: Whole-body vibration and the risk of low back pain and sciatica: a systematic review and meta-analysis, International archives of occupational and environmental health 88 (2015) H. 4. S. 403–418.

[5] Punnett, L. und Wegman, D. H.: Work-related musculoskeletal disorders: the epidemiologic evidence and the debate, Journal of electromyography and kinesiology : official journal of the International Society of Electrophysiological Kinesiology 14 (2004) H. 1. S. 13–23.

[6] Rehn, B.; Nilsson, T.; Olofsson, B. und Lundström, R.: Whole-body vibration exposure and non-neutral neck postures during occupational use of all-terrain vehicles, The Annals of occupational hygiene 49 (2005) H. 3. S. 267–275.

[7] Kuratorium für Waldarbeit und Forsttechnik e.V.: OnTrack – Forwarding the Future. https://www.kwf-online.de/index.php/forschungsprojekte/forschungsarchiv/ontrack/518-ontrack-kurzfassung?highlight=WyJvbnRyYWNrIl0=, Zugriff am: 14.12.2018.

[8] Skogforsk: Xt28 Pendelarmsskotaren. https://www.skogforsk.se/contentassets/d120dff37a2c4e5197d211a873dc1ab8/tsg-xt28_2016.pdf, Zugriff am: 12.12.2018.

[9] Hohenlohe-Waldenburg, F. P. z.: Tandemachse DE102016014004A1.

[10] Witzel, P.: Ein validiertes Reifenmodell zur Simulation des fahrdynamischen und fahrkomfortrelevanten Verhaltens von Ackerschleppern bei Hindernisüberfahrt: Dissertation Universität Hohenheim 2016.

[11] Witzel, P.: The Hohenheim Tyre Model: A validated approach for the simulation of high volume tyres – Part I: Model structure and parameterisation, Journal of Terramechanics 75 (2018). S. 3–14.

[12] Ismoilov, A.; Sellgren, U. und Andersson, K.: Development of dynamic base model of a bogie suspended forwarder, Proceedings of the Institution of Mechanical Engineers, Part K: Journal of Multi-body Dynamics 231 (2017) H. 2. S. 357–371.

Linear Hybrid Dynamical Control of Digital Displacement Units

Niels H. Pedersen, Per Johansen, Torben O. Andersen
Department of Energy Technology, Aalborg University
Pontoppidanstraede 111, 9220 Aalborg East, Denmark
E-mail: nhp@et.aau.dk, pjo@et.aau.dk, toa@et.aau.dk

ABSTRACT

This paper concerns development of control strategies for energy efficient fluid power digital displacement machines® (DDM). The DDM technology yields an efficient reduction in displacement levels by deactivating independently cylinder pressure chambers by electromagnetically controlled on-off valves. Since the continuous dynamics of each pressure chamber is activated/deactivated discretely at fixed shaft positions, the DDM dynamics belongs to the class of hybrid dynamical systems. However, control development for hybrid system is in general very complex due to the use of Lyapunov stability theory for both continuous and discrete systems. This paper shows stability based on hybrid dynamical theory for a linear continuous plant actuated by a DDM, which dynamics has been approximated by a linear discrete model. It is shown that the control design problem is identically to that of a fully discrete description of the system based on a zero-order-hold approximation of the continuous design. Furthermore, the problem of having a nonlinear plant, multiple DDMs or an angle dependent asynchronous control update rate for a variable speed DDM is addressed, where measures of stability analysis is discussed.

KEYWORDS: Fluid Power, Digital Displacement, Hybrid system, Control model, Event-driven

1 INTRODUCTION

Development of control strategies for digital displacement machines (DDM) is considered an important aspect with respect to ensuring proper operation of the hydraulic system actuated by the digital pump/motor units. However, this is a complicated task since the continuous dynamics of each pressure chamber is activated/deactivated discretely as function of the shaft angle. As a result, the system dynamics belongs to the class of hybrid dynamical system, interconnecting continuous and discrete dynamics. This may explain why most state-of-the-art control strategies neglect the dynamics of the DDM when designing the control system for the actuated plant [1, 2, 3, 4, 5, 6]. A continuous approximation of a DDM is proposed by Pedersen et. al [7], but is only valid for a relatively high number of cylinders, at high displacements and for relatively low frequency excitations. A discrete approximation has been derived by Johansen et. al. [8] and is used for closed loop control in [9, 10, 11]. Similar to the continuous model, the

discrete model is only valid for a relatively high number of cylinders, high displacements (linearly). Additionally, it is only applicable for a single machine with fixed shaft speed. To increase the validity and accuracy, hybrid dynamical models have been proposed by Pedersen et. al [12, 13] and Sniegucki et. al [14]. Model based control design for hybrid systems is based on Lyapunov stability theory for both nonlinear continuous and discrete system and is thus challenging even for relatively simple systems [15, 16, 17, 18, 19]. This paper presents a linear representation of the hybrid dynamical formulation presented in [12] and shows stability of a linear continuous actuated plant with use of Lyapunov stability theory for hybrid systems. Since the considered hybrid system consist of linear continuous and discrete state equations, a linear state feedback controller is sufficient to guarantee stability. It is shown that the control tuning problem may be performed by classical DLTI pole placement method, where the continuous plant dynamics is approximated with a zero-order-hold input. Furthermore, the challenge of having a state (angle) dependent sampling rate, nonlinear continuous plant and multiple DDMs is discussed as further work.

2 NONLINEAR MATHEMATICAL MODEL

The hybrid dynamical model is constructed based on a description of the nonlinear dynamics of the DDM. The model equations are only presented briefly, where a more detailed description is found in [10, 20, 12, 13]. The same nonlinear model describing the DDM dynamics may be found in [21]. The nonlinear mathematical model is established based on the illustration of the DDM and a single pressure chamber shown in Fig. 1.

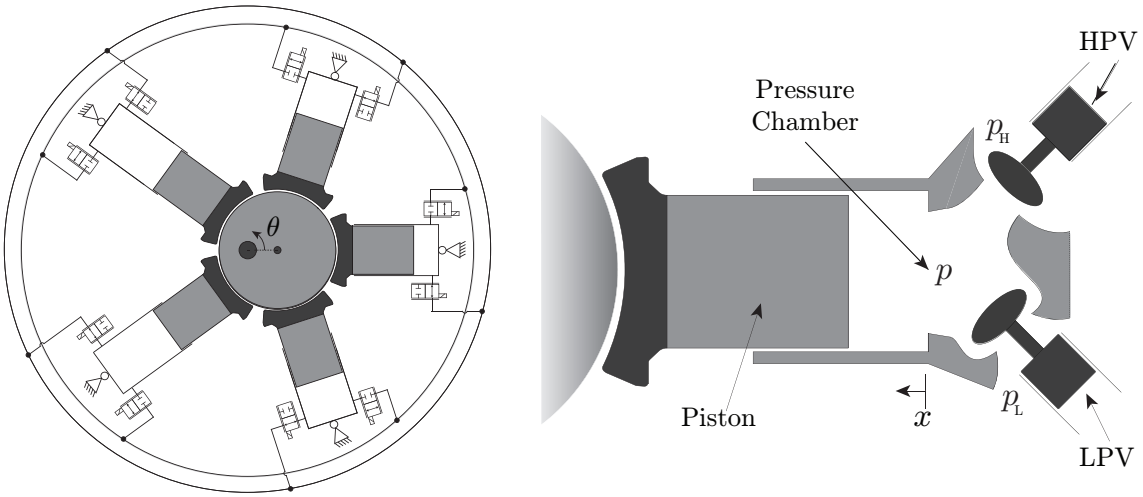

Figure 1: Illustration of the radial piston type digital displacement machine (5 cylinder machine) and definition of variables used for the mathematical model [20, 22].

The piston displacement for the i'th cylinder, x_i, is described as function of the shaft angle by

$$x_i = r_e\,(1-\cos(\theta_i)) \qquad \theta_i = \theta + \frac{2\pi}{N_c}\,(i-1) \qquad i \in \{1,\ldots,N_c\} \tag{1}$$

where r_e is the eccentric shaft radius and N_c is the number of cylinders. The displacement volume is thus given as $V_d = 2\,r_e A_p$, where A_p is the piston area. The chamber volume for

the i'th cylinder, V_i, and its time derivative are then given by

$$V_i = \frac{V_\mathrm{d}}{2}\left(1-\cos(\theta_i)\right)+V_0 \qquad \dot{V}_i = \frac{V_\mathrm{d}}{2}\sin(\theta_i)\,\dot{\theta} \tag{2}$$

where V_0 is the minimum chamber volume. The continuity equation is used to describe the pressure build-up for the i'th cylinder given by

$$\dot{p}_i = \frac{\beta_\mathrm{e}(p_\mathrm{i})}{V_\mathrm{i}}\left(Q_{\mathrm{H},i}-Q_{\mathrm{L},i}-\dot{V}_i\right) \tag{3}$$

where β_e is the pressure dependent effective bulk modulus. Q_L and Q_H are the flows through the low and high pressure valve respectively. The orifice equation is used to describe the flows through the valves and are given to be

$$Q_{\mathrm{L},i} = \frac{x_\mathrm{L,i}}{k_\mathrm{f}}\sqrt{|p_i-p_\mathrm{L}|}\,\mathrm{sign}\left(p_i-p_\mathrm{L}\right) \qquad Q_{\mathrm{H},i} = \frac{x_\mathrm{H,i}}{k_\mathrm{f}}\sqrt{|p_\mathrm{H}-p_i|}\,\mathrm{sign}\left(p_\mathrm{H}-p_i\right) \tag{4}$$

where $x_\mathrm{L}\in[0,1]$ and $x_\mathrm{H}\in[0,1]$ are normalized valve plunger positions, while k_f is the valve flow coefficient. When considering the fundamental machine dynamics it is deemed sufficient to model the valves as a simple first order system given as

$$\dot{x}_\mathrm{H,i} = \frac{1}{\tau_\mathrm{v}}\left(u_\mathrm{H,i}-x_\mathrm{H,i}\right) \qquad \dot{x}_\mathrm{L,i} = \frac{1}{\tau_\mathrm{v}}\left(u_\mathrm{L,i}-x_\mathrm{L,i}\right) \tag{5}$$

where u_H and u_L are the inputs to the high and low pressure valve respectively, while t_v is the valve time constant. The torque contribution from the i'th pressure chamber is derived to be given by

$$\tau_i = \frac{d\,V_i\left(\theta_i\right)}{d\theta}\,p_i = \frac{V_\mathrm{d}}{2}\sin(\theta_i)\,p_i \tag{6}$$

For a full stroke operated DDM, the binary valve inputs may only be altered discretely at fixed shaft positions. Since the nonlinear model comprises several states for each cylinder chamber, using the nonlinear model for control development is considered extremely difficult. Therefore, a significantly simpler model of the DDM is used which neglects the pressure dynamics of the individual chamber and thereby directly describes the output torque or flow.

3 DISCRETE DYNAMICAL DDM MODEL

Considering the pressure build-up in each chamber to be significantly faster than the remaining machine dynamics, the flow and torque throughput may be approximated by [23, 9, 11, 10]

$$\begin{aligned} Q_\mathrm{H} &\approx \frac{dV(\theta)}{d\theta}\frac{d\theta}{dt} = \frac{V_\mathrm{d}}{2}\sin(\theta)\,\dot{\theta} = \mathcal{D}(\theta)\,\dot{\theta} \\ \tau &= \frac{dV(\theta)}{d\theta}\,p \approx \frac{V_\mathrm{d}}{2}\sin(\theta)\,p = \mathcal{D}(\theta)\,p \end{aligned} \tag{7}$$

Since the binary input may only be altered once for every cylinder per revolution, the sampling angle is given by $\theta_\mathrm{s} = 2\,\pi/N_\mathrm{c}$. The displacement fraction between samples may then be evaluated by

$$\mathcal{D}[k] = \frac{\Delta V[k]}{\theta_\mathrm{s}} = \frac{\left(V\left(\theta[k+1]\right)-V\left(\theta[k]\right)\right)N_\mathrm{c}}{2\,\pi} \tag{8}$$

where the discrete control update angle is given as

$$\theta[k] = \phi_0 + \theta_s\ (k-1) \qquad\qquad i \in \{1,...,N_c\} \tag{9}$$

where ϕ_0 is the local shaft angle where the LPV is closed to initiate an active stroke. In this paper a digital displacement motor is considered, but the presented method also applies for a pump. The change is volume for the motoring stroke is evaluated by

$$\Delta V[k] = \begin{cases} 0 & \theta[k], \theta[k+1] \notin [0\,; \phi_H] \\ V(\theta[k+1]) - V(\theta[k]) & \theta[k], \theta[k+1] \in [0\,; \phi_H] \\ V(\theta[k+1]) - V(0) & \theta[k] < 0 < \theta[k+1] \\ V(\phi_H) - V(\theta[k]) & \theta[k] < \phi_H < \theta[k+1] \end{cases} \tag{10}$$

where ϕ_H is the angle where the motoring stroke is ended by closing the HPV. The discrete state model comprises of memory states of the input decisions (active or inactive) and are given by the matrix-vector representation as

$$\underbrace{\begin{bmatrix} u(k) \\ u(k-1) \\ u(k-2) \\ \vdots \\ u(k-m+1) \end{bmatrix}}_{z(k+1)} = \underbrace{\begin{bmatrix} 0 & 0 & \cdots & 0 & 0 \\ 1 & 0 & \cdots & 0 & 0 \\ 0 & 1 & \cdots & 0 & 0 \\ \vdots & \vdots & \ddots & \vdots & \vdots \\ 0 & 0 & \cdots & 1 & 0 \end{bmatrix}}_{A_u} \underbrace{\begin{bmatrix} u(k-1) \\ u(k-2) \\ \vdots \\ u(k-m+1) \\ u(k-m) \end{bmatrix}}_{z(k)} + \underbrace{\begin{bmatrix} 1 \\ 0 \\ 0 \\ \vdots \\ 0 \end{bmatrix}}_{B_u} u(k) \tag{11}$$

$$\mathcal{D}(k) = \begin{bmatrix} \mathcal{D}[1] & \mathcal{D}[2] & ... & \mathcal{D}[m] \end{bmatrix} z(k) + \mathcal{D}[0]\, u(k)$$

The chamber pressure buildup as function of the shaft angle is described, by neglecting the fast transient flow dynamics and gives

$$\frac{dp}{dt}\frac{dt}{d\theta} = \frac{dp}{d\theta} = -\frac{\beta_e}{V(\theta)}\frac{dV(\theta)}{d\theta} = \underbrace{-\frac{\beta_e}{\frac{V_d}{2}(1-\cos(\theta)) + V_0}\frac{V_d}{2}\sin(\theta)}_{f_p(\theta)} \tag{12}$$

A discrete representation of the chamber pressure may then be written as [14].

$$p(k+1) = \begin{cases} p_H & if\ \ (\bar{x}_L = 0 \wedge \bar{x}_H = 1) \vee p(k+1) > p_H \\ p(k) + f_p(\theta[k]) & if\ \ \bar{x}_L = 0 \wedge \bar{x}_H = 0 \\ p_L & if\ \ (\bar{x}_L = 1 \wedge \bar{x}_H = 0) \vee p(k+1) < p_L \end{cases} \tag{13}$$

By normalizing the discrete pressure by $p(k) = \bar{p}(k)\, p_H(k)$, the torque throughput of the discrete model is given by $\tau(k) = \mathcal{D}(k)\, \bar{p}(k)\, p_H(k)$. The resulting output maps for the torque and flow thus becomes

$$\begin{aligned} \tau_m(k) &= \underbrace{\begin{bmatrix} \mathcal{D}[1]\,\bar{p}[1] & \mathcal{D}[2]\,\bar{p}[2] & ... & \mathcal{D}[m]\,\bar{p}[m] \end{bmatrix} p_H}_{C_\tau} z(k) + \underbrace{\mathcal{D}[0]\,\bar{p}[0]\,p_H}_{D_\tau} u(k) \\ Q_m(k) &= \underbrace{\begin{bmatrix} \mathcal{D}[1] & \mathcal{D}[2] & ... & \mathcal{D}[m] \end{bmatrix} \omega}_{C_q} z(k) + \underbrace{\mathcal{D}[0]\,\omega}_{D_q} u(k) \end{aligned} \tag{14}$$

For simplicity ω and p_H are considered constant in this paper, which yields the same model as when linearizing at zero displacement. A validation of the discrete model is done

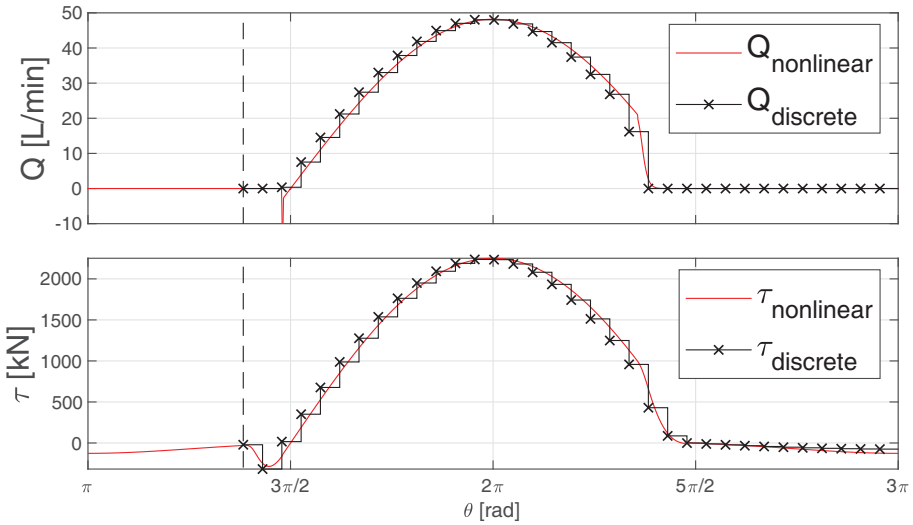

Figure 2: Comparison of discrete and non-linear model response with 42 cylinders. $\omega = 100\,\text{rpm}$, $p_\text{H} = 300\,\text{bar}$, $p_\text{L} = 10\,\text{bar}$ [24].

by an impulse response comparison between the discrete and nonlinear model, where the results are shown in Fig. 2. It is seen that the discrete model is fairly accurate in describing the DDM dynamics as long as the number of cylinders are fairly high. This discrete model representation of the DDM dynamics is combined with the continuous plant dynamics to obtain a hybrid dynamical description of the hydraulic system.

4 LINEAR HYBRID DYNAMICAL MODEL

Control of a continuous plant actuated by a DDM with discretely updated inputs, may be classified as a hybrid dynamical system. A hybrid system comprises of both continuous differential equations and discrete difference equations. A hybrid system is in general formulated as [19]

$$\mathcal{H}: \quad x \in \mathbb{R}^n \quad \begin{cases} \dot{x} & \in F(x), & x \in C \\ x^+ & \in G(x), & x \in D \end{cases} \tag{15}$$

$\dot{x}$ denotes the state time derivative and x^+ denotes the state value after a jump. The sets and map used to describe the hybrid dynamical system are:

- The flow set C $\subset \mathbb{R}^n$
- The flow map F: C $\to \mathbb{R}^n$
- The jump set: D $\subset \mathbb{R}^n$
- The jump map: G: D $\to \mathbb{R}^n$

As long as the state x belongs to the flow set C, x is described by the differential inclusion given by the flow map F and when x belongs to the jump set D, x is described by the difference inclusion given by the jump map G.

In this paper, the discrete linear time invariant (DLTI) approximation of the DDM dynamics derived in (11) and (14) is used for stability analysis in the sense of a hybrid dynamical systems. However, to enable a description in the hybrid domain where the dynamics is described in serial connection (either flowing or jumping) requires a refor-

mulation given by

$$\underbrace{\begin{bmatrix} z(k) \\ z(k-1) \\ z(k-2) \\ \vdots \\ z(k-m) \end{bmatrix}}_{z^+} = \underbrace{\begin{bmatrix} 0 & 0 & \cdots & 0 & 0 \\ 1 & 0 & \cdots & 0 & 0 \\ 0 & 1 & \cdots & 0 & 0 \\ \vdots & \vdots & \ddots & \vdots & \vdots \\ 0 & 0 & \cdots & 1 & 0 \end{bmatrix}}_{A_z} \underbrace{\begin{bmatrix} z(k-1) \\ z(k-2) \\ \vdots \\ z(k-m) \\ z(k-m-1) \end{bmatrix}}_{z} + \underbrace{\begin{bmatrix} 1 \\ 0 \\ 0 \\ \vdots \\ 0 \end{bmatrix}}_{B_z} u(k) \tag{16}$$

$$\begin{aligned} \tau_\mathrm{m} &= \underbrace{\begin{bmatrix} \mathcal{D}[0]\,\bar{p}[0] & \mathcal{D}[1]\,\bar{p}[1] & \ldots & \mathcal{D}[m]\,\bar{p}[m] \end{bmatrix}}_{C_{z\tau}} p_\mathrm{H}(k)\, z^+ \\ Q_\mathrm{m} &= \underbrace{\begin{bmatrix} \mathcal{D}[0] & \mathcal{D}[1] & \ldots & \mathcal{D}[m] \end{bmatrix}}_{C_{zq}} \omega(k)\, z^+ \end{aligned} \tag{17}$$

In this paper, a linear actuated plant with continuous dynamics given by $\dot{x} = A\,x + B_\mathrm{p}\,u_\mathrm{p}$ is considered, where u_p is either the torque, τ_m, or flow, Q_m, dependent on the controlled variable (speed or pressure). The linear hybrid model of the continuous plant actuated by the DDM is given to be

$$\left.\begin{aligned} \dot{x} &= A\,x + B\,z \\ \dot{z} &= 0 \\ \dot{\chi} &= 1 \end{aligned}\right\} \chi \in [0,T] \quad \left.\begin{aligned} x^+ &= x \\ z_\mathrm{u}^+ &= A_\mathrm{z}\,z + B_\mathrm{z}\,u \\ \chi^+ &= 0 \end{aligned}\right\} \chi = T \tag{18}$$

where χ is a timer generating the control updates when reaching $T = 2\,\pi/(\omega\,N_\mathrm{c})$. The input matrix B is defined as $B_\mathrm{p}\,C_z$, where $C_\mathrm{z} = C_{z\tau} \wedge C_{z\tau}$ depending on whether the output is torque or flow. Similarly, $C_\mathrm{u} = C_\tau \wedge C_q$ for the DLTI model.

5 STABILITY AND FEEDBACK CONTROL

Control design of hybrid dynamical systems is done by stability analysis featuring a Lyapunov function candidate. The objective is to show Uniformly Globally Pre-asymptoically Stability (UGPaS) for the hybrid system with respect to the set $\mathcal{A}$. The definition of UGPaS for the hybrid dynamical system $\mathcal{H}$ is defines as [19]:

(Sufficient Lyapunov Conditions) Let $\mathcal{H} = (C,F,D,G)$ be a hybrid system and let $\mathcal{A} \subset \mathbb{R}^n$ be closed. If V is a Lyapunov function candidate for $\mathcal{H}$ and there exist $\alpha_1, \alpha_2 \in \mathcal{K}_\infty$, and a continuous positive definite function $\rho : \mathbb{R} \to \mathbb{R}_{\geq 0}$ such that

$$\begin{aligned} &\bullet \quad \alpha_1(|x|_\mathcal{A}) \leq V(x) \leq \alpha_2(|x|_\mathcal{A}) && \forall x \in C \cup D \cup G(D) \\ &\bullet \quad \langle \nabla V(x), f(x) \rangle \leq -\rho(|x|_\mathcal{A}) && \forall x \in C, \forall f \in F(x) \\ &\bullet \quad V(g(x)) - V(x) \leq -\rho(|x|_\mathcal{A}) && \forall x \in D, \forall g \in G(x) \end{aligned} \tag{19}$$

Then $\mathcal{A}$ is Uniformly Globally p re-Asymptotically Stable for $\mathcal{H}$.

where $\mathcal{A} = \{0\} \times \{0\} \times [0, T_s]$ for the states $\begin{bmatrix} x & z & \chi \end{bmatrix}$. Since the hybrid system is linear, it may be optimally controlled by a linear controller. Inserting the control law $u = K x_1$, where $x_1 = \begin{bmatrix} x & z \end{bmatrix}^T$ and $K = \begin{bmatrix} K_1 & K_2 \end{bmatrix}$ yields the closed loop system dynamics given by

$$\left.\begin{aligned} \dot{x} &= A x + B z \\ \dot{z} &= 0 \\ \dot{\chi} &= 1 \end{aligned}\right\} \chi \in [0, T] \quad \left.\begin{aligned} x^+ &= x \\ z^+ &= A_z z + B_z K x_1 \\ \chi^+ &= 0 \end{aligned}\right\} \chi = T \tag{20}$$

The flow and jump maps may be written in a compact form as

$$\begin{aligned} f(x_1) &= \begin{bmatrix} A_f x_1 \\ 1 \end{bmatrix} \quad g(x_1) = \begin{bmatrix} A_g x_1 \\ 0 \end{bmatrix} \\ A_f &= \begin{bmatrix} A & B \\ 0 & 0 \end{bmatrix} \qquad A_g = \begin{bmatrix} I & 0 \\ B_z K_1 & A_z + B_z K_2 \end{bmatrix} \end{aligned} \tag{21}$$

The stability analysis is then made through the use of the following definitions [19]

$$H := e^{(A_f T)} A_g \qquad\qquad W(x_1) := x_1^T P x_1 \tag{22}$$

where P is a positive definite and symmetric matrix. It follows that $x_1(t+T, j+1) = H x_1(t, j)$, where H describes the closed loop system dynamics. The dissipation of energy may be shown by evaluating the change in $W(x_1)$ due to a jump, which must satisfy (23) for $\varepsilon > 0$

$$W(H x_1) - W(x_1) = x_1^T (H^T P H - P) x_1 \leq -\varepsilon |x_1|^2 \tag{23}$$

Meaning that $H^T P H - P \prec 0$ or equivalently $|\lambda(H)| < 1$ [19]. Considering the Lyapunov function candidate

$$\begin{aligned} V(x) &:= e^{(-\sigma x_2)} W\left(e^{(A_f(T-x_2))} x_1\right) \\ &:= \underbrace{e^{(-\sigma x_2)}}_{\succ 0} x_1^T \underbrace{\left(e^{(A_f(T-x_2))}\right)^T P \left(e^{(A_f(T-x_2))}\right)}_{\succ 0} x_1 \end{aligned} \tag{24}$$

where $\sigma > 0$. It may be established that the Lyapunov candidate function, $V(x)$, fulfills the requirements in (19) for UGPaS. Since the exponential functions and P are always positive definite, it can be verified that

$$\underline{c} |x|_{\mathcal{A}}^2 \leq V(x) \leq \bar{c} |x|_{\mathcal{A}}^2 \qquad\qquad \forall x \in C \cup D \tag{25}$$

where $\underline{c} > 0$ and $\bar{c} > 0$, given that $\underline{c} < \bar{c}$ and thus the first requirement in (19) is fulfilled. For the second requirement in (19), it may be established that

$$\begin{aligned} \langle \nabla V(x), f(x) \rangle &= -\underbrace{\sigma e^{(-\sigma x_2)}}_{\succ 0} x_1^T \underbrace{\left(e^{(A_f(T-x_2))}\right)^T P \left(e^{(A_f(T-x_2))}\right)}_{\succ 0} x_1 \leq -\beta |x_1|^2 \\ \langle \nabla V(x), f(x) \rangle &= -\beta |x|_{\mathcal{A}}^2 \qquad\qquad \forall x \in C \end{aligned} \tag{26}$$

where $\beta > 0$. The third requirement may be established to yield (27), when considering that $x_2 = T$ when jumping.

$$\begin{aligned} V(g(x)) - V(x) &= e^{(-\sigma x_2)} \left(W\left(e^{(A_\mathrm{f}(T-x_2))} A_\mathrm{g} x_1 \right) - W(x_1) \right) \\ &= e^{(-\sigma T)} \left(W(H x_1) - W(x_1) \right) \\ &= \underbrace{e^{(-\sigma T)}}_{\succ 0} \left(-\varepsilon |x_1|^2 \right) \leq -\gamma |x|_{\mathcal{A}}^2 \qquad \forall x \in D \end{aligned} \tag{27}$$

The hybrid dynamical system is hence shown to be UGPaS for those values of K such that $|\lambda(H)| < 1$.

6 CONTROLLER SYNTHESIS

The objective for control design is hence to determine the controller gain K, such that $|\lambda(H)| < 1$. When evaluating H, it is found that the closed loop dynamics is given to be

$$H = \underbrace{\begin{bmatrix} A_\mathrm{d} & B_\mathrm{d} C_\mathrm{z} \\ 0 & I \end{bmatrix}}_{e^{(A_\mathrm{f} T)}} \underbrace{\begin{bmatrix} I & 0 \\ B_\mathrm{z} K_1 & A_\mathrm{z} + B_\mathrm{z} K_2 \end{bmatrix}}_{A_\mathrm{g}} = \begin{bmatrix} A_\mathrm{d} + B_\mathrm{d} C_\mathrm{z} B_\mathrm{z} K_1 & B_\mathrm{d} C_\mathrm{z} \left(A_\mathrm{z} + B_\mathrm{z} K_2 \right) \\ B_\mathrm{z} K_1 & A_\mathrm{z} + B_\mathrm{z} K_2 \end{bmatrix} \tag{28}$$

where A_d and B_d are the discrete system matrices for the continuous plant. The objective is hence to determine the controller gains $K = \begin{bmatrix} K_1 & K_2 \end{bmatrix}$ to yield the desired pole-locations. It may be found that the control design problem is the same as for a sample-and-hold DLTI description of the control system. The open loop description of the DLTI model yields

$$\begin{bmatrix} x(k+1) \\ z(k+1) \end{bmatrix} = \begin{bmatrix} A_\mathrm{d} & B_\mathrm{d} C_\mathrm{u} \\ 0 & A_\mathrm{u} \end{bmatrix} \begin{bmatrix} x(k) \\ z(k) \end{bmatrix} + \begin{bmatrix} B_\mathrm{d} D_\mathrm{u} \\ B_\mathrm{u} \end{bmatrix} u(k) \tag{29}$$

Inserting the control law $u(k) = \begin{bmatrix} K_1 & K_2' \end{bmatrix} \begin{bmatrix} x(k) & z(k) \end{bmatrix}^T$ yields

$$\begin{bmatrix} x(k+1) \\ z(k+1) \end{bmatrix} = \begin{bmatrix} A_\mathrm{d} + B_\mathrm{d} D_\mathrm{u} K_1 & B_\mathrm{d} \left(C_\mathrm{u} + D_\mathrm{u} K_2' \right) \\ B_\mathrm{u} K_1 & A_\mathrm{u} + B_\mathrm{u} K_2' \end{bmatrix} \begin{bmatrix} x(k) \\ z(k) \end{bmatrix} \tag{30}$$

Comparing by coefficient between (28) and (30) reveals that $K_2 = \begin{bmatrix} K_2' & 0 \end{bmatrix}$ in which case the closed loop system dynamics are equivalent to that given in (28). Therefore, one state in the hybrid formulation becomes indifferent, since the current updated input may not be used to generate the current input. For this linear system, a hybrid formulation is hence not needed and the significantly simpler DLTI description may be used for control design. However, if a nonlinear continuous plant, varying speed DDM or multiple DDMs in a transmission is considered, a hybrid dynamical system formulation is likely a necessity. However, the identification of a Lyapunov function may be very difficult to find. An important problem is variable speed operation of the DDM, where the objective is to show that $|\lambda(H)| < 1$ where H is varying as function of the rotational speed being a state.

$$H = e^{A_\mathrm{f} T} A_\mathrm{g} \qquad\qquad T = \frac{2\pi}{\omega N_\mathrm{c}} \tag{31}$$

It has been attempted to transform the system dynamics to the shaft position domain, which results in a nonlinearity in the continuous plant dynamics due to

$$\frac{dx}{dt} = f(x(t), u(t)) \qquad \frac{dx}{dt}\frac{dt}{d\theta} = \frac{dx}{d\theta} = \frac{1}{\omega(\theta)} f(x(\theta), u(\theta)) \qquad \omega \neq 0 \tag{32}$$

The introduction of the nonlinearity greatly increases the complexity of finding a Lyapunov function if it is not linearized. Also the theory of dynamical systems on time-scales has been found insufficient in solving the problem of variable speed operation, since the time-scale (speed) has to be known priori to ensure stability. Therefore, further research in stability proof and controller synthesis for variable speed operated DDM(s) and nonlinear actuated plants is required.

7 CONCLUSION

This paper concerned control development for digital hydraulic pump/motor units, which is highly challenged by the non-smooth dynamical behavior. The paper presented a linear hybrid dynamical description of a linear continuous plant actuated by a digital displacement machine with discretely updated input. A stability proof was conducted for a linear feedback controller through the use of a control Lyapunov function. It was further shown that the control design problem for the hybrid system is identical to that of using a purely discrete model with zero-order-hold input to the discrete approximated continuous plant. It was further discussed how the hybrid formulation may be used for control of a nonlinear plant, variable speed DDM operation and multiple DDMs in a transmission, where the purely discrete formulation is no longer applicable. However, the difficultly of finding a Lyapunov function for a hybrid system is considered very challenging for any nonlinear or time varying plant. Therefore, a great amount of further research is necessary to solve these challenging mathematical problems.

8 ACKNOWLEDGMENT

This research was funded by the Danish Council for Strategic Research through the HyDrive project at Aalborg University, at the Department of Energy Technology (case no. 1305-00038B).

References

[1] M. Ehsan, W. Rampen, and S. Salter, "Modeling of digital-displacement pumpmotors and their application as hydraulic drives for nonuniform loads," *Journal of Dynamic Systems, Measurement and Control, vol. 122, no. 1, pp. 210215*, 2000.

[2] M. Heikkila and M. Linjama, "Displacement control of a mobile crane using digital hydraulic power management system," *Mechatronics 23(4), pp. 452 - 461*, 2013.

[3] S. Nordaas, M. K. Ebbesen, and T. O. Andersen, "The potential of a digital hydrulic winch drive system," *Proc. of the Ninth Workshop on Digital Fluid Power, Aalborg, Denmark*, 2017.

[4] S. Nordaas, M. K. Ebbesen, and T. O. Andersen, "Feasibility study of a digital hydraulic winch drive system," *Proc. of the Ninth Workshop on Digital Fluid Power, Aalborg, Denmark*, 2017.

[5] B. S. R. Armstrong and Q. Yuan, "Multi-level control of hydraulic gerotor motor and pumps," *Proceedings of the 2006 American Control Conference, Minneapolis, Minnesota, USA*, June 2006. Proceedings of the 2006 American Control Conference Minneapolis, Minnesota.

[6] X. Song, "Modeling an active vehicle suspension system with application of digital displacement pump motor," *Proceedings of the ASME 2008 International Design Engineering Techical Conference/Computers and Information in Enegineering Conference, Brooklyn - New York, Vol. 5, pp. 749-753*, 2008.

[7] N. H. Pedersen, P. Johansen, and T. O. Andersen, "Feedback control of pulse-density modulated digital displacement transmission using a continuous approximation," *Submitted to IEEE/ASME Transactions on Mechatronics*, 2018.

[8] P. Johansen, D. B. Roemer, T. O. Andersen, and H. C. Pedersen, "Discrete linear time invariant analysis of digital fluid power pump flow control," *Journal of Dynamic Systems, Measurement and Control*, 2017.

[9] N. H. Pedersen, P. Johansen, and T. O. Andersen, "Lqr feedback control development for wind turbines featuring a digital fluid power transmission system," 2016.

[10] N. H. Pedersen, P. Johansen, and T. O. Andersen, "Optimal control of a wind turbine with digital fluid power transmission," *Nonlinear Dynamics*, 2018.

[11] N. H. Pedersen, P. Johansen, and T. O. Andersen, "Event-driven control of a speed varying digital displacement machine," *Proceedings of ASME/BATH FPMC Symposium on Fluid Power and Motion Control, Sarasota, Florida, USA*, 2017.

[12] N. H. Pedersen, P. Johansen, and T. O. Andersen, "Non-linear hybrid control oriented modelling of a digital displacement machine," *Proc. of 9th Workshop on Digital Fluid Power, Aalborg, Denmark*, 2017.

[13] N. H. Pedersen, P. Johansen, and T. O. Andersen, "Four qudrant hybrid control oriented dynamical system model of digital displacement units," *Proc. of the Bath/ASME Symposium on Fluid Power and Motion Control, Bath, UK*, 2018.

[14] S. M, G. M, and K. U, "Optimal control of digital hydraulic drives using mixed-integer quadratic programming," September 2013. 9th IFAC Symposium on Nonlinear Control System, Toulouse.

[15] R. G. Sanfelice and A. R. Teel, "Lyapunov analysis of sample-and-hold hybrid feedbacks," 2005+.

[16] A. R. Teel, R. G. Sanfelice, and R. Goebel, "Hybrid control systems," 2009.

[17] R. G. Sanfelice, "Feedback control of hybrid dynamical systems," *Encyclopedia of Systems and Control*, 2015.

[18] R. Goebel, R. G. Sanfelice, and A. R. Teel, "Hybrid dynamical systems," *IEEE control systems magazine*, 2009.

[19] R. Goebel, R. G. Sanfelice, and A. R. Teel, *Hybrid Dynamical Systems - Modeling, Stability and Robustness*. Princeton, 2012.

[20] N. H. Pedersen, P. Johansen, and T. O. Andersen, "Challenges with respect to control of digital displacement hydraulic units," *Modeling, Identification and Control*, 2018.

[21] N. H. Pedersen, P. Johansen, and T. O. Andersen, "Analysis of the non-smooth dynamical effects and suitable operation and control strategies for digital displacement units," *Proc. of the 10th Digital Fluid Power Conference, Tampere, Finland*, 2019.

[22] N. H. Pedersen, *Development of Control Strategies for Digital Displacement Units*. PhD thesis, Aalborg University, 2018.

[23] P. Johansen, D. B. Roemer, H. C. Pedersen, and T. O. Andersen, "Discrete linear time invariant analysis of digital fluid power pump flow control," *Journal of dynamic system measurement and control, ASME, accepted for publication*, 2016.

[24] N. H. Pedersen, *Development of Control Strategies for Digital Displacement Units*. PhD thesis, Deparment of Energy Technology, Aalborg University, 2018.

Investigation of the fault tolerance of digital hydraulic cylinders

Viktor Donkov[1], Torben Andersen[1], Morten Kjeld Ebbesen[2], Matti Linjama[3] , Miika Paloniitty[3]

[1]Aalborg University
Pontoppidanstraede 111
9220 Aalborg East, Denmark
E-mail: vhd@et.aau.dk

[2]University of Agder
Jon Lilletuns vei 9
4879 Grimstad, Norway

[3]Tampere University of Technology
Korkeakoulunkatu 10
FI-33720 Tampere, Finland

ABSTRACT

This paper investigates the fault tolerance of Discrete Displacement Cylinders (DDCs) controlled with a Model Predictive Controller(MPC). Due to the nature of DDCs there are multiple components such as several pressure chambers, constant pressure rails, and on/off valves, which operate in parallel. Some of these components do similar jobs, i.e. more than one cylinder chamber provides a positive force when pressurized. This modularity in design is an often stated benefit of digital hydraulics because failed components have less influence on the behaviour of the whole system. The exact influence of faults in the components, when the fault is detected and when it is not, is shown through a sensitivity study. Certain faults are tested in a laboratory setting to verify the simulation results. The results show that different component failures lead to different types of loss of capability of the system because the components are not equivalent in size. Furthermore the results show that the performance of the system is better when the fault is detected and the controller is able to take appropriate action.

KEYWORDS: Discrete Displacement Cylinders, Digital Hydraulics, Fault Tolerance

1. INTRODUCTION

Digital hydraulics started as an attempt to increase the energy efficiency of classic hydraulic systems by exchanging more complex components with simple components, which are either fully on or off. In certain ways, it tries to emulate the benefits electrical power systems have acquired from the use of transistors. This trend tries to make parts simpler and shift the functionality of the system from hardware to software. The main benefit and goal of the trend is energy efficiency, but there can be other benefits as well. Some digital hydraulic systems require multiple components operating in parallel. In this paper the focus will be on Discrete Displacement Cylinders (DDCs). DDCs are cylinders with more than two chambers. In order to produce different force levels the pressure in the different chambers is changed by connecting them to one of several pressure lines. The number of chambers together with the number of possible pressure levels define the resolution of the force output. Furthermore, a larger number of possible pressure levels also increases the energy efficiency of the system as the losses introduced by switching from one pressure to another are reduced when the two pressures are closer together [8]. The number of valves which are needed to connect the cylinder and the pressure lines grows proportionally. From one perspective the increased number of components is a minus due to the more complicated maintenance, but from a different perspective the large number of components such as valves and accumulators providing pressure means that only a certain subset of them are needed for a particular loading. In this article the extent of this inherent fault tolerance will be investigated. The faults investigated are valves stuck open and valves stuck closed. This is done because valves in digital hydraulic

systems are under considerable load, and these are common failure modes for them [3]. Fault tolerance for digital flow control units has been investigated for instance in [2]. For this reason failures in one valve, when more valves are connected in parallel, will not be investigated. Instead, if several valves are used in a pressure line, all will experience a failure. In section 2 the test setup will be presented. In section 3 the mathematical model describing it will be presented. This model will be used to test the majority of the faults, with only some of them implemented on the real test stand. In section 4.4 the model will be verified showing a good agreement with reality. In section 5 the faults will be described and the results will be shown. Finally in section 6, conclusions will be drawn and possible future work will be suggested.

2. TEST STAND

The test stand (Fig.1) is a commonly used test stand for digital hydraulics at Tampere University. The stand consists of a metal bar connected at the center with two places for extra mass to be attached on each end. The metal bar acts as a seesaw and in this case is actuated by a four-chamber cylinder. A constant velocity on/off pump supplies the system. In order to create the constant pressure rails three accumulators are used. The controller is implemented on a Dspace RealTime(RT) target using Matlab's compiler feature. The cylinder chambers are connected to the pressure rails through 21 type KSDE Rexroth valves, another four valves are used for charging the pressure rails. The hydraulic circuit can be seen in Fig.6. The large amount of valves is required because chamber A1 is four times larger than chamber A2. For the pressure in these chambers to rise equally fast, the same ratio of flow should be delivered to both of them. Since the valves are the same size, chamber A1 uses four valves per pressure line, chamber B1 uses two valves, and chamber A2 uses one valve. With three pressures to connect to, the total number of valves are twelve, six, and three. With different sized valves and a new manifold specifically designed for this circuit, fewer components could have been used. The amount of hoses and fittings would have been reduced as well. This would have increased the energy efficiency of the system. Due to monetary and time reasons this was not done. Instead the manifolds and valves already available were arranged in a way that provides the desired capabilities. The specific components used in the test stand can be seen in Tab.1.

Figure 1. Test stand

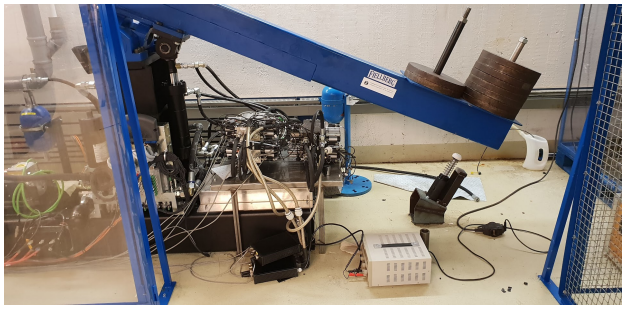

Figure 2. Hydraulics

Table 1. Components of the test stand

Component	Specification	Component	Specification
Cylinder	Norrhydro 85/63/40/28-250	Valves	Rexroth KSDE 10 L/min@5bar
Accumulators x 3	4 L	Pump	Rexroth UPE2 7 L/min
RT target	Dspace ds1006 1 core 2GHz		

3. MODEL

This section presents the mathematical model describing the test stand. The section is divided into two parts - the mechanical model of the seesaw and the hydraulics system which will drive the cylinder.

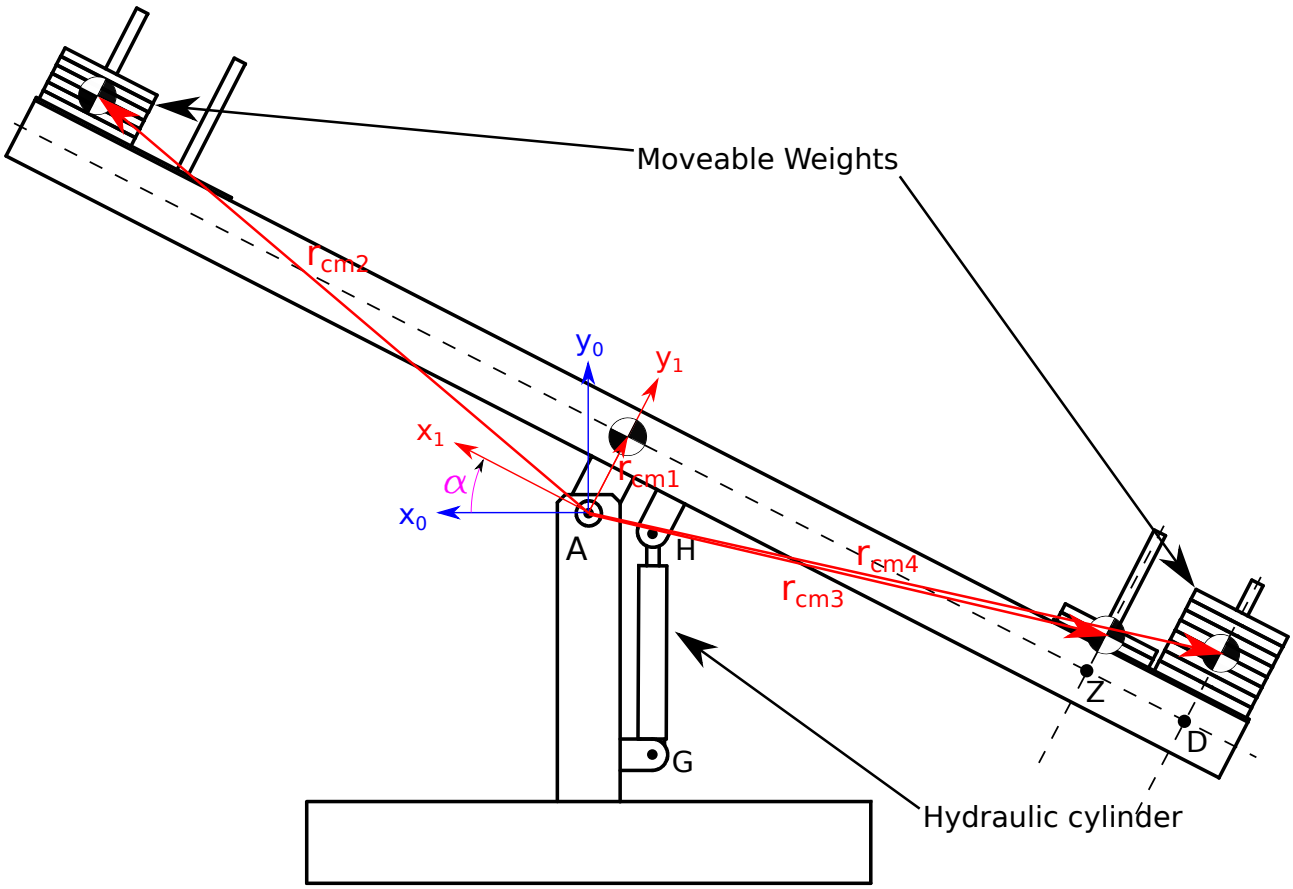

Figure 3. Kinematics

3.1. Seesaw model

Fig.3 shows the naming convention used in the model. The angle α is defined as the rotation between the stationary reference system denoted as $[x_0, y_0]$ and the rotating reference system denoted $[x_1, y_1]$, as seen in Fig.3. The cylinder is attached on the right side of the column. With that in mind, the cylinder stroke is smallest at $\alpha = 0.5$. The axis x is positive to the left, because the coordinate systems have been defined for the cylinder attached to the left of the column as in [4], this convention has been kept here for consistency. The lengths of the vectors in the appropriate coordinate systems can be seen in Tab.2. In order to calculate the load force the gravitational forces due to the 4 point masses are converted to a torque around point A using the kinematics of the system. This torque is them converted to a one dimensional force acting along the length of the cylinder. The torque due to gravity depends on angle α. The ratio between cylinder force and torque around point A also varies with α. The kinematics are also used to convert the total system inertia to a equivalent mass attached to the top of the cylinder. This mass varies with the same parameter as the load force. In Fig.4 and Fig.5 the calculated values for the load force and the equivalent mass on the cylinder according to the rotation angle α can be seen. The connection between cylinder stroke and α is used to make a one dimensional model with the nine valve as inputs and the cylinder stroke as output.

Table 2. Table of vector lengths in the appropriate coordinate system

Vector	x [m]	y [m]
AZ_1	-1.65	0.26
AD_1	-2	0.26
AH_1	-0.2025	0.05
AG_0	- 0.205	-0.760

3.2. Hydraulics

The hydraulics circuit used can be seen in Fig.6

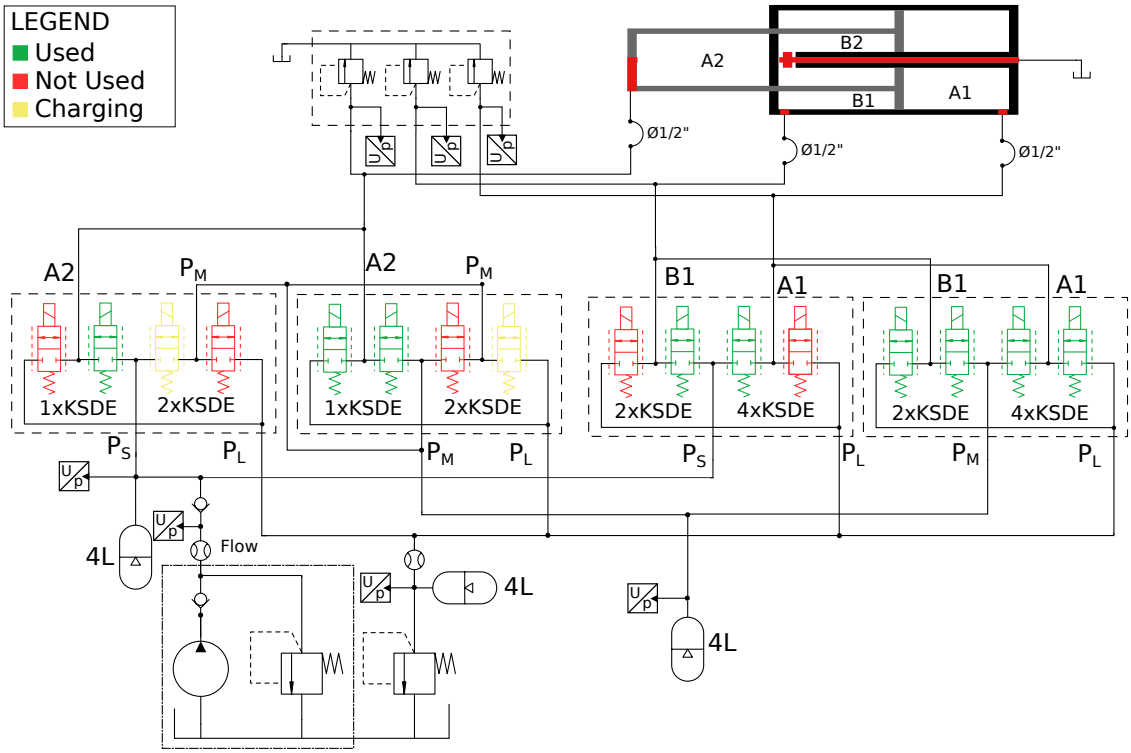

Figure 6. Hydraulic Circuit

3.2.1. Cylinder

The cylinder has four chambers, but only three will be used. According to this, the cylinder provides force as

$$F_{cyl} = A_{A1}p_{A1} - A_{B1}p_{B1} + A_{A2}p_{A2} \tag{1}$$

where the A_{A1} stands for area of chamber $A1$, and p_{A1} is the pressure in that chamber. The three pressure lines p_S, p_M, and p_L are selected as 12 MPa, 3 MPa, and 1 MPa respectively. The three chamber areas have

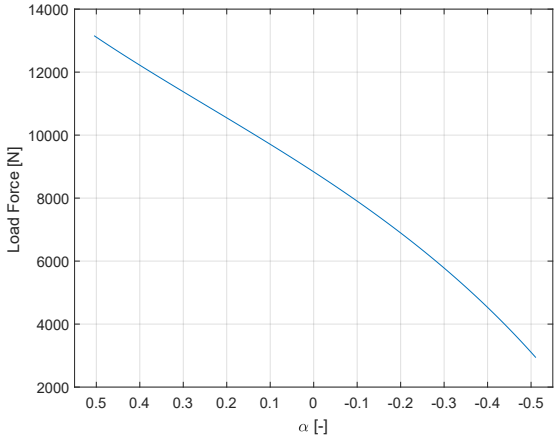

Figure 4. Load force as a function of α.

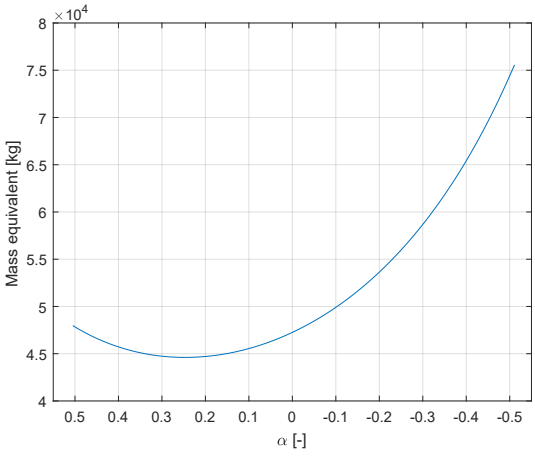

Figure 5. Equivalent mass seen by the cylinder as a function of α.

sizes according to the diameters in Tab.1. The available force levels can be seen in Fig.7. The blue dot at 9 kN corresponds to the average of the load force. This is taken from the trajectory and the load force calculated in Fig.4.

3.2.2. Hoses

The hoses in the system are modelled according to the method used in [5]. The time derivatives of the flow and the pressure for each hose segment are modelled as

$$\dot{Q}(k) = \frac{A\,(p(k) - p(k+1))}{L\rho} \tag{2}$$

$$\dot{p}(k) = \frac{\beta(p(k))}{AL}\,(Q(k-1) - Q(k)) \tag{3}$$

where A and L are the area and length of the hose segment, ρ is the density of oil, and (k) denotes segment number, $\beta(p(k))$ is the bulk modulus of the oil as a function of the pressure in that segment. Fig.8 also illustrates this convention. Losses in the hoses and fittings are ignored.

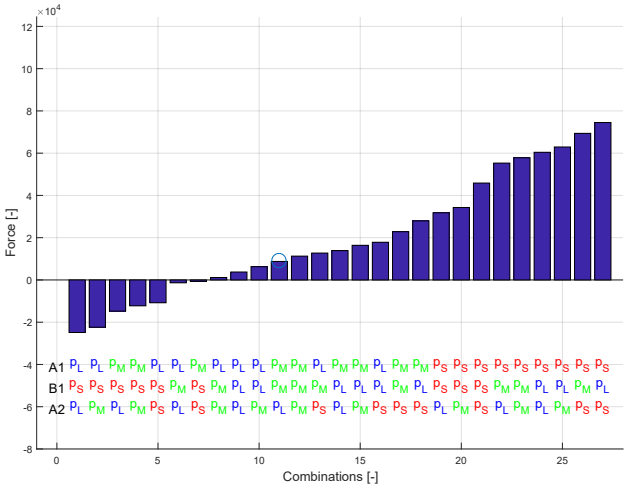

Figure 7. Available force levels

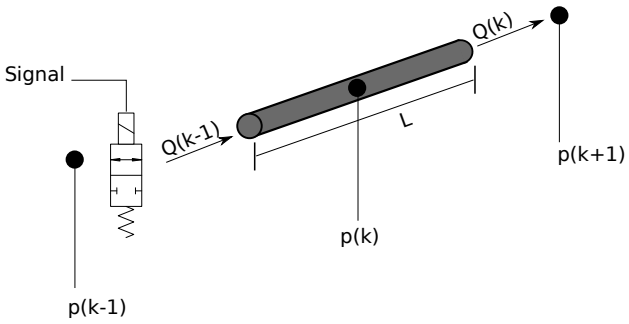

Figure 8. Model of the hoses between the cylinder chamber and the valve.

3.2.3. Accumulator

The accumulators are modelled according to the method used in [5]. The model is based on the temperature and volume of the gas as

$$\dot{T} = \frac{T_{wall} - T}{\tau} - \frac{RT\dot{V}_g}{c_v V_g} \tag{4}$$

$$\dot{V}_g = \dot{p}_{acc}\frac{V_{oil}}{\beta_v} - Q_{in} \tag{5}$$

where T_{wall} is the temperature of the accumulator wall, τ is the heat exchange time constant, R is the thermal resistance of the accumulator, c_v is the heat capacitance, $\dot{p}_{acc}$ is the gradient of the pressure in the accumulator, V_{oil} is the volume of the oil, β_v is the bulk modulus of the oil, and Q_{in} is the flow of oil into the accumulator. The volume of the oil is found from the current volume of the gas and the size of the accumulator

$$V_{oil} = V_{acc} + V_0 - V_g \tag{6}$$

From these equations the change in pressure of the hydraulic fluid can be described by

$$\dot{p}_{acc} = \frac{Q_{in} + \frac{1}{1+\frac{R}{c_v}}\frac{V_g}{T}\frac{1}{\tau}\,(T_{wall} - T)}{\frac{V_{oil}}{\beta_v} + \frac{1}{1+\frac{R}{c_v}}\frac{V_g}{p_{acc}}} \tag{7}$$

From Eq.4, Eq.5 and Eq.7 the dynamics of an accumulator can be described. A simple combinatorial logic based controller is used to charge the p_S and p_M accumulators. A threshold is selected as 0.5 MPa below the desired pressure. For the high pressure line, if p_S falls below this value (11.5 MPa), the pump is turned on. For the middle pressure line, if p_M reaches 2.5 MPa charging doesn't start unless the high pressure line is above the desired value. That is AND(p_M <2.5 MPa, NOT(p_S < 11.5 MPa)). If the charging condition is fulfilled two valves are opened between the high and middle pressure lines. The charging occurs with a large pressure drop across the charging valves and is very inefficient. The two valves between middle and low pressure lines can be used to drain the accumulators. This is done by opening all of the charging valves which connects p_S to p_M to p_L.

4. CONTROL

The cylinder is controlled with a Model Predictive Controller (MPC). The problem is be optimized with the differential evolution algorithm as in [1]. The MPC is based on [6]. Since it was shown in [6] that the controller has problems with changing mass and load force, the algorithm will be augmented by incorporating integral action according to the method used in [7].

4.1. Prediction

A linear model will be used to predict the system states:

$$x_c(k+1) = A_c x_c(k) + B_c u(k) \tag{8}$$

$$y(k) = C_c x_c(k) \tag{9}$$

In this equation x_c is a state vector containing the three pressures in the chambers p_{A1}, p_{B1} and p_{A2}, the position and velocity of the cylinder. $u(k)$ is a vector of nine Boolean values - indicating whether a valve is open or closed, $y(k)$ is the position of the cylinder. The specifics and a longer discussion of the system can be seen in the previously mentioned reference [6]. In order to introduce the integral action into the controller a new control vector has to be introduced: $\Delta u(k) = u(k) - u(k-1)$. Furthermore, a "change in system state" vector is introduced: $\Delta x_c(k) = x_c(k) - x_c(k-1)$ which allows the system equations to be rewritten as:

$$\Delta x_c(k+1) = A_c \Delta x_c(k) + B_c \Delta u(k) \tag{10}$$

$$y(k+1) - y(k) = C_c A_c \Delta x_c(k) + C_c B_c \Delta u(k) \tag{11}$$

A few more steps are needed. A new state vector is introduced as:

$$\bar{x}(k) = \begin{bmatrix} \Delta x_c(k) \\ y(k) \end{bmatrix} \tag{12}$$

This allows the rewriting of Eq.10 and Eq.11 into:

$$\bar{x}(k+1) = \bar{A}\bar{x}(k) + \bar{B}\Delta u(k) \tag{13}$$

$$y(k) = \bar{C}\bar{x}(k) \tag{14}$$

Here the matrices are defined as:

$$\bar{A} = \begin{bmatrix} A_c & 0 \\ C_c A_c & I \end{bmatrix} \quad \bar{B} = \begin{bmatrix} B_c \\ C_c B_c \end{bmatrix} \quad \bar{C} = \begin{bmatrix} 0 & I \end{bmatrix} \tag{15}$$

were I and 0 are an identity matrix and a matrix of zeros with the appropriate sizes.

For multi-step prediction a new output vector is defined as:

$$\hat{y} = G\Delta\hat{u} + \hat{x}_o \tag{16}$$

where $\hat{y}$ and $\Delta\hat{u}$ are:

$$\hat{y} = \begin{bmatrix} y(k+1) \\ y(k+2) \\ \vdots \\ y(k+M) \end{bmatrix} \qquad \Delta\hat{u} = \begin{bmatrix} \Delta u(k) \\ \Delta u(k+1) \\ \vdots \\ \Delta u(k+M) \end{bmatrix} \tag{17}$$

The matrices are built as:

$$G = \begin{bmatrix} B & 0 & \cdots & 0 \\ AB & B & \cdots & 0 \\ \vdots & \vdots & \ddots & \vdots \\ A^{M-1}B & A^{M-2}B & \cdots & B \end{bmatrix} \tag{18}$$

$$\hat{x}_o = \begin{bmatrix} \bar{C}\bar{A} \\ \vdots \\ \bar{C}\bar{A}^M \end{bmatrix} \tag{19}$$

where M is the prediction horizon.

4.2. Cost function

Now that the system's states are predicted the optimal control vector has to be chosen according to some condition. Since the aim is to follow a position trajectory, the position state can be selected as an output by choosing the correct C_c matrix. Then an error vector can be defined as

$$\bar{e} = \begin{bmatrix} e(k) \\ e(k+1) \\ \vdots \\ e(M) \end{bmatrix} = \begin{bmatrix} r(k) \\ r(k+1) \\ \vdots \\ r(M) \end{bmatrix} - \begin{bmatrix} y(k) \\ y(k+1) \\ \vdots \\ y(M) \end{bmatrix} \tag{20}$$

where $r(k)$ is the position reference for time instant k. This vector can be included in the cost function that is to be minimized. In [6] the cost function J was chosen as:

$$J = \omega_1 \hat{e}^T \hat{Q} \hat{e} + \omega_2 \left| F\hat{u} \right|_1 \tag{21}$$

where $\hat{Q}$ is a diagonal matrix with weight and F is a difference matrix built according to [6]. This cost function has some good properties - it is always positive and lower bounded, so it exhibits convex properties. The first term punishes error, while the second punishes pressure switching, which has been shown to be the major source of losses in a DDC [8]. Cost functions of this shape are fairly often used [9], but unfortunately the squaring of matrices proved too heavy to be completed online by the RT target. For this reason the cost function was simplified to

$$J = \omega_1 \left| \hat{e} \right|_1 + \omega_2 \left| F\hat{u} \right|_1 \tag{22}$$

The cost function is still positive definite and lower bounded, but the calculations are completed much faster. For the RT implementation a population of 50 combinations with a maximum setting of 100 generations always completed in less than the 60 ms. This was the setting on the watchdog timer. This timer was selected because the comparatively low inertia and the fast trajectory required from the controller to run at this frequency. The population size and maximum generations were selected to ensure that the computations are completed in the required time. With larger population size and more generations a better optimum can be found at each time step. This of course requires better hardware.

4.3. Delay compensation

In order to cope with the delays of the valves and the computation delay, delay compensation has been implemented similar to [10]. With a lower frequency controller these delays can be ignored, but due to the low inertia

of the test stand a rather fast switching frequency of 16.6667Hz (60 ms) is required. The delay compensation is implemented by further delaying the selected command, so that the the force is delivered at the correct instant. The prediction is moved one step forward to match this. In the laboratory case, the calculation delay and transfer delay is large enough on its own, so no artificial delay is added.

The difference can be seen in Fig.9 and Fig.10. The red line is the force calculated by the controller. The blue line is the actual delivered force. It can be seen in Fig.9 that due to the valve delay and the pressure dynamics the actual force reaches the desired value with a substantial delay. With delay compensation, the delivered force matches the desired force more accurately. This improves both accuracy and energy efficiency; otherwise force commands could be achieved one time step later leading to excessive switching.

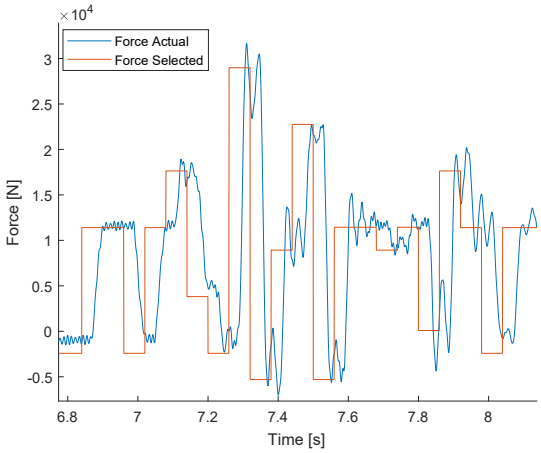

Figure 9. Without delay compensation

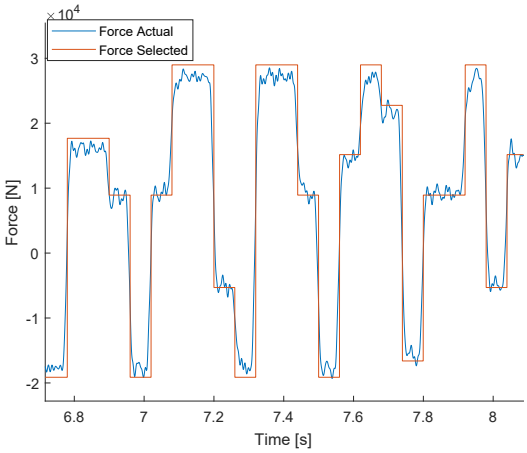

Figure 10. With delay compensation

4.4. Velocity estimation

With the delay compensation using the predicted pressures, the only real feedbacks to the controller are position and velocity. A velocity sensor was not available, so the velocity was estimated from the position signal. The position signal itself has noise which interferes with the proper estimation, so the position signal was filtered with

$$x_{p,filt}(k) = \frac{\Sigma x_p(k \cdots k-4) - max(x_p(k \cdots k-4)) - min(x_p(k \cdots k-4))}{3} \tag{23}$$

where $x_{p,filt}(k)$ is the filtered cylinder position at time instant k, and it depends on the previous four sampled values. The sampling was done at 1000 Hz. From this filtered signal the velocity could be obtained by

$$\dot{x}_{p,est} = \frac{5x_{p,filt}(k) + 3x_{p,filt}(k-1) + x_{p,filt}(k-2) - x_{p,filt}(k-3) - 3x_{p,filt}(k-4) - 5x_{p,filt}(k-5)}{35t_{s,vel}} \tag{24}$$

where $t_{s,vel}$ is the sample time for the estimation, which was chosen to be 5 ms. Both filter and velocity estimation are done according to [11].

4.5. Model Verification

Fig.11 shows the comparison between a real trajectory run and a simulation. In this test no faults are introduced. Fig.12 shows the comparison, but when a fault between chamber A2 and the supply pressure is introduced for the whole trajectory. In both test runs the simulation behaves similarly to the real plant. These verification tests were done with the controller in the closed loop.

For the first test run (Fig.11), the efficiency measure of the simulation is 19.93 J/mm. This is calculated by taking the energy used to follow the trajectory and dividing it by the total length of movement. The accuracy of the simulation run is 449.61 m. This was calculated by taking the difference of the reference and the

actual position of the cylinder, then finding the absolute value of this error for sampled time instances and then summing the values.

For the real system, the position error sum is 1510 m and the efficiency measure is 46.77 J/mm. The position error number differs significantly from the simulated case, but the actual tracking performance appears quite similar in the figure. A possible reason is that a small difference gets integrated fast to a large value. More importantly the efficiency measure differs significantly. The reason for this was found to be the fact that the pressures in the accumulators were dropping faster than in the model. When the supply pressure in the middle line reached a low enough value it was charged from the high pressure accumulator by opening two valves connected in parallel. This rather costly charging wastes a lot of energy. Since the middle pressure drops slower in the simulation the costly charging is not used and energy efficiency is improved. The reason for this difference could not be found in the limited time in which the test stand was available, but possible reasons are valve opening overlap and errors in the simulation model. For the fault case, the simulation's position error is 920.29 m and the efficiency measure is 21.84 J/mm, whereas for the real test stand the position error is 1498 m and the efficiency measure is 44.30 J/mm. The model does not describe the real situation perfectly, but since the goal of the paper is to find if the system is able to function under specific faults this level of agreement was considered satisfactory for the purpose of the fault tolerance study.

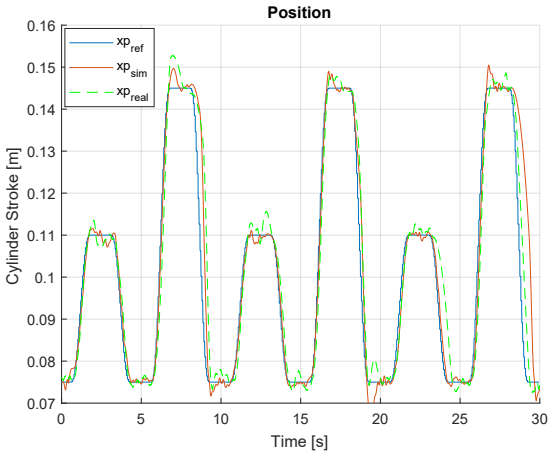

Figure 11. Comparison of model and real measurements without fault

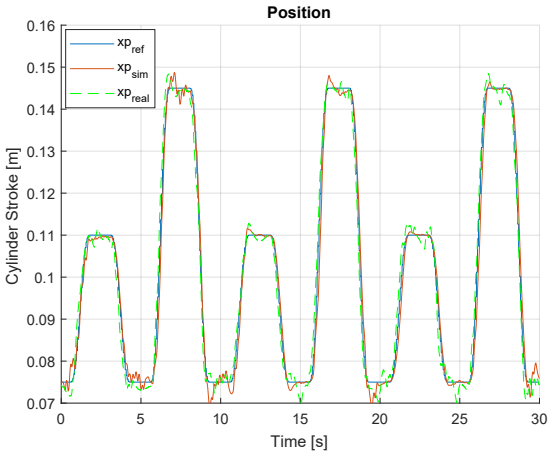

Figure 12. Comparison of model and real measurements with fault

5. FAULT TOLERANCE STUDY

For the fault study a fault in the valve between a chamber and a pressure line is introduced for the entire trajectory run. The same trajectory is used for all tests. Two types of faults are studied - a valve stuck closed and a valve stuck open. For chamber A1 where four valves are used per pressure line the fault is introduced in all four valves. In this sense the four valves are considered as one big valve. The same is done for chamber B1. Later in this section a weight is introduced in the control structure in order to improve the fault tolerance of the system. For the study it is assumed that the fault is detected and isolated. The actual fault detection and isolation have not been investigated in this paper and are instead left for future work. Multi-chamber cylinders are inherently fault tolerant to some faults. This can be seen in Tab3. In this table faults are denoted as "$*$ to $\bullet$", which can be understood as a fault in the valve connecting pressure line $*$ to chamber $\bullet$. The results, which can be considered critical, i.e. total inability to complete the work, have red coloured cells. Most often in these cases, the cylinder would reach one or the other end stop and stay there. For instance when chamber A1 is always connected to the high pressure line, the cylinder force is too large for the cylinder to move in the negative direction.

The basis for the fault tolerance in this part of the study is the fact that some of these valves do not need to be used to follow the predefined trajectory. It can be seen that the faults in the low pressure line are the most

critical, because they result in failures. In almost all cases the fault resulted in degraded performance in either the accuracy or the energy efficiency of the controller.

Table 3. Results with valve stuck closed without detection

Fault	Pos Error	Energy	Fault	Pos Error	Energy	Fault	Pos Error	Energy
p_s to A1	615.57	20.32	p_m to A1	1694.33	33.62	p_l to A1	12220.05	18.03
p_s to B1	1417.39	18.52	p_m to B1	659.43	26.85	p_l to B1	9062.45	14.41
p_s to A2	810.23	20.16	p_m to A2	735.09	25.70	p_l to A2	9231.42	19.53

The results for the same faults, but with a fault tolerance addition to the controller can be seen in Tab.4. The same convention has been followed, and the critical faults are coloured in red. If the fault is detected, the fault tolerance is improved as can be seen by the fact that some of the faults which were critical have been recovered from. The only thing necessary to introduce the fault tolerance in the controller is to augment the cost function as

$$J = \omega_1 \left|\hat{e}\right|_1 + \omega_2 \left|W_f F \hat{u}\right|_1 \tag{25}$$

where W_f is a diagonal matrix with a large weight at the position of the faulty valve and ones at all other positions of the diagonal. The cost of using that particular valve becomes very large and other force combinations are preferred. The weight selected here was chosen arbitrarily large, until those valves are never picked by the controller. In the case where a valve is stuck open, the weights can be put on the other two pressure lines. This makes combinations, where the valve (which is stuck open) is chosen to be open, is preferred. Using these weights is an easy way to represent constraints in a differential evolution algorithm. For all faults the weight on position error ω_1 had to be increased. This was necessary due the fact that the controller now needs to pick less energy efficient combinations.

Table 4. Results with valve stuck closed with detection

Fault	Pos Error	Energy	Fault	Pos Error	Energy	Fault	Pos Error	Energy
p_s to A1	490.19	36.45	p_m to A1	486.97	20.67	p_l to A1	1034.89	22.83
p_s to B1	509.69	18.22	p_m to B1	414.85	21.49	p_l to B1	590.81	46.28
p_s to A2	422.55	29.98 6	p_m to A2	487.97	24.86	p_l to A2	376.04	30.12

The same investigation has been done for faults where the valve is stuck open instead. The results are presented in Tab.5 and Tab.6. It can be seen that valves stuck open lead to critical failures in almost all cases when the the fault is not detected. Part of the severity of the failures is the fact that when a valve is stuck closed, it influences the performance only if the controller chooses to use it. If a valve is stuck open, it influences the performance at all times. It also leads the controller to short-circuit the pressure lines. This drains the accumulators, and the available pressures change significantly. The results in Tab.6 show that with proper detection and changes to the controller the fault can be recovered from. Again the weight on position error had to be increased in order to force the controller to use the more costly switching combinations more often.

Table 5. Results with valve stuck open without detection

Fault	Pos Error	Energy	Fault	Pos Error	Energy	Fault	Pos Error	Energy
p_s to A1	38422.09	13.38	p_m to A1	4208.14	29.85	p_l to A1	15956.17	1.43
p_s to B1	31687.24	15.63	p_m to B1	596.53	21.75	p_l to B1	2735.25	46.93
p_s to A2	31879.61	9.23	p_m to A2	16711.33	49.24	p_l to A2	13078.48	21.69

Table 6. Results with valve stuck open with detection

Fault	Pos Error	Energy	Fault	Pos Error	Energy	Fault	Pos Error	Energy
p_s to A1	23455.80	13.65	p_m to A1	473.98	25.87	p_l to A1	853.26	17.15
p_s to B1	17781.12	20.80	p_m to B1	522.98	20.05	p_l to B1	876.16	12.58
p_s to A2	778.69	38.51	p_m to A2	618.81	22.57	p_l to A2	721.17	32.92

6. CONCLUSION AND FUTURE WORK

In this paper an investigation of the fault tolerance of multi-chamber cylinders was conducted. To facilitate this study a mathematical model of the test stand was created. Tests were conducted to verify that the model exhibits similar behaviour to the real test stand. Model predictive control with fault tolerance capabilities was implemented in the model and on the real system. A study of the fault tolerance of the controller was performed both when the fault is detected and isolated and when it is not. During this study it was found that faults where the valve is stuck open are the most critical. Furthermore, it was found that when the fault is detected and isolated, the controller can function normally by utilizing different switching patterns. Some faults are severe enough that even with this fault tolerant controller they cannot be recovered from. For future work online fault detection and isolation should be investigated in order for this fault tolerant control strategy to be useful.

ACKNOWLEDGMENT

The research in this paper has received funding from The Research Council of Norway, SFI Offshore mechatronics, project number 237896/O30.

7. REFERENCES

References

[1] A. Hedegaard Hansen, M. F Asmussen, and M. M. Bech, "Model predictive control of a wave energy converter with discrete fluid power power take-off system," *Energies*, vol. 11, no. 3, p. 635, 2018.

[2] L. Siivonen, M. Linjama, M. Huova, and M. Vilenius, "Jammed on/off valve fault compensation with distributed digital valve system," *International Journal of Fluid Power*, vol. 10, no. 2, pp. 73–82, 2009.

[3] N. C. Bender, H. C. Pedersen, A. Plöckinger, and B. Winkler, "Reliability analysis of a hydraulic on/off fast switching valve," in *Proc. of The Ninth Workshop on Digital Fluid Power, Aalborg, Denmark*, 2017.

[4] M. Linjama and M. Huova, "Model-based force and position tracking control of a multi-pressure hydraulic cylinder," *Proceedings of the Institution of Mechanical Engineers, Part I: Journal of Systems and Control Engineering*, vol. 232, no. 3, pp. 324–335, 2018.

[5] A. H. Hansen, H. C. Pedersen, and R. H. Hansen, "Validation of simulation model for full scale wave simulator and discrete fuild power pto system," in *9th JFPS International Symposium on Fluid Power*. Japan Fluid Power System Society, 2014.

[6] V. H. Donkov, T. O. Andersen, H. C. Pedersen, and M. K. Ebbesen, "Application of model predictive control in discrete displacement cylinders to drive a knuckle boom crane," in *2018 Global Fluid Power Society PhD Symposium (GFPS)*. IEEE, 2018, pp. 408–413.

[7] M. A. Stephens, C. Manzie, and M. C. Good, "Model predictive control for reference tracking on an industrial machine tool servo drive," *IEEE Transactions on Industrial Informatics*, vol. 9, no. 2, pp. 808–816, 2013.

[8] R. H. Hansen, T. O. Andersen, and H. C. Perdersen, “Analysis of discrete pressure level systems for wave energy converters,” in *Fluid Power and Mechatronics (FPM), 2011 International Conference on*. IEEE, 2011, pp. 552–558.

[9] S. Boyd, N. Parikh, E. Chu, B. Peleato, J. Eckstein *et al.*, “Distributed optimization and statistical learning via the alternating direction method of multipliers,” *Foundations and Trends® in Machine learning*, vol. 3, no. 1, pp. 1–122, 2011.

[10] P. Cortes, J. Rodriguez, C. Silva, and A. Flores, “Delay compensation in model predictive current control of a three-phase inverter,” *IEEE Transactions on Industrial Electronics*, vol. 59, no. 2, pp. 1323–1325, 2012.

[11] A. Harrison and D. Stoten, “Generalized finite difference methods for optimal estimation of derivatives in real-time control problems,” *Proceedings of the institution of mechanical engineers, part I: journal of systems and control engineering*, vol. 209, no. 2, pp. 67–78, 1995.

AS SIMPLE AS IMAGINABLE - AN ANALYSIS OF NOVEL DIGITAL PUMP CONCEPTS

MSc Samuel Kärnell, PhD Liselott Ericson
Department of Management and Engineering, Division of Fluid and Mechatronic Systems
Linköping University, Sweden
E-mail: samuel.karnell@liu.se

ABSTRACT

This paper focuses on how digital displacement can be achieved in a *wobble plate pump* by connecting the cylinders in the pump to different groups and using by-pass valves to control the flow from each group. The idea is to make a simple and inexpensive electronically controlled pump. The paper deals with two main aspects, the *cylinder configuration* and the *valve configuration*. The *cylinder configuration* refers to how the cylinders in the pump can be grouped and how different groupings will affect the flow pulsations. The *valve configuration* refers to the by-pass solution. Two principally different solutions are analysed: one that uses 3-way by-pass valves and one that makes use of check valves in combination with 2-way on/off-valves. A comprehensive simulation model has been used as a tool for analysing flow pulsations for the different design configurations. The results show that a cylinder configuration with 3+6 cylinders delivers low flow pulsations for all three displacement settings. However, if more displacement settings are desired, an interesting finding is that a configuration with 3+6+12 cylinders is only slightly better than a configuration with 2+4+8 cylinders, from a pulsation amplitude point of view. This is due to the pre-compression in the cylinders. Regarding the valve configuration, it has been shown that both of the analysed configurations might suffer from problems during switching, especially if the valves are slow.

KEYWORDS: Digital hydraulics, digital displacement, pumps

1 INTRODUCTION

The title of this paper includes the term *digital pump*. So, first of all, what is a digital pump? The definition is not clear, and it has been subject to debate [1]. However, if we choose to stick to the somewhat simplistic definition that a digital pump is *a flow source with discrete displacements*, several types of digital pumps can be mentioned. Some examples are

- Fixed pumps with by-pass valves
- Parallel connected fixed pumps with by-pass valves
- Dual-displacement pumps
- Digital displacement pumps (full stroke control)

The first and the second items in the list are very similar. The difference is that pumps with by-pass valves can only be on or off whilst parallel connected pumps offer more discrete alternatives. Dual-displacement pumps offer two nonzero discrete outputs and the number of discrete outputs from a digital displacement pump can generally be very high.

Pumps with by-pass valves are widely used and can be found on e.g. trucks where the by-pass valve is activated (or deactivated) when the hydraulics are not being used. The valve short circuits the outlet with the tank, which means idling mode. Parallel connected pumps are basically multiple pumps with isolated outlets connected to the same shaft. If the pumps are fixed, they will come under our definition of a digital pump. In the case of two isolated outlets (i.e. two pumps), the machine usually goes under the name tandem pump or double pump. A common application for these is log splitters, where one pump can be deactivated by a pressure-controlled by-pass valve (sometimes called unloading valve). Tandem pumps are also common on e.g. trucks and excavators. In the case of the truck, it can be that the outlets are connected when e.g. a hooklift is used, but are then separated to power other functions, such as a snowplough and an auger, during driving. In 1984, Moorhead published an article [2] on parallel connected pumps. He proposed what he called a *digital pump system* for an injection moulding machine and focused on the potential energy and cost savings. The idea was to use parallel connected pumps instead of a variable pump. Even then, he stated that the approach was not new. Still there has not been much research in the area, even though there are many ways to design these machines. However, some work has been done, including Heitzig [3] and Locateli [4]. Both of them focus on the example of a configuration of pumps that are binary scaled (i.e. 1, 2, 4...) and they have shown promising results regarding energy efficiency and controllability. However, the deterring thing with their concepts is the large number of required on/off valves.

A quite different kind of digital pump is the dual-displacement pump, and as the name implies, it only offers two different discrete outputs. However, the two outputs are *on* and *slightly on*. Dual-displacement pumps are most often found in speed-controlled systems. The reason for this is that the size of the electric motor can be kept down since a smaller displacement reduces the torque requirement. Examples of manufacturers of dual-displacement pumps are Moog, Parker Hannifin and Eaton. Moog offers radial piston pumps [5] where the stroke ring position has two defined positions. The positions can be mechanically adjusted with screws. An electronically controlled valve, which directs the pilot pressure acting on the ring, is then used to set the displacement. Parker Hannifin and Eaton use the same principle but for axial piston machines, where the swashplate angle can be varied between two values [6] [7].

However, most people in the fluid power community probably think of the Scottish company Artemis Intelligent Power (AIP) when they hear the term *digital pump*. AIP are pioneers in the technique they call Digital Displacement (DD), and the first patent for the technique was filed in as early as 1989 [8]. In DD machines, each cylinder is individually controlled by electronically controlled valves. Principally, it is possible to use full stroke control or part stroke control. However, note that part stroke control allows for a continuous displacement setting which would exclude it from our definition of a digital pump (which could indicate problems with the definition). Nevertheless, AIP has done a lot of work and a recent success was the implementation of a DD pump in an excavator [9]. Research on DD-machines has also been carried out at universities around the world. In Aalborg they have focused on the valves and the control, see for example [10] [11]. At Purdue University, they have also tested some control strategies [12] [13] [14]. Another university in the US that has studied the potential is the University of Minnesota. They have focused on PWM controlled rotary valves [15] and recently they have also tested some interesting control algorithms for more conventional control [16]. In Tampere, they built a pump [17] and later also a transformer based on DD technology [18].

When it comes to system design, variable flow is often desired for efficiency-related reasons. However, conventional variable pumps are known for being costly and for having low efficiency at part displacement, due to relatively high regulator losses and compression losses, among other factors. DD pumps do not suffer from these losses to the same extent and they therefore appear to be highly efficient and promising in many ways, but they are complex and place very high demands on the valves. A simpler alternative with only a few discrete displacements could be a good compromise between cost and system efficiency, which is why the concepts presented in this paper can be of interest.

2 THE NOVEL DIGITAL PUMP CONCEPTS

Parallel connected pumps have two principally independent main design parameters. One is what the pump elements should look like and the other is the configuration of the by-pass valves. It was previously stated that a pump that is simple was desired. The idea is therefore to use a conventional wobble plate pump (WPP) and simply arrange its cylinders in groups that form the parallelly connected pump elements. By doing so, one could obtain a compact digital pump unit with good performance.

2.1 The Wobble Plate Pump

A WPP is basically an inline pump with a rotating swashplate, i.e. the wobble plate. The commutation is managed by check valves. Each cylinder has two check valves, one for the inlet and one for the outlet. The working principle of a WPP is shown in Fig. 1. The fact that the pistons are not rotating makes the WPP applicable for the digital pump application. A pump with port plate commutation would require several outlet ports, which in turn would mean that the cylinders must be placed at different radii. This could be problematic when the number of groups increases, and pumps with port plates are therefore not considered here, even though such double pumps do exist (e.g. [19]). However, note that a WPP with check valves cannot run as a motor.

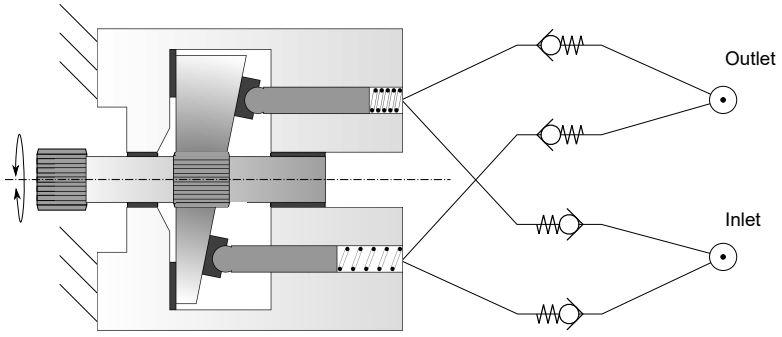

Figure 1: Working principle of a two-piston wobble plate pump.

2.2 Cylinder Configuration

For reasons of simplicity and cost, it is desirable to have as few controllable valves as possible. However, one must weigh the number of valves against the number of desired discrete displacements. When using binary scaling, the available displacement settings will be equally spread over the displacement range and the number of discrete displacements can be described as in Eq. 1, where n_d is the number of displacement settings and n_v the number of valves. The number of required cylinders depend on whether or not the cylinders are equally sized. If equally sized cylinders are assumed, the number of required cylinders is then described as in Eq. 2, where $n_{g,min}$ is the number of cylinders in the smallest group, i.e. the smallest pump element. The number of required cylinders for different numbers of discrete displacements and different numbers of cylinders in the smallest group is presented in Fig. 2(a).

$$n_d = 2^{n_v} \tag{1}$$

$$n_{cyl} = n_{g,min}\ (2^{n_v} - 1) \tag{2}$$

When the number of cylinders in the smallest group, $n_{g,min}$, and the number of groups, n_v, have been set, a decision on how the cylinders should be grouped must be made. The number of possible solutions escalates

$n_{g,min}$ \ n_v / n_d	1 / 2	2 / 4	3 / 8	4 / 16
1	1	3	7	15
2	2	6	14	30
3	3	9	21	45

(a) Number of required cylinders. The configurations within the dashed blue box are illustrated in Fig. 2(b).

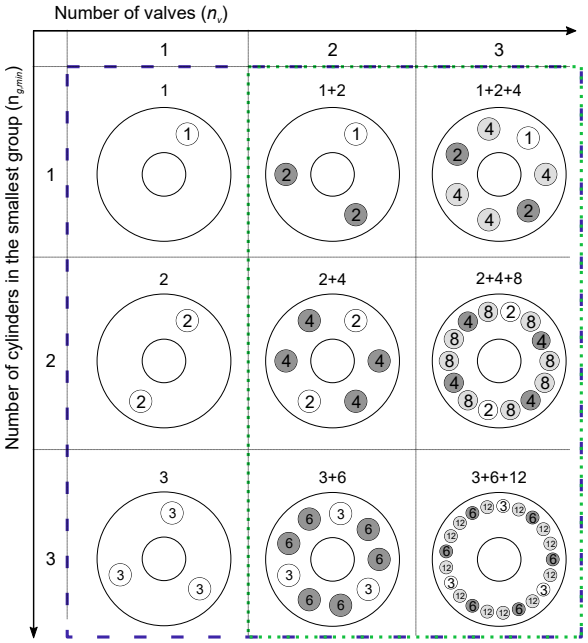

(b) Optimal grouping of cylinders for different configurations. The number in the cylinder corresponds to the number of cylinders in its group. The ones within the green dotted box will be analysed further.

Figure 2: Number of required cylinders and how they should be grouped.

quickly with increasing $n_{g,min}$ and n_v. However, many solutions are inappropriate for reasons related to flow pulsations. To get as smooth flow as possible, it is reasonable to spread the cylinders in each group as far as possible. A proper way to decide the best solution is therefore to minimise the sum of the actual angle between each group member and the angle that represents equally spread cylinders. This would give minimal kinematic flow pulsations. The results of this grouping strategy for different configurations are presented in Fig. 2(b). It is this grouping that has been used throughout this paper.

2.3 Valve Configuration

The different pump elements must be able to be controlled individually. The by-passing can be handled in several ways. The two concepts that are dealt with in this paper are presented in Fig. 3. One concept makes use of 3-way by-pass valves and the other uses 2-way by-pass valves. Both concepts require one control valve for each pump element. However, the 2-way solution also requires one check valve for each pump element. Observe that these concepts could be used together with any pump units.

When looking at the valve configurations in Fig. 3, some might question the novelty of the concepts. In fact, the 2-way configuration (Fig. 3(b)) was basically illustrated as the definition of parallel connected pumps in Linjama's state of the art review on digital fluid power [20] and the 3-way by-pass configuration (Fig. 3(a)) has similarities with the systems presented in the earlier mentioned examples from Heitzig and Locateli [3] [4]. The novelty is the complete pump system working as a variable pump.

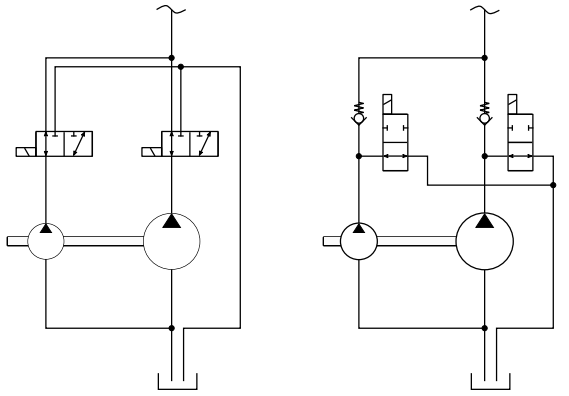

(a) Digital pump with 3-way by-pass valves.

(b) Digital pump with 2-way by-pass valves.

Figure 3: Two possible valve configurations for a digital pump with two pump elements.

2.4 General Control

In its simplest form, the controller for the pumps basically is an open loop controller. It only has to read a displacement reference and then output a value from a table, see Fig. 4. However, for many applications this will probably not work particularly well since it can cause a lot of switching. A lot of switching means much losses - compression losses, throttling losses and losses due to the short circuit of the inlet and outlet (mainly for the 3-way by-pass configuration). Therefore, it might be relevant to use a function in the control algorithm that takes switching losses into account. Furthermore, the relative valve timing can be an important performance factor. This will be discussed later in section 4.

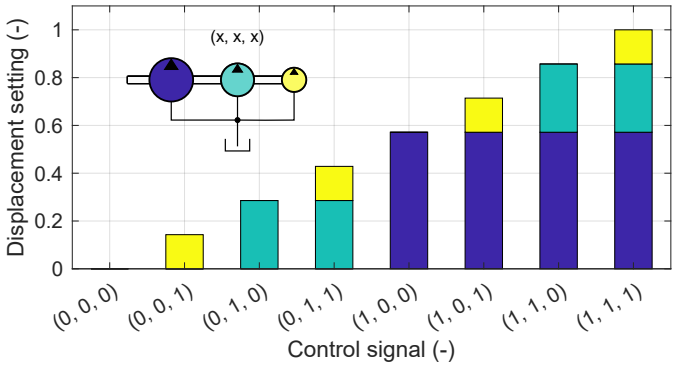

Figure 4: Principal control of any pump configuration with three binary scaled groups.

3 SIMULATION MODEL

The results presented in the following sections are based on simulations. The simulation models that have been used are based on a model of a commercial WPP with a displacement of 70 cm^3/rev, 10 pistons and a rated maximum speed of 2200 rpm. The model is built in the software Hopsan and is an improved version of the one presented by the authors in [21]. Leakage, restriction and friction parameters in the model have been adapted to fit efficiency and cylinder pressure measurements.

The difference between the original WPP model and the digital pump models is basically the additional by-pass section. The by-pass valves are modelled with defined switching times for each direction. The opening areas

change linearly during the switching. During comparison between a WPP and a digital pump, the number of cylinders on the WPP has been adjusted to be the same as the digital pump. The cylinder diameters were adjusted in order to make the displacement 70 cm^3/rev for all configurations if nothing else is stated.

4 FLOW PULSATIONS

Flow pulsations of pumps are of interest since they are closely related to the noise level. For the pump concepts presented here, flow pulsations are considered as critical and also as one of the strongest arguments against them. This is because the placing of the active cylinders can be somewhat strange. The simulated amplitudes for different displacement settings for different pump configurations are shown in Fig. 5(a). It should be stated that these amplitudes are depending on how much of the stroke that is used before the check valves opens. This means that parameters such as rotational speed and oil compressibility affect the result. Nevertheless, it is interesting to compare them with the amplitudes of the kinematic flow (i.e. the flow due to the piston movements, without any compression-related effects regarded). These are shown in Fig. 5(b).

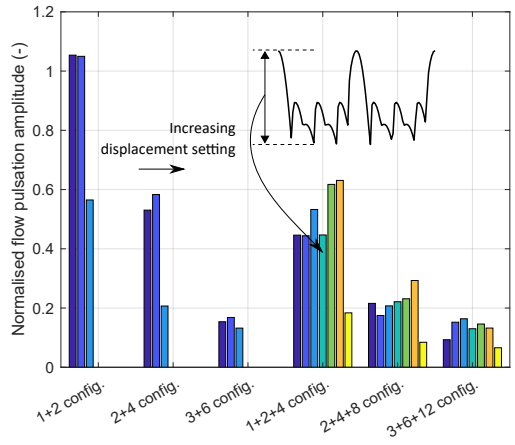

(a) Normalised flow pulsation amplitudes for various cylinder configurations and different displacement settings. The shown amplitudes are for 3-way by-pass simulations at 1000 rpm and 35 MPa.

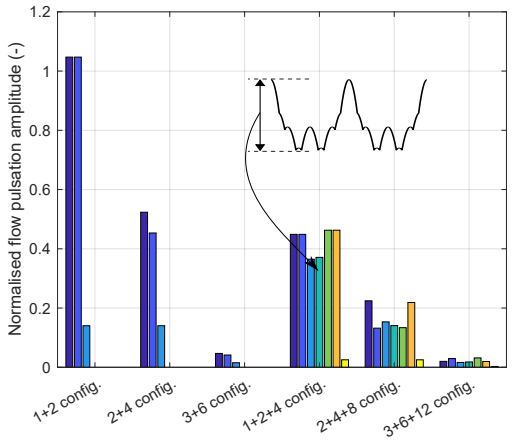

(b) Normalised kinematic flow pulsation amplitudes for various cylinder configurations and different displacement settings.

Figure 5: Simulated flow pulsations versus kinematic flow pulsations. The amplitudes are normalised to the ideal flow at full displacement. The observed configurations are the ones within the green dotted line in Fig. 2.

The static behaviours (i.e. no switching) are very similar for the 2-way and 3-way by-pass configurations, and in Fig. 6 and 7 it can be seen that the compression phase of the stroke has a high impact on the amplitudes. A slightly different performance between the 2-way and the 3-way configuration can also be noted. This is due to the characteristics of the additional check valves in the 2-way configuration. Nevertheless, during switching, the two configurations show completely different characteristics.

The 2-way by-pass configurations experience problems with delays due to the slow closing and opening of the valves. This is because pressure cannot be built up until a valve is completely closed. The pump element will therefore not give any flow to the system until the valve is fully closed. On the other hand, the pressure drops quickly when a valve starts to open. This means that the pump will not produce any flow during certain switchings, which can be seen in Fig. 7. This makes the switching less predictable for the user compared to the 3-way configuration. Furthermore, a small peak in flow can be noted after every switch due to the characteristics of the check valves. The 3-way by-pass configurations experience quite different problems compared to the 2-way configuration. They mainly struggle with backflow during switching, since there is a short circuit between the inlet and the outlet for a short time.

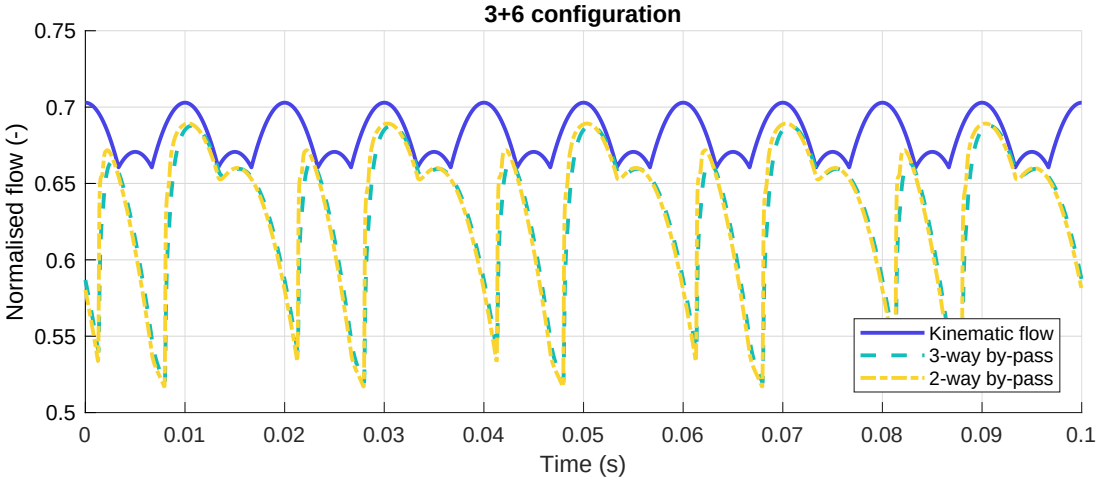

Figure 6: Flow pulsations for a pump with 9 cylinders and 2 valves at the displacement setting $\varepsilon = 2/3$. The figure shows the flow for both 2-way by-pass and 3-way by-pass configuration running at 1000 rpm and 35 MPa, as well as the kinematic flow. The flows are normalised to the ideal geometrical flow.

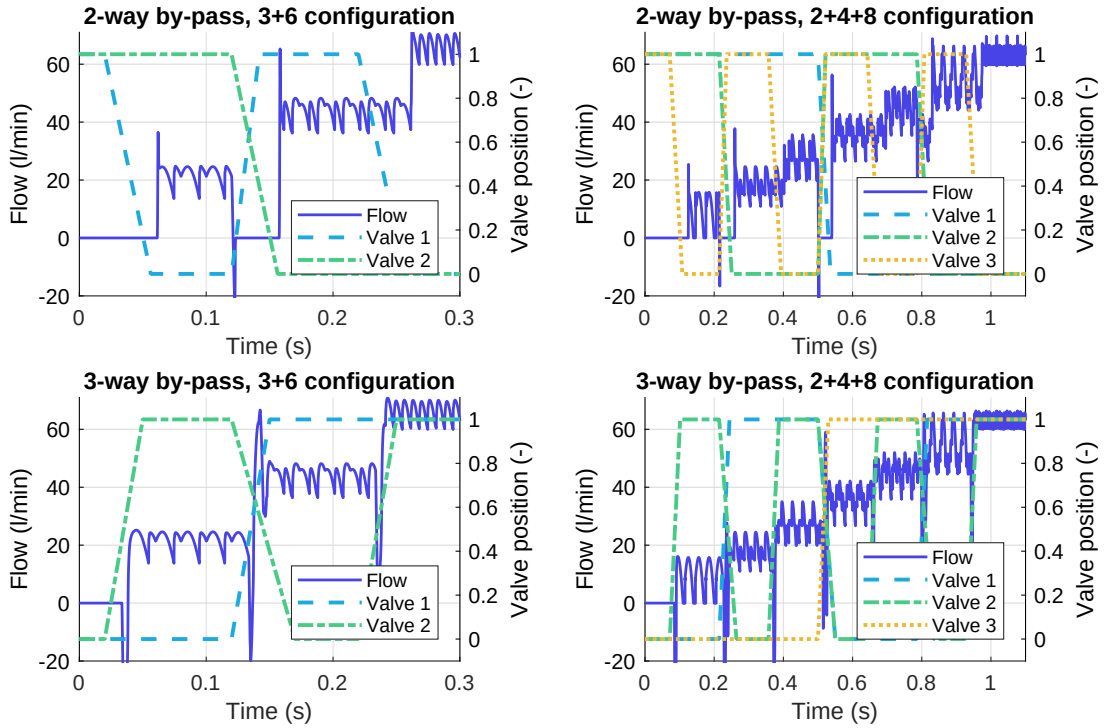

Figure 7: Flow pulsations and switching behaviour for different cylinder and valve configurations. For a 2-way by-pass, a valve position at 1 means idling whilst it means pumping for a 3-way by-pass. The time to get from 0 to 1 was set at 30 ms and from 1 back to 0 at 50 ms. The working conditions were 1000 rpm and 35 MPa.

4.1 3-way by-pass - Switching Considerations

As already mentioned, the 3-way by-pass design suffers from backflow. This is due to the design of the valve that should be underlapped, see Fig. 8(a). The reason why it should be underlapped is because high pressure build-up upstream from the valve has to be avoided. Fig. 8(b) shows how the maximum pressure for a specific cycle varies with the underlap and the opening time of the valve. One can see that fast valves can accept less underlap. For cartridge valves, the typical opening time is 30-100 ms. However, here the opening areas change linearly during the switching time. This is a simplification that may make the slow valve performance look worse than the actual case, where delays in the power electronics takes up some of the switching time and where the spool does not move with a constant velocity.

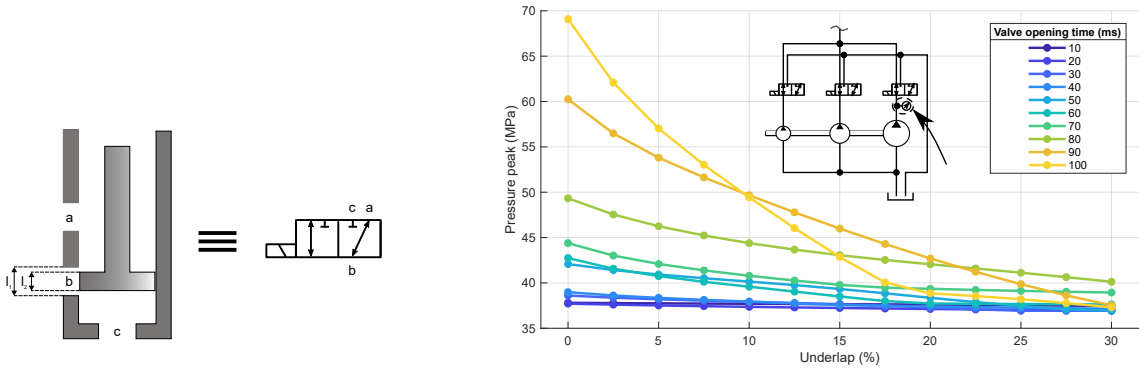

(a) Principal illustration of the directional spool valve in the 3-way by-pass configuration. The underlap is defined by the relationship between l_2 and the difference between l_1 and l_2. 0 % underlap means that l_1 and l_2 are equal.

(b) Maximum pressure during a displacement switch from $3/4$ to $4/7$ as a function of the underlap and the switching time of the valve. The opening areas change linearly during the switching. The switching time was here equally set in both directions and the results are for a rotational speed of 1265 rpm and a differential pressure of 35 MPa.

Figure 8: 3-way valve design.

The underlap means that there is a short circuit between the inlet and outlet during switching. If a slow valve is used, the losses due to this short circuit are substantial, and so are the flow pulsations. Furthermore, this can affect the position of the load, which can be a critical aspect. Additional check valves can be placed on the outlet line to reduce this problem. However, this will cause a higher pressure drop.

One approach to handling the flow pulsations can also be to adjust the valve timing. By making sure that the shorting is not taking place at the same time for several valves, the pulsation amplitude can be reduced. This can be seen in Fig. 9(a). The fact that single-actuated solenoid valves generally have different switching times for different directions makes this happen automatically, but it can also be done via the controller. However, the losses will not be affected by this - they will only occur at different moments in time.

4.2 2-way by-pass - Switching Considerations

The major problem with a 2-way by-pass is that the flow can disappear when two valves are operating in parallel, since the check valve closes immediately when a valve starts to open up to the tank, but only starts to open when a valve is fully closed. However, this problem can be avoided by adding a time delay that corresponds to the opening or closing time. See Fig. 9(b). The disadvantage with this is that one must know the switching time, otherwise there will be either a short peak or a drop in flow rate, depending on whether the delay is too long or too short. Another aspect to consider is whether one should add a delay in the switching when a pump element is deactivated. This could result in a more symmetrical and predictable behaviour.

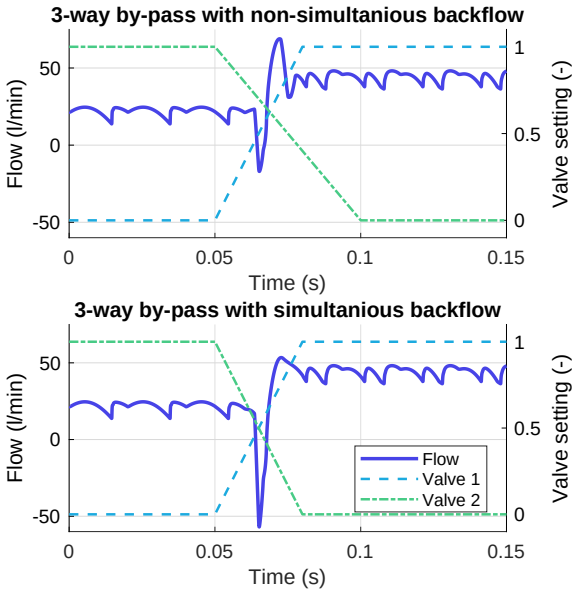

(a) Difference in flow pulsation amplitude for a 3-way by-pass valve with 3+6 cylinders when two valves are generating backflow at the same time versus when the backflows are taking place at different times. The underlap of the valve was 10 %.

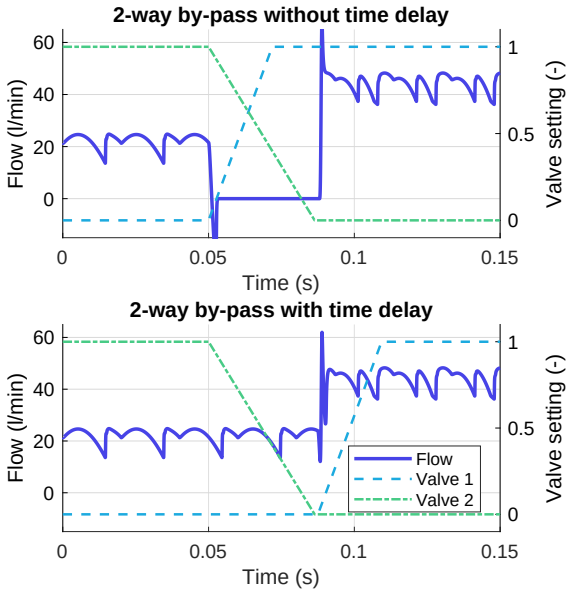

(b) How a time delay in the controller can improve the performance of a 2-way configuration with 3+6 cylinders. It can be seen that undesired changes in flow rate can be avoided by controlling the valves sequentially.

Figure 9: Switching considerations. The switching was from the displacement setting $\varepsilon = 1/3$ to $\varepsilon = 2/3$ and the working conditions were 1000 rpm and 35 MPa.

5 EFFICIENCY

The efficiency of the digital pumps is highly dependent on the capacity of the additional valves. Small valves will cause low efficiency at high speeds due to high pressure drops. Therefore, it should be kept in mind that the efficiencies shown in this section can be improved quite easily by simply increasing the size of the valves. Furthermore, the reference pump has a relatively low efficiency, which is illustrated in Fig. 10. The figure also shows how the efficiency and power losses vary with the displacement setting for different pressure levels on a 3-way by-pass. All valves on the 3-way by-pass are normally in idling mode and require a pressure drop of 1.5 MPa at 60 l/min. The power consumption for an activated valve was set at 33 W.

Note that the efficiency of a 3-way by-pass and a 2-way by-pass is equal if the pressure drop over the check valve is the same as for the 3-way valve. There is only a difference in efficiency between the 3-way and 2-way by-passes when switching is taken into account, which has not been analysed here. Also note that the power loss due to the valve arrangement is almost independent on both the system pressure and the displacement setting if the pressure drop to the system and the pressure drop to tank are equal.

6 DISCUSSION

The analysis has not changed anything regarding the statement that the concepts are simple. The cylinder configurations with three cylinders in the smallest group probably offers acceptable pulsation levels for many applications at all displacement settings, but configurations with more than two groups require very high numbers of cylinders (21, 45...). The alternative with 2+4+8 cylinders is relatively good regarding pulsation amplitudes, and 14 cylinders is still a reasonable number. Too many cylinders would make the pump more expensive and is therefore undesirable. However, note that the frequency is important for how the noise is

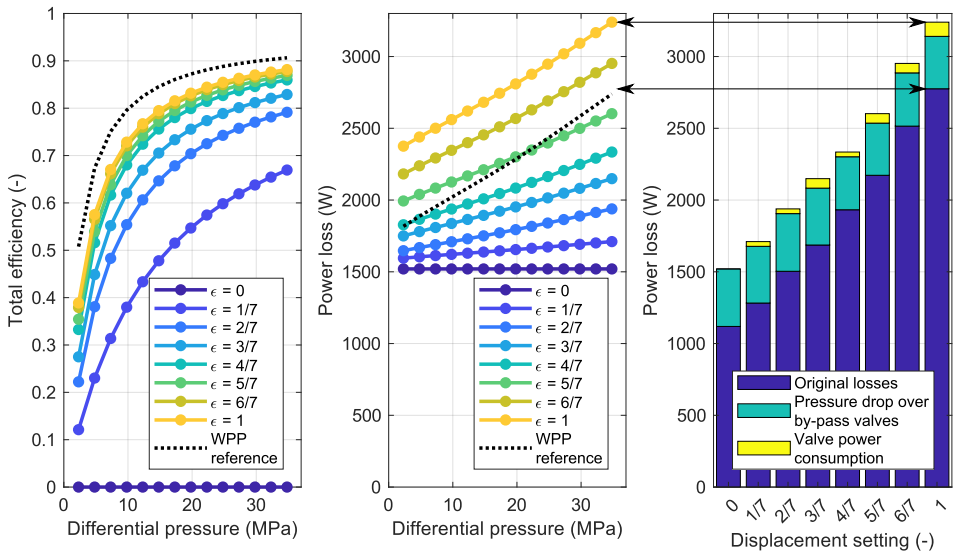

Figure 10: Efficiencies and average power losses for a 3-way by-pass configuration with 7 pistons and 50 cm^3/rev at different displacement settings when running at 1000 rpm. Simulated data for a WPP is also shown as a reference. The bar graph shows the distribution of power losses at 35 MPa and 1000 rpm for different displacement settings. Original losses correspond to the losses in the reference WPP.

perceived and that the frequency distribution has not been analysed. Another detail that has not been taken into account is the cylinder pressure rate. A high cylinder pressure rate (i.e. fast pressure build-up) can cause much structure-borne noise. However, it would also make the check valves in the WPP open faster which would make the flow pulsation amplitudes get closer to the kinematic flow pulsation amplitudes shown in Fig. 5(b). In other words, there is a trade-off between structure-borne and fluid-borne noise.

Nevertheless, the 3-way by-pass design showed problems with backflow and/or high pressure build-up. The backflow can be solved by adding check valves downstream from the 3-way valve, but that would lower the efficiency due to higher pressure drops. Furthermore, the number of required components would be the same as for the 2-way by-pass configuration, but the 2-way configuration would have better efficiency. The main problem with the 2-way by-pass is that the valves should ideally be controlled sequentially. This is problematic if the switching times for the valves changes with working condition and during the lifetime. A solution to this could be to measure the valve position. However, that would make the pump more complex which is not desirable. It is probably a better alternative to use faster valves. Nevertheless, another drawback with the 2-way by-pass configuration is that it can be perceived as less predictable for the user since the flow rate sometimes changes immediately and sometimes only after a full valve movement. A faster valve would also solve this problem, if it is considered as a problem. A detail that also should be mentioned is that the 2-way configuration cannot work as a motor. That is not a problem when using a WPP since it cannot work as a motor either, but it is a potential drawback if using other pump elements.

When it comes to efficiency some might argue against the pump concepts presented here and point out the poor performance. First of all, it should then be clearly stated that the original pump does not offer very satisfactory performance. This could be improved by changing other pump parameters than those relating to the presented concepts. However, the concepts have one principal drawback, compared to other pumps: the flow has to pass through an additional valve and, as mentioned earlier, the size of these valves has a high impact on efficiency. The power consumption of the valves is, however, relatively low.

Another aspect regarding the valves is that the valve for the smallest group will switch more frequently than the other valves. This means that it is likely to fail before other components are even close to being worn out. And if one valve fails, many driving modes, i.e. displacement settings, will be lost.

7 CONCLUSIONS

Different cylinder and valve configurations for digital pump concepts have been presented and analysed. Two cylinder configurations are considered the most interesting: the 3+6-configuration and the 2+4+8-configuration. Regarding the valve configurations, simulations have shown that both the 3-way and 2-way by-pass configurations can work properly, but some challenges have also been revealed. Strategies to overcome these have been discussed, but the conclusion is: faster valves means less problems.

The main argument for considering the presented concepts at all is that they can offer electronically controlled displacement in a simple way. However, if a large number of discrete displacements is required, many cylinders will be needed. The pump will then become more expensive and therefore less attractive, but if a rather low number of discrete values is considered sufficient it can be a useful alternative - assuming that flow pulsations are not highly critical. The pump can then offer the good high-pressure performance of a piston pump and still be in a reasonable price range, since relatively simple valves can be used for control and since no additional sensors are needed.

8 FUTURE WORK

Since this is the first time the concepts have been considered, much remains to be explored. From the pump and valve perspective, the switching is something that deserves more attention. Furthermore, it is of interest to analyse how the noise emission of the different cylinder configurations are perceived and how the pulsations propagate. From a system perspective there is also a lot to investigate. For example, it is highly relevant to analyse how these digital pump concepts could work together with a shunt valve to produce a continuous, electronically controlled variable flow.

9 ACKNOWLEDGEMENTS

The authors would like to thank Sunfab Hydraulics AB for their contributions to this paper as well as the Swedish Energy Agency, who are sponsoring the project STEALTH - Sustainable Electrified Load Handling, App. no 44427-1, of which this work is a part.

REFERENCES

[1] Peter Achten, Matti Linjama, Rudolf Scheidl, and Stefan Schmidt. 2012. Discussion: Is the future of fluid power digital? *Proceedings of the Institution of Mechanical Engineers, Part I: Journal of Systems and Control Engineering*, 226(6):724–727.

[2] JR Moorhead. 1984. Saving energy with digital pump systems. *Machine Design*, 56(4):40–44.

[3] Stefan Heitzig, Sebastian Sgro, and Heinrich Theissen. 2012. Energy efficiency of hydraulic systems with shared digital pumps. *International journal of fluid power*, 13(3):49–57.

[4] Cristiano Cardoso Locateli, Paulo Leonel Teixeira, Edson Roberto De Pieri, Petter Krus, and Victor Juliano De Negri. 2014. Digital hydraulic system using pumps and on/off valves controlling the actuator. In *8th FPNI Ph. D symposium on fluid power*, pages V001T01A009–V001T01A009. American Society of Mechanical Engineers.

[5] Moog Inc. 2017. Electrohydrostatic pump unit. CDL49052-en, Rev. D.

[6] Eaton. 2015. *Variable speed drive pump solution*. E-PUIO-CC002-E.

[7] Parker Hannifin Corporation. 2017. *Drive Controlled Pump Effiziente hydraulische Antriebe mit System*. HY11-3351/DE.

[8] S.H. Salter and W.H.S. Rampen. 1991. Improved fluid-working machine. WO Patent App. PCT/GB1990/001,478.

[9] Matthew Green, Jill Macpherson, Niall Caldwell, and W.H.S Rampen. 2018. Dexter - the application of a digital displacement pump to a 16 tonne excavator. *Proceedings of the BATH/ASME 2018 Symposium on Fluid Power and Motion Control*.

[10] Daniel Beck Roemer. 2014. *Design and Optimization of Fast Switching Valves for Large Scale Digital Hydraulic Motors*. PhD thesis, Aalborg University.

[11] Niels H Pedersen, Per Johansen, and Torben O Andersen. 2017. Event-driven control of a speed varying digital displacement machine. In *ASME/BATH 2017 Symposium on Fluid Power and Motion Control*, pages V001T01A029–V001T01A029. American Society of Mechanical Engineers.

[12] Michael A Holland. 2012. *Design of digital pump/motors and experimental validation of operating strategies*. PhD thesis, Purdue University.

[13] Kyle Joseph Merrill. 2012. *Modeling and analysis of active valve control of a digital pump-motor*. PhD thesis, Purdue University.

[14] Farid El Breidi. 2016. *Investigation of digital pump/motor control strategies*. PhD thesis, Purdue University.

[15] Haink Tu. 2014. *High Speed Rotary PWM On/Off Valves for Digital Control of Hydraulic Pumps and Motors*. PhD thesis, University of Minnesota.

[16] Hao Tian, Perry Y Li, and James D Van de Ven. 2017. Using an angle domain repetitive control to achieve variable valve timing for a digital displacement hydraulic motor. In *Proc. of The Ninth workshop on digital fluid power, Aalborg, Denmark*.

[17] J Tammisto, M Huova, M Heikkilä, M Linjama, and K Huhtala. 2010. Measured characteristics of an in-line pump with independently controlled pistons. In *7th International Fluid Power Conference (7th IFK), 22-24 March 2010, Aachen, Germany*.

[18] Mikko Heikkilä, Jyrki Tammisto, Mikko Huova, Kalevi Huhtala, and Matti Linjama. 2010. Experimental evaluation of a digital hydraulic power managment system. In *The Third Workshop on Digital Fluid Power, Tampere, Finland*, pages 129–142.

[19] "Sunfab Hydraulics AB". 2019. Dual flow pumps. https://www.sunfab.com/se/products/dual-flow-pumps/?lang=eng.

[20] Matti Linjama. 2011. Digital fluid power: State of the art. In *12th Scandinavian International Conference on Fluid Power, Tampere, Finland, May*, pages 18–20.

[21] Samuel Kärnell, Alessandro Dell'Amico, and Liselott Ericson. 2018. Simulation and validation of a wobble plate pump with a focus on check valve dynamics. In *2018 Global Fluid Power Society PhD Symposium (GFPS)*, pages 1–8. IEEE.

DIGITAL HYDRAULIC IMV SYSTEM IN AN EXCAVATOR – FIRST RESULTS

Miikka Ketonen, Matti Linjama
Laboratory of Automation and Hydraulics / Tampere University of Technology
Korkeakoulunkatu 10, FI-33720 Tampere, FINLAND
miikka.ketonen@tut.fi

ABSTRACT

This study presents the conversion process of the working hydraulics on a 20 ton wheeled excavator from a load sensing system into a digital hydraulic independent metering valve system. Independent metering valves enable better energy efficiency by allowing reduction of throttling losses and by allowing energy recuperation and harvesting with different control modes. Digital hydraulics with parallel connected on/off valves offers robustness, more deterministic valve opening and improved durability compared to analogue IMV systems realised with proportional valves. The paper studies the feasibility of a digital hydraulic valve system in a high flowrate construction machine with multiple actuators operating simultaneously with a single electronically pressure controlled pump. Paper includes the process steps of design, feasibility analysis, building of the machine and the first measurements to validate the system operation and to show the performance compared to the original load-sensing system.

KEYWORDS: independent metering valves, digital hydraulics, construction machinery

1. INTRODUCTION

In future, machine building industry is going to have to adopt new technologies to increase the overall machine efficiency. When looking into the near future, only viable technology to produce large mobile machines with reasonable power-weight ratio is still hydraulics. Majority of the work machines are built with a hydraulic-mechanical load sensing system or with an open-centre valve system, and with proportional spool valves that link the inflow and outflow metering edges together. These technologies have been developed for more than 50 years and are well known and trusted by the customers. These technologies have been tuned up over the years to give the operator adequate controllability to the machine in various environments and operation conditions. Modern mobile proportional valve systems have become rather complex when additional features such as pressure compensators and regenerative functions have been added to the system. To improve energy efficiency, reduce system complexity, and to improve flexibility of the valve system, independent metering valves have been proposed to replace traditional spool-valves.

Independent metering valve technology has been subject for many studies (e.g. [1]–[5]). Earliest commercial independent metering valve solutions were available from companies Monti in seventies and from Vickers in eighties [6]. Modern commercial IMV-valve systems are available e.g. from Husco Incova [7] and Eaton [8], but the reliability and durability is not yet accepted widely by the construction machine builders. Safety regulations and concerns are one of the reasons slowing down the implementation of IMV-technology in

construction machines. During the last few years, studies related to IMV-technology have been focusing on improving the safety, improving the dynamic properties, and making the mode switching during actuator motion smooth [9]–[12]. Summaries on the current state of the research and the challenges to defeat have been done by Ding et al. [13] and Eriksson and Palmberg [6].

Three different valve types have been used in IMV-systems. Benefits and disadvantages of these technologies can be seen from table 1. Benefits of spool-type valves are accurate flowrates and possibility to build IMV-system with only two 3/3-valves. Poppet type valves can be leak-free and the manufacturing tolerances are not as tight as with the spool valves.

Table 1. IMV-valve types

Spool-valves	Poppet-valves	Digital valves (with parallel connected poppet-type on/off-valves)
+ Accurate flowrates + IMV system possible with 2-3 valves - Requires spool position measurement - Leaks - High manufacturing tolerance - Sensitive to contaminated oil	+ Leak free +/- Robustness to contaminated oil - Control linearity related to pilot control linearity	+ Leak free + Exact valve opening + Tolerant for valve failures + Robustness to contaminated oil + Fast valve response - Limited control resolution - Pressure peaks

In this study, the focus is on parallel connection technology with PCM (pulse code modulation) control. D-IMV system consists of DFCUs (Digital Flow Control Unit) that control a single metering edge. In PCM coded DFCU, one DFCU consists of a set of different sized valves that create 2^n-1 different opening combinations i.e. states [14]. A DFCU can be built with any-type of on/off-valves, but best properties are achieved with directly controlled poppet-type valves that are leak-free and have no pilot pressure control inside the valves. Pilot controlled on-off valves add uncertainty to the response time of the valve, which can lead to state transition problems when changing the opening of the DFCU. Main advantages compared to proportional IMV-valves are the exact discrete valve openings without position measurements, robustness of the mass-produced simple on/off-valves and reliability from having multiple valves in parallel that can be reconfigured in case any of the jams either open or close [15]. Digital hydraulic valves are used in few industrial applications, e.g. in Valmet paper machines [16] and the technology has been studied in various academic studies. Challenges remain on bringing the technology to mobile machine industry where the operator comfort is one of the most important factors. Current on/off-valve technology sets limits to the D-IMV design in terms of size and cost, as well as repeatability of dynamic properties that limit the valve capacity and can cause unexpected pressure peaks to the system.

Different operating modes with four-valve IMV system are presented in Figure 1. In this paper, abbreviations of type PTe or TPr are used, where the first letter stands for the pressure connected to the A-chamber and the second letter for stands for the line connected to the B-chamber. The third letter stands for the movement direction: e for extending or r for retracting.

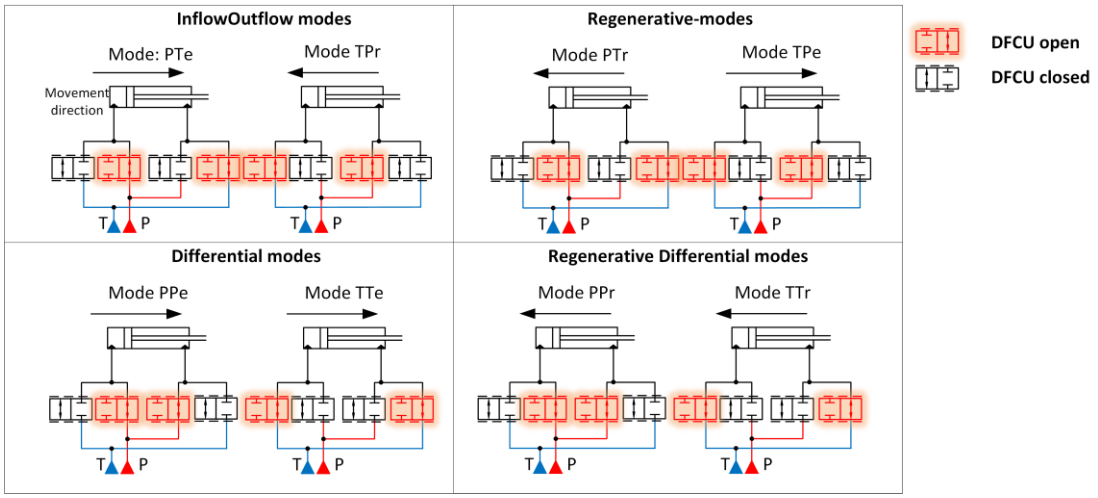

Figure 1. Different modes of IMV-systems and the abbreviations used in this paper

The process flow of converting the hydraulic-mechanic load sensing system into a D-IMV is presented in Figure 2. Each step is described in this paper, but the Feasibility analysis, the Simulation study and the valve properties are presented more detailed in [17]–[19].

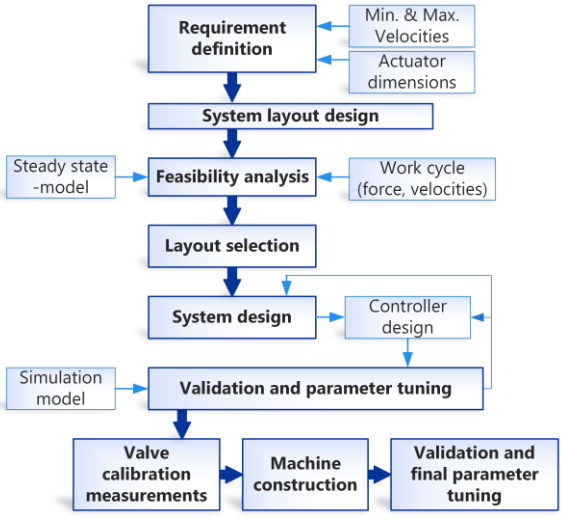

Figure 2. Conversion process flow chart for retrofitting D-IMV to a work machine.

2. TEST PLATFORM

A 21-ton Volvo EW210C wheeled excavator was selected as the platform for the conversion. It has a single pump capable of producing a flowrate of approximately 400 l/min to operate the work hydraulics and the drivetrain. The valve system is a hydraulic-mechanical load-sensing type system with closed-centre down-stream pressure compensated valves. Schematics for the hydraulic system is presented in figure 3. This machine has a typical hydraulic system found in European construction machines in the mid-size range.

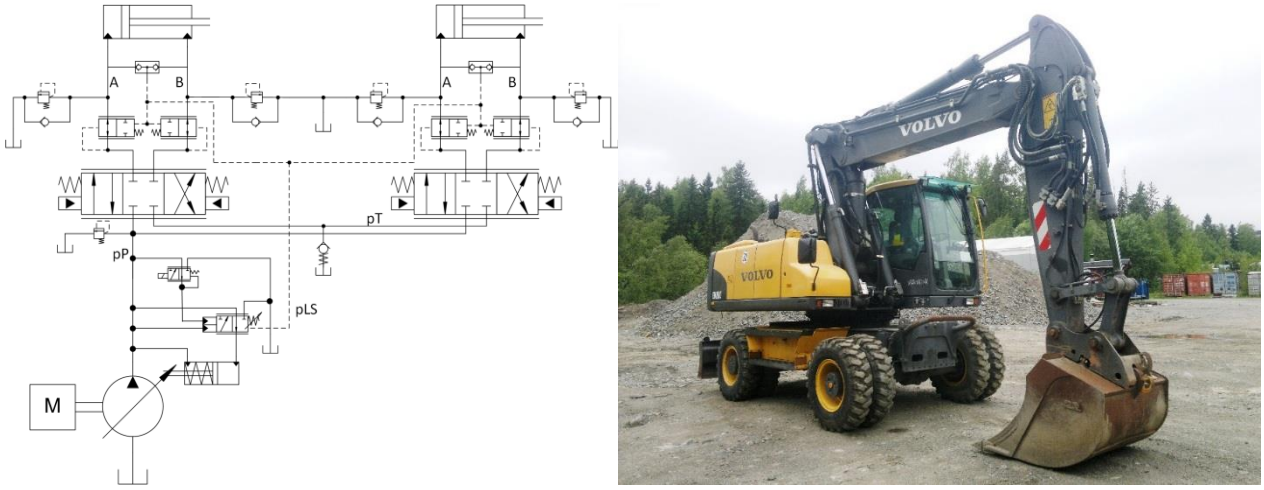

Figure 3. Illustrative schematic diagram of the load-sensing working hydraulic system of Volvo EW210C.

The D-IMV conversion was done to the Boom, Arm, Bucket and Swing actuators. Other actuators, such as the travel function and the secondary boom, were separated from the D-IMV system and operated with proportional valves. Excavator was fitted with inline flow measurement of the pump outlet, pressure sensors in actuator chambers, in the supply line and in the return line, and with actuator position sensors. Fuel consumption was also measured with online fuel measurement system.

3. SYSTEM DESIGN

3.1. Requirements

Requirements for the hydraulic system were measured from the excavator before conversion. Maximum velocities of the actuators were measured with step response tests from which the corresponding actuator chamber inflows and outflows were calculated. Maximum velocities and flowrates are presented in table 2.

Table 2. Maximum velocities of the actuator and corresponding chamber flowrates.

	Boom	**Arm**	**Bucket**	**Swing**
Max. vel. extending [m/s, deg/s]	0.14	0.25	0.42	50
Flow (A-port / B-port) [l/min]	228 / 119	247/141	262/135	149 / 149
Max. vel. rectracting, [m/s, deg/s]	- 0.18	-0.29	-0.48	-50
Flow (A-port / B-port) [l/min]	289 / 145	285/163	299/154	149 / 149

Actuator forces are limited by the pump pressure, which is limited by a pressure relief valve in the load-sensing circuit. In normal operation the maximum pump pressure is limited to 32,5 MPa and in power boost mode the limit is 36 MPa. This sets the maximum operation pressure for the digital valves and the maximum pressure difference at which the valves must open.

3.2. Baseline tests

For the baseline, real work and standard-based cycles were measured with the original excavator. Real work measurements included 90-degree truck loading work with five professional operators repeating the cycle 10 times each. The Standard-based cycles are defined by the JCMAS (Japan Construction Mechanization Association Specification) and it includes simulative work motions of truck loading and ground levelling [20]. Standardized cycles were used as references for designing and simulating the controller in the simulation

phase. Simulation results were presented in [18]. The cycle used in the measurements of this paper is the grading cycle presented in figure 4.

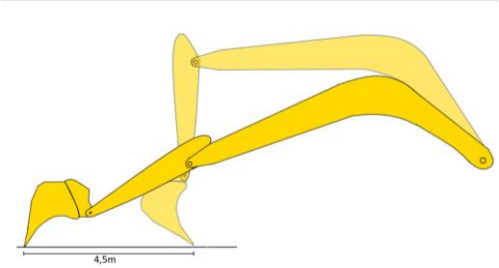

Figure 4. Grading cycle determined in JCMAS H020 Standard.

JCMAS tests were conducted to achieve repeatable results as the actual grading of the ground is highly depending on operator skills and ground conditions. The problem with the JCMAS test is that it mimics very light duty work, and in real work cycles the forces and velocities of the actuators varies a lot. In digging cycles the difference is bigger than in grading as grading is often relatively light work also in the real life. For both of these cycles, the actual work that is done is close to zero as no earth is moved and the actuators return to the initial positions in the end of the cycle.

3.3. Feasibility analysis

The first step to analyse the advantages of digital hydraulic valve system was to calculate the steady state energy consumptions in different operation points. This analysis is presented by the author in [17]. Figure 5 presents the hydraulic power loss analysis of two actuators with constant velocities. Equations were formed for a standard proportional valve system and for independent metering valve system (Digi) with a load sensing supply pressure control. In this study, no distinction between analog and digital IMV-systems were done. Calculations included also a pressurized return line system (Digi pT) where the return line included an accumulator and a pressure relief valve, and a system where an extra middle pressure line (Digi MP) was introduced consisting of an accumulator charged with the main pump and two additional DFCUs per actuator. From the equations, color maps were built to analyze the efficiency within the whole velocity and force range of a single or multiple actuators.

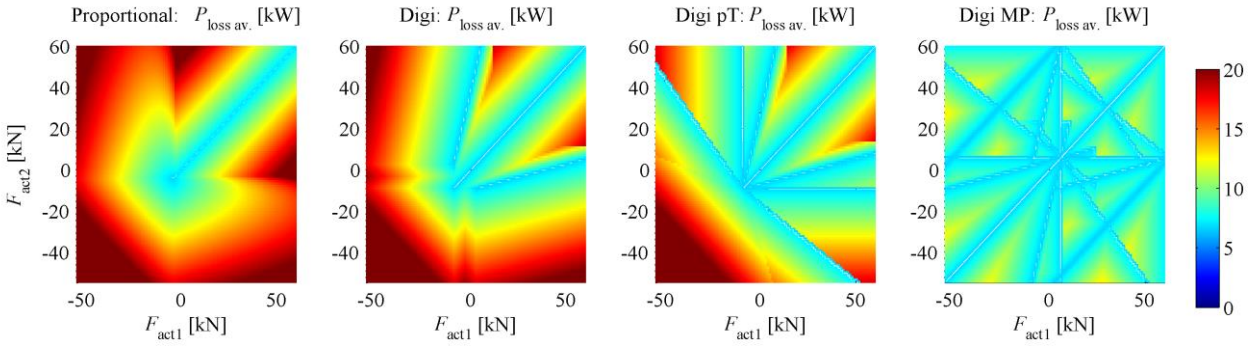

Figure 5. Power losses of two-actuator system with constant positive cylinder velocities and equal cylinder dimensions.

Calculations in Figure 5 show for two-actuator case, what are the losses of the different systems. Steady state calculations included also the mean values within all velocity and load points and the operation points gathered from the base line measurements of the original machine. Results in [17] for the digging cycle indicated energy loss reduction up to -50 % for the MP-system, -18% for the pressurized return line system, and -10 % for the D-IMV-system.

3.4. System layout for the D-IMV excavator

Main research topics to be researched with this excavator included high flow rate digital hydraulic valve design and the feasibility of implementing this technology to mobile machines. Steady state feasibility studies showed the best energy efficiency results with the pressurized return line and with the extra middle pressure line system, but for this build, the layout of Figure 6 was selected to accommodate the main research topics. The pump unit is the same as in the original machine with the addition of an electronic pressure relief valve controlling the LS-pressure signal entering the pump pressure controller. The original valve package was removed and hydraulic joysticks were replaced with electronic joysticks. Safety valves attached to the cylinders stayed intact, but the controlling valves were replaced to electronic 3/2-proportional valves.

The valve system is simplified as most functions and adjusting is done programmatically. There is no pressure compensation valves in the system or other auxiliary valves used with traditional LS-valves, except for the shock relief and anti-cavitation valves.

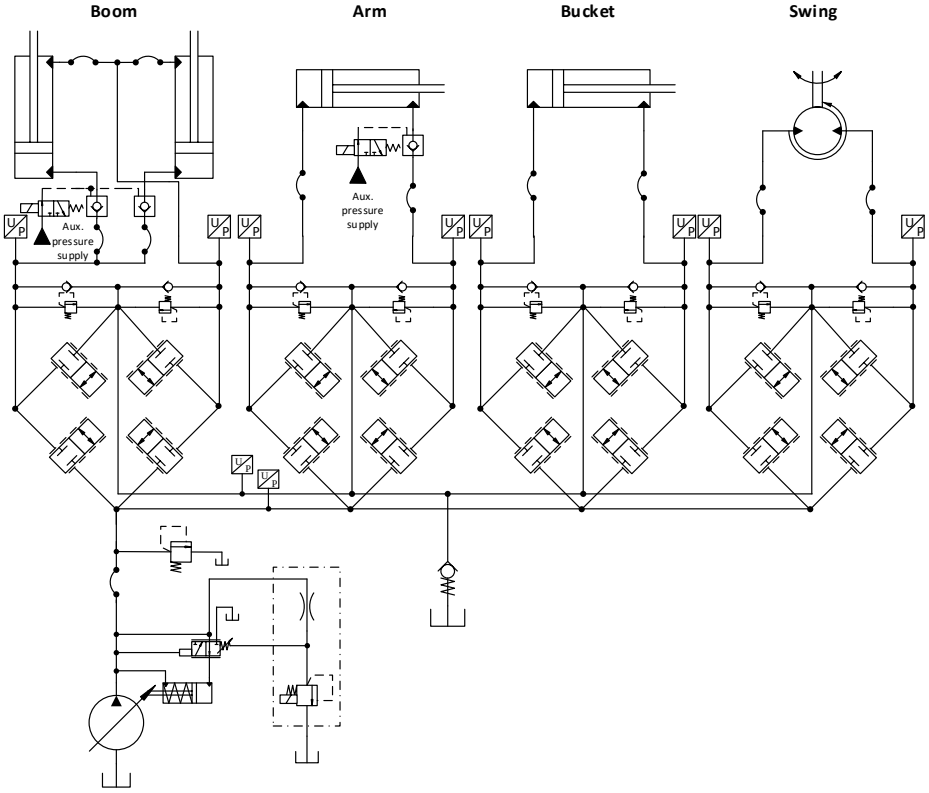

Figure 6. Hydraulic circuit of the Digital hydraulic excavator.

To avoid cavitation in the actuator chambers, the return line pressure is increased as in the original machine to around 1MPa. Cooling system, travel functions and other auxiliary operations are realized as with the original machine.

3.5. Controller design

Control of each actuator is distributed to the actuator ECUs (Electronic control unit). One of the ECUs operates as a master-ECU that handles the pump controlling, flow sharing functions, joystick filtering, communication with other ECUs of the machines, and other safety related tasks. Actuator controller structure includes two steps: first best mode is selected and then correct opening of the DFCUs is calculated.

Upper level control

Controller principle was presented in detail in [18] and is quickly summarized in this chapter. The upper-level D-IMV control principle is presented in Figure 7.

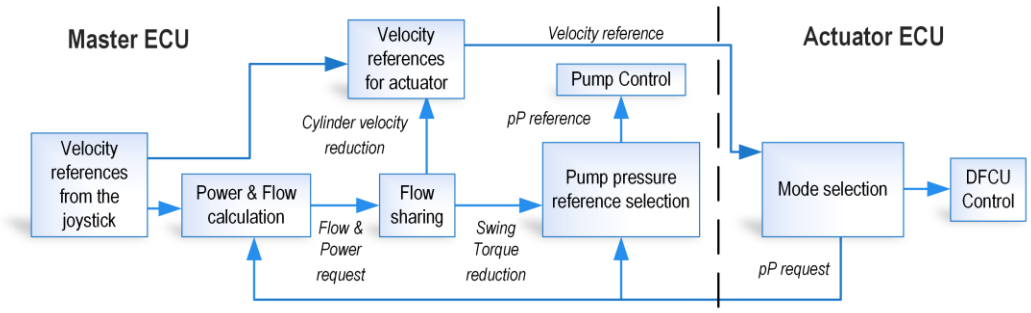

Figure 7. Pump pressure and velocity reference control principle.

After velocity-references have been calculated from the joystick position, the required power and flow from the pump are estimated. The power is estimated from the actuator velocity references and from the maximum value of pump pressure requests from the actuators. In case the desired flowrate exceeds the available flowrate from the pump, velocity references are reduced so that the maximum pump flowrate is not exceeded. In case the power demand is over the engine power limit, cylinder velocity references are reduced and the swing torque is limited by reducing the pP-request from the swing-ECU.

The Flow sharing controller calculates the over-demand ratio of flow or power and reduces the actuator velocities and swing pump pressure reference. The over-demand ratio is rate-limited and filtered to achieve smooth feeling for the operator.

Mode selection

Main tasks of the mode controller are presented in Figure 8. Mode controller calculates the best mode, reference for the pump controller and reference values for the flow controller.

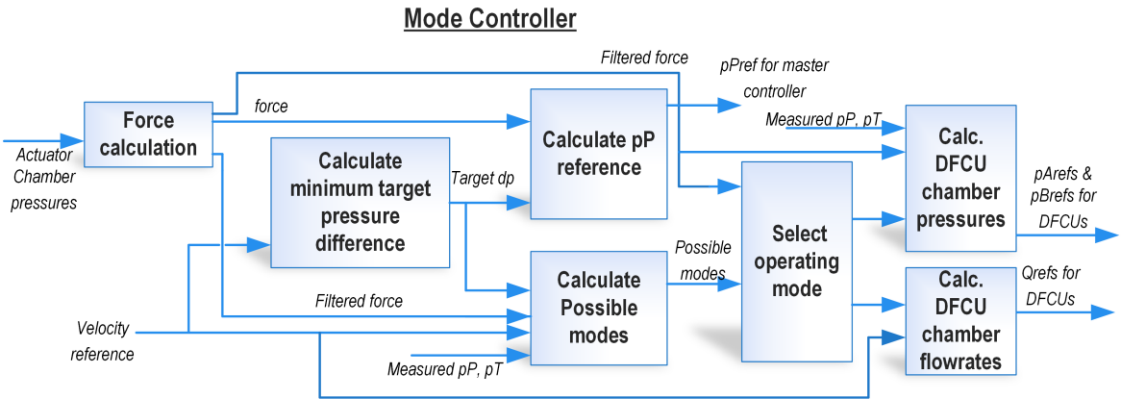

Figure 8. Mode controller

First, the actuator force is calculated from the measured pressures at the DFCU actuator ports. The unfiltered force is used to calculate the pump pressure reference (*pPref*) with a standard mode to achieve high rise-time for the supply pressure. *pPref* is calculated by adding the minimum target pressure difference (*dpmin*) to the maximum load pressure. To increase the flowrate capacity of the DFCUs, *dpmin* is allowed to increase after the velocity reference exceeds the level at which all the valves are open. The d*pmin* values are calculated for both, the inflow (*dpmin_in*) and the outflow side (*dpmin_out*) separately to increase flexibility and to minimize throttling losses. Parameter *dp_IOratio* is used to lower the *dpmin_out* with equation

$$dpmin\_out = dp\_IOratio \times dpmin\_in \quad (1)$$

The possibilities of different operation modes are calculated with the filtered force, measured pump pressure and return line pressure, and target pressure difference. Best possible operation mode is selected in a state-machine that handles mode transitions and selection of mode based on pre-determined order of preference. After the mode selection, reference pressures and flowrates are calculated for the DFCU flow controller. The

flow references are calculated directly from the velocity reference and the pressure references are calculated based on the measured *pP* and *pT*, thefiltered force and the desired *dpmin*-values.

DFCU flow controller

In the flow controller, best valve opening combination is calculated for each active DFCU. The controller calculates flowrates for each opening combination with the chamber pressure reference values received from the mode selection algorithm. The flowrates of each valve is calculated with equation

$$Q_{valve_i}(p_1, p_2) = \begin{cases} K_{1i}(p_1 - p_2)^{x_{1i}}, & b_{1i}p_1 < p_2 \leq p_1 \\ K_{1i}[(1 - b_{1i})p_1]^{x_{1i}}, & p_2 \leq b_{1i}p_1 \\ -K_{2i}(p_1 - p_2)^{x_{2i}}, & b_{2i}p_{21} < p_1 \leq p_2 \\ -K_{2i}[(1 - b_{2i})p_1]^{x_{2i}}, & p_1 \leq b_{2i}p_2 \end{cases} \quad (2)$$

where K_{1i} is the flow coefficient, x_{1i} is the exponent and b_{1i} is the critical pressure ratio of a single valve in the flow direction 1→2, and K_{2i}, x_{2i}, and b_{2i} are the parameters for the opposite direction, and p_1 and p_2 are pressure references. Parameters are received from the calibration measurements of the DFCUs done in a test bench. Flowrate combinations are calculated with equation

$$\overline{Q}_{all\_comp} = \overline{Q}_{valves} \times ctrl\_mtrx \quad (3)$$

,where *ctrl_mtrx* is 7×127 logical matrix including all valve opening combinations. The controller selects the best combination by minimizing the cost function of equation 4 that includes costs for the flow error and for the switching amount.

$$u_{state} = \min\left(\left(\bar{Q}_{all\_comp} - Q_{ref}\right)^2 + w_{sw} \times swtchng\_mtrx(u_{prev})\right) \quad (4)$$

In equation 4, Q_{ref} is the desired flowrate, w_{sw} is the weighting factor for the switching term and $swtchng\_mtrx(u_{prev})$ is an 1x127 array including valve state changes from the current DFCU state to each possible new state. Values of the $swtchng\_mtrx$ are weighted with the valve size to weight more valve state changes that include large valves. This is to done to avoid unnecessary state transitions when two states have almost equal flow rate errors.

3.5.1. Features added to improve controllability

Some features had to be added to the controller designed and presented in [18] during the machine construction phase. The main changes that needed to be done to improve the system are presented below.

1. *Motion start*

To achieve smooth motion start, chamber pressure references for the flow controllers are gradually changed from measured values to calculated values. This enables smooth valve opening in case high pressures are trapped in the actuator chambers when the motion was previously stopped.

Joystick filtering is also important factor in smoothness of the motion. Non-linearity was added to the joystick along with a variable frequency low-pass filtering to give the operator better feeling to the machine. The cut-off frequency of the filter is changed as a function of the output velocity reference so that small movements to the joystick are visible in the velocity reference without lag.

2. *Removing bad state changes*

In some cases it was noted that the bad state changes, i.e. changes when states to be switched do not share any common valves, caused unexpected pressure peaks due to non-simultaneous valve switching. Phenomenon was reduced by preventing modes where one of the largest valves is the only valve open. To reduce this phenomenon further, also states, where only one of the largest valve and either one of the two smallest valves are open, are prevented

3. Pump pressure control

For smooth actuator motions, supply pressure must follow the reference as accurately as possible. Too slow incline rate creates unwanted lag in the system and while too rapid decline rate affects the actuator velocity control. To achieve fast incline and smooth decline in pump pressure, bi-directional pressure reference filtering was implemented. Selection algorithm for the pressure reference is presented in Figure 9.

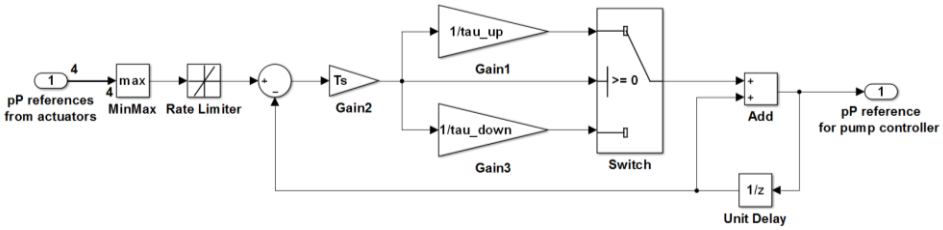

Figure 9. Pressure reference filtering algorithm.

4. Mode transition

First attempt to make the operation mode transitions smooth was to change the modes as fast as possible. The valves allow the mode change to happen fully in around 20 ms, but it was noticed that the pump pressure control would not be as fast as needed. Fast switching from differential mode to inflow-outflow mode resulted in a temporary velocity drop and affected to the supply pressure level, which disturbed other actuators moving simultaneously. To achieve smooth transition, a transition state is used when moving from one state to another.

When mode transition is started, both DFCUs related to the same actuator chamber are simultaneously open for a short period. After DFCUs have been switched fully, pressure reference calculation for the chambers are switched from the previous mode to the new mode. Example for the mode change from extending normal mode (PTe) to extending differential mode (PPe) is presented in figure 10.

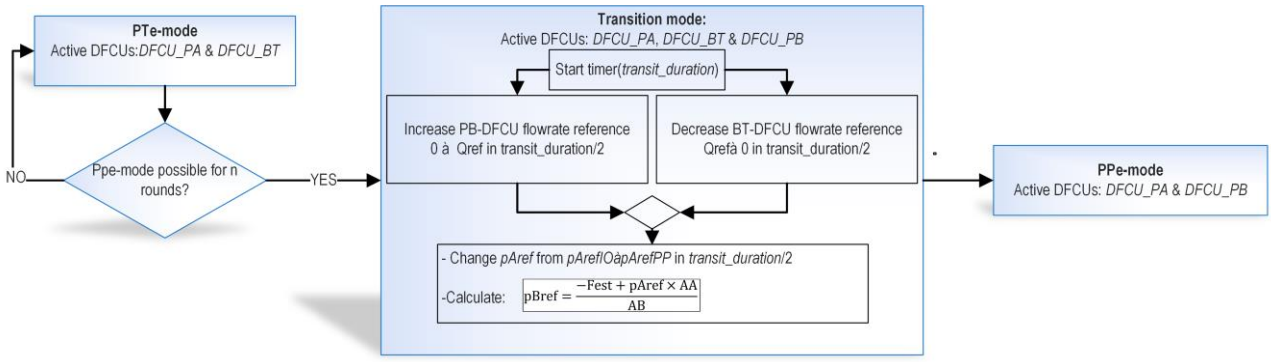

Figure 10. Transition from standard mode (PTe) to differential mode (PPe).

In the Figure 10, mode transition is started from the mode PTe after the new mode has been possible for *n* sample time periods. Pump pressure reference is calculated with the new mode right after changing to the transition mode. DFCU flowrates for the PB-DFCU and BT-dfcus are changed between each other in the first half of the transition period. Total flow to the B-chamber is kept as required by the velocity reference during the mode transition. To keep the chamber pressures adequate for both outflow side DFCUs, pressure references are kept in a proper level for both modes during the flow transition and then smoothly changed according to the new mode during the second half of the transition period.

4. IMPLEMENTATION

4.1. Valve design

The designed valve package includes four identical valve blocks with maximum design flowrates described in table 2 of chapter 3. Each of the valve blocks includes four DFCUs and each DFCU includes seven on/off valves, making total of 112 on/off-valves for four actuators. To increase the DFCU control resolution, and to control the valves with PCM-control strategy, part of the valves have a metering orifice installed on the tip of the valve. Typical set of orifice sizes and the realized flowrates with different opening combinations are presented in Figure 6. The valve design and properties are presented in detail by the author in [19].

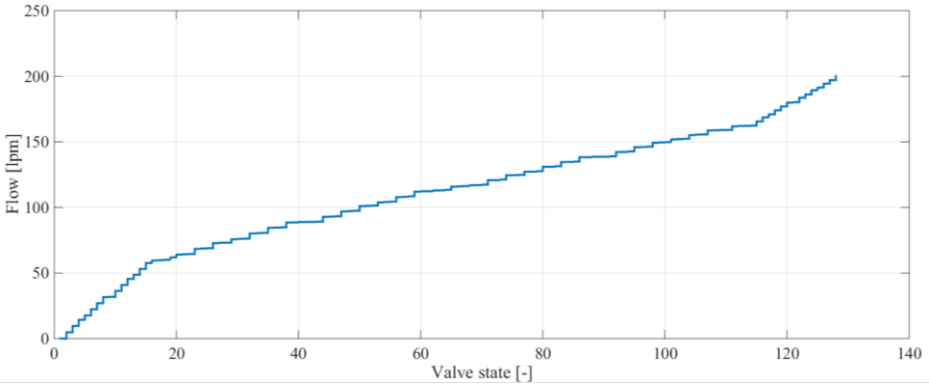

Figure 11. Flow-state curve of Bucket PB-DFCU with an orifice series of 1.4mm, 2mm, 2.8mm, 4mm, -, -, - with 1.5MPa pressure difference over the valves.

The valve package installed in the centre pit of the excavator is presented in figure 6 along with a single D-IMV valve block. The hoses above the valves are going to the actuators while pump and return line connections are underneath the blocks.

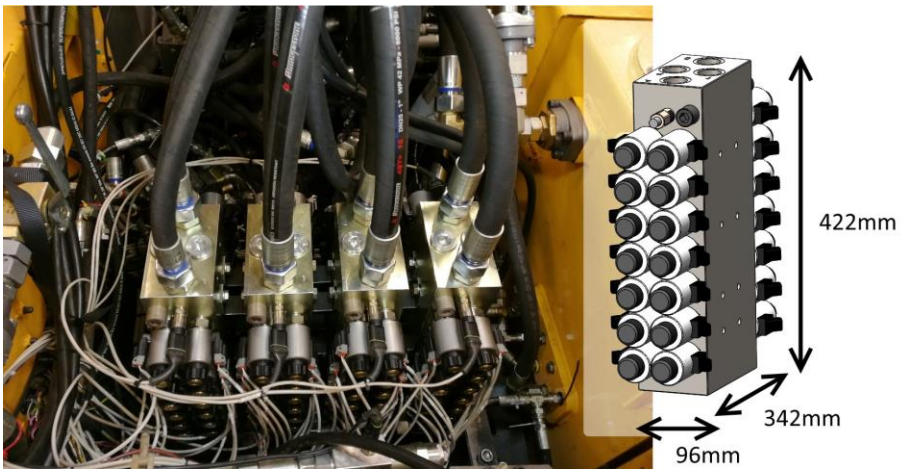

Figure 12. D-IMV installed in the excavator and a single valve block.

The 2/2-valve used is a Bucher WS22GDA-series valve with with maximum flowrate of around 140 l/min and a nominal flowrate of around 37 l/min at 0.5 MPa. Valve opening time was measured to be 18-21 ms and closing time 14 ms with the used 12 VDC-coil.

4.2. Control electronics and layout

The ECUs used were Bosch Rexroth Bodas RC36/20 and RC28/20 controllers that have a 150MHz and 180MHz Tricore processors. Reason that four mobile controllers were selected instead of a single more powerful e.g. industrial PC, was that the RC20-Series ECUs have enough high current PWM-outputs and

therefore no additional power boosters were needed between the valves and the RCs. Currently available boosters for digital valves are meant for industrial applications and are not convenient to use in working machines. ECUs are communicating through CAN bus with each other.

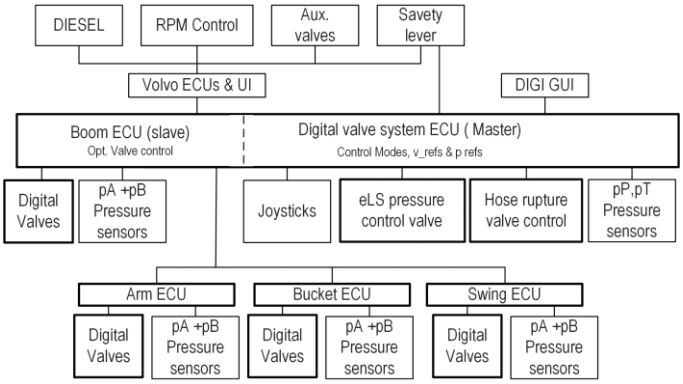

Figure 13. Controller architecture for the D-IMV excavator.

RC20-series Bodas controllers have 36 or 28 PWM-outputs depending on the model,that can produce a boost voltage with the 24VDC supply voltage to increase the valve opening time for the 12 VDC coils. These ECUs do not have means to reduce the voltage over the coil rapidly when closing the valve. To increase the closing time, two methods were used. For the PWM-outputs of RC20-36, fast closing was realized with an additional MOSFET integrated to valve cable to the ground-side, that was controlled off when closing the valve. This method is described in more detail in[19]. Second method was to insert 7V zener-diode to the ground-side of the solenoid so that the it would work as a current restriction during the valve closing. This method generates constant heat when the valve is open, but it was found to increase the closing of the valve enough to match the valve opening and closing times close to each other.

5. TUNING

This chapter describes the process of tuning the. Controller testing and parameter tuning is done in most parts with the simulation model in the design phase. To compensate model inaccuracies, some of the parameters have to be verified and tuned for the real world system. Parameters related to the flow control of the DFCUs can be fully verified when testing the valves in the test bench. Steps to tune rest of the parameters include:

1. **Pump controller**: Valve current/pressure relation is measured first with direct current input to get the look-up table parameters. Then PI-controller is tuned with step response tests. Minimum and maximum pressures were set to match the original machine. After rest of the tuning procedures are done, PI-controller parameters are re-evaluated to improve the operation of the pump controller further.
2. **Joystick**: Joystick filtering is tuned to have a pleasant operation without lag in the motion start. Non-linearity is set to roughly match the original system.
3. **D-IMV actuator parameters:** Individual operations were tested one by one to find good balance between efficient operation and good dynamics with the normal operation modes. Initially the pressure difference target parameter *dpmin_in* was set to 3 MPa and the *dp_IO_ratio* to 1. After some iterations, *dpmin_in* was set to 1.5 MPa and *dp_IO_ratio* to 0.5 to for cylinder actuators and 3 MPa and 1 for the swing actuator. Target pressure difference was allowed to increase up to 3 MPa with high velocities. For the retracting direction, *dpmin_in* was allowed to increase up to 4.5 MPa to match the maximum velocities of the arm and bucket cylinders in the original system.
4. **Mode transitions**: For the first tests, only modes PTe, TPr, PPe and TTr were allowed. Two different transition times were used in mode controller. For mode changes PTe⇔PPe, transition time of 0.6 seconds was selected, and for mode changes TPr⇔TTr , transition time of 0.15 seconds was

adequate for smooth operation. Parameters were tuned as small as possible to improve energy efficiency.

5. **Flow sharing:** Flow sharing was tuned to reduce all actuator velocities equal amount. Asymmetric filter of the over-demand signal was tuned fast enough to prevent the engine from stalling and the rising back to one slow enough for operator comfort.

6. VALIDATION

Figure 14 presents a comparison of the original LS system and the D-IMV system in the JCMAS grading cycle. Tests were done in both cases with the maximum engine rpm setting, with equal hydraulic oil temperatures (35°C), and as fast as possible while keeping the bucket at around 30cm from the ground. In both cases, the arm actuator is driven to the end of the cylinder at the end of the cycle at around 15-16 seconds. The input power is calculated from the measured pump pressure and flowrate while the output power is calculated from the measured chamber pressures and measured velocities.

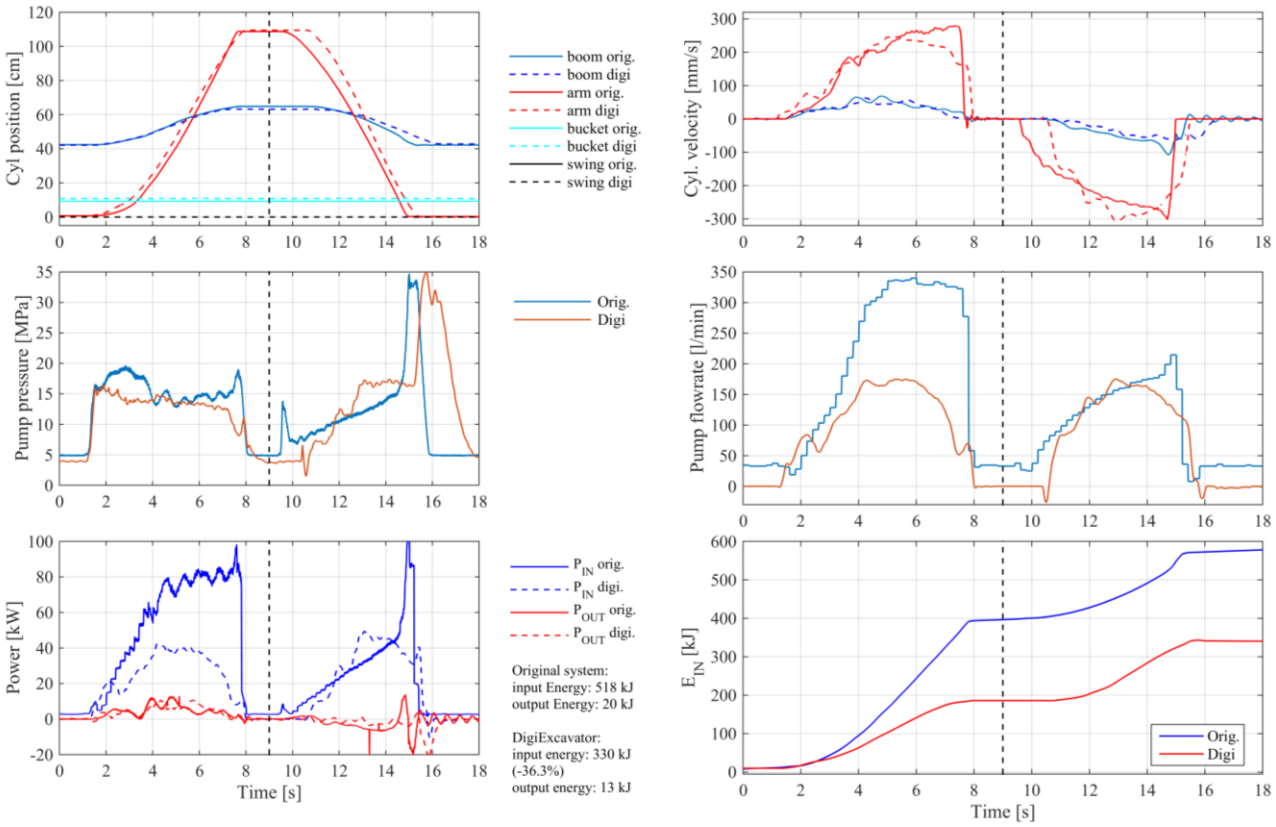

Figure 14. Comparison of the load-sensing system and D-IMV system in a JCMAS-based grading cycle where boom and arm are actuated in a manner that the bucket tip moves on a horizontal line.

The input energy was reduced by 36% in this example. Idle phases are disregarded from the energy calculations, but it was noticed that the original system had around 3kW when idling while the D-IMV system had zero losses. With the idle losses included, the reduction was 41%. It can be seen that output energy is close to zero in both systems since the only work that is done is related to the cylinder frictions. Figure 15 presents the actuator modes of the D-IMV system used during the cycle.

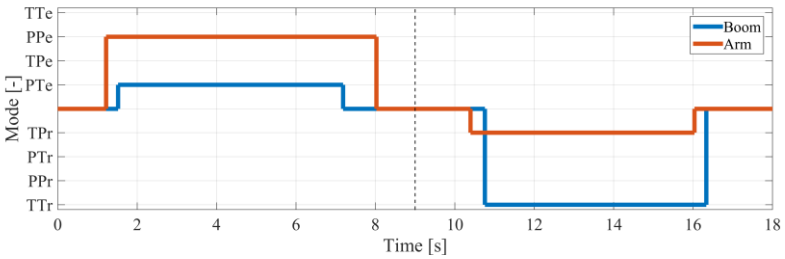

Figure 15. Operation modes used during the cycle.

In the first 9 seconds, the LS-system uses the whole engine capacity to extend both cylinders while the D-IMV system uses only around half of the engine capacity. Pump pressure is determined by the boom actuator pressure and it is slightly smaller with the D-IMV than with the LS due to smaller pressure margins. Boom operates in normal PTe mode and the arm uses differential mode PPe.

After 9 seconds, the energy consumption is equal with both systems. The D-IMV system uses normal mode TPr to retract the arm cylinder and regenerative differential mode TTr to lower the boom. The original system lowers the boom also without flowrate from the pump because of the regenerative function integrated to the boom valve. The calculated flowrate of the outflow-side of the arm cylinder rises to over 300 l/min which required to allow the target pressure difference to increase up to 4.5 MPa. This led to rather high losses on the valve to rather high.

7. DISCUSSION

These first tests show that is possible to build D-IMV system for a mobile machine with flowrates up to 300-400 l/min, and that commercial components are available. These first tests showed that in the common grading work cycle, input energy was reduced 36 %. Challenges remain on fully removing all the undesired pressure notches on the system that the operator can feel. More detailed analysis on the dynamic properties are left for the later studies, but these measurements show that roughly identical velocity trajectories can be achieved.

In the presented work cycle, operator could have used smaller engine rpm with the D-IMV system than with the LS-system while still achieving equal output power. The smaller engine revolutions would bring the engine closer to the optimal operation point of the engine in terms of efficiency. The work cycle presented a typical bad scenario for the traditional LS-systems where one actuator requires high pressure and another actuator requires high flowrate.

It was noticed that it is possible to use the regenerative mode PTr at the boom actuator in the second phase of the cycle, but it can generate negative flowrate to the pump and it is also prone to cavitation in the B-chamber because it requires flow supply from the return line. Utilization of the differential mode TTe also requires flow to be supplied from the return line and these modes require an accumulator or other actuators to produce the required flowrate to return line and consume the flowrate generated to the supply line. Utilization of these modes need modifications to the hydraulic circuit and are left for further studies, as well as the analysis of the efficiency in the digging cycle of the JCMAS-standard, and the efficiency in actual real digging work.

REFERENCES

[1] A. Jansson and J.-O. Palmberg, “Separate controls of meter-in and meter-out orifices in mobile hydraulic systems.,” in *SAE Transactions*, 1990, p. 99(2):377-383.

[2] M. Elfving, “On Fluid Power Control, A Concept for a Distributed Controller of Fluid Power Actuators,” Linköping University, Sweden, 1997.

[3] B. Nielsen, “Controller Development for a Separate Meter-In Separate Meter-Out Fluid Power Valve for Mobile Applications,” p. 237, 2005.

[4] A. Shenouda *et al.*, “Quasi-Static Hydraulic Control Systems and Energy Savings Potential Using Independent Metering Four-Valve Assembly Configuration,” 2006.

[5] S. Liu, R. W. H. Laboratories, and B. Yao, “Coordinate control of energy-saving programmable valves,” in *Proceedings of 2003 ASME International Mechanical Engineering Congress, Washington, D.C United States of America*, 2003.

[6] B. Eriksson and J. Palmberg, “Individual metering fluid power systems: challenges and opportunities,” *Proc. IMechE Vol. 225 Part I J. Syst. Control Eng.*, pp. 196–211, 2011.

[7] Husco International, “Husco EHPV-datasheet.” .

[8] Eaton Corporation, “Eaton CMA - Advanced Mobile Valve with Independent Metering.” [Online]. Available: https://www.eaton.com/Eaton/ProductsServices/Hydraulics/Valves/MobileValves/CMA/index.htm. [Accessed: 22-Jan-2019].

[9] B. Beck and J. Weber, “Enhancing safety of independent metering systems for mobile machines by means of fault detection,” in *The 15th Scandinavian International Conference on Fluid Power, SICFP’17, June 7-9, 2017, Linköping, Sweden*, 2017, pp. 92–102.

[10] M. Rannow, “Fail Operational Controls for an Independent Metering Valve,” *Eat. Corp. web Publ.*, 2016.

[11] G. Kolks and J. Weber, “Modiciency - Efficient industrial hydraulic drives through independent metering using optimal operating modes,” in *10th International Fluid Power Conference (IFK2016)*, 2016, pp. 105–120.

[12] R. Ding, B. Xu, J. Zhang, and M. Cheng, “Bumpless mode switch of independent metering fluid power system for mobile machinery,” *Autom. Constr.*, vol. 68, no. November 2018, pp. 52–64, 2018.

[13] R. Ding, J. Zhang, B. Xu, and M. Cheng, “Programmable hydraulic control technique in construction machinery: Status, challenges and countermeasures,” *Autom. Constr.*, vol. 95, no. August, pp. 172–192, 2018.

[14] M. Linjama, “Is It Time For Digital Hydraulics?,” in *The Eighth Scandinavian International Conference on Fluid Power, SICFP’03, May 7-9, 2003, Tampere, Finland*.

[15] L. Siivonen, M. Linjama, M. Huova, and M. Vilenius, “Pressure Based Fault Detection and Diagnosis of a Digital Valve System,” in *Power Transmission and Motion Control (PTMC 2007). Centre for Power Transmission and Motion Control, Bath, UK.*, 2007.

[16] Valmet, “Digital hydraulics.” Web publications, Available: https://www.valmet.com/globalassets/media/downloads/white-papers/process-improvements-and-parts/wpp_digihydraulics.pdf. [Accessed: 25-Jan-2019].

[17] M. Ketonen, M. Linjama, and K. Huhtala, “Retrofitting digital hydraulics – An analytical study,” in *9th International Fluid Power Conference (IFK)*, 2014, pp. 327–337.

[18] M. Ketonen and M. Linjama, “Simulation study of a digital hydraulic independent metering valve system on an excavator,” in *The 15th Scandinavian International Conference on Fluid Power, SICFP’17, June 7-9, 2017, Linköping, Sweden*, 2017.

[19] M. Ketonen and M. Linjama, “High flowrate digital hydraulic valve system,” in *Proceedings of The 9th Workshop on Digital Fluid Power*, 2017.

[20] Japan Construction Mechanization Association, “Earth-moving machinery – Test methods for energy consumption – Hydraulic excavators,” 2010.

EXPERIMENTAL INVESTIGATION OF CHURNING LOSSES IN A HIGH-SPEED AXIAL PISTON PUMP

Ying Li, Bing Xu, Junhui Zhang, Gan Liu
State Key Laboratory of Fluid Power and Mechatronic Systems, Zhejiang University
Zheda Road 38
310027 Hangzhou, Zhejiang, China
E-mail: benzjh@zju.edu.cn

ABSTRACT

Churning loss has a significant influence on the mechanical efficiency in axial piston pumps. This paper focuses on experimental investigations on the churning losses and introduces a test rig to measure the influence of various parts on churning loss in an axial piston pump. The description of the test method is presented in detail, followed by sample results of the churning losses measurement. According to the measuring results under test conditions, it is found that the churning loss is mainly related to cylinder block and pistons, and has little relation with swash plate and variable mechanism.

KEYWORDS: axial piston pump, churning losses, experimental study.

1. INTERODUCTION

Axial piston pumps are widely used in industrial and construction machinery due to their high limit load pressure and high power density. However, pump efficiency is decreased with the increase of operating parameters because of increasing power losses [1, 2]. The power losses in axial piston pump have three main means, namely the volumetric losses caused by the leakage flow losses, the mechanical losses due to the friction losses and churning losses in the stirred fluid caused by the internal rotating components [3-6].

A small improvement in the overall efficiency of axial piston pumps may significantly increase the global efficiency of the fluid power systems. Volumetric losses and mechanical losses have been investigated in axial piston pumps to reduce energy dissipation in the past few decades. The main focus is on the piston/cylinder block pair, slipper/swash plate pair and cylinder block/valve plate pair. Murrenhoff et al. [7-9] showed that coated pistons and surface texturing of axial piston pumps can achieve very low friction between piston and bushing, and this could improve the energy efficiency. Ivantysynova et al. [10, 11] presented a contoured piston to improve the load carrying ability of the gap in an axial piston pump. The results showed that the micro-surface shaping of the piston can reduce both volumetric losses and torque losses in both pumping and motoring mode. Hooke et al. [12, 13] measured clearances under slippers subjected to tilting couples and then confirmed the theoretical predictions. Yamaguchi et al. [14-16] presented the design criteria of the optimum size of slipper in axial piston pump to obtain the minimum power losses, minimum size (or maximum load-carrying capacity) and maximum moment stiffness. The numerical models with detailed valve plate and piston barrel kidney geometries have been used to analyze and optimize the pump design to improve the efficiency [17-19]. They compared the volumetric losses and mechanical losses among different design parameters of valve plates, and demonstrated the principle

advantages. The fluid film that existed between the valve plate and the cylinder block was experimentally measured and studied in Ref. [20, 21]. The results were applied to revise the shape of the valve plates to increase the stability and the efficiency of the piston pumps. Xu et al. [22] introduced several suggestions for decreasing extra cylinder block tilting moments and inhibiting the tilting effect on the volumetric losses and mechanical losses in a high-speed axial piston pump. These suggestions included improving machining precision, reducing the total mass of a single piston-slipper assembly, and decreasing the nominal pitch circle radius of piston bores.

The churning losses, which are mainly studied in this paper, are caused by the internal rotating components stirring the fluid in axial piston pumps and have been a research focus in recent years for its dominant effect on pumps when speed ups to 10000~15000 r/min. The high-speed of pumps are mainly applied in aeronautics and astronautics areas, in comparison with axial piston pumps with nominal speed of 1500~3000 r/min. The first theoretic approach about churning losses was done by Jang [23] in 1997. After that, Håkan [24] carried out that the proportion of churning losses was 20% of total losses under low pressure operating conditions in axial piston pumps. In 2015, Ivantysynova et al. [25] established the temperature simulation model through taking churning losses into consideration in axial piston pumps. Murrenhoff et al. [26] optimized the fluid state in the casing filled with oil to reduce the churning losses. Xu et al. [27, 28] investigated the effect of pistons and cylinder block on churning losses in axial piston pumps at various ranges of speed. They also indicated some methods such as insert and nano-coating to reduce the churning losses caused by the rotating cylinder block.

As can be seen from the above theoretical studies, churning loss has a significant impact on efficiency in axial piston pumps. Although the churning loss model for pistons and cylinder block was established, the effect of other parts on churning loss was not analyzed. According to the published literature, it may be found that there was no experimental validation to confirm the influence of various parts on churning loss in an axial piston pump. Therefore, the objective of this paper is to build up a test rig to measure directly the influence of various parts on churning loss in an axial piston pump. The measured results will give a further understanding of churning loss and contribute to more comprehensive theoretical models for the efficiency of axial piston pumps.

2. TEST METHOD FOR CHURNING LOSSES

It is not easy to analyze the churning losses directly using a piston pump because the friction losses cannot be segregated among three friction pairs and these frictions may have a great influence on the measured churning losses. Therefore, a churning losses test bench has been designed at the State Key Laboratory of Fluid Power and Mechatronic Systems, Zhejiang University in order to assess the behaviour of churning losses in axial piston pumps.

As shown in Figure 1, a churning losses test bench consists of a test pump, a temperature sensor, a pressure sensor, a torque/speed sensor and an electric motor. The churning losses power is deduced by subtracting the wet and dry casing torque acting on the shaft as shown in

$$P_c = M_c\omega = \left(M_w - M_d\right)\omega \tag{1}$$

where ω is the rotation angular velocity, Mc is the experimental churning losses torque, M_w is the experimental torque acting on the shaft with oil in the casing, and M_d is the experimental torque acting on the shaft without oil.

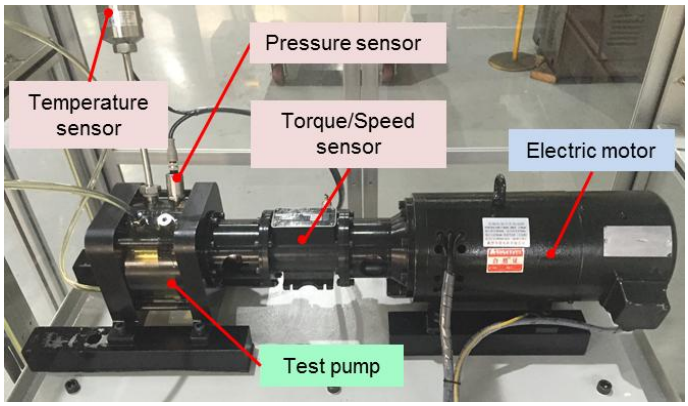

Figure 1. A churning losses test bench.

The tests are conducted at constant pressure, constant temperature and varied speeds within 1500 and 16000 rpm as shown in Tab.1.

Table 1. Operating conditions

Parameters	Value	Unit
Test speed	1500/3000/6000/9000	rpm
Test temperature	35	°C
Test pressure	1.02	bar

It seems that the churning losses may be captured using the above method. But the test pump needs to be designed specially in order to get the influence of various parts on churning loss in an axial piston pump. As shown in Fig. 2, the test pump is designed based on a high-speed axial piston pump prototype used for aircraft in References [22]. There are nine pistons mounted within the cylinder bores at equal angular intervals around the centreline of the cylinder block. These nine pistons are fixed by the specific screws and gaskets mounted within the cylinder bores. In order to remove the effect of spline friction torque losses on churning losses. The cylinder block and shaft are integrated together. The swashplate and variable mechanism are fixed in the coverplate. A clearance should be maintained between the pistons and the swashplate to avoid friction between the pistons and swashplate.

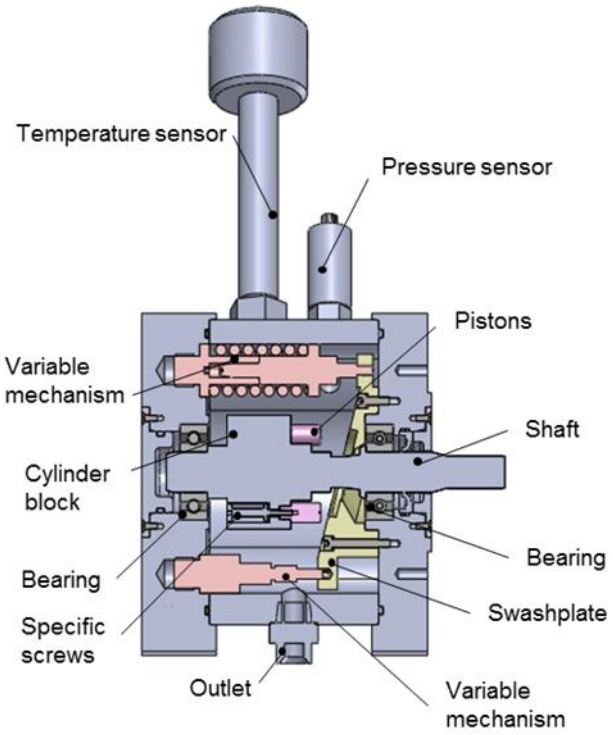

Figure 2. A frontal cross-section of the test pump.

The churning loss torque of various parts can be obtained by the subtracting the wet casing torque acting on the shaft from the dry casing torque acting on the shaft on the test pump. The test of churning losses torque due to the cylinder block M_{cc} can be expressed as:

$$M_{cc} = M_{wcc} - M_{dcc} \tag{2}$$

where M_{wcc} is the measured torque acting on the shaft due to the cylinder block with oil in the casing, and M_{dcc} the measured torque acting on the shaft due to the cylinder block without oil in the casing.

The test of churning losses torque due to the pistons M_{cp} can be expressed as:

$$\begin{aligned} M_{cp} &= M_{ccp} - M_{cc} \\ &= M_{wccp} - M_{dccp} - M_{wcc} + M_{dcc} \end{aligned} \tag{3}$$

where M_{ccp} is the experimental churning losses torque due to the cylinder block and pistons, M_{wccp} is the measured torque acting on the shaft due to the cylinder block and pistons with oil in the casing, and M_{dccp} the measured torque acting on the shaft due to the cylinder block and pistons without oil in the casing.

The test of churning losses torque due to the swashplate M_{cs} can be given as:

$$\begin{aligned} M_{cs} &= M_{ccps} - M_{ccp} \\ &= M_{wccps} - M_{dccps} - M_{wccp} + M_{dccp} \end{aligned} \tag{4}$$

where M_{ccps} is the experimental churning losses torque due to the cylinder block, pistons and swashplate, M_{wccps} is the measured torque acting on the shaft due to the cylinder block, pistons and swashplate with oil in the casing, and M_{dccps} the measured torque acting on the shaft due to the cylinder block, pistons and swashplate without oil in the casing.

The test of churning losses torque due to the variable mechanism M_{cv} can be expressed as:

$$\begin{aligned} M_{cv} &= M_{ccpsv} - M_{ccps} \\ &= M_{wccpsv} - M_{dccpsv} - M_{wccps} + M_{dccps} \end{aligned} \tag{5}$$

where M_{ccpsv} is the experimental churning losses torque due to the cylinder block, pistons, swashplate and variable mechanism, M_{wccpsv} is the measured torque acting on the shaft due to the cylinder block, pistons, swashplate and variable mechanism with oil in the casing, and M_{dccpsv} the measured torque acting on the shaft due to the cylinder block, pistons, swashplate and variable mechanism without oil in the casing.

3. MEASUREMENT RESULTS

Fig. 3 shows the measuring results of the churning losses torque for cylinder block, pistons, swashplate and variable mechanism. The measured torque was selected after the test pump had been operated for several times and reached a relatively steady state. By analyzing the test curves in Fig. 3 it can be seen that cylinder block and pistons have a dominant influence on churning losses both at low speeds and high speeds. This can be explained by the fact that pistons and cylinder block are two main rotating parts in the test pump. In addition, the swash plate has little effect on the churning losses, while the variable mechanism plays a role in reducing the churning losses with the increase of rotating speed. Because the swashplate locates in the non-core flow region. It has little influence on the churning losses torque. The variable mechanism reduces the volume of oil inside the test pump and effectively reduces the amount of turbulent pulsating fluid. Therefore, the variable mechanism can reduce the churning losses at high speed.

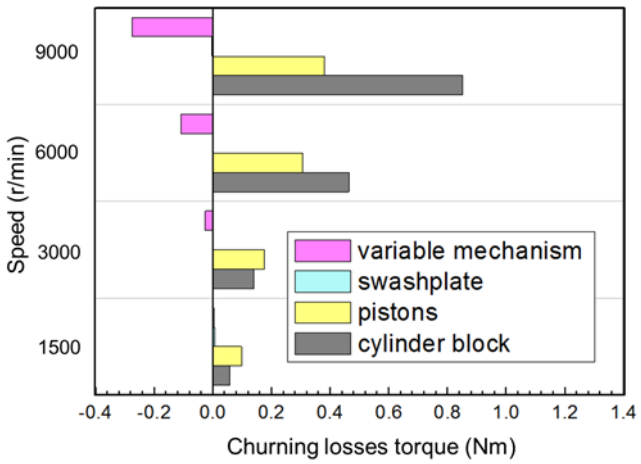

Figure 3. Measuring results of the churning losses torque

Fig. 4 illustrates the proportion of churning losses produced by the cylinder block, pistons, swashplate and variable mechanism at different speeds. The proportion of cylinder block to churning losses increases obviously with the increase of rotating speed, while the proportion of plunger to churning losses decreases obviously with the increase of rotating speed. Because the resistance of one piston may be smaller due to the cycled assembly of the pistons, and the flow state of the rotating cylinder may change from laminar to turbulent at high rotation speed as shown in Ref. [28]. The swashplate has a slight effect on stirring loss at low speed because the swashplate reduces the clearance between part of the shaft and the housing internal surface at low speeds. At high speed, the swashplate located in the non-core turbulent region has little influence on the churning loss torque. Variable mechanism accounts for a small proportion of churning loss at low speed and plays a role in reducing churning loss with the increase of rotating speed. The capacity of variable mechanism to reduce churning loss increases with the increase of rotating speed. It can be explained that the variable mechanism reduces the gap between the cylinder block and the housing internal surface, thus increasing the laminar viscous friction caused by the rotating cylinder block at low speeds. The laminar flow turns into the turbulent flow with the increase of rotating speed, the variable mechanism cannot create churning losses, the variable mechanism affects the churning losses because it reduces the volume of oil inside the test pump. Thus, the variable mechanism effectively reduces the amount of turbulent pulsating fluid and decreases the churning losses at high speeds.

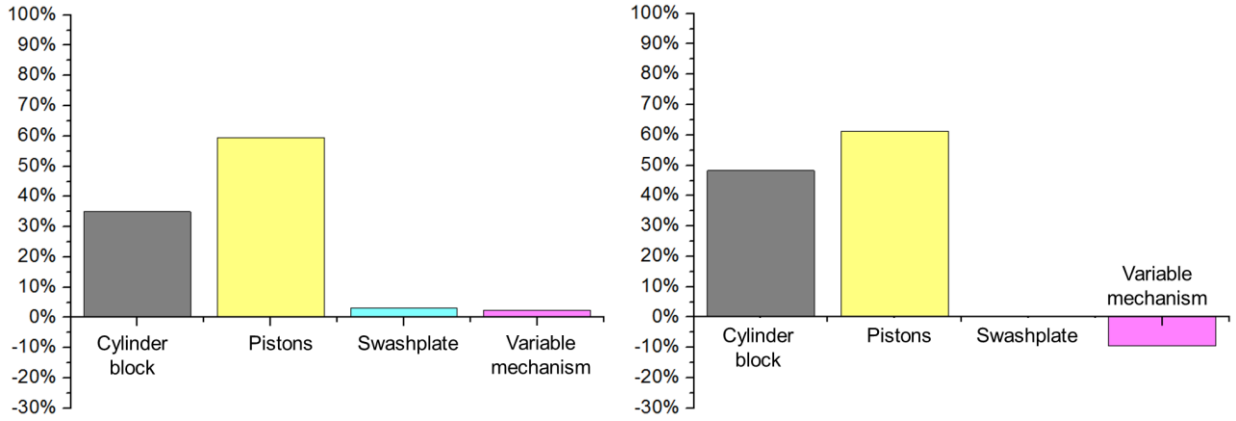

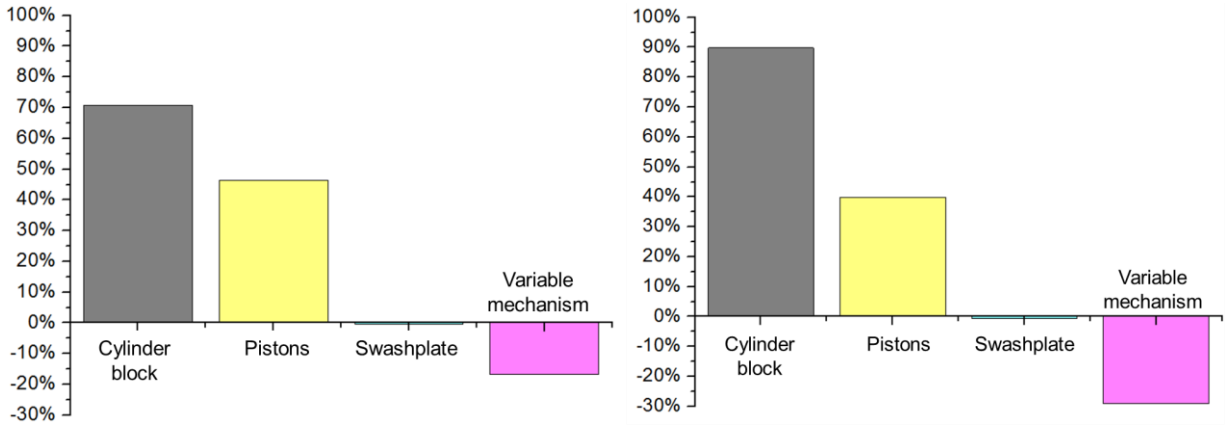

Figure 4: Percentage of churning losses for various parts at different speeds: (a) 1500rpm; (b) 3000rpm; (c) 6000rpm; (d) 9000rpm

4. CONCLUSION

In this study, a churning loss test rig is introduced to experimentally investigate the effect of cylinder block, pistons, swashplate and variable mechanism on churning loss in an axial piston pump. The focus of this work mainly lies in the description of the test method for churning losses torque and the presentation of the measuring results.

Presented measurements exhibit the capacity of the test rig to detect the net churning losses in an axial piston pump at both low speeds and high speeds. According to the experimental data, it can be concluded that the churning loss is mainly related to cylinder block and pistons. The swash plate has little effect on the churning losses, while the variable mechanism plays a role in reducing the churning losses at high speed. These experimental findings may provide new insights into the churning loss.

Taking advantages of the full capability of the test rig, future research on churning losses will focus on reducing the churning losses based on considering the influence of various parts on churning loss in axial piston pumps.

ACKNOWLEDGMENTS

The financial support received from the National Natural Science Foundation of China (No. U1737110, 51890882) are gratefully acknowledged.

REFERENCES

[1] McCandlish D, Dorey RE. The mathematical modelling of hydrostatic pumps and motors. Proceedings of the Institution of Mechanical Engineers, Part B: Journal of Engineering Manufacture, 1984, 198(3): 165-174.

[2] Manring ND. Torque on the cylinder block of an axial-piston swash-plate type hydrostatic pump. PhD thesis, Iowa State University, America, 1996.

[3] Bronshteyn LA, Kreiner JH. Energy efficiency of industrial oils. Tribology transactions, 1999, 42(4): 771-776.

[4] Murrenhoff H, Piepepenstock U, Kohmäscher T. Analysing losses in hydrostatic drives. In Proceedings of the JFPS International Symposium on Fluid Power, September 15-18 2008, Toyama, Japan, pp. 103-108.

[5] Jeong HS, Kim HE. A novel performance model given by the physical dimensions of hydraulic axial piston motors: Experimental analysis. Journal of Mechanical Science and Technology, 2007, 21(4): 630-641.

[6] Gao M, Huang H, Li X, Liu Z. A Novel Method to Quickly Acquire the Energy Efficiency for Piston Pumps. Journal of Dynamic Systems, Measurement, and Control, 2016, Vol. 138, 1-9.

[7] Murrenhoff H, Stephan S, Wear and friction of ZRCG-coated pistons of axial piston pumps, International Journal of Fluid Power, 7(3): 13-20, 2006.

[8] Leonhard L, Murrenhoff H. Deterministic Surface Texturing for the Tribologic Contacts in Hydrostatic Machines, In Proceedings of the 7th International Fluid Power Conference, 7. IFK, March 22-24, 2010, Aachen, Germany, pp. 49-58.

[9] Murrenhoff H, Klocke F, Leonhard L, Derichs C. Mathematische Modellierung, Optimierung und Herstellung mikrostrukturierter Kontaktflächen für hydraulische Verdrängereinheiten - OptiKonS. Abschlussbericht zum Forschungsprojekt, RWTH Aachen, Fraunhofer-IPT, Aachen, Germany, 2010.

[10] Seeniraj GK, Ivantysynova M. Impact of valve plate design on noise, volumetric efficiency and control effort in an axial piston pump, In Proceedings of the ASME 2006 International Mechanical Engineering Congress and Exposition, November 5-10, 2006, Chicago, USA, pp. 1- 8.

[11] Wondergem A, Ivantysynova M. The Impact of Micro-Surface Shaping of the Piston on the Piston/Cylinder Interface of an Axial Piston Machine, In Proceedings of the 10th International Fluid Power Conference, 10. IFK, March 8-10, 2016, Dresden, Germany, pp. 289-300.

[12] Hooke CJ, Li KY. The lubrication of slippers in axial piston pumps and motors—the effect of tilting couples, Proceedings of the institution of mechanical engineers, part C: journal of mechanical engineering science, 203(5): 343-350, 1989.

[13] Koc E, Hooke CJ. Considerations in the design of partially hydrostatic slipper bearings, Tribology International, 30(11): 815-823, 1997.

[14] Kazama T, Yamaguchi A. Optimum design of bearing and seal parts for hydraulic equipment, Wear, 161(1): 161-171, 1993.

[15] Wang X, Yamaguchi A. Characteristics of hydrostatic bearing/seal parts for water hydraulic pumps and motors, Tribology international, 35(7): 425-433, 2002.

[16] Kazama T. Numerical simulation of a slipper model for water hydraulic pumps/motors in mixed lubrication, In Proceedings of the 6th JFPS International Symposium on Fluid Power, 6. JFPS, November 7-10, 2005, TSUKUBA, Japan, pp. 509-514.

[17] Lin SJ, Akers A, Zeiger G. The Effect of Oil Entrapment in an Axial Piston Pump, Journal of Dynamic Systems, Measurement, and Control, 107(4): 246–251, 1985.

[18] Manring ND, Zhang Y. The Improved Volumetric-Efficiency of an Axial-Piston Pump Utilizing a Trapped-Volume Design, Journal of Dynamic Systems, Measurement, and Control, 123(3): 479–487, 2001.

[19] Manring ND. Valve-Plate Design for an Axial Piston Pump Operating at Low Displacements, Journal of Mechanical Design, 125(1): 200–205, 2003.

[20] Ahn SY, Rhim YC, Hong YS. Lubrication and Dynamic Characteristics of a Cylinder Block in an Axial Piston Pump, In Proceedings of the 3th World Tribology Congress III, 3.WTC, January, 2005, Washington, DC, pp. 223–224.

[21] Kim J, Kim H, Lee Y, Jung J, Oh S, Measurement of Fluid Film Thickness on the Valve Plate in Oil Hydraulic Axial Piston Pumps (Part II: Spherical Design Effects), J. Mech. Sci. Technol., 19(2): 655–663, 2005.

[22] Xu B, Chao Q, Zhang JH, Chen Y. Effects of the dimensional and geometrical errors on the cylinder block tilt of a high-speed EHA pump, Meccanica, 52(10): 2449-2469, 2017.

[23] Jang DS. Verlustanalyse an Axialkolbeneinheiten, RWTH Aachen University, Aachen, Germany, 1997.

[24] Håkan O. Power losses in an axial piston pump used in industrial hydrostatic transmissions. In Proceedings of the Eighth Scandinavian International Conference on Fluid Power, May 7–9, 2003, Tampere, Finland, pp. 491-505.

[25] Shang L, Ivantysynova M. Port and case flow temperature prediction for axial piston machines. International Journal of Fluid Power, 2015, 16(1): 35-51.

[26] Enekes CP. Ausgewählte Maßnahmen zur Effizienzsteigerung von Axialkolbenmaschinen. PhD thesis, RWTH Aachen University, Germany, 2012.

[27] Xu B, Li Y, Zhang JH, Chao Q. Modeling and analysis of the churning losses characteristics of swash plate axial piston pump, In Proceedings of the 7th International Conference on Fluid Power and Mechatronics, 7. FPM, August 5-7, 2015, Harbin, China, pp. 22-26.

[28] Zhang JH, Li Y, Xu B, Pan M, Lv F. Experimental Study on the Influence of the Rotating Cylinder Block and Pistons on Churning Losses in Axial Piston Pumps, Energies, 10(5): 662, 2017.

SWASHPLATE PLATE TYPE AXIAL PISTON PUMP NOISE DIAGNOSTICS FOR DESIGN

Paul Kalbfleisch[1], Dan Ding[1], Abhimanyu Baruah[1], Dr. Monika Ivantysynova[1] †, Germano Franzoni[2], Howard Zhang[2],
Purdue University[1] & Parker Hannifin Corporation[2]
1500 Kepner Dr
Lafayette in 47905-6578
E-mail: pkalbfle@gmail.com

ABSTRACT

The characterization of the noise admitted by positive displacement machine is an important metric in designing positive displacement machines and their corresponding systems. Many companies in industry design their pump's noise based on confidential heuristical traditions, verified by simple measurements of sound pressure. A research initiative between Parker Hannifin and Maha Fluid Power Research Center at Purdue University will introduce a new methodology for diagnosing for designing existing pumps to reduce noise. This paper will provide a high-level overview of the proposed methodology. The methodology consists of organizing the unit's oscillatory energy into five stages of the structural acoustic process, where each stage can be independently characterized using various experimental and empirical modeling methods.

KEYWORDS: Noise, Vibration, Harshness, Swashplate, Axial Piston, Acoustic, near field holography, Computer order tracking, signal processing, spherical harmonic, Structural acoustic.

1. INTRODUCTION

Traditionally, the vast majority of NVH research has been focused on the source/generation of noise. As the new direction in research is modeling the influence of the structure, the proposed experimental methodology will provide a crucial step in the diagnosis and organizing the unit's oscillatory energy through the five stages of the structural acoustic process. The proposed In-situ experimental diagnostics system is highlighted using a 44cc, nine piston pump, open circuit, electro-hydraulically controlled swash plate type axial piston unit. The methodology verifies the steady-state operation to assume a cyclostationary signal with a dominating deterministic component, periodic about the fundamental shaft rotational frequency (f_0). The development of the computer order tracking and the creation of a synthetic array allows for the replacement of very expensive microphone arrays while still capturing the majority of sound energy.

2. TRADITIONAL NOISE, VIBRATION, AND HARSHNESS METHODS

Different companies have different confidential noise design methodologies. Some have briefly shared insights into their understanding starting with Stan Skaistis at Vicker's pump company [1]. Skaistis represents the first literature in separating the sources of audible airborne noise as a function of "liquid borne noise" and "structure

borne noise". Following Skaistis' lead, Becker, at Vickers, concluded the rate of displacement chamber compression was correlated with acoustic loudness [2]. This led to the field of designing the rate of displacement chamber compression to effect noise through port timing modifications. The design of port timing later matured into defining the port timing geometry through the use of a valve plate design. This modular design system allowed for an easier change in port timing, independent of the port geometries.

Entering later, academia made a large contribution to pump noise design through the major collaboration of British Universities standardizing "structure borne noise" (SBN) and "liquid borne noise" now "fluid borne noise" (FBN) [3]. Following the SBN/FBN paradigm, researchers have been exploring for many methodologies and design techniques for reducing pump noise [4].

Categorizing past research based on the current five stages structure acoustic paradigm, most of the research focused only on the generation of noise. Beginning with FBN, research focused on modeling the pumps source impedance [2], [5]–[7] and measurement of line/sources impedances [8]–[11]. Later, the direct modeling of the pump's oscillating flow/pressure was conducted [12]–[14]. Substantially much less research has focused solely on SBN [15]–[17]. Motivated by professor Edge [4], a significant amount of the research focused on both FBN and SBN was completed in order to either model, measure, or minimize pump noise [18]–[26].

While a fast amount of research and effort focused on the generation stage of noise. Very little focus has been given on the effects of the structural response and sound radiation of oscillatory energy. The current direction of research into understanding the radiation of sound from pumps in through finite element and boundary element modeling (FEM/BEM) [27]–[34].

In contrast to the previous research, the proposed methodology aims to understand/map how a pump's internal fluid pressure oscillations propagate through the pump and radiate to perceived audible noise. In contrast with current FEM/BEM modeling efforts, which take months to create for every pump, the current methodology can diagnosis the sources of noise within a matter of hours/days. This faster route to understanding allows for a much easier adaption of industrial researchers to diagnosis/design their machines.

3. NVH DIAGNOSTIC METHODOLOGY

The proposed diagnostic methodology begins with the categorization of the oscillatory energy into five stages or domains (Fig. 1). Beginning with the *Generation* of noise sources within the pump, these pressure fields *Transmit* energy to the pump structural/case. This is a coupled process based on the complex mechanical impedance at each forcing location. The corresponding local change in material position/velocity is then *propagated* throughout the solid body based on the structural impedance.

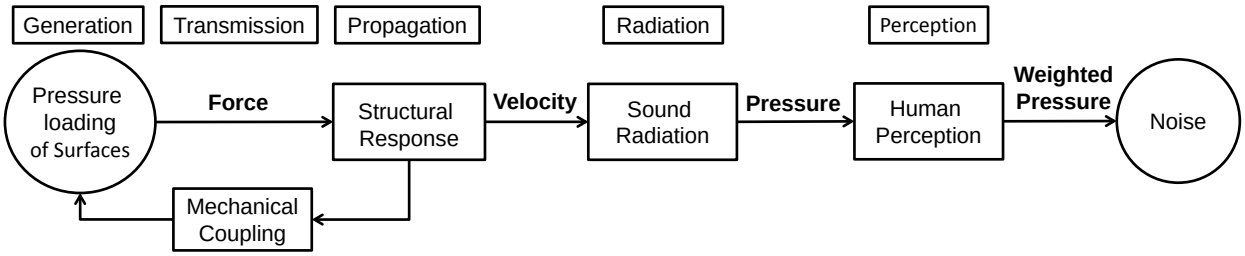

Figure 1. Five Stage Structural Acoustic Process

Propagating waves in a solid medium in contact with a fluid (air) will create another transfer of energy to the adjacent air through *Radiation*. The small amplitude propagating fluctuations in pressure, density, velocity, and temperature that escape the reactive effects of the near field will eventually propagate away from the pump (far field). This complex, spatial varying, radiation pattern of sound will create a spatially unique frequency content for all locations in the far field. Finally, the process of modeling how a human interprets this highly varying complex sound field is the *Perception*.

The proposed diagnostic methodology aims to experimentally identify and categorizes the dominating contributors to perceived airborne noise emitted by a swash plate type axial piston pump. The eventual identification and separation of the various physical phenomena affecting noise can later be modeled and modified on an individual basis.

3.1. Experimental Facilities

All five stages of the structural acoustic process currently assume Cyclostationary symmetry, assuming purely periodic signals plus noise. To accommodate this signal processing assumption the tests were performed under steady-state operation in accordance with ISO 4409 [35]. Similarly, to help physically reduce the effects of external sound sources, including wall reflections, the pump was tested in Purdue Universities Maha Fluid Power Research Center's semi-anechoic testing chamber (Fig. 2A) [36]. This chamber is in accordance with International pump testing standards [37]–[39].

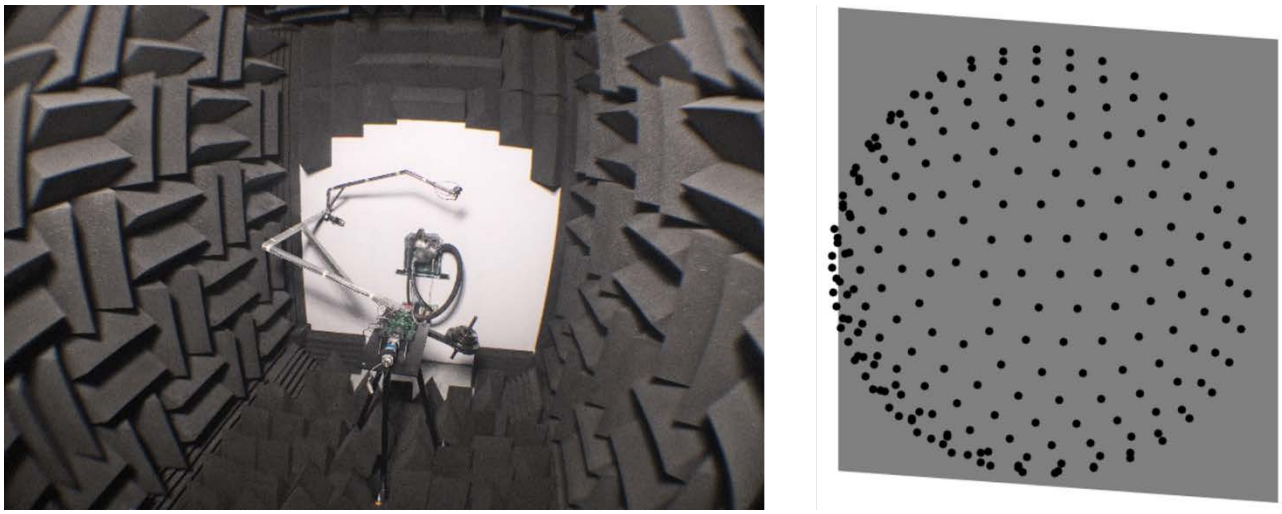

Figure 2. Maha Research Center Acoustic Chamber (Left). 225-point measurement surface (Right).

The measurement of sound was performed using a custom-designed robot [36] sampling 225 equally spaced measurements locations at a radial distance of 1 meter from the pump (Fig. 2B). The structural response was measured using 10 channels of PCB 352C03 and 6 channels of PCB 356A02 accelerometers equally spaced around the pump case. The generation stage was sampled with high bandwidth (Kistler 603B1) piezoelectric pressure transducers in the swash plate control cylinder pressure, and both port pressures. All 23 (16 accelerometers, 3 microphones, 3 pressures, 1 shaft trigger) channels of sensors were taken synchronously using National instrument 9234 cards, sampling at 51.2 kHz. The swash plate control moments have been historically researched to be a dominant source of noise [18]–[26]. Therefore the measuring of the swash plate control cylinder was theorized to be a good experimental way of measuring the control moments. Considering a closed system, a change in swash plate force would be equally balanced by a corresponding change in cylinder pressure. The closed system assumption can be considered when the dynamics of the moments are greater than the bandwidth of the control valve.

4. SIGNAL ANALYSIS

The measurement of quality raw data is more importantly coupled with the signal analysis methods to extract the useful information. The following signal process highlights the synchronizing of NVH data based on the periodicity of the shaft. The strong periodicity of NVH data allows the authors to create a novel *Synthetic Microphone Array* allowing for the utilization of more modern array techniques.

4.1. Energy Audit

Signal energy is defined as Eq. (1) and it conserves in both time domain and frequency domain:

$$E = \sum_{n=0}^{N-1} |p[n]|^2 = N \sum_{k=1}^{N} |P[f_k]|^2 \quad (1)$$

Where $P[f_k]$ is the discrete frequency spectrum of $p[n]$. Eq. (1) enables the computation of energy contribution at different frequencies. Theoretically, the fluid ripple and swash plate moments have only the frequency contents at the *Pump Harmonics*, which are the integer multiples of ninth (nine pistons) shaft order. Therefore, the first energy group was the pump harmonics. It is usually observed from the spectrums that the most energetic frequencies occur at the multiple of shaft orders. Thus, the second group is all the shaft orders excluding pump harmonics, called side band. All the remaining frequency content, not at shaft orders, are included in the broadband group.

The frequencies are further split into three ranges. The low frequencies (0Hz - 8.5 shaft order; 9 pistons) are usually not related to the pump harmonics. The middle frequencies are the main frequencies of interest and begin with the 8.5 shaft order up to the limitation of the current accelerometers 10 kHz. The last and least important group is the high-frequency region (10 kHz to 20 kHz) where the structural response cannot be measured with the accelerometers and is usually dominated by broadband noise. The accumulation of measurement errors in many of the signal analysis tools tends to taint the trust in the conclusion drawn from this region.

Table 1. Energy Audit Signal Energy [Pa²]

	Noise Floor	Turning Noise Floor	Pump Harmonics	Non-pump Orders	Broadband
Low	1.26e-3	4.19e-3	0	2.13e-2	2.53e-1
Mid	7.90e-6	1.51e-3	**6.09e0**	**1.83e-1**	5.32e-1
High	1.20e-5	5.42e-5	2.74e-3	2.13e-2	2.97e-1

The main conclusion to draw from table one shows the majority of sound energy is found within the middle frequency region in the Pump Harmonics and Non-pump Orders. This confirms the following developed signal analysis tools are useful for characterizing the vast majority of a pump's radiated/audible sound energy.

4.2. Instantaneous Angular Speed (IAS)

The majority of shaft related NVH data is assumed to be periodic in time with a period of one shaft rotation f_0. The use of a one pulse per revolution (PPR) trigger channel is used to record the rotation of the shaft. However, the instantaneous angular shaft speed (IAS) variations occurring faster than once per revolution (shaft order > 1) need to be accounted for. Such that any variation in angular speed (ω) will affect/warp the time domain data.

$$dt = \frac{d\theta}{\omega} \quad (2)$$

The estimation of angular speed through the discrete sampling of rotational angle (θ) fundamentally creates a low-pass filtered estimation of speed [40]. Such that the spectrum of the first-order estimated, angular speed $\bar{\Omega}$ in the angle domain is:

$$\bar{\Omega}(f_0) = \Omega(f_0) \cdot e^{-\frac{j4\pi^2 f_0}{p}} \cdot sinc_\pi\left(f_0 \frac{2\pi}{p}\right) \quad (3)$$

This low-pass filtering of the IAS creates a minimal limitation on the encoder resolution (p). Of the various errors analyzed, the *Quantization error* due to the finite sampling of angular speed with a finite sampling

frequency f_s dominated. The calculation of the quantization error is upper bounded by assuming a maximum measured timing error, of the rising edge of the encoder signal, has a maximum of one sample. Therefore, the quantization error is based on the ratio of time between the two samples and the samples per encoder segment S.

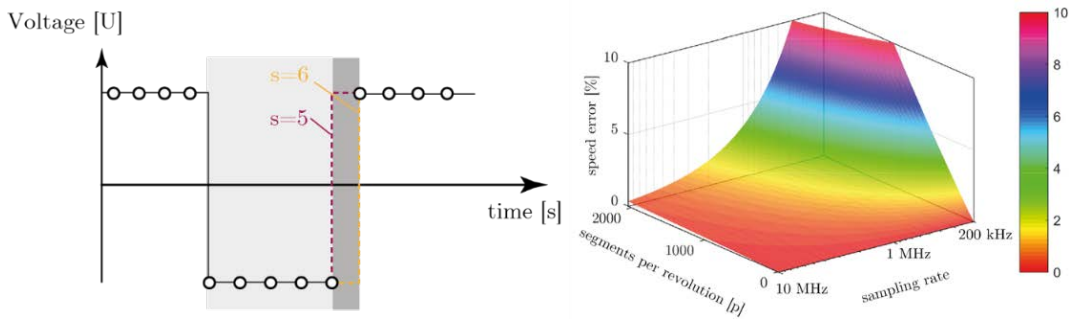

Figure 3. Quantization error of encoder (Left). Quantization error @ 1000 rpm for various p and fs (Right).

The derivations, found by Horn [41], conclude to a dependency on the relationship between the operating speed f_0, the encoder resolution p, and the sampling frequency f_s.

$$\Delta\omega_{IAS,\%} = \frac{100\Delta\omega_{IAS}}{\omega_{IAS}} = \frac{10\pi p {f_0}^2}{3(f_s - p)} \tag{4}$$

Sizing the encoder resolution requires a balance of the positive effect of more angular sampling and the negative consequences of aliasing in the angle domain. To date, there is no physical method of filtering the angular sampling with an anti-aliasing filter and therefore an appropriate encoder resolution should consider both [40].

Similarly, the low-pass filtering of the quantization error creates a minimal value for the sampling frequency f_s. Throughout the current research, various combinations of angular sampling frequency (p) and temporal sampling frequency (fs) were utilized until final values of 1024 pulses per revolution (PPR) square wave encoder (TTL) creating 2048 encoder sections (p) and a sampling frequency of 500 kHz (f_s) [41]. An example result of the study is exemplary of the consistent, surprising, and convenient conclusion that the IAS speed for these measurements is very small. Figure 4 highlights the results of measuring the shafts IAS under three testing conditions; without a pump, with a pump, and with a pump with intentional speed variations caused by oscillating the swash plate command.

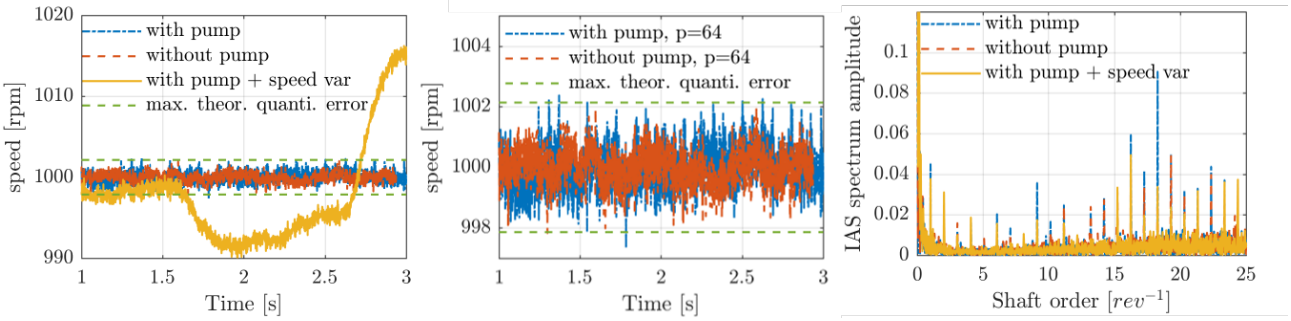

Figure 4. Comparison of IAS measurements @ 1000 rpm; 500kHz, 2048p downsampled to 64p

Figure 4 shows the speed variation due to the addition of the pump remains similar to an empty shaft and both remain below the measurement limitation (quantization error ± 2 rpm). Therefore, for this particular measurement setup up and pump, the angular shaft speed can be assumed constant (0 Hz only). Therefore, the synchronized NVH data in the angle domain can also be considered synchronized in time without further processing.

4.3. Computed Order Tracking (COT)

The presence of quantization error and sampling at a frequency not an integer multiple of the fundamental shaft rotation frequency will create cycle-to-cycle and sensor-sensor differences in the length of each revolution. Therefore, the numerous measured revolutions will have slightly different measurement vector lengths. In order to perform averaging techniques and signal/signal processing, all signals must process the same vector length for each revolution. The process of converting equally time step sampled signals (Δ) into equally angle step signals ($\Delta\Theta$) is called *Computed Order Tracking (COT)*. Once resampled into angle domain, the now synchronized signals can be further processed in a comparative manner.

Of the various COT methods, a simplistic and rather intuitive method of *Resampling* was chosen based on Bechhoefer [42] using cubic spline interpolation [43]. The current method of Resampling is always *Up-sampling*, such that every revolution has more samples than before. This is to guarantee no information is lost in downsampling of signals. Figure 5 illustrates the using of simultaneously sampling an encoder signal (E_i) with a measured NVH signal (x_i). Using a *zero-crossing* edge detection, each equally spaced segment of the encoder is now known and the data can be resampled. The final product of resampling creates J number of revolutions each with S number of samples in each. The signal is now resampled to have equal angle step signals samples ($\Delta\Theta$).

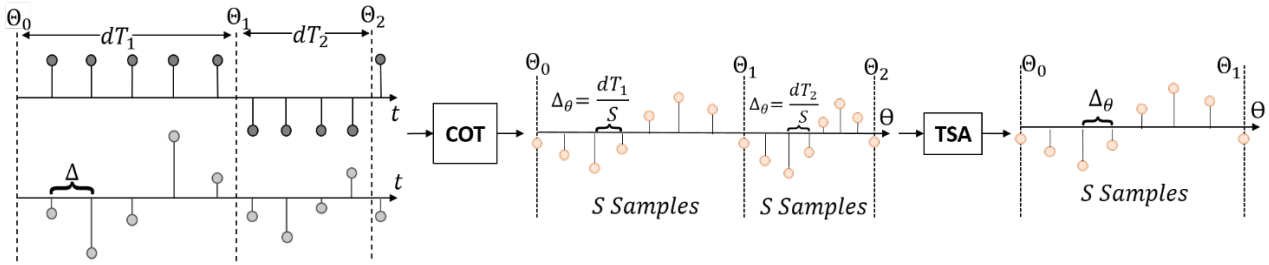

Figure 5. Computed Order Tracking Process

The measured signals can be thought of as having shaft-correlated components and non-shaft correlated components. Notable examples of non-deterministic signals would include electrical noise, background acoustic noise, and stationary or 2nd order Cyclostationary pump noise sources [44] such as turbulent flow or friction. Therefore, it is convenient to extract the consistent and shaft-correlated components of measured signals as the *Deterministic* component with the *Residual* remaining. Such that every signal with J revolutions will contain a shared deterministic component and J unique residuals. This cycle-to-cycle averaging is useful for the reduction of non-shaft correlated noise sources. The extraction of the deterministic component is done by simply computed an average of the J revolutions of each measured signal. The frequency response of the *Time Synchronous Averaging (TSA)* process creates a comb filter [45] such that the magnitude of the normalized averaging transfer function (H(jw)) is shown in Equation 5.

$$\left|H\left(\frac{f}{f_0}\right)\right| = H(z)_{z=e^{-j\omega\Delta}} = \frac{1}{J}\frac{\sin\left(J\pi\frac{f}{f_0}\right)}{\sin\left(\pi\frac{f}{f_0}\right)} \tag{5}$$

Normalized to the fundamental rotational frequency f_0, the effect is to create a band-pass allowing only the integer multiples of shaft frequency (f_0) and filtering the remaining frequencies. While averaging has a positive effect on filtering noise sources uncorrelated to the shaft rotation, an unwanted effect is removing any useful information in those frequencies.

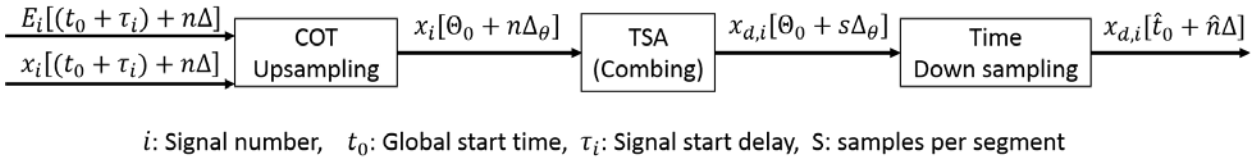

Figure 6. Computed Order Tracking Signal Chain

Figure 6 summarizes the use of the i^{th} encoder signal (E_i) and the i^{th} sensor signal (x_i) to Upsample x_i into the angle domain so that the *Time Synchronous Averaging (TSA)* can be performed. Recalling the instantaneous angular speed was found to be constant, the constant (Δ_θ) is downsampled to return the signal to the original sampled time step (Δ).

4.4. Synthetic Microphone Array

Equipped with multiple microphones at different locations measuring simultaneously, microphone arrays are capable of many advanced processing techniques. Although the robot measurements are non-synchronous, a synthetic microphone array can be created by making a few assumptions and utilizing the COT and TSA techniques.

When a pump is running at steady state, which means the load, shaft speed, and oil temperature are all constant, the fluid borne noise source (flow ripple) and structural borne noise source (swash plate moment) are theoretically the same in every shaft revolution. If assuming the system response is time-invariant, the sound generated in every shaft revolution should also be the same, which in reality is the deterministic part. Therefore, at every measurement location, by extracting the deterministic part starting from the same shaft angle, the sequential measurements can be synchronized to create a synthetic microphone array, and therefore unlock the array processing techniques.

4.5. Acoustic Array Techniques

In general, there are two main categories of microphone array processing techniques: far-field methods and near-field methods [46]. Far-field methods are usually referred to as beamforming, and near-field methods mainly include near-field acoustical holography (NAH).

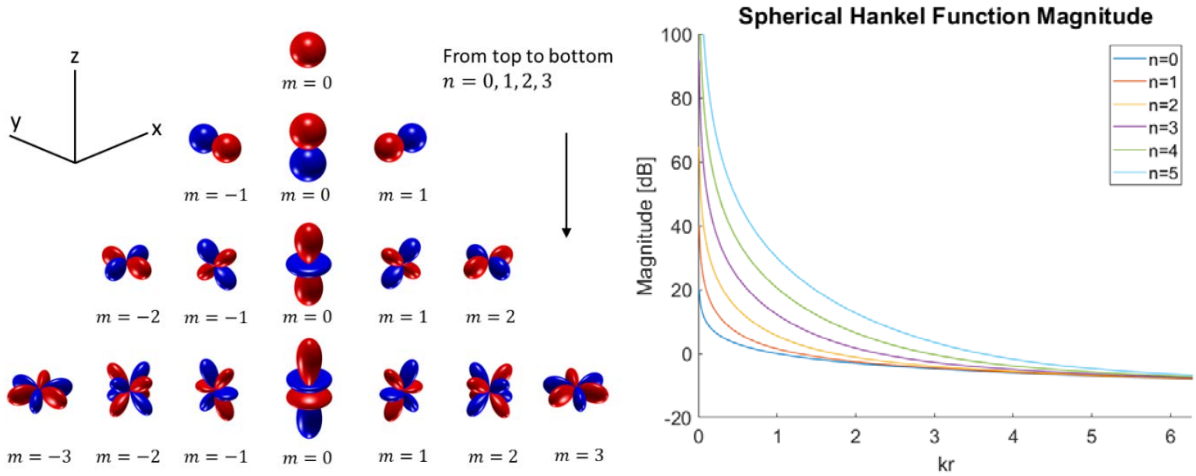

Figure 7. Spherical Harmonic Function (Left) and Spherical Hankel Function (Right)

NAH was chosen for the diagnostics in this paper because it could reveal more information. Within the scope of NAH, many different methods have been developed, including Fourier NAH, Inverse Boundary Element Method (IBEM), Equivalent Source Method (ESM), etc [46]. The spherical coordinate system inherently fits this analysis because of the hemispherical grid. Therefore, the Helmholtz equation's solution in the spherical

coordinate system was chosen to form the basis for Equivalent Source Method. In the spherical coordinate system, the wave equation has a general solution shown as:

$$p(\theta, \varphi, r, \omega) = \sum_{n=0}^{\infty} \sum_{m=-n}^{n} c_{nm} Y_n^m(\theta, \varphi) h_n(kr) \tag{6}$$

where $Y_n^m(\theta, \varphi)$ is called *Spherical Harmonic Function* describing the directional characteristics, n and m are two integers called order and degree of spherical harmonic functions respectively (Fig. 7A), and $h_n(kr)$ is called *Spherical Hankel Function* characterizing the radial behaviours of spherical harmonics at different order n (Fig. 7B). Once the coefficients c_{nm} are known, the sound pressure at an arbitrary position in space can be computed. This paper estimates the coefficients c_{nm} by minimizing the squared error between fitted value and measured sound pressure. Thus, this method is called *Helmholtz Least Square Method* (HELS) [47], [48]. One advantage of this method is the spherical harmonic functions form an orthogonal basis in Hilbert space $L_2(S^2)$ [49]. Therefore, the total radiated sound power measured on the spherical surface is the sum of the sound power distributed on different spherical harmonic contents. Each spherical harmonic can be equivalently considered as an independent simple noise source. These independent sources sometimes have direct connection with specific vibration pattern. Furthermore, given the same energy input, some of spherical harmonics radiates more sound power than the others. As results, by analysing the spherical harmonic spectrum, the major sound radiation contributors can be inferred, and potential sound radiation reduction solution can be found.

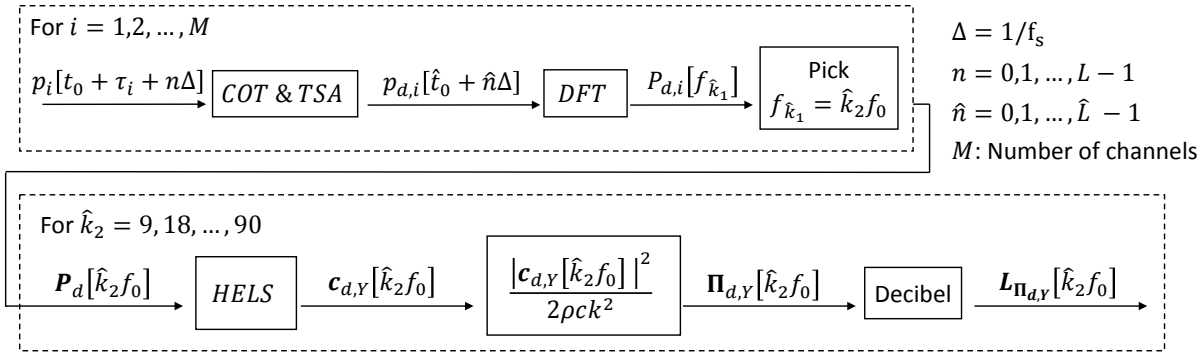

Figure 8. Spherical Harmonic Spectrum Signal Chain

On the implementation, Discrete Fourier Transform (DFT) was firstly applied on the deterministic part found on each measurement location. Equation 6 only describes the pressure at a single frequency, therefore one complex pressure is picked at one measurement location. All the 225 "picked" complex pressure at the same frequency are then used to form a vector and send to the HELS block (Fig. 8). Using the spherical wave coefficients c_{nm}, the sound power can be directly calculated [50].

$$\Pi = \frac{1}{2\rho c k^2} \sum_{n=0}^{\infty} \sum_{m=-n}^{n} |c_{nm}|^2 = \sum_{n=0}^{\infty} \sum_{m=-n}^{n} \Pi_{nm} \tag{7}$$

Where Π is the total sound power and Π_{nm} denotes the sound power at order n and degree m.

5. DIAGNOSTIC CASE STUDY

The proposed In-Situ experimental diagnostics system is highlighted using a 44cc, 9 piston pump, open circuit, electro-hydraulically controlled swash plate type axial piston unit. The unit was tested at numerous different operating conditions, but only one is used for highlighting the utility of the current system; 1200 rpm, 200 bar, 90% displacement. Three different valve plates (VP1, VP2, and VP3) were measured as the highlighted design changes.

Table 2. Case Study Sound Pressure Levels (dBA) Overview

	Overall Mean	1st Harm	2nd Harm Level
VP1	77.37	70.08	63.01
VP2	73.25	61.34	64.07
VP3	72.72	61.09	58.98

The case study will show how the same pump begins with VP1 dominated by the first harmonic SPL. Reducing first harmonic by 8.7 dBA through the design of VP2 reduces the overall SPL by 4dBA. Continuing onto VP3, maintaining first harmonic levels while simultaneously reducing the second harmonic by four dBA reduces the overall SPL by an additional 0.5dBA. Noting we see smaller compromising increases in other frequencies such as the fourth harmonic (Fig. 9).

To give an understanding of how the change in valve plate design correlates to noise, the five stages of the structural acoustic process are mapped. Working backward with using the average pressure spectrums and spherical harmonic spectrum for the Radiation, the velocity phase diagrams for the Transmission/Propagation, and swash plate control pressure for the Generation.

5.1. Spectrum Overview

Starting with the narrowband spectrum in figure 9, the mean and maximum value (for each frequency) of the 225-microphone measurement locations shown. As a reference, the sound chamber's noise floor is shown to measurement quality, as ISO 3745 [51] recommends 10-20dB headroom. While the microphones are accurate for frequencies up to 20 kHz, only the spectrum below 5 kHz has significant SPL contributions.

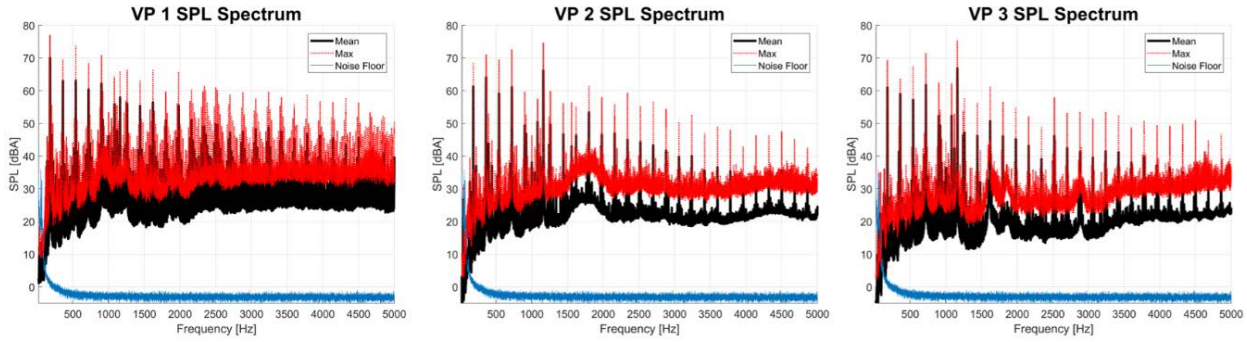

Figure 9. Narrowband A-Weighted Sound Pressure Levels

After decomposing the sound field into the various spectral components, each frequency can further be decomposed into the spherical harmonic basis (given a radius). Figure 10 shows a new graphical representation of the sound field, called the *Spherical Wave Spectrum*. Here the chosen main frequencies of interest are displayed on the y-axis (first 10 pump harmonics) each with their spherical wave decomposition on the x-axis. Finally, the color represents the decomposed sound power (A-weighted) possessed by each spherical basis function. Referring to figure 7A, the spherical harmonic index is simply the counting of the spherical wave basis functions. For reference, the n^{th} spherical harmonic orders are separated with vertical white lines to distinguish the main simple radiators such as the one monopole (n=0), three dipoles (n=1), five quadrupoles (n=2), etc.

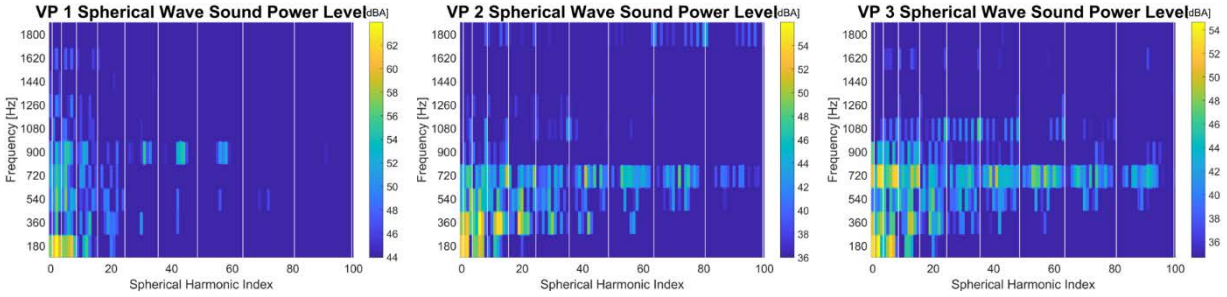

Figure 10. A-weighted Spherical Wave Spectrum

Examining the specific measured data, we start by recognizing the strong vertical dipole (n=1, m=0; index = 2) dominating the first pump harmonic (9th shaft order; 180 Hz) for all three valve plates designs. We observe as the frequency increases so does the contribution of higher spherical orders. As VP2 and VP3 decrease the first and second harmonic respectively, the fourth harmonic (720 Hz) now is increasing in sound power over a very wide diversity of spherical orders. This shows a very complicated spatial distribution of sound resulting in the positive consequence of lower radiation efficiencies (Hankel function) and the negative consequence of significantly more complex model required.

A brief explanation for the intentional exclusion of the vibration spectrum was based on its inability to provide further clarity. The sampling of the sound field through 225 measurement locations provide an accurate approximation to the lower spherical harmonic order (n<14). However, 16 locations appear to be insufficient to completely characterizing the surface velocity field of a complicated irregular object, which also appears to have a high modal density (due to the presence of higher spherical harmonic orders). Nevertheless, their partial characterization of the surface velocity field does provide useful confirming information.

Concluding the overview of measured data is the spectrum of the measured control cylinder pressure. As previously mentioned the moments have been historically found to correlate well with the radiated sound power. Comparing the measured control pressure (Generation) and the A-weighted sound pressure spectrum (Radiation/Perception) now show much larger deviations as the influence of the structural response and radiation resistance/efficiency start to play an increasing role at higher frequencies where more complicated interference patterns arise.

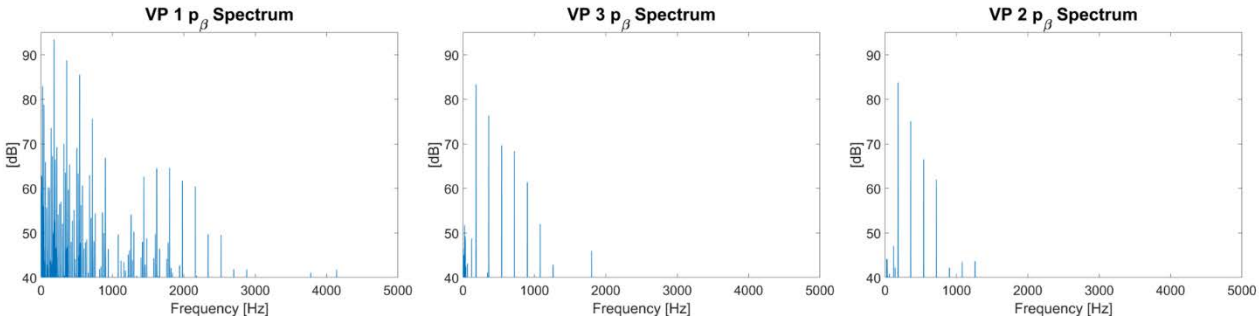

Figure 11. Control Cylinder pressure, p_β Spectrum

The inlet and outlet port pressures were measured and were subjectively found not to correlate well with the measured sound. As later shown the swashplate moments, approximated by the control cylinder pressure, explain the sound field well.

5.2. First Pump Harmonic Reduction

Recalling from the overview section, the main reduction in overall sound pressure level from VP1 and VP2 is due to the reduction in the first pump harmonic. Followed by a roughly similar level in VP3. To help explain

how the generation of the swash plate moment effects the total sound power the five structural acoustic stages are mapped for the specific frequency (180 Hz).

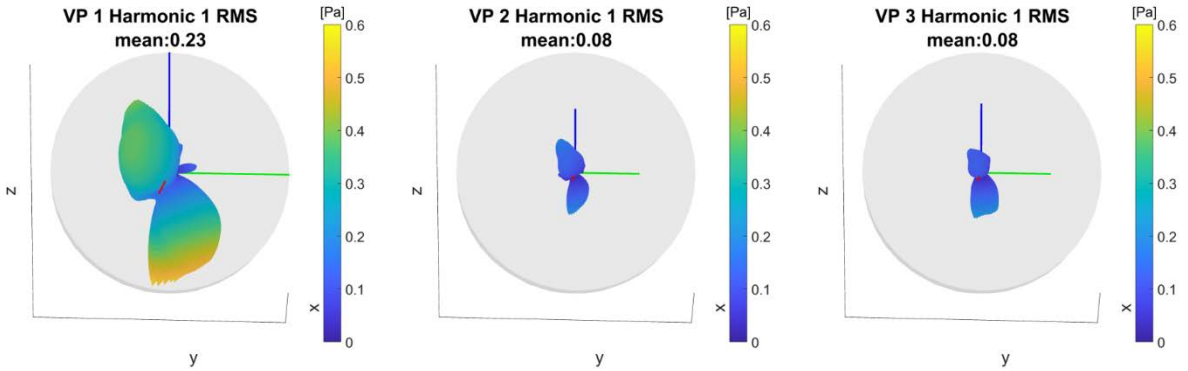

Figure 12. First pump harmonic (9th order) sound field rms

Beginning with the radiation of sound, figure 12 shows the shape of the measured sound field. Notice the shape for all three designs strongly resembles a vertical dipole.

Note, the various locations of the sound field have different phasing (dipoles are 180 deg phased). Therefore, to show the time average amplitudes for the sound field, the root mean square of the pressure is displayed. Notice a rms reduction of 0.23 to 0.08 corresponds to a SPL dB drop of 9.2dB.

The phase diagram of the measure velocities is shown (Fig. 13) to represent the structural response stage because it is known from the *Linearized Euler's Equation* [52] the surface velocity is closely related to the surface acoustic pressure. Here the phase diagram shows the magnitude of each measure velocity radially, and the phase information in angle.

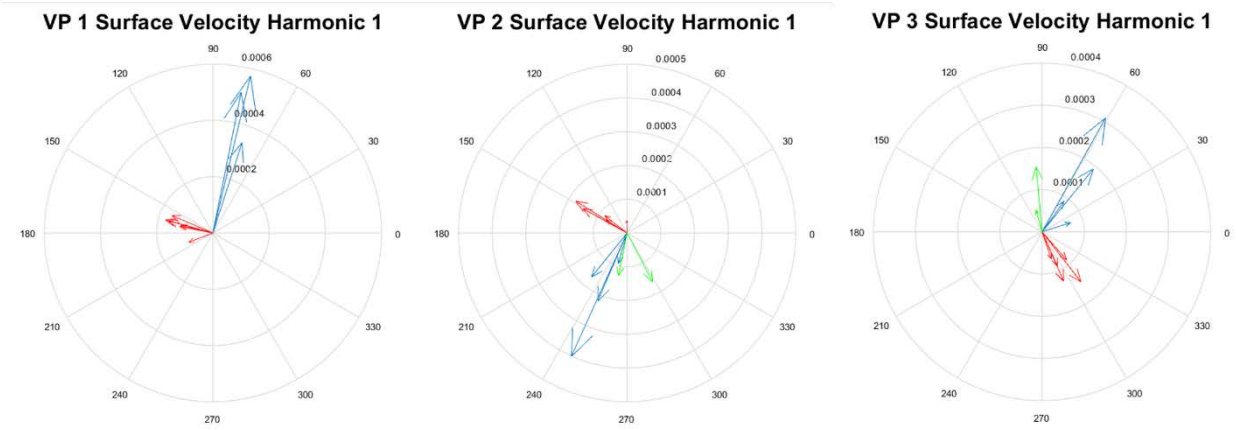

Figure 13. 9th Shaft Order Velocity Phase Diagrams (blue: x-direction, red: y-direction, green: z-direction)

The narrow distribution of phase shows the various sides of the pump moving together (in phase) creating a whole body cantilever motion, producing low spherical harmonic orders (dipole.) The 90-degree phase difference between blue and red shows a circular whole-body motion of the pump, however, the blue's magnitude dominates producing a strong vertical dipole.

The structural response is theorized to be dominantly a function of frequency (linear system, similar forcing locations, etc.) and similar spherical harmonics means similar radiation resistance/efficiency. Therefore, generation of noise and the perception of noise can be linearly correlated well with a 9.5 dB drop in p_β is matched with the 9.2 dB drop in SPL (rms 0.23 to 0.08). Looking at the velocity, we do not observe a similar good correlation due to undersampling and insufficient averaging of the surface velocity.

5.3. Second Pump Harmonic Reduction

Continuing onto the comparison of VP2 and VP3 we have observed the main difference in overall sound power is due to the reduction in the second pump harmonic frequency (360 Hz). Figure 14 shows the shape of the second pump harmonic sound field. Recall from the spherical wave spectrum to see this shape can be considered a linear combination of many different spherical harmonics. As the spherical harmonics are orthogonal functions and therefore conserve power, the total radiation efficiency for this frequency can be seen as a linear combination of all the contributing spherical harmonics. Therefore, the correlation between the measured far field is more complicated than the first harmonic dipole.

As the spatial complexity increases, we see increasing importance in the role of where the sound is sampled. Notice, if a single microphone location is sampled to compare designs VP1 and VP2, they can measure very different values of sound pressure. However, the overall rms, when sampled well, is very similar (1dB difference).

Now comparing VP2 and VP3 we notice the drop in mean sound pressure (0.03 rms, 5dB) accompanied by a change in the shape and therefore spherical harmonic content as well as radiation efficiency.

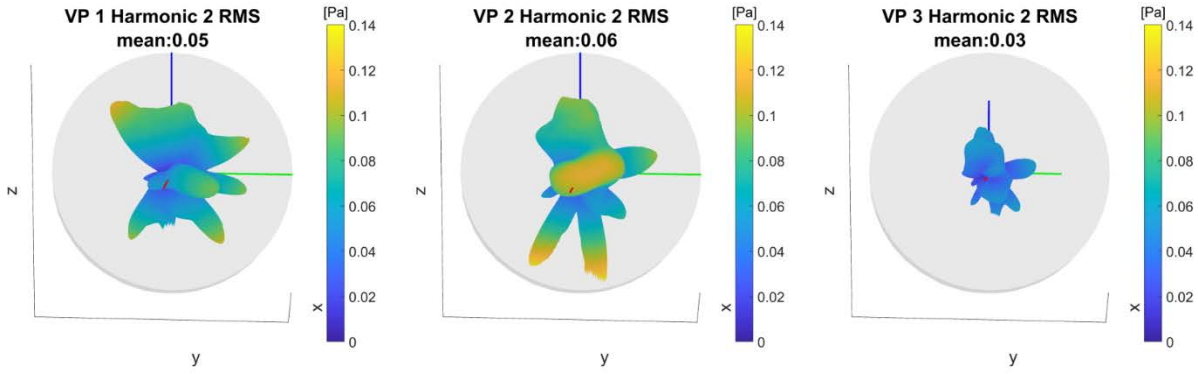

Figure 14. Second pump harmonic (18th order, 360 Hz) sound field rms

We see a general correlation between velocity and sound, however, notice more variance in the phase will correspond with the various sections of the pump moving independently causing destructive interference in the near field. This will create high order spherical harmonics, which radiate less efficiently and change the linearity of correlation.

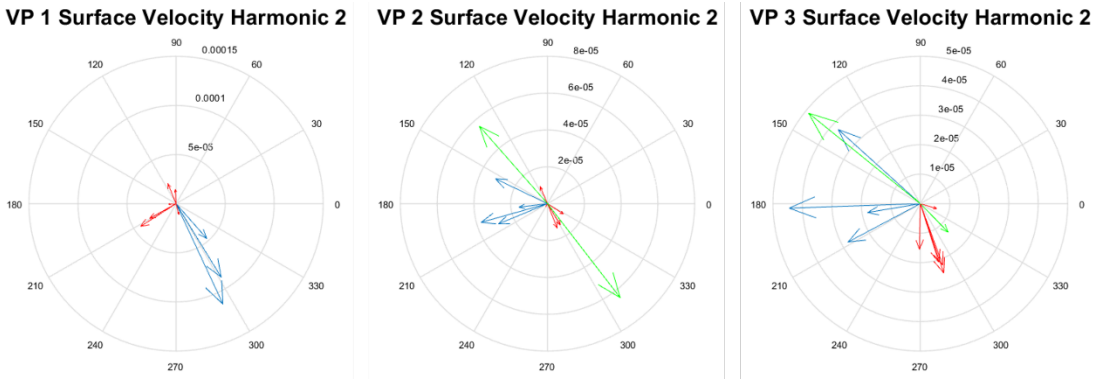

Figure 15. 18th Shaft Order Velocity Phase Diagrams

Recalling the control pressures p_β, we see a very interesting influence of radiation efficiency. The VP3 p_β is higher and the velocities are similar to VP2, however, the sound power decreased. This is due to the increase in spherical harm content also seen by more variation in the velocity phase.

6. CONCLUSIONS

Traditionally, the vast majority of NVH research has been focused on the source/generation of noise. As the new direction in research is modeling the influence of the structure, the proposed experimental methodology will provide a crucial step in the diagnosis and organizing the unit's oscillatory energy through the five stages of the structural acoustic process. The combination of a shaft encoder and the development of the IAS, COT, and TSA algorithms accumulate into the creation of a synthetic array. This process allows for the replacement of very expensive microphone arrays while still capturing the majority of sound energy.

The proposed In-Situ experimental diagnostics system allows for faster diagnosing of design for industrial use, while providing additional information for academics to develop more sophisticated modelling. The current case study shows how the effects of the structural response and acoustic radiation can influence the relationship between the generation and perception of noise.

NOMENCLATURE

List of Abbreviations

COT	Computer Order Tracking
DFT	Discrete Fourier Transform
ESM	Equivalent Source Method
HELS	Helmholtz Least Square Method
IAS	Instantaneous Angular Speed
IBEM	Inverse Boundary Element Method
NAH	Near-field Acoustical Holography
NVH	Noise, Vibration, and Harshness
PPR	Pulses Per Revolution
SPL	Sound Pressure level
TSA	Time Synchronous Averaging
TTL	Transistor–Transistor Logic
VP	Valve Plate

List of Symbols

c_{mn}	Spherical wave coefficient	
dB	Decibel	
E	Signal Energy	[units^2]
E_i	Encoder Signal	
f	frequency	[Hz]
f_0	Fundamental shaft frequency	[Hz]
f_s	Temporal Sampling frequency	[Hz]

h_n	Spherical Hankel Function	
j	Imaginary number	
k	Wave number	[m^{-1}]
$\hat{k}_2$	Shaft harmonic	
L	Total number of samples within each M microphone measurement	
$\hat{L}$	Time synchronized number of samples within each M microphone measurement	
L	Signal Level	[dB]
L_2	Hilbert Space	
M	Number of microphone channels	
n	Sample number within each M microphone measurement	
$\hat{n}$	Time synchronized sample number within each M microphone measurement	
p	Sound pressure	[pa]
p_d	Deterministic sound pressure	[pa]
p	encoder resolution, segments (2*PPR)	[seg/rev]
S	Samples per segment (after TSA)	
t	Time	[sec]
t_0	measurement start time	
T	Fundamental period (shaft rotation)	[sec]
x_i	Sensor signal (for Computer order tracking)	
Y_n^m	Spherical Harmonic Function	
z	z domain; discrete Laplacian domain	
Δ	Sampling time step	[sec]
Δθ	Sampling angle step	[rad]
Π	Sound power	[W]
Ω	Angular speed Spectrum	[rad
θ	Shaft rotational angle	[rad]
(θ, φ, r)	Spherical coordinate system	
ω	Shaft angular speed	[rad/s]
τ_i	Time delay for each M microphone measurement	[sec]

REFERENCES

[1] S. Skaistis, “Sounds of Hydraulics, Pumps and Motors,” *Design News*, Detroit Michigan, pp. 14–19, 1962.

[2] R. J. Becker, “Quieting Hydraulic Systems and Components,” *SAE Tech. Pap.*, 1970.

[3] British Hydromechanics Research Group, *Quieter Fluid Power Handbook*. BHRA Fluid Engineering, 1982.

[4] K. Edge, “Designing Quieter Hydraulic Systems Some Recent Developments and Contributions,” in *Proceedings of the JFPS International Symposium on Fluid Power*, 1999, vol. 1999, no. 4, pp. 3–27.

[5] K. Edge, “The Theoretical Prediction of the Impedance of Positive Displacement Pumps.” p. 10, 1980.

[6] M. Pettersson, K. Weddfelt, and J. Palmberg, “Methods of Reducing Flow Ripple from Fluid,” *SAE Tech. Pap.*, vol. 100, no. 1991, pp. 158–167, 1991.

[7] J. E. Drew, D. K. Longmore, and D. N. Johnston, “Theoretical analysis of pressure and flow ripple in flexible hoses containing tuners,” *Proceedings of the Institution of Mechanical Engineers, Part I: Journal of Systems and Control Engineering*, vol. 212, no. 6. pp. 405–422, 1998.

[8] E. Kojima and H. Nagamura, “Characteristics of Fluidborne Noise Generated by Fluid Power Pump (4th Report),” *Bulletin of the Japan Society of Mechanical Engineers*, vol. 27, no. 232. pp. 2188–2195, 1984.

[9] D. N. Johnston and K. Edge, “A Test Method for Measurement of Pump Fluid-Borne Noise Characteristics,” 1991, vol. 100, no. 1991, pp. 148–157.

[10] D. N. Johnston and J. E. Drew, “Measurement of positive displacement pump flow ripple and impedance,” *Proceedings of the Institution of Mechanical Engineers, Part I: Journal of Systems and Control Engineering*, vol. 210, no. 1. pp. 65–74, 1996.

[11] I. Standard, “ISO 10767-1 Hydraulic Fluid Power - Determination of Pressure Ripple Levels Generated in Systems and Components Part 1: Precision Method for Pumps,” vol. 1996, 1996.

[12] X. Zhang, J. Cho, S. S. Nair, and N. D. Hanring, “Damping on the swash plate of an axial-piston pump,” *Proceedings of the 2000 American Control Conference*, vol. 5, no. 96. Chicago, Illinois, pp. 3590–3594 vol.5, 2000.

[13] W. F. Breig *et al.*, “A Practical Method to Predict NVH in an Automotive Hydraulic System,” in *SAE 2005 World Congress & Exhibition*, 2005.

[14] S. Wang, H. Sakura, and A. Kasarekar, “Numerical modelling and analysis of external gear pumps by applying generalized control volumes,” *Math. Comput. Model. Dyn. Syst.*, vol. 17, no. 5, pp. 501–513, 2011.

[15] A. Palmen, “Noise reduction of an axial piston pump by means of structural modification,” *4th Int. Fluid Power Conf. - IFK 2004*, vol. 48, no. 4, pp. 121–132, 2004.

[16] A. Bonanno and F. Pedrielli, “A Study on the Structureborne Noise of Hydraulic Gear Pumps,” *Proc. JFPS Int. Symp. Fluid Power*, no. 7–3, pp. 641–646, 2008.

[17] T. Kim and M. Ivantysynova, “Active Vibration/Noise Control of Axial Piston Machine Using Swash Plate Control,” in *ASME/BATH 2017 Symposium on Fluid Power and Motion Control*, 2017, p. Olems, L. (2000) ‘Investigations of the temperatur.

[18] J. Cho, X. Zhang, N. D. Manring, and S. S. Nair, “Dynamic Modelling and Parametric Studies of an Indexing Valve Plate Pump,” *Int. J. Fluid Power*, vol. 3, no. 3, pp. 37–48, Jan. 2002.

[19] M. Ivantysynova, C. Huang, and S.-K. Christiansen, “Computer Aided Valve Plate Design - An Effective Way to Reduce Noise,” *SAE Tech. Pap.*, 2004.

[20] R. Klop and M. Ivantysynova, “Validation of a Coupled Pump-Motor-Line Model to Predict Noise Sources of Hydrostatic Transmissions,” *Proc. 6th FPNI PhD Symp.*, p. Olems, L. (2000) ‘Investigations of the temperatur, 2010.

[21] G. Kumar Seeniraj, M. Zhao, and M. Ivantysynova, “Effect of combining precompression grooves, PCFV And DCFV on pump noise generation,” *Int. J. Fluid Power*, vol. 12, no. 3, p. Olems, L. (2000) ‘Investigations of the temperatur, 2011.

[22] R. Klop, K. Williams, D. Dyminski, and M. Ivantysynova, “A Simulation Study to Reduce Noise of Compact Power-Split-Drive Transmissions,” *Proc. 20th Power Transm. Motion Control Symp. (PTMC 2007)*, p. Olems, L. (2000) ‘Investigations of the temperatur, 2007.

[23] R. Klop and M. Ivantysynova, “Influence of Line Length Concerning Noise Source Generation in Hydrostatic Transmissions,” no. 1986, p. Olems, L. (2000) ‘Investigations of the temperatur, 2008.

[24] G. Kumar Seeniraj and M. Ivantysynova, “A multi-parameter multi-objective approach to reduce pump noise generation,” *Int. J. Fluid Power*, vol. 12, no. 1, p. Olems, L. (2000) ‘Investigations of the temperatur, 2011.

[25] R. Klop and M. Ivantysynova, “Investigation of noise sources on a series hybrid transmission,” *Int. J. Fluid Power*, vol. 12, no. 3, p. Olems, L. (2000) ‘Investigations of the temperatur, 2011.

[26] P. K. Kalbfleisch, “Computational Valve Plate Design,” 2015.

[27] T. Yamazaki, Ã and E. Kojima, “Prediction of sound power radiated from oil hydraulic pump using FEM and BEM,” vol. 2, pp. 103–105, 2003.

[28] T. R. Milind, S. R. Sonawane, A. Sarker, M. A. Beyer, and H. Wang, “Noise Prediction of Axial Piston Pumps,” in *Proceedings of the 37th International & 4th National Conference on Fluid Mechanics and Fluid Power FMFP2010*, 2010, no. December.

[29] T. Opperwall and A. Vacca, “A combined FEM/BEM model and experimental investigation into the effects of fluid-borne noise sources on the air-borne noise generated by hydraulic pumps and motors,” *Proc. Inst. Mech. Eng. Part C J. Mech. Eng. Sci.*, vol. 228, no. 3, p. Olems, L. (2000) ‘Investigations of the temperatur, 2014.

[30] C. Schleihs, H. Murrenhoff, and F. P. Drives, “Modal Analysis Simulation and Validation of a Hydraulic Motor,” in *JFPS International Symposium*, 2014, pp. 582–589.

[31] C. Schleihs and H. Murrenhoff, “Acoustical Simulation of a Hydraulic Swash Plate Motor,” in *ASME/BATH 2015 Symposium on Fluid Power and Motion Control*, 2015, p. 9.

[32] T. R. Milind and M. Mitra, “Boundary Element Modeling of the Acoustic Radiation of an Axial Piston Pump : Numerical Implementation,” in *International Congress on Computational Mechanics and Simulation*, 2016, pp. 1–10.

[33] M. Mitra and T. R. Milind, “Numerical Rigid and Flexible Multibody Dynamic Modeling of an Axial Piston Pump : Validation , Comparison and Parametric Studies,” in *International Congress on Computational Mechanics and Simulation*, 2016, pp. 1–15.

[34] T. R. Milind and M. Mitra, “Numerical Modeling of the Structural Acoustic Radiation and Sound Pressure Fields of an Axial Piston,” in *International Congress on Computational Mechanics and Simulation*, 2016, no. 2003.

[35] I. Standard, “ISO 4409:2007 Hydraulic Fluid Power: Positive-Displacement Pumps, Motors and Integral Transmissions: Methods of Testing and Presenting Basic Steady-State Performance.” 2007.

[36] P. Kalbfleisch, T. Kim, and M. Ivantysynova, “Robotic Arm for Automatic Sound Intensity Measurements,” in *BATH/ASME 2016 Symposium on Fluid Power and Motion Control*, 2016.

[37] I. Standard, “ISO 16902-1 Hydraulic Fluid Power — Test Code for the Determination of Sound Power Levels Using Sound Intensity Techniques: Engineering Method — Part 1: Pumps,” *Program*, vol. 2003, 2011.

[38] I. Standard, “ISO 3745:2012: Acoustics -- Determination of Sound Power Levels and Sound Energy Levels of Noise Sources Using Sound Pressure -- Precision Methods for Anechoic Rooms and Hemi-Anechoic Rooms,” 2012.

[39] I. Standard, “ISO 4412-1:1991 Hydraulic fluid power -- Test code for determination of airborne noise levels -- Part 1: Pumps.” p. 20, 1991.

[40] H. André, F. Girardin, A. Bourdon, J. Antoni, and D. Rémond, “Precision of the IAS monitoring system based on the elapsed time method in the spectral domain,” *Mech. Syst. Signal Process.*, vol. 44, no. 1–2, pp. 14–30, 2014.

[41] S. Horn, “Investigation of the Shaft Speed Fluctuation Effect on Steady State Vibro-Acoustic Measurements in Axial Piston Pump,” Technische Universitat Dresden, 2018.

[42] E. Bechhoefer and M. Kingsley, “A review of time synchronous average algorithms,” *Annu. Conf. Progn. Heal. Manag. Soc.*, pp. 1–10, 2009.

[43] P. D. McFadden, “Interpolation techniques for time domain averaging of gear vibration,” *Mech. Syst. Signal Process.*, vol. 3, no. 1, pp. 87–97, 1989.

[44] J. Antoni, “Cyclostationarity by Examples,” *Mech. Syst. Signal Process.*, vol. 23, no. 4, pp. 987–1036, 2009.

[45] S. Braun, “The synchronous (time domain) average revisited,” *Mech. Syst. Signal Process.*, vol. 25, no. 4, pp. 1087–1102, 2011.

[46] M. R. Bai, J.-G. Ih, and J. Benesty, *Acoustic Array Systems: Theory, Implementation, and Application*. Singapore: John Wiley & Sons Singapore Pte. Ltd., 2013.

[47] Z. Wang and S. F. Wu, “Helmholtz equation–least-squares method for reconstructing the acoustic pressure field,” *J. Acoust. Soc. Am.*, vol. 102, no. 4, pp. 2020–2032, 1997.

[48] S. F. Wu, H. Lu, and M. S. Bajwa, “Reconstruction of transient acoustic radiation from a sphere,” *J. Acoust. Soc. Am.*, vol. 117, no. 4, pp. 2065–2077, 2005.

[49] B. Rafaely, *Fundamentals of Spherical Array Processing*, vol. 8. Berlin, Heidelberg: Springer Berlin Heidelberg, 2015.

[50] E. G. Williams, *Fourier Acoustics: Sound Radiation and Nearfield Acoustical Holography*. Washington. D.C.: Academic Press, 1999.

[51] I. Standard, “ISO 3745:2012: Acoustics -- Determination of Sound Power Levels and Sound Energy Levels of Noise Sources Using Sound Pressure -- Precision Methods for Anechoic Rooms and Hemi-Anechoic Rooms,” 2012.

[52] L. E. Kinsler, A. R. Frey, A. B. Coppens, and J. V Sanders, *Fundamentals of acoustics*, 4th ed., vol. 1. Wiley, 1999.

POWER DENSITY INCREASE IN AXIAL PISTON PUMPS BY USE OF NUMERICAL DESIGN OF EXPERIMENTS

Franck Maurice[1,2], Louis-Claude Porel[1], François Porel[1], Eric Noppe[2], Benoit Eynard[2], Zohra-Cherfi Boulanger[2]
([1]) HYDRO LEDUC
Allée René Leduc, Azérailles, France

([2]) Université de Technologie de Compiègne,
Roberval FRE CNRS 2012, Compiègne, France,
franck.maurice@utc.fr

ABSTRACT

This paper deals with the increase in power density of an axial piston pump using numerical Design of Experiments (DoE). Piston pumps are an important source of fluid power in hydraulic systems. The strength of these technologies, whether radial, bent axis, or axial, relies on their high power density. Increasing the overall efficiency and making products reliable in terms of lifetime for high-pressure uses are the main concern of hydraulic components manufacturers. Our work focuses on a HYDRO LEDUC pump type “TXV indexable”. An optimisation strategy using 1D and 3D simulations relying on Design of Experiments will be described. The pump is characterised on a test rig to get a set of experimental data. A numerical model of the pump is then built on the Amesim® software and represents a virtual test rig. To improve the power density of the pump, the Design of Experiments methodology is applied to the valve plate, with the aim of finding a satisfying geometry which allows to meet the desired fatigue life requirements as well. Using response surface optimisation methodology, a new optimal geometry is implemented into the Amesim® model to validate the gain in power density of the pump. From the results of the simulations performed on the Amesim ® virtual test rig, the new design of the valve plate is validated. The power density of the pump equipped with the new valve plate has increased by 7%.

KEYWORDS: Axial piston pump, swashplate, power density, optimization, design of experiments, numerical simulation, AMESIM®, ANSYS®.

1. INTRODUCTION

Fluid power plays a fundamental role in all mechanical systems that require high mass power. Its scope extends to many areas such as the transport of commodities and people, machine tools, agricultural and industrial vehicles.

Rising energy prices, environmental constraints and global market demands are forcing hydraulic equipment manufacturers to produce increasingly competitive, efficient and reliable components. The conventional way to optimising a product, consists in performing cycles of experiments/errors, which is costly in terms of time and money and can lead to the optimisation process failure. Piston pumps are widely used for their high power density and high efficiency in power transmissions. Over the last decades, computing capacity has sharply

increased and numerical simulation has become the mainstream way to improving product performances. There are numerous studies dealing with piston pumps, whether it is to describe physical phenomena, optimisation and/or modelling solutions. Knowledge on hydraulic pumps and motors has been detailed and mathematically formulated by J. Ivantysyn and M. Ivantysynova [1]. N. Manring [2] focused more particularly on axial piston pumps and gave a complete mathematical analysis to design each component and control device. Many studies deal with mathematical descriptions of physical phenomena that occur into axial piston pumps. For example, Zeiger and Akers [3], Schoenau, Burton and Kavanagh [4] and Lin [5] studied the torque acting on the swashplate and gave a comprehensive mathematical model to estimate the mean torque for steady state conditions. Bergada, Ganesh Kumar and Watton [6] gave a complete analysis of flow losses and the resulting flow pressure dynamics in a piston pump. They also analysed the pressure, the flow and the torque between the barrel and port plate in an axial piston pump [7]. A significant number of studies dedicated to implementing mathematical models describing piston pumps behaviour can be found in a rich and abundant literature. All of these studies enable to build models on in-house or commercial software environment. Piston pumps can be modelled using 1D simulation or 3D CFD simulation based on finite volume. Research is carried out at Purdue University, where a software fully dedicated to simulating piston pumps (CASPAR) has been developed. CASPAR is a 3D CFD piston pumps simulation tool that takes into account dynamic and thermo-elastic effects on fluid [8]. Numerous papers stem from CASPAR, Schenk and Ivantysynova worked out a transient thermo-elasto-hydrodynamic lubrication model for the slipper and swashplate [9]. Ivantysynova, Huang and Christiansen presented a computer based design method for valve plate design using CASPAR to reduce noise [10]. Other softwares dedicated to pump simulation are also used for pump modelling and optimisation. Pumplinx® is a commercial 3D CFD software code developed by Simerics Inc that contains different templates for a wide range of pumps, motors and valves. Ding, Visser, Jiang and Furmanczyk demonstrated and validated Pumplinx® performance and cavitation simulation results for different pump technologies such as centrifugal pump, gérotor and piston pumps [11]. Frosina, Marinaro, Senatore and Pavanetto studied different valve plate designs of an axial piston pump through Pumplinx® and found a valve-plate geometry that decreases by 40% the flow ripple using pre-compression filter volume (PCFV) [12]. Another example of work led on Pumplinx® is the study of Weber and Kunkis, where the authors studied the speed limit of an axial piston pump. Cavitation phenomenon simulated fitted with experimental measurements. According to the CFD simulation results, they proposed a new inlet pump design that would increase the speed limit [13]. 3D CFD model enables to model pumps behaviour by taking into account complex physical phenomena such as fluid thermo-elastic and solid deformation effects. Despite the accuracy of the results given by 3D CFD modelling, optimisation process through 3D CFD simulation can yield large computing times. That is why 1D modelling is sometimes preferred to 3D modelling. Usually, lumped parameter approach is used for system level, whereas 3D simulation is used for local approach. In lumped parameter approach, each element of the system is represented by an individual discrete component where the performance is based on empirical data or theoretical correlation. Lumped parameter simulation environment is widely used in the industry for designing, modelling and optimising systems. Many studies are based on that approach as can be read in reference [14] where the authors Casoli, Anthony and Ricco presented results from an Amesim® simulation of an excavator hydraulic system. Our work consists in increasing an axial piston pump performances and we have chosen to use numerical simulation to achieve this objective. Given that 3D CFD-simulation is time-consuming, a system approach of the pump in 1D modelling appears more suitable. Numerous papers have shown that 1D modelling presents good correlation between simulations and experiments. Manco, Nervegna, Lettini and Gilardino have developed in-house submodels into the Amesim® environment to simulate the behaviour of an axial piston pump. They showed that the Amesim® model of the pump is in accordance with experimental measurements [15]. Gilardino, Manco and Nervegna [16] made an analysis of the steady state and dynamic behaviour of displacement control of an axial piston pump by building its model into Amesim®. They showed accurate results between Amesim models and experimental results. Bedotti, Pastori, Scolari and Casoli found excellent results in 1D simulation in agreement with experimental data to predict the dynamic response of the swash plate [17]. Corvaglia and Rundo modelled an axial piston pump on Pumplinx® and on Amesim® in order to confront the simulations results [18]. It appeared that Amesim could simulate the pump with different levels of details and catch interactions between the fluid and the dynamics of some components, which is not as easy to simulate with a 3D CFD environment. They concluded

that 3D effects do not play a significant role in the analysis of the operating conditions of the pump. We also identified a trend that consists in coupling 1D approach and 3D approach as part of co-simulations, Roccatello, Manco and Nevegna created a co-simulation process between ADAMS and Amesim to model an axial piston pump [19]. Hence, the use of 1D simulation to simulate the performances of the piston pump is justified. Most research focuses on improving one aspect at a time, for example reducing noise emission [12]. In our investigations, we have taken a system approach and achieved an effective virtual test rig. The work presented in this paper aims to raise the power density of the pump by improving the design of the valve plate. Our contribution is to implement an optimization methodology relying on multi-response design of experiments using, jointly, lumped parameter fluid modelling and 3D fatigue analysis applied to an axial piston pump.

The power density of the pump can be raised by increasing its speed limit. Indeed, from a certain rotational speed, cavitation occurs and the pump is no longer able to maintain its flow rate. At this moment, the real flow rate curve gets off the theoretical flow rate curve. The theoretical flow rate of a pump is given by the rotational speed times the pump displacement.

$$Q = \frac{N \times Dis}{1000} \tag{1}$$

In equation 1, Q (l/min) is the theoretical flow rate of the pump, Dis (cm^3/rev) is the pump displacement and N (rpm) is the rotational speed of the pump. The power density (kW/kg) is defined as follows:

$$P_M = \frac{\Delta P \times Q}{600 \times M} = \frac{\Delta P \times N \times Dis}{600000 \times M} \tag{2}$$

ΔP (bar) is the pressure difference between the inlet and outlet ports of the pump and M (kg) is its mass.

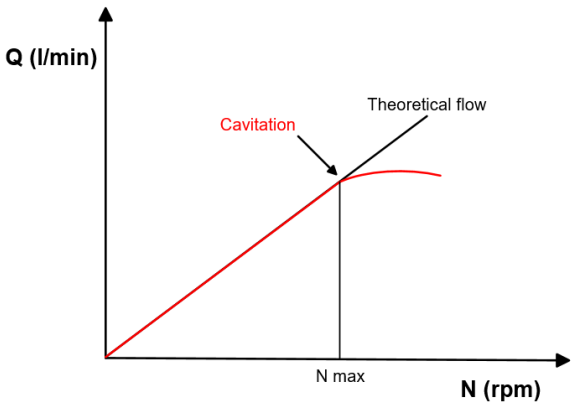

Figure 1. Curve of the flow rate as a function of the pump's rotational speed

Thus, for a given pressure, the maximal rotational speed of the pump limits its power density. Figure 1 shows an example of a characteristic flow rate curve of a pump. Hence, an increase in the power density of the pump is equivalent to a raise in its rotational speed limit, in other words, the goal is to shift the occurrence of cavitation to higher rotational speeds. The presentation of our work is divided into three parts, the first one is dedicated to the pump modelling, the second focuses on valve plate design optimisation using fatigue analysis through design of experiments and the last one aims to validate the new valve plate design.

2. AXIAL PISTON PUMP MODELLING

2.1. Operation of an axial piston pump

A shaft drives the barrel in a rotational motion. The pistons move into the chambers of the barrel and the swash plate angle α induces the reciprocating motion of the pistons. The barrel is held against the valve plate by the

force of the compression spring. The pistons' slippers slide on the swash plate and are maintained against it by the slipper retainer. During one half-shaft rotation, a piston moves from the lower dead point to the upper dead point. The hydraulic fluid is admitted into the piston's chamber through the suction kidney of the valve plate. During the second half-shaft rotation, the piston moves from the upper dead point to the lower dead point. The hydraulic fluid is expelled from the piston's chamber through the discharge kidney of the valve plate. In the case of a variable displacement pump, a displacement control device supplies the displacement control cylinder that makes the angle of the swash plate change.

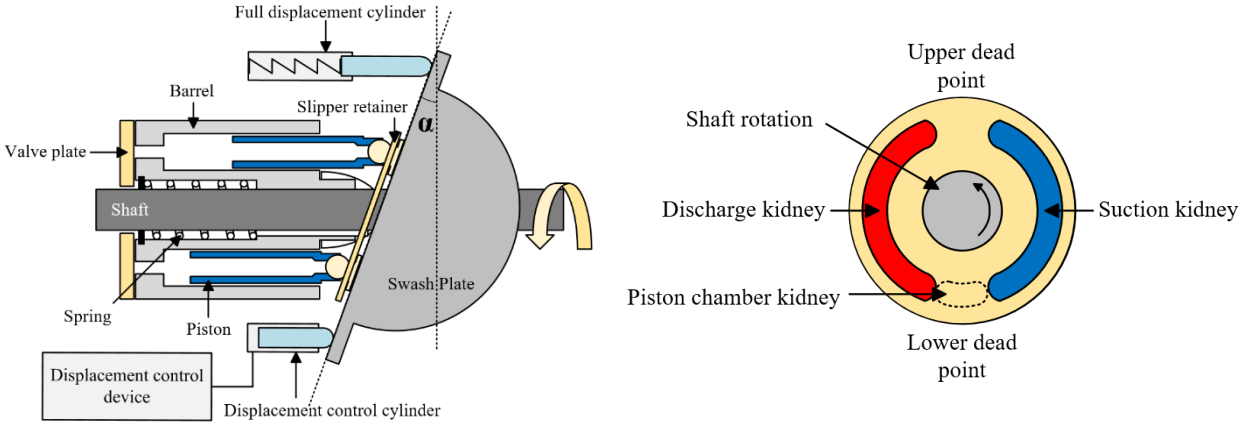

Figure 2. Axial piston pump and valve plate diagrams

In order to build the axial piston pump model as part of system approach, we have made a set of experiments to characterize the pump's performances. The data obtained from test rig measurements will be used to compare experimental and simulation results. They will be also used to fix several parameters to fit the 1D model with experimental values.

2.2. Characterization of the pump on the test rig

The considered pump is designed for open loop circuit. To characterise pump performances, manufacturers perform measurements of the flow rate (as a function of the rotational speed) that gives the speed limit of the pump. They also measure the flow rate (as a function of the discharge pressure) that gives the curve of the volumetric efficiency of the pump. We made two sets of experiments to characterise the pump's performances;

- Flow rate as a function of the rotational speed and suction pressure,
- Flow rate in as a function of the discharge pressure and the rotational speed

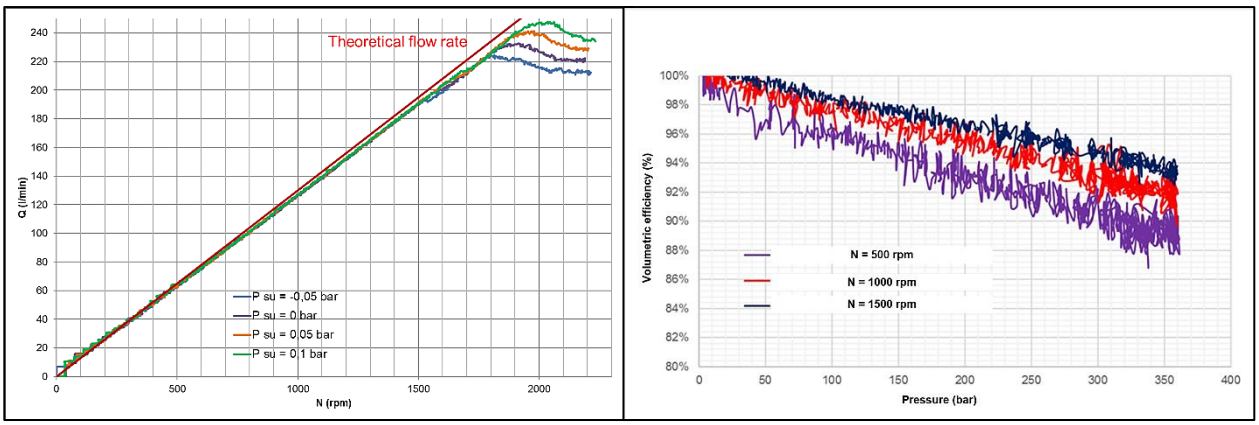

Figure 3. Example of flow rate as a function of the rotational speed and suction pressure (left) and flow rate as a function of the discharge pressure and the rotational speed (right)

From the curves of the flow rate in as a function of the rotational speed, it has been seen that the suction pressure imposes a rotational speed limit to the pump. The lower is the suction pressure, the earlier pump cavitation occurs. From the curves of the flow rate as a function of the discharge pressure, it has been noticed that the volumetric efficiency decreases with the discharge pressure. When the rotational speed rises, the volumetric efficiency of the pump increases. Thanks to this set of experimental data, it will be possible to confront and fit the Amesim® model of the pump with the measurements obtained on the test rig.

2.3. Mathematical model of the pump

2.3.1. Basic equations

The volumetric efficiency is given by the ratio between real pump flow rate and theoretical pump flow rate.

$$\eta_V = \frac{Q_R}{Q_{Th}} = \frac{Q_{Th} - Q_L}{Q_{Th}} \tag{3}$$

Where Q_{Th} corresponds to the theoretical flow rate and Q_R is the real flow rate. Q_R is the theoretical flow rate minus all leakages Q_L. In an axial piston pump, leakages are due to the discharge pressure and are located as follows:

- Leakages between the slippers and the swashplate
- Leakage between the valve plate and the barrel
- Leakages between the pistons and their bores
- Leakages into the displacement control device for a variable displacement pump.

The mechanical efficiency is given by the ratio between the theoretical torque and the real torque (also called the absorbed torque).

$$\eta_M = \frac{C_{Th}}{C_R} = \frac{C_{Th}}{C_{Th} + C_{fr}} \tag{4}$$

Where C_R is the real torque, C_{Th} is the theoretical torque and C_{fr} is the friction torque due to the friction forces acting between the different moving parts of the pump. We also define the overall efficiency of the pump as being equal to the volumetric efficiency multiplied by the mechanical efficiency.

$$\eta_{overall} = \eta_V \times \eta_M \tag{5}$$

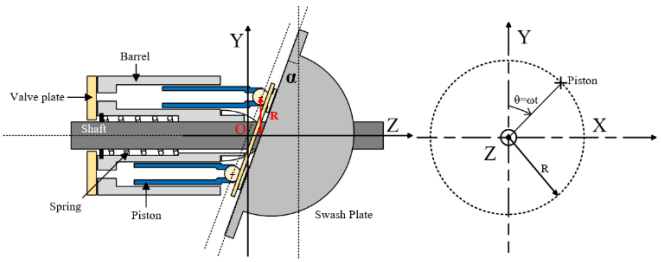

Figure 4. Schematic of an axial piston pump to describe the kinematics of the piston

- Piston's displacement is given by:

$$x(t) = -R_p \times \epsilon_{Dis} \times \tan(\alpha) \times (1 - \cos(\omega t)) \tag{6}$$

Rp is the pitch radius of the pistons, α is the angle of inclination of the swashplate and ω is the rotational speed of the pump. In function of the operating conditions of the pump (rotational speed, displacement, discharge pressure), the point of action of the pistons resultant forces moves on the swashplate. That involves that the swashplate can oscillate and the angle of inclination is not constant [20]. We introduce ϵ_{Dis} which represents the fraction of displacement, this latter depends on the operating conditions. To simplify the model, we set this ratio equal to one. From the Eq. (6), the velocity and the acceleration of the piston can be derived as follows.

$$v(t) = \frac{dx(t)}{dt} = -\omega R_p \times \epsilon_{Dis} \times \tan(\alpha) \times \sin(\omega t) \tag{7}$$

$$a(t) = \frac{dv(t)}{dt} = -\omega^2 R_p \times \epsilon_{Dis} \times \tan(\alpha) \times \cos(\omega t) \tag{8}$$

2.3.2. Amesim® implementation

A mathematical model of the pump is already implemented into the Amesim® environment [21]. This approach neglects tribological aspects, and the gap heights between different moving parts of the pump are considered constant. To match the real behaviour of the pump as measured experimentally, the mathematical model of the pump has to be extended. Indeed, that model does not take into consideration leakage between the barrel and the valve plate, and between the swashplate and the slippers. We also extended the definition of the fluid in order to take into account the variation of fluid viscosity depending on the simultaneous variation of pressure and temperature. To consider the effect of air imprisoned into the fluid and of the pressure on the isothermal bulk modulus, its expression has been changed.

- Leakage between the piston and its bore [21]:

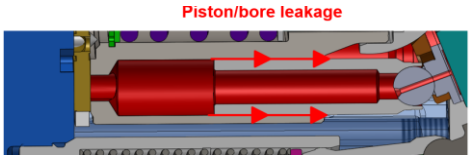

$$Q_{PB} = -\frac{\Delta P}{12\mu l_c} r_c^3 \pi d_p \left[1 + \frac{3}{2}\left(\frac{\epsilon}{r_c}\right)^2\right] + \frac{v^+ + v^-}{2} r_c \pi d_p \tag{9}$$

The expression of the leakage between the piston and its bore, given by Eq. (8), is a combination of the Poiseuille flow due to pressure gradient and the Couette flow due to the movement of the piston. Where ΔP is the pressure variation between the suction port and the discharge port of the pump, μ is the dynamic viscosity of the fluid, r_c is the radial clearance between the piston and its bore, d_p and l_c are respectively the diameter and the wet length of the piston, ϵ is the eccentricity between the piston's axis and its bore's axis and, v^+ and v^- are the relative velocities between the piston and its bore.

- Leakage between the barrel and the valve plate [2], [15]

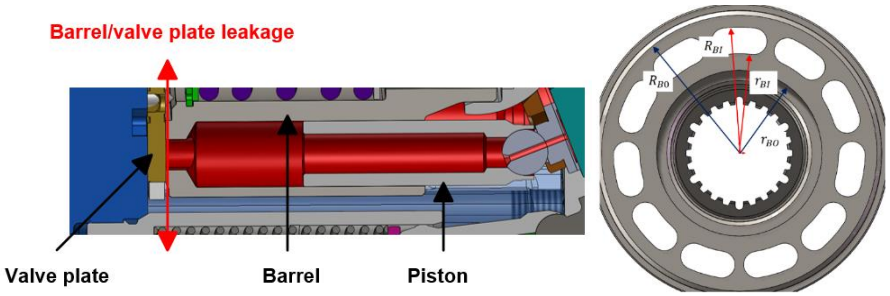

$$Q_{BV} = \frac{\pi}{6\mu} \times \frac{\Delta P}{2} \times \left(\frac{1}{ln\left(\frac{R_{BO}}{r_{BO}}\right)} + \frac{1}{ln\left(\frac{R_{BI}}{r_{BI}}\right)}\right) \times h^3 \tag{10}$$

Between the barrel and the valve plate, leakage occurs in the hydrostatic balance area. Equation. (10) comes from the Reynolds equation for radial stationary flow. R_{BO}, r_{BO}, R_{BI} and r_{BI} are the radii of the hydrostatic balance between the barrel and the valve plate, h represents the height of the fluid film. Because of the complexity to describe the dynamic behavior of the fluid film, according to literature, the latter is supposed to remain constant, stationary, and equal to 10 μm.

- Leakage between the slipper and the swashplate

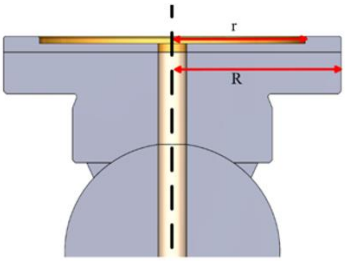

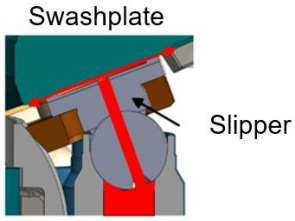

Under the same hypothesis as for the leakage between the barrel and the valve plate, the leakage between the slipper and the swashplate is given by [2], [15]:

$$Q_{SS} = \frac{\pi}{6\mu} \times \frac{P_D h^3}{ln\left(\frac{R}{r}\right)} \tag{11}$$

For the same reasons underlined for the leakage between the barrel and the valve plate, the height of the film fluid film between the slipper footings and the swashplate is supposed to remain constant, stationary and equal to 10 µm.

- Isothermal bulk modulus [2]

The fluid used for the experimental characterization of the pump is a ISO VG 32 type hydraulic fluid. The air imprisoned within the hydraulic fluid is not equal to zero. Therefore, the effective isothermal bulk modulus has been considered. The theoretical expression of the latter is defined as follows:

$$\beta_e = \beta_0 \left[1 + c \times \left(1 - \frac{2k_1}{\gamma}\right)\right] + k_1 \left[1 + c\left(1 - \frac{k_1}{\gamma}\right)\right] \times P - \left(\frac{\beta_0^2 c}{\gamma}\right) \times \frac{1}{P} \tag{12}$$

In Eq. (12), β_e is the effective isothermal bulk modulus, c is the volumetric ratio of the air imprisoned within the fluid, β_0 is the liquid's nominal bulk modulus when pressure is equal to zero, $k_1$is an empirical coefficient that can be set to 25 [2], γ is the ratio of specific heats and P is the pressure. According to literature [6], [2] and experimental measures, β_0 is equal to 10000 bar and c has been adjusted to 1%.

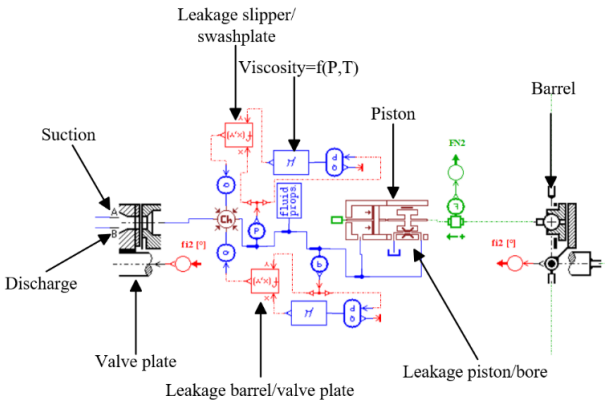

Figure 5. Extended model of the piston in Amesim

- Valve plate geometry

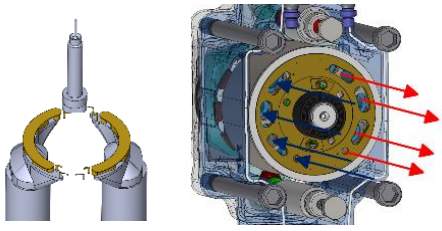

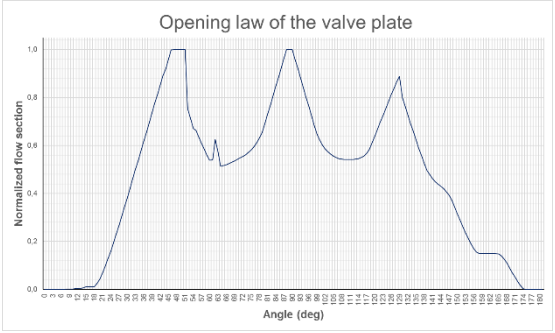

Figure 6 Extracted fluid volume of the pump and opening section law of the valve plate

To represent the geometry of the valve plate, the fluid volume of the pump has been extracted. From this fluid volume file, by moving the piston degree by degree, the opening law of the valve plate has been defined. The opening section related to the barrel kidney through the valve plate is measured for a full barrel rotation. This opening law is integrated into the Amesim valve plate submodel.

2.4. Results and comparison

We have confronted the results of the simulation with those from the experiments. To validate the model, we targeted an error lower than to 5% (cavitation and efficiency). It appears that the Amesim model fits well with the behaviour of the pump observed on the test rig. We obtained good results to predict cavitation and the volumetric efficiency with an error lower than 5%. The Amesim model of the pump has been extended to the others pumps of the same range. We have similarly observed good correlations between the experiments and

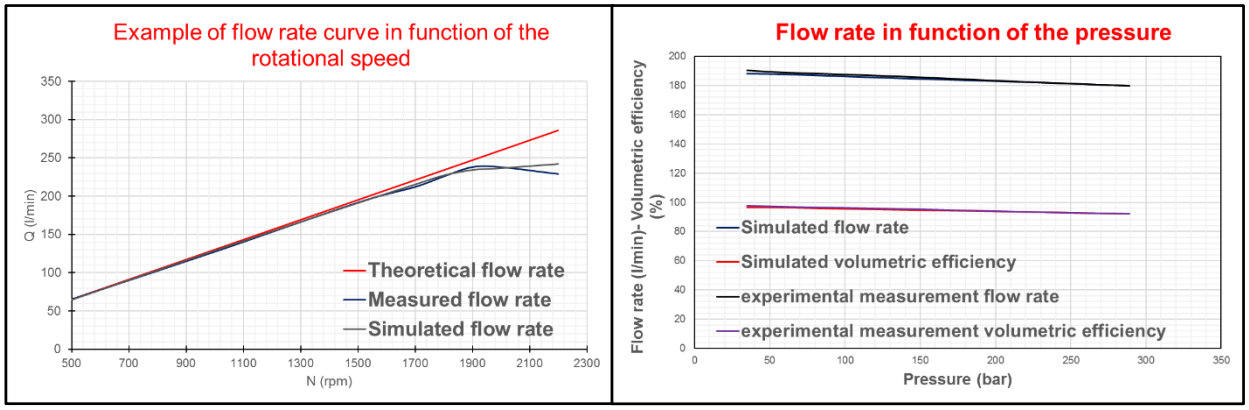

Figure 7 Examples of experimental and simulation results confrontation

the simulation. Figure 7 gives two examples of the experiments and simulations curves for the flow rate in as a function of the rotational speed and the flow rate as a function of the discharge pressure.

We have tested and validated the pump's mathematical model, and it can be considered that we have modelled an effective virtual test rig. From this point, we can lead investigations on the design of the valve plate to increase the power density of the pump and validate it on the Amesim® virtual test rig. In the third part of this paper, we will present the design optimisation of the valve plate.

3. OPTIMISATION OF THE VALVE PLATE DESIGN

3.1. Optimisation process

Many studies dealing with design optimisation relying on numerical simulation can be found. For example, Castorani, Landi and Germani studied the optimal configuration of an energy recovery ventilator through virtual prototyping using design of experiments [22]. They performed response surface methodology (RSM) from a centred composite design of experiments to find the optimal configuration. Response surface methodology is widely used to solve optimisation problems and design exploration. Design of experiments used for response surface methodology are second order designs. They allow to establish second order mathematical models, among these designs of experiments, we have quoted composite, Doehlert , Box-Behnken and uniform design of experiments [23]. Cho used Taguchi orthogonal tables to study the optimal design of the valve plate to minimise the maximum stress [24]. He defined the best parameter configurations by leading an analysis of variance (ANOVA). To improve the power density of the pump, we perform response surface methodology through centred composite design of experiments. To achieve this aim, we target the following objectives:

- Maximize the total section of the suction port of the valve plate (see *Figure 8*),

- Maximize the section of the central kidney of the valve plate (see *Figure 8*),
- Guarantee the same lifetime as the current valve plate,
- Maintain the maximal stress (Von Mises) below the elastic limit of the materials.

The optimization process of the valve plate we performed is shown on *Figure 8*.

To perform the stress and the fatigue calculations as well as the optimisation process, we use ANSYS® static analysis and optimisation modules.

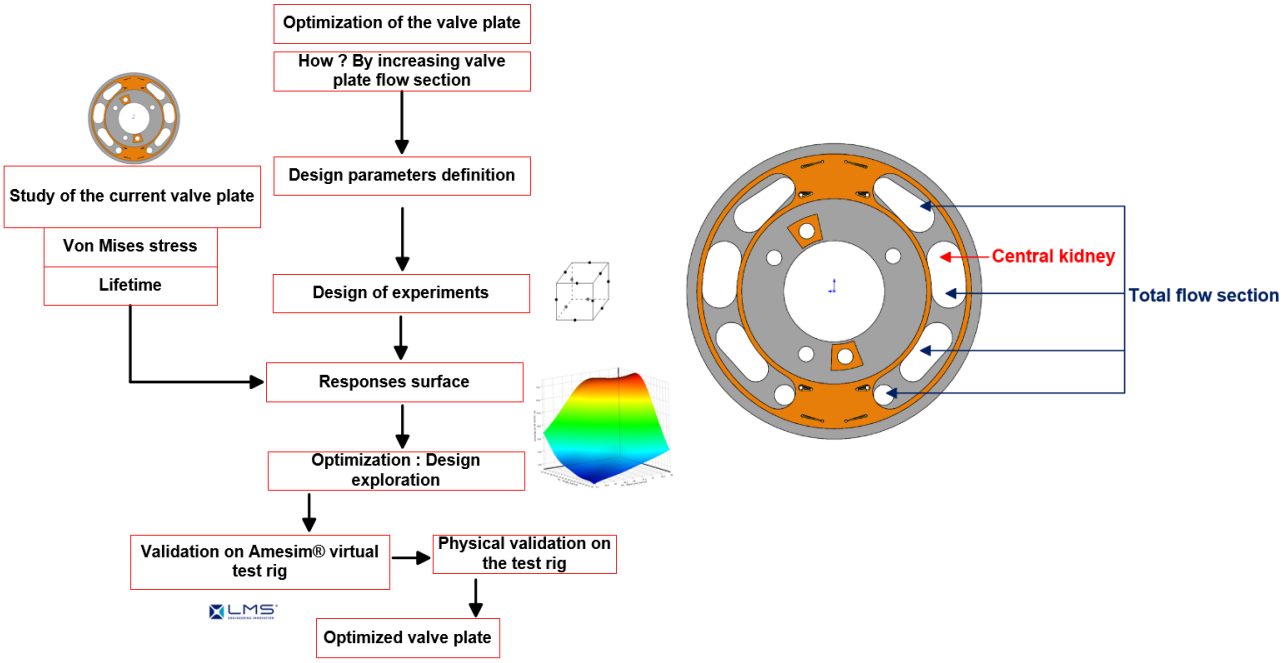

Figure 8. Optimisation process of the valve plate

3.2. Study of the current valve plate

In the optimisation process given on *Figure 8*, the first part of the work consists in studying the current valve plate. The objective is to define a lifetime constraint to which the optimised valve plate has to answer. According to experimental fatigue cycles applied in laboratory, the number of cycles is high (higher than 10^4), hence stress life approach is adopted [25]. The stress definition is constant amplitude zero-based loading. The fatigue analysis is led into a comparative approach to fix a lifetime constraint in the design exploration of the new valve plate. That is why, we use standard steel material data and its SN-curve to perform the fatigue analysis. The fatigue strength factor (Kf) is set to one and there is no mean stress theory [25]. The results of the static analysis and the fatigue analysis give a maximal stress equal to 270 Mpa (<elastic limit) and a lifetime equal to 575 hours (see *Figure 9*). Nota, 575 hours is not the absolute lifetime of the current valve plate, but this gives the references values to lead a comparative analysis.

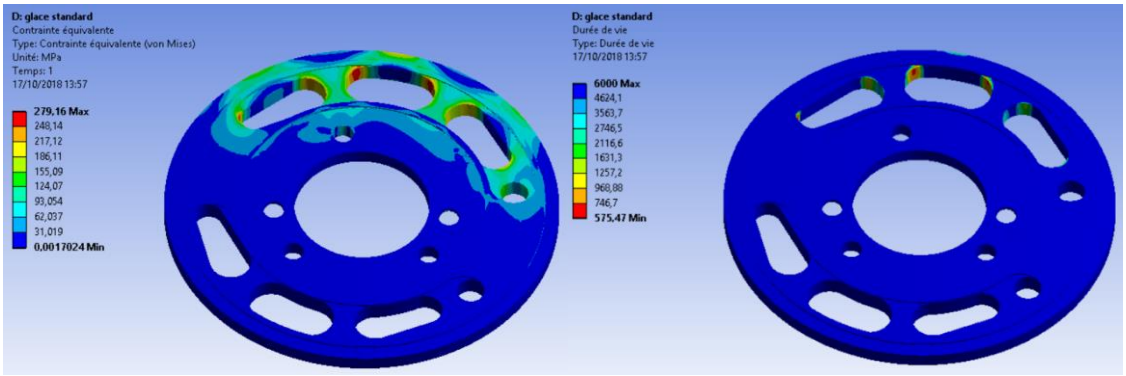

Figure 9. Result of the simulations, equivalent Von Mises stress (on the left) and fatigue lifetime (on the right)

3.3. Design of experiments and responses surface

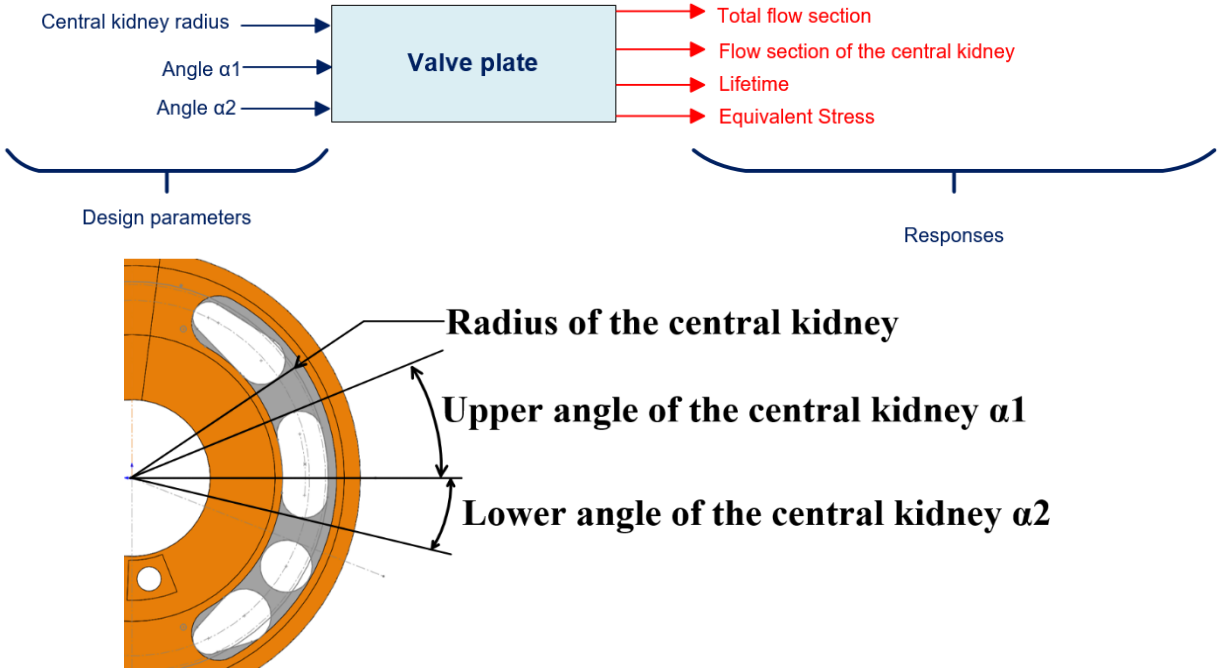

Figure 10. Design of experiment parameters

We studied different types of valve plate. In this paper, we illustrate the optimisation methodology through one example. Parameters and the diagram of the design of experiment are detailed on *Figure 10*. We have defined three design parameters. Each parameter has two modalities and we choose a centred composite design of experiments. The mathematical model of the responses is obtained from the design of experiments by Kriging. This method was chosen because it gave the best correlation between the simulation results and the metamodel. *Figure 11* is an example of response surface and links the lifetime to the radius of the central kidney and the angle α_1.

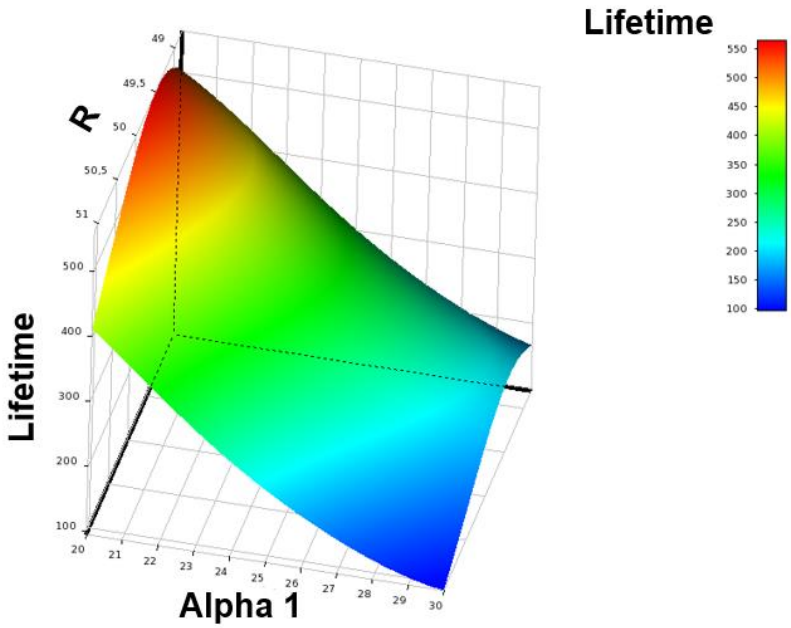

Figure 11. Response surface obtained from kriging method

3.4. Determination of an optimal parameters configuration

Screening method was employed to find the parameter configurations that answer the constraints and the objectives described in part 2.2. As it can be noticed on the Figure 8, we performed a fatigue analysis of the current valve plate. The results of this latter in terms of equivalent stress and lifetime give the mechanical objectives that the new valve plate have to manage. In terms of geometrical objectives, we want to maximise the flow section of the central kidney. We also aim to find the higher values of the angular parameters. Indeed, the central kidney (see Figure 10) corresponds to the area where the velocity of the piston is maximal. What it means that increases the flow section of the central kidney, while maximising the values of α_1 and α_2 allow the piston to better suck the hydraulic fluid from the suction line.

The objectives and constraints of the optimisation study are shown on the Table 1.

		Objectives/Constraint
Parameters	R (mm)	None
	α1 (deg)	Maximise
	α2 (deg)	Maximise
Responses	Flow section of the central kidney (mm^2)	Higher than 280 mm^2
	Lifetime (hours)	Higher or equal to 575 (hours)
	Equivalent Stress (MPa)	Lower or equal to 320 (MPa)

Table 1 Objectives and constraint of the optimization study in function of the parameters and the responses

Applying optimisation on ANSYS®, we found an optimal parameters configuration and results are given in Table 2. The current data of the valve plate are given into brackets.

Parameters	**R (mm)**	**48,78 (51.02)**
	α1 (deg)	**52,45 (35.1)**
	α2 (deg)	**25,35 (16.3)**
Response	**Flow section of the central kidney (mm^2)**	**331,23 (319)**
	Lifetime (hours)	**578 (575)**
	Equivalent Stress (MPa)	**280 (280)**

Table 2 Results

3.5. Validation of the optimised design of the new valve plate

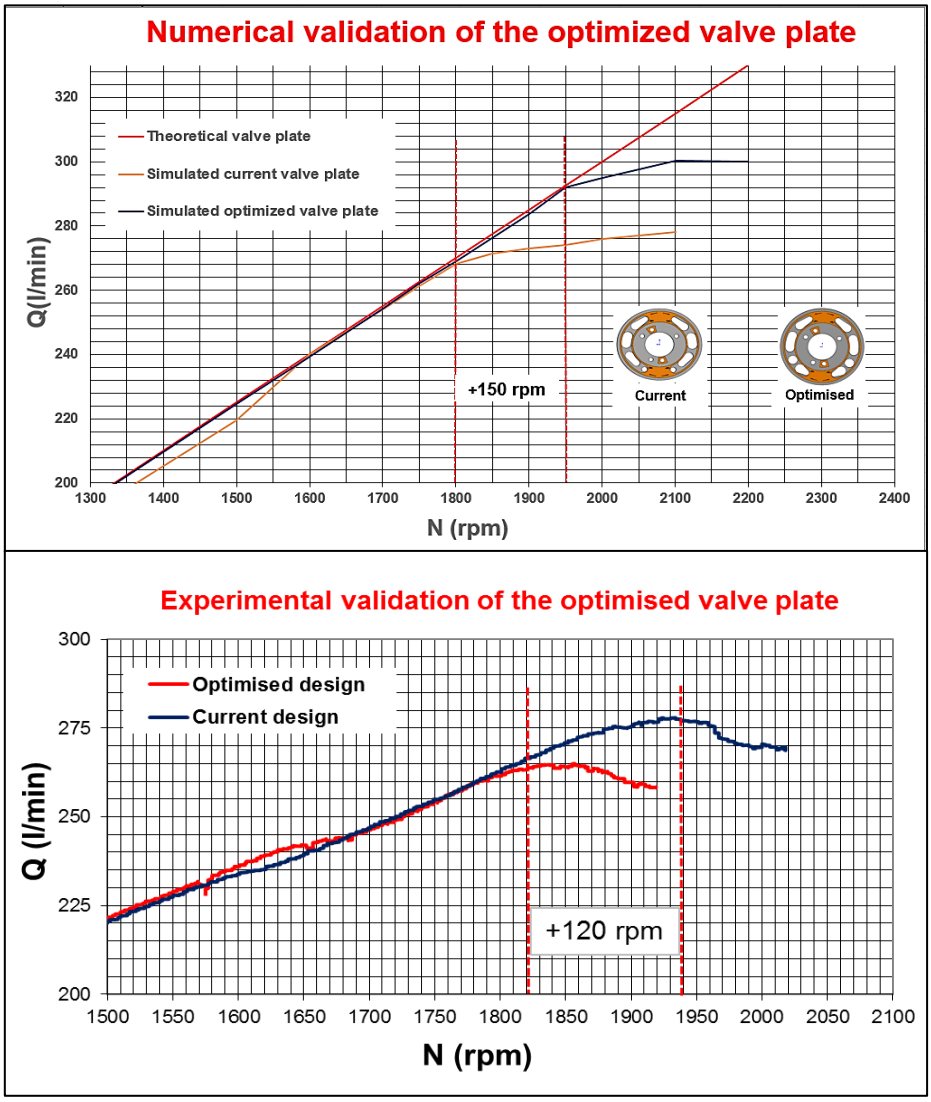

Figure 12. Validation of the optimized valve plate

From these results, the new valve plate geometry was implemented into the Amesim® model. A simulation of the flow rate in function of the rotational speed was carried out to validate the increase in power density. After the validation of the new valve plate design on the Amesim® model of the pump, a physical prototype has been manufactured to validate physically the gain in power density. The hydraulic fluid used is Total Equivis ZS 32 and its temperature was maintained to 30°C, the suction and the discharge pressure were equal to zero bar. The result of the simulation and the experimental test are shown on Figure 12. According to Figure 12, cavitation occurs from a rotational speed equal to 1800 rpm for the current valve plate, 1950 rpm for the optimised valve plate. The error between the optimised valve plate simulation and experimental measure is lower than 1%. The increase in power density of the pump is equal to 7%. The flow rate difference between the optimised valve plate simulation and experimental measure relies on the fact that physical parameters could be adjusted, such as the ratio of air imprisoned into the fluid or the fluid film height between the slippers and swashplate or between the barrel and the valve plate. This difference can also be explained from manufacturing variations. The new valve plate design has been validated by the simulation (virtual test rig) and experimentally. It can be added that modifications of the flow sections of the kidney could affect pressure ripples, volumetric and mechanical efficiency. However, we have considered that the main parameters that have an influence on these performance criteria are the design parameters of the hydrostatic balance, the ideal timing angle design, the precompression and decompression grooves design located in the commutation

areas. We did not perform any modification of these latter, that is why we have considered that modifying cross sections flow into the valve plate suction and discharge kidney does not affect pressure ripples, volumetric and mechanical efficiency. The next step is a fatigue test of the prototype pump equipped of the optimised valve plate. Moreover, to make sure that the new valve plate geometry does not affect the flow/pressure pulsation and noise, we will compare the measures of flow/pressure pulsations and noise of the pump equipped with the current and the optimised valve plate.

4. CONCLUSION

In this paper, we have presented an optimisation strategy relying on numerical modelling and design of experiments to increase the power density of an axial piston pump. A virtual test rig of the pump has been implemented on Amesim® and validated by physical experiments. We have led investigations on the valve plate design to maximise its flow sections according to fatigue constraints through numerical design of experiments on ANSYS®. After the validation of the new valve plate design in terms of increase in power density on the Amesim® virtual test rig, we have manufactured this optimised valve plate. This latter has been validated on the test rig and the power density of the pump has been increased by 7%. In future studies, we will employ the same strategy to continue investigations on the valve plate design to further increase the power density of the pump. Linking 1D modelling and 3D simulation through design of experiments is a strategy we have developed and can be applied to others issues. This latter enables to find best designs, reduce the time and the cost of the optimisation process. In future studies, we will lead the same method applied to the valve plate focusing on two goals, increase the power density and decrease flow/pressure pulsations. The control of the pump will be added to the Amesim® model in order to decrease the power to be supplied for controlling the pump using the same optimisation strategy. We will also enhance the Amesim® model by considering tribological aspects for example to describe better the film fluid behaviour between different moving part of the pump. This enhanced model will allow to focus on hydrostatic balance design, for example between the valve plate and the barrel to increase the volumetric efficiency.

5. NOMENCLATURE

η_V	Volumetric efficiency	μ	Kinematic viscosity (Pa.s)
η_M	Mechanical efficiency	l_c	Wet length of the piston (m)
$\eta_{overall}$	Overall Efficiency	r_c	Radial clearance (m)
Q_R	Real Flow rate (l/min)	d_p	Piston diameter (m)
Q_{Th}	Theoretical flow rate (l/min)	ϵ_{dis}	Fraction of displacement
Q_L	Leakage flow rate (l/min)	$v^+ and\ v^-$	Relative velocities piston/bore (m/s)
Q_{PB}	Piston/bore leakage flow rate (m^3/s)	Q_{BV}	Leakage between the barrel and the valve plate (m^3/s)
N	Rotational speed (rpm)		
P	Pressure (bar)		
C_{Th}	Theoretical torque (N.m)	Q_{SS}	Leakage between the slipper and the swashplate (m^3/s)
C_R	Real torque (N.m)		
C_{fr}	Friction torque (N.m)		
$x(t)$	Displacement of the piston (m)	R_{B0}	Large outer radius of the valve plate-barrel hydrostatic balance (m)
$v(t)$	Velocity of the piston (m/s)		
$a(t)$	Acceleration of the piston (m^2/s)	r_{B0}	Small outer radius of the valve plate-barrel hydrostatic balance (m)
R_p	Pitch radius of the piston (m)	R_{BI}	Large inner radius of the valve plate-barrel hydrostatic balance (m)
α	Angle of inclination of the swashplate (rad)		
ω	Rotational speed (rad/s)		
ϵ	Eccentricity		

r_{BI}	Small inner radius of the valve plate-barrel hydrostatic balance (m)	β_{el}	Simplified effective bulk modulus (bar)
β_e	Effective bulk modulus (bar)	γ	Ratio of specific heats
β_0	Liquide Liquid nominal bulk modulus (bar)	P_d	Pressure discharge (Pa)
		Dis	Displacement (cm^3/r)

References

[1] J. Ivantysyn and M. Ivantysynova, Hydrostatic pumps and motors: principles, design, performance, modelling, analysis, control and testing, New Delhi: India Tech Books internat, 2003.

[2] N. Manring, Fluid Power Pumps and Motors Analysis, Design, and Control, New York: Mc Graw Hill Education, 2013.

[3] G. Zeiger and A. Akers, "Torque on the Swashplate of an Axial Piston Pump," *Journal Of Dynamic Systems, Measurement, and Control,* vol. 107, pp. 220-226, 1985.

[4] G. Schoenau, R. Burton and G. Kavanagh, "Torque on the swasplate of an axial piston pump," *Journal of Dynamic Systems, Measurement and Control,* vol. 112, pp. 122-132.

[5] S. Lin, A. Akers and G. Zeiger, "The effect of Oil Entrapment in an axial Piston Pump," *Journal of Dynamic Systems, Measurement, and Control,* vol. 107, pp. 246-251, 1985.

[6] J. Bergada, S. Kumar and J. Watton, "A complete analysis of axial piston pump leakage and output flow ripples," *Applied Mathematical Modelling ,* no. 32, pp. 1731-1751, 2012.

[7] J. Bergada, J. Watton and S. Kumar, "Pressure, Flow, Force, and Torque Between the Barrel and Port Plate in an Axial Piston Pump," *Journal of Dynamic Systems Measurement and Control ,* vol. 130, pp. 011011-1; 011011-16, 2008.

[8] M. Ivantysynova and U. Wieczorek, "CASPAR a computer-aided design tool for axial piston machines," Bath, 2000.

[9] A. Schenk and M. Ivantysynova, "A transient Thermoelastohydrodynamic lubrication model for the axial slipper/swashplate in axial piston machines," *Journal of Tribology,* vol. 137, pp. 031701 1-10, 2015.

[10] M. Ivantysynova, C. Huang and S.-K. Christiansen, "Computer Aided Valve Plate Design - An effective Way to Reduce Noise," *SAE Commercial Vehicle Engineering Congress and Exhibition,* no. 2004-01-2621, 2004.

[11] H. Ding, F. Visser, Y. Jiang and M. Furmanczyk, "Demonstration and validation of a 3D CFD simulation tool prediction pump performance and cavitation for industrial applications," *Journal of Fluids Engineering,* vol. 133, pp. 011101 1-14, 2011.

[12] E. Frosina, G. Marinaro, A. Senatore and M. Pavanetto, "Effects of PCVF and Pre-compression Groove on the Flow Ripple Reduction in Axial Piston Pumps," *IEEE,* 2018.

[13] J. Weber and M. Kunkis, "Experimental and numérical assessment of an axial piston pump's speed limit," *Fluid Power and Motion Control,* 2016.

[14] P. Casoli, A. Alvin and L. Ricco, "Modeling Simulation and Experimental Verification of an Excavator Hydraulic System-Load Sensing Flow sharing Valve Model," *SAE international,* 2012.

[15] S. Manco, N. Nervegna, A. Lettini and L. Gilardino, "Advances in the simulation of the axial piston pumps," *5th International Symposium on Fluid Power JFPS,* vol. 1, pp. 251-258, 2002.

[16] L. Gilardino, S. Manco, N. Nervegna and F. Viotto, "An experience in simulation : The case of a variable displacement axial piston pump," *ASME Dynamic Systems and Control Conference,* vol. 1, pp. 267-274, 2009.

[17] A. Bedotti, P. Mirko, F. Scolari and P. Casoli, "Dynamic modelling of the swashplate of a hydraulic axial piston pump fo condition monitoring application," *Energy Procedia,* 2018.

[18] A. Corvaglia and M. Rundo, "Comparison of 0D and 3D Hydraulic Models for Axial Piston Pumps," *Energy procedia,* pp. 114-121, 2018.

[19] A. Roccatello, S. Manco and N. Nervegna, "Modelling a variable Displacement Axial Piston Pump in a Multibody Simulation Environment," *Journal of Dynamic Suystems, measurement, and Control,* vol. 129, pp. 456-468, 2007.

[20] L. Ericson, "Swash Plate Oscillations due to Piston Forces in Variable In-line Pumps," *The 9th International Fluid Power Conference,IFK,* 2014.

[21] 2. S. I. S. NV, *AMESIM Demos.*

[22] V. Castorani, D. Landi and M. Germani, “Determination of the optimal configuration of energy recovery ventilator through virtual prototyping and DoE techniques,” *Procedia CIRP ,* vol. 50, pp. 52-57, 2016.

[23] J. Goupy, “Modélisation par les plans d'expériences,” in *Mesures-Analyses Instrumentation et méthodes de mesure*, Techniques de l'Ingénieur, 2016.

[24] I. S. Cho, “A study on optimum design for the valve plate of a swash plate-type oil hydraulic piston pump,” *Journal of Mechanical Science and Technology,* vol. 6, no. 29, pp. 2409-20413, 2015.

[25] ANSYS, The Fatigue Module of ANSYS Mechanical, 2018.

A NOVEL EXERGY EFFICIENT PNEUMATIC VACUUM PUMP

Dr. Olivier Reinertz, Prof. Dr. Katharina Schmitz
RWTH Aachen University, Institute for Fluid Power Drives and Systems (ifas)
Campus Boulevard 30, 52074 Aachen, Germany
Olivier.Reinertz@ifas.rwth-aachen.de

ABSTRACT

The usage of wasted exergy of pneumatic pressure regulators to deliver a sufficient vacuum pressure for adjacent gripping systems carries significant energy and cost saving potentials. Unfortunately, nowadays pneumatic vacuum generators are unable to fulfil the resulting demands. Therefore, a novel suitable pneumatic membrane vacuum generator is introduced. At first, the underlying thermo-dynamical effects during vacuum generation and pressure reduction in pneumatic systems are analytically investigated to highlight the existing optimization potentials. Thereof, the underlying principles of the novel component are deduced, the modelling of the device is described and geometrical parameters are analytically defined. Furthermore, a corresponding energy efficient control algorithm is presented. Finally, the behaviour of the device in typical load cases is assessed by dynamic multi-domain simulation in DSHplus. The results show broad applicability of the device in relevant applications and significant energy saving potentials compared to state of the art products.

KEYWORDS: Vacuum Pump, Membrane, Valve Timing

1. INTRODUCTION

Compressed air is known as an expensive energy source. Therefore, the reduction of air consumption of contemporary pneumatic systems is focused by the machines' manufacturers and operators. One widely used approach is to reduce the inlet pressure of systems or modules as far as possible by integrating pressure regulators. By this, the density of the compressed air and thus air consumption is decreased. Nevertheless, system efficiency stays far below the theoretical optimum by lowering the air pressure and not using the contained decompression exergy. Thus, the development of a device using decompression exergy carries substantial potential for efficiency improvement.

Up to now, there is no component on the market which can recuperate this exergy in order to drive additional features. As the combination of pneumatic drives and vacuum effectors is very common in actual production machines, it is aspired to use the excessive exergy to deliver a sufficient vacuum pressure for adjacent gripping systems. Unfortunately, neither actual ejectors nor other pneumatic vacuum generators are able to work with only small differential pressures and at elevated back pressures. Therefore, a novel vacuum generator for this purpose and its dynamic simulation are presented in this paper.

2. EXERGY ASSESSMENT OF STATE OF THE ART PRESSURE REGULATORS

The design of automation systems requires amongst others the sizing of the included pneumatic components. An exact dimensioning is hindered by the available standard sizes of the components and uncertain external influences, as e.g., fluctuations in supply pressures, friction forces, and process forces. Therefore, pneumatic actuators are commonly oversized. By driving these actuators in open loop control, additional measures for efficiency improvements on the control side are extensive and thus rarely used. Thus, the oversized volumes of the actuator chambers and the dead volumes of the interconnecting hoses are completely pressurized over a working cycle.

When neglecting leakages, such systems' air consumption is proportional to the number of cycles, the size of the pressurized volumes, and the density of the pressurized air. From this very fundamental correlation, some commonly used measures for efficiency improvements of pneumatic systems can be deduced, which have been published in different guidelines, e.g., by EnEffAH-Project consortium [1] and the Bundesamt für Energie BFE [2]:

- Optimize component sizing
- Regularly check for and eliminate leakages
- Lower the system pressure (and thus the density) to the required value

Moreover, already at a realizable pressure reduction of 500 mbar, the usage of an additional pressure regulator for a subsystem is already worthwhile [2]. To assess the impact of such a pressure regulator, two exemplary applications (case A and B) are specified in the following table. The table also includes the required media properties of compressed air for all following calculations.

Table 1. Application examples and compressed air media data

Application examples		**Case A**	**Case B**
Supply pressure	p_0	6 bar	6 bar
Regulated pressure	p_A	5.5 bar	3 bar
Ambient temperature	T_{atm}	293 K	293 K
Compressed air media data			
Density at standard conditions	ρ_S	1.183 kg/m³	
Temperature at standard conditions	T_S	293 K	
Specific gas constant	R	288 J/(kg·K)	
Isentropic coefficient	κ	1.4	
Heat capacity	c_p	1008 J/(kg·K)	

When heat transfer over the component's surface and kinetic and potential energy of the in- and outflow are neglected, the pressure reduction is isothermal for ideal gases. Hence, the exemplary reduction in the pressure regulator from p_0 to p_A yields a decrease in density of 8.33 % in case A and 50 % in case B by ideal gas law. As the flow demand of the system stays constant, supplied air mass and thus exergy demand of the investigated systems is decreased by the same amount. Nevertheless, during throttling in the pressure regulator, exergy is wasted.

The difference in specific exergy between the in- and outflow of the pressure regulator gives a deeper understanding of the occurring throttling losses and thus the usable exergy by an energy harvesting component. According to Krichel [3] and Lucas [4], the flow specific exergy e_a in point a can be described by:

$$e_a = \frac{\dot{E}_a}{\dot{Q}} = c_p \cdot \rho_S \cdot (T_a - T_{atm}) + T_{atm} \cdot \rho_S \cdot \left(R \cdot ln\left(\frac{p_a}{p_{atm}}\right) - c_p \cdot ln\left(\frac{T_a}{T_{atm}}\right)\right) \quad (1)$$

Here, T_a represents the air temperature and p_a its pressure in point a. The ambient conditions are described by the temperature T_{atm} and the pressure p_{atm}. Thus, the change in specific exergy over the pressure regulator $\Delta e_{0\rightarrow A}$ can be written as:

$$\Delta e_{0\to A} = c_p \cdot \rho_S \cdot (T_0 - T_A) + T_{atm} \cdot \rho_S \cdot \left(R \cdot ln\left(\frac{p_0}{p_A}\right) - c_p \cdot ln\left(\frac{T_0}{T_A}\right)\right) \quad (2)$$

With the supply pressure p_0 and the required pressure p_A for the application. The difference in exergy over the pressure regulator is described by an isothermal decompression at ambient temperature. Thus, the exergy difference over the device is given by:

$$\Delta e_{0\to A_{isothermal}} = T_{atm} \cdot \rho_S \cdot R \cdot ln\left(\frac{p_0}{p_A}\right) \quad (3)$$

The resulting values are summarized in the following table 2. Significant amounts of wasted and thus recoverable exergy are present in nowadays pressure regulators.

Table 2. Wasted exergy and air savings for application examples

Application examples		**Case A**	**Case B**
Mass flow reduction		8.33 %	50 %
Change in exergy	$\Delta e_{0\to A_{isothermal}}$	8.686 kJ/m³	69.194 kJ/m³
Wasted exergy at 100 l/min		14.5 W	115.3 W

3. DEDUCTION OF A NOVEL VACUUM GENERATOR PRINCIPLE

As has been shown so far, a huge amount of exergy is wasted in pressure regulators to reduce air consumption of pneumatic systems by lowering the air pressure. Up to now, there is no component on the market recuperating this exergy for driving additional features, as, e.g., a vacuum pump. The challenge is to develop a device, which is able to use small pressure differences at elevated absolute pressures for broad applicability while optimizing its internal efficiency over a broad range of pressures as far as possible.

As the device should be usable at varying supply and regulated pressures with sufficient performance, the device must be tuned to allow maximum efficiency at the lowest relevant input power. This occurs at pressure differences of 500 mbar, the lowest pressure difference for efficient pressure regulator installation [2]. In the scope of this paper, the device is considered to be placed in parallel to a pressure regulator, thus lowering the flow through the regulator without necessity for p_A control. A vacuum reservoir is used to allow for fast evacuation of suction grippers connected to the reservoir by switching valves. The suitability of such configuration for fast and efficient vacuum gripping devices has been shown by Straub and Schaaf [5]. A device enabling multivariable control for efficiency, vacuum pressure and regulated pressure will be focused in future publications.

In the following, a membrane or piston type pressure transformer serves as basis for the vacuum generator development. The impact of the regulated pressure p_A on the driving force should be minimized. Therefore, a symmetric double acting actuator is used to drive the vacuum pump. For symmetry reasons, also a symmetric double acting vacuum pump is used.

The internal efficiency of the drive can be optimized by intelligent valve timing only filling the drive chambers with the required pressure and using decompression energy to the highest possible extent. As the harvesting device should be able to operate at fluctuating pressures, adaptive valve timing for commutation is required. Therefore electromagnetic switching valves and an electronic control unit are used.

Figure 1 shows schematics of possible realizations as piston and membrane devices. The pressure requirements can easily be matched by sizing the displacement volumes of the driving and the pumping unit accordingly. Thus, also at low vacuum pressures, low differential pressures on the drive side can already be sufficient for driving the pump. On the other hand, the drive cross-section should be minimized to avoid high flow requirements of the device and thus to optimize efficiency and component costs.

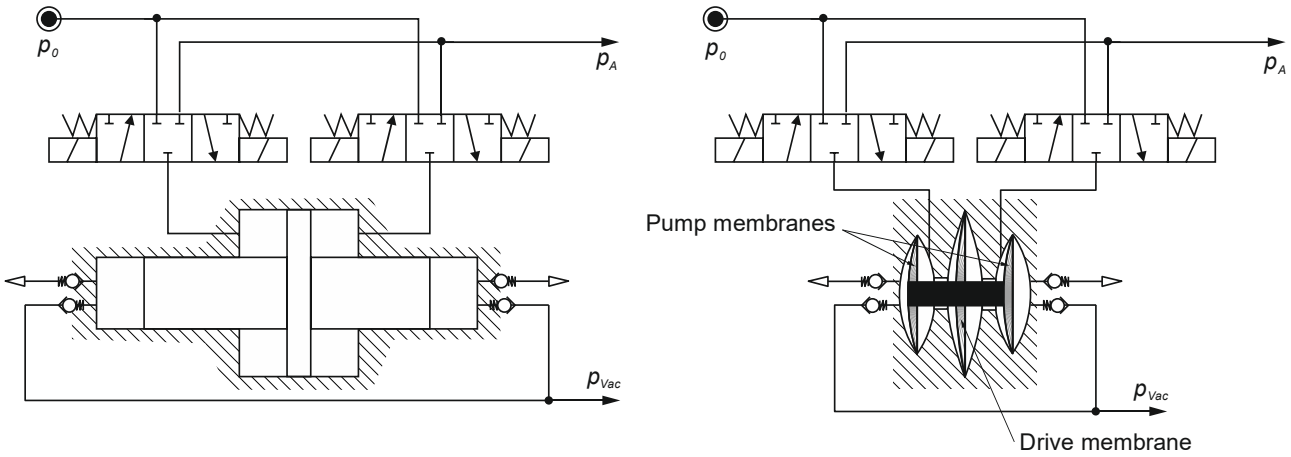

Figure 1. Vacuum Generator schematics; left: piston type, right: membrane type

At first, the device is statically analyzed. Therefore, the volumes are normalized on the pump chamber's volume. A dead volume of 10 % in each chamber and pressure differences on the check valves of 50 mbar are included in the calculation and an isentropic change of state in the chambers is assumed. A vacuum pressure of 300 $mbar_{abs}$ is targeted.

Figure 2 shows the force demand of the two vacuum chambers and the resultant force over the stroke which has to be delivered by the pneumatic drive on the left side. On the right side, the pressure volume correlation for the drive and pump chambers are depicted for the two load cases A and B. With increasing volume of the vacuum pump chamber, the pressure first lowers and then stays constant at suction level. During back stroke, the air in the chamber is first compressed before being discharged to the environment. As long as the drive fulfills the motion task, the supply and regulated pressure have no impact on the cycle of the vacuum chamber.

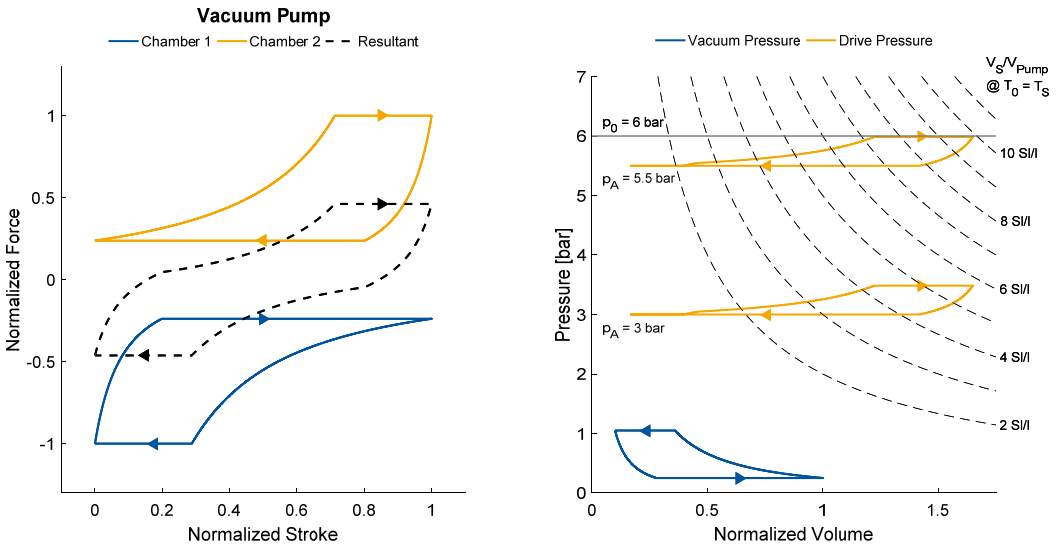

Figure 2. Force requirement and pV-Diagram of the piston generator

As for this static calculation mass inertias of the moving parts are neglected, the pressure course of the drive chamber directly results from the resultant vacuum force. The low pressure side of the drive is loaded with the back pressure p_A, so that the absolute values change with the investigated load case. With the driving pressure difference of only 500 mbar, a vacuum pressure of 300 $mbar_{abs}$, and additional pressure losses on the check valves, the drive's displacement volume needs to be 165 % of the pump's displacement volume.

The isolines in the right diagram show the specific air consumption of the drive. As the highest driving force is required at the highest chamber volume a huge supply air demand occurs.

A mechanical possibility for optimizing the efficiency lies in the pressure volume correlation. By equalizing the force requirement over the stroke, a smaller drive chamber can be used. This means, the force on the first part of the stroke needs to be increased for lowering it to the stroke end. A possible solution is to use a sufficient mass inertia of the movable part. The downside of this approach is that it limits the maximum frequency of the transformer and leads to strong vibrations. The favored solution is to introduce a spring with negative spring constant. A mechanical realization is, e.g., achieved by disk springs or prestressed membranes. The resultant force stroke and pressure volume correlations are shown in figure 3. Due to the smaller drive displacement volume of only 125 % of the pump displacement volume and the lower pressure demand at the stroke end, air consumption is reduced by 30 %.

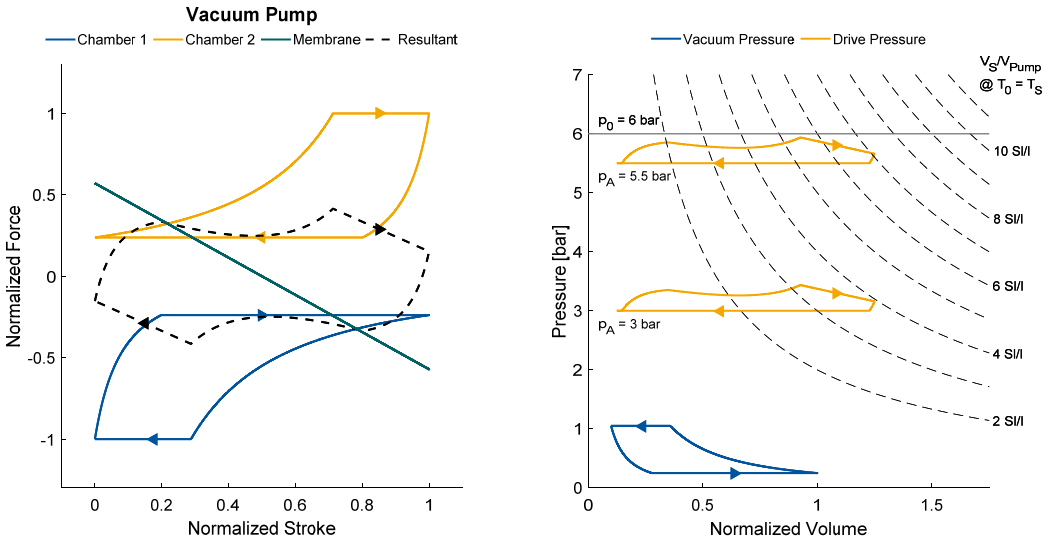

Figure 3. Force requirement and pV*-Diagram of the prestressed membrane generator*

It becomes obvious, that the air consumption is strongly influenced by the regulated pressure. Therefore, the following figure 4 compares the statically calculated specific flow demands of the piston and prestressed membrane type vacuum generator discussed so far.

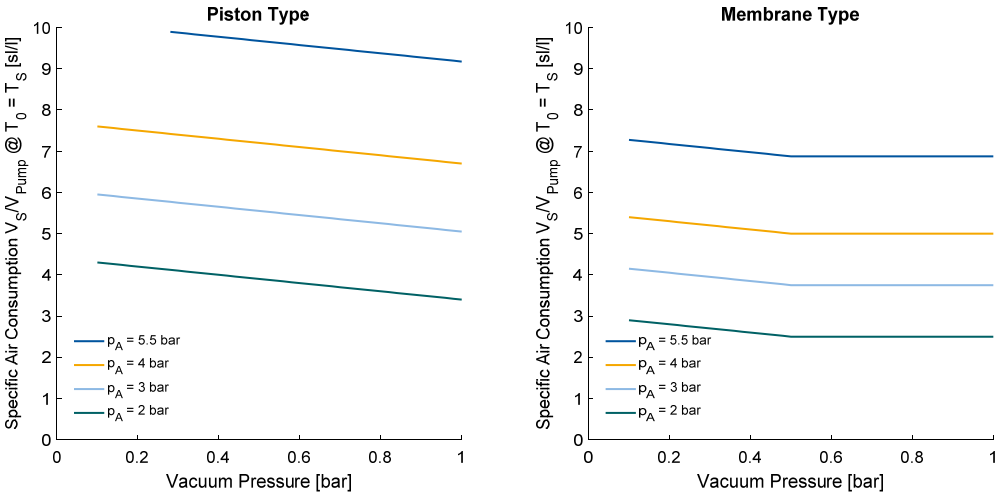

Figure 4. Specific air requirements of piston and membrane type generator

As the displacement of the piston type generator was tuned for a vacuum pressure of 300 $mbar_{abs}$, lower pressures cannot be achieved at the smallest driving pressure difference of 500 mbar. Despite its smaller drive displacement, the membrane generator has sufficient headroom to realize vacuum pressures of down to approximately 100 mbar also at the smallest driving pressure difference. The horizontal lines at vacuum pressures above 500 $mbar_{abs}$ in case of the membrane generator are due to the fact, that no force at the

stroke end is required at all for these operational points. Therewith, the air requirement is independent from the vacuum pressure and limited to the necessary amount of air to achieve the regulated pressure in the drive chamber at the end of the stroke.

For an assessment of the generators efficiency, the specific work provided by its drives needs to be calculated. It results from the pressure/volume diagram [6]:

$$\frac{W_{Pump}}{V_{Pump}} = \int \frac{V}{V_{Pump}} \cdot dp \tag{4}$$

The drive's exergetic efficiency η can be calculated out of this specific work, the specific exergy per pump volume resulting from the air consumption in figure 4, and the supply and regulated pressures.

$$\eta = \frac{W_{Pump}}{E_{Drive}} = \frac{W_{Pump}}{V_S \cdot T_{atm} \cdot \rho_S \cdot R \cdot ln\left(\frac{p_0}{p_A}\right)} \tag{5}$$

Figure 5 shows the exergetic efficiency of the drive for the different load cases analyzed so far. It is visible, that efficiency rises with smaller differences between driving and regulated pressure, so that in cases of low supply energy, efficiency and thus power output is maximized. The local efficiency optimum at vacuum pressures below 500 mbar is due to the local maximum in performed work at the vacuum pump and the small influence of vacuum pressure on required air flow.

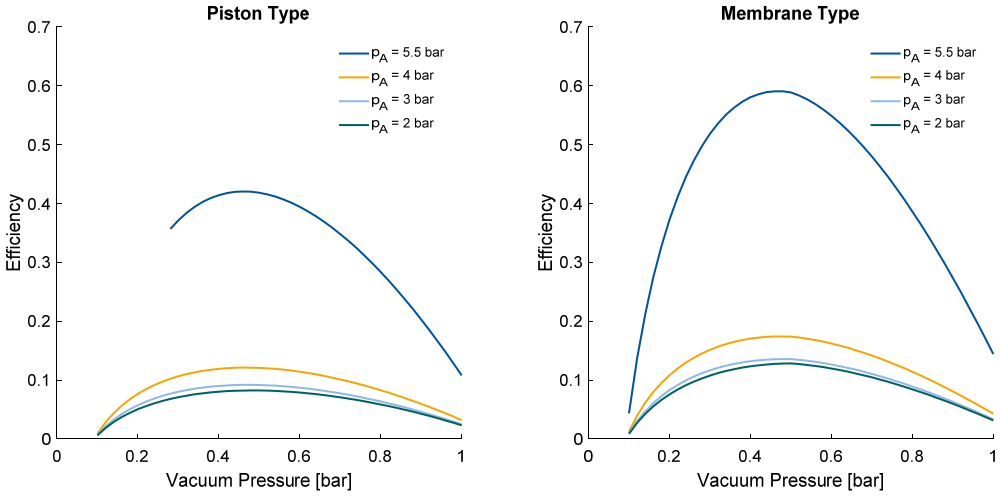

Figure 5. Efficiency of the Vacuum Generator Drive

4. PARAMETER ESTIMATION

First of all, the definition of design parameters requires the modelling of the device and its mechanics. The force of a differential pressure loaded membrane with deflection x, thickness t, diameter d, Young's modulus E, Poisson's ratio v and pretension σ_0 can be described by the physically motivated empirical equation (6) given by Schomburg [7]:

$$F = \frac{\pi}{3} \cdot \left[\frac{16}{3}\frac{E \cdot t^3}{1-v^2} \cdot \frac{x}{r^2} + 4t\sigma_0 \cdot x + 6\frac{5184}{5005}\frac{E \cdot t}{1-v^2} \cdot \frac{x^3}{r^2} - \Delta p \cdot r^2\right] \tag{6}$$

Thereof, the active pressure area A_p, required to describe the volume of the chamber delimited by the membrane, and the spring ratio c at $x = 0$ are deduced:

$$A_p = \frac{\pi}{3} \cdot r^2 \tag{7}$$

$$c = \left.\frac{dF}{dx}\right|_{x=0} = \frac{\pi}{3} \cdot \left[\frac{16}{3}\frac{E}{1-v^2} \cdot \frac{t^3}{r^2} + 4t\sigma_0\right] \tag{8}$$

Obviously, for sufficient compression stress, expressed by negative values of the pretension σ_0, the required negative spring rate is achieved. As the pretension can be used for adjustment, the realizable membrane

thickness is not constrained by the required spring rates. Nevertheless, the hyperbolic third term in the membrane equation is amplified by the membrane thickness, so that linearity is best for small values.

Due to the mechanical creeping of elastomers, elastomeric membranes would lose pretension over time. Therefore, a design with one pretensioned steel membrane for the drive and two non pretensioned elastomeric pump membranes is considered in the following. As the pump membranes could be additively manufactured in their housing, a membrane thickness of 0.5 mm is a good compromise between manufacturing, material homogeneity and bending stresses. Manufacturing of the membranes should be realized in neutral position. In contrast, the inner steel membrane is manufactured with a certain initial deflection. In the manufactured position x_0 the steel membrane is free of external and internal forces. Thus, by setting the external force F and the pressure gradient Δp equal to zero in the membrane equation, the pretention of the membrane σ_0 in position $x = 0$ is achieved and the spring rate c_D is a function of the pretension stroke:

$$c_D = -2\pi \cdot \frac{E_D}{1-{\upsilon_D}^2} \frac{5184}{5005} \cdot \frac{t_D \cdot {x_0}^2}{{r_D}^2} \tag{9}$$

Meanwhile, the spring rate of the pump membranes c_P is given by:

$$c_P = \frac{16}{9}\pi \cdot \frac{E_P}{1-{\upsilon_P}^2} \cdot \frac{{t_P}^3}{{r_P}^2} \tag{10}$$

To estimate the required spring rate for the application, it is assumed that half of the minimal driving pressure difference is sufficient to hold the device in the end position. With this assumption and the pressure difference over the check valves Δp_{Check}, the spring force in end position $F_{Spring,max}$ amounts to

$$F_{Spring,max} = -\left(2 \cdot \Delta p_{Check} + p_{atm} - p_{Vac} - \frac{(p_0 - p_A)}{2}\right) \cdot A_p \tag{11}$$

Thus, the optimal spring rate of the system of three interconnected membranes c_{Res} can be roughly estimated by:

$$c_{Res} = 2 \cdot c_P + c_D = \frac{F_{Spring,max}}{x_{max}} \tag{12}$$

Herein, nonlinear membrane behavior is neglected and a linearization of the force stroke relationship in the neutral position is used, which is only a valid assumption for small membrane strokes. The required pretension stroke of the steel membrane x_0 for the above stated spring rate is defined by

$$\Rightarrow x_0 = r_D \sqrt{\left(\frac{F_{Spring,max}}{x_{max}} - \frac{32}{9}\pi \cdot \frac{E_P}{1-{\upsilon_P}^2} \cdot \frac{{t_P}^3}{{r_P}^2}\right) \cdot -\frac{1-{\upsilon_D}^2}{2\pi \cdot t_D \cdot E_D} \frac{5005}{5184}} \tag{13}$$

Out of these equations and constraints, the main parameters of the device in the following table are deduced. The material properties of the pump membranes are given for additively manufactured PA12 thermoplastics while the drive membrane's parameters are given for stainless steel X5CrNiMo17-12-2 (1.4401) [8, 9].

The resulting deflection forces of the membranes are depicted in figure 6. A linearization results from equalizing the spring constant in centre position with the required force at stroke end. This leads to increasing deviations between required force and membrane force to the stroke ends. As multiple additional influences have been disregarded, e.g., the pressure loss over the valves, mass inertia of the moving part, etc., the resulting accuracy is sufficient for preliminary sizing of the membranes. The dynamic simulation model presented in chapter 6 includes the before mentioned nonlinearities and additional effects.

Table 3. Resulting design parameters

Operational and General Parameters		
Pressure Difference at Check Valves	Δp_{Check}	50 mbar
Supply Pressure	p_0	6 bar
Max. Regulated Pressure	p_A	5.5 bar
Min. Vacuum Pressure	p_{Vac}	300 mbar
Membrane Stroke	x_{max}	1 mm
Surface gradient	A_{Drive}/A_{Pump}	125 %
Pump Membranes		
Young's modulus	E_P	1800 MPa
Poisson's ratio	v_P	0.4
Radius	r_P	50 mm
Thickness	t_P	0.5 mm
Drive Membrane		
Young's modulus	E_D	180 GPa
Poisson's ratio	v_D	0.3
Radius	r_D	75 mm
Thickness	t_D	0.1 mm
Pretension Stroke	x_0	2.5 mm

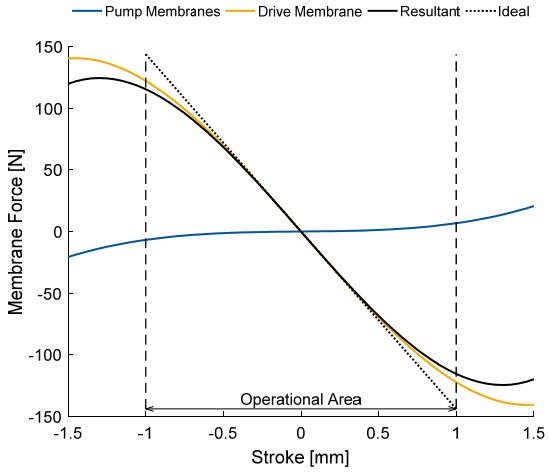

Figure 6. Membrane mechanics

5. CONTROL ALGORITHM

The control algorithm consists of two parts: An outer closed loop pressure control of the vacuum pressure and an inner open loop valve switching control, which optimizes efficiency of the device by valve timing.

A simplified representation of the outer pressure control loop is given in Figure 7. Out of the actual pressure difference, the pressure control generates a set frequency for the drive f_{Set} which is constrained to positive values and limited by a dynamically adjusted maximum frequency f_{max}. The frequency limitation is load dependent and set by the drive control. The drive actuates the vacuum pump with an oscillation frequency f_{Drive}. The resulting suction flow of the pump leads to a pressure change in the capacity. Due to inevitable dead volumes in the pump chamber, a dependency of the actual pressure on the effective suction flow

exists. All external flows into the vacuum system, which result from leakage or suction processes, additionally influence the pressure build-up in the vacuum capacity.

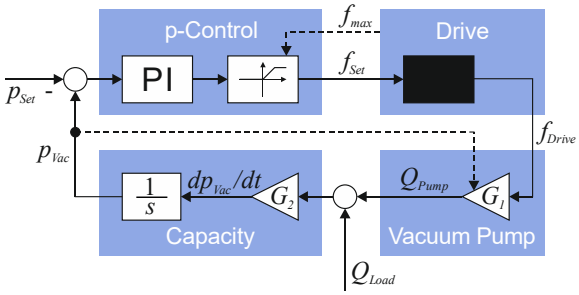

Figure 7. Closed Loop Pressure Control

Due to the integrating part in the controlled process, already a simple proportional pressure control is sufficient to control vacuum pressure without an offset as long as no external inflow occurs. Nevertheless, an integrating part in the controller prevents flow proportional contouring errors during external flow demands.

The required switching control of the drive's valves is realized with a time based sequential control. The flow chart is presented in figure 8. The inlet valves PA and PB are pulse time controlled to prevent the drive chambers from being filled to inlet pressure without necessity. The pulse width adjustment optimizes efficiency by closing the inlet valve as early as possible.

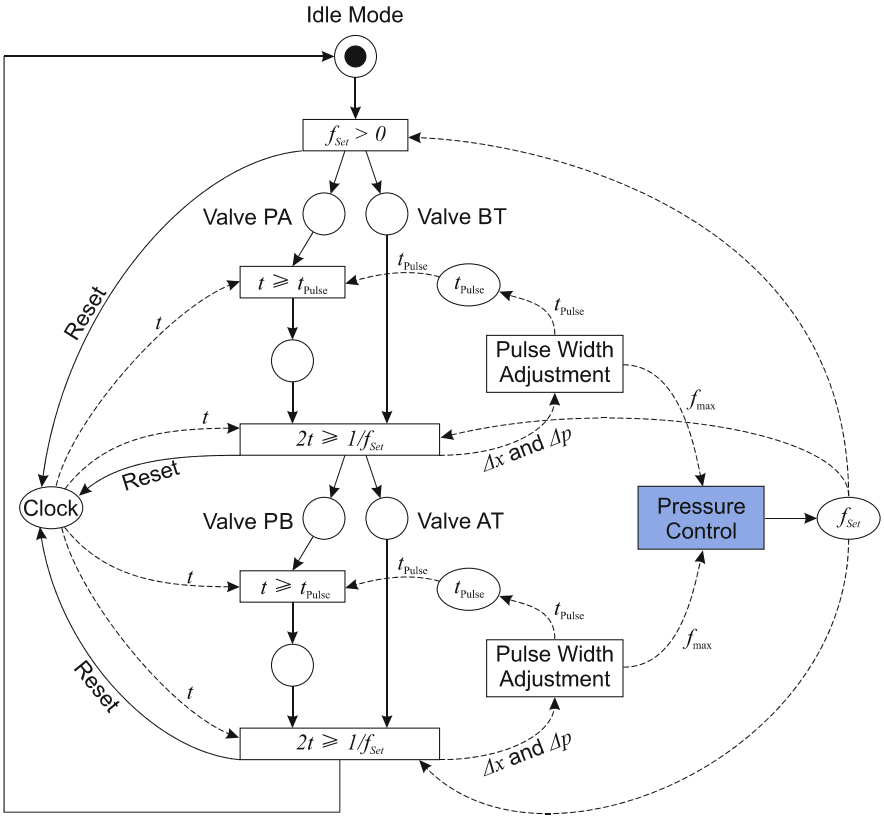

Figure 8. Open Loop Drive Control

As a result of the negative spring constant and the membrane sizing, the required driving pressure difference is nearly independent of the supplied, regulated and vacuum pressure. Therefore a differential pressure control is applied, regulating the pressure difference in the driving chambers at stroke end by varying the inlet valves' pulse time. The set value of the control is the design pressure difference of 500 mbar. As during motion, higher pressure differences can appear, unwanted oscillations in pulse width can result in case the differential pressure is not measured in end position, e.g., when the device does not move fast enough. Therefore an additional stroke sensor is installed surveying the actual stroke. If in one cycle the end stop is not hit, the pulse width is automatically increased for the next cycle.

6. DYNAMIC SIMULATION

A dynamic simulation model of the device is build up in the one-dimensional simulation program DSHplus. Therefore, a user library was implemented including a membrane model and the above described application specific time discrete control. Figure 9 shows the model in DSHplus.

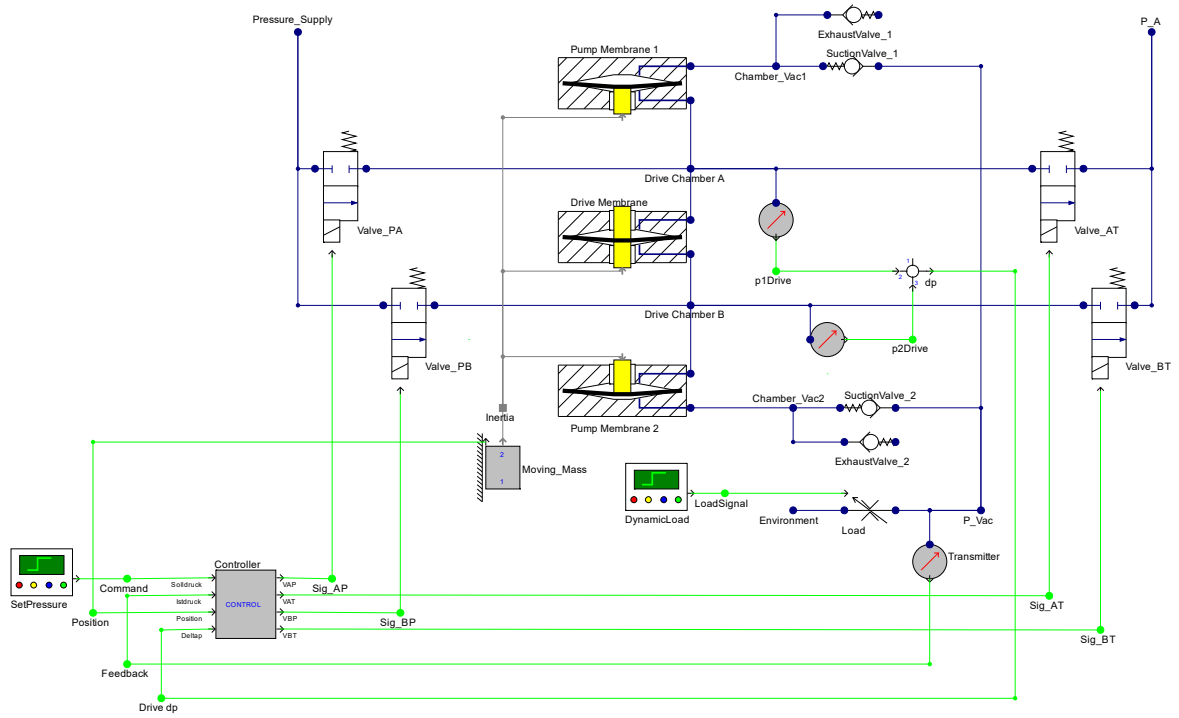

Figure 9. Simulation model in DSHplus

For parameterization of the fast switching valves, data of Spider Valves from Staiger were used, ensuring lifetimes of up to 4 billion cycles [10]. All relevant parameters not listed in table 3 are summarized in table 4.

Table 4. Additional parameters for dynamic simulation

Valves		
Location	Inlet	Outlet
Valve Type	VA204-103	VA204-105
Nominal Diameter	2 mm	4 mm
Opening Time	5 ms	
Closing Time	5 ms	
Conductance (C-value)	22.5 Sl/(min bar)	90 Sl/(min bar)
Critical Pressure Gradient (b-value)	0.528	
Additional Parameters		
Moving mass	5 g	
Evacuated Volume	1.5 l	
Control frequency	1 kHz	

At first, the ability to generate vacuum out of a small pressure difference is tested with the parameters from case A. For comparison, the same test for load case B is also depicted. After the vacuum capacity reaches its set pressure of 300 $mbar_{abs}$ the load valve opens and an external inflow occurs which has to be balanced by the vacuum generator.

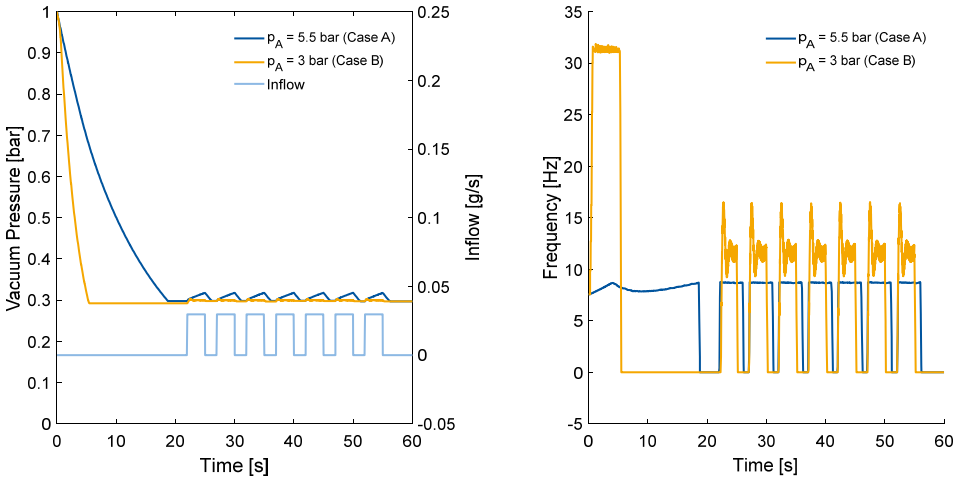

Figure 10. Dynamic Behavior of the Vacuum Generator

It becomes obvious, that the control performance of the vacuum generator in case B is better, as higher input power is available and thus a pressure or flow demand can be matched with smaller reaction time. In load case A, the input power is not sufficient to continuously compensate the load flow. Instead, when the load flow is active, vacuum pressure increases and lowers down after the load valve is closed. Hence, the frequency of the device is determined by the switching control. In case B, sufficient input power is available to compensate the load flow. Hence, the device's frequency is adjusted by the pressure control loop. Some characteristic oscillations in frequency can be observed resulting from PI-pressure control.

Figure 11 shows the pressure/volume diagram of the device in dynamic operation and the efficiency map resulting from dynamic simulation. It is obvious, that the statically predicted behavior is matched with excellent accuracy. The small deviations between static calculation and dynamic simulation result from throttling losses at the valves, mass forces of the moving part and thermodynamics in the vacuum pump and drive chambers.

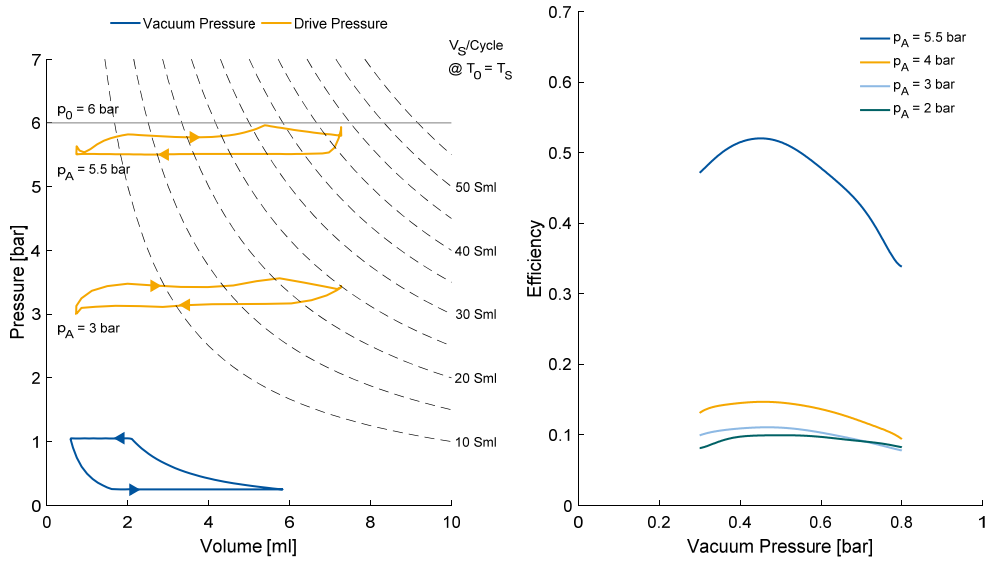

Figure 11. Characteristic results from dynamic simulation

7. CONCLUSION AND OUTLOOK

Significant amounts of exergy are wasted in nowadays pneumatic pressure regulators. Therefore, a novel vacuum generator which uses parts of this exergy and can be placed in parallel to a pressure regulator is introduced and analysed. The working principle consists of two drive and two pump chambers separated by membranes. The drive chambers are controlled by electromechanical switching valves and an electronic control. To optimize performance and efficiency, a bistable mechanical element, acting as a spring with negative spring constant, was introduced. The function and performance of the device and its control was validated by static calculations and in dynamic simulation.

Due to the promising results shown in this paper, in a next step, a prototype development and measurements will be envisaged. Key aspects will be the membrane stresses and forces during operation as well as membranes' life time. Therefore, FEM calculation and geometrical optimization need to be realized during prototype development. Moreover, a multivariable control to allow the operation of the device as vacuum generator and pressure regulator in parallel without additional components will be investigated.

REFERENCES

[1] N.N. 2006. *"EnEffAH - Energy efficiency in production in the drive and handling technology field - Basic principles and measures"*, Brochure, EnEffAH – Project Consortium, Stuttgart

[2] N.N. 2015. *"Leitfaden Druckluft-Optimierung"*, EnergieSchweiz, Bundesamt für Energie BFE, Bern (in German)

[3] Krichel, S. & Sawodny, O. 2012. *"Exergy Flow Diagrams as Novel Approach to Discuss the Efficiency of Compressed Air Systems"*, Proceedings of the 8th International Fluid Power Conference (8. IFK), March 26 – 28, Dresden

[4] Lucas, K. 2004. *"Thermodynamik – Die Grundgesetze der Energie- und Stoffumwandlungen"*, 4th edition, Springer, Berlin (in German)

[5] Straub, D. & Schaaf, W. 2018. *"Experimental and Theoretical Investigation of Lightweight Pumps and Fluid Reservoirs for Electrically Driven Vacuum Systems in Automated Handling Processes"*, Proceedings of the 11th International Fluid Power Conference (11. IFK), Vol. 1, March 19-21, Aachen

[6] Murrenhoff, H. & Reinertz, O. 2014. *"Fundamentals of Fluid Power – Part II: Pneumatics"*, Lecture Notes, Translation of the 2nd revised German edition of 2014, Shaker, Aachen

[7] Schomburg, W.-K. 2015. *"Introduction to Microsystem Design"*, 2nd Edition, Springer, Berlin

[8] N.N. 2017. *"HP 3D printing materials"*, Product brochure, HP Development Company, L.P.

[9] N.N. 2003. *"DIN EN 10151 Stainless steel strip for springs - Technical delivery conditions"*, EN 10151:2002, Beuth, Berlin

[10] N.N. 2018. *"VA 204-1"*, Product Datasheet, Staiger GmbH & Co. KG, Erligheim

RESEARCH ON DYNAMIC CHARACTERISTICS OF A SUCTION CANTILEVER VALVE IN MINIATURE HIGH PRESSURE COMPRESSOR BASED ON EQUIVALENT MODEL

Deng Yipan[1], Miao Na[1], Liu Yinshui[1], Wu Shan[2], Wu Defa[1]
[1] State Key Lab of Digital Manufacturing Equipment and Technology, Huazhong University of Science and Technology
[2] Wuhan Technology and Business University
Wuhan, Hubei, China
dengyipan@hust.edu.cn

ABSTRACT

In this paper, a cantilever valve for miniature high-pressure compressor is proposed. An equivalent model of cantilever valve has been presented to obtain the equivalent stiffness and equivalent mass for the valve motion equation. Based on the equivalent model and thermodynamic process in the cylinder, A theoretical analysis has been constructed to reveal the dynamic characteristics of the suction valve. Crucial parameters such as reed thickness and valve lift are analysed to reveal their effects on the performance of suction valve, as well as the miniature high pressure compressor. It can be found that both reed thickness and valve lift exert an more obvious effect on closing process of suction valve comparing to opening process. Volumetric efficiency can be improved by reducing valve lift. Based on the numerical investigation, the optimized parameters can be obtained for reliable performance of the miniature high pressure compressor.

KEYWORDS: miniature high pressure compressor, cantilever valve, equivalent model, dynamic characteristics.

1. INTRODUCTION

Miniature high pressure compressor has gained much attention in the applications of refrigeration, infrared cooling and cold-gas stores ejection for aeronautics and astronautics systems, which put strict restrictions to dimension and weight of carry-on equipment [1-3]. Compared with traditional high pressure compressor, the in-cylinder volume of miniature high pressure compressor are relatively smaller, especially for high-pressure stage. As generally known, suction valve and discharge valve play an extreme important role in influencing the performance (in-cylinder mass, volumetric efficiency, indicated work et. al) of reciprocating compressors. In traditional large-scale reciprocating compressor, suction valve and discharge valve usually comprise a valve plate, a valve seat, a spring and a lift limiter. This type of valves generally occupy a large space, have relative larger clearance volume and spring stiffness, which limits their application to miniature high pressure compressor in our research. In some small reciprocating compressors with low discharge pressure, reed or cantilever valves have been successfully applied. However, their dimensions are quite large and the applications to high pressure compressors are rarely reported.

Valve dynamic characteristics have great influence on the performance of reciprocating compressors and many past studies have been conducted to the investigation. A simulation model with single-degree-of-freedom system was established by Costagliola [4] to describe the valve motion in the form of two non-linear differential

equations. Based on this basic methods, Sun [5] proposed a new method to simulate the valve dynamics by comprehensively considering the various factors, such as heat transfer, leakage and gas pulsation. Elhaj [6], Farzaneh-Gord [7] and Wang [8] improved the model and carried out fault detection on reciprocating compressor valves. In order to understand the flow conditions and valve motions in detail, modern methods were inclined to induce commercial CFD software to simulate the thermodynamic process and valve dynamic behaviour in reciprocating compressors. Matos [9, 10]carried out a numerical methodology to simulate the dynamic behaviour of reed type valves of reciprocating compressors used in refrigeration, the force acting on the reed and the flow through the valves were obtained and revealed. Lang [11] used a FSI methodology to study the suction valves of a hermetic reciprocating compressor and the overall compressor performance are analysed by varying suction valve parameters. Choi [12] and Hwang [13] investigated the valve dynamics in linear compressor based on fluid-structure interaction. Pereira [14] analysed the influence of piston on effective areas of reed-type valves of small reciprocating compressors through a 3D numerical model. Zhang [15] described the simulation and experimental studies of the transient motion of suction valves. Zhao [16] presented a 3D CFD model of a double acting reciprocating compressor and transient flow inside the compressor and the interaction between valve motion and pressure pulsation were resolved simultaneously.

Except from the simulation methodology mentioned above, experimental investigation were also conducted to reveal the valve dynamics in reciprocating compressors. Buligan [17] and Nagy [18] carried out valve lift measurement in compressor by optical techniques and they discussed the effects on optical signals of a variety of disturbing inputs and environmental effects. Venkatesan [19] validated experimentally a mathematical model of a reed valve in reciprocating air compressor and parameters such as compressor speed, discharge pressure and clearance volume were evaluated. Wang [20] conducted experimental investigation on valve impact and inclining motion of valve in a reciprocating compressor and they analysed the factors influencing the valve dynamics. Wang [21] presented an experimental study of the fault (include leakage, valve flutter, delayed closing and improper lift) diagnosis of reciprocating compressor valves with acoustic emission technology and simulated valve motion. Ma [22] did experimental investigation of the valve dynamics in order to design a self-acting valve with a high efficiency and long life span for the trans-critical CO_2 compressor.

Among all these research mentioned above, they mainly focused on the valve dynamics of reciprocating compressor with a large bore cylinder and a relative low working pressure. The parameters including stiffness, mass, clearance volume and flow area will differ greatly when cylinder miniaturizes and pressure elevates. Thus the traditional valve structure may be not suitable for miniature high pressure due to the improper stiffness and clearance volume, as well as other crucial parameters.

In the present study, cantilever valve applicable to miniature high pressure compressor has been proposed. A theoretical analysis has been constructed to reveal the dynamics of the suction valve. An equivalent model of cantilever valve has been presented to obtain the equivalent stiffness and equivalent mass for the valve motion equation. Based on the theoretical model, the effects of important parameters such as reed thickness and lift on the suction valve dynamics have been studied.

2. EQUIVALENT MODEL OF SUCTION CANTILEVER VALVE AND THERMODYNAMIC MODELLING

The miniature high-pressure compressor is presented in Figure 1. and the parameters is shown in Table 1. The MMSC consists mainly of a main shaft, a swash plate, four-stage piston assemblies, cylinder block with four various liner holes, suction valves, discharge valves and an integrated inter cooler. Swash plate is positioned at a fixed angle on the bevel of main shaft. Slippers are held tightly in contact with the swash plate. The pistons move reciprocally when the main shaft rotates. With the collaboration of suction valves, discharge valves and inter cooler, gas inhaled from the gas inlet is compressed stage-by-stage to form a high pressure. Finally, the pressurized gas is discharged from the gas outlet. As learn from Table 2, the dimension of every stage cylinder are limited due to the overall compacted size of compressor. Therefore, neither traditional valves with independent spring nor linear reed valve can be introduced into the miniature compressor due to their relative large dimension.

Schematic of cantilever valves applicable for the miniature high pressure compressor is shown in Figure. 2. The cantilever valves are made of elastic steel, an annular cantilever is formed to increasing the deformation length in a limited space. Lift limiters are used to guarantee stable motion of the valves. By this method, an integrated flow-distribution pairs are presented for every stage of the miniature high pressure compressor.

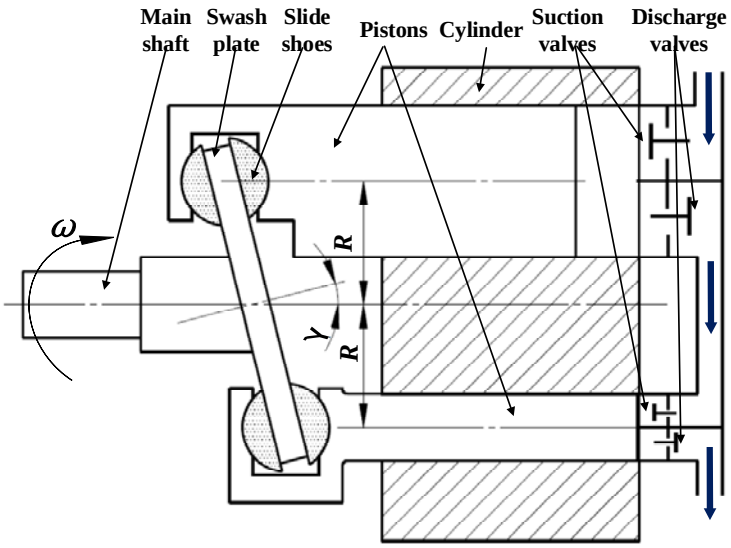

Figure 1. Schematic of miniature high pressure compressor (only two stages are shown)

Table 1. Parameters of miniature high-pressure compressor

Required Parameters	Value
Maximum delivery pressure (MPa)	41
Flow rates (SL min^{-1})	10
Weight (kg)	4
Dimension (mm)	Φ110×200
Piston stroke (mm)	12.6

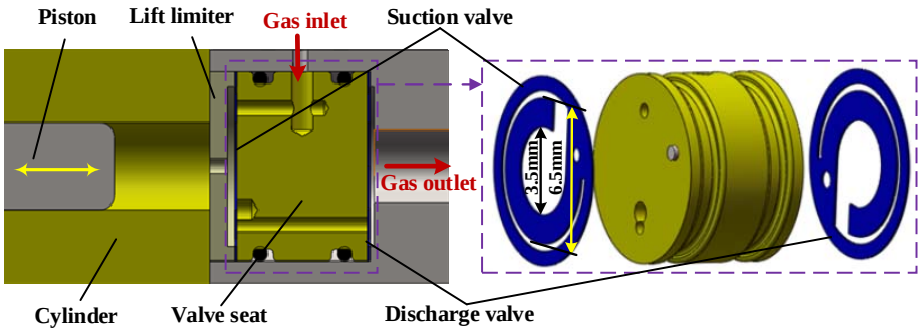

Figure 2. Cantilever valve design in miniature high pressure compressor

2.1. Equivalent model of cantilever valve

In this section, an equivalent model of cantilever valve is presented. The equivalent stiffness and equivalent mass were calculated [23].

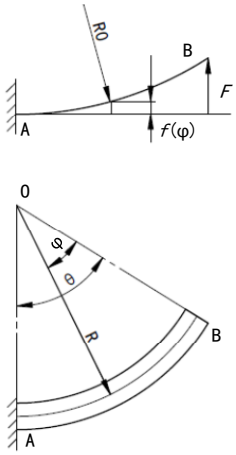

Figure 3. Model of cantilever valve.

According to Cassette theorem and Rayleigh method, the deformation of the cantilever valve can be expressed as following.

$$f(\varphi)=\frac{FR^3}{bh^3}\left\{\left[\frac{12}{E}\left(\frac{1}{2}(\theta-\varphi)\cos\varphi-\frac{1}{4}\sin(2\theta-\varphi)+\frac{1}{4}\sin\varphi\right)\right]+\frac{1}{\beta G}\left[(\theta-\varphi)\left(1+\frac{1}{2}\cos\varphi\right)-\sin(\theta-\varphi)-\sin\theta+\frac{1}{4}\sin(2\theta-\varphi)+\frac{3}{4}\sin\varphi\right]\right\} \quad (1)$$

Where b and h are width and thickness of cantilever, E and G are elasticity modulus, shear modulus of cantilever material. Parameter β is the coefficient relating to the torsional deformation of rectangular section.

And the deformation of position B under a force of F can be calculated as:

$$f(B)=\frac{FR^3}{bh^3}\left[\frac{12}{E}\left(\frac{1}{2}\theta-\frac{1}{4}\sin 2\theta\right)+\frac{1}{\beta G}\left(\frac{3}{2}\theta-2\sin\theta+\frac{1}{4}\sin 2\theta\right)\right] \quad (2)$$

So the equivalent stiffness of the cantilever can be written as:

$$k=\frac{F}{f(B)}=\frac{bh^3}{R^3}\left[\frac{12}{E}\left(\frac{1}{2}\theta-\frac{1}{4}\sin 2\theta\right)+\frac{1}{\beta G}\left(\frac{3}{2}\theta-2\sin\theta+\frac{1}{4}\sin 2\theta\right)\right]^{-1} \quad (3)$$

The equivalent mass of the cantilever is derived as following,

$$M_e=\rho bhR\int_0^{\theta}F^2(\varphi)d\varphi \quad (4)$$

Where $F(\varphi)$ can be given as following.

$$F(\varphi)=\frac{f(\varphi)}{f(B)} \quad (5)$$

Based on the simplified equivalent model of cantilever valve, the motion equation can be given by following.

$$\begin{cases}\dfrac{d^2y_i}{d\theta^2}=\dfrac{1}{M_{ei}\omega^2}\left[\beta_i A_i(p_i-p_c)-k_i(y_i+y_{i0})\right]\\ \dfrac{d^2y_o}{d\theta^2}=\dfrac{1}{M_{eo}\omega^2}\left[\beta_o A_o(p_c-p_o)-k_o(y_o+y_{o0})\right]\end{cases} \quad (6)$$

Where M_{ei} and M_{eo} are equivalent masses of suction and discharge cantilever valve. Coefficient of β_i and β_o account loss of the energy due to the orifice flow. Also. subscripts i, o and c stand for suction, discharge and control volume condition respectively.

2.2. Energy conservation law

Energy conservation law (the first law of thermodynamic) for the inside gas of the cylinder as a control volume can be written as [5,6] :

$$\frac{d(E_c)}{d\theta} = \frac{dQ}{d\theta} + \frac{dm_i h_i}{d\theta} - \frac{dm_o h_o}{d\theta} + \frac{dW}{d\theta} \tag{7}$$

In this equation, The work term can be computed as following:

$$\frac{dW}{d\theta} = -p_c \frac{dV_c}{d\theta} \tag{8}$$

Where p and V represent pressure and volume respectively. $dQ/d\theta$, $dm/d\theta$, h are heat transfer rate, mass flow rate and enthalpy respectively. $d(E_c)/d\theta$ is the change rate of internal energy, Under the assumption that variation in kinetic and potential energies are neglected. $d(E_c)/d\theta$ can be written as

$$\frac{d(E_c)}{d\theta} = \frac{d(m_c u_c)}{d\theta} \tag{9}$$

2.3. Mass conservation law

Considering the in-cylinder gas of compressor as a control volume, the mass conservation equation can be expressed by following:

$$\frac{dm_c}{d\theta} = \frac{dm_i}{d\theta} - \frac{dm_o}{d\theta} \tag{10}$$

Where $dm_i/d\theta$ and $dm_o/d\theta$ are the mass flow rate through suction and discharge valve respectively, which can be computed from following equations.

$$\begin{cases} \dfrac{dm_i}{d\theta} = \dfrac{C_{di}\rho_i A_i}{\omega}\sqrt{2|p_i - p_c|} \\ \dfrac{dm_o}{d\theta} = \dfrac{C_{do}\rho_o A_o}{\omega}\sqrt{2|p_c - p_o|} \end{cases} \tag{11}$$

Where C_{di} and C_{do} are flow coefficient of suction and discharge valves, and, ρ_i and ρ_o are gas density of suction and discharge passages respectively. additionally, in equation (11), A_i and A_o are the flow areas through the suction and discharge valves which take place from cylinder respectively.

2.4. Real gas equation of state

The most basic Redlich-Kwong equation of state is used to describe the thermodynamic properties of pressure, temperature and specific volume for a real gas.

$$p = \frac{R_g T}{v - b} - \frac{a}{T^{0.5} v(v + b)} \tag{12}$$

Where p , T , v are gas pressure, temperature, specific volume in the cylinder, respectively. R_g is the gas constant and its value of air is 287 J/(kg·K) and a , b are property constants.

2.5. Piston motion equation

The exact expression for instantaneous position of the piston displacement from Top Dead Center (TDC) in terms of the shaft angle can be given by following:

$$S(\theta) = R(1-\cos\theta)\tan\gamma \tag{13}$$

Where R and γ are radius of cylinders distribution circle and swash plate angle respectively.

3. RESULTS AND DISCUSSIONS

An explicit Runge-Kutta method was used to solve the mathematical model and we adopted MATLAB to implement the simulation. The last stage of miniature high pressure compressor is taken as study objective due to the highest pressure range and minimum cylinder diameter. The cylinder diameter is 6 mm and sealing pressure ranges from 9.11 MPa (suction) to 41.00 MPa (discharge). Effects of reed thickness and lift limiter on dynamic characteristics of suction valve are analysed and the results as well as discussions are presented in following sections.

3.1. Effects of reed thickness

In this section, the effects of reed thickness on dynamic characteristics of the suction cantilever valve are presented. The investigated thicknesses ranges from 0.15 mm to 0.25 mm and the valve lift is set as 0.2 mm.

The variation of displacement ratio of suction valve against different reed thickness is shown in Figure. 4. It should be noted that displacement ratio refers to actual displacement against maximum lift. We can learn that reed thickness has no remarkable influence on the opening process of suction valve. Once the valve plate reaches to the lift limiter, a slight bounce is formed and then valve plate adheres to lift limiter rapidly. Additionally, under three different thickness, the bouncing curves coincide almost completely. However, reed thickness exerts an more obvious effect on closing process of suction valve. As shown in the partial enlarged drawing in Figure. 4, the closing time is different as reed thickness varies. Reducing reed thickness will postpone the closing time slightly and thus increasing gas mass from the suction valve. It can also be noticed that with a thickness of 0.15 mm, the suction valve experiences an obvious bounce during closing process, while this phenomenon is absence in other two situations.

Volumetric efficiency can be defined as following.

$$\eta_{\mathrm{v}} = \frac{m_{\mathrm{real}}}{m_{\mathrm{ideal}}} = \frac{m_{\mathrm{real}}}{V_{\mathrm{cy}}\rho_{\mathrm{i}}} \tag{14}$$

Where ρ_{i} is suction air density, V_{cy} is in-cylinder volume and m_{real} is mass flow into cylinder chamber per cycle.

Figure. 5 a) and b) show the variation of in-cylinder mass with shaft angle and volumetric efficiency against different reed thickness, respectively. It can be reflected that increasing the thickness from 0.15 mm to 0.20 mm reduces the maximum in-cylinder gas mass from 4.53×10^{-5} kg, which indicates a volumetric efficiency drop from 74.9% to 69%. The rising curves of in-cylinder mass with shaft angle show a high consistency. Additionally, it can be learned that as the thickness increases to 0.25 mm, volumetric efficiency has a slight drop of 0.5% comparing to 0.20 mm.

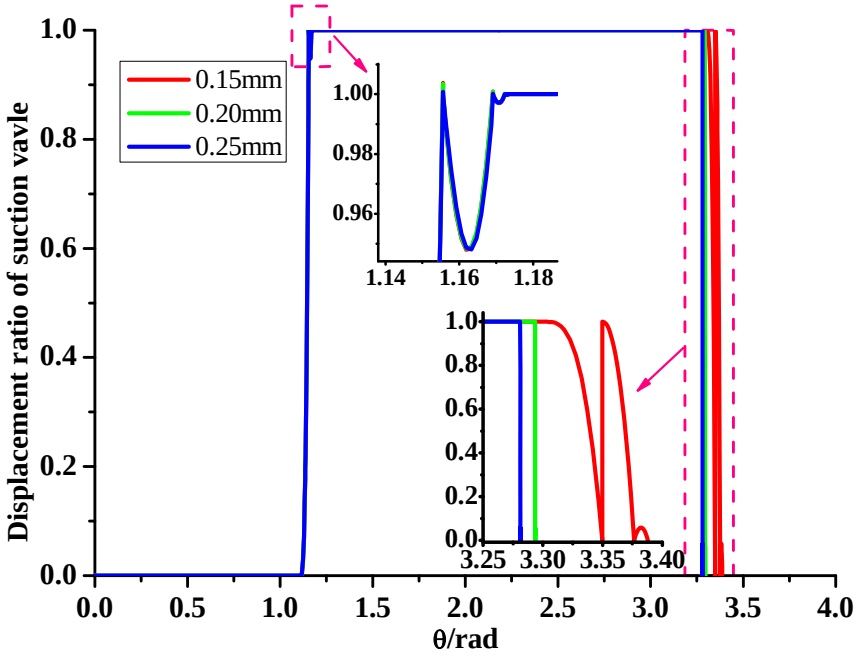

Figure 4. Variation of displacement ratio of suction valve against different reed thickness

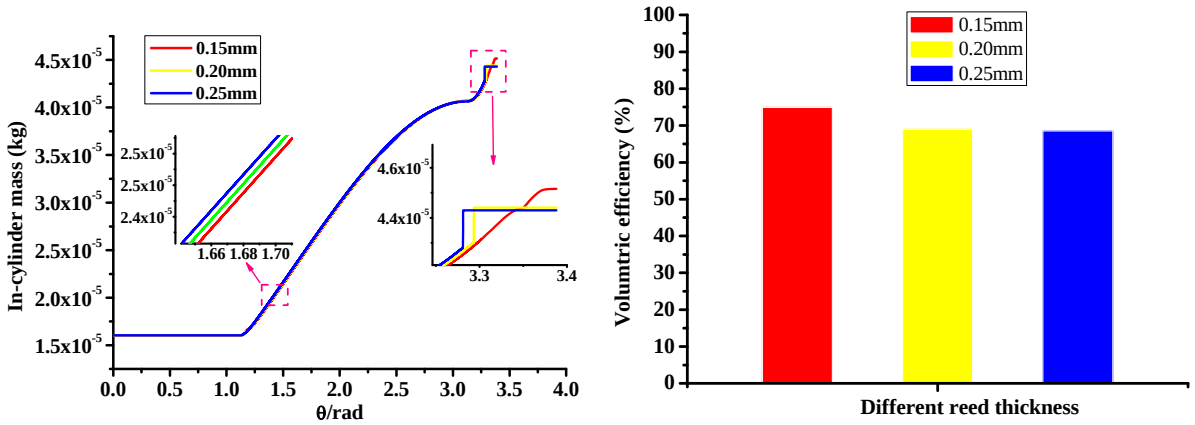

Figure 5. Variation of a) in-cylinder mass with shaft angle b) volumetric efficiency against different reed thickness.

3.2. Effects of lift limiter

In this section, we present the effects of reed thickness on dynamic characteristics of the suction cantilever valve. The investigated valve lift values range from 0.15 mm to 0.25 mm and the reed thickness is set as 0.2 mm.

Figure. 6 presents the variation of displacement ratio of suction valve against different lift. The variation trend is similar to Figure. 4 and we can learn that valve lift has no remarkable influence on the opening process of suction valve. A slight bounce is formed after the valve plate reaches to the lift limiter and then valve plate adheres to lift limiter rapidly. Valve lift has a slight influence on the bouncing curve during opening process, bouncing amplitude increases with the increasing of valve lift. It can be also discovered that valve lift exerts an more obvious effect on closing process of suction valve. As shown in the partial enlarged drawing in Figure. 6, the closing time is different as valve lift varies. Closing time can be postponed slightly as valve lift decreases. It can also be noticed that with a lift value of 0.15 mm, the suction valve experiences an obvious bounce during closing process, while this phenomenon is absence in other two situations.

Figure. 7 a) and b) show the variation of in-cylinder mass with shaft angle and volumetric efficiency against different valve lift, respectively. We can learn that valve lift has an obvious effect on both minimum and maximum in-cylinder gas mass. This can be explained that different valve lift brings about different dead volume and thus influence the in-cylinder mass curves.

It can learned from Figure. 7 b) that increasing valve lift reduces the volumetric efficiency. The volumetric efficiencies are 75.6%, 71.5% and 67.7% respectively when the lifts are set as 0.10 mm, 0.15 mm and 0.20 mm. So for improving the performance of the compressor, dead volume should be limited strictly to a low level.

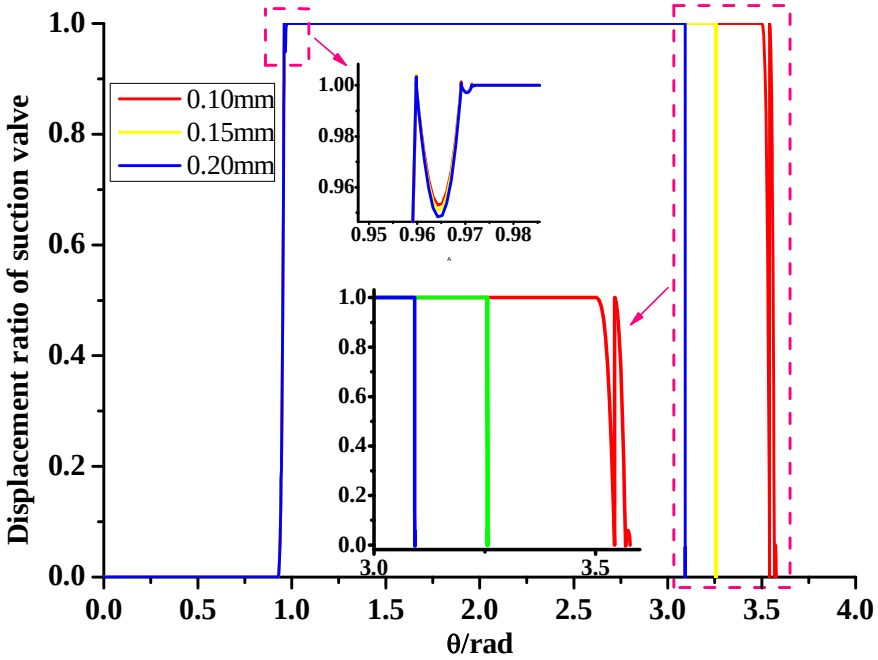

Figure 6. Variation of displacement ratio of suction valve against different lift

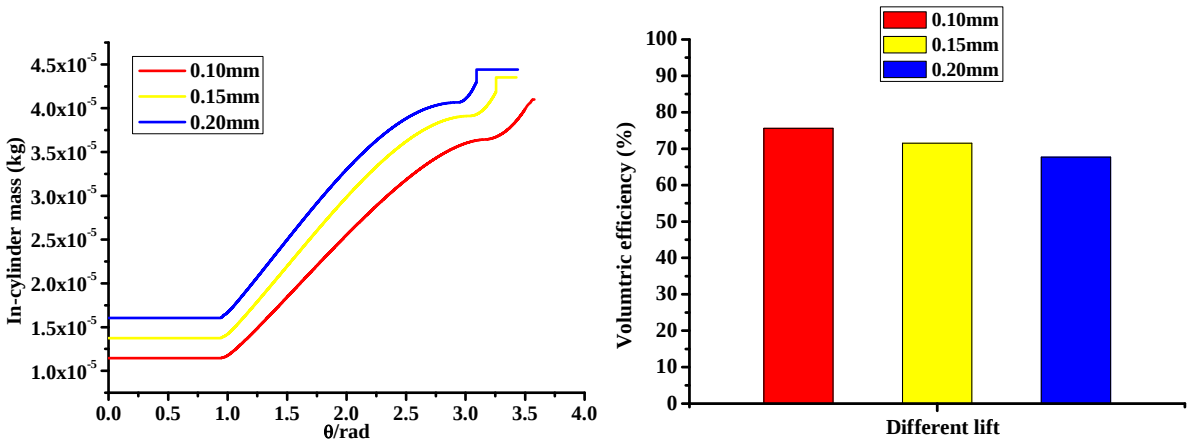

Figure 7. Variation of a) in-cylinder mass with shaft angle b) volumetric efficiency against different lift.

4. CONCLUSIONS

In current study, cantilever valve applicable to miniature high pressure compressor has been proposed. A theoretical analysis has been constructed to reveal the dynamic characteristics of the suction valve. An equivalent model of cantilever valve has been presented to obtain the equivalent stiffness and equivalent mass for the valve motion equation. Based on the numerical analysis, it can be found reed thickness and valve lift exert an more obvious effect on closing process of suction valve comparing to opening process. Additionally,

volumetric efficiency can be improved by reducing valve lift and dead volume should be limited strictly to a low level for improving the performance of the compressor. Based on the numerical investigation, the optimized parameters can be obtained for reliable performance of the miniature high pressure compressor.

Due to relative small size of the valves and compressor, it is impossible to measuring the valve movements directly to strengthen the simulation model. However, measuring the gas pressure both in-cylinder and out-cylinder are feasible. In our future research, corresponding experimental investigation will be carried out and FE analysis on valve deformation will be conducted for strengthen the simplified mathematical models.

REFERENCES

[1] Y. Liu, N. Miao, Y. Deng, D. Wu. 2019. "Efficiency evaluation of a miniature multi-stage compressor under insufficient inter-stage cooling conditions". International Journal of Refrigeration;97:169-179.

[2] Y. Luo and X. Wang. 2010. "Exergy analysis on throttle reduction efficiency based on real gas equations," Energy, vol. 35, pp. 181-187.

[3] Y. Deng, Y. Liu, F. Li, P. Tian, and N. Miao. 2017. "Research on Sealing Performance in High Pressure Oil-Free Miniature Air Compressor," p. V001T01A023.

[4] M. COSTAGLIOLA, 1950. "THE THEORY OF SPRING-LOADED VALVES FOR RECIPROCATING COMPRESSORS," JOURNAL OF APPLIED MECHANICS-TRANSACTIONS OF THE ASME, pp. 415-420.

[5] S.-Y. Sun and T.-R. Ren. 1995. "New method of thermodynamic computation for a reciprocating compressor: Computer simulation of working process," International Journal of Mechanical Sciences, vol. 37, pp. 343-353.

[6] M. Elhaj, F. Gu, A. D. Ball, A. Albarbar, M. Al-Qattan, and A. Naid. 2008. "Numerical simulation and experimental study of a two-stage reciprocating compressor for condition monitoring," Mechanical Systems and Signal Processing, vol. 22, pp. 374-389.

[7] M. Farzaneh-Gord and H. Khoshnazar. 2016. "Valve fault detection for single-stage reciprocating compressors," Journal of Natural Gas Science and Engineering, vol. 35, Part A, pp. 1239-1248.

[8] Y. Wang, C. Xue, X. Jia, and X. Peng. 2015. "Fault diagnosis of reciprocating compressor valve with the method integrating acoustic emission signal and simulated valve motion," Mechanical Systems and Signal Processing, vol. 56–57, pp. 197-212.

[9] F. Matos, A. Prata, and C. Deschamps. 2002. "Numerical simulation of the dynamics of reed type valves, 16th Int," in Compressor Engineering Conference at Purdue, 2002, pp. 16-19.

[10] F. Matos, A. Prata, and C. Deschamps. 2000. "A numerical methodology for the analysis of valve dynamics,".

[11] W. Lang, R. Almbauer, and D. Jajcevic. 2010. "Usage and validation of a fluid structure interaction methodology for the study of different suction valve parameters of a hermetic reciprocating compressor," The International Journal of Multiphysics, vol. 4, pp. 65-81.

[12] Y.-s. Choi, J.-h. Lee, W.-b. Jeong, and I.-G. Kim. 2010. "Dynamic behavior of valve system in linear compressor based on fluid-structure interaction," Journal of Mechanical Science and Technology, vol. 24, pp. 1371-1377.

[13] I. S. Hwang, S. J. Park, W. Oh, and Y. L. Lee. 2017. "Linear compressor discharge valve behavior using a rigid body valve model and a FSI valve model," International Journal of Refrigeration, vol. 82, pp. 509-519.

[14] E. L. L. Pereira and C. J. Deschamps. 2011. "Influence of piston on effective areas of reed-type valves of small reciprocating compressors," HVAC&R Research, vol. 17, pp. 218-230.

[15] J. Zhang, Y. Wang, X. Li, Z. Jiang, Y. Xie, and Q. Zhu. 2016. "A Simulation Study on the Transient Motion of a Reciprocating Compressor Suction Valve Under Complicated Conditions," Journal of Failure Analysis and Prevention, vol. 16, pp. 790-802.

[16] B. Zhao, X. Jia, S. Sun, J. Wen, and X. Peng. 2018. "FSI model of valve motion and pressure pulsation for investigating thermodynamic process and internal flow inside a reciprocating compressor," Applied Thermal Engineering, vol. 131, pp. 998-1007.

[17] G. Buligan, N. Paone, G. Revel, and E. Tomasini. 2002 "Valve lift measurement by optical techniques in compressors, 16th Int," in Compressor Engineering Conference at Purdue, 2002, pp. 16-19.

[18] D. Nagy, R. A. Almbauer, W. Lang, and A. Burgstaller. 2008. "Valve lift measurement for the validation of a compressor simulation model,".

[19] J. Venkatesan, G. Nagarajan, R. V. Seeniraj, and R. Murugan. 2010. "Experimental validation of a mathematical model of a reed-valve reciprocating air compressor from an automotive-braking system," International Journal of Automotive Technology, vol. 11, pp. 317-322.

[20] Y. Wang, C. Xue, J. Feng, and X. Peng. 2013. "Experimental investigation on valve impact velocity and inclining motion of a reciprocating compressor," Applied Thermal Engineering, vol. 61, pp. 149-156.

[21] Y. Wang, A. Gao, S. Zheng, and X. Peng. 2016. "Experimental investigation of the fault diagnosis of typical faults in reciprocating compressor valves," Proceedings of the Institution of Mechanical Engineers, Part C: Journal of Mechanical Engineering Science, vol. 230, pp. 2285-2299.

[22] Y. Ma, Z. He, X. Peng, and Z. Xing. 2012. "Experimental investigation of the discharge valve dynamics in a reciprocating compressor for trans-critical CO2 refrigeration cycle," Applied Thermal Engineering, vol. 32, pp. 13-21.

[23] S. Pan, Y. Wu, X. Lin, K. Guang, S. Ou. 2016. "Calculation of Cantilever Springs in Compressor Plate Valves," Fluid Machinery, vol. 44, No.3. (In Chinese)

MATHEMATICAL MODELLING OF PNEUMATIC STEADY FLOW THROUGH TUBES WITH HEAT TRANSFER IN MATLAB/SIMULINK AND ITS EXPERIMENTAL VERIFICATION

Riku Ito, Eiji Murayama, Yukio Kawakami, Kazuo Nakano
Shibaura Institute of Technology
Graduate School of Science and Engineering
Department of Mechanical Engineering
307 Fukasaku, Minuma-ku, Saitama City, Saitama, 337-8570 Japan
E-mail: md18011@shibaura-it.ac.jp

ABSTRACT

The purpose of this research is the development of simulation models of pneumatic steady flow through tubes with wall friction and external heat transfer by making use of MATLAB/Simulink® for system engineers. We considered straight uniform tubes which were heated or cooled to maintain the wall temperature at certain constants. The developed model consists of the thermal entry region model and the Fanno region model, which is connected in series to the former model. The heat transfer effects through walls are modelled by utilizing the Chilton-Colburn analogy in the thermal entry region model. On the other hand, adiabatic tube-walls are assumed in the Fanno region model, because of the small temperature difference between the walls and internal air. In the experiment, compressed air was supplied from a constant temperature tank to a copper tube set in a water jacket to adjust the wall temperature. The pressure at both ends of the tube and the mass flow rate were measured. The usefulness of the newly developed models was verified by comparing the simulation results with the experimental results.

KEYWORDS: Pneumatic, Turbulent internal flow, Heat transfer, Simulation models

1. INTRODUCTION

Estimating steady flow characteristics of pneumatic pipe lines is important for designing pneumatic systems. However, it is impossible to express the flow characteristics of turbulent steady pneumatic flow with heat transfer from or to tubes in closed forms, even if a one-dimensional modelling scheme of the flow were acceptable. Trial and error is inevitable to derive related solutions. Many contributions to these fields have been reported as shown in the following examples. Humble *et al* [1] measureed average friction coefficients of air flowing through tubes for an over-all range of surface temperature from 297K to 1,700K. The data for low surface temperature agree fairly well with those for no heat addition. It was shown graphically that the difference between the data and the Kármán-Nikuradse correlation became wider as the surface temperature increased. Deissler [2] analysed the local Nusselt number in the entrance regions of tubes and parallel plates. The results of numerical computations were shown graphically for various flow conditions and they were compared with the experimental data in NASA. Sleicher and Tribus [3] solved the fundamental equations by the usual method of separation of variables and the local Nusselt numbers were expressed in the form of an infinite series of eigenfunctions for the case of uniform wall temperature and the case of uniform heat flux at

the wall. Benedict and Carlucci [4] presented the generalized Fanno tables and graphs for the adiabatic flow. Wartelle [5] proposed the approximate solutions represented by the simple equations and an approximation using a quarter ellipse. Notter and Sleicher's [6] equation solved the turbulent Graetz problem numerically for the lower eigenvalues and constants for Reynolds numbers in the range $10^4<Re<10^6$ and for Prandtl numbers in the range $0<Pr<10^4$. The calculated local Nusselt number for uniform wall temperature agreed well with the experimental data. Bandyopadhyay and Majumdar [7] reported the modelling of compressible flow with friction and heat transfer in a constant area pipe using the generalized fluid system simulation program (GFSSP) developed by the NASA Marshall Space Flight Center. The axial distributions of the pressure and Mach number were shown graphically for Fanno flow, Rayleigh flow and the case of combined friction and heat transfer. Satoh *et al* [8] presented approximate solutions to the critical pressure ratio for Fanno flow, and proposed a simulation model on MATLAB/Simulink® computing software assuming a constant friction coefficient. Gautier *et al* [9] presented experimental results obtained when characterising long pneumatic tubes according to the variable upstream pressure test and the constant upstream pressure test recommended under the ISO /FDIS 6358 standard. The effects of the up-stream pressure on the flow characteristics were examined experimentally. Hullender *et al* [10] presented the explicit equations to calculate the approximate mass velocity of compressible steady flow in pipes by making use of the empirical equations for the friction factor. A comparison of the mass velocity as a function of the inlet pressure for isothermal and adiabatic flow with laboratory data demonstrated very little difference in the graph. Shiraishi *et al* [11] presented simple methods to calculate approximate characteristics for the Fanno flow in considering the dependency of the friction factor on the Reynolds number on the MATLAB/Simulink®. The untility of the simulation was shown by comparing the calculations to the experimental results. Murayama *et al* [12] extended the simulation models given by [11] for a single pipe line to a model of serially connected pipes with different diameters. Urata [13] presented the flow rate equation for the subsonic Fanno flow in a circular tube. It was concluded that the relative difference of mass flow rates between Fanno and isothermal flows was less than 1% in most practical combinations of pressure, friction coefficient and pipe length-diameter ratio. Nakano *et al* [14] simplified the root finding process in the former model [11], [12] for Fanno flow on MATLAB/Simulink® by making use of the steady state characteristics of feedback control mechanisms. Chabane *et al* [15] proposed a novel analytical formulation of the mass flow rate in pneumatic pipes by taking into account the pipe friction factor and its dependency on the flow Reynolds number. It was pointed out that iterative procedures were still necessary to calculate the friction factor and the mass flow rate. Pneumatic systems are generally operated under different circumferential temperature and so the effects must be studied. Though many researches have been reported, simple and user-friendly models to simulate steady pneumatic internal flow taking account of effects of the pipe-wall temperature are not available. We intended to develop a new simple model to simulate pneumatic steady flow through tubes with wall friction and external heat transfer.

Symbols

c : Speed of sound, D : Inner diameter of tube, f : Friction factor, h : Heat transfer coefficient, L : Length of tube, M : Mach number, p : Pressure (Static), q_m : Mass flow rate, T : Temperature (Static), x : Axis coordinate, κ : Specific heat ratio, μ : Viscosity, ρ : Density

Subscripts

0 : Stagnation state, 1 : Upstream end of each region, 2 : Downstream end of each region,
e : Thermal entry region, F : Fanno flow region w : Wall

2. MATHEMATICAL MODEL

2.1. Fundamental equations

The following assumptions are made to construct the mathematical models of pneumatic internal flow through tubes. The flow is one dimensional, viscous, compressible and steady. Each tube is straight and its cross-sectional area is constant along the tube axis *x*. The viscous drag force on a wet surface is evaluated by the Fanning friction factor *f*. The wall temperature T_w is uniform and constant. The heat transfer from or to the tube wall is considered using Newton's law of cooling. From these conditions the following equations are deduced as shown in reference [16].

$$\frac{\mathrm{d}M^2}{M^2} = \frac{\kappa M^2\left(1+\frac{\kappa-1}{2}M^2\right)}{1-M^2}\frac{4f}{D}\mathrm{d}x + \frac{\left(1+\kappa M^2\right)\left(1+\frac{\kappa-1}{2}M^2\right)}{1-M^2}\frac{\mathrm{d}T_0}{T_0} \tag{1}$$

$$\frac{\mathrm{d}T_0}{T_w - T} = \frac{4h_w}{D\rho u c_p}\mathrm{d}x = \frac{4\mathrm{St}}{D}\mathrm{d}x \tag{2}$$

We adopted Chilton-Colburn's analogy to simplify the mathematical model. The Stanton number St is related to the Prandtl number Pr and the friction coefficient *f* by the analogy [17].

$$\mathrm{St} = \frac{f}{2\mathrm{Pr}^{2/3}} \tag{3}$$

Substituting Eq. (2) and Eq. (3) into Eq. (1), the following equation is obtained.

$$\frac{\mathrm{d}M^2}{M^2} = \frac{\kappa M^2\left[1+\frac{(\kappa-1)}{2}M^2\right]}{1-M^2}\frac{4f}{D}\mathrm{d}x + \frac{\left(1+\kappa M^2\right)}{1-M^2}\frac{\left(\frac{T_W}{T}-1\right)}{2\mathrm{Pr}^{2/3}}\frac{4f}{D}\mathrm{d}x \tag{4}$$

Neglecting the heat transfer, Eq. (4) reduces to the following Fanno flow equation.

$$\frac{\mathrm{d}M^2}{M^2} = \frac{\kappa M^2\left(1+\frac{\kappa-1}{2}M^2\right)}{1-M^2}\frac{4f}{D}\mathrm{d}x \tag{5}$$

2.2. Thermal entry region and its length

The hydrodynamic entry length for the turbulent internal flow is so short in comparison with the thermal entry length that we assume the hydro-dynamically fully developed turbulent velocity profile is already achieved at the inlet where the heat transfer starts. The total pneumatic line consists of the thermal entry region and the successive downstream region. In the former region, the air temperature approaches asymptotically to the constant wall temperature from the entering air temperature; and in the later region, the temperature difference between the wall and the inside air is negligible. Then we assumed that the heat transfer at the wall could be neglected in the later region, and the flow characteristics were represented as Fanno flows. The two serially connected regions and related state variables are shown in Fig. 1.

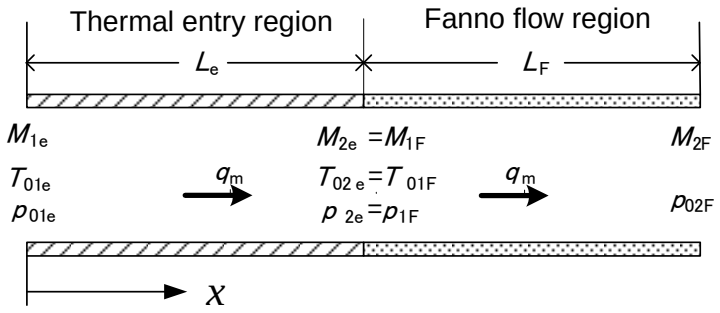

Figure 1. Two serially connected regions and related state variables

The dimensionless mixed-mean temperature $\theta_{\mathrm{m}} = (T_{\mathrm{w}} - T)/\left((T_{\mathrm{w}} - T_{1\mathrm{e}})\right)$ of the incompressible fluid flow in a circular tube with a constant wall temperature is presented in the form of infinite-series -solutions with the eigenvalues $\lambda_{\mathrm{n}}(\mathrm{Re})$ and the related functions $G_{\mathrm{n}}(\mathrm{Re})$. The first term in the series is dominant and so the higher terms can be neglected. The dimensionless temperature θ_{m} can be evaluated approximately by the following simple equations [5], [18].

$$\theta_m \cong 8\frac{G_0}{{\lambda_0}^2}\exp\left[-{\lambda_0}^2\frac{2(x/D)}{\mathrm{RePr}}\right] \tag{6}$$

where $\lambda_0(\mathrm{Re})$ and $G_0(\mathrm{Re})$ are given in the references.

In general, the Mach number *M* is smaller than about 0.3~0.4 at most in the entry region of the compressible internal flow through tubes. Equation (6) may be applied approximately to the air-flow in the thermal entry region discussed in this research. The length-mean Nusselt number $\mathrm{Nu_m}$ is obtained by a similar process.

$$\frac{\mathrm{Nu_m}}{\mathrm{Nu_\infty}} = \frac{\frac{1}{x^+}\int_0^{x^+}\mathrm{Nu_x}\,dx^+}{{\lambda_0}^2} = 1 + \frac{\mathrm{Re\,Pr}}{2{\lambda_0}^2(x/D)}\ln\frac{{\lambda_0}^2}{8G_0} = 1+\delta \tag{7}$$

The ratio $\mathrm{Nu_m}$ / $\mathrm{Nu_\infty}$ tends asymptotically to unity as $x \to \infty$. We defined the region in which δ is greater than 0.01 as the thermal entry region from the view-point of the thermal developing behaviour. Solving Eq. (7) for x, the thermal entry length L_{e} is expressed as follows.

$$\frac{L_{\mathrm{e}}}{D} \cong \frac{\mathrm{Re\,Pr}}{2\delta{\lambda_0}^2}\ln\frac{{\lambda_0}^2}{8G_0} \tag{8}$$

The length-mean dimensionless temperature Θ in the thermal entry region is obtained by integrating θ_{m} from x =0 to L_{e}.

$$\Theta = \frac{\int_0^{L_{\mathrm{e}}}\frac{8G_0}{{\lambda_0}^2}\exp\left(-{\lambda_0}^2\frac{2\,x/D}{\mathrm{Re\,Pr}}\right)dx}{L_{\mathrm{e}}} = \delta\frac{8G_0/{\lambda_0}^2}{\log_{\mathrm{e}}\left({\lambda_0}^2/8G_0\right)}\cdot\left[1-\left(8G_0/{\lambda_0}^2\right)^{1/\delta}\right] \tag{9}$$

Varying the Reynolds number from 20,000 to 200,000 changes $8G_0/{\lambda_0}^2$ from 0.959 to 0.978. We chose the approximate value 0.975 which is the value of $8G_0/{\lambda_0}^2$ at Re=100,000. As a result, the length-mean dimensionless temperature Θ is given as:

$$\Theta \cong 0.35 \tag{10}$$

The effect of the Reynolds number on thermal entry length L_{e} is not very strong. We evaluate the length L_{e} by substituting constants for Re = 100,000 in Eq. (8).

$$L_{\mathrm{e}}=242D \tag{11}$$

We replaced the temperature *T* in Eq. (4) with a constant temperature T_{r} for the sake of mathematical simplification derive an approximate solution. The constant temperature T_{r} is related to the length-mean dimensionless temperature Θ as follows

$$T_{\mathrm{r}} = (1-\Theta)T_{\mathrm{w}} - \Theta T_{1\mathrm{e}} = 0.65T_{\mathrm{w}} - 0.35T_{1\mathrm{e}} \tag{12}$$

Then, Eq. (4) was reduced to the next form which could be easily integrated.

$$\frac{\mathrm{d}M^2}{M^2} = \frac{\kappa M^2\left(1+\frac{\kappa-1}{2}M^2\right)+(1+\kappa M^2)\beta}{1-M^2}\frac{4f_e}{D}\mathrm{d}x \tag{13}$$

where $\beta = \frac{\frac{T_{\mathrm{w}}}{T_{\mathrm{r}}}-1}{2Pr^{2/3}}$.

The constant β is positive in the heating process, and negative in the cooling process.

3. MATLAB/SIMULINK MODELS

3.1. Fanno flow region model

The Simulink model of the Fanno flow is the same as the model developed in our former report [14]. The Reynolds number in the Fanno flow region is:

$$\mathrm{Re_F} = \frac{DcM}{\nu} = \frac{4}{\pi D \mu_\mathrm{F}} q_\mathrm{m} = \frac{4}{\pi D \mu_\mathrm{F}} \frac{\pi D^2}{4} \sqrt{\frac{\kappa}{RT_{01\mathrm{F}}}} p_{1\mathrm{F}} M_{1\mathrm{F}} \sqrt{\frac{2+(\kappa-1){M_{1\mathrm{F}}}^2}{2}} \tag{14}$$

The friction factor f_RF is given as the function of $\mathrm{Re_f}$ by Blasius formula and Filonenko's equation for a wide Reynolds number range [14].

$$f_\mathrm{RF} = g(\mathrm{Re_F}) = G(p_{1\mathrm{F}}, M_{1\mathrm{F}}) \tag{15}$$

On the other hand, the friction factor f_F in the Fanno flow region is derived using the moment transfer theory as a function of the Mach numbers at both ends of the region.

$$f_\mathrm{F} = \frac{D}{4L_\mathrm{F}} \left\{ \frac{1}{\kappa {M_{1\mathrm{F}}}^2} - \frac{1}{\kappa {M_{2\mathrm{F}}}^2} + \frac{\kappa+1}{2\kappa} \ln \left[\frac{{M_{1\mathrm{F}}}^2}{{M_{2\mathrm{F}}}^2} \frac{2+(\kappa-1){M_{2\mathrm{F}}}^2}{2+(\kappa-1){M_{1\mathrm{F}}}^2} \right] \right\}$$
$$= F_\mathrm{F}(M_{1\mathrm{F}}) - F_\mathrm{F}(M_{2\mathrm{F}}) \tag{16}$$

Friction factors f_RF and f_F must be equal.

$$f_\mathrm{RF} - f_\mathrm{F} = 0 \tag{17}$$

Equations (15), (16) and (17) are solved as the steady-state response of the Simulink model shown in Fig. 2 for the given inputs $p_{1\mathrm{F}}$ and $M_{1\mathrm{F}}$ [14].

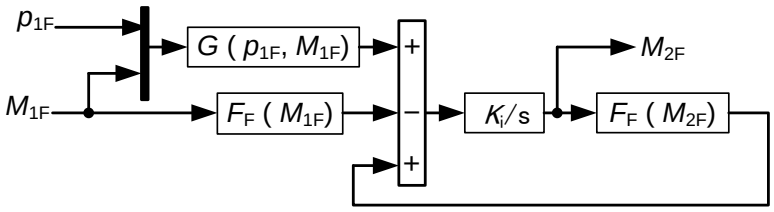

Figure 2. Basic Simulink model in Fanno flow region

The static pressure ratio between the inlet and outlet of the Fanno flow region is:

$$\frac{p_{2\mathrm{F}}}{p_{1\mathrm{F}}} = \frac{M_{1\mathrm{F}}}{M_{2\mathrm{F}}} \sqrt{\frac{2+(\kappa-1){M_{1\mathrm{F}}}^2}{2+(\kappa-1){M_{2\mathrm{F}}}^2}} \tag{18}$$

3.2. Thermal entry region model

The basic Simulink model of the thermal entry region is obtained by a similar mathematical procedure in the case of the Fanno flow region. The Reynolds number and related friction factor in this entry region are written as follows:

$$\mathrm{Re_e} = \frac{4}{\pi D \mu_\mathrm{e}} \frac{\pi D^2}{4} \sqrt{\frac{\kappa}{RT_{01\mathrm{e}}}} p_{1\mathrm{e}} M_{1\mathrm{e}} \sqrt{\frac{2+(\kappa-1){M_{1\mathrm{e}}}^2}{2}} \tag{19}$$

$$f_\mathrm{Re} = g(\mathrm{Re_e}) = G(p_{1\mathrm{e}}, M_{1\mathrm{e}}) \tag{20}$$

Eq. (13) is rearranged by factorization.

$$\frac{4f_{\mathrm{e}}}{D}\mathrm{d}x = \frac{2}{\kappa(\kappa-1)}\frac{(1-M^2)}{M^2(M^2-z_1)(M^2-z_2)}\mathrm{d}M^2 \tag{21}$$

The integral of Eq. (21) is:

$$f_{\mathrm{e}} = \frac{D}{L_{\mathrm{e}}}\frac{2}{\kappa(\kappa-1)}\ln\left[\left(\frac{M_{2\mathrm{e}}{}^2}{M_{1\mathrm{e}}{}^2}\right)^{a_0}\left(\frac{M_{2\mathrm{e}}{}^2-z_1}{M_{1\mathrm{e}}{}^2-z_1}\right)^{a_1}\left(\frac{M_{2\mathrm{e}}{}^2-z_2}{M_{1\mathrm{e}}{}^2-z_2}\right)^{a_2}\right]$$

$$= F_{\mathrm{e}}(M_{1\mathrm{e}}) - F_{\mathrm{e}}(M_{2\mathrm{e}}) \tag{22}$$

Constants z_1, z_2, a_0, a_1, a_2 and the function $F_{\mathrm{e}}(M)$ are shown as follows.

$$b = \frac{1+\beta}{\kappa-1} \qquad c = \frac{2\beta}{\kappa(\kappa-1)} \qquad z_1 = -b+\sqrt{b^2-c} \qquad z_2 = -b-\sqrt{b^2-c}$$

$$a_0 = \frac{1}{z_1 z_2} \qquad a_1 = \frac{z_2(z_1-1)}{z_1 z_2(z_2-z_1)} \qquad a_2 = \frac{z_1(z_2-1)}{z_1 z_2(z_1-z_2)}$$

$$F_{\mathrm{e}}(M) = -\frac{D}{2L_{\mathrm{e}}}\frac{1}{\kappa(\kappa-1)}[2a_0\ln(M) + a_1\ln(M^2-z_1) + a_2\ln(M^2-z_2)]$$

These two friction factors must be equal.

$$f_{\mathrm{Re}} - f_{\mathrm{e}} = 0 \tag{23}$$

Equations (20), (22) and (23) can be solved by making use of the Simulink model shown in Fig. 3 [14].

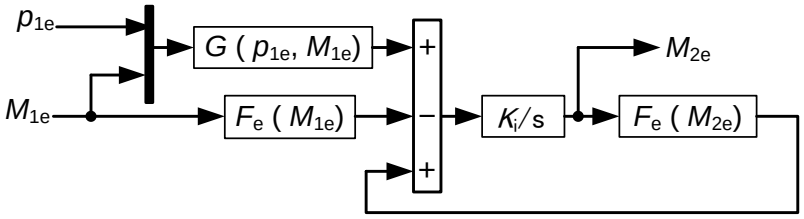

Figure 3. Basic Simulink model in thermal entry region

The static pressure ratio and the static temperature ratio between the inlet and outlet of the thermal entry region are written as follows.

$$\frac{p_{2\mathrm{e}}}{p_{1\mathrm{e}}} = \left(\frac{M_{1\mathrm{e}}{}^2-z_1}{M_{2\mathrm{e}}{}^2-z_1}\right)^{\frac{B}{\kappa-1}}\left(\frac{M_{1\mathrm{e}}{}^2-z_2}{M_{2\mathrm{e}}{}^2-z_2}\right)^{\frac{C}{\kappa-1}} \tag{24}$$

$$\frac{T_{2\mathrm{e}}}{T_{1\mathrm{e}}} = \left(\frac{M_{2\mathrm{e}}}{M_{1\mathrm{e}}}\right)^2\left(\frac{p_{2\mathrm{e}}}{p_{1\mathrm{e}}}\right)^2 \tag{25}$$

where,

$$B = \frac{d_1 z_1 z_2(1+kz_1) - d_2 z_1(1+kz_2) + d_3(1+kz_2)}{(z_1-z_2)(1+kz_1)(1+kz_2)} \qquad C = \frac{-d_1 z_1 z_2(1+kz_2) + d_2 z_2(1+kz_1) - d_3(1+kz_1)}{(z_1-z_2)(1+kz_1)(1+kz_2)}$$

$$d_1 = k(k-1) \qquad d_2 = 1+k(k-1)(z_1+z_2) \qquad d_3 = 1+k(k-1)z_1 z_2$$

3.3. Total serially connected model

The thermal entry region model and the Fanno flow region model are connected directly so as to fulfil the common end conditions at the junction as follows.

$$L = L_{\mathrm{e}} + L_{\mathrm{F}} \tag{26}$$

The common mass flow rate is given by

$$q_{\mathrm{m}} = \frac{\pi D^2}{4}\sqrt{\frac{\kappa}{RT_{01}}}p_1\sqrt{1+\frac{(\kappa-1)}{2}M_1^2}M_1 \tag{27}$$

$$M_{2\mathrm{e}} = M_{1\mathrm{F}} \tag{28}$$

$$p_{2\mathrm{e}} = p_{1\mathrm{F}} \tag{29}$$

$$T_{02\mathrm{e}} = T_{01\mathrm{F}} \tag{30}$$

The total Simulink model is shown in Fig. 4. The system constants D, L, L_{e}, θ, $T_{01\mathrm{e}}$, T_{w} and the physical constants are given in the m-file. The Mach number $M_{1\mathrm{e}}$ is the consolidated input to the total model. The initial value of the integrator in each region model is set. The mass flow rate q_{m}, the total pressure p_{o2F}, and the Mach number at the outlet of the Fanno flow region, are obtained as outputs of the model. The details of each block is shown in Appendix.

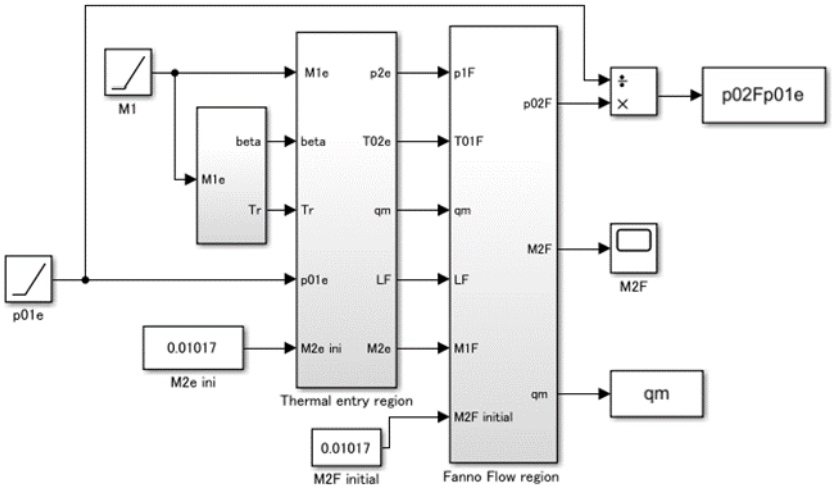

Figure 4. Total Simulink model

4. EXPERIMENTAL VALIDATION OF THE SIMULATION MODEL

4.1. Experimental apparatus

The experimental circuit is shown in Fig. 5, and this circuit is arranged according to ISO 6358-2.

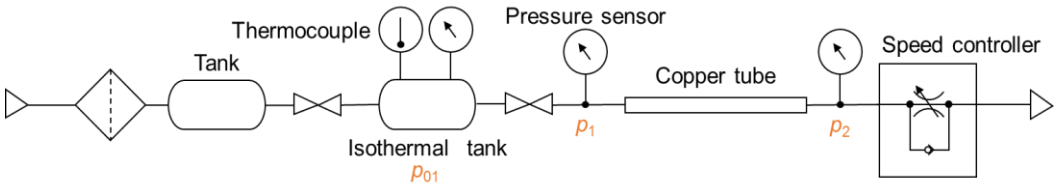

Figure 5. Experiment circuit

The mass flow rate was calculated from the pressure change of the isothermal tank. Commercial copper tube was used at the test section. The inner diameters of both sides of the tube were measured using pin gauge. The results were shown in Table 1. The average of the measured diameters was adopted for the numerical calculation of the simulation model.

Table 1. Inner diameters of cooper tube

Nominal inner diameter *D*	Measured *D* inlet	Measured *D* outlet
2 [mm]	2.025 [mm]	2.025 [mm]
4 [mm]	3.900 [mm]	3.925 [mm]

A water jacket was used to cool and warm the copper tube as shown in Fig. 6 and Photo 1. The copper tube was inserted in a heat-resistant vinyl chloride pipe, and cool or warm water was filled up between the both tubes. We covered the heat resistant vinyl chloride pipe with thermal insulation material to maintain the water temperature. The wall temperature was measured using thermocouples.

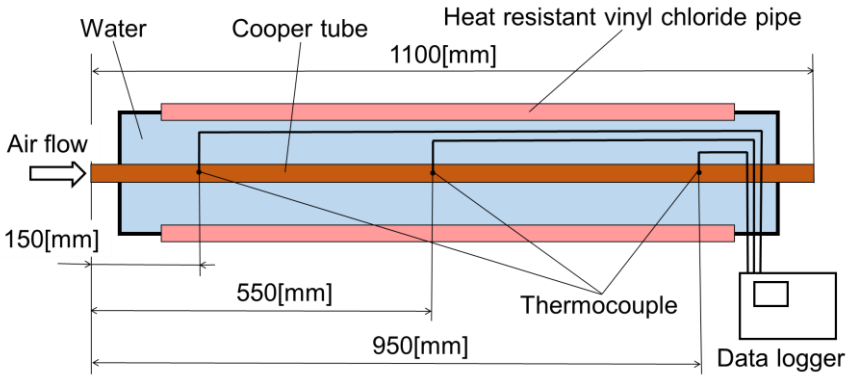

Figure 6. Arrangement of the water jacket for heating and cooling the copper tube

Photo 1. The heat-resistant vinyl chloride pipe covered with thermal insulation material

4.2. Experimental procedure

Experiments were performed as per the following steps.

1. Set the speed controller at the adjustmenting position and close the outlet valve of the isothermal tank
2. Select the upstream side pressure level P_{test} to be tested.
3. Charge the isothermal tank up with air to a pressure higher than P_{test}.
4. Close the inlet valve of the isothermal tank.
5. Open the outlet valve of the isothermal tank.
6. Measure the isothermal tank pressure p_{01}, the inlet pressure p_1, and outlet pressure p_2, continuously until the inlet pressure p_1 decreases to less than P_{test}.
7. Close the outlet valve of the isothermal tank.
8. Return to Step 1 and change the position of the speed controller and the pressure level P_{test}.
9. Repeat each step.

The mass flow rate q_m was calculated from the measured time records of p_{01} at intervals in which p_1 nearly crossed the level of P_{test}.

4.3. Experimental results

The experimental results and the simulation results are shown in Figs. 7 and 8. The experimental results are the average value of measurements repeated three times and are shown by marks, while the simulation results are shown with solid lines. Also, they are colour-coded for each wall temperature. The blue, black and red correspond to 276K, 298K and 333K respectively.

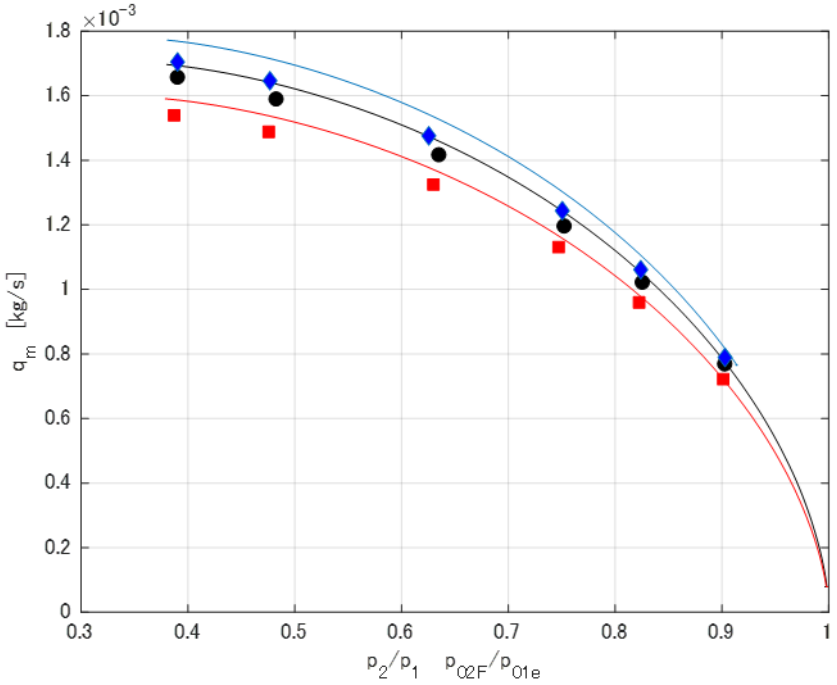

Figure 7. Comparison of calculated and experimental results

D=2.025 mm, L=1.1 m, p_1=0.6 MPa, T_{01e}=293 K

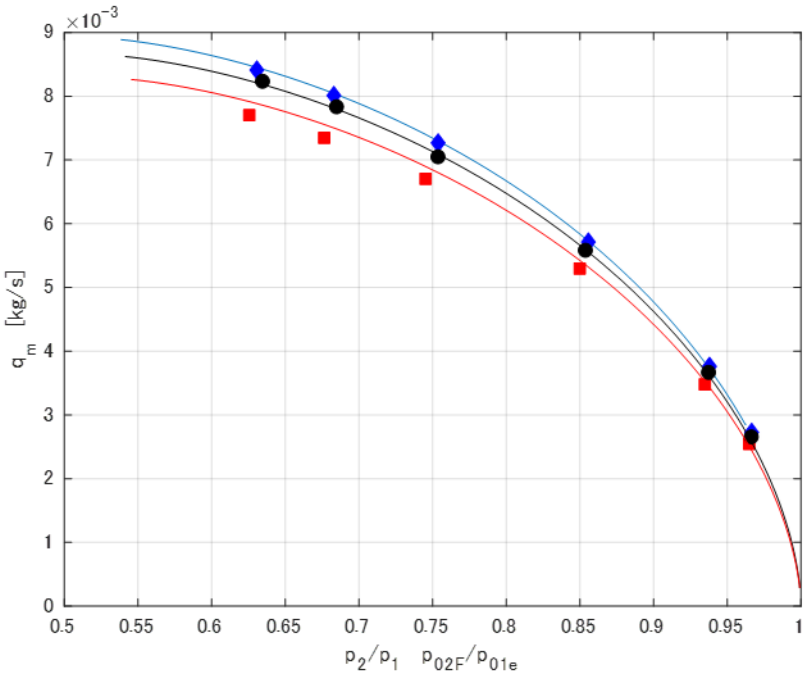

Figure 8. Comparison of calculated and experimental results
D=3.913 mm, L=1.1 m, p_1=0.6 MPa, T_{01e}=293 K

Although the simulation results were slightly different from the experimental results, the tendency of the thermal effects has been qualitatively demonstrated and the simulation model may be practically useful in predicting flow characteristics.

5 CONCLUSION

It was confirmed through comparison with experimental results that the newly developed simulation model for pneumatic steady flow through tubes with wall friction and external heat transfer could predict the characteristics of the flow to the extent practically acceptable. In this model, we treated the heat transfer effects in the thermal entry region as a consolidated parameter system. That approximation worked well here, but it might be necessary to improve the accuracy of the simulation to consider distributed heat transfer effects in future.

REFERENCE

[1] Humble, L. V., Lowdermilk W. H., and Desmon L. G.: Measurements of average heat-transfer and friction coefficients for subsonic flow of air in smooth tubes at high surface and fluid temperatures, NACA Report 1020, Washington, USA, 1951, pp. 343-357.

[2] Deissler, R. G.: Turbulent heat transfer and friction in the entrance regions of smooth passages, Trans. ASME, Nov. 1955, pp. 1221-1233.

[3] Sleicher, Jr., C. A. and Tribus, M.: Heat transfer in a pipe with turbulent flow and arbitrary wall-temperature distribution, Trans. ASME, May, 1957, pp.789-797.

[4] Benedict, R. P. and Carlucci, N. A., Flow with losses, Trans. ASME, J of Basic Eng. January 1965,pp.37-49.

[5] Notter, R. H. and Sleicher, C. A.: A solution to the turbulent Graetz problem-III Fully developed and entry region heat transfer rates, Chemical Engineering Science, Ver. 22, 1972, pp. 2073-2093.

[6] Wartelle, C., Caractéristiques de débit des appareils à fluids compressibles, Les Mémoires Techniques du CETIM, n°13, September 1972, pp.1-46
[7] Bandyopadhyay, A. and Majumdar, A.: Modeling of compressible flow with friction and heat transfer using the generalized fluid system simulation program (GFSSP), TFAWS, NASA, Sept. 2007, pp.1-14
[8] Satoh, K., Kawakami, Y., and Nakano, K.: Estimation of a critical pressure ratio of a pneumatic pipe-line and its simulation, Proc. 7th JFPS Inte. Symp. On Fluid Power, Toyama, Japan, 2008, pp.413-417.
[9] Gautier, D., Chabane, S., Sesmat, S., and Hubert, D.: Pneumatic pipe Line: Experimental approach, CETIM report, France 2010, pp. 1-9
[10] Hullender, D., Woods, R. and Yi-Wei Huang: Single phase compressible steady flow in pipes, Trans. ASME J. Fluids Eng. January 2010 vol. 132, pp. 014502-1-014502-4
[11] Shiraishi, T., Murayama, E., Kawakami, Y., and Nakano, K.: Approximate simulation of pneumatic steady flow characteristics in tubes with friction, Proc. 8th JFPS Int. Sym. On Fluid Power, Okinawa, JAPAN, 2011, pp. 242-247
[12] Murayama, E., Kobori, S., Kawakami, Y., and Nakano, K.: Simulation on Steady Pneumatic Flow in Tube, FLUCOME, Nara, Japan, OS3-04-2. 2013, pp. 1-7
[13] Urata, E., A flow rate equation for subsonic Fanno flow, Proc IMechE, Part C: J Mechanical Engineering Science 2013; 227(12): 2724–2729.
[14] Nakano, K., Murayama, E., and Kawakami, Y.: On simplifications of simulation models for pneumatic turbulent flows through tubes, 9th JFPS Inter. Sym. Matsue, Japan, 2014, pp.702-707.
[15] Chabane, S., Sesmat, S., Hubert, D., Gautier, D., Wartelle, C., and Bideaux, E., Reynolds number–dependent mass flow rate calculation for pneumatic pipes, Proc IMechE Part I: J Systems and Control Engineering 2015 Vol. 229(5) 419–428.
[16] Shapiro, A. H.: The Dynamics and thermodynamics of compressible fluid flow, Ronald Press, 1954, Vol.I, p.230.
[17] Bird, R. B., Stewart, W. E., and Lightfoot, E. N.: Transport Phenomena, Wiley & Sons, 1960, p. 382, p.401.
[18] Kays, W., Crawford, M., and Weigand, B.: Convective and Mass Transfer, 4th ed. McGraw-Hill, 2005

Appendix

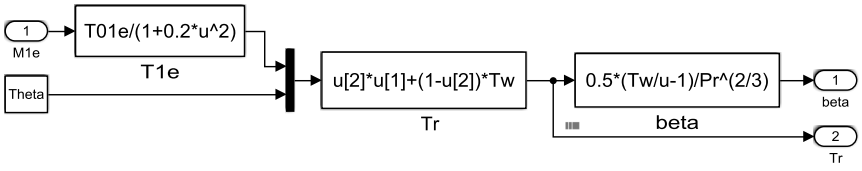

Figure A.1 Beta and Tr of Simulink model

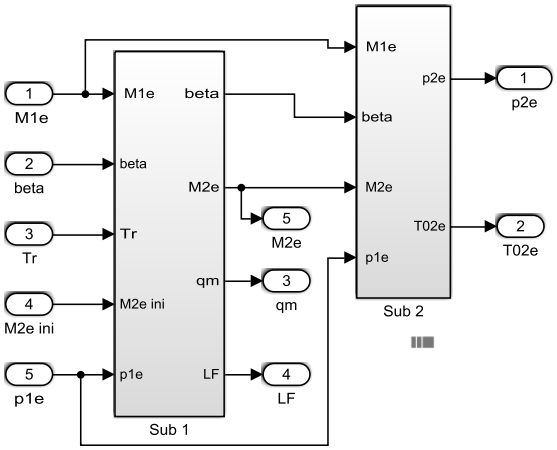

Figure A.2 Thermal entry region of Simulink model

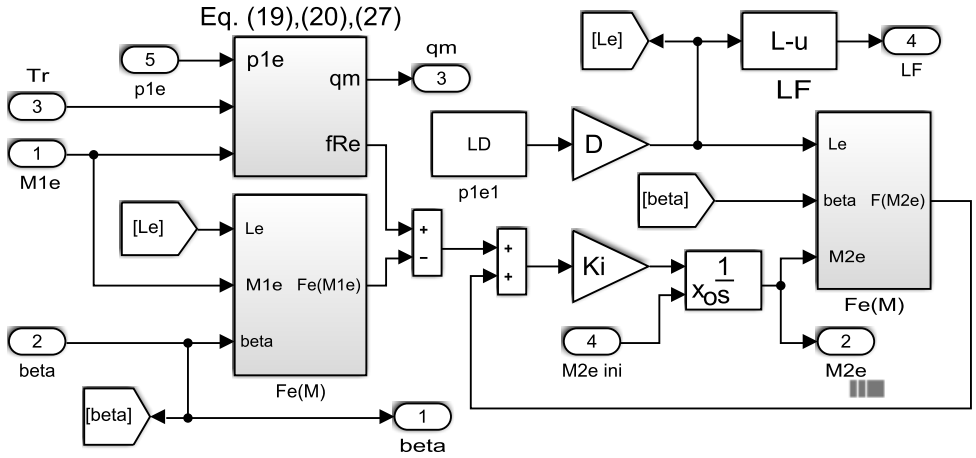

Figure A.3 Sub 1 of Simulink model

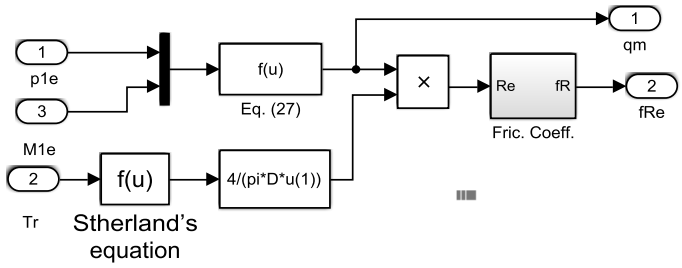

Figure A.4 q_m and fRe of Simulink model

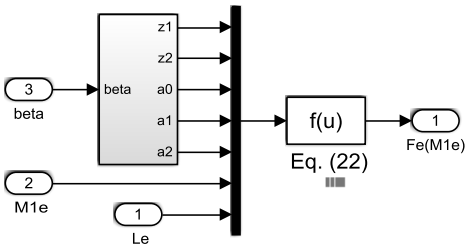

Figure A.5 Fe(M1e) of Simulink model

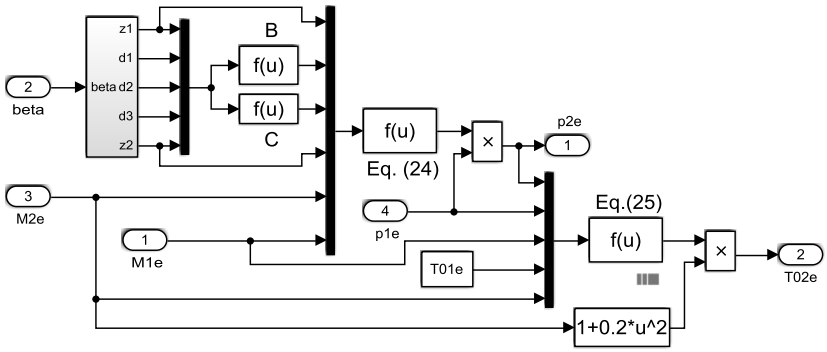

Figure A.6 Sub 2 of Simulink model

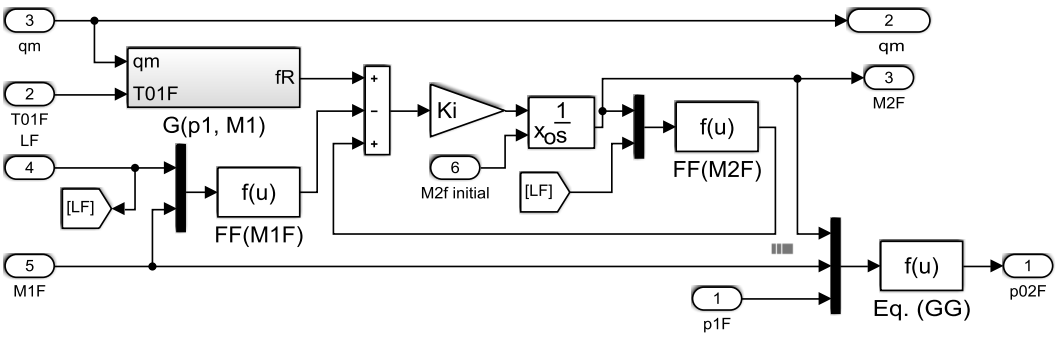

Figure A.7 Fanno flow region of Simulink model

DATA CORRELATION MODEL FOR HYDRAULIC FLUID FILTER CONDITION MONITORING

Anton Jokinen[1], Olof Calonius[1], Jagan Gorle[2], Matti Pietola[1]
[1] Aalto University, Department of Mechanical Engineering,
Espoo, Finland
[2] Parker Hannifin, Hydraulic and Industrial Process Filtration EMEA,
Urjala, Finland
anton.jokinen@aalto.fi

ABSTRACT

In fluid power systems, one of the most common causes of failure is contamination of the hydraulic fluid. Without filtering the fluid gets contaminated with harmful particles over time, which will cause excessive wear of components or even block motion of parts in flow control valves. In order to avoid machine downtime, it is important to monitor that adequate technical performance level of the fluid is maintained at all times.

This study contributes to condition-based maintenance of hydraulic fluid filter units by establishing a correlation equation, based on comprehensive laboratory tests and incorporated in a simulation model, relating the pressure drop over the filter unit with the main variables describing the operating conditions of the fluid system as well as with filter operating time.

The paper describes how the correlation equation and the simulation model was constructed. The results indicate that good correlation was obtained (R-square value 0.98) with the constructed equation between the physical variables and the temporal development of the pressure drop over the filter. The model can be used as a building block for a smart filter unit that can predict its lifetime.

KEYWORDS: hydraulic fluid filter, correlation model, condition monitoring

1. INTRODUCTION

In fluid power systems, one of the most common causes of failure is contamination of the hydraulic fluid [1]. In addition to its main function, i.e., to transfer energy, the fluid acts as a lubricant between moving parts in the components, enabling control of friction, wear and operating temperature.

In order to avoid machine downtime and loss of production, it is important to maintain adequate technical performance level of the fluid at all times. This is done by filtering, without which the fluid gets contaminated with harmful particles over time. Excessive concentration of particles in the fluid will cause excessive wear of components or can even block motion of parts in flow control valves. Wear can also cause insufficient efficiency in pumps, or their failure. Jammed parts in control valves can cause unreliable and erratic motion in actuators. These potential detrimental effects stress the importance of maintenance of fluid filter units.

Filter elements are usually replaced according to pre-defined time-schedules, but this is inefficient as the maintenance actions are not based on the actual time-history of the filter unit and the fluid system. Time-based

maintenance can either lead to premature replacement of filters, or lead to excessive contamination levels in the fluid due to unforeseen sudden increase of particle load during the presumed service period. Condition-based maintenance of filter elements can be made possible by continuously measuring the pressure drop over the filter element and using the measured value in a filter model to predict the remaining lifetime of the element.

Filtering can also play an important role in assessing ship machinery condition (e.g., the thruster gear run condition), as wear particle concentration rate is also influenced by the removal rate of wear particles from the lubrication system. [2, 3]

Modelling the pressure drop associated with fluid flow through fibrous or porous media have been presented by several researchers over the years. However, the studies can be restricted to estimating pressure drop due to flow though clean fibrous filters [4, 5], or flow of air through porous material [6, 7]. This stresses the importance of filter testing and modelling involving contaminated fluid and gradual pressure build-up over the cartridge due to contamination retention. While the research on contamination retention in hydraulic filtration is not as extensive as in, say, industrial air filtration, in [8] a study was conducted for predicting the service life of a hydraulic filter based on the operating conditions. In the mentioned study, a model was developed for monitoring the condition of a hydraulic return line filter in a hydraulic servo system of a hot strip mill. The study presented a methodology for taking into account the influence of flow rate on the pressure difference over the filter by using down-stream pressure measurement instead of utilizing expensive flow meters. However, temperature measurement was not implemented, and thus the study did not take the influence of viscosity on the pressure difference over the filter into account.

For this study, comprehensive laboratory tests have been made in order to produce filtration performance data relating the effect of flow rate, contaminant particle concentration, and fluid temperature to the pressure drop measured over the filter element. [9]

In this paper, the laboratory test results will be analysed and mathematical correlation expressions will be derived from the experimental data giving estimates for the pressure drop over the filter as a function of the operating conditions and service time. While these mathematical correlation expressions represent the near-term goal, the aim of the future research is to develop Internet-of-things (IoT) enabled, smart filtering connected to the overall computerized condition monitoring solution in the machine system, e.g., in a ship. The purpose is to be able to compare filter performance data that have been recorded in the machine system with the estimate given by the mathematical expressions, in order to detect the operating state of the filter cartridge and to predict its remaining lifetime by producing an estimate (trend) of how the pressure drop will evolve over time.

2. METHODS

The study to create a correlation model for the pressure drop across a filter element was twofold: perform laboratory tests at different fluid conditions, and develop a model based on said laboratory tests that could predict the pressure drop based on the different conditions. Section 2.1. examines the laboratory tests that were carried out, followed by the explanation of the succeeded modelling procedure in Section 2.2.

2.1. Experimental

The experimental part consisted of measuring the filter pressure drop at different oil conditions. For this purpose, a test bench with multiple sensors monitoring the different conditions was utilized. The filter type used in the experiments was a 5 µm rated commercial filter with glass fibre media that has an effective surface area of 0.154 m^2 through 57 pleats. The oil that was used was the standard ISO VG 32 hydraulic oil. [9]

The different oil conditions considered for this study were the oil flow rate, temperature, and gravimetric contamination level. For adjusting the gravimetric contamination level, the fluid was subjected to ISO medium test dust (ISO12103-1-A3) at different rates resulting in four different contamination levels at 2 mg/l, 5 mg/l, 8

mg/l and 10 mg/l. The flow rates were set to 40 l/min, 80 l/min and 120 l/min, and the fluid temperatures were adjusted to 30 °C, 40 °C, 50 °C, and 60 °C, [9]. Figure 1 illustrates the types of effect that the different oil conditions have on the pressure drop development over time. The different experiments were carried out until a pressure drop of 5 bar had been reached, and the sampling period used for the measurements during each experiment was two seconds. As a summary, the tests included four different contamination levels, three different flow rates, and four different fluid temperatures, resulting in 48 experiments in total. The experimental set-up was described in more detail in [9].

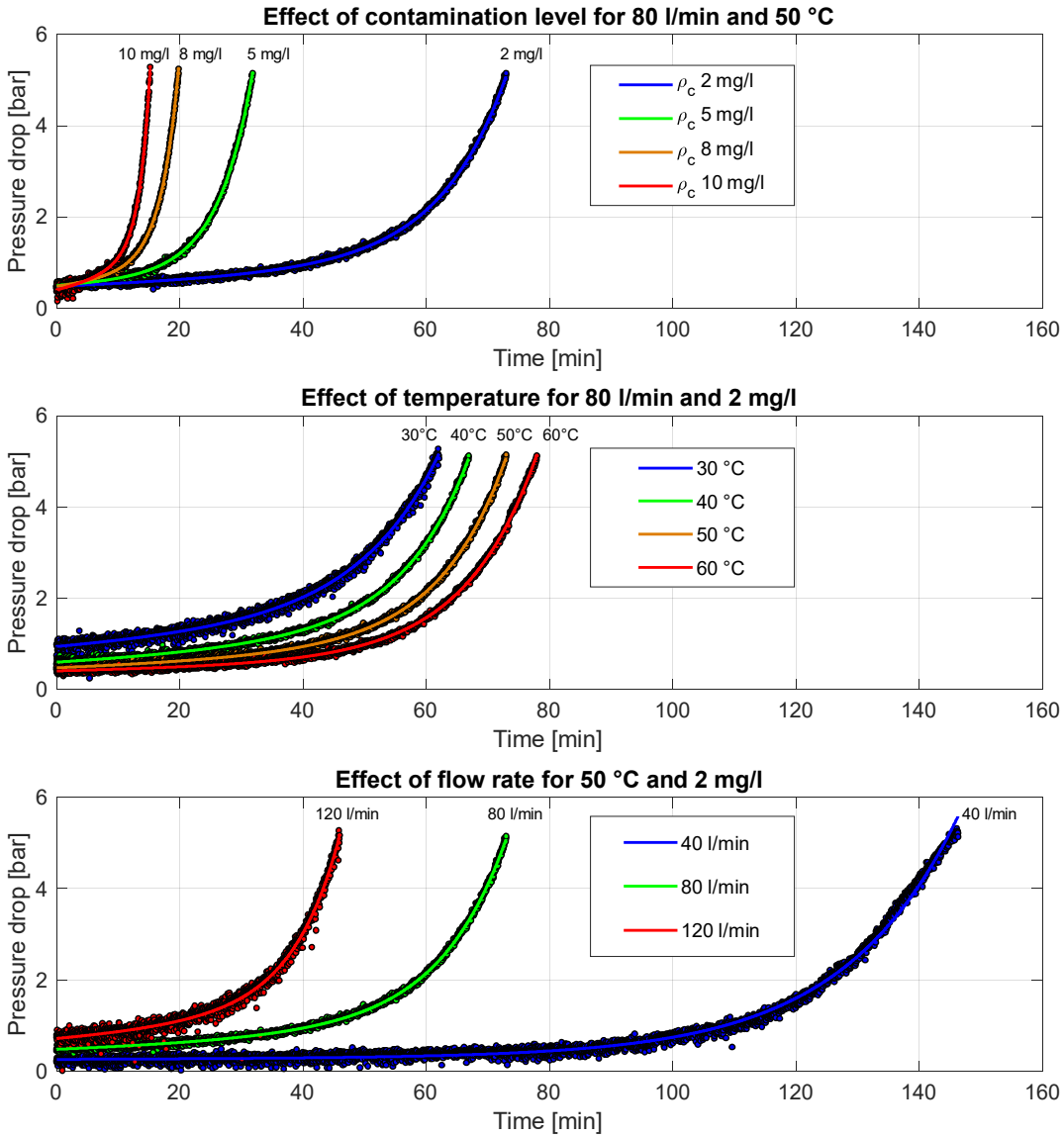

Figure 1. Examples of how the pressure drop developed when operation conditions were changed.

2.2. Model description

The main goal of this study was to establish a single model that will describe the development of the pressure drop across the filter element throughout its entire service life. Based on the experimental data, the model will consist of an equation of physical variables:

$$\Delta p = f(t, q_V, T, \rho_c), \tag{1}$$

where t is time, q_V is volumetric flow rate, T is temperature, and ρ_c is mass concentration of the contaminant i.e. the gravimetric contamination level. The approach used for constructing the model was regression analysis.

2.2.1. Equation for ∆p

The first objective in the regression analysis was to find a general form for the equation (1) through curve fitting. The curve fitting was performed in the MATLAB environment for all the different 48 experiments, with the pressure drop Δp as the output and time t as the only initial input. Different models were experimented with, but the best fitting was discovered to be with an exponential function that has two exponential terms. The method utilized for finding the exponential fitting was the nonlinear least squares method, which is characterized by

$$\min_{\beta} \sum_{i=1}^{n} r_i(x)^2 = r_1(x)^2 + r_2(x)^2 + \ldots + r_n(x)^2, \quad (2)$$

where the function $r_i(x)$ is

$$r_i(x) = y_i - f(x_i, \beta), \quad (3)$$

where y_i is the sample, which is Δp in our case, and $f(x_i, \beta)$ is the corresponding fitting function value for the value x_i of the independent variable with a parametrization vector β. The intention was to minimize (2) by applying the Trust-Region search algorithm, which is especially suited for solving nonlinear problems. [10,11]

As the best fitting was found to be with an exponential function that has two exponential terms, the equation for Δp could now be expressed as

$$\Delta p(t) = ae^{bt} + ce^{dt}, \quad (4)$$

where a, b, c and d are coefficients that vary at different flow rates, temperatures and contamination levels. This exponential fitting for Δp resulted in an R^2 value of over 0.99 for all but one of the original 48 experimental results.

The fitted curve includes certain observable trends that are typical for exponential functions. The curve is characterized by a low and steady increase in Δp at the beginning along the time-axis, which can also be seen from Figure 1 that showcases the measurement data. After the initial steady increase, the rate of change for Δp increases markedly towards the end of the experiment, Figure 1. However, the region of increased rate of change for Δp is not as apparent at lower temperatures, i.e. at higher fluid viscosities.

The next modelling objective was to present the coefficients a, b, c and d in (4) with the help of the physical variables q_V, T and ρ_c. This was initially approached by the means of manual search, e.g. keeping some physical variables constant, such as flow rate and temperature, and varying a single variable, such as contamination level, and determining whether it had any effect on the coefficients a, b, c or d. The coefficients a and c were found to be mainly influenced by the fluid flow rate and temperature, as their sum represents the pressure drop at time instant zero. Therefore, the coefficients a and c can be expressed as

$$a + c = \Delta p(0) = \Delta p_0, \quad (5)$$

where the initial pressure drop across the filter element at time instant zero is denoted as Δp_0. This initial pressure drop occurs when the filter is still “clean” and has not been subjected to a stream of particles. This is also depicted in the uppermost graph in Figure 1, where the initial pressure drops are similar despite the differences in the gravimetric contamination level.

The initial pressure drop could be expressed with the help of the Ergun equation (1952), which is an extension of the Darcy’s law (1856) for a pressure drop for a fluid flowing through a packed bed. The Ergun equation for a pressure drop is given as [12]

$$\Delta p = \frac{150\mu(1-\epsilon)^2 v_s L}{d_p^2 \epsilon^3} + \frac{1.75(1-\epsilon)\rho v_s^2 L}{d_p \epsilon^3}, \quad (6)$$

where μ is the dynamic viscosity, ϵ is the porosity of the bed, v_s is the superficial velocity of the fluid, L is the length of the bed, and d_p is the particle diameter. According to the Ergun equation, the effect of fluid viscosity is linear, and the effect of fluid velocity is quadratic for the pressure drop across a packed bed. For our modelling purposes, the initial pressure drop Δp_0 for different cases was obtained by linear interpolation from the measurement data, as a function of flow rate and temperature.

Despite the initial pressure drop being independent of the fluid contamination level, the coefficient c was perceived to have a decreasing trend versus higher contamination levels, though no such trend was observed with the coefficient a. An example of this is demonstrated in Figure 2, where the contamination level is varied but the flow rate and temperature are kept constant at 120 l/min and 50 °C, respectively. This trend was observed at almost all different sets of a fixed flow rate and temperature.

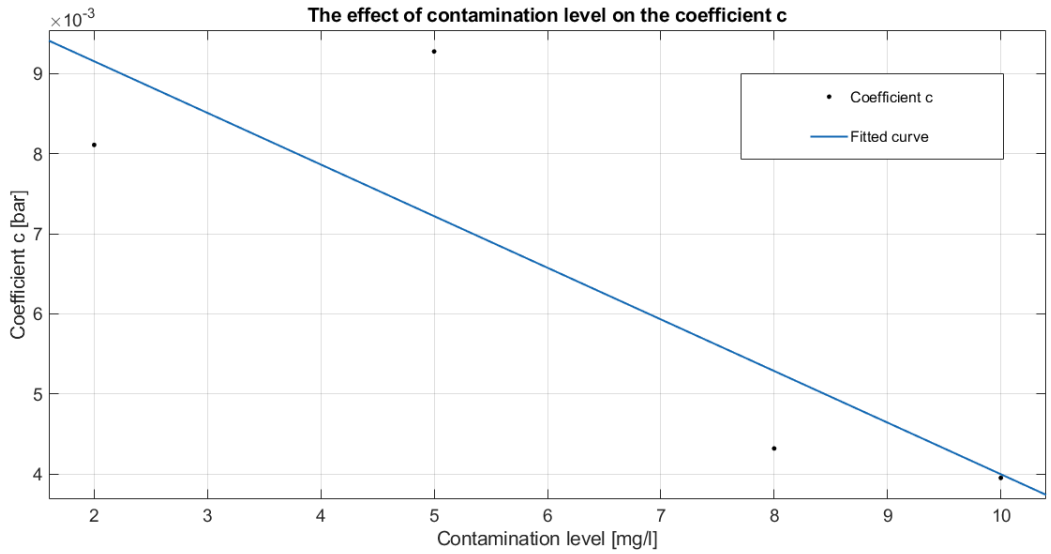

Figure 2. The coefficient c at different contamination levels, while the flow rate and temperature are kept constant (at 120 l/min, 50 °C)

The flow rate and temperature were varied separately as well, to determine how much they affected the coefficient c. After doing this inspection manually, a general form for the coefficient c was approximated as:

$$c = \left(x_1 q_v \rho_c + x_2 q_v^{x_3}\right)\nu + x_4 q_v^{x_5} \rho_c + x_6 q_v, \tag{7}$$

where x_1 through x_6 are constants and ν is the fluid kinematic viscosity. Note that this equation uses fluid viscosity as one of its variables rather than temperature. The relationship between fluid viscosity and temperature for the ISO VG 32 oil kinematic viscosity (in cSt) was given in [9] as:

$$\nu = 300.98 T^{-0.585}, \tag{8}$$

where the temperature T is expressed in °C. Now that a general form for c had been acquired, the coefficient a could be expressed with the help of (5):

$$a = \Delta p_0 - c = \Delta p_0 - \left(\left(x_1 q_v \rho_c + x_2 q_v^{x_3}\right)\nu + x_4 q_v^{x_5} \rho_c + x_6 q_v\right), \tag{9}$$

A similar approach was taken for the coefficients b and d in (4), to approximate how the different physical variables affected them. The effect of contamination level was found to be very linear for both of the coefficients. The temperature was perceived to have little to no effect, however the effect of flow rate was noticeably linear and similar across different contamination levels. Figure 3 depicts an example of the effect of contamination level and flow rate on the coefficient b.

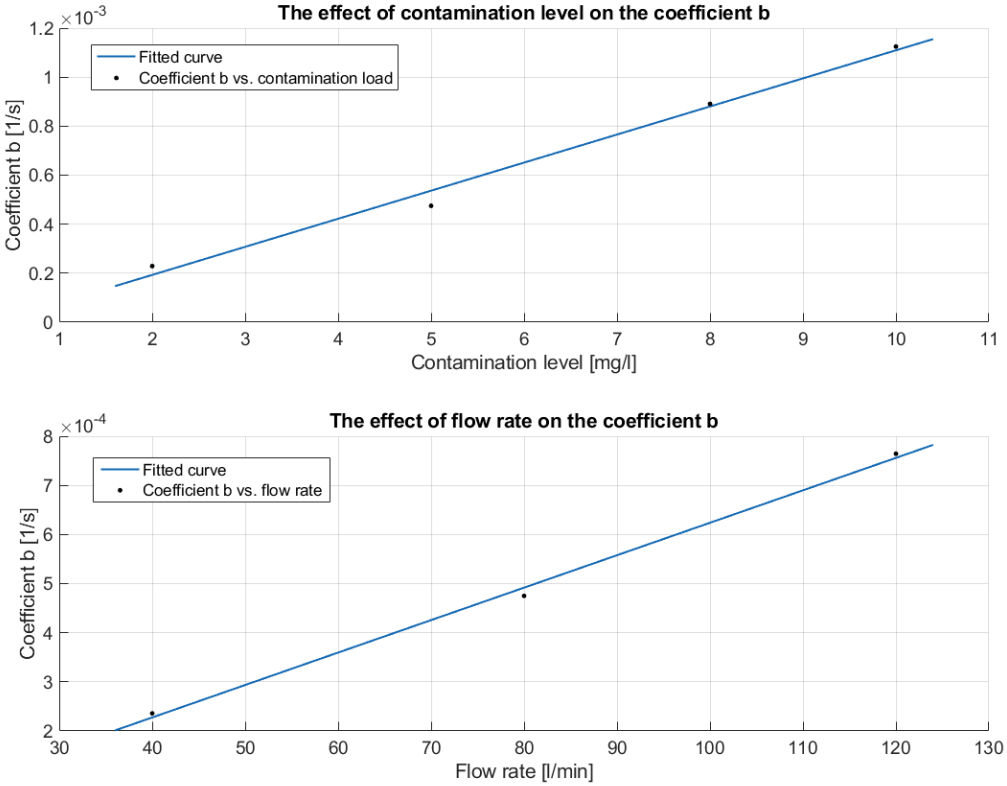

Figure 3. The effect of contamination level on b (at 80 l/min, 40 °C), and the effect of flow rate on b (at 5 mg/l, 40 °C)

As both of the coefficients b and d were discovered to vary very linearly based on the contamination level and flow rate, the two coefficients could be expressed as:

$$b = x_7 q_v \rho_c, \tag{10}$$

and

$$d = x_8 q_v \rho_c, \tag{11}$$

where x_7 and x_8 are constants. Combining the resulting functions for a, b, c and d into (4) provides us a general form for the pressure drop equation:

$$\Delta p = \left(\Delta p_0 - \left(\left(x_1 q_v \rho_c + x_2 q_v^{x_3}\right)\nu + x_4 q_v^{x_5} \rho_c + x_6 q_v\right)\right) e^{x_7 q_v \rho_c t} + \left(\left(x_1 q_v \rho_c + x_2 q_v^{x_3}\right)\nu + x_4 q_v^{x_5} \rho_c + x_6 q_v\right) e^{x_8 q_v \rho_c t} \tag{12}$$

The constants x_1—x_8 were initially obtained manually while deriving this equation. However, for better accuracy, the coefficients were later refined using parameter optimization, which is discussed in the following sub-section.

2.2.2. Parameter optimization

After deriving the mathematical model (12) for the pressure drop across the filter element, the next task was to optimize the parameters x_1—x_8 in order to improve the accuracy of the model. The experimental results for Δp were resampled into equally long lists, to avoid excessive importance of the longer experiments, mainly those that occurred at lower flow rates and contamination levels. Some of the measurements were excluded for this stage as they were inconsistent with the majority. The excluded measurements contained all the experiments done at flow rate of 40 l/min at temperatures 50 and 60 °C, therefore eight experiments in total from the original 48 experiments were excluded. The included measurements were combined into a single output list, and an input matrix that included the corresponding time, flow rate, viscosity and contamination

level, was created. The problem was approached similarly as in (2), where it was treated as a cost function to be minimized. For this case, the function to minimize was:

$$\min_x \frac{1}{2n}\sum_{i=1}^{n}(\Delta p_i - \Delta\hat{p}_i)^2, \quad (13)$$

where Δp_i is the measured pressure drop obtained from the output list, and $\Delta\hat{p}_i$ is the estimated pressure drop calculated with (12) using the values from the input matrix. x is a vector to optimize, containing the parameters x_1—x_8, i.e., the constants of (12) that are to be determined. The amount of sample points n is 14683, which is the length of the list that contains the measured Δp values. The search algorithm used was the Nelder-Mead simplex algorithm [10], and the values that had previously been obtained manually for x_1—x_8 were used as an initial guess for the algorithm. The accuracy of the optimized, final function will be examined in the Results section.

2.2.3. Simulink model

The final step in the model establishment procedure was to simulate the response of equation (12) at different cases of flow rate, temperature and contamination level. For this purpose, a model in the Simulink environment was constructed. The model uses constant values for x_1—x_8 that were acquired through the parameter optimization, and as inputs the aforementioned physical variables: fluid flow rate, temperature and contamination level, as well as time. The fluid kinematic viscosity is calculated in the simulation using equation (8), and an initial pressure drop across the filter element is interpolated from the flow rate and temperature. The simulation has been programmed to end once a pressure drop of 5 bar has been reached. The simulation results were validated by comparisons with the experimental data, which shall be discussed in more detail in the following section.

3. RESULTS

This section examines the modelling results. The Simulink model that utilizes equation (12) was experimented with at different flow rates, temperatures and contamination levels. The simulation outcomes were compared against the experimental data. Some of the comparisons are demonstrated in Figure 4 to illustrate the accuracy of the developed model. The simulation results for the early phase in the pressure drop development are largely accurate, though for some cases, clear deviation between the simulated and measured results can be observed at the end.

Table 1 assesses the goodness of equation (12), when compared against all the measured data that was included for the optimization process, i.e. the list of 14683 different Δp measurements.

Table 1. Validation of function (12) when compared against the measured data.

Goodness of fit	Value
SSE	303
R^2	0.985
RMSE	0.144

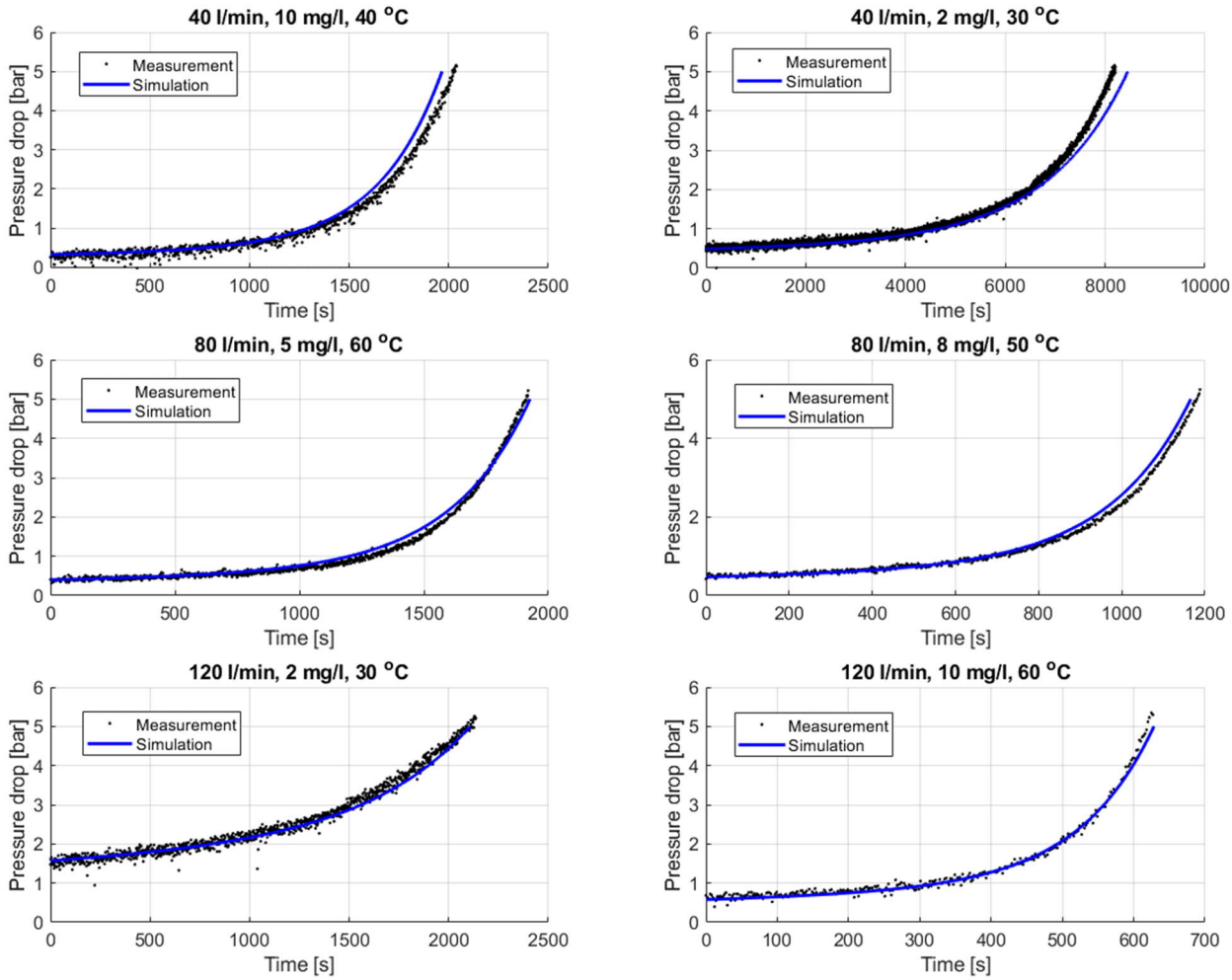

Figure 4. Comparing simulated and measured pressure drops.

4. DISCUSSION

The model developed in this study can predict the development of Δp up to 5 bar with a high degree of accuracy. Eight of the original 48 experiments were excluded from this inspection due to their inconsistent results. All of the excluded cases were 40 l/min cases, which might account for more noticeable discrepancies between the simulated and measured results for the 40 l/min comparisons in Figure 4. However, when considering that the model was assessed against 40 experiments that each had three independently varied physical variables, an R^2 value of 0.985 can be deemed high enough to showcase a clear correlation between the different physical variables and the development of Δp. The greatest variance between the simulated and measured results can typically be observed at the end of the simulation, though the greatest inconsistencies in the experimental results also occurred at the end, making the end of the Δp curve the greatest area of uncertainty.

The equation (12) that was derived in this study is an equation of the filtration time that works only if the different oil parameters are assumed to be constants. To have the equation work better with variable parameters, the equation should be written without time as one of its variables. One possibility would be to rewrite the equation as a function of filtered mass instead of time, where the filtered mass would be defined as the cumulative integral of mass that has entered the filter, calculated from the oil contamination level and flow rate. Another possibility could be to examine the derivatives of different Δp curves to investigate whether a clear point where the Δp starts to climb excessively could be identified. As the fitting function is exponential in nature, differentiating it would be simple.

Another aspect is that the model developed in this research could be entirely media specific, and there is no guarantee that it would work with other filter types. The coefficients that were considered constants in this study would most likely vary based on the filter media. In addition, as laboratory tests that were performed at careful conditions were the basis of this research, further confirmation of the accuracy of the developed model would require additional field-testing.

5. CONCLUSIONS

The objective in this study was to develop a correlation model for the pressure drop across a filter element that is subjected to a stream of contaminated oil at different oil contamination levels, flow rates and temperatures. The study resulted in exponential equation (12) that could be used to calculate the developing pressure drop based on the aforementioned oil parameters. The model was validated against experimental data, and was found to match the empirical results with a high degree of accuracy with a coefficient of determination R^2 of over 0.98. This demonstrated a clear correlation between the oil parameters and the pressure drop development over the filter element, which is typically used for determining the remaining service life of the filter.

This study has been done as part of an initial research in order to investigate correlations between oil conditions and filter service time. The ultimate goal of the research is to develop an intelligent oil filter that can predict its remaining lifetime. This information would be used in predictive maintenance that would eliminate unnecessary filter replacements, and prevent downtime due to a filter failure. As the research is still in its early phase, more work needs to be done to develop the correlation models. Possible future prospects include a correlation model based on filtered mass, and an investigation of the rate of change of the pressure drop data, in order to more accurately detect the beginning of the actual blocking phase of the filter lifetime.

ACKNOWLEDGMENTS

This work was made as a part of a Finnish research consortium - INTENS, hosted by VTT Oy, and funded by Business Finland (project # 7733/31/2017).

NOMENCLATURE

ν	Kinematic viscosity	[mm^2/s]
ρ_c	Mass concentration of contaminant, i.e., the gravimetric contamination level	[mg/l]
a, b, c, d	Coefficients for pressure drop	[-]
Δp	Pressure drop	[bar]
Δp_0	Initial pressure drop over a filter	[bar]
q_V	Volumetric flow rate	[l/min]
t	Time	[s]
T	Temperature	[°C]
x_1—x_8	Constants for pressure drop	[-]
SSE	Sum of squares due to error (summed square of residuals)	[-]
R^2	R-square (coefficient of determination)	[-]
RMSE	Root Mean Squared Error (standard error of the regression)	[-]

REFERENCES

[1] Frith, R.H. & Scot, W. 1993. Control of solids contamination in hydraulic systems – An overview. Wear, Vol. 165, pp. 69–74.

[2] Henneberg, M., Eriksen, R.L. & al. 2015. A quasi-stationary approach to particle concentration and distribution in gear oil for wear mode estimation. Wear, Vol. 324–325, pp. 140–146.

[3] Henneberg, M., Eriksen, R.L. & Fich, J. 2016. Modelling and measurement of wear particle flow in a dual oil filter system for condition monitoring. Wear, Vol. 362–363, pp. 153–160.

[4] Jaisinghani, R.A. & Sprenger, G.S. 1981. Resistance to Flow of Liquids in Fibrous Beds Applied to Cartridge Filtration. Filtration & Separation, March/April 1981, pp. 131–134.

[5] Fenton, M.B.M. 1994. Flow and Heat Transfer Modelling of an Automotive Engine Lubrication System. Dissertation, University of Warwick, June 1994, 8 + 11 + 384 p. http://go.warwick.ac.uk/wrap/3494, Accessed 2018-09-12.

[6] Lage, J.L., Antohe, B.V. & Nield, D.A. 1997. Two Types of Nonlinear Pressure-Drop Versus Flow-Rate Relation Observed for Saturated Porous Media. Journal of Fluids Engineering, Sep 1997, Vol. 119, pp. 700–706.

[7] Dukhan, N. Picón-Feliciano, R. & Álvarez-Hernández Á.R. 2006. Air Flow Through Compressed and Uncompressed Aluminium Foam: Measurements and Correlations. Journal of Fluids Engineering, Sep 2006, Vol. 128, pp. 1004–1012.

[8] Rinkinen, J., Laukka, J. & Karinen, K. 1999. Online condition diagnosis of hydraulic filter in hot strip mill. The Sixth Scandinavian International Conference on Fluid Power, SICFP'99. Tampere, Finland. 26-28.5.1999, pp. 635–649.

[9] Gorle, J.M.R., Heiskanen, V-M., Nissi, S. & Majas, M. 2018. Effect of temperature, contamination and flow rate on hydraulic filtration. MM Science Journal 2018, pp. 2490-2493. https://doi.org/10.17973/MMSJ.2018_10_201852.

[10] Rios, L.M. & Sahinidis, N.V. 2013. Derivative-free optimization: a review of algorithms and comparison of software implementations. Journal of Global Optimization, Vol. 56, pp. 1247–1293. https://doi.org/10.1007/s10898-012-9951-y.

[11] Gould, N., Orban, D. & Toint, P. 2005. Numerical methods for large-scale nonlinear optimization. Acta Numerica, Vol. 14, pp. 299–361.

[12] Niven, R.K. 2002. Physical insight into the Ergun and Wen & Yu equations for fluid flow in packed and fluidised beds. Chemical Engineering Science, Vol. 57, pp. 527–534.

COUPLED FLUID-THERMAL-STRUCTURAL ANALYSIS OF TWO-PHASE FLOW IN A HYDRAULIC TANK

Jagan Gorle
Hydraulic and Industrial Process Filtration EMEA, Parker Hannifin, Salmentie 260, 31760 Urjala, Finland
gorle.jmr@gmail.com

ABSTRACT

In addition to storing the hydraulic oil, the hydraulic tanks are expected to cool the fluid, eliminate the air and water content, and avoid condensation and solid deposition. Besides these functional capabilities, the optimum use of internal volume is desired, which ensures better vorticity distribution in the tank. Being the reservoir and supplier of preconditioned oil, a typical tank design should meet certain standards as oil cleanliness is concerned. On the other hand, the design of a hydraulic tank, as an integral part of the hydraulic power unit, is often subject to space management and hence enormous design complexity. In this context, virtual engineering practices for flow and structural analysis during designing and redesigning phases of the tank's development process have become decisive in reaching the final outcome.

In this study, a coupled-field investigation, using Computational fluid dynamics and solid dynamics (CFD & CSD), has been performed for flow and structural mechanics of a hydraulic oil reservoir at real-time operating conditions. The size of the tank is approx. 0.047 m^3 and the return line steadily supplies the oil at 1.96 kg/s. First, the thermofluid flow analysis, with initial volumes of oil and air, was performed using Volume of Fluid (VOF) model with second order solution accuracy. The flow and heat transfer characteristics were studied in detail. The resulting thermal and pressure loads on the tank walls were obtained by exporting the CFD solution to CSD solver. The coupled field was then analysed for stresses in the tank's structure. This simulation-driven product design provides a useful knowledge base for further exploration of complex structured hydraulic tanks.

KEYWORDS: Hydraulic tank, Computational fluid dynamics (CFD), Computational solid dynamics (CSD), coupled field analysis

1. INTRODUCTION

Determining a better design for the structural components in engineering applications is a never-ending problem. It is imperative to explore all possible dimensions of physics to find the best design solution of a part if it plays an important role in establishing the right flow conditions along with maintaining the structural integrity. The effectiveness of virtual engineering including numerical simulations in this context has been demonstrated in several applications [1-3], thanks to *high-performance computing* capabilities. However, there is a gap in the literature on the application of numerical methods in analysing the performance of a hydraulic tank, which is one of the common areas of engineering.

The return flow to a hydraulic tank often brings the foreign matter of different physical and chemical properties. Although the solid contamination can be separated from the oil stream using a return line filter [4], the air bubbles however inevitably pass through the filter and enter the tank, and then the suction line [5]. Also, a sudden drop in oil pressure in the tank can lead to cavitation and increases the chance of bubbles in the tank

[6]. On the other hand, the return line fluid usually has the temperature corresponding to the system operating conditions which is imparted to the tank's internal structure [7], while the external surface of the tank is exposed to ambient conditions. This creates considerable temperature gradients in the tank's structure. The structural behaviour of the tank in response to the flow pressure as well as the variable thermal loads thus constitutes a multiphysics problem with the aspects of sloshing [8,9], bubble motion [10], turbulence [11], heat transfer [12] and structural dynamics. Considering the geometrical complexity and practical limitations, the experimental analysis of such a system is not feasible. High-fidelity computational analysis using suitable solvers is rather a promising approach, not only to investigate the fluid and structural dynamics of the system but also to identify the critical zones that need to be improved.

2. PROBLEM DEFINITION

The inlet configuration of a hydraulic tank has a direct influence on the overall flow pattern and hence the force acting on the internal surface of the tank. To examine this, the tank geometry, supplied by Volvo Construction Equipment, France, is considered in this study (Figure 1). The volume of the tank is 0.047 m^3, but the oil volume is maintained at 0.031 m^3 and the rest of the space is occupied by air. A mixture of oil at 0.96 kg/s and air at 5E-7 kg/s from the return line enters the tank through the funnel. The suction line of the tank which is assimilated as constant pressure zone serves as the outlet of the flow domain. Due to the spacing and operational constraints, the geometry of the tank is fixed with a possibility to alter the funnel positioning. Therefore, the following five funnel configurations are considered to investigate the effect of inlet properties on the overall flow pattern.

Case 1 - Funnel @ 0°: Reference design, which has an angled open bottom so that the flow enters the tank in the downward direction.

Case 2 - Funnel @ 90°: Funnel is turned by 90° about its own axis in the clockwise direction.

Case 3 - Funnel @ 180°: Funnel is turned by 180° about its own axis in the clockwise direction.

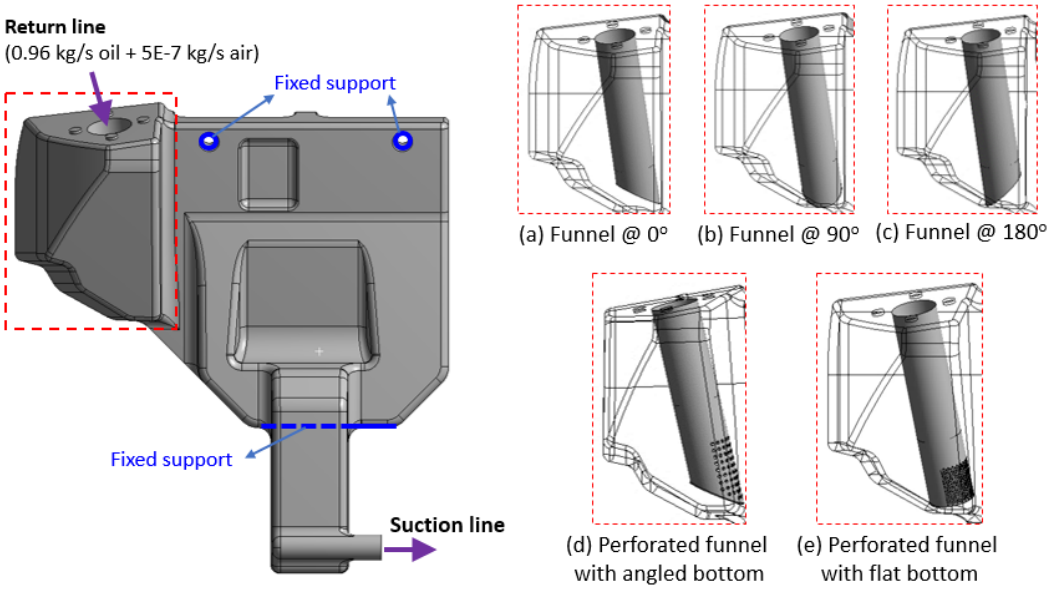

Figure 1. Tank design under study. Five different funnel configurations were examined. (a-c) The funnel with angled opened bottom, turned in the clockwise direction, was analysed at 0°, 90° and 180° respectively. (d) The funnel has a closed bottom with 6 mm sized perforations over 180° azimuth that accounted for an open area of 0.0029 m^2. (e) The funnel has a flat bottom with 3 mm sized perforations over 210° azimuth with an open area of 0.0036 m^2.

Case 4 - Perforated funnel with an angled bottom: Funnel with the same orientation as in case 1 has closed bottom. 102 nozzles, each of 6 mm in diameter, are made over 180^o azimuth so that the flow enters the tank normal to the funnel's axis. Corresponding open area through perforations on the funnel is 0.0029 m^2.

Case 5 - Perforated funnel with a flat bottom: Same as Case 4 but with a flat bottom. The nozzle size is 3 mm with an effective open area on the funnel is 0.0036 m^2, spreading across 210^o azimuth.

The tank is made of Nylon 6, and used to store and circulate the hydraulic oil of ISO VG 32. The properties of fluid phases and tank material are furnished in Table 1.

Table 1. Physical properties of the oil and air considered in the simulation setup

Property	**Oil[1]**	**Air[1]**	**Nylon 6[2]**
Density (kg/m^3)	870	1.2256	1140
Viscosity (kg/m.s)	0.02784	0.000017894	-
Specific heat (J/kg.K)	1943	1006	-
Thermal conductivity (W/m.K)	0.12	0.0242	0.28
Coefficient of thermal expansion	-	-	0.000147
Elastic modulus (GPa)	-	-	1.06
Poisson's ratio	-	-	0.35
Bulk modulus (GPa)	-	-	1.18
Shear modulus (GPa)	-	-	0.39
Yield strength (MPa)	-	-	43.1
Ultimate strength (MPa)	-	-	49.7

1 For multiphase flow analysis in the tank
2 For static structural analysis of the tank

3. METHODOLOGY

The present study adopted a sophisticated numerical methodology, from the geometry creation and computational meshing through the coupling between the structural and flow solvers and post-processing of the results. Following sub-sections present the details of the deployed methodology.

3.1. Pre-processing

The pre-processing of the computational work consists of geometry development and domain discretization. While the tank's geometry is retained for the analysis of computational solid dynamics (CSD), the internal volume of the tank is extracted for the study of computational fluid dynamics (CFD). The finite volume discretization for CFD study, as shown in Figure 2(a), comprises unstructured tetrahedral mesh with fine resolution on the geometrical curvatures and propinquity regions. Homogeneity of the distribution of mesh nodes and undistorted cell creation is ensured by thorough control over the quality parameters such as orthogonal quality and cell aspect ratio. With 95% of the cells with the orthogonal quality above 0.9 and 97% with the cell aspect ratio below 6, the developed meshes are regarded as having a quality distribution of mesh nodes. Rigorous mesh dependency studies were performed and a grid with 2.2 million nodes (1.3 million cells) is found to have enough resolution. Beyond this, the mesh size has little effect on the solution behaviour. However, the variation in the mesh size is approximately 10% depending on the simulation case with the same definition of mesh parameters. Five inflation layers are created over the solid boundary of the fluid domain to model the wall-bounded viscous layer, where the non-dimensional wall distance $y+$ is consistently kept in the range of [30, 300]. This enables the use of standard wall functions in the definition of the turbulence model.

The finite element model for structural analysis considers the tank's geometry without the funnel as the objective is to evaluate the response of only the tank's structure. As shown in Figure 2(b), the mesh consists of fine tetrahedral solid elements to capture the small and complex geometrical features. The mesh size is

350,700 nodes with 184,544 cells. The tank has three fixed supports as highlighted in Figure 1 (left). The structure of the tank is assumed to be isotropic and homogeneous linear elastic in nature.

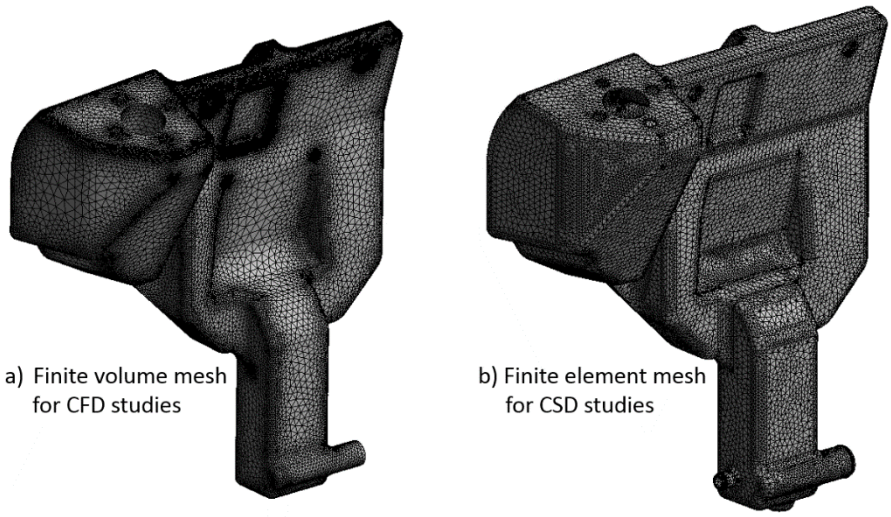

Figure 2. Computational meshes for CFD (left) and CSD (right) analysis

3.2. Coupling between fluid and solid fields

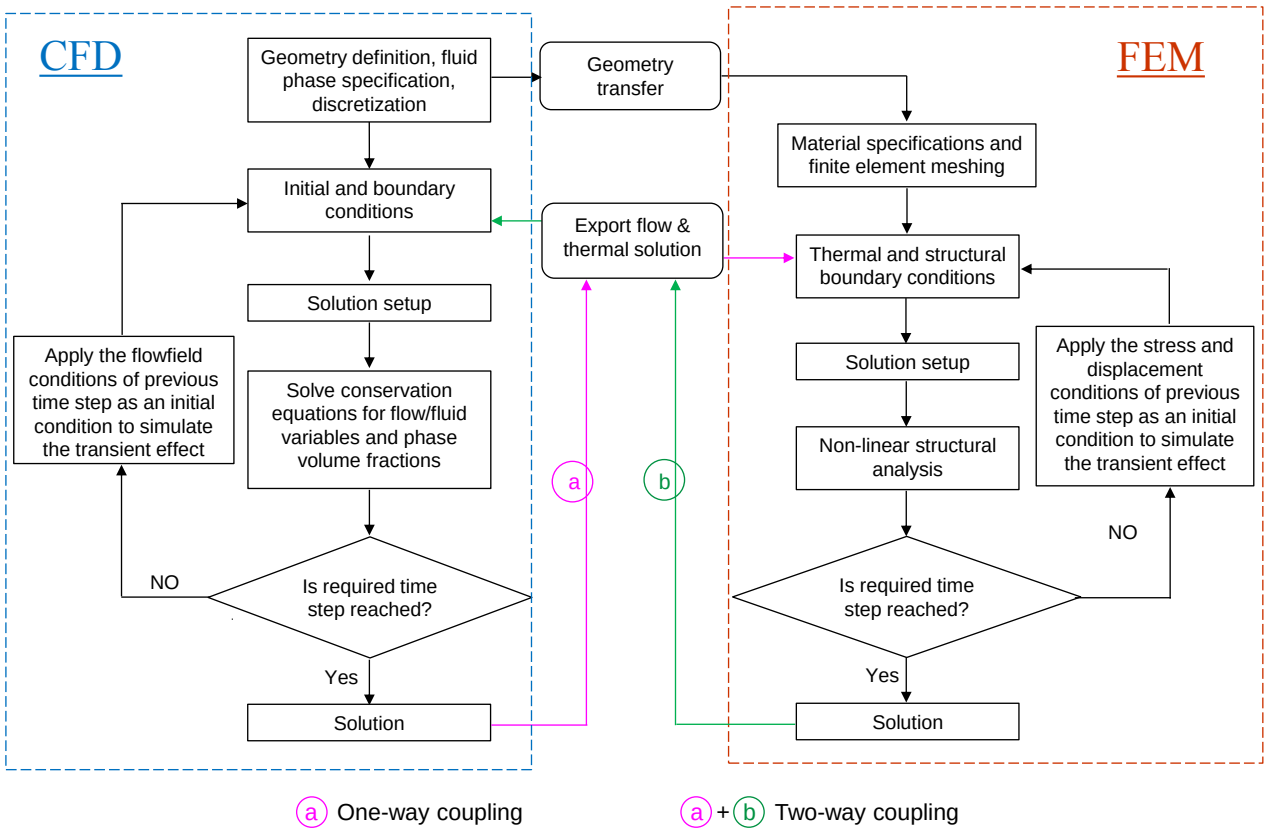

Figure 3. Workflow of fluid-structure interaction

The fluid temperature and flow conditions in the hydraulic tank has a considerable effect on the structural response of the tank. The resulting stress and displacement of the tank walls are directly governed by the interaction of the turbulent two-phase flow and the structure with precise material properties. While the fluid flow is simulated by defining the right turbulence parameters for an incompressible viscous solver, the structural deformation is computed by means of the mechanics of flexible solids, assuming a linear elastic behaviour of the used material. The interaction between the fluid and solid mechanics is modelled by a

constraint boundary condition for computational solid dynamics (CSD) solver based on finite element method, the numerical value of which is given by computational fluid dynamics (CFD) solver, based on finite volume method. Because the coupling is completely localized on the internal skin of the tank, this surface acts as an interface between the fluid and solid domains. The fluid-structure interaction (FSI) is limited only to one-way coupling i.e. from fluid to solid because the resulting structural displacement is so small that it has negligible influence on the hydraulic flow in return. The workflow of this approach is depicted in Figure 3.

3.3. Computational modelling

The governing equations for continuity, momentum, energy and phase volume fraction (α) for steady incompressible two-phase flow using the Volume of Fluid (VOF) method are:

$$\nabla.(\rho\vec{V}) = 0 \tag{1}$$

$$\nabla.(\rho\vec{V}\vec{V}) = -\nabla p + \nabla.\{\mu(\nabla\vec{V} + \vec{V}^T)\} + \rho\vec{g} + \vec{f} \tag{2}$$

$$\nabla.(\rho h\vec{V}) = \nabla.(k_{eff}\nabla T) + S_h \tag{3}$$

$$\vec{V}.\nabla\alpha_G = 0 \tag{4}$$

where ρ, μ, $\vec{V}$, p and $\vec{f}$ are the density, viscosity, velocity, pressure and force source term of the mixture, respectively. ρ, μ and $\vec{f}$ can be computed from the volume fractions of liquid and gaseous phases, α_L and α_G, respectively. This is mathematically defined as

$$\rho = \alpha_L\rho_L + \alpha_G\rho_G \tag{5}$$

$$\mu = \alpha_L\mu_L + \alpha_G\mu_G \tag{6}$$

$$\vec{f} = \sigma\frac{2\rho k_G\nabla\alpha_G}{\rho_L+\rho_G} \tag{7}$$

where σ is the surface tension and the curvature k_G is the divergence of the unit surface normal. The *finite volume* based CFD solver, Ansys Fluent with steady Reynolds Averaged Navier Stokes (RANS) approach. The flow turbulence is modelled using the bivariate model, standard *k-ε*, where the following transport equations for turbulent kinetic energy (*k*) and its dissipation rate (*ε*) are solved.

$$\rho V_i\frac{\partial k}{\partial x_i} = \mu_t\left[\frac{\partial V_j}{\partial x_i} + \frac{\partial V_i}{\partial x_j}\right]\frac{\partial V_j}{\partial x_i} + \frac{\partial}{\partial x_i}\left\{\frac{\mu_t}{\sigma_k}\frac{\partial k}{\partial x_i}\right\} - \rho\varepsilon \tag{8}$$

$$\rho V_i\frac{\partial \varepsilon}{\partial x_i} = C_{1\varepsilon}\left(\frac{\varepsilon}{k}\right)\mu_t\left[\frac{\partial V_j}{\partial x_i} + \frac{\partial V_i}{\partial x_j}\right]\frac{\partial V_j}{\partial x_i} + \frac{\partial}{\partial x_i}\left\{\frac{\mu_t}{\sigma_\varepsilon}\frac{\partial \varepsilon}{\partial x_i}\right\} - C_{2\varepsilon}\rho\frac{\varepsilon^2}{k} \tag{9}$$

where σ_k, σ_ε, $C_{1\varepsilon}$, $C_{2\varepsilon}$ and C_μ are empirical constants. As tuned to canonical flows, these constants carry the values 1.0, 1.3, 1.44, 1.92 and 0.09 respectively.

The velocity field was obtained from momentum conservation equations and the pressure is determined by the incompressibility constraint transformed into a pressure equation. The velocity-pressure coupling followed Semi-Implicit Method for Pressure-Linked Equations (SIMPLE) algorithm. Numerical simulations with second-order accuracy were performed on an eight-core Lenovo W540 workstation (16 GB ram, 2.8 GHz).

The pressure on the walls of the fluid domain is mapped, interpolated and exported to the structural mechanics' solver as the pressure, statically acting on the internal surface of the tank. With no inertial effects to the load conditions, the displacement field {*x*} is solved for in the following matrix equation.

$$[K]\{x\}=\{F\} \tag{10}$$

where [*K*] is the constant, based on *small deflection theory*, and [*F*] is static load.

4. RESULTS AND DISCUSSION

The numerical findings of the this study include the effect of funnel positioning and perforations on the global flow pattern, phase distribution in the tank and structural behaviour as a result of turbulent flow in the tank. Following sub-sections will present and contrast the considered designs for the flow and structural variables.

4.1. Effect of funnel positioning

The streamline distribution of oil phase in the tank with different funnel positions is depicted in Figure 4. With 0^o turned funnel, the oil stream takes the form of swirling flow in the downstream of the funnel to make a quick turn through the vertical channel '*c*' and then to the suction line (Figure 4a). This passage is characterized by a streamline-cluster, while the right end of the domain '*e*' has fewer streamlines as the local flow is relatively silent. The swirling action becomes more profound as the funnel is turned in the clockwise direction by 90^o and 180^o (Figure 4b and 4c), and possibly enhances mixing in the dead zones. This promotes the recirculation of flow in region '*r*'. From the streamline pattern, the funnel at 90^o is more effective than the other two designs as the flow distribution is concerned. One of the requirements of hydraulic tank design is to maximize the use of tank's volume without static zones.

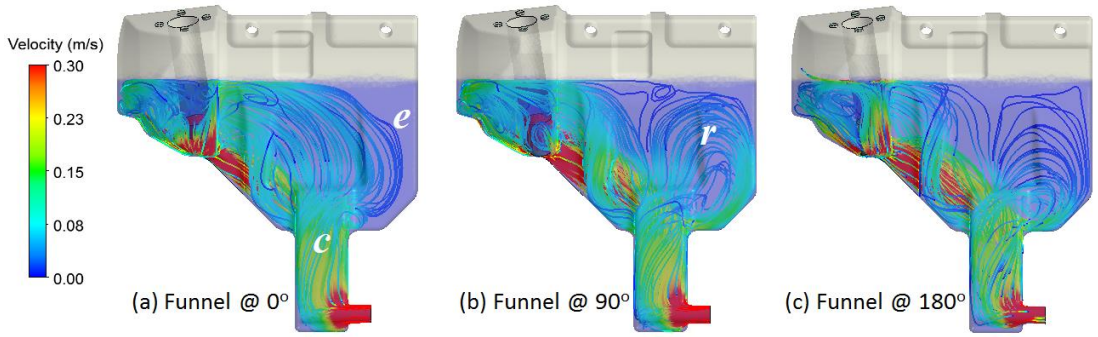

Figure 4. Streamline distribution in the tank with different funnel positions

The distribution of secondary phase i.e. air in the tank for the selected funnel positions is presented in Figure 5. The preliminary qualitative observations from the steady state contour plots reveal that there is no appreciable sloshing effect in the tank. The amount of air reaching the region '*e*' is reduced with the turning angle of the funnel. When the funnel is at 0^o, the confined flow passage at the bottom of the funnel causes the oil stream to impinge on the solid surface, which involves an abrupt energy exchange. The air retains the momentum to move wider in the tank. With the funnel at 90^o and 180^o, the maximum volume fractions of the air appear near the funnel with reduced void fractions in the downstream locations. These observations are further quantified by computing the quantity of air entering the suction line, which is presented in Table 2. It is found that funnel at 0^o causes 77% of the incoming air to enter the suction line, whereas it is 64% with the funnel at 90^o. On the other hand, the half-turned funnel displays the best among the three designs with only 28% of the air entering the suction line.

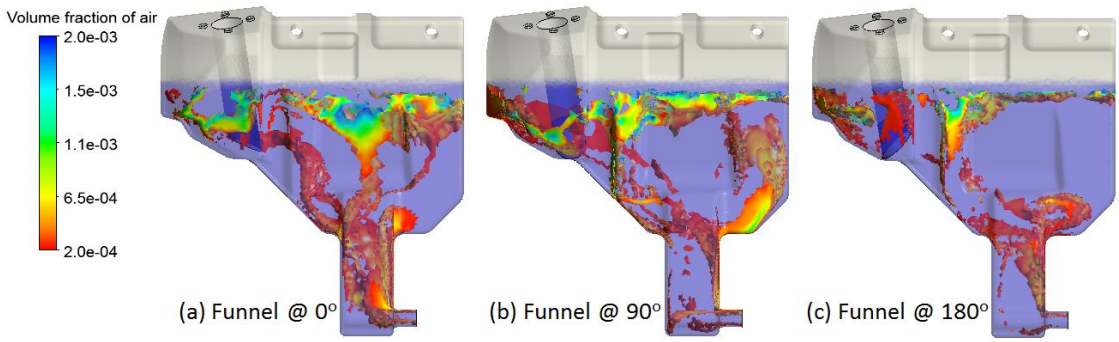

Figure 5. Void fraction when 5E-7 kg/s air flows into the tank through return line

The strength analysis based on the CFD-predicted pressure which is imparted to the internal walls of the tank includes the magnitude of the resulting stresses and deformation of the structural material, which enables to identify the critically loaded/displaced locations and evaluate the structural safety of the tank. As depicted in Figure 6, the tank is primarily distinguished in 3 locations, l_1, l_2 and l_3 as the structural deformation is concerned. Irrespective of the design, the location l_2 is found to be the most vulnerable, followed by l_3, as these are the farthest away from the fixed supports. The designs however differ significantly from each other in terms of the magnitude of displacement. Looking at the peaks of structural deformation, the design with unturned funnel has the maximum of 0.0002 m in the location l_2, and that with the funnel at 90° has almost six times higher in the location l_3. The behavior of the design with half turned funnel is close to the case of unturned funnel.

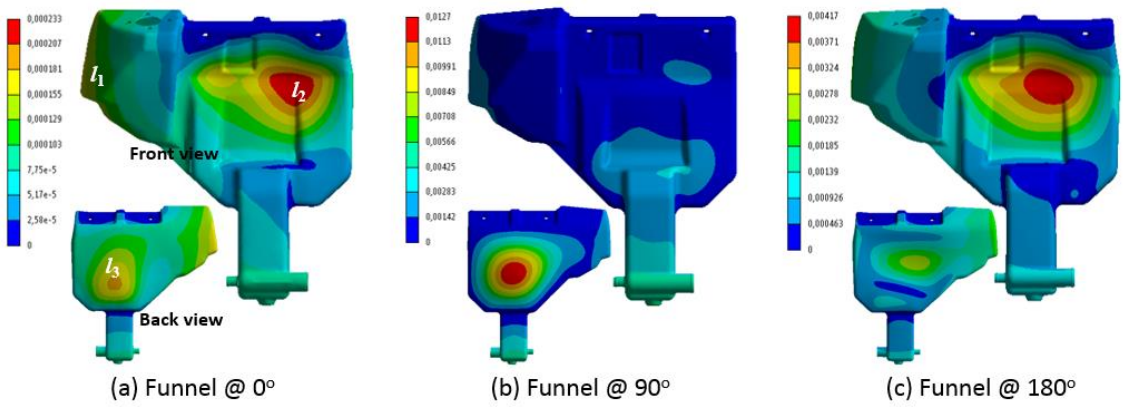

Figure 6. Structural deformation in m resulting from the flow dynamics in the tank

One of the ways to quantify the energy transfer from the flow to the tank's structure is to calculate the wall shear stress (WSS). The effect of funnel position on the shear stress distribution is computed from the surface integral of WSS. Although the effective flow sectional area before entering the tank is the same in the cases 1-3, the angular orientation of the funnel opening has a significant impact on the skin friction of tank walls. Half-turned funnel in case 3 has the lowest stress of 1.108 Pa.m^2, which is approximately 19% lesser than the unturned case and 22% than the quarter-turned case. Furthermore, the heat transfer was computed from the total heat transfer rate across the oil-solid contact, which follows the same trend of surface integrated WSS. The funnel positioning in cases 1-3 has a considerable effect on the thermal convection phenomenon. Funnel turned by 180° exhibits the lowest rate of heat transfer of 235 W, which is approximately 18% lower than that in cases 1 and 2.

Table 2. Comparison between different funnel configurations for the parameters of flow and structural dynamics

	Funnel @ 0°	**Funnel @ 90°**	**Funnel @ 180°**	**Perforated funnel - angled bottom**	**Perforated funnel - flat bottom**
Amount of air through outlet	77 %	64 %	28 %	13 %	38 %
Area integrated wall shear stress (Pa.m^2)	1.365	1.412	1.108	1.761	1.832
Heat transfer rate (W)	284	285	235	297	300
Max. deformation (m)	0.0002	0.0127	0.0042	0.0040	0.0127
Max. equivalent stress (Pa)	1.63E+8	4.32E+7	3.19E+7	3.19E+7	1.20E7
Min. safety factor	1.537	0.997	1.352	1.353	2.186

4.2. Effect of perforation

Several studies, but in the other fields of application, noted that the global flow pattern can appreciably change by adapting simple alterations to the inlet geometry [13]. One such experiment is performed in this study where the direction of the inflow is changed. The bottom face of the funnel is closed and the flow is forced to enter the tank through a series of perforations as described in Figure 1(d) and (e). This inlet configuration has a significant impact on the flow momentum, which results in an improved oil stream distribution in the tank. Figures 7(a) and 7(b) illustrate the streamline pattern from the perforated funnel with angled and flat bottom designs, respectively. Unlike the bottom opened funnel, the uniformity of the flow pattern certainly increases with the perforated design. This is reflected in the phase distribution as well (Figure 8). Recalling that the perforated funnel with angled bottom has the 6 mm nozzles, spread across the 180^{o} over a height of 0.108 m, it is evident with the perforated funnel with angled bottom that the secondary phase reaches the oil surface in the most efficient manner compared to all other cases, resulting in only 13% of air going into the suction line. On the other hand, the perforated funnel with flat bottom has 38% of the air entering the suction line. This is possibly due to the fact that the half-sized nozzles in this case are closely placed across an azimuth of 210^{o} over a height of 0.068 m. This leads to the quicker mixing of emanating jets and hence a faster momentum exchange than that in the other case. This effect is also visible in the surface integrated wall shear stress and heat transfer characteristics, which are substantially higher in the cases of perforated funnels than the open-bottom funnels, as seen from Table 2. The contracted flow injection through the funnel nozzles and hence increased mass flux in this case results in higher heat transfer rate. This is consistent with the penetration theory [14]. In spite of lower open area through perforations in case of the angled bottom than that of flat bottom, the difference of nozzles' size and their spatial distribution makes both designs to have almost identical heat transfer rates.

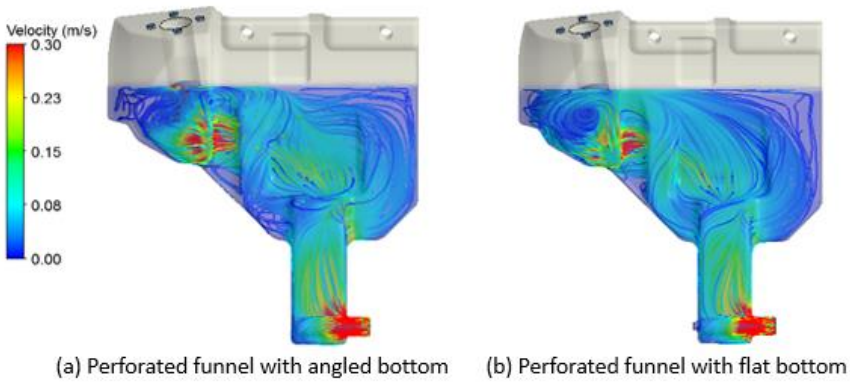

Figure 7. Effect of perforated funnel with angled and flat bottom on the streamline pattern

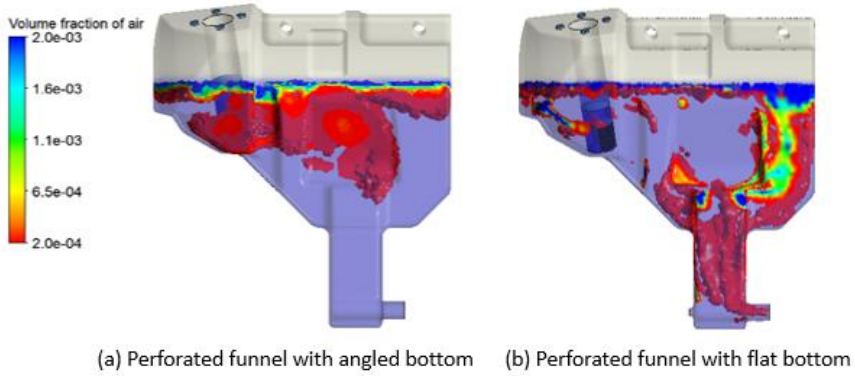

Figure 8. Secondary phase (air) distribution in the tank with the multiphase flow through perforated funnel on the return line

Also, the angular pattern of the nozzles in the case of flat bottom funnel creates much different structural dynamics than that of angled bottom. With more evenly spread flow in the tank, the maximum deformation with

angled bottom funnel is 0.004 m, which is more than three times lesser than that in the case of flat bottom funnel. Another major difference between the two designs is that the location of maximum displacement is on the opposite sides of both cases i.e. in l_2 with angled bottom funnel and at l_3 with flat bottom funnel, as visualized in Figure 9. The effect of inlet design on the structural dynamics is further studied for equivalent stress (von-Mises). As listed in Table 2, the perforated funnel with flat bottom displays the lowest maximum stress of 1.2E+7 Pa, and 90^o turned funnel creates four times of this, which is the highest among all. However, the peak stresses occurring in any case is less than the ultimate strength of the material, Nylon 6, which ensures the operation of the tank is in the elastic region. Nevertheless, the critical locations containing weak zones may be subject to structural failure. The study is extended to observe the locations of the lowest factor of safety in all cases. Although the factor of safety below 3 is observed in all cases, this is identified at streaks of certain corners of the tank. The overall safety factor is 15 or above, which confirms the structural safety in all cases.

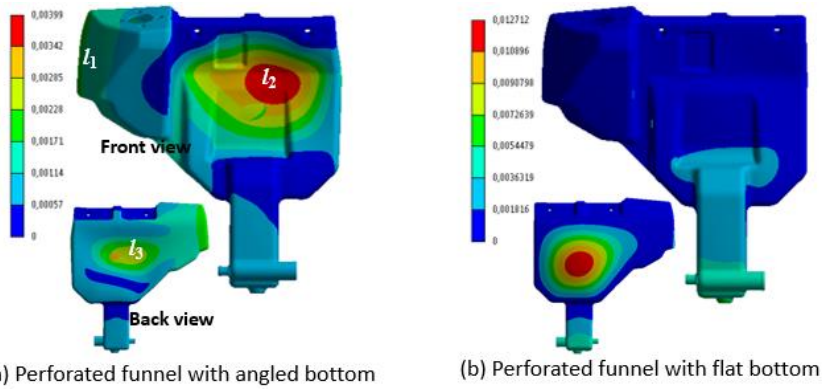

(a) Perforated funnel with angled bottom (b) Perforated funnel with flat bottom

Figure 9. Structural deformation of the tank with perforated funnel on the return line

5. CONCLUSIONS

The predictive capabilities of computational fluid and solid dynamics enabled to understand the coherent phenomena and make a rationale based decision in developing the fluidic systems. As the reservoir and supplier of lubrication oil, a hydraulic tank inevitably receives the contamination in the form of air, which is detrimental to the downstream components if it is allowed to pass through the suction line. In this study, two-phase flow on a hydraulic tank and the structural interaction of the flow was numerically investigated using one-way coupled fluid-structure interaction model. The coupled-field analysis was made on the tank with five different funnel designs. The flow and structural dynamics were critically compared between the test cases, which played an important role in finalizing the design with better performance. Negligible sloshing effect is the common trait in all the cases. With better flow distribution, the perforated funnels have lesser air contamination entering the suction line than the bottom opened funnels and exhibit superior heat transfer rates. The investigation on the phase distribution in the present study is limited to the volume fractions of the air in the oil, and amount of air at the outlet. However, the phase stability, breakdown of liquid slug and corresponding transition characteristics are critical to further improve the internal flows of a hydraulic tank. The magnitude of structural response owing to the turbulent flow pattern in the tank in the cases of the funnel at 180^o and perforated funnel with angled bottom are almost identical, whereas perforated funnel with flat bottom created the safest overall design. These results can be extended to other configurations such as different material specifications, design modifications, flow pattern improvement, structural optimization etc. to realize better multi-physical performance.

ACKNOWLEDGMENTS

The cooperation of Volvo Construction Equipment, France, is acknowledged.

REFERENCES

[1] Gorle, J.M.R., Chatellier, L., Pons, F. & Ba, M. 2017. Operation of Darrieus turbines in constant circulation framework. Physics of Fluids, Vol. 29, p. 075103. https://doi.org/10.1063/1.4993162

[2] Gorle, J.M.R., Terjesen, B.F. & Summerfelt, S.T. 2018. Hydrodynamics of octagonal culture tanks with Cornell-type dual-drain system. Computers and Electronics in Agriculture, Vol. 151, pp. 354-364. https://doi.org/10.1016/j.compag.2018.06.012

[3] Tič, V. & Lovrec, D. 2012. Design of modern hydraulic tank using fluid flow simulation. International Journal of Simulation Modelling, Vol. 11, No. 2, pp. 77-88. https://doi.org/10.2507/IJSIMM11(2)2.202

[4] Gorle, J.M.R., Heiskanen, V-M., Nissi, S. & Majas, M. 2018. Effect of temperature, contamination and flow rate on hydraulic filtration. MM Science Journal 2018, pp. 2490-2493. https://doi.org/10.17973/MMSJ.2018_10_201852

[5] Totten, G.E., Sun, Y.H. & Bishop, R.J. Jr. 1997. Hydraulic Fluids: Foaming, Air Entrainment, and Air Release - A Review. SAE Technical Papers, https://doi.org/10.4271/972789

[6] Maiga, M.A., Coutier-Delgosha, O. & Buisine, D. 2015. Cavitation in a hydraulic system: The influence of the distributor geometry on cavitation inception and study of the interactions between bubbles. International Journal of Engine Research, Vol. 17, No. 5, pp. 543-555. https://doi.org/10.1177/1468087415590742

[7] Wu, C., Xu, C., Mao, X., Li, B., Hu, J. & Liu, Y. 2017. Heating analysis in constant-pressure hydraulic system based on energy analysis. IOP Conf. Series: Earth and Environmental Science, Vol. 100, p. 012147. https://doi.org/10.1088/1755-1315/100/1/012147

[8] Singala, V., Bajaj, J., Awalgaonkara, N. & Tibdewalc, S. 2014. CFD Analysis of a kerosene fuel tank to reduce liquid sloshing, Procedia Engineering, Vol. 69, pp. 1365-1371. https://doi.org/10.1016/j.proeng.2014.03.130

[9] Močilan, M., Žmindák, M., Pecháč, P. & Weis, P. 2017. CFD Simulation of Hydraulic Tank. Procedia Engineering, Vol. 192, pp. 609-614. https://doi.org/10.1016/j.proeng.2017.06.105

[10] Sakama, S., Tanaka, Y., Higashi, H., Goto, H. & Suzuki, R. 2014. Air Bubble Separation and Elimination from Working Fluids for Performance Improvement of Hydraulic Systems. Proc. IFPE 2014, March 4-8, 2014, Las Vegas, USA. 8 p. https://doi.org/10.13140/2.1.4927.4245

[11] Patwardhan, A.W. 2002. CFD modeling of jet mixed tanks. Chemical Engineering Science, Vol. 57, No. 8, pp. 1307-1318. https://doi.org/10.1016/S0009-2509(02)00049-0

[12] Konev, V., Polovnikov, E., Krut, O., Merdanov, S. & Zakirzakov, G. 2017. Investigation and development of the thermal preparation system of the trail builder machinery hydraulic actuator. IOP Conf. Series: Materials Science and Engineering, Vo. 221, p. 012001. https://doi.org/10.1088/1757-899X/221/1/012001

[13] Gorle, J.M.R., Terjesen, B.F., Holan, A.B., Berge, A. & Summerfelt, S.T. 2018. Qualifying the design of a floating closed-containment fish farm using computational fluid dynamics. Biosystems Engineering, Vol. 175, pp. 63-81. https://doi.org/10.1016/j.biosystemseng.2018.08.012

[14] Schlünder, E.U. 1971. Wärmeübergang an bewegte Kugelschüttungen bei kurzfristigem Kontakt. Chemie Ingenieur Technik, Vol. 43, pp. 651-654. https://doi.org/10.1002/cite.330431103

LIGHTWEIGHT PISTON ACCUMULATOR FOR HYDRAULIC HYBRID DRIVE SYSTEMS

Thorsten Hillesheim
Technical Director Division Accumulators
Freudenberg Sealing Technologies GmbH & Co. KG, Germany
Sinzigerstr. 47, D-53424 Remagen
thorsten.hillesheim@fst.com

ABSTRACT

Freudenberg Sealing Technologies (FST) has developed innovative solutions for high and low pressure accumulators for hydraulic hybrid energy storage systems. These systems support demand for more energy efficient and fuel saving solutions. For vehicles with heavy stop and go duty cycles, a hybrid accumulator system can be an optimal choice to recover brake energy and reduce overall fuel consumption. During braking, the kinetic energy is converted to stored energy via a gas-filled accumulator system. This stored energy is then available when needed for accelerating the vehicle from a stopped position. This makes a significant contribution to reduced fuel consumption, lower CO_2 emissions and also enables downsizing of other vehicle system components. In addition, wear on braking systems is significantly reduced, contributing to an overall improvement in total cost of ownership. Hydraulic hybrid accumulator systems can be used in cars and mobile applications, including smaller delivery vans, refuse trucks, and other vocational vehicles with high stop and go duty cycles. FST has now succeeded in reducing the weight of the storage system (consisting of a high pressure and low pressure piston accumulator), thus making its application even more attractive for mobile use. Hydraulic Hybrid Accumulator systems are also an alternative to electric hybrid solutions for smaller vehicles.

The low weight of the new high pressure accumulator made of steel was achieved through specific structural improvements. These include dome end caps, a reduced weight aluminum piston, and reduced material thickness on the pressure vessel. These improvements make it possible to achieve weight reduction of 60 percent (or 45 kg) on a 20-liter nitrogen gas accumulator. The newly developed low-pressure accumulators consist of a housing, cover and piston out of aluminum. The integral connection of the cover to the housing is completed by means of electromagnetic pulse welding. The use of this welding technique, a first for FST, ensures high stability of the overall process. To reduce wear in the in piston guide diameter, a gas-tight friction coating has been applied. Pressure and temperature sensors are installed for condition monitoring and an overpressure relief valve is provided to ensure safe function in the event of a vehicle fire or other vehicle event.

KEYWORDS: Piston accumulator, hydraulic hybrid, light weight design, reduced fuel consumption, reduced CO_2 emissions

1. INTRODUCTION

Hydraulic energy recuperation from braking with the help of hydraulic accumulators helps to meet the demand for fuel-saving solutions. Freudenberg Sealing Technologies has now succeeded in not just sharply reducing the weight of low pressure and high pressure piston accumulators but – thanks to special designs and a new joining technology – in achieving significantly greater efficiency as well. Along with low costs and the lowest possible weight, the requirements involve the load capacity of the media separator with regard to gas/hydraulic oil, the influence of temperature and the possible impairment of functionality in the event of the loss of pre-loading due to the permeation of the nitrogen through the media separator.

2. ADVANTAGES OF HYDRAULIC ACCUMULATORS

In vehicles with hybrid powertrains, support for the internal combustion engine comes either from an electric or a hydraulic drive in most cases. This not only reduces fuel consumption and accordingly CO_2 emissions – it also enables the downsizing of individual components. The main component of a hydraulic drive is the hydraulic accumulator. It consists of one section for gas and another for liquid; the two sections are separated by a media separator. The task of the hydraulic accumulator is the recapture of kinetic energy from the braking process (recuperation). During braking, the hydraulic accumulator is initially filled against the gas pressure. When it is needed, the energy stored in this way is available for the vehicle's acceleration. In that process, the gas expands again and drives a hydraulic motor using the medium. The motor delivers the stored energy to the vehicle via the transmission, supporting the internal combustion engine, which shifts its operating point and optimizes its operation. The use of an accumulator use is thus especially efficient in light commercial vehicles with numerous stop-and-go cycles. But hydraulic accumulators are also an alternative to electric hybrid systems in passenger cars, small delivery vehicles and mobile work machines. Compared to the lithium-ion battery of an electric hybrid, they indeed have a lower capacity, but they charge up much faster and provide high energy in the shortest possible time thanks to their enormous power density.

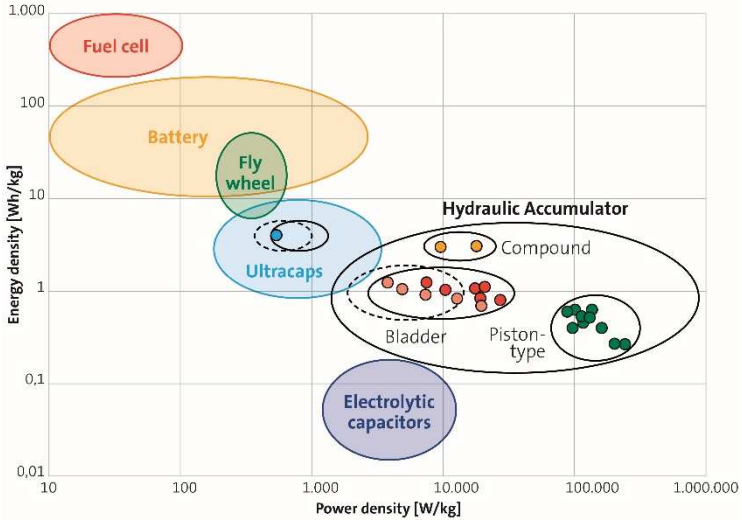

Figure 1: Ragone plot [1]

Unlike batteries, hydraulic accumulators also exhibit no age-related loss of capacity and operate at low temperatures without any difficulty. It is also relevant that brake wear is reduced with the use of a hydraulic hybrid since the share of the kinetic energy absorbed by the hydraulic accumulator does not need to be reduced by the braking system.

3. OPTIMIZED DESIGN

Systems for serial and parallel hydraulic hybrids primarily consist of two accumulators – one low-pressure and the other high-pressure. While the low-pressure accumulator supplies the closed circuit, the high-pressure accumulator handles the energy storage during the braking process. Freudenberg Sealing Technologies has now succeeded in significantly lowering the weight of the overall storage system, thus making it even more attractive for mobile use. The reason: The lower the weight of the hydraulic accumulator, the lower the vehicle's fuel consumption. Besides the lowest possible weight and low costs, other requirements involve the load capacity of the media separator with regard to gas/hydraulic oil, the influence of temperature and the potential precharge pressure loss due to permeation.

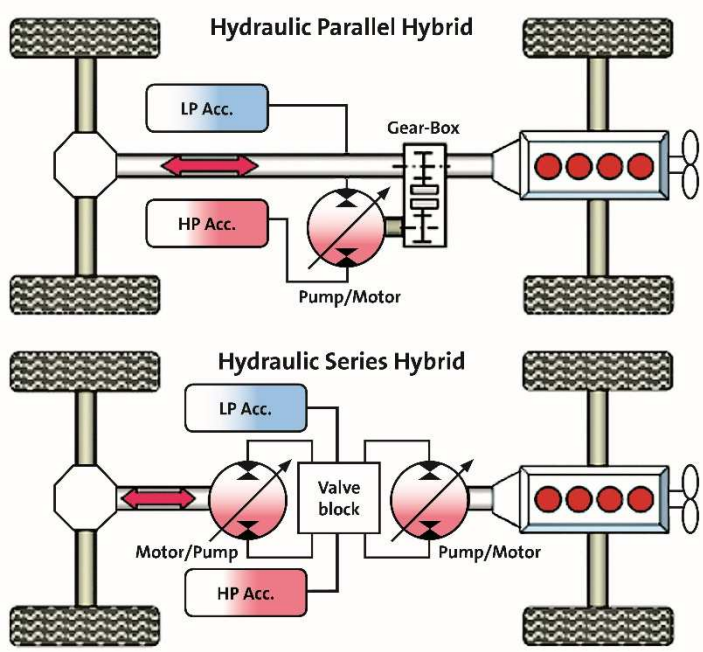

Figure 2: System architecture hydraulic hybrid systems [2]

The low-pressure and high-pressure accumulators developed by Freudenberg Sealing Technologies are designed as piston accumulators. This is associated with significantly less wear as well as improved permeation characteristics resulting from the fairly small elastomer surface with accordingly reduced permeation by the nitrogen. This reduces the loss of the gas precharge pressure, which has a direct effect on the lifespan and maintenance intervals of the accumulator. Particularly with horizontal installation (typically in small vehicles and commercial vehicles), bladder accumulators also exhibit an asymmetric flexing motion. This results in increased wear and thus reduced service life. This is promoted further by the effect of the vehicle's movements, since the oil volume follows every braking and acceleration sequence.

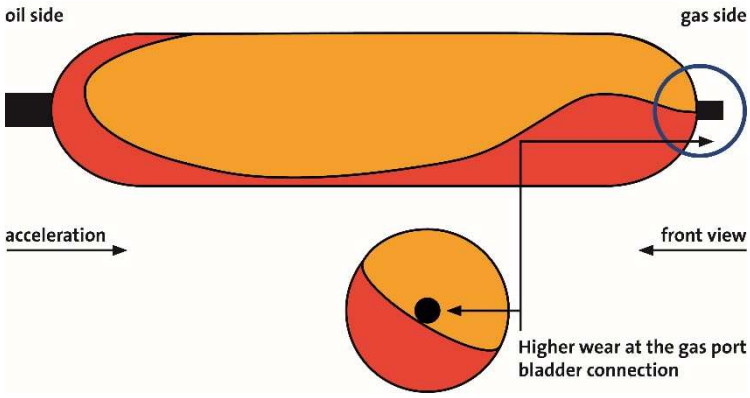

Figure 3: Influences to accumulator durability

Freudenberg Sealing Technologies also has decades of experience in the so-called “lifetime filling” of piston accumulators in the automotive field. Thanks to the right materials and the optimal seal design, extremely long life spans are being achieved. For example, an approximately 1-million-km endurance test by one customer showed only slight loss of gas precharge.

4. EMPT PROCESS

Aluminum was selected as the material for the housing, end cap and piston of the newly developed low-pressure accumulator; it was the optimal choice in balancing material costs and potential weight reduction. The firmly joined connection between the two end caps and the housing is carried out with electromagnetic pulse forming technology (EMPT). It is based on the contactless forming of electrically conductive materials using strong magnetic fields. Depending on the energy and material, the reshaping itself takes place within 10 to 200 micro-seconds.

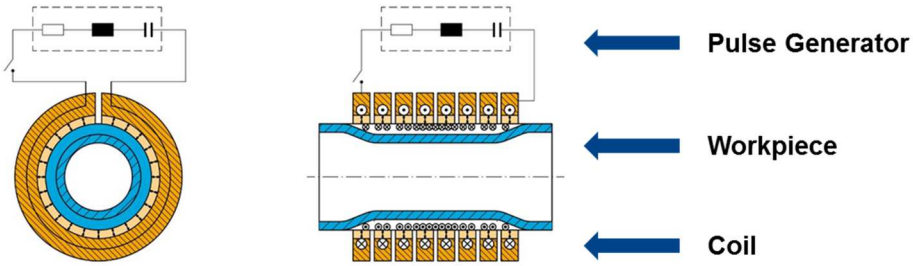

Figure 4: Principle electromagnetic pulse technology

Freudenberg Sealing Technologies is using this technology for the firmly bonded joining of accumulators made from aluminum.

Unlike mechanical crimping, there is no tool wear due to the contactless process, and there is much less contamination during production. High stability is another advantage, as is the precise dosing of the amount of energy, which in turn allows highly accurate replicability. In addition, a new gas-tight anti-friction coating was developed for the aluminum housing to achieve optimal guide and wear behavior.

5. WEIGHT SAVINGS

The low weight of the new steel high-pressure accumulator was achieved with a variety of measures: a housing made of high-strength steel, dome-shaped end caps, an aluminum piston as media separator, and a reduction in the thickness of the pressure vessel's material. The housing wall's thickness is only marginally greater in certain areas, for example, at the ends where the end caps are attached. Even the shape of the end caps has been optimized. With their new design, they are the best possible compromise between weight and axial length under high pressure loads.

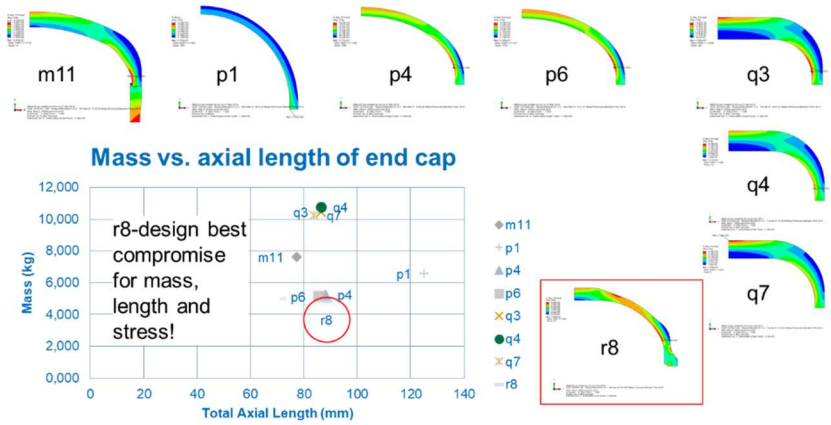

Figure 5: Design study

If one assumes the standard industry design for a 20-liter piston accumulator weighing about 110 kg, the weight can be reduced to 45 kg with a conventional material (lightweight design using steel). This is equivalent to a weight savings of 59 percent for a high-pressure accumulator 800 mm in length, designed for a maximum pressure of 350 bar. The firmly joined connection of the caps and housing is reliably executed with electronic beam welding. The advantages are a low expenditure of energy, low heat input and thus reduced deformation, along with an oxidation-free connection of the materials. Still more weight reduction for high-pressure accumulators is possible with other plastics reinforced with carbon and glass fibers (CFK/GFK) as described below.

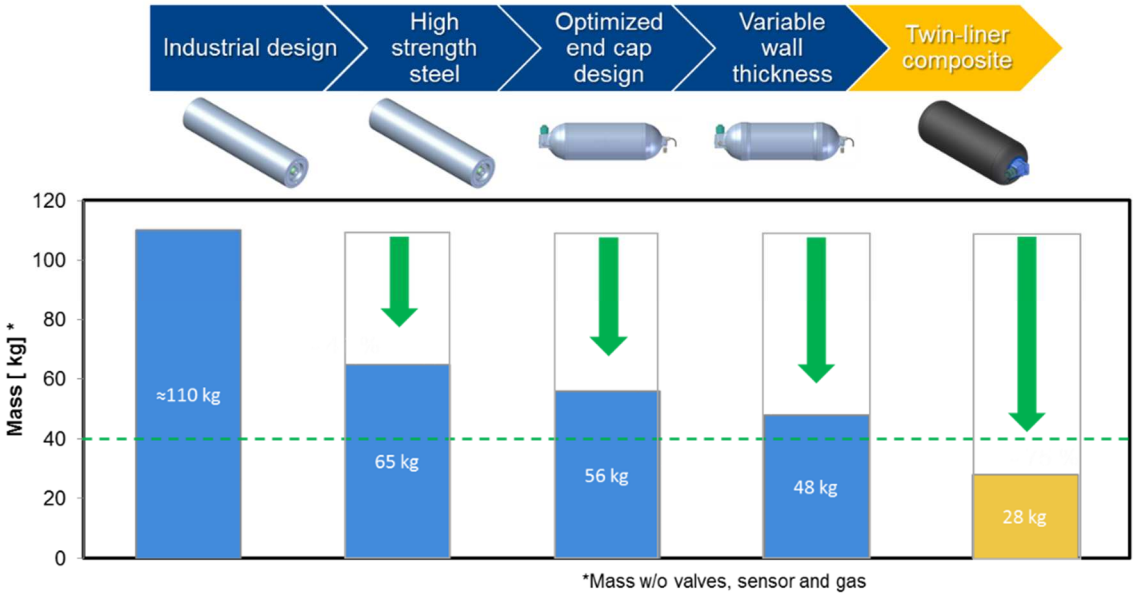

Figure 6: Overview weight reduction

6. NOISE REDUCTION

The noise generation that takes place when the piston strikes the end stop during a full discharge has also been optimized. In the new high-pressure accumulators, this is handled with hydraulic damping. Wide-ranging simulations of piston speeds were carried out to achieve this. Special sealing systems (elastomer/PTFE) with low friction are used in both hydraulic accumulators, which has a positive effect on efficiency and hysteresis. The result is good dynamic behavior with high efficiency and low permeation. The monitoring of the two accumulators' condition takes place with a combined pressure and temperature sensor. At the gas end, safety is assured with pressure and temperature sensors. On the liquid side, there is also a valve for filling the entire system. It can also be used to prevent potential air pockets with evacuation. A rupture disk is a safeguard in the event of overpressure, and a fuse in the event of a vehicle fire.

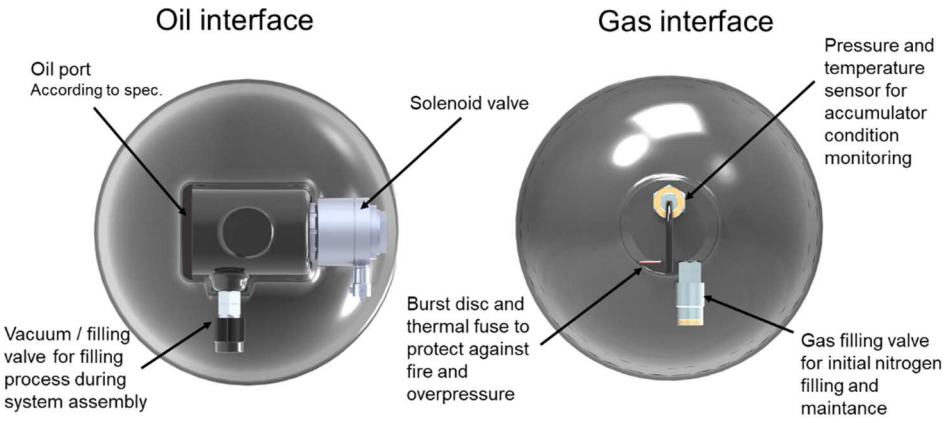

Figure 7: Design of high pressure accumulator

7. COMPOSITE SOLUTIONS

The use of carbon- and glass fiber-reinforced plastics (CFK/GFK) illustrates how great the potential remains for weight reduction in high-pressure accumulators. In combination with an aluminum piston, the weight for single- or twin-liner designs is reduced to 21 and 28 kg respectively. But measures are needed to deal with the low weight of the single liner, which features an external CFK hull, to prevent potential widening under high pressure. This can certainly be achieved with thicker walls and a particularly strong fiber, but they increase the costs.

On the other hand, the twin-liner, for which Freudenberg Sealing Technologies has filed a patent, also reduces weight significantly. Besides an external hull made of CFK/GFK, a liner in which the piston moves is integrated in its interior. The end caps have also been optimized with regard to geometry and potential fiber windings.

8. SUMMARY

Freudenberg Sealing Technologies has developed a new accumulator system for hydraulic hybrids to recapture kinetic energy from the braking process.

Figure 8: Low and high pressure accumulator

This reduces fuel consumption and CO_2 emissions. The high efficiency of this innovative solution is based on, among other aspects, the significant weight savings resulting from a special design and new joining techniques.

REFERENCES

[1] Dr. Christine Ehret, Dr. Gerhard R. Geerling, Dr. Markus G. Kliffken, Frank Nagel. Reference 1. Hydrostatic Regenerative Braking System (HRB); Conference on Hybrid Drives for Mobile Work Machines; February 2007, Karlsruhe, Germany.

[2] Rydberg, Karl-Erik. Reference 2. Energy Efficient Hydraulic Hybrid Drives; 11th Scandinavian International Conference on Fluid Power SICFP09, June 2-4, 2009, Linköping, Sweden.

METHODS FOR DETERMINATION OF THE GAP HEIGHT IN WATER-LUBRICATED CONTACTS

Florian Schoemacker, Katharina Schmitz
Institute for Fluid Power Drives and Systems (ifas), RWTH Aachen University
Campus-Boulevard 30, 52074 Aachen, Germany
E-mail: florian.schoemacker@ifas.rwth-aachen.de

ABSTRACT

Applications, which require the pressure fluid to be environmentally safe, often use water hydraulics as motion technology. If the tribological contacts of the components are chosen to be lubricated with water as well, the gap height is reduced compared to oil lubrication due to the lower viscosity of water. Because of occurring wear and increased leakage the pressure load of the components is limited. This limitation is investigated for the purpose of the piston slipper / swash plate contact of an axial piston pump. This research is based upon simulation using a model containing the Reynolds-Equation and a solid contact model. Furthermore deformation of the slipper surface is considered.

KEYWORDS: water hydraulics, piston slipper, hydrodynamic pressure distribution, solid contact pressure, gap height distribution, deformation

1. INTRODUCTION

Applications for water hydraulics are nowadays found in press and mining, as well as food and pharmaceutic industries. For these applications the pressure medium needs to be non-flammable and non-toxic. If water-lubricated components are used, the pressure level of the hydraulic system is limited to about 160 to 210 bar [1]. The limitation is caused by wear and leakage in tribological contacts. Due to the lower viscosity of water in comparison to oil, a relatively small gap height is needed to build up sufficient pressure in order to bear high loads. This results in mixed friction, since the gap height is of the same magnitude as the surface roughness. Therefore plastic materials are often used for the tribological contacts in water piston pumps.

Tribological contacts for water lubrication need to be investigated thoroughly in order to design a robust contact regarding the low gap height, mixed friction and leakage. The contact between the piston slipper and swash plate in axial piston machines has been studied for oil and water hydraulics in various research projects. This paper deals with a simulation model including hydrodynamics and solid contact pressure, in order to determine the gap height for the motion of the slipper in water-lubricated contacts using plastic materials. In this work the results are discussed regarding the pressure level limitation in water hydraulic systems.

1.1. State of the Art

Böinghoff [2] investigated the contact of piston slippers and swash plates in oil hydraulic axial piston machines. He introduced the idea of the theoretical compensation ratio as a value for the load-carrying capacity of slippers and discussed the effect of a tilted piston slipper on the pressure field. Böinghoff also analytically described the gap height and leakage in the contact. Furthermore he experimentally investigated the friction and leakage behaviour for different slipper pad geometries.

Donders [3] focused on the optimisation of piston pumps for HFA fluids, which is a solution of water containing up to 5 % of additives supporting lubrication. In his research he also investigated the contact between the slipper and the swash plate. Donders experimentally determined the gap height, friction coefficient and leakage for the tribological contact. The gap height is measured to be in range of 4 to 6 µm.

Manring et al. [4] investigated the effect of linear deformations using an analytical solution of a hydrostatic slipper bearing. Calculations were done for concave and convex deformations. A convex deformation signifies that the gap height at the outer radius of the slipper collar is greater than at the inner radius. The deformation of a concave slipper is vice versa. A concave deformation leads to a higher, a convex deformation to a lower load carrying capacity. The leakage is increased in both cases.

Kazama [5] developed a simulation model for the slipper/swash plate contact for mixed lubrication with water. He used the Average Flow Model of Patir and Cheng and the asperity-contacting model of Greenwood-Williamson in his simulation. Therefore this simulation model considers several side-effects that occur during mixed lubrication. Kazama investigated the effect of an eccentric position of the piston pressure force, which leads to greater inclination angles of the slipper, a higher contact pressure. He also investigated the dynamic behaviour of the gap height due to the pressure load of the piston's displacement chamber.

Rokala [6] thoroughly investigated the contact between slipper and swash plate for axial piston machines in order to verify the function of the tribological contact in a variable displacement water pump. This means that due to the changing swash plate angle the load force for the slipper contact varies as well. For this purpose Rokala developed a test bench containing a swash plate with a variable angle and a piston/slipper assembly. He measured the gap height of the slipper during operation to be about 7 to 10 µm. Furthermore a simulation of the deformation of the slipper was carried out and the resulting pressure distribution was calculated. Rokala concludes that the development of a variable displacement water pump is possible.

For tribological contacts in water hydraulic components, the knowledge of the resulting gap height during operation of the system is far more concerning that in the case of oil hydraulics, due to the reduced viscosity of the fluid. The references state an experimental as well as a simulative approach to this topic. Research at ifas has shown that the major important effect on the load carrying capacity and therefore the gap height is the deformation of the sliding surfaces due to the use of plastic materials in water hydraulics [7]. The simulation has been carried out for a slipper without motion leaving out hydrodynamic effects.

2. GEOMETRY AND MATERIAL SELECTION

For the analysis, the geometry of a piston slipper of axial piston pumps has been chosen. Designs of axial piston pumps can be found in both oil hydraulics and water hydraulics. The research focuses on axial piston pumps with a nominal speed of 1500 rpm and a pressure level up to 300 bar. As pressure medium tap water and respectively HFA fluid is used. The geometrical parameters as well as the material properties are stated in **Fig. 1**.

Piston Slipper	
Geometry	**Value**
D_{Piston}	17 mm
D_{Pocket}	13 mm
D_{Slipper}	20 mm
$q_{\text{C,th}}$	0.93
$q_{\text{C,in}}$	0.58

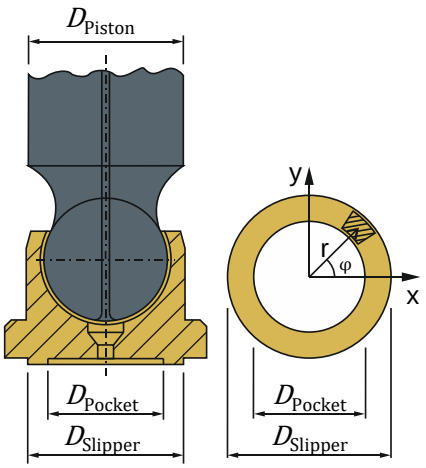

Water Hydraulic Contact	
Medium	**Properties**
Water	Density: 1000 kg/m^3
	Viscosity: 1·10^{-6} m^2/s
Stainless steel	Modulus of elasticity: 210·10^9 N/m^2
	Poisson's ratio: 0.3
Plastic (PEEK)	Modulus of elasticity: 3.6·10^9 N/m^2
	Poisson's ratio: 0.42

Figure 1. Geometry of a piston slipper of an axial piston pump

In the piston slipper contact the load force is usually hydrostatically compensated to a certain degree which reduces the remaining load for the hydrodynamic bearing. The disadvantage of this method is that a hydrostatic compensation causes leakage. In conclusion a compromise has to be found between high load carrying capacity and low leakage. In order to estimate the amount of the hydrostatically compensated load while designing the contact, usually the theoretical compensation is stated as the force ratio $q_{\text{C,th}}$ calculated using **Eq. 1**.

$$q_{\text{C}} = \frac{F_{\text{Fluid}}}{F_{\text{Piston}}} \Rightarrow q_{\text{C,th}} = \frac{p_{\text{HP}} \cdot D_{\text{Pocket}}^2 \cdot \frac{\pi}{4} + \int_{D_{\text{Pocket}}/2}^{D_{\text{Slipper}}/2} \left(p_{\text{HP}} - p_{\text{HP}} \cdot \frac{\ln(2 \cdot r / D_{\text{Pocket}})}{\ln(D_{\text{Slipper}}/D_{\text{Pocket}})} \right) \cdot 2\pi \cdot r \cdot dr}{p_{\text{HP}} \cdot A_{\text{Piston}}} = \quad \text{(Eq. 1)}$$

$$q_{\text{C,th}} = \frac{p_{\text{HP}} \cdot \left(D_{\text{Slipper}}^2 - D_{\text{Pocket}}^2 \right) \cdot \frac{\pi}{8} / \ln\left(D_{\text{Slipper}} / D_{\text{Pocket}} \right)}{p_{\text{HP}} \cdot D_{\text{Piston}}^2 \cdot \frac{\pi}{4}} = \frac{D_{\text{Slipper}}^2 - D_{\text{Pocket}}^2}{2 \cdot D_{\text{Piston}}^2 \cdot \ln\left(\frac{D_{\text{Slipper}}}{D_{\text{Pocket}}} \right)}$$

For this equation the piston slipper has a circular geometry and a logarithmic pressure drop for the sliding surface is assumed. This assumption bases upon a constant gap height, which causes the pressure drop due to leakage, and no sliding motion of the piston. But the remaining, non-compensated load would actually close the gap. This means that the theoretical compensation does not apply to real contacts.

If only the load carrying capacity of the slipper's inner pocket is calculated (without the logarithmic pressure drop over the collar), the theoretical compensation would yield to $q_{\text{C,in}}$ = 0.58. Compared to the overall theoretical compensation ($q_{\text{C,th}}$ = 0.93) for the chosen geometry, the difference indicates that the load carrying capacity depends strongly on the pressure profile over the slipper's collar. Therefore the resulting gap height is affected by the pressure build-up during motion and also deformation of the surfaces. In order to consider these impact factors, the pressure profile needs to be calculated using the Reynolds-Equation.

3. SIMULATION MODEL OF FLUID FILM PRESSURE

The Reynolds-Equation (**Eq. 2**) is widely used for simulating lubricated contact problems and is also applicable for water lubrication because water is a Newtonian fluid as well as oil. The Reynolds-Equation is given below in polar coordinates.

$$\frac{\partial}{\partial r}\left(r \cdot \frac{h^3}{12 \cdot \mu} \cdot \frac{\partial p}{\partial r} \right) + \frac{\partial}{\partial \varphi}\left(\frac{h^3}{12 \cdot \mu} \cdot \frac{1}{r} \cdot \frac{\partial p}{\partial \varphi} \right) - \frac{u_r}{2} \cdot \frac{\partial}{\partial r} \cdot (r \cdot h) - \frac{u_\varphi}{2} \cdot \frac{\partial h}{\partial \varphi} = \frac{\partial h}{\partial t} \cdot r \quad \text{(Eq. 2)}$$

For this research the dynamic change of the gap height is neglected ($\frac{\partial h}{\partial t} \cdot r = 0$). In the form given in **Eq. 2** the Reynolds-Equation is only capable of calculating fluid film pressure. The slipper / swash plate contact is discretized using finite volume elements which are described in the polar coordinate system. This choice of

coordinate system fits the geometrical appearance of the fluid film in the tribological contact. The discretization is shown in **Fig. 2**. In the x-y-plane finite volume elements are placed in a way that the position is given in the polar coordinate system. For each element the gap height is known and the local pressure is calculated using the Reynolds-Equation resulting in an overall pressure distribution for the contact.

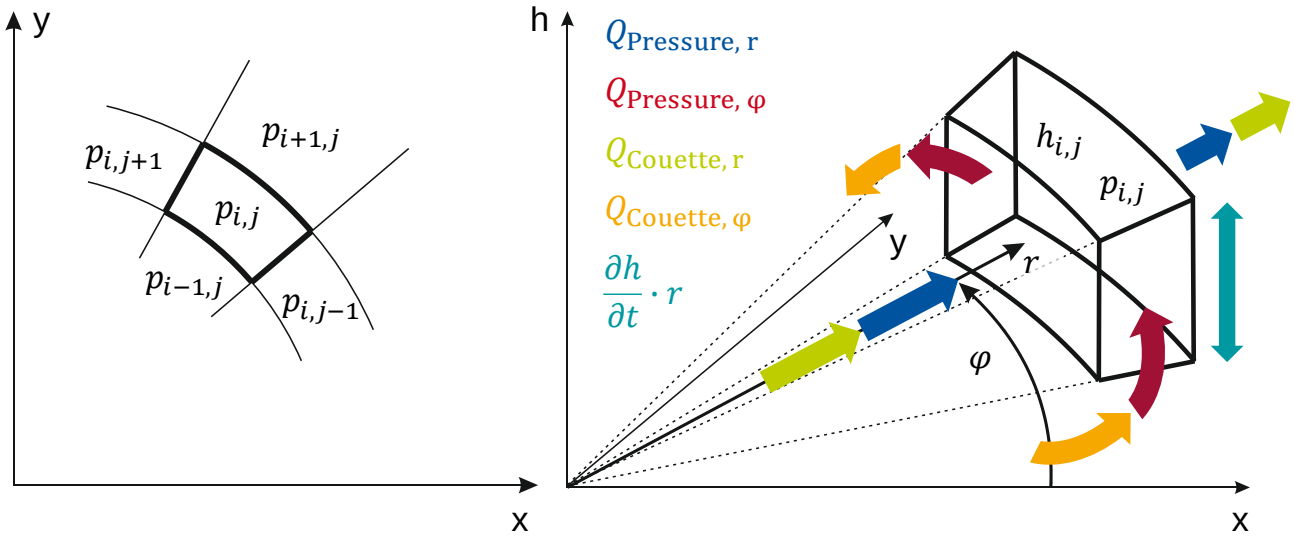

Figure 2. Polar coordinate system

In general the Reynolds-Equation describes the dynamic change of an infinite element's volume due to the difference of input and output flow of the pressure Q_{Pressure} and Couette Q_{Couette} flow. Therefore, for one element the volume flows can be discretized using the following formulas.

$$Q_{\text{Pressure, r}} = \frac{\left(r - \frac{dr}{2}\right) \cdot d\varphi \cdot \left(\frac{h_{i-1,j} + h_{i,j}}{2}\right)^3}{12 \cdot \eta} \cdot \frac{p_{i-1,j} - p_{i,j}}{dr} - \frac{\left(r + \frac{dr}{2}\right) \cdot d\varphi \cdot \left(\frac{h_{i,j} + h_{i+1,j}}{2}\right)^3}{12 \cdot \eta} \cdot \frac{p_{i,j} - p_{i+1,j}}{dr} \quad \text{(Eq. 3)}$$

$$Q_{\text{Pressure, φ}} = \frac{dr \cdot \left(\frac{h_{i,j-1} + h_{i,j}}{2}\right)^3}{12 \cdot \eta} \cdot \frac{p_{i,j-1} - p_{i,j}}{r \cdot d\varphi} - \frac{dr \cdot \left(\frac{h_{i,j} + h_{i,j+1}}{2}\right)^3}{12 \cdot \eta} \cdot \frac{p_{i,j} - p_{i,j+1}}{r \cdot d\varphi}$$

$$Q_{\text{Couette, r}} = \frac{\left(r - \frac{dr}{2}\right) \cdot d\varphi \cdot \frac{h_{i-1,j} + h_{i,j}}{2} \cdot v_r}{2} - \frac{\left(r + \frac{dr}{2}\right) \cdot d\varphi \cdot \frac{h_{i,j} + h_{i+1,j}}{2} \cdot v_r}{2}$$

$$Q_{\text{Couette, φ}} = \frac{dr \cdot \frac{h_{i,j-1} + h_{i,j}}{2} \cdot v_\varphi}{2} - \frac{dr \cdot \frac{h_{i,j} + h_{i,j+1}}{2} \cdot v_\varphi}{2}$$

$$Q_{\text{Pressure, r}} + Q_{\text{Pressure, φ}} + Q_{\text{Couette, r}} + Q_{\text{Couette, φ}} = 0$$

In this research the circular movement of the slipper on the swash plate is simplified as a linear sliding motion in only the x-direction. Therefore the formulas for the Couette flow are dependent on v_x instead of the individual velocities v_r and v_φ. The alteration leads to the formulas below (**Eq. 4**).

$$Q_{\text{Couette, r, in}} = \frac{1}{2} \cdot \frac{h_{i,j} + h_{i+1,j}}{2} \cdot v_x \cdot 2 \cdot \left(r + \frac{dr}{2}\right) \cdot \sin\left(\frac{d\varphi}{2}\right) \cdot \cos\varphi \qquad \text{(Eq. 4)}$$

$$Q_{\text{Couette, r, out}} = \frac{1}{2} \cdot \frac{h_{i-1,j} + h_{i,j}}{2} \cdot v_x \cdot 2 \cdot \left(r - \frac{dr}{2}\right) \cdot \sin\left(\frac{d\varphi}{2}\right) \cdot \cos\varphi$$

$$Q_{\text{Couette, }\varphi\text{, in}} = \frac{1}{2} \cdot \frac{h_{i,j-1} + h_{i,j}}{2} \cdot v_x \cdot dr \cdot \sin\left(\varphi - \frac{d\varphi}{2}\right)$$

$$Q_{\text{Couette, }\varphi\text{, out}} = \frac{1}{2} \cdot \frac{h_{i,j} + h_{i,j+1}}{2} \cdot v_x \cdot dr \cdot \sin\left(\varphi + \frac{d\varphi}{2}\right)$$

4. SIMULATION OF SLIPPER CONTACT WITH SOLID CONTACT PRESSURE

Most tribological contacts run in the mixed-lubrication regime, thus the load is partly carried by hydrostatic, hydrodynamic and solid contact pressure, **Fig. 3**. The hydrostatic and hydrodynamic pressure distribution can be calculated using the Reynolds-Equation stated as **Eq. 2**. In order to achieve a hydrodynamic pressure build-up the slipper needs to be tilted against the corresponding surface during movement. Due to the lower viscosity compared to oil, the gap height of the hydrodynamic fluid film will be reduced in the case of water lubrication. Therefore the load part carried by solid contact pressure will be increased.

The solid contact pressure results from the interaction of the asperities on rough surfaces. In order to calculate the gap height distribution via simulation, in addition to the Reynolds-Equation (**Eq. 2**) a model for the solid contact pressure is needed because the gap height depends on each pressure distribution.

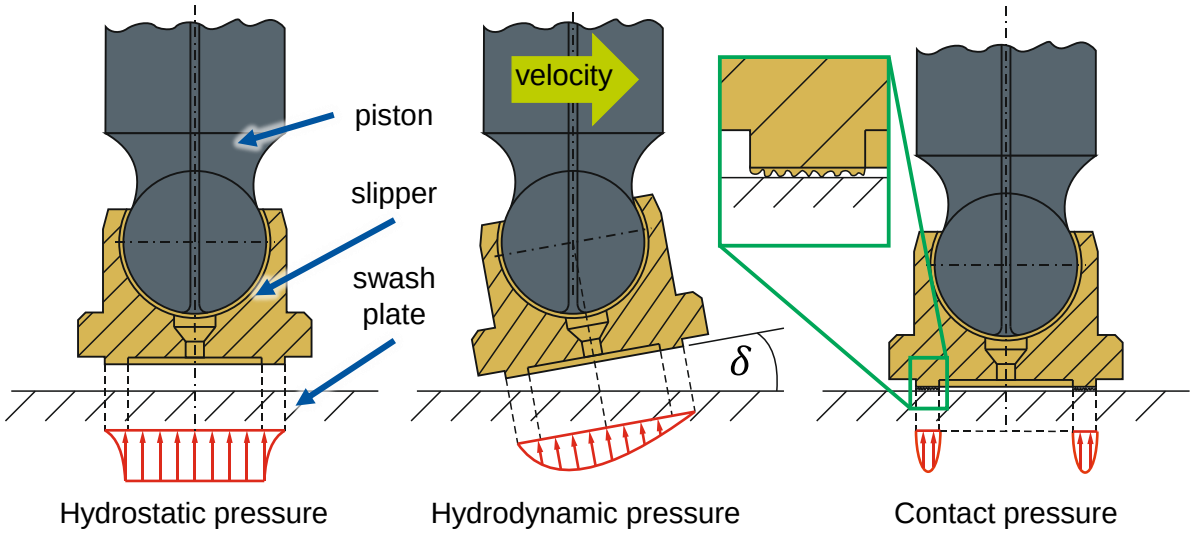

Figure 3. Pressure distribution due to different effects

4.1. Greenwood-Tripp / Patir-Cheng model

In the field of calculating solid contact pressure, the Greenwood model is widely used. The model exists in two different versions: one model considering only one rough surface (Greenwood-Williamson) and one model considering two rough surfaces (Greenwood-Tripp [8]). The model describes the dependency of the solid contact pressure towards the gap height and the surface roughness. In this research the Greenwood-Tripp model is used because both surfaces are assumed as rough, like in most tribological contacts. The solid contact pressure is calculated using **Eq. 5** [8].

$$p_c(h) = \frac{16 \cdot \sqrt{2}}{15} \cdot \pi \cdot E' \cdot (\eta \cdot \beta \cdot \sigma_{\mathrm{GT}})^2 \cdot \sqrt{\frac{\sigma}{\beta}} \cdot F_{5/2}\left(\frac{h}{\sigma_{\mathrm{GT}}}\right) \quad \text{(Eq. 5)}$$

The model requires several input parameters. E' is the reduced elastic modulus of both surfaces combined. η (1/m²) is the density of asperities on a finite area, β (µm) the radius of the summits of those asperities and σ_{GT} (µm) the standard deviation of the summit's heights. These three parameters are not independent and usually their product is given as 0.05. The standard deviation is also needed to calculate the dimensionless gap height. In the model σ_{GT} is defined as the standard deviation of the heights above the reference plane. Therefore it differs from the surface property Rq which is used by mechanical engineers to describe rough surfaces and equals the standard deviation σ of the surface roughness distribution, see **Fig. 4**. For the modelling σ_{GT} is reduced to 70 % of Rq and respectively σ.

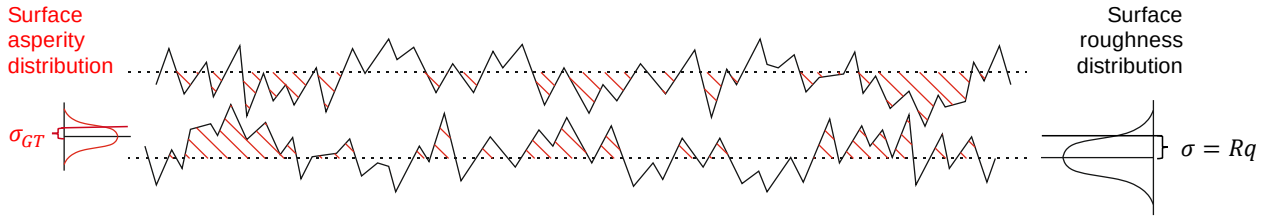

Figure 4. Description of the asperity distribution for models

The function $F_{5/2}$ is the probability that for a given gap height contact occurs between the asperities. The function is stated in **Eq. 6** and for the distribution of asperity heights a Gaussian distribution is implemented.

$$F_{5/2}\left(\frac{h}{\sigma_{\mathrm{GT}}}\right) = \int_u^\infty (s-u)^{\frac{5}{2}} \cdot \phi^*(s) \cdot ds = \frac{1}{\sqrt{2\pi}} \cdot \int_u^\infty (s-u)^{\frac{5}{2}} \cdot e^{-s^2/2} \cdot ds \quad \text{(Eq. 6)}$$

In addition to the Greenwood-Tripp model, the Patir-Cheng average flow model, **Eq. 7** [9], needs to be included because in the case of surface asperities coming into contact, the fluid flow is altered as well. In comparison to the original Reynolds-Equation, the average flow model includes flow factors for the pressure ($\phi_{p,r}$, $\phi_{p,\varphi}$) and shear flow ($\phi_{s,r}$, $\phi_{s,\varphi}$), increasing or decreasing the volume flows depending on the texture of the asperities. The result of this equation is the average pressure for a given finite volume element which has an average gap height.

$$\frac{\partial}{\partial r}\left(\phi_{p,r} \cdot r \cdot \frac{h^3}{12 \cdot \mu} \cdot \frac{\partial \bar{p}}{\partial r}\right) + \frac{\partial}{\partial \varphi}\left(\phi_{p,\varphi} \cdot \frac{h^3}{12 \cdot \mu} \cdot \frac{1}{r} \cdot \frac{\partial \bar{p}}{\partial \varphi}\right) - \frac{u_r}{2} \cdot \frac{\partial}{\partial r} \cdot \left(r \cdot \bar{h}_T\right) - \frac{u_r}{2} \cdot \sigma \cdot \frac{\partial}{\partial r} \cdot \left(r \cdot \phi_{s,r}\right) \quad \text{(Eq. 7)}$$
$$- \frac{u_\varphi}{2} \cdot \frac{\partial \bar{h}_T}{\partial \varphi} - \frac{u_\varphi}{2} \cdot \sigma \cdot \frac{\partial \phi_{s,\varphi}}{\partial \varphi} = \frac{\partial \bar{h}_T}{\partial t} \cdot r$$

The flow factors are calculated using the formulas of Patir and Cheng for a Peklenik factor of 1. The Peklenik factor describes the direction of a textured surface and results in an increased or decreased flow factor whether the texture supports or prevents fluid flow in the considered direction. For a factor of 1, no surface texture is given, and the flow factors are independent of the flow direction.

4.2. Gap height with rough surfaces

The described model, Reynolds-Equation combined with the Greenwood-Tripp model and Patir-Cheng model, has been implemented in the MATLAB software. The gap height has been estimated so that the load is carried by the fluid film pressure (hydrostatic and hydrodynamic) and the solid contact pressure. Thus, the load carrying capacity equals 1 because the entire load is balanced (**Eq. 8**).

$$q_{\mathrm{C,eff}} = \frac{F_{\mathrm{Fluid}} + F_{\mathrm{Contact}}}{F_{\mathrm{Piston}}} = \frac{\int (p_{\mathrm{Fluid}}(r,\varphi) + p_{\mathrm{Contact}}(r,\varphi)) \cdot dA}{p_{\mathrm{HP}} \cdot D_{\mathrm{Piston}}^2 \cdot \frac{\pi}{4}} = 1 \quad \text{(Eq. 8)}$$

The model has been used for calculating several different speeds, surface roughnesses and tilting angles. The simulation parameters used for the investigation are given in **Table 1**.

Table 1. Simulation parameters

Name and variable	Parameter and unit
Pressure p	50, 100, 150, 200, 250, 300 bar
Speed v	1, 2, 6 m/s
Tilting angle δ	0.005, 0.01°
Surface roughness σ	0, 0.4, 1.6 µm

The values for the speed result from a cylinder block with a pitch radius of 0.038 m, which is rotating with 250, 500 and 1500 rounds/min. A surface roughness with a standard deviation of σ = 0.4 µm is often used for sliding surfaces as a technically smooth surface. Bönghoff has shown that the tilting angle is set according to the friction in the piston-bushing contact and in the spherical joint [2]. The angle is estimated to be about 0.01°. The same value has been measured by Donders [3] and Rokala [6] as well for water hydraulic slippers. **Fig. 5** shows the simulation results for tilting angles of 0.005° and 0.01°.

The resulting gap height strongly depends on the given tilting angle of the slipper and the sliding speed. The gap height is in the range of 1 to 3 µm, increasing with greater speeds. Results show that the impact of the asperities depends on the standard deviation of the height distribution, causing the gap height to slightly increase with higher asperities. Furthermore the leakage is decreased if the asperities have the magnitude of the gap height. Thus, for rather smooth surfaces the effect can be neglected.

Donders [3] has measured the gap height to be in the range of 2 to 3 µm for slipper using HFA-fluid and the slipper had an inclination angle of about 0.01°. Rokala [2] instead measured a gap height above 7 µm. Compared to the results of the simulation, the results of Donders are of the same range. But the results of Rokala seem to be fairly large, being in the range of oil hydraulic slipper contacts. Rokala used piston slippers with plastic materials on the sliding surface. Due to the use of plastic slippers, large deformations occur in the slipper contact. The geometry used by Rokala results in a concave deformation leading to an increase of the load carrying capacity. This aspect needs to be studied for this research's geometry as well because the deformation of plastic slipper surfaces can be of the magnitude as the gap height itself.

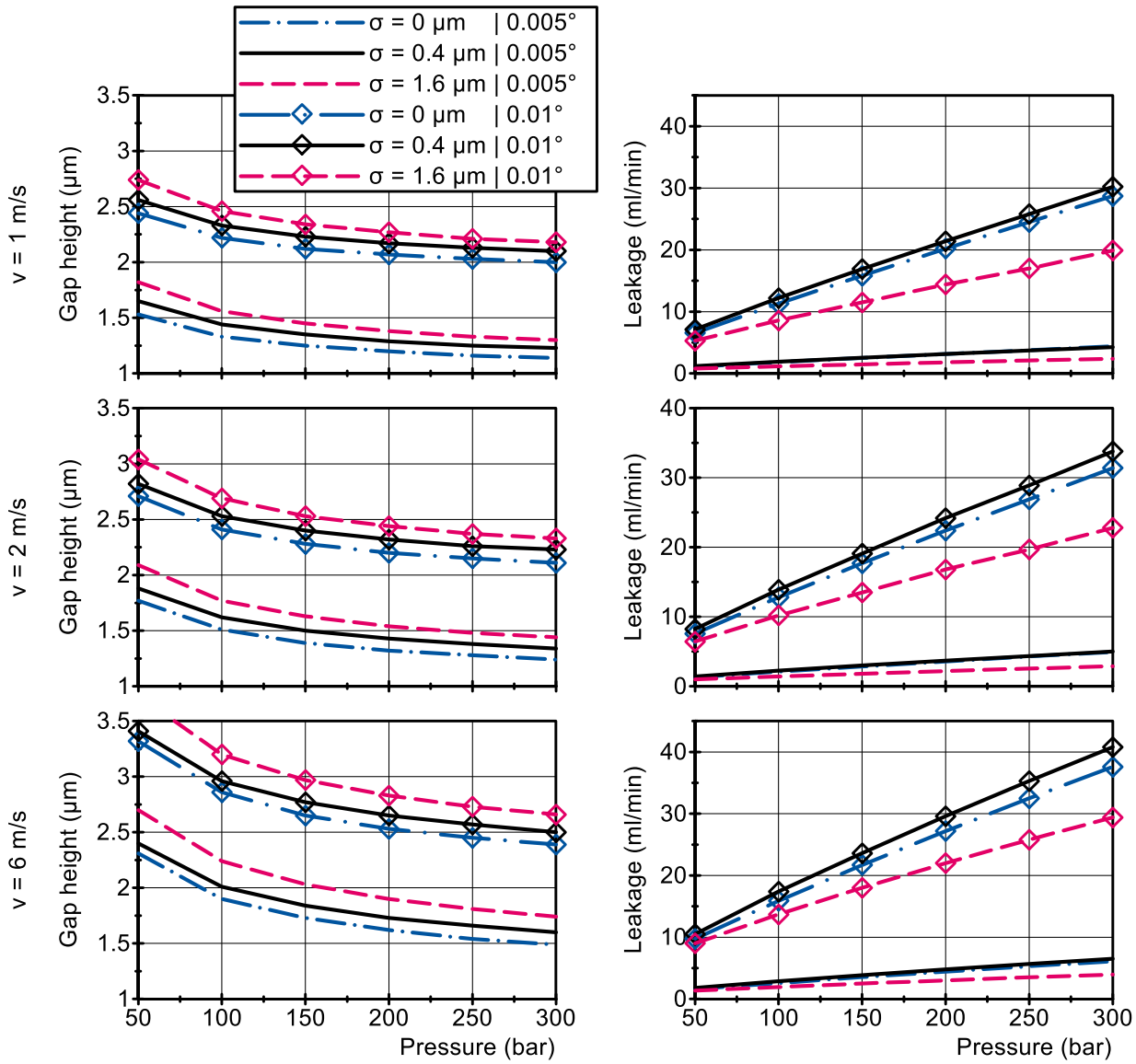

Figure 5. Results for tilting angles δ of 0.005° and 0.01°

5. DEFORMATION

The impact of the deformation of the slipper pad's surface on the gap height is further investigated. For this purpose the simulation model is combined with an additional simulation in ANSYS Workbench. The plastic material is assumed to be linear elastic with the given material properties in **Fig. 1**. The deformation is rather small compared to the nominal thickness of the disc (1 mm). At first the pressure distribution is calculated using the MATLAB code and afterwards the deformation of the surface is calculated in ANSYS. The new gap height distribution is taken from the deformation result and given as an input once again into the MATLAB code. This iteration process is performed several times until the gap height changes are in the range of 0.001 µm.

For the simulation the following parameters have been used: σ = 0.4 µm, δ = 0.01°. The results are shown in **Fig. 6** and **Fig. 7** for 100 and 300 bar and the piston is moving at 6 m/s. The deformation in the FEM-representation is exaggerated by a factor of 200.

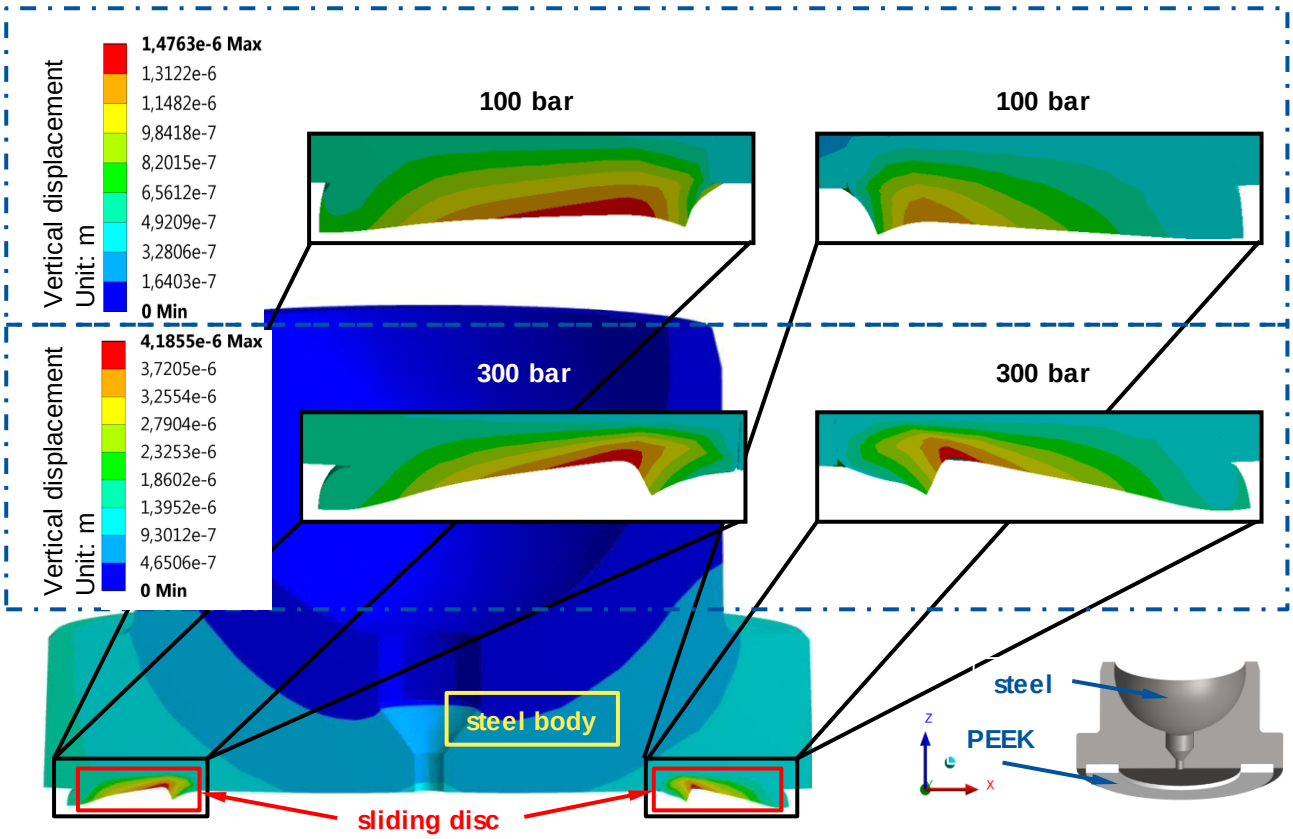

Figure 6. Deformation given as vertical displacement in ANSYS (v = 6 m/s ,σ = 0.4 µm, δ = 0.01°)

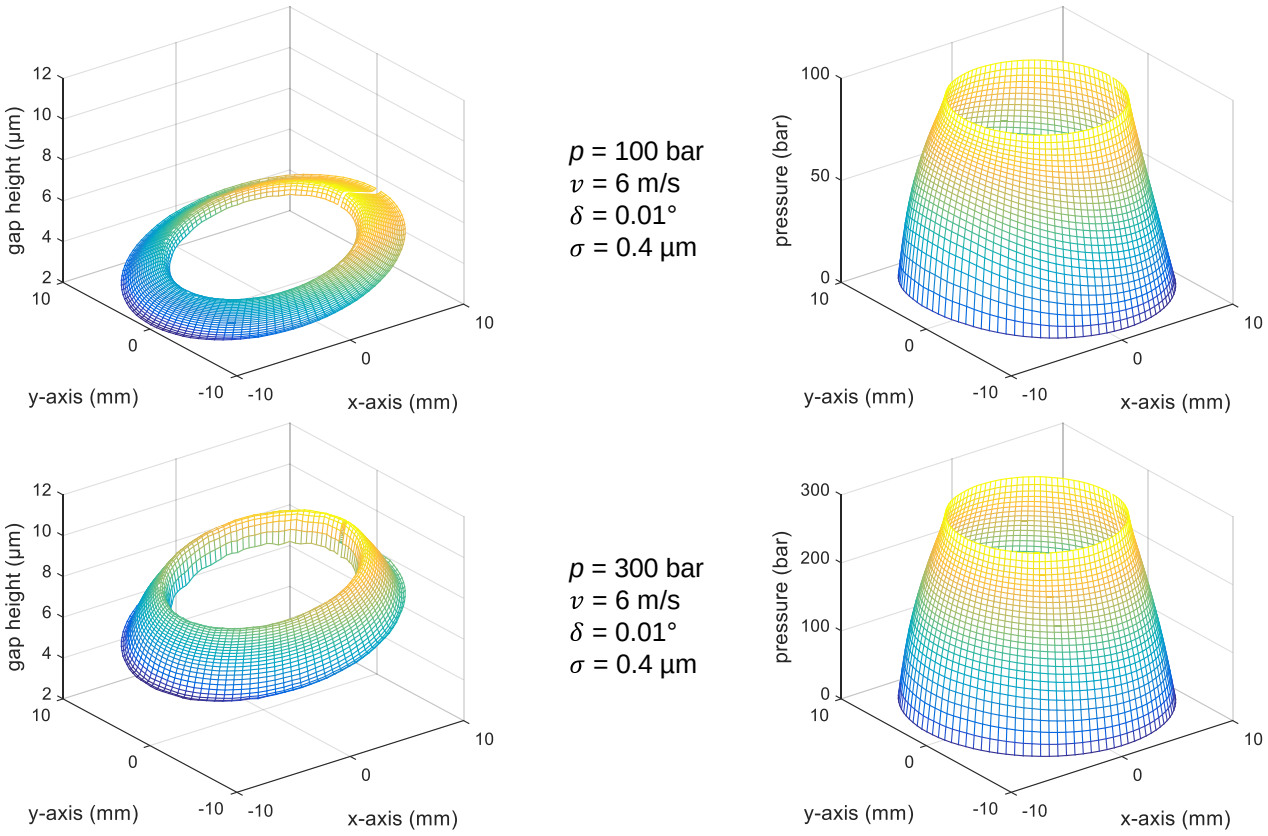

Figure 7. Results of MATLAB corresponding to Fig. 7

The deformation shows a distribution for the radius and the angle due to the moving of the slipper and the resulting pressure distribution. The deformation for 300 bar pressure is about 3 times greater compared to

100 bar. Furthermore the deformation is concave according to Manring [4]. The deformation allows the pocket pressure to spread under the slipper pad and the pressure gradient from pocket to case pressure increases. Therefore the load-carrying capacity is increased leading to a higher gap height and therefore to increased leakage.

A convex deformation, which leads to a lower load-carrying capacity and therefore lower gap heights, is not reasonable for water lubrication because the already small gap height would be reduced even further. This concept can for example be used for oil hydraulics, with greater gap heights, or even for fully hydrostatic compensated piston slipper contacts. In these contacts leakage is quite high and increases significantly with pressure. Therefore a tribological system which closes the gap with increasing pressure is reasonable.

This simulation has been done for several pressures and speeds. The resulting gap height and leakage of the slippers is shown in **Fig. 8**. The gap height is the nominal gap height, which is the distance of the plane surface to the middle of the tilted undeformed surface plane of the slipper. To this nominal gap height the gap height distribution caused by the deformation has to be added. Therefore the local gap height, necessary for the Reynolds-Equation, is greater than the nominal gap height.

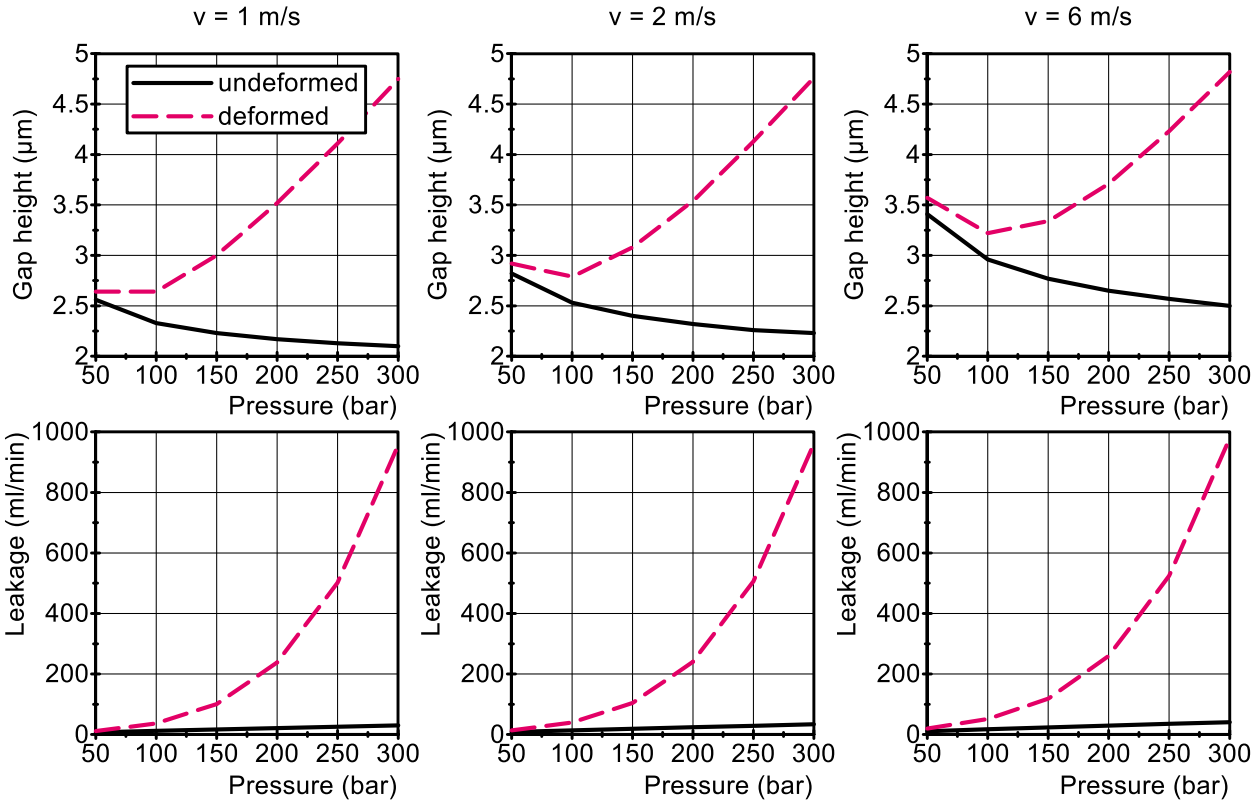

Figure 8. Results (σ = 0.4 µm, δ = 0.01°)

Fig. 9 shows that an undeformed, rigid body slipper tends to close the gap even though the pressure increases. This behaviour is changed entirely once the deformation is considered. The increase of the gap height over pressure is about 1 to 2 µm which is quite large compared to the original gap height. Furthermore the leakage is increased by a factor of 25, leading to leakages of up to 1 l/min. This amount counts for one piston. The overall leakage will lead to a significant decrease of efficiency. From these results, the limitation for water lubrication can be estimated to about 200 bar, which results in 0.2 l/min leakage. A further pressure build up to 300 bar increases the leakage by factor 5 and results in 0.5 kW power loss.

6. CONCLUSION

The investigation of the slipper / swashplate with water lubrication has been conducted using a simulation model containing the Reynolds-Equation including with the Greenwood-Tripp and Patir-Cheng models. Furthermore the model has been combined with a simulation of the surface deformation for a plastic slipper pad, carried out in ANSYS Workbench.

The results show that the typical gap height of the water-lubricated slipper contact is in the range of about 2 to 4 µm, which is also given by literature references. The deformation of the surface increases the gap height as well. The increase in leakage shows the limitation for pressure in water-lubricated contacts using plastic materials.

The investigation is only theoretical and needs yet to be validated using experiments with the given geometry and materials. A disadvantage of this way of modelling are not known input parameters and the loss of accuracy due to the use of simplification.

The benefit of this research is a statement of the limits of water lubrication in the piston slipper / swashplate contact according to the pressure range and the used materials, e.g., plastic materials.

7. ACKNOWLEDGEMENTS

Supported by:

Federal Ministry
for Economic Affairs
and Energy

on the basis of a decision
by the German Bundestag

The research work leading to this publication was funded by the German Federal Ministry for Economic Affairs and Energy under the reference ZF4199603KO6 as a cooperation project between Institute of Fluid Power Drives and Systems (IFAS), RWTH Aachen University and Hauhinco Maschinenfabrik GmbH & Co.KG. The responsibility for the content of this paper lies with the authors. The authors are grateful for the funding.

NOMENCLATURE

Variable	Description	Unit
μ	Dynamic viscosity	(Pa · s)
h	Nominal gap height	(mm)
D_{Piston}	Diameter of piston	(mm)
D_{Pocket}	Diameter of pocket in slipper contact, inner diameter	(mm)
D_{Slipper}	Outer diameter of slipper contact	(mm)
q_{C}	Compensation of normal load force	(-)
p_{HP}	Piston displacement chamber pressure	(bar)
$p_{(r,\varphi)}$	Pressure profile in slipper contact	(bar)
p_{c}	Solid contact pressure	(MPa)
R_{TK}	Radius of pitch circle	(mm)
A_{eff}	Area in slipper contact for pressure profile	(mm^2)
δ	Inclination angle	(°)
v	Speed in lateral direction	(m/s)
σ	Standard deviation of surface roughness	(µm)

REFERENCES

[1] E. Trostmann et al. 2001. Tap water as a hydraulic pressure medium. Marcel Dekker, Inc., New York.

[2] O. Böinghoff. 1977. Untersuchungen zum Reibungsverhalten der Gleitschuhe in Schrägscheiben-Axialkolbenmaschinen. PhD thesis, TU Braunschweig.

[3] S. Donders. 1997. Optimisation of High-Pressure Piston Pumps for HFA-Fluids. Proceedings of the 5th Scandinavian International Conference on Fluid Power, May 28-30 1997, Linköping, Sweden.

[4] N. Manring et al. 2002. The Impact of Linear Deformations on Stationary Hydrostatic Thrust Bearings. Journal of Tribology, volume 124, issue 4, pp. 874-877.

[5] T. Kazama. 2005. Numerical simulation of a slipper model for water hydraulic pumps/motors in mixed lubrication. Proceedings of the 6th JFPS International Symposium on Fluid Power, Tsukuba.

[6] M. Rokala. 2012. Analysis of slipper structures in water hydraulic axial piston pumps. PhD thesis, Tampere University of Technology, Tampere.

[7] F. Schoemacker & H. Murrenhoff. 2018. Piston slippers for robust water hydraulic pumps. Proceedings of the 11th International Fluid Power Conference, March 19–21 2018, Aachen, Germany.

[8] J.A. Greenwood & J.H. Tripp. 1970. The contact of two nominally flat rough surfaces. Proceedings of the Institution of Mechanical Engineers, Volume 185, Issue 1, pp. 625-653.

[9] N. Patir & H.S. Cheng. 1978. An average flow model for determining effects of three-dimensional roughness on partial hydrodynamic lubrication. Journal of Lubrication Tribology, volume 100, issue 1, pp. 12-17.

OPTIMIZATION OF SILENCING GROOVE FOR PORT PLATE OF WATER HYDRAULIC AXIAL PISTON PUMP

Hao Pang[1], Yinshui Liu[1], Shan Wu[2], Defa Wu[1], Qian Cheng[1]
1. State Key Laboratory of Digital Manufacturing Equipment and Technology,
Huazhong University of Science and Technology.
2.Department of General Course, Wuhan Technology and Business University.
Wuhan, Hubei, China.
panghao@hust.edu.cn

ABSTRACT

Water hydraulic axial piston pump is a key component in water hydraulic system. One of the most important drawbacks of water hydraulic system is noise and vibration, which mainly originate from the water hydraulic pump. And the noise and vibration mainly caused by pressure and flow ripple of pump. So there are great number of researches to reduce pressure and flow ripple, for example, the silencing groove of port plate. In this paper, the port plate of a water hydraulic axial piston pump with U-shaped silencing groove is investigated. Through establishing the pressure and flow mathematical model of a water hydraulic pump considering the silencing groove, the silencing groove of port plate is optimized. The simulation results show that the pressure and flow ripple with optimized port plate is decreased. Then the experiment verifies that the optimized silencing groove can be to reduce the pressure ripple.

KEYWORDS: water hydraulic, piston pump, pressure ripple, silencing groove.

1. INTRODUCTION

Water hydraulic axial piston pump, owing to high out-pressure and little leakage, are more and more widely used in water hydraulic system. As the main power source, water hydraulic axial piston pump is also the main noise and vibration source [1-3]. Noise and vibration are harmful since they can cause the component failure and hearing loss of machine operator. In order to reduce the noise and vibration of water hydraulic axial piston pump, one of best way is to reduce the noise and vibration source. The emitted noise of axis piston pump is composed of two types: fluid-borne noise and structure-borne noise [4-6]. As the sources of fluid-borne noise, the flow and pressure ripple are dominant contributor to the noise generation.

In recent years, there have been many researches to reduce the noise and vibration level of axial piston pump, in which many researchers have studied the port plate. Different types of silencing grooves were proposed to decrease the flow and pressure ripple. Harrison et al. [7] proposed a novel check valve port plate which was inherently speed, flow, and pressure sensing to reduce the pressure ripple of axis piston pump and the measurement results showed that the air-borne noise was reduced up to 6 dB by using this port plate. Guan, Jiao et al. [8] established the single- and multi-piston pump model considering the fluid compressibility, orifice restriction effect, fluid resistance in the capillary tube, and the leakage flow, based on an aviation axial-piston pump with damp holes in port plate The effects of the pre-pressurization fluid path on the flow ripple and the instantaneous pressure in the piston chamber have been studied and optimized design recommendations

have been given out. Xu, Sun et al. [9] proposed a design method for the transition region of valve plate to decrease the flow-pressure ripple and noise based on the matching of flow area. Mandal, Saha et al. [10] established a mathematic model of silencing groove and theoretically simulated the flow ripple for different leading-side groove in fixed-displacement axis piston pump. Yin and Nie et al. [11] studied pressure and vibration characteristics of seawater axis piston pump with different port plate which was designed with non-grooved, U-shaped and triangle-based pyramid (TP) silencing groove. It was concluded that the pressure and vibration amplitudes of the pump with TP silencing groove is lower. Xu B, Zhang J.H [12] researched a distribution method of axis piston pump with pressure equalization mechanism

According to researches mentioned above, all of them can't give a valid method to optimize the silencing groove for port plat of a water hydraulic axial piston pump. The present paper studies the flow and pressure ripple of a water hydraulic axial piston pump whose valve plate adopts combinatorial U-shaped silencing groove through establishing the theoretical model that considers the water compressibility, restriction effect of silencing groove and the leakage flow. The simulation results including the dynamic pressure in the piston chamber, the discharge flow of single piston and the pressure and flow ripple of the pump are realized by MATLAB/Simulink frame. With reference to the simulation results, the silencing groove is optimized. The experimental results show that the flow and pressure ripple, noise and vibration of optimized silencing groove is smaller than that of non-optimized silencing groove.

2. MATHEMATICAL MODEL

In order to investigate the effect of the U-shaped silencing groove on the pressure and flow ripple of water hydraulic axial piston pump. a mathematic model is established to study the effect of working medium characteristics on the piston chamber pressure. According to previous researches [9], the pressure and flow modelling principle of WHAPP is shown in *Figure*. *1*. Pin and Pout are the inlet and outlet pressure of the pump, respectively. P_{ci} is the piston chamber pressure. q_{ci} and q_{di} are respectively the absorption flow rate and discharging flow rate of single piston, respectively. q_{cli} is the leakage flow rate through the clearance between piston and cylinder bore. q_{sli} is the leakage flow between slipper and swash plate. q_{VL} is the leakage flow rate through the clearance between port plate and valve plate. According to the flow continuity equation, kinematical equations of pistons, pressure and flow equation of damp, the mathematical model of the water hydraulic pump will be gotten.

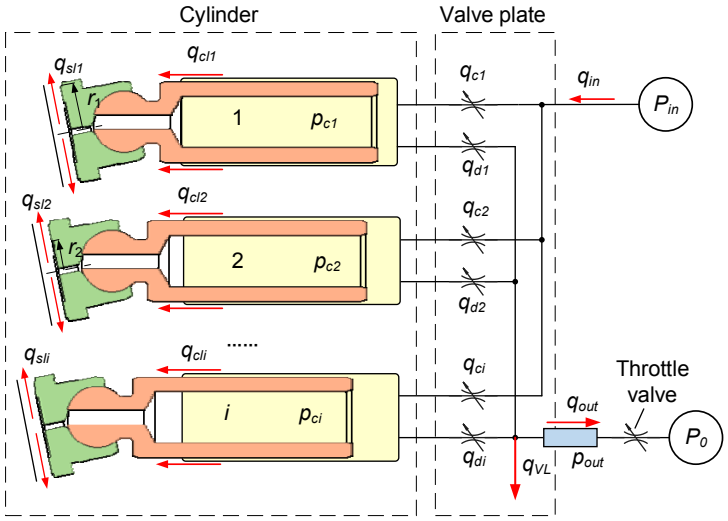

Figure 1. Modelling principle diagram of water hydraulic axial piston pump

Assuming that the top dead center (TDC, as shown in *Figure.2*) of valve plate is the initial position of piston, the displacement of piston *i* is expressed as follow:

$$s_{pi} = \frac{D_C}{2}\left(1 - cos(\omega t + (i-1)\frac{2\pi}{N})\right)tan\beta \quad (1)$$

Where D_C is the diameter of pistons distribution circle, ω is the angular velocity of WAHPP, β is the tilting angle of swash plate, N is the number of piston. So the velocity of piston along axial direction can be expressed as follow:

$$v_{pi} = \frac{ds_{pi}}{dt} = \frac{\omega D_C}{2} sin(\omega t + (i-1)\frac{2\pi}{N})tan\beta \quad (2)$$

Owing to the small clearance between slipper and swash plate, the flow between slipper and swash plate can be regarded as laminar flow. So the leakage flow rate through the gap between slipper and swash plate is described as:

$$q_{sli} = \frac{\pi\delta_s^3(P_{ci} - P_{in})}{6\mu ln k_s} \quad (3)$$

Where δ_s is the clearance between slipper and swash plate, μ is the dynamic viscosity of working medium, k_s is the structure parameter of slipper and $k_s=r_1/r_2$. r_1, r_2 are the outside and inside sealing area radius of slipper as shown in *Figure 1*.

As the same reason, the flow between piston and cylinder bore is also regarded as laminar flow. The leakage flow rate through the clearance between piston and cylinder bore is composed of two parts: one is caused by differential pressure, another is caused by piston reciprocating in cylinder. The leakage flow rate caused by differential pressure is expressed as follow:

$$q_{clpi} = \frac{\pi d\delta_p^3(P_{ci} - P_{in})}{12\mu(l + s_{pi})} \quad (4)$$

Where d is the diameter of piston, δ_p is the clearance between piston and cylinder bore, l is the length of piston left in cylinder bore.

The flow rate caused by piston motion is expressed as follow:

$$q_{clmi} = -\frac{\pi d\delta_p v_{pi}}{2} \quad (5)$$

Thus, the leakage flow rate through the clearance between piston and cylinder bore is:

$$q_{cli} = q_{clpi} + q_{clmi} \quad (6)$$

Piston reciprocates in cylinder bore. So the theoretical flow rate is:

$$q_{Ti} = \frac{1}{4}\pi d^2 v_{pi} \quad (7)$$

According to the liquid continuity equation and the definition of elastic modulus, the equation is gotten:

$$\frac{dp_{ci}}{dt} = \frac{B}{V_{ci}}(q_{Ti} - q_{sli} - q_{cli} - q_i) \quad (8)$$

Where B is the elastic modulus of working medium, V_{ci} is the volume encircled by piston and cylinder barrel is expressed as follow:

$$V_{ci} = V_{c0} + \frac{1}{4}\pi d^2\frac{D_C}{2}\left(1 + cos(\omega t + (i-1)\frac{2\pi}{N})\right)tan\beta \quad (9)$$

Where V_{c0} is minimum volume encircled by piston and cylinder barrel. q_i is the actual flow rate of piston chamber and can be expressed as:

$$q_i = q_{ci} + q_{di} \quad (10)$$

Where q_{ci}, q_{di} are respectively the absorption flow rate and discharging flow rate. *Figure.2* shows the position relationship between piston and the kidney groove. The working medium is absorbed and discharged into the piston chamber through the kidney groove, and the flow area change with the position of piston. Assuming that the flow satisfies the pressure-flow relationship of thin-wall orifice, the actual flow rate can be expressed as:

$$q_{ci} = C_d A_{ci} \sqrt{\frac{2|P_{ci} - P_{in}|}{\rho}} \operatorname{sgn}(P_{ci} - P_{in}) \tag{11}$$

$$q_{di} = C_d A_{di} \sqrt{\frac{2|P_{ci} - P_{out}|}{\rho}} \operatorname{sgn}(P_{ci} - P_{out}) \tag{12}$$

Where C_d is flow coefficient, A_{ci} is the flow area when the piston passes over suction side. A_{di} is the flow area when the piston passes over discharge side, ρ is the density of working medium.

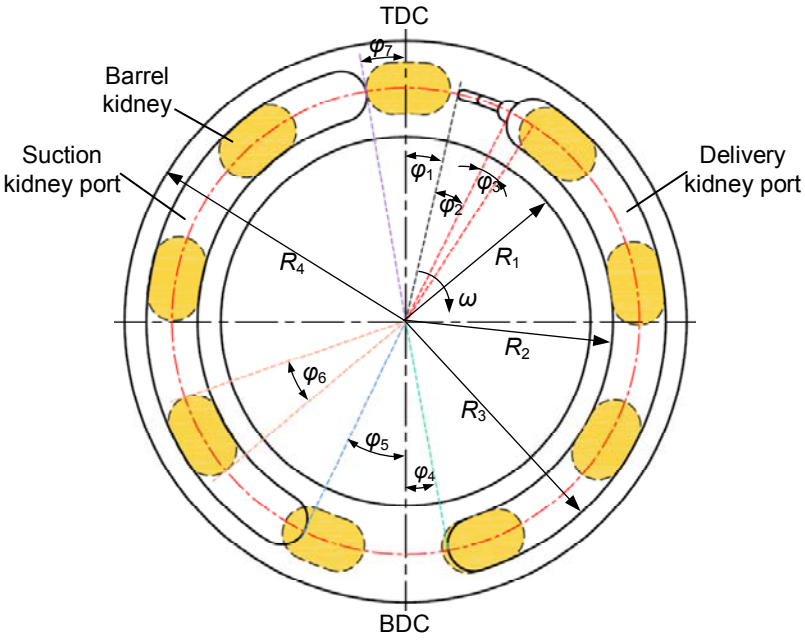

Figure 2. Valve plate with U-shaped silencing groove

The flow area A_{ci} and A_{di} change with the rotation angle of piston shown in *Figure 2* and *3*. Taking the TDC as the initial position of piston, the middle point of piston coincides with the TDC and the barrel kidney is tangent to suction kidney port at this point, as shown in *Figure.2*. Take the 1st piston as an example to calculate the discharge area A_{di} and suction area A_{ci}. When ωt (the rotation angle of piston) is at [0, φ_9], the barrel kidney doesn't connect with the discharge and suction kidney port. So the flow area is written as

$$A_{d1}=A_{c1}=0 \qquad 0 \le \omega t \le \varphi_9 \tag{13}$$

When ωt is at [φ_9, $\varphi_9+\varphi_{10}$], the barrel kidney connects with the Ⅰ stage of silencing groove, as shown in Fig.3. And the discharge area A_{di} is the cross area of silencing groove and can be described as

$$A_{d1} = a_1 h_1 \qquad \varphi_9 < \omega t \le \varphi_9 + \varphi_{10} \tag{14}$$

Where a_1 is the length of intersection line of barrel kidney and silencing groove and h_1 is the depth of silencing groove as shown in *Figure.3*. In this angle range, a_1 changes with rotation angle of piston ωt. Assuming that a_1 changes linearly with ωt, the a is given by

$$a_1 = \frac{m_1}{\varphi_{10}}(\omega t - \varphi_9) \qquad \varphi_9 < \omega t \le \varphi_9 + \varphi_{10} \tag{15}$$

Where m_1 is the width of silencing groove Ⅰ, Ⅱ stage. When ωt is at [$\varphi_9+\varphi_{10}$, φ_{11}], a_1 remains unchanged and equals to be m_1. So the discharge area A_{d1} can be expressed as

$$A_{d1}=m_1 h_1 \qquad \varphi_9 + \varphi_{10} < \omega t \le \varphi_{11} \tag{16}$$

Using the same analytical method as described above, the discharge area A_{d1} and suction area A_{c1} can be gotten when the 1st piston rotates with the cylinder barrel.

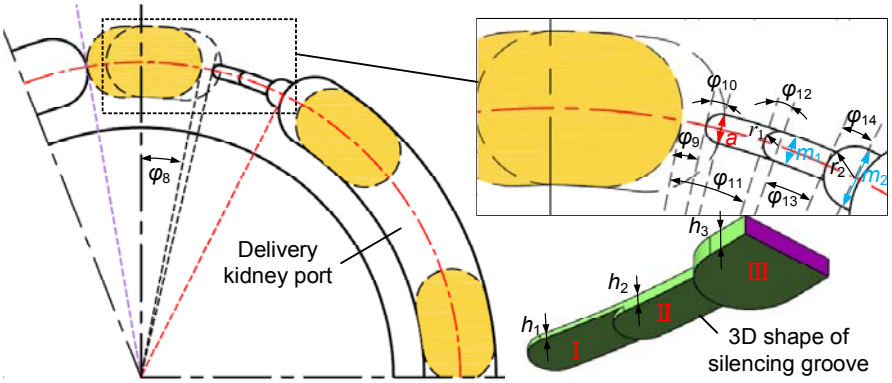

Figure 3. Position relationship between piston and the kidney groove

$$A_{d1}=\begin{cases} 0 & 0 \le \omega t \le \varphi_9 \\ \dfrac{m_1}{\varphi_{10}}(\omega t-\varphi_9)h_1 & \varphi_9 < \omega t \le \varphi_9+\varphi_{10} \\ m_1h_1 & \varphi_9+\varphi_{10} < \omega t \le \varphi_{11} \\ m_1h_1+\dfrac{m_1}{\varphi_{12}}(\omega t-\varphi_{11})(h_2-h_1) & \varphi_{11} < \omega t \le \varphi_{11}+\varphi_{12} \\ m_1h_2 & \varphi_{11}+\varphi_{12} < \omega t \le \varphi_{11}+\varphi_{12}+\varphi_{13} \\ m_1h_2+\dfrac{m_2h_3-m_1h_2}{\varphi_{14}}(\omega t-\varphi_{11}-\varphi_{12}-\varphi_{13}) & \varphi_{11}+\varphi_{12}+\varphi_{13} < \omega t \le \varphi_{11}+\varphi_{12}+\varphi_{13}+\varphi_{14} \\ m_2h_3 & \varphi_{11}+\varphi_{12}+\varphi_{13}+\varphi_{14} < \omega t \le \varphi_9+\varphi_2 \\ m_2h_3+\dfrac{\pi(R_3-R_2)^2-m_2h_3}{8\varphi_3}(\omega t-\varphi_1-\varphi_2) & \varphi_9+\varphi_2 < \omega t \le \varphi_9+\varphi_2+2\varphi_3 \\ \dfrac{\pi(R_3-R_2)^2}{4}+[\dfrac{A}{\varphi_6-2\varphi_3}-\dfrac{\pi(R_3-R_2)^2}{4(\varphi_6-2\varphi_3)}](\omega t-\varphi_1-\varphi_2-2\varphi_3) & \varphi_9+\varphi_2+2\varphi_3 < \omega t \le \varphi_9+\varphi_2+\varphi_6 \\ A & \varphi_6+\varphi_2+\varphi_6 < \omega t \le \pi-\varphi_4-\dfrac{\varphi_6}{2} \\ A-[\dfrac{A}{\varphi_6-2\varphi_3}-\dfrac{\pi(R_3-R_2)^2}{4(\varphi_6-2\varphi_3)}](\omega t-\pi+\varphi_4+\dfrac{\varphi_6}{2}) & \pi-\varphi_4-\dfrac{\varphi_6}{2} < \omega t \le \pi+\dfrac{\varphi_6}{2}-\varphi_4-2\varphi_3 \\ \dfrac{\pi(R_3-R_2)^2}{4}-\dfrac{\pi(R_3-R_2)^2}{8\varphi_3}(\omega t-\pi+-\dfrac{\varphi_6}{2}+\varphi_4+2\varphi_3) & \pi+\dfrac{\varphi_6}{2}-\varphi_4-2\varphi_3 < \omega t \le \pi+\dfrac{\varphi_6}{2}-\varphi_4 \\ 0 & \pi+\dfrac{\varphi_6}{2}-\varphi_4 < \omega t \le 2\pi \end{cases}$$

(17)

$$A_{c1}=\begin{cases} 0 & 0 \le \omega t \le \pi+\varphi_5-\dfrac{\varphi_6}{2} \\ \dfrac{\pi(R_3-R_2)^2}{8\varphi_3}\left(\omega t-\pi-\varphi_5+\dfrac{\varphi_6}{2}\right) & \pi+\varphi_5-\dfrac{\varphi_6}{2} < \omega t \le \pi+\varphi_5+2\varphi_3-\dfrac{\varphi_6}{2} \\ \dfrac{\pi(R_3-R_2)^2}{4}+\left(\dfrac{A}{\varphi_6-2\varphi_3}-\dfrac{\pi(R_3-R_2)^2}{4(\varphi_6-2\varphi_3)}\right)(\omega t-\pi-\varphi_5-2\varphi_3+\dfrac{\varphi_6}{2}) & \pi+\varphi_5+2\varphi_3-\dfrac{\varphi_6}{2} < \omega t \le \pi+\varphi_5+\dfrac{\varphi_6}{2} \\ A & \pi+\varphi_5+\dfrac{\varphi_6}{2} < \omega t \le 2\pi-\varphi_7-\dfrac{\varphi_6}{2} \\ A-\left(\dfrac{A}{\varphi_6-2\varphi_3}-\dfrac{\pi(R_3-R_2)^2}{4(\varphi_6-2\varphi_3)}\right)(\omega t-2\pi-\varphi_7+\dfrac{\varphi_6}{2}) & 2\pi-\varphi_7-\dfrac{\varphi_6}{2} < \omega t \le 2\pi+\dfrac{\varphi_6}{2}-\varphi_7-2\varphi_3 \\ \dfrac{\pi(R_3-R_2)^2}{4\varphi_7}(\omega t-2\pi-\dfrac{\varphi_6}{2}+\varphi_7+2\varphi_3) & 2\pi+\dfrac{\varphi_6}{2}-\varphi_7-2\varphi_3 < \omega t \le 2\pi \end{cases}$$

(18)

Where A is the area of barrel kidney. R_2, R_3 is the inside and outside radius of delivery/suction kidney port respectively. As for other pistons, for example ith piston, A_{di}, A_{ci}, have the same form as A_{d1}, A_{c1}, only needing to turn the ωt into $\omega t+2\pi/N(i-1)-2m\pi$, where m is the number of cylinder revolving cycles. The value of φ_1~φ_{14} are listed in *Table.1*. Substituting these parameters into equation (17) and equation (18), the curves of A_{di} and A_{ci} changing with time are shown in *Figure 4* when the speed of cylinder barrel is 1500r/min.

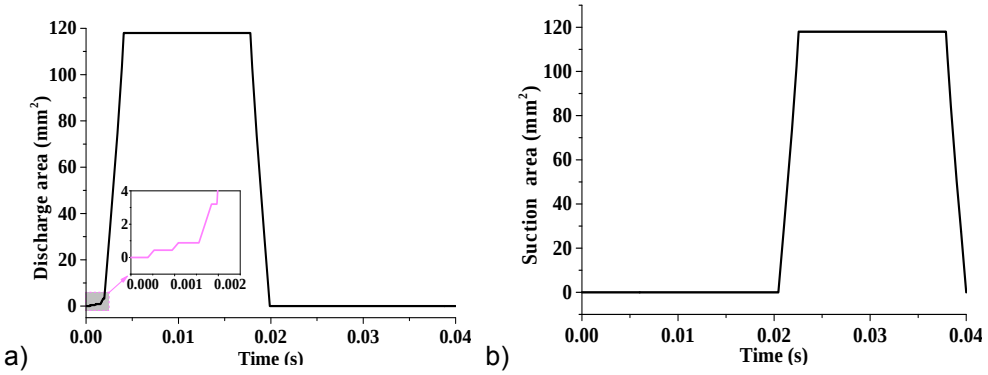

Figure 4. a) Flow area A_{di} changes with time; b) Flow area A_{ci} changes with time

Table 1. The value of design parameters for valve plate

Parameter	Value	Parameter	Value	Parameter	Value
φ_1 /°	13	φ_8 /°	9.5	R_2 /mm	38.1
φ_2 /°	14.21	φ_9 /°	3.5	R_3 /mm	47.8
φ_3 /°	6.48	φ_{10} /°	1.27	m_1 /mm	2
φ_4 /°	10.52	φ_{11} /°	8.5	m_2 /mm	4
φ_5 /°	12.98	φ_{12} /°	1.27	h_1 /mm	0.22
φ_6 /°	19	φ_{13} /°	4.23	h_2 /mm	0.44
φ_7 /°	9.5	φ_{14} /°	2.6	h_3 /mm	0.8

Considering the leakage flow rate and the working medium compressibility, the outlet pressure is gotten:

$$\frac{dP_{out}}{dt}=\frac{B}{V_{PO}}\left(\sum_{i=1}^{N}q_{ci}-q_{VL}-q_{out}\right) \tag{19}$$

Where q_{out} is the actual flow rate of pump, V_{PO} is the volume of pipe between pump and throttle valve, q_{VL} is the leakage flow rate through the clearance between port plate and valve plate. q_{VL} is expresses as:

$$q_{VL}=\frac{k\pi\delta_V^3}{6\mu}\left[\frac{1}{\ln(R_2/R_1)+\ln(R_4/R_3)}\right](P_{out}-P_{in}) \tag{20}$$

Where δ_V is the clearance between cylinder barrel and port plate, R1 and R4 are shown in *Figure.2*, k is related to the structure parameters of port plate. The flow rate through throttle valve is expressed as:

$$q_{out}=C_dA_{PO}\sqrt{\frac{2(P_{out}-P_0)}{\rho}} \tag{21}$$

Where A_{PO} is the flow area of throttle valve, P_0 is the ambient pressure.

3. SIMULATION RESULTS AND OPTIMIZATION OF PORT PLATE

3.1. Simulation results and validation of model

The equations developed in section 2 are two first-order differential equations for pressure dynamics along with a set of algebraic equations for the flow. Simultaneous solution of these equations provides the pressure and flow characteristic of individual piston as well as the overall pump. The equations are solved using MATLAB/Simulink version 14.0. *Table 2* lists the value of the pump's design parameters and the characteristic parameters of water used in the mathematical model. In *Table 2*, A_{po} denotes the flow area of throttle valve and is a variable to change the outlet pressure of the pump. When the outlet pressure is 14Mpa, the value of A_{po} is shown in *Table 2*. For staring the simulation, time t is set as the input to the Simulink block along with the pressure in piston chamber, outlet pressure, outlet flow and individual piston's flow as the output. A Runge-Kutta fourth-order solver with a fixed step equal to 1×10^{-9}s has been employed. Substituting the parameters in the *Table 2*, the simulation results are shown in *Figure 5* to *7*.

Table 2. Value of the parameters used in the mathematical model

Parameter		Value	Parameter		Value
D_C	/×10^{-3}m	86	V_{co}	/×10^{-6}m^3	10
N	/-	9	d	/×10^{-3}m	23
β	/ rad	π/12	C_d	/-	0.6
δ_S	/×10^{-6}m	5	R_1	/×10^{-3}m	35
r_1	/×10^{-3}m	26	R_2	/×10^{-3}m	38.1
r_2	/×10^{-3}m	20	R_3	/×10^{-3}m	47.8
P_{in}	/×10^{-6}Pa	0	R_4	/×10^{-3}m	51
V_{po}	/×10^{-6}m^3	353.4	l	/×10^{-3}m	39.5
δ_P	/×10^{-6}m	15	A_{po}	/×10^{-5}m^2	1.54
δ_v	/×10^{-6}m	5	k	/-	0.42
B	/×10^{9}Pa	2.373	ρ	/×kg·m^{-3}	1000
μ	/×10^{-3}Pa·s	0.93	ω	/ rad/s	50π

Figure 5 shows the simulation and the experimental results of outlet pressure characteristics of the water hydraulic pump.at 14MPa. In comparison to the ripple of the simulation results with respect to the experimental results, the fluctuation characteristics of pressure curves is very similar. But there is a slight difference in fluctuation amplitude. The fluctuation amplitude of simulation is about 1.24MPa and the experimental is about 1.01MPa. From the *Figure 5*, the reasonable agreement between the flow pressure ripples from the simulation and experiment is observed, so the mathematical model for the water hydraulic axial piston pump is acceptable. *Figure 6* shows the outlet flow characteristics of the water hydraulic axial piston pump by simulation. As the same as outlet pressure, the flow also oscillates with time and the number of oscillations in a cycle is equal to the number of pistons.

Figure 7 shows the piston chamber pressure of the water hydraulic axial piston pump in two revolutions. According to *Figure 7*, we can know that the pressure ripple is very similar to outlet pressure ripple. In addition, the pressure in piston chamber sharply rises at 0s and 0.04s, and the piston is located at the TDC at this time. The pressure rises to biggest at t=0.0417s and the maximum value is up to approximate 20MPa exceeding the average pressure 6MPa as shown in *Figure 7*, which may cause the pump large pressure-flow ripple and vibrating intensely. At this time, the rotation angle of piston is ωt=50×π×(0.0417-0.04)×180/π=15.3° and the barrel kidney is connecting to Ⅲ stage of silencing groove. So the process of pressure rising is mainly influenced by the silencing groove. Thus, the silencing groove must be optimized to decrease the pressure-flow ripple. *Figure 8* shows the single piston flow in two revolutions. From *Figure 8*, we can see that the fluid reverses back into piston chamber from the discharge kidney port, as shown in enlarged drawing. At t=0.026s and 0.0606s, the fluid reverses back into suction kidney port from piston chamber and the maximum flow reaches to 41.22L/min.

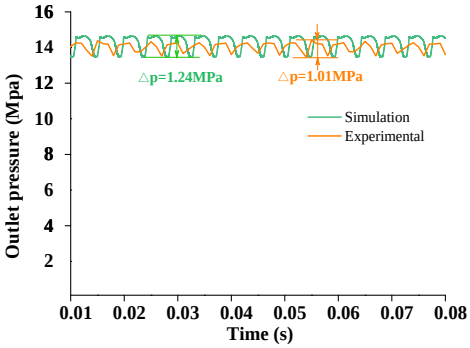

Figure 5. Outlet pressure of the water hydraulic pump

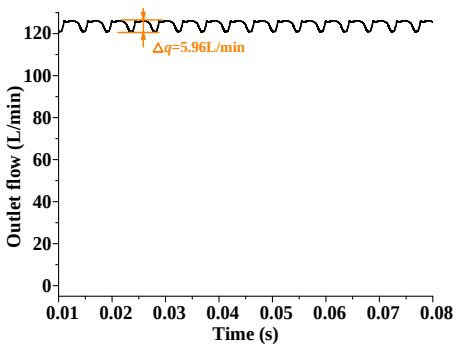

Figure 6 Outlet flow of the water hydraulic pump

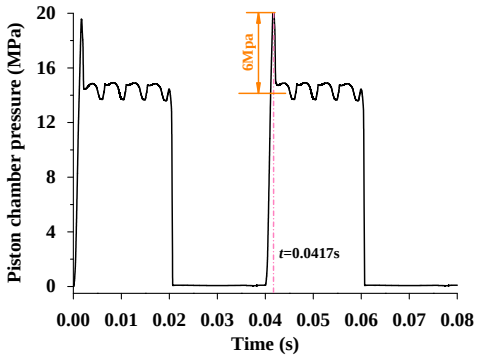

Figure 7. Piston chamber pressure of the pump

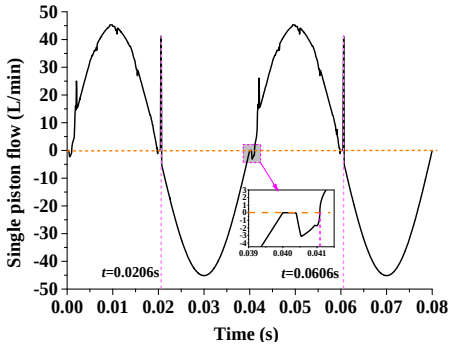

Fig.8 Single piston flow of the pump

3.2. Optimization of the port plate

With reference to the modeling process of the mathematical model of the pump, the effect of silencing groove on the pressure-flow ripple of piston chamber includes two factors: the cross section area and the position of the silencing groove. The optimization for the port plate is mainly concentrated on this two factors to decrease the pressure-flow ripple. From the *Figure 7*, the chamber pressure is too high at the initial stage of discharge fluid, which is caused by the flow generated by piston motion and the flow reversing back into piston chamber form the discharge kidney port. Thus, the angle φ_1 that determines the position of silencing groove should change larger to decrease the flow reversing back into piston chamber and the cross section area of silencing groove should change larger to increase the flow through the silencing groove. The optimized port plate is shown in *Figure 9*. the optimized silencing groove has two stages and the parameters shown in *Figure 9* are listed in *Table 3*.

After optimizing the silencing groove of the port plate, the simulation results are shown in *Figure 10* to *13*. From the *Figure 10 a)*, the time that the piston contacts with silencing groove is delayed to make the piston chamber pressure increasing to be only related with piston motion. The length of silencing groove is shortened to decrease the time that silencing groove communicates with piston chamber, which can extremely decrease the fluid volume reversing back into piston chamber from the discharge port and restrain the flow ripple. These can be explained by *Figure 13*. In *Figure 13*, the flow rate reversing back into piston chamber reaches to biggest at 0.0005s and 0.0405s, equal to 4.5L/min. In comparison with *Figure 8*, the reversing flow rate is bigger (the biggest value in *Figure 8* is 3.5L/min), but the time that piston chamber communicates with silencing groove (0.0003s) is shorter than that (0.0007s) in *Figure 8*. On the whole, the fluid volume reversing back into piston chamber with the optimized port plate is decreased, which is of benefit to reduction the flow ripple amplitude. As shown in *Figure 6* and *14*, the flow ripple amplitude decreases from 5.96L/min to 5.33L/min. Meanwhile, the outlet pressure amplitude reduces from 1.24MPa (shown in *Figure 5*) to 1.17MPa (shown in *Figure 11*) and the maximum value of piston chamber pressure decreases from 20MPa (shown in *Figure 7*) to 15.6MPa (shown in *Figure 12*). What's more, the increasing of angle φ_5 makes the piston chamber pressure decrease (shown in *Figure 12*), which results in reducing the fluid flowing into suction kidney port from piston when the piston connects with suction kidney port. As shown in *Figure 8*, the instantaneous flow feeding into

suction kidney port from piston reaches to biggest, about 41.22L/min, at 0.0206s and 0.0606s. But in *Figure 13*, the instantaneous flow decreases to 5.5L/min. Reference to the simulation results, the pressure-flow ripple is to be reduced with optimized port plate.

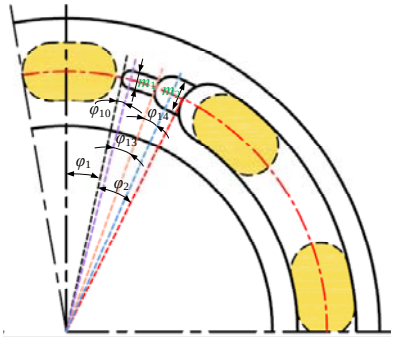

Figure 9. The optimized port plate

Table 3. The value of design parameters for valve plate

Parameter	Value	Parameter	Value	Parameter	Value
φ_1 /°	17	φ_{13} /°	1	m_2 /mm	6
φ_2 /°	11.02	φ_{14} /°	4	h_1 /mm	0.5
φ_5 /°	12.98	m_1 /mm	3	h_3 /mm	0.8
φ_{10} /°	2				

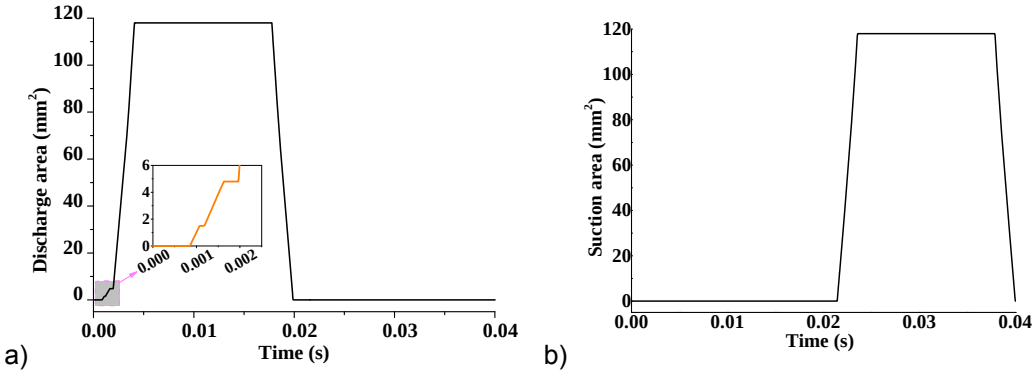

Figure 10. a) discharge area; b) Suction area change with time of optimized port plate

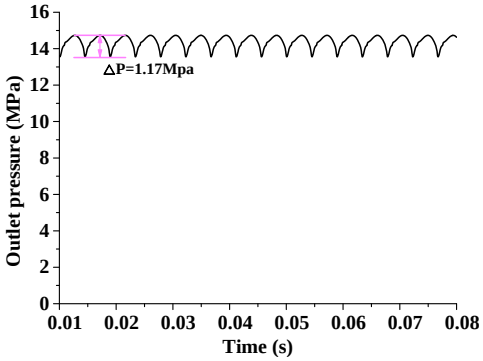

Figure 11. Outlet pressure ripple with optimized port plate

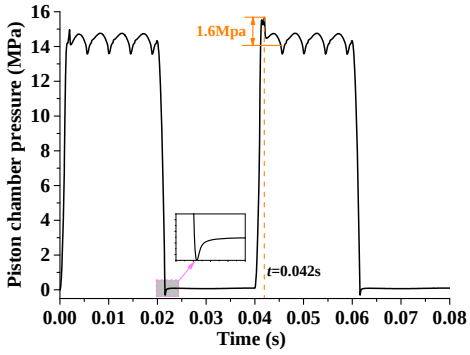

Figure 12. Piston chamber pressure with optimized port plate

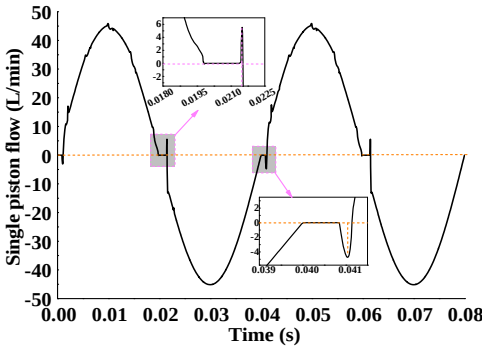

Figure 13. Single piston flow with optimized port plate

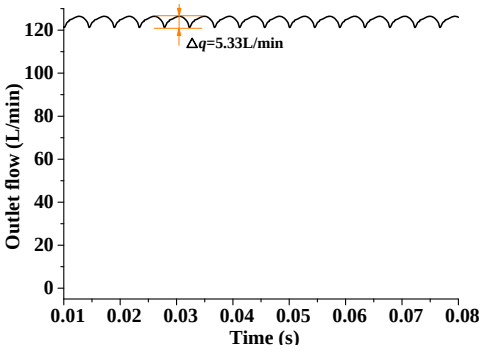

Figure 14. Outlet flow with optimized port plate

3.3. Experimental validation

In order to get the actual effect of the optimized port plate, an experiment is carried out to measure the outlet pressure, noise and vibration of a water hydraulic axis piston with optimized port plate and non-optimized port plate. The schematic of the experimental hydraulic system is shown in the Fig. 15, including electric motor, WHAPP, pressure gauge, vacuum pressure gauge, throttle valve, relief valve and flowmeter. The height of the tank is greater than pump 1.5m (equivalent to 0.015MPa inlet pressure of the pump) to prevent cavitation. A sound-absorbing cover that is made of sound-proof cotton is employed to isolate the noise emitted from the electric motor. The inverter is used to adjust the rotation speed of WHAPP. The discharge pressure is adjusted by the throttle valve and displayed by the pressure gauge (measuring range: 0-25MPa, accuracy: 0.25%). The inlet pressure is measured by the vacuum pressure gauge. The flow rate is measured by flowmeter (measuring range: 0-150L/min, accuracy: 0.25%). The Vibro-acoustics acquisition system (as shown in Fig.16) includes the data acquisition pad (LAN-XI Type: 3050-B-060 6ch, Brüel & Kjær), microphone (type 4189-A-021, Brüel & Kjær), and piezoelectric accelerometers (type 4525-B-003, Brüel & Kjær). The noise is measured by the microphone, which is placed in front of the end cover with a distance of 1 m from the WHAPP. The vibration is measured by accelerometer which can measure the vibration acceleration of X, Y, Z direction at same time.

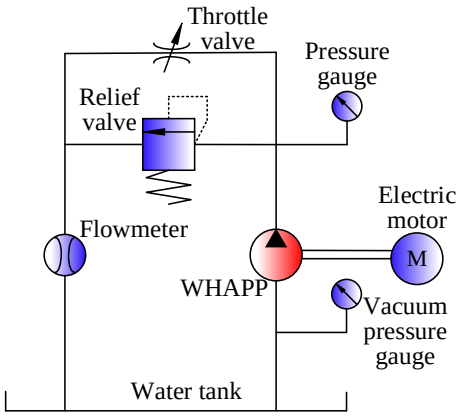

Fig. 15 Schematic of the hydraulic system

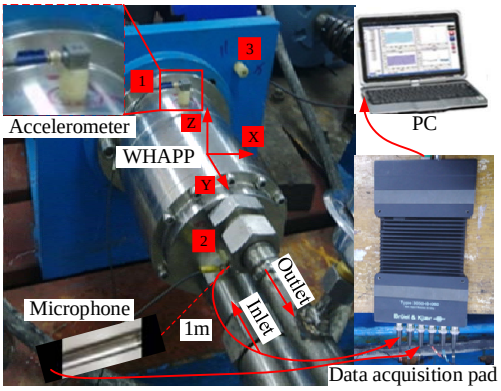

Fig.16 Vibro-acoustics acquisition system

The experimental results are shown in *Figure 17* to *19*. *Figure 17* shows the outlet pressure ripple of water hydraulic axis piston pump at 8MPa, 12MPa, 14MPa. It's illustrated in *Figure 17* that the pressure ripple amplitude with optimized port plate is smaller than that with non-optimized port plate and the pressure ripple decreases with the decrease of the outlet pressure. *Figure 18* shows the vibration acceleration of the pump at different speed and pressure. It is obvious from *Figure 18* that the vibration characteristics with optimized port plate is better (lower vibration acceleration) than non-optimized port plate. As same result as vibration characteristics, the noise is lower with optimized port plate than that with non-optimized port plate as shown in *Figure 19*. From these experimental results, we can get that the optimized port plate can be to decrease the pressure-flow ripple and improves the performance of the water hydraulic axial piston pump. The optimized method is effective for optimizing silencing groove.

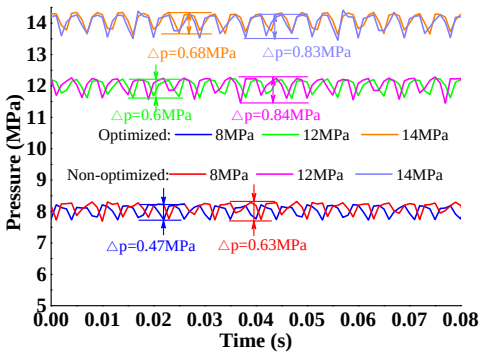

Figure 17. Outlet pressure ripple at 8MPa, 12MPa, 14MPa

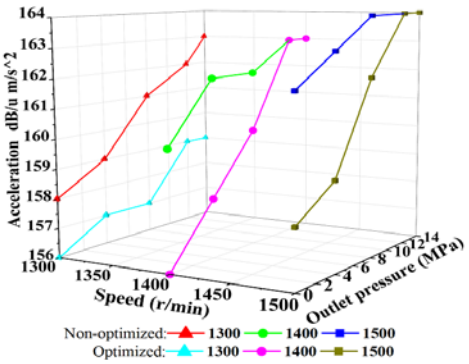

Figure 18. Vibration characteristics at different pressure and speed

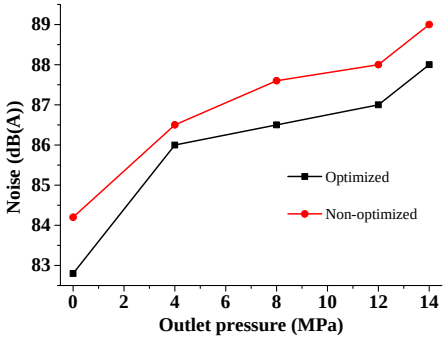

Figure 19. Noise changes with pressure at speed 1500 r/min

4. CONCLUSION

In this paper, a detailed model of pressure and flow for a water hydraulic piston pump has been achieved. Based on the model, the dynamic pressure and flow curves changing with time have been obtained. According these curves, it is found that the silencing groove has great influence on pressure and flow ripple. Then an effective method has been proposed to optimize the silencing groove of port plate. Especially, the optimized port plate has been verified by a series of experiments. The result revealed that the pump with optimized port plate had better performance of vibration and noise. Meanwhile, the experiment results also validated the model could describe the pressure and flow characteristics of the water hydraulic axial piton pump.

5. REFERENCE

[1] I. S. Cho and J. Y. Jung, A study of pressure ripple characteristics in a bent-axis type oil hydraulic piston pump, Journal of Mechanical Science and Technology, 27 (12) (2013)3713-3719.

[2] J. H. Shin, Computational study on dynamic pressure in a swash-plate axial piston pump connected to a hydraulic line with an end resistance, Journal of Mechanical Science and Technology, 29 (6) (2015) 2381-2390.

[3] I. S. Cho, A study on the optimum design for the valve plate of a swash plate-type oil hydraulic piston pump, Journal of Mechanical Science and Technology, 29 (6) (2015)2409-2413.

[4] Seeniraj, G.K., Ivantysynova, M, Impact of valve plate design on noise, volumetric efficiency and control effort in an axial piston pump. Proceedings of IMECE, 2006, Chicago.

[5] Seeniraj, G.K., Ivantysynova, M, Noise reduction in axial piston pump machines based on multi-parameter optimization. Proceedings of 4th FPNI-PhD Symposium, 2006, Sarasota, p.235-246.

[6] Vacca, A., Klop, R., Ivantysynova, M, A numerical approach for the evaluation of the effects of air release and vapor cavitation on effective flow rate of axial piston machines. International Journal of Fluid Power, 11(1):33-45, 2010.

[7] Harrison A M, Edge K A. Reduction of axial piston pump pressure ripple[J]. Proceedings of the Institution of Mechanical Engineers Part I Journal of Systems & Control Engineering, vol214(1), pp. 53-64., 2000.

[8] Guan, C., et al. Theoretical study of flow ripple for an aviation axial-piston pump with damping holes in the valve plate. Chinese Journal of Aeronautics 27(1): 169-181., 2014.

[9] Xu, B., et al. A new design method for the transition region of the valve plate for an axial piston pump. Journal of Zhejiang University-SCIENCE A 16(3): 229-240., 2015.

[10] Mandal, N. P., et al. Theoretical simulation of ripples for different leading-side groove volumes on manifolds in fixed-displacement axial-piston pump. Proceedings of the Institution of Mechanical Engineers, Part I: Journal of Systems and Control Engineering 222(6): 557-570., 2008.

[11] Yin, F., et al. Effect analysis of silencing grooves on pressure and vibration characteristics of seawater axial piston pump. Proceedings of the Institution of Mechanical Engineers, Part C: Journal of Mechanical Engineering Science, vol. 231, pp. 1390-1409, 2016.

[12] Xu, B., Zhang, J.H., Yang, H.Y., Simulation research on distribution method of axial piston pump utilizing pressure equalization mechanism. Proceedings of the Institution of Mechanical Engineers, Part C: Journal of Mechanical Engineering Science, 227(3):459-469, 2013.

ADAPTIVE MODEL PREDICTIVE TRACKING CONTROL OF TAP–WATER DRIVEN MUSCLE USING HYSTERESIS COMPENSATION WITH BOUC–WEN MODEL

Ryo Inada, Kazuhisa Ito
Shibaura Institute of Technology
Graduate School of Mechanical Engineering
307 Fukasaku, Minuma-ku, Saitama, 337-8570 Japan
E-mail: md18012@shibaura-it.ac.jp, kazu-ito@shibaura-it.ac.jp

Shigeru Ikeo
Sophia University
Department of Engineering and Applied Sciences
7-1 Kioicho, Chiyoda-ku, Tokyo, 102-8554 Japan
s_ikeo@sophia.ac.jp

ABSTRACT

Recently, high-precision displacement control of McKibben type artificial muscles driven by tap water has attracted attention because the muscle exhibits advantages including high flexibility, low cost, light weight, and high-power density and is promising in terms of industrial applications that necessitate high cleanliness. However, the muscle generally has hysteresis characteristics, and the characteristics depend on the load. Therefore, it is difficult to obtain high-precision displacement control. The authors introduce the Bouc–Wen model to obtain a model that describes hysteresis characteristics, and propose a linearization technique by using the inverse of the model. Furthermore, in order to obtain robustness for load and high control performance, we apply an adaptive model predictive control with a servo mechanism by using its linearization technique to the muscle. The experimental results indicate that the proposed method improved control performance by 66% when compared to that of the conventional method under different load conditions.

KEYWORDS: McKibben type artificial muscle, Tap water hydraulics, Model predictive tracking control, Constrained recursive least square, Bouc–Wen model

1. INTRODUCTION

McKibben type artificial muscles attracted attention because they exhibit advantages including high flexibility, low cost, light weight, and high-power density in medical, welfare, and robotics [1], [2]. In most cases, artificial muscles are driven by pneumatics although they have noise generated by compressors and are not suitable for use in industrial machineries that require high cleanliness. Kobayashi *et al*. [3] proposed muscle driven by tap water (hereafter termed as the tap water driven muscle) because it has higher response and does not require a pump since it uses tap water as working fluid instead of pneumatics. Given the aforementioned aspects, the application of the tap water driven muscle is promising in rehabilitation and support systems at home or machineries that require high cleanliness. Conversely, the muscle has strong hysteresis

characteristics due to nonlinear shrinkage behavior and friction between components. Additionally, the characteristics depend on the load applied to the muscle. In order to solve the aforementioned problems, a few model-based controls are already applied to the muscle control and include the model reference adaptive control [4], sliding mode control [5], and H_∞ control [6]. However, the control methods are designed based on linear model and their performances are potentially limited because linearized models ignore the effects of hysteresis. Therefore, control systems based only on the linear model of the artificial muscles cannot achieve sufficient control performance. Furthermore, nonlinear control strategies are also used for displacement control of the muscle [7] [8]. However, the control methods are designed based on the first-principles-model, and its model requires a complex structure to express nonlinearity and knowledge on the estimated objects and prior measurements to estimate the model parameters.

In the study, we apply model predictive control (MPC) with a linearization technique using the Bouc–Wen model to describe hysteresis characteristics with a relatively simple structure for the muscle system. In previous studies, various hysteresis models based on Prandtl–Ishlinskii, Preisach, or Bouc–Wen model [9]-[11] are proposed. However, Prandtl–Ishlinskii or Preisach models are complicated and require high computational power to obtain their inverse models because the models require many grids and corresponding parameters. Therefore, the inverse of the Bouc–Wen model is adopted in the study. The MPC generates a control input to optimize an evaluation function including the state/output on the specified finite time future interval and input penalty and also deals with constraints (for e.g., input and state) in the design step. Given the aforementioned aspects, MPC is widely used in various field including aerospace and automotive industries [12]. The control method depends significantly on precision of the mathematical model because it is used to predict states of the plant. Therefore, we implement the muscle model by combining the linear model with the Bouc–Wen model, which describes hysteresis characteristics to obtain high control performance. However, it is not possible to apply the MPC with multi coincidence points to the muscle system in a straightforward manner with a popular MPC solver, such as CVXGEN, which generates the code to solve a convex programming problem [13] because the model exhibits nonlinearities. In order to apply CVXGEN, the study proposes a linearization technique for the muscle system by designing a proper input that compensates the effect of hysteresis characteristics by using the inverse of the Bouc-Wen model.

Additionally, a conventional MPC cannot perform an integral operation on its own. Therefore, steady state error may still persist although the predictor in MPC exhibits high accuracy. In order to solve the problem, an MPC with a servo mechanism is applied. Furthermore, in order to improve robustness for the load, the study introduces an adaptive model predictive control (AMPC) that consists of the MPC with recursive least square (RLS) algorithm, which is an adaptive algorithm with robustness for measurement noise. However, in terms of application, the generated control input can diverge if a few estimated parameters corresponding to the effect of hysteresis convergence to an extremely small value. Therefore, constrained RLS algorithm is introduced to AMPC based on preliminary identification to constrain the parameter estimation within a certain region. In order to demonstrate the effectiveness of the proposed method, experiments are conducted, and the results are compared to the unique coincidence point AMPC that directly uses the model under two different load conditions.

The study is organized as follows: Section 2 summarizes the symbols used in the study. Section 3 derives a model of the muscle that combines the linear model with the Bouc–Wen model and explains parameter estimation algorithm using the constrained RLS algorithm for the proposed model. Furthermore, the section provides the parameter estimation results and compares the fitness with that of the linear model. Section 4 develops hysteresis cancellation input using the Bouc–Wen model to linearize the muscle system and designs the AMPC controller. Section 5 presents the experimental results under two different load conditions and discusses control performances. Section 6 describes conclusions and future work.

2. NOMENCLATURE

a_i, b_i	System parameters
A_i	Hysteresis parameter that determines an amplitude
C	Constrained region in the parameter space
H_p	Prediction horizon
H_u	Control horizon
$l(k)$	Displacement of the muscle
$\hat{l}(k)$	Output of the model
n	Hysteresis parameter that determines smoothness
$P(k)$	Covariance matrix
Q	Weight on the tracking error
Q_s	Weight on the integrator
R	Weight on change of input
$r(k)$	Reference trajectory
$u(k)$	Valve input voltage
$u_c(k)$	Control input by MPC with the servo mechanism
$y_{hy}(k)$	Virtual hysteresis variable
β, γ	Hysteresis parameters that determine the shape of the hysteresis
$\Delta u(k)$	Change of valve input voltage
$\Delta u_c(k)$	Change of control input by MPC with the servo mechanism
θ	Parameter space
θ_0	Initial value of the estimated parameter vector
$\hat{\theta}(k)$	Estimated parameter vector
$\varphi(k)$	Regressor vector

3. MODELING OF THE MUSCLE USING THE BOUC–WEN MODEL AND ESTIMATION OF ITS PARAMETERS

3.1. Modeling of McKibben muscle using the Bouc–Wen model

Several Bouc–Wen models are already proposed for describing hysteresis of a McKibben muscle. Generally, these types of models are represented via a differential equation. However, the study deals with a discretized model to apply the MPC. In this study, Eq.(1) which gives better fitness in preliminary identification was introduced. The muscle model that combines a linear model with the discretized Bouc–Wen model is given as follows:

$$\begin{cases} \hat{l}(k) = a_1 l(k-1) + a_2 l(k-2) + b_1 u(k-1) + y_{hy}(k-1) + y_{hy}(k-2) \\ y(k-i) = A_i \left\{ l(k-i) - l(k-i-1) \right\} - \beta_i \left| l(k-i) - l(k-i-1) \right| \left| y_{hy}(k-i-1) \right|^{n-1} y_{hy}(k-i-1) \\ \qquad\qquad -\gamma_i \left\{ l(k-i) - l(k-i-1) \right\} \left| y_{hy}(k-i-1) \right|^{n} + c_i y_{hy}(k-i-1), \quad (i = 1, 2) \end{cases} \tag{1}$$

where k denotes time step. It should be noted that the model includes not only the muscle characteristics but also proportional valve characteristics. As shown in Eq.(1), the model consists of a linear model, which extends from the first term to the third term, and the Bouc–Wen model, which includes the fifth and sixth terms.

3.2. Linearization technique for the proposed model

We propose a linearization technique for the proposed model to apply code generator, *e.g*. CVXGEN that solves the quadratic programming problem with linear constraints.

The desired plant is defined as follows:

$$l(k) = a_1 l(k-1) + a_2 l(k-2) + b_1 u_c(k-1) \tag{2}$$

We substitute Eq.(2) into Eq.(1) to obtain the following hysteresis cancellation input:

$$u(k) = u_c(k) - \frac{1}{b_1}\left[y_{hy}(k) + y_{hy}(k-1) \right] \tag{3}$$

where $u_c(k)$ is to be designed in Section 4.2. By applying the input, we linearize and apply CVXGEN to the muscle system.

3.3. Constrained RLS algorithm for the Bouc–Wen model

Each parameter of the proposed model is estimated by the constrained RLS algorithm, and the parameter updating law for RLS algorithm [14] is expressed as follows:

$$\begin{cases} \hat{\theta}(k) = \hat{\theta}(k-1) + \dfrac{P(k-1)\varphi(k-1)}{1+\varphi^T(k-1)P(k-1)\varphi(k-1)}\left[l(k) - \varphi^T(k-1)\hat{\theta}(k-1)\right] \\ P(k-1) = P(k-2) - \dfrac{P(k-2)\varphi(k-1)\varphi^T(k-1)P(k-2)}{1+\varphi^T(k-1)P(k-2)\varphi(k-1)} \end{cases} \tag{4}$$

where $\varphi(k)$ and $\hat{\theta}(k)$ are defined as Eqs.(5) and (6), respectively, to identify parameters of the Bouc–Wen model as follows:

$$\varphi(k) = \begin{bmatrix} l(k) \\ l(k-1) \\ u(k) \\ l(k) - l(k-1) \\ l(k-1) - l(k-2) \\ \left|l(k) - l(k-1)\right| y_{hy}(k-1) \\ \left|l(k-1) - l(k-2)\right| y_{hy}(k-2) \\ \left\{l(k) - l(k-1)\right\} \left|y_{hy}(k-1)\right| \\ \left\{l(k-1) - l(k-2)\right\} \left|y_{hy}(k-2)\right| \\ y_{hy}(k-1) \\ y_{hy}(k-2) \end{bmatrix} \tag{5}$$

$$\hat{\theta}(k) = \left[\hat{a}_1(k) \quad \hat{a}_2(k) \quad \hat{b}_1(k) \quad \hat{A}_1(k) \quad \hat{A}_2(k) \quad \hat{\beta}_1(k) \quad \hat{\beta}_2(k) \quad \hat{\gamma}_1(k) \quad \hat{\gamma}_2(k) \quad \hat{c}_1(k) \quad \hat{c}_2(k)\right]^T \tag{6}$$

where n=1 in Eq.(1). Specifically, in order to identify parameters, we conduct parameter estimation experiment assuming that $y_{hy}(k)$ shows the difference between displacement and linear model, namely $y_{hy}(k)=l(k) - [a_1 l(k\text{-}1)+a_2 l(k\text{-}2)+b_1 u(k\text{-}1)]$ [15].

Here, b_1 in hysteresis cancellation input (3) are unknown. Therefore, b_1 should be replaced with its estimation $\hat{b}_1(k)$.

$$u(k) = u_c(k) - \frac{1}{\hat{b}_1(k)}\left[y_{hy}(k) + y_{hy}(k-1)\right] \tag{7}$$

In terms of application, it is necessary to consider the constrained region to ensure that $\hat{b}_1(k)$ does not converge to a small value because the generated control input (7) may diverge if $\hat{b}_1(k)$ in denominator of hysteresis cancellation input converge to an extremely small value. Therefore, it is necessary to introduce the constrained RLS algorithm. The constrained RLS algorithm is run by the following algorithm [14].

Algorithm: Eq.(4) is calculated; if $\hat{\theta}(k) \in C$, then the algorithm is continued: else,

Step 1. Transform the coordinate basis for the parameter space by defining the following:

$$\rho = P^{-1/2}(k-1)\theta \tag{8}$$

and denote $\bar{C}$ as the image of C under the linear transformation $P^{-1/2}(k-1)$.

Step 2. Orthogonally project the image, $\hat{\rho}(k)$, of $\hat{\theta}(k)$ under $P^{-1/2}(k-1)$ on the boundary of $\bar{C}$ to yield $\hat{\rho}'(k)$

where the following expression holds:

$$\hat{\rho}(k) = P(k-1)^{-1/2}\hat{\theta}(k) \tag{9}$$

Step 3. Put

$$\hat{\theta}(k) = \hat{\theta}'(k) \triangleq P^{1/2}(k-1)\hat{\rho}'(k) \tag{10}$$

and continue.

Remark: The transformation $\rho = P^{-1/2}(k-1)\theta$ yields the following:

$$\begin{aligned} V(k) &= \left[\hat{\theta}(k) - \theta_0\right]^T P(k-1)^{-1}\left[\hat{\theta}(k) - \theta_0\right] \\ &= \left[\hat{\rho}(k) - \rho_0\right]^T \left[\hat{\rho}(k) - \rho_0\right] \end{aligned} \tag{11}$$

where

$$\rho_0 = P^{-1/2}(k-1)\theta_0 \tag{12}$$

Given that $\hat{\rho}'(k)$ is an orthogonal projection of $\hat{\rho}(k)$ on $\bar{C}$ and $\rho_0 \in \bar{C}$, the following inequality holds:

$$\left\|\hat{\rho}'(k) - \rho_0\right\| \le \left\|\hat{\rho}(k) - \rho_0\right\| \tag{13}$$

and hence

$$\left[\hat{\theta}'(k) - \theta_0\right]^T P(k-1)^{-1}\left[\hat{\theta}'(k) - \theta_0\right] \le \left[\hat{\theta}(k) - \theta_0\right]^T P(k-1)^{-1}\left[\hat{\theta}(k) - \theta_0\right] \tag{14}$$

From the result, we observe that $[\hat{\theta}(k) - \theta_0]^T P(k-1)^{-1}[\hat{\theta}(k) - \theta_0]$ corresponds to a non-increasing function when $\hat{\theta}(k)$ is projected on the constrained region *C*.

3.4. Experimental setup

The experimental setup used in the study is shown in Fig.1. The circuit consists of two proportional valves (KFPV300-2-80, Koganei Corporation), a pressure sensor (FP101, Yokogawa Electric Corporation), a linear encoder (DX-025, MUTOH Industries Ltd.), and a PC (including MATLAB/Simulink and dSPACE 1103). The McKibben muscle used in the experiments is an in-house custom-built muscle with a length of 400 [mm]. The average supply pressure corresponds to 0.25 [MPa].

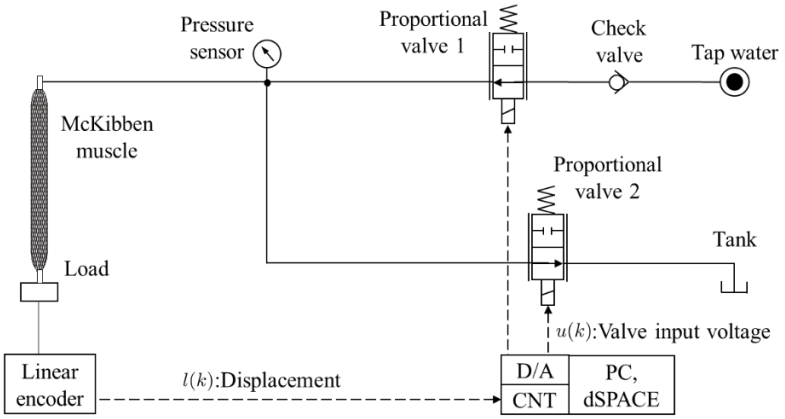

Figure 1. Experimental circuit for displacement control of the McKibben muscle

3.5. Experiment for parameter estimation of the Bouc–Wen model

We conduct parameter estimation for the Bouc–Wen model by using the constrained RLS algorithm. Figure 2 shows a part of the input and output data using parameter estimation. As shown in Fig.2, the input corresponds to a sinusoidal wave with an amplitude of 3 [V], offset of 5 [V], and frequency of 0.1 [Hz]. In the experiment, the sampling period corresponds to 0.1[s], and the load applied to the muscle corresponds to 44 [N]. The initial

value of the covariance matrix $P(-1)$ corresponds to a diagonal matrix with a value of 10^3 for each element, and the initial estimated parameter vector corresponds to zero. Table 1 summarizes the constrained region of the parameters of the linear part that are obtained via a preliminary system identification experiment. The constrained region is determined via the mean value and distribution of each parameter.

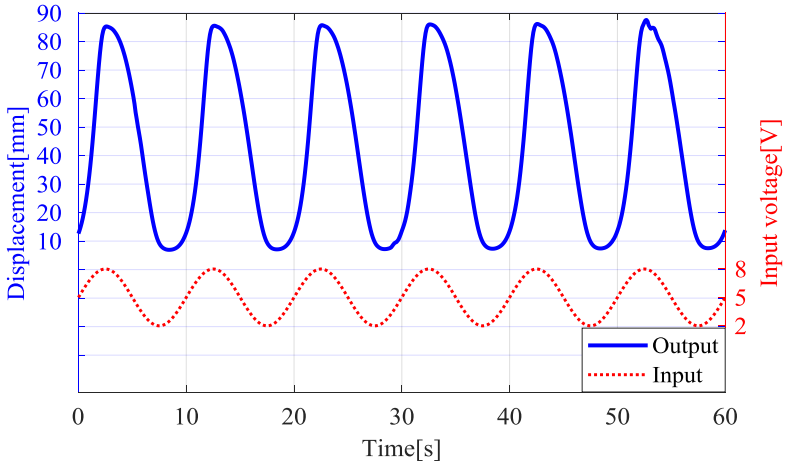

Figure 2. Part of input and measurement of displacement data for identification

Table 1. Constrained region of the parameters of the linear model

	a_1	a_2	b_1
Maximum value	1.260	-0.278	1.184
Minimum value	1.208	-0.334	0.607

Table 2 shows estimated parameters of the proposed model. It is estimated that the parameters converge in approximately 100 [s] although the constrained RLS algorithm runs after 100 [s]. Figure 3 shows a comparison of the proposed model by using the estimated parameters shown in Table 2 and the linear model in the experiment. As shown in Fig.3, the accuracy of the proposed model evidently improves when compared to that of the linear model while the linear model exhibits high error with respect to hysteresis. Additionally, Table 3 shows fitness between predicted output of the model and experimental measurement data. As shown in the Table, fitness for five steps ahead between predicted output of the proposed model and experimental measurement data improves by 13 [%] when compared to that of the linear model. From the results, hysteresis characteristics of the muscle are compensated via appropriately combining the linear model with the Bouc–Wen model and constrained RLS algorithm estimated parameters of the Bouc–Wen model.

Table 2. Parameters of the proposed model as estimated by the RLS algorithm

Parameter	a_1	a_2	b_1	A_1	A_2	β_1	β_2	γ_1	γ_2	c_1	c_2
Value	1.260	-0.304	0.607	0.222	-0.088	-0.684	0.333	0.387	-0.098	0.290	0.156

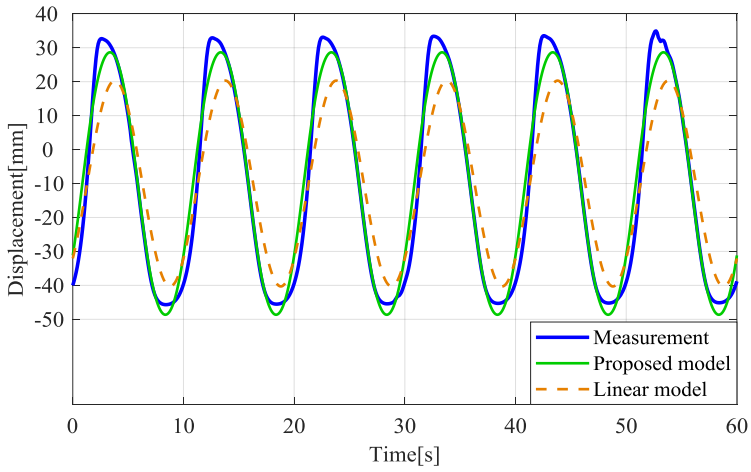

Figure 3. Comparison of the proposed model and linear model in the experiment

Table 3. Fitness between each predicted output of the model and experimental measurement data

Model \ Prediction	1 step ahead	3 steps ahead	5 steps ahead
Proposed model	99.6 [%]	98.4 [%]	96.5 [%]
Linear model	95.9 [%]	91.2 [%]	86.2 [%]

4. CONTROLLER DESIGN

4.1. MPC with a unique coincidence point

The MPC with a unique coincidence point corresponds to the simplest case and directly deals with nonlinear model. Firstly, designers select a prediction horizon H_p and subsequently reference trajectory $r(k)$ that adequately defines an output track reference from current output $l(k)$ to H_p steps ahead of the predicted output $\hat{l}(k+H_p|k)$. Subsequently, $\hat{l}(k+H_p|k)$ is uniquely calculated by Eq.(15) as follows:

$$\hat{l}(k+H_p \mid k) = \hat{l}_f(k+H_p \mid k) + S(H_p)\Delta u(k) \tag{15}$$

where $\hat{l}_f(k+H_p)$ and $S(H_p)$ are response that is obtained at the coincidence point when $u(k\text{-}1)$ is kept during H_p steps and unit step response of the model at H_p step later, respectively. Additionally, the change of input is defined as follows:

$$\Delta u(k) = u(k) - u(k-1) \tag{16}$$

It should be noted that the control method assumes that the optimal input $u(k)$ will only change at times k, k+1, …, $k+H_p$-1, and will remain constant after that. Finally, the controller generates optimal change of input that causes the predicted output to coincide with the reference trajectory at $k+H_p$ steps, namely $r(k+H_p|k) = \hat{l}(k+H_p|k)$. Thus, the optimal change of input $\Delta u(k)$ is obtained as follows:

$$\Delta u(k) = \frac{r(k+H_p \mid k) - \hat{l}_f(k+H_p \mid k)}{S(H_p)} \tag{17}$$

From the result, we obtain a unique solution even when the nonlinear model is used. The algorithm iterates at each step.

4.2. AMPC with the servo mechanism

The MPC with a unique coincidence point was introduced in the previous section. In order to improve control performance, we introduce MPC with multi coincidence points to obtain a higher control performance. The evaluation function of MPC with the servo mechanism [16] is described as follows:

$$J(k) = \sum_{i=1}^{H_p} \left| \hat{l}(k+i \mid k) - r(k+i \mid k) \right|^2_{Q(i)} + \sum_{i=0}^{H_u-1} \left| \Delta \hat{u}_c(k+i \mid k) \right|^2_{R(i)} + \sum_{i=1}^{H_p} \left| \hat{x}_s(k+i \mid k) \right|^2_{Q_s(i)} \tag{18}$$

where $\Delta \hat{u}_c(k+i \mid k)$ is defined as Eq. (19)

$$\Delta \hat{u}_c(k+i \mid k) = \hat{u}_c(k+i \mid k) - \hat{u}_c(k+i-1 \mid k), i = 0, ..., H_u - 1 \tag{19}$$

The model derived by identification or estimation via the RLS algorithm does not have a physical interpretation of the state vector. Therefore, a non-minimum state space representation is introduced as follows:

$$\begin{cases} \mathbf{x}(k+1) = \begin{bmatrix} a_1 & a_2 \\ 1 & 0 \end{bmatrix} \mathbf{x}(k) + \begin{bmatrix} b_1 \\ 0 \end{bmatrix} u_c(k) \\ l(k) = [1 \quad 0]\mathbf{x}(k) \end{cases} \tag{20}$$

where $\mathbf{x}(k)=[I(k)\ I(k\text{-}1)]^T$. Additionally, $x_s(k)$ is expressed as follows:

$$\begin{cases} x_s(k+1) = x_s(k) + e(k) \\ e(k) = r(k) - I(k) \end{cases} \tag{21}$$

Here, we provide the input constraint of input voltage of control valves that is represented by Eq.(22) and $\Delta u_c(k)$ is derived by minimizing Eq.(18) subject to Eq.(22) as follows:

$$0 \le \hat{u}_c(k+i \mid k) - \frac{1}{\hat{b}_1(k)}\left\{y_{hy}(k) + y_{hy}(k-1)\right\} \le 10,\ i = 0, 1\ldots, H_u - 1 \tag{22}$$

Control performance of MPC significantly depends on the precision of the model because it is used to predict the state of the system as denoted in previous sections. Therefore, if the predictor has parameter error and/or parameters of the muscle are changed by the load, then the MPC does not work well. In order to solve the problem, we incorporate the RLS algorithm in the predictor of MPC. Figure 4 shows the block diagram of the proposed method that corresponds to an adaptive model predictive control (AMPC), which combines MPC with the constrained RLS algorithm with the servo mechanism using the hysteresis cancellation input.

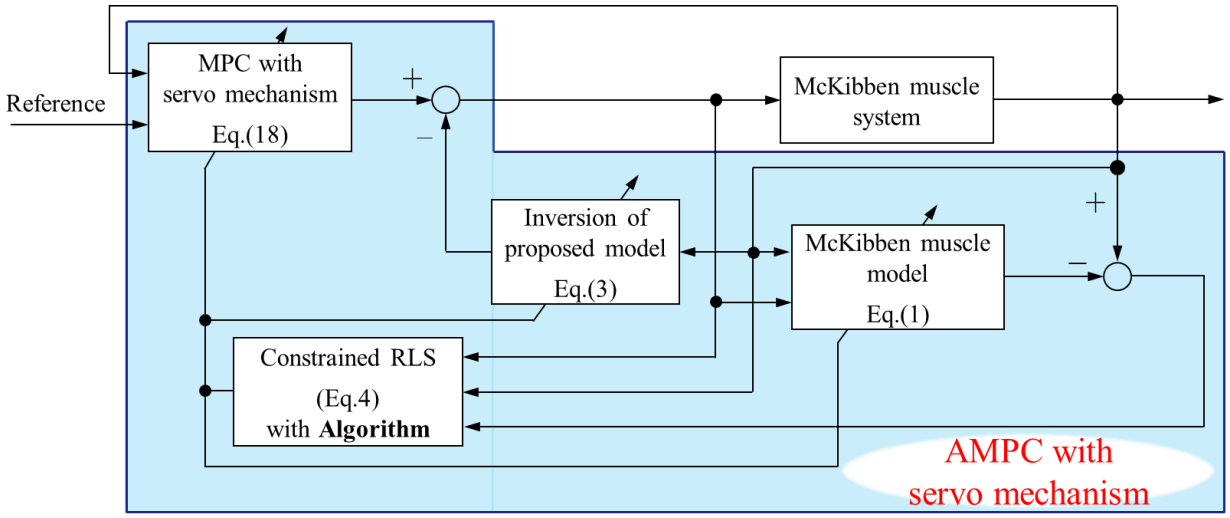

Figure 4. Schematic block diagram of the AMPC with the servo mechanism using hysteresis cancellation input

5. EXPERIMENTAL RESULTS

5.1. Experimental condition of displacement control

All data are obtained under the conditions corresponding to a sampling period of 0.1 [s] and a reference sinusoid wave with an offset of 35 [mm], amplitude of 30 [mm], and frequency of 0.1[Hz]. Experiments are conducted under loads corresponding to 44 [N] and 68 [N]. Tracking control performance in the steady state response from 10 [s] to 40 [s] is evaluated by Eq.(23).

$$\bar{e} = \frac{1}{300}\sum_{k=100}^{400} | r(k) - I(k) | \tag{23}$$

In the experiment, MPC with the servo mechanism is applied as the proposed method. Table 4 shows control parameters for the displacement control in which the conventional method corresponds to MPC with a unique coincidence point.

Table 4. Control parameters for the displacement control

Item	Proposed method	Conventional method
Prediction horizon H_p	5	2
Control horizon H_u	5	
Weight on tracking error $Q(i)$, i = 1, …, H_p	{5, 5, 5, 5, 5}	
Weight on change of input $R(i)$, i = 1,…, H_u	{10, 10, 10, 10,10}	
Weight on Integrator $Q_s(i)$, i = 1, …, H_p	{1, 1, 1, 1, 1}	
Initial value of covariance matrix $P(-1)$	diag [500, 500, 500, 50, 50, 50, 50 ,50, 50, 50, 50]	

5.2. Experimental results of the conventional method and proposed method without constrained RLS algorithm

In order to observe the effect of the number of coincidence points, we conduct experiments of displacement control with the proposed and conventional methods without the constrained RLS algorithm. It should be noted that the experiment uses a fixed predictor, which is obtained via a parameter estimation experiment under 44 [N]. Figures 5 and 6 show experimental results of the conventional and proposed methods without the constrained RLS algorithm and prediction error of the predictor in each method without the constrained RLS algorithm from 10 to 40 [s], respectively. Additionally, Figs. 7 and 8 show experimental results of the conventional and proposed methods without the constrained RLS algorithm when the load is changed to 68 [N] and prediction error of the predictor in each method without the constrained RLS algorithm from 10 to 40 [s], respectively.

Table 5 summarizes the calculation results for control performance. Based on Table 5, the performance of the proposed method improved by more than 43% when compared to that of the conventional method under both loaded conditions, although the prediction error degraded when compared to that of the conventional method. From the results, we observe that the effect for the number of coincidence points and integrator are stronger than that of the prediction error. Therefore, this indicates that it is valid for the muscle to give multi coincidence points with hysteresis cancellation input. However, experimental results under the load of 68 [N] indicate that the approach exhibits a higher tracking error than that of the result under load 44 [N] as shown in Table 5. This is due to the modeling error because the model parameters are estimated via the parameter estimation experiment with the load of 44 [N]. Hence, we incorporate the constrained RLS algorithm in each method to compensate for the error.

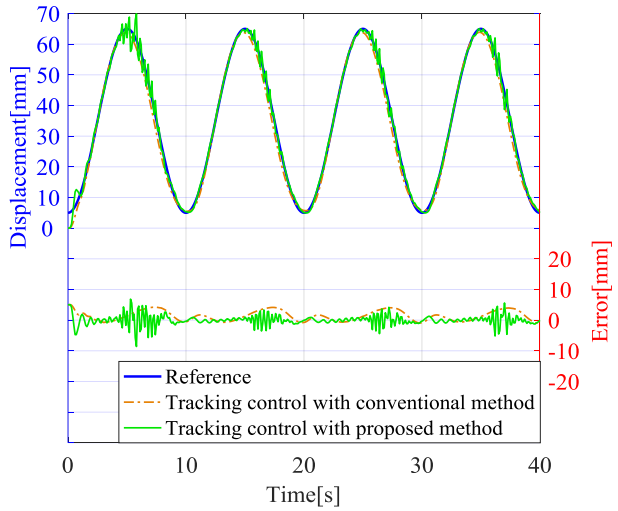

Figure 5. Tracking response of the proposed method and conventional method without the constrained RLS algorithm under the load corresponding to 44 [N]

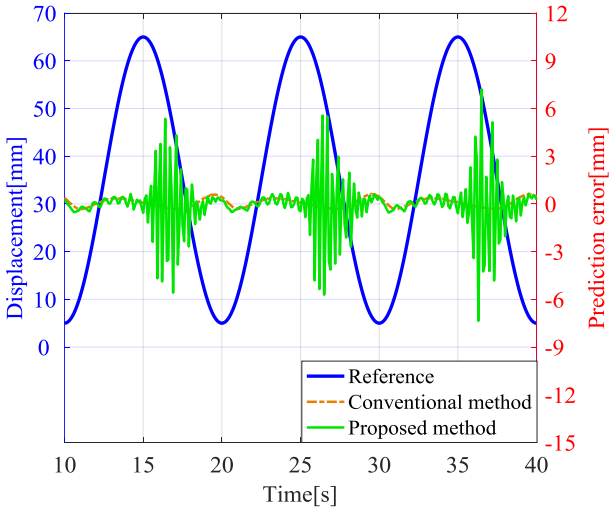

Figure 6. Prediction error of predictor in each method without the constrained RLS algorithm from 10 to 40 [s] under the load corresponding to 44 [N]

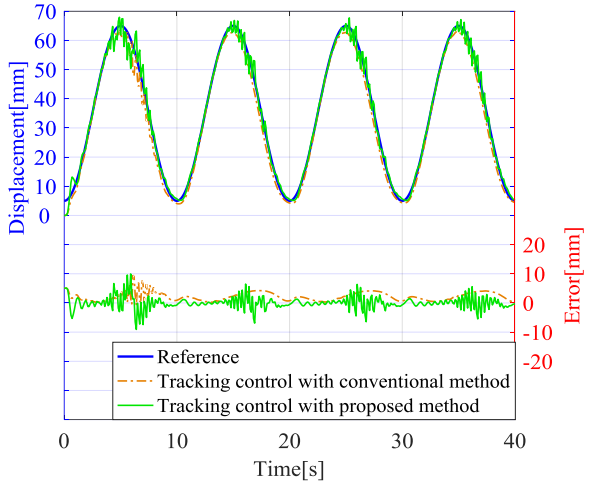

Figure 7. Tracking response of the proposed method and conventional method without the constrained RLS algorithm under the load corresponding to 68 [N]

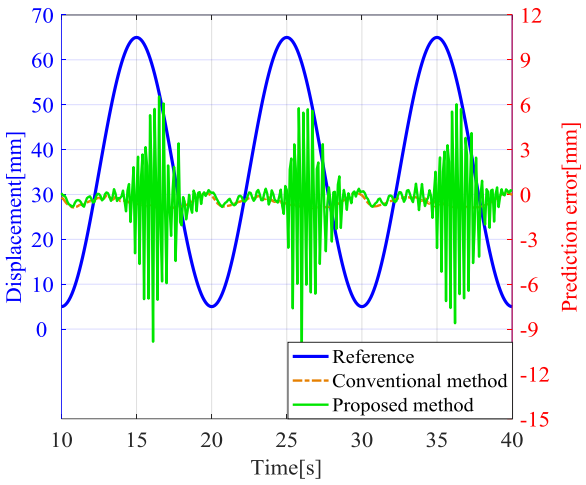

Figure 8. Prediction error of predictor in each method without the constrained RLS algorithm from 10 to 40 [s] under the load corresponding to 68 [N]

Table 5. Comparison of the mean absolute value for the control performance of each method without the constrained RLS algorithm under loads corresponding to 44[N] and 68[N]

Load \ Method	Conventional method without constrained RLS	Proposed method without constrained RLS
44 [N]	1.58 [mm]	0.90 [mm]
68 [N]	2.13 [mm]	1.20 [mm]

5.3. Experimental results of the conventional method and proposed method with the constrained RLS algorithm

In order to demonstrate the effectiveness of AMPC, we introduced the constrained RLS algorithm to each method and conducted experiments of displacement control with the proposed and conventional methods with its algorithm. Figures 9 and 10 show experimental results of the conventional and proposed methods with the constrained RLS algorithm under the load of 44 [N] and predication error of predictor in each method with the constrained RLS algorithm from 10 to 40 [s], respectively. Additionally, Figs.11 and 12 show experimental results of the conventional and proposed methods with the constrained RLS algorithm when the load is changed to 68 [N] and predication error of predictor in each method with the constrained RLS algorithm from 10 to 40 [s], respectively.

As shown in Figs. 9 and 11, the proposed method with the constrained RLS algorithm clearly improves control performance when compared to that without the algorithm. Additionally, the constrained RLS algorithm reduces prediction error as shown in Figs.10 and 12. Table 6 summarizes the calculation results for control performance. Based on Table 6, the proposed method with the constrained RLS algorithm significantly improves control performance by more than 63 % when compared to that of the conventional method under both load conditions. Furthermore, the proposed method obtains almost the same control performance under different load conditions as shown in Table 6. This implies that the constrained RLS algorithm has robustness for the load change and compensates for the modeling error of the predictor. Additionally, the conventional method does not possess an integrator and only has a coincidence point while the proposed method has both functions. Conversely, the proposed method tracks the reference well under different load conditions. Therefore, the experimental results indicate that the AMPC with the servo mechanism is effective for the muscle with load fluctuations.

Conversely, the prediction error exists as shown in Figs 10 and 12 although we apply the constrained RLS algorithm to the proposed method. This is due to modeling error of the proposed model because the Bouc–Wen model is unable to express asymmetric hysteresis characteristics. Therefore, it is necessary to introduce asymmetric the Bouc–Wen model to obtain a high precision model. Additionally, Figs. 9 and 11 indicate that

outputs oscillate from 0 to 10 [s]. The online parameter estimation caused the oscillation. The control performance of the AMPC with the servo mechanism worsens while parameters are being estimated. Therefore, it is necessary to introduce a few thresholds whether adaptive algorithm runs (or not) to avoid the phenomenon.

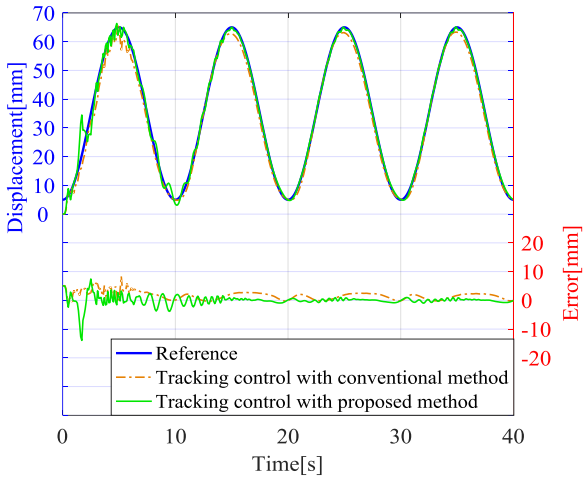

Figure 9. Tracking response of the proposed method and conventional method with the constrained RLS algorithm under the load corresponding to 44 [N]

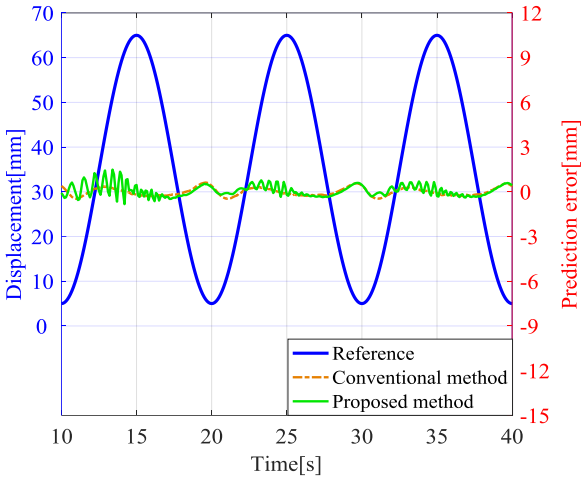

Figure 10. Prediction error of predictor in each method with the constrained RLS algorithm from 10 to 40 [s] under the load corresponding to 44 [N]

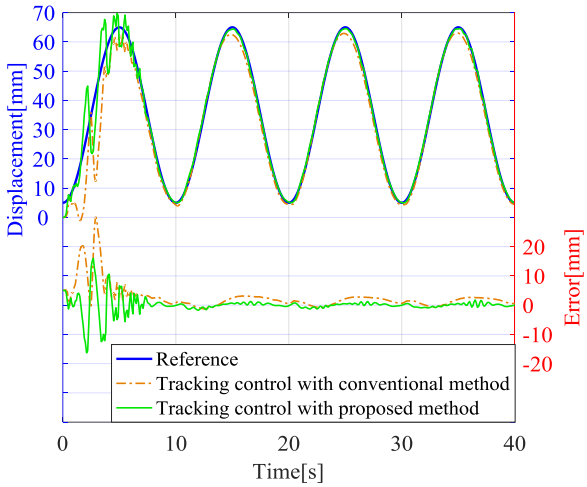

Figure 11. Tracking response of the proposed method and conventional method with the constrained RLS algorithm method under the load corresponding to 68 [N]

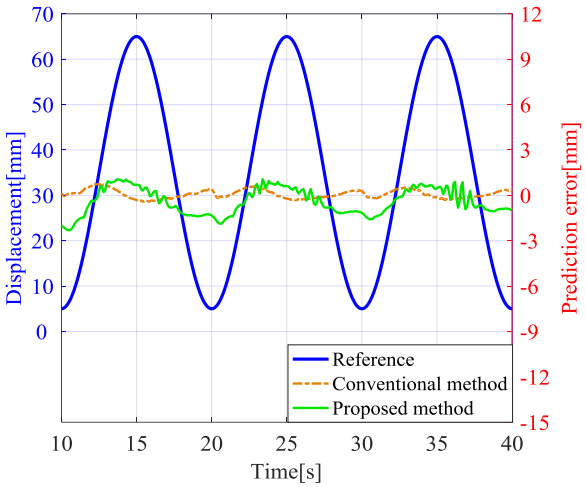

Figure 12. Prediction error of predictor in each method with the constrained RLS algorithm from 10 to 40 [s] under the load corresponding to 68 [N]

Table 6. Comparison of mean absolute value for control performance of each method with the constrained RLS algorithm under loads corresponding to 44[N] and 68[N]

Method / Load	Conventional method without constrained RLS	Proposed method without constrained RLS
44 [N]	1.34 [mm]	0.49 [mm]
68 [N]	1.50 [mm]	0.51 [mm]

6. CONCLUSION

The study proposed modeling, linearization technique, and controller design of the muscle system and examined control performance based on experiments. The proposed model indicated high fitness relative to

the measured output. Subsequently, inverse of the proposed model was utilized to compensate for hysteresis characteristics. We applied adaptive model predictive control with a servo mechanism to the muscle to obtain high control performance and robustness for load. Thus, adaptive model predictive control with the servo mechanism using the linearization technique improved control performance by 63% when compared to that of the adaptive model predictive control using unique coincidence point and exhibited robustness for the load.

A future study will involve developing a model expressing asymmetric hysteresis characteristics that depends on the direction of muscle extension.

REFERENCES

[1] M. Z. M. Dzahir, S. Yamamoto, Recent Trends in Lower-Limb Robotic Rehabilitation Orthosis: Control Scheme and Strategy for Pneumatic Muscle Actuated Gait Trainers, Robotics, Vol.3, Issue 2, pp.120-148, 2014

[2] B. Tondu, P. Lopez, Modeling and Control of McKibben Artificial Muscle Robot Actuators, IEEE Control Systems Magazine, Vol.20, Issue 2, pp.15-38, 2000

[3] W. Kobayashi, K. Ito, S. Yamamoto, Displacement Control of Water Hydraulic McKibben Muscles with Load Compensation, JFPS International Journal of Fluid Power, Vol.8, No.2, pp.107-112, 2015

[4] A. S. Nouri, *et al*., Generalized Variable Structure Model Reference Adaptive Control of One-Link Artificial Muscle Manipulator in Two Operating Modes, Proceeding of IEEE International Conference on Systems, pp.1944-1950, 1994

[5] P. Carbonell, Z. P. Jiang, D. W. Repperger, Nonlinear Control of a Pneumatic Muscle Actuator: Backstepping vs. Sliding-mode, Proceedings of 2001 IEEE International Conference on Control Applications, pp.167-172, 2001

[6] A.P. Arrese, *et al*., Modeling in Modelica and Position Control of a 1-DoF Set-up Powered by Pneumatic Muscles, Mechatronics, Vol.20, Issue 5, pp.535-552, 2010

[7] X. Shen, Nonlinear Model-based Control of Pneumatic Artificial Muscle Servo Systems, Control Engineering Practice, Vol.18, Issue 3, pp.311-317, 2010

[8] J. Wu, *et al*., Nonlinear Disturbance Observer-Based Dynamic Surface Control for Trajectory Tracking of Pneumatic Muscle System, IEEE Transaction on Control Systems Technology, Vol.22, No.2, 2014

[9] C. J. Lin, *et al*., Hysteresis Modelling and Tracking Control for a Dual Pneumatic Artificial Muscle System using Prandtl-Ishlinskii Model, Mechatronics, Vol.28, pp.35-45, 2015

[10] T. Kosaki, M. Sano, Control of a Parallel Manipulator Driven by Pneumatic Muscle Actuators Based on a Hysteresis Model, Journal of Environment and Engineering, Vol.6, No.2, pp.316-327, 2011

[11] H. Aschemann, D. Schindele, Comparison of Model-Based Approaches to the Compensation of Hysteresis in the Force Characteristic of Pneumatic Muscles, IEEE Transactions on Industrial Electronics, Vol.61, No.7, pp.3620-3629, 2014

[12] J. M. Maciejowski, Prediction Control with Constraints, Pearson education, p.290, 2002

[13] J. Mattingley, S. Boyd, CVXGEN: A Code Generator for Embedded Convex Optimization, Optimization and Engineering, Vol.13, Issue 1, pp.1-27, 2012

[14] G. C. Goodwin, K. S. Sin, Adaptive Filtering Prediction and Control, Dover Publications, pp.58-94, 2009

[15] Z. Wei, B. L. Xiang, R. X. Ting, Online Parameter Identification of the Asymmetrical Bouc–Wen Model for Piezoelectric Actuators, Precision Engineering, Vol.38, Issue 4, pp.921-927, 2014

[16] T. Tomatsu, *et al*., Model predictive Trajectory Tracking Control for Hydraulic Excavator on Digging Operation, 2015 IEEE Conference on Control Applications Part of 2015 IEEE Multi-Conference on Systems and Control, pp.1136-1141, 2015

THE EFFECTS OF BULK MODULUS ON THE DYNAMICS OF CONTROLLED INDEPENDENT METERING SYSTEM

Goran Stojanoski, Gerhard Rath, Martin Gimpel
University of Leoben, Chair of Automation, Leoben, Austria
Sandvik Mining and Construction, Zeltweg, Austria
Peter-Tunner-Straße 25 A-8700 Leoben
E-mail goran.stojanoski@unileoben.ac.at

ABSTRACT

The bulk modulus significantly affects the dynamics of hydraulic systems. In this paper, various known approaches for modelling the bulk modulus are investigated and tested. The models include: volumetric compression, solubility of air in oil and oil temperature. These models have been modified here to enable their use in a simulation environment which includes position controlled hydraulics. The results confirm, that air content in and the temperature of the oil can considerably lower the bulk modulus and the overall stiffness of the hydraulic system. This paper shows the different impacts that the low bulk modulus has on pressure and flow controllers as part of the independent metering control strategy. Additionally, the contributions of the pressure and flow controlled cylinder sides on the overall stiffness of the system are analysed and demonstrated. To minimize these effects, a new approach, which pre-pressurizes the rod side of the hydraulic cylinder according to the stiffness of the piston side is proposed. This approach alleviates the shortcomings of previous scientific research and improves the energy efficiency of the system. Furthermore, the results of the new approach are compared with already existing methods, where the set value for the pressure on the rod side is pre-set to a constant value. Depending on the pressure region in which the system operates and the speed of position change this new approach can increase the energy efficiency by 5-15%.

Keywords: bulk modulus, hydraulic actuator, independent metering, energy efficiency

1. INTRODUCTION

The bulk modulus is one of the most important parameters of hydraulic systems and it is often referred to as the reciprocal term of compressibility. It reflects both the stiffness of the system and the speed of transmission of pressure waves [1]. The oil pressure, air content in oil, oil temperature, pipe rigidity and molecular structure of the oil can affect the value of the bulk modulus. The equivalent of the bulk modulus, which includes the effects of all these parameters, has been defined as effective bulk modulus [2]. Feng [3] shows that the compressibility of the oil has the most dominant effect on the stiffness of the hydraulic actuator (around 80%). The pressure applied to the oil, the air content in and the temperature of oil mostly affects its compressibility. Schrank [23] showed that the pressure change in a sealed volume highly depends on the air content in the oil. To this day, a number of theoretical models which describe the bulk modulus dependence on these parameters have been introduced. Merritt [2] introduced a theoretical model for the calculation of the bulk modulus, but

does not include the air dissolving effect. Nykänen [4] derived a theoretical model for the oil-air mixture, which is a significant improvement on the Merritt model. Unlike Nykänen, Cho [5] used the correct tangent bulk modulus definition for the oil-air mixture and achieved better results. Furthermore, Gholizadeh [1] modified the Nykänen model for the true value of the tangent bulk modulus of the oil-air mixture. Yu [6] developed a theoretical model, which gave the pressure dependent variation of free and dissolved air. The theoretical base of the Yu model corresponds with the Wylie [7] model. Kajaste [8] modified the Wylie model for non-isothermal processes and labels it as the Wylie-Yu model. He further modified the model for the pressure increase according to [9] and [10] where it is shown that the relationship between the pressure and the bulk modulus is often regarded as linear. Sunghun [11] offered a new theoretical model in which he adds the pressure influence of the oil into the equation for the theoretical bulk modulus calculation. Gholizadeh [1], introduced a new model, where he sets forth two equations for calculating the bulk modulus of the oil: the first one when the pressure is lower than the critical pressure (air is not dissolved); and the second: when the pressure of the system is higher than the critical value of the pressure (most of the air is dissolved). Moreover, in high-pressurised systems, such as the one presented in this paper, we avoid low-pressure areas where the models are mostly inconsistent. However, in their experiments for ultra-high pressures and temperatures, Yang [22] finds differences between some of the models and the real test data.

The independent metering position controlled systems with two valves offer the possibility to control the back pressure and pre-set its value. If the value of the back pressure is higher, the pressure on the active side of the cylinder will also increase. This will increase the natural frequency of the system and improve the systems ability to handle oscillations. This is very useful when high inertia loads are moved. Although this option is not always energy efficient, it is commonly used in hydraulics to avoid oscillations caused by the lower bulk modulus values. In his paper, Cetin [12] introduces a combined PID - Fuzzy logic controller, which shows better results than the PID controller at the lower bulk modulus values, but he does not address the issue of the energy consumption. Wang [13] introduces a method of degassing where he successfully lowers the air content in the system for 0.01%. Anwer [20] shows that the system needs more power when the temperature increases, but he uses a simplified system with one controlled servo valve. In addition, Anwer [20] and Hassan [21] verify in their experiments that the increasing temperature decreases the supply pressure on the system. Moreover in [19], Harker presents a new method where he identifies the system parameters very accurately.

In this paper most of the abovementioned models were tested under the same conditions and compared to the results presented in [8] and [11]. The Wylie-Yu (Kajaste) model, was further modified for the temperature increase (as presented in [11]) and implemented into an independent metering position controlled system, which moves a heavy load. The air content in and the temperature of the oil in the system were modified in order to see the effects of the low bulk modulus values caused by these parameters on the system. It is shown that the contribution of the values of the low bulk modulus is not equal for the pressure controlled cylinder side and for the flow controlled cylinder side. Additionally, both flow and pressure controllers show delayed response as the bulk modulus value is declining. At the same time, the amplitude of the pressure controller is intensively lowered. The new approach presented in this paper offers a gradual increase of pressure on the backside according to the value of the bulk modulus on the piston side. This allows the system to achieve the desired position at all times without experiencing oscillations or significant delays. This new approach was compared to the conventional independent metering control strategies implemented in the valves, which has the possibility to pre-set a constant value for the pressure on the rod side of the cylinder. An improvement in the energy efficiency of the system is achieved and shown.

2. MODEL OF THE SYSTEM

2.1. Bulk Modulus

The bulk modulus of a fluid is defined as the change of pressure divided by the change of volume. There are four types of bulk modulus. It depends if the process is adiabatic or isothermal and if we use the secant or the

tangent definition for the bulk modulus. The secant bulk modulus (eq. 2) is more suitable for big pressure changes, whereas the tangent bulk modulus (eq. 1) is more adequate for smaller pressure changes. The tangent bulk modulus is defined as:

$$K = -V\left(\frac{\partial P}{\partial V}\right)_{S,T}, \tag{1}$$

where K is the value of the bulk modulus and V is the initial volume after compression. Equation 2 represents the secant bulk modulus

$$K_s = -V_0\left(\frac{\Delta P}{\Delta V}\right)_{S,T}, \tag{2}$$

where V_0 is the initial volume of the fluid, ΔP is the change in pressure, ΔV is the change in volume and S and T represent the adiabatic and isothermal process respectively.

2.2. Different Models for Theoretical Calculation of the Effective Bulk Modulus

In hydraulic systems the change of pressure is not linear with the change of volume [15]. As mentioned in section 2.1 the bulk modulus can be defined as tangent or secant. For given pressure, the tangent bulk modulus is defined as the slope of the tangent of the curve (eq. 1) and the secant bulk modulus (eq. 2) is defined as the slope of the line connecting the pressure with the origin.

2.2.1. Merritt Model

Under the assumptions: solubility of air in oil was not considered; the container is rigid; air was treated as perfect gas; no surface tensions and if oil and air are assumed to have the same temperature and pressure, the model from Merritt [2] for the effective bulk modulus, can be written as

$$K_{Merritt} = \frac{K_0}{1 + x\left(\frac{K_0}{np} - 1\right)}, \tag{3}$$

where he takes the standard definition for the secant bulk modulus, but doesn't include the effect of the rising pressure on the air content in the oil. Because of this, the value for the bulk modulus using this model will be lower than the effective bulk modulus. In eq. 3, x represents the air content in oil.

2.2.2. Nykänen Model

Nykänen [4], eq. 4 delivered a model in which he does not use the standard definition for the tangent bulk modulus.

$$K_{Nykanen} = \frac{x\left(\frac{p_0}{p}\right)^{\frac{1}{n}} + (1-x)e^{-\frac{p}{K_0}}}{\frac{x}{np}\left(\frac{p_0}{p}\right)^{\frac{1}{n}} + \left(\frac{(1-x)e^{-\frac{p}{K_0}}}{K_0}\right)} \tag{4}$$

2.2.3. Cho and Nykänen Modified Models

The model from Cho [5]

$$K_{Cho} = \frac{(1-x) + \left(\frac{p_0}{p}\right)^{\frac{1}{n}} x}{\frac{x}{np}\left(\frac{p_0}{p}\right)^{\frac{1}{n}} + \frac{(1-x)}{K_0}}, \tag{5}$$

used the tangent value for the bulk modulus eq. 5 and delivers improved results when compared with the previous two models described with eq. 3 and eq. 4. Furthermore, Gholizadeh [1], showed that when referring

to the effective bulk modulus we should use the tangent value for the bulk modulus. In the same manner he modified the Nykänen model for the tangent bulk modulus of the air and liquid mixture and received the same equation as for the model in eq. 5. It can be seen from Fig. 1 that, when using the standard tangent value for the Nykänen model, we receive higher values for the effective bulk modulus.

2.2.4. Yu and Gholidazeh Models

Yu [6] introduced a model accounting for the dissolving of the air in oil. He also provided a simplified form of his equation which disregards the air dissolving effect. As our system works with higher starting pressures, we assume that most of the air is dissolved. Furthermore, as shown in section 2.2.5, Kajaste modified the Yu and Wylie models for non-isothermal conditions (eq. 8).

On the other hand, Gholizadeh provides two equations, where he describes the dissolving of air in oil in one and the compression of air in oil in another (eq. 6). As explained before, because of the high starting pressures, the equation which describes the air dissolving in oil, was not used.

$$K_{Gholizadeh} = \frac{V_{l0}\left(1+\frac{m_p}{K_0}(p-p_0)\right)^{-\frac{1}{m_p}} + \left(\frac{p_0}{p}\right)^{\frac{1}{n}}\left(\frac{T}{T_0}\right)x}{\frac{1}{K_l}V_{l0}\left(1+\frac{m_p}{K_0}(p-p_0)\right)^{-\frac{1}{m_p}} + \frac{1}{np}\left(\frac{p_0}{p}\right)^{\frac{1}{n}}\left(\frac{T}{T_0}\right)x} \tag{6}$$

The value of the volume V_{l0}, was calculated from the cylinder we used in Fig. 3 and the equation presented in [1]. The coefficient m_p represents the pressure related term.

2.2.5. Wylie-Yu Model Modified by Kajaste

The model of Wylie [7] describes the effective bulk modulus described as the ratio between the pressure difference and the volume change of the fluid and air mixture. Equation 7 describes the isothermal case

$$K_W = \frac{K_l}{1+\left(\frac{m_g RT}{p}\right)\left(\frac{K_l}{p}-1\right)}. \tag{7}$$

Kajaste [8] further modified eq. 7 for non-constant temperature and labels it ‘Wylie-Yu model for theoretical calculation of the effective bulk modulus’ eq. 8.

$$K_{Wk} = \frac{K_l}{1+x\left(\frac{p_0}{p}\right)^n\left(\frac{K_l}{np}-1\right)} \tag{8}$$

If the value for the K_l in eq. 8 is modified for the pressure increase coefficient [9] m_p and temperature increase coefficient n_T [11], the equation for the bulk modulus of the liquid is

$$K_l = K_0 + m_p p + n_T T, \tag{9}$$

as presented in [11]. However, Kajaste in [9] takes the values for K_0 which correspond to the measurements for different temperatures. In order to be able to compare this model with the IFAS model we modify eq. 8 with eq. 9, as presented in [11].

2.2.6. IFAS Model

The IFAS model developed by Kim [11], addresses the tangent bulk modulus of the oil with the pressure increase term already implemented in the equation

$$K_{IFAS} = \frac{(1-x)\left(1+\frac{m_p(p-p_0)}{K_0}\right)^{-\frac{1}{m_p}} + x\left(\frac{p_0}{p}\right)^{\frac{1}{n}}}{\frac{1}{K_0}(1-x)\left(\frac{p_0}{p}\right)^{\frac{1}{n}}\left(1+\frac{m_p(p-p_0)}{K_0}\right)^{-\frac{m_p+1}{m_p}} + \left(\frac{x}{np_0}\right)\left(\frac{p_0}{p}\right)^{\frac{n+1}{n}}} \tag{10}$$

2.2.7. Comparative Analyses for Isothermal Conditions

After principal investigation of the models under different conditions, all of the models were simulated and compared under the same conditions. Figure 1 shows the bulk modulus values of the different models presented in the sections above. When compared with the results presented in [11], the Wylie-Yu (Kajaste) 2.2.5 model and the IFAS 2.2.6 model show the most consistent results. Because of this, the two models were further compared for non-isothermal conditions and non-constant temperature.

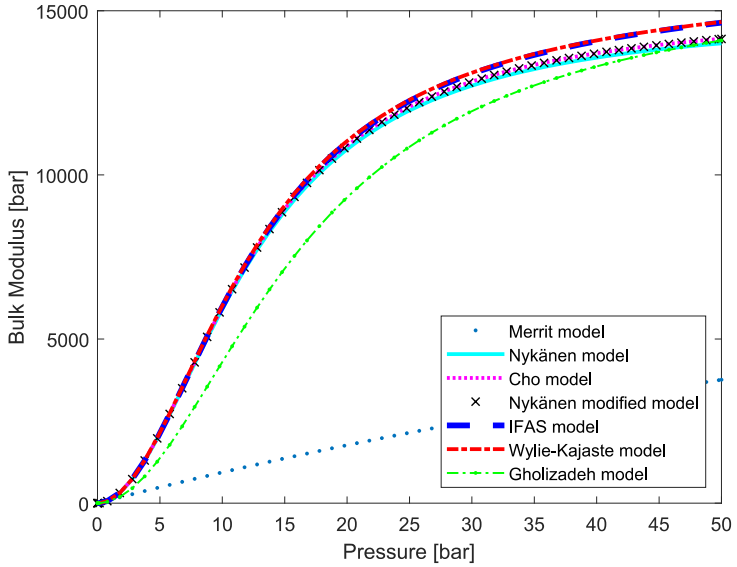

Figure 1. Comparison of the different models under the same conditions, x= 1%, n= 1 (isothermal condition), p_0= 1 bar, m_p= 11.4, K_0= 15000 bar and p= [0-50] bar.

2.2.8. Comparative Analyses of the Wylie-Yu (Kajaste) and IFAS Models for Non-Isothermal Conditions

Here the two models were compared under non-isothermal conditions. Pressure ranges between p= [0-80] bar, the temperature of the oil between T= [0-60]°C the air content in the oil is x= 0.013%, the bulk modulus value K_0= 18670 bar (ISO VG 46 oil), the temperature related term n_T = -80 bar/°C, the pressure related term m_p= 11.4 and the polytropic constant n= 1.4, as presented. Figure 2 shows the value of the bulk modulus calculated with the two models under the given conditions.

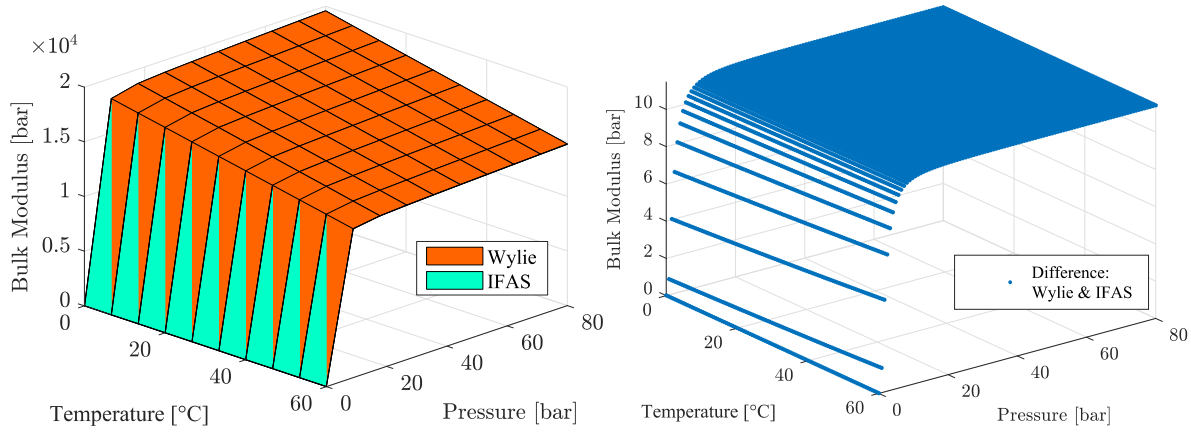

Figure 2. Wylie-Yu (Kajaste) and IFAS models under the same conditions, x= 0.013%, T= [0-60]°C, K_0= 18760 bar, n= 1.4, n_T= -80 bar/°C, m_p= 11.4 and p= [0-80] bar.

The results correspond well with the results presented in [11]. Further, in Fig. 2 the difference between the two models is evaluated at every point. Even at higher pressures and adiabatic conditions the similarities are

evident. Because of this reason, the results stated in [16] and the lower complexity of eq. 8, the Wylie- Yu (Kajaste) model was incorporated in our simulation model.

2.3. Hydraulic System

The hydraulic and mechanical systems are shown in Fig. 3 and Fig. 4. They are simplified models of the systems used in the new state of the art cutting machine, which is part of the EIT Raw Material project 'Rock Vader'.

The main parts in the hydraulic system are a double acting cylinder, two proportional valves that allow individual control of the flows q_A and q_B and the pressures p_A and p_B. The flows and the pressures are controlled with PID controllers. Additional components such as load sensing and pressure compensators are not displayed.

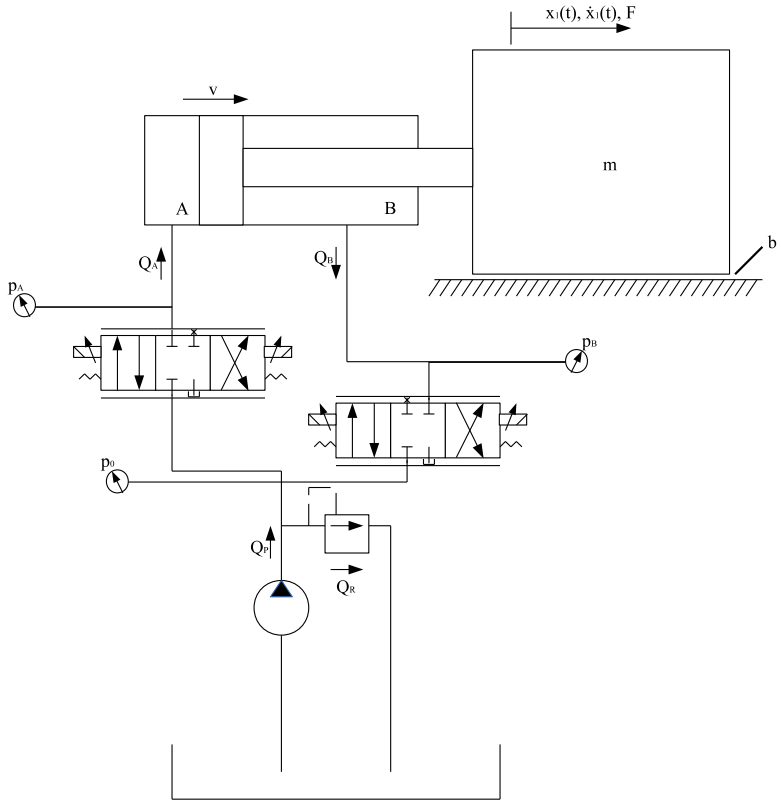

Figure 3. Hydraulic system.

2.4. Mechanical System

The mechanical model consists of a big mass, that rotates around a given point O (Fig. 4). For simulation purposes, the model of the mass is concentrated in a single point M. The lever with length L is regarded as massless. A hydraulic cylinder moves the mass M horizontally by applying force on the smaller lever with length l. The system is moving horizontally, not being affected by the force of gravity.

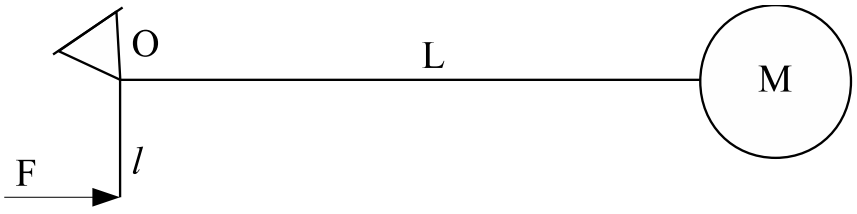

Figure 4. Sketch of the mechanical system.

For small motions the dynamic mass of the system is regarded as

$$m = \left(\frac{L}{l}\right)^2 M. \tag{11}$$

2.5. Mathematical Model

The position of the mass is shown in Fig. 3 and described as x_1. According to this, the equation of motion for this system is

$$m\ddot{x} = p_A(t)A_A - p_B(t)A_B - b\dot{x}_1(t). \tag{12}$$

In a hydraulic system like the one in Fig. 3, multiple components can be a source of friction. The flow of the oil through an orifice contributes to the friction. Additionally, the steel construction of the system can contribute to the friction sum. Further, the sealing of the cylinder offers a non-linear friction behaviour. The main contribution by the actual machine is coming from the load that performs a cutting process. For simplifying the equations we presumed it to be viscous with the coefficient b eq. 12. The motion of the system is controlled by two independent valves as shown in Fig. 3. These types of valves provide several independent metering control strategies in order to achieve constant flow and desired pressure values [17]. This allows direct control of the pressures p_A, p_B and flows q_A, q_B. In our situation, we use the flows as inputs for the change in pressure

$$\begin{aligned} \dot{p}_A(t,p) &= \frac{1}{C_A(x_0,p,T_0)}(q_A(t) - \dot{x}_1(t)A_A), \\ \dot{p}_B(t,p) &= \frac{1}{C_B(x_0,p,T_0)}(q_B(t) + \dot{x}_1(t)A_B). \end{aligned} \tag{13}$$

The initial conditions for eq. 13 are defined at 30 bar. The hydraulic capacitance for volume V can be calculated with

$$C_A(x_0,p,T_0) = \frac{V_A}{K_A(x_0,p,T_0)} \quad C_B(x_0,p,T_0) = \frac{V_B}{K_B(x_0,p,T_0)}. \tag{14}$$

In our situation the bulk modulus is calculated with the eq. 8, which means that eq. 14 can be modified to

$$C_A(x_0,p,T_0) = \frac{V_A}{K_{Wk_A}(x_0,p,T_0)} \quad C_B(x_0,p,T_0) = \frac{V_B}{K_{Wk_B}(x_0,p,T_0)}. \tag{15}$$

The hydraulic capacitance depends on multiple factors. One of the factors is the volume of the chambers, which, in our situation is taken to be non-identical for the piston and rod side of the cylinder. At the same time, the position of the piston can affect the capacitance, but in our model this was disregarded, as the change in position is small. We also assume that the connections between the valves and the cylinder are rigid. The bulk modulus K is changed according to the pre-set conditions of the oil in the system. This changes the capacitance values accordingly. The independent metering valves like in [17] offer additional pressure and flow measurements, which help with maintaining a constant flow and desired pressure values. According to [2], the flow through an orifice can be defined as

$$Q = C_d w x_v(t)\sqrt{\frac{2(p_S - p_{A,B})}{\rho}}, \tag{16}$$

where C_d= 0.61 and w represent the area gradient of the valve. This value is normally given in the specification data of the valve. In order to be able to use eq. 16 in real time simulation the flow can be calculated using Q_N, ΔP_N and y where

$$\begin{aligned} Q_v &= K_v y\sqrt{\Delta P_v}, \\ K_v &= \frac{Q_N}{y_{max}\sqrt{\Delta P_N}}. \end{aligned} \tag{17}$$

The nominal flow and pressure drop are parameters that can easily be found into the valve catalogues, y represents the input voltage into the valve and $\sqrt{\Delta P_v}$ represents the pressure difference in over the valve.

The hydraulic supply power in the simulation is calculated with equation

$$P_w = p_s Q_s, \tag{18}$$

where p_s is the supply pressure and Q_s is the supply flow.

3. SIMULATIONS AND RESULTS

3.1. Case Study

In order to confirm some of the effects mentioned in the previous chapters and further investigate the issue of the bulk modulus, the system shown in Fig. 3 and Fig. 4 was tested and simulated with Simulink®. The mass of the system is presented as M= 400,000 kg and the friction b= 10^7 Ns/m (identified value from measurements during operation in cutting experiment). The hydraulic cylinder areas are A_A= 0.0616 m² and A_B= 0.0302 m². The length of the cylinder is h= 0.65 m. As input we used an external position PI controller with set value of 0.01 m. The flows and the pressures inside the valve are controlled with PID controllers. The values for the temperature and the air content are chosen according to the values received from the real working conditions. Depending if the load is active or passive there are multiple control strategies that can be implemented into the system embedded controller [17]. Most of them are tested and demonstrated in [18]. In this case, the system is not affected by gravity, so we assume that the load is passive. A positioning experiment was done and the results are shown in Fig. 5, Fig. 6 and Fig. 7.

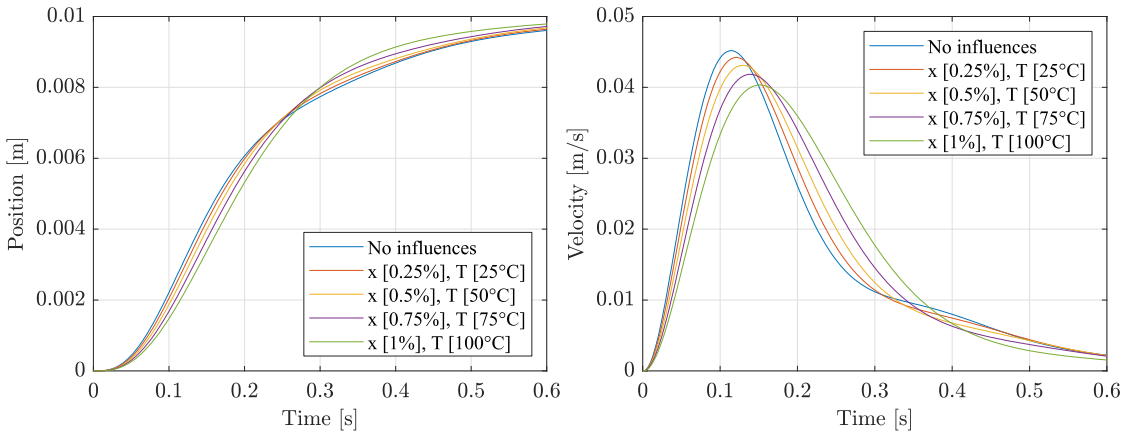

Figure 5. Position and velocity, at different air content (x), temperature (T) and pressure (p).

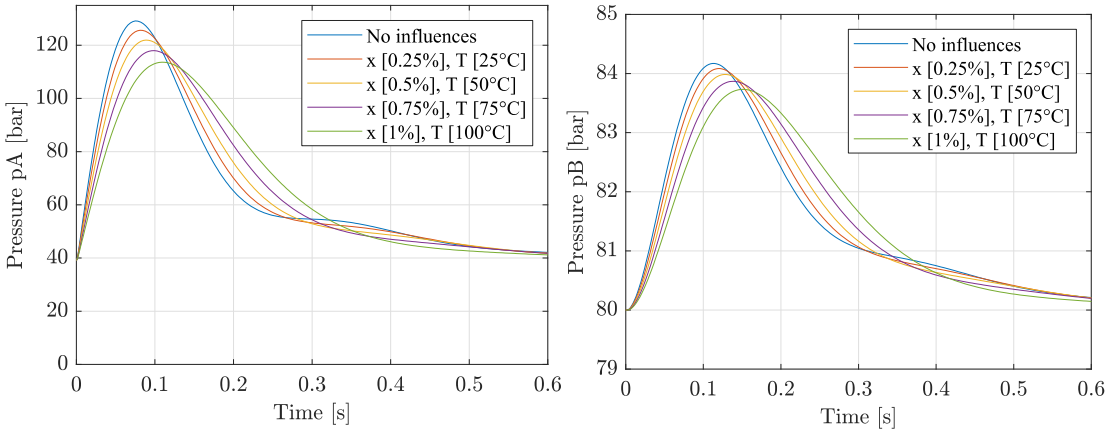

Figure 6. Pressures P_A and P_B, at different air content (x), temperature (T) and pressure (p).

Figure 5 shows that with the decrease in bulk modulus the position of the system delays. Further the system peak velocity is declining. In Fig. 6 a significant decrease in pressure on the piston side is visible, which is flow

controlled. Additionally, the rod side, which is pressure controlled shows very small changes from the constant set value of 80 bar. Figure 7 displays the effects that the bulk modulus has on the system controllers. It is apparent that the position controller recognizes the decrease in bulk modulus and tries to increase the flow into the system. This actuates the flow controller accordingly. On the rod side, the pressure controller shows linear behaviour to the change in bulk modulus. It delays as the bulk modulus value declines and the amplitude decrease is significant.

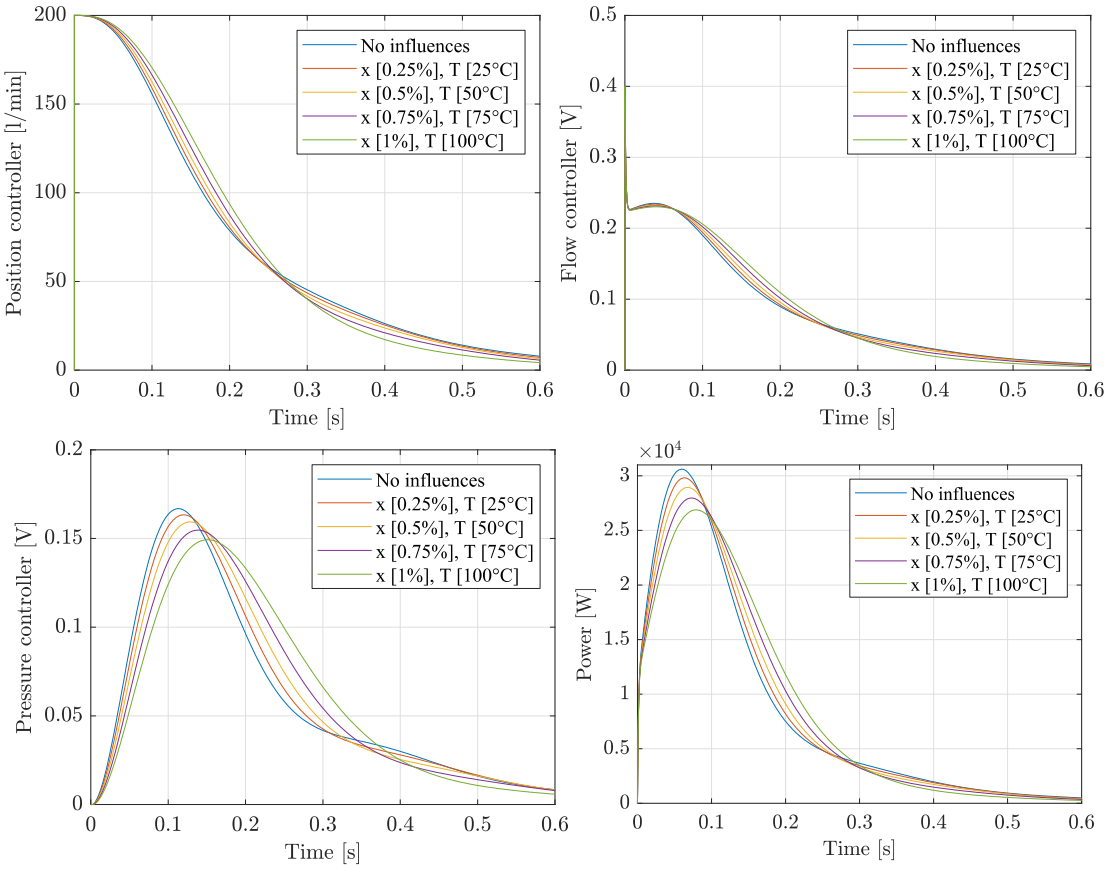

Figure 7. Outputs of the controllers and the supply power, at different air content (x), temperature (T) and pressure (p).

From the hydraulic supply curves shown in Fig. 7, it is evident that the system is using more power when the bulk modulus is higher and less power when the bulk modulus is lower. One reason for this is the decrease in pressure on the piston side. This shows that the independent metering strategy did not take into account the change of the bulk modulus. Also, the figures above led us to believe that the flow and pressure controlled cylinder sides do not have equal contribution to the stiffness of the system.

3.2. Comparison of Flow and Pressure Controlled Sides

In order to see which controller performs better under these conditions, two additional simulations were carried out. These simulations confirm our previous assumption that the flow controller (piston side) affects the overall stiffness of the system much more severely when compared with the pressure controller (rod side). In the first additional simulation the value of the piston side bulk modulus was affected by the pressure of, temperature of and the air content in the oil. The rod side bulk modulus value was only affected by the pressure of the oil.

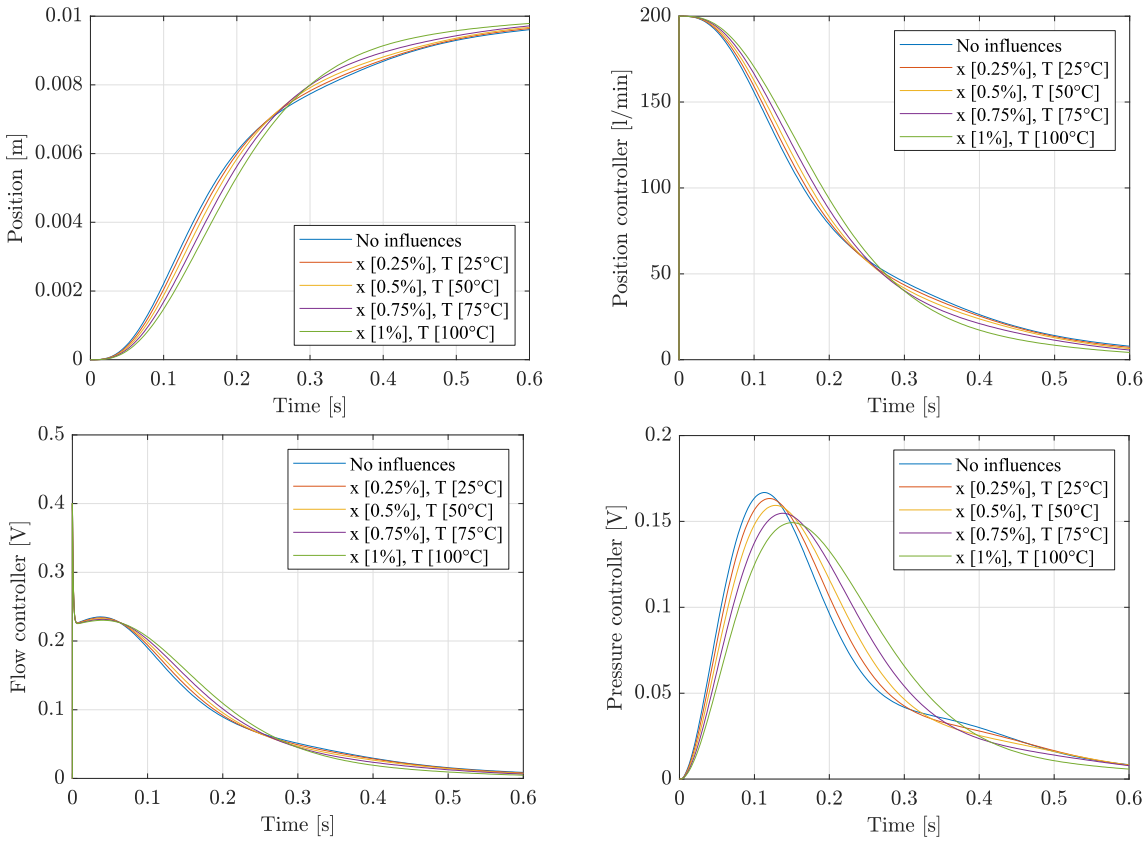

Figure 8. Outputs of the position and the controllers,
piston side bulk modulus value affected by: air content (x), temperature (T), pressure (p),
rod side bulk modulus value affected by: pressure (p).

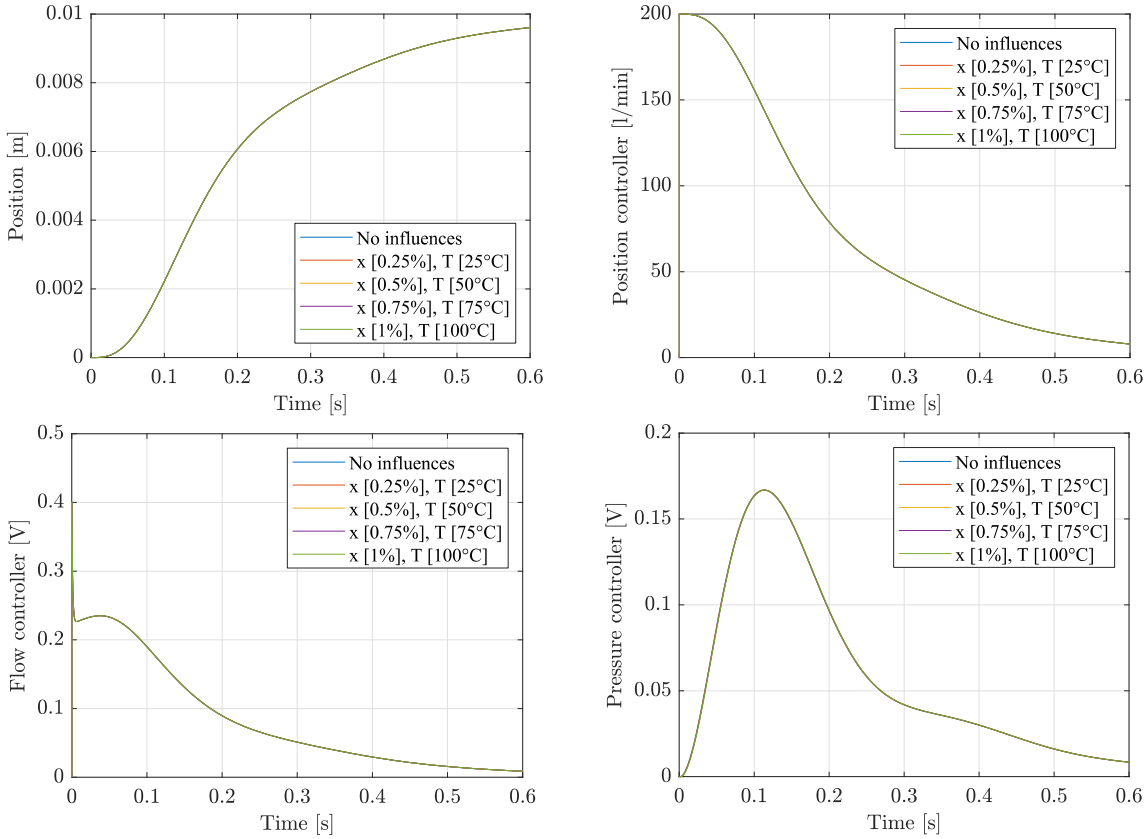

Figure 9. Outputs of the position and the controllers,
piston side bulk modulus value affected by: pressure (p),
rod side bulk modulus value affected by: air content (x), temperature (T), pressure (p).

Figure 8 shows that the position and the controllers exhibit behavior similar to that shown in Fig. 5 and Fig. 7. In the second additional simulation, the piston side bulk modulus value was only affected by the pressure. The rod side bulk modulus value was affected by the air content in, temperature and pressure of the oil. Figure 9 shows that, in this case the effects on the system dynamics are minor. This leads us to the conclusion that the pressure controller has an advantage in this type of systems and under these conditions. In addition, by identification of the bulk modulus value, we should focus on the flow controlled side. Moreover, this opens a possibility, to modify the starting pressure of the pressure controller side according to the bulk modulus value on the flow controlled side of the cylinder, or more accurately to the oil conditions.

3.3. New Approach, with Adaptive Back Pressure Control

The independent metering control strategies, have the advantage to modify the values of the starting pressures of the piston and rod side. Normally they are set experimentally, depending on the system demands. We have already shown that the air content in and the temperature of oil significantly affect the stiffness of the system. As the bulk modulus equations are incorporated into the hydraulic cylinder calculation for the capacitance eq. 13, we can very easily calculate how much the value of the bulk modulus has been affected by the air content in, temperature and pressure of oil. According to this, a control algorithm was implemented (Fig. 10, Fig. 11), which determines three scenarios: when the system is stiff; when the system is mid-stiff and when the system has a lower stiffness (low bulk modulus values). Because of the advantage of the pressure controller we observed the bulk modulus value only on the flow controlled side. In accordance with this, the back pressure is preset to a value which allows the system to achieve the desired position. The values for the back pressure are set experimentally.

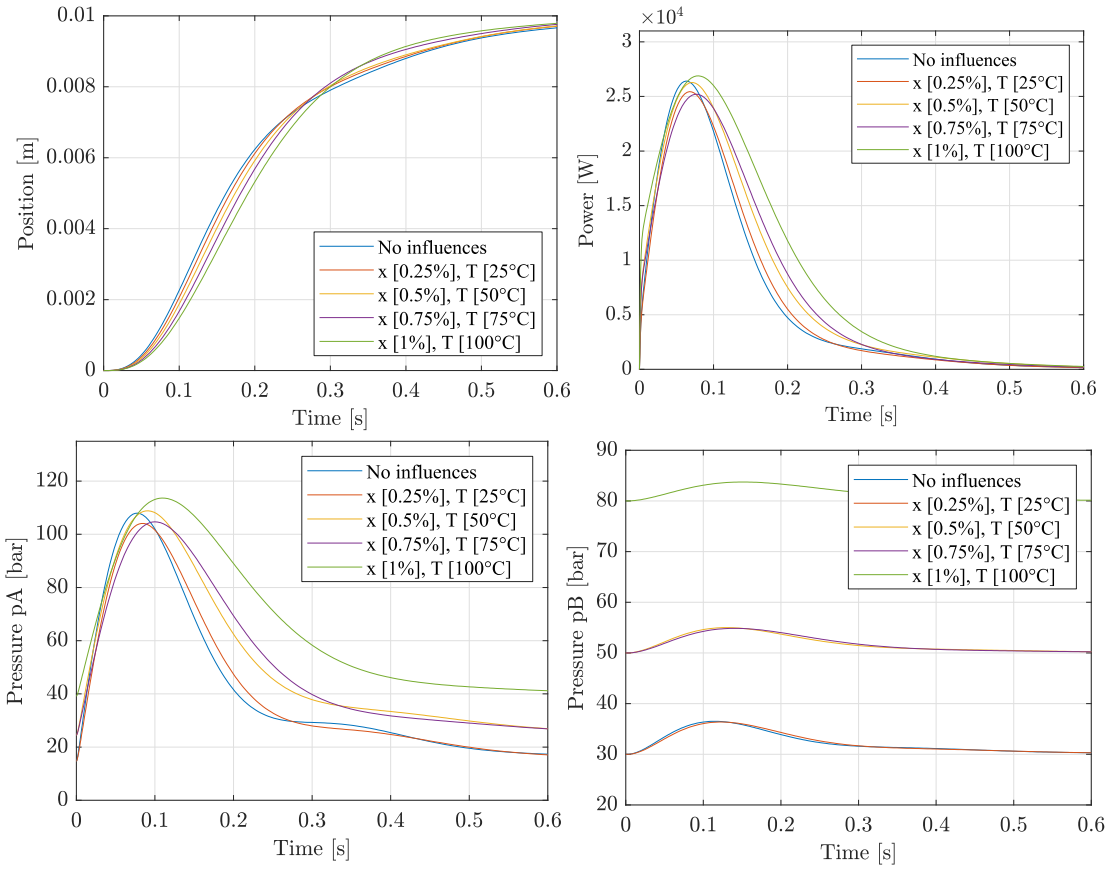

Figure 10. Outputs of the position, power and the pressures p_A and p_B, with adaptive back pressure control.

Figure 10 shows that the system is able to achieve the desired position fast without any oscillations. Furthermore, it is visible that the values for the back pressure change depending on the oil condition (stiffness of the system) of the piston side. This is most visible by the power curve shown in Fig. 10.

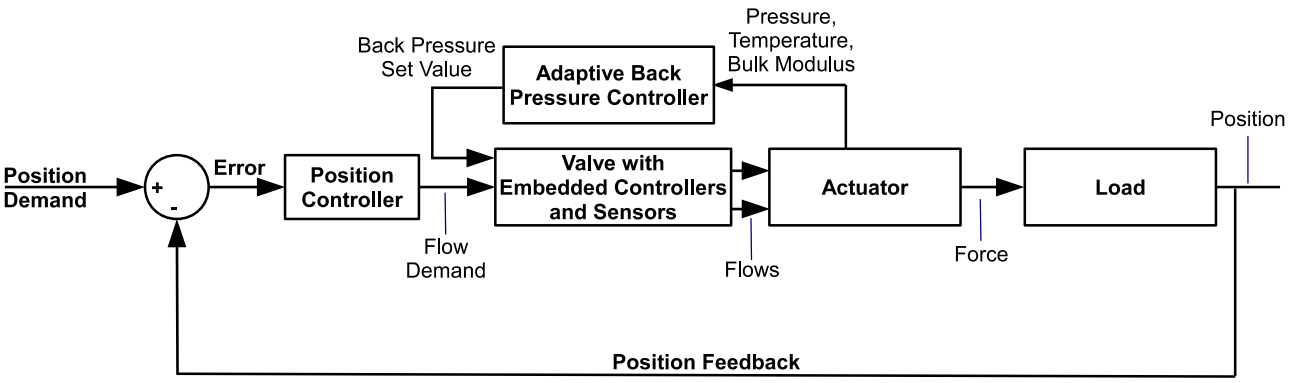

Figure 11. Block diagram of the overall system with adaptive back pressure controller.

The goal of this approach was to be able to improve the power curves shown in Fig. 8, where the system was using most of its power while having no influence on the value of the bulk modulus. This improvement is most visible in Fig. 12, where the average power consumption of the system under the given conditions for the two previously given scenarios is visible.

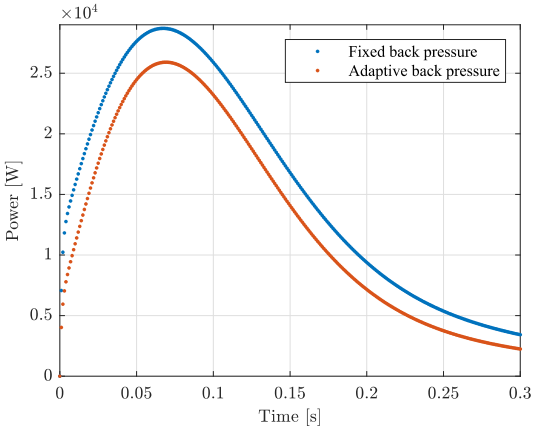

Figure 12. Average power consumptions for the system under the previously given conditions.

4. CONCLUSIONS

The results achieved with the methods presented in this paper lead to the conclusion that: to obtain optimal control performance it is important to take into account and model the bulk modulus. This requires the modelling of both the entrained air and temperature effects on the bulk modulus of the oil. In this paper different theoretical models for bulk modulus are analysed and compared. One is further implemented in an independent metering position controlled system. The results demonstrate that a higher energy efficiency has been achieved. Future work will focus on the requirements for optimal performance in other types of independent metering systems and implementation in real independent metering valves.

ACKNOWLEDGEMENT

This project was partially funded by the *EIT Raw Materials project Rock Vader.*

5. NOMENCLATURE

Notation	Denotation	Unit	Notation	Denotation	Unit
K	Tangent bulk modulus	Pa	m_g	Mass of free gas	kg
K_s	Secant bulk modulus	Pa	m	Dynamic mass	kg
K_0	Bulk modulus of the liquid	Pa	m_p	Pressure related term	
K_l	Bulk modulus of liquid, corrected	Pa	M	Mass of the load	kg
$K_{Merritt}$	Bulk modulus by Merritt model	Pa	L	Length of bigger lever	m
$K_{Nykanen}$	Bulk modulus by Nykänen model	Pa	l	Length of smaller lever	m
K_{Cho}	Bulk modulus by Cho model	Pa	h	Length of cylinder	m
$K_{Gholizadeh}$	Bulk modulus by Gholizadeh model	Pa	F	Cylinder force	N
			R	Gas constant	J/molK
			x	Amount of free air at p_0	%
K_W	Bulk modulus by Wylie model	Pa	x_1	Position of the load	m
K_{Wk}	Bulk modulus by Wylie-Yu (Kajaste) model	Pa	$\dot{x}_1$, v	Speed of the load	m/s
			y	Valve opening	V
K_{IFAS}	Bulk modulus by IFAS model	Pa	n	Polytropic constant	
V_0	Initial fluid Volume	m^3	n_T	Temperature related term	bar/°C
V	Fluid volume	m^3	ΔP	Pressure change	Pa
V_{g0}	Volume of gas	m^3	ΔV	Volume change	m3
V_{l0}	Volume of liquid	m^3	b	Viscous friction coefficient	Ns/m
p	Absolute pressure	Pa	A_A, A_B	Areas, piston and rod side	m^2
p_0	Initial pressure	Pa	C_A, C_B	Hydraulic capacitance	m^3/Pa
p_s	Supply pressure	Pa	Q	Oil flow through a valve	m^3/s
p_N	Nominal pressure for Q_N	Pa	Q_N	Nominal oil flow of a valve	m^3/s
p_A	Pressure chamber A	Pa	Q_s	Supply oil flow of a valve	m^3/s
p_B	Pressure chamber B	Pa	q_A	Oil flow into chamber A	m^3/s
P_w	Supply power	W	q_B	Oil flow into chamber B	m^3/s
ΔP_v	Pressure drop over the valve	Pa	w	Area gradient	
T	Absolute temperature	K			

REFERENCES

[1] H. Gholizadeh. 2014. Modelling and Experimental Evaluation of the Effective Bulk Modulus for a Mixture of Hydraulic Oil and Air. PhD Thesis, University of Saskatchewan, Canada, 2013.

[2] H.E. Merritt. 1967. Hydraulic Control Systems. John Wiley & Sons Inc., New York.

[3] H. Feng, Q. Du, Y. Huang & Y. Chi. 2017. Modelling study on stiffness characteristics of hydraulic cylinder under multi-factors. Journal of Mechanical Engineering, May 2017, pp. 447–456.

[4] T.H.A. Nykänen, S. Esque & A.U. Ellman. 2000. Comparison of different fluid models, Bath Workshop on Power Transmission and Motion Control, Bath, United Kingdom, pp. 101–110.

[5] B-H. Cho, H-W. Lee & J-S. Oh. 2000. Estimation Technique of Air Content in Automatic Transmission Fluid by Measuring Effective Bulk Modulus. Technical report, pp. 57–61.

[6] Y. Jinghong, C. Zhaoneng & L. Yuanzhang. 1994. The Variation of Oil Effective Bulk Modulus with Pressure in Hydraulic Systems. Journal of Dynamic Systems, Measurement and Control. pp. 146–150.

[7] E.B. Wylie, V.L. Streeter. 1978. Fluid Transients. McGrawn Hill Inc., United States of America.

[8] J. Kajaste, H. Kauranne, A. Ellmann & M. Pietola. 2005. Experimental Validation of Different Models for Bulk Modulus of Hydraulic Fluid. The Ninth Scandinavian International Conference on Fluid Power, June 1-3, Linköping, Sweden

[9] E. Kuss. 1976. PVT Daten bei hohen Drücken. DGMK Berichte, Forschungsbericht 4510, Hanover.

[10] J. Watton, Y. Xue. 1994. A New Direct Measurement Method for Determining Fluid Bulk Modulus in Oil Hydraulic Systems. FLUCOME'94, August 29 – 1 September 1994, Toulouse, France.

[11] K. Sunghun, H. Murrenhoff. 2012. Measurement of Effective Bulk Modulus for Hydraulic Oil at Low Pressure. Journal of Fluids Engineering, March 2012.

[12] S. Çetin, A.V. Akkaya. 2010. Simulation and hybrid fuzzy-PID control for positioning of a hydraulic system. An International Journal of Nonlinear Dynamics and Chaos in Engineering Systems, Springer Science, August 2010, pp. 465–476.

[13] J. Wang, G. Gong & H. Yang. 2008. Control of bulk modulus of oil in hydraulic systems. In IEEE/ASME International Conference on Advanced Intelligent Mechatronics, July 2-5 2008, Xi'an, China pp. 1390–1395.

[14] A.M. Hurst & J. VanDeWeert. 2016. A Study of Bulk Modulus, Entrained Air, and Dynamic Pressure Measurements in Liquids. Journal of Engineering for Gas Turbines and Power, October 2016, pp. 1–9.

[15] A.T.J. Hayward. 1967. Compressibility equations for liquids: a comparative study. British Journal of Applied Physics, February 1967, pp. 965–977.

[16] J. Kajaste, H. Kauranne, A. Ellmann & M. Pietola. 2006. Computational Models for Effective Bulk Modulus of Hydraulic Fluid. Second International Conference on Computational Methods in Fluid Power, August 2-3 2006, Aalborg, Denmark, pp. 1–7.

[17] E.H. Group. 2015. Advanced independent metering mobile valve, December 2015.

[18] G. Stojanoski. 2017. Modelling, Simulation and Control of a Hydraulic System with Individual Meter-in and Meter-out. Master thesis, University of Leoben, Leoben, Austria.

[19] M. Harker, G. Rath. 2018. Global Least Squares for Time-Domain System Identification of State-Space Models. 7th Mediterranean Conference on Embedded Computing (MECO), June 10-14 2018, Budva, Montenegro, pp. 590-595.

[20] A.F. Anwer. 2013. Effect of Oil Temperature on the Performance of a Hydraulic Linear System Controlled With Electro Hydraulic Servo Valve. Production Engineering and Design Department, Faculty of Engineering, El-Minia University, March 2013, El-Minia, Egypt.

[21] J.M. Hassan, S.Y. Ibrahim. 2009. An Experimental Study Into The Effect Of Temperature And Pressure on The Hydraulic System. Eng.&Tech. Journal Vol.27, September 2009, pp. 2531-2545.

[22] Y. Shudong, T. Aihua, L. Yulin, Z. Junxiang, Z. Peng & Z. Lin. 2016. Experimental measurements of bulk modulus for two types of hydraulic oil at pressures to 140MPa and temperatures to 180°C. 10th International Fluid Power Conference, March 8-10 2016, Dresden, Germany, pp. 193-204.

[23] K. Schrank. 2015. Eindimensionale Hydrauliksimulation mehrphasiger Fluide. PhD Thesis, Rheinisch-Westfälische Technische Hochschule Aachen (RWTH Aachen), Aachen, Germany, 2015.

ANALYSIS AND TEST OF MODEL-BASED FAULT DETECTION METHODS FOR MOBILE MACHINERY USING INDEPENDENT METERING SYSTEMS

B. Beck, S. Köhler, J. Weber
Technische Universität Dresden
Institute of Mechatronic Engineering
Chair of Fluid-Mechatronic Systems (Fluidtronics)
Helmholtzstraße 7a
01069 Dresden, Germany
benjamin.beck@tu-dresden.de

ABSTRACT

Regarding further improvements of machine efficiency through a consequent digitalisation, electrohydraulic drive systems using independent metering valves are increasingly the focus of the application. However, the system complexity in combination with a higher effort on control algorithms, software architectures and especially safety as well as reliability aspects are hurdles to integration. Previous contributions answered the safety and reliability questions concerning the system structure and showed one possible fault detection method based on limit checking to fulfil the safety requirements according to ISO 13849. Nevertheless, the detection performance is upgradeable and a deep diagnosis is not achievable with limit checking. Subsequently, this contribution handles the development and test of model-based detection using parity equations with respect to integration into a conventional mobile control unit.

KEYWORDS: independent metering, machine safety, ISO 13849, model-based fault detection

NOMENCLATURE

Formula sign	Description	Unit
A_i	Area	m^2
DC	Diagnostic Coverage	%
D_V	Valve's damping	$-$
F_L	Load force	N
h	Feedback gain	s^{-1}
i	Current	A
k_i, q_i	Coefficients	$m^3/(s \cdot \sqrt{Pa})$
K'	Effective bulk modulus	Pa
n_1	Rotational speed pump	min^{-1}
p_i	Pressure	Pa

$\dot{p}_i$	Pressure build-up	Pa/s
PL	Performance Level	$-$
PL_r	Required Performance Level	$-$
Q_i	Volume flow	m^3/s
r	Residuum	Various
$r_{i,max}$	Residuum upper limit	Various
$r_{i,min}$	Residuum lower limit	Various
R	Coefficient of determination	$-$
s	Laplace variable	s^{-1}
t, t_e	Time , dead time	s
T_1	Time constant	s
y	Model output variable	Various
y_c	Cylinder stroke	m
$\dot{y}_c$	Cylinder velocity	m/s
y_{meas}	Measured variable	Various
y_V	Valve spool stroke	m
$\dot{y}_V$	Valve spool velocity	m/s
$\ddot{y}_V$	Valve spool acceleration	m/s^2
V_i	Volume	m^3
Δp_i	Pressure difference	Pa
Δt	Cycle time	s
Δy_{TCP}	Tool-centre-point difference	m
ω_V	Valve's characteristic circular frequency	s^{-1}

1. INTRODUCTION

Driven by the digitalisation trend as well as further efficiency improvements and the increasingly strict emission standards, alternative electrohydraulic drive systems like independent metering come to the fore. But due to higher acquisition costs, complex system layout and control algorithms, suitable software concepts and especially fault management aspects to fulfil the different safety requirements, this technology has not yet been established on the market in series production. There are only a few example applications [1, 2].

Previous contributions demonstrated which kind of system architectures meet the different safety requirements of mobile machines [3]. One suitable valve structure in combination with pressure sensors and a single-variable control approach was applied to an excavator test rig at the research institute [4]. This system can reach a maximum Performance Level $PL = e$ according to ISO 13849 if the Diagnostic Coverage is $DC = 99\,\%$, which depends on the fault detection. Due to simplicity and easy integration as well as usability, a limit checking fault detection system was developed and tested in [5]. Experimental tests using only pressure sensors showed that the safety critical faults can be detected, but the unintended movement of the equipment's tool centre point during detection and reaction is too high by the amount of $0.593\,m$. Furthermore, a deep fault analysis is not achievable with conventional methods like limit checking, leading to the fact that other methods

are necessary for further improvements. Because data-driven approaches need a very big database of measurements and failure information, come mostly along with black-box models, which have to be trained and therefore allow no view inside the system and no extrapolation, system model-based methods will be analysed in the following. An overview of model-based methods for conventional hydraulic drive systems can be found in [6, 7]. The idea is to run a model parallel to the system, preferably on the used electronic control unit (ECU). Thereby, real-time aspects arise. Nevertheless, the model calculates an output signal depending on the input signals and the considered effects. The residuum r describes the difference between the model output y and the related sensor signal y_{meas}. The goal of every model-based method is to get a zero residuum during normal operation and a significant change in case of an error. Münchhof describes in [6] that parity equations are most suitable for valve-controlled hydraulic drive systems due to low computational effort and easy integration compared to extended Kalman filters (EKF), which are widely spread in literature [8, 9]. Figure 1 summarizes these aspects and shows the overall concept used for this contribution. The main part of this contribution will discuss the aspects shown in the lower left grey rectangle, especially the set-up of the ordinary differential equation (ODE) system.

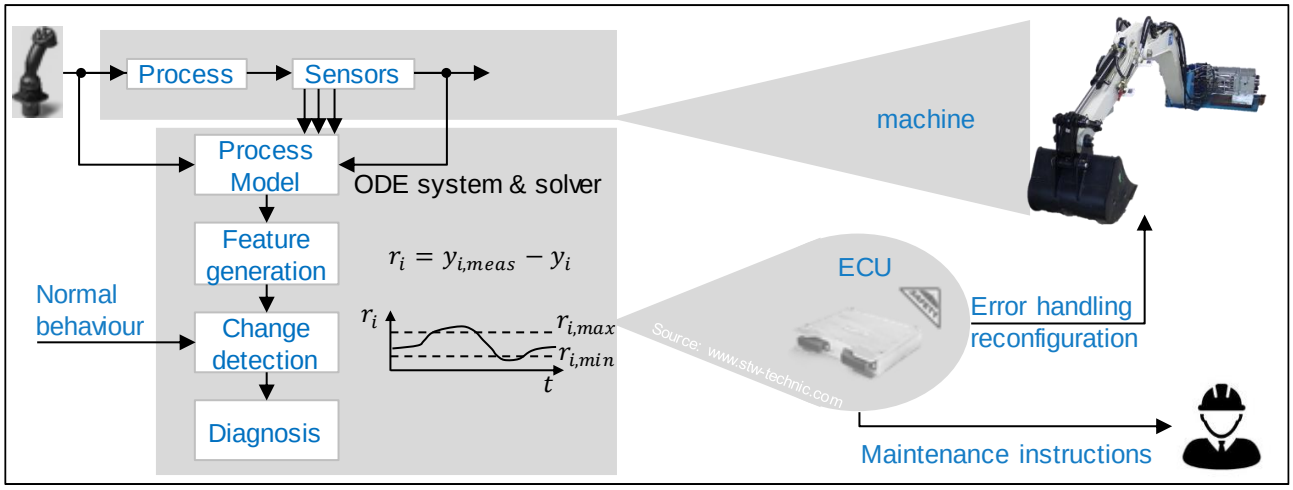

Figure 1. Principal procedure of fault detection and diagnosis

The quality of every model-based technique depends on the model. The following questions must be answered considering the available hardware and modelling information:

1. Which effects have to be modelled?
2. Which component information is available? Thereby white-, grey-, black box or mixed modelling techniques as described in [10] become applicable. A light-grey box model is preferred due to deeper diagnosis.
3. Are numerical integration methods required?
4. In this case, which approaches are easy to integrate and deliver a robust as well as precise solution at feasible time steps with the available ECU?

Münchhof used parity equations in combination with parameter estimation [6]. Thereby, a detection of sensor biases of approx. $1\,\%$ of the maximum deflection was possible. Nevertheless, many, partly difficult accessible sensors are needed within this method and the test rig comprises a greatly simplified load unit and conventional 4/3 proportional valves for industrial applications. Nurmi showed with measurements in a crane application with typical mobile but conventional 4/3 proportional valves based on a reduced-order model in combination with an adaptive threshold generating algorithm that sensor biases of three bar could be detected [11]. However, this contribution on the one hand uses cylinder position, chamber pressure, tank pressure, pilot pressure and pressure sensors between the pressure compensator and the main spool to obtain the reduced order model. On the other hand, a time constant of $\Delta t = 0.5\,ms$ is necessary to solve the equations which is indeed not applicable with state of the art mobile control units.

The goal of this contribution is to develop and test a suitable fault detection system based on parity equations with respect to low hardware effort, fast detection and usage of a typical mobile control unit with $\Delta t = 1\,ms$. In the following, the analysed system, the modelling as basis for the parity equations, the software integration and the test using a software-in-the-loop environment as well as a test rig will be described.

2. SYSTEM DESCRIPTION

Basis of the design of the fault detection is the excavator test rig at the research institute. The system consists of the subsystems supply unit, input, logic, output, actuator and the work equipment. Besides the typical conventional subsystems motor-pump-unit, electronic control unit (ECU), differential cylinders connected to monobloc boom and stick, the valve system with independent metering forms the centre of investigations. Since the test rig, model validation and control strategy were described in detail in the publications [4, 5], only the system behaviour is summarized and supported by Figure 2 in the following.

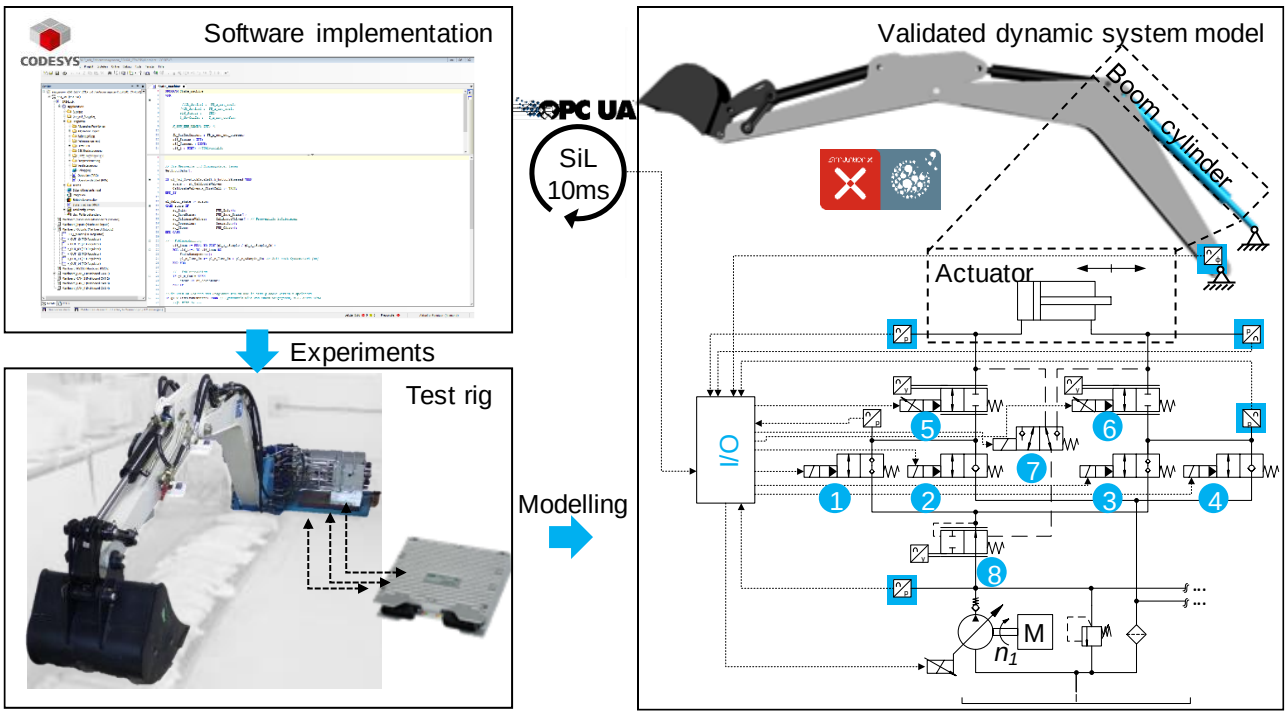

Figure 2. System overview and the different development and test environments

The supply unit comprises an electric motor, which is operated at a constant speed of $n_1 = 24.17\,s^{-1}$. An electronically controlled variable displacement axial piston pump, operated in closed-loop control, is connected to the motor. As I/O unit an ESX-3XL from STW is used [12]. It contains the control algorithm for each axis, the operation mode management, the failure insertion algorithm for the test of system faults and the fault detection algorithms as well as the numerical solver. Installed to the boom and stick cylinder there are two valve blocks with independent metering. Each block consists of two 2/2 bidirectional pilot-operated proportional spool valves (no. 5-6) for velocity and pressure control and four 2/2 bidirectional switching poppet valves (no. 1-4) for connecting each cylinder chamber with pump or tank line. A load independent movement is achieved through an individual pressure compensator (IPC; element no. 8). To ensure that the inlet flow is constantly regulated by the IPC, an additional switching valve (no. 7) was installed. The company Hydraforce supported the valves. Measuring the system and chamber pressures is essential for the cylinder movement with independent metering. In addition, the pressure signals between the switching and proportional valves as well as the cylinder position signals, which are calculated through the measured angles in the corresponding joints, are used for the model-based fault detection.

To support an early stage development, a detailed dynamic system model was setup up in the Modelica-based system simulation software SimulationX and validated through measurements [5]. A software-in-the-loop (SiL)

test environment using OPC UA allows the test of the integrated algorithms in CODESYS with the validated model in SimulationX. Syntax as well as runtime errors were eliminated before running the experiments.

3. MODELLING AND DESIGN ASPECTS OF PARITY EQUATIONS

In the following, the mathematical description as the basis for the parity equations will be discussed subsystem-wise concerning the four aforementioned questions. The nomenclature displayed in Figure 3 is used to set up the system equations.

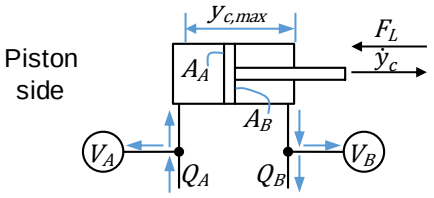

	Extension against load	Extension with load	Retraction against load	Retraction with load
$\dot{y}_c$	+	+	-	-
F_L	+	-	-	+

Figure 3. Nomenclature for system equations

3.1. General system properties

The focus is in particular set on the boom cylinder including its valve control system. Focusing on the boom cylinder enhanced comparability of the model-based fault detection results to the ones based on limit checking in [5]. By small adjustments, the algorithms can be transferred to the stick and bucket cylinder. The axial piston pump is controlled in a closed-loop pressure control. By metering the load pressures, the piston displacement is set, that the difference between pump and highest load pressure remains at constant level as described in the following equation.

$$\Delta p_{LS} = p_0 - p_{max} = const. = 1.4\ MPa. \tag{1}$$

The pressure compensator in combination with the 3/2-way valve guaranties a constant pressure drop $p_1 - p_A$ or $p_1 - p_B$ over the proportional and switching valves for each hydraulic consumer. The nominal value can be justified by the spring preload of the pressure compensator and amounts usually $0.7 - 1.2\ MPa$.

3.2. Hydraulic fluid

Hydraulic fluids take part in modelling in the form of two parameters, namely density ρ and effective bulk modulus K'. Density is used to calculate turbulent flow losses. Effective Bulk modulus is used to calculate compression volume flows of hydraulic capacities. Density usually depends on fluid temperature and pressure. On the one hand, temperature effects are generally excluded in system simulation. On the other hand, compression factors of oils are in the range of $7\ Pa$. Therefore, a constant density is used. The bulk modulus is one of the most complex parameters in modelling hydraulic components. Besides of influences of fluid temperature and pressure, also amount of free and dissolved air and mechanical elasticities of hose walls matter. Therefore, different empirical equations for this calculation have been developed in the past. Approaches of Lee, Eggert and Hoffman are well known in literature [13]. In this contribution, a linear approach was chosen based on simulation data. As system simulation is showing, the bulk modulus for cylinder and pipe volumes is in the main pressure field, $1 - 30\ MPa$, linear to its hydraulic pressure. As a result, the following equation suggested by the authors is used:

$$K' = 1000\ MPa + 11 \cdot p\ . \tag{2}$$

3.3. Hydraulic cylinder

The cylinder connects the physical domains by transforming hydraulic into mechanic energy. The volume flow balance for each cylinder chambers contains three different terms:

1. The volume flows through the valves 5 / 6 (Q_A / Q_B),
2. Volume flows due to the cylinder movement Q_{cA} / Q_{cB} and
3. Volume flows due to oil compression in the corresponding volume Q_{vA} / Q_{vB}.

This leads to the following equations for the piston and rod side of the cylinder:

$$Q_A(t) = Q_{cA}(t) + Q_{vA}(t) \quad / \quad Q_B(t) = Q_{cB}(t) - Q_{vB}(t), \text{ with} \tag{3}$$

$$Q_{KA}(t) = A_A \cdot y_c(t) \quad / \quad Q_{KB}(t) = A_B \cdot y_c(t) \text{ and} \tag{4}$$

$$Q_{VA}(t) = \dot{p}_A(t) \cdot \frac{V_A + y_c(t) \cdot A_A}{K'_A} \quad / \quad Q_{VB}(t) = \dot{p}_B(t) \cdot \frac{V_B + (y_{c,max} - y_c(t)) \cdot A_B}{K'_B} \tag{5}$$

Internal and external leakages are neglected due to minimal impact. Focusing on the hydraulic domain, the equation of motion shall not be discussed.

3.4. Valves

Since the switching valves only control the cylinder's movement direction, the static and dynamic behaviour of the proportional valves have to be modelled exactly. These properties have been measured on a valve test rig in an early development stage of the proposed system. The results revealed that the dynamic behaviour could be simplified by a second order transfer function (PT2) with delay time. This leads to the following equation for the relationship between actuating current i and the valve's spool stroke y_V:

$$\ddot{y}_V(t) + 2D_V\omega_V\dot{y}_V + \omega_V^2 y_V(t) = f(i(t - t_e)) \cdot \omega_V^2 \tag{6}$$

Due to the electrohydraulic pilot stage, the static relation between current and valve stroke $f(i)$ is strongly non-linear in the field of positive main valve overlap, but linear in the section beyond. Due to the fact that only valve strokes outside the overlap are significant to the cylinder movement, the overlap will not be modelled. With regard to parameterization of the flow rate, the valve stroke is standardized to values 0 – 1, resulting in the following equation:

$$y_V = \left(i - i_{Overlap}\right) \cdot \frac{1}{i_{max} - i_{Overlap}} = 0 \ldots 1 \tag{7}$$

Valve edges are usually sharply designed. As a result, turbulence flow can be assumed and the flow rate can be characterized as following:

$$Q = \frac{Q_{Nenn}}{\sqrt{\Delta p_{Nenn}}} \cdot \frac{y_V}{y_{V,max.}} \cdot sign(\Delta p) \cdot \sqrt{\Delta p} \tag{8}$$

Requirement for its validity is a linear dependency between valve stroke and flow cross section. Mobile hydraulic valves usually do not have this characteristic, because of different requirements like fine positioning as well as high velocities. Hence, the proportional valves are approximated by a broken-rational polynomial within equation 8, which leads to the following formula:

$$Q = K(y) \cdot sign(\Delta p) \cdot K_{\Delta p} \text{ with} \tag{9}$$

$$K(y) = \frac{k_5 {y_V}^5 + k_4 {y_V}^4 + k_3 {y_V}^3 + k_2 {y_V}^2 + k_1 y_V + k_0}{{y_V}^4 + q_3 {y_V}^3 + q_2 {y_V}^2 + q_1 y_V + q_0} \tag{10}$$

For reducing computing effort, the gradient of the root function is limited by a linear approach between $0 - 0.1\ MPa$ according to:

$$K_{\Delta p} = \begin{cases} m \cdot |\Delta p|, & IF\ |\Delta p| < \Delta p_{off} \\ \sqrt{|\Delta p|}, & IF\ |\Delta p| > \Delta p_{off} \end{cases} \tag{11}$$

The parameterization of $K(y)$ is made with a least square regression on measured valve data. Thereby the focus is set on Δp about $1.1\ MPa$, which correlates to the pressure difference the pressure compensator shall provide. The difference between the original and the approximated characteristic diagram of the proportional valve is displayed in Figure 4. Despite a very high coefficient of determination $R^2 = 0.9995$ at the desired pressure difference $\Delta p = 1.1\ MPa$ there are local deviations of $|\Delta Q_{max}| = 8 \cdot 10^{-4}\ m^3/s$ in the whole characteristic diagram. Considering the positive overlap and without standardization, the approximation would be even worse. The local deviations are the best indicator for evaluating the approximation quality. Because of the IPC, the approximation at the desired pressure drop can especially be used for the detection model at the velocity-controlling valve.

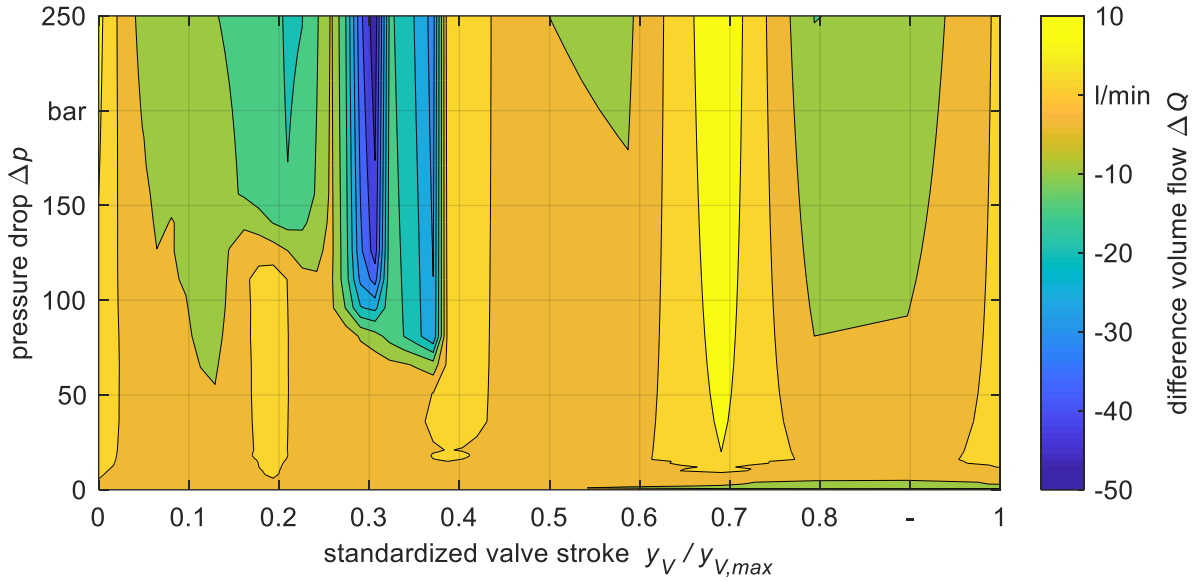

Figure 4. Difference between original and approximated characteristic diagram of the proportional valve

3.5. Sensors

Due to generating realistic input values for parity equations, flow and potential variables of system simulation have to be adapted. Therefore, sensor properties, namely dynamics and deviations, have to be modelled. Because of high natural frequencies of position and pressure sensors PT1-elements with small time factors $T_1 = 1\ ms$ are introduced. Deviation is taken into account by overlapping variables with white noise. Variance can be orientated towards accuracy classes of sensors. The cycle time is aligned to the sampling rate. All measuring signals have the addition "$meas$" in the index of the associated variable.

3.6. Resulting system equations, parity equations and numerical solver

Summarizing the aforementioned analyses, the overall system is strongly coupled, non-linear and has the order 10. The control currents of the valves $i_{1\ldots6}$, as well as tank pressure p_T and the node pressures serve as input variables. To set up the parity equations, the non-linear, strongly coupled equation system is to be reshaped according to the outputs. For this, equations with different input quantities are to be formulated. The goal is to generate strictly isolated residuals, e.g. residuals that react in different ways on varying errors. It should be noted that the model inputs as well as the model outputs have to be gaugeable. However, information of the control device, such as e.g. nominal volume flows Q_{set} and setpoint valve currents $i_{1\ldots6}$ of the control can be used as model inputs. Furthermore, it should be considered that the resulting equations have to be solvable on a mobile control unit. As a result, sampling rates of the sensors and the step sizes of the solution methods have to be in a range of $\Delta t = 10\ \mathrm{ms}$. In addition, the system order is limited to a maximum of 4 degrees to margin the computational effort. It could be shown in [5] that the proportional valve no. 6 is a highly safety-critical element. Against this background, the following aspects will be discussed with reference

to the cylinder chamber B. The corresponding equations can be set up equivalently for cylinder side A. Based on an eigenvalue analysis developed at the research centre [14], it could be shown that a numerical solution of the pressure due to the very low time constant and thus requirements for the sampling rate of $\Delta t \leq 1\ \mathrm{ms}$ is not effective with mobile-compatible control units. Therefore, a parity equation with the cylinder path as the output based on valve no. 6 will be exemplified in the following. Furthermore, a first order system of equations must be set up for a numerical solver. With these prerequisites and eq. (2, 3, 4, 5, 6, 7, 9, 10, 11), the following parity equation system results:

$$\vec{\dot{y}} = \frac{d}{dt} \cdot \begin{pmatrix} y_{V6} \\ \dot{y}_{V6} \\ y_c \end{pmatrix} = \begin{pmatrix} \dot{y}_{V6} \\ \omega_{V6}^2 \cdot (i(t-t_e) - 2 \cdot \frac{D_{V6}}{\omega_{V6}} \cdot \dot{y}_{V6} - y_{V6}) \\ \frac{1}{A_B} \cdot \left(K_{\Delta p} \cdot sign(\Delta p) \cdot K(y_{V6}) - \dot{p}_B(t) \cdot \frac{V_B + (y_{c,max} - y_c(t)) \cdot A_B}{K'_B} \right) \end{pmatrix} \text{ with} \tag{12}$$

$$\Delta p = p_B - p_{B,2}\ , \tag{13}$$

$$\dot{p}_B = \frac{\Delta p_B}{\Delta t} \text{ and} \tag{14}$$

$$y_c = \int \dot{y}_c \cdot dt\ . \tag{15}$$

From eq. (15), it can be stated that the system has integrative behaviour. Due to system input errors or model inaccuracies, the residuum will drift over the movement. Error detection based on these drifting residuals is not expedient due to limit violations occuring in the error-free case. Using the cylinder velocity as model output would solve this problem but development effort for adequate filters of the measured velocity were needed in this case. Another possible countermeasure is the introduction of a model feedback h to limit the drift. This measure is similar to a closed-loop control with constant gain. The transmission behaviour of the parity system changes to that of a PT1-element. Errors or inaccuracies are therefore no longer integrated over the movement. The residuals can only assume a maximum value depending on model inaccuracies as well as input errors. The transmission behaviour of the actually measured cylinder path is likewise in the form of a PT1-element, the resulting residual arising from the superposition of the two transmission characteristics. The choice of the model feedback h is a compromise between the drift compensation and a sufficient sensitivity of the residual against errors. In analyses at the research centre that would go beyond the scope of this publication, it could be shown that the feedback h should be corresponding to the maximum frequencies of the system. Using the eigenvalue analysis mentioned above, the feedback for the proposed parity equation yields $h = 2\,Hz$ which corresponds to the dynamic of the proportional valves. As a result, the calculated cylinder velocity in eq. 12 is added by the term

$$\dot{y}_c = \dot{y}_c - (y_{c,meas} - y_c) \cdot h\ . \tag{16}$$

In reality, due to model inaccuracies, deviations in the cylinder velocity will occur which in the first instance result from differences in volume flow balances. Based on this finding, the following equation can be derived:

$$r_i(s) = y_{c,meas}(s) - y_c(s) = \frac{-\Delta Q}{A} \cdot \frac{1}{s+h} = \frac{-\Delta Q}{A \cdot h} \cdot \frac{1}{\frac{s}{h}+1}\ . \tag{17}$$

The residual r_i thus depends on the model inaccuracy ΔQ, the area of the considered cylinder chamber A, and the model feedback h. The model inaccuracy is based in the quasi-static case mainly on the differences of the approximated to the real flow characteristics of the hydraulic valves. In the dynamic case, the compression volume flows and the associated errors have a significant impact on the calculation result. The model feedback h not only scales the residual r_i in combination with the respective cylinder area A, but also determines the time constant T_1 of the transmission behaviour (PT1). Besides this knowledge about dynamic aspects, eq. 17 can be used to calculate the quasi-static model error with

$$\lim_{s \to 0} r_i(s) = \frac{-\Delta Q}{A} \cdot \frac{1}{h}\ . \tag{18}$$

In addition, the maximum model error is an indicator for the limits of the residuals, which are used to finally calculate the faults. Regarding the exemplary chosen parity equation and the aforementioned parameters ($|\Delta Q_{max}|(@1.1\,MPa) = 4.48 \cdot 10^{-5}\ \frac{m^3}{s}, A_B = 0.0037699\,m^2, h = 2\,s^{-1}$), eq. 18 leads to maximum deviations of

$|r_{max}| = 6\,mm$. Temperature influences and tolerance deviations between individual valves of the same type will naturally change the maximum volume flow differences and thus the maximum model deviations. However, an initial parameterization of the error detection can be carried out and must then be optimized by experiments.

Finally, a numerical solver must be chosen. Against the background of a simple implementation in the control unit, an explicit one-step method is initially to be used. The forward Euler method is particularly suitable. Starting from an initial value, the value lying further by one time step is approximated according to:

$$y_{t+\Delta t} = y_t + \Delta t \cdot \dot{y}_t \tag{19}$$

4. IMPLEMENTATION AND TESTS

The standard ISO 13849-2 defines fault types for mechanical, electrical, electronical, pneumatic and hydraulic elements. Due to contaminated oil, jammed valves are common faults, especially in mobile hydraulic applications. Uncontrollable system behaviour is one of the resulting consequences. As shown and discussed in a previous publication [5], this safety critical fault occurs during jammed valves no. 4 or 6 in the proposed system. Due to the highest impact on the system, a fully opened valve no. 6 during extension of the boom cylinder (lowering) will be the basis for the following tests. Different set-velocities will be used to analyse their influence on the residuals.

4.1. Software implementation

As mentioned above, the parity equations have been implemented into CODESYS and tested with the validated SimulationX model of the test rig. An object-oriented approach was chosen in order to encapsulate functionalities, keep the code clear and to ensure easy interchangeability via interfaces. In the course of further investigations, other approach functions for mapping the valves and the oil behaviour as well as other numerical solvers can be implemented with acceptable time expenditure. The resulting software concept is shown in Figure 5.

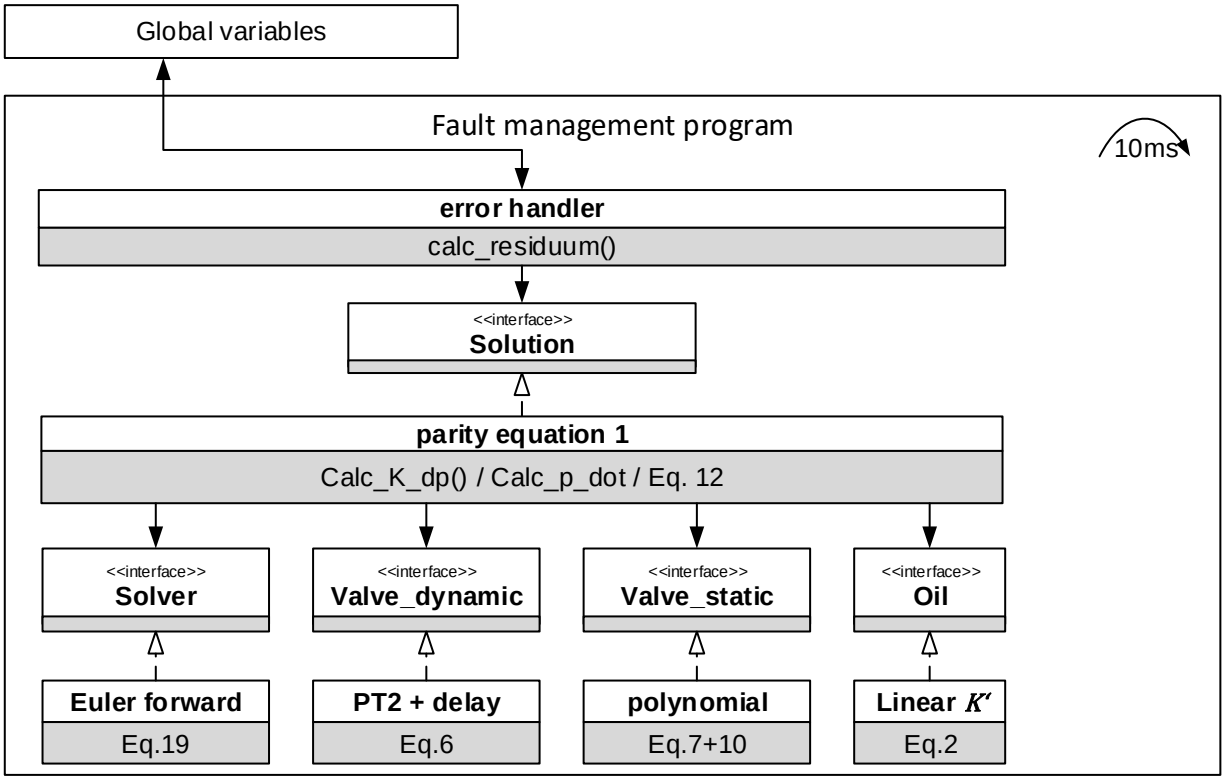

Figure 5. Software architecture of the fault management system

4.2. SiL Tests and Measurements

The target and actual value of the normalised boom cylinder velocity as well as the residual during a lifting lowering cycle of the boom is displayed over time in Figure 6. On the left side, the energy efficient modes of the independent metering system were forbidden through the software. This results in a conventional lowering movement. On the right side, the lowering movement takes place in the high-pressure-regeneration (*hp-reg*) mode. Thus, both cylinder chambers are connected to the pump during lowering. In addition, lower target values of the velocity were chosen. It can be stated that the residual remains in a tighter band with low velocities and the normal mode. In contrast to the calculated limits above, these values have to be chosen twice to third as high. This is mainly due to the assumed ideal system behaviour in the model and the approximated static valve behaviour as well as the solution method in combination with the sampling rate.

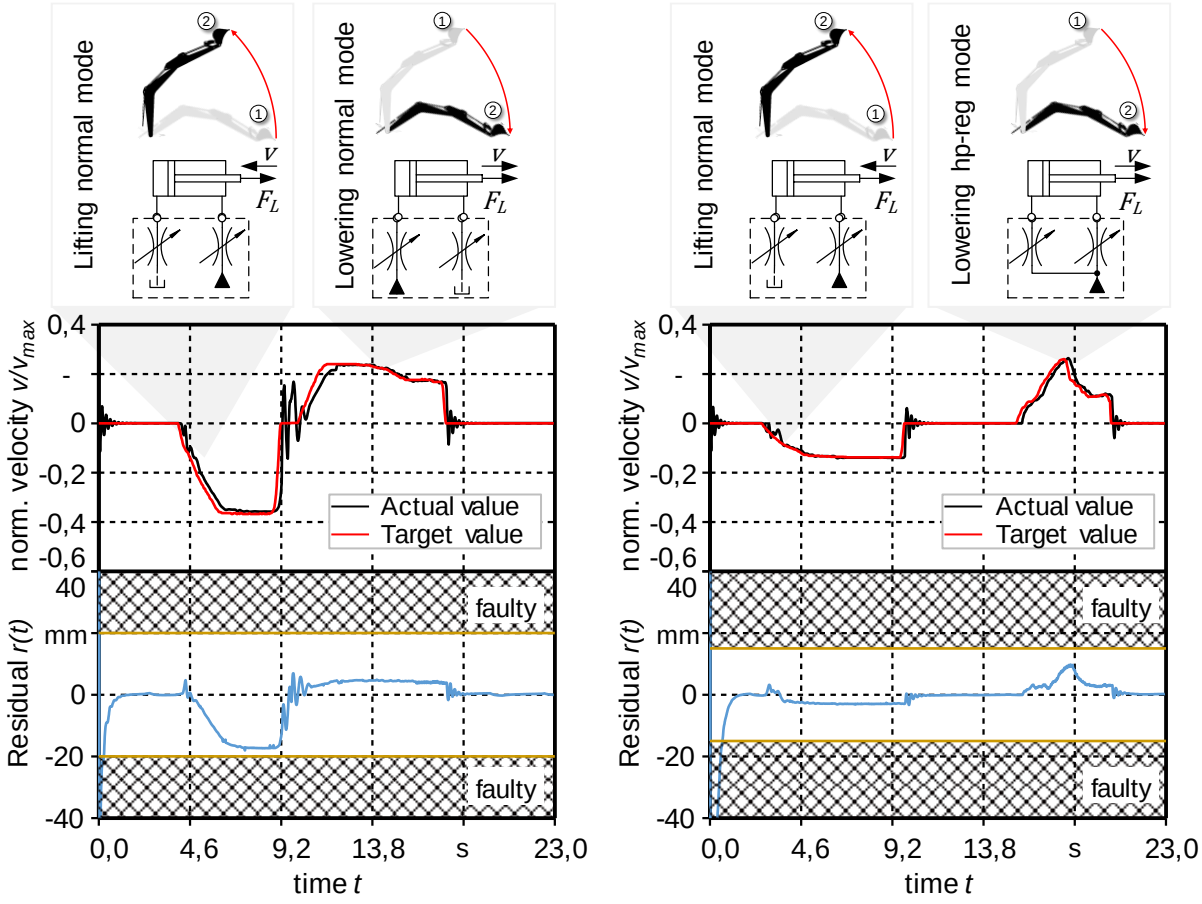

Figure 6. SiL during lifting and lowering cycle of boom without a fault
left: only normal mode; right: with hp-reg mode

In the next step the safety critical fault – a fully open valve no. 6 during lowering – was investigated. The results of the corresponding SiL is displayed in Figure 7. In this case the fault detection was deactivated to analyse the fault impact on the system and the residual over time. It can be seen that the fault impact in normal mode (left side) is much higher than in *hp-reg* mode (right side). Since in normal mode, the cylinder chamber side facing the load is connected directly to the tank via the incorrectly fully opened proportional valve, the cylinder moves unhindered into the stop. In *hp-reg* mode, however, there is still the possibility of influencing the speed via the opposing proportional valve no. 5. Therefore, the fault impact is lower. Nevertheless, the detection and even isolation of that fault is of great importance because of reconfiguration of the system.

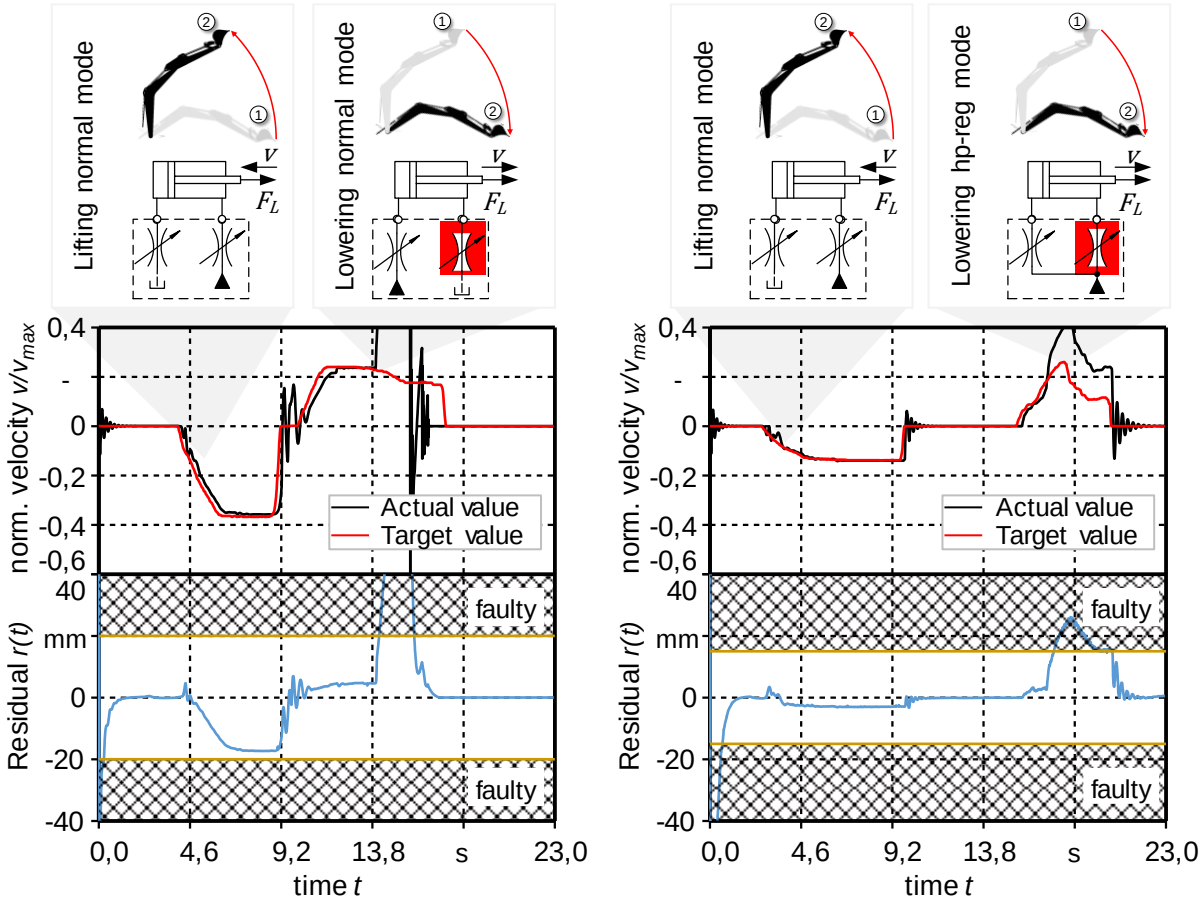

Figure 7. SiL during lifting and lowering cycle of boom with max. open valve no. 6 during lowering and deactivated detection; left: only normal mode; right: with hp-reg mode

Finally, the results of the same movement with comparison to normal and typical independent metering modes but this time with activated fault detection are displayed in Figure 8. The implementation time of the faults is summarized in Table 1. At this time, there is a significant change in the corresponding valve stroke signal, here valve no. 6. It can be seen that the residual yields the upper limit of $r_{max} = 20\,mm$ immediately after the fault insertion in both operation modes. As a result, the save state is activated which means that all valves are closed and the cylinder velocity becomes zero. The detection time is the difference between fault insertion time and the corresponding time where the outputs become zero and lie in the range of $\Delta t_{detect} = 0.28 - 0.54\,s$. These differences result from the aforementioned impact of the fault type in the operation modes. At this point, the functionality of the model-based fault detection with parity equation is proven. A final evaluation of the performance can be derived from the measurements in the following.

Table 1. Fault insertion times for the used test environments

SiL – only normal	SiL – with *hp-reg*	Measurement – only normal	Measurement – with *hp-reg*
$t_{insert} = 13.9\,s$	$t_{insert} = 16.9\,s$	$t_{insert} = 18.5\,s$	$t_{insert} = 19.5\,s$

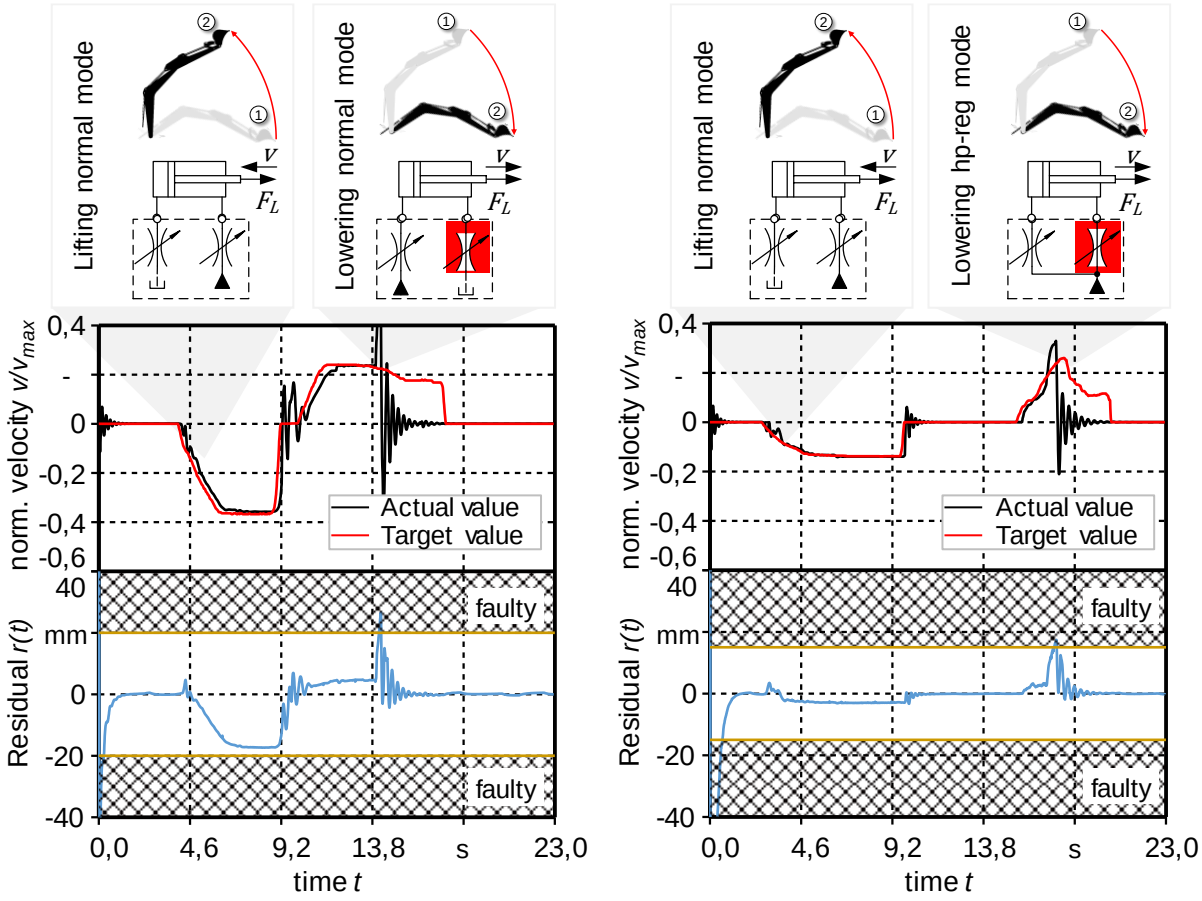

Figure 8. SiL during lifting and lowering cycle of boom with max. open valve no. 6 during lowering and activated detection; left: only normal mode; right: hp-reg mode

The measurement results are displayed in Figure 9. In this case only the cycle with normal mode is shown due to the bigger impact of the fault on the system. Between $0 - 14\ s$ the boom is lifted without a fault. The residual remains at a constant value of $r = 15\ mm$. This is equal to the simulation and results from the aforementioned inaccuracies in the static valve behaviour. Between $15 - 20\ s$ the lowering movement takes place. At approx. $18.5\ s$ the fault is inserted. Regarding the residual signal it can be derived that the detection of the fault is immediately after the insertion by an amount of $0.1\ s$. The Boolean value of the fault as well as the states of the implemented state machine is displayed too. It is noticeable that when the fault value becomes one the state becomes the value one too, which means the *save_state* causing all outputs to become zero.

Table 2. Measured performance of model-based detection

	Measurement – only normal	Measurement – with *hp-reg*
Detection time $\Delta t_{detect}\ [ms]$	100	300
Fall height $\Delta y_{TCP,max}\ [mm]$	262	180

On the right side of Figure 9 the corresponding tool-centre-point path (TCP) is displayed. The red dots highlight the movement during the occurrence of the fault. In the time between fault formation and fault reaction, the excavator arm lowers by approx. $202\ mm$. Compared to conventional limit checking methods with pressure sensors as analysed in [5], this means an improvement of $56\ \%$. In *hp-reg* mode, the detection time is a little bit higher, but the impact on the fall height is lower as can be seen in Table 2.

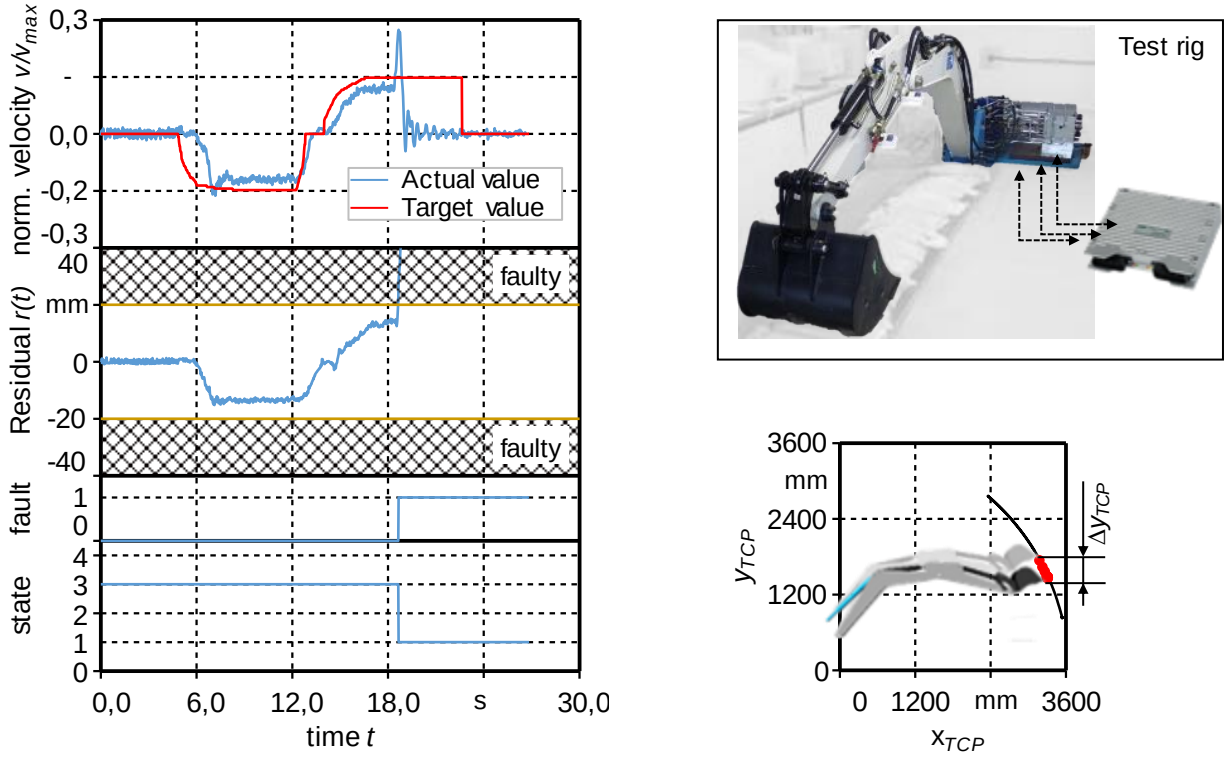

Figure 9. Measurement on excavator test rig during lifting and lowering cycle of boom with max. open valve no. 6 during lowering in normal mode and activated detection

5. CONCLUSION AND OUTLOOK

A parity equation based on a model of the boom cylinder could be derived. The behaviour of the parity equation has been analysed and measures were introduced to compensate undesired effects. The Euler forward solver enables the numerical integration of the equation, which is also implementable on mobile ECUs. A software concept with high flexibility and interchangeability was proposed. Tests in a software-in-the-loop environment have been carried out. It could be shown that the limits for checking the residual depend on the cylinder set velocity. This is mainly due to deviations in the valve's characteristic behaviour and the quality limits of the numerical solver within the restricted sample rate. Nevertheless, safety critical faults can be detected and diagnosed with 56 % higher performance as with conventional methods like limit checking direct on the sensor signal. While the initial effort to build the model-based recognition system is higher, this performance enhancement combined with a diagnostic capability makes this approach attractive for further analysis.

In future research activities, sampling rates, computational and communication step sizes, solution methods, signal filtering, and computational effort have to be considered in the context of real ECUs. Especially the class of Runge-Kutta methods for numerical integration are promising. In addition, the effects of currently neglected influences, such as temperature, valve hysteresis, component manufacturing tolerances or sensor noise, are to be further investigated. In order to monitor all consumers, the obtained results should also be transferred to stick and bucket. Due to the structural similarity, only the system parameters of the model equations, such as cylinder, rod area or line volumes, have to be adapted accordingly. Finally, a concept to integrate the whole diagnosis system into the state machine of the independent metering system with all its modes have to be developed and tested.

REFERENCES

[1] Caterpillar. 2019. Reliable and Productive. https://www.cat.com/en_GB/campaigns/npi/xe-series/966mxe.html, access on March 29, 2019.

[2] Eaton. 2016. CMA200 Advanced Independent-Metering Mobile Valve.

[3] B. Beck, J. Weber. 2016. Safety and Reliability of Independent Metering Systems in Mobile Machinery. In Risk, Reliability and Safety: Innovating Theory and Practice: Proceedings of ESREL 2016 (Glasgow, Scotland, 25-29 September 2016), published by L. Walls, M. Revie, T. Bedford, Taylor & Francis Group, pp. 2602-2609.

[4] J. Lübbert, A. Sitte, B. Beck, and J. Weber. 2016. Load-Force-Adaptive Outlet Throttling: An Easily Commissionable Independent Metering Control Strategy, BATH/ASME 2016 Symposium on Fluid Power and Motion Control, pp. FPMC2016-1793.

[5] B. Beck and J. Weber. 2017. Enhancing safety of independent metering systems for mobile machines by means of fault detection. The 15th Scandinavian International Conference on Fluid Power, June 7 - 9, 2017, Linköping, Sweden, pp. 92–102.

[6] M. Münchhof. 2006. Model-Based Fault Detection for a Hydraulic Servo Axis. Dissertation, TU Darmstadt, Darmstadt, Germany.

[7] J. Nurmi. 2017. On Increasing the Automation Level of Heavy-Duty Hydraulic Manipulators with Condition Monitoring of the Hydraulic System and Energy-Optimised Redundancy Resolution. Dissertation Tampere University of Technology, Tampere, Finland.

[8] L. An and N. Sepehri. 2008. Leakage Fault Detection in Hydraulic Actuators Subject to Unknown External Loading. International Journal of Fluid Power, vol. 9, no. 2, pp. 15–25.

[9] J. Nurmi and J. Mattila. 2012. Detection and isolation of leakage and valve faults in hydraulic systems in varying loading conditions, Part 2: fault detection and isolation scheme. International Journal of Fluid Power, vol. 13, no. 1, pp. 17–27.

[10] R. Isermann. 2006. Fault-diagnosis systems: an introduction from fault detection to fault tolerance. Berlin: Springer.

[11] J. Nurmi and J. Mattila. 2013. Detection and Isolation of Faults in Mobile Hydraulic Valves Based on a Reduced-Order Model and Adaptive Thresholds. ASME/BATH 2013 Symposium on Fluid Power and Motion Control, Sarasota, USA, pp. FPMC2013-4435.

[12] Sensor-Technik Wiedemann GmbH. 2019. ESX-3XL. access on April 2, 2019

[13] P. Beater. 1999. Entwurf hydraulischer Maschinen: Modellbildung, Stabilitätsanalyse und Simulation hydrostatischer Antriebe und Steuerungen.

[14] O. Koch et al. 2014. Real-time models for hardware-in-the-loop simulation of hydraulic drive and control systems. in 9th International Fluid Power Conference (9th IFK): 24th - 26th March 2014, Aachen, Germany. Vol. 2: Conference: Tuesday, March 25th, Aachen, 2014, vol. 2, pp. 178–193.

SIMULATION RESEARCH ON TEMPERATURE RISE CHARACTERISTICS OF PERMANENT MAGNET SPRING RELIEF VALVE

Lianming Su[1] , Guolei Si[2] , Liman Yang[1] , Yunhua Li[1] , Junhui Chen[2], Yan Shi[1], Dongkai Shen[1]
1.Beihang University, School of Automation Science and Electrical Engineering
2.Sichuan Aerospace Fenghuo Servo Control Technology Corporation
Beihang University, XueYuan Road No.37, HaiDian District, Beijing, China
E-mail: slm201009@buaa.edu.cn

ABSTRACT

Aiming at the characteristics of high-pressure and large-flow of aerospace servo system, a permanent magnet spring relief valve is designed. The permanent magnet spring of the valve was designed by means of analytical calculation and experimental validation. Because of taking the advantage of magnetic force characteristics, the magnet spring is superior to coil spring. Therefore, the permanent magnet spring relief valve has higher reliability, pressure regulation accuracy and thrust-weight ratio. However the permanent magnet spool is sensitive to temperature, if the temperature of the spool is too high in the working condition, the magnetism of the permanent magnet will be weakened, which will affect the stability of the relief valve. Therefore, in order to verify whether the temperature rise generated under rated condition will affect the magnetic properties of the permanent magnet spool, the temperature rise of the relief valve under rated condition is theoretically analysed first, and the source of heat and the way of loss are clarified. Secondly, the heat generated in the relief valve is calculated by the finite element simulation in COMSOL, and the temperature of the relief valve is observed. The results show that the temperature rise of the relief valve under rated condition does not affect the magnetic properties of the permanent magnet spool, which ensures the stability of the permanent magnet spring relief valve under rated conditions.

KEYWORDS: Permanent magnet spring relief valve, thermal simulation, temperature characteristic

1. INTRODUCTION

The relief valve plays an important role in the hydraulic system, it can adjust the oil pressure in the system to ensure the constant pressure and safety of the hydraulic system. Therefore relief valves are important part of any complete hydraulic system. It's quality and performance affect the performance of the whole hydraulic system. In the aerospace hydraulic system, most of the relief valves work in the environment with high pressure and high flow, therefore, the safety and stability of the relief valve are much higher [1]. Traditional relief valves mostly use coil spring as the pressure regulation element and resetting element, but the traditional coil springs may appear fatigue fracture, hydrogen embrittlement fracture, corrosion fracture, pressure instability and tilt stuck during working period [2]. In order to avoid the occurrence of these faults, a method of replacing the conventional coil spring with a permanent magnet spring was proposed [3, 4].

Compared with traditional relief valve, the permanent magnet spring relief valve has the advantages of small moving parts, no wear, low power consumption, long life, low noise and no lubrication. Meanwhile, the permanent magnet spring relief valve has a larger stiffness, through the reasonable design can make it has a

better linear characteristics in the vicinity of the working point, and it can overcome the shortcomings of the traditional coil spring, improve the performance of the relief valve [5].

The temperature of valve will rise during the working process because of the pressure loss of the oil, Xiaohong Liu [6] established a two-dimension CFD simulation in order to research the stuck phenomenon of the hydraulic slide valve due to the temperature rise in working condition. She summarized the influencing factors of temperature rise of the valve body in different working pressures, radial clearances and different opening sizes. Song Li [7] from Zhejiang University also researched the temperature rise and deformation of two different types of throttle valves. The temperature field was obtained based on CFD simulation, which provided a reference for the research of temperature rise during the working process of valve. The temperature rise of the relief valve is related to the pressure loss of the oil. Compared with the traditional relief valve, the permanent magnet spring relief valve uses a permanent magnet material named neodymium iron boron (NdFeB) [8, 9] to instead of the traditional coil spring, which has achieved good performance[5], however the magnetic properties of the permanent magnet materials are more sensitive to operating temperature, D Huger [10] studied the influence of temperature cycle on NdFeB materials, indicated that the high temperature would demagnetize the permanent magnet material, so it is important to analysed the temperature rise of the valve spool during rated condition to ensure the stability of the permanent magnet relief valve.

2. WORKING PRINCIPLE AND THE HEATING CAUSE OF PERMANENT MAGNET SPRING RELIEF VALVE

2.1. The working principle of permanent magnet spring relief valve

The working principle of the permanent magnet spring relief valve is shown in Figure 1. The relief valve is composed of three permanent magnets of NdFeB material [11], which are respectively a valve spool and a permanent magnet base located above and below the valve spool. The top and bottom permanent magnet base and the valve spool respectively constitute a repulsion and suction spring, and the preload of the valve is formed by the combined of the repulsive and suction force. When the valve port pressure is greater than the rated pressure, the valve spool is pushed up, and the relief valve is unloaded as a safety valve, the pressure of the pipeline is controlled, the schematic diagram of the valve is shown in figure 2.

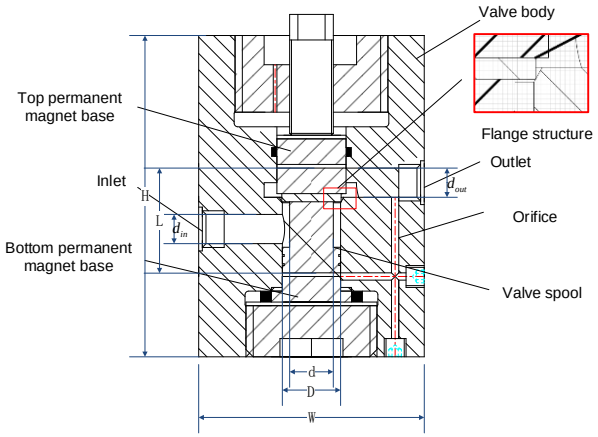

Figure 1. The structure of Permanent magnet spring relief valve

The flange structure of the permanent magnet valve spool can reduce the hydraulic power during the opening of the valve port, and balance the pressure fluctuation when the permanent magnet spring is open. Through design optimization, the relief valve achieves the main structural dimensional parameters shown in Table 1 and the static performance specifications of Table 2.

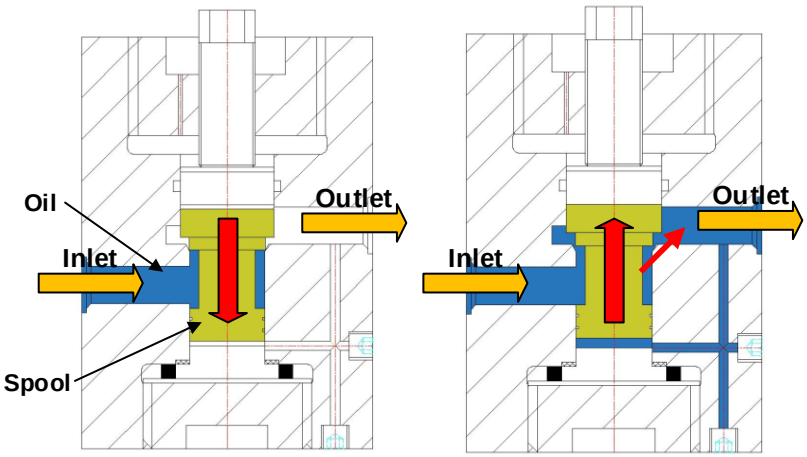

Figure 2. The schematic diagram of the valve

In addition, it should meet the dynamic performance index which the pressure overshoot should be less than 10% of the rated pressure value and the transient recovery time should be less than 0.3s.

Table 1. Main structural size parameters of the relief valve

Parameter	D	d	L	W	d_{in}	d_{out}	H
Value (mm)	16	12	28.69	62	8	8	88

Table 2. Static characteristic index

Opening pressure (MPa)	≥ 20
Preset pressure (MPa)	$21^{+0.65}_{-0.2}$
Rated flow ($L/\min$)	30^{+2}_{0}
Full open pressure (MPa)	≤ 22.5
Full open flow ($L/\min$)	≥ 50
Closed pressure (MPa)	≥ 19
Return pressure (MPa)	0.9 ± 0.1

2.2. The energy loss during the working process of relief valve

When the oil flows in the permanent magnet spring relief valve, there is resistance due to the viscosity of the oil, which is the reason of energy loss in the relief valve. This energy loss is manifested in the reduction of pressure from the inlet to the outlet of the relief valve, so this energy loss is often called as pressure loss. When the hydraulic oil flow in the valve, due to the viscous effect of the oil, there is frictional shear stress between adjacent flow layers and the fluid particles in contact with the wall surface will adhere to the wall surface of the pipe, the velocity of flow is zero, and in the normal direction along the wall surface the velocity of the flow increases rapidly, and there must be relative motion between adjacent flow layers. Work is done necessary to overcome the frictional resistance, consume some of the mechanical energy in the fluid, and dissipate it in the form of internal energy. Where the flow velocity changes greatly, the energy loss is large, and the generate of the heat is also large, which is the main reason for the temperature rise of the relief valve during operation.

When the oil passes through the restrictor and the damping hole of the relief valve, due to the rapid change of the flow state, collision, friction and vortexes will occur between fluid particles, and a large local pressure loss will occurs in the nearby. A sudden increase or decrease in the cross section will result in local pressure loss. The local pressure loss expression is:

$$\Delta p_l = \xi \frac{\rho v^2}{2} \tag{2.1}$$

Where ξ is the local loss constant, it is related to the shape of the pipe (restrictor) and the roughness of the inner wall of the pipe under turbulent conditions, and usually determined by the experiment, in the area of the damping hole and restrictor of the valve, the dimension change rapidly, so the pressure changes sharply, which generated a large amount of heat. v is the velocity of the oil and ρ is the density of the oil.

2.3. Estimate the temperature rise of the relief valve by power loss method

During the working process of the relief valve, the flow velocity changes fastest at the valve port, so it is also the place where the heat is concentrated. The overall temperature rise of the relief valve during the working process can be estimated by the power loss method. The main idea of the power loss method is to hypothesis the power loss generated when the oil flows through the valve is all converted into heat, and one part of the heat is absorbed by the oil, the other part of the heat is lost due to the heat exchange between the valve spool and the valve body. According to the law of energy conservation, it can be described as:

$$\left(p_i - p_e\right) q_i = q_i \rho C_p \left(T_e - T_i\right) + Q_{js} \tag{2.2}$$

Where T_i and p_i is the temperature and pressure of the inlet of the relief valve, T_e and p_e is the temperature and pressure of the outlet of the relief valve, C_p is the constant pressure specific heat capacity of oil, q_i is the oil flow through the relief valve, Q_{js} is the heat dissipation flow of the relief valve. In the heat generating problem, $\left(p_i - p_e\right) q_i$ is the heating power generated by the pressure change of the oil in the relief valve, $q_i \rho C_p \left(T_e - T_i\right)$ is the heat that raises the temperature of the oil, and Q_{js} is the heat that dissipated through the valve spool and valve body, this part of heat is not well estimated by power loss method due to the complex flow field and temperature field distribution inside the relief valve, but more accurate results can be calculated by finite element simulation. If this part of heat is omitted, the temperature raise of oil is hard to estimated correctly, there is systematic error in this method, and the temperature distribution can't be obtained either.

3. FINITE ELEMENT SIMULATION OF PERMANENT MAGNET SPRING RELIEF VALVE

In order to visually research the temperature distribution of the permanent magnet spring relief valve under the rated working condition, the finite element simulation [12] method can be used to simulate the heating condition of the relief valve under the rated working condition.

Finite element method or finite element analysis is a very effective tool for obtaining approximate solutions of complex differential equations. It is a basic principle of modern digital technology and an advanced means of exploring the objective laws of matter in scientific research. COMSOL is used as an finite element simulation software to simulate the temperature distribution of relief valve under different valve opening degrees, and explores the temperature rise of the permanent magnet spring relief valve during working process.

The finite element simulation in COMSOL mainly uses the 'turbulent flow' model in the 'fluid flow' module library, the 'solid heat transfer' and 'fluid heat transfer' models in the 'heat transfer' module, and the 'non-isothermal flow' in the 'multiphysics' model. The 'turbulence' model is used to simulate the flow of oil in the relief valve, and it can calculate the pressure and velocity distribution of the oil in the valve. The 'solid heat transfer' and 'fluid heat transfer' model are used to simulate heat transfer and heat convection among the oil, valve and the air around the valve. The 'non-isothermal flow' model is used to simulate the heat generated from the viscous dissipation of oil and pressure changes in the relief valve.

The computational model used in this paper is the standard $k-\varepsilon$ model. This model is the most widely used two-equation model. It has been extensively tested in scientific research and engineering. The standard $k-\varepsilon$ model is suitable for the flow model with high Reynolds number, which was proposed by Launder and Spalding in 1972 [13]. The two unknowns of the kinetic energy k and its dissipation rate ε are determined by the following two transport equations:

$$\begin{aligned}\frac{\partial}{\partial t}(\rho k)+\frac{\partial}{\partial x_i}(\rho k u_i)&=\frac{\partial}{\partial x_j}\left[\left(\mu+\frac{\mu_t}{\sigma_k}\right)\frac{\partial k}{\partial x_j}\right]+\rho G_k-\rho\varepsilon\\ \frac{\partial}{\partial t}(\rho\varepsilon)+\frac{\partial}{\partial x_i}(\rho\varepsilon u_i)&=\frac{\partial}{\partial x_j}\left[\left(\mu+\frac{\mu_t}{\sigma_\varepsilon}\right)\frac{\partial\varepsilon}{\partial x_j}\right]+C_{1\varepsilon}\frac{\rho\varepsilon}{k}G_k-C_{2\varepsilon}\frac{\rho\varepsilon^2}{k}\end{aligned} \tag{3.1}$$

Where G_k represents the turbulent energy generation term due to the average velocity gradient:

$$G_k=\frac{\mu_t}{\rho}\frac{\partial u_i}{\partial x_j}\left(\frac{\partial u_i}{\partial x_j}+\frac{\partial u_j}{\partial x_i}\right) \tag{3.2}$$

Turbulent viscosity μ_t is expressed by turbulent kinetic energy k and dissipation rate ε:

$$\mu_t=\frac{\rho C_\mu k^2}{\varepsilon} \tag{3.3}$$

C_{1s} and C_{2s} is the empirical constant value, which is recommended by Launder and Spalding. σ_k and σ_s is the Prandtl constant value corresponding to the turbulent kinetic energy k and dissipation rate ε.

3.1. Building the geometric model of relief valve

Four geometric models with different valve opening sizes 0.10 mm, 0.12 mm, 0.15 mm and 0.18 mm are established in SOLIDWORKS, and import the geometric models into COMSOL using the LiveLink® feature in COMSOL in order to investigate the temperature rise of the relief valve under different opening sizes.

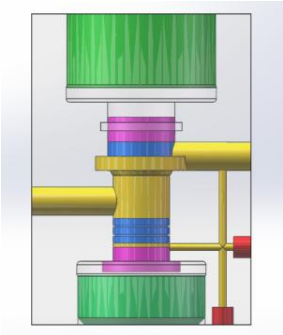

Figure 3. The geometry model of relief valve

The geometry model of relief valve is shown in figure 3, the yellow part of the geometry model is the fluid area, the purple parts are the top and bottom permanent magnet bases and the blue part is the valve spool, which are the main objects of the research.

3.2. Set material properties

There are three materials in the simulation model of permanent magnet spring relief valve. The liquid part is No.10 aircraft hydraulic oil (SH 0358-1995), its density is set to constant, $\rho_{oil}=850kg/m^3$,according to the empirical formula, the viscosity of No.10 aircraft hydraulic oil (SH 0358-1995) is related to the pressure and

temperature, and the equation is shown below[14]:

$$\eta = \eta_{\text{oil100}} \exp((\ln \eta_{\text{oil100}} + 9.67)(-1 + (1 + 5.1 \times 10^{-9} p)^{2.3 \times 10^{-8}} ((T - 138) / (T_{\text{oil100}} - 138))^{-1.16})) \quad (3.4)$$

The thermal conductivity and the specific heat of hydraulic oil are related to the temperature, and the equation is shown below:

$$k = 0.145 - \frac{0.145 - 0.135}{433 - 293} \times (T - 293) \quad (3.5)$$

$$c = \frac{(1.69 + 0.0038(T - 273))}{\sqrt{\rho_{\text{oil10}} / 1000}} \times 1000 \quad (3.6)$$

The permanent magnet spring part is NdFeB material, and its physical properties are shown in Table 3:

Table 3. The physical properties of NdFeB material

Parameter	Value	Unit
Specific heat capacity	120	$J / kg \cdot K$
Density	7400	kg / m^3
Heat conductivity coefficient	7.7	$W / (m \cdot K)$

The rest part of the relief valve is Cr18Ni9Ti, and the physical properties are shown in Table 4:

Table 4. The physical properties of Cr18Ni9Ti

Parameter	Value	Unit
Specific heat capacity	501.6	$J / kg \cdot K$
Density	7850	kg / m^3
Heat conductivity coefficient	16.3	$W / (m \cdot K)$

3.3. Set boundary conditions

The boundary conditions of the flow field is shown in Table 2, where the inlet pressure is 21 MPa , and the outlet pressure is 0.9 MPa .

In the temperature field boundary condition settings, the initial temperature of the solid portion is set to be 293.15 K , which is approximately room temperature, and the initial temperature of the fluid portion is 323.15 K , which is the temperature of the inlet oil. In order to simulate the heat exchange between the valve body and the air, the heat flux is added to the heat transfer module, and the air temperature is set to be 293.15 K . The heat exchange between the air and the valve body surface is convective heat transfer, which can be expressed by the following formula:

$$q_0 = h\left(T_{ext} - T\right) \quad (3.7)$$

Where q_0 is the convective heat density, $T_{ext} - T$ is the temperature difference between the valve body surface and the air, the proportional constant h is called the convective heat transfer coefficient and can be obtained from the input of the geometric of the valve body in COMSOL.

3.4. Meshing the model of the relief valve

COMSOL Multiphysics can automatically mesh the model. In order to facilitate observation and simplify the calculation, only half of the whole geometry is used for simulation, and the split surface is set to a symmetrical boundary. This division method greatly improves the computational efficiency and saves

computational time.

In the mesh setting, the type of mesh is selected to be the physical control meshing, and the meshing result is shown in Figure 4, the total of the division units is 334251, and in order to calculate the flow field part accurately, the boundary of the flow field uses the boundary layer meshing.

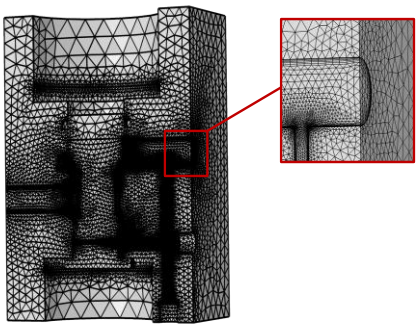

Figure 4. Meshing result

3.5. The result of the simulation

The steady-state calculation results are shown in Figure 5.

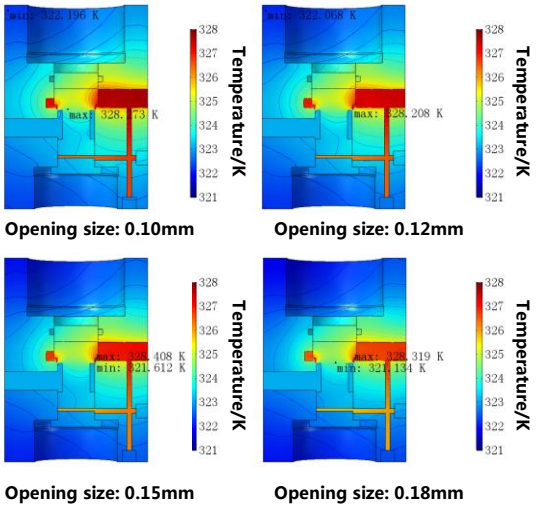

Figure 5. The temperature distribution of valve with different opening size

In Figure 6, it shows the temperature distribution of the permanent magnet part of the relief valve under different valve opening sizes in rated conditions. It can be seen from the figures that the pressure at the valve port changes sharply and due to the viscosity of the fluid, the mechanical energy in the fluid is converted into heat energy, so the temperature of the valve spool rises the most in the valve port, meanwhile, the other part of the valve spool is relatively low. At the same time, comparing the overall temperature rise of the relief valve under four valve opening sizes, it can be known that as the opening size of the valve port increases, the temperature rise of the relief valve becomes lower, the main reason is that with the opening of the valve port, more heat is taken away by the oil, leaving less heat to make the temperature of relief valve rise.

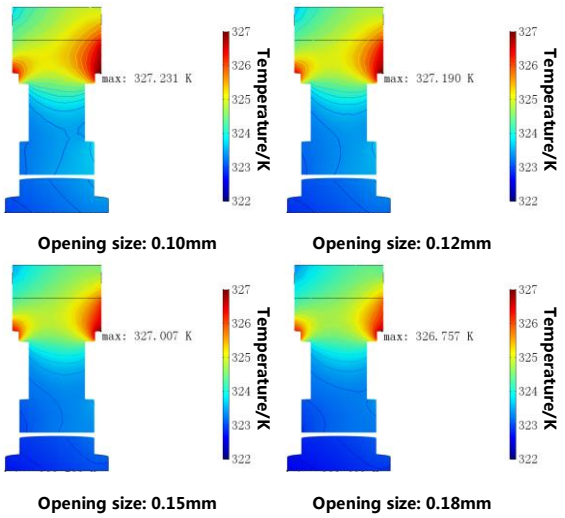

Figure 6. The temperature distribution of valve spool

According to the simulation results of the flow field in COMSOL, Figure 7 shows the flow rate under different valve opening sizes of the permanent magnet spring relief valve. As the opening size of the valve port increases, the flow rate gradually increases, so that the heat dissipation of relief valve is accelerated. The velocity field of the relief valve in different opening sizes are shown in Figure 8, the flow line in figure represents the flow direction of the oil in the valve, and the different colors indicate the different temperature of the fluid. According to the flow line, as the opening of the valve port increases, the overall temperature rise of the relief valve shows a downward trend, and it can be intuitively seen that the temperature rise is mainly concentrated in places where the pressure changes drastically. The pressure gradient causes the mechanical energy in the oil to be converted into internal energy, which leads to the temperature rise of the valve body.

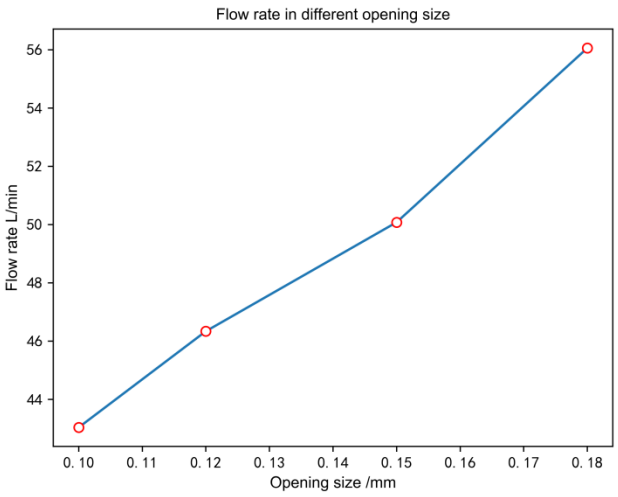

Figure 7. The flow rate in different opening size

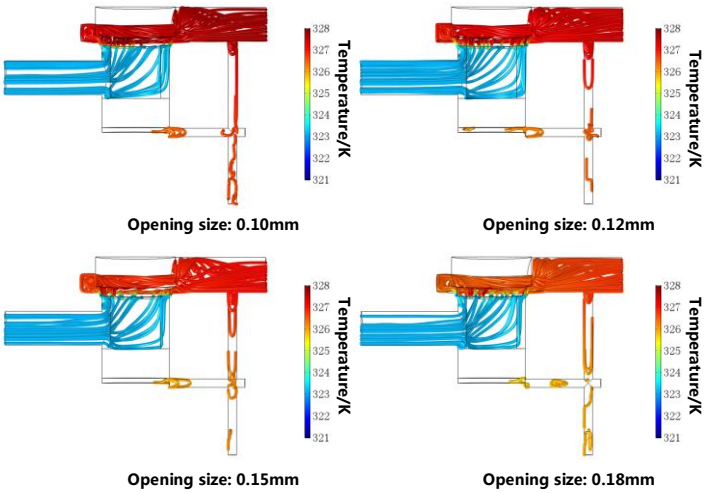

Figure 8. The flow line in different opening size

The highest and lowest temperature of relief valve and relief valve spool is shown in figure 9, it can be summarized from the figure that the temperature distribution of the valve is between 320 K and 328 K , and the highest temperature rise is about 5 K .

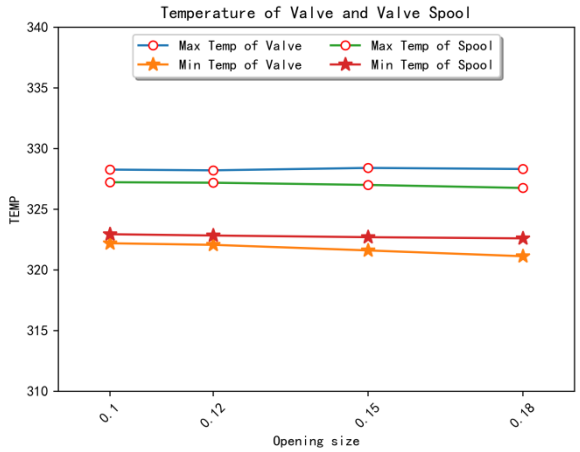

Figure 9. Temp of Valve and Valve Spool

After the finite element simulation, the heat taken away by the oil flow and the heat lost to the air by heat exchange can be calculated. Select the surface of fluid in COMSOL, and the normal heat flux can be calculated, the amount of the heat flux is about 9.02 kW . And the total work that the oil has been done in the relief valve is about 10.05 kW , which can be calculated by the formula of the heat loss method in section 2. In consequence, the most part of the heat is taken away by the oil and the heat exchange between the oil and the valve, the heat for raising the temperature of valve spool and body is less. Therefore, the temperature rise of the valve spool and body is not high. The temperature of the permanent magnet valve spool is more dependent on the initial temperature of the oil, controlling the inlet temperature of oil can effectively prevent the temperature of permanent magnet spool of the valve from being too high, thereby ensuring the stable operation of the permanent magnet spring relief valve.

4. CONCLUSION

In order to research the heat generation of the permanent magnet spring relief valve during rated condition and ensure whether the temperature rise of the relief valve can affect the magnetic properties of the permanent magnet spring. Firstly, the heat generation of the permanent magnet spring relief valve is

analyzed by mathematical modeling and summarized the reason of temperature rise of the relief valve. Secondly, in order to obtain the specific temperature rise of the permanent magnet spring relief valve, especially the permanent magnet part of the valve, the finite element analysis method is used to obtain the temperature distribution of the valve. Through the analysis of the temperature cloud diagram, the highest temperature of the relief valve under steady state condition is 328.4 K , which is much lower than the maximum working temperature of the permanent magnet material [13]. Finally, it can be proved that the heat generated by the oil during working process of the relief valve can be controlled by designing the appropriate heat sink, controlling the initial temperature of oil from inlet, and in this way the heat generated by the oil during working process will not affect the performance of the relief valve.

REFERENCES

[1]. Bukowski, J.V., R.E. Gross,W.M. Goble. The Adhesion Failure Mode in Stainless Steel Trim Spring Operated Pressure Relief Valves. ASME 2012 Pressure Vessels and Piping Conference. 2013.

[2]. Zhu, Y., Y. Wang,Y. Huang, Failure analysis of a helical compression spring for a heavy vehicle's suspension system. Case Studies in Engineering Failure Analysis, 2014. **2**(2): p. 169-173.

[3]. Qian, K.X.. Novel magnetic spring and magnetic bearing. Magnetics IEEE Transactions on, 2003. **39**(1): p. 559-561.

[4]. Si, G.L.. Study on Relief Valve with Permanent Magnetic Spring. Advanced Materials Research, 2011. **328-330**: p. 224-227.

[5]. Fu, C.. Design and mechanical performance analysis of relief valve with permanent magnet spring. IEEE International Conference on Aircraft Utility Systems. 2016.

[6]. Liu Xiaohong, Ke Jian, CFD Study on radial clearance temperature field of hydraulic spool valve. Journal of Mechanical Engineering, 2006. **42**(s1): p. 235-238.

[7]. Li Song, Research on temperature increase of valve flow and spool deformation. 2008, Zhejiang University.

[8]. Lee, R.W., Hot-pressed neodymium-iron-boron magnets. Applied Physics Letters, 1985. **46**(8): p. 790-791.

[9]. Novák, M., J. Černohorský,M. Košek. Detailed measurement and simulation of FeNdB permanent magnet used for magnetic spring. Power Electronics and Motion Control Conference. 2013.

[10]. Huger, D. ,D. Gerling. The effects of thermal cycling on aging of Neodymium-Iron-Boron magnets. IEEE International Conference on Power Electronics and Drive Systems. 2015.

[11]. Sagawa, M.. Nd-Fe-B Permanent Magnet Materials. Japanese Journal of Applied Physics, 1987. **26**(6): p. 785.

[12]. Bathe, K.J., Finite element procedures. 2015. **106**(4).

[13]. Szablewski, W., B. E. Launder and D. B. Spalding, Mathematical Models of Turbulence. 169 S. m. Abb. London/New York 1972. Academic Press. Preis geb. $ 7.50. ZAMM - Journal of Applied Mathematics and Mechanics / Zeitschrift fÃ¼r Angewandte Mathematik und Mechanik, 2010. **53**(6): p. 424-424.

[14]. Zhanling, J., Analysis and Control for Thermal-Fluid-Structure Coupling Characteristics in Airborne Power Transmission Components, in The school of Mechatronic Engineering. 2016, Beihang University: Beijing.

ELECTRO-HYDRAULIC PROPORTIONAL PRESSURE REDUCING VALVE FOR INDEPENDENT METERING VALVE WITH A SPOOL-POPPET HYBRID ACTUATOR

So-Nam Yun[1], Haroon Ahmad Khan[1], Yang-Lae Lee[1], Jeong-Man Jin[2], Yoshito Tanaka[1]
[1]Korea Institute of Machinery & Materials
156 Gajeongbuk-ro, Yuseong-gu, Daejeon, 34103, Republic of Korea
[2]SF Hyworld
141 Charyongdanji-ro, Uichang-gu, Changwon-si, Gyeongsangnam-do, Republic of Korea
Ysn688@kimm.re.kr

ABSTRACT

This study is related to Independent Metering Valve (hereinafter IMV) which is a hot area of excavator research because of having increased energy saving operation and better controllability. An IMV is a combination of two valves; one is main valve (containing spool or poppet) and the other is a pilot valve. The flow rate is controlled by the movement of spool or poppet in the main valve while the movement of the spool or poppet is controlled by pilot pressure provided by the pilot valve. In this study, the pilot valve was chosen to be electro-hydraulic proportional pressure reducing valve (hereinafter EPPR valve). An IMV circuit for excavator was suggested and a model for the EPPR valve was built and analysed. Finally proportional characteristics of solenoid actuator of EPPR valve from the analysis results were derived and the endurance test was carried out for 18 million cycles.

KEYWORDS: Attraction force, Excavator, Independent metering valve, Proportional pressure reducing valve, Proportional solenoid, Spool actuator

1. INTRODUCTION

In hydraulic machinery, like excavators, there are unnecessary pressure drops when transferring hydraulic power from one point to another. Some pressure drops are necessary and some are unnecessary for the operation of the hydraulic machinery. It is always desirable to achieve better fuel efficiency by reducing the unnecessary pressure losses. This can be achieved by the proper design configuration of the hydraulic circuit. One such design is the IMV configuration.

Excavators have hydraulic circuits for delivering the high pressure hydraulic oil from pumps to the cylinder actuators such as the boom, arm or bucket cylinders. Flow control valves have a primary role in the hydraulic circuits. To provide the flow, two types of methods are possible, one is coupled control and another is independent control. In coupled control, the flow going into the hydraulic cylinder and the flow coming out of the hydraulic cylinder is metered by the movement of a single spool or poppet, so the movement of one edge changes the movement of the other edge. This leads to unnecessary pressure drops which can be avoided if the two edges are controlled separately which is how an IMV valve operates. By lowering the unnecessary pressure drops, IMV valves have the ability to reduce the fuel consumption rate of excavators by up to 20%. The energy saving potential of IMV has been reported by [1, 2, 6].

Different types of techniques and configurations are possible to achieve independent metering. For example figure 1 shows one of the countless ways in which an IMV system configuration can be realized.

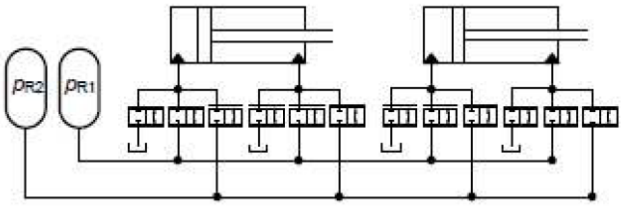

Figure 1. One of the IMV circuits studied by [2]

The problem in this configuration is that there are two accumulators and the number of valves per cylinder is 6, which makes the weight of the excavator very heavy. As proved by Kyujeong Choi et al. [7], if we choose a 4 valve circuit of IMV it will be highly energy efficient.

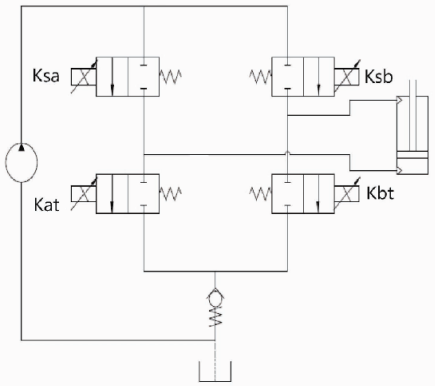

Figure 2. IMV Configuration investigated by Kyujeong Choi et al. [7]

The IMV configuration chosen for this study consists of 4 flow control valves or 4 IMVs as shown in figure 4. Each IMV consists of two parts. First part is a main flow control valve which contains a linearly movable component, to be called from now on a spool-poppet/ spool-poppet hybrid, whose displacement provides the opening area for the main flow. The second part is the EPPR valve. The function of the EPPR valve is to provide and control the pilot pressure. Higher the pilot pressure, higher would be the displacement of the spool-poppet and higher would be the flow area. So the flow opening area which provides the main flow rate is controlled by the output/control pressure of the EPPR valve.

An EPPR valve was developed in this study for use in the IMV. The proposed EPPR valve has a pin inside the spool for provision of a feedback pressure force to the spool against the solenoid force on the spool due to the electric current input. We call it a pin-type EPPR valve because the area of pin is the main design parameter which determines the range of the pressure that can be supplied for a certain solenoid actuator. A supply pressure line is needed for operation of EPPR valve, the input is in the form of a current to the solenoid and the output is in the form of the reduced pressure whose maximum value is the same as the supply pressure. For the main spool-poppet hybrid valve, the input is the pressure from the EPPR valve.

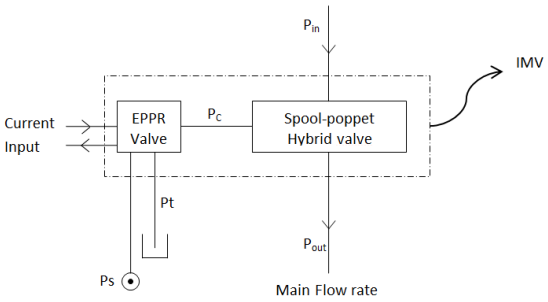

Figure 3. Functional Layout of IMV demonstrating the different ports and connection

The understanding of EPPR valve characteristics before it is practically applied to the IMV of excavator is very important for estimating the IMV and thus the overall performance of the hydraulic circuit which is the main purpose of this study. Simulation was performed using the SimulationX software and experiments were conducted using the hydraulic test equipment.

2. THEORETICAL ANALYSIS

Figure 4 shows a hydraulic circuit for controling the cylinder of conventional type excavator, and Figure 5 shows a semi-imv circuit. Figure 6 shows the full Independent metering valve circuit for excavator. In case of conventional type excavator, 4/3 way directional control valve is applied, and more advanced stage than the conventional valve of the excavator is the semi-IMV skill.

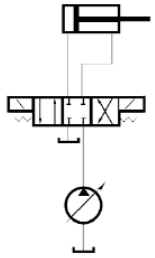

Figure 4. Hydraulic circuit for 4/3 valve control

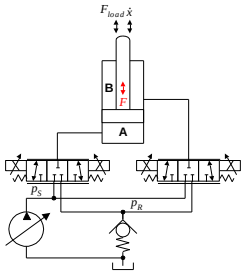

Figure 5. Semi-IMV circuit

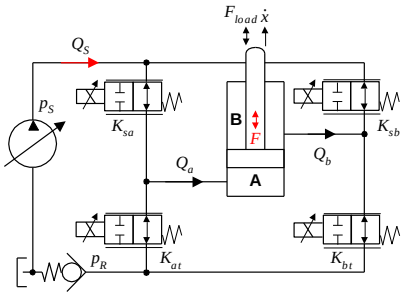

Figure 6. Full IMV circuit

Figure 7 is the study object model of EPPR valve which will be applied to IMV for excavator. The proposed EPPR valve has a pin inside the spool for provision of a feedback pressure force to the spool against the solenoid force on the spool due to the electric current input. We call it a pin-type EPPR valve because the area of pin is the main design parameter which determines the range of the pressure that can be supplied for a certain solenoid actuator.

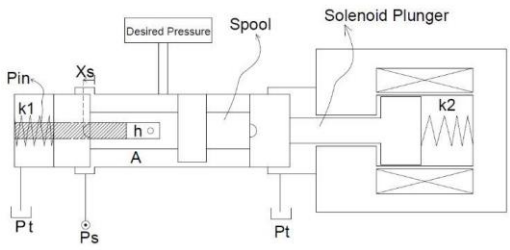

Figure 7. Study object model of EPPR valve

Fig. 8 is analysis model of the study object EPPR valve and was built by SimulationX software. For simulation given conditions are as follows:

- Supply pressure is kept constant.
- Oil density is contant as well and is not affected by oil temperature variation.

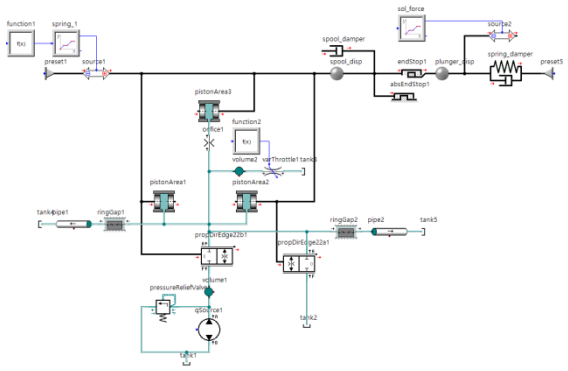

Figure 8. Analysis model of the EPPR valve

Figure 9 is the results when supply pressure and input attraction force are 50[bar] and 15[N], respectively. Then output reducing pressure is 35[bar].

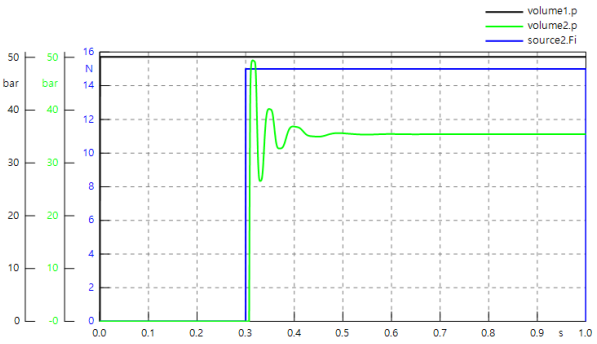

Figure 9. Step response result(supply pressure: 50[bar], Input attraction force: 15[N])

Figure 10 shows the results when supply pressure and input attraction force are 50[bar] and 10[N], respectively. Then the steady state value of output reducing pressure is 21[bar].

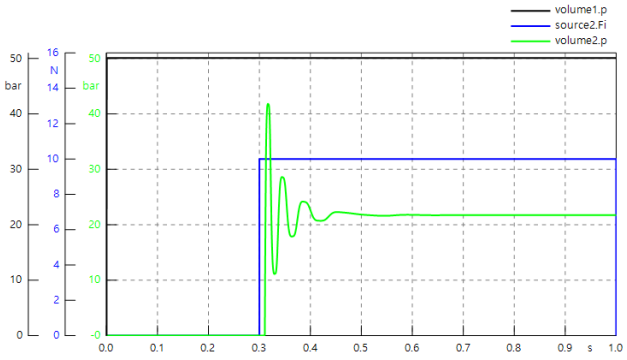

Figure 10. Step response result(supply pressure: 50, Input attraction force: 10[N]

Figure 11 shows the results when supply pressure and input attraction force are 50[bar] and 10[N], respectively. Then, the steady state value of output reducing pressure is 8[bar].

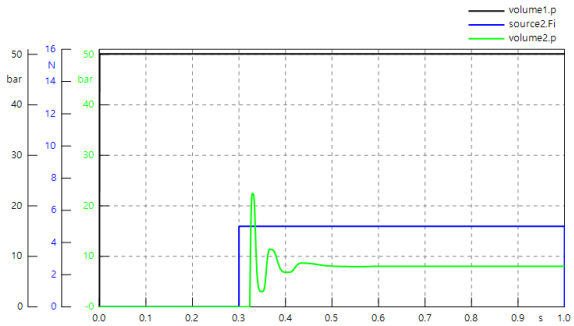

Figure 11. Step response result(supply pressure: 50, Input attraction force: 5[N]

From Figure 9, Figure 10 and Figure 11, we can know that the output control pressures are proportional to the input currents and the response characteristics are very stable.

3. EXPERIMENTAL SETUP AND METHOD

3.1. Experimental setup

Figure 12 shows a test circuit and a control/measurement diagram for performance evaluation of the fabricated EPPR valve with a pin function. Test circuit was based on the KS(Korea Standard) and JIS(Japan Industrial Standard) that was also designed for checking the temperature, pressure and flow from sensors. Current which is supplied to the object valve by test items is regulated by PC or function generator.

Figure 13 is the experimental setup and was built from Figure 12.

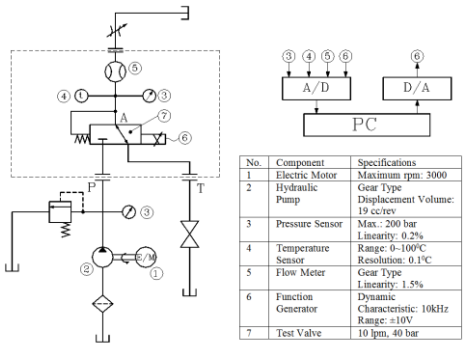

No.	Component	Specifications
1	Electric Motor	Maximum rpm: 3000
2	Hydraulic Pump	Gear Type Displacement Volume: 19 cc/rev
3	Pressure Sensor	Max.: 200 bar Linearity: 0.2%
4	Temperature Sensor	Range: 0~100°C Resolution: 0.1°C
5	Flow Meter	Gear Type Linearity: 1.5%
6	Function Generator	Dynamic Characteristic: 10kHz Range: ±10V
7	Test Valve	10 lpm, 40 bar

Figure 12. Hydraulic circuit for performance test of the fabricated EPPR valve

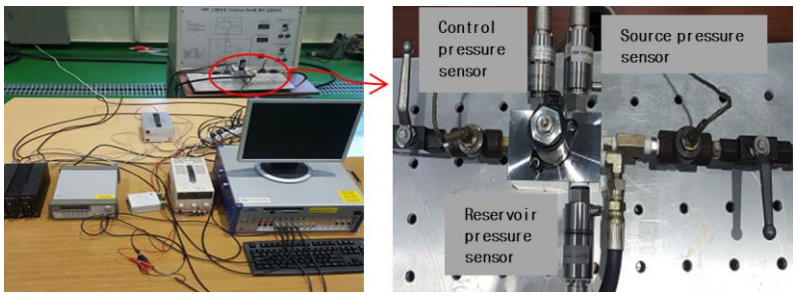

Figure 13. Experimental setup for the fabricated EPPR valve

3.2. Experimental method

In this study, static and dynamic tests of the fabricated EPPR valve were conducted and endurance test was carried out for finding the life time. Before starting the experiments of static, dynamic and endurance tests, experimental setup and sensors were calibrated.

3.3. Results and discussion

Figure 14 is an experimental result of a kind of movement behaviour of proportional solenoid plunger. From this study endurance and performance of EPPR valve are confirmed and the validity for hydraulic excavator application of the fabricated EPPR valve is proved.

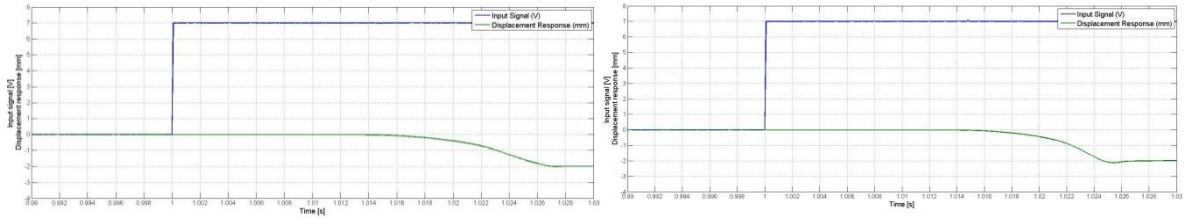

Figure 14. Step response results of the fabricated proportional solenoid actuator

Figure 15 shows step response characteristics of the fabricated EPPR valve. From Figure 15. The response characteristics are very stable and experimental results are corresponded well with the simulation results of Figure 9.

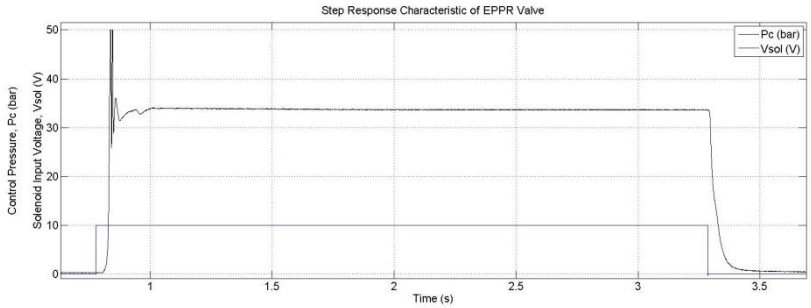

Figure 15. Step response result of the fabricated EPPR valve

4. CONCLUSIONS

In this study, hydraulic circuit of IMV and EPPR valve with a proportional solenoid actuator for the next generation excavator was suggested. The suggested proportional solenoid actuator and the EPPR valve were fabricated and experimented. Summarized results are as follows:

- Performance measurement of fabricated proportional solenoid actuator was carried out and applicability for the excavator was also confirmed.
- It was confirmed that the endurance characteristics of the fabricated proportional solenoid actuator are superior after 18 million cycles.
- EPPR valve model was built and dynamic characteristics were investigated.
- From the simulation and the experimental results, the response characteristics are very stable.
- Finally, the validity of the theoretical analysis method was also confirmed from the experimental results.

REFERENCES

[1] S. A. Nahian et al, “Introduction of Independent Metering Valve for Energy Saving Excavator System”, Journal of Drive and Control 12(1), 2015, pp.45~52.

[2] Milos Vukovic et al, “ STEAM – a hydraulic hybrid architecture for excavators”, International Fluid Power Conference, Dresdon, pp. 151~162, 2016

[3] N.N, Keith A. Tabor, 2005, “A novel method of controlling a hydraulic actuator with four valve independent metering using load feedback”, SAE commercial vehicle engineering conference, SAE 2005-01-3639.

[4] So-Nam Yun, Young-Bog Ham, Jung-Ho Park and Haroon Ahmad Khan, 2017, “Proportional solenoid actuator for independent metering valve of the next generation construction vehicles”, SICFP 2017, pp.1~3.

[5] H.E. Merrit, 1967, Hydraulic control systems, John Wiley & Sons, USA.

[6] Shenouda A and Book W., 2005, “Energy saving analysis using a four-valve independent metering configuration controlling a hydraulic cylinder”, SAE technical paper 2005-01-3632.

[7] Kyujeong Choi et al., “Energy-saving in excavators with application of independent metering valve”, Journal of Mechanical Science and Technology 29 (1) (2015) pp. 387~395

[8] A. Forrai, T. Ueda and T. Yumura, 2005, “A simple approach to electromagnetic actuator control based on asymptotically exact linearization”, Archive of Applied Mechanics, 74(8), pp. 550-562

[9] Y. Wang, T. Megli and M. Haghgooie, 2002, “Modeling and control of electromechanical valve actuator”, Society of Automotive Engineers, pp. 1-10.

[10] A.E. Balau, C.F. Caruntu, D.I. Patrascu, L. Lazar, M.H. Matcovschi and O. Pastravanu, 2009, “Modeling of a pressure reducing valve actuator for automotive applications”, Proc. Of IEEE International Conference on Control Applications, Saint Petersburg, pp. 1356-1361.

ANALYTICAL APPROACH TO CALCULATE THE ROTATION ANGLE-DEPENDENT COMPENSATION RATIO OF THE CYLINDER BLOCK – VALVE PLATE CONTACT IN AXIAL PISTON MACHINES

Seong-Ryeol Lee[1]*, Stephan Wegner[2], Hubertus Murrenhoff[1], Katharina Schmitz[1]
[1]RWTH Aachen University, Institute for Fluid Power Drives and Systems (ifas), Aachen, Germany
[2]Stackpole Powertrain International GmbH, Aachen, Germany
[1,2]Campus-Boulevard 30, Aachen, Germany
E-mail: seong.lee@ifas.rwth-aachen.de

ABSTRACT

Hydraulic piston machines are commonly used in many industry fields because of their high power density and high efficiency. One of the most important components in axial piston machines that determines the efficiency is the valve plate, which is in lubricated contact with the rotating cylinder block. The fluid force, generated by the fluid film and acting against the load force, lifts the cylinder block to reduce the solid friction with the valve plate. The ratio of the fluid and load force, called compensation ratio or balance ratio, is used in the industry as design parameter, representing a number for the complex trade-off between losses and robust operation under all conditions. To calculate the compensation ratio, many analytical calculation methods have been introduced on a fixed position. In practice, however, the effective pressurized area varies depending on the angle of rotation, therefore changing the fluid force. Thus, the calculation method has an inconsistent accuracy over one revolution, depending on the shape of the valve plate.

This paper discusses an analytical approach to calculate the rotation angle-dependent compensation ratio of the cylinder block and valve plate. A proposed calculation method differs from the conventional method in that it can calculate the rotation angle dependent compensation ratio. In order to check the accuracy of the proposed method, the analytical results are compared to simulation results using a verified EHD (Elasto-Hydrodynamic) simulation under the same operating conditions. The comparison shows that the maximum error is less than 2 %. Moreover, the relation of the compensation ratio and the design parameters is analyzed.

KEYWORDS: Axial piston machine, Cylinder block, Valve plate, Compensation ratio, Balance ratio

1. INTRODUCTION

Hydraulic piston machines are commonly used in many industry fields because of their high power density, broad operation range and high efficiency. Their principle allows to be used as a pump to supply hydraulic power to the circuit, or vice versa, as a motor that converts the hydraulic power into mechanical power. The realized design includes wobble plate, bent axis and swash plate machines. Among them, the swash plate machine is widely used because of its short fluid routes and simple and compact structure. Figure 1 shows the common design of the swash-plate type axial piston machine. The machine consists of several components, such as piston, piston shoe, swash plate, cylinder block and valve plate. The pistons are connected to high or low pressure by kidney-shaped openings in the valve plate, depending on their stroke. The cylinder block rotates with the pistons in relation to the fixed valve plate. One of the most important components in the axial

piston machines that determines their efficiency is the valve plate. The valve plate main functions are commutation and separation of high and low pressure. Also, it functions as hydrostatic and hydrodynamic journal bearing simultaneously [1]. In the contact, a fluid film is formed between the contact surfaces of the cylinder block and the valve plate, and the fluid force is generated by the fluid film. The fluid force compensates the load force acting on the valve plate and allows the cylinder block to rotate with less solid friction. When the fluid force is bigger than the load force, the gap height increases, causing a growth of leakage in the cylinder block-valve plate contact. Therefore, the ratio of the fluid force and the load force is used as an important design parameter and defined as the compensation ratio or the balance ratio in Eqn. 1.

$$C = \frac{F_{fluid}}{F_{load}} \tag{1}$$

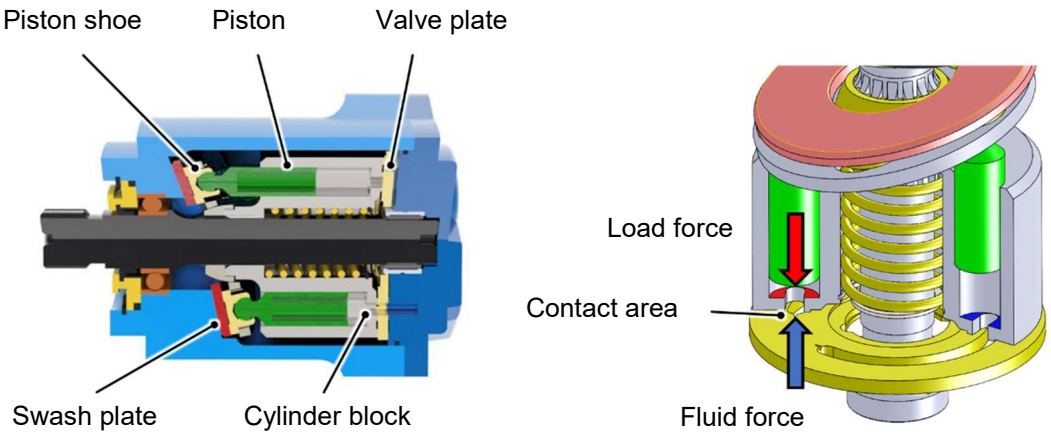

Figure 1. General composition of swash-plate type axial piston machine

Figure 2 shows two examples of the compensation ratio for one rotation. When the compensation ratio is equal to 1, the fluid force and the load force are balanced and the acceleration of the cylinder block becomes zero. When the compensation ratio exceeds 1, the gap between the cylinder block and the valve plate is increased and the sealing effect decreases. This causes leakage and volumetric loss at the cylinder block-valve plate contact. Conversely, in case the compensation ratio becomes smaller than 1, the gap becomes smaller in height and the sealing effect is increased. However, as the fluid force decreases, the contact force increases as well as the solid friction, causing hydraulic-mechanical losses. Therefore, in order to minimize the total loss of the cylinder block-valve plate contact, many manufacturers generally design the valve plate to have the ratio of about 0.9 to 0.95 [2, 3].

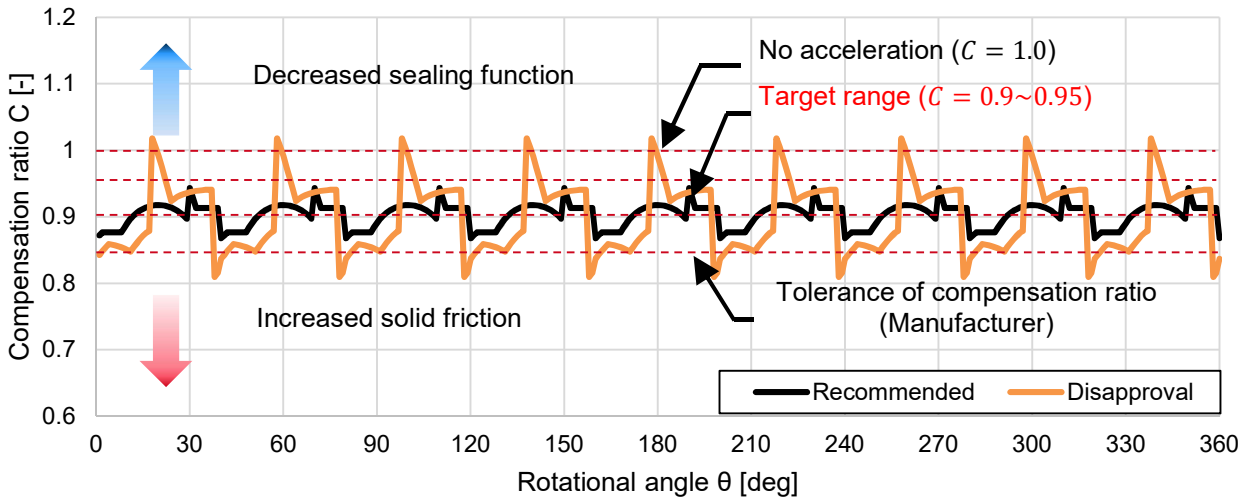

Figure 2. Rotational angle dependent compensation ratio of the cylinder block – valve plate contact

The compensation ratio can also be used to analyze the cylinder block motion on the valve plate. Manring [4] studied the analytical calculation of the cylinder block's tipping motion using the compensation ratio, and Achten [5] showed that the fluid force is needed to prevent the barrel from tipping via simulation of two valve plates, which have a different compensation ratio.

There are many calculation methods of the compensation ratio. In their works Brangs [6], Ivantysn [3], Manring [7], Jang [8], Donders [9], Wegner [10] present different simplified methods to calculate the compensation ratio. Wegner [10] analyzed the calculation methods by comparing them with the results of 2D-EHD simulations and showed that the error of the results differs according to the geometry of the valve plate. The calculation methods only cover two states during the full rotation (within a machine having an odd number of pistons, the number of pressurized pistons alternates). In other words, the calculation methods cannot calculate according to the rotation angle of the cylinder block as shown in Fig. 2. However, it is inevitable to consider the rotation angle of the cylinder block when analyzing the relationship between the cylinder block and the valve plate because the area of the fluid film varies with the rotation angle. For that reason, the calculation methods have different results for the same geometry, even though the methods obtain a relatively good value. Therefore, 3D or 2D simulations are generally performed to interpret the behavior of the cylinder block. The simulation analysis has a relatively high accuracy but requires high computational efforts. In addition, it is hard to find a correlation according to the change of each design parameter.

This paper describes an analytical calculation method of the compensation ratio in the cylinder block - valve plate contact under consideration of the cylinder block`s rotation. Some assumptions are introduced to simplify the calculation. To calculate the effective area where the fluid force acts according to the rotation angle of the cylinder block, the position of the kidney is classified into several cases according to the constraints. The analytical calculation results are compared with the results from validated 2D-EHD simulation by applying various geometry parameters and the accuracy of the proposed method is also analyzed via comparison with the simulation results.

2. ANALYTICAL CALCULATION METHOD OF COMPENSATION RATIO

2.1. Assumptions

Figure 3 shows the geometry and areas necessary for the calculation of the compensation ratio in the cylinder block and valve plate. The rotation angle of the cylinder block is defined as the angular position of an arbitrary kidney. In this calculation method, several assumptions are applied for a simplified calculation of a simple geometry of the components.

- Only the static pressure affects as force-generating and thus no further forces (for example, ambient pressure, additional contact pressure, friction, spring force, etc.).
- The contact surfaces are flat. For real geometries that have a spherical contact, it is projected onto a plane.
- The cylinder block rotates without tipping, so the gap height is constant over time.
- The contact surfaces of the contact partners are parallel. Therefore, there is no effect from rotational speed.
- Only cylinder blocks with nine pistons are compared. However, the calculation method is generally valid and can be applied to any number of pistons.
- There is no effect from temperature, so density and viscosity are assumed to be constant.
- There is no deformation of the components.
- Only valve plates without notches and groves are considered to simplify the calculation.

The pressure distribution over the contact area is calculated via the Reynolds equation, which is shown in Eqn.2. as general form. The equation is composed of three terms, which are squeeze flow, shear flow and pressure flow.

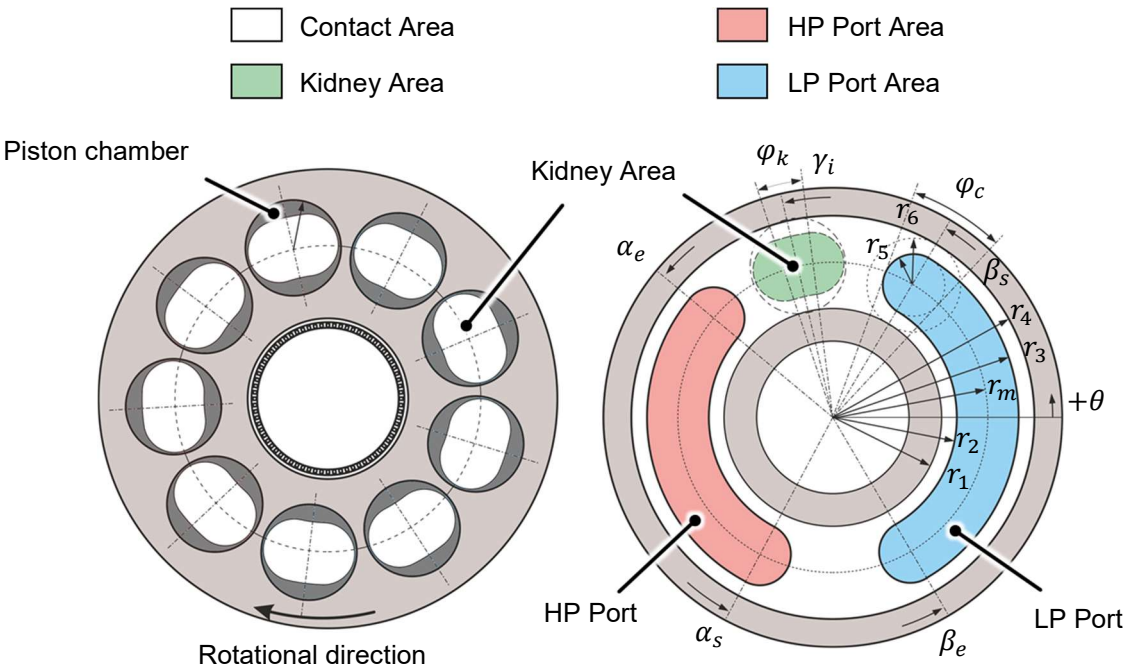

Figure 3. Cylinder block and valve plate design parameters

$$\frac{\partial(\rho h)}{\partial t} + \nabla \cdot \left(\frac{\rho h}{2} (\overrightarrow{v_t} + \overrightarrow{v_b}) \right) - \nabla \cdot \left(\frac{\rho h^3}{12\eta} \nabla p \right) = 0 \tag{2}$$

As introduced in Ref. [10], the pressure distribution in the radial direction can be calculated with the assumptions from the simplified Reynolds equation. Figure 4 shows the pressure distribution in radial direction with a constant gap height. The blue line is solved by the simplified Reynolds equation and the red line is the linear pressure distribution. Since the areas under each line are almost the same, it is assumed that half of the maximum pressure is applied to the ring areas (A_{ring}) to simplify the calculation.

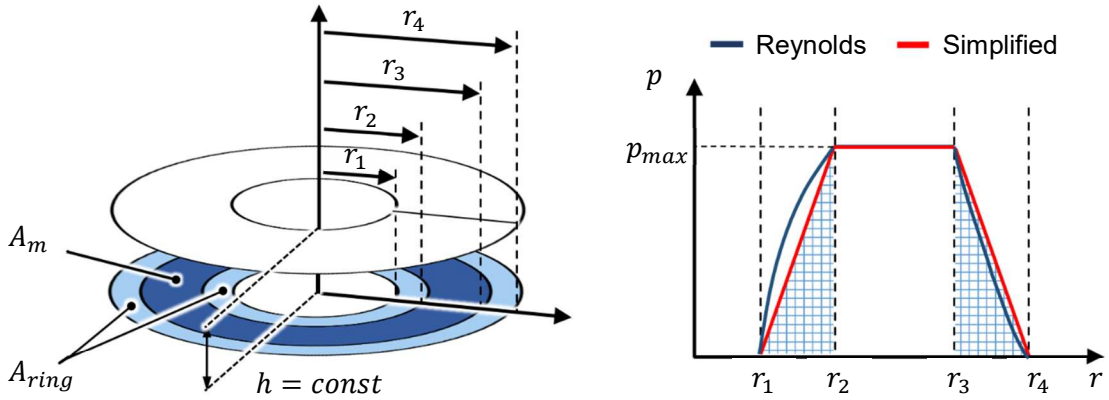

Figure 4. Pressure distribution into radial direction on valve plate

The pressure of each piston chamber is simply defined by correlation of the angles (see Eqn.3) and shown in Fig.5. The angular position of each kidney in the cylinder block is expressed in Eqn.4.

$$p_i = \begin{cases} p_{HP}, & \beta_s + \frac{\varphi_c}{2} + \varphi_k \le \gamma_i < \alpha_s + \frac{\varphi_c}{2} + \varphi_k \\ 0, & Otherwise \end{cases} \tag{3}$$

$$\gamma_i = \theta + \frac{360°}{n_t} \cdot (i-1), \qquad where\ i = 1, 2, \cdots, n_t \tag{4}$$

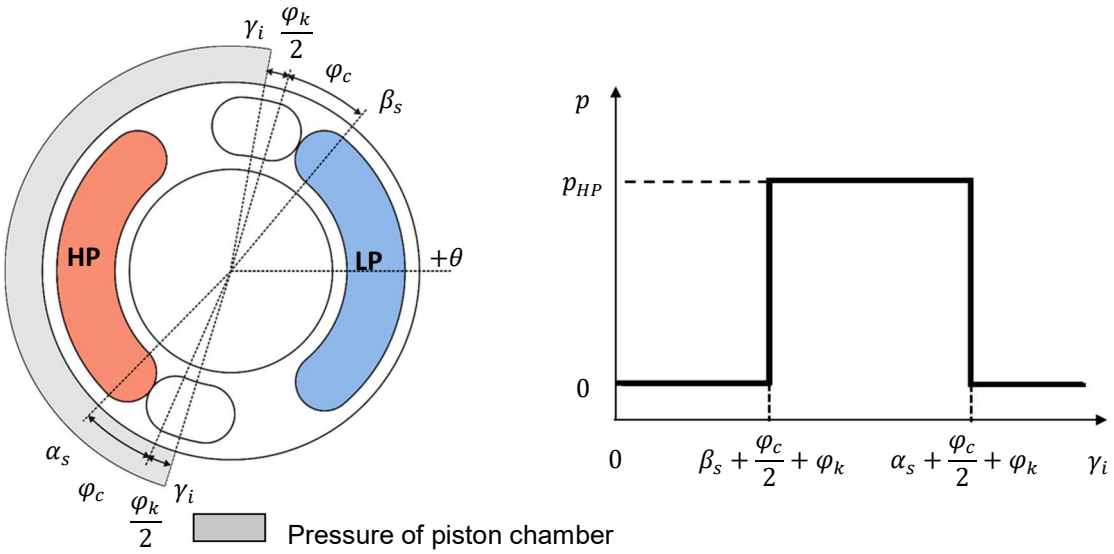

Figure 5. Simplified pressure curve of piston chamber

2.2. Effective pressurized area and load force area

Figure 6 shows segments of the pressurized area on the unrolled valve plate. Since the valve plate is fixed without rotation, the area of the valve plate port and the sealing land area at the adjoining valve plate are constant. However, as the cylinder block rotates, the kidneys extend the length of the valve plate port. Thus, the effective pressurized area can be divided into the fixed areas and the extended areas which vary with the rotation angle. The fixed pressurized area is represented in Eqn.5 and Eqn.6.

$$A_{m.fix} = \pi({r_3}^2 - {r_2}^2)(\alpha_s - \alpha_e)/360° + \pi {r_5}^2 \tag{5}$$

$$A_{ring.fix} = \pi({r_4}^2 - {r_3}^2 + {r_2}^2 - {r_1}^2)(\alpha_s - \alpha_e)/360° \tag{6}$$

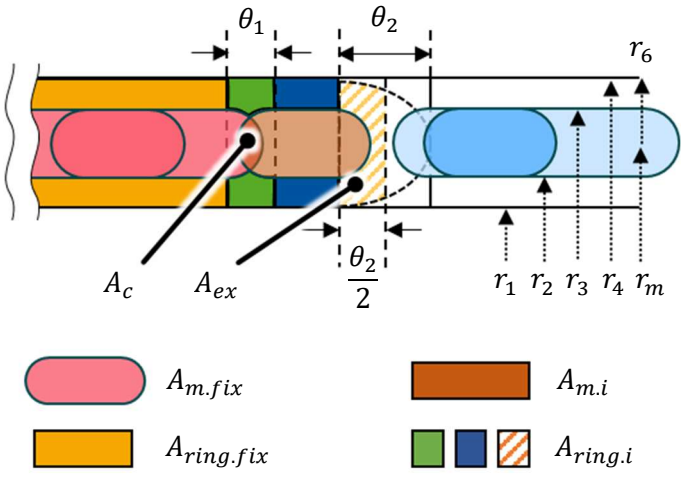

Figure 6. Segments of fluid force area on unrolled valve plate

The cross-sectioned area (A_c) and effective extended area (A_{ex}) are dependent on the rotational angle. The cross-sectioned area is a function of θ_1 and represented in Eqn.7. The cross-sectioned area is used to calculate the exact middle and ring area. A_c is zero at $\theta_1 = r_5/\pi r_m$. Since the effected extended area in the end of the kidney is difficult to calculate analytically, the area is generalized and simplified as Eqn.8 in this paper. The equation represents the cross-hatched region in Fig.6. and is a function of θ_2. In this equation, kidney radius (r_5) and radius of the contact area (r_6) are geometrically calculated as $r_5 = (r_3 - r_2)/2$ and $r_6 = (r_4 - r_1)/2$.

$$A_c(\theta_1) = {r_5}^2 \cos^{-1}\left(\theta_1 \frac{\pi r_m}{r_5}\right) - \pi r_m \theta_1 \sqrt{{r_5}^2 - (\pi r_m \theta_1)^2} \tag{7}$$

$$A_{ex}(\theta_2) = {r_6}^2 \left(\theta_2 \sqrt{(1 - {\theta_2}^2)} + sin^{-1}(\theta_2)\right) - \frac{\pi {r_5}^2}{2} \tag{8}$$

The commutation kidney area of the cylinder block is represented in Eqn.9.

$$A_k = \pi {r_5}^2 + \pi({r_3}^2 - {r_2}^2)\frac{\varphi_k}{360°} \tag{9}$$

Figure 7 shows the extended pressurized effective areas nearby the i^{th} kidney in each case on the unrolled valve plate. Also, generalized constraints of the cases are described in Table 1 and Table 2. The constraints correlate between one kidney and the high or low pressure port angle in the valve plate. The first constraint indicates a relationship of the port angle with the angular position of the i_{th} kidney, and the second one is with $i - 1^{th}$ or $i + 1^{th}$ kidney. As shown in Fig.7, a combination of two constraints determines one case of the kidney position. Sequentially, the first to the fourth case is rotational movements of the kidney from the high-pressure port to the low-pressure port. The fifth and the sixth case show that the kidney is commutated with the high pressure port. The first constraints define the effective areas excluding the green hatched area (A_{ex}), which is determined by the second constraints. Case 1 has three sub-cases and the other cases have two sub-cases each. The first through the third sub-case are related to $i - 1^{th}$ kidney and the others to $i + 1^{th}$ kidney.

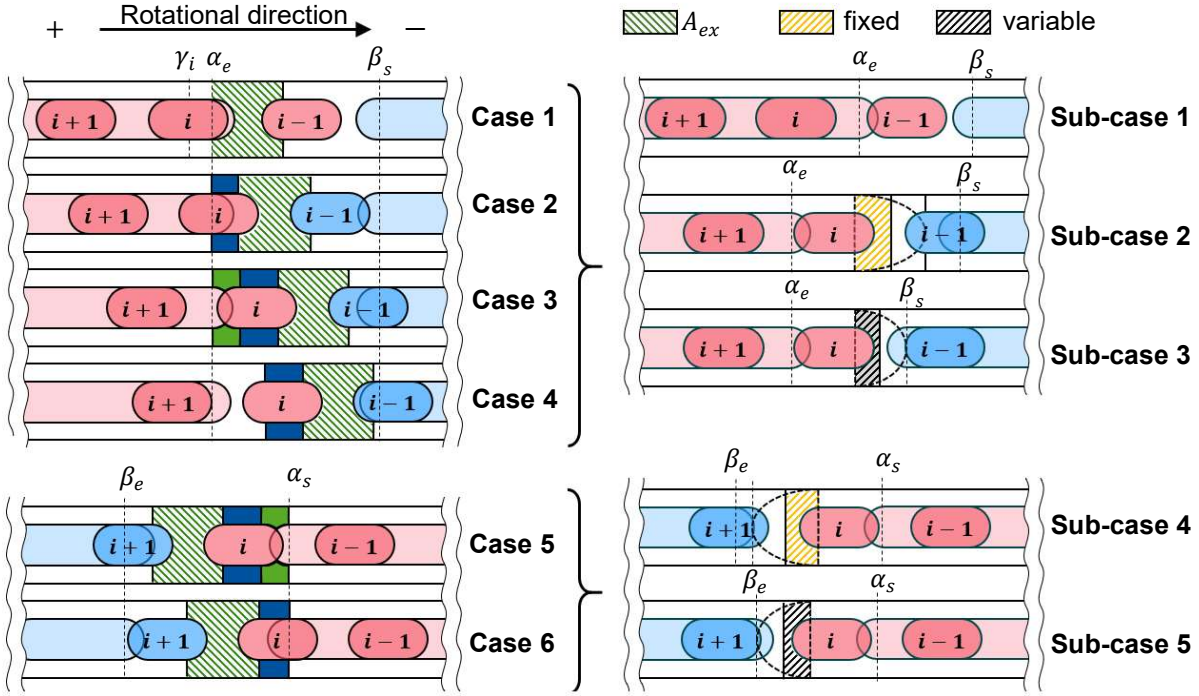

Figure 7. Cases of the kidney position on the valve plate related to kidney angle

Table 1. Constraints and variables for cases of kidney position

Case	Constraints of i^{th} kidney	a [deg]	b [rad]	c	d
1	$\alpha_e + \frac{\varphi_k}{2} < \gamma_i \leq \alpha_s - \frac{\varphi_k}{2}$	0	$\frac{r_5}{\pi r_m}$	0	1
2	$\alpha_e - \frac{\varphi_k}{2} < \gamma_i \leq \alpha_e + \frac{\varphi_k}{2}$	$\alpha_e - \gamma_i + \frac{\varphi_k}{2}$	$\frac{r_5}{\pi r_m}$	0	1
3	$\alpha_e - \frac{\varphi_k}{2} - \varphi_c < \gamma_i \leq \alpha_e - \frac{\varphi_k}{2}$	$\alpha_e - \gamma_i + \frac{3\varphi_k}{2}$	$\left(\alpha_e - \gamma_i + \frac{\varphi_k}{2}\right)\frac{\pi}{180°}$	1	1
4	$\alpha_s + \frac{\varphi_k}{2} + \varphi_c < \gamma_i \leq \alpha_e - \frac{\varphi_k}{2} - \varphi_c$	φ_k	$\frac{r_5}{\pi r_m}$	0	1
5	$\beta_s + \frac{\varphi_k}{2} < \gamma_i \leq \beta_s + \frac{\varphi_k}{2} + \varphi_c$	$\gamma_i + \frac{3\varphi_k}{2} - \alpha_s$	$\left(\gamma_i + \frac{\varphi_k}{2} - \alpha_s\right)\frac{\pi}{180°}$	1	0
6	$\beta_s - \frac{\varphi_k}{2} < \gamma_i \leq \beta_s + \frac{\varphi_k}{2}$	$\gamma_i + \frac{\varphi_k}{2} - \alpha_s$	$\frac{r_5}{\pi r_m}$	0	0

Table 2. Constraints and variable for sub-cases of kidney position

Sub-case	Constraints of $i-1^{th}$ kidney	Constraints of $i+1^{th}$ kidney	e [deg]
1	$\alpha_e - \frac{\varphi_k}{2} - \varphi_c < \gamma_{i-1} \leq \alpha_s$	None	0
2	$\beta_s - \frac{\varphi_k}{2} < \gamma_{i-1} \leq \beta_s + \frac{\varphi_k}{2} + \varphi_c$	None	$\frac{360°}{n_t} - \frac{\varphi_k}{2}$
3	$\beta_e + \frac{\varphi_k}{2} < \gamma_{i-1} \leq \beta_s - \frac{\varphi_k}{2}$	None	$\gamma_i - \frac{\varphi_k}{2} - \beta_s$
4	None	$\alpha_e + \frac{\varphi_k}{2} < \gamma_{i+1} \leq \alpha_s - \frac{\varphi_k}{2}$	$\frac{360°}{n_t} - \frac{\varphi_k}{2}$
5	None	$\alpha_e + \frac{\varphi_k}{2} - \varphi_c < \gamma_{i+1} \leq \alpha_e + \frac{\varphi_k}{2}$	$\beta_e - \gamma_i - \frac{\varphi_k}{2}$

The varied pressurized effective areas are represented in Eqn.10 and Eqn.11. These equations are composed of variables according to each case, as shown in Table 1 and Table 2.

$$A_{m.i} = \pi({r_3}^2 - {r_2}^2)\frac{a}{360°} - A_c(b) \tag{10}$$

$$A_{ring.i} = \pi({r_4}^2 - {r_3}^2 + {r_2}^2 - {r_1}^2)\frac{a}{360°} + A_c(b) - \mathrm{c} \cdot \pi {r_5}^2 + d \cdot A_{ex}(e) \tag{11}$$

Since the angular position of each kidney is changed with the rotational angle of the cylinder block, the kidney position case is also changed in each rotational angle depending on the constraints. Figure 8 represents example of the cases for rotation angles. The number of pistons in high pressure (n_{hp}) is equal to the number of kidneys that have a case.

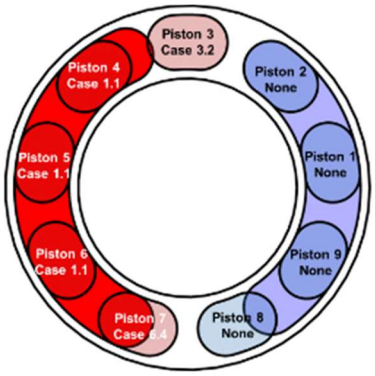

Figure 8. Example of kidney cases for one rotational angle

The effective fluid force area is represented in Eqn.12. In the equation, the ring areas are multiplied by 0.5. This is because half of the high pressure is applied to this area as described above. Sum of the load force areas is represented in Eqn.13. The rotational angle-dependent compensation ratio is simply defined and represented in Eqn.14.

$$A_{fluid}(\theta) = A_{m.fix} + \frac{A_{ring.fix}}{2} + \sum_{i=1}^{n_t} \left\{ A_{m.i}(\theta) + \frac{A_{ring.i}(\theta)}{2} \right\} - n_{hp} A_k \tag{12}$$

$$A_{load}(\theta) = n_{hp}\left(\pi {r_p}^2 - A_k\right) \tag{13}$$

$$C(\theta) = \frac{A_{fluid}(\theta)}{A_{load}(\theta)} \tag{14}$$

3. 2D EHD(ELASTO-HYDRODYNAMIC) SIMULATION

In this paper, a 2D-EHD simulation, developed by Wegner [10, 11], is used as a reference value for an evaluation of the analytical calculation method. This is calculated by means of a simulation model which discretizes the contact surface and whose calculation is therefore also accessible to complex geometrical conditions. Figure 9 shows a simulation example of the mesh grid and result of a pressure field calculation. In this simulation, geometry parameters of the valve plate, such as inner and outer diameter as well as curvature, are applied to generate a basic grid. Then, objects such as valve plate and cylinder block kidneys or commutation notch and bores, are defined on the basic grid dependent on the geometry parameters and rotational angles. A fixed time step pattern is introduced and the grid generation is finalized by a refinement step, performing one revolution of the cylinder block to add nodes on the object edges for every time step. The model allows the generation of spherical geometries. For comparison with the analytical calculations the consideration of load forces is switched off and the simulation is performed setting the gap height to a constant value. For the exact calculation of the pressure field, pressure boundary conditions are given in the elements of the contact surface (for example, edge areas, high pressure and low pressure kidney, pilot holes, etc.). For unconstrained nodes, the pressure is solved using the Reynolds equation discretized for the mesh in the form of finite volumes. Contrary to the analytical calculation, the pressure field is calculated correctly even in the hard-to-describe areas, such as the kidney end area. A detailed description of the simulation is presented [10]. Each node of the grid represents an area fraction of the contact, so that the multiplication by pressure corresponds to a force. Summing the forces at the nodes in the contact results in the fluid force exerted by the pressure field on the cylinder block. The movement of the cylinder block is fixed for the calculations carried out in this work, so that the same conditions for the simulation and the analytical calculation result. The simulation is conducted at discrete angular positions and the analytical calculation is also performed at the same positions for the comparison.

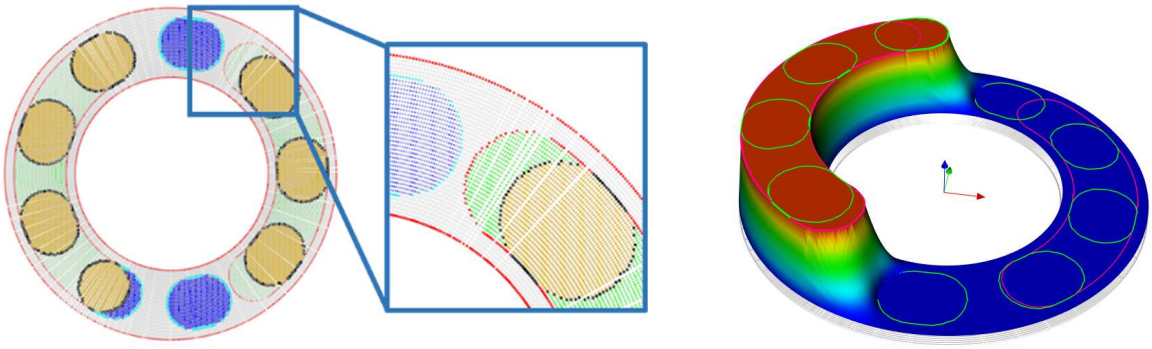

Figure 9. Example of mesh grid and pressure field in 2D-EHD-Simulation

4. RESULTS

In this paper, six geometries were generated to verify the proposed method by comparing them with simulation results in the same condition. As shown in the assumptions, the geometries of the valve plate are applied on the flat plane without commutation holes or notches. The geometries of the valve plate and commutation kidneys of the cylinder block are shown in Fig.10, and the parameter values are listed in Table 3. All geometries have nine pistons. At every geometry, the valve plate port on the left side is the high pressure port (red) The low pressure port on the right side is colored in blue. The geometries are selected to study the tendency of the compensation ratio by changing several parameters based on the first geometry.

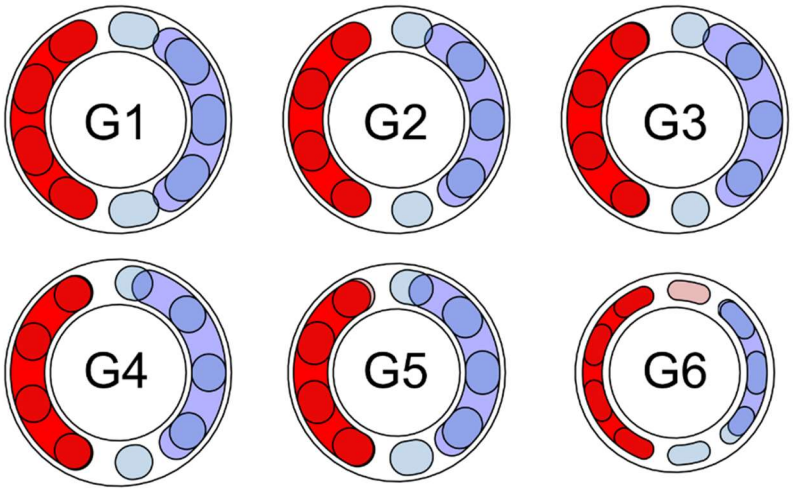

Figure 10. Representation of sample geometries

Table 3. Geometry parameter of cylinder block and valve plate

Denotation	Symbol	Unit	G1	G2	G3	G4	G5	G6
Inner radius of VP	r_1	*mm*	30	30	30	30	28	28.8
Inner radius of Kidney	r_2	*mm*	32.5	32.5	32.5	32.5	30.5	32.05
Outer radius of kidney	r_3	*mm*	47.5	47.5	47.5	47.5	45.5	40.65
Outer radius of VP	r_4	*mm*	50	50	50	50	48	43.9
Angle of Kidney	φ_k	*deg*	10	4	2	2	6	16
Total number of Piston	n_t	-	9	9	9	9	9	9
Radius of Piston	r_p	*mm*	12.5	12.5	12.5	12.5	12	9.85
Start angle of HP port in VP	α_s	*deg*	245	242	242	242	242	248
End angle of HP port in VP	α_e	*deg*	115	118	118	118	120	112
Start angle of LP port in VP	β_s	*deg*	60	60	60	70	55	50
End angle of LP port in VP	β_e	*deg*	-50	-50	-50	-50	-50	-40

Figure 11 shows the analytical calculation results and the comparison with the simulation results. The results are calculated and simulated with 1-degree steps for 40 degrees, which is one piston period. The valve plate ports are fixed and the rotational direction of the commutation kidneys is clock-wise as pump operation (from 20 deg to -20 deg). As shown in all the results, when five kidneys are connected to the high pressure, the compensation ratio is smaller than when there are only four. This is because the load force is the product of the load force area and the number of pistons connected to the high pressure. It is designed so that the force per piston is less than the load force. It can also be seen that the compensation ratio varies with the rotation angle of the cylinder block, since the effective pressure area varies depending on the angular position of the cylinder block. During the angular position where the number of high pressure pistons changes from 4 to 5, the compensation ratio changes drastically. This is because the number of pistons connected to high pressure changes and the piston pressure is assumed to be discretely divided into high pressure and low pressure.

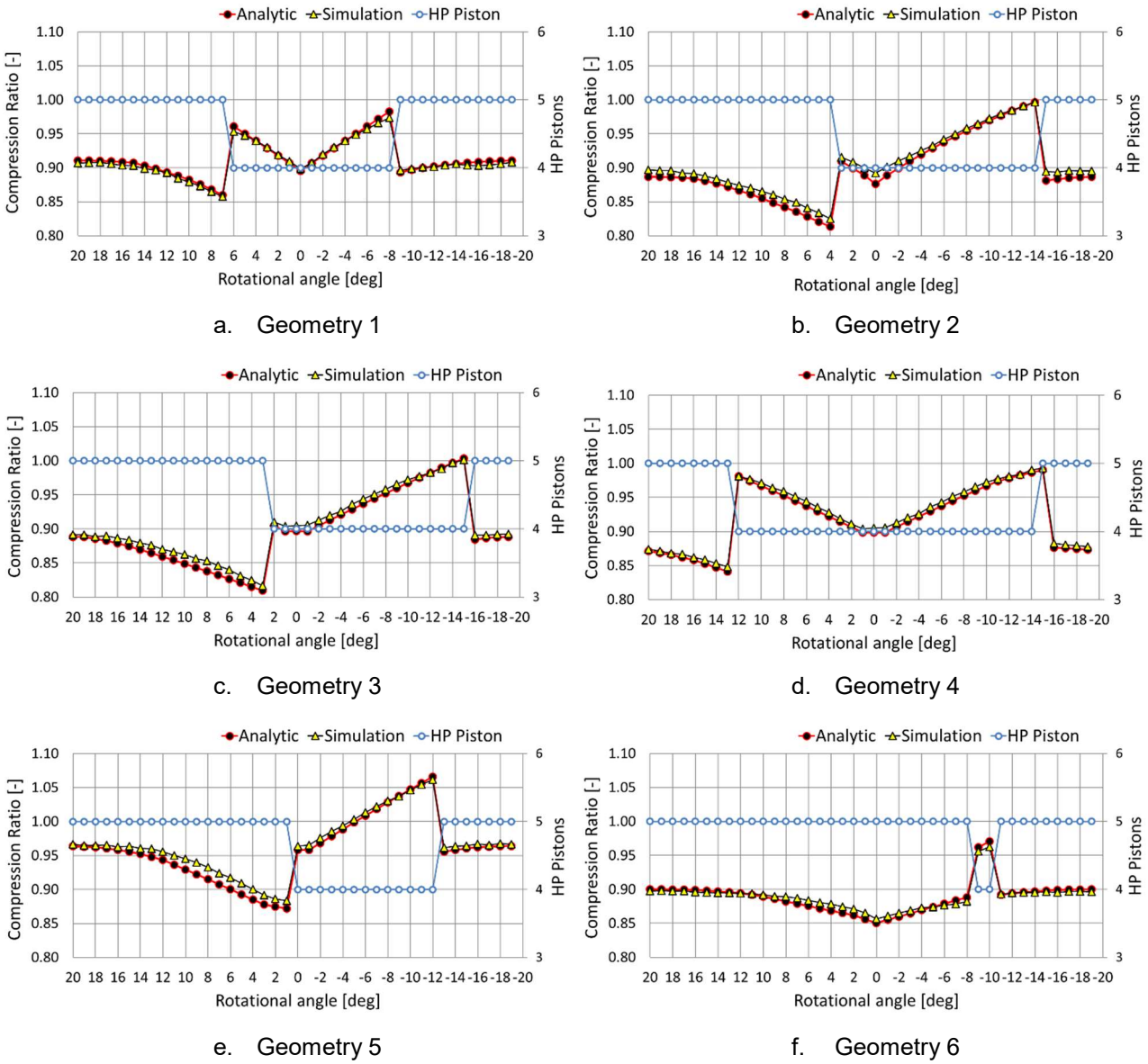

Figure 11. Comparison results of compensation ratio

As shown in Fig.11, Geometry 1 is the case where the high pressure port in the valve plate is symmetrical for the x-axis and its length is exactly same as four kidneys. When the rotational angle is zero, the compensation ratio is the smallest in the section where the number of high pressure pistons is four. Based on this point, the compensation ratio increases into either direction in the section, because the kidneys extend the sealing land and increase the effective pressurized area.

Geometry 2 also has the symmetrical high-pressure port for the x-axis and kidney angle is 4 degrees. Four kidneys overlap exactly with the HP ports at zero rotational angle. Geometry 2 shows a tendency of the graph to be shifted in the direction of rotation of the cylinder block as compared with Geometry 1. This is because the section of the four HP pistons is also shifted.

Geometry 3 has a smaller kidney angle than Geometry 2. Therefore, at zero position, the HP port angle is larger than the angle of the four kidneys. In this case, it is shown in the graph that the compensation ratio is constant from 1 degree to -1 degree. The reason is that the fluid force and the load force are constant in the section because the four HP pistons can be located within the HP port without cross-section. Geometry 4 has a LP port that is 10 degrees longer. Therefore, the section, where the piston is maintained at a high pressure, is shorter than the other geometries. In other words, the section with four HP pistons is longer than the other.

In contrast to geometry 3 and 4, geometry 5 has a smaller HP port angle than the angle of the four kidneys at zero position. Therefore, there is no section with constant compensation ratio in the graph.

Geometry 6 has parameters obtained by measuring the components of a high-efficiency commercial pump. Due to the assumptions, pilot holes and notches are not considered in the calculation. The result of this shape is different from the others. Compared to the other geometries that showed a large change rate according to the rotation angle, geometry 6 has a relatively smooth change rate. This is because the LP port is short and the section, where the number of HP pistons is kept at 5, is relatively long compared with the other geometries. This tendency is achieved when Eqn.14 is satisfied.

$$\alpha_s - \beta_s > \varphi_c + \varphi_k + 4 \cdot 40° \tag{14}$$

In addition, by adjusting the angular position where the piston connects to the HP port through the notch or pilot hole on the valve plate, the protruding section can be removed.

Figure 12 shows the accuracy of the analytical calculation method based on the simulation results. As shown in the results, the maximum error according to each rotational angle does not exceed 2 %. The standard error for all geometries was also about 0.5 %, which showed high accuracy for all rotational angles.

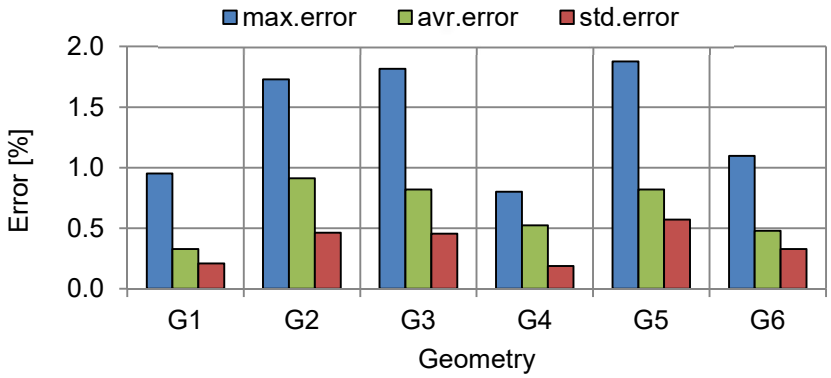

Figure 12. Accuracy of proposed calculation method

5. CONCLUSION

In this paper, a new analytical calculation method is introduced to calculate the compensation ratio in the cylinder block - valve plate contact with consideration of the cylinder block`s rotation. Some assumptions are applied to simplify the Reynolds equation. The effective fluid force area is generalized into 6 cases and 5 sub-cases via the constraints, which are related to the kidneys` angular position. Six geometries are generated and the tendency of the compensation ratio is studied by simulation and analytical calculation. It is confirmed that the angular parameters, such as the valve plate port angle and kidney angle, have a large effect on the variation of the rotation angle-dependent compensation ratio. In addition, the calculation shows that the compensation ratio varies greatly depending on the number of pistons connected to the high pressure kidney. Moreover, the geometric design conditions of the valve plate are shown to have a less oscillating compensation ratio. Also, the accuracy of the analytical calculation is checked by comparison with results from a verified 2D-EHD simulation. The comparison error shows less than 2 % maximum error.

As a general observation, the compensation ratio varies greatly, showing that a simple calculation may not cover peaks either high or low values. Peaks to lower levels may result in high friction, higher levels may increase leakage. These periods may be very short but occur with a high period, effecting wear, noise, heat generation and other effects. At this point the analytical calculation is limited (e.g., because the squeeze film effect is not considered) but shows the importance of a detailed design of this contact.

As future work, the tilting angle of the cylinder block will be added to the analytical calculation and the influence of the rotational speed of the pump will be studied through simulation and analytical calculation. In addition, an analytical calculation method for the cylinder block’s tipping motion will be studied.

NOMENCLATURE

A	Area
C	Compensation ratio
h	Gap height
p	Pressure
r	Radial geometry parameter
v	Velocity of contact partners
α	Angle of high pressure port in valve plate
β	Angle of low pressure port in valve plate
γ	Angular position of cylinder block's kidney
η	Fluid Viscosity
θ	Rotational angle
ρ	Fluid density
φ	Angular geometry parameter

REFERENCES

[1] Schmitz.K & Murrenhoff.H., 2018. Grundlagen der Fluidtechnik, Teil 1: Hydraulik, pp. 158-160.

[2] Manring.N., 2013. Fluid Power Pumps and Motors - Analysis, Design and Control. McGraw-Hill Education.

[3] Ivantysn.J., 1993, Hydrostatische Pumpen und Motoren. Vogel Fachbuch, 1993.

[4] Manring.N., 2000, Tipping the Cylinder Block of an Axial-Piston Swash-Plate Type Hydrostatic Machine. Journal of Dynamic Systems, Measurement, and Control, Mar 2000, Vol.122, pp. 216–221.

[5] Achten.P. & Eggenkamp.S., 2017, Barrel Tipping in Axial Piston Pumps and Motors. The 15th Scandinavian International Conference on Fluid Power, Jun 7-9 2017, Linköping, Sweden, pp. 381–391.

[6] Brangs.E., 1965, Über die Auslegung von Axialkolbenpumpen mit ebenem Steuerspiegel. Dissertation, RWTH Aachen.

[7] Manring.N., 1996, Torque on the Cylinder Block of an Axial-piston Swash-plate Type Hydrostatic Pump. Retrospective Theses and Dissertations.

[8] Jang.D., 1997, Verlustanalyse an Axialkolbeneinheiten. Dissertation, RWTH Aachen.

[9] Donders.S., 1998, Kolbenmaschinen für HFA-Flüssigkeiten. Dissertation, RWTH Aachen.

[10] Wegner.S., Gels.S. & Murrenhoff.H., 2017, Vergleich analytischer Berechnungsmethoden des Entlastungsgrades im Kolbentrommel-Steuerspiegel-Kontakt in Axialkolbenmaschinen. O+P Fluidtechnik, Nov-Dec 2017, pp.60-69.

[11] Wegner.S., Löschner.F., Gels.S. & Murrenhoff.H., 2016, Validation of the Physical Effect Implementation in a Simulation Model for the Cylinder Block/Valve Plate Contact Supported by Experimental Investigations. Mar 8-10 2016, IFK 2016, Dresden, Germany.

FLUID DYNAMIC SIMULATION OF HYDRAULIC ORBITAL MOTORS

Venkata Harish Babu Manne*[,1], Matteo Pellegri[1], Andrea Vacca[1], Kyle Merrill[2]
1: Maha Fluid Power Research Center, Purdue University, Lafayette, Indiana, USA
2: Parker Hannifin Corporation, Pump and Motor Division, Greeneville, Tennessee, USA
(*) corresponding author email id: manne0@purdue.edu

ABSTRACT

This paper presents an approach for the simulation of the fluid displacing action realized by Orbit Gerotor Motors. The goal of the proposed approach is to achieve a correct simulation of the internal flow features of the motor, of the port flow fluctuations as well as to predict the volumetric efficiency, for various operating conditions, in terms of shaft speed and port pressures. The simulation tool is based on coupling of different models: a geometric tool to estimate the instantaneous chamber volumes and port areas, a lumped parameter model that simulates the fluid dynamics of the motor and a 2D-CFD model to simulate the leakage flows. The geometric tool considers the measured CAD profiles of the gear geometry inclusive of the machining tolerance data as input, and it provides as output the information needed by the following fluid dynamic models, such as the instantaneous volume of each internal chamber, the connecting areas realized by the commutator and the internal timing slots. A lumped parameter model implemented in AMESim permits the evaluation of the main flow features, including the instantaneous chambers' pressures and the port flows. A 2D-CFD model complements the main flow simulation performed by the lumped parameter model to simulate the internal lubricating gaps. The model is based on the Reynolds equation applied to the actual gap geometry. The pressure-gradient driven velocity is integrated across the boundaries to calculate the leakage flow rate. The most significant results of the model are illustrated in the paper, taking as reference a commercial unit produced by Parker Hannifin Corp. The features of the internal pressurization and of the internal leakage flows are described. The model validation is also provided, by comparing the predicted volumetric efficiency map with the one derived from a test campaign obtained on a series of production units.

KEYWORDS: Orbital Motors, CFD, Volumetric Efficiency, Fluid Dynamics Simulation

1. INTRODUCTION

Orbital motors, also called Geroler Motors are a type of internal gear machines. These machines are fixed positive displacement units and find a wide range of applications in low speed high torque (LSHT) applications in agricultural, construction, forestry, public utility and lawn equipment. Orbital motors work similar to the other type of well-known internal gear machines, Gerotors. Two gears exist in a Gerotor, one with external teeth and the other with internal, both rotate about their own centres which are divided by the eccentricity of the machine. In case of orbital motors, only one gear, rotor, exists and the displacement is achieved by the rolling/sliding motion of vanes which provide relative motion between the moving rotor and stator. The rotor's centre's nominal locus can be traced as a circle. Fig. 1 illustrates a typical construction of Gerotor and Orbital motors.

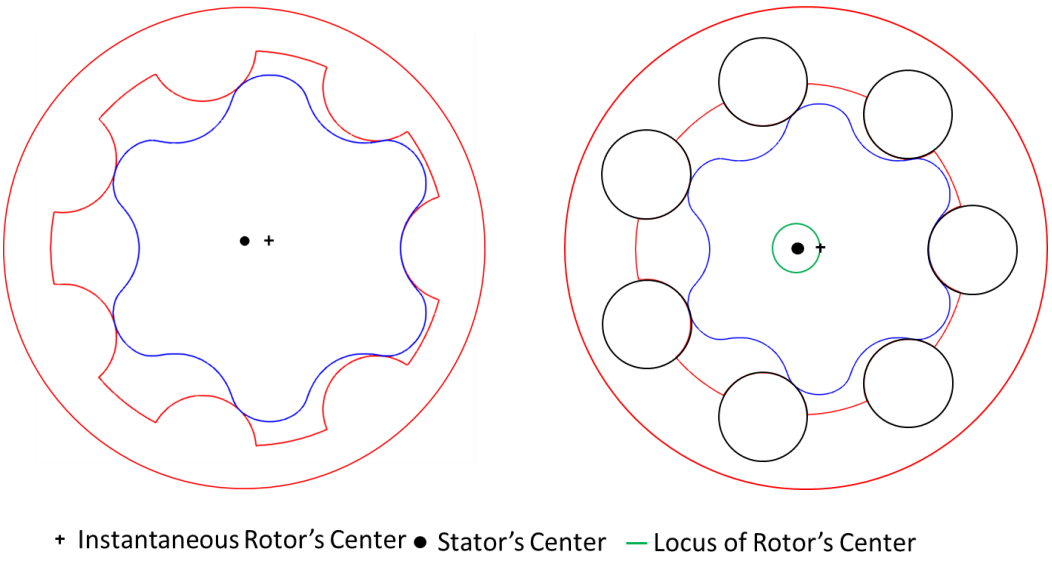

Figure 1. Gerotor and Orbital motors

Gerotors and Orbital motors differ mainly in the displacement volume for a given size of machine. The rotor-stator set of orbital motors acts as a gear reducer with gear ratio of 1: N, where N is the number of stator/ outer gear teeth. The volume displaced by Gerotor for a shaft revolution can be represented as (Nervegna N. [1]):

$$V_{ger} = (N-1) \cdot V_0 \quad (1)$$

The volume displaced by orbital motor [1] for the same number of stator teeth, N, over a shaft revolution, would be:

$$V_{orb} = (N-1) \cdot N \cdot V_0 \quad (2)$$

Consequently, the displacement volumes of a gerotor and orbital motor can be represented as:

$$V_{orb} = N \cdot V_{ger} \quad (3)$$

Orbital motors offer the advantage of higher specific power compared to Gerotors. The speed of operation can be related [1] as:

$$\omega_{orb} = \frac{\omega_{ger}}{N} \quad (4)$$

Thus, orbital design of internal gear machines is used to obtain high torque at low speeds. Gaining insights on their operation can help improve their design and efficiency. Very few scientific reports exist that deal with the fluid dynamic analysis of orbital machines. Many researchers [2-5] reported findings on the torque analysis, especially the mechanical losses and startability, but very few analysed the fluid dynamics of orbital machines. Dasgupta et.al.[6] performed theoretical and experimental studies on the steady state performance of an orbital hydraulic motor by utilizing the bondgraph technique and achieved close agreement with the experimental results. They modelled resistances of flow path with semi-empirical approach using simulation and experimental investigations. Although good agreement with experimental studies was reached, the requirement of empirical tuning makes this approach infeasible as a design tool. Ding et.al.[7] developed a CFD model for orbital motor by treating the dynamically changing rotor fluid volume as a deforming/moving mesh and achieved good agreement of the average flow results with that of experiments. Although a good agreement with experimental results was achieved, the proposed CFD approach lacks the advantages offered by lumped parameter models such as low simulation time which provides feasibility of optimization studies and the possibility of simulating the system connected to the ports.

A simulation model of Gerotors was created by author's research group and experiments were performed to evaluate the validation of the model [8]. An independent comparison of a lumped parameter model and a CFD-based model with experimental results was performed to analyse these two different approaches [9]. It was observed that lumped parameter models can sufficiently represent the performance of the unit especially if the

micro-motions of the rotor are considered in the model. Similarly, Manco et al. [10] formulated a control volume lumped parameter model, based on continuity and orifice equations. A similar formulation was extended for a more generic case by Schweiger et al. [11] who also included a more detailed calculation for the internal leakages. Even though lumped parameter approach reduces the simulation time considerably, the leakages in complex machines have to be evaluated separately using a CFD-based approach for improvement of prediction capability.

The past work, including mentioned papers, usually considered the nominal geometry for the evaluation of flow features of the positive displacement units. Considerations based on the real profile of the pumping element are seldom taken into consideration, but can indeed provide insights on the effect of geometric imperfections or of machining tolerances. A tool capable of capturing the effect of geometric imperfections can provide insights of the actual operation of the machine and can be used as a design tool. In this work, a simulation model was created to gain insights on the operation of orbital machines. A lumped parameter fluid dynamic model is employed to evaluate the major fluid-dynamic aspects of the unit whereas the leakages in the lubricating gaps are evaluated using a CFD-based approach. The lumped parameter approach investigated by past researchers [6,10,11] included several simplifications of flow features whereas the CFD approach [7] is infeasible for optimization or design studies. Hence the current approach is optimal as a design tool. Different construction types of orbital Motors exist, the main difference being the way the pressurization timing is achieved. For validation, Parker Hannifin's TL240 unit is considered. In the following section, the details of the reference unit and its pressurization mechanism are described.

Reference Orbit Unit:

Major details of the unit for continuous operation are presented in Table 1 [12].

Parameter	Value
Number of Rotor Teeth	6
Geometric Displacement	238 cc/rev
Maximum Oil Flow rate	68 l/min
Maximum Differential Pressure	190 bar
Maximum Torque	620 Nm

Table 1. Major details of the TL240 unit for continuous operation

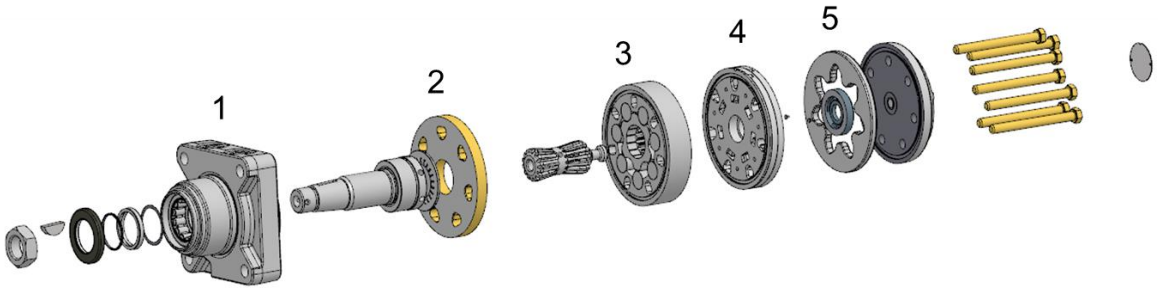

Figure 2. Exploded view of the TL240 unit: 1. Ports Block 2. Manifold on the shaft side 3. Rotor-Vane set 4. Windows Manifold 5. Commutator

The exploded view of the orbital motor and the five major parts under consideration are presented in fig. 2. The ports block, 1, has provision to provide the inlet flow to the machine and to collect the outlet flow. All the parts of the machines are stacked together by studs. These studs pass through the parts 2-5 presented in the figure. The slots provided in the parts 2-5 for the studs are larger than the cross-section of the studs. This is to provide a flow passage from the ports block, 1, to the commutator, 5. The commutator performs the orbiting action, it either opens or closes the windows in the windows manifold, 4. Each window is connected to a displacement chamber, DC, in the Rotor-Vane set. Thus, the timing for the connections of the volumes in the

Rotor-Vane set is realized by the motion of the commutator. In particular, the flow enters through the windows manifold into the Rotor-Vane set where the pressurized inlet fluid drives the rotor. After the maximum volume of the DC is reached, the commutator switches the port, connecting the flow to a slot (not visible in fig.2) provided through the shaft for the fluid to enter which is directly opened to the ports block, 1. The windows manifold, 4, performs the action of connecting the gear's control volumes and the inlet/outlet environments as dictated by the commutator. It should be noted that the inlet/outlet ports can be switched to rotate the shaft in the opposite direction.

Fig. 3 represents the windows under consideration along with the commutator. It can be observed that the windows are exposed to the inside of the commutator or the outside which correspond to the inlet/outlet (blue in Fig.3) and outlet/inlet environments (red in Fig.3) respectively depending on the direction of rotation of shaft required. For a certain duration of angle, the window area is completely enveloped by the commutator thus providing zero cross-porting.

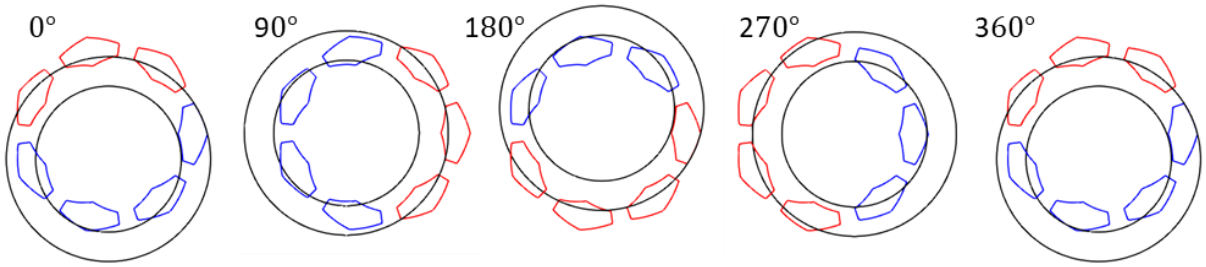

Figure 3. Commutator and Windows for 360° of revolution of rotor

2. SIMULATION MODEL

In this work, attention is primarily paid to evaluation of the fluid dynamic aspects of the orbital motor. The structure of the present simulation tool is presented in fig.4. The three main modules of the simulation tool are: the geometric module, the fluid dynamics module and the gap module. These three modules are developed on three different platforms: C++ is used for the geometric module, the fluid dynamics module is implemented in AMESim, while the gap module uses OpenFOAM open source libraries. The geometric module considers CAD drawings as inputs and provides various inputs required by the fluid dynamics module. Pressure values of the TSVs are provided as inputs by the fluid dynamics module to the gap module whereas leakage values are provided as inputs by the gap module to the fluid dynamics module. The three modules are detailed further.

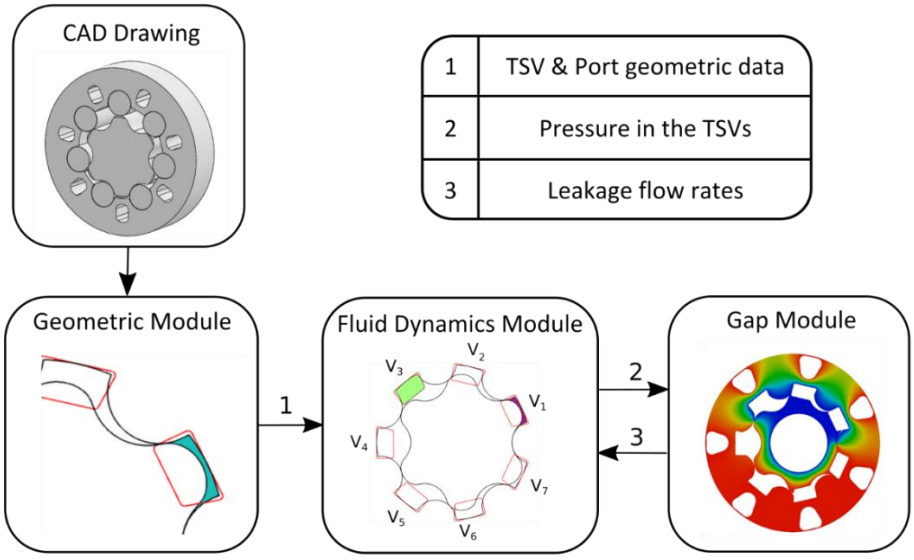

Figure 4. Orbit Multi-Domain Simulation Tool

2.1. Geometric Module

The geometric module works as a pre-processor by providing the required input data to the fluid dynamics module. The geometric module is not based on the analytical definition of the profiles, but on the numerical calculations performed on the measured CAD profile data (in TXT format) of the rotors, vanes and the socket positions. The module is implemented in C++ and utilizes the open-source GSL libraries. The output of the model is given in TXT format and can be used for stand-alone considerations of the motor geometry and as input to the AMESim fluid dynamics module. The geometric module is divided into two sub-modules, the commutator geometry module and the gear geometry module

2.1.1. Commutator Geometry Module

The commutator geometry module deals with the evaluation of the geometrical features of only the commutator and windows manifold, thus generating the porting communication data of the motor with the inlet/outlet environments. Using the GSL libraries, the instantaneous area of communication and hydraulic diameter are evaluated for each of the windows as the commutator performs the orbiting motion. The data is stored in the TXT format for further use by the fluid dynamics module. Fig. 5 represents part of the output generated by the commutator geometry module. For one of the windows, the communication area to the inlet and outlet environment are presented.

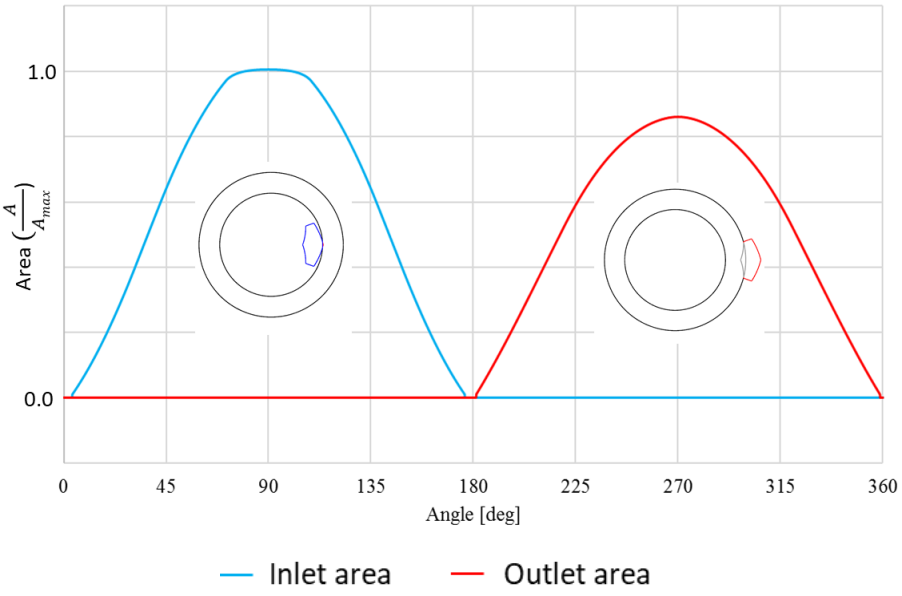

Figure 5. Window area exposed to Inlet/Outlet environment for one Rotor-Vane DC, for a full revolution of the rotor

2.1.2. Gear Geometry Module

Even though the orbit motor is nominally periodic, all the parameters are evaluated individually for all the chambers and over a full shaft revolution since a real profile of rotor and real parameters of vanes, sockets are considered. The gear geometry module evaluates several features of the rotor-vanes-stator body set. Some of these features are the instantaneous DC volumes, the volume derivative, the port areas and hydraulic diameters of communication of each of the chambers to the windows manifold, tooth tip gap heights and tooth tip gap lengths. The vanes-stator body set can be reconstructed as a stator. Fig. 6 represents the position of rotor, windows and the stator for different angles of orbit motion. The reference DC is coloured in grey. Vanes are numbered in counter-clockwise direction starting from the extreme right vane.

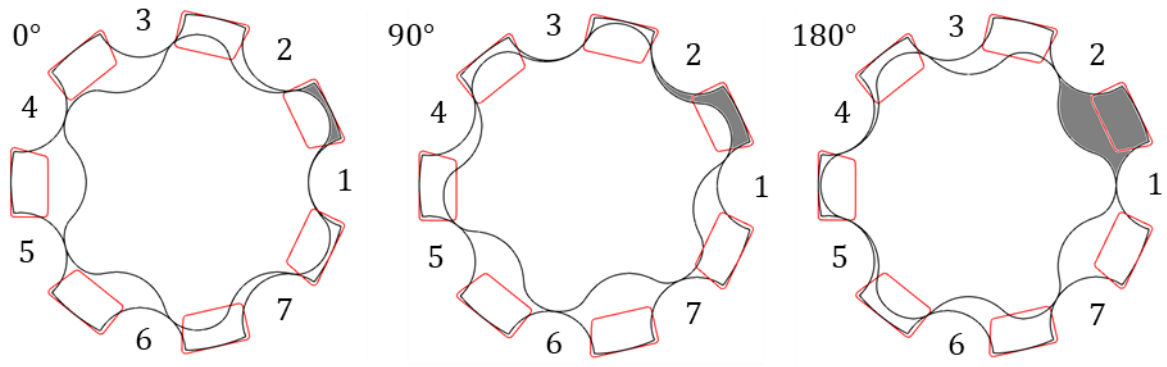

Figure 6. Rotor, Windows and Stator for various angles of orbit motion

One of the important features evaluated by the gear geometry module is the tooth tip gap between adjacent control volumes, which can be one of the major contributor of leakages. The gap height is evaluated as the minimum distance between the rotor and any of the vanes. Once the gap height is evaluated, an equivalent gap length, l_t, is defined as the distance between two points positioned inside adjacent control volumes where the gap height is $h_t^* = h_t \cdot (1 + t)$. More details on this are reported in [9].

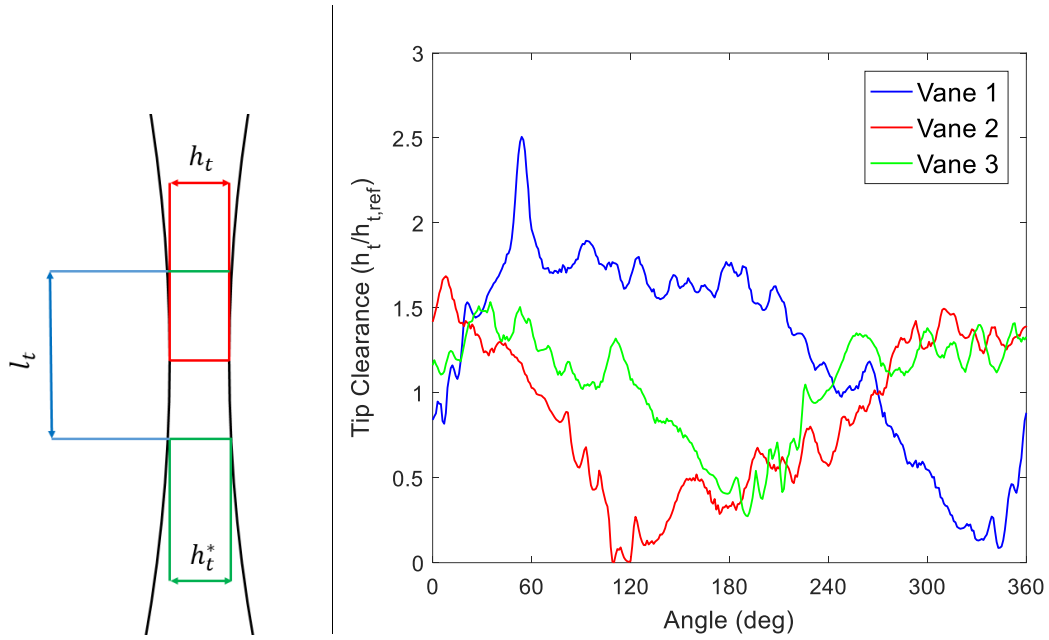

Figure 7. Tooth tip clearance definition and representative dimensionless values for one revolution of the Rotor

Fig. 7 represents the tooth tip clearance values, at three of the seven vanes, obtained from the geometric module implemented. The capability of the model in accounting for manufacturing imperfections can be observed. The variations of tooth tip clearance shown in fig. 6 will have non-negligible implications on the fluid-dynamic behaviour of the unit. Other geometrical features such as the DC volumes or the porting areas are not significantly affected by the actual geometrical features, so the variations of these parameters between different DCs could be potentially neglected, although they are considered in the current model.

2.2. Fluid Dynamics Module

The lumped parameter fluid dynamic module permits the evaluation of pressure inside the DC by considering the dynamic porting provided by the commutator and windows manifold. The fluid domain of the pump is discretized into a finite number of sub-volumes. In each sub-volume, the properties of flow are assumed to be uniform and dependent only on time. The high bulk modulus of fluid and small volume size makes this assumption reasonable. The different sub-volumes are connected to each other and to the inlet and outlet

environments. The connections between these control volumes and the connections of each of these control volumes to the inlet/outlet ports are treated as variable orifices. Based on the flow communicated between each of the control volumes and with the inlet and outlet ports, the variation of pressure, p, inside each of the control volumes with respect to time is determined through the pressure build-up equation:

$$\frac{dp_i}{dt} = \frac{1}{V_i}\frac{dp}{d\rho}\Big|_{p=p_i} \cdot \left[\sum \dot{m}_{in,i} - \sum \dot{m}_{out,i} - \rho|_{p=p_i}\frac{dV_i}{dt}\right] \quad (5)$$

The mass entering and leaving each control volume is evaluated using two different approaches: for the connection between the DCs and the inlet/outlet ports, the orifice equation with a variable orifice coefficient, α has been used assuming a dependence of this coefficient on the Reynolds number.

$$\dot{m} = \frac{p_i - p_p}{|p_i - p_p|} \cdot \rho|_{p=\overline{p_{i,p}}} \cdot \alpha \cdot A_{i,P} \cdot \sqrt{\frac{2 \cdot (p_i - p_p)}{\rho_{p=\overline{p_{i,p}}}}} \quad (6)$$

The Reynolds number, Re, is defined in this case as:

$$Re = \frac{D_h}{\nu}\sqrt{2 \cdot \frac{\Delta p}{\rho}} \quad (7)$$

With $D_h = \frac{4A}{P}$. The correlation between the discharge coefficient and the Reynolds number has been approximated with the following relationship

$$\alpha = \alpha_{max} \cdot \tanh\left(\frac{2 \cdot Re}{Re_{crit}}\right) \quad (8)$$

The values of Re_{crit} and α_{max} represent fully turbulent condition. When the fully turbulent condition is met, $(Re \geq Re_{crit})$, α saturates to its maximum value α_{max}. $Re_{crit} = 1000$ and α_{max} = 0.7 have been used in the current work: these values fall in the range prescribed by McCloy and Martin[13].

The connections corresponding to the rotors' inner-teeth clearance are treated assuming a condition of laminar flow. This is a fair assumption considering the geometry of orifice and the relative motion between the two surfaces. A laminar flow equation including Couette and Poiseuille terms is implemented as follows:

$$\dot{m} = \rho\left[-\frac{h_t^3}{12\mu}\frac{p_i - p_j}{l_t} + \omega_{outer} \cdot 2\pi \cdot r_{outer} \cdot \frac{h_t}{2} - \omega_{inner} \cdot 2\pi \cdot r_{inner} \cdot \frac{h_t}{2}\right] \cdot b \quad (9)$$

The flow through the lubricating gaps is assessed separately and described in the next section. The corresponding evaluated leakage values are included in the Fluid Dynamics Module.

The developed AMESim sketch is presented in fig. 8. Several of the components are developed in AMESim Submodel editor, others being the default components available in AMESim. The equations mentioned above are already implemented in AMESim along with the fluid model. Thus, development of a new fluid model is not required. The developed components can easily be connected to each other to build an entire circuit. The parts 1,2,3 presented in fig. 8 are: 1. components to handle the communication of leakages evaluated by CFD module 2. components for the communication of data from commutator geometry module 3. component for the communication of data from main geometry module.

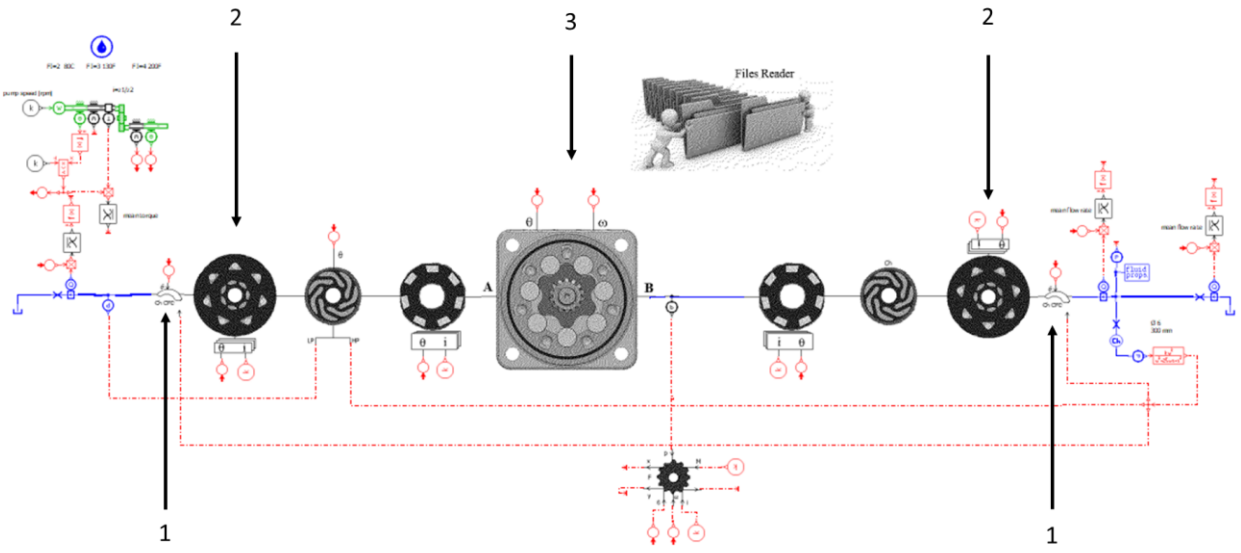

Figure 8. Fluid dynamics model developed in AMESim environment

2.3. Gap Module

2.3.1 Geometry of Lubricating Interfaces

Three lubricating gaps exist in the orbit motor under consideration. The gap between commutator and casing, will be referred to as the commutator gap. The other two gaps exist on either sides of the rotor and will be referred to as the lateral gaps and are further detailed in the following sections.

Commutator Gap

The lateral gap between the commutator and casing allows the orbiting commutator to move relative to the casing. The commutator is essentially an annular metal component that connects the timing windows manifold to the inlet/outlet pressures. If the inside of the commutator is subjected to inlet pressure, the outside is subjected to the outlet pressure and vice versa. The orbiting commutator and the windows manifold are presented in fig. 9.

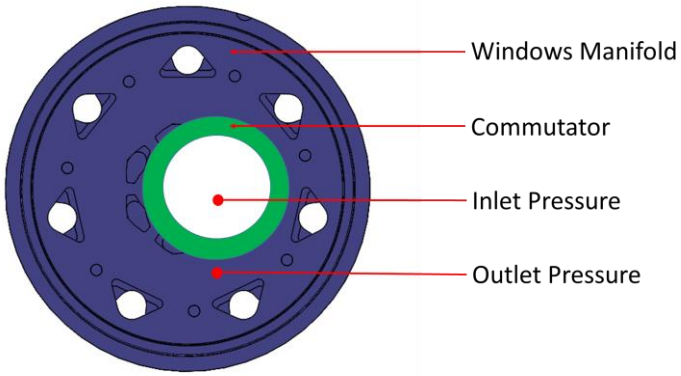

Figure 9. Orbiting commutator and Windows manifold

Lateral Gaps

Lateral gaps allow the rotor to rotate within the surrounding stationary fixtures. They exist on either sides of the rotor:

(i) On the side of shaft

(ii) On the side of windows manifold

These gaps are represented in fig. 10. The component in the middle, (b), is the gear set with rotor, vanes and stator body. The component to the right, (c), is the windows manifold. The component to the left, (a), represents the manifold on the shaft side.

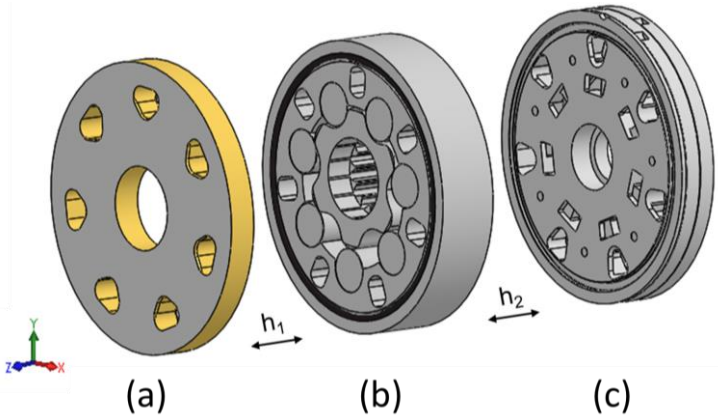

Figure 10. Rotor and Stator sandwiched between stationary parts

Thickness of the Lubricating Gaps

The spatial gap thickness in the gap domain is determined from the measured lengths of the parts. The thicknesses at different parts of the machine are presented in fig. 11. By subtracting the rotor's thickness from the stator's thickness, the combined gap thickness on either sides of the rotor, $2 \cdot \mu_{g,max}$ was obtained. Similarly, by subtracting the vanes' thickness from the stator's thickness, the combined gap thickness on either sides of the vanes were evaluated. An average of all the measured thickness at the vanes, found to be $2 \cdot \mu_{g,max}$, is considered in the model. The gaps are approximated to have equal thickness on either sides as the gears are spatially pressurized in the same way which leads to a nullified net axial force. Thus, the gap thickness next to rotor and vanes on either side would be $\mu_{g,max}$. A nominal thickness of $0.3 \cdot \mu_{g,max}$ is assumed for the gap at the stator body. The commutator gap thickness is difficult to estimate as it varies based on the manufacturing tolerance of many parts involved in the assembly. A nominal thickness of $\mu_{g,max}$ is assumed for the commutator gap as it is similar to the pair of rotor-stator. All the gaps are in the order of magnitude of 10 microns.

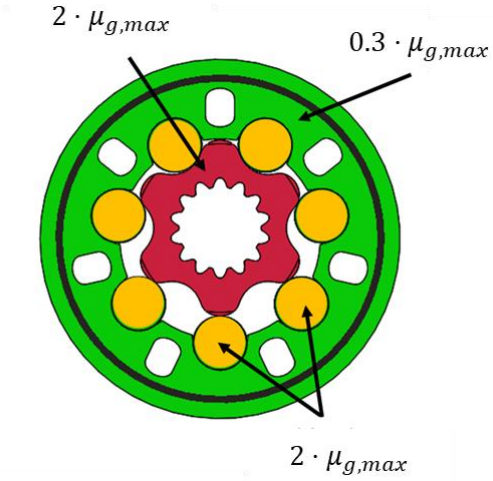

Figure 11. Tip gap heights at different positions of rotor-stator pair

2.3.2 Modelling the Lubricating Interfaces

The flow features in thin films can be described using the Reynolds equation which is a well-known and fundamental equation in tribology. The equation predicts the pressure distribution within the flow domain accounting for different sources of pressure generation. The equation is derived from three dimensional Navier-Stokes equations. Detailed derivation can be found in the work of [14].

$$\nabla \cdot \left(\left(-\frac{\rho h^3}{12\mu} \right) \nabla p \right) + \frac{\rho \mathbf{v}_b}{2} \cdot \nabla(h) + \rho \mathbf{v}_b \cdot \nabla(h_b) + \rho \left(\frac{\partial h_t}{\partial t} - \frac{\partial h_b}{\partial t} \right) = 0 \qquad (10)$$

Considering steady state, incompressible flow, neglecting body forces and symmetric constant axial gaps, the Reynolds equation can be reduced to:

$$\frac{\partial}{\partial x} \left(h^3 \frac{\partial p}{\partial x} \right) + \frac{\partial}{\partial y} \left(h^3 \frac{\partial p}{\partial y} \right) = 0 \qquad (11)$$

This diffusive steady state problem implies that the solution of pressure, p, is influenced solely by its value at the boundaries. The values of pressure at the boundaries can be extracted from the lumped parameter fluid dynamic model discussed earlier. The Reynolds equation is not valid outside the gap region where the flow is turbulent such as the interface between gears and the ports, in the DCs. The gap geometry on which the Reynolds equation has to be solved should be limited solely to the gap geometry as represented in fig. 12. Although the Reynolds equation is a steady state equation, the gap shape is not constant and varies with the rotation of rotor.

The complex mesh to be generated on which the Reynolds equation has to be solved is developed using the open source CFD platform, OpenFOAM. The mesh was generated starting from the CAD file of the motor and ANSYS Workbench has been used to generate Fluent (.msh) type mesh which is primarily made of hexahedrons. This mesh type is compatible with OpenFOAM mesh converter. OpenFOAM is equipped with mesh handling capabilities such as mesh rotation, snappyHexMesh [15]. SnappyHexMesh utilizes the Stereo Lithography (.stl) files of ports to remove the port regions, where the flow is turbulent, from the background mesh. The sample mesh of lateral gap between rotor and the windows manifold is presented in fig. 12. Mesh sensitivity analysis is performed to confirm that the results are not mesh sensitive beyond 2.5 million cells in the lateral gap and 0.5 million cells in the commutator gap.

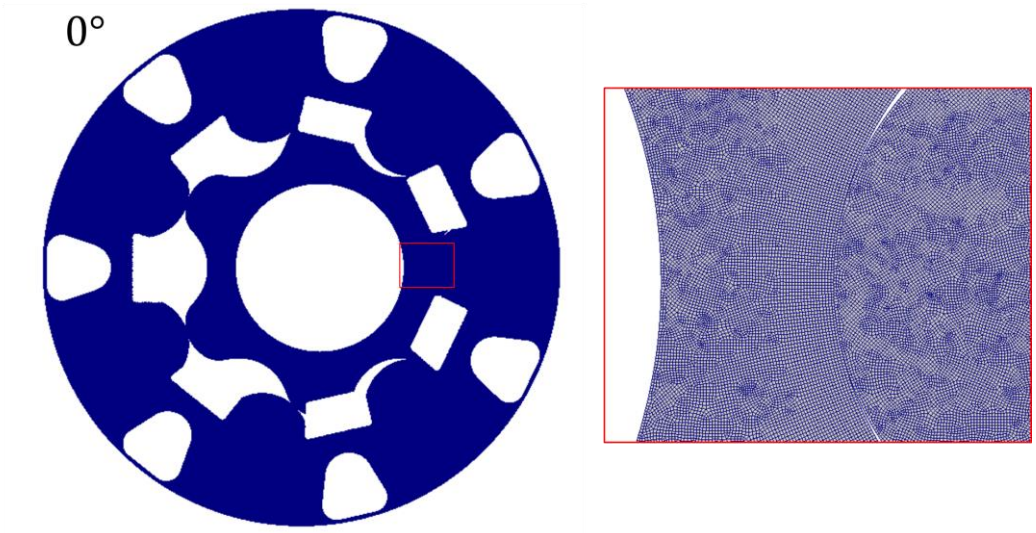

Figure 12. a. Generated Mesh for the lateral gap on the window side, approximately 2.5 million cells.

b. Magnified view of a portion of mesh

2.3.3 Boundary Conditions

Dynamic pressure values extracted from the lumped parameter fluid dynamic model are provided as boundary conditions to the gap model. The boundaries of mesh where the suction, delivery and chamber pressure boundary conditions are applied are represented in fig. 13. The exterior of the mesh which corresponds to the polymer seal is subjected to a solid wall boundary condition which implies a zero pressure gradient.

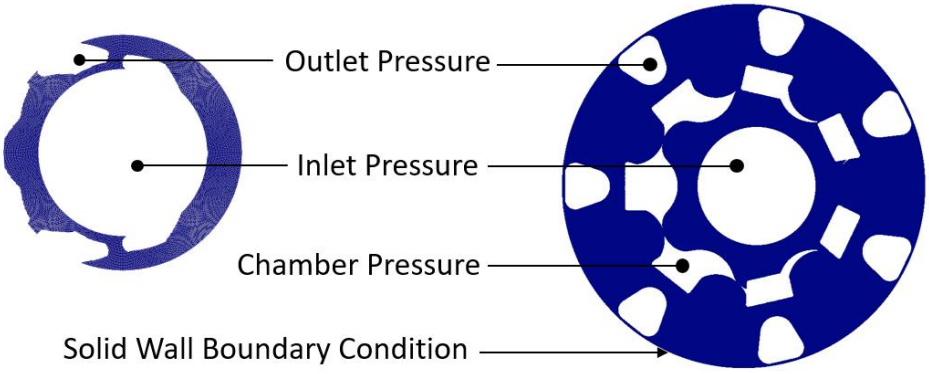

Figure 13. Boundary conditions of commutator gap and lateral gap

2.3.4 Evaluation of Leakages

The leakages across the boundaries are a function of both the pressure gradient and the relative motion between the moving parts and stationary parts. Referring to the representative mesh in fig. 14, the leakages can be calculated as:

$$Q_{leak} = \sum_i Q_{i,leak} = \sum_i \int\int_{A_i} v_i \cdot n_i dA_i \qquad (12)$$

$$= \int_0^{\delta} ds \int_0^{h} (u \cdot n_x + v \cdot n_y) dz$$

$$Q_{leak} = \sum_{i=1}^{N} \left[-\frac{\delta_i}{12} \left(\left(n_{1i} \frac{1}{\mu} \frac{\partial p}{\partial x}\Big|_i + n_{2i} \frac{1}{\mu} \frac{\partial p}{\partial y}\Big|_i \right) h^3 \right) + \delta_i \cdot \frac{h}{2} (ux + vy) \right] \qquad (13)$$

Where δ_i represents the face width of a cell, h represents the height of gap at the cell, u and v represent the relative velocity of top surface with respect to the bottom surface of the gap interface which in the current scenario would be the rotor's velocity.

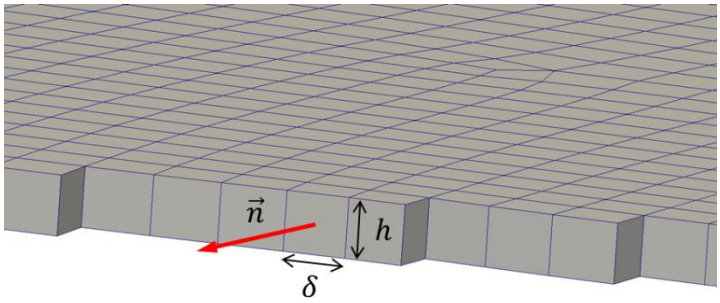

Figure 14. Sample image of the lateral gap mesh

3 RESULTS AND VALIDATION

3.1 Flow Ripple

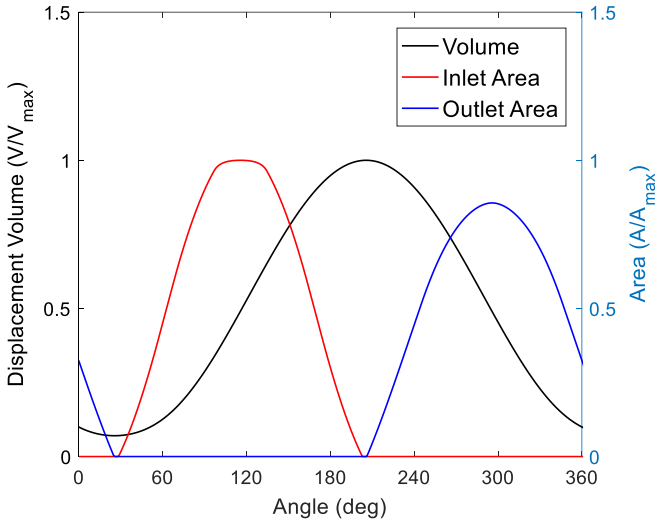

Figure 15. Displacement volume, port areas over an orbit rotation

The lumped parameter model permits to output the geometrical features such as the instantaneous DC volume and the connecting areas to the inlet/outlet ports (fig. 15). The displacing action of the motor is clearly visible from the figure: the DC is connected to the inlet port while its volume increases, whereas the outlet port opens when the volume decreases. It can be observed that there is zero cross porting between the inlet and outlet ports.

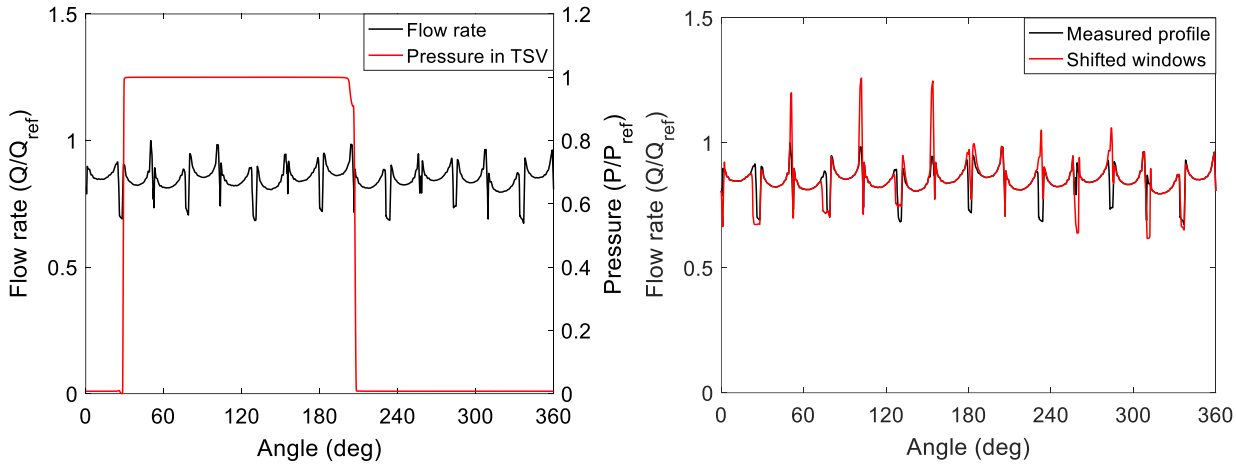

Figure 16. a. Flow rate evaluated in the outlet line and pressure in one of the TSV

b. Comparison of flow ripple of measured profile with the case of shifted windows

The TSV pressure and flow ripple evaluated at one of the operating conditions are shown in fig. 16a. It can be observed that the flow rate is not periodic. This is a result of considering real geometry of rotor, vanes and socket positions in the geometry model. Due to the porting provided, none of the TSVs are subjected to P_{ref} for a small angular duration. This results in a dip of the flow outlet of TSVs through the primary flow path and the leakages, which reflects as dips in the flow rate shown in fig.16a.

To illustrate the sensitivity of flow rate with geometry, one of the measured geometry configurations is modified by shifting the windows manifold (c in fig. 10). The windows manifold is shifted in the $+X$ direction within the assembly tolerance limit. Shifting the windows does not alter the relative opening and closing of inlet/outlet

ports. Instead, the primary affect shifting the windows causes would be a phase shift between the instantaneous displacement volume and the inlet/outlet port areas in different magnitudes for different TSVs. The ideal timing of outlet port opening would be when the displacement chamber volume starts to reduce. The phase shift introduces new timing to different TSVs, some TSVs would be affected by the opening of outlet port earlier than the start of reduction of displacement volume, which would cause a reduction in instantaneous flow rate. For some TSVs, the outlet port would open later than the onset of reduction of volume which causes spikes in instantaneous flow rate. The result of this configuration is compared with that of the unchanged geometrical configuration in fig. 16b. It can be observed that the flow rate has higher magnitude of peaks and dips for larger angular duration for the case of shifted windows. It should be noted that the effect of assembly/machining tolerances of different parts can affect the flow features and should be studied in combination which can be achieved by the current tool.

3.2 Pressure Distribution in the Lubricating Gaps and Leakages

The Reynolds equation is solved for the lubricating gaps between commutator and casing and the lateral lubricating gaps on either sides of the rotor. The resultant reference pressure distribution in the commutator gap and in the lateral gap next to the windows manifold side are presented in fig. 17.

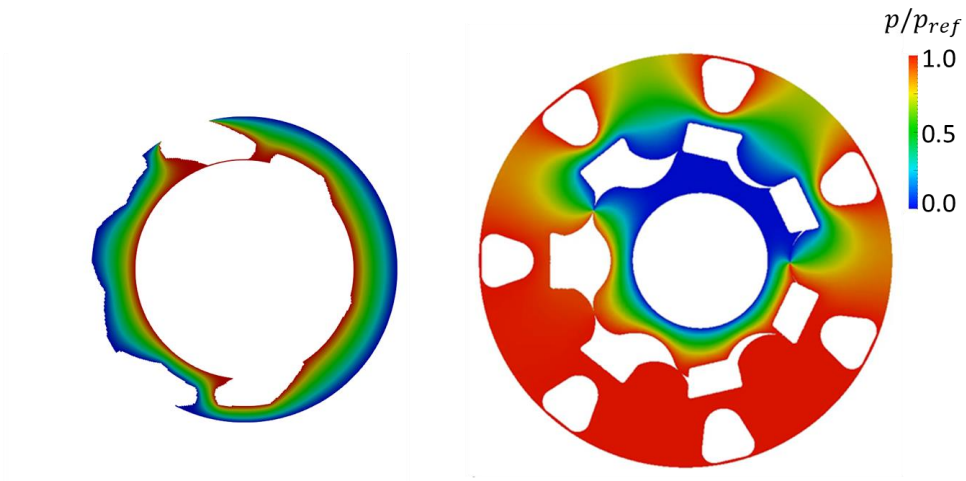

Figure 17. Pressure distribution in the commutator gap and the lateral gap

The leakages are evaluated for different operating conditions and are further accounted in the lumped parameter model to evaluate the net flow rate. Reference leakage values for the lateral gap between rotor and manifold on window side and the commutator gap are presented in fig. 18. The negative values of leakages can be interpreted as flow leaving the environment whereas positive values as flow entering the environment.

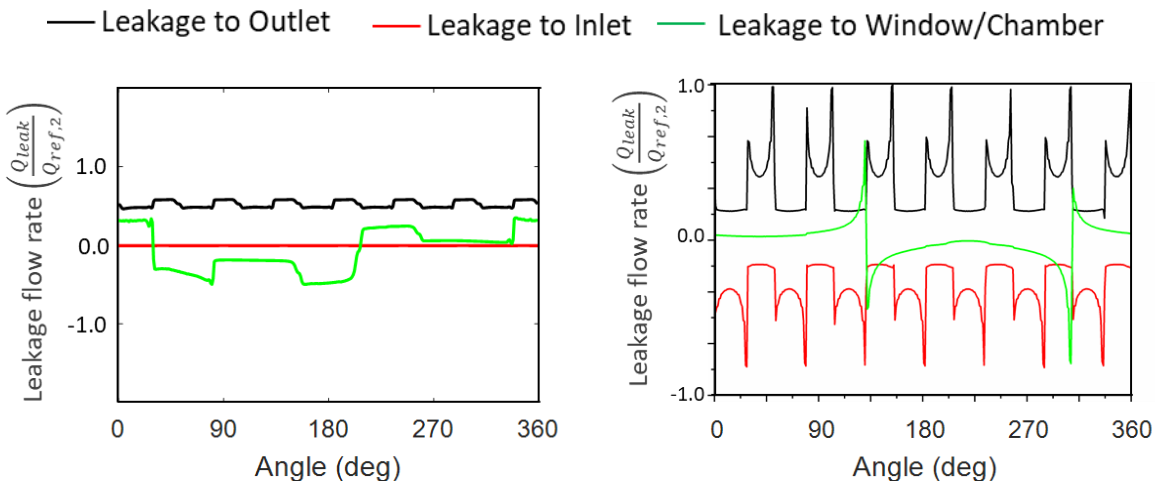

Figure 18. Leakages in the 1. lateral gap and 2. commutator gap

It can be observed that the boundary conditions of the commutator gap and the gaps between the rotor and manifolds are different in nature. The boundary conditions for the commutator gap would always be the inlet and outlet pressures of the motor whereas the boundary conditions of the lateral gap on either sides of the rotor would depend on the instantaneous pressure in the DC volumes between the rotor and vanes. Hence, the commutator gap can be assumed to have Poiseuille flow with fixed pressure differential but varying effective length and height as these properties change with the rotation of rotor. This is considering the fact that for the LSHT application motor, the speed of operation is relatively low and the contribution of Couette term towards the net leakage is marginal. The pressure driven flow can be represented as:

$$Q = \Delta P \cdot \frac{b}{12\mu \cdot l} h^3 \qquad (14)$$

Here the factor, $C = \frac{b}{l}$ has to be evaluated at different angles of rotation of rotor. For this purpose, the gap model is run at different operating conditions to evaluate the leakages at the imposed $\Delta P, h$. The evaluated factor, C, is indeed found to be constant for different $\Delta P, h$ pairs and only a function of the geometry, angle. This resultant factor, C at different pairs of pressure differential and gap height is presented in fig. 19.

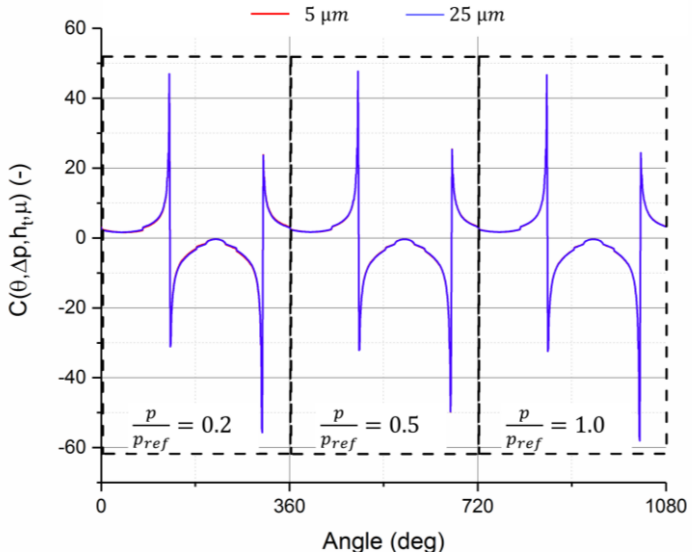

Figure 19. Factor C, evaluated for different pressures and gaps

The factor C is periodic. This shows that it can be passed to the lumped parameter model as a look-up table parameter. This creates the possibility of an on-line coupling of the leakages generated by the commutator with the lumped parameter fluid dynamic model without an off-line CFD simulation. The fluid dynamic model accounts for the leakages in the commutator gap with the introduced factor C as:

$$\underbrace{Q_{leak}(\theta) = \Delta p(\theta)}_{calculated} \cdot \overbrace{\frac{\tilde{h}^3}{12\mu}}^{imposed} \cdot \underbrace{C(\theta)}_{read} \qquad (15)$$

The leakages in lateral lubricating gaps on either sides of the rotor have to be evaluated offline and introduced into the lumped parameter model as the boundary condition depends on the pressure in the DC volumes.

3.3 Volumetric Efficiency

3.3.1 Measured Volumetric Efficiency

A series of tests were performed on different TL240 production units produced by Parker Hannifin corp. The ISO schematic of the experimental setup is presented in fig. 20. Experiments are performed at a specified inlet

flow rate and pressure to the motor to evaluate the volumetric efficiency at constant fluid temperature of 54.4°C. The experiments are performed on 15 randomly selected production units of TL240 orbital motor with hydraulic oil Mobil DTE 26. A four quadrant electric motor is employed as a brake to provide the necessary load to the orbit motor.

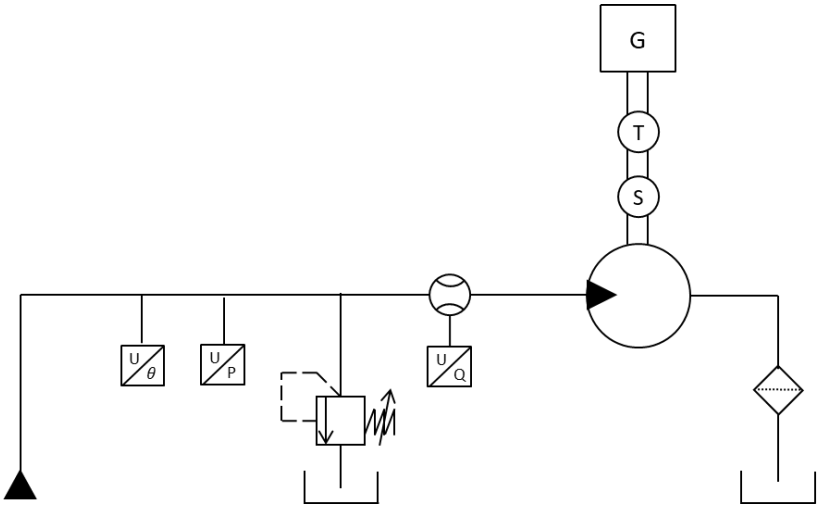

Figure 20. ISO schematic of the test set-up

The mean of the flow rates for these 15 units at different operating conditions is chosen to verify the capability of the simulation model. Also, keeping in mind the variation of results across the units, the coefficient of variation, COV, ratio of standard deviation to mean, is evaluated. The COV represents how reliably the mean value represents the performance of a given production unit. It was observed that the COV is less than 2 for most of the operating conditions measured and 10 at some extreme operating conditions. Because of this, the average of the values measured can be considered as valid and representative of the production units. COV of 10 is observed for low flow rates and high pressures. This is expected because at low flow rates, the contribution of leakages towards net flow rate would be high for a given pressure differential and the leakages are highly dependent on the gap thickness which can vary across the units.

In the present test circuit, a pressure variation of up to 3% of the mean value is observed at many operating conditions. Hence, the instantaneous flow ripple observed from test could not be compared with that of simulation. Instead, volumetric efficiency, a representation of the average flow rate, is evaluated for the validation of simulation tool. The measured volumetric efficiencies are normalized with respect to the maximum volumetric efficiency observed among all the operating conditions and presented in fig. 21.

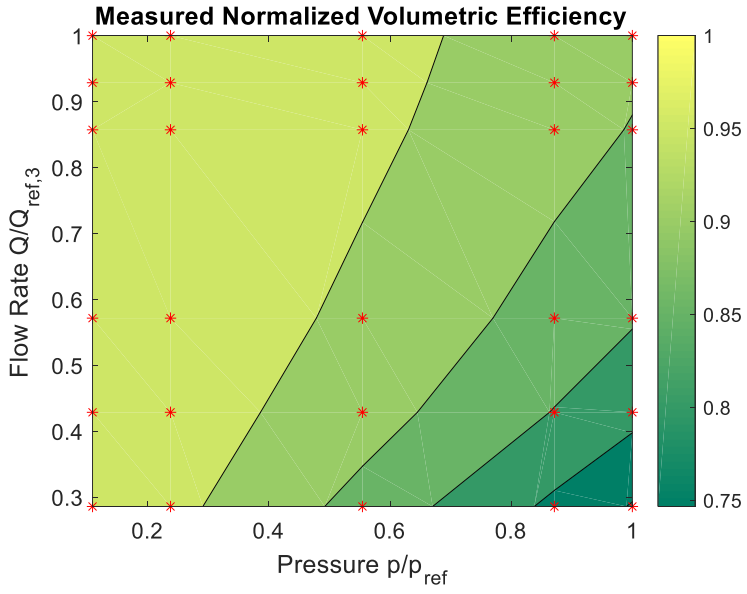

Figure 21. Measured normalized volumetric efficiency map

3.3.2 Validation

The co-simulation between the lumped parameter fluid dynamic model and the gap model is performed till convergence of flow rate for different operating conditions. The comparison of the simulated volumetric efficiency with that of experiments is shown in fig. 22. The simulated volumetric efficiencies are normalized with respect to the maximum volumetric efficiency obtained from the measurements. It can be observed that the simulation model is capable of predicting the flow rate for different operating conditions of the motor. The presented results show good agreement with the measured data and shows the capability of the simulation tool in predicting the flow dynamics of the motor.

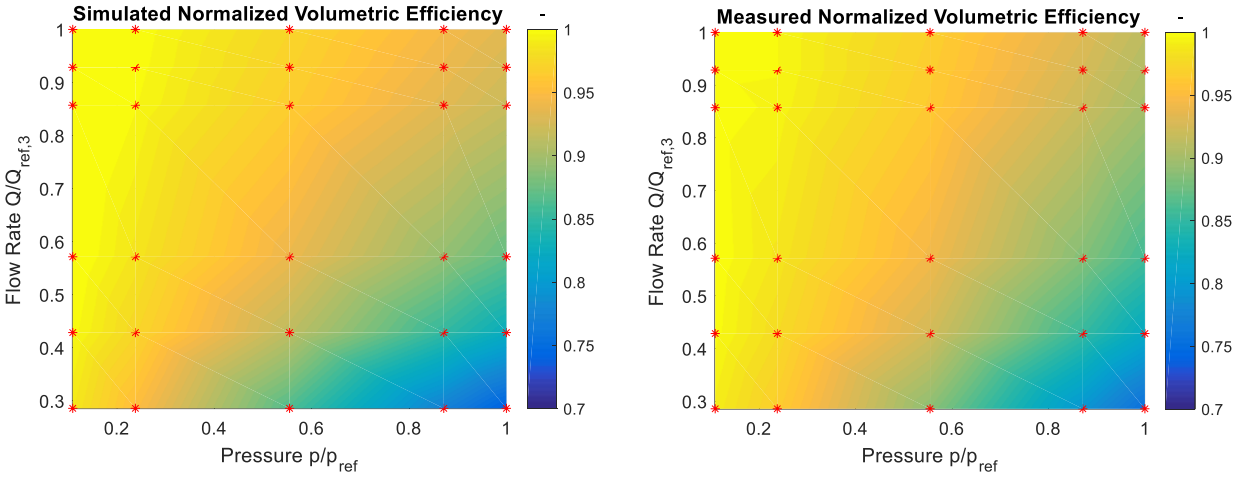

Figure 22. Simulated and Measured volumetric efficiency maps

The absolute difference in percentage error of volumetric efficiency is shown in fig. 23. It can be observed that the maximum error is approximately 2 and it occurs in the region of high COV of the measured results.

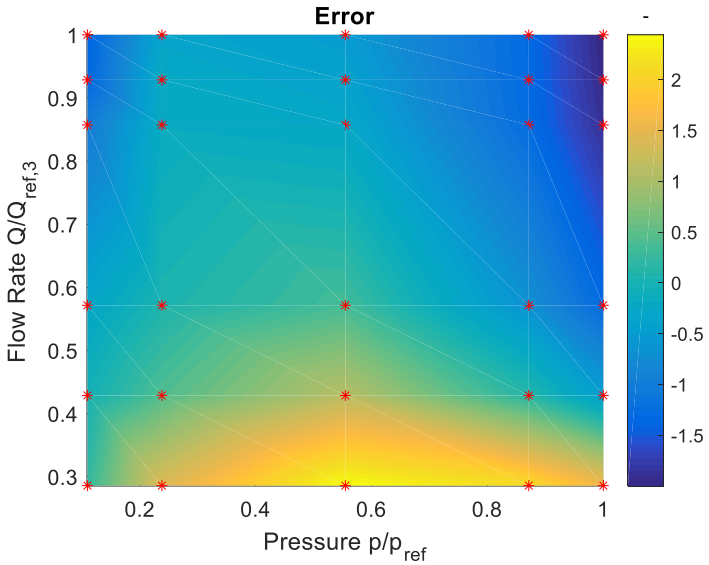

Figure 23. Error between the simulated and measured volumetric efficiencies

4 CONCLUSION

This paper presented an approach for the detailed fluid dynamic simulation of the operation of orbital type machines. The internal flow features such as flow fluctuations as well as volumetric efficiency for different operating conditions can be evaluated by the simulation model created. A geometry module was developed to evaluate the geometrical features of the machines. This geometry module considered the geometrical features

of the commutator, window manifold and the rotor-stator set to provide output of displacement volume, tip gap heights, lengths and port areas. The geometry module considers TXT files of the geometry, thus both nominal and measured profiles can be used as inputs. The lumped parameter fluid dynamic module evaluates the main flow features and permits the extraction of instantaneous chamber pressures and flow fluctuations. The gap module evaluates the leakages through the lubricating gaps present in the machine that has complex geometries. Reynolds equation simplified specific to the current geometry is solved numerically in the gap module. The resultant leakages are provided as input to the lumped parameter model to evaluate the net flow rate. Measurements are performed on the production units of TL240 to evaluate the average volumetric efficiency map. The simulated volumetric efficiency results show good agreement with the measured results thus proving the capabilities of simulation tool. The created simulation tool is fast and can predict the effect of actual machining tolerance. Therefore, the simulation tool can be used in the design process to understand the effect and optimize different design parameters of the unit.

REFERENCES

[1] Nervegna N., 2003, Oleodinamica e Pneumatica, Componenti Vol.2, Anno Accademico 2005-2006.

[2] Michael P., Burgess K., Kimball A., Wanke T., 2009, Hydraulic Fluid Efficiency Studies in Low-Speed High-Torque Motors, SAE 2009 Commercial Vehicle Engineering Congress & Exhibition, 2009-01-2848.

[3] Michael P., Garcia J. M., Scott S B., Devlin M. T., Martini A., 2012, Lubricant Chemistry and Rheology Effects on Hydraulic Motor Starting Efficiency, Tribology Transactions, 55: 549-557.

[4] Garcia J. M., 2011, Surface Effects on Start-up Friction and their Application to Compact Gerotor Motor Design, Ph.D. Thesis, Purdue University.

[5] Maiti R., 1993, Torque Characteristics of Epitrochoid Generated Orbital Rotary Piston Type Hydraulic Motors, Mech. Mach. Theory Vol. 28, No. 2. pp. 225-231.

[6] Dasgupta K., Mukherjee A., Maiti R., 1996, Theoretical and experimental studies of the steady state performance of an orbital rotor low-speed high-torque hydraulic motor, Proc Instn Mech Engrs, Vol 210.

[7] H Ding et al 2012, A CFD model for Orbital Gerotor Motor, IOP Conf. Ser.: Earth Environ. Sci. 15 062006.

[8] Pellegri M., Vacca A., Devendran R., 2016, A Lumped Parameter Approach for GEROTOR Pumps: Model Formulation and Experimental Validation, 10th International Fluid Power Conference, Dresden, Germany.

[9] Pellegri M., Vacca A., Frosina E., Buono D., Senatore A., 2017, Numerical analysis and experimental validation of Gerotor pumps: A comparison between a lumped parameter and a computational fluid dynamics-based approach, J Mechanical Engineering Science, Vol. 231(23) 4413–4430.

[10] Manco S., Nervegna N., Rundo M., 2002, A contribution to the design of hydraulic lube pumps, Int J Fluid Power 3(1):21–32

[11] Schweiger W., Vacca A., 2011, Gerotor pumps for automotive drivetrain applications: a multi domain simulation approach GRPs in AWD-powertrain systems, SAE Int J Passeng Cars Mech Syst 4(3):1358–1376, doi:10.4271/ 2011-01-2272.

[12] TL Series Catalog, [Online], http://www.parker.com/Literature/Hydraulic%20Pump%20&%20Motor/HY13-1590-010-TL-Series.pdf

[13] McCloy D and Martin HR. Control of fluid power: analysis and design. Newyork: E.Horwood, 1980

[14] S. Dhar, A Study of Fluid Structure and Thermal Interactions in the Lubricating Interface Between Gears and Lateral Bushes in External Gear Machines, PhD Thesis, Purdue University, West Lafayette, USA, 2014.

[15] C. Direct, “snappyhexmesh,” [Online], Available: https://www.openfoam.com/documentation/user-guide/snappyHexMesh.php.

Nomenclature

A	Area (m^2)
A_{max}	Maximum port area, inlet/outlet
b	Width (m)
D_h	Hydraulic diameter (m)
DC	Displacement Chamber
G	Generator
ger	Gerotor
h	Height (m)
h_t	Tooth tip gap height
l	Length (m)
l_t	Tooth tip gap length
$\dot{m}$	Mass flow rate (kg/s)
orb	Orbital Motor
P	Perimeter
p	Pressure (Pa)
p_p	Pressure of the inlet/outlet environment
p_{ref}	Maximum operating pressure of the motor
Q	Volumetric flow rate (m^3/s)
Q_{ref}	Average flow rate
$Q_{ref,2}$	Maximum value of leakage
$Q_{ref,3}$	Maximum flow rate for continuous operation of the motor
S	Speed sensor
T	Torque meter
TSV	Tooth Space Volume
V	Volume (m^3)
V_0	Displacement volume of one DC (m^3)
V_{max}	Maximum volume of the DC (m^3)
α	Coefficient of discharge
μ	Fluid viscosity $(Pa \cdot s)$
$\mu_{g,max}$	Maximum of all gap heights
ρ	Density (kg/m^3)
ω	Angular velocity (rad/s)

DOUBLE-PUMP (R)EVOLUTION – HIGHER EFFICIENCY AND LOWER NOISE LEVEL FOR VARIABLE SPEED PUMP DRIVES

Tobias Speicher*, Tobias Thies*, Oliver Kettenhofen+, Jochen Gessat*
htwsaar – Hochschule für Technik und Wirtschaft des Saarlandes, Forschungsgruppe Fluidtechnik, Göbenstraße 40, D-66117 Saarbrücken, Germany*
InnoMa System GmbH, Heinrich-Hertz-Straße 11, D-66773 Schwalbach-Hülzweiler, Germany+
E-Mail: tobias.speicher@htwsaar.de

ABSTRACT

REGARDING THE TREND OF OPTIMIZING ENERGY EFFICIENCY AND MEETING UPCOMING REGULATIONS OF ENERGY CONSUMPTION, THERE ARE MANY WAYS TO REFINE EXISTING HYDRAULIC DRIVE SYSTEMS. BASED ON THE ENERGY-ON-DEMAND STRATEGY, BESIDES VARIABLE DISPLACEMENT APPROACHES, ONE IMPORTANT WAY TOWARDS MORE EFFICIENT SYSTEMS ARE VARIBALE SPEED DRIVEN SYSTEMS. THIS WORK FOCUSES ON VARIABLE SPEED DRIVEN SYSTEMS WITH DOUBLE GEAR PUMPS CONSISTING OF A SMALL HIGH PRESSURE STAGE AND A LARGE STAGE FOR MID/LOW PRESSURE BUT HIGH FLOW LEVELS. COMPARED TO A SYSTEM WITH A LARGE FIXED DISPLACEMENT SINGLE PUMP, THESE SYSTEMS REDUCE THE TORQUE LEVEL NEEDED AT THE DRIVE SHAFT AND THEREFORE ALLOW A SMALLER MOTOR, REDUCING INITIAL COSTS AND INCREASING THE EFFICIENCY. A NEW DOUBLE PUMP CONCEPT USING DIFFERENT PUMP PRINCIPLES FOR HIGH AND MID/LOW PRESSURE STAGE IS INTRODUCED. IT IS SHOWN THAT, COMPARED TO EXISTING SYSTEMS, THE NEW DESIGN IS SUPERIOR IN ENERGY EFFICIENCY AND FLUID BORN NOISE. ALSO ITS BEHAVIOR IN ONE OF THE MOST CHALLENGING OPERATIONAL POINTS, HOLDING HIGH PRESSURE WITH SMALL OR EVEN NO FLOW AT ALL, IS THERMALLY STABLE.

KEYWORDS: Variable Speed Pump Drives, Double Pump Systems, Energy Efficiency, Design Strategy

1. INTRODUCTION

Ever-expanding commodity prices and energy costs fan the flames of the trend towards energy efficient process solutions and increased efficiencies of drive systems. The emphatic demand for CO_2 savings and the optimal utilization of energy in technical applications are already part of legally required guidelines. For manufacturing companies, energy costs are a significant part of their operating costs. Customers of, e.g. machine tools, therefore show intensified interest in power-saving solutions for their machines. The manufacturers of hydraulic drive technologies are hereby obliged to provide drive technologies for energy efficient realization of functions like feed motion, clamping operation et cetera.

In this context, novel system architectures for hydraulic drives gain increasing significance. Valve-controlled systems, as a matter of principle lossy due to their energy losses at the cross sections of the valves, are

replaced by energy on demand drives. Variable displacement pumps or variable speed pump drives allow a needs-based use of the system [1], [2]. Possible savings in energy consumption, compared to conventional hydraulic drives, are estimated to up to 40% [3], what generates significant cost advantages for the user and simultaneously reduces the ecological footprint. First systems were introduced in applications such as forming, cutting and pressing processes [4] as well as in forging or injection molding machines [5], [6]. In the meantime, almost every manufacturer of hydraulic systems offers variable speed pump drives.

Rapid progress in the electrical drive technology has therefore promoted the fast market presence of electro-hydraulic motor-pump-units (MPU). However, there is no continuous development but an assembly of existing components more or less suitable for the individual application. In difference to variable displacement systems, with fixed displacement pumps, this “Bottom-Up” approach can easily lead to oversized systems and therefore misses the target of an energetic and economic optimum.

This issue is addressed by a process-driven „Top-Down“-approach with all tools necessary that allows more efficient process solutions. These are also quantifiable and therefore even permit economic and eco-friendly decisions.

The presented work uses this process-driven approach for the development of a new hybrid type of double-pump (HT-DP) for variable speed driven hydraulics. These systems, consisting of two hydraulic pumps, as shown in *figure 1*, connected to the same drive shaft and driven by one electrical motor, are especially used in applications where high flow and high pressure is needed, but not at the same time. A combination of a small high-pressure pump and a large pump for low pressure and high flow reduces the maximum torque needed and allows the use of a much smaller motor. That reduces the initial costs of the system and, at the same time, increases its efficiency.

This study shows how, by a combination of a high-pressure internal gear pump (IGP) and an external gear pump (EGP) with helical gearing, the system efficiency of a pump drive, used in an automotive folding device, can be further increased. It is also shown that the new system produces only small pressure pulsation and therefore emits less fluid borne noise than existing products. Last but not least, it is shown that the new pump combination also shows good thermal stability for the most challenging operating point in variable speed pump drives - holding high pressure level with only low flow levels.

Figure 1. Currently used double-pump system with two internal gear pumps

2. GEAR PUMP BASICS

Geared machines transform energy with losses, which, as stated by the DIN ISO 4391 [7], divide into two main types of losses (*cf. table 1)*. On the one hand, there are volumetric losses, which are caused by spacing, sealing gaps and pressure- or temperature induced deformation of material. On the other hand, there are hydro-mechanical losses that are caused by friction of moving parts and viscous friction, pressure losses due to flow-deflection in the pump as well as the compressibility of the fluid.

Type of losses	Definition	Sum of losses for a hydraulic pump
Volumetric losses	$\eta_{vol} = \frac{Q_{eff}}{Q_{theo}} = \frac{Q_{eff}}{n \cdot V_{geom}}$	$\eta_{pump} = \eta_{vol} \cdot \eta_{hm} = \frac{Q_{eff}}{n \cdot V_{geom}} \cdot \frac{\Delta p \cdot V_{geom}}{2 \cdot \pi \cdot M_{eff}} = \frac{Q_{eff} \cdot \Delta p}{M_{eff} \cdot \omega}$
Hydro-mechanical losses	$\eta_{hm} = \frac{M_{theo}}{M_{eff}} = \frac{\Delta p \cdot V_{geom}}{2 \cdot \pi \cdot M_{eff}}$	

Table 1. Losses of a hydraulic pump as defined by DIN ISO 4391

Gear pumps, within the group of fixed-displacement pumps, are preferably used mainly due to their cost advantage over other types and are divided by their design into external gear pumps and internal gear pumps.

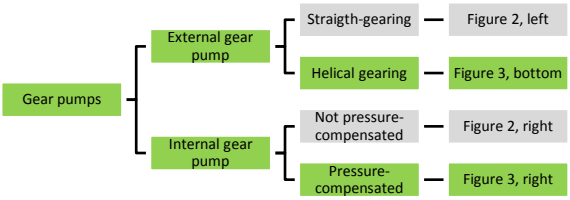

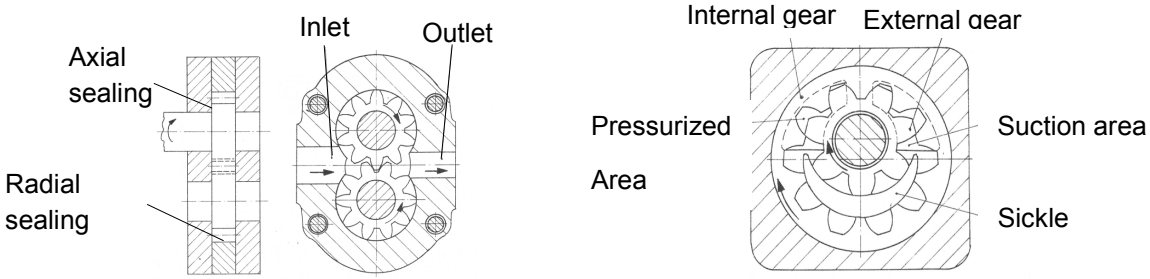

Figure 2. Unifilar drawing of an external and an internal gear pump

For the case of this study, especially two pump designs are taken into consideration. On the one hand a pressure-compensated internal gear pump, especially used for high-pressure applications. This is due to its design that is based on a divided sickle, which reacts to pressure by reducing the spacing between the internal- and external gear and thus minimizing volumetric losses. On the other hand a, also pressure-compensated, helical geared external gear pump that is constructed to reduce flow pulsation and noise emission.

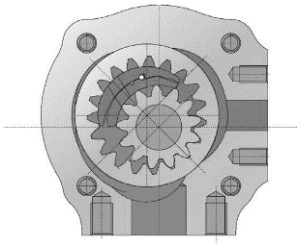

The continuous contact of the two gears allows constant flow without noise emission caused by trapped oil between the tooth flanks. The internal axial forces produced by this type of gearing are compensated with hydrostatic notches, therefore no longer hampering the usability of these pumps [9].

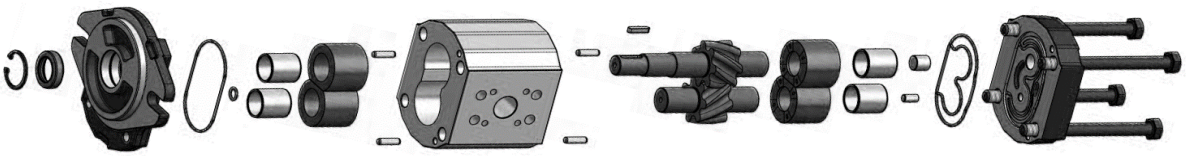

Figure 3. Sectional drawing of a pressure compensated IGP [8], exploded view of a helical geared HEGP [8]

3. ENERGY FLOW ANALYSIS AND EFFICIENCY

The idea to increase energy efficiency by combining different pump principles to the new double-pump layout shown in this work is based on the results of previous studies. There, a process-driven optimization strategy for variable speed pump drives was developed and applied to different systems. This strategy [8] is based on three complementary approaches:

In general, the system efficiency can be optimized by using components with fewer losses or by optimization of existing components especially for their use in applications with variable speed pumps. These measures are combined under the topic “Efficient components”.

Beyond this fundamental requirement to use components as efficient as possible, also the best possible interaction of all pump drive components has to be ensured. An unpropitious combination can shift the point of operation of one component to an unfavorable range, causing an unnecessary decrease of the system efficiency. “Matching pump drive components” therefore is the second approach of optimization.

Finally, no optimization is complete without the inclusion of the process – the systems requirements to the MPU define its points of operation. Vice versa, it is also wise to fit the systems requirements to the strengths and weaknesses of the pump drive. This third approach is the “Adjusted process layout”.

The center of this strategy is the measurement and in-depth analysis of the energy flow of motor-pump-units from its electrical supply to the hydraulic process – from source to function. The energy flow helps identifying the strengths and weaknesses of the components, analyzing interdependencies between the MPU’s components and the interaction with the process.

This analysis is now applied to the process of a variable speed driven folding machine (*cf. figure 4*) in search for a new double-pump solution with best possible efficiency. This process consists of two positioning steps, performed with high flow but only low pressure, and the folding step itself, where high pressure is applied by only minimal flow is needed.

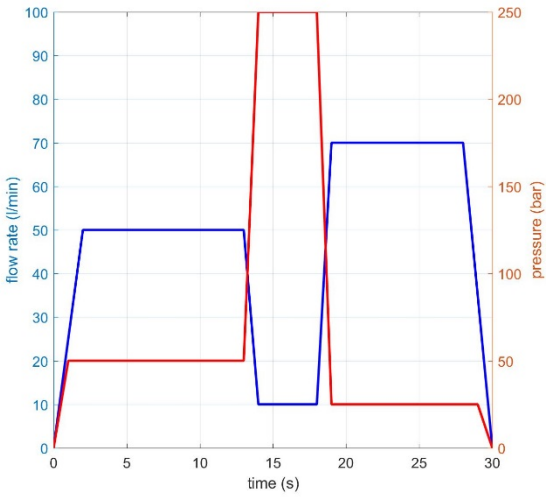

Figure 4. Simplified load cycle of the folding process

3.1. Experiments

The pump studies are based on the standards defined by the ISO 4409 [10] and [11]. Exemplary, those are used as guidance to establish the actual displacement of a pump and measure pump- and system efficiency, as well as regulations on how to depict such measurement results.

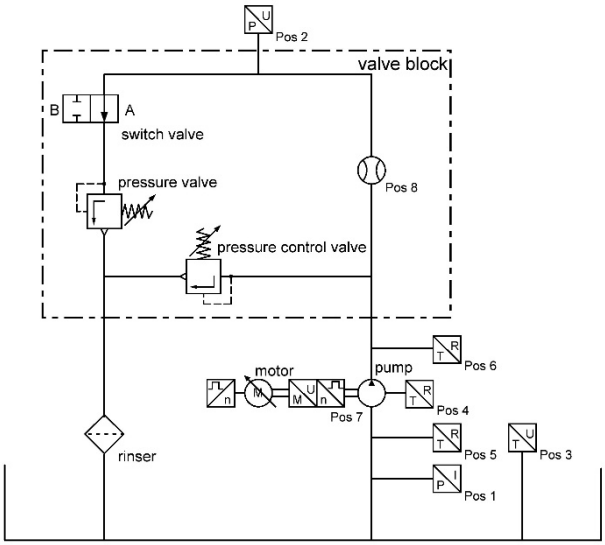

Figure 5. Schematics of pump measurements

Type of sensor	Pos.
Suction pressure	1
System pressure	2
Temperature (oil tank)	3
Temperature (casing)	4
Oil temperature (suction area)	5
Oil temperature (pressurized area)	6
Torque Rotational speed	7
Volume flow	8

Table 2. Overview of Sensors

Measurements of the efficiency produce data for the degree of energy conversion with regard to the overall operating range of the pump and the measuring unit. Boundaries of the operating range are defined by either the pump or the measurement unit as maximum pressure, volume flow, torque as well as temperature limit values of the pump are exceeded. The measurement of the leakage behavior serves as mean to establish the internal leakage whilst building up pressure against a closed tube end. Here internal leakage is the flow volume of oil pressed through sealing gaps from the pressurized area to the suction area.

Figure 5 depicts the schematics of pump measurements and the positioning of the used data sensors (cf. *table 2*) within the system layout.

The switch valve is used to choose between leakage measurement and efficiency measurement. Switch setting A (*open*) enables the circular flow needed for performing the efficiency measurement while switch-setting B (*closed*) closes the circuit to provide the setup needed to run the leakage measurement. The pressure relief valve protects the measurement unit against excess pressure. *Figure 6* illustrates the configuration of the temperature sensors applied to the test pumps. Here, the temperature of the casing, of the oil in the suction area and in the pressurized area as well as the temperature of the oil tank are monitored.

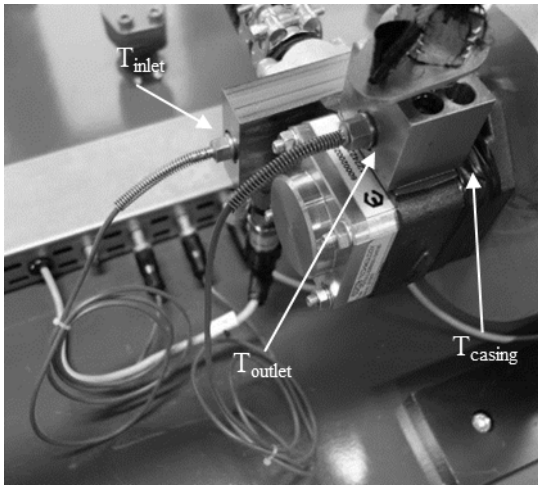

Figure 6. Arrangement of temperature measurement

3.2. Results

Previous studies on pump drives with gear pumps [8] confirmed that the efficiency is not only, as commonly known, depending on the operating point but also highly different throughout pump principles. It reveals that internal gear pumps, particularly with pressure compensation, are by far to be preferred for high-pressure applications, especially when there is also only little flow. In contrast, both types of external gear pumps show much higher energy efficiency when driven at high rotational speed but only small pressure level (cf. *figure 7*).

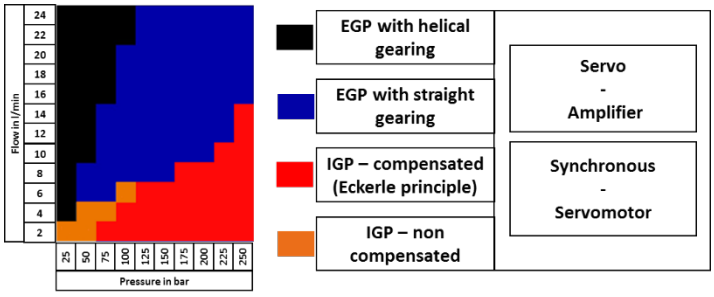

Figure 7. System with highest efficiency - comparison of four pump principles

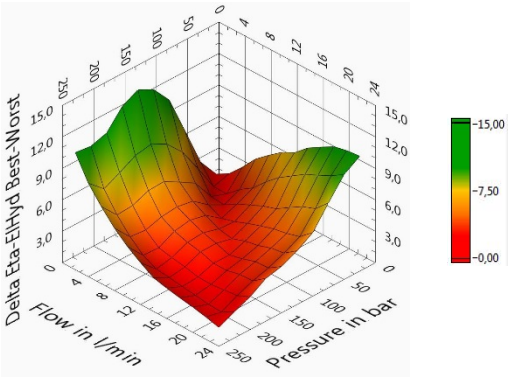

Figure 8. Potential efficiency increase – best to worst system comparison

The potential increase is displayed in figure 8 by the difference of the efficiencies between the best and the worst system and reaches values of more than 10%. For most applications with a single pump, this potential can hardly be used to the fullest because every state of operation has to be done by the same pump.

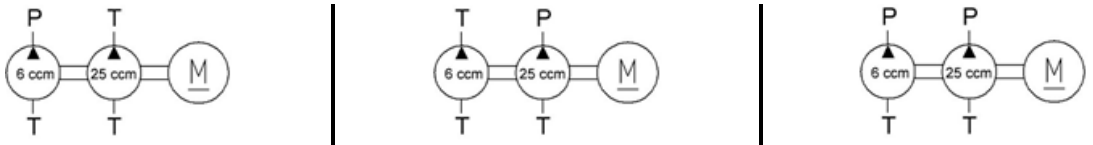

Mode 1 - pressure only applied to 6cm³ stage

Folding device: p up to 250bar, n up to 2000rpm

Mode 2 – pressure only applied to 25cm³ stage

Folding device: not used

Mode 3 – pressure applied to both stages

Folding device: p up to 50bar, n up to 2500rpm

Figure 9. Three modes of operation

For example, the internal gear pump that performs best at high pressures also has to work at high rotational speed and low pressure where, compared to an external gear pump, its efficiency decreases. However, for

double-pump systems where the function of each stage is separated, this situation changes - a combination of two principles makes the full potential accessible. To verify the success, two state of the art single type double-pump (ST-DP) systems are examined to provide the reference point of efficiency.

Both double-pumps are a combination of a 6cm³ and a 25cm³ pump, one with two internal gear pumps (IGP ST-DP) and the other with two external gear pumps (HEGP ST-DP), in this case with helical gearing. All three possible modes of operation, as shown in *figure 9*, are tested but only modes 1 and 3 are now further investigated, because mode 2 is not only rarely used but also shows similar behavior as mode 3.

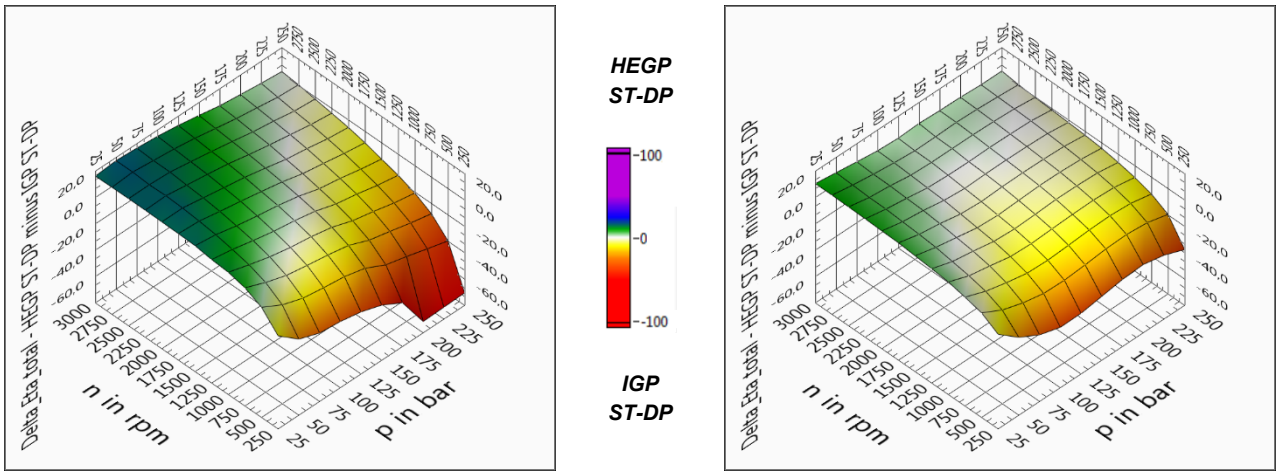

Figure 10. Difference in double-pump efficiency for mode 1 operation

Figure 11. Difference in double-pump efficiency for mode 3 operation

Figures 10 and *11* show the differences between the efficiencies of the two single type double-pump systems. They reveal the same strengths and weaknesses as for single pump systems, the superior efficiency of the internal gear double-pump for high pressure and of the external helical gear double-pump for high flow.

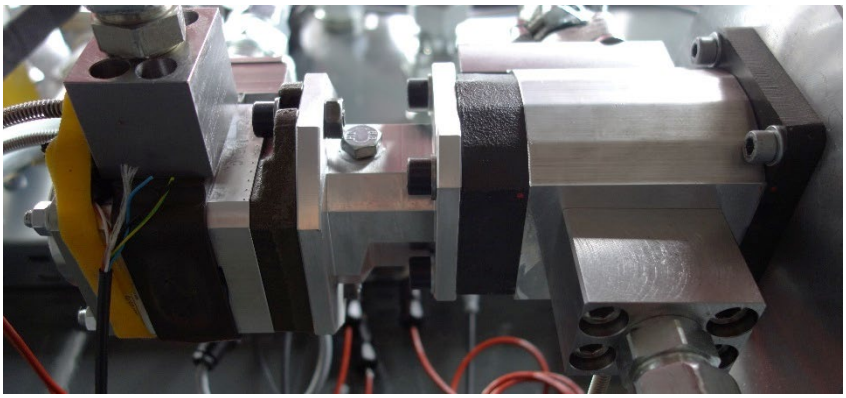

Figure 12. Hybrid type double-pump (HT-DP) with IGP (left) and HEGP (right) on the test rig

To access these superior efficiencies, the new hybrid type double-pump uses a 6cm³ internal gear pump for high pressure together with a 25cm³ external gear pump with helical shaped teeth for low pressure and high flow. *Figure 12* shows the HT-DP with the mechanical adaptation of the two pumps on a single drive shaft mounted to the test rig.

Name	HEGP-6	HEGP-25	HEGP-DP	IGP-6	IGP-25	IGP-DP
Displacement	6.4 cm3	25.2 cm3	31.2 cm3	6.3 cm3	25.2 cm3	30.7 cm3
Nominal Pressure	275 bar	208 bar	225 bar	330 bar	250 bar	250 bar
Max. RPM	3600 rpm	2500 rpm	2500 rpm	4000 rpm	3000 rpm	2500 rpm

(HEGP-DP = HEGP-6 and HEGP-25, IGP-DP = IGP-6 and IGP-25, HT-DP = IGP-6 and HEGP-25)

Table 3. Specifications of the pumps researched

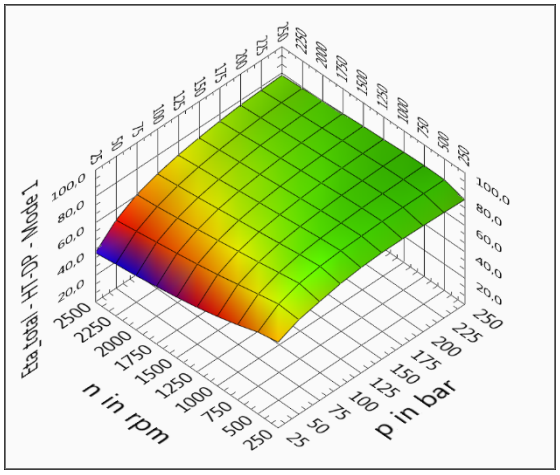

Figure 13. Pump efficiency of the hybrid type double-pump for mode 1 operation

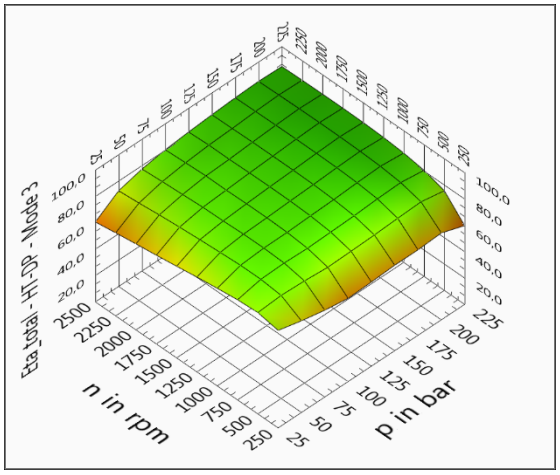

Figure 14. Pump efficiency of the hybrid type double-pump for mode 3 operation

A comparison of the efficiencies of the hybrid type double-pump to the single type internal gear double-pump shows that efficiency increases as expected. In mode 1, with only the 6cm³ internal gear pump applying pressure, the efficiency increases for the whole working range of the double-pump (cf. *figure 15*). Especially for high pressure and very low rotational speeds, the increase is up to 10%. With higher rotational speed, the gain in efficiency decreases but is still higher than for the single type internal gear double-pump. The better efficiency is possible because the 25cm³ external helical gear pump, with less internal friction than the internal gear pump, produces fewer losses when idling.

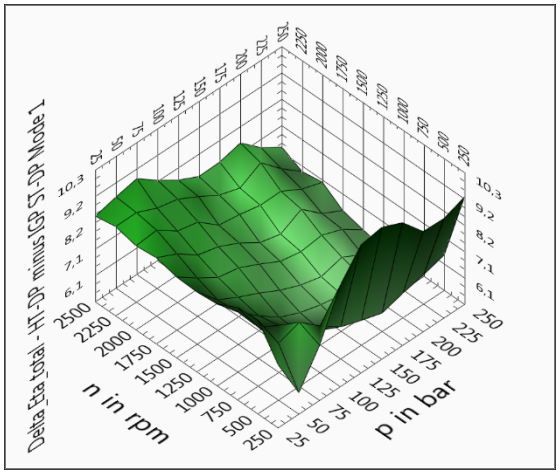

Figure 15. Difference in efficiency between the HT-DP and internal gear ST-DP for mode 1 operation

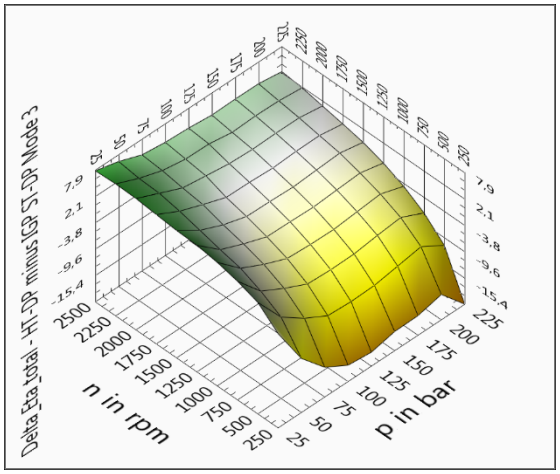

Figure 16. Difference in efficiency between the HT-DP and internal gear ST-DP for mode 3 operation

For mode 3 with both pump stages applying pressure, the situation changes. Here, an increased efficiency shows only for high rotational speeds and lower pressure. Up to 8% higher efficiency is possible (cf. *figure 16*) for highest speed in combination with low pressure. With increasing pressure and lower rotational speed, the situation changes and the efficiency of the internal gear double-pump is superior. This is mainly due to the higher internal leakages and increasing hydro-mechanical losses of the helical geared pump at higher pressures. Nevertheless, taking the process into consideration, this part of the working range is not relevant and therefore this is no disadvantage.

The pump shall deliver high flow at lower pressure (in mode 3, about 2500 rpm with less than 50bar) and high pressures at lower speeds (in mode 1, less than 2000 rpm with up to 250bar), and for both operational points, the new hybrid type double-pump is up to 10% more efficient than a current state of the art system such as the internal gear system.

4. PRESSURE PULSATION

A second topic that needs to be addressed when developing a pump or pump drive system is the pulsation of flow and pressure. Especially the pressure pulsation not only causes fluid born noise and therefore negatively effects the user comfort but also influences functions and, in combination with the line system connected, can cause serious damages when amplified by resonances.

4.1. Experiments

The measurement of the pressure pulsation is performed with a special test rig [12] using a RaLa, a low-reflection line terminator (cf. *figure 17*). This component allows, by adjustment of its wave resistance to that of the line coming from the pump, a minimization of wave reflections and resulting resonances in the measurement system. This adjustment is carried out by an orifice with downstream balancing volume.

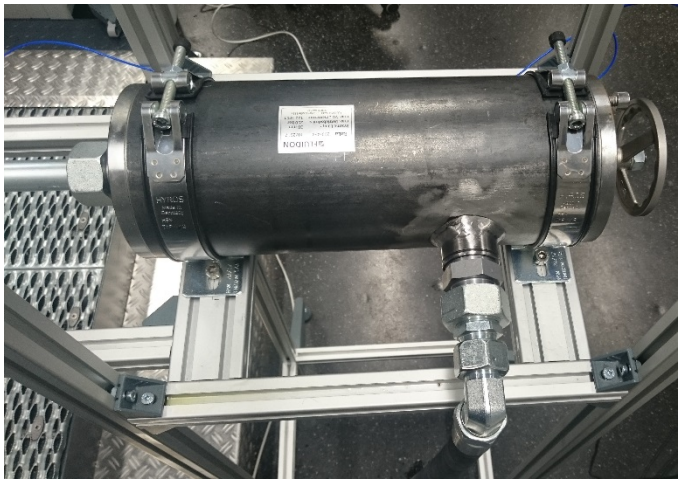

Figure 17. Low-reflection line terminator (RaLa)

The pressure pulsation is measured at two places by piezoelectric pressure transducers, placed exactly one meter apart from each other. One is placed next to the pump outlet, the other one next to the RaLa.

Every part of the line system from the pump outlet to the RaLa has exactly the same diameter, because any change in diameter would cause additional reflections, which would have a negative influence to the results. By use of that special test rig layout (cf. *figure 18*), it is now possible to measure the pressure pulsation with nearly no influence of the rig itself.

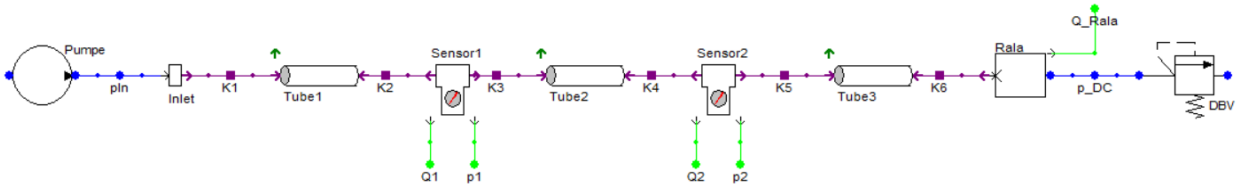

Figure 18. Schematic of the test rig for pressure pulsation measurement, displayed by its DSHplus model

For the design of the new hybrid-type double-pump, three types of pump principles are taken into consideration. These are the pressure compensated internal gear pump with divided sickle and two external gear pumps, one type with straight and one with helical gearing. Both types of external gear pumps meet the demands in terms of efficiency but there are huge differences in matters of noise level and pressure pulsation. A comparison of the three pulsations (cf. *figure 19*) shows results as expected and in accordance to literature [10], [11]. The highest pulsation with more than 2.5 bar peak-to-peak shows the external gear pump with straight gearing, mostly caused by oil trapped between the teeth flanks where the two gears interact. The internal gear pump shows less pulsation, only about 1 bar peak-to-peak. For both pumps, the measured pulsation frequency is the product of the number of teeth (in this case 12 teeth for the external and 13 teeth for the inner gear of the internal gear pump) and the rotational speed.

On the other end of the spectrum is the pump with helical gearing that has less than 0.5 bar of peak-to-peak pulsation. This is due to the shape of teeth that provides nearly constant flow and due to the missing of trapped oil between tooth flanks, usually the main reason for pressure pulsation and noise emission in gear pumps.

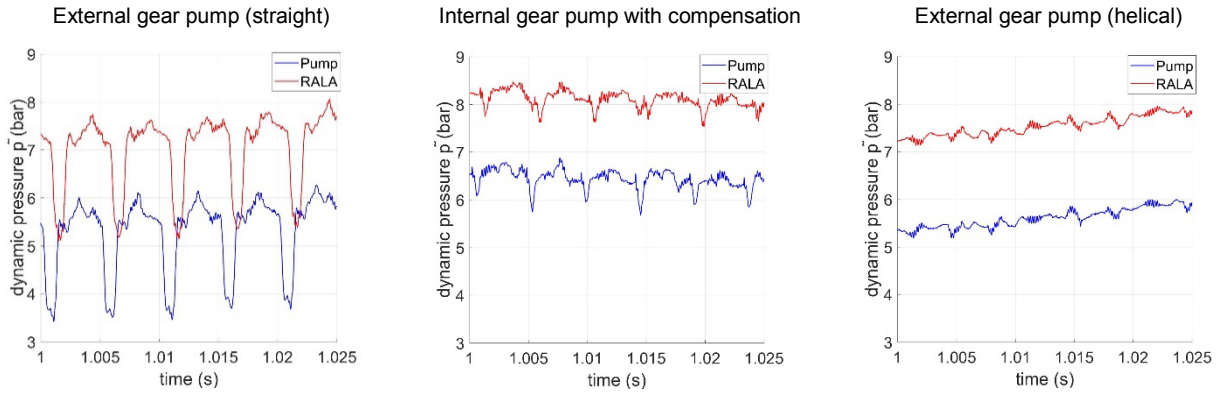

Figure 19. Dynamic pressure pulsation of different gear pumps – signals of pressure transducers next to the pump and the RaLa without offset correction (@ 150 bar and 1000 rpm)

Besides the influence of the pump principle, the two additional influences are the rotational speed and the pressure level. Both are shown in the figures above for the internal gear pump. With increasing rotational speed, the pressure pulsation also increases (cf. *figure 20*) – this is due to the faster pressurization of the oil trapped between the gear flanks. Pressure pulsation also increases when higher pressure is applied (cf. *figure 21*).

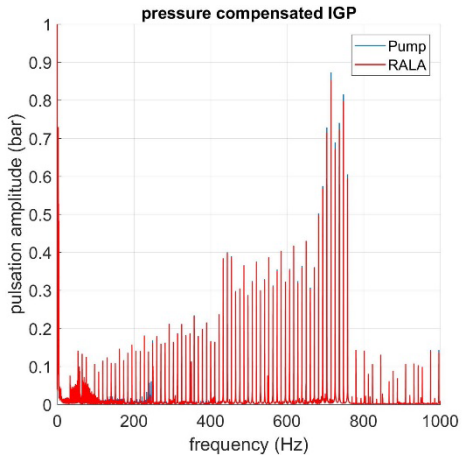

Figure 20. Spectrum of pressure pulsation for this internal gear pump at 150 bar for 250 to 3500 rpm in steps of 50 rpm

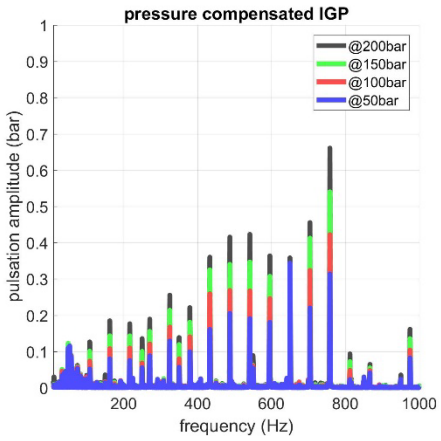

Figure 21. Spectrum of pressure pulsation for this internal gear pump – influence of pressure level

4.2. Results

A boundary condition of the folding device the hybrid-type double-pump is designed for, as introduced in chapter 3, is that the maximum peak-to-peak pulsation of the pump may not exceed 1bar. With the helical geared pump, especially at pressures not exceeding 100 bar, this critical value is no restraint. For the high-pressure stage with internal gear pump, the maximum permissible value is only exceeded for maximum speed and a pressure level of 150bar and higher. Overall, these operational points shall not be used or other measures must be taken, e.g. dampening by use of adjusted hose lines [15].

5. THERMAL BEHAVIOUR

Efficiency not only is about saving money or becoming eco-friendly, the losses also have major influence on the thermal behavior of each pump. Especially, this becomes significant for variable speed pump drives where, in contrast to conventional hydraulic systems, more challenging load states occur. The thermally most

challenging is providing high pressure but with little or even no flow at all, e.g. for positioning action of a load or applications like a hydraulic press. Without the cooling effect of the hydraulic fluid flowing through, the pump heats up and can reach or even exceed its temperature limit, which causes increased wearing or even failure. Therefore, another requirement to the hybrid-type double-pump, to all variable pump drives, is a good thermal behavior under these harsh load conditions. It is known that internal gear pumps are able to perform in pressure hold systems [13], [14], but because thermal behavior is critical for the process the hybrid-type double-pump will be applied to, it is further examined.

5.1. Experiments

The aim of these experiments is to find out how long a pump chosen for the high-pressure stage of the hybrid-type double-pump can hold pressure. To create a measure for the thermal behavior, the pumps are monitored when performing the worst-case scenario – pressure hold. The valve connecting the pump to the load simulation unit is closed, the pressure then adjusted to 200 bar, the peak pressure applied in the process the pump is applied to, by controlling the rotational speed of the pump. The pump speed is only a result of its internal leakages that need to be compensated to hold the pressure level and a small external leakage (0.1 l/min) defined by the process. Therefore, besides the small power to the external leakage flow, all mechanical power at the pumps drive shaft is transformed into thermal energy inside the pump. Without an appreciable oil flow and its cooling effect, the pump can only cool down by emitting thermal energy to the surrounding air by convection. There can also be heat transfer between the pump and the motor, its direction depending on the system and load situation. The test starts with the test rig, pump and components necessary for pump adaption at 40 °C (+/-1 °C) and is finished when the pump temperature exceeds the allowed range (in this case 90 °C) or if the temperature reaches a constant value (does change less than 0.5 °C in 10 minutes time).

5.2. Results

It shows that the temperature of the pump housing in proximity to the bearings as a function of time provides us with a suitable measure to compare the thermal behavior of pumps to each other. This temperature is chosen because it represents the median of the different temperatures measured and is the least susceptible to external influences. In *figure 22*, this temperature is displayed for pumps with different displacements, three internal and, for a better rating of the results two external gear pumps. In addition to the temperature*, figure 23* shows the power that is, due to the losses, transferred into thermal energy and heats up the pump. Three effects influencing the temperature behavior can be identified.

Name	EGP-8ccm	EGP-19ccm	IGP-6ccm	IGP-8ccm	IGP-19ccm
Displacement	8.2 cm3	18.8 cm3	6.3 cm3	7.8 cm3	19 cm3
Leakage @ 200 bar, 40 °C	0.98 l/min	1.4 l/min	0.17 l/min	0.4 l/min	0.39 l/min
Principle	External gear pump		Internal gear pump		

Table 4. Overview of the five pumps compared

First, as expected, it shows that especially the two external gear pumps (cf. red and dark blue curves in *figure 22*) are not eligible to hold pressure for more than a few seconds; they reach their temperature limit after two respectively 6 minutes. That situations changes for the three internal gear pumps with pressure compensation where the two smaller pumps even reach a constant temperature level far below their limit, allowing them to hold pressure also for longer periods. This huge difference is mainly caused by the much higher internal leakages of the external gear pumps (cf. *table 4*) and the resulting higher rotational speed needed to compensate it. Therefore, the power at the pump drive shaft is also much higher, thus increasing the thermal energy added to the pump. This leads to the first conclusion – typical external gear pumps are less suitable for applications where pressure hold appears for longer phases, internal gear pumps should be preferred.

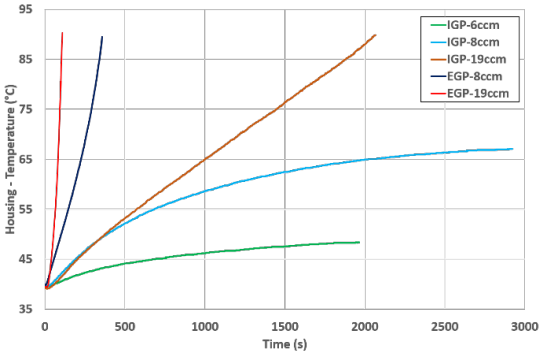

Figure 22. Pump housing temperature over time

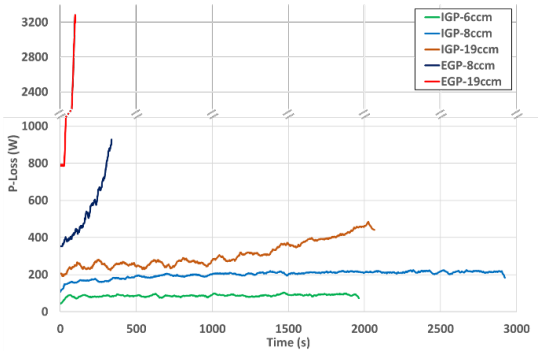

Figure 23. Power transferred into thermal energy due to volumetric losses and friction

Secondly, the different temperature dependencies on the leakages for the two principles show its huge influence when comparing EGP-19ccm and IGP-19ccm in *figures 22* and *23*. Both pumps reach their temperature limit at 90 °C, but the increase of power that is transformed to thermal energy is significantly different, caused by their leakages. For the internal gear pump, power only increases to 2.5 times the initial value, from about 200 W at 40 °C to less that 500 W at 90 °C, but for the external gear pump, this is to 4 times its initial value, from 800 W at 40 °C to more that 3200 W at 90 °C. This is another characteristic in favor of internal gear pumps. To this point, the results are according to the results presented in literature [13].

Finally, there is the interaction between pump size and its displacement, which is the most significant effect for the design process of the hybrid-type double-pump. It is illustrated by the comparison of the three internal gear pumps, all size-two pumps but with different displacements and different thermal behavior. This is a result of the balance between input and dissipation of heat. Besides the small amount of thermal energy that is transported by the small external leakage flow, their ability to dissipate warmth to the surroundings is only defined by the geometry of the housing and the connection to the motor. There, the difference between the three pumps is only minor, because the only differences in their geometry are the width of their gear, to achieve different displacements, and the corresponding difference in the length of the housing. Therefore, the different behavior of the three pumps is a result of the different heat input, as shown in *figure 23*. Only with small displacement, the amount of heat produced by the internal losses is smaller than the amount of heat that can be dissipated and the pump does not overheat. It can be concluded that for applications with longer periods of pressure hold, only small internal gear pumps show an uncritical thermal behavior. Larger pumps produce too much heat due to their higher losses, the time span for pressure hold operation is shortened. This proves another advantage of the introduced hybrid-type double-pump layout.

6. SUMMARY AND CONCLUSION

This paper introduces a new hybrid type double-pump consisting of an internal gear pump as small stage (6cm^3) and an external gear pump with helical gearing as large stage (25cm^3). It is proposed for applications where high pressure and high flow is needed, but mostly not simultaneously. Using the previously introduced optimization strategy [8], it shows that using the small stage for high-pressure operation and both stages together to provide high flow, this allows up to 10% increase in efficiency in comparison to state of the art systems. Further, its pressure pulsation is examined and it is proven that, by use of the helical geared pump as the large stage, the pulsation and noise emission can be minimized.

Finally, the thermal behavior under harsh load conditions is addressed. On the example of the worst-case scenario, continuous pressure hold without flow through the pump, internal and external gear pumps are compared. It shows that the small displacement internal gear pump, as used for the high-pressure stage of the introduced hybrid-type double-pump, is the best option for this load case and can provide long time performance without overheating. For all three topics, the introduced pump has at least equal but mostly superior properties compared to state of the art systems.

As an overall conclusion, it can be stated that revolution and evolution are not mutually exclusive. It needs a combination of both to create new and improved systems. Revolutions, like combining two different pump principles, together with evolutions, like the optimal combination of components by use of innovative, process-driven optimization approaches.

7. ACKNOWLEDGEMENTS

The work in this paper is part of the project “EFIplus – Effizienzsteigerung und Zuverlässigkeitsoptimierung energiesparender Motorpumpen-Aggregate”, funded by the BMBF (German Federal Ministry of Education and Research, FKZ:13FH021IX4). The permission for publication is gratefully acknowledged.

REFERENCES

[1] Helbig, A. 2007. Energieeffizientes elektrisch-hydraulisches Antriebssystem am Beispiel der Kunststoff-Spritzgießmaschine, Diss. TU Dresden, Germany.

[2] Neubert, T. 2002. Untersuchung von drehzahlveränderbaren Pumpen, Diss. TU Dresden, Germany

[3] Götze et.al. 2014. Energetisch-wirtschaftliche Bewertung des Einsatzes drehzahlgeregelter Antriebe in Werkzeugmaschinen, TU Chemniz, Germany.

[4] Brahmer, B. 2012. CLDP – Hybrid Drive using Servo Pump in Closed Loop, Voith Turbo H+L, Eighth International Fluid Power Conference, May 26-28 2012, IFK Dresden, Germany.

[5] Siemer, E. 2012. Variable-Speed Pump Drive System for a 5000 kN Ring Expander, Eighth International Fluid Power Conference, May 26-28 2012, IFK Dresden, Germany.

[6] Schiffers, R. 2012. Energy Efficiency of Various Hydraulic Drives used in Injection Moulding Machines, Eighth International Fluid Power Conference, May 26-28 2012, IFK Dresden, Germany.

[7] DIN ISO 4391:1984-10, Hydraulic fluid power, pumps, motors and integral transmissions, parameter definitions and letter symbols

[8] Speicher, T. 2018. Process-driven component adjustment on variable speed pump drives – development of a strategy to increase the overall energy efficiency, Eleventh International Fluid Power Conference, March 19-21 2018, IFK Aachen, Germany.

[9] Bosch Rexroth, AZPJ External Gear Pump - Silence Plus – Datasheet RD 10094, 07/2016

[10] ISO 4409:2007, Hydraulic fluid power -- Positive-displacement pumps, motors and integral transmissions -- Methods of testing and presenting basic steady state performance.

[11] Ivantysyn, J.+M. 1993. Hydrostatische Pumpen und Motoren, Vogel Fachbuch, Würzburg, Germany.

[12] Goenechea, E. 2007. Mechatronische Systeme zur Pulsationsminderung hydrostatischer Verdrängereinheiten, RWTH Aachen, Dissertation, Aachen, Germany.

[13] Kazama, T. 2015 Comparison of temperature measurements and thermal characteristics of hydraulic piston, vane and gear pumps, J-Stage Mechanical Engineering Journal, Japan

[14] Lana, E. 2006 A New Evaluation Method for Hydraulic Gear Pump Efficiency through Temperature Measurements, SAE 2006

[15] Speicher, T., Baum, H. 2014 New system optimization opportunities by simulation based line tuning, Ninth International Fluid Power Conference, March 24-26 2014, IFK Aachen, Germany.

MULTI-DISCIPLINARY MODEL FOR PRELIMINARY DESIGN OF ELECTRO-MECHANICAL SERVO PUMP

Xu Han*, Tatiana Minav**, Jian Fu*, Yongling Fu*, Matti Pietola**,Peng Zhang***
*Beihang University, 37 Xueyuan Road, Haidian District, Beijing, China
** Aalto University, Otakaari 1, 02150 Espoo, Finland
*** Beijing Institute of Precision Mechatronics and Controls, Beijing, China
E-mail thanxu@buaa.edu.cn

ABSTRACT

A new electro-mechanical servo pump (EMSP) is proposed for high-power variable pump fixed motor electro-hydrostatic actuator for heavy-duty vehicle application. The EMSP has a highly integrated structure with the displacement regulating unit inside the same shell. This results in more challenges for sizing during design stage. Therefore, a dedicated multidisciplinary model for the EMSP preliminary design is presented in this paper. Initially model parameters are analysed and classified into different categories. As a result, only a fraction of parameters such as pump displacement, motor nominal torque, etc. was employed for active EMSP sizing to achieve more effective trade off and optimization. Rest of parameters were generated automatically with various methods such as scaling laws, product database, and empirical equations. Next, the hydraulic, electrical and thermal dynamic characteristics were investigated in the model. Finally, a multidisciplinary model equipped with the parameter generation tools was proposed as a practical tool for the EMSP preliminary design. At last, dynamic simulation results of hydraulic, electrical and thermal under typical cycles were utilised to verify the model functionality. The performance of the given EMSP design option can be evaluated by the proposed model, which makes the preliminary design and optimization feasible.

KEYWORDS: electro-mechanical servo pump, preliminary design, multi-disciplinary model, limited parameters, fixed motor variable pump electro-hydrostatic actuator

1. INTRODUCTION

Nowadays, development of the vehicles is proceeding to electrification for economic and environmental reasons. Accordingly, it is beneficial if the actuators utilised in the vehicles would be more electrical. So, the development of electro-mechanical actuator (EMA) and electro-hydrostatic actuator (EHA) is emerging [1]. According to [2], two basic types of EHAs are available: variable motor fixed pump EHA (EHA-VMFP) and fixed motor variable pump EHA (EHA-FMVP). At the early stage of EHA development, the EHA-VMFP was preferred for its simplicity and thermal aspect advantages [3]. However, with the evolution of the vehicles, new requirements for actuators are demanded. For instance, higher power actuators are required for heavy-lift launch vehicles for the deep space exploration plans in US and China [4]. Meanwhile, EHAs are also being brought into many heavy marine vehicles [5]. However, applications in these heavy vehicles usually require actuators with power more than 40 kW. This high level power leads to the Electro-Magnetic Interference (EMI) and heat generation issues of the EHA-VMFP power electronics becomes more challenging. In addition, the dynamic performance also degrades since high power servo motors cannot achieve so high dynamics as low

power ones. Therefore, EHA-FMVP becomes more attractive for these applications because of its low power control unit, i.e. the pump displacement control unit.

To be consistent with the more electric actuator concept, the control unit of the variable pump that equipped in the EHA-FMVP should be driven by an electric motor directly, rather than the common utilised solution based on cylinder and valve. Figure 1 illustrates additional hydraulic circuit, which is required for hydraulically controlled pump and proposed electrically driven solution. The electrical unit also achieves better contamination resistance ability than hydraulic control unit. Therefore, a new electro-mechanical variable displacement servo pump specially for EHA-FMVP application is under development. In this new proposed design, the cylinder and control valve of the conventional axial piston servo pump are replaced with a ball screw and a variable speed servo motor, as displayed in Figure 2. All components are integrated inside one common shell, which allows this new pump to be more compact and omit the auxiliary hydraulic power for displacement control.

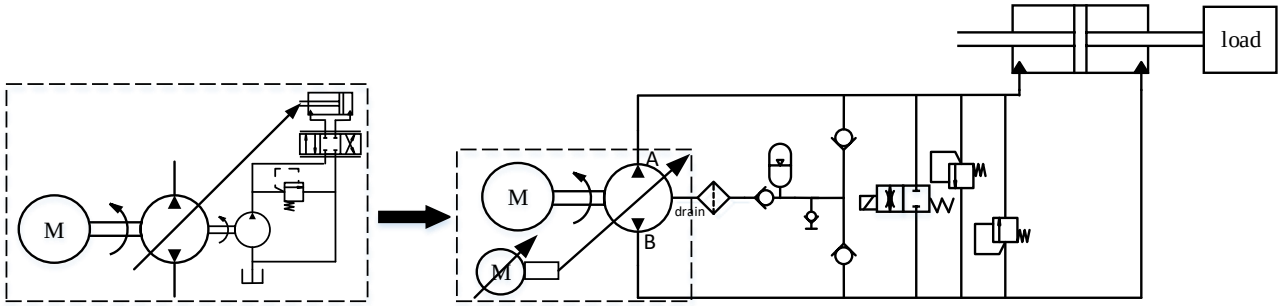

Figure 1. EHA-FMVP equipped with electro-variable displacement pump

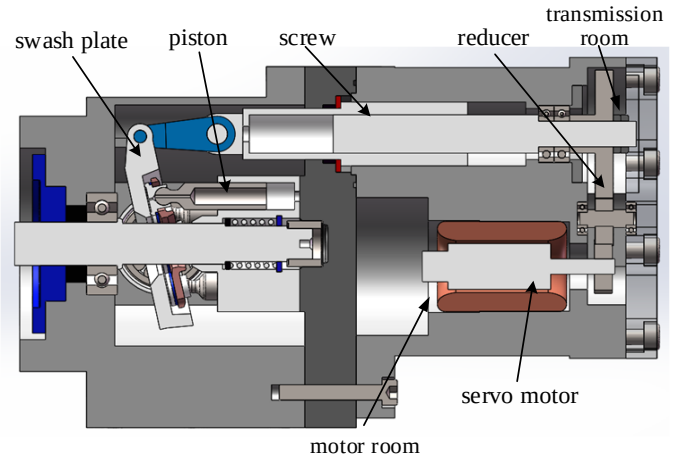

Figure 2. The section view of the electro-mechanical servo pump (EMSP)

The integrated structure of this new pump requires careful sizing during design phase due to a nature of this highly coupled multi-disciplinary product. The development process of the electro-mechanical servo pump is illustrated in Figure 3. In the preliminary design phase, dominated parameters should be iteratively defined to meet the performance requirements. Modelling and simulation is the most efficient method to assess each design option and reduce effort. Hence, a multi-disciplinary model that can simulate the product attributes with different sets of dominated parameters is necessary. However, only limited information is available in the preliminary design phase, resulting to difficulties in determining model parameters. On the other hand, only a fraction of model parameters can be actively regulated during optimization design, rather than changing all the parameters at the same time. Therefore, this paper concentrates on development of a multi-disciplinary model with automatic parameter generation functions for the preliminary design of the electro-mechanical servo pump (EMSP).

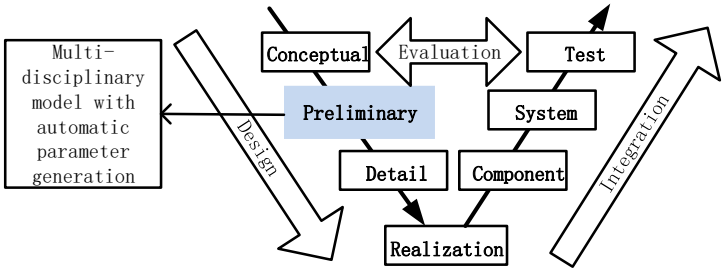

Figure 3. Development process of the electro-mechanical servo pump (EMSP)

In this paper, the hydraulic, electrical and thermal multi-disciplinary dynamic model for preliminary design of the electro-mechanical variable displacement servo pump is developed. First, the EMSP is introduced and the dominant parameters in the preliminary design are selected and analysed. Second, the hydraulic and electrical dynamic model is established and investigated in following sections. Third, the lumped parameter thermal model module is added to the dynamic model. At last, simulation based on the developed model is conducted to verify the model functionality.

2. FORMULATION OF MODEL PARAMETERS

The electro-mechanical servo pump consists of several major components. During the preliminary design, each major component of EMSP needs to be depicted with numbers of parameters. All parameters of these major components named as dominant parameters. However, to trade off and optimize the EMSP from a system point of view, only limited parameters can be treated as the active variable parameters in order to speed up process of preliminary design stage. In addition, only limited parameters permissible for actively adjusting as dominated parameters are usually not independent, e.g. the inertia of the motor rotor depends on the motor power, torque and structure design. Therefore, the model utilises only a fraction of parameters, that named as active parameters in this study. Other parameters should be generated automatically. Thus, the parameter identification and classification is the background of the successful modelling. This section presents the model parameter formulation. Modelling introduced in the following sections.

The EMSP consists of a basic axial piston pump unit, a ball screw, a gearbox, a servo motor, electronics and sensors. For position controlled EHA, the EMSP should be in a displacement controlled mode. In the preliminary design, crucial parameters of these components should be decided to ensure the required performance of the EMSP. In addition, the decided parameters in the preliminary design should be used as the input to the following detailed design.

The dominated parameters of EMSP are listed in Table 1. The parameters are classified into 3 categories: active, driven and empirical. Active parameters are defined and adjusted by designers directly. Driven parameters depend on the active parameters of the component. Empirical parameters depend on the chosen material and manufacturing process.

All dominated parameters in Table 1 are the targets in preliminary design of the electro-mechanical servo pump, since they are necessary for the pump performance evaluation. However, the driven and empirical parameters can be achieved only by detail design of each component, which is impractical in the system design phase. Therefore, these parameters should be generated. Author in [6,7] proposed scaling law models and variable power law meta-models (VPLM) for simulation parameter generation tools of mechatronic systems. In this paper, proposed scaling law models are employed for part of driven parameters generation, e.g. mass, inertia, volume. Note: In spite of the accuracy advantages, VPLM is not used in this study as required component level parameters are not available in this system level design.

However, scaling law models do not work well on the efficiency and thermal parameters. These parameters are highly depending on the material, manufacture and structural factors. The exact values may be not available until the final product finished. However, products within the same serial and manufacturer usually

share similar feature. Finally, in this research these parameters are based on empirical functions provided by the manufacturer.

Table 1. Dominated parameters of the electro-mechanical servo pump

No.	Component	Name	Category	Symbol	Unit
1	Pump	Maximum displacement	Active	D_{pmax}	m^3
2		Nominal pressure	Active	P_{pn}	Pa
3		Nominal speed	Active	S_{p}	rad/s
4		Inner volume	Driven	V_{p}	m^3
5		Mass	Driven	M_{p}	kg
6		Mechanical efficiency	Empirical	E_{pm}	-
7		Volumetric efficiency	Empirical	E_{pv}	-
8		Thermal resistance	Empirical	R_{pt}	K/W
9	Motor	Nominal voltage	Active	V_{mn}	V
10		Nominal torque	Active	T_{mn}	Nm
11		Max torque	Driven	T_{mmax}	Nm
12		Max speed	Driven	S_{mmax}	rad/s
13		Resistance	Driven	R_{m0}	Ω
14		Inductance	Driven	L_{m0}	H
15		Torque constant	Driven	C_{mt}	Nm/A
16		Inertia	Driven	I_{m}	kgm^2
17		Mass	Driven	M_{m}	kg
18		Viscous friction	Driven	f_{m}	Nm/(rad/s)
19		Thermal resistance	Empirical	R_{mt}	K/W
20	Gearbox	Ratio	Active	i_g	-
21		Nominal torque	Driven	T_{g}	Nm
22		Max torque	Driven	T_{gmax}	Nm
23		Max speed	Driven	S_{gmax}	rad/s
24		Efficiency	Empirical	E_{g}	-
25		Thermal resistance	Empirical	R_{gt}	K/W
26	Ball screw	Nominal load	Active	F_{sn}	N
27		Lead	Active	l_{s}	m
28		Maximum speed	Driven	S_{smax}	m/s
29		Diameter	Driven	D_{s}	m
30		Mass	Driven	M_{s}	kg
31		Inertia	Driven	I_{s}	kgm^2
32		Efficiency	Empirical	E_{s}	-
33		Thermal resistance	Empirical	R_{st}	K/W
34	Controller	Gain	Active	P_{c}	-

For the gearbox and ball screw, some parameters can only be chosen from discrete numbers, e.g. screw lead is chosen from 5 mm, 10 mm, 15 mm, etc. Values apart from these numbers are unavailable for the constraints of the mechanism schematics or the manufacture process. Therefore, a customized parameter generation method based on product database is developed. The screw lead and diameter value that feed to the model can only be oriented from the product database. Firstly, the closest diameter value in the database which satisfy the force requirement is chosen. Then the closest lead value to the assignment is chosen. For the gearbox, actually, the nominal torque and the ratio are both the identical parameters. But due to the discrete parameter property and constraint from the screw force, only ratio i_{g} is chosen as active parameter. The gearbox nominal torque T_{g} is calculated as:

$$T_{\mathrm{g}} = \begin{cases} \min(\mathrm{T}_{\mathrm{gdata}}(n)), \text{ when } \mathrm{T}_{\mathrm{gdata}}(n) > T_{\mathrm{s}} \text{ and } 0.8 \cdot i_{\mathrm{g}} < \mathrm{i}_{\mathrm{gdata}}(n) < 1.2 \cdot i_{\mathrm{g}} \\ \mathrm{T}_{\mathrm{gdata}}(n), \text{ where } \left|\mathrm{i}_{\mathrm{gdata}}(n) - i_{\mathrm{g}}\right| = \text{minimum and } \mathrm{T}_{\mathrm{gdata}}(n) > T_{\mathrm{s}}, \text{ otherwise} \end{cases}, \tag{1}$$

where $\mathrm{T_{gdata}}$, $\mathrm{i_{gdata}}$ are the torque and ratio vector from the product database, n is the index of the object value, T_s is the loaded torque to the gearbox. Equation (1) is used to decide the gearbox nominal torque value after the screw and gearbox ratio is selected. Finally, based on the methods aforementioned automatic parameter generation tool is formed, all the driven and empirical parameters can be obtained after the active parameters are assigned.

The following section introduces the modelling on the basis of these parameter generation tools.

3. DYNAMIC MODELLING OF HYDRAULIC AND ELECTRICAL COMPONENTS

Power, lifetime, dynamic characteristics, efficiency, and weight are the general requirements for the servo pump. In this paper, the preliminary design of EMSP needs to address these requirements. Therefore, the model for the preliminary design should be able to possess the dynamic simulations of hydraulic and electrical domains, as well as considering the thermal effects. This section presents modelling of the hydraulic and electrical parts. The thermal modelling is presented in Section 4.

3.1. Electrical modelling

Electro-mechanical servo pump is equipped with an EMA (consisting of a servo motor, a gearbox and a ball screw) as the displacement control unit. Since the model is for system preliminary design, linear model is considered first [8]. The differential equations to model the servo motor are:

$$u_\mathrm{m}(t) = i_\mathrm{m}(t)\cdot R_\mathrm{m} + L_\mathrm{m}\frac{di_\mathrm{m}(t)}{dt} + C_\mathrm{mt}\frac{d\theta_\mathrm{m}(t)}{dt}, \tag{2}$$

$$i_\mathrm{m}(t)\cdot C_\mathrm{mt} = I_\mathrm{m}\cdot\frac{d^2\theta_\mathrm{m}(t)}{dt^2} + f_\mathrm{me}\frac{d\theta_\mathrm{m}(t)}{dt} + T_\mathrm{ml}(t)\cdot \tag{3}$$

where u_m is the input voltage to the servo motor, i_m is the current response of the servo motor, R_m is the resistance of the servo motor winding, L_m is the inductance of the servo motor winding, C_mt is the torque constant of the servo motor, θ_m is the angular displacement of the servo motor, I_m is the rotational inertia of the servo motor, f_me is the friction coefficient of the servo motor, T_ml is the load torque of the servo motor. The rotational friction effects of the gearbox and screw nut are transferred to the motor shaft side equivalently. So, the gearbox and the ball screw models can be simplified to proportional gains. The model of the ball screw translational motion is:

$$F_\mathrm{s}(t) = m_\mathrm{s}\cdot\frac{d^2S_\mathrm{s}(t)}{dt^2} + f_\mathrm{s}\cdot\frac{dS_\mathrm{s}(t)}{dt} + F_\mathrm{psp}, \tag{4}$$

where F_s is the output force to the ball screw, f_s is the total friction effects of the screw and pump swash plate, m_s is the total mass of the screw and pump swash plate (inertia is equalized to the linear motion side), S_s is the translational speed of the ball screw, F_psp is the load force to the ball screw.

3.2. Hydraulic modelling

The hydraulic modelling focuses on the piston pump. The piston pump dynamic is governed by following equations:

$$Q_\mathrm{p}(t) = S_\mathrm{p}\cdot D_\mathrm{pmax}\cdot\frac{\tan\gamma_\mathrm{psp}}{\tan\gamma_\mathrm{pspmax}} - Q_\mathrm{pil} - Q_\mathrm{pol}, \tag{5}$$

$$T_{\mathrm{p}}(t)=\Delta p_{\mathrm{p}}\cdot D_{\mathrm{pmax}}\cdot\frac{\tan\gamma_{\mathrm{psp}}}{\tan\gamma_{\mathrm{pspmax}}}+T_{\mathrm{pf}}\cdot \tag{6}$$

where Q_{p} is the output flow of the pump, S_{p} is the rotational speed of the pump, D_{pmax} is the maximum displacement of the pump, γ_{psp} is the inclination angle of the pump swash plate, γ_{pspmax} is the maximum inclination angle of the pump swash plate, Q_{pil} is the inner leakage flow of the pump, Q_{pol} is the outer leakage flow of the pump, T_{p} is the input torque of the pump, Δp_{p} is the pressure difference between the pump port A and B, T_{pf} is the friction torque of the pump shaft. Since the pump operates at constant speed in EHA-FMVP, there is no torque item produced by inertia in equation (6). A model to interface the piston pump and the EMA should also be developed to generate the system level model. The EMA is used to control the pump swash plate inclination. The EMA translational output is converted to the swash plate rotation by a linkage, as illustrated in Figure 4. It can be seen that the arm length R_{psp}, which contributes to the motion conversion function, depends on the distribution radius of the pistons R_{ppd}, piston radius R_{pp} and the screw radius R_{s}. However, R_{ppd} and R_{pp} are not system level parameters and they should not be introduced to the model. Therefore, R_{ppd} and R_{pp} are generated by a particular tool. The following equations are usually utilized by the manufacturers to generate piston pump parameters:

$$m_{\mathrm{p}}=\frac{R_{\mathrm{ppd}}}{R_{\mathrm{pp}}}\approx\frac{Z}{0.75\cdot\pi}, \tag{7}$$

$$D_{\mathrm{pmax}}=\frac{\pi D_{\mathrm{pp}}{}^{2}}{4}\cdot D_{\mathrm{ppd}}\cdot\tan\gamma_{\mathrm{pspmax}}\cdot Z, \tag{8}$$

where $m_{\mathrm{p}}$is the empirical rate of the pump piston distribution radius and pump piston radius, piston quantity Z is usually 7 or 9, D_{pp} is the diameter of the pump piston, D_{ppd} is the distribution diameter of the pump pistons. To balance the tolerance for both cases, Z is defined to be 8. In practice, the piston amount in the pump is usually odd, but here is considered reasonable since it's just for displacement control unit sizing. The maximum inclination degree of the swash plate γ_{pspmax} is usually 15~20^0, the mean value of 17.5^0 is defined. Then once the maximum pump displacement is defined, R_{ppd} and R_{pp} can be achieved and R_{psp} is derived.

F_{psp} in equation (5) is equal to swash plate torque T_{psp} divided by R_{psp}. So, the T_{psp} derivation still need to be decided. Author in [9] conducted detail research on the swash plate control torque. However, the developed models rely on highly detail pump parameters, which are not available in the system level model. Since the control torque with respect to the swash plate inertia and rotational friction is included in the equation (5), T_{psp} is mainly contributed by the hydraulic pressure in the piston cylinder, as following equation:

$$T_{\mathrm{psp}}=\sum_{i=0}^{Z-1}p_{\mathrm{pp}i}\cdot\frac{\pi D_{\mathrm{pp}}{}^{2}}{4}\cdot\frac{D_{\mathrm{ppd}}}{2}\cdot\cos\left(\varphi_{\mathrm{ps}}+i\cdot\frac{2\pi}{Z}\right),\ \varphi_{\mathrm{ps}}\in[0,2\pi], \tag{9}$$

where i is the piston number, φ_{ps} is the angular displacement of the pump shaft, p_{pp} is the pressure acted on the piston. The piston pressure p_{pp} is equal to the pump port A pressure when the piston locates in the 0~π range of the valve plate, on the other hand, the piston pressure is equal to the pump port B pressure when the piston locates in the $\pi\sim2\pi$ range of the valve plate. T_{psp} is calculated by substituting equation (8) to (9).

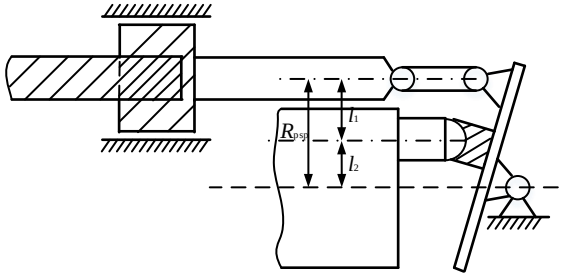

Figure 4. Linkage between EMA and swash plate

4. THERMODYNAMIC MODELLING

The thermal characteristics of the electro-mechanical servo pump must be evaluated during the preliminary design since it adopts a highly integrated structure. The lumped parameter modelling method is used since it only requires limited parameters. Lumped parameter thermal modelling can be divided into three major steps: model architecture definition, heat generation modelling, and heat transfer modelling. Heat transfer results from the thermal resistance definition are supplied by the manufacturer. This section introduces the model architecture and heat generation modelling parts.

4.1. Model Architecture

In lumped parameter modelling, system is divided into nodes with exchanged variables. The parts within low thermal resistance are defined as one node, and parts with high connected thermal resistance are divided into different nodes. All the EMSP components are integrated inside one shell, although the shell is assembled with several parts, it can be defined as one node since all the parts are metal that contacts with each other directly and maintain a low connected thermal resistance. On the other hand, although the electrical motor winding is a sub-component of the motor element, it should be decided as a separated node since it retains a high thermal resistance with the contacted parts of the motor. As a result, the EMSP is divided into 9 nodes.

After nodes definition, the connections between them are defined to achieve the complete architecture. A connection between the two nodes is needed as long as they have identical heat transfer. The connections are thermal resistances, these values are defined by the empirical functions provided by the manufacturer. Authors in [10-11] proposed different thermal model architectures for piston pumps. These architectures are extended to formulate the thermal model architecture of EMSP. At last, the complete architecture is demonstrated in Figure 5. The fluid volume and solid structure are the nodes of the thermal model. The thermal dynamic responses of them are calculated based on general thermodynamics equations, for details refer to [12-13]. Nodes outside the EMSP are also defined since the thermal boundary and constraints are necessary for thermal simulation.

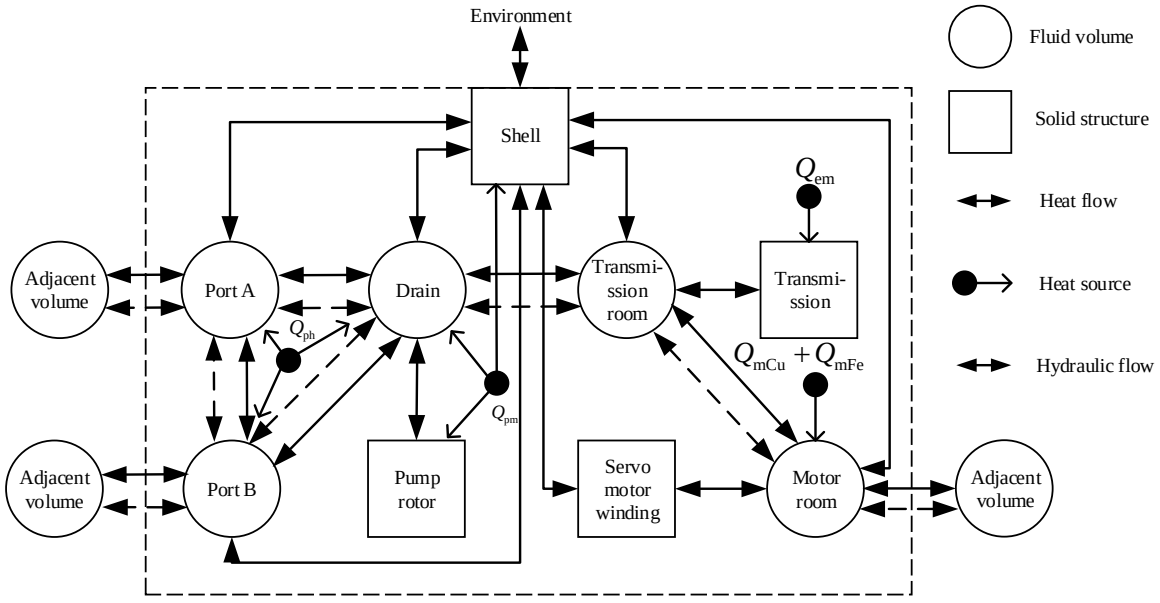

Figure 5. Thermal model architecture of the electro-mechanical servo pump

4.2. Heat generation modelling

The heat generated in the EMSP is from the energy losses. Losses generated from each component are analysed below.

- Piston pump

The losses are usually classified into mechanical loss P_{pm} and volumetric loss P_{pv}. For system level, compact models with limited definition parameters are chosen [14], as follows:

$$P_{\mathrm{pm}} = E_{\mathrm{pm}} \cdot S_{\mathrm{p}}{}^{2} \cdot D_{\mathrm{p}} \cdot \Delta p_{\mathrm{p}}, \tag{10}$$

$$P_{\mathrm{pv}} = \Delta p_{\mathrm{p}} \cdot (Q_{\mathrm{pil}} + Q_{\mathrm{pol}}) = E_{\mathrm{pv}} \cdot D_{\mathrm{p}} \cdot \Delta p_{\mathrm{p}}{}^{2}. \tag{11}$$

where E_{pm} is the mechanical efficiency coefficient, E_{pv} is the hydraulic efficiency coefficient, D_{p} is the pump displacement.

- Electro-mechanical actuator

The EMA is consisting of a servo motor, a gearbox and a ball screw. Losses from servo motor are mainly copper, iron and mechanical losses. The mechanical loss are considered together with the mechanical transmission parts. The copper loss P_{mCu} and iron loss P_{mFe} are as follows:

$$P_{\mathrm{mCu}} = R_{\mathrm{m0}} \cdot (1 + K_{\mathrm{mr}}(TEM_{\mathrm{m}} - \mathrm{TEM}_{0})) \cdot i_{\mathrm{m}}{}^{2}, \tag{12}$$

$$P_{\mathrm{mFe}} = K_{\mathrm{mFe}} \cdot S_{\mathrm{m}}{}^{1.5}. \tag{13}$$

where R_{m0} is the motor resistance at reference temperature, K_{mr} is the thermal coefficient of the motor resistance, K_{mFe} is the coefficient of motor iron loss, S_{m} is the rotational speed of the servo motor. The mechanical loss of the motor, gearbox, ball screw and attached swash plate assembly P_{em} is treated as viscous friction, as follows:

$$P_{\mathrm{em}} = K_{\mathrm{em}} \cdot S_{\mathrm{m}}{}^{2}, \tag{14}$$

where all the mechanism viscous friction coefficients are equalized to the motor shaft viscous friction coefficient K_{em}. Based on derivation above, the thermal model can be implemented.

Now all the model elements are developed and the complete model of EMSP can be established. Following section introduces the overall model and conduct the simulations.

5. SIMULATION RESULTS

The model was implemented in the AMESim simulation environment. First, the hydraulic and electrical model is established. The architecture is demonstrated in Figure 6. Second, thermal model described in Section 4 is added. The model characters an object-oriented feature. The entire AMESim model is illustrated in Figure 7. Typical duty cycles are feed to the model and simulation results are obtained. The duty cycle definition is given in Table 2. The full range from the swash plate 0 degree to the maximum inclination of one side is regarded as 100% amplitude. The discharging port is loaded as illustrated in Figure 8, while the sucking port is under constant pressure equal to 0.1 MPa. The schematic of simulation settings is demonstrated in Figure 8. Besides, a dynamic duty test defined with 2% amplitude and 8~20 Hz frequency command is performed. During dynamic test, the EMSP is under full load condition.

Requirements of the electro-mechanical servo pump are derived from the EHA-FMVP. The EMSP rotation speed S_{p} is assigned to be constant 7000 rpm. The full load pressure is 28 MPa and the maximum displacement is 13.2 mL/rev. Other active parameters are also defined by preliminary sizing: servo motor supply voltage V_{m} is 28 VDC, servo motor nominal torque T_{mn} is 0.77 Nm, gearbox ratio i_{g} is 1.5, ball screw nominal force F_{sn} is 2930 N, ball screw lead l_{s} is 0.005 m. Other simulation parameters are generated by the tools that developed in Section 2.1. The dynamic performance simulation results are demonstrated in Figure 9. During the command frequency span 8~20 Hz, the EMSP displacement response amplitude is above -3dB and the phase shift is above -90^{0}.

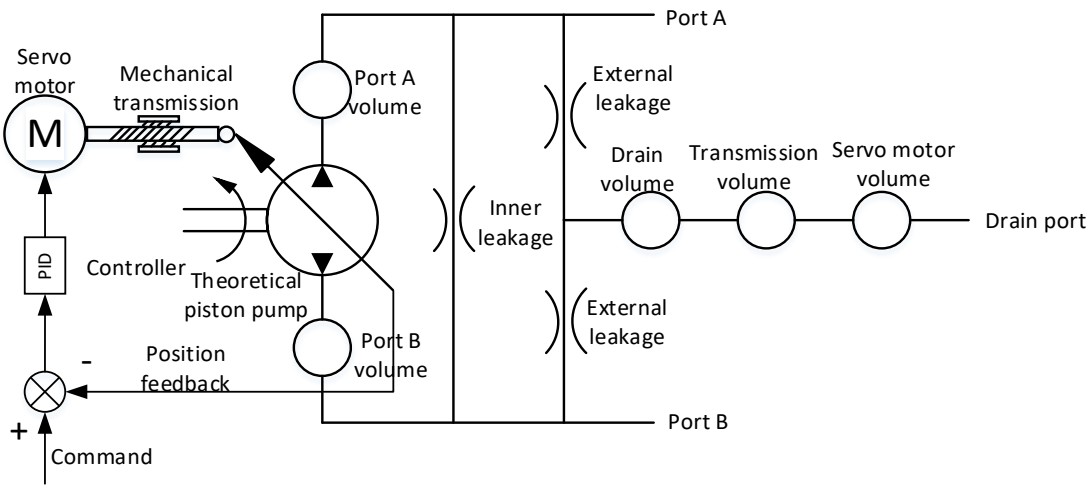

Figure 6. Model architecture of the electrical and hydraulic disciplines

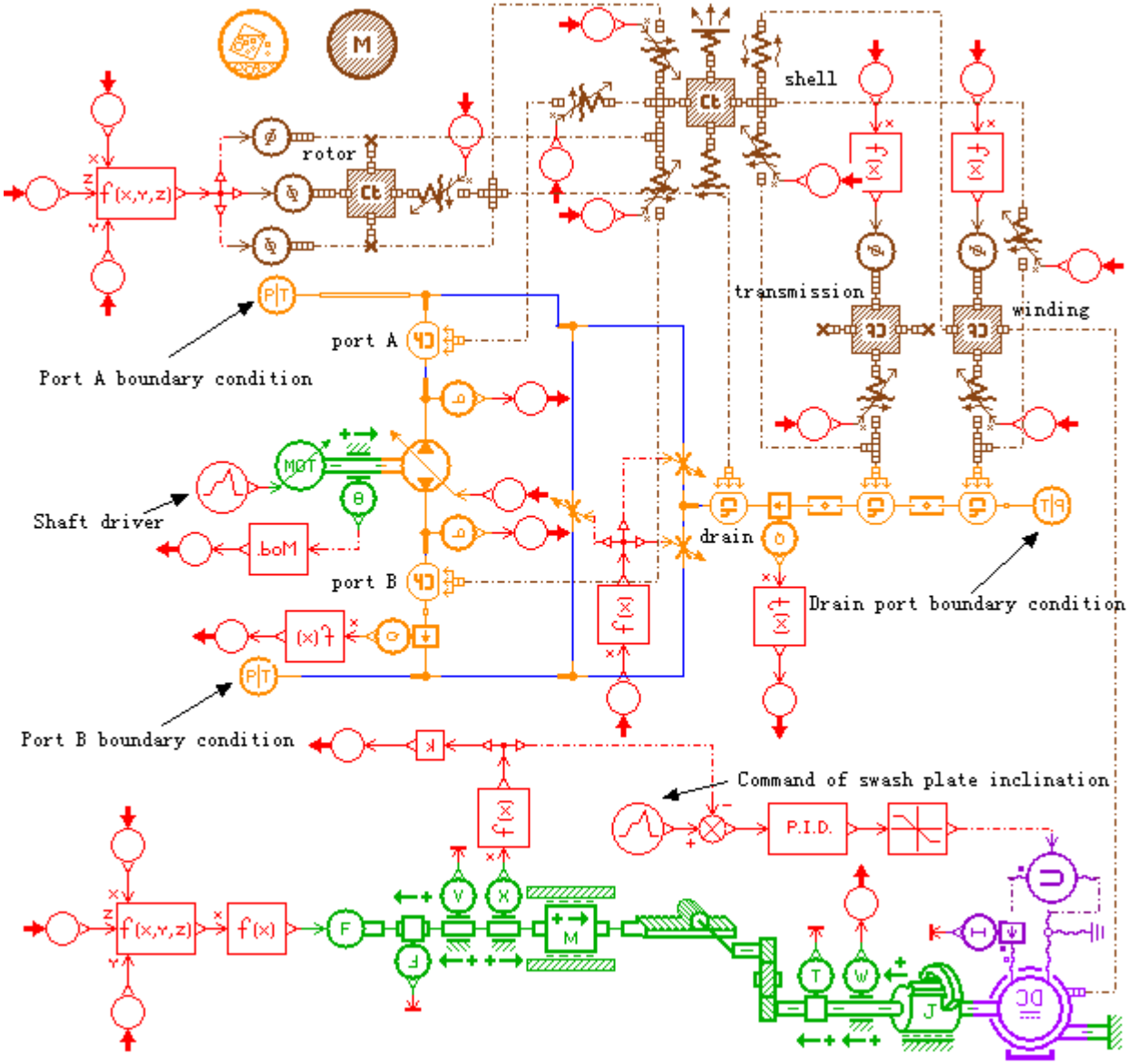

Figure 7. Model implementation in Amesim

Table 2. Typical servo pump test duty cycle

Phase No.	Duration, [s]	Loaded percentage of full load, [%]	Command amplitude rate, [%]	Command frequency, [Hz]
1	3	100	100	0.3
2	12	50	50	0.6
3	35	10	10	1.5
4	50	5	2	3

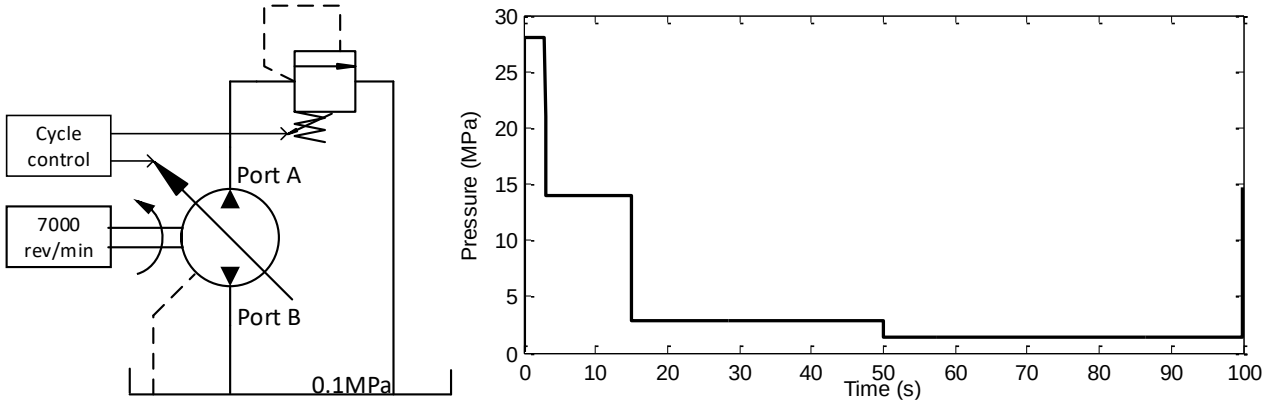

a) Schematic of simulation settings

b) Loaded pressure of the pump discharging port

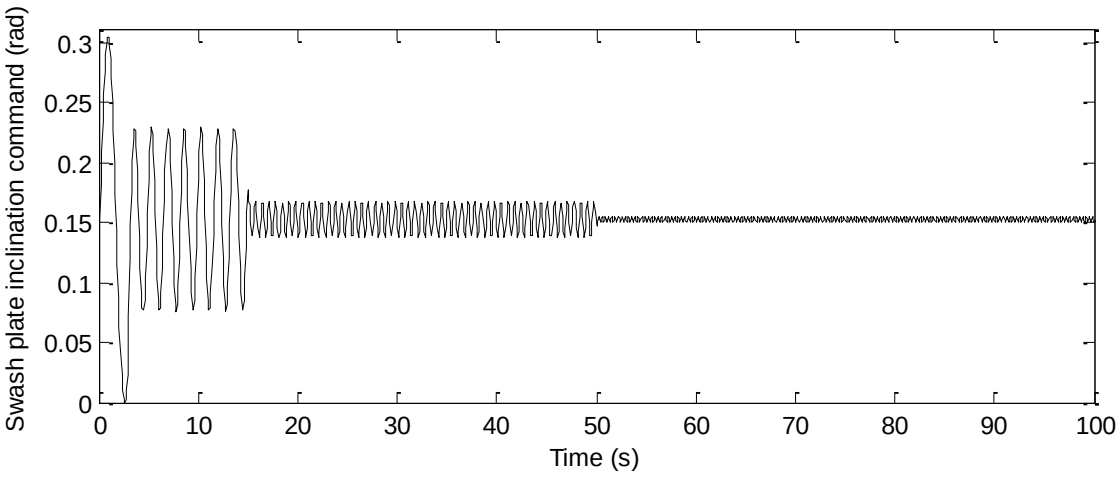

c) Command of the swash plate inclination

Figure 8. Schematic of simulation settings and duty cycle

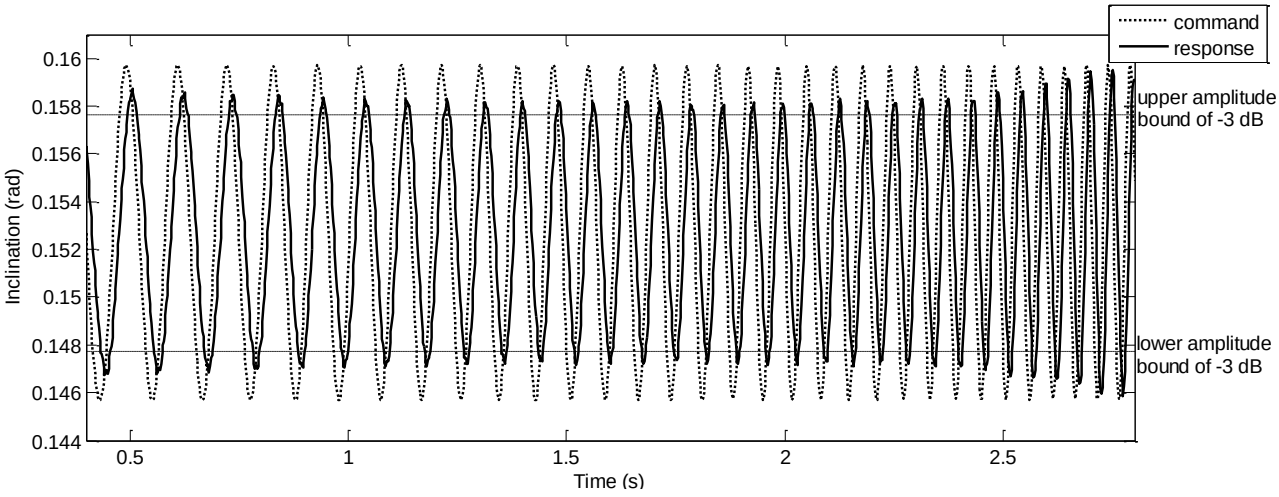

Figure 9. Dynamic simulation results

The thermal simulation results under the typical servo pump test duty cycle are displayed in Figure 10. Simulation duration is 10 minutes (6 cycles). The environment temperature is set at constant 20 ℃. Port B nearly maintains the constant 20 ℃ since it keeps on sucking constant temperature oil from outside. Port A is discharging oil that is a little higher than 20 ℃ since the EMSP heat up the oil. The temperature rising speed in phase I is much faster than following phases since the applied load in phase I is heavier. The temperature of the oil at the drain port is the highest because it collected most of the heat produced by the pump volumetric losses. Shell's temperature reaches to 22 ℃ at last since it is in the environment with effective free convection. The highest temperature part is the pump rotor, which absorbs most of the heat that produced by the highest loss part (kinematic pair friction) and with a highest thermal resistance.

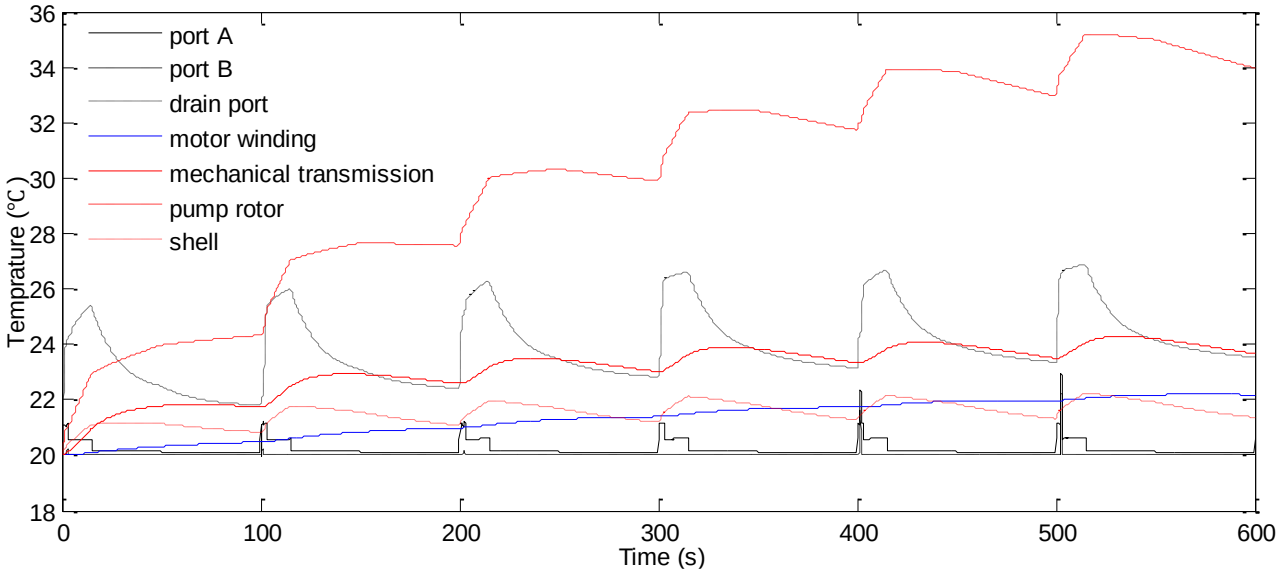

Figure 10. Thermal simulation results

From the simulation results, it can be concluded that the model achieves the functionality of acceptable EMSP performance in the preliminary design phase. This simulation results can be utilised for the further evaluation of the power, efficiency, lifetime, dynamic response and thermal attributes.

6. CONCLUSIONS AND FUTURE PERSPECTIVES

6.1. Conclusions

A multidisciplinary model specific for the electro-mechanical servo pump preliminary design stage is proposed in this paper. To be a practical as preliminary design tool, the model only employs 9 parameters for actively sizing. Other parameters for defining the model are generated automatically with developed and proposed tools in this study. This feature promotes the design evaluation and optimization to be more efficient and fast. All the active and generated parameters constitute to the preliminary design objectives, which decide the targeted performance of the EMSP and the input to the detail design phase. The created model maintains the ability of performance evaluation of hydraulic, electrical and thermal components independently. Simulations with swept frequency command verified the functionality of electrical and hydraulic components of the proposed model. Moreover, simulations under typical duty cycles verified the model functionality of simulating the thermal dynamics of the different parts in EMSP.

6.2. Future Perspectives

The parameter generation tool was implemented for creating the model parameters. This brings requirement for continuous improvement of the parameter generation tools to allow the simulation results be more reliable

and accurate. Additionally, the sensitivity analysis of the generated parameters should be conducted to support the following design procedures with consideration on parameter uncertainties. The test of the electro-mechanical servo pump is ongoing and the model validation will be conducted and presented in future publications.

NOMENCLATURE

D_{p}	Pump displacement	mL/rev
D_{pp}	Diameter of the pump piston	m
D_{ppd}	Distribution diameter of the pump pistons	m
f_{me}	Equivalent friction coefficient of the motor, gearbox and ball screw rotational motion	Nm/(rad/s)
F_{psp}	Load force to the ball screw	N
F_{s}	Output force to the ball screw	N
i_{m}	Current response of the servo motor	A
K_{mFe}	Coefficient of servo motor iron loss	$\mathrm{Nm{\cdot}s^{0.5}}$
K_{mr}	Thermal coefficient of the servo motor resistance	-
L_{m}	Inductance of the servo motor winding	H
m_{p}	Empirical rate of the pump piston distribution radius and pump piston radius	-
Q_{p}	Output flow of the pump	L/min
Q_{pil}	Inner leakage flow of the pump	L/min
Q_{pol}	Outer leakage flow of the pump	L/min
R_{m}	Resistance of the servo motor winding	Ω
S_{m}	Rotational speed of the servo motor	rad/s
S_{s}	Translational speed of the ball screw	m/s
t	Time	s
TEM_0	Reference temperature of the servo motor winding	℃
TEM_{m}	Temperature of the servo motor winding	℃
T_{ml}	Load torque of the servo motor	Nm
T_{p}	Input torque of the pump	Nm
T_{pf}	Friction torque of the pump shaft	Nm
T_{s}	Loaded torque to the gearbox	Nm
u_{m}	Input voltage to the servo motor	V
θ_{m}	Angular displacement of the servo motor	rad
γ_{psp}	Inclination angle of the pump swash plate	rad
γ_{pspmax}	Maximum inclination angle of the pump swash plate	rad
Δp_{p}	Pressure difference between the pump port A and B	MPa

ACKNOWLEDGEMENT

The authors would like to acknowledge the support from Beihang University in China and School of Engineering, Aalto University in Finland.

REFERENCES

[1] J Mare, J Fu. 2017. Review on signal-by-wire and power-by-wire actuation for more electric aircraft. Chinese Journal of Aeronautics, 2017, 30(3): 857-870.

[2] Alle N, Hiremath S, Makaram S, et al. 2016. Review on electro hydrostatic actuator for flight control. International Journal of Fluid Power, 2016, 17(2): 125-145.

[3] Garrison M, Steffan S. 2006. Two-Fault Tolerant Electric Actuation Systems for Space Applications. 42nd AIAA/ASME/SAE/ASEE Joint Propulsion Conference & Exhibit, July 9-12, 2006, Sacramento, California.

[4] Smith S, Irving J. 2006. Electro Hydrostatic Actuators for Control of Undersea Vehicles. Joint Undersea Warfare Technology Fall Conference, 2006, Groton, Conneticut.

[5] Bildstein M. 1998. EHA for flight testing on Airbus A321 power losses of fix pump EHA versus variable pump EHA. Recent Advances in Aerospace Hydraulics, November 24-25, 1998, Toulouse, France, pp. 101-103.

[6] Marc B, Jonathan L, Fabien H, et al. 2012. Estimation models for the preliminary design of electromechanical actuators. Proceedings of the Institution of Mechanical Engineers, Part G: Journal of Aerospace Engineering, 2012, 226(3): 243-259.

[7] Sanchez F, Budinger M, Hazyuk I. 2017. Dimensional analysis and surrogate models for the thermal modeling of multiphysics systems. Applied Thermal Engineering, 2017, 110: 758-771.

[8] Fu J , Mare J C , Yu L , et al. 2018. Multi-level virtual prototyping of electromechanical actuation system for more electric aircraft. Chinese Journal of Aeronautics, 2017, 31(5): 892-913.

[9] Manring N D. 1999. The Control and Containment Forces on the Swash Plate of an Axial-Piston Pump. Journal of Dynamic Systems, Measurement, and Control, 1999, 121(12): 599-605.

[10] Li K, Lv Z, Lu K, et al. 2015. Thermal-hydraulic modeling and simulation of piston pump in electro-hydrostatic actuator system. International Conference on Fluid Power & Mechatronics. IEEE, 2015.

[11] Guo M, Wang S, Wang X, et al. 2017. Six-unit control volumes thermal model of the swashplate axial piston pump in electro-hydrostatic actuator systems. Guidance, Navigation & Control Conference. IEEE, 2017.

[12] Li C, Jiao Z. 2008. Calculation Method for Thermal-Hydraulic System Simulation. Journal of Heat Transfer, 2008, 130(8): 1-5.

[13] Cheng-Gong LI, Jiao Z X. 2006. Thermal-hydraulic Modeling and Simulation of Piston Pump. Chinese Journal of Aeronautics, 2006, 19(4):354-358.

[14] Kauranne H O J, Kajaste J T, Ellman A U, et al. 2003. Applicability of Pump Models for Varying Operational Conditions. ASME International Mechanical Engineering Congress. 2003.

ON THE SATURATION DYNAMICS OF THE OIL FILM ON A HYDRAULIC CYLINDER ROD DURING EXTENSION

Tobias Mielke, Katharina Schmitz
Institute for Fluid Power Drives and Systems (ifas), RWTH Aachen University
Campus-Boulevard 30, 52074 Aachen, Germany
Tobias.Mielke@ifas.rwth-aachen.de

ABSTRACT

Water can be dissolved into conventional pressure fluids, based on mineral oil, to a certain extend. In this matter the dynamics of the absorption process is unknown.

In this work, the saturation dynamics of water into a thin oil film on the rod of a hydraulic cylinder is investigated. A physically motivated model is derived to describe the processes. The model is able to describe any saturation process of water in oil and is therefore independent of the oil mass or volume. Furthermore absorption experiments are carried out on a large oil volume compared to lubrication layers. The gained data is used to parameterize the model. Finally the findings are transferred to the dimension of the oil layer on the rod.

KEYWORDS: oil, water, film layer, absorption, rod, cylinder

1. INTRODUCTION

Hydraulic systems and machines use a fluid to transmit mechanical energy. A pump converts mechanical energy, usually coming from an electric motor or a combustion engine, into volume flow and pressure. The flow is then directed through pipes and valves to the actor, usually a cylinder. The actor transforms the hydraulic energy back into mechanical energy (in the case of the cylinder into a force and velocity of the rod). Usually only very little attention is paid to the fluid itself, aside from most failures of hydraulic machinery induced being due to contamination of the fluid.

Three types of contamination can be determined: solid particles, foreign fluids (dissolved or as a free phase) and gaseous content (dissolved or as bubbles). To ensure a long life time of the hydraulic machines, those contaminations should be kept out of the system, which is done by implementing filters and by designing reservoirs in such a matter, that little or no air can dissolve into the oil so that present bubbles can rise up to the fluid surface to exit the fluid. To extract foreign fluids, like water, only limited technologies are available which are also limited in their capabilities [1]. Therefore, the entrance of water into the hydraulic system has to be limited.

Water accounts for 20% of the life expectancy failure [2]. It impacts the life expectancy in various ways such as oxidation on metal surfaces, ageing of the fluid, hydrolysis of sealing materials and many more. Therefore it is crucial to understand the entrance behaviour of water into a hydraulic system to evaluate the life expectancy of hydraulic machinery. Water can enter the hydraulic system via two paths: through the air filter in the reservoir and through dynamic seals. In the latter case, water may be present as a free phase, which

has been studied in another paper by the author [3] or dissolved in the lubricating film remaining on the rod when extended which is discussed in this paper. Upon contact with humidity in the air, water enters the lubricating film and is entrained into the system when the rod is retracted. The dynamics of the saturation process are unknown. The lubricating films on the piston rod are very thin so the process cannot be measured directly. Therefore, the saturation process is investigated on a bigger oil volume by means of a theoretical model and experiments. Then it is rescaled to the dimensions of the film.

2. LUBRICATION FILM HEIGHTS AND SATURATION CURVES

In this chapter, the amount of water, which can be dissolved in the fluid, is described. In addition, findings regarding the formed film on the rod during extension of the cylinder are briefly explained.

2.1. Saturation curves of mineral oil based pressure fluids

In a previous work [4], saturation curves for a mineral oil based fluid were derived. It was shown, that only a little amount of water can be dissolved within the fluid before forming a free phase. Furthermore it was demonstrated, that more water can be dissolved at higher temperatures. *Figure 1* displays the saturation curve for a very widely used mineral oil based fluid, HLP 46 [5]. The unit of saturation is mg/kg, which means “mg” of water dissolved in “kg” oil.

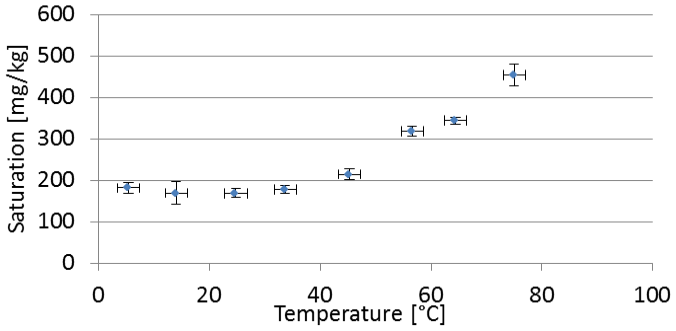

Figure 1. Saturation curve of a HLP 46

In [1] saturation curves for HEES, a fluid based on synthetic ester which is considered as bio-degrable, is derived. It was demonstrated, that with a rise in temperature more water can be dissolved. At 3 °C 920 ppm (“parts per million”) water are dissolved, whereas at 72 °C 2750 ppm of water are dissolved.

Bio-degrable fluids account for approx. 2.9% of the market share of the lubricants [6] and are therefore neglected in the frame of this work.

2.2. Film heights on the rod

The task of rod seals is to prevent leakage into the environment and therefore allowing a pressure build-up in the rod chamber of a cylinder. Meanwhile, the friction occurring in the contact zone of rod and seal during movement should be as low as possible. In addition, wear should be kept at a minimum to ensure a long lifetime. To meet these various requirements, the seal is designed in such a manner, that during extension, a very thin oil film can pass the seal to separate the surfaces in the contact zone. That film sticks to the rod during extension and is dragged back into the system through the sealing during retraction. The film layer brings down friction and prevents wear to a certain extend. Important in this matter is the ability to retract the film back in because otherwise leakage occurs.

Various research works have been carried out to measure the film height on the rod. In [7] an interferometer was used. A groove ring as the sealing element was investigated. *Figure 2* displays the measured film height along the circumference of the rod. The pressure to be sealed off was 0 bar which is very common for that kind of operation of the cylinder.

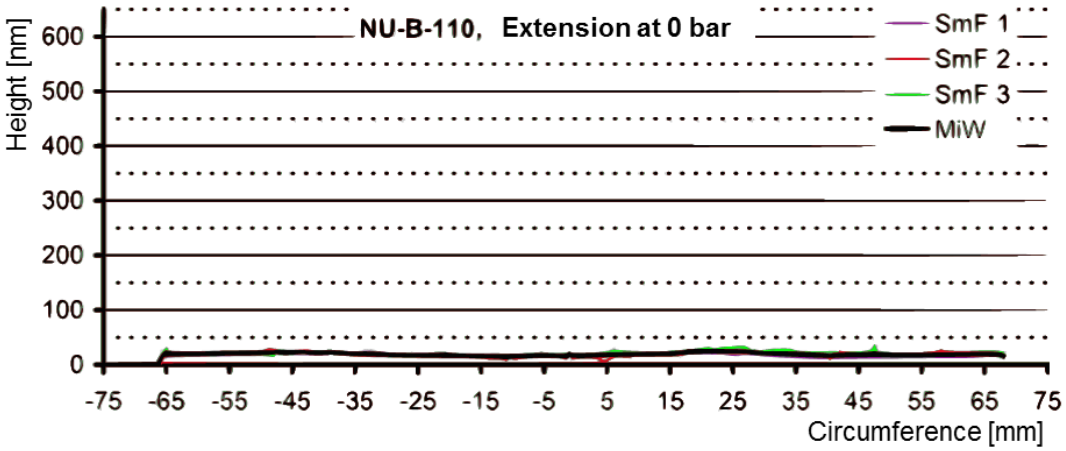

Figure 2. Film height on rod during extension [7]

The height distribution around the circumference of the rod is relatively even and constant. An average height of approx. 35 nm is measured.

Other researchers found film heights of approx. 1 µm [8], 0.5 µm [9], 2.4 µm [10] and 0.05 µm [11] for different seals, fluids, pressures and rod velocities. Overall, it can be stated, that the film height's magnitude is in the order of the surface roughness of the contacting surfaces or lower. In this work, various film heights are considered.

3. MODEL OF SATURATION PROCESS

In this chapter, the model for describing the dynamics of the saturation process of an oil film with water is derived.

3.1. Model

For modelling, it is assumed, that the water content in the oil layer on the rod is distributed evenly within the fluid's volume. A water mass flow perpendicularly enters the oil layer through the surface exposed to the air, *figure 3*. A is the area the mass flow enters and h the height of the oil mass.

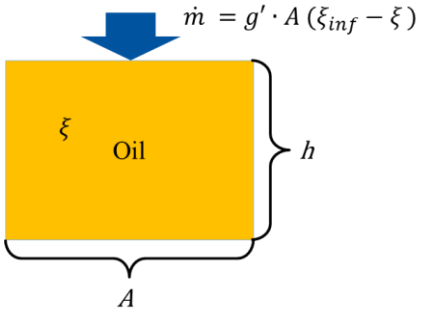

Figure 3. Film height on rod during extension

The driving difference for the mass flow is the difference between the current water mass concentration ξ and the concentration reached at infinite exposure time ξ_{inf}. The mass concentration is defined according to eq. (1).

$$\xi = \frac{m_i}{m_{tot}} \quad \text{Eq. (1)}$$

m_i is the mass of material i and m_{tot} the total mass. In the following, ξ is the mass content of water in oil and the total mass m_{tot} equals the mass of the oil m_{Oil}. The latter is valid due to the very little amount of water which can be dissolved into the oil.

The mass flow of water is modelled by eq. (2).

$$\dot{m} = g' \cdot A\,(\xi_{inf} - \xi) \quad \text{Eq. (2)}$$

g' is the proportionality constant which describes the saturation process. It is assumed, that g' is independent from the oil mass and therefore applicable for any kind of saturation process under the same environmental conditions. It is furthermore assumed, that the value depends on the temperature due to the higher energy content of a molecule on an elevated temperature level.

The oil's water content changes with the entering water mass flow. Applying the law of continuity to the water content in the oil leads to the differential equation eq. (3).

$$\frac{\partial \xi}{\partial t} m_{Oil} = \frac{\partial \xi}{\partial t} \cdot A \cdot h \cdot \rho_{oil} = \dot{m} = g' \cdot A\,(\xi_{inf} - \xi) \quad \text{Eq. (3)}$$

The oil mass is calculated by means of the volume (cross-sectional area A and height h) and the density of the oil ρ_{oil}.

Summarizing and solving the differential equation using suitable boundary conditions (ξ_{start} is the water mass content at the beginning of the investigation) gives the following analytical description of the saturation process (cf. eq. (4)).

$$\xi = \xi_{inf} + \left(\xi_{start} - \xi_{inf}\right) e^{-\frac{g' \cdot t}{h \cdot \rho_{oil}}} \; (= c \cdot e^{-a \cdot t} + b) \quad \text{Eq. (4)}$$

The unknown parameter in this equation is g' which can be determined by measured data and fitting the equation (using the parameters a, b and c). The scale factor of the saturation process is the height of the oil mass h, which is independent from the other factors. The solution should therefore be transferable to any scale.

4. EXPERIMENTAL INVESTIGATION

In this section, the experimental investigations are explained. First, the used test bench is described. After that, the conducted tests and their results are displayed.

4.1. Test setup

To investigate the saturation dynamics of water in oil, the same test bench to determine the saturation curves is used [11]. It consists of a vessel in which an oil condition sensor, which measures the relative water content of the oil Rh, is installed. Rh is defined as the mass of the dissolved water divided by the maximum water mass $m_{\mathrm{w,max}}$ the oil can dissolve. $m_{\mathrm{w,max}}$ is called the saturation point at that specific temperature and is based on the oil mass needed to dissolve that amount of water. The relation between Rh and ξ is given in eq. (5).

$$\xi = Rh \cdot m_{\mathrm{w,max}} \qquad \text{Eq. (5)}$$

The vessel is placed on a stirring plate to homogenize the oil sample during the tests. To support the homogenizing process, obstacles are placed in the oil to induce vertical velocities. The vessel and the stirring plate are placed in a climatic chamber, which controls the air humidity and the air temperature. The conditioned air of the climatic chamber is applied directly onto the oil's surface via a funnel using a commercially available PC fan. The complete test setup is shown in *figure 4*.

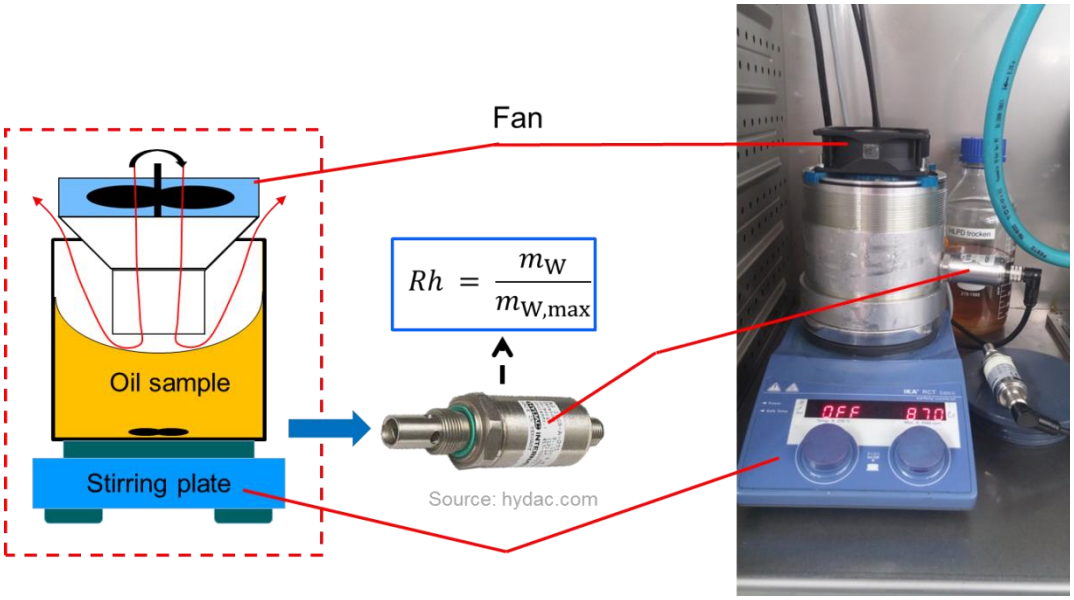

Figure 4. Test-set-up, left scheme, right in climatic chamber

The oil was filled into the previously intensively cleaned vessel and is brought into the air-conditioning chamber. The stirrer ensures constant thermal and mixture homogenization of the oil. The fan is inserted into the vessel and switched on. Then the climatic chamber is closed and the temperature and air humidity is set to a low value of 15%. After reaching a stable state condition of the oil's humidity (which happens to occur after approx. 2.5 h to 3 h, hence the waiting time was set to 4 h), the air humidity was changed to a high value, 85%, which is reached within minutes. Rh is recorded. After an additional 4 h, the procedure is stopped and the oil is dried by setting the air humidity back to the low value. In addition, the temperature is changed. After achieving stable state conditions again, the procedure is repeated. 30 °C, 40 °C, 50 °C and 60 °C are set for temperature.

Three different oil heights (50 mm, 60 mm and 78 mm, at ambient temperature) are measured to validate the assumption of independency of factor g'.

4.2. Results

In this section, first the results of the measurement and the results for the fitted model are shown as sample for one operating point. In addition, the data processing and the determined results are explained.

In the following, in equations (2) till (4) ξ is subsidised by eq. (5) and further simplified.

4.2.1. Measurement

Matlab was used to process the raw data and to fit the model to the data. The used function is called fittype and it uses a nonlinear fitting algorithm. Besides the fact, that the rising time of the air humidity in the chamber is neglectable compared to the rise of the humidity of the oil, it is taking into account for the processing of the data.

In the following *figure 5* the measured relative humidity at different temperatures and an oil height of 78 mm are shown. The blue curves represent the measured raw data; the red curves represent the fitted model. It can be seen, that there is a good accordance between both curves. The same is observed for other measured operating points. The authors conclude that the chosen physical model (cf. section 2.1) is correct.

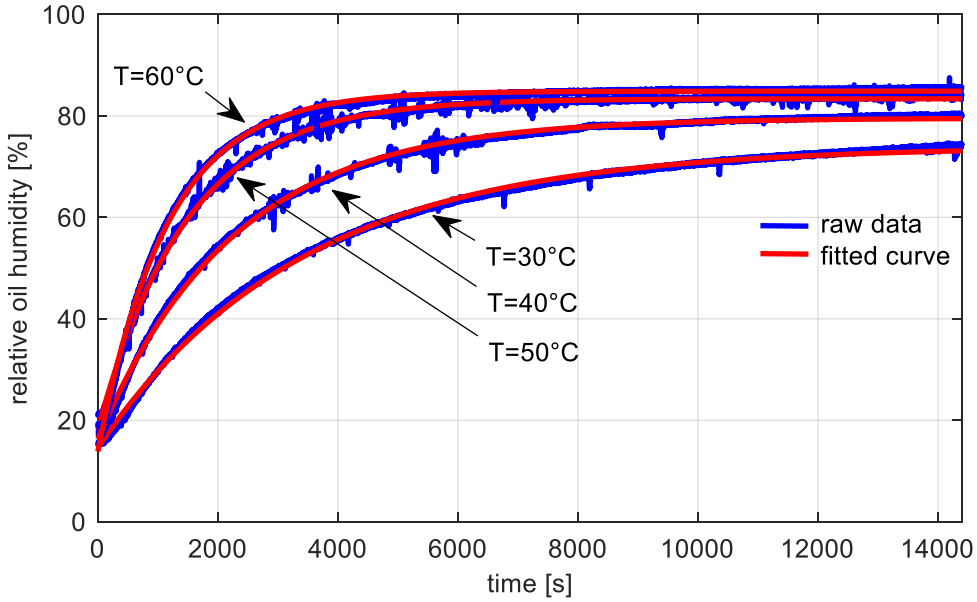

Figure 5. Measured raw data and fitted model

4.2.2. Data processing

The data fitting process delivers the results for the factors a, b and c. a consists of the density ρ_{Oil}, the height h of the oil sample and the parameter g' according to eq. (6)

$$a = \frac{g'}{h \cdot \rho_{Oil}} \qquad \text{Eq. (6)}$$

Oil's density changes with a change in temperature. Therefore the height of oil in the vessel changes, too. Eq. (7) gives an equation to calculate the density at temperature T, using a known density $\rho_{Oil,0}$ at a temperature T_0 [12].

$$\rho_{Oil} = \frac{\rho_{Oil,0}}{1 + \gamma \cdot (T - T_0)} \qquad \text{Eq. (7)}$$

γ is the expansion coefficient and has the value of $7 \cdot 10^{-4} \frac{1}{K}$ for mineral oil based fluids.

Using the law of mass conservation and assuming that the cross sectional area of the vessel does only change to a neglectable extent with a change in temperature, the height h at temperature T can be calculated according eq. (8), using the height h_0 at temperature T_0.

$$h = h_0 \cdot (1 + \gamma \cdot (T - T_0)) \qquad \text{Eq. (8)}$$

Having all these parameters corrected for temperature, g' and be calculated using eq. (6).

Table 1 gives the results for g' for the various working points.

Table 1. Results for g'

Height [mm]	Temperature [°C]	g' [1/s kg/m³ mm]
78 mm	30	20.01199
	40	30.25709
	50	46.1107
	60	58.65539
60 mm	30	19.22787
	40	28.05758
	50	38.33294
	60	55.26552
50 mm	40	24.97649
	50	38.15378
	60	58.37661

It is notable that the values for g' depend more on temperature than the height of the oil. To prove the independency of the height, the values of the same temperature but of different heights are averaged. The standard deviation of the averaging is taken as a measure for proof.

In *figure 6* the values as well as the standard deviation are displayed. Note, that the standard deviation for the temperatures 30 °C and 60 °C is within the accuracy of the senor used (± 3 %) whereas the deviation for 40 °C and 50 °C ranges up to 7.80 % and 9.07 % respectively. Nevertheless, the deviation ranges do not interfere and therefore no fundamental misinterpretation of the data is assumed.

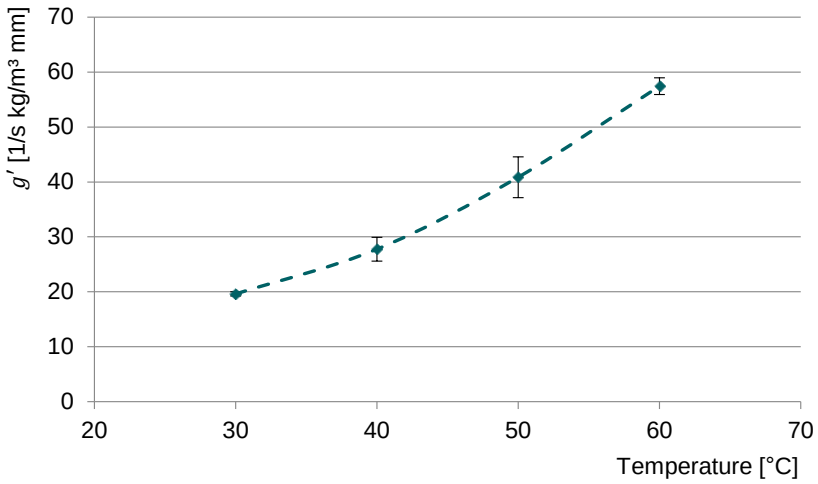

Figure 6. g' values and standard deviation

It is further notable that with an increase in temperature, g' increases exponentially. Further investigation will be carried out to evaluate the causes.

5. RESCALING

As it has been shown, the describing factor of the saturation process g' is independent of the oil height and only relies on the temperature. Therefore the determined factors can be applied to the dimension of the lubrication film height on the rod of a hydraulic cylinder. To do so, h in eq. (4) is varied.

It is important to know at which exposure time t_α the water content in the film reaches a certain level (defined as percentage α of ξ_{inf}). Using eq. (9), t_α can be calculated:

$$t_\alpha = \frac{h \cdot \rho_{oil}}{-g'} \cdot \ln\left(\frac{(\alpha-1)\cdot\xi_{inf}}{\xi_{Start}-\xi_{inf}}\right) \quad \left(= \frac{h \cdot \rho_{oil}}{-g'} \cdot \ln\left(\frac{(\alpha-1)\cdot b}{c}\right)\right) \qquad \text{Eq. (9)}$$

Using this equation and measured data for b and c, t_α for a = 95 %, different temperatures and different film heights are calculated. *Figure 7* shows the gained results.

At low temperatures and thick film heights, $t_{95\,\%}$ is relatively high compared to higher temperatures and thinner layers. Overall, it can be stated, that 95 % saturation is reached within 1 second.

Transferring these findings to the real application of hydraulic cylinders, the following conclusions can be made:

- On contact with a humid atmosphere, the oil layer is quickly saturated. The dissolved water is entrained into the cylinder during retraction.
- In the real application, the problem is not 0-dimensional but 3-dimensional. Therefore more water flows have to be considered, especially along the rods axis. Nevertheless, the findings give a good impression of the of the problem time magnitude.

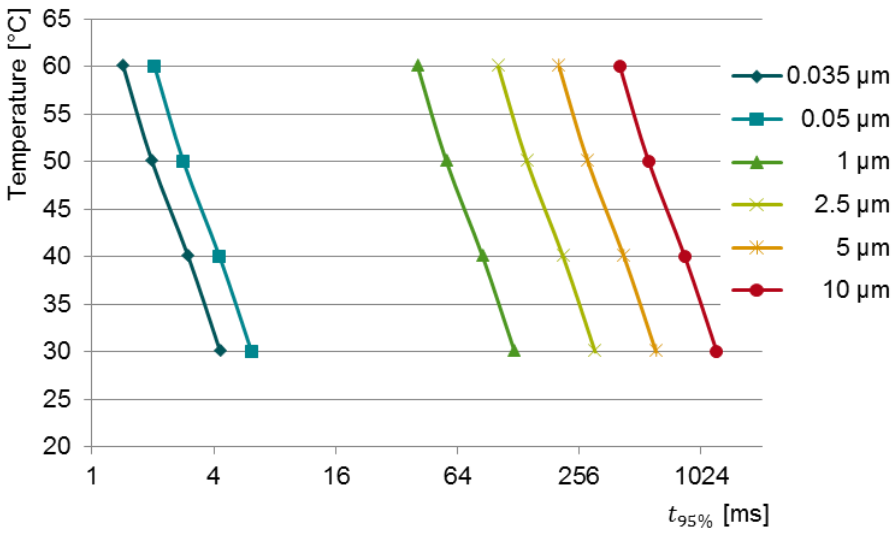

Figure 7. $t_{95\,\%}$ for different heights and temperatures

6. SUMMARY AND CONCLUSIONS

In this work, the saturation dynamic of a thin oil layer on a rod of a hydraulic cylinder with water is investigated. As the dimension of such a layer is very thin, a direct observation is not possible, nor measurable.

To meet these circumstances, a 0-dimensional, physical motivated model of the saturation process was derived and solved, taking the boundary and start conditions into account. The dynamics describing factor in this context is the factor g', which is assumed to be independent from the entire oil mass and the height of the oil layer.

An experimental investigation was carried out. A vessel, which was filled with the investigated oil, has an oil condition sensor incorporated. With this setup the relative humidity of the oil can be measured. The apparatus is put on a stirring plate (to homogenize the oil) and into a climate chamber to set temperature and humidity. Air is applied directly on the oil by a conventional PC-fan.

The measured data was used to fit the model. Doing so, g' was derived.

In addition, the findings were transferred to the dimensions of the film on the rod. A time t_α was introduced, which describes the time period it takes to saturate the layer to α % of the final value. It was found, that the saturation process is relatively fast (typically below 1 s for α=95 %). Therefore, the authors conclude that the film layer is practically completely saturated upon contact with a humid atmosphere.

References

[1] Kempermann, C. Ausgewählte Maßnahmen zur Verbesserung der Einsatzbedingungen umweltschonender Druckübertragungsmedien. PhD-Thesis, RWTH Aachen, 1999

[2] Rabinowicz, E. Lecture presented to the American Society of Lubricating Engineers, Bearing Workshop, USA, 1981

[3] Mielke, T., Schmitz, K., Murrenhoff, H. Entrainment of free water into hydraulic systems through the rod sealing, 11th International Fluid Power Conference, March 19-21, 2018, Aachen Germany

[4] Mielke, T., Murrenhoff, H., Schmitz, K. Wasserzutritt in hydraulische Systeme, O+P Fluidtechnik, 07-08/2018

[5] N.N. Druckflüssigkeiten-Hydrauliköle-Teil 2- Hydrauliköle HLP, Mindestanforderungen, DIN 51524-2, DIN-Norm, Beuth-Verlag, 2017

[6] Böttger, M. Markanalyse für den Bereich der Bioschmierstoffe. BIOSCHMIERSTOFF-KONGRESS 2014. 12.-13.11.2018, Hagen Germany

[7] Nißler, U. Dichtheit von Hydraulikstangendichtringen aus Polyurethan. PhD-Thesis, Stuttgart, 2015

[8] Yoshimura, K., Suzuki, N., Mizuta, H. Oil Film Formation of Reciprocating Seals Observed by Interferometry, Tribology Online, 9, 3, 106-112, 2014

[9] Crudu, M. H., Fatu, A., Cananau, S. A numerical and experimental friction analysis of reciprocating hydraulic 'U' rod seals. Proc IMechE Part J: JEngineering Tribology 226(9) 785-794. 2012

[10] Field, G.J., Nau, B.S. Film thickness and friction measurement during reciprocation of rectangular section rubber seal ring. Proceedings of the 6th International Conference on Fluid Sealing. München, C5. 45-56. 1973

[11] Wernecke, P.W. Untersuchung der physikalischen Vorgänge in Spalten von Hydraulikdichtungen. PhD-Thesis, RWTH Aachen, 1983

[12] Schmitz, K., Murrenhoff, H. Fundamentals of Fluid Power – Part 1: Hydraulics. Lecture Notes. RWTH Aachen University, 2018

STICK SLIP PREVENTION OF HYDRAULIC ROD AND PISTON SEALS IN THE BOUNDARY CONDITION

Seppälä, Timo (1); Wilke, Mandy (2); Jordan, Holger (2)
1: Trelleborg Sealing Solutions Finland Oy
2: Trelleborg Sealing Solutions Germany GmbH, Germany
timo.seppala@trelleborg.com

ABSTRACT

Continuous trends in the hydraulic world lead to increasing power and efficiency. Weight is a driver for that and therefore hydraulic systems also are under the view of light weight constructions. The all known Stick Slip Effect then can easier occur in terms of vibration and noise creation in such an application.

With sealing elements, the respective choice of different materials and or design variations the engineering normally looks into possible solutions to overcome the problem. As the tribological system is somehow sensitive and some application related variations such as speed or pressure fluid viscosity again can bring a solution to limits. The paper presents a new sealing solution, which now allows to eliminate stick slip due to an intelligent combination of materials.

In the situation of stick slip at a sealing contact area some micro movements can be damped by using the dampening character of an elastomeric material to eliminate vibration and noise [1, 2].

KEYWORDS: Hydraulic sealing system, stick slip effect, elimination of vibration, damping character of elastomeric material

1. INTRODUCTION

Continuous trends in the hydraulic world lead to increasing power and efficiency. Weight is a driver for that and therefore hydraulic systems are also under the view of light weight constructions. The well-known stick slip effect then can easier occur in terms of vibration and noise creation in such an application.

With sealing elements, the respective choice of different materials and/or design variations the engineering normally looks into possible solutions to overcome the problem. The tribo-logical system is somehow sensitive. Even small application related variations in speed or pressure fluid viscosity can lead to stick slip. This paper presents a new sealing solution, which now allows to eliminate stick slip due to an intelligent combination of materials. In the situation of stick slip at a sealing contact area some micro movements can be damped by using the dampening character of an elastomeric material to eliminate vibration and noise.

This paper extends the presented and published content [1,2] to eliminate stick slip effects in rod sealing systems to piston sealing systems.

Stick slip describes the friction force variations of at least two machine component surfaces while moving. Changing conditions of the friction within the gap lead to a variation between boundary and hydrodynamical

friction. The result is a discontinuous movement. By increasing the velocity, the boundary friction behavior disappears, and the system runs with a continuous hydrodynamical movement. Stick slip behavior with focus on sealing elements occurs especially at low velocity application or while the system parameters change from boundary to hydrodynamical friction (figure 1).

Stick slip describes the friction force variations of at least two machine component surfaces while moving. Changing conditions of the friction within the gap lead to a variation between boundary and dynamic friction. The result is a discontinuous movement. By increasing the velocity, the boundary friction behavior disappears, and the system is running with a continuous movement. Using classical mechanics, the phenomenon of stick-slip of a hydraulic cylinder can be described by the combination of spring and damper, see figure 1.

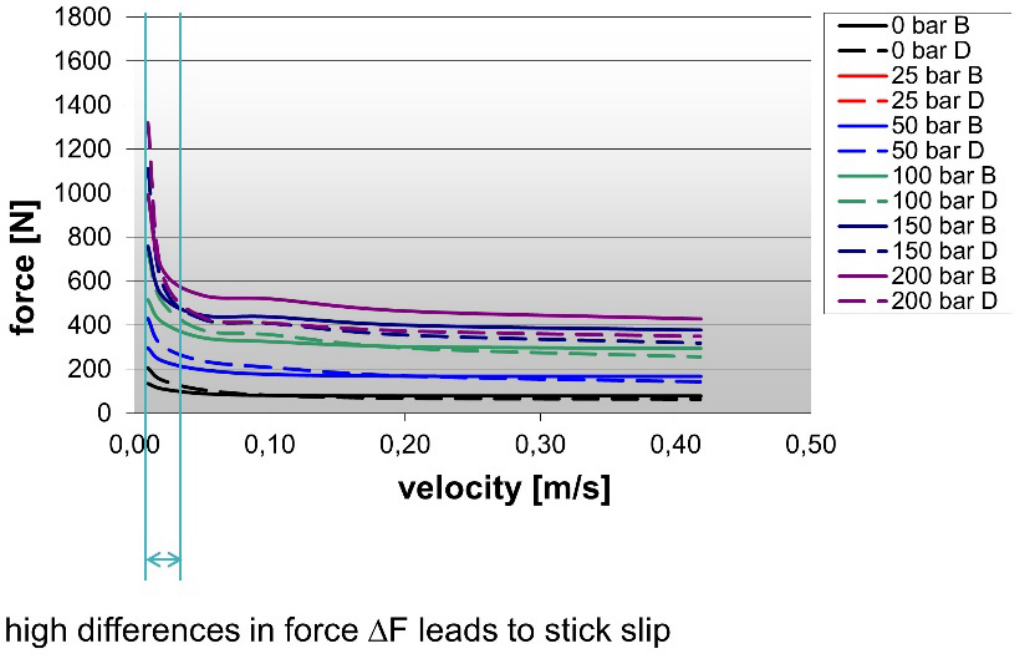

Figure 1. Example of a friction force measurement of rod seals with stick slip tendency at low velocities on a chrome coated rod with a polyurethane sealing element before (solid line) and after endurance (dotted lines)

2. THEORETICAL ASPECTS OF THE RELATION BETWEEN SEALING AREA AND FRICTION ON TRANSLATORICAL MOVEMENT

If the principle of spring and damper is applied on elastomer materials within dynamical hydraulic seal applications, the storage modulus E' and loss modulus E'' according to the elastomer technology has to be considered, compare [3].

$$E^*(i\omega, T) = E'(\omega, T) + E''(i\omega, T) \qquad (1),$$

The loss angle δ represents the phase offset of elongation and tension and is the quotient of loss modulus and storage modulus:

$$tan\delta = \frac{E''}{E'} \qquad (2).$$

According to these values of the behavior of the stored energy the impact on the damping feasibility can be described. Focus are on two parameters. First the stored energy which can be released due to elastic reset behavior of the material. Second the absorbed energy which comes into the material due to internal movement and friction between the molecule chains. These values are measurable for example with a DMA (Dynamic-Mechanical-Analysis). Figure 3 shows an example of the output of a DMA measurement with a constant frequency of 1 Hz and increasing temperature. As an alternative measuring method, the temperature can be constant, and the frequency will be increased.

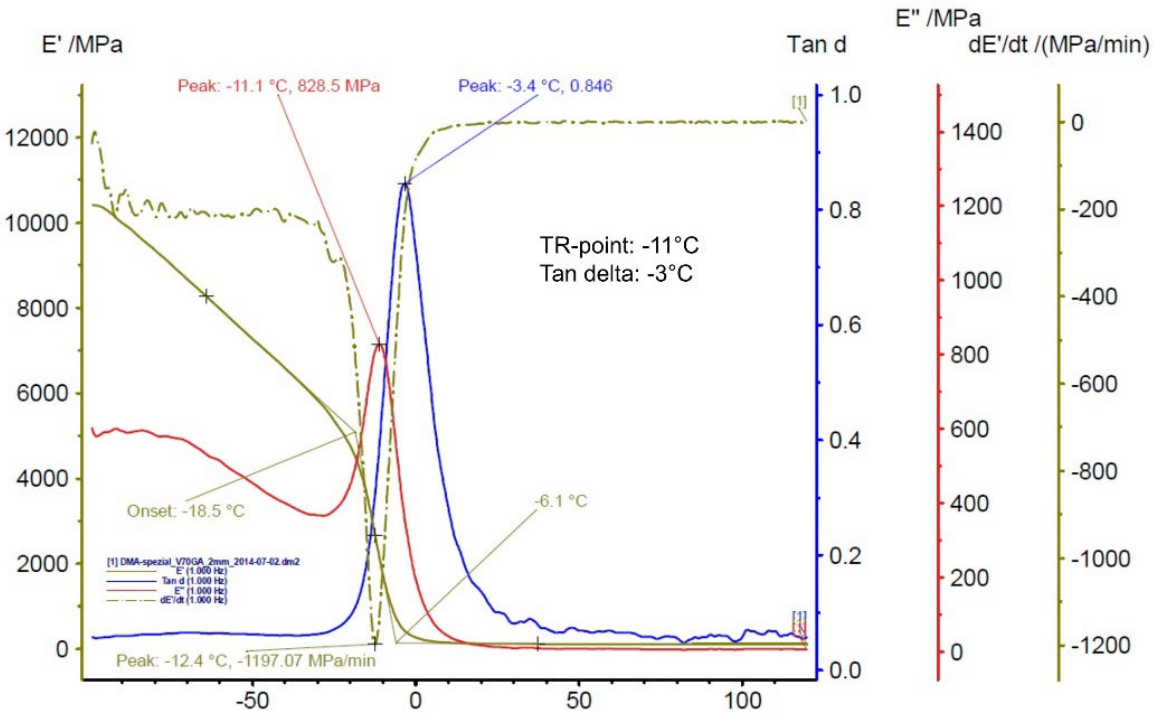

Figure 2. Example of elastomer DMA measurement

3. TEST ON ROD SEALS

To measure the different friction impacts a 3-axis acceleration measuring device was installed on a typical test rig for rod seal tests. The next figure 3 describes the components of the test rig including the measurement direction of the acceleration sensor.

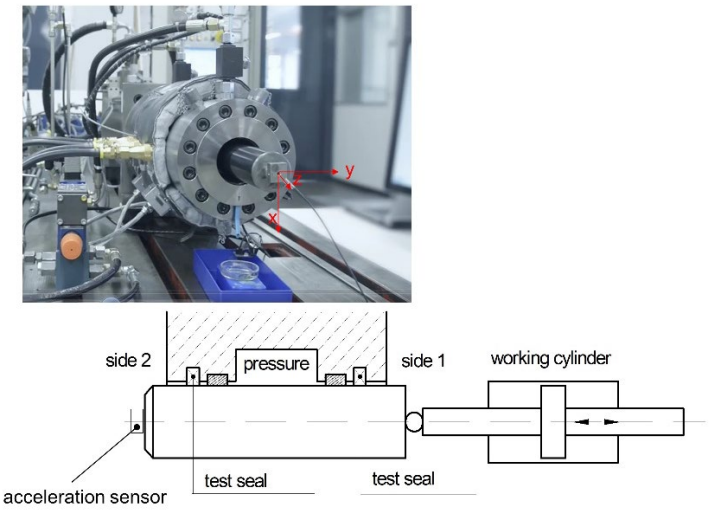

Figure 3. Components of test rig for rod seals

The acceleration is measured during the rod movement with different pressure levels at different velocities. Afterwards the acceleration is transformed into vibration frequencies of the rod for the directions x, y and z.

To optimize the measurement results and to provoke the stick slip phenomenon an Al2O3 coated rod with a very unfavorable counter surface topography was used (figure 4), which is also common in some hydraulic cylinder applications.

Figure 5 shows the measured diagrams of the acceleration sensor in the x-y-z axis while z is rod movement direction (compare figure 3). The results are cyclic harmonic vibration in all three directions. An additional channel shows the friction force during the movement be-tween the cylinder and test rod.

With help of Fourier transformation, the measured accelerations were transferred into frequency spectra, see figure 6. The result is a multidimensional harmonic vibration. Influences on the vibrations at equal test conditions are design and material of used seals.

To limit the variety, the design of the tested polyurethane seal remained the same during all tests. All other parameters like velocity (0.01 to 0.4 m/s), pressure (0 to 20 MPa) and temperature (30 to 50°C) have been varied always in the same defined way fully automated. In these tests, a standard mineral oil HLP 46 was used. Damping elements with modified axial widths were tested to examine the damping conditions of the system. The material of the damping element remained the same during all tests (compare DMA fig. 2).

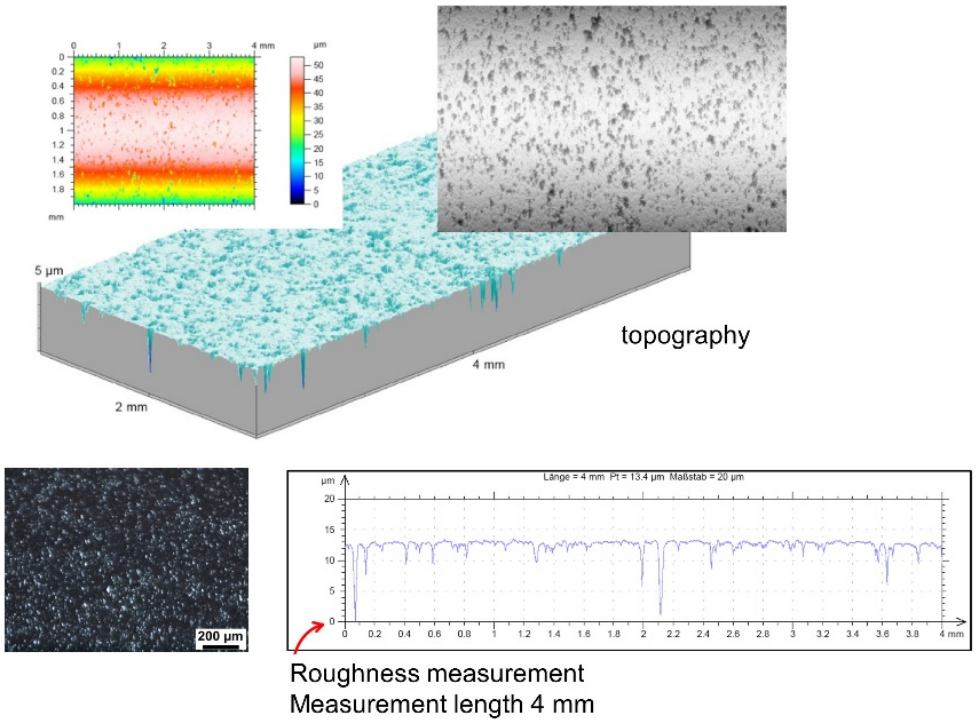

Figure 4. Used Al_2O_3 Counter Surface, roughness measurement, topography and height profile [1]

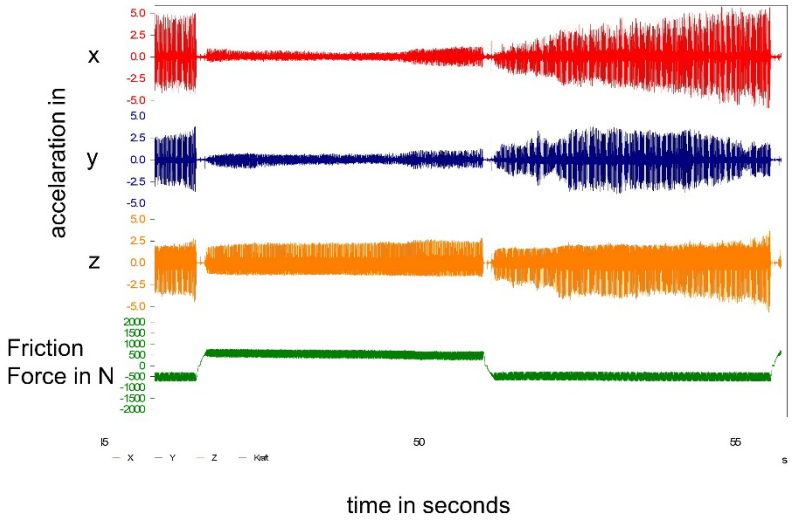

Figure 5. Acceleration in x, y and z direction with friction at 0 MPa and 0.01m/s [4]

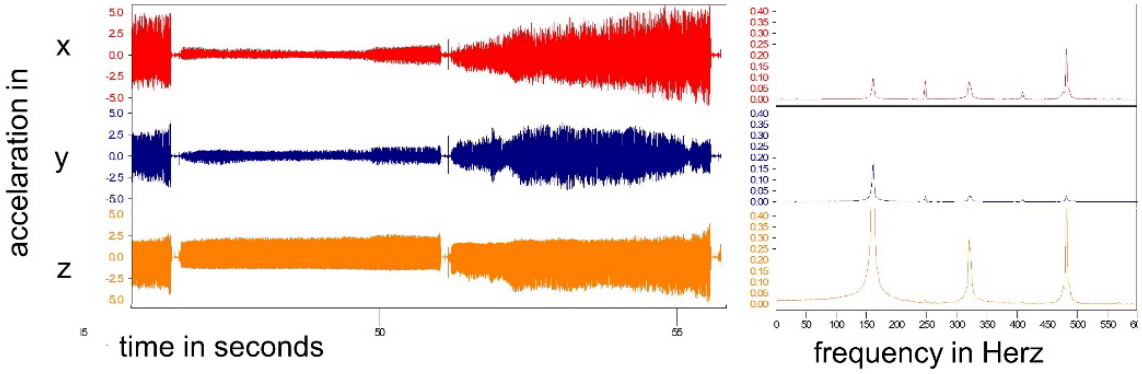

Figure 6. Acceleration in x, y and z direction on the left and frequency spectrum on the right at 0 MPa and 0.01 m/s [1]

Figure 7 describes the assembly of the damping element within the sealing groove without pressure load. The test results show a damping effect, which is depending on the dimension of the damping element due to their plastic elastic behavior explained in chapter 3, see figure 9 and 10. These results can be achieved at the shown low pressure as well as on higher pressure loads and at different oil temperatures and velocities.

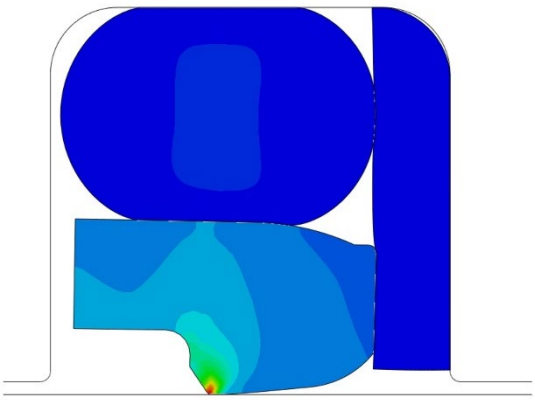

Figure 7. O-ring energized seal with axially damping element [1]

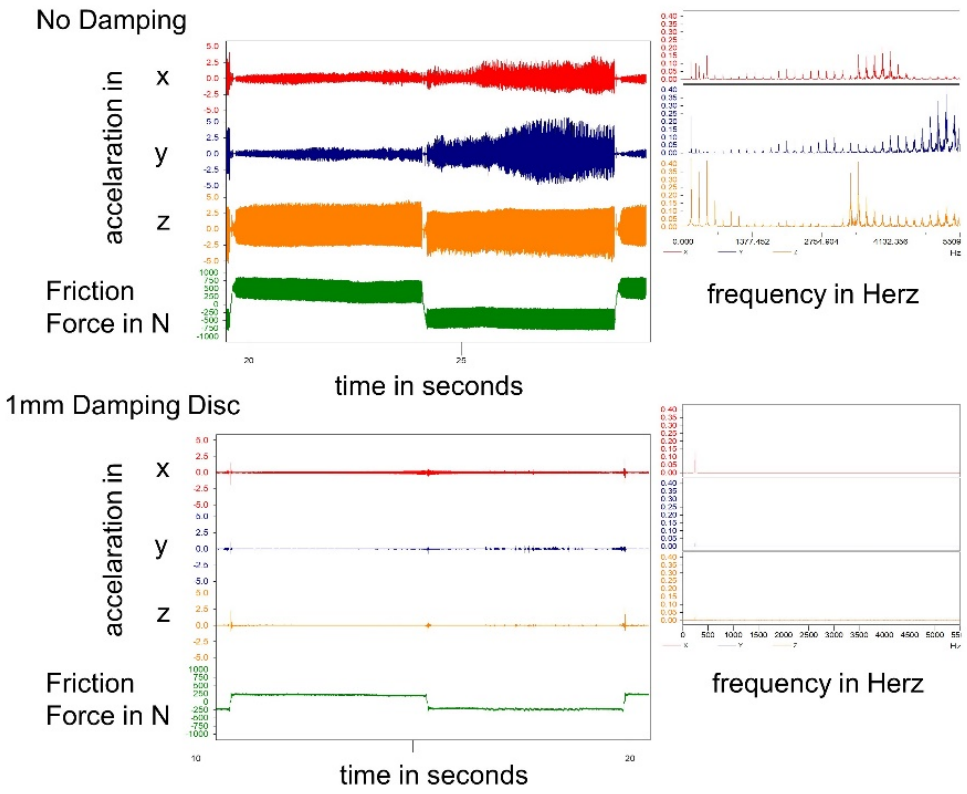

Figure 8. Acceleration values with and without damping element at 0 MPa and 0,02 m/s /4/

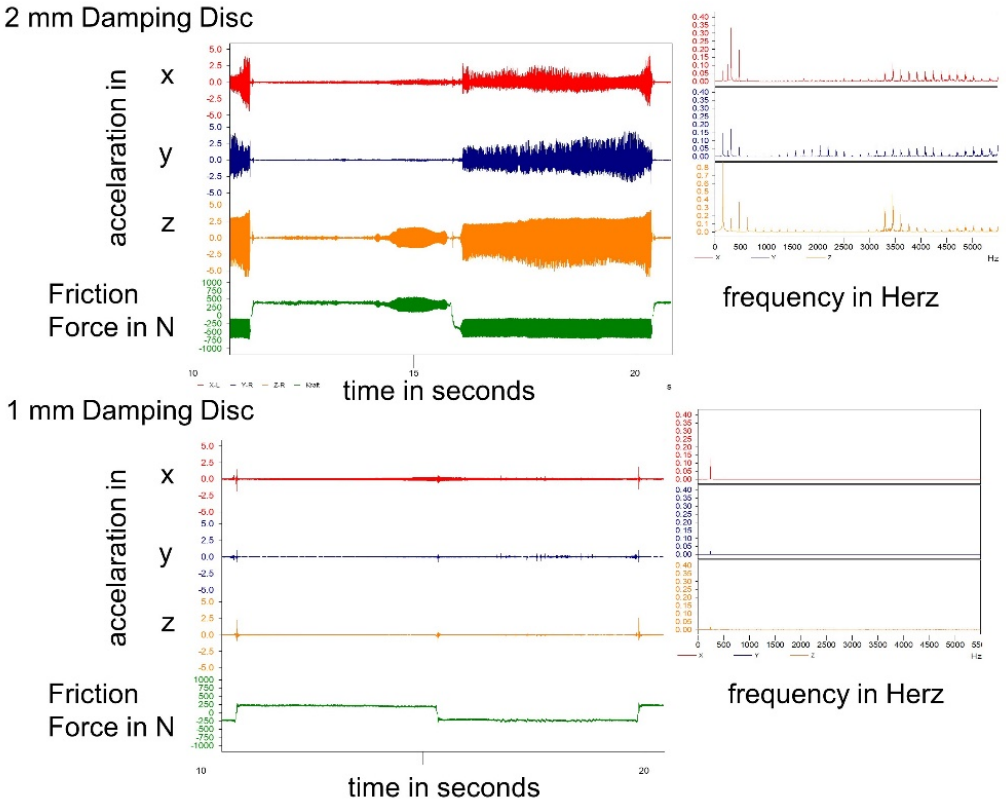

Figure 9. Acceleration values with 2 mm and 1 mm damping element at 0 MPa and 0,02 m/s /4/

4. TEST ON PISTON SEALS

To determine the damping effect on piston sealing systems, additional tests were conducted. Since the system has different criteria and parameters within the in- and out-stroke the feasibility had to be approved. For this purpose, a piston test rig was modified and prepared with an acceleration sensor to determine the damping effect. The test parameters were a pressure change (30 to 2 MPa) with a velocity of 0.11 m/s at a temperature of 70 °C. Several damper designs were tested to achieve the best possible damping effect. A standard piston seal was measured before and after applying the final special damping element. Following figure 10 shows the vibrations without and with damping element.

The measurements show that a sufficient damping effect is possible although the test system parameters change between in and out stroke.

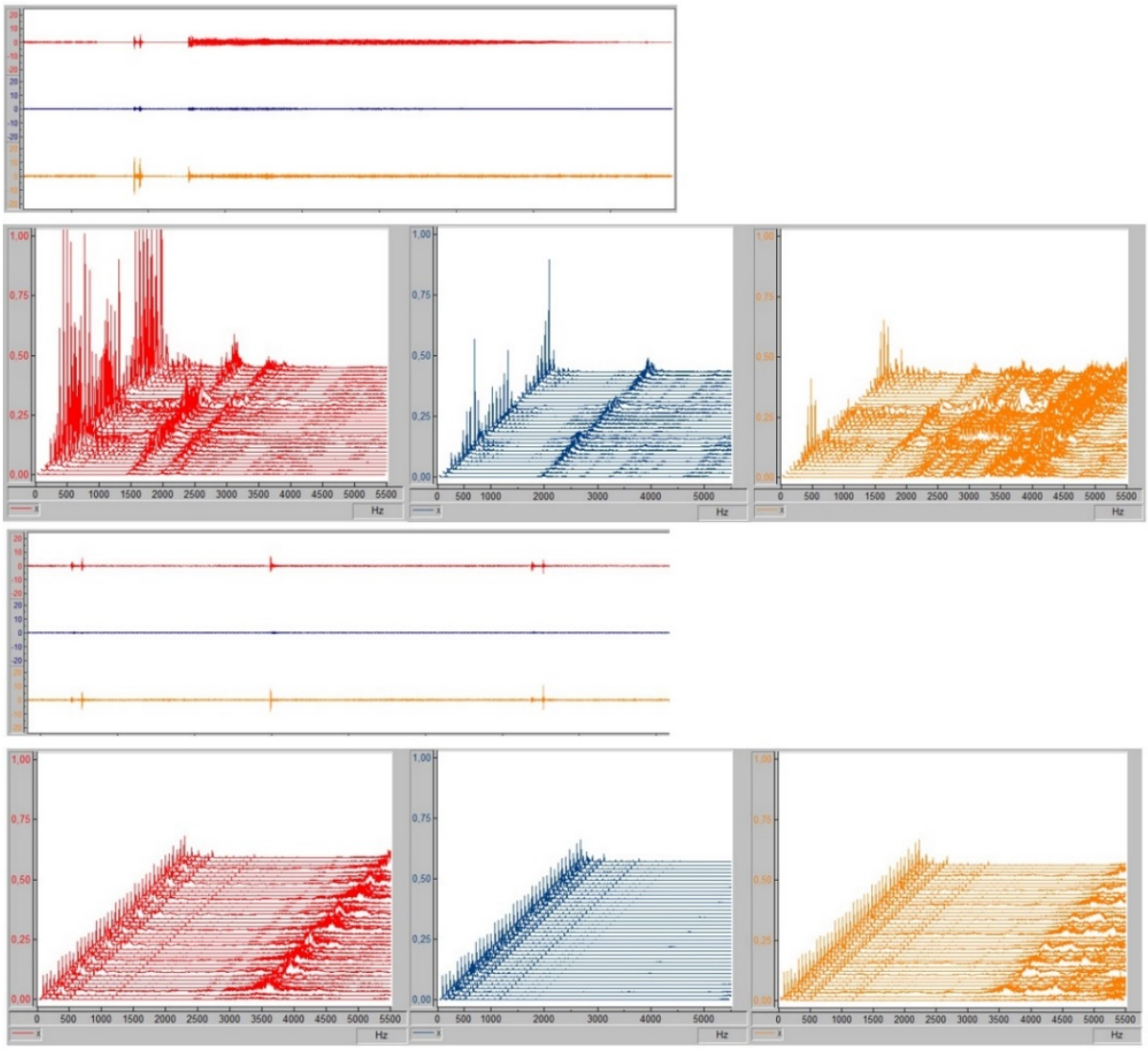

Figure 10. Comparison vibration before and after applying damping element

5. CONCLUSIONS

With a correct choice of material and design the movement behavior of contact seals can be influenced. The result is an improved sealing system completely avoiding stick slip effects when the sealing position is the source of vibrations. The reason for the damping effect is the plastic elastic behavior of the damping elements.

NOMENCLATURE

F_N	Normal Force
F_R	Friction Force
v	velocity
E	modulus of elasticity
(x)*	complex dimension of x
(x)`	real part of x
(x)``	imaginary part of x
i	imaginary unit
ω	angular frequency
T	Temperature
δ	loss angle

REFERENCES

[1] Wilke, M.; Jordan H. 2016. 19th International Sealing Conference: Friction Behav-iour of Contact Seals in the boundary condition (Stick Slip), October 12-13, 2016, Stuttgart, Germany, pp. 500–505.

[2] WILKE, M.; JORDAN, H.: Zum Verhalten von berührenden Dichtungen im Wechsel von Haft- zu Gleitreibung (Stick Slip), ISBN 978-3-8163-0684-9, pp. 500 – 505, 19th ISC, Stuttgart, 12th - 13th of October 2016.

[3] PETERS, J.: Zur Modellierung des mechanischen und kalorischen Verhaltens polymerer Werkstoffe, ISBN 978-3-8322-9907-1, Shaker Verlag, Aachen 2001.

[4] WILKE, M.; JORDAN, H.: Friction Behavior of Contact Seals in the Boundary Condition (Stick-Slip), Fluid Sealing 2018, 24th International Conference on Fluid Sealing, Manchester 6th – 7th of March 2018, S. 43, ISBN 2194-0754, 2018.

Experimental investigation of the hard-hard contact in seat valves

Tobias Mielke, Marcel Rückert, Ximena Ayala Galindo, Katharina Schmitz
Institute for Fluid Power Drives and Systems (ifas), RWTH Aachen University
Campus-Boulevard 30, 52074 Aachen
tobias.mielke@ifas.rwth-aachen.de

ABSTRACT

Static sealing valves are machine elements of critical importance in various fluid power applications. Their main task is the prevention of leakage and thus the upholding of a pressure difference. Seals with metallic contacts are used, among other things, for seat valves. Despite the seemingly simple design, it is still not possible to correctly predict the leakage depending on their mechanical properties, design and operating parameters. Therefore, efforts are carried out to increase the knowledge on the mechanisms involved in the hard-sealing contact to be able to predict the leakage based on a physical model which also aids in potential optimization. [1] In this Paper, the critical contact area of the sealing parts is investigated. TO do so a test rig is built up. the sealing parts, consiting of a ball and a seat, are exposed to different loads. The resulting malleable deformation is measured and compared.

KEYWORDS: seat valve, hard-hard contact, contact mechanics, contact area

1. INTRODUCTION

Seat valves are widely used in the industry for multiple tasks. The sealing mechanism is performed by two parts, the seat and the sealing element (in this study a ball), which form a line contact. The pressure to be sealed drops at that line contact.

The contact is of particular importance for prediction of leakage due to the surface asperities and the plastic deformation as a consequence of repeated stress reversals. The multiscale and inherently non-linear properties of the contact make it challenging to model the physics of the problem in classical mechanics. An analytical solution is only possible in a small number of cases, and the experimental procedures are limited or not feasible [2]. Using numerical tools, it is possible to simulate the contact mechanics of the sealing bodies without relying on assumptions, taking the material properties and non-linear contact interface and the macroscopic characteristic into consideration [3].

To validate the simulation, a test rig was designed and built to investigate leakage on sealing seats of varying geometric, hydraulic and mechanical parameters.

The geometry and surface properties of sealing bodies are analysed with an optical microscope, before and after the sealing process. The contact area is visible due to the plastic deformation of the micro asperities. The material properties change with scale because certain features, such as grains, occur at a specific scale or become less influential at different scales [4]. Because of these scale-dependent material properties, such as decreasing elastic modulus with increasing scale, the hard sealing body impresses the very rough surface of the seat. [1]

To be able to confer the results, the valve geometry is simplified to a symmetric problem and the design of the valve is similar to common seat valves. Also the hydraulic boundary conditions in the experiment reflect the real world industrial applications. A stainless steel bearing ball contacts a disk with a conical bore. To be able

to measure the real contact area a very rough and soft surface in one of the bodies is needed. Furthermore a hard surface of the seat is investigated for different working conditions.

In this work, the test rig used to conduct the measurements is explained first. After that, the considered sealing parts are explained. Third, the measured malleable deformation due to the sealing process is measured and explained. Finally the results are compared with calculations.

2. ANALYTICAL DESCRIPTION OF CONTACT ZONE

The contact zone of the sealing components is exposed to very high mechanical loads during the sealing process. This is due to the line contact, which makes the actual contact area very small. To calculate the pressing, the theory of Hertz applies [7]. Assuming two cylinders touching, eq. (1) can be used to calculate the resulting maximum pressing in the zone. That assumptions is valid as it represents the unwind contact line.

$$p_{H,max} = \sqrt{\frac{F_{CF} \cdot E}{\pi \cdot l_{Seat} \cdot (1-\nu^2)} \left(\frac{1}{2r_{DE}} + \frac{1}{2r_{DS}}\right)} \quad \text{Eq. (1)}$$

F_{CF} is the pressing force, E the bulk modulus, ν the Poisson ratio, l_{Seat} the length of the contact line and r_{DE} and r_{DS} the radii of the sealing components in the contact zone. In the investigated case with straight and even contact area, $\lim_{r_{DE} \to 0} = \infty$ applies, simplifying eq. (1) to eq. (2).

$$p_{H,max} = \sqrt{\frac{F_{CF} \cdot E}{2\pi \cdot l_{Seat} \cdot (1-\nu^2) \cdot r_{DS}}} \quad \text{Eq. (2)}$$

The length of the contact line l_{Seat} can be computed using eq. (3).

$$l_{Seat} = \pi \cdot d_{Seat} = 2\pi \cdot r_{Seat} \quad \text{Eq. (3)}$$

Figure 1 displaces the contact geometry.

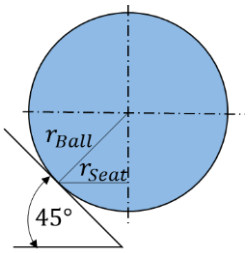

Figure 1. Contact geometry

r_{Seat} can be calculated using the cosine of 45° times r_{Ball}.

Load alternations play a crucial role regarding the life time of seat valve. This has been demonstrated in the case of ball bearings [8]. The expected cycles of loads decreases significantly with an increase in load. In the case of ball bearings, slip has a big impact as well. The higher the slip, the lower the load the bearing can withstand for the projected life expectancy. If effects like slip applies for seat valves as well, meaning that a relative movement of the ball and the seat during closing and opening leads to a decrease of life expectancy, is still subject to pending research.

3. TEST RIG

In order to investigate the sealing mechanism of hard-hard contact of seat valves, a test rig is built up at the test facilities of the Institute of Fluid Power Drives and Systems (ifas). It consists of the hydraulic circuit and the actual test chamber where the sealing parts are mounted.

3.1. Test chamber

In figure 2 the test chamber of the test rig is depicted. It contains the actual valve geometry which is subject to this research.

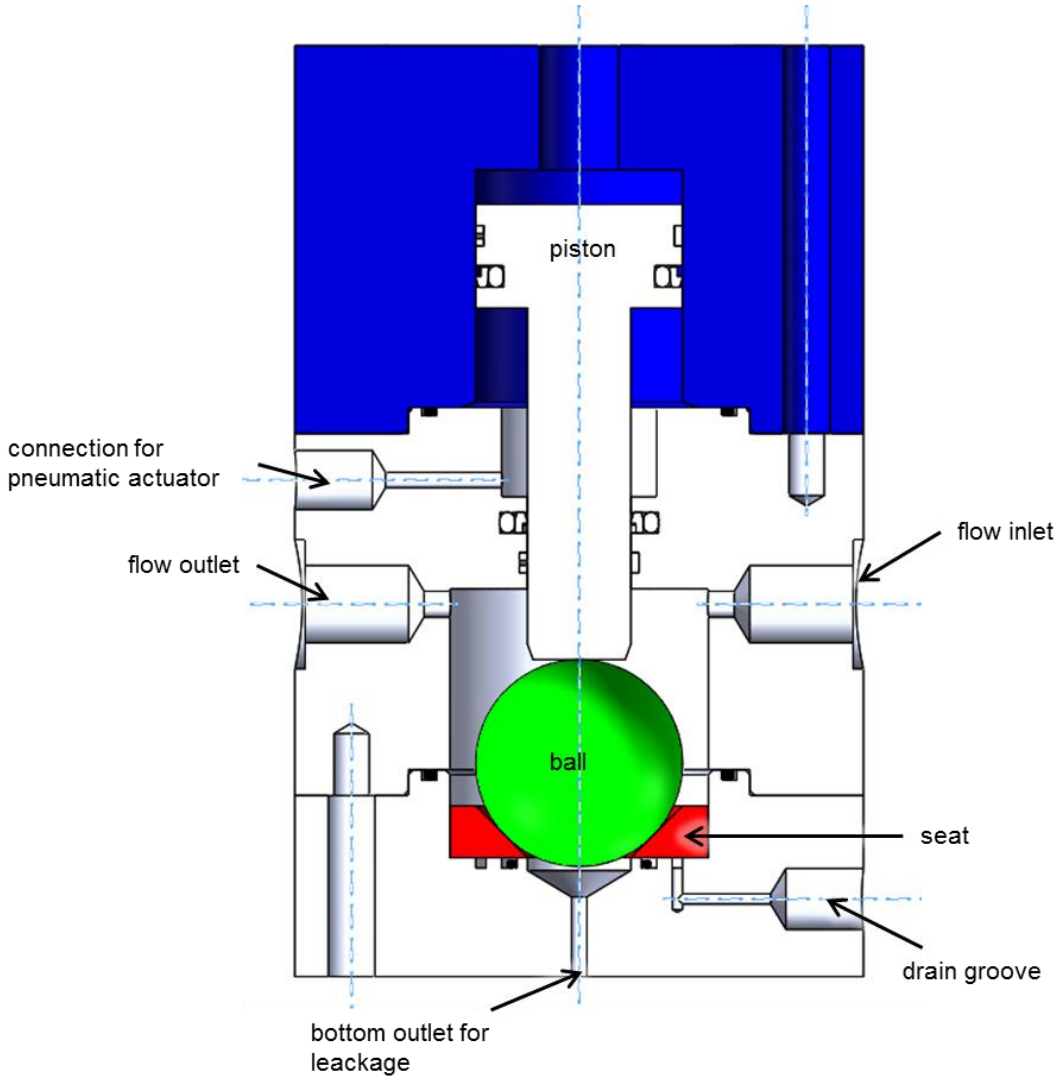

Figure 2. Test chamber

The test rig is designed in such a manner, that the actual sealing components, a standard steel ball which can be bought off the shelf and a circular plate with a cone-shaped bore in the center, can easily be replaced. They are also made very simple, so that a variety of seats can be tested without blowing up manufacturing costs or lead time. The pressure to be sealed sets the force in the contact zone of the components. This is simulated by a hydraulic actuated piston which acts on the ball. It is supplied by an external pressure source. The resulting force is then calculated by measuring the pressure and multiplying it with the area of the piston. For a back stroke, pressurised air is applied on the rod side of the piston. Seals prevent leakage form the piston side into the rod side and further, into the chamber where the sealing seat is. The friction of the seals of the rod is neglected.

For leakage investigations a fluid flow can be directed through the chamber. For leakage tests, a low viscosity fluid, like water, will be used. The parts of the test rig in contact with the test fluid are made of stainless steel to prevent oxidation of the surfaces. The leakage through the sealing contact passes through the bottom outlet is collected and measured with a scale. The observation of the leakage is therefore possible.

As the plate is only sealed with a gap to the housing. Therefore fluid and its pressure could act on the back of the plate which would disturb the calculated force balance in the contact zone. Another issue occurring from the gap is flow which can pass through the bottom outlet. To prevent both, measures are implemented into the test chamber. First, an O-ring is brought in to stop the flow into the outlet. Second, a groove is between the O-ring and the gap. The groove is connected to the environment and therefore no pressure can be built up.

3.2. Hydraulic circuit

The fluid flow is conveyed by a pneumatically driven pressure amplifier. Flow ripples are typical for such an amplifier. To smooth flow ripples out, an accumulator is connected to the outlet of the amplifier which takes up excess flow and delivers flow during periods of a lack of flow from the amplifier. To support the smoothening a throttle is incorporated into the feed line to the test chamber. In further research, the influence of particles on the sealing mechanism will be investigated. Those will be brought into the system through a tank in front of the amplifier and filtered out after the test chamber. Pressure and temperature sensors are implemented to measure the conditions in the test chamber. The entire hydraulic circuit is depicted in Figure 3.

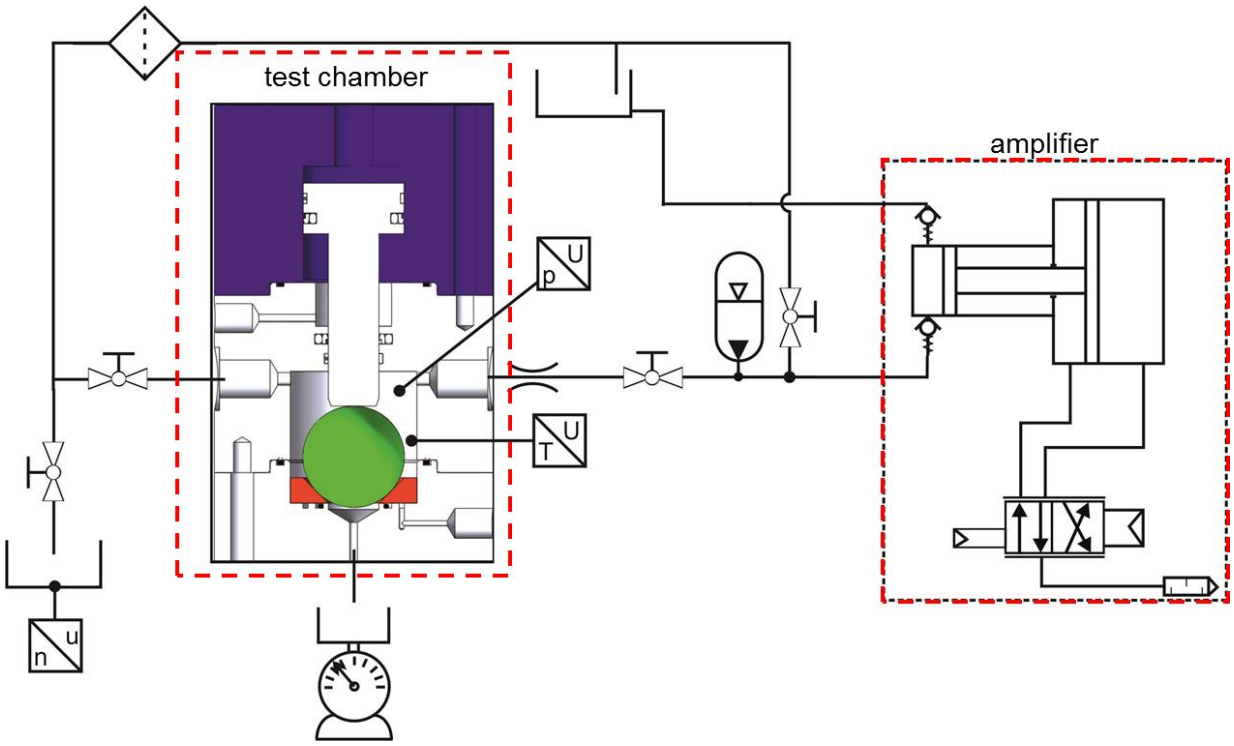

Figure 3. Hydraulic circuit

3.3. Sealing parts

In this section, the sealing parts, ball and seat, are explained in more detail.

3.3.1. Ball

The balls used in this research are off-the-shelf purchasable. Previous investigations have shown that the expected leakage is very low which leads to long test runtimes. In order to keep the test times to an absolute minimum and to have an easy assembly of the test rig, a large ball diameter is selected. This leads to a large contact zone and therefore to relatively high leaking.

The diameter of the balls is 40.000 mm with an accuracy of t_{Dws} of 0.7 µm and they are made of the material 1.4034 (X46Cr13), which is a stainless martensic chromium steel. The grade of the balls is G100 and the surface is extra polished resulting in a surface roughness of R_a=0.05 µm. The hardness, measured with the Rockwell scale [5], is between 55 and 60 The balls are standardized according to DIN 5401 [6].

3.3.2. Seat

The seat is basically a circular plate with a conical bore. The bore has an angle of 90 and the diameter is selected in such a way, that the ball touches the seat in the bore and not on the upper or lower edge.

The seat is made of the material 1.4122 (X39CrMo17-1), which is also a stainless martensic chromium steel, and has a surface roughness of R_a=6.3 µm and a thickness of 10 mm. Figure 4 shows the cross- sectional view of the seat.

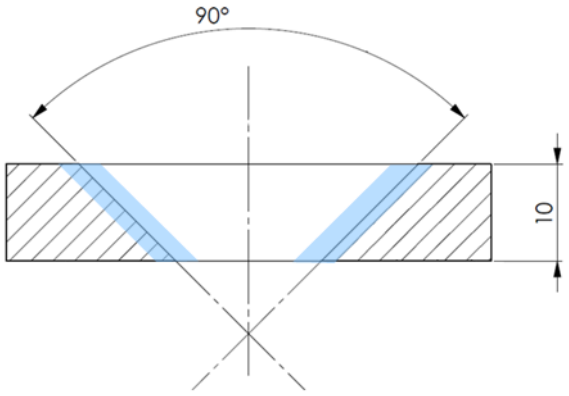

Figure 4. Seat

The surface of the bore can be manufactured with different textures to investigate its impact on the seal mechanism. In this work, only circular grooves are considered. Furthermore, two hardness's are investigated, a hard and a soft one.

3.4. Test rig assembly

The assembled test rig is depicted in figure 5. The pressure for actuating the piston is delivered by a hand driven pump. The pressure is set by a pressure relief valve and measured with an analogues gauge.

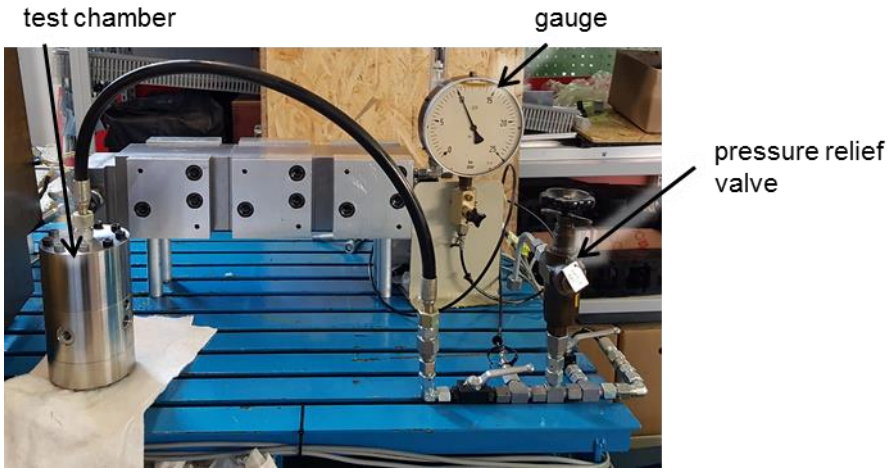

Figure 5. Assembled test rig

The seat and the ball are built into the chamber and compressed with different pressures for different times. After that, the contact zone between both parts is measured with a 3D-microscop to investigate the surface changes of the seat due to the applied force.

4. MEASUREMENT RESULTS

In this section,first, the measured malleable deformation of the seat is shown. Two measurement series were carried out: A soft sealing seat was exposed to different pressures on the piston (5 bar, 10 bar, 25 bar and 100 bar) with different time durations. Second, a hard seat was exposed for different times to a piston pressure of 20 bar and 25 bar, see .Table 1.

Table 1. Measurement matrix for the soft and hard sealing seat

Hard	Pressure [bar]	Duration [min]
	20	5
	25	90
Soft	Pressure [bar]	Duration [min]
	5	5
	10	5
	25	5
	25	90
	100	5

Figure 6 shows the tested specimens. After each test cycle, the sealing seats were cleaned and investigated with a 3D-microscope. A visual indication for malleable deformation can be seen in Figure 6 (right). The picture shows the hard sealing seat after a 25 bar and 90 min exposure. To investigate whether the visual indicators really are malleable deformation, a closer look into the microscope recordings needs to be taken.

Figure 6. Test specimen (left) and resulting malleable deformation for the hard sealing seat (right)

4.1. Soft seat

After each pressure- and time-step, the specimen was investigated using a 3D-microscope. Figure 7 shows the magnified contact area with slight malleable deformations. It is obvious that the sealing body did leave marks on the seat. Additionally, these marks indicate that the assumption of a line contact between body and seat is hardly true. This, of course, depends on the geometry used for body and seat.

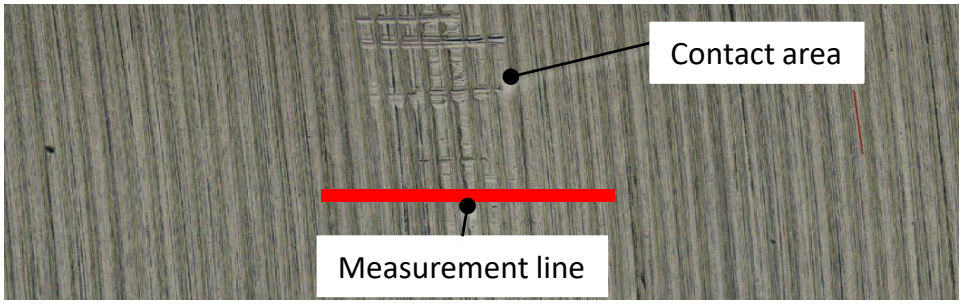

Figure 7. Magnification of the contact area on the sealing seat.

A closer look into the roughness pathway is shown in Figure 8. A length of 900 µm was evaluated. The path is indicated in Figure 7 as the measurement line. Analysing the stochastic roughness, the 200 µm contact area shows some noticeable behaviour. Within the contact area, the pathway shows deviations from the frequency with which the roughness peaks appear. The surface appears to flat out. At 100 bar cylinder pressure, the material behaviour of the sealing seat changes from elastic to plastic behaviour. Before the 100 bar measurement, the roughness pathway did not indicate any deformation or flatting out within the contact area.

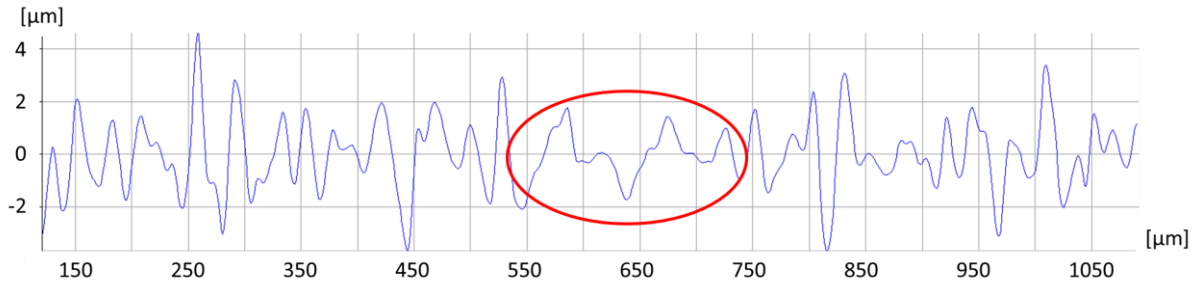

Figure 8. Roughness pathway across the contact area of the soft sealing seat

4.2. Hard seat

With the results of the soft sealing seat, the hard sealing seat was set up with a cylinder pressure of 25 bars and 90 min time. The resulting roughness pathway is illustrated in Figure 9. As expected, due to mainly elastic deformation, no noticeable changes within the roughness pathway can be identified.

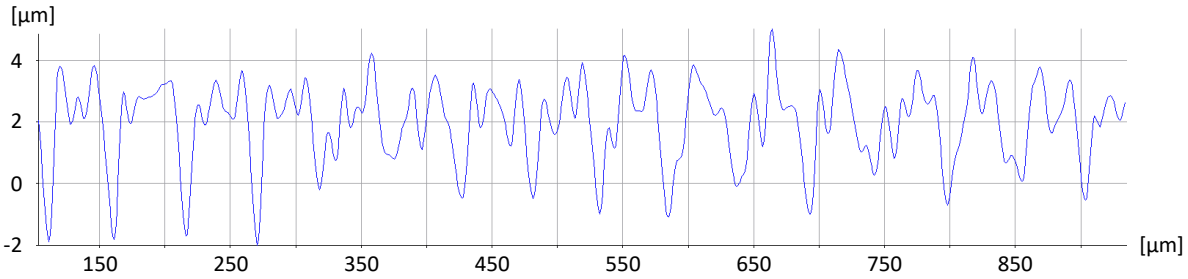

Figure 9. Roughness pathway across the contact area of the hard sealing seat

5. CONCLUSION AND OUTLOOK

Within this paper, a test-rig to induce defined contact pressures between two metallic sealing bodies was presented. When looking at a ball-plane contact, a line contact is assumed in between these two partners. At that line, the pressure to be sealed drops. Fluid can pass through the channels formed by the surface roughness of the sealing bodies. To prevent that, elastic and sometimes malleable deformation occurs within the contact area to close all relevant fluid channels. The assumed line contact becomes an actual area contact due to the said deformation. The contact pressure can be calculated analytically using Hertz´s law. In the frame of this work, different operating points were investigated. The contact was loaded with different pressures and different exposure times and the resulting malleable deformation was measured. Those showed neither at the soft nor at the hard sealing seats malleable deformations, since the material is mostly stressed within the elastic regime.

In coming research, alternating loads onto the contact will be subject for research. Doing so, a comprehensive FEA will be carried out and its results will be compared to measurements. The results will be used to calculated the flow through the remaining channels formed by asperities of the surface roughness. Furthermore, the results will be validated with the presented test rig, which will be extended to perform the required test.

ACKNOWLEDGEMENTS

This work was funded by the German Research Foundation (DFG) in the scope of the Project „Modellbildung metallischer Dichtsitze” (MU1225/42-1). The authors would like to thank DFG for its support.

REFERENCES

[1] Schmidt, M., Dichtheit als Entwicklungsschwerpunkt für Sitzventile hochdynamisch schaltender Zylinderantriebe. Dissertation RWTH Aachen. 2010

[2] Wriggers, P., Computational Contact Mechanics, Second Edition, ISBN-10 3-540-32608-1 Springer Berlin Heidelberg New York. 2002

[3] Popp, A., Mortar Methods for Computational Contact Mechanics and General Interface Problems. Dissertation Technische Universität München. 2012

[4] Ashby, M. F., and Jones, D. R. H., Engineering Materials 2: An Introduction to Microstructures and Processing. Oxford University. 2013

[5] N.N, Metallic materials – Rockwell hardness test-Part 1: Test method, International Standard ISO 6508-1, Beuth, 2016

[6] N.N, Wälzlager – Kugeln für Wälzlager und allgemeinen Industriebedarf, German Industrial Standard DIN 5401, Beuth, 2002

[7] Hertz, H.: Ueber die Berührung fester elastischer Körper, Jour. für die reine und angewandte Mathematik, 92, S. 156–171, 1881.

[8] Niemann, G.; Winter, H.; Höhn, B.-R.: Maschinenelemente – Band 1: Konstruktion und Berechnung von Verbindungen, Lagern, Wellen, 4. Aufl., Springer [u. a.], Berlin, 2005.

IMPROVED PERFORMANCE ON RECIPROCATING SEALS DUE TO OPTIMIZED LUBRICATION IN THE SEALING SYSTEM

Wilke, Mandy (1); Jordan, Holger (1); Seppälä, Timo (2)
1: Trelleborg Sealing Solutions Germany GmbH, Germany
2: Trelleborg Sealing Solutions Finland Oy
mandy.wilke@trelleborg.com

ABSTRACT

The performance requirements of multiple sealing systems for reciprocating movements are continuously increasing with friction, wear and service time being key performance criteria. The new concept, presented in this paper, is about adjusting lubrication conditions of all single sealing elements within a sealing system so the load on each element can be reduced and the performance in terms of friction-wear-lifetime can be optimized.

Best practice in demanding fluid power sealing applications is a primary and a secondary seal. The primary seal does the sealing job for as long as possible and the secondary seal is the redundancy, there when it is needed. The challenge for this secondary sealing element is length of life under dry running conditions. The more effective the primary seal in sealing in lubricant to the hydraulic system, the drier the running conditions of the secondary seal. Starvation of lubrication can lead to wear issues that come in to play in the case of a needed redundancy. The paper describes the dilemma in terms of optimizing the performance of the primary and secondary seal and brings up a new seal concept, where the risk of leakage of lubricant is balanced to ensuring performance of the primary seal and the extended life of the secondary seal. This is achieved by allowing a better, thicker oil film under the most pressure loaded first sealing element to reduce the load on that seal [1, 2].

KEYWORDS: Energy efficiency, lifetime improvement, hydraulic sealing system with improved lubrication, alternative coating technologies for counter surfaces

1. INTRODUCTION

The performance requirements of multiple sealing systems for reciprocating movements are continuously increasing with friction, wear and service time being key performance criteria. The new concept, presented in this paper, is about adjusting lubrication conditions of all single sealing elements within a sealing system so the load on each element can be reduced and the performance in terms of friction-wear-lifetime can be optimized.

Best practice in demanding fluid power sealing applications is a primary and a secondary seal. The primary seal does the sealing job for as long as possible and the secondary seal is the redundancy, there when it is needed. The challenge for this secondary sealing element is length of life under dry running conditions. The more effective the primary seal in sealing lubricant to the hydraulic system is, the drier the running conditions of the secondary seal. Starvation of lubrication can lead to wear issues that come into play in the case of a

needed redundancy. This paper describes the dilemma in terms of optimizing the performance of the primary and secondary seal and brings up a new seal concept, where the risk of leakage of lubricant is balanced to ensuring performance of the primary seal and the extended life of the secondary seal. This is achieved by allowing a better, thicker oil film under the most pressure loaded first sealing element to reduce the load on that seal.

A well-known and essential challenge within the sealing function of dynamic machine components is the tightness and durability. Next to this the aspect of efficiency is focused more and more. In most applications sealing positions are consumption areas as well, due to friction and additional conditions, that have an impact on the total machine efficiency and costs. The broad range of requirements within applications, e.g. tightness, durability and consumption, varies with material and design of the seal or the sealing system. A significant amount of investigations in the area of hydraulic rod seals contain the specification and measuring of lubrication thickness, conveying effectiveness and leakage [3, 4, 5]. All studies rely on the thesis according to Müller [6], which represents the optimum sealing performance, depending on a triangle formed pressure distribution curve with the maximum close to the sealing edge on pressure load side. To evaluate the efficiency, it is furthermore necessary to include friction as a main influence [2, 7, 10].

Within the application the parameter of the sealing system meets the parameter of the hard-ware. At dynamic sealing systems the sealing gap has a significant influence on friction, abrasion and durability. In the contact area of seal and counter surface the tribological behavior, which comprises friction and abrasion, is mainly depending on the lubrication condition. This leads to the idea to optimize the lubrication condition with modifications of each sealing element regarding its individual function and stress [2, 7, 10].

This paper extends the presented and published content [8, 10] of the concept which contains all previous mentioned points and furthermore improves the lubrication condition for the whole sealing system by adjusting the loads for each element. To achieve this, the lubrication amount and quality have to be optimized.

2. CURRENT STATE OF THE ART

If only the theoretical aspects of the lubrication thickness between seal and counter surface are considered, e.g. the inverse hydrodynamic thesis according to Blok [9], the thickness is directly adjusted by the gradient of the contact pressure distribution, also described by Müller and other authors [6, 3, 4, 5].

A reduced gradient during the outstroke of the rod leads to a modified lubrication distribution and thickness within the sealing gap, which has a positive effect on friction and load. During the instroke the system condition necessitates to have a flat pressure distribution gradient as well. Sealing systems with high elasticity and low modulus have the tendency to create a high angled gradient due to shape modelling under pressure load. The result is a reduced lubrication conveying capacity, which has a negative impact on the endurance of the rod seal, compare [10].

According to the literature the solution is usually to apply a back-up element made of a material with a higher modulus, e.g. Buffer Ring made of polyurethane (PUR) in combination with back-up ring made of polyoxymethylene (POM). Never the less the back-up element gets pressurized as well, which leads again to high angled pressure distribution gradients within the contact areas to the counter surface. This has the same negative influences as mentioned above for the sealing element.

If focus is on friction level and stroke initial force polytretrafluorethylene (PTFE) is the preferred sealing material. The following chapter describes the applying of the improved lubrication concept on a standard PTFE slipper seal and the opportunity to solve challenges in combination with new coating technology regarding counter surfaces.

3. IMPROVEMENT OF LUBRICATION WITHIN SEALING SYSTEMS

Key of the new concept is to modify the contact pressure distribution on all parts of the seal that contact to the counter surface, that the result is a symmetrical and flat distribution gradient, Figure 1.

If the sealing system contains back-up rings, the edges of these are modified with radii to optimize the lubrication condition.

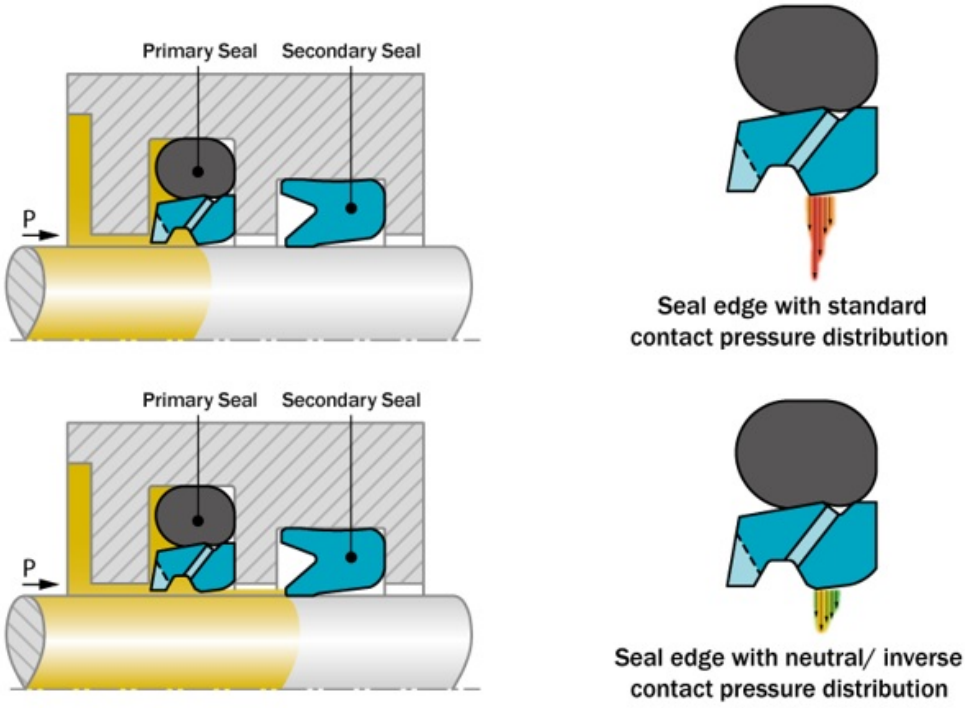

Figure 1. Comparison between typical sealing system with common contact pressure distribution to sealing system with optimized lubrication

In a tandem system, e.g. in a hydraulic actuator, the primary seal is usually pressurized most and gets the highest load. If the system has low lubrication simultaneously, the performance limits are reached quite fast, which result in an unfavorable consumption, duration and efficiency. An improved lubrication on the primary seal with an integrated valve function pushes the limits of friction and abrasion behavior into a positive way for the system and the application.

4. TEST RESULTS

To determine the influence within the tribological system, different test rigs with a variety of test parameters were used.

Friction is measured at different pressure to velocity (p x v) values. The runtime behavior is an estimation during test runs according to temperature, velocity and pressure. An evaluation of the counter surface structure and roughness is especially necessary at test runs with short stroke travels and high frequency tests up to 50 Hz (+/- 0,5 mm). Figure 2 shows the parameters and the test rig for abrasion evaluations.

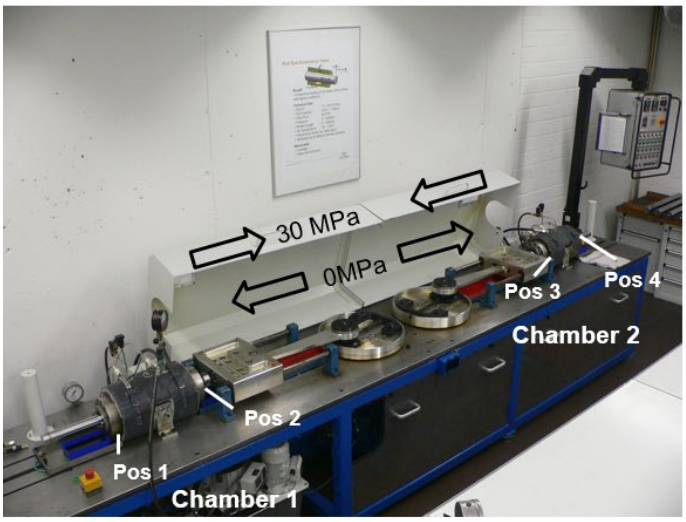

- Drive — Sinusoidal movement
- Stroke — 300 mm
- Pressure — 0/30 MPa
- Velocity — 0,7 m/s
- Oil temp. — 50 °C
- Cycles — 1.000.000 DS
- Rod — Ø 50 mm Laser Cladded
- Fluid — HLP 46

Figure 2. Test rig for abrasion evaluation on rod seals

The tested laser cladded counter surface provides unfavourable properties from a tribological point of view. The surface shows relatively high Rz values in combination with a ratio be-tween one and two (Rvk/Rpk). According to these values the surface structure is open, figure 3.

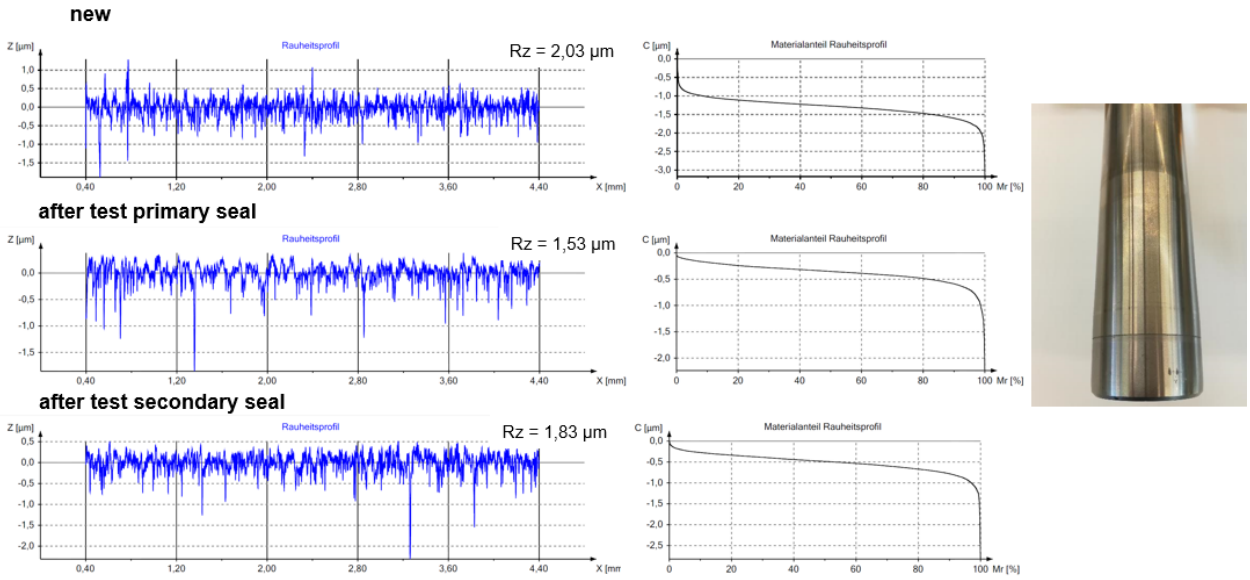

Figure 3. Roughness values of laser cladded counter surface

Standard sealing systems in combination with described counter surface did experience in-creased abrasion and wear rates. An improvement within the sealing system results in a better performance level and therefore longer lifetime and lower wear rates. Figure 4 shows friction comparison between standard sealing systems and the lubrication improved sealing system including PTFE primary seal with different velocities and pressure steps. The diagram shows a stable and low range friction behavior of the improved lubrication system compared to the standard sealing system.

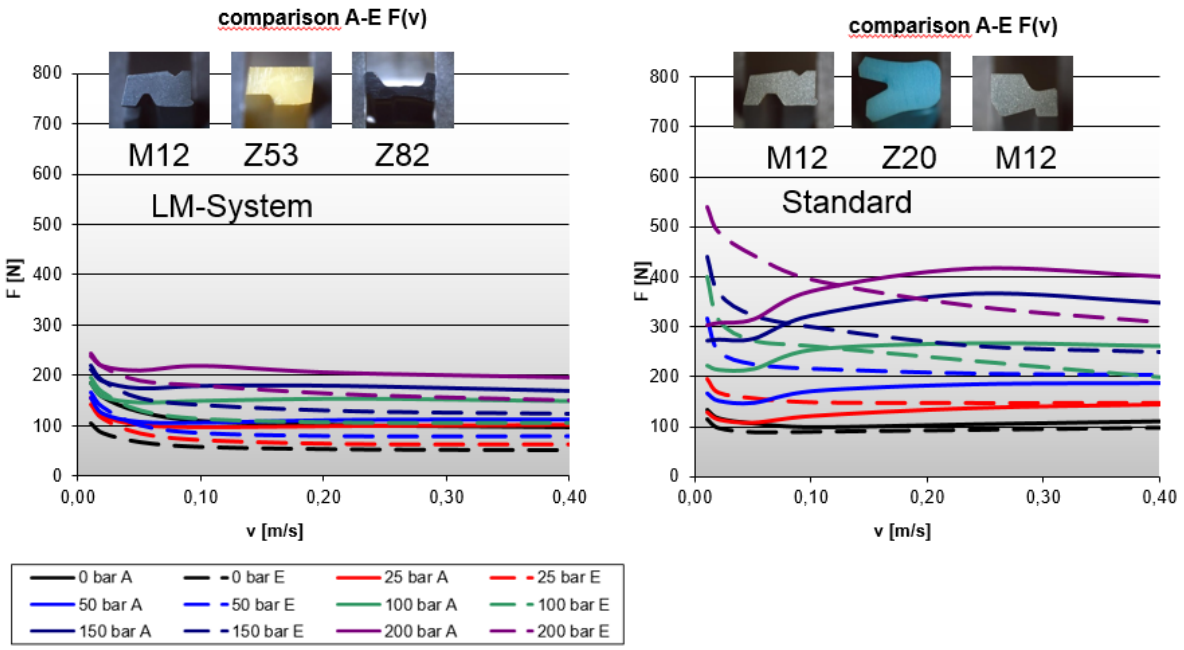

Figure 4. Comparison friction behavior of sealing systems

Additional benefits are clear, while regarding the wear on the seals, which is deviated from the pretension loss (delta W-dimension). Figure 5 shows the comparison between the sealing profiles. The pretension loss on primary seal has been reduced from 6,8% on 3,8% due to the effect of lubrication improvement [2, 7, 10]. Next to this the effect is apparent on the friction measurements. Figure 6 shows friction comparison between standard PUR sealing systems and the lubrication improved sealing system with different velocities and pressure steps.

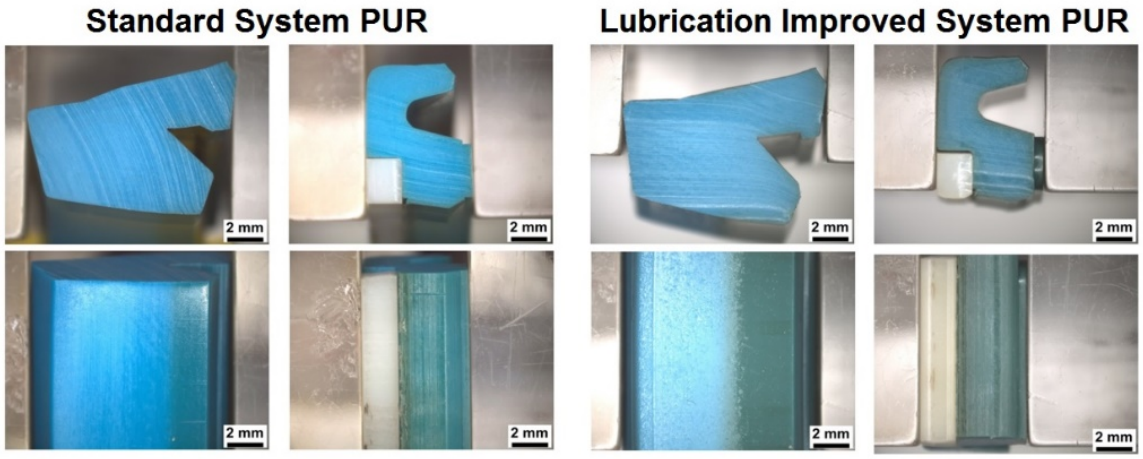

Figure 5. Comparison of wear on sealing systems [2, 7, 10]

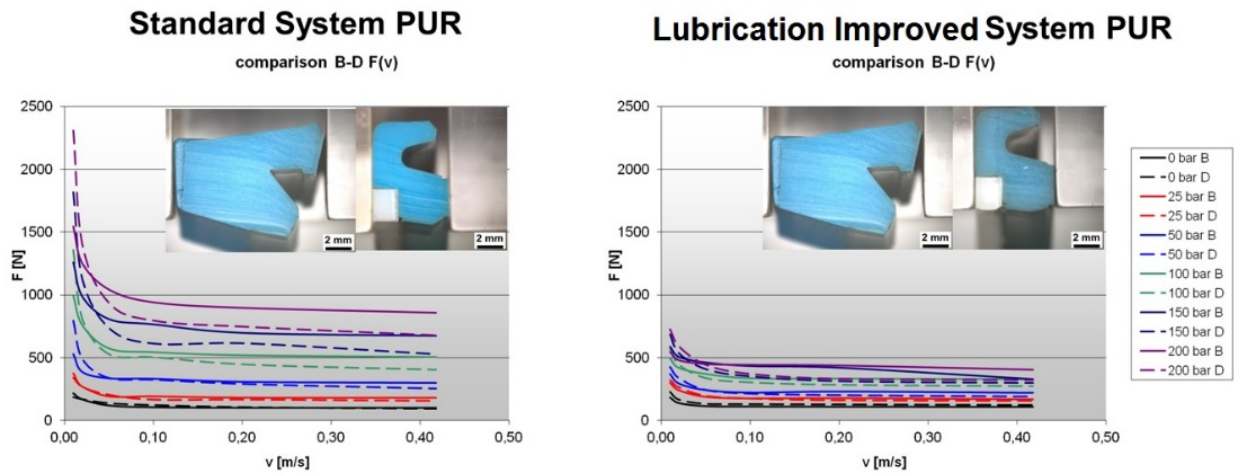

Figure 6. Comparison friction behavior of sealing systems [2, 7, 10]

The summarized advantages are clear regarding the combination of a tremendously reduced friction and very low wear rates on the primary seals. Additional benefits are achievable at short stroke applications. Again, very good results were achieved regarding the lifetime of secondary seal and furthermore on run in behavior on the counter surface. For this purpose, the same test rig mentioned in Figure 2 was used with modified parameter to a stroke length of 10 mm and a constant pressure of 25 MPa. The velocity was 4 mm/s, at 80 °C and 1 million cycles. After the test no changes of roughness on the counter surface, neither on primary or secondary sealing area, was measurable (Figure 7).

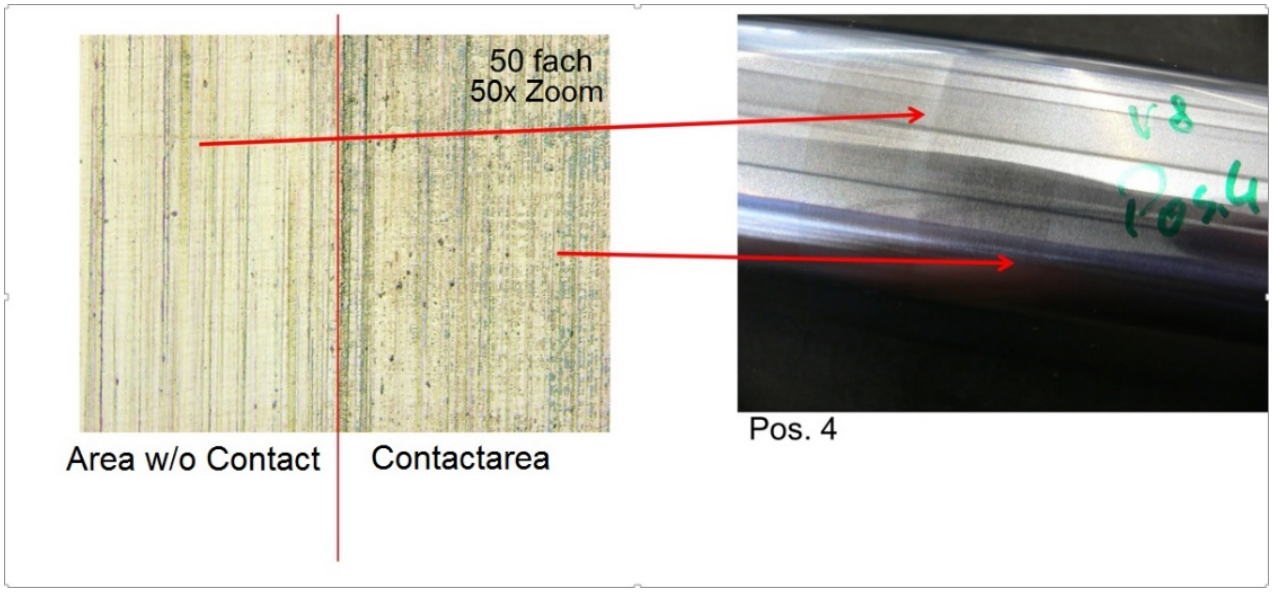

Figure 7. Counter surface after short stroke test with 1 million cycles [2, 7, 10]

Next to these benefits of the improved lubrication are visible at high frequency applications. Figure 8 shows the pretension loss of the primary and secondary seal after a 288 hours high frequency test (1/20 Hz, 5 MPa and 80 °C).

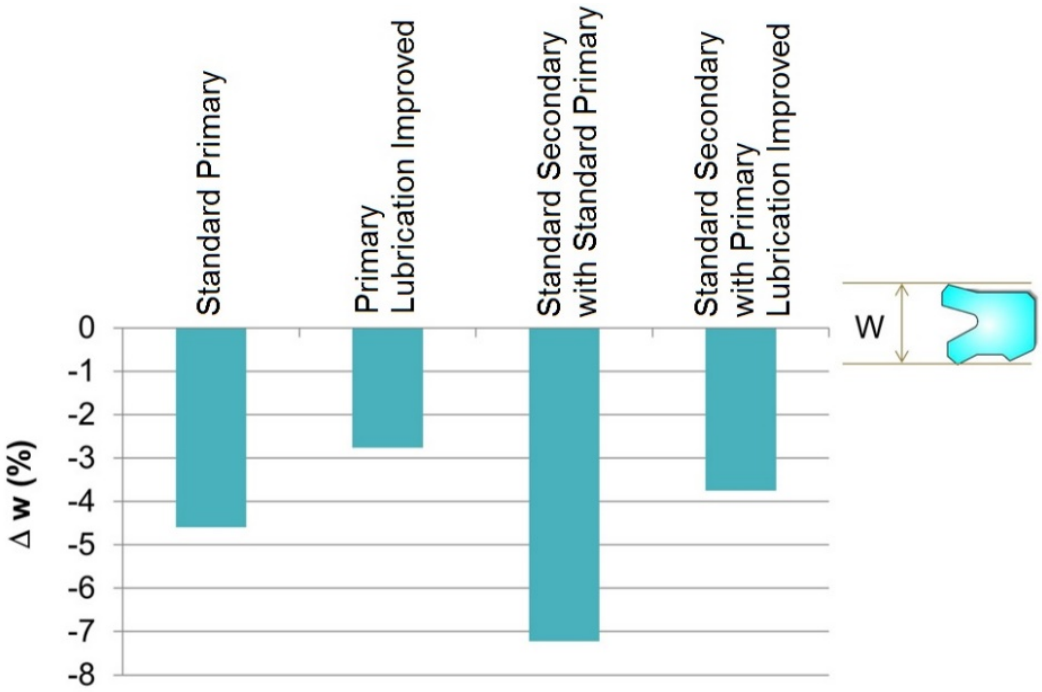

Figure 8. Pretension loss of primary and secondary seal [2, 7, 10]

The reduced load on the tribological system in total can also be seen as an increasing of the robustness of the sealing system. This leads to a favorable improvement of the system life-time concerning very abrasive counter surface topographies. As an example, an Al_2O_3 coated rod was used for comparison tests.

The topography of the rod shows typical structures for this kind of coating, the Rz values are around 2,5 µm. Figure 9 shows a 3-D contact measured surface structure and profile cut. The profile and wear pictures of the tested sealing system in combination with above mentioned mating surface verify the positive effect of the flat pressure distribution gradient.

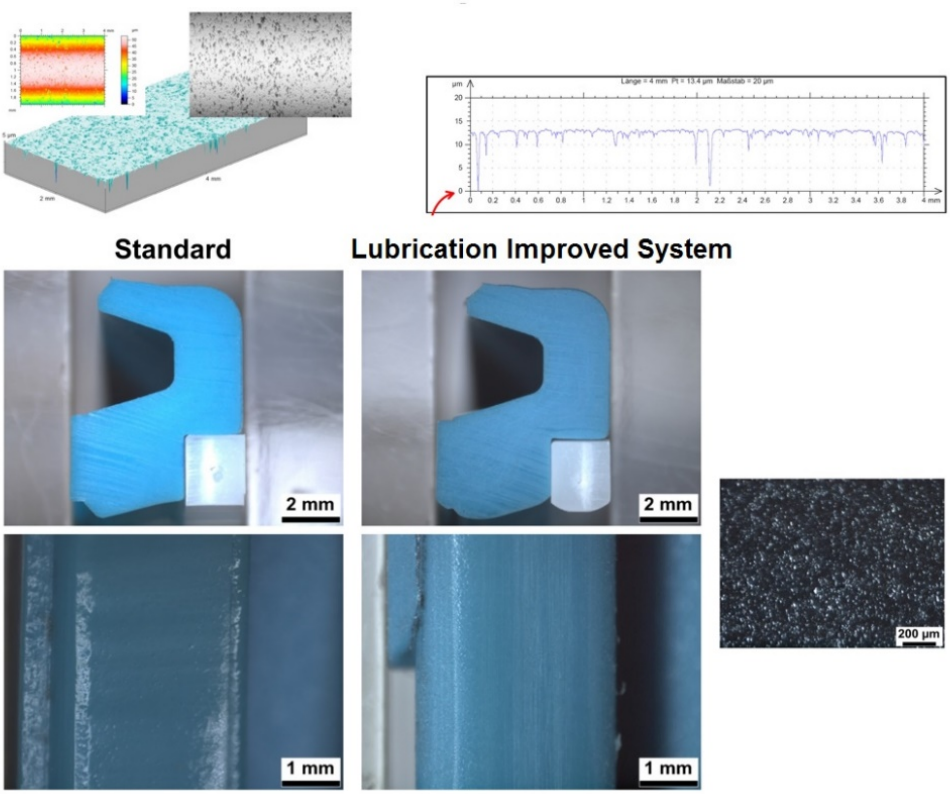

Figure 9. Comparison wear on seal in combination with Al_2O_3 counter surface [2, 7, 10]

5. CONCLUSIONS

In general, it can be stated that a lubrication improvement of sealing systems is possible with all sealing materials and the modification pushes the performance limits of all material groups. Even big diameters manufactured on a centre lathe out of e.g. PTFE or UHMPE compounds are feasible. Due to lubrication improved sealing systems the performance limits of load, friction, wear and total lifetime can be increased tremendously. FEA simulations helped to create the concept, which was later compared and approved by in house tests.

NOMENCLATURE

R_z	Average Maximum Height of the Profile	[µm]
R_{vk}	Reduced Valley Depth	[µm]
R_{pk}	Reduced Peak Height	[µm]

REFERENCES

[1] Wilke, M.; Jordan H. 2016. 19th International Sealing Conference: Zur Leistungssteigerung von translatorischen Dichtungen durch Schmierfilmoptimierung im Verband des Dichtsystems, October 12-13, 2016, Stuttgart, Germany, pp. 633–639.

[2] Wilke, M.; Jordan H. 2016. Steigerung des Leistungsvermögens translatorischer Dichtungen durch Schmierfilmoptimierung im Dichtsystem. In: O+P Fluidtechnik für den Maschinen- und Anlagenbau, 4/2016, pp. 70 – 73, ISSN 0341-2660, 2016.

[3] Hörl, L., Haas, W., Innovative Dichtungsbewertung durch Schmierfilm-Dickenmessung, In: 12th International Sealing Conference, Stuttgart, Germany, pp. 434 – 446, October 10-11, 2002

[4] Nißler, U., Haas, W., Simulation und Versuch bei Hydraulikdichtringen, In: 14th International Sealing Conference, Stuttgart, Germany, pp. 497 – 510, October 10-11, 2006

[5] Nißler, U., Haas, W., Hörl, L., Unterschiede in der Dichtheitsbewertung durch verschiedene Bewertungsverfahren, In: 12th International Sealing Conference, Stuttgart, Germany, pp. 355 – 368, October 07-08, 2008

[6] Müller, H. K., Abdichtung bewegter Maschinenteile, Medienverlag Ursula Müller, 1990.

[7] Wilke, M., Jordan, H., Leistung translatorischer Dichtungen steigern – Schmierfilmoptimierung im Dichtsystem, In: Fluid, 6/2016, pp. 24-27, 2016

[8] Jordan, H., Mehrteiliges Stangendichtsystem für hydraulische Anwendungen zur Steigerung der Leistungsfähigkeit und Lebensdauer bei höchster Belastung, In: 14th International Sealing Conference, Stuttgart, Germany, pp.335-343, October 10-11, 2006

[9] Blok, H., Inverse problems in hydrodynamic lubrication and design directives for lubricated flexible surfaces, In: Proc. Symp. on Lubrication and Wear, Houston, Texas, 1963

[10] Jordan, H., Wilke, M., Zur Leistungssteigerung von translatorischen Dichtungen durch Schmierfilmoptimierung im Verband des Dichtsystems, In: 19th International Sealing Conference, Stuttgart, Germany, pp.633-639, October 12-13, 2016

CLASSIFICATION OF MACHINE FUNCTIONS: A HYDRAULIC EXCAVATOR CASE STUDY

Nathan J Keller, Monika Ivantysynova, Andrea Vacca, Yixuan Sun, Yifei Zhou, Guang Lin
Maha Fluid Power Lab
Purdue University
1500 Kepner Drive, Lafayette, IN 47905
kellern@purdue.edu

ABSTRACT

The increase in mobile machine automation and data collection has allowed mobile equipment manufacturers to push to implement their machines with smart machine learning algorithms to assist in the condition monitoring of the system. Machine learning algorithms are broken into two main categories, supervised and unsupervised learning. Supervised learning requires previously labelled training data, while unsupervised learning does not require labelled data and infers patterns by itself. Classification is a sub-class of supervised learning. Three common classification algorithms are briefly discussed, decision trees, Support Vector Machines (SVM), and K-Nearest Neighbor (KNN).

The goal of this research is to successfully classify the machine functions on a hydraulically driven mini-excavator. Machine function classifications can provide points of reference for future online condition monitoring techniques and algorithms. Therefore, this work will be used as a springboard into more traditional condition monitoring techniques to monitor the health of the hydraulic system on mobile equipment.

To accomplish the aforementioned goal it seemed important to first explore common types of classification algorithms available. Then, a displacement controlled mini-excavator was instrumented to record many different parameters during a typical truck loading cycle. Each data point was assigned a label that corresponds to the current function of the machine; travelling, unloading, swinging, digging, or idling. The data was then taken with the corresponding labels and trained in a decision tree learning algorithm. The algorithm was then tested to determine the accuracy of labelling unseen data.

This work focuses on the classification of the machine functions on a Bobcat 435 mini excavator that is equipped with a displacement controlled hydraulic system and is instrumented with several thermocouples, pressure transducers, angle sensors, speed sensors, and accelerometers. The data collected during a representative truck loading cycle is fed into a decision tree training algorithm to predict machine functions on unseen data.

Four different classification models were run varying the number of input features. It was shown that the command signals from the operator are the most important input features and contribute the most to the model accuracy and performance.

KEYWORDS: Condition monitoring, machine learning, classification, supervised learning, mobile machine maintenance, Internet of Things (IoT), decision trees, k-nearest neighbor (KNN), support vector machine (SVM)

1. INTRODUCTION

Maintenance for mobile equipment hydraulic systems has recently been an area of major concern and emphasis for Original Equipment Manufacturers (OEMs) and operators. When a mobile machine experiences unplanned downtime, they are often a significant distance from a repair facility. For instance, agricultural tractors, mining equipment, and forestry equipment often work kilometers from repair shops. When a mobile machine unexpectedly breaks down, the owners and operators can lose significant amounts of money and time repairing the machine. Not only do they lose money and time repairing the machine but also in the machine productivity. However, health and safety concerns are among the most important motivators for improving the productivity and reliability of mobile equipment.

The rise of the Internet of Things (IoT) and automation for mobile machinery is driving hydraulic systems to become smarter. IoT requires data to be collected from the machine and sent to data processing sites within wireless clouds. Mobile machine automation requires more controller inputs from sensors and faster response times for the control systems because of the absence of operators and an increased number of automated actuators [1], [2]. This opens the door for more sophisticated methods of machine maintenance utilizing online machine learning and diagnostic systems.

The goal of this research is to successfully classify the machine functions on a hydraulically driven mini-excavator. Machine function classifications can provide points of reference for future online condition monitoring techniques and algorithms. Therefore, this work will be used as a springboard into more traditional condition monitoring techniques to monitor the health of the hydraulic system on mobile equipment.

To accomplish the aforementioned goal it seemed important to first explore common types of classification algorithms available. Then, a displacement controlled mini-excavator was instrumented to record many different parameters during a typical truck loading cycle. Each data point was assigned a label that corresponds to the current function of the machine; travelling, unloading, swinging, digging, or idling. The data was then taken with the corresponding labels and trained in a decision tree learning algorithm. The algorithm was then tested to determine the accuracy of labelling unseen data.

The structure of this paper is as follows: Section 2 is a brief review of classification in machine learning, which includes pre-processing, decision trees, support vector machines, and k-nearest neighbor; Section 3 contains the case study of the hydraulic mini-excavator, which includes the machine instrumentation, machine function labelling, and the results from the classification algorithm used; Section 4 then concludes the paper with a summary, and a list of future works.

2. CLASSIFICATION REVIEW

A classifier takes input data then assigns the input of a set to discrete output classes. The objective of the classification algorithm is to learn the mapping of the input to the output. Practically, this means a model or rule is developed that allows the machine learning algorithm to make future predictions based on past data. Classification helps designers and operators extract more information about the system. The more information known about the system, then the better it can be designed to become more reliable and productive for the consumer. In addition to predicting future behavior and extracting more information about the system, learning systems perform a compression [3]. A compression is done by creating a rule or model from the data and explaining the behavior of the system simpler than the data itself. Three main types of classification algorithms will be discussed: decision trees, support vector machines (SVM), and k-nearest neighbor (KNN).

2.1. Pre-processing

Pre-processing data is the process of transforming or altering the data before it is fed into the machine learning algorithm. Pre-processing can improve the results of the machine learning algorithm if done correctly and is

considered one of the most important factors in determining the performance of the algorithm [4]. Pre-processing can involve reducing the dimensionality of the dataset or scaling the input variables.

Reducing the dimensionality of the dataset seems, at first, could be detrimental to the final performance of the learning system since information is discarded. However, it can actually improve the performance. In fact, adding too many input variables or features can reduce the performance of the system [4]. A reason is because of overfitting. Overfitting occurs when the model can fit the training data very well but is not able to generalize well on the testing data.

Some methods to reduce dimensionality can be to combine some of the original inputs into linear combination of one another. Another methods to dimensionality reduction is to simply choose some of the inputs and discard the rest. This approach can be used if several of the input variables are known to contain little information or if strong correlation is known between variables [4]. However, the approach of discarding input variables requires prior knowledge of the system and should only be done if each variable is understood or a principle component analysis (PCA) is conducted.

Pre-processing can also involve scaling or altering the input variables. An example where this may be useful is when both accelerations and pressure transducers are used as input variables. The accelerations may have units of m/s^2 while the pressure transducer may have units of *Pa*. The values of these parameters could differ from each other in multiple orders of magnitude. Therefore, a simply scaling or normalization technique can compress the data into a simpler form without losing information. Some additional pre-processing techniques can be found in [5]–[7].

2.2. Decision Trees

Decision trees are one type of classification algorithm that can be used for nonlinear mapping from input variables to a set of output variables. A decision tree is a decision making method that provides each of the possible choices a probability according to a decision system [8]. Decision trees break up a complex decision making process into several simpler and smaller decisions. Trees are easy to interpret and can provide needed insight into the data [9].

The decision process starts at the root and continues through nodes and branches until the leaf node is reached, see Figure 1. The root is at the top of the tree, while the leaf nodes are the bottom portions of the tree that do not continue to split. Leaf nodes represent the output [3]. A large tree is first constructed and then pruned to minimize the complexity and cost of the algorithm [9]. Several stopping rules and pruning methods have be proposed in literature. In 1984 Breiman et al. proposed a method to successively grow and selectively prune the tree, using cross-validation to choose the subtree with the lowest estimate misclassification rate [10]. For a more detailed description of decision trees see [3], [9].

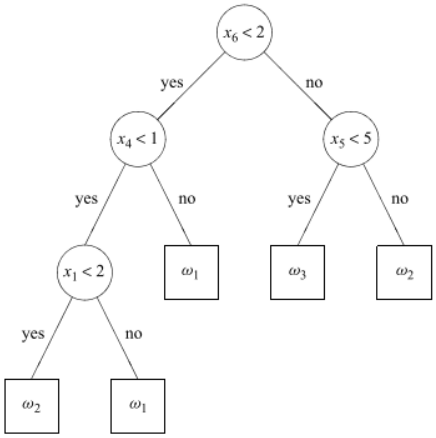

Figure 1. Simple decision tree [9].

2.3. Support Vector Machines

Support Vector Machines (SVM) are non-probabilistic binary classifiers that were invented by Vladimir Vapnik and Alexey Chervonenkis in 1963 and further refined by Vapnik and Corinna Cortes in 1995 [11]. SVMs are limited to producing only two outputs and have only been available for use with supervised learning. However, in 2001, SVMs were first used as clustering algorithms in unsupervised machine learning techniques[12].

SVMs begin with finding the optimal hyperplane, which differentiates between the two classes, as seen in Figure 2. The distance between the hyperplane and the nearest data point from either set is called the margin. A larger margin means the algorithm is more robust and reliable. A hyperplane that has a lower margin but correctly classifies the data is given priority over a hyperplane that has a smaller margin but is not as accurate at classifying the data. The hyperplane shown in Figure 2 is linear, but it can take the form of many shapes, such as an ellipse, by using the kernel trick invented by Boser, Guyon, and Vapnik in 1992 [13]. For more details on SVMs see [11].

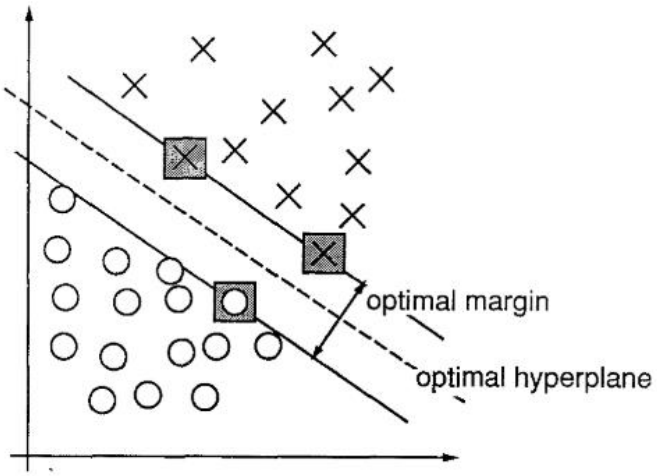

Figure 2. Support Vector Machine (SVM) example [11].

2.4. K-Nearest Neighbor

K-nearest neighbor (KNN) is a non-parametric and one of the best known classification and regression machine learning algorithms [14], [15]. The basic principle of KNN is that it assigns an unclassified data point to the classification of the nearest of a set of previously classified points. In other words, the unclassified data point takes on the classification its “nearest neighbor.”

Figure 3 shows a binary classification scheme, a classification of blue circles and red *X*. The unclassified data point is shown as a green triangle. This particular example compares the unclassified data point to the nearest three previously classified points, corresponding to *k=3*. The unclassified data point is closest to one blue circle and two red *X* and would then be classified as an *X* because majority rules.

Many techniques can be employed when developing a KNN algorithms. However, a few rules must be met to achieve optimum performance when choosing the value of nearest neighbors, *k*. For a binary or two class problem, *k* must be an odd number to avoid ties that could arise in the algorithm [16]. Additionally, k must not be a multiple of the number of classes to also avoid ties. One of the most common techniques in determining the nearest neighbors using the Euclidean distance method. This and other techniques are explained in more detail in [17].

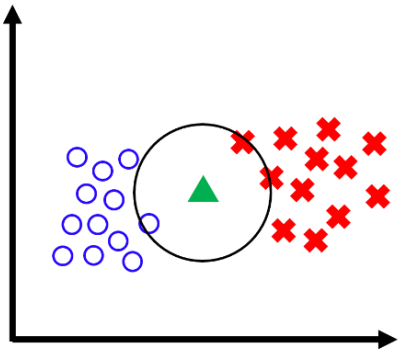

Figure 3. K-Nearest Neighbor (KNN) example.

3. EXCAVATOR CASE STUDY

The mobile hydraulic equipment that is used to collect the sample data for this classification study is a Bobcat 435 mini excavator, see Figure 4. This type of excavator has a 2-liter, 4-cylinder turbocharged 36.5 kW engine. However, this is a displacement controlled (DC) prototype machine. For more information on displacement control see [18]–[21]. The machine instrumentation, data sampling, machine function labelling, and classification results will be shown in this section.

Figure 4. DC prototype Bobcat 435 mini excavator at Maha Fluid Power.

3.1. Machine Instrumentation

The hydraulic schematic of the prototype excavator at Maha Fluid Power Labs can be seen in Figure 5 shows the novel pump switching system for displacement controlled systems. The main sensors installed on this machine can be seen in Table 1. More information on the functions of the pump switching DC hybrid excavator can be found in [22]. However, it is important to note the instrumentation that is equipped on the hydraulic system. Notice that for each hydraulic unit the swashplate position is measured and the pressure at each of the pressure ports. What is not shown below is that each unit is also equipped with thermocouples at both pressure ports and the drain port. Additionally, Unit 1 is instrumented with a triaxial accelerometer mounted on the case to measure vibrations. However, the pump case accelerations were neglected for this particular study.

Figure 6 shows each measured parameters on the excavator. For this study, measurements were only considered for Unit 1 because of its commonality of being used in several different operational functions, as will be described in a later section. In addition to the hydraulic parameters, many other parameters were measured such as the ambient temperature around the machine to get a temperature difference between the pump and ambient conditions, the engine speed, joystick command, and travel lever commands. The joystick commands can be seen in Figure 7. The minor functions such as the offset and blade lift and lower have been neglected in this study due to their infrequent use.

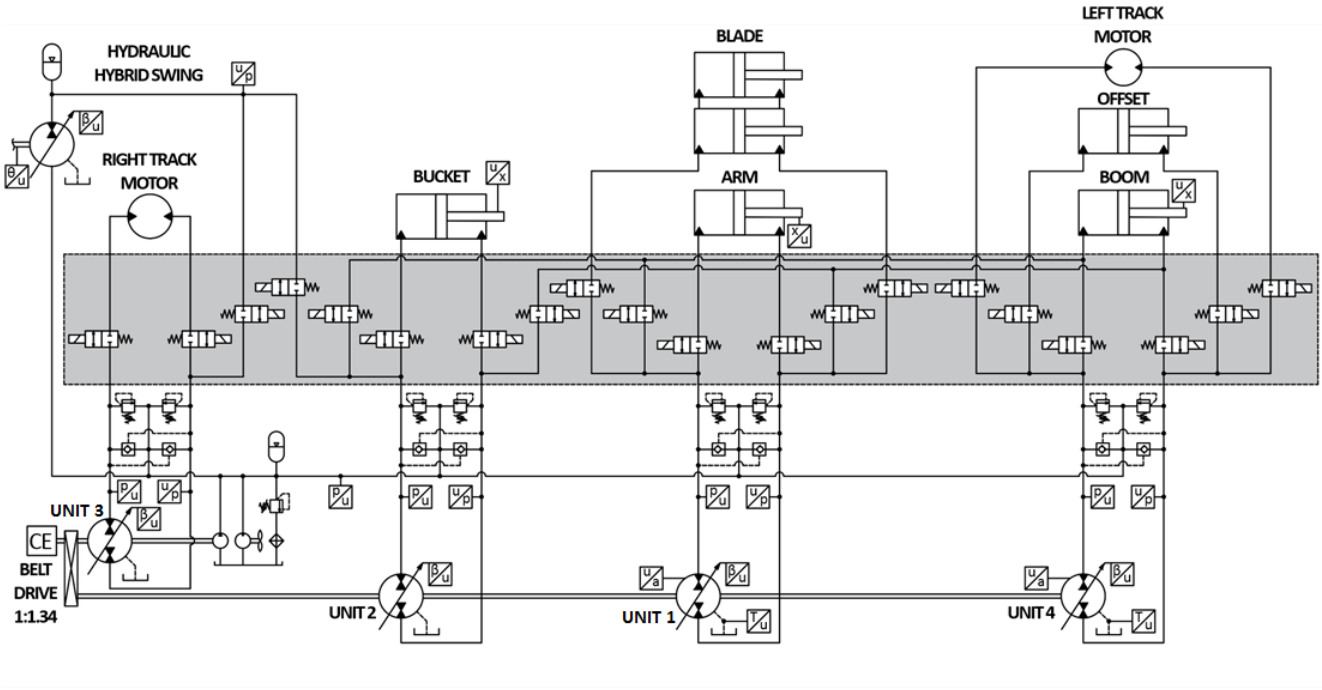

Figure 5. Hydraulic schematic of DC prototype excavator equipped with pump sharing throttle-less switching valves at Maha Fluid Power Laboratory at Purdue University [22].

Table 1. Main sensor data for sensors equipped on excavator prototype.

Company	Model	Type	Full Scale	Accuracy
Parker	IQAN-SP500	Diaphragm strain gauge	0-500 bar	5 bar
Omega	KMQSS-062G-6	Thermocouple	0-1250 ◦C	2.2 ◦C or 0.75%
PCB Piezotronics	356A16	Piezoelectric Triaxial Accelerometer	±50 g	100 mV/g or ±10%
Parker	RS60	Hall Effect	47°	1.4°

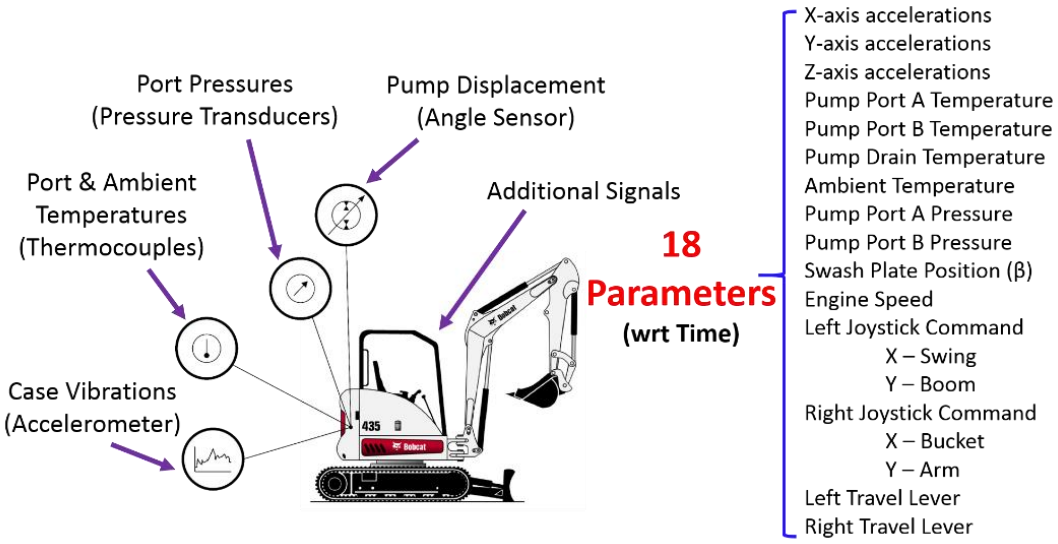

Figure 6. Measured parameters on experimental machine.

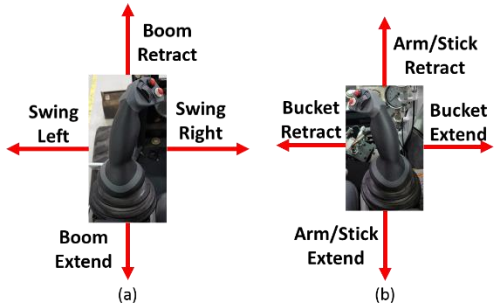

Figure 7. (a) Left joystick controls and (b) right joystick controls.

3.2. Machine Function Labelling

The four main functions of interest are travel, unloading, swing only, and digging. These four functions are common when operating the mini excavator. A simple and common duty cycle that was chosen is the truck loading cycle. In this cycle, the excavator digs, swings approximately 90 degrees, unloads the bucket at a height, and repeats the cycle. It is uncommon in this cycle for the machine to travel, but it is still included as a possibility as the operator may need to make adjustments to the machine position with respect to the truck or hole. Figure 8 shows the excavator operating during a truck loading cycle.

Figure 8. Simulated truck loading cycle.

Classification is a form of supervised learning and therefore requires labelled data during the training process. The machine functions are labelled by what the operator is commanding with joysticks and travel levers. If the operator operates either the right or left travel levers, then the data points will be labelled as traveling. If neither of the travel levers are operated but either the arm or bucket cylinders are given a retraction command, then

the data will be labelled as unloading. If neither travel nor unloading are occurring but the swing joystick is active, then the data will be labelled as swinging. If none of the above functions are occurring but the arm cylinder or bucket cylinder are commanded to extend, then the data is labelled as digging. Finally, if none of the above conditions are met, then the machine is considered at idle and the data is labelled accordingly. The function labelling logic can be seen in Table 2 and for the corresponding joystick commands, see Figure 7.

The order of function labelling needs to be performed in the order shown in Table 2. The reason swing is labelled after unloading is because an operator will often swing while unloading. However, an operator will not be swinging while actively digging. It is interesting to note that the boom command is not used in any of the labelling of machine functions. The boom is typically involved in both the digging and unloading.

Table 2. Logic for assigning classification labels to data.

Classification Label	Function Command	Condition	Additional Function Command
Travel	Left Travel Lever	OR	Right Travel Lever
Unloading	Retract Arm Cylinder	OR	Retract Bucket Cylinder
Swing	Swing Right	OR	Swing Left
Digging	Extend Arm Cylinder	OR	Extend Bucket Cylinder
Idle	No Command	-	-

3.3. Representative Truck Loading Cycle

A representative truck loading cycle was previously developed, but some data from the cycle can be seen within this section. Figure 9 shows the actual classification during two complete cycles for an excavator performing a truck loading operation. The majority of the time spent during a typical cycle is almost evenly split between digging and unloading. However, the swinging operation only contributes a small amount of time throughout the cycle.

The measured pressures of Unit 1, the main pump associated with the arm cylinder, are illustrated in Figure 10. As expected, the digging function shows higher pressures with more oscillations as the operator digs through the earth. The unloading pressures are significantly lower than the pressures seen during the digging operation. Figure 11 shows the displacements of Unit 1 during these two cycles of a truck loading operation. The pump displacement is quite oscillatory as the operator attempts digging through the earth. The oscillations in the displacements correspond to the pressure oscillations in Figure 10.

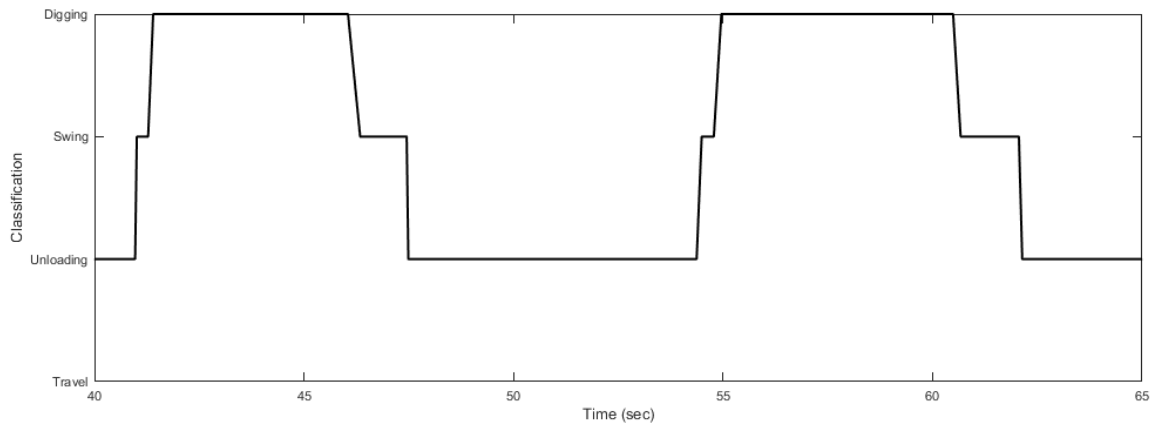

Figure 9. Representative truck loading cycle.

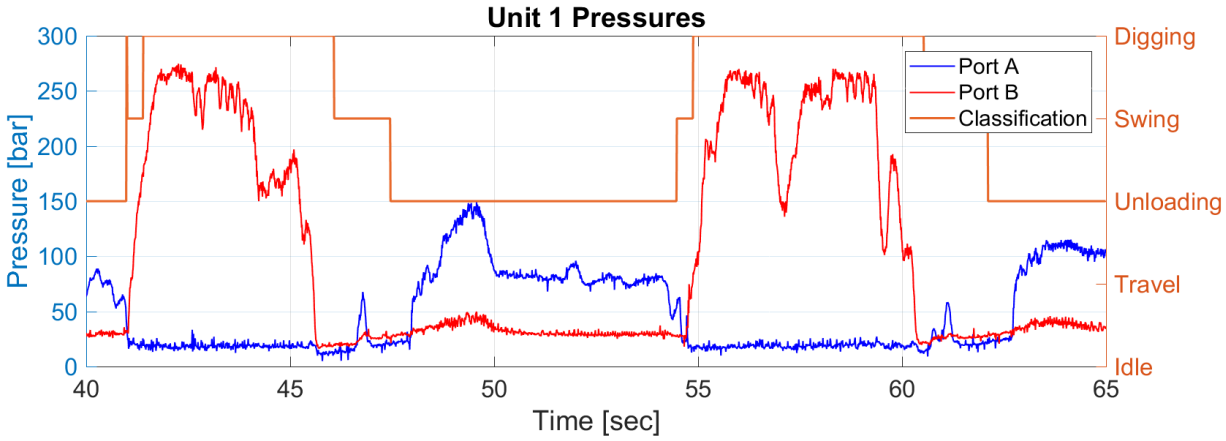

Figure 10. Common pressure trends for Unit 1, arm pump, during a typical truck loading cycle.

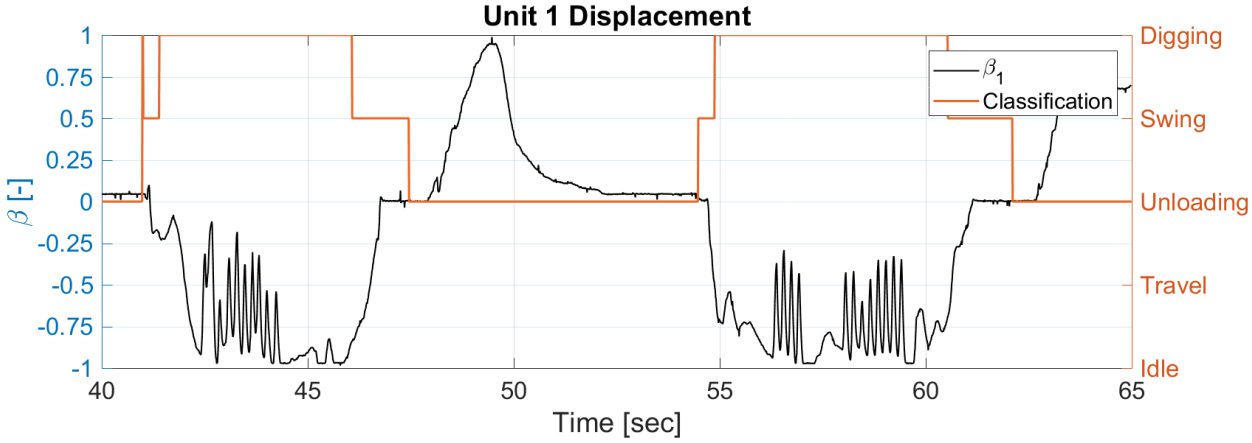

Figure 11. Common displacements of Unit 1, arm pump, during a typical truck loading cycle.

3.4. Classification Results

The decision tree algorithm has been chosen for this case study due to the simplicity of the algorithm and its functionality for this problem. The training process was done employing Scikit-Learn, a machine learning library in Python [23], [24]. Similar results are also given if using MATLAB. No normalization or standardization was done on the data and the categorical classes were represented by integers: 0 (idle), 1 (travel), 2 (unload), 3 (swing), and 4 (dig).

Approximately 20 cycles of dig, swing, and unload were performed while data was collected. In addition to the typical truck loading cycle, a small segment of machine travel was also performed. In total, 30,000 data points were collected and used in the training and testing of the decision tree algorithm. 80 percent of the data, 24,000 data points, was used for training the model. This corresponds to approximately 16 complete cycles. The model was tested on the remaining 20 percent of the data, 6,000 data points, or approximately 4 cycles. This ratio of training and testing is a common ratio.

The labelled data corresponds to 535 samples of travelling, 13,190 samples of unloading, 5,914 samples of only swinging, and 10,362 samples of digging. No samples were labelled as idling because the machine never experienced an idle function during the selected sample of 30,000 data points.

Figure 12 illustrates the testing accuracy of the decision tree algorithm and training set size for this particular case. Starting from 10, one cycle, as the sample size increases, the testing accuracy rapidly increases and approaches 1. The testing accuracy reaches an almost constant value after 1,000 training samples, 10 cycles. It is clear that the initial decision tree models were trained using a significantly larger training set size than was

required, 24,000 versus 1,000. It logically would make the training time longer than using approximately a training set size of 1,000. However, the increase in training time was negligible for this case.

Four models were developed using the decision tree algorithm. Each model used different input parameters to see how the input selection affected the performance of the final model. The first model, Figure 13, includes each of the 15 input parameters; pressures, temperatures, engine speed, command signals, and unit displacement. This model is shown to have an accuracy of 99.97% when run using the test data. The second model, Figure 14, was run using only the joystick and lever control signals. The results of the model showed to have the same accuracy as the first model, 99.97%. Notice how well the two models match the correctly labelled data.

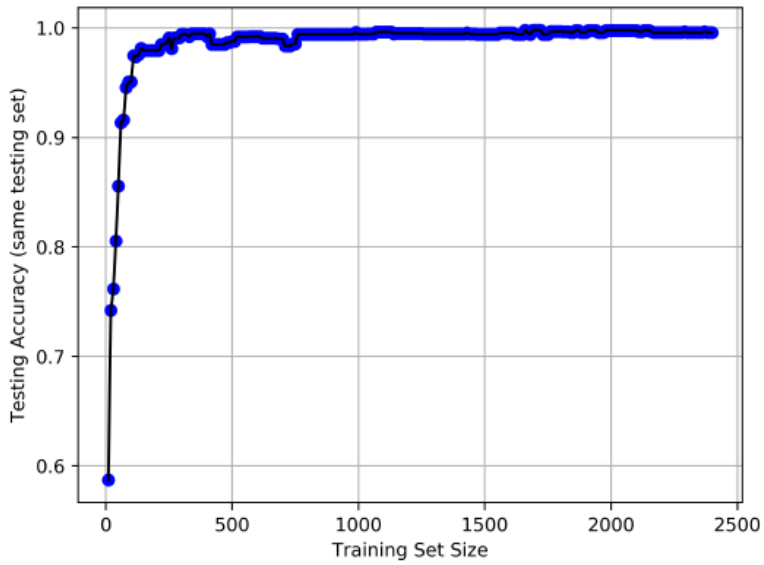

Figure 12. Testing accuracy versus training set size.

The third model, Figure 15, was run using each input parameter minus the command signals. The model run using the same testing data showed a reduction in accuracy by 2.23%, giving an accuracy of 97.74%. A few misclassifications begin to become noticeable.

Finally, the fourth model, Figure 16, was run without time stamps or command signals but used all other signals. This model further decreased the accuracy of the model to 92.36%. The amount of misclassifications is clearly visible if the model is not trained using the command signals.

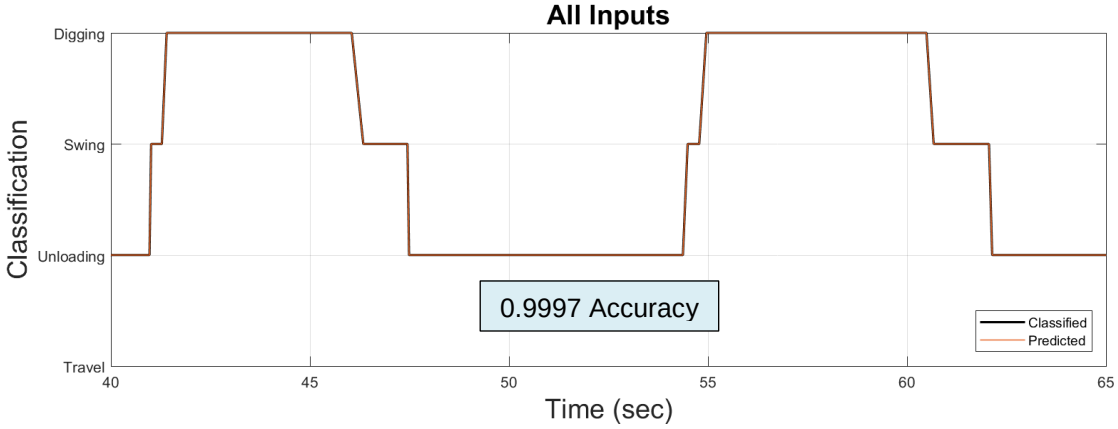

Figure 13. Classification results using all 15 inputs and time.

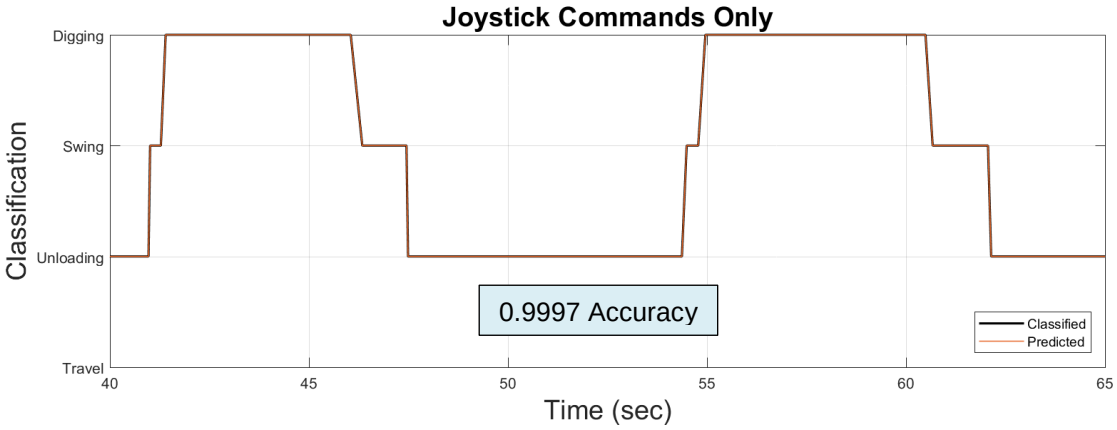

Figure 14. Classification results using only joystick commands.

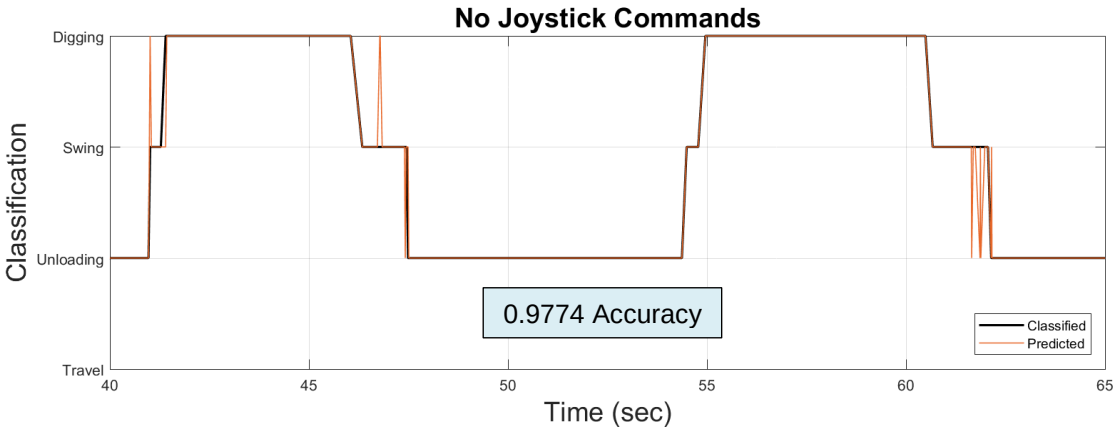

Figure 15. Classification results using all inputs and time minus the joystick commands.

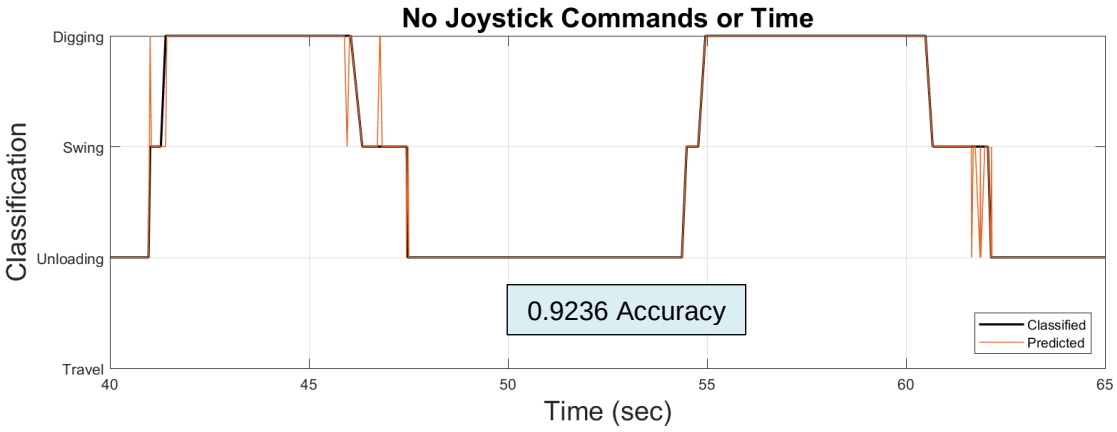

Figure 16. Classification results using all inputs minus joystick commands and time.

Finally, it is important to discuss which features were the most important in the truck loading cycle. From the four different models it is clear to see that the command signals were the most important features, but some are more important than others. Figure 17 shows the importance factor of each 15 input feature. The arm command, feature (2), has an importance factor of about 0.45 followed closely by the swing command, feature 10, at approximately 0.37. The most important conclusion to be drawn from this illustration is that all parameters other than the command signals could be considered negligible in the classification of machine functions.

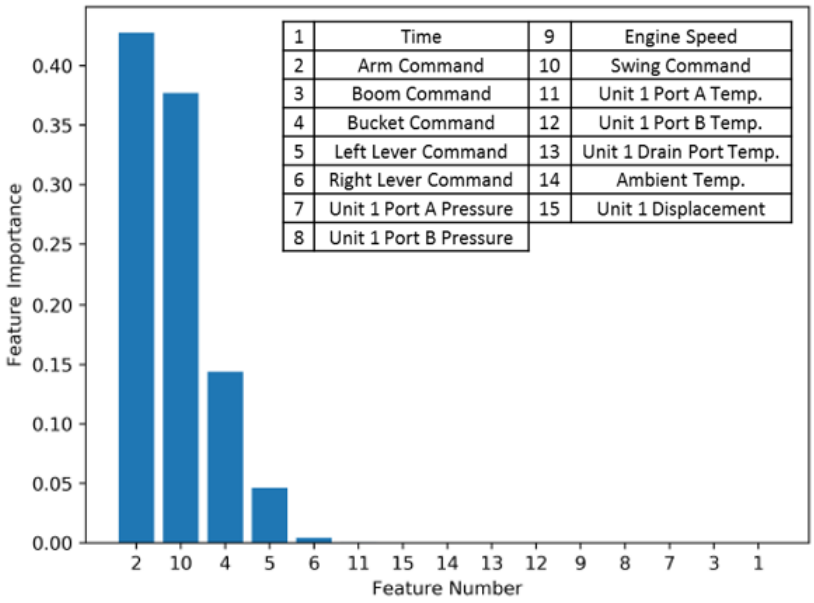

Figure 17. Feature importance for this particular segment of the truck loading duty cycle. (2) Is the arm command, (10) is the swing command, (4) is the bucket command, (5) is the left lever command, and (6) is the right lever command.

4. CONCLUSION AND FUTURE WORK

The goal of this research is was to successfully classify the machine functions on a hydraulically driven mini-excavator and was accomplished by analysing different classification algorithms, namely the decision tree, instrumenting an excavator, developing a representative truck loading cycle, collecting data and applying a decision tree algorithm to that data.

The DC prototype excavator had been equipped with thermocouples and pressure transducers in each of the pumps' pressure and drain ports, swashplate position sensors, ambient temperature thermocouples, an engine tachometer, actuator command signals, and accelerometers. The data was then labelled as either travelling, unloading, swinging, unloading, or idling corresponding to the different machine functions based on input joystick commands.

Once the data had been correctly labelled, 80% of it was sent through a decision tree training algorithm to generate a model that could correctly classify unseen data as one of the before mentioned machine functions. The model was then tested using the remaining 20% of the data to determine the model accuracy.

Four models were generated that gave varying degrees of accuracy, depending on the input parameters used in the model training. However, it was noticeable that the command signals were the most important, as shown by the model using only the command signals, which gave an accuracy of 99.97%. This was further confirmed by a feature importance rating that showed the command signals are the important features that are considered the machine learning algorithm, and the other signal do not contribute anything the model performance.

Some next steps for this work will include generating artificial faults with incremental degrees of severity to detect pump failures using the machine function classification algorithm that was trained in this work to give the condition monitoring algorithms points of reference in their decision making.

In conclusion, this study can help bring the mobile equipment world into the 21st Century by connecting the machines to clouds and machine learning systems. With machine functions being understood, then condition monitoring techniques can have more solid reference points to help determine the health of the hydraulic components and system.

REFERENCES.

[1] Case International Harvester, “Case IH Autonomous Concept Vehicle,” 2018. [Online]. Available: https://www.caseih.com/northamerica/en-us/Pages/campaigns/autonomous-concept-vehicle.aspx. [Accessed: 19-Dec-2018].

[2] R. Gehm, “Autonomous Plows Ahead,” *Off-highw. Eng.*, vol. 24, no. 6, pp. 12–15, 2016.

[3] E. Alpaydin, *Introduction to Machine Learning Second Edition*, 2nd ed. Massachusetts Institute of Technology, 2010.

[4] C. Bishop, *Neural Networks for Pattern Recognition*. Clarendon Press, 1995.

[5] D. J. Hand, “Discrimination and classification,” *Wiley Ser. Probabilty Math. Stat.*, 1981.

[6] P. Devijver and J. Kittler, *Pattern recognition: A statistical approach*. Prentice hall, 1982.

[7] K. Fukunaga, “Intrinsic dimensionality extraction,” *Classif. Patter Recognition, Reduct. Dimens.*, vol. 2, no. Handbook of Statistics, pp. 347–360, 1982.

[8] D. M. Magerman, “Statistical Decision-Tree Models for Parsing,” 1995.

[9] A. R. Webb, *Statistical Pattern Recognition*, 2nd ed. John Wiley & Sons Ltd, 2002.

[10] L. Breiman, J. Friedman, R. Olshen, and C. Stone, *Classification and regression trees*. Wadsworth International Group, 1984.

[11] C. Cortes and V. Vapnik, “Support-Vector Networks,” *Mach. Learn.*, vol. 20, no. 3, pp. 273–297, 1995.

[12] A. Ben-Hur, D. Horn, H. Siegelmann, and V. Vapnik, “Support vector clustering,” *J. Mach. Learn. Res.*, vol. 2, pp. 125–137, 2001.

[13] E. Boser, I. M. Guyon, and N. Vapnik, “A training algorithm for optimal margin classifiers,” in *Proceedings of the fifth annual workshop on Computational learning theory*, 1992, pp. 144–152.

[14] N. S. Altman, “An Introduction to Kernel and Nearest-Neighbor Nonparametric Regression,” *Am. Stat.*, vol. 46, no. 3, pp. 175–185, 1992.

[15] A. K. Jain, “Data clustering: 50 years beyond K-means,” *Pattern Recognit. Lett.*, vol. 31, no. 8, pp. 651–666, 2010.

[16] R. Duda, P. Hart, and D. Stork, *Pattern Classification*, 2nd ed. Wiley-Interscience, 2000.

[17] E. Grimson, J. Guttag, and A. Bell, “6.0002 Introduction to Computational Thinking and Data Science.” Massachusetts Institute of Technology: MIT OpenCourseWare, 2016.

[18] R. Rahmfeld and M. Ivantysynova, “Energy Saving Hydraulic Actuators for Mobile Machines,” in *1st Bratislav Fluid Power Symposium*, 1998.

[19] R. Rahmfeld and M. Ivantysynova, “Displacement Controlled Wheel Loader - a simple and clever solution,” in *Fourth International Fluid Power Conference (IFK)*, 2004.

[20] C. Williamson, “Power Management for Multi-Actuator Mobile Machines with Displacement Controlled Hydraulic Actuators,” Purdue University, 2010.

[21] J. Zimmerman, “Toward Optimal Multi-Actuator Displacement Controlled Mobile Hydraulic Systems,” Purdue University, 2012.

[22] E. Busquets, “Advanced Control Algorithms for Compact and Highly Efficient Displacement-Controlled Multi-Actuator and Hydraulic Hybrid Systems,” Purdue University, 2016.

[23] “scikit-learn,” 2018. [Online]. Available: https://scikit-learn.org/stable/. [Accessed: 18-Dec-2018].

[24] “Python,” 2018. [Online]. Available: https://www.python.org/. [Accessed: 18-Dec-2018].

HYDRAULIC HYBRID WORKING MACHINES PROJECT – LESSONS LEARNED

Adj. Prof. Matti Linjama*, Dr. Tech. Mikko Huova*,
M.Sc. Jyrki Tammisto*, Dr. Tech Mikko Heikkilä*, Prof. Seppo Tikkanen*,
Dr. Tech. Jyrki Kajaste**, Dr. Tech. Miika Paloniitty*, Prof. Matti Pietola**
*Tampere University
Korkeakoulunkatu 6, 33720 Tampere, Finland
**Aalto University
PO Box 11000, 00076 Aalto, Finland
matti.linjama@tuni.fi

ABSTRACT

A big research project was implemented in Finland in 2016-2018 to find economically and technologically feasible ways to improve fuel efficiency of hydraulic working machines. Two main approaches were hydraulic hybrids and independent metering. Objective was also to study experimentally the effect of Diesel engine loading profile on emissions. An analysis tool was developed to estimate the fuel consumption of working machines using measured load cycle data and dozens of solutions were analysed. This paper summarizes the main findings of the project. Important finding is that simple “accumulator + control valve” type hybrid is a low-cost and effective method to reduce fuel consumption. The second finding is that hybridization alone reduces fuel consumption by approximately 15 per cent in the machines studied quite independently on the hybridization solution. An exception is multi-pressure systems, which have potential for bigger fuel savings. The third finding is that independent metering is equally effective in the reduction of losses. The most effective solution is the combination of independent metering and hybridization where 28 per cent reduction in the fuel rate together with 12 per cent faster cycle time is demonstrated.

KEYWORDS: Hydraulic hybrid, independent metering, working machines, energy efficiency

1. INTRODUCTION

Hydraulically operated working machines are used e.g. in earth moving, construction, mining and forestry applications. The common features of these machines are high utilization rate, big engine powers and harsh conditions. The efficiency of current hydraulic solutions is relatively poor. These facts yield big fuel consumption, typically between 10 000 and 100 000 litres per year per machine. Several different approaches have been studied to improve the fuel efficiency, but quite few of them are in common use. Hydraulic hybrids have been studied much [1–3], but real applications are few. Caterpillar has introduced a hydraulic hybrid excavator in 2012 and about 25 per cent reduction in the fuel consumption has been claimed [4]. Mantsinen [5] uses hydraulic balancing cylinder connected to an accumulator for the lift actuator of their larger material handling machines. They state that the reduction of fuel consumption is up to 35 per cent. Another widely studied energy saving method is independent metering valves [6–8]. The Caterpillar’s solution combines independent metering and hydraulic hybrid. Relatively new approach is to use a variable speed drive for each

actuator [9], but this results in relatively bulky system. A prototype of fully electric compact excavator has also been introduced by Volvo [10]. The solution is probably too expensive for the market.

A big research project (Hydraulic hybrid working machines – HHybrid) was implemented in Finland in 2016-2018 to find economically and technologically feasible ways to improve fuel efficiency of hydraulic working machines. The main approaches were hydraulic hybrids, independent metering and hardware-in-the-loop simulations. This paper summarizes the main results of the project.

2. HYDRAULIC HYBRIDS

2.1. Classifications

The hydraulic hybrid solutions can be roughly divided into the following types:

- Hybrid without extra pump-motors, traditional valves
- Hybrid without extra pump-motors, independent metering valves
- Hybrid with extra pump-motor(s), traditional valves
- Hybrid with extra pump-motor(s), independent metering valves
- Two-pressure system STEAM [2] and its variants
- Multi-pressure systems

2.2. Hydraulic hybrids without extra pump-motors

The simplest form of hydraulic hybrid without extra pump-motors is the use of balancing cylinder connected to an accumulator [5]. This passive solution is suitable for lift cylinders only and was not studied in the HHybrid project. Another example about hybrid without extra pump-motors presented by Amrhein and Neumann [11]. The idea is to recuperate the energy from the lowering of the boom to an accumulator and connect the accumulator to the suction side of the pump. This requires the replacement of the open circuit pump with the closed circuit pump. This solution was not studied further, because it is intended for lift cylinders only. The third example is “throttled accumulator” in which an accumulator is connected to the supply line via a two-way proportional valve [7, 12, 13]. The circuit diagram is show in Figure 1. This simple solution can be used with traditional or independent metering valves. The replacement of the traditional load sensing system by electric load sensing is required.

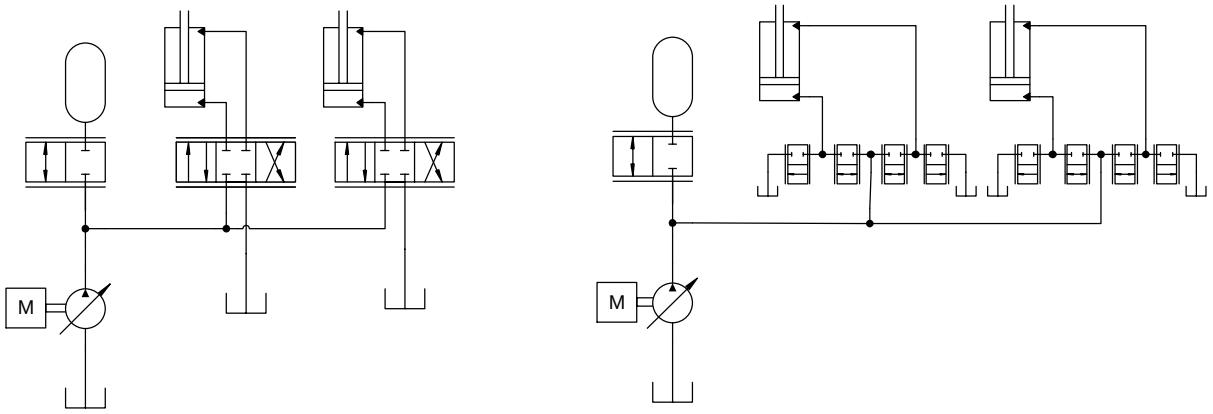

Figure 1. Throttled accumulator with traditional valves (left) and independent metering valves (right).

2.3. Hybrids with extra pump-motor(s)

The hybrid with extra pump-motor(s) is the most common type of hydraulic hybrids. Only two examples are given here, hydraulic flywheel [14] and the hybrid introduced by Erkkilä *et al.* [15]. The hydraulic flywheel is shown in Figure 2. The benefit of the approach is that it can be installed in parallel with the existing system. The drawback is that the installed pump displacement increases, which increases pump-motor losses. The hybrid introduced by Erkkilä *et al.* is shown in Figure 3. The benefit of this approach is that the flow rates of the pump-motors are summed and the installed displacement does not necessarily increase. Several variants of this solution can be generated by adding more valves into the system.

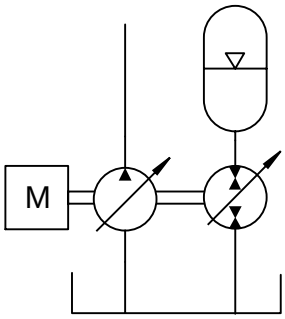

Figure 2. Hydraulic flywheel.

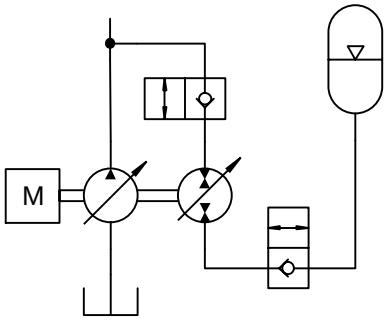

Figure 3. Hybrid presented by Erkkilä et al. [15].

2.4. STEAM and its variants

The STEAM system has two supply pressures, which are implemented by accumulators and a loading pump [2]. The solution is intended for excavators. Two variants are shown in Figure 4. In the first variant, logic valves are used to select the supply and return port pressures for traditional valves. This solution may have transients when changing the state of logic valves. Another variant has six two-way proportional valves per actuator and no four-way or logic valves are needed. This solution allows smooth mode transitions. Although the latter version is independent metering system, it does not necessarily reduce losses compared to the first variant, because supply pressures are constant. Significantly reduced fuel consumption and increased productivity has been demonstrated with STEAM. Weak point is that the utilization ratio of accumulators is poor due to almost constant supply pressures.

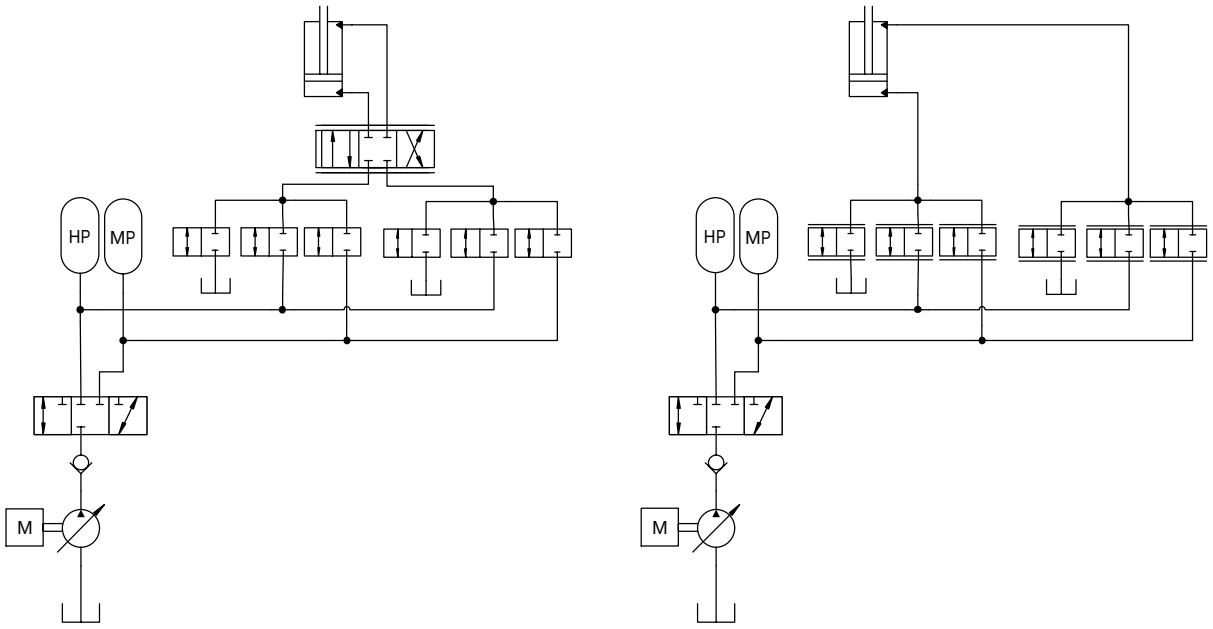

Figure 4. Two variants of the STEAM system.

2.5. Multi-pressure systems

The idea of STEAM can be extended by increasing the number of supply pressures. An example of five-pressure system is shown in Figure 5. The system has 25 different forces depending on the state of the logic valves. If the inertia of the actuator is large, the motion control can be implemented without proportional valves by controlling directly the force of the actuator. An alternative method is to replace logic valves by two-way proportional valves. In this case, small inertias can be also controlled. The analysis results show that the increase of the number of supply pressures reduces significantly losses up to six or seven pressures, and the multi-pressure systems are the most energy efficient solution among all alternatives. The obvious drawback is complexity of valve systems and piping.

Another approach is to implement multiple pressures locally at actuators. This approach is called distributed hybrid or hybrid actuator, because each actuator has its own accumulator. An example of a six-pressure system is shown in Figure 6. The idea is to generate several lower pressures from the supply pressure by small converter cylinders. This kind of system has been studied by Huova *et al*. [16]. Results are promising both in terms of energy efficiency and control performance. This solution was further studied in the HHybrid project.

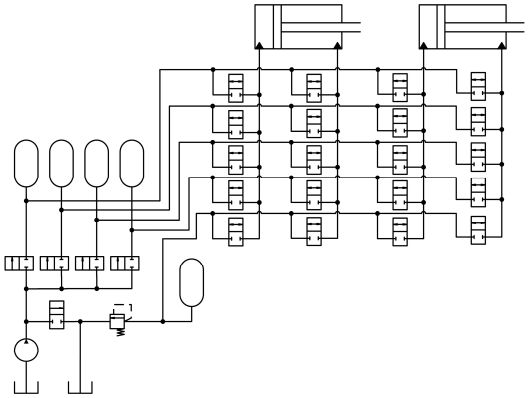

Figure 5. Example of multi-pressure system implemented by accumulators.

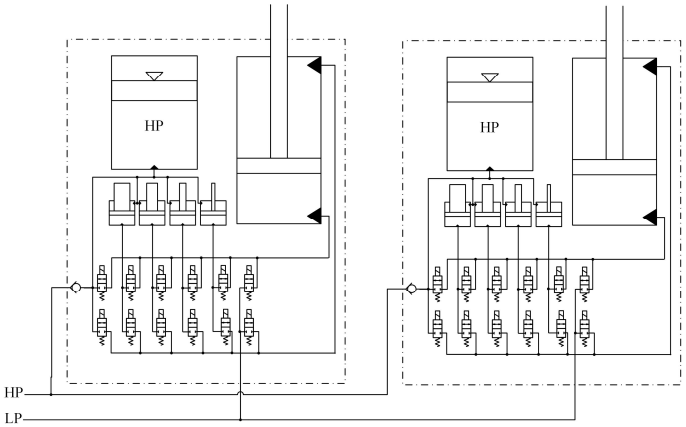

Figure 6. Example of multi-pressure system implemented by converter cylinders.

3. THE HHYBRID PROJECT

3.1. Objectives and approaches

The main objective of the HHybrid project was to find economically and technologically feasible ways to improve fuel efficiency of hydraulic working machines. The second objective was to study experimentally the effect of Diesel engine loading profile on emissions and fuel consumption. The hypothesis was that the smooth loading profile reduces both fuel consumption and harmful emissions. The third objective was to find out the effect of parasitic losses (accumulator heat losses, pipes, hoses, manifolds, friction etc.) on the fuel consumption.

The main approaches for the energy saving were hydraulic hybrids, independent metering and distributed hybrids. The emissions research used Hardware-in-the-Loop (HIL) simulations in order to find out the effect of the loading profile on the emissions.

3.2. Participants and roles

The HHybrid project had two research units and five companies. Tampere University of Technology (TUT) was the responsible for hybrid solutions, independent metering and experimental validation while Aalto University was responsible for energy efficient components. Two machine manufacturers were involved: Ponsse as a manufacturer of cut-to-length forest machines and Vilakone as a manufacturer of municipal tractors. Two component manufacturers were Bosch Rexroth and Finnish cylinder manufacturer Hydroline. Fiellberg is an engineering company with special interest on distributed hybrid solutions.

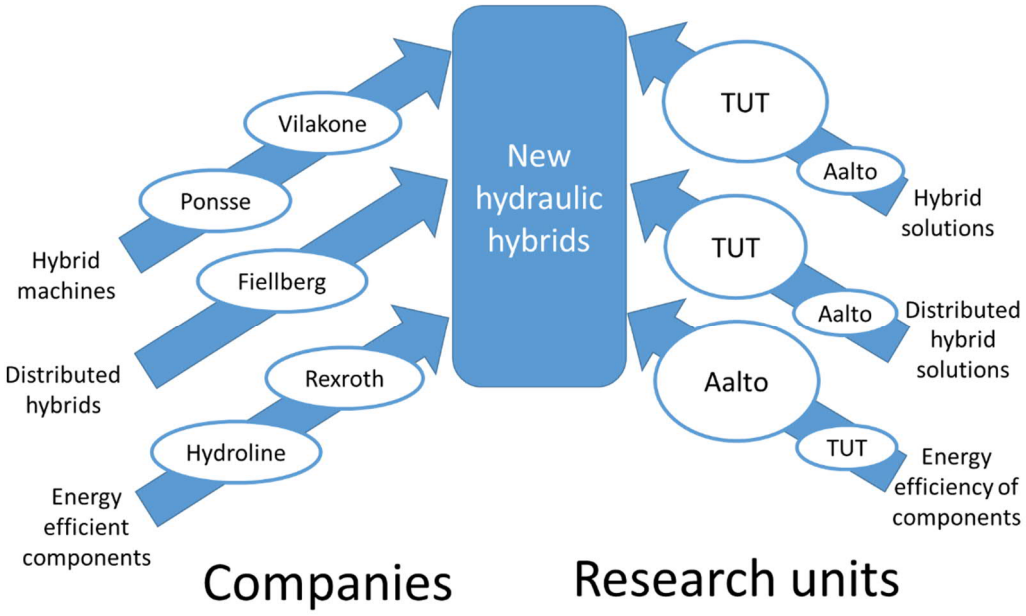

Figure 7. Participants and roles.

3.3. Implementation

The flow chart of the project is shown in Figure 8. The first task was to seek for hydraulic hybrid solutions found in the literature, combine them and invent new hybrid solutions. Over twenty solutions were identified and 15 of them were selected for further analysis. Two baseline machines – Wille 665 municipal tractor [17] and TUT's forest forwarder – were measured. The measurements consisted actuator positions and pressures, Diesel engine RPM, and supply pump flow and pressure. This set of data is called load cycle data. An analysis tool was developed and it was used to estimate the fuel consumption of the baseline machines and different hybrid solutions. The real fuel consumption was not measured from the machines. The Diesel torque was calculated using the analysis tool and this together with the Diesel RPM were used as the input to the Hardware-in-the-Loop (HIL) system. The output of the HIL system was measured fuel consumption and emissions. The second part of the project was the implementation of independent metering and one hybrid solution in the TUT's forwarder. The outputs of the measurements were load cycle data and performance of the hybridized machine. Analysis tool was used to estimate the fuel consumption of the hybridized machine, and HIL was used to find out the real fuel consumption and emissions.

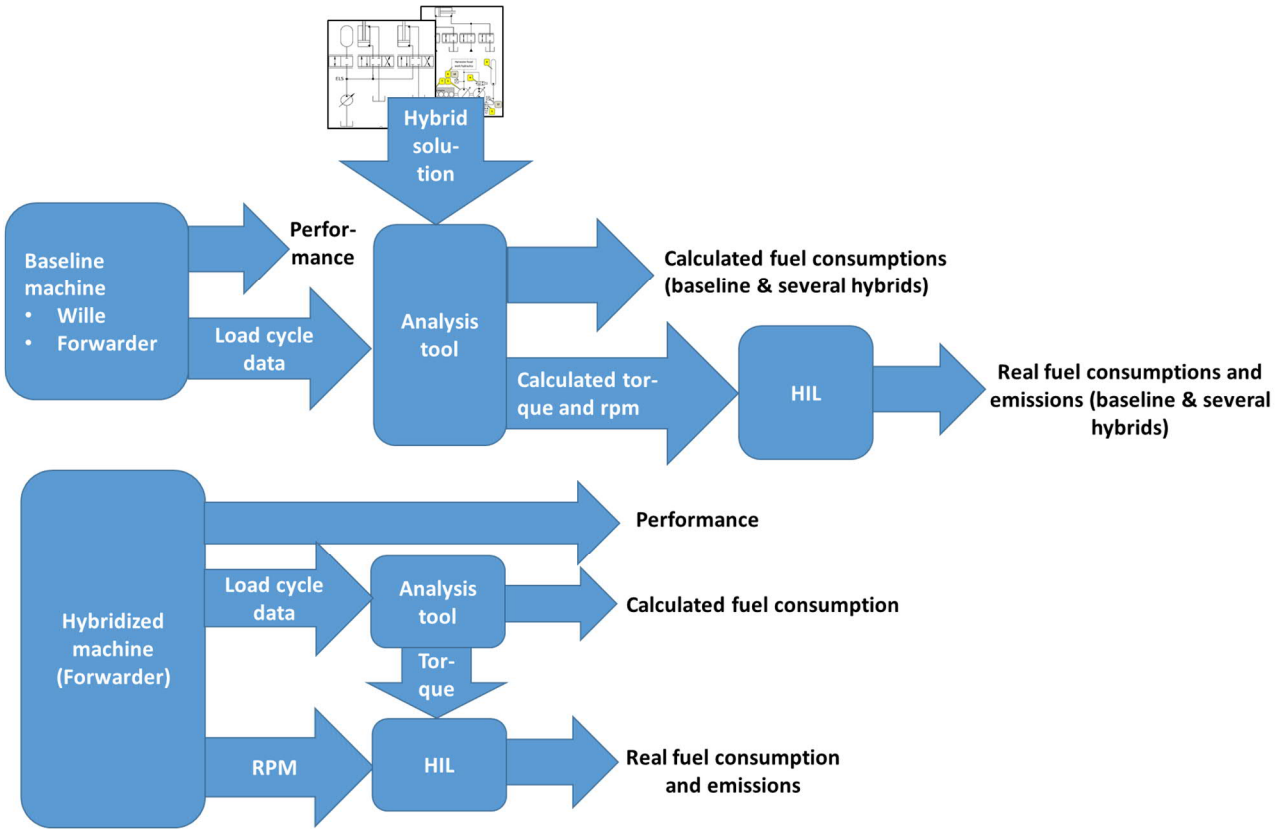

Figure 8. The implementation of the HHybrid project.

4. ANALYSIS TOOL

One important result of the project is the analysis tool, which can be used to estimate losses and fuel consumption of hybrid solutions. The tool is modular and currently 15 solutions are coded into it. The tool uses generic efficiency maps for Diesel and pump-motors. Simple control logic is implemented for each solution in order to select supply pressure, control modes and pump-motor angles. When compared to the HIL measurements, typical error in the fuel consumption is less than ten per cent. However, the main target is not to find out the absolute fuel consumption, but to compare the fuel consumption of different solutions. The operation principle of the tool is shown in Figure 9. The input to the tool is measured or simulated work cycle data. Outputs include valve, pump-motor and Diesel losses, mechanical work done, fuel consumption and torque profile.

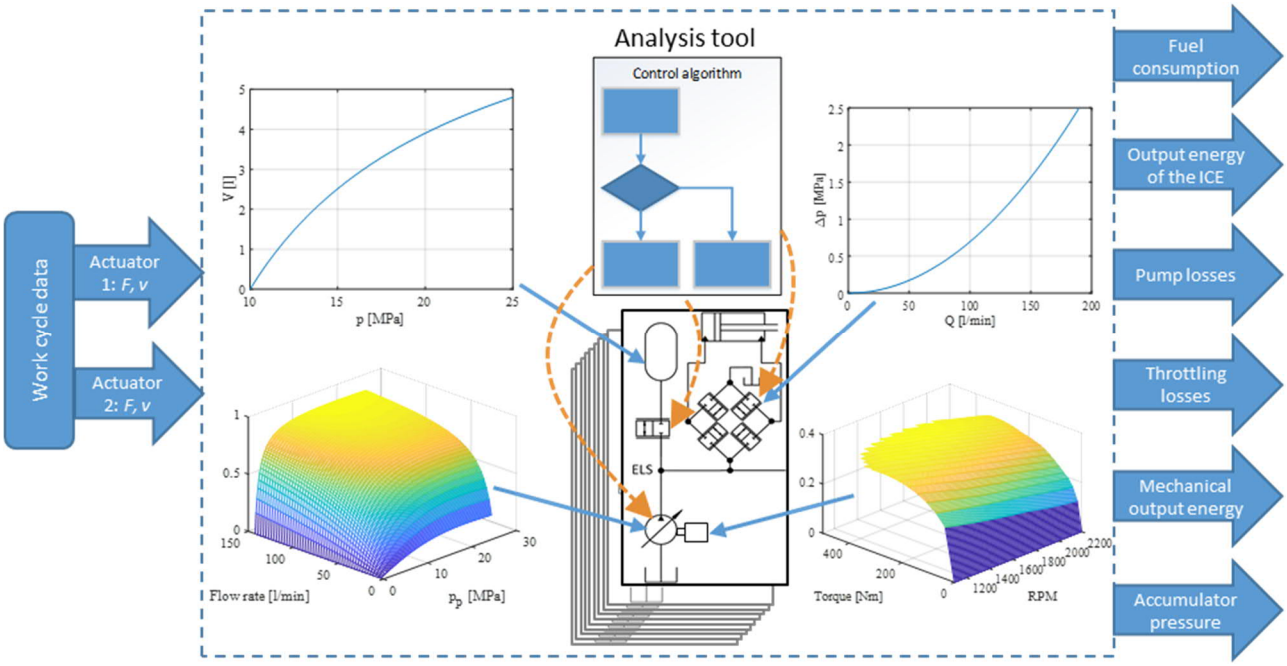

Figure 9. Operation principle of the analysis tool.

5. HARDWARE-IN-THE-LOOP ENVIRONMENT

The HIL test bench allows testing of different loading cycles of the Diesel engine. Thus, the effect of hybridization on engine's fuel consumption and emissions can be evaluated in case of the real engine and emulated working cycle. The system consists of Diesel engine, hydraulic loading unit (Bosch Rexroth), measurement equipment for the fuel consumption and emissions, and control hardware. A simplified drawing of the system is shown in Figure 10. The modern four-cylinder, turbocharged heavy-duty engine has rated power of 84 kW. Hydraulic secondary unit having two variable displacement pump-motors fed by a hydraulic power unit generates the engine load. Swivel angles of the pump-motors are controlled via Bosch Rexroth Control Cabined according to the measured shaft torque and torque reference sent from a dSPACE DS1103 system. The DS1103 is also used for sending an RPM request for the Diesel engine. Fuel consumption of the engine is measured using AVL KMA and emissions with AVL GAS PEMS and AVL PM PEMS. The studied Diesel engine has no exhaust gas treatment; thus, the raw emissions are investigated.

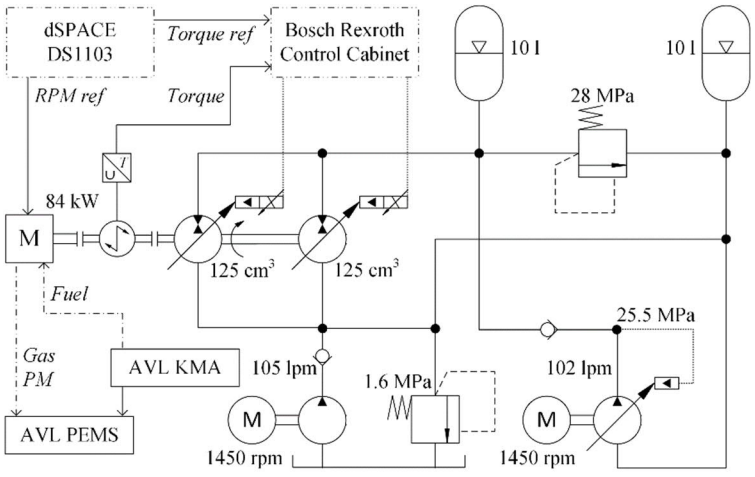

Figure 10. The simplified hydraulic circuit diagram of the HIL system.

6. ENERGY EFFICIENT COMPONENTS

One objective of the project was to analyse the effect of parasitic losses on the fuel economy. Parasitic losses include cylinder friction, flow losses in pipes and manifolds, flow losses in logic valves and heat losses at accumulators. It was expected that the heat losses at accumulators are large, because the efficiency of the traditional accumulator is poor with certain load cycles [18]. Energy efficient accumulator is an active research topic [19, 20] and one solution is already in the market [21]. In the cases studied, accumulators are used actively without any long steady periods. Losses are small with such load cycles and therefore traditional accumulators were used. One important finding is that the accumulator must be about 50 per cent larger in this kind of cycles when compared to the ideal gas equation. The cylinder friction was found small and the effect on the fuel consumption is assumed minor. Significant flow losses up to 1.5 MPa were found in the extension actuator of the forwarder. The deeper analysis showed that extension actuator seldom determines the supply pressure and the effect on the system losses is small. Flow losses of the other actuators were found to be below 0.2 MPa. The manifold used with the distributed valves was analysed by CFD and the estimate for the maximum flow loss is 0.15 MPa. It can be concluded that the system is well designed and parasitic losses increase the supply pressure up to by 0.35 MPa. Typical supply pressure is 15-20 MPa and the power demand thus increases by 2 per cent at maximum actuator velocities.

Logic valves are used in several hybrid solutions, for example in the STEAM and multi-pressure systems. The requirements are high flow capacity, bi-directional flow and relatively fast response. Because such valves do not exist in the market, a prototype of a high-capacity logic valve was build [22]. Fast solenoid valves from Bucher Hydraulics [23] were used as pilot valves to control standard NS16 cartridge. Results are promising: flow capacity of 200 l/min at 0.23 MPa pressure differential and response time of 11-13 ms for opening and 30-36 ms for closing [22].

7. SELECTION OF HYBRIDIZATION METHOD

The selection of the hybridization method is based on the estimated fuel consumption (using the analysis tool) and complexity of the solution. The analysis results for the Wille 665 municipal tractor are presented in [7, 12, 13]. The experimental results with the forwarder will be published soon and are similar. The fuel consumption reduces about 15 per cent quite independently on the hybridization method. When independent metering is applied, another 15 per cent reduction in the fuel consumption is achieved. The combination of independent metering and hybridization reduces fuel consumption about 30 per cent. The STEAM reduces fuel consumption about 26 per cent. Multi-pressure systems have potential for up to 40 per cent reduction, but they were considered too different from traditional systems. The selected hybrid is the throttled accumulator with independent metering (see Figure 1), because the fuel efficiency is good and the solution is the simplest one.

8. HYBRID FORWARDER

The forest forwarder (Ponsse Caribou S10) shown in Figure 11 was used as a platform for hybridization. It is relatively old (model for 2000) and its emissions and fuel economy differ significantly from the modern Diesel engines. For this reason, the fuel consumption and emissions were not measured, but the analysis tool and HIL system were used instead. The independent metering was applied to the four main actuators – slewing, lift, luffing and extension (see Figure 12). The main parameters of the machine are given in Table 1. Diesel RPM and pump size can be reduced significantly in the hybrid machine, because the accumulator is used as the extra flow source.

Table 1. Main parameters of the forwarder.

	Baseline machine	**Independent metering only**	**Hybrid machine**
Diesel engine	Perkins 1004-40TW, 91 kW		
Average Diesel engine RPM	1600 r/min	1420 r/min	1260 r/min
Control valves	Parker K170LS	Husco EHPV	Husco EHPV
Pump	130 cc (Load sensing)	130 cc (Electric load sensing)	71 cc (Bosch Rexroth, Mooring type)
Accumulators	-	-	2 x 10 l, p_0 = 12.5 MPa

Figure 11. TUT's Ponsse Caribou S10 forwarder.

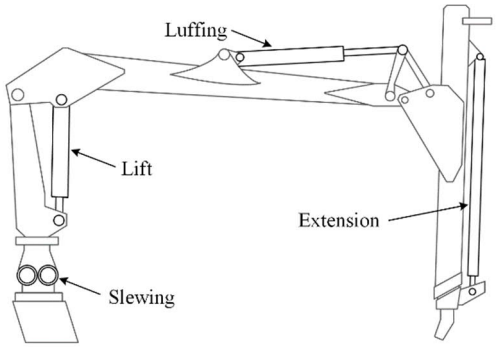

Figure 12. Main actuators of the forwarder manipulator.

9. MAIN RESULTS

9.1. Diesel engine control

Dynamic programming was used to find the optimal rotational speed of the Diesel engine [13]. This result was compared to the constant speed with the lowest possible RPM using the analysis tool. Differences in the estimated fuel consumption were minor in both machines. Low and constant RPM is thus very close to the optimal solution, and is recommended strategy because of its simplicity. This result is not obvious from the efficiency map of the Diesel engine. This emphasises the fact that it is important to optimize whole system.

9.2. Experimental results with forwarder

9.2.1. Baseline measurements

The baseline machine was measured by using a professional operator in December 2017. The task was to unload and load one set of logs (58 pine logs, approximately 10 solid cubic meters). The measurement was repeated two times. The logs were fresh and thus relatively heavy. Quite normal rotational speed of 1600 r/min was used.

9.2.2. Independent metering

The forwarder was measured with the 130 cc pump and independent metering in June 2018. The logs were dry and lighter, and the mechanical work done was thus smaller. However, the analysis showed that this has negligible effect on the fuel consumption. It was possible to reduce the rotational speed to 1420 r/min, because of reduced losses and the use of differential connection when possible. The main result is that both energy efficiency and control performance improves with well-tuned independent metering valves. In this case, Husco EHPV valves were used and their performance was found good. An important benefit of these valves is the ability to control flow in both flow directions. The fuel rate reduced 14 per cent and the cycle time reduced 13 per cent. A challenge is that independent metering requires lot of control code. This applies especially on the control of pressure differentials, control modes (inflow-outflow vs. regenerative) and supply pressure. In spite of this, it was possible to implement whole control code and I/O of four actuators in two embedded controllers (Epec 5050, [24]). The sampling time was 20 ms.

9.2.3. Hybrid machine with throttled accumulator and independent metering

The implementation of the throttled accumulator was straightforward: Accumulator plus control valve and additional control code. Husco EHPV valve was used to control the flow rate into and from the accumulator. Small 20 litres accumulator was enough to reduce peak power requirement from the Diesel significantly. The measurements were performed in November 2018. It was possible to use smaller pump (71 cc) and Diesel engine RPM (1260 r/min) because of hybridization. The estimated fuel rate reduced by 28 per cent and total fuel amount by 36 per cent compared to the baseline machine. The cycle time was similar to the pure independent metering case – 12 per cent faster than the baseline.

9.3. Results with multi-pressure systems

Simulations were used in the analysis of the performance and energy efficiency of the multi-pressure approach in the forwarder. The first finding was that the luffing and extension joints have too small inertia to be used with the secondary control approach. Therefore, the multi-pressure approach was applied only on the slewing and lift actuators. Luffing and extension actuators were used in the electric load-sensing mode with traditional 4/3 proportional valves. Their losses reduced also compared to the baseline machine, because there were only two actuators in the LS circuit. The simplified hydraulic circuit diagram of the system is shown in Figure 13. The multi-pressure system (MPS) was implemented by four converter cylinders (see Figure 6) and the total number of pressures was thus six. Only one set of converter cylinders was used for two actuators. The main findings are that the performance of the secondary controlled swing and lift actuators is good, losses reduce dramatically and the estimate of the fuel rate reduction is 36 per cent. The multi-pressure approach of Figure 6 was also studied experimentally in the swing actuator of a micro excavator [25]. The results are promising, losses reduce dramatically and control performance is similar to the original load-sensing system.

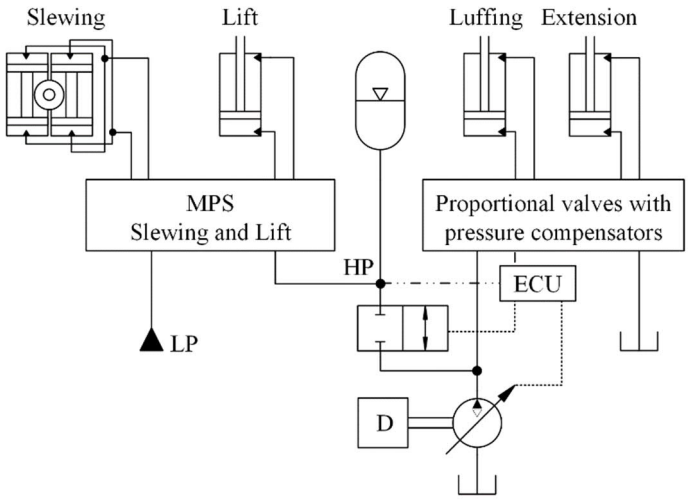

Figure 13. Simplified hydraulic circuit diagram of the multi-pressure system in forwarder.

9.4. Energy saving potential of the municipal tractor

Figure 14 presents the analysis results for the municipal tractor when the measured load cycle data from a short Y-cycle is used. It is seen that the hybridization and independent metering have similar effect on the fuel consumption. The best results are obtained with STEAM, throttled accumulator with independent metering, and parallel pump solution of Figure 3 with independent metering.

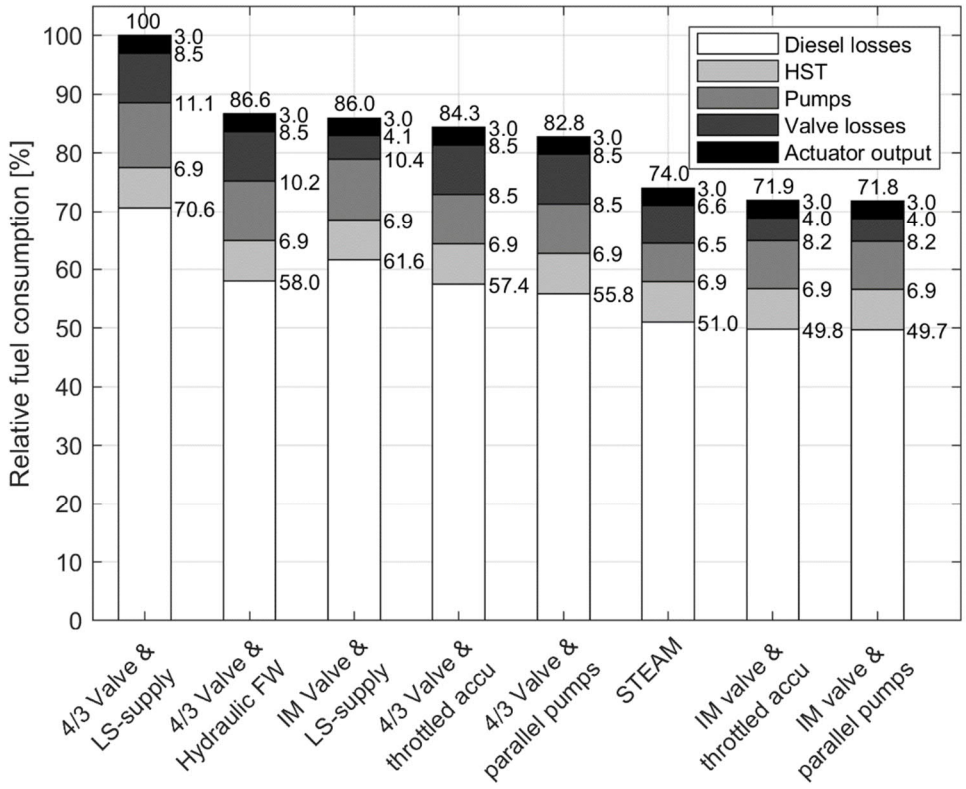

Figure 14. Analysis results for the municipal tractor. IM means independent metering and FW flywheel.

9.5. HIL

A sample result with the HIL system is shown in Figure 15 when the measured load cycle from the baseline machine is used as the input. It is seen that the torque follows quite perfectly the target value. The lowest plot shows that the engine control unit (ECU) and real-time fuel measurement (KMA) give consistent results, but the ECU has faster dynamics.

The research hypothesis was that the smoother loading profile of the Diesel engine reduces harmful emissions. The emissions measurements with different hybrid versions show that this is not the case. In general, all raw emissions decrease but usually less than fuel consumption. The exception is CO emissions where hybrid versions have significantly bigger emissions. This may be caused by the lower rotational speed of the Diesel engine or measurement error.

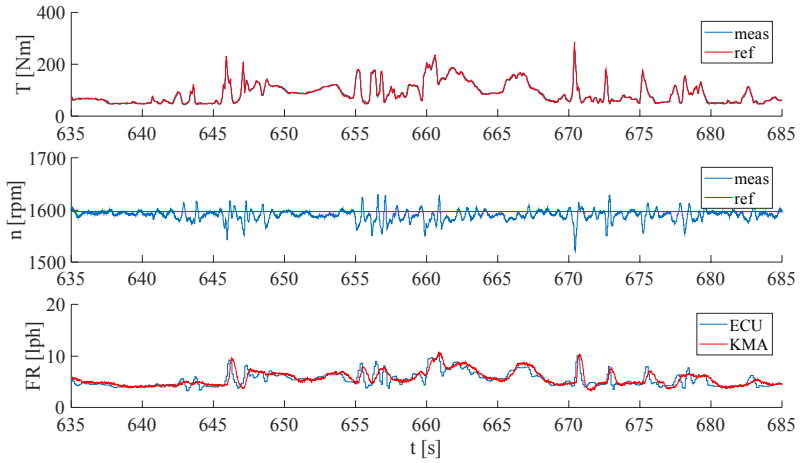

Figure 15. Measured torque, rotational speed and fuel rate of the HIL system. Two fuel rates are shown: one from the engine control unit (ECU) and another from a real-time fuel rate sensor (KMA).

10.LESSONS LEARNED

The main findings of the project can be summarized as follows:

- It is important to analyse hybrid solutions by using measured load cycle data from realistic working conditions. It is not possible to know in advance, which solution is the best for the given machine and load cycle.
- Optimization of subsystem, such as Diesel efficiency, does not give the best fuel economy. It is important to analyse the system as whole.
- Independent metering and hybridization have quite similar energy saving potential in the studied machines. The combination of them is recommended for the best fuel economy.
- It is important to minimize the installed pump displacement. Pump losses are significant and pumps must be rotated all the time.
- It is important to minimize the rotational speed of the Diesel engine. This reduces losses of pumps and auxiliary components. Running Diesel engine at the lowest possible constant speed is simple and efficient control strategy in the machines studied.
- Contrary to intuition, the simple throttled accumulator is a competitive hybrid solution.
- Parasitic losses are minor in the forwarder. Accumulator losses are also small if accumulators are used actively.
- Setting up a HIL environment is laborious, but it is a good approach to study the effect of hybridization and independent metering on the fuel consumption and emissions. Several solutions can be studied quickly when the system is operational.

- Secondary controlled multi-pressure approach has very big energy saving potential, but it is best suited for high inertia actuators.
- Hybridization reduces emissions of the Diesel engine because the fuel consumption reduces. The loading profile seems not to have any significant effect on emissions but this topic needs further research.

11. CONCLUSIONS

The research made in the HHybrid project shows that systematic analysis is needed to evaluate the energy efficiency of working machines. It is essential to have load cycle data from real operation conditions. It is also important to analyse several solutions in order to find the best one for the given machine. Surprisingly many different hydraulic hybrid solutions exist and it is not possible to rank them without proper load cycle data and accurate analysis tool.

The results of the project are promising. Significant fuel savings can be achieved with a simple and low-cost throttled accumulator. This combined with independent metering reduces the estimated fuel rate of the forwarder by 28 per cent. At the same time, the productivity of the machine improves by 14 per cent. The approach can be applied to any boom control system with or without independent metering. When the load cycle data is available, HIL is good approach to evaluate the fuel consumption and emissions of several hybrid solutions. The analysis tool can be used to generate the loading profile for the Diesel engine.

To summarize, hydraulic hybrid technology – especially when combined with independent metering – is a low-cost approach to reduce fuel consumption of working machines. Torque and power needed from the prime mover reduce significantly. If the prime mover is Diesel engine, lower rotational speed can be used or the engine can be downsized. If electric prime mover is used, power and torque requirements are relaxed, which allows smaller electric components, lower costs and longer operation time.

ACKNOWLEDGEMENT

The research was made at Tampere University of Technology (Tampere University since 2019) and Aalto University. The research was funded by Challenge Finland project 1604/31/2016 by Business Finland / Tekes. Sincere thanks to the operator Manne Viljamaa from Tampere University of Applied Sciences.

REFERENCES

1 Hippalgaonkar, R., Ivantysynova, M. & Zimmerman, J. 2012. Fuel savings of a mini-excavator through a hydraulic hybrid displacement controlled system. 8th International Fluid Power Conference, March 26–28, 2012, Dresden, Germany, pp. 139–153 (Vol. 2).

2 Vukovic, M., Leifeld, R. & Murrenhoff, H. 2016. STEAM – a hydraulic hybrid architecture for excavators. 10th International Fluid Power Conference, March 8–10, 2016, Dresden, Germany, pp. 151–162 (Vol. 3).

3 Einola, K. & Kivi, A. 2015. First experimental results of a hydraulic hybrid concept system for a cut-to-length forest harvester. The Fourteenth Scandinavian International Conference on Fluid Power, May 20–22, 2015, Tampere, Finland, 13 p.

4 Anon. 2012. Caterpillar unveils first hybrid excavator. Caterpillar press release 335PR12, October 16, 2012.

5 Mantsinen HybriLift. https://www.mantsinen.com/en/products/material-handlers/key-features/. Visited 10.12.2018.

6 Eriksson, B. 2010. Mobile fluid power systems design with a focus on energy efficiency. PhD thesis, Linköping University, Linköping, Sweden, 2010.

7 Huova, M., Tammisto, J., Linjama, M. & Tervonen, J. 2018. Fuel Efficiency Analysis of Selected Hydraulic Hybrids in a Wheel Loader Application. The BATH/ASME 2018 Symposium on Fluid Power and Motion Control, September 12–14, 2018, Bath, UK, 10 p.

8 Yao, B. & Liu, S. 2002. Energy-saving control of hydraulic systems with novel programmable valves. The 4th World Congress on Intelligent Control and Automation, June 10–14, 2002, Shanghai, China.

9 Zhang, S., Minav, T. & Pietola, M. 2017. Improving efficiency of micro excavator with decentralized hydraulics. ASME/BATH 2017 Symposium on Fluid Power and Motion Control, October 16–19, 2017, Sarasota, 8 p.

10 Anon. Volvo CE unveils 100% electric compact excavator prototype. Volvo CE press release May 16, 2017.

11 Amrhein, J. & Neumann, U. 2012. PRB – regeneration of potential energy while boom-down. 8th International Fluid Power Conference, March 26–28, 2012, Dresden, Germany, pp. 63–71 (Vol. 2).

12 Huova, M., Heikkilä, M., Linjama, M., Tikkanen, S. & Huhtala, K. 2018. Comparison of Energy Saving Methods for Loader. The 10th Colloquium Mobile Hydraulics (MHK 2018), October 16–17, 2018, Brunswick, Germany, 12 p.

13 Heikkilä, M., Huova, M., Tammisto, J., Linjama, M. & Tervonen, J. 2018. Fuel Efficiency Optimization of a Baseline Wheel Loader and its Hydraulic Hybrid Variants Using Dynamic Programming. The BATH/ASME 2018 Symposium on Fluid Power and Motion Control, September 12–14, Bath, UK, 10 p.

14 Hydraulic Flywheel HFW. https://www.boschrexroth.com/en/xc/products/product-groups/mobile-hydraulics/systems-and-functional-modules/hydraulic-flywheel-hfw/index. Visited 11.12.2018.

15 Erkkilä, Bauer, F. & Feld, D. 2013. Universal energy storage and recovery system – a novel approach for hydraulic hybrid. The 13th Scandinavian International Conference on Fluid Power, June 3–5, 2013, Linköping, Sweden, 8 p.

16 Huova, M., Aalto, A., Linjama, M. Huhtala, K., Lantela, T. & Pietola, M. 2017. Digital hydraulic multi-pressure actuator – the concept, simulation study and first experimental results. International Journal of Fluid Power, Vol. 18, No. 3, pp. 141-152. DOI: http://dx.doi.org/10.1080/14399776.2017.1302775.

17 Wille 665. https://www.willemachines.com/machines/665. Visited 11.12.2018.

18 Juhala, J., Kajaste. J. & Pietola, M. 2014. Experimental analysis of heat losses in different types of hydraulic accumulators. The 8th FPNI PhD Symposium on Fluid Power FPNI2014, June 11–13, 2014, Lappeenranta, Finland, 7 p.

19 Juhala, J., Kajaste, J. & Pietola, M. 2011. Improving energy efficiency of hydraulic accumulator. The Twelfth Scandinavian International Conference on Fluid Power, May 18–20, 2011, Tampere, Finland, pp. 99–110 (Vol. 2).

20 Stroganov, A. & Sheshin, L. 2011. Improvement of heat-regenerative hydraulic accumulators. The Twelfth Scandinavian International Conference on Fluid Power, May 18–20, 2011, Tampere, Finland, pp. 301–315 (Vol. 3).

21 Anon. 2018. Accumulators, Sustainable Hydraulics, Bladder accumulator with foam-filled bladder. Hydac Technews 2018.

22 Saleem, S. 2018. Pilot operated cartridge valve – dynamic characteristics measurements for energy efficient operation and application. M.Sc. thesis, Aalto University.

23 Anon. 2015. 2/2 cartridge seat valve, Size 5. Bucher Hydraulics brochure 400-P-121110-EN-00/09.2015.

24 Epec 5050 control unit. http://www.epec.fi/control-system-products/epec-5050-control-unit/. Visited 11.12.2018.

25 Ahmed, H., Gottberg, O., Kauranne, H., Kajaste, J., Calonius, O., Huova, M., Linjama, M., Elonen, J., Kahra, P. & Pietola, M. 2019. Multi-pressure actuator in enhancing energy balance of micro-excavator. To be published in The Sixteenth Scandinavian International Conference on Fluid Power, May 20-22, 2019, Tampere, Finland.

ENERGY EFFICIENCY OPTIMIZATION OF ELECTRIC POWERTRAIN OF UNDERGROUND LOAD-HAUL-DUMP MINING LOADER BY MEANS OF DYNAMIC PROGRAMMING

Marius Baranauskas[1*], Tatiana Minav[2], Anouar Belahcen[1], Anton Jokinen[2], Kari Tammi[2], Matti Pietola[2]

1. Department of Electrical Engineering and Automation, School of Electrical Engineering, Aalto University, Espoo, Finland
2. Department of Mechanical Engineering, School of Engineering, Aalto University, Espoo, Finland

*marius.baranauskas@aalto.fi

ABSTRACT

The emissions of heavy-duty underground mobile machinery put the health of human workers at risk and increase the overall maintenance cost of the underground mine due to extra ventilation expenses. Besides, tightening emission standards for non-road vehicles are pushing towards greener solutions, hence fully electric powertrains are becoming a viable alternative to conventional solutions. A fully electric powertrain provides mechanical power with no local emissions and it is characterized by a superior energy efficiency compared to conventional diesel powered machines. This paper analyzes a case study of a real-size load-haul-dump mining loader equipped with a fully electric powertrain. An optimal speed profile is generated for the mining loader by means of Bellman's dynamic programming algorithm in MatLab environment. The optimal speed profile demonstrated a 9.1% decrease in energy consumption comparing to a profile composed of constant speed and constant acceleration. As the traction motors are operated in the higher efficiency areas, they generate less heat prolonging the lifetime of the powertrain components.

KEYWORDS: dynamic programming, load-haul-dump mining loader, electric powertrain, energy efficiency

1. INTRODUCTION

The emissions of non-road mobile machinery (NRMM) in underground mines are one of the major issues of the mining industry. The exhaust of conventional diesel engines contribute to an already harsh working environment for human workers. Ensuring their well-being requires safety precautions, proper ventilation and air-conditioning systems. The ventilation systems are necessary to combat the increased temperatures and reduced oxygen levels. Mining history shows that most disasters are caused by ventilation issues - fires, dust explosions, gas outbursts and windblasts [1]. As the underground mines become deeper and hotter, the ventilation systems become more complex and, therefore more expensive. Consequently, the ventilation becomes a considerable part of the underground mine maintenance.

Electrification of NRMM powertrains is a proposed solution in order to improve the working conditions in underground mines and to reduce the ventilation expenses. Electric powertrains not only are local emission-free but also have a potential to increase an overall energy and work efficiency. The electrification of heavy-duty NRMM has been a field of extensive research due to various environmental concerns and enforced

upcoming Tier V regulations for non-road engines [2]. Therefore, the powertrain electrification is an appealing research topic, as tightening emission standards are pushing towards greener solutions.

Globally 75% of underground mines use load-haul-dump (LHD) mining loaders for handling loose material during the excavation [3]. LHD vehicle (figure 1) is a type of NRMM similar to front end loaders but designed for the roughest hard mining applications. They are highly maneuverable, rugged and exceptionally productive, however most of the LHD powertrains are driven by large diesel engines, which are neither efficient nor sustainable. An implementation of fully electric powertrains is a great alternative to the conventional solutions.

Figure 1. A full-size LHD mining loader in Aalto University laboratory

Fully electric powertrains for the LHD applications are still a novelty, and currently, diesel driven powertrains dominate the transportation market [4]. Conventional powertrains have numerous flaws comparing to fully electric powertrains. The diesel engine for the conventional applications is normally selected according to the highest possible load even though duty work cycles are composed of short high-power peaks, resulting in long idling periods during regular operation. Electric motors, on the other hand, can provide high torque at low speeds and provide better controllability via variable frequency drives (VFD) effectively outperforming the diesel counterpart. In conjunction with an inherently lower energy efficiency, the internal combustion motors are clearly inferior to the electric motors.

However, energy storage technology still limits the application of electric NRMM powertrains. Currently available Li-ion batteries are still at least 15 times less energy dense than the diesel fuels. Massive battery packs must be installed to provide enough power, increasing the overall mass of the vehicle. Thus, an efficient use of stored energy is necessary in order to implement fully electric powertrains cost-effectively. This can be achieved by regenerative braking and by optimizing the energy efficiency of electric traction motors.

2. OBJECTIVES

An electric powertrain allows power regeneration during braking and since the LHD mining loader is a heavy vehicle, large amounts of energy can be recovered. The harder the braking, the more energy is regenerated but the faster the vehicle moves, the more power is consumed. While the LHD mining loader does not have a standard work cycle like other mobile machines, a generic duty cycle can be formulated empirically. The automation of this movement introduces an opportunity for an optimization concerning the energy efficiency and work efficiency. Improving the energy efficiency means reducing the energy cost per unit of distance (kWh/km). Improving the work efficiency means reducing the time taken to complete the duty cycle, which can be interpreted as material moved per unit of time (tons/h). Simultaneously improving work efficiency and energy efficiency, however, is contradictory. While the one increases, normally, the other one decreases. The proposed optimization method determines the optimal operating points for the best performance regarding the power consumption.

The aim of this research is to reduce the power consumption of the traction motors by utilizing an optimization algorithm developed by means of dynamic programming (DP). This is realized by creating a dynamic

deterministic model of the LHD powertrain in MatLab environment and applying the optimization algorithm. The optimization code includes a simulation of a generic work cycle and a DP function that minimizes the consumed energy. The simulation generates a minimal energy speed profile, calculates the total energy consumption and time elapsed during the duty cycle. The energy consumption results are then compared with a profile composed of a constant speed and a constant acceleration (a non-optimal speed profile).

The following section overviews the electric NRMM state of the art and relevant DP applications. Section 4 briefly discusses the LHD mining loader case study in Aalto University. The model of LHD mining loader and the description of the method, including the definition of the duty cycle and the problem formulation, are presented in section 5. The simulation results are presented in section 6, sensitivity analysis - in section 7. The discussion of the results and the future prospects for this study are outlined in sections 8 and 9, respectively.

3. STATE-OF-THE-ART

Currently, three types of electric powertrains are available according to their main power source [5]. Electric power can be fed by overhead lines (or rails), tethered trailing cables or energy storage devices. The overhead lines require the most infrastructure and their use is limited. High maintenance and low adaptability makes it highly unlikely to become a mainstream solution in the future. Trailing cables are the cheapest solution and it is already used in practice, but it suffers from low mobility and versatility [6]. In addition, cable failures are a potential hazard. The battery-powered loaders provide the greatest flexibility and reliability. However, it is estimated that 1.5-2 tons of batteries are needed for 2-2.5 hours of worktime. Typical Li-ion batteries require at least 2 hours of charging, which results in 50% downtime [5]. Alternatively, a spare set of batteries is needed for normal operation – one battery is operational while the other one is being charged.

Electric powertrains for NRMM are commercially viable in all power classes [5]. The low power electric powered vehicles (under 10kW) are the most technologically feasible and have the largest variety of products in the market. They are particularly attractive for the applications where the environment requires low noise levels and no emissions. In mid-power class, only a handful of products exists but as the power increases the attractiveness of the electric powertrain increases as well. Most NRMM (as well as LHD mining loaders) are equipped with a hydraulic power transmission for high torque manipulations such as buckets and booms. Hydraulic power is also used for traction purposes in slowly moving machines, as currently no alternatives are available, which is one of the drivers for this study. The electromechanical transmission outperforms hydraulic at higher power and higher speeds. Finally, high-power class of stationary applications is almost exceptionally driven by electromechanical powertrains as the energy efficiency becomes more relevant and overheating becomes an issue. LHD mining loaders fall into mid-high power range category where the powertrain electrification is feasible and energy efficiency optimization can be profitable.

Various optimization algorithms were developed in recent years but the dynamic programming (DP) method is the most widely used [7]. Dynamic programming (DP) is an optimization technique that is based on Bellman-Ford algorithm [8], which solves the problem by breaking it down to simple recursive sub-problems, solving them and reusing the solutions. The algorithm solves the problem from the final state backwards in time and stores the relevant information about the optimal trajectory to all intermediate points. The DP method is a powerful tool to solve problems such as finding the shortest path or calculating a minimal cost of an industrial process. It is sometimes called “careful brute force algorithm” because it involves an exhaustive search in polynomial time i.e. the problem length increases the time consumed linearly. However, it solves the optimization problem omitting the redundant operations of a basic recursion algorithm. Even if the problem is not inherently optimization, it can be reformulated and used with a DP algorithm, making it a very powerful and universal tool suitable for many different applications.

An open-source MatLab DP function [9] introduced in [10] is the backbone of this study. DP approach was used in optimizing the fuel efficiency of conventional road vehicles [11], [12], hybrid road and non-road vehicles [13], [14] and energy optimal speed profiles were analyzed for electric city busses in [15]. However, the method was never applied for electric NRMM powertrains, thus this article addresses this niche.

4. DESCRIPTION OF RESEARCH PLATFORM

A real-size 14.5-ton LHD mining loader with a 4-ton lifting capacity is available as a case study in Aalto University. The scope of the previous research was twofold – the development of direct driven hydraulics (DDH) and fully electric powertrain. Figure 2 presents a block schematic of the powertrain components. The main traction power source is a 362V Li-Ion battery constructed in Aalto University [16].

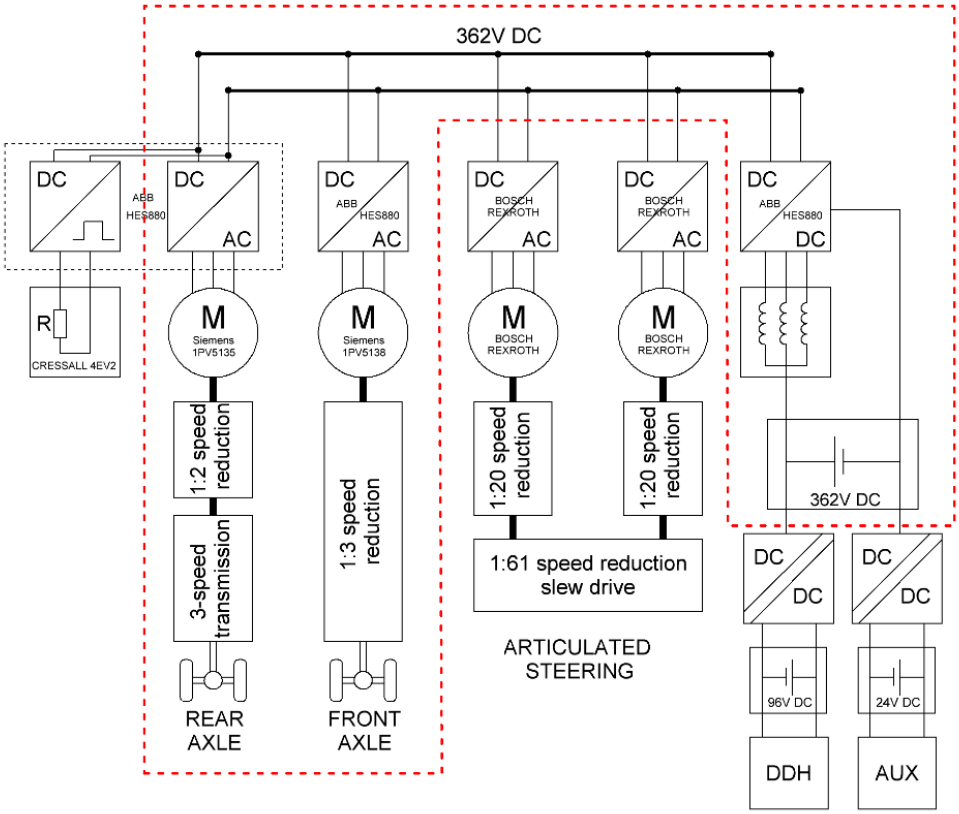

Figure 2. Block schematic of LHD powertrain

Numerous articles were published regarding DDH, proving it to be superior to conventional hydrostatic hydraulics in terms of efficiency and reliability [17], [18]. During the past projects, the conventional hydrostatic powertrain was replaced by electromechanical equivalent as seen in figure 3. The steering mechanism, as well as DDH and auxiliary systems are energy efficient and consume significantly less power than the traction motors [19], thus, they are excluded from this study. This study focuses on the energy optimization of the electric powertrain. The simulation model includes only the elements highlighted in red demonstrated in Figure 2. The traction motors are the focus for the energy optimization and the parameters used in the simulations are presented in table 1.

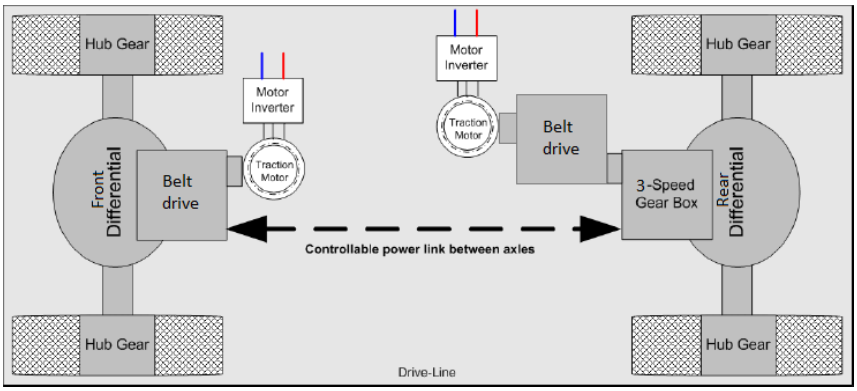

Figure 3. Electromechanical drivetrain configuration [18]

The front and the rear axles are driven by separate asynchronous traction motors, which are controlled by VFD. The torque produced by the front axle traction motor is transferred to wheels via 2:1 belt drive, differential and hub gears with speed reduction ratios of 6 and 5.125. The rear axle configuration is almost identical but there is a 3-speed gearbox in between the belt drive and the rear differential gears. The gearbox ratio is set to 1:1 for the simulations. The axles are not connected mechanically and a controllable power link is present. In this case, the rear traction motor is considered primary and during a normal operation is loaded more than the secondary, front motor. The rear motor acts an auxiliary traction power when the front wheels are slipping or hovering in mid-air. However, for the sake of simplicity, the simulation, further described in section 5, assumes that both motors are loaded evenly.

Table 1. Traction motor parameters

	Value	Unit
Motor type	Asynchronous motor	-
Control mode	Direct torque control	-
Nominal voltage	440	V
Nominal frequency	133.7	Hz
Nominal speed	3920	rpm
Nominal power	85	kW
Nominal $cos\phi$	0.87	-
Polepairs	2	-

5. MODEL DESCRIPTION

The powertrain of the LHD mining loader described in the previous section is simulated in MatLab environment. This study analyzes the energy consumed by the main powertrain, i.e. the traction motors that are powered by a central battery pack. The simulation omits the power consumed by the steering motors for its high efficiency and low power consumption. Thus, the simulation can be realized as a movement on a one-dimensional path. Other LHD mining loader subsystems, such as work hydraulics and auxiliary systems, are excluded from the simulations or simplified to a constant load. Moreover, transmission box, gears, frequency converters and battery charging are simulated with a constant efficiency factor and complex vehicle dynamics are excluded from the simulation.

Standard duty cycle are undefined for NRMM because of their vast variety and often very specific applications. A generic duty cycle for LHD mining loader has been defined based on empirical data [20]. The generic duty work cycle of an LHD mining loader is presented in figure 4. The unloaded LHD moves 80 m 4% uphill, then 205 m 12% downhill and 55 m on flat ground. At the loading place it picks up 4 000 kg of loose material and drives back to the dumping place. The duty cycle was realized as a discrete system that consists of the position change, the time elapsed from the start of the duty cycle, speed limits, a reference speed, and an inclination angle. Therefore, this model can be used as a tool for other similar applications as the parameters can be easily changed.

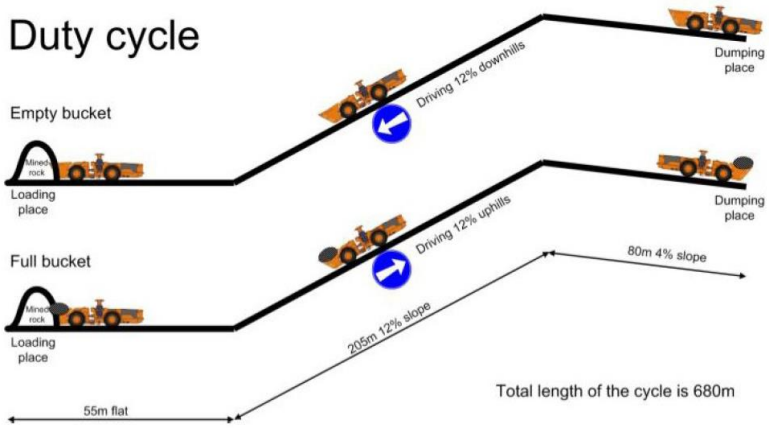

Figure 4. LHD generic duty cycle [20]

The objective of the DP optimal control is to determine the control signals which cause the process to minimize (or maximize) some performance criterion at the same time satisfying the physical constraints. In this case, the performance criterion is the energy consumed over a single duty cycle.

$$\min_{u_k \in U_k} \sum_{k=0}^{N-1} P_{batt}(u_k, k) \cdot T_d(u_k, k) \tag{1}$$

where P_{batt} is the power drawn from the battery, u_k is the control signal, ranging from 0 to 1, T_d is the time-step (1 second in this case) and k is the number of steps. Optimizing the work cycle of an LHD mining loader can be beneficial because it mostly operates at periodic duty cycles over its lifetime. The duty cycle operation is highly energy consuming, so even a small decrease in energy consumption, will result in many kWh saved. To avoid sudden battery power surges, a penalization of acceleration was introduced, which essentially puts a price for changing the speed with respect to consumed power. Lower overall power consumption and smoother duty cycles extend the lifetime of the powertrain components, most notably the battery pack.

The wheel torque is calculated as follows.

$$T_w = (mg\mu_r cos\alpha + mgsin\alpha + ma)r_w \tag{2}$$

where m is the mass of the vehicle, μ_r – rolling coefficient, α – inclination angle and r_w – wheel radius.

Electric motor torque is calculated as:

$$T_m = \frac{T_w}{k_g \cdot k_m \cdot \eta_d} + T_{m0} \tag{3}$$

where k_g is the final gear ratio, k_m – motor belt drive gear ratio, η_d – total drivetrain efficiency, T_{m0} - motor drag torque.

The battery current is calculated as:

$$I_b = \eta_e \cdot \frac{U - \sqrt{U^2 - 4 \cdot r \cdot P_{be}}}{2 \cdot r} \tag{4}$$

where η_e is the Coulombic efficiency of the battery, U – voltage, r – internal resistance and P_{be} – total battery power required.

A more detailed description of the duty cycle, model and the DP algorithm application is presented in [21].

6. RESULTS

By employing the DP algorithm with the LHD powertrain model, an optimal speed profile was generated. Figure 5 compares the power demand of an optimal speed profile and a non-optimal speed profile composed of constant speed and constant acceleration, 4.167 m/s and 3 m/s^2 respectively. The non-optimal (original) speed profile corresponds to the most aggressive driving style by the machine operator. The driver uses the maximum torque available to accelerate and drives at the speed limit. The acceleration of 3 m/s^2 is the maximum acceleration that the LHD mining loader can reach on a flat ground considering the drivetrain configuration and the traction motors working at full torque. The speed of 4.167 m/s (15 km/h) is the limit in most manned underground mines [20]. However, the LHD mining loader in Aalto laboratory is capable of reaching higher speeds due to high-speed asynchronous traction motors. In addition, DP speed profile can only be applied in at least semi-automated underground mines where the chance of human error is reduced and speed limits may be increased. Thus, to demonstrate the potential of DP algorithm capabilities, the maximum speed for the model is increased to 30 km/h.

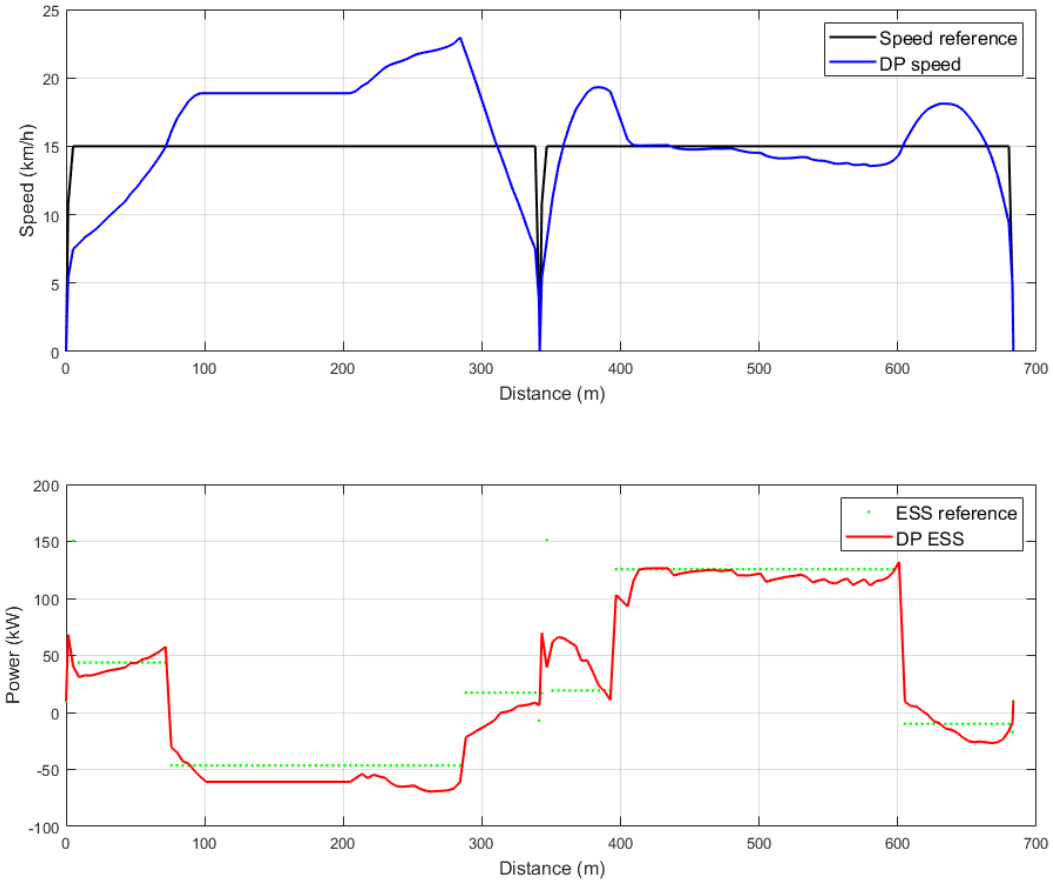

Figure 5. Optimal speed profile

The figure 5 illustrates the comparison between the reference and DP speed profiles. The first half of the upper graph represents the unloaded vehicle moving towards the loading place. DP algorithm suggests slower acceleration and deceleration but a higher speed during the steep downhill part to recover more energy. The second half represents the loaded vehicle moving towards the dumping place. The DP speed profile is more similar to the reference profile here except for the bumps in speed before and after the steep uphill part where the most energy is saved. The lower graph compares DP ESS (energy storage system - P_{batt}) with the reference ESS. Positive power here means power consumption and negative – power regeneration. ESS power (green dots) is visually higher than DP ESS power (red line) in most areas indicating the overall energy consumption decrease.

Figure 6 shows a different speed profile representation – the speed-torque duty cycle is overlaid with the energy efficiency map of the traction motors. The traction motors are asynchronous electric machines with the

highest efficiency at the high speed areas. Thus, the DP algorithm is forcing the operation points towards those areas.

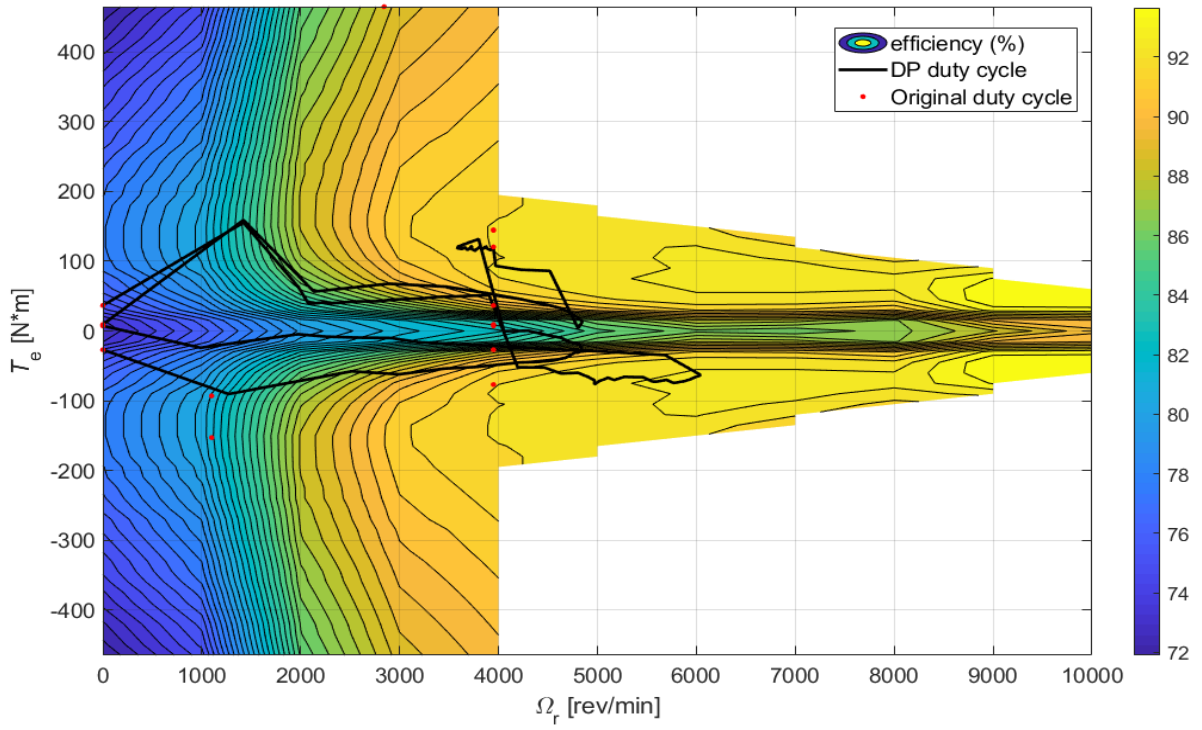

Figure 6. Traction motor efficiency map and duty cycle operation area

Table 2 presents the energy consumption comparison between the original and DP optimal speed profiles. The results are split into two parts – before and after loading of the vehicle. The first part is a lighter vehicle moving mostly downhill, the second – heavier and uphill. The DP algorithm shows better results in both power consumption and power regeneration. The total energy consumption decreased by 9.1%.

Table 2. Energy consumption

	Original results, Wh/km	DP results, Wh/km
1st half	-839.6	-1066
2nd half	5516.9	5316.2
Total	**2338.65**	**2125.1**

Table 3 presents the time elapsed of the original and DP speed profiles. It can be interpreted as an LHD mining loader work efficiency. The faster the duty cycle is completed, potentially the more material per hour is moved. The increase in the work efficiency is insignificant in these simulation results but they are considered in the sensitivity analysis in the following section. The simulation time is recorded to analyse the availability of real-time applications further analysed in the next section. While DP optimization method is used in various applications, it is primarily an offline tool due to its rather high computation power requirements.

Table 3. Time elapsed

	Original results, s	DP results, s	Simulation time, s
1st half	83.5	81.6	49.7
2nd half	83.5	84.2	97.8
Total	**167**	**165.8**	**147.5**

7. SENSITIVITY ANALYSIS

The outcome of the simulation is heavily affected by two independent arbitrary parameters – the time step and the acceleration penalization coefficients. Thus, the sensitivity analysis consists of two parts. The first part corresponds to the accuracy of the simulation i.e. the time step or the simulation points which are inversely proportional as seen in figure 7. Naturally, higher accuracy should provide better results (lower power consumption) for a price of longer simulation time. The second part of the sensitivity study analyses the penalization of the acceleration. The cost function defined in (5) penalizes the change in speed with respect to consumed power.

$$C\{1\} = \alpha P_{batt}/10^6 + \beta a \tag{5}$$

It was introduced due to sudden spikes in power consumption using a DP speed profile. The results presented in the previous section were simulated with arbitrary coefficients - 167 points corresponding to 1 s time step and $\alpha = \beta$ meaning that 1 m/s^2 is as costly as 100kW.

7.1. Time step and simulation points

The expected trade-off for a more accurate power consumption simulation is an increased simulation time. The time step lower than 1 s increases the simulation time drastically (figure 8). The time step higher than 1 s, on the other hand, causes inaccuracies in the vehicle and duty cycle models thus that is not recommended. Figure 9 illustrates the power consumption simulation dependency on the number of simulation points. A downwards trend can be observed however, the decrease in power consumption is rather low. Thus, an argument can be made that time step of 1 s is reasonable for this study.

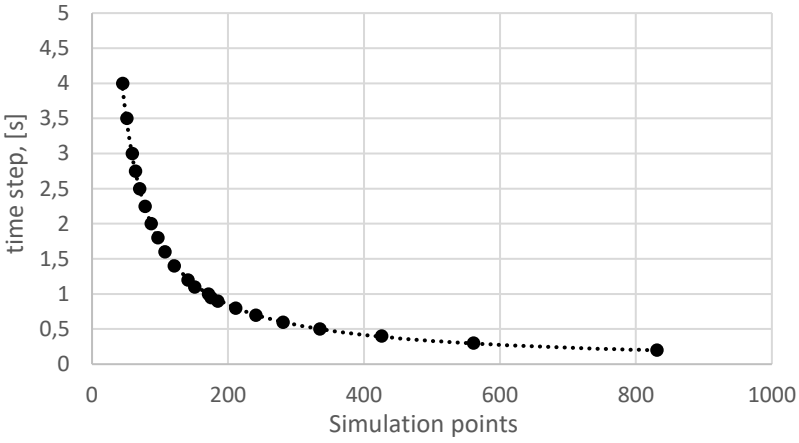

Figure 7. Time step vs simulation points

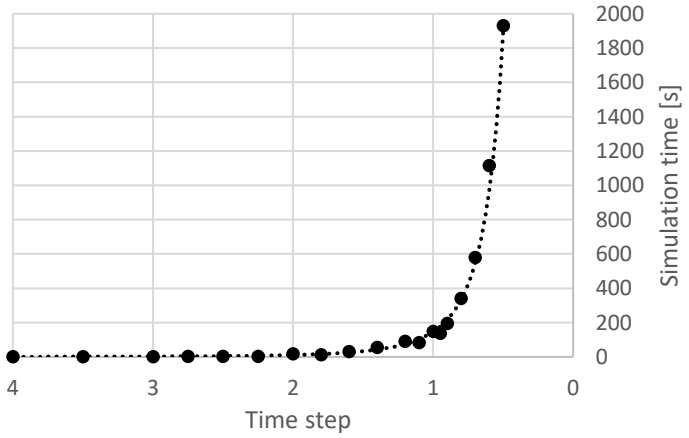

Figure 8. Simulation time

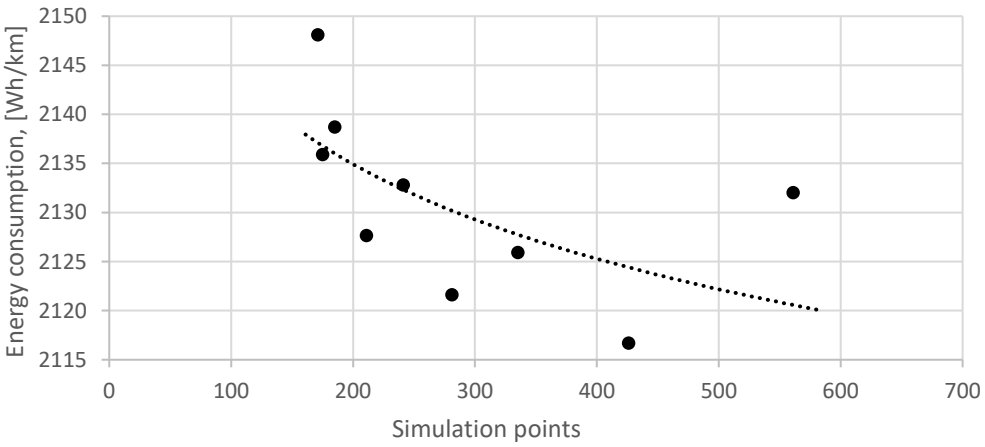

Figure 9. Power consumption depending on simulation points

7.2. Acceleration penalization

The acceleration penalization was introduced in order to smoothen the duty cycle – to avoid sudden power surges. Coefficients of the equation (5) are normalized:

$$\alpha + \beta = 1 \tag{6}$$

and presented in figure 10 versus the energy consumption and the duty cycle duration. The increasing weight of power consumption in the cost function (α) showed erratic behaviour and only a slight downwards trend in energy consumption per unit distance (black dots). However, the duty cycle duration or work efficiency displayed a clear decrease (brown dots) with higher values of α. Depending on the goal of the optimization, whether the energy consumption or the work efficiency is the focus, the coefficients can be selected accordingly. However, the energy consumption axis ranges from 2118 to 2134, which is less than 1%. The change in energy consumption is miniscule, while the change in duty cycle duration is more noticeable. Nevertheless, $\alpha = \beta$ represented this DP application adequately.

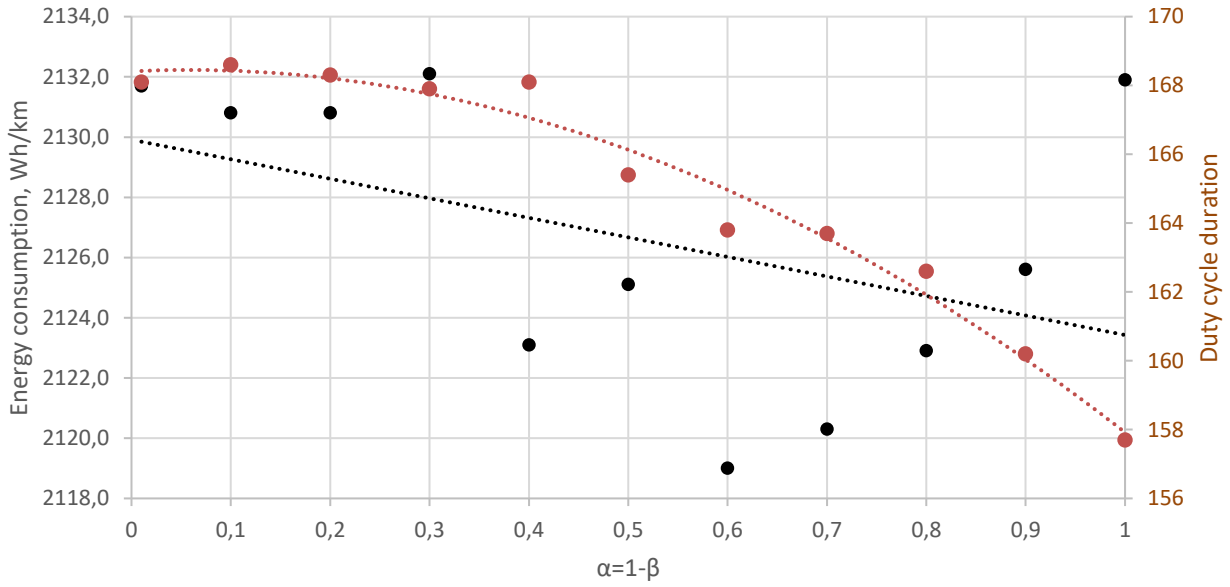

Figure 10. Energy consumption and duty cycle duration dependency on coefficients α and β

8. DISCUSSION

By applying DP algorithm, the energy consumption per unit of distance decreased by 9.1% comparing to a non-optimal speed profile from Table 2. It is worth mentioning that the energy consumption decrease positively affect the lifetime of the LHD powertrain components. Furthermore, more efficient traction motors generate less heat reducing the chance of failure. The electric traction motors are applied in their full capacity, as the electric motor operating point is moving all over speed-torque map, reaching the highest efficiency areas. Moreover, the motors do not operate in over-torque regions (over 250 Nm), which leaves a reasonable safety margin for the calculation errors and an unexpected load increase in a real world underground mine applications. Naturally, a simulation is a simplified example of a real world application and certain factors simply cannot be accounted for.

The aim of this research was to illustrate the potential and the limitations of the DP optimization algorithm. A precise energy consumption decrease can be measured only in the actual work environment i.e. an underground mine. Since the utilized reference cycle was artificial, concrete conclusions could not be drawn. The decrease of energy consumption by 9.1% cannot be realistically proven due to the artificial nature of the procedure. However, it serves as an indicator for the potential of the optimization technique and a prospect for continued research.

Similar optimization methods can be used for any type of powertrain even a conventional, diesel-powered one. However, the results might not be as significant because the diesel engine speed-torque efficiency map is entirely different and only electric powertrains enable power regeneration, which is the key for improving the energy efficiency. In addition, the optimization requires increased level of mine automatization, which hinders the DP application for conventional NRMM powertrains. The use of DP algorithms is an advantage of using electric powertrains for NRMM applications.

Successful results of this study prompt potential research topics relating to further DP applications and the development of this case study.

9. FUTURE WORKS

The MatLab simulation discussed concentrates on minimizing the total energy consumption over a duty cycle. However, in certain cases, work efficiency is more important than energy efficiency, especially considering the low price of electric power. The optimization for work efficiency can be achieved by editing the cost function in MatLab code and prioritizing the total elapsed time over the energy consumption. To improve the optimization process further, certain coefficients could be introduced to calculate energy efficiency and work efficiency trade-off. These calculations would be based on the economic aspect and the unique application of NRMM in question.

This article is based on a case study with a fixed set of equipment. A future study could speculate and discuss the results with different equipment, most notably a different type of traction motors. Permanent magnet electric machines have a favorable efficiency map and are more suited to work as generators i.e. the energy recovery could be improved. The DP algorithm would drive the speed function towards lower speeds as the efficiency is higher at that area, contrary to the induction motors. DP can be a universal tool used for any type of powertrain optimization including a conventional diesel powered one. While the research is focused on the electrification of powertrains, diesel powertrains still dominate the market and improving their efficiency can attract the attention of industry.

The modelling process can be improved, by including air drag simulation for an increased accuracy, steering and work hydraulics simulation, uneven load simulation and a gradual change in inclination change in duty cycle description. In addition, a very recent study in [22] applies the same DP method for fuel efficiency optimization of NRMM work hydraulics. It shows the potential of applying DP algorithms for DDH work hydraulics present in the case study. Even though the power consumption of DDH is significantly lower than powertrain's, energy optimization of auxiliary motors might allow the equipment downsizing.

Although the reference cycle is based on real work cycles, it is an artificial formulation. This kind of artificial cycle can be used to compare different optimization techniques and judge the DP performance in relation to them.

In conclusion, this study introduced DP algorithms as a powerful tool for energy consumption optimization of electric NRMM applications. Significant energy consumption reduction was achieved by applying an optimal DP speed profile, while increasing the traction motor efficiency over the generic duty cycle. However, DP remains an offline optimization tool due to relatively high simulation time.

REFERENCES

[1] Brake, R. 2006. The Importance of Underground Mine Ventilation. FAusIMM, Mine Ventilation Australia. Bulletin, pp. 21-22

[2] Dieselnet, 2016.11, EU: Non-road Engines. Retrieved: 2018.10.24 https://www.dieselnet.com/standards/eu/nonroad.php

[3] Tatiya, R.R. 2013, Surface and underground excavations – methods, techniques and equipment.

[4] Manzi, P, 2018, Market Beat, January 2018. Nada.

[5] Paraszczak, J. et al., 2014. Electrification of Loaders and Trucks – A Step towards More Sustainable Underground Mining. International conference on renewable energies and power quality, April 8-10, 2014, pp.81-86

[6] Lajunen, A. et al., 2016. Electric and hybrid electric non-road mobile machinery -present situation and future trends. EVS29 Symposium, Montréal, Québec, Canada, June 19-22, 2016, pp. 1-12

[7] Back, M. 2004, Predictive powertrain control for hybrid electrical vehicles, IFAC Symposium on Advances in Automotive Control. April 2004, pp. 439-444.

[8] Bellman, R. (1958). On a routing problem. Quarterly of Applied Mathematics.

[9] ETH, 2018, Institute for Dynamic Systems and Control – Downloads. Retrieved: 2018.10.26. http://www.idsc.ethz.ch/research-guzzella-onder/downloads.html

[10] Sundstrom, O. Guzzela, L. 2009. A generic dynamic programming Matlab function. 18th IEEE conference on control applications. Saint Petersburg, Russia, July 8-10, 2009, pp. 1625-1630.

[11] Mensing F. et al. 2011. Vehicle Trajectory Optimization for Application in Eco-Driving. IFSTTAR Bron – LTE.

[12] Mensing F. et al. 2013. Trajectory optimization for eco-driving taking into account traffic constraints. Elsevier, Transportation research, pp. 55-61

[13] Zhu. Q. et al. 2015. Comparative study of fuel reduction methods for hybrid excavators. Scandinavian International Conference on Fluid Power, May 22-24, Tampere, Finland.

[14] Lot. A, et al. 2013. Green driving optimization of a series hybrid electric vehicle.

[15] Lajunen, A. 2013, Energy-optimal velocity profiles for electric city buses, The 25th World Battery, Hybrid and Fuel Cell Electric Vehicle Symposium & Exhibition, pp. 886-891

[16] Hentunen, A. 2013. Development and validation of a Li-ion battery pack for non-road mobile machinery applications

[17] Minav, T. et al. 2016 Series Hybrid mining loader with zonal hydraulics, Implementation of zonal integrated future fluid power systems (IZIF)

[18] Lehmuspelto, T. et al. 2015, Full-scale Series Hybrid Mining Loader with Zonal Hydraulics. ECV

[19] Turunen, A. et al. 2018, Experimental investigation of direct drive hydraulic units implemented in a mining loader. GFPS

[20] Lajunen, A. 2010, Energy consumption simulations of a conventional and hybrid mining loader. The 25th World Battery, Hybrid and Fuel Cell Electric Vehicle Symposium & Exhibition. Shenzhen, China, Nov. 5-9, 2010.

[21] Baranauskas, M. Energy efficiency optimization of powertrain of electric underground load-haul-dump mining loader – a case study. Master's thesis. Aalto University, ELEC.

[22] Heikkilä M. et al. 2018. Fuel efficiency optimization of a baseline wheel loader and its hydraulic hybrid variants using dynamic programming. FPMC2018, Bath UK, September 12-14, 2018 pp. 1-10

AUTOMATIC PROCESS PATTERN RECOGNITION FOR MOBILE MACHINERY

Martin Starke, Frank Will
Technische Universität Dresden, Endowed Chair of Construction Machinery
Münchner Platz 3, 01062 Dresden
martin.starke@tu-dresden.de

ABSTRACT

In nowadays-used mobile construction machinery, the knowledge of the usage profiles is in fact not available. This lack causes a design phase, which is characterized by assumptions. This affects every development step in which the application has a significant influence on the design, what in nearly every section is the case (e.g. dimensioning of structural-mechanical part, drive system development, hydraulic structure construction). This paper presents the development of a process pattern recognition (PPR). Process patterns are from an engineering perspective a class of uniform or similar working cycles. The developed system will answer the question which working-cycles the machine executes during its lifetime.

KEYWORDS: process pattern, pattern recognition, machine learning, usage profiles

1. INTRODUCTION

The versatile use of typical construction machinery in field is a crucial criterion during the development process. Nobody knows which tasks the operator executes and furthermore how sensitive they will be done. Additionally to this operator-guided process, the changing environmental conditions, which include the weather and the consistence of the working medium, have to be observed during the design-phase.

The researchers at the TU Dresden started in further projects to deal with these issues. In [6] a definition of so-called process patterns was introduced with the aim of developing a method capable of classifying load consequences. As mentioned before, process patterns are defined as a class of uniform or similar working cycles. This definition was applied within the context of the project by measuring the loads exerted on relevant components and allocating load consequences with a similarly damaging effect to specific process patterns. The resultant classes provided a basis for the determination of process-dependent instances of partial damage that can be superpositioned and extrapolated to a specific period of machine operation. A key prerequisite to realize this is the knowledge of the machine's probable operating parameters. Against this backdrop a method enabling the definition of usage profiles for mobile machines was developed [8]. The broad range of knowledge already available in the field of pattern recognition in parallel areas of application such as image and speech recognition was used as a foundation for the selection and adaptation of algorithms enabling the definition of customer usage profiles that in turn facilitate the realistic measurement of mobile construction machines when in operation. The resultant algorithms enabled the online recognition of working cycles and the allocation thereof to pre-defined process patterns during machine operation. Real-time data evaluation kept data storage requirements to a minimum despite the very long observation periods involved, as only the frequency with which individual patterns occurred needed to be recorded. The researchers could show, that this method

basically enables the user to record the occurring working patterns. The extension of this method leads to the requirement of an automatically data preparation to get independent from the special sensor signals and makes the method applicable to different types of machines.

Based on the most typical wheel loader's pattern called y-cycle the whole development is presented in this contribution. In chapter 2 the basics of an HMM and its suitability for the application to the example is presented. Besides this chapter introduces the reader in the definition of the HMM and what the definition of the state and transition probabilities means. Furthermore the suitable sensor signals, which are necessary for a most accurate recognition rate, are discussed. After the validation of the developed method is shown, chapter 3 decribes the actual development with the extension of the method for the efficiency analysis and the structure of the recognition system. Finally, chapter 4 concludes the paper's content.

2. HIDDEN MARKOV MODELS AND THE Y-CYCLE

2.1. Hidden Markov Models

The first step included the choice of suitable algorithms for this application. The aim to detect patterns from signals is similar to parallel areas such as speech and image recognition. Every recognition-method has the similar structure, shown in Figure 1.

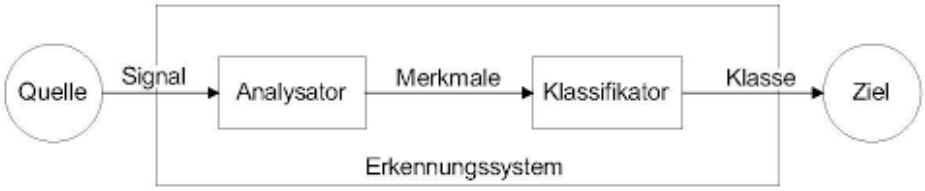

Figure 1. Structure of a recognition system [4]

The workflow contains the signal source, which is imported to the analyser, where the data preparation, e.g. frequency filtering, is being executed. After that a classification and the decision, to which class the signal is allocated is done. The main difference between the available algorithms is the conversion of the physical signal to the characteristic classification type. For this application the typical pattern recognition methods have been investigated. These were the template matching procedure (TM), artificial neuronal nets (NN), support-vector-machines (SVM) and hidden markov models (HMM), which are described in detail in [3].

HMMs meet the requirements. First of all that they offer the opportunity to deal with a continuing data stream. In the field of online application, this is the most important issue, which had to be fulfilled. Furthermore HMMs can manage the high variation of the duration of the working cycles, which occurs in nearly every successive cycle. The separation of the single working cycle out of one dataflow had to be ensured in the pattern recognition. With HMMs this is convertible.

HMMs are widely used within the context of word recognition ([5],[1]). This involves the overlaying of the speech signal with a window function and the calculation of the frequency spectrum. The maxima observed at characteristic frequencies within the spectrum depend on the tone spoken, and are summarised in a feature vector which is transferred to the HMM. A pre-trained vocabulary is then used in combination with the Viterbi algorithm to determine the word with the maximum level of probability. Their mode of operation makes HMMs highly suitable for the recognition of sequences of various lengths, with analysis of the previous signal history used to create a type of memory. The relatively simple mathematical operations involved and the compact description of process patterns with the aid of probability distribution make the procedure especially suitable for implementation on a microcontroller.

2.2. Model definition

This chapter will handle the theoretical basics of the HMM and the realization of the method regarding to the application as pattern recognition algorithm in mobile machinery. The shown example is a wheel loader's y-cycle.

The basic idea behind the HMM is to interpret the issue under investigation as a temporal sequence of so-called states. The machine can only be in one of the n possible states (Z). In addition, it is assumed that the state of the system at time t+1 is only ever dependent on the immediately preceding time t. Nevertheless it is not possible to either observe such states in practice or measure them using sensors. Observable variables (V) (sensor signals) are instead used to determine the hidden state of the system. Transferred to the y-cycle there are 4 states the machine could belong to: Driving into the heap of excavated material, driving out of the heap, driving to the point of unloading and driving from the point of unloading back to the point of loading (see Figure 2).

Figure 2. Wheel loader's y-cycle

It is possible to determine which of the 4 states the machine is currently in by analysing measured sensor signals (here: the force applied by the lifting cylinder and the driving speed) in combination with transition and output probabilities. These probabilities are the main parameters of the model definition. Transition probabilities $a_{i,j}$ describe the probability of the machine being in state j at time t if it was in state i at the previous time increment t-1 (equation (1)).

$$P\big(Z(t) = Z_j \big| Z(t-1) = Z_i\big) = a_{i,j} \qquad (1)$$

If you have a system with n possible states, the transition probabilities are summarised in A, a nxn matrix. The diagonal elements describe the probability of the machine of staying in the same state in two following time steps. Above and underneath the diagonal elements are the probabilities of changing in the next or the prior state located.

In addition to the transition probabilities, the observation probabilities $b_{n,m}$ are the second element of HMMs, which have to be determined. They describe the probability of a specific sensor value being observed in the machine in the respective state. The observation probabilities are being summarised in B, a nxm matrix. This includes the n states and m possible sensor values.

Transition and observation probabilities are defined with the aid of training data. For each process pattern a HMM has to be trained. As mentioned before the shown pattern in this contribution is a wheel loaders y-cycle. The training is one of the basic problems for HMMs. Given are the observation sequence and the sequence of the states. The first aim is to fill the matrices A and B. This is realized with a simple counting-algorithm of the states, the observations and their transitions and to classify them into the frequency matrix. One main problem, which occurs before the training proceeds, is the definition of the state sequence. In contrast to typical applications of the HMM, e.g. speech recognition as shown in [7], the training problem could not be solved with the Baum-Welch-Algorithm or the Viterbi-training. Instead an instance counting is used to train the HMM. The goal to compute the HMM which produces a state sequence out of observations can be realized by counting the hidden state transitions and the output emissions and by determining the probabilities of the occurrence. To realize this, there is a need to assign the state sequence to the measured observation. Mieth showed in [8] a semiautomatic way to implement this by developing a special GUI used in this contribution.

Figure 3 shows a figure with the assignment of four states to the wheel loaders driving speed. This is the data basement for the described HMM training.

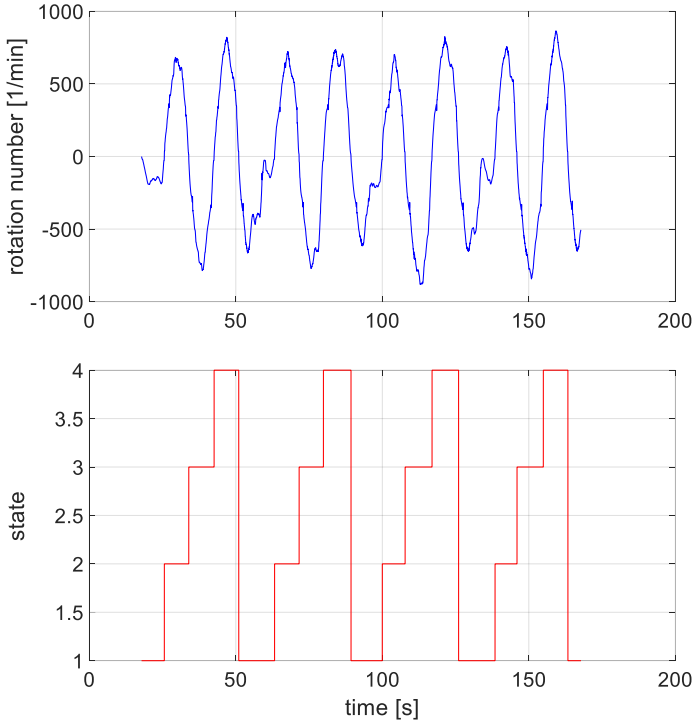

Figure 3. State distribution

$$A = \begin{bmatrix} a_{1,1} & \cdots & a_{1,n} \\ \vdots & \ddots & \vdots \\ a_{n,1} & \cdots & a_{n,n} \end{bmatrix}$$

$$A_{0.1} = \begin{bmatrix} 0000 \\ 0000 \\ 0000 \\ 0000 \end{bmatrix} \quad A_{0.2} = \begin{bmatrix} 1000 \\ 0000 \\ 0000 \\ 0000 \end{bmatrix} \quad A_{0.3} = \begin{bmatrix} 1000 \\ 0000 \\ 0000 \\ 0000 \end{bmatrix}$$

$$A_{0.4} = \begin{bmatrix} 0{,}75 & 0{,}25 & 0 & 0 \\ 0 & 0 & 0 & 0 \\ 0 & 0 & 0 & 0 \\ 0 & 0 & 0 & 0 \end{bmatrix} \quad A_{0.5} = \begin{bmatrix} 0{,}75 & 0{,}25 & 0 & 0 \\ 0 & 1 & 0 & 0 \\ 0 & 0 & 0 & 0 \\ 0 & 0 & 0 & 0 \end{bmatrix}$$

$$A_{0.6} = \begin{bmatrix} 0{,}75 & 0{,}25 & 0 & 0 \\ 0 & 0{,}5 & 0{,}5 & 0 \\ 0 & 0 & 0 & 0 \\ 0 & 0 & 0 & 0 \end{bmatrix} \quad A_{0.7\ldots0.9} = \begin{bmatrix} 0{,}75 & 0{,}25 & 0 & 0 \\ 0 & 0{,}5 & 0{,}5 & 0 \\ 0 & 0 & 1 & 0 \\ 0 & 0 & 0 & 0 \end{bmatrix} \quad A_{1.0} = \begin{bmatrix} 0{,}75 & 0{,}25 & 0 & 0 \\ 0 & 0{,}5 & 0{,}5 & 0 \\ 0 & 0 & 0{,}8 & 0{,}2 \\ 0 & 0 & 0 & 0 \end{bmatrix}$$

$$A_{1.1} = \begin{bmatrix} 0{,}75 & 0{,}25 & 0 & 0 \\ 0 & 0{,}5 & 0{,}5 & 0 \\ 0 & 0 & 0{,}8 & 0{,}2 \\ 0 & 0 & 0 & 1 \end{bmatrix} \quad A_{1.2} = \begin{bmatrix} 0{,}75 & 0{,}25 & 0 & 0 \\ 0 & 0{,}5 & 0{,}5 & 0 \\ 0 & 0 & 0{,}8 & 0{,}2 \\ 0 & 0 & 0 & 1 \end{bmatrix} = A$$

time [s]	states
0,1	1
0,2	1
0,3	1
0,4	2
0,5	2
0,6	3
0,7	3
0,8	3
0,9	3
1,0	4
1,1	4
1,2	4

Figure 4. Synthetic example for instance counting transition matrix A

Figure 4 shows an abstract overview, which illustrates the training after the state definition with the instance counting method. The counting for the observation sequence is not described in detail, because it is done a similar way.

During the recognition subsequently the trained HMM determines the states with the highest level of probability at each time increment as well as the overall probability of the state sequence up to that point with the aid of the Viterbi algorithm.

2.3. Suitable sensor Signals

As mentioned before the wheel loader y-cycle suitable sensor signals for the recognition were the force applied by the lifting cylinder and the driving speed. These were not random chosen but in fact determined before

applying the trained HMM. It was the next task to find the variables, which yielded the most accurate prediction of hidden states. This was achieved with the aid of a discriminant analysis according to Fisher, which was used to investigate the spread of two variables. A variable was deemed to be suitable if the spread of the measured values between two different states was significantly greater than the spread yielded by the sensor within a state. The discriminant analysis is based on the assessment of variances of the information of the class affiliation. The sensor signals n are merged to the defined states S and the spread s_w within one state is calculated with equation (2).

$$s_w = \frac{1}{n-S}\sum_{i=1}^{S}\sum_{j=1}^{n_i}\left(x_{ij} - \bar{x}_i\right) * \left(x_{ij} - \bar{x}_i\right)^T \qquad (2)$$

x_{ij} … $data\ point\ j\ of\ class\ i$

$\bar{x}_i$ … $median\ of\ data\ points\ of\ class\ i$

The spread s_b between the classes is calculated with the equation shown in (3).

$$s_b = \frac{1}{S}\sum_{i=1}^{S}(\bar{x}_i - \bar{x}) * (\bar{x}_i - \bar{x})^T \qquad (3)$$

If the spread between the states is higher than within the states the quotient D, called fisher-criteria, is getting higher than 1 and the signal is suitable.

$$D = \frac{s_b}{s_w} \qquad (4)$$

For the existing measurement data of the y-cycle the force applied by the lifting cylinder and the driving speed gave the best results (Figure 5) and will be used for the recognition.

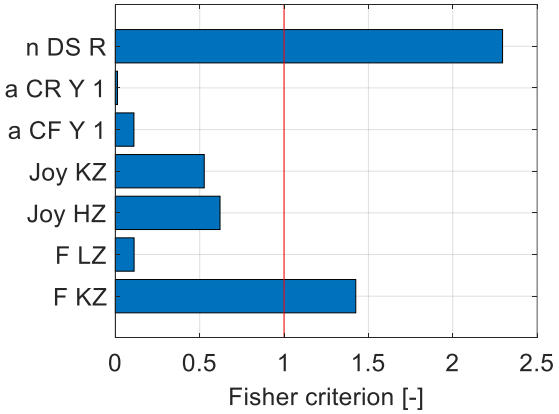

Figure 5. Result discriminant analysis

2.4. Validation

The algorithm required for pattern recognition and the processing of training data in preparation for the training of the HMM was realised in the MATLAB environment. The validation was executed with different data sets of the wheel loaders y-cycle measured in a former project. The installed machine was a Liebherr L 576. The data sets are characterised by different drivers and due to this varying sequence times of the single cycle. This issue enables the investigation of the operator leverage. Because every process in the field is operator-guided this is a very important point.

This contribution bases on the work of Mieth. He showed in [8] that the pattern recognition in the described way is basically possible. He used the former mentioned GUI to assign states to the sensor signals and hereupon teaches the HMMs. After that, he implemented them on a ESX-3M control device from Sensortechnik

Wiedemann. For the validation, he uses a machine model integrated in a HiL test bench in combination with the control device. An interface was integrated into the machine model in order to enable the machine operator to interact with them using control devices in the form of a joystick and pedals. Additionally to this virtual validation, he implemented the control device on an excavator. He investigated his algorithms with two different operators. The cycles were carried out in a random order but in roughly equal numbers. This made it possible to compare the time curves recorded for the sensor signals against the results yielded by the recognition system, thus enabling the determination of the rates of recognition achieved. The recognition rates achieved 80 to 83 % in the case of process pattern excavating and 76 to 85 % in the case of process pattern scraping. The testing of the actual machine yielded a recognition rate of the working cycle excavating of 76%. The recognition rate was slightly lower than at the preliminary examinations. This could be attributed to a large extent to the fact, that during the validation measurements, machine states repeatedly occurred that were only insufficiently covered by training data.

For the validation of the HMMs described in this paper first the influence of the data set and with that the described operator leverage is shown. Therefor the states were assigned to every of the 4 data sets by the manual GUI like Mieth uses it and after that with every data set a HMM was trained. This approach is a kind of supervised learning. The next step was to apply the 4 data sets to the trained HMM and calculate the recognition rate. The referred way to determine suitable signals was applied and the mentioned sensor signals were used for the recognition. The results are shown in Table 1.

Table 1. Results HMM training and application

		Data set (train)				
		1	2	3	4	
Data set (use)	1	96,6	93,3	50	23,3	Recognition rate [%]
	2	56,7	90	33,3	33,3	
	3	50	0	50	36,7	
	4	13,3	73,3	73,3	80	

Different data sets lead to different recognition rates. A replicable relationship between train data and use data was not detectable. Although the states were previously assigned to the data sets, the recognition rate alternates between 100% to 0% and this was not suitable for a detection system.

2.5. Between conclusion and problems

The examination of the method showed, that in former contributions the HMMs lead to adequate recognition rates if states will be assigned in a manual way to the training data. Furthermore, the investigation of the y cycle's data set with the data-preprocessing leads to different recognition rates with a big spread. Both issues are crucial for the extension of the data-preprocessing in a way, that the states have not been assigned manual to the data set, that the determination of suitable sensor signals has to be simplified or better avoided to meet the effect of the train data and in the end the training has to be automated. All these issues will lead to an unsupervised learning of unknown patterns and the later detection of them and thereby to an automatic system for process pattern recognition.

3. QUADRANT METHOD

3.1. Development

The approach, described in the following chapters, was first chosen due to the requirement of the independence of certain sensor signals. The second issue described, the automatically assignment of the states, can also been realised with this method. The basic idea is the regard of every single load and its working point in the speed-force- respectively speed-torque-diagram. Not the absolute values are examined, but only the appearance in the quadrant of the particular diagram of the load in every time step is observed (Figure 6).

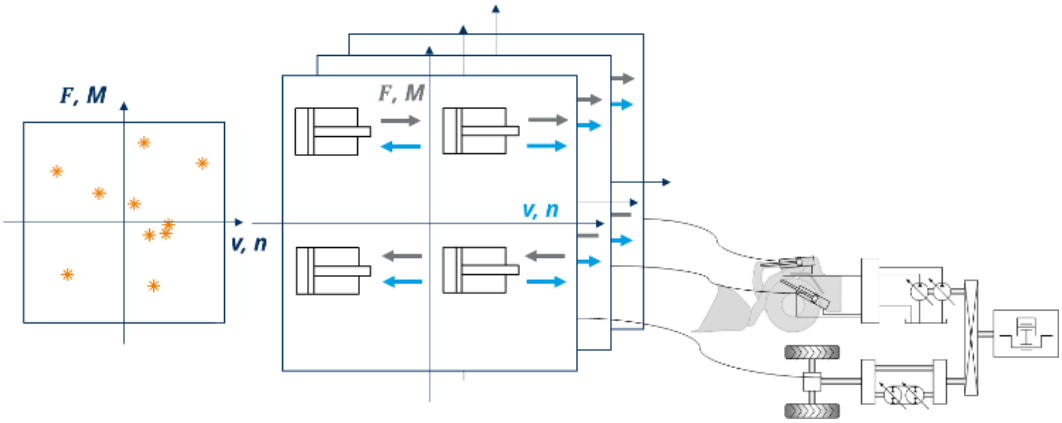

Figure 6. Quadrant method

By regarding the wheel loader, the lifting cylinder for example can be grouped into ascending with pulled load, ascending with pushed load, levelling with pulled load and levelling with pushed load. The approach includes all on mobile machine installed actuators (cylinder and hydraulic motors). At the wheel loader three actuators can be adducted. These are the drivetrain motor, the bucket cylinder and the lifting cylinder. In every time step, the combination of each actuator's quadrant will be determined. This accounts for $5^3 = 125$ possible combinations. Table 2 shows an example of the determination of the combination distribution at the first six time steps.

Table 2. Determination of the combination distribution

		load						combination
		1		2		3		
Time step	1	1	1	1	-1	0	0	1
	2	1	-1	1	1	0	0	2
	3	1	-1	-1	1	-1	1	3
	4	1	1	1	-1	0	0	1
	5	1	1	1	1	0	0	4
	6	1	-1	1	1	0	0	2

These are the four mentioned quadrants and additionally the idleness both of the cylinders and the motor. It was defined, that if one of the regarded actuator's potential (speed) or flow variable (force, torque) is equal zero, the variable, which is unequal zero, will be set zero. This is possible because in both cases the power is calculated to zero (equation 5).

$$P = F,M(flow) * v,n(potential) \qquad (5)$$

This leads to five possible positions for every actuator. With three actuators this leads to 125 possible combinations. By computing the combination in every time step a distribution is achieved, which is the substructure both of the training and of the application of the HMM. The first of the defined goals, the independence of certain sensor signals is attained. The next step is the elimination of the manual assignment of the states to the observed sensor signals. For this purpose, a classification into four classes of the determined combinations is executed. The result is a four-state-distribution which is trained on the HMM. This is a possibility to assign the states to the sensor signals or in this case to the combination distribution without doing this manually. The idea behind this procedure is the occurrence of the same quadrant combinations within the process patterns. Due to that, the calculated state distribution (Figure 7) is repeatable. This described method was implemented as an algorithm in the MATLAB environment. With the resulting data (Figure 7) a HMM was trained.

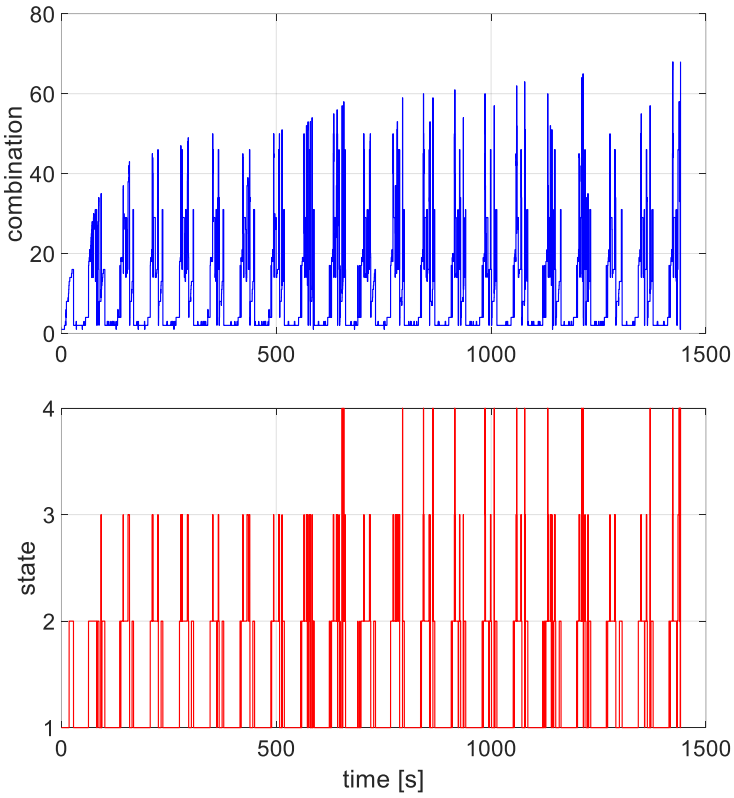

Figure 7. Results quadrant method

3.2. Validation of the quadrant method

To get comparable results the data sets of the wheel loaders y-cycle were taken again and the combination distributions were calculated with the developed algorithm. After that, the HMMs were trained and applied with these data sets. The calculation with the computed recognition rates of the trained HMMs shows Table 3.

Table 3. Results HMM training and application after quadrant method

		Data set (train)				
		1	2	3	4	
Data set (use)	1	100	100	100	100	Recognition rate [%]
	2	100	100	100	100	
	3	100	100	100	100	
	4	100	100	100	100	

By using the preprocessed data every train data set with every use data set achieves 100% of the recognition rate. This is first of all an improvement of the results in 2.4 and a promising substructure for the further development of the recognition system.

3.3. Application of the quadrat method

3.3.1. Efficiency evaluation

The manual assignment of the data-preprocessing and thereby the states definition of the sensor signals is a working method, if a big amount of data of one specific process pattern applied on one specific machine is available for the training of the HMM. The quadrant method is focussing both on a machine comprehensive application of the HMM and on the creation of an interface for an efficiency evaluation. Within the second part of the research project an efficiency model was developed, which is not described in detail in this paper. The point of contact to the described method is that the evaluation of the efficiency can only be answered with the knowledge of the usage profiles. With the detected patterns, an efficiency evaluation can be executed. Only the working point distribution is necessary. The quadrant method provides, besides the mentioned issues, the opportunities that working points are considered in the step before determining the combinations of the actuators. The combining of the usage profile with the efficiency model is simply realisable. This is a further application of the quadrant method and shows the potential of this approach.

3.3.2. Macro HMM and detection system

The development of a detection system and thereby the interface of the efficiency model is described in this chapter. The training of an HMM with automatized generated states and combinations distributions was shown in 3.1. However, the recognition system has to detect different patterns and besides has to learn unknown patterns, what correlates with an unsupervised learning. In [2] Balke mentioned therefor a macro HMM, which is suitable for the detection of different patterns. The structure of such a macro HMM of a wheel loader with the process patterns y-cycle, pushing, idling and driving is shown in Figure 8.

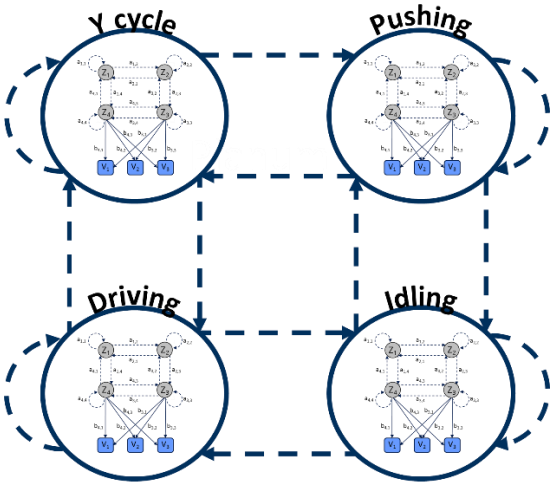

Figure 8. Structure of a macro HMM

In a macro HMM an important issue is how the HMMs are passed during the calculation. Either in a serial way with starting and end conditions for every HMM in the macro HMM or parallel like shown in the following chapter. Because no further data sets of the wheel loader with other process patterns were available other data of different machines were taken to set up a macro HMM. Three different process patterns were finally used. In addition to the mentioned y-cycle, two different data sets of two excavators were applied with the patterns digging and levelling. As an important edge condition the number of states, which were calculated with the quadrant method, has to be the same in every data set, which is applied in the macro HMM. This is the case, because every data set is parallel calculated in every HMM of the macro HMM and after that a comparison of the state distributions calculated by the HMM and the quadrant method is executed. Also as an intermediate step a classification of the combinations before computation had to be conducted, as the size of the observation matrix is determined with the training the applied data set has to have the same size. If these conditions are met, the recognition system (Figure 9) is able to calculate.

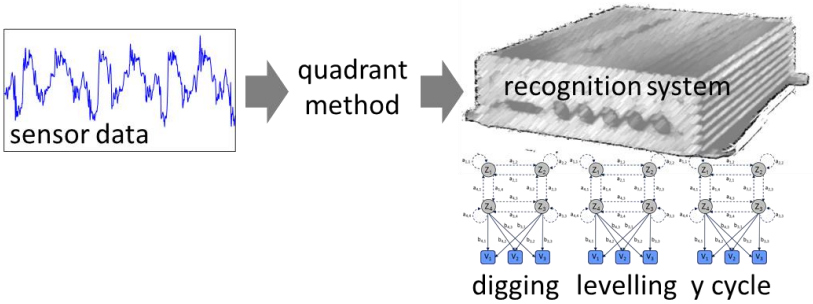

Figure 9. Structure of the recognition system

In the next chapter the criterions, which are used to detect the correct process pattern, are discussed. At first the probability of the most probable path of every HMM in the macro HMM is considered. This probability is calculated with the observation sequence, which presents the classified distribution of the combinations determined with the quadrant method. The HMM which produces the highest probability is the excepted pattern. For the second criterion the distribution of the path with the highest probability is taken. The preprocessing with the quadrant method enables the comparison of the computed path with the path the quadrant method calculated. The comparison includes the calculation of the variance of both distribution in every time step and the mean value computation. The least value represents the probable pattern. For the third criterion both state distributions are used again and the correlation coefficient of both is determined. The highest value is assigned to the most probable pattern. Because the pattern detection was very defective, these three different criterions were introduced. In the calculation the criterions are weighted. The values for this weighting were determined in an iterative process.

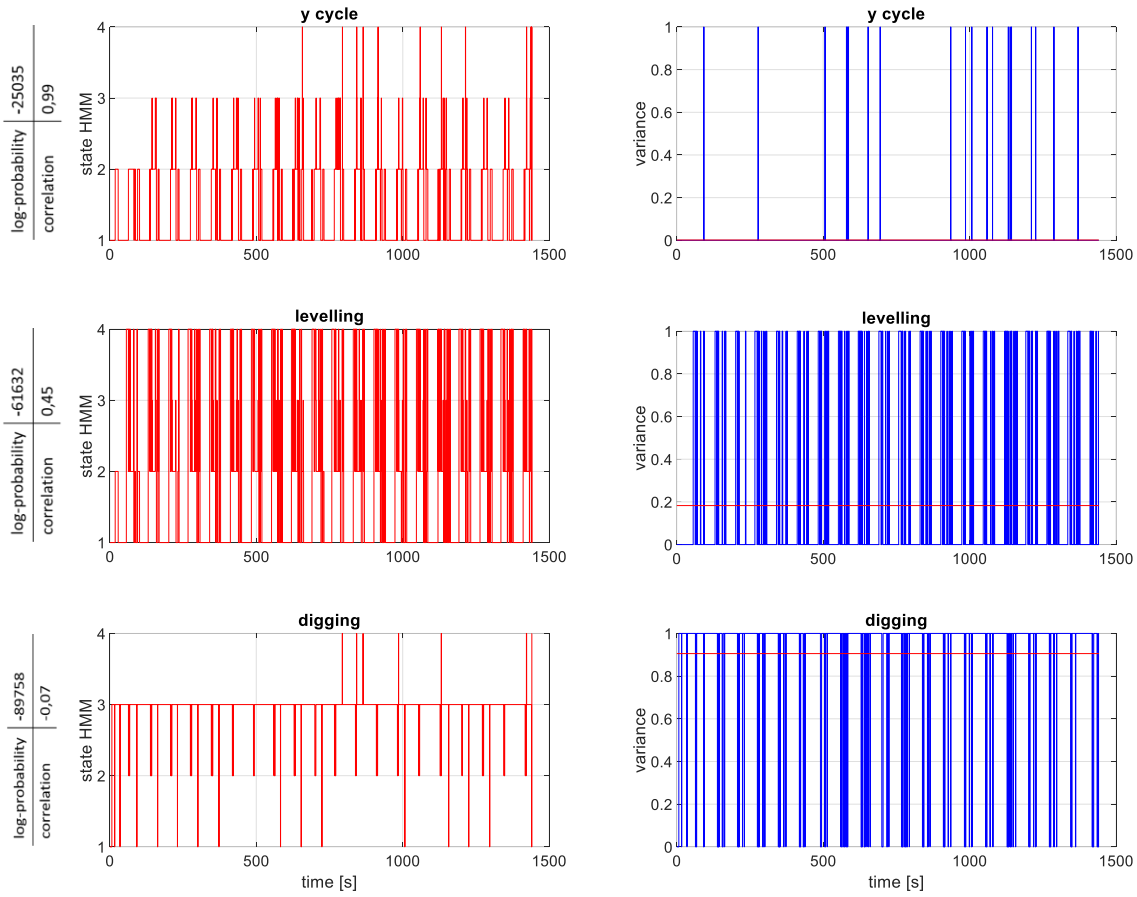

Figure 10. Results of the single HMMs with one of the y-cycles data set

Figure 10 shows the results of the single HMMs of the recognition system applied with one of the y-cycle's data set. The combination distribution (Figure 7) is best calculated by the HMM trained with y-cycle's data. The variance of both the computed and the state distribution determined with the quadrant method is shown on the right side. As you can see the y-cycle's HMM has the least variance and thereupon the least mean value (red line). Also the probability of the most probable path and the correlation coefficient have the highest values in the y-cycle's HMM. In this case, every of the three defined criterions are matched for the right process pattern.

In further investigations with other data sets the results of the detection were consistently positive. Every pattern was detected from the data sets. Each of the 4 y-cycle were detected and also the levelling and the digging. The y-cycle's HMM was trained with only one of the four data sets. The 3 other data sets, the HMM never saw before, were confident detected. The same results were achieved by using data of another unknown third excavator with the pattern digging.

When occurring an unknown pattern the system gives out a warning and the possibility to learn this new pattern. If this new pattern is done again the system will be able to detect it. Thus the recognition system becomes more intelligent with every new pattern.

4. CONCLUSIONS AND OUTLOOK

The paper shows on the one hand the realization of a method for the recognition of known patterns for a specific machine. On the other hand the extension of this method with a suitable data-preprocessing and with that the possibility of the detection and the learning of unknown patterns are given. Additionally the system is applicable to every single machine. Furthermore the shown method will be refined to an online procedure. The first problem, which has to be solved, is the consideration of a small time window or better every time step. The algorithms for cycle counting have also to be improved for an online application. Main problems are the determination of the start and end times of the patterns. At the moment the system can only detect different

patterns. A first attempt to identify these times by examining the decrease of the calculated probability in the HMM leads to promising results. The further development of these aspects will be the next step.

Generally the process pattern recognition concept presented is exercisable across a wide range of applications. It facilitates the targeted optimisation of both development tasks and reverse engineering. The application of the concept in other engineering disciplines is also conceivable, like shown as a means of assessing the efficiency of a drive system using knowledge of process pattern-specific energy-related circumstances within the machine gained over a long observation period.

The representative usage profiles for mobile construction machines yielded by the concept unquestionably offer huge added value for both machine manufacturers and their suppliers. The intelligent adaptation of control and drive parameters during machine operation represents another potential area of application due to the real-time capability of recognition systems of this type. The fact that the concept is based on the use of standard sensors and control devices simplifies the transfer thereof to a variety of conventional construction machines.

5. ACKNOWLEDGEMENT

The project Ref. No. AiF 19613 BR/1 was financed and supervised by the Research Association Mechanical Engineering (FKM). In the scope of the Programme to promote Industrial Collective Research it was funded by the German Federation of Industrial Research Associations (AiF) with means of the Federal Ministry of Economic Affairs and Energy (BMWi) on the basis of a decision by the German Bundestag.

[1] Abdulla, W.; Kasabov, N.: The Concepts of Hidden Markov Model in Speech Recognition. Technical Report, University of Otago, 1999

[2] Balke, W.: Hidden Markov Model, Video Retrieval (09.06.11), episode 10, multimedia databases. Technische Universität Braunschweig et al. 2011. https://doi.org/10.5446/340

[3] Gruen, A. W.: Adaptive Least Squares Correlation: a Powerful Image Matching Technique. South African Journal of Photogrammetry, Remote Sensing and Cartography, 14(3): 175-187

[4] Hoffmann, R.: Signalanalyse und -erkennung: Eine Einführung für Informationstechniker. Springer-Verlag, Berlin-Heidelberg, 1998

[5] Juang B. H.; Rabiner L. R.: Hidden Markov Models for Speech Recognition. Technometrics, vol. 33, 1991

[6] Kunze, G.; Mieth, S.: Lastkollektivmethode FVB. Final report on IGF research project no. 15852 BR: Dresden, 2012

[7] Rabiner, L. R.: A tutorial on hidden Markov models and selected applications in speech recognition, Proceedings of IEEE, vol. 77, no. 2, pp. 257–286, 1989

[8] Weber, J.; Mieth, S.: Process Assist: Methode zur Online Prozessmustererkennung für die Ermittlung von Kundenkollektiven an mobilen Baumaschinen. Final report on IGF research project no. 18014 BR: Dresden, 2016

CARBON FOOTPRINT DETERMINATION OF AN ELECTRO-HYDRAULIC COMPACT AXLE (EHA) BASED ON DIN EN ISO 14067

Maximilian Waerder M.Sc. M.Sc., Stephan Merkelbach M.Sc., Univ.-Prof. Dr.-Ing. Katharina Schmitz
Institute for Fluid Power Drives and Systems (ifas), RWTH Aachen University
Campus Boulevard 30, 52074 Aachen, Germany
E-mail: maximilian.waerder@ifas.rwth-aachen.de

ABSTRACT

This paper introduces the methodology of calculating the product carbon-footprint (PCF) of industrial linear actuators by the example of an electro-hydraulic compact axle (EHA). The EHA system design and the manufacturing process is highly complex since it contains many components of different domains (i.e., mechanical, hydraulic and electronic parts). Therefore, the system must be be virtually disassembled into its components to the extent that an individual determination of the PCFs is possible. For a straight understanding of the method, the paper is subdivided into three major topics: description of PCF determination method, exemplary calculation of an EHA PCF and, finally, its critical review. The PCF calculation is based on DIN EN ISO 14067 and, thus, classifies the ecological impact of the individual life cycle steps (i.e., material production, product development, commissioning, use and maintenance as well as the end-of-life) referring to the global warming potential (GWP). As a conclusion, this paper reveals the opportunities of analysing the ecological impact of industrial components (especially fluid power industry) and the current existing difficulties of implementation and objective interpretation of different results.

KEYWORDS: Fluid Power, Hydraulics, Life Cycle Assessment, Carbon-Footprint, Sustainability, Global Warming Potential

1. INTRODUCTION

The ongoing discussion about greenhouse gas concentration in the atmosphere constitutes a problem that humanity has been facing since over a century. Due to increasing energy consumption and the lack of appropriate steps towards different technologies and global regulations, the carbon dioxide (CO_2) concentration in the atmosphere reaches all-time highs annually [1]. In order to quantify the amount of carbon dioxide production to distinguish sustainable from strongly polluting systems the carbon footprint (CFP) has been established [2]. The first approaches though, mainly treated the CFP of entire countries or nations respectively (especially in terms of energy consumption by transportation, infrastructure and heating efforts) [3]. However, in the production sector, CFP analysis plays still a minor role, although the ecological impact is comparatively high but the regulatory boundaries are either non-existing or not straightforward.

Since the individual processes and impacts of former analysis objects (e.g., nations or houses) differ significantly from the production of industrial product, the general CFP approach has been adapted into the so-called product carbon footprint (PCF). The PCF shifts the focus toward a product-oriented analysis containing the ecological impact of the entire life cycle (including raw material production, acquisition of supply parts, manufacturing, assembling, testing, distribution and the end-of-life). While there are several national

approaches (cf. the british standard PAS 2050 or the GHG Protocol Product Life Cycle Accounting and Reporting Standard), this paper focuses on the new international standard DIN EN ISO 14067 [4]. All standards are in accordance with the DIN EN ISO 14040 [5] and 14044 [6], which define the fundamental methodology of life cycle assessment. Although many approaches regarding a user-friendly application of the CFP calculation exist, the difficulty still lays in three major aspects – the aggregation of necessary data, the correct accounting of the use-case and the adaption to the respective users. In industrial manufacturing and distribution, these aspects are even more significant. Fluid power components, for example, become technologized to a greater trend due to the ongoing digitalisation. Furthermore, the cost efficient and reliable manufacturing is one of the key values of today's economic success leading to a variety of complex product designs, machinery as well as processes. Therefore, the PCF is divided into functional units along the entire life cycle of the product.

It should also be mentioned at this point that this contribution is not designed referring to the standards ISO 14026, ISO 14044 and the technical specification ISO/TS 14071, which define appropriate methods of critical prove and communication of CFP results. The contribution rather focuses on the CFP evaluation and interpretation of very specific industrial components (especially fluid power) and the difficulties encountered during data aggregation, analysis and scenario observation.

2. STATE OF THE ART AND METHODOLOGY OF DIN EN ISO 14067

According to a general definition of the CFP given by [7], the CFP describes the sum of all gaseous emissions that are "… relevant to climate change and associated with human production or consumption activities". This includes direct as well as indirect emissions. All emissions of those greenhouse gases (GHG) that occur during production steps or the usage of the product, e.g., by burning fossil fuels in combustion engines, are therein considered direct emissions whereas the term indirect emissions covers GHG that are emitted during auxiliary processes like the generation of electric energy for the actuation of electric motors, for example.

An overview of different approaches for the calculation of the CFP focusing on highly differing topics is given by [3]. It is obvious that the goal and scope of the study alters with the subject that is examined. For example, studies regarding a specific product have a different scope and target audience than studies that focus on events like the Olympics. Many CFP-studies concentrate on the examination and optimization of the supply chains instead of describing the CFP of one specific product. Examples for this approach were shown by [8] or [9]. Aim of these studies is to show the highest potential for the reduction of GHG-emissions in the supply chains and production processes and not to generate exact values for the overall emissions connected to the product. There are only few studies known in literature that focus on the CFP of industrial goods in general or fluid power drives in particular. The authors in [10] describe a comparative analysis of pneumatic and electromechanical linear drives with regard to the Chinese market. It is shown that the results depend on many boundary conditions that need to be defined in the first step of the analysis and should be published together with the results to ensure their confirmability as well.

Following on from this, efforts have been made recently to standardize the course of CFP-analyses yielding the current DIN EN ISO 14067. The CFP itself is the result of a life cycle analysis (LCA) with respect to the single working category of the climate change. Therefore, the DIN EN ISO 14067 refers to the more general description of DIN EN ISO 14040 and 14044 that define the procedures during an LCA. The LCA is therein split into four parts, which are shown in figure 1.

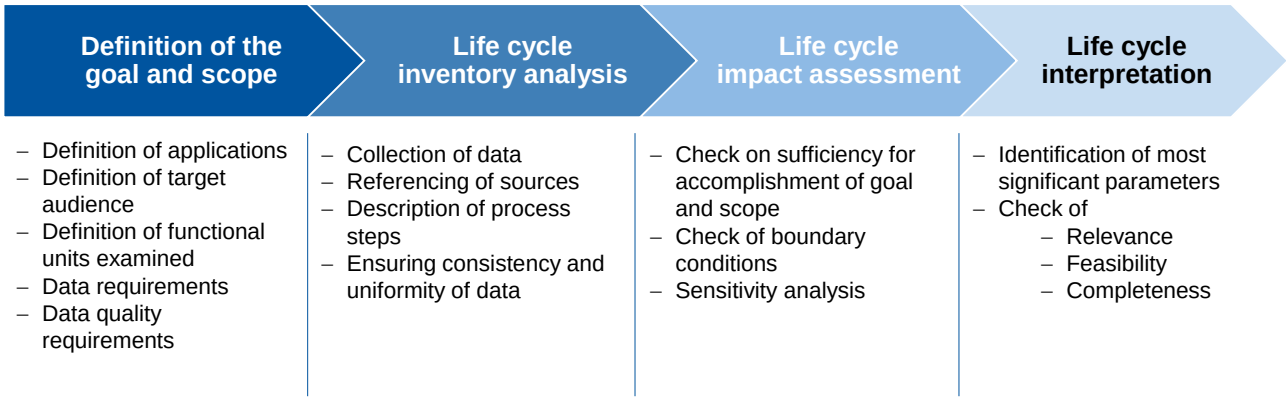

Figure 1. Step of LCA according to ISO 14044

Depending on the target audience and the requirements of the results, the level of detail to which the analysis is performed varies. Besides the quality of the collected data, this may also include the number of parts and processes that are actually examined, e.g., not every screw or production step must be included if these parts are considered negligible. If two or more different products shall be compared, the level of detail of the data must match of course.

In the second step, the necessary data has to be collected, which is by far one the most challenging part of the analysis. There are ongoing approaches of collecting climate relevant data in form of CO_2-equivalents for any gaseous emission in databases to enable the CFP analysis (cf. thinkstep GaBi, ecoinvent, JRC, ProBas, etc.). However, two problems prevent most of the users from the use of the data. On the one hand, a majority of the data is only available for a fee, which depends on the content and amount of data needed. On the other hand, many products and processes are so specific that general data sets are not applicable. For example, the different efficiency of machines and their usage to manufacture components cannot be averaged to one single, valid CO_2-equivalent. Thus, there is the need of performing and collecting further individual analyses to enhance the data basis. In order to define necessary data, in PCF analysis the product is analysed as one or more functional units along the entire life cycle. Since this modelling differs significantly from one product to another, the example for an EHA is given in chapter 4.1.

The last parts of the analysis are the impact assessment and interpretation of the results. As the goal is usually not only the quantification of one single PCF but also the comparison of different design or manufacturing approaches, the result analysis deals with the identification of high impact steps and categories. Thus, the parameters of the most significant potential for ecological improvements are derived. Furthermore, the results show the aspects that can be neglected in further observations, which is important to reduce the need of specific data, for example. Finally, there are three important basic characteristics of the LCA. Firstly, it is an iterative approach, which means that the entire analysis utilizes the subsequent results of the different steps in order to improve the overall analysis quality. Due to the complex structure of current products, the analysis is based on transparency secondly. Thus, the result interpretation and comparison of different LCA are accomplished in the right manner. The last property is the holistic approach that enables the identification of trade-offs by a cross-media point of view.

3. SYSTEM DESCRIPTION

EHA, which are a hydraulic system concept of a pump-controlled actuator in a closed circuit, are on a rising edge since the compact and enclosed design simplifies the implementation of the actuator into a current, mainly electronically controlled system. While former systems used variable displacement pumps and constant motors as the power supply, todays approaches tend to shift the adjustability towards the motor by variable speed drives. Thus, the hydraulic system is even more robust. In order to understand the introduced approach of a PCF analysis, it is now performed using the example of such an EHA.

An exemplary system is shown in figure 2 containing a variable speed drive, a constant pump/motor unit and the actuator, which converts the rotational into a translational movement. Besides, there is an accumulator and several valves. The accumulator and check valves enable the compensation of the different volume flow requirements since the actuator has different areas (A1 and A2). Furthermore, the low-pressure side is pre-charged by the accumulator, which avoids cavitation effects. There are plenty of different EHA designs, which differ primarily in the power supply, control techniques and valve structure. For the time being, the design itself is inferior since only all parts, their composition and origins have to be known for PCF analysis. Only the ecological impact of the operating is closely related to the system design, which will be discussed in chapter 4.5 more detailed.

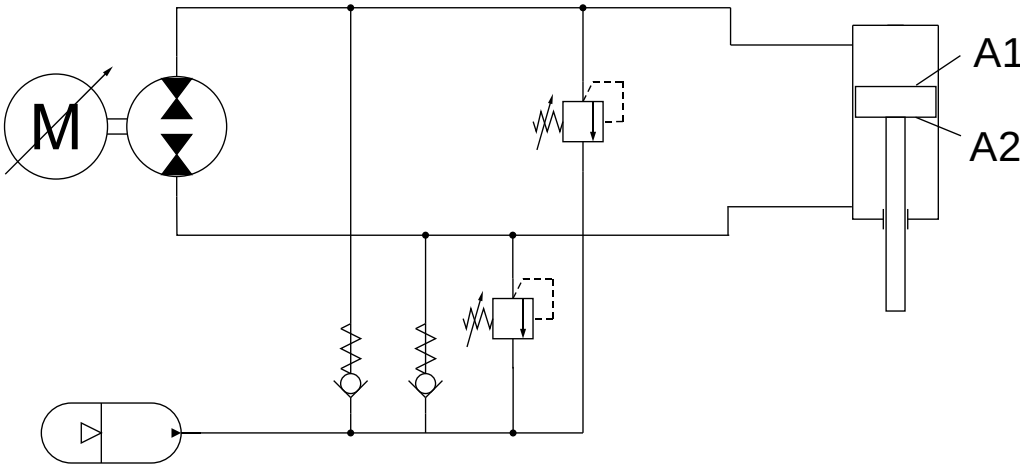

Figure 2. Circuit diagram of a general EHA

To illustrate the power class of the system, table 1 summarizes the most important parameters. These parameters are not relevant for the analysis of the PCF, but they help to classify the results, which differs among different power classes. Furthermore, in this study only one precise system of a specific manufacturer is analysed and, thus, the results cannot be generalized.

Table 1. System Parameters

Property	Value	Unit
Dimensions (LxWxD)	1400x500x300	mm
System pressure	250	bar
Max. stroke	50	mm
Max. force	500	kN
Max. velocity (at 50% f_{max})	100	mm/s

4. PCF ANALYSIS OF THE EHA

The following PCF is based on an exemplary EHA, which is produced in Ulm, distributed and used in Aachen, Germany. The results only consider the global warming potential of 100 years exposure (GWP100) given in CO_2-equivalent, which can be identified as the goal of the study. Since the available data basis is not sufficient, the manufacturing and operating must be neglected in the total PCF. Yet, a methodology for the estimation of

unknown data of these steps is introduced (cf. chapter 4.3 and 4.5). The scenario of the PCF study has major impact on the results, which is why it has to be considered in the analysis and their interpretation. Change of the scenario and other parameters will be discussed in chapter 5.

4.1. Model of System Structure embedded in LCA

After the definition of the goal and boundary conditions, the PCF analysis continues with the separation of the product in functional units and their assignment towards a state of the product life cycle, i.e., raw material extraction, production, distribution, operating and recycling (cf. figure 3). The arrows correspond to a material or product flux, which is necessary for the subsequent object. The materials consist of metal components (i.e. copper, aluminium, steel and cast iron) on the one hand and plastics (i.e., polyether ether ketone (PEEK) and ethylene propylene diene methylene (EPDM)) on the other hand. Furthermore, there are minor material components (e.g., rare earths) which are not considered in figure 3 but in the overall analysis for reasons of clarity and comprehensibility.

Eventually, it makes sense to cluster product groups (e.g., valves or seals) since the incoming fluxes are quite equal and, usually, they are either purchased by one supplier or manufactured at one division. Figure 3 also shows that during production, there are residuals of the different, manufactured parts. They are either recycled or discarded, which must be considered in the PCF. A similar situation occurs during operating, when spare parts have to be changed and damaged components have to be disposed. In the described scenario, a direct distribution is considered. However, usually there are one or more intermediaries, which also consume resources, ergo, emit CO_2.

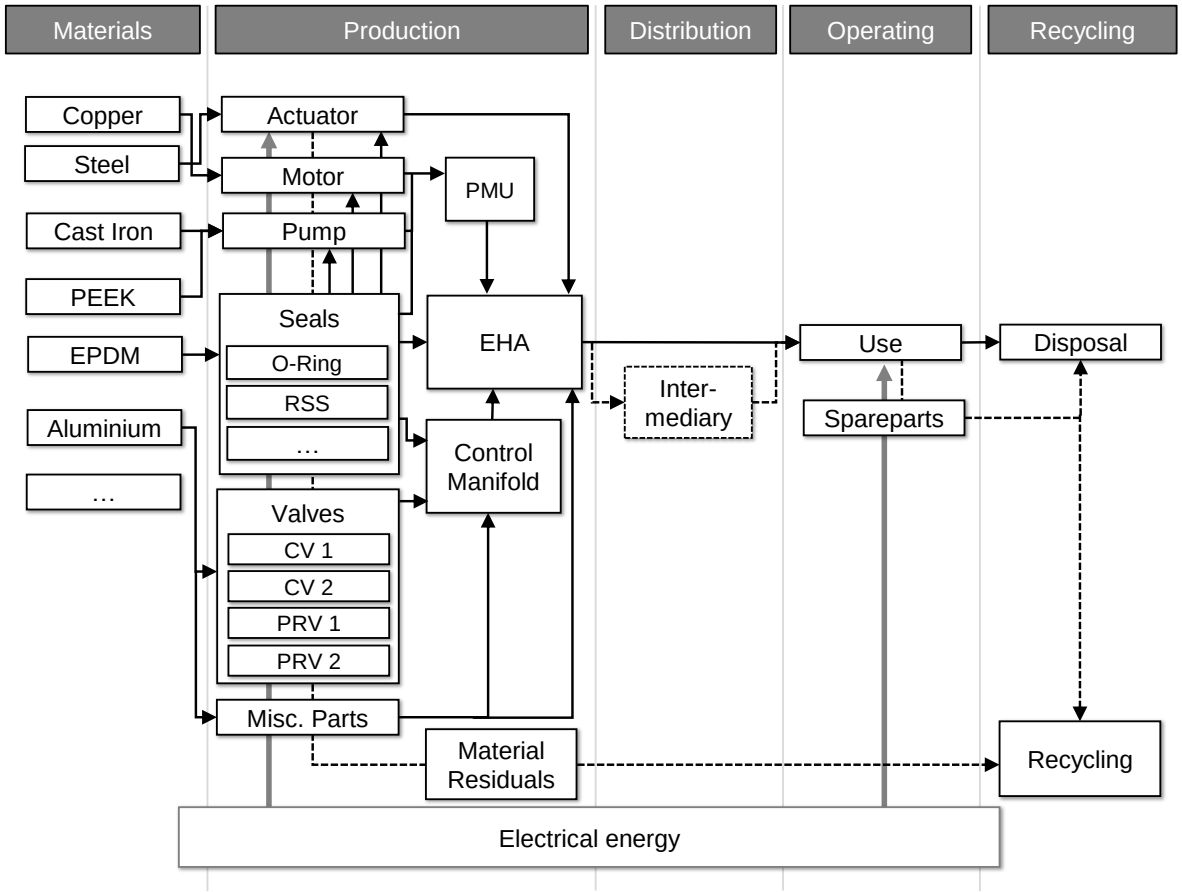

Figure 3. Model of functional units along the life cycle

4.2. Step 1 – Raw Material Extraction

In chapter 4.1, the major part of materials has been stated yet, but now they are quantified in order to calculate the CO_2-equivalent. The mass distribution is extracted from the assembly's part list, which is an important information source for PCF calculation. The data used for the calculation of CO_2-equivalents in this chapter originates from the Probas database [11]. Figure 4 shows the absolute material distribution of the EHA. It is obvious that the highest mass fraction (approx. 80%) is given by steel and cast iron components, which not only correlates with the used volume but also with the densities of the materials.

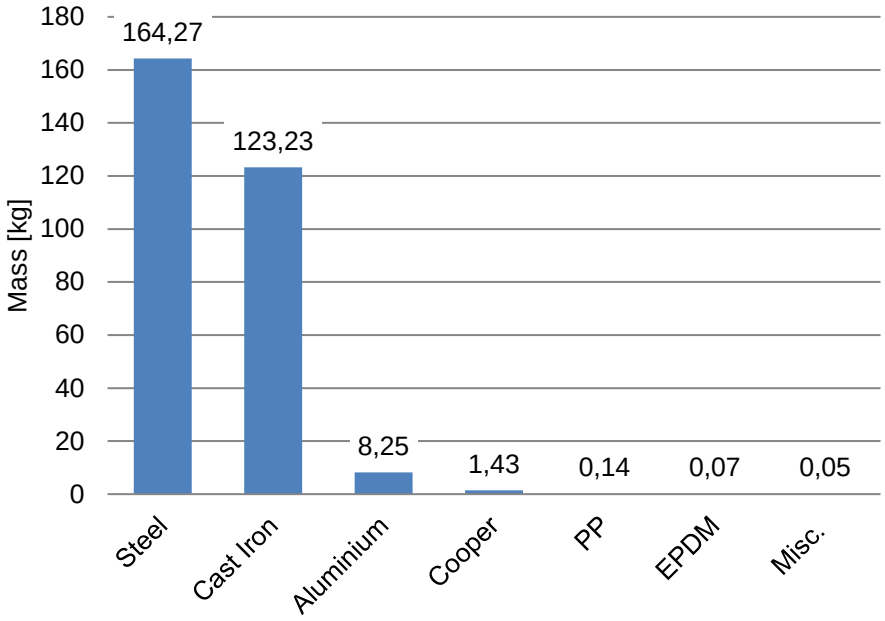

Figure 4. Material distribution of the EHA

The corresponding CO_2-equivalents can be calculated, which is summarized in figure 5. The CO_2 consumption adds up to 652,4 kg in total. Comparing figure 4 and figure 5, it is an important conclusion that the ecological impact is not directly correlated to the mass distribution, but also considers the different raw material extraction procedures (cf. steel and cast iron). This also yields the potential of exchanging materials to achieve a better ecological footprint. Furthermore, the Probas data only give an average CO_2-equivalent, which may differ depending on the actual suppliers. Thus, a proper choice of the supplier can also affect the ecological footprint of the product.

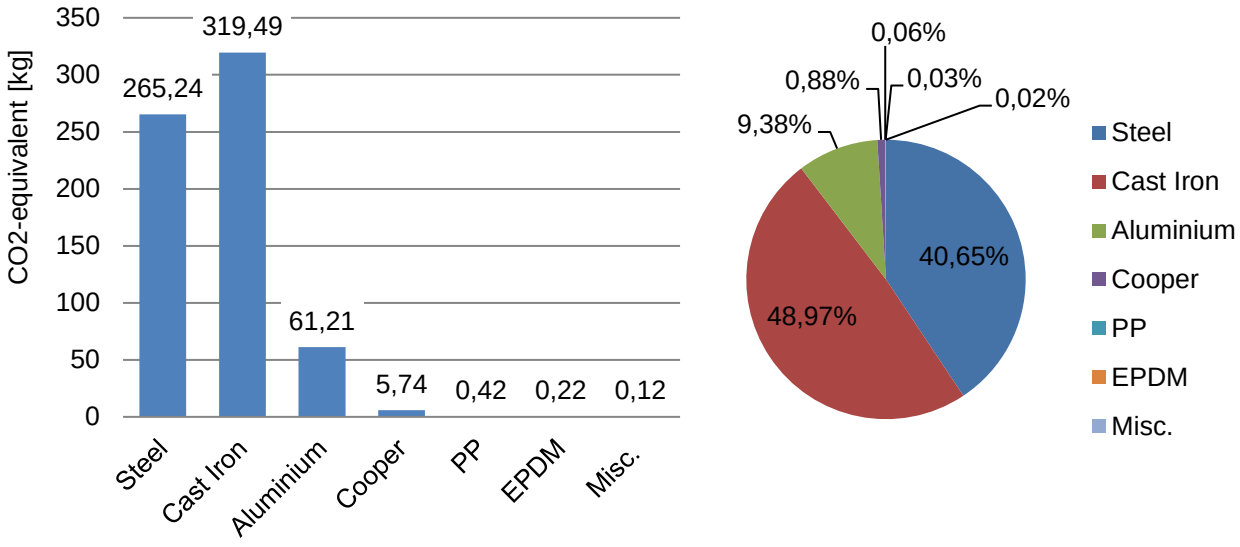

Figure 5. Absolute (left) and relative (right) CO_2-equivalent of material distribution

4.3. Step 2 – Production

As mentioned in the introduction of chapter 4, there is no valid data for the different manufacturing process of industrial components. This is mainly caused by the variety of processes, machines and even possibilities to create specific parts. Thus, the only accurate way of considering the manufacturing for PCF calculation is the measurement of energy and material consumption of the machinery. A way of estimating this part of PCF, a simple approach is to suggest a single product line. If the energy consumption of all machines are known, that can be related to the manufacturing of a single product, the yearly consumption could be divided by the total number of produced elements to achieve the product specific energy coast. Since the authors were not able to perform this kind of measurement, it will be neglected in the total PCF.

4.4. Step 3 – Distribution

The defined scenario assumes a direct distribution from Ulm to Aachen (Germany), after the assembly of the final product. Now, there are two important aspects of the distributive ecological impact. Firstly, how many components (or mass respectively) has to be transported for which distance and, secondly, which vehicle or system is used. Table 2 shows a summary of average CO_2-equivalent of the four standard kind of direct transportation (i.e., rail, truck, ship and airplane) in grams per tons and km of the product. The distance between the locations can be estimated to 520 km by truck and 500 km by train, approximately. The total mass of the system including packaging yields 374 kg. Thus, the transportation of a single EHA to Aachen requires 4,38 kg by rail and 18,96 kg by truck. It becomes very clear, that a national distribution in Germany leads to CO_2 consumptions that are negligible in comparison to the production and operation of it. Yet, the distribution over several thousands of kilometres by plane has a much greater impact.

Table 2. Average GWP of different transportation [12]

Transportation	CO_2-equivalent in g/tkm
Rail	23,4
Truck	97,5
Ship	33,4
Airplane	1539,6

4.5. Step 4 – Operation

The operation of the EHA starts after the arrival at the customer or the location of usage respectively. Since the unit is powered by an electrical variable-speed motor, the operating impact is induced by the electrical power consumption of the unit and the kind of power supply of the factory. As mentioned already, the balancing of operating power consumption and ecological impact respectively is not trivial. There are three approaches, which should be preferred by the order.

1. Continuous measurement of energy consumption is the most accurate way, yet, it is usually quite expensive since it is not available for standard applications.
2. White-box modelling and parameterisation of the system. With the help of a valid system model, not only the actual load cycle but also different setups can be estimated. Thus, an optimisation analysis can also be performed. A simple model approach is given in [13], for example. However, in this study the necessary parameters are not known.
3. In [14] a simplified approach is suggested in order to calculate the actual power consumption by using efficiency maps of the drive by the help of the known load cycle. The estimation is not as good as of method 2, but the required amount of information and the effort of implementation is less.

Since the information for method 3 are not available either, the impact of operating in the total PCF is questionable. However, in order to assess the ecological impacts of the operating phase, which is usually the longest, a rough estimation is given.

The maximum power consumption of the EHA is roughly 25 kW. It is assumed, the average power consumption for a typical load cycle equals 50%. Furthermore, the axis is in operation for 6 days per week (1 day off for maintenance) and 3 years at 50% duty cycle. Referring to equation (1), the total time on duty yields 11738 h. Under the assumption of the mentioned, constant power consumption, the total energy consumption yields 146725 kWh. The Probas data states a current energy CO_2-equivalent for an actual energy mix of 166128 kg/TJ, which adds app to 87750 kg CO_2-equivalent.

$$t_{duty} = 0{,}5 \cdot 24h \cdot (365 - 1 \cdot 52) \cdot 3 = 11738\,h \qquad \text{Eq. (1)}$$

In other words, the CO_2 consumption of production is exceeded after 87,2 hours of operation. It is obvious, that the relationship between the life cycle steps of high power drives is unambiguous.

4.6. Step 5 – End of life

As illustrated in figure 3, there are intermediate goods coming from production or the exchange of spare parts as well as the entire product that has to be dealt with at the end-of-life. Furthermore, it must be differentiated between the disposal of the product and recycling of it or the system components respectively. In case of an already accounted recycling for the raw materials, it must be neglected in end-of-life. In this study, it is assumed that the raw materials are partially taken from recycled material, which is why the CO_2 of this segment equals zero. If there are any recycling processes the amount of CO_2 equivalent has to be accounted negatively.

4.7. Total PCF and remarks

As a conclusion, the sum of all life-cycle segments leads to the total sum of CO_2 consumption of the entire EHA life, which is summarized in table 3. The total sum of CO_2-equivalent consumption yields 87750 kg, which is mainly induced by the operating energy consumption (approx. 99,3 %).

There are a few remarks that have to be mentioned in order to ensure a correct understanding of the results. The uncertainty of the data is quite high and inhomogeneous with respect to the alternative raw material procurement, manufacturers, distributions and especially ways of operating. As it can be clearly seen, the operating energy consumption defines the ecological effects almost by itself. However, depending on the specific application, it cannot be generalised insofar as to neglect the other life-cycle segments. For example, there are application where the duty cycle of the actuator as well as its power class is considerably lower, which change the relations coherently.

Table 3. Summary of CO_2-equivalent consumption of the EHA

Life-cycle-segment	CO_2-Consumption in kg	Rel. amount in %
Raw Material Extraction	652,4	0,74
Production	-	-
Distribution	18,96	0,02
Operating	87750	99,24
End-of-life	0	0
Total Sum	**88402**	

5. SUMMARY AND OUTLOOK

This paper describes the actual methodology of describing a product carbon footprint (PCF) based on the standard DIN EN ISO 14067 applied to the field of linear actuators, more precisely electro-hydraulic compact axles (EHA). While the actual process of PCF calculation is rather trivial, the difficulty lies in the collection of valid data and its correct accounting with respect to the functional system along its life cycle. Therefore, the first step of every PCF analysis is the definition of the entire life cycle as well as the material/product flow along, which is carried out for an exemplary 25 kW EHA in this contribution. The scenario is described as the life cycle of one exemplary EHA, which is produced from local resources and distributed to another city in Germany. The time of usage is roughly estimated to 3 years at an average power consumption. Finally, the total PCF yields 88402 kg CO_2-equivalent.

In order to build a transparent basis for discussion, the most important part is pointing out all assumptions made, the origin of applied data and the methods of calculating intermediate values. Especially the comparison of different product variants or products of different manufacturers must be based on the same reference point. The example of the observed EHA shows, that a comparison of different power classes of linear actuators, which also have diverse duty cycles, is not reasonable. A more rational approach is given by the sensitivity analysis of reliable data, e.g., the change of material composition, manufacturing processes and machines or different duty cycle for the same object of observation.

For an increase of ecological awareness of the industry sector, there is the need of further effort regarding the collection of valid and open source data, simplification of the calculation for specific products and maybe regulatory boundaries forcing large industries to deal with it as well.

REFERENCES

[1] *Carbon Dioxide Information Analysis Center Atmospheric Carbon Dioxide Concentration.* [Online] Available: http://cdiac.ess-dive.lbl.gov/trends/co2/modern_co2.html. Accessed on: Jan. 30 2019.

[2] H. Hottenroth, *Carbon Footprints für Produkte: Handbuch für die betriebliche Praxis kleiner und mittlerer Unternehmen*, 2014.

[3] D. Pandey, M. Agrawal, and J. S. D. Pandey, “Carbon footprint: current methods of estimation,” (eng), *ENVIRON. MONIT. ASSESS*, vol. 178, no. 1-4, pp. 135–160, 2011.

[4] *Treibhausgase – Carbon Footprint von Produkten – Anforderungen an und Leitlinien für Quantifizierung (ISO 14067:2018);*, 14067, 2019.

[5] *Umweltmanagement – Ökobilanz – Grundsätze und Rahmenbedingungen (ISO 14040:2006)*, 14040, 2009.

[6] *Umweltmanagement - Ökobilanz - Anforderungen und Anleitungen (ISO 14044:2006)*, 14044, 2006.

[7] T. Wiedmann and J. Minx, “A definition of ‘carbon footprint’,” *Ecological economics research trends*, vol. 1, pp. 1–11.

[8] Benjaafar, S. Benjaafar, Y. Li, and M. S. Daskin, “Carbon Footprint and the Management of Supply Chains: Insights From Simple Models,” (fre), *IEEE Transactions on Automation Science and Engineering*, vol. 10, no. 1, pp. 99–116, 2013.

[9] Sundarakani *et al.,* “Modeling carbon footprints across the supply chain,” (spa), *International journal of production economics*, vol. 128, no. 1, pp. 43–50, 2010.

[10] Zhang, Y. Zhang, and M. Y. Cai, “Overall life cycle comprehensive assessment of pneumatic and electric actuator,” (eng), *Chinese Journal of Mechanical Engineering*, vol. 27, no. 3, pp. 584–594, 2014.

[11] Umwelt Bundesamt, *ProBas ProBas - Prozessorientierte Basisdaten für Umweltmanagementsysteme.* [Online] Available: http://www.probas.umweltbundesamt.de/php/index.php. Accessed on: Mar. 19 2019.

[12] Umwelt Bundesamt, *Daten zum Verkehr.* [Online] Available: https://www.umweltbundesamt.de/sites/default/files/medien/publikation/long/4364.pdf. Accessed on: Jan. 30 2019.

[13] R. L. Tovo, F. J. Vargas, and L. C. S. Goes, “Creation of Virtual Environment with AMESim and its Integration with MATLAB/Simulink,” in 2016.

[14] D. Vanhooydonck *et al.,* “Calculating energy consumption of motor systems with varying load using iso efficiency contours,” in *ICEM 2010 The XIX International Conference on Electrical Machines: Proceedings*, 2010.

ENERGY EFFICIENCY ANALYSIS OF A NOVEL HYDRO-ELECTRIC HYBRID DRIVING SYSTEM FOR HYDRAULIC EXCAVATOR BOOM

Hao Yunxiao, Quan Long*, Ge Lei, Xia Lianpeng, Li Zepeng, Zhao Bin
Key Lab of Advanced Transducers and Intelligent Control System of Ministry of Education and Shanxi Province, Taiyuan University of Technology
No.79 West Street Yingze, Taiyuan, Shanxi, P.R.China 030024
haoyunxiaosuper@163.com

ABSTRACT

Energy recovery and reutilization is an important way to improve the energy efficiency of hydraulic excavators. In this paper, a novel hydro-electric hybrid driving system adopting hydraulic cylinder and electromechanical cylinder is proposed. The non-rod chamber of the hydraulic cylinder is connected to a hydraulic accumulator, which can realize the direct conversion of the potential energy and hydraulic energy. Due to the less energy conversion links, the recovery and reutilization rates of the potential energy are significantly improved. Adopting the electromechanical cylinder as the active actuator, the electric energy can be directly converted into working device's potential energy. The energy transfer chain of the proposed system is shorter than other transmission systems, and the proposed system will have very high energy efficiency. The working principle is first introduced, a test rig and a co-simulation model are built to validate the feasibility and the energy-saving effect of the proposed system. The test results show that the proposed system has good operating characteristics; compared with a separate meter-in and meter-out system, the peak power of the boom system is reduced by 77.5% and the energy consumption by 71.7%.

KEYWORDS: Hydraulic excavator, Hydro-electric hybrid driving, Energy recovery and reutilization, Energy saving, Electromechanical cylinder

1. INTRODUCTION

As one of the most widely used construction machinery, hydraulic excavator has the disadvantages of high energy consumption and poor emission. Thus, studying the energy saving for hydraulic excavator has important practical significance. During the boom lowering process, due to the throttling loss of the control valves, a large amount of the potential energy is converted into heat energy and dissipated. According to relevant research, the wasted potential energy is about 15% of the hydraulic pump output energy in one standard excavation cycle [1]. Therefore, recovering and reutilizing the potential energy is important for the energy saving of the hydraulic excavator.

Many scholars have done intensive researches on the methods of recovering the potential energy. According to the references, the main ways to recover the potential energy mainly consist of electric recovery technology and hydraulic recovery technology. The electric recovery technology is mainly applied to electric hybrid hydraulic excavator [2-3]. In the electric recovery system, the hydraulic cylinder provides high pressure oil to drive a hydraulic motor, and then the hydraulic motor drives an electric generator. In this way, the potential energy is converted into electric energy and stored in the electric energy storage unit. The Komastu Company,

the Hitachi Company, the Caterpillar Company and the Sany Company have developed and launched electric hybrid hydraulic excavators with electric recovery technology. Ahn et al. propose an electric recovery system with bypass throttling valve. The operation performance is improved by adjusting the electric generator speed and the throttling valve opening. The energy recovery efficiency is about 12% [4]. Wang et al. set a proportional valve between the hydraulic cylinder and hydraulic motor to keep the valve pressure difference constant by adjusting the generator torque. The results show that the system operation performance is improved and the energy recovery efficiency is 40%-50% [5, 6]. In the system proposed by Lin, a hydraulic motor is set in series with a proportional directional valve and parallel with a throttle valve. The energy recovery efficiency is about 35%-39% [7]. To reduce the installed power and capacity of the electric energy recovery unit, Lin uses a hydraulic accumulator to prolong the energy conversion time. The results show that the installed power of the electric energy recovery unit can be reduced by 60% [8]. Zhang et al. use a volume speed control scheme that two hydraulic pumps driven by a variable speed electric motor are used to control the boom hydraulic cylinder [9].

In the hydraulic recovery scheme, because of the hydraulic accumulator's nonlinear pressure characteristics, the hydraulic accumulator should be connected to the hydraulic cylinder non-rod chamber through control valves [10] or hydraulic transformer [11]. Zhao et al. propose a scheme that the hydraulic accumulator is connected to the non-rod chamber of the hydraulic cylinder through a proportional directional valve. To reuse the stored energy, the high pressure oil from the hydraulic accumulator is led into the inlet of the hydraulic pump through a proportional throttling valve [12]. Stored high pressure oil also can be introduced to the inlet of a pilot pump [10] or be used to drive a hydraulic motor connected to the engine [13]. However, there is a large of throttling loss during energy recovery and reutilization process. Shen et al. use hydraulic transformer and hydraulic accumulator to recover the potential energy in a hydraulic excavator based common pressure rail. The stored energy can be used through the hydraulic transformer without throttling loss [14]. To further improve the energy recovery and reutilization efficiency, the hydraulic-pneumatic balancing scheme can be used. Its characteristics have been studied in reference by Liang [18] and Hao [19]. Koitto et al. adopt a single-rod cylinder and a double-rod cylinder to drive a stationary industrial lifting application. A closed pump controlled system is used to drive a double-rod cylinder, and a hydraulic accumulator is connected with the non-rod chamber of a single-rod cylinder to compensate for the gravitational force of the load [20]. Xia et al. study the characteristics of the hydraulic-pneumatic balancing scheme where a three-chamber cylinder having an energy storage chamber is adopted [21].

It is known from the above analysis that in the electric energy recovery system, the potential energy is converted into electric energy through three energy conversion forms (potential energy-hydraulic energy-mechanical energy-electric energy) and six transfer links (hydraulic cylinder-hydraulic valve- hydraulic motor-electric generator-inverter circuit-super capacitor or battery). Considering the regeneration of the stored energy, there are many energy conversion links and long energy transfer chain in electric recovery system, and the overall energy efficiency is low. Although using hydraulic transformer has good potential energy recovery effect, no available commercial components can be used as yet, and the system with hydraulic transformer is complicated [21]. The hydraulic-pneumatic balancing scheme has high energy recovery and reutilization rate, but valve controlled system is used in main hydraulic circuit which also causes a large of throttling loss [19].

To address the above issues, a novel hydro-electric hybrid driving system adopting hydraulic cylinder and electromechanical cylinder is proposed. The proposed system realizes the integrating of the driving and the potential energy recovery of the boom. In theory, the hydraulic cylinder and accumulator are used to balance the gravity of the working device (including boom, arm, and bucket) and recover the potential energy. As an active actuator, the electromechanical cylinder is used to control the velocity and position of the boom. Due to the least energy transfer links no matter in the energy recovery and reutilization circuit or the driving circuit, the proposed system has high energy efficiency.

The rest of this paper is organized as follows. In section 2, the working principles of the proposed system is introduced. In section 3, the mathematical model is built. The operating and energy efficiency characteristics of the proposed system are respectively simulated and tested in section 4 and 5. Finally, the conclusions are presented in Section 6.

2. WORKING PRINCIPLE

Figure 1 shows the working principle of the proposed hydro-electric hybrid driving system. In the proposed system, hydraulic cylinder and electromechanical cylinder are used to drive the boom. The non-rod chamber of the hydraulic cylinder is connected with a hydraulic accumulator. By selecting appropriate pressure and capacity of the hydraulic accumulator, the gravity of the boom can be compensated by the output force of the hydraulic cylinder. The electromechanical cylinder includes a servo motor, a reducer, a ball screw, and a cylinder block. Its working principle is that the ball screw is used to convert the rotational motion of the servo motor to the linear motion. Compared with the hydraulic cylinder, the capacity of the electromechanical cylinder is larger, and the cost is higher.

In the proposed scheme, the electromechanical cylinder is used as active actuator, the velocity and position of the boom are controlled by adjusting the rotation speed and direction of the servo motor in electromechanical cylinder. The hydraulic cylinder is used as passive actuator and follows the movement of the electromechanical cylinder. When the boom is lowered, the hydraulic oil in the non-rod chamber is pressed into the hydraulic accumulator under the gravity of the boom. In this way, the potential energy is directly converted into hydraulic energy. When the boom is lifted, the high-pressure oil in the hydraulic accumulator is led into the non-rod chamber, and the hydraulic energy is converted into the potential energy again. The main function of the hydraulic cylinder is to compensate for gravity of the boom and reduce the output power of the electromechanical cylinder, which means the hydraulic cylinder does not directly involved in the control of the boom velocity and position.

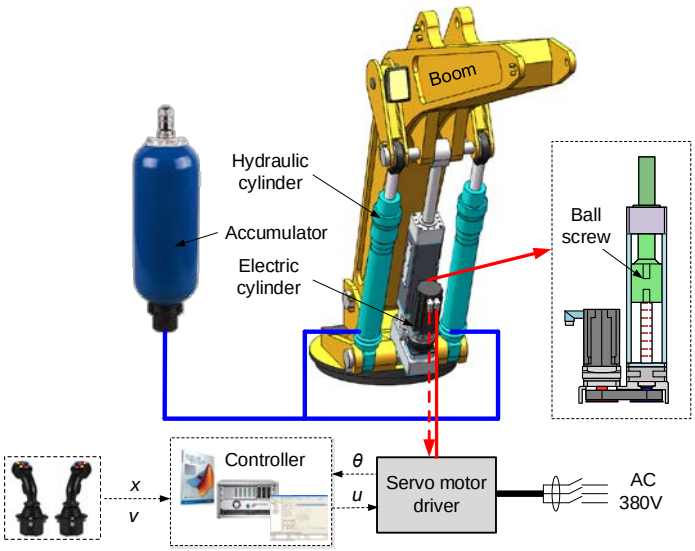

Figure 1. Working principle of the proposed system

3. MATHEMATICAL MODEL

The rod chamber of the hydraulic cylinder is directly connected to the oil tank, so its effect on the system can be neglected. The flow equation of the non-rod chamber is shown as Eq. (1).

$$q_{\mathrm{h}} = A_{\mathrm{A}}\dot{x} + \frac{V_{\mathrm{A}}}{\beta_{\mathrm{e}}}\dot{p}_{\mathrm{A}} + C_{\mathrm{L}}p_{\mathrm{A}} \tag{1}$$

where A_{A} is the non-rod chamber area, p_{A} is the non-rod chamber pressure, x is the boom position, C_{L} is the leakage coefficient, β_{e} is the bulk modulus of the hydraulic oil, V_{A} is the oil volume in non-rod chamber, $V_{\mathrm{A}}=V_{\mathrm{A0}}+A_{\mathrm{A}}x$.

Neglecting the leakage between the hydraulic accumulator and the hydraulic cylinder, the laminar flow resistance between the two elements is

$$q_{\mathrm{h}} = R_{\mathrm{l}}(p_{\mathrm{AC}} - p_{\mathrm{A}}) \tag{2}$$

where R_1 is the liquid guide of laminar flow, $R_1=\pi d^4/128\mu l$, d is the diameter of the hose, μ is the hydraulic oil viscosity, l is the length of the hose, p_{AC} is the hydraulic accumulator pressure.

The change of the gas in the hydraulic accumulator is an adiabatic process, and the gas state equation is

$$p_{\mathrm{AC}} V_{\mathrm{AC}}^{\ k_{\mathrm{a}}} = p_0 V_0^{\ k_{\mathrm{a}}} \tag{3}$$

where V_{AC} is the gas volume of the hydraulic accumulator, p_0 and V_0 are the pre-charge pressure and gas volume of the accumulator, k_a is the adiabatic index, k_a=1.4.

The following equation can be obtained by differentiating the two sides of the Eq. (3).

$$\frac{dp_{\mathrm{AC}}}{dt} = -\frac{k_{\mathrm{a}} p_0}{V_0}\frac{dV_{\mathrm{AC}}}{dt} \tag{4}$$

The flow equation of the hydraulic accumulator is

$$q_{\mathrm{AC}} = -\frac{dV_{\mathrm{AC}}}{dt} \tag{5}$$

The flow rate of the hydraulic cylinder is the same with that of the hydraulic accumulator.

$$q_{\mathrm{h}} = \frac{R_{\mathrm{l}} k_{\mathrm{1}} \mathrm{s}}{R_{\mathrm{l}} + k_{\mathrm{1}} \mathrm{s}} p_{\mathrm{A}} \tag{6}$$

where $k_1 = \dfrac{V_0}{k_{\mathrm{a}} p_0}$.

According to the above equations, the relationship between the pressure of the non-rod chamber and the position of the hydraulic cylinder is

$$p_{\mathrm{A}} = \frac{(R_{\mathrm{l}} + k_{\mathrm{1}} s) A_{\mathrm{A}} \beta_{\mathrm{e}}}{R_{\mathrm{l}} k_{\mathrm{1}} s - (R_{\mathrm{l}} + k_{\mathrm{1}} \mathrm{s}) V_{\mathrm{A}} s - C_{\mathrm{L}} (R_{\mathrm{l}} + k_{\mathrm{1}} \mathrm{s})} x = G_1(s) x \tag{7}$$

The servo motor used in the electromechanical cylinder is a permanent magnet synchronous motor. The voltage equation of the motor is shown in Eq. (8).

$$\begin{cases} U_{\mathrm{d}} = R_{\mathrm{s}} i_{\mathrm{d}} + L_{\mathrm{d}} \dfrac{di_{\mathrm{d}}}{dt} - \omega L_{\mathrm{q}} i_{\mathrm{q}} \\ U_{\mathrm{q}} = R_{\mathrm{s}} i_{\mathrm{q}} + L_{\mathrm{q}} \dfrac{di_{\mathrm{q}}}{dt} + \omega L_{\mathrm{d}} i_{\mathrm{d}} + \omega \psi_{\mathrm{f}} \end{cases} \tag{8}$$

where i_d and i_q are the excitation current and torque current; L_d and L_q are the equivalent inductance; ω is the rotation speed of the rotator; R_s is the stator resistance; Ψ_f is the magnetic flux linkage.

By using the i_d=0 control strategy, the electromagnetic torque equation is

$$T_{\mathrm{e}} = \frac{3}{2} p_{\mathrm{n}} \psi_{\mathrm{f}} i_{\mathrm{q}} \tag{9}$$

where p_n is the pole pairs.

In the servo motor driver, the speed loop and the current loop have fast response speed, so the two loop can be considered as a first-order inertia link.

$$G_2(s) = \frac{k_1}{T_1 s + 1} \tag{10}$$

where k_1 is the gain, T_1 is the time constant.

The relationship between the electromechanical cylinder's linear velocity and the servo motor's rotational speed is

$$\dot{x} = \frac{\dot{\theta} L_{\mathrm{p}}}{2\pi \mathrm{k}} \tag{11}$$

where θ is the rotation angle of the servo motor, k is the reduction rate, L_{p} is the helical pitch of the ball screw.

The relationship between the electromechanical cylinder's output force and the servo motor's output torque is

$$T_{\mathrm{ce}} = \frac{F_{\mathrm{ce}} L_{\mathrm{p}}}{2\pi \mathrm{k} \eta} \tag{12}$$

where T_{ce} is the output torque of the servo motor, F_{ce} is the output force of the electromechanical cylinder, η is the efficiency of the ball screw.

The boom is driven by the hydraulic cylinder and the electromechanical cylinder, the force balance equation is

$$p_{\mathrm{A}} A_{\mathrm{A}} + F_{\mathrm{ce}} = m\ddot{x} + B_2 \dot{x} + F_{\mathrm{L}} \tag{13}$$

where m is the equivalent mass of the working device, B_2 is the damp coefficient，F_{L} is the load of the system.

The mechanical motion equation of the servo motor is

$$J_{\mathrm{e}} \ddot{\theta} = T_{\mathrm{e}} - B_{\mathrm{e}} \dot{\theta} - T_{\mathrm{ce}} \tag{14}$$

where J_{e} is the moment of inertial, B_{e} is the viscous friction coefficient.

By analysing the above equations, the equivalent equation of the system is

$$J\ddot{\theta} + B\dot{\theta} = T_{\mathrm{e}} - T_{\mathrm{L}} \tag{15}$$

where J is the moment of inertial equivalent to the servo motor shaft, B is the damp coefficient equivalent to the servo motor shaft, T_{L} is the load torque equivalent the servo motor shaft.

$$J = J_{\mathrm{e}} + \frac{1}{\mathrm{k}^2} \frac{\mathrm{L}_{\mathrm{p}}^2 m}{4\pi^2 \eta} \qquad \mathrm{B} = \mathrm{B}_{\mathrm{e}} + \frac{1}{\mathrm{k}^2} \frac{\mathrm{L}_{\mathrm{p}}^2 B_2}{4\pi^2 \eta} \qquad T_{\mathrm{L}} = \frac{\left(F_{\mathrm{L}} - p_{\mathrm{A}} A_{\mathrm{A}}\right) \mathrm{L}_{\mathrm{p}}}{2\pi \eta k}$$

Figure 2 shows the transfer function block diagram of the hydro-electric hybrid driving system. Due to the high transmission accuracy of the ball screw, the accurate control of the boom can be realized only by using closed-loop control of the rotation speed or angle of the servo motor. It can be seen from Figure 2 that, to control the boom position, the feedback point is taken from the rotation angle of the servo motor. The load force and the output force of the hydraulic cylinder are disturbances, and the output torque of the servo motor is changed along with the variety of the load force and hydraulic cylinder output force. For the velocity and position of the boom, the hydraulic cylinder can be considered as a disturbance. As the active actuator, the electromechanical cylinder is used to control the velocity and position of the boom.

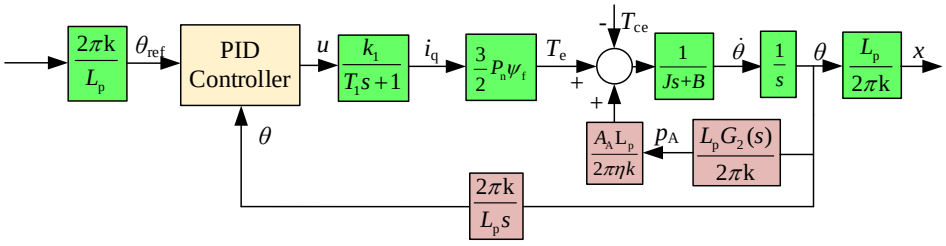

Figure 2. Transfer function block diagram of the proposed system

4. SIMULATION RESEARCH

To evaluate the characteristics of the proposed system, a mechanical-electrical-hydraulic co-simulation model is built in ITI SimulationX software as shown in Figure 3. In order to eliminate the influence of eccentric load, two hydraulic cylinders and one electromechanical cylinder are used to drive the boom. The simulation model includes the multi-body dynamics model, the hydraulic system model and the electrical system of a 6-ton hydraulic excavator. By using this model, the mechanical structure dynamical property can be calculated in real time, and the forces acting on the hydraulic cylinders and electromechanical cylinder can simulate the actual load of the hydraulic excavator. The simulation parameters are shown in Table 1.

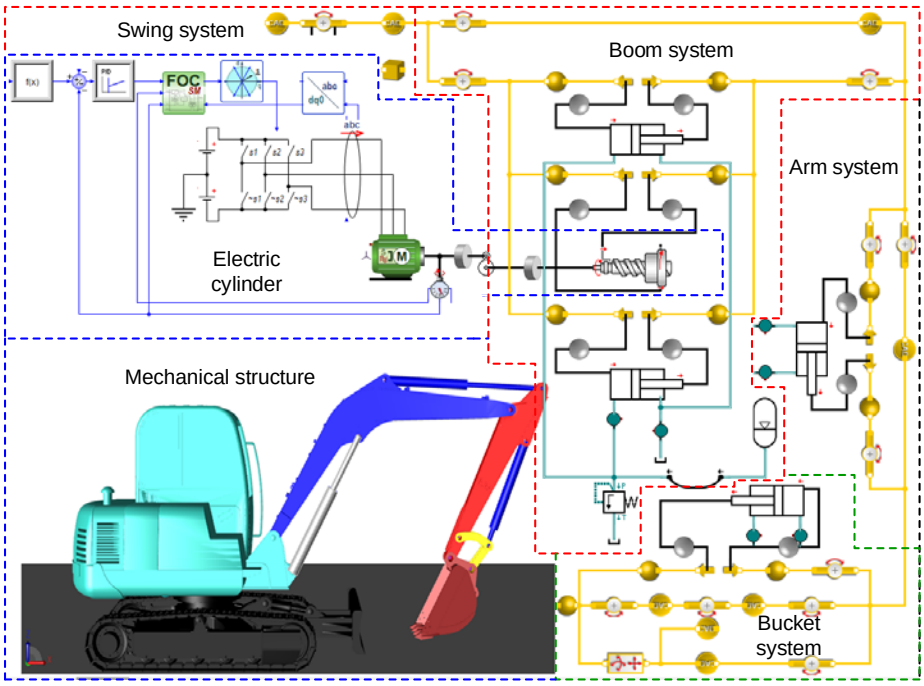

Figure 3. Mechanical-electrical-hydraulic co-simulation model of the proposed system

Table 1. Simulation parameters

Symbols	Value	Unit
d_A	63	mm
V_{A0}	31	ml
d	20	mm
μ	$4.0x10^{-2}$	Pa·s
l	2	m
p_0	5.5	MPa
V_0	20	L
C_L	0.001-0.005	(l/min)/bar
p_n	4	
Ψ_f	0.383	Wb
k	1.5	
J_e	0.012	kgm^2
B_e	0.003-0.004	Nm/(rad/s)
L_p	10	mm/r
η	0.92-0.98	

As a key element, the pressure and capacity of the hydraulic accumulator have a great influence on the energy efficiency of the system. When there is no cargo in the bucket, the system's energy efficiency under different conditions is simulated and analysed, and the simulation results are shown in Figure 4. Due to the

stored hydraulic oil volumes are the same under different accumulator pressure, the accumulator stored energy increases along with the increase of the accumulator pressure. If the accumulator pressure is too low or too high, the accumulator cannot completely recover the potential energy or stored energy drives the servo motor working in generator mode, which resulting in energy waste. It can be seen in Figure 4a that the energy consumed by electromechanical cylinder decreases first and then increases along with the increase of the accumulator pressure. When the accumulator pressure is 8.5 MPa, the energy consumed by electromechanical cylinder is the least. However, the above simulation results are obtained when there is no cargo in bucket. Considering the mass of the cargo, the accumulator pressure is selected as 9 MPa to obtain good energy efficiency and reduce the installed power of the electromechanical cylinder.

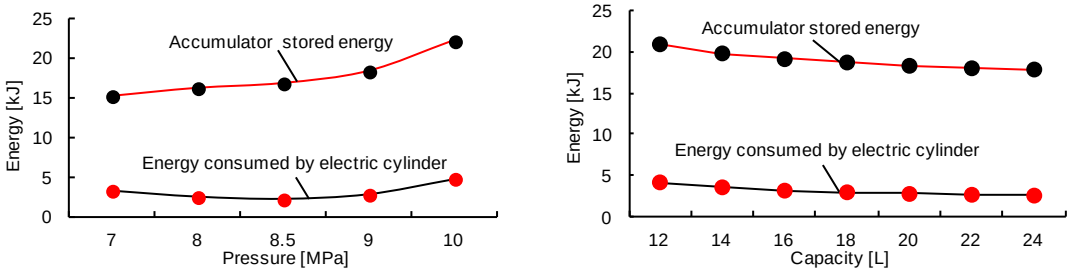

(a) Accumulator pressure (b) Accumulator capacity

Figure 4. Influence of the accumulator parameters on the energy characteristics

When the accumulator pressure is set 9 MPa, Figure 4b shows the energy characteristics of the system under different accumulator capacities. According to the characteristics of the hydraulic accumulator, to store the same hydraulic oil volume, the larger the accumulator capacity is, the smaller the pressure increases. As shown in Figure 4b, the accumulator stored energy decreases along with the increase of the accumulator capacity. When balance pressure is 9 MPa, the system is at the edge of an overbalanced state where the hydraulic cylinder force is larger than the gravity of the working device. Combining the analysis results of Figure 6a, it's known that the larger the accumulator capacity is, the lower the energy consumed by the electromechanical cylinder becomes. Due to the limitation of installation space in the hydraulic excavator, the accumulator capacity is selected as 20 L.

When the accumulator pressure is set 9 MPa and capacity is set 20 L. Figure 5 shows the simulation results of the system's operation characteristics. The operation velocity of the boom is stable without fluctuation and the overshoot is small. Due to the pressure loss of the hose, there is a small pressure difference between the non-rod chamber and the hydraulic accumulator when the boom moves. The simulation results show that the largest pressure difference is about 0.4 MPa when the boom velocity is 100 mm/s. It means that there is a little energy loss between the accumulator and hydraulic cylinder during the energy recovery and reutilization process.

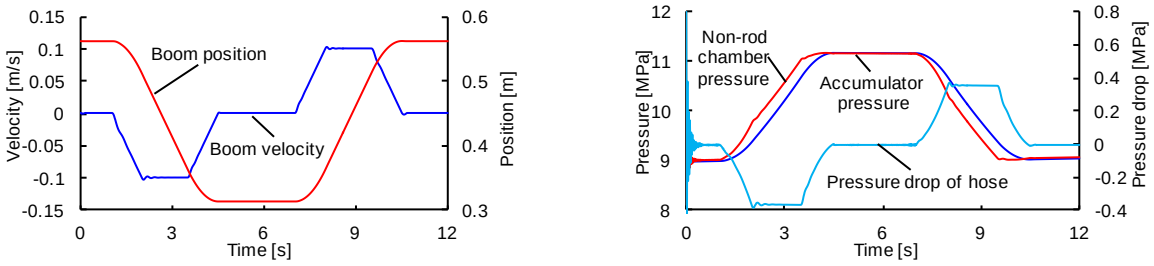

(a) Position and velocity (b) Pressure curves

Figure 5. Simulation results of the operation characteristics of the proposed system

Figure 6 shows the simulation power curves of the proposed system. During the lowering process, the electromechanical cylinder works in motoring condition, the electric power is low and the peak-power is about 2 kW. Due to the low pressure loss of the hose, the loss power of the hose is about 0.2 kW. Thus, a large part of the potential energy is recovered by the hydraulic accumulator.

When the boom is lifted, due to the hydraulic cylinder force is larger than the gravity of the working device. It can be seen in Figure 6 that the electromechanical cylinder will work in generating condition. As shown in Figure 6, the required power to lift the boom is mainly provided by the hydraulic accumulator.

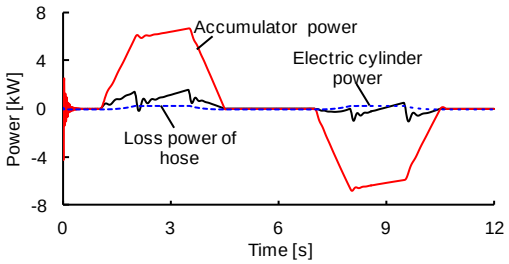

Figure 6. Simulation power curves of the proposed system

The efficiency of the hydraulic accumulator also will influence the energy efficiency of the system. The main factor affecting the efficiency of the hydraulic accumulator is the heat flow between the ambient and the gas of the hydraulic accumulator. According to the first Law of thermodynamics, the change rate of internal energy U of the hydraulic accumulator is given by the sum of mechanical power P_{mech} and heat flow P_{th}.

$$\frac{\mathrm{d}U}{\mathrm{dt}}=P_{\mathrm{mech}}+P_{\mathrm{th}} \tag{16}$$

The mechanical power is obtained from the absolute gas pressure p_{AC} and the change rate of gas volume V_{AC}. The mechanical power curve of the hydraulic accumulator is shown in Figure 6.

$$P_{\mathrm{mech}}=-p_{\mathrm{AC}}\frac{dV_{\mathrm{AC}}}{dt} \tag{17}$$

According to the fundamental theory of heat transfer, the heat flow P_{th} between the ambient and the gas can be expressed as

$$P_{\mathrm{th}}=\alpha_{\mathrm{t}}A_{\mathrm{t}}\left(T_{\mathrm{am}}-T_{\mathrm{gas}}\right) \tag{18}$$

Setting the ambient temperature at 25 ℃, the accumulator gas temperature variation and the heat flow are shown in Figure 7. When the boom is lowered, the accumulator gas is compressed, and the gas temperature is increased from 25 ℃ to 41.3 ℃. When the boom doesn't move, the gas temperature is decreased from 41.3 ℃ to 40.2 ℃ due to that the gas heat is dissipated into the ambient. When the boom is lifted, the accumulator gas volume is increased, and the gas temperature is decreased from 40.2 ℃ to 24.5 ℃. As shown in Figure 6, the larger the gas temperature is, the higher the heat flow becomes. The largest heat flow is about 0.08 kW. Moreover, the time for the extending, stopping and retracting of the hydraulic cylinder of the boom is short, it's known that the energy loss caused by the heat exchange between the gas and the ambient can be neglected considering the accumulator mechanical power as shown in Figure 6. Thus, the heat flow between the gas and the ambient has little influence on the energy efficiency of the accumulator.

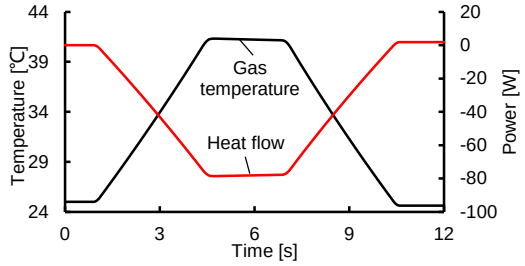

Figure 7. Gas temperature and heat flow power

5. EXPERIMENT STUDY

To validate the feasibility of the proposed scheme, a test rig of a separate meter-in and meter-out (SMIMO) system is firstly built and the characteristics of the SMIMO system are tested. In the SMIMO system, two three-position four-way directional valves are used to control the rod and non-rod chamber separately. The diameter of the hydraulic cylinder piston is 100 mm and the diameter of the rod is 70 mm. Then, a test bench of the hydro-electric hybrid driving system is established on a 6-ton hydraulic excavator, and the testing principle and picture are shown in Figure 8. Table 2 shows the component parameters. In the testing systems, Atos pressure sensors are used to detect the pressures of the hydraulic cylinders and accumulator, a MTS magneto-strictive displacement sensor is used to detect the position and velocity of the boom, a WT3000 power analyser is used to detect the power of the electromechanical cylinder, and a dSPACE 1103 is used as controller and data acquisition. The servo-motor of the electromechanical cylinder is a Phase U31004F type motor and the servo-driver is Phase AXN.22.44.

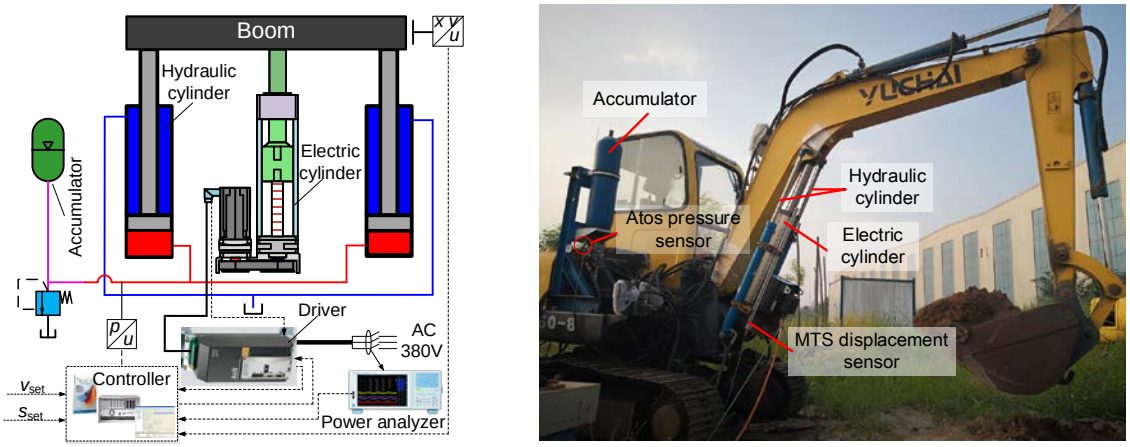

(a) Testing principle (b) Test rig photograph

Figure 8. Testing principle and test rig photograph of the proposed system

Table 2. Simulation parameters

Components	Value	Unit
Boom mass	305	kg
Arm mass	180	kg
Bucket mass	200	kg
Electromechanical cylinder mass	74	kg
Parker turbine meter range	0-150	L/min
Atos pressure sensor range	0-25	MPa
MTC displacement sensor range	0-900	mm
	0-±1500	mm/s

During the test process, the operators use an electric joystick to realize the open-loop control of the velocity and position of the boom. In order to compare the characteristics of the SMIMO system and the proposed system, the maximum velocity and operation distances are respectively set as 100 mm/s and 250 mm in the two systems. Figure 8 shows the operating characteristics of the SMIMO system and the proposed system.

In the proposed system, the pressure of the accumulator decreases from 10.5 MPa to 8.9 MPa when the boom is lifted and then the pressure is increased from 8.9 MPa to 10.5 MPa when the boom is lowered. The volume of the hydraulic cylinders and accumulator is large and the control performance of the electromechanical cylinder is high. It can be seen in Figure 8a that the boom velocity is stable and the overshoot is low. In the SMIMO system, when the boom is lifted, the pressure fluctuation number is five, the

boom velocity has large overshoot, and the adjustment time is about 1.5 s. When the boom is lowered, the pressure in the non-rod chamber of the SMIMO system is about 8 MPa and the boom velocity is stable, which means the gravity of the working device can be balanced by the hydraulic cylinder output force at this time. It's known that compared with the SMIMO system, the boom velocity is more smoothly by using the proposed system.

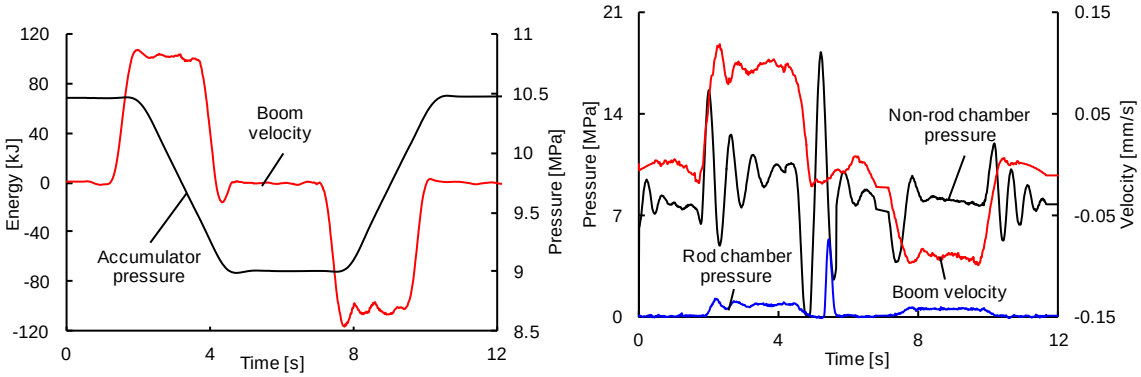

(a) Proposed system (b) SMIMO system

Figure 9. Operating characteristics of the SMIMO system and the proposed system

In the SMIMO system, the pump output power is calculated as follows.

$$P_{sm}=p_p A_{A1} v \tag{19}$$

where p_p is the pump pressure in SMIMO system, A_{A1} is the non-rod chamber area, v is the boom velocity.

The loss power between the pump and the hydraulic cylinder is calculated as follows.

$$P_L=(p_p-p_{A1})A_{A1}v \tag{20}$$

where p_{A1} is the non-rod chamber pressure in SMIMO system.

The pump output energy in the SMIMO system is calculated as follows.

$$E_{SM}=\int p_p A_{A1} v dt \tag{21}$$

When the boom is lowered, the potential energy loss power is obtained as follows.

$$P_{PL}=-p_{A1}A_{A1}v \tag{22}$$

The wasted potential energy is calculated as follows.

$$E_{PL}=\int p_{A1}A_{A1}vdt \tag{23}$$

In the proposed system, the power of the electromechanical cylinder P_{ec} is obtained by the WT3000 power analyser. The electromechanical cylinder energy is calculated as follows when the $P_{ec} \geq 0$.

$$E_{ec}=\int P_{ec}dt \tag{24}$$

The accumulator output energy is calculated as follows.

$$E_{ac}=\int A_A p_{AC} v dt \tag{25}$$

Figure 10 shows the energy characteristics of the SMIMO system and the proposed system. In the SMIMO system, as shown in Figure 10a, the peak power of the hydraulic pump is 13.8 kW which is fits in with the non-rod chamber pressure curve as shown in Figure 9b. The energy loss caused by the throttling effect is 6.1 kJ when the boom is lifted. When the boom is lowered, a flow regeneration control strategy is used that the non-rod chamber is connected to the rod chamber through the control valves, and the pump does not output energy.

However, a large of potential energy is wasted as shown in Figure 9a. By calculating, the wasted potential energy is 14.8 kJ. Because the simulation model cannot take full account of all frictional forces, it can be seen in Figure 9b that the tested electromechanical cylinder power and energy are larger than the simulation results. However, the change rule of the test results is consistent with the simulation results.

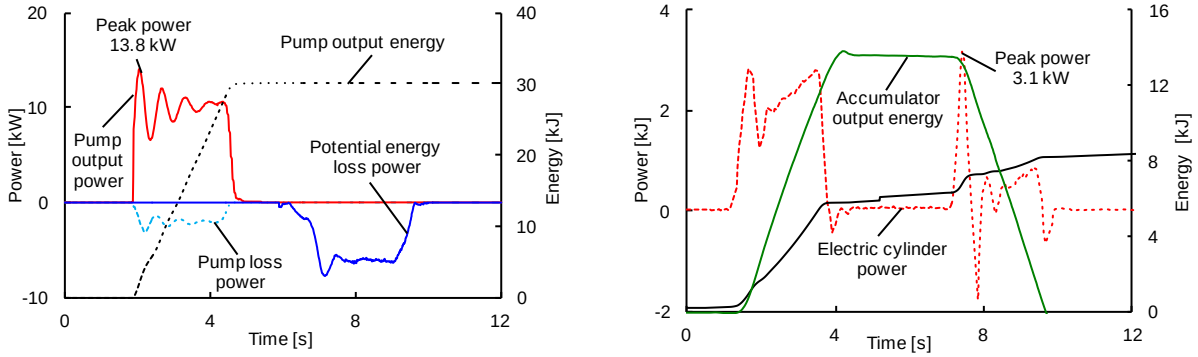

(a) SMIMO system (b) Electromechanical cylinder

Figure 10. Energy characteristics of SMIMO system and proposed system

In the proposed system, as shown in Figure 10b, the boom lifting and lowering distances are the same. The accumulator stores about 14.4 kJ energy during the lowering process and provides 14.3 kJ energy to lift the boom, which means there is little heat exchange between the accumulator gas and ambient. Because the hydraulic accumulator outputs high pressure oil to the hydraulic cylinders to drive the boom, it can be seen in Figure 10b that the power and energy of the proposed system are both less than those of the SMIMO system. At the initial phase of the boom lowering process, the electromechanical cylinder is in motor condition and outputs force to accelerate the boom lowering. The peak power of the proposed system is 3.1 kW, and the peak power is decreased by 77.5% compared with the SMIMO system.

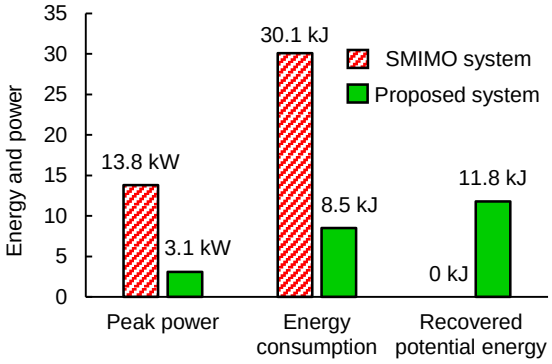

Figure 11. Energy saving effect of the proposed system

Figure 11 shows the energy saving effect of the proposed system. During the boom lowering process, the consumed energy of the electromechanical cylinder is 2.4 kJ. By calculating, the recovered potential energy by the hydraulic accumulator is 11.8 kJ. Thus, the energy recovery rate of the proposed system is about 79.7%. When the boom is lifted and lowered one time, the hydraulic pump output energy of the SMIMO system is 30.1 kJ and the energy consumed by the electromechanical cylinder is 8.5 kJ. Thus, by using the proposed system, the energy consumption can be reduced by 71.7%.

6. CONCLUSION

(1) The proposed system integrates the driving and energy recovery and reutilization by using the same device. Due to the less energy conversion links and shorter transfer chains, the proposed system has high

potential energy recovery and reutilization efficiency. Moreover, the proposed scheme is also suitable for other heavy-duty manipulator.

(2) The simulation results show that when the velocity is 100 mm/s, the maximum pressure loss between the accumulator and hydraulic cylinder is 0.4 MPa, and the largest loss power caused by the hose is about 0.2 kW. The accumulator pressure and capacity have great influence on the energy efficiency of the system. According to the simulation results, the capacity is selected as 20 L and the initial pressure is selected as 9 MPa.

(3) The testing results show that the proposed scheme has good operating performance, the boom can be operated smoothly. By using the proposed scheme, the potential energy of the working device can be recovered by 79.7%. Compared with the separate meter-in and meter-out system, the peak power is decreased by 77.5% and the energy consumption is reduced by 71.7%.

ACKNOWLEDGMENT

The authors would like to give their acknowledgment to National Natural Science Foundation of China (No. 51875385 and 51675364) for the financial support on the project.

REFERENCES

[1] Zimmerman J, Pelosi M, Williamson C, Ivantysynova, M. 2007. Energy consumption of an LS excavator hydraulic system. ASME 2007 International Mechanical Engineering Congress and Exposition, November 11-15 2007, Washington, USA, pp. 117-126.

[2] He X, Jiang Y et al. 2018. Review of hybrid electric systems for construction machinery. Automation in Construction, vol. 92, pp. 286-296.

[3] Wang H, Huang Y, Khajepour A, et al. 2017. A novel energy management for hybrid off-road vehicles without future driving cycles as a priori. Energy, vol. 133, pp. 929-940.

[4] Ahn K K, Truong D Q. Development of energy saving hybrid excavator using hybrid actuator. 2009. Proceedings of the Seventh International Conference on Fluid Power Transmission and Control, April 7-10 2009, Hangzhou, China, pp. 205-209.

[5] Wang T, Wang Q. 2014. Efficiency analysis and evaluation of energy-saving pressure compensated circuit for hybrid hydraulic excavator. Automation in Construction, vol. 47, pp. 62–68.

[6] Wang T. Study on boom energy recovery element and system of hybrid excavator. Dissertation, Zhejiang University, 2013.

[7] Lin T, Wang Q. Hydraulic accumulator-motor-generator energy regeneration system for a hybrid hydraulic excavator. 2012. Chinese Journal of Mechanical Engineering, vol. 25(6), pp. 1121-1129.

[8] Lin T, Huang W, Ren H, et al. 2016. New compound energy regeneration system and control strategy for hybrid hydraulic excavators. Automation in Construction, vol. 68, pp. 11-20.

[9] Zhang S, Minav T, Pietola M. Improving efficiency of micro excavator with decentralized hydraulics. 2017. ASME/BATH 2017 Symposium on Fluid Power and Motion Control, American Society of Mechanical Engineers, October 16-19 2017, Florida, USA, pp. 1-8.

[10] Casoli P, Riccò L, Campanini F, et al. 2016. Hydraulic hybrid excavator—mathematical model validation and energy analysis. Energies, vol. 9, no. 12, pp. 1-12.

[11] Shen W, Huang H, Pang Y, et al. 2017. Review of the energy saving hydraulic system based on common pressure rail. IEEE Access, vol. 5, pp. 655-669.

[12] Zhao D, Chen M, Dai Q, et al. 2011. System of arm potential energy recovery in hybrid hydraulic excavators. Journal of Jilin University (Engineering and Technology Edition), vol. 41, no. 1, pp.150-154.

[13] Kim, Y, Kim P and Murrenhoff H. 2016. Boom potential energy regeneration scheme for hydraulic excavators. BATH/ASME 2016 Symposium on Fluid Power and Motion Control, September 7-9 2016, Bath, UK, pp. 1-7.

[14] Shen W, Jiang J, Su X, et al. 2015. Control strategy analysis of the hydraulic hybrid excavator. Journal of the Franklin Institute, vol. 352, no. 2, pp. 541-561.

[15] Liebherr-Hydraulik bagger GmBH. Piece of working equipment. US Patent 2010/0018195A1, January 28 2010.

[16] Asam D, Fehse J. Method of operating an energy recovery cylinder. US Patent 8938956, January 27 2015.

[17] Quan L, Dong Z, Hao H, et al. A lifting machinery working device control circuit. CN Patent 105523478A, April 27 2016.

[18] Liang X. On improving energy utilization in hydraulic booms. Dissertation, Tampere University of Technology, 2002.

[19] Hao Y, Quan L, Cheng H, et al. 2018. Potential energy directly conversion and utilization methods used for heavy duty lifting machinery. Energy, vol. 155, pp. 242-251.

[20] Koitto T, Kauranne H, Calonius O, et al. 2018. Experimental Investigation of a Directly Driven Hydraulic Unit in an Industrial Application. 11th International Fluid Power Conference, 19–21 March 2018 Aachen. Aachen: RWTH Aachen University, vol.2, pp. 348–361.

[21] Xia L, Quan L, Ge L, et al. 2018. Energy efficiency analysis of integrated drive and energy recuperation system for hydraulic excavator boom. Energy Conversion and Management, vol.156, pp. 680–687.

[22] Vukovic M, Sgro S, Murrenhoff H. STEAM–a holistic approach to designing excavator systems. In: Proceedings of the 9th International Fluid Power Conference, Aachen, Germany, March 24-26, 2014: 24-26.

THEORETICAL STUDY ON THE ENERGY REGENERATION MECHANISM OF A SWITCHED INERTANCE HYDRAULIC SYSTEM WITH CYLINDER AND LOAD

S.Maekawa, Y.Inoue, M.Sonobe N.Sugano
Mechanical Engineering Research Laboratory, Kobe Steel Ltd.
Maekawa.satoshi@kobelco.com

ABSTRACT

The energy efficiency of the conventional flow control of hydraulic systems using the pressure loss of throttle valves, which are widely used in construction machinery, is very low. If a switched inertance hydraulic system (SIHS) is used, a significant improvement in the energy regeneration efficiency can be expected. This is a kind of PWM control system for switching between a high-pressure source and a low-pressure source at high speed. The purpose of this study was to propose a new analysis method which can consider the valve pressure loss, the elasticity of oil and the influence of the hydraulic cylinder mass and load in a typical hydraulic system. This method can help us understand the mechanism of energy regeneration and the effect of parameters on the energy regeneration efficiency. As a new analysis method, a flow response calculation method using modal analysis with approximate equations is proposed. This is performed by separation into the low-order modes affected by a hydraulic cylinder and the mass of the mechanical parts and the high-order modes affected by the elasticity of oil in the piping. Next, a new definition of the energy regeneration efficiency is proposed, expressed by the product of the average component and the vibration component. A method to grasp how the two types of mode components influence the energy regeneration efficiency by changing various parameters is proposed. As a result of comparing the results obtained by eigenvalue analysis and time history response analysis with finite element model (FEM), it is shown that the proposed method is valid. Some calculations are carried out using the proposed flow response calculation method and the definition of efficiency. The mechanism of the energy regeneration in a typical hydraulic system is clarified and the effect of parameters on the energy regeneration efficiency is noted.

KEYWORDS: SIHS, Energy Regeneration, Modal Analysis, Construction Machinery

1. INTRODUCTION

In the current hydraulic system, when decelerating from a state in which mechanical parts directly connected to a hydraulic cylinder are moving, a method of generating braking pressure by a pressure loss of a valve is often used. However, if that method is used, all the kinetic energy stored in the mass of the mechanical parts is dissipated. In recent years, digital hydraulics has attracted attention as a control method of a hydraulic system, and energy saving by SIHS has been proposed [1] [2] [3] [4] [5]. Pan et al. show that energy saving is possible by using SIHS in a simple system with piping and valves experimentally [2]. They propose an analytical method based on linear wave theory and show that the regeneration rate drops greatly at the resonance frequency of piping due to the elasticity of oil. However, when considering energy regeneration by SIHS in construction machinery, it is necessary to grasp how the addition of a hydraulic cylinder etc. affects

energy saving performance. For dynamic phenomena in hydraulic systems including hydraulic cylinders, time historical response simulation methods of mechanical and hydraulic coupling systems using FEM may be used [6] [7], but they are not suitable for the purpose of grasping the mechanism of energy regeneration. Therefore, in this study, a flow response calculation method using modal analysis is proposed for a system including a hydraulic cylinder and the mass of the mechanical parts, and the influence of energy regeneration mechanism and its parameters is grasped. Also in this study, the regeneration rate of the whole system is considered, expressed by the product of the average regeneration rate determined by the static average flow rate and the oscillation regeneration rate determined by the dynamic oscillation flow rate. In modal analysis, we consider the low-order modes (the 1st order mode and the 2nd order mode) which is greatly influenced by a hydraulic cylinder and the mass of the mechanical parts and the high-order modes (the 3rd and higher order modes) which is greatly influenced by the vibration due to the elasticity of oil in the piping separately. Then, we consider about phenomena for each group of classified modes and understand complexly intertwined phenomena as a sum of independent simple phenomena. Modal parameters used for model analysis can be obtained by eigenvalue analysis using FEM, but in this study they are obtained from the approximate equations derived approximately by using properties peculiar to the system including a hydraulic cylinder. It also shows that it is possible to understand the mechanism of energy regeneration and grasp the influence of parameters by investigating how the responses of each classified mode contribute to two regeneration rates.

2. RESPONSE FLOW ANALYSIS METHOD USING MODE ANALYSIS

2.1. Flow response analysis method of a system including a hydraulic cylinder

Figure 1 shows a control system of generating brake pressure by throttling the valve opening area on the meter-out side of the hydraulic cylinder. Since a pressure loss of the valve is used, all the kinetic energy stored in the mass of the mechanical parts is dissipated. On the other hand, Figure 2 shows a control system of switching the high-pressure source and the low-pressure source at high speed by using PWM control of the valves (SIHS). SHIS is a system that generates inertia force of oil at the low pressure connection and regenerates it as strain energy to the high-pressure source by using its inertial force at the high pressure connection.

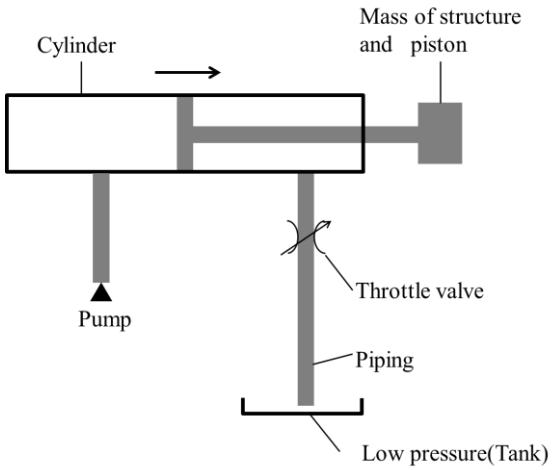

Figure 1. Conventional hydraulic system

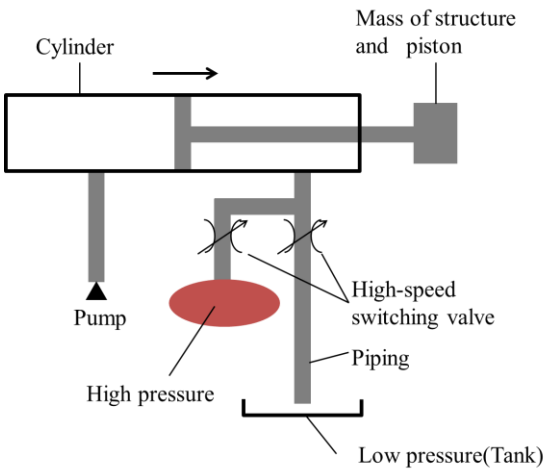

Figure 2. Switched inertance hydraulic system(SIHS)

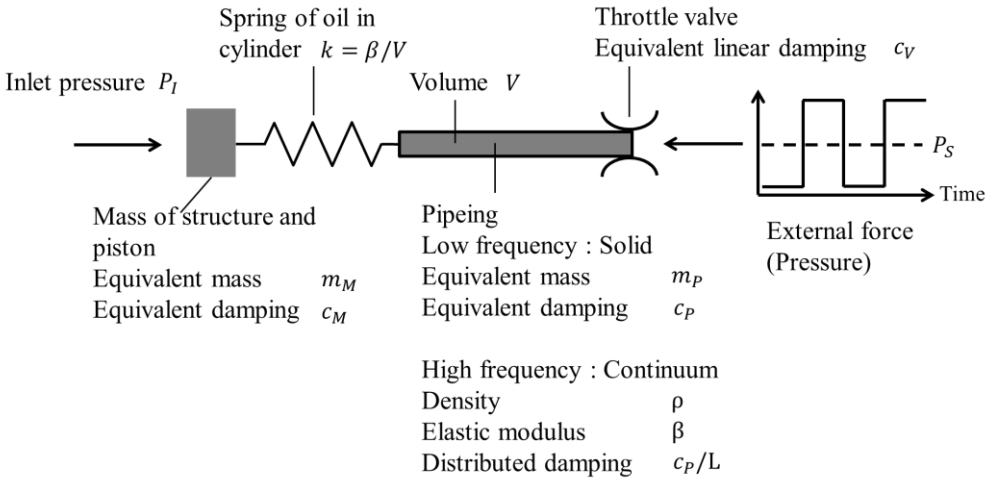

Figure 3. Mathematical model for SIHS including a hydraulic cylinder

We consider an analysis model as shown in Figure 3, which simplifies the model of Figure 2. For the handling of the meter-in side, we assume that constant pressure will be applied to the cylinder for simplicity. The average flow rate Q_S is obtained by the following equation from the average pressure P_S, the pressure on the inlet side P_I, and the damping of each part , c_P(piping), c_V(valve), c_M(between the cylinder and the piston). Where c_S is the sum of the damping associated with pressure drop.

$$Q_S = \frac{P_I - P_S}{c_P + c_V + c_M} = \frac{P_I - P_S}{c_S} \tag{1}$$

Modal parameters can be obtained from the approximate equations derived approximately by using properties peculiar to the system, and the flow response is calculated using them.

Assuming that the mass of the mechanical parts is M, the damping is C, and the cross-sectional area of the cylinder is A_C, the equivalent mass m_M and the equivalent damping c_M coordinated to the hydraulic system with pressure as the external force are given by the following equation:

$$m_M = M/A_C^{\,2} \tag{2}$$

$$c_M = C/A_C^{\,2} \tag{3}$$

For the oil in the cylinder section, assuming that the cross-sectional area of the cylinder is sufficiently greater than the cross-sectional area of the piping, the effect of the mass is neglected and modeled with an equivalent spring. The spring constant k corresponding to the balance of the flow rate in the cylinder is expressed by the following equation using the volume V of the cylinder and the bulk modulus β of oil:

$$k = \beta/V \tag{4}$$

The oil in the piping system is considered as a rigid body in the low frequency domain where elasticity can be ignored and it is modeled by the equivalent mass m_P and the equivalent damping c_P. On the other hand, the oil in the piping system is considered as a continuum in the high frequency domain where elasticity cannot be ignored and it is modeled by the bulk modulus β, the density ρ, the length L, the cross-sectional area A_P, and the piping friction per unit length μ.

Since the 1st order mode is a rigid body mode and the elasticity of oil is negligible, the natural frequency f_1 is 0Hz. In this case, the modal mass m_1 and the modal damping c_1 of the 1st order mode are expressed by the following equation:

$$m_1 = m_M + m_P \tag{5}$$

$$c_1 = c_P + c_V + c_M \tag{6}$$

In the 2nd order mode, it is generally assumed that its natural frequency is considerably lower than the natural frequency of the piping system due to the elasticity of oil, and it can be assumed that the oil in the piping is a rigid body. In this case, considering the natural frequency of the two-mass system at both ends free where the spring constant k obtained by the equation (4) exists between the mass of the oil and the mass of the mechanical parts, the natural frequency f_2 and the natural angular frequency ω_2 is expressed by the following equation:

$$\omega_2 = 2\pi f_2 = \sqrt{\frac{k\left(m_P + m_M\right)}{m_P m_M}} \tag{7}$$

Since the vibrational mode of the 2nd order mode is the opposite direction for m_M and m_P and the ratio of the size is the reciprocal of the mass ratio, if it is adjusted so that the vibrational mode component in the valve becomes 1, the modal mass m_2 is expressed by the following equation:

$$m_2 = m_P + m_M\left(m_P / m_M\right)^2 \tag{8}$$

The 2nd order modal damping is calculated assuming that the vibrational mode of the 2nd order mode does not change even if damping is added, and calculation is performed in the same way as the modal mass calculation method. Considering the proportionality constant of the spring proportional type damping η and the additional modal damping ratio ζ as the damping other than the fluid resistance, the modal damping c_2 is expressed by the following expression:

$$c_2 = c_P + c_V + c_M\left(m_P / m_M\right)^2 + \eta m_2 {\omega_2}^2 + 2\zeta_j m_2 \omega_2 \tag{9}$$

The 3rd and higher order modes are modes in which the oil in the piping system is deformed. In these modes, the influence from the cylinder and the mechanical parts is considered to be negligible for simplicity since the frequency is considerably higher than in the 2nd order mode. In this case, since these modes can be regarded as oscillations of piping system free of both ends, the natural frequency f_j and the natural angular frequency ω_j of the j-th (j>=3) order mode are expressed by the following equations:

$$\omega_j = 2\pi f_j = \frac{\pi\left(j-2\right)}{L}\sqrt{\frac{\beta}{\rho}} \tag{10}$$

Where j is the order of the mode. Since all the vibrational modes are represented by trigonometric functions, the modal mass m_j is expressed by the following equation, which is 1/2 of the equivalent mass of the piping m_P:

$$m_j = \frac{\rho L}{\pi A}\int_0^{\pi} \cos^2\left(j\theta\right) d\theta = \frac{\rho L}{2A} = \frac{m_P}{2} \tag{11}$$

The modal stiffness k_j is expressed by the following equation:

$$k_j = {\omega_j}^2 m_j = {\omega_j}^2 m_P / 2 \tag{12}$$

As with the 2nd order modal damping c_2, assuming that the vibrational mode of the j-th order mode does not change even if the damping is added, considering the proportionality constant of the spring proportional type damping η and the additional modal damping ratio ζ as the damping other than the fluid resistance, the modal damping c_j is expressed by the following equation:

$$c_j = c_P/2 + c_V + 2\zeta_j m_j \omega_j + \eta m_j \omega_j^2 = c_P/2 + c_V + \zeta m_p \omega_j + \eta m_P \omega_j^2/2 \quad (13)$$

In a system in which the above approximation is established, it is considered that the 1st order mode or the 2nd order mode is a mode markedly affected by an additional hydraulic cylinder and the mass of the mechanical parts and the 3rd and higher order modes are modes determined by vibration characteristics of only the oil in the piping. The frequency response of the j-th order vibration flow rate at the excitation point $g_j(i\omega)$ and frequency response function up to the n-th order mode $G_n(i\omega)$ are expressed as follows using the obtained modal parameters:

$$G_n(i\omega) = \sum_{j=1}^{n} g_j(i\omega) = \sum_{j=1}^{n} \frac{i\omega}{\left(-\omega^2 + \omega_j^2\right) m_j + i\omega c_j} \quad (14)$$

Assuming that the valve switching angular frequency is Ω and the excitation force of the l-th order harmonic obtained by a Fourier series expansion of the vibration pressure p_D applied to the outlet end is $F_l\cos(l\Omega t-\varphi_l)$, the vibration flow rate q_D that takes into account the m-th order harmonic is expressed by the following equation:

$$\begin{aligned} q_D &= \sum_{l=1}^{m} F_l \left\{ \mathrm{Re}\left[G(il\Omega)\right]\cos(l\Omega t - \phi_l) - \mathrm{Im}\left[G(il\Omega)\right]\sin(l\Omega t - \phi_l) \right\} \\ &= \sum_{j=1}^{n}\sum_{l=1}^{m} F_l \left\{ \mathrm{Re}\left[g_j(il\Omega)\right]\cos(l\Omega t - \phi_l) - \mathrm{Im}\left[g_j(il\Omega)\right]\sin(l\Omega t - \phi_l) \right\} = \sum_{j=1}^{n}\sum_{l=1}^{m} q_{Dlj} = \sum_{j=1}^{n} q_{DMj} = \sum_{l=1}^{m} q_{DFl} \end{aligned} \quad (15)$$

Since the flow response q is obtained by the sum of the average flow rate Q_S and the vibration flow rate q_D, it is expressed by the following equation:

$$q = Q_S + q_D = Q_S + \sum_{j=1}^{n}\sum_{l=1}^{m} q_{Dlj} = Q_S + \sum_{j=1}^{n} q_{DMj} = Q_S + \sum_{l=1}^{m} q_{DFl} \quad (16)$$

2.2. Definition of energy regeneration rate

The energy regeneration efficiency ε is considered to be the ratio of the energy regenerated to the high-pressure source P_H to the energy applied to the system by the pressure P_I applied to the meter-in side during one cycle. Assuming that P_I and P_H are constant during one cycle, the energy regeneration efficiency ε is expressed by the following equation:

$$\varepsilon = \frac{E_H}{E_I} = \frac{dP_H Q_H}{P_I Q_S} = \frac{dP_H}{P_I} \times \frac{Q_H}{Q_S} = \varepsilon_S \times \varepsilon_D \quad (17)$$

Where E_I is the energy flowing into the system in one cycle, E_H is the energy regenerated to the high-pressure source, Q_S is the average flow rate, Q_H is the flow rate regenerated to the high-pressure source. In what follows, we use ε_S to refer to the average regeneration rate and ε_D to refer to the vibration regeneration rate. The average regeneration rate ε_S is expressed by the following equation and it is proportional to the duty ratio d assuming that P_I and P_H are constant during one cycle:

$$\varepsilon_S = \frac{P_S}{P_I} = \frac{dP_H}{P_I} \quad (18)$$

On the other hand, the vibration regeneration rate ε_D is given by the ratio of Q_H to Q_S and can be calculated Q_S and Q_{DH} obtained from the vibration flow:

$$\varepsilon_D = \frac{Q_H}{Q_S} = 1 + \frac{Q_{DH}}{Q_S} = 1 - \frac{U_{DH}}{Q_S} = 1 - U_{DHN} \quad (19)$$

Since Q_{DH} takes a negative value, the complementary vibration flow rate $U_{DH} = -Q_{DH}$ is introduced and the value normalized by Q_S is U_{DHN}.

3. VALIDATION OF THE PROPOSED METHED

3.1. Validity of modal parameters by theoretical equation

Before a flow response calculation, we verify the validity of the approximate equations. In particular, we consider the validity of calculating the modal parameters by assuming that the oil in the piping is assumed to be rigid in the low-order modes and by ignoring the coupling with a hydraulic cylinder and the mass of the mechanical parts in the high-order modes. As an example, for a system that is $m_M=m_P=1$, $f_2=12$[Hz], $f_3=153$[Hz], we compare the results obtained by the proposed method with the eigenvalue analysis results calculated by FEM. Table 1 shows the natural frequencies of the models with free ends at both ends and piping only, and Table 2 shows the natural frequencies of the models with m_M and k added to the piping. In Table 1 and 2, since the proposed method is theoretical solutions and FEM is approximate solutions including a discretization error, there are some errors in the high-order modes, but the results of both are in good agreement. Comparing the results of the FEM in Tables 1 and 2, it can be confirmed that even if a cylinder is added to the piping, the increase in the natural frequency of the high-order modes is small. Therefore, ignoring coupling with a hydraulic cylinder and the mass of the mechanical parts has no problem, and it is considered to have sufficient accuracy as approximate solutions for clarifying the mechanism. From the above results, if the natural frequencies of the 2nd order mode and the 3rd order mode are sufficiently far apart, the approximate equations of the proposed method may be sufficiently accurate.

Table 1. Natural frequencies of the piping calculated by theoretical equation and FEM

Natural frequency	Eq.(10)	FEM
f_1 [Hz]	0.0	0.0
f_2 [Hz]	153.0	153.0
f_3 [Hz]	306.0	306.3
f_4 [Hz]	459.0	460.0
f_5 [Hz]	612.0	614.5
f_6 [Hz]	765.0	769.9
f_7 [Hz]	918.0	926.5
f_8 [Hz]	1071.0	1084.5
f_9 [Hz]	1224.0	1244.2
f_{10} [Hz]	1377.0	1405.8

Table 2. Natural frequencies of the piping with a cylinder calculated by the approximate equations and FEM

Natural frequency	Eq.(7) (10)	FEM
f_1 [Hz]	0.0	0.0
f_2 [Hz]	12.0	11.9
f_3 [Hz]	153.0	153.5
f_4 [Hz]	306.0	306.5
f_5 [Hz]	459.0	460.2
f_6 [Hz]	612.0	614.6
f_7 [Hz]	765.0	770.0
f_8 [Hz]	918.0	926.6
f_9 [Hz]	1071.0	1084.6
f_{10} [Hz]	1224.0	1244.3

3.2. Validity of the flow response calculation method

We consider the validity of the flow response calculation result by the proposed method. Apply $\lambda_I=P_I / P_H=0.8$, d=0.5, f=110[Hz] as the external force to the model used in eigenvalue analysis in Section 3.1. In addition to $c_M=60$ and $c_P=90$ as the damping, the proportionality constant of the spring proportional type damping $\eta=1\times10^{-6}$ is set. Figure 4 shows the normalized flow response q_N calculated by the proposed method and FEM. The result of Figure 4 calculated by considering the mode up to the 20th order and Fourier series expansion of the vibration pressure p_D up to the 32nd order using the proposed method. In Figure 4(a)

and 4(b), since the proposed method is a theoretical solution and FEM is an approximate solution including a discretization error, there are some errors in the high-order modes, but the results of both are in good agreement.

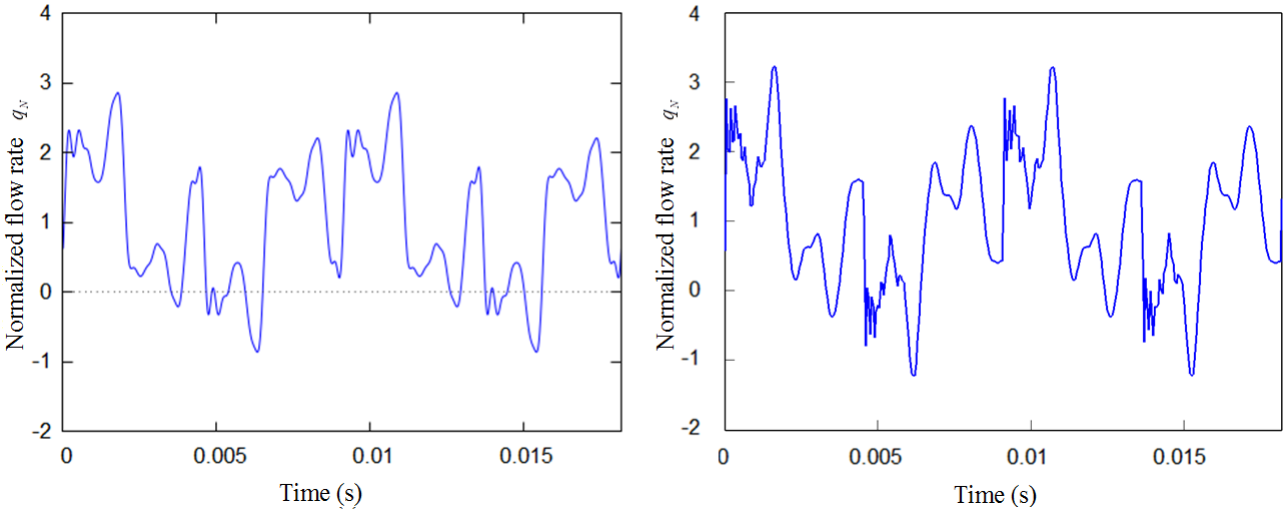

(a) The proposed method *(b) FEM*

Figure 4. Normalized flow response q_N calculated by the proposed method and FEM

4. ENERGY REGENERATION MECHANISM AND INFLUENCE OF PARAMETERS

Using the calculation results of the flow response, we examine the influence energy regeneration mechanism and influence of parameters. Figure 5 shows the results of a flow response calculation in the valve switching frequency f = 40Hz, 110Hz, 153Hz in the example of section 3.2. Figure 5 shows one cycle, the first half is the low pressure connection period and the second half is the high pressure connection period (d=0.5). The flow rates shows in Figure 5 are all normalized with Q_S, and the index N is added to the variables. Figure 5 also the results of a single degree of freedom model equivalent to the electrical system and the results are calculated under the same external force conditions as in the other cases. Figure 5 shows the average flow rate: Q_S (green solid), the vibration flow rate: q_D (red solid), the average value of q_D in the low pressure connection period: Q_{DL} (orange solid), the average value of q_D in the high pressure connection period: Q_{DH} (blue solid), the low-order modes of q_D: q_{D2} (peach dashed), the high-order modes of q_D: q_{D3}(light brown dashed) and vibration flow rate in a single degree of freedom model: q_{DE}(purple solid). Table 3 shows U_{DHN}, the low-order modes of U_{DHN}: U_{DH2N}, the high-order modes of U_{DHN}: U_{DH3N} in the valve switching frequency f = 40Hz, 110Hz, 153Hz.

Table 3. U_{DHN}, U_{DH2N}, U_{DH3N} in the valve switching frequency f = 40Hz, 110Hz, 153Hz (d=0.5)

f	40[Hz]	110[Hz]	153[Hz]
U_{DHN}	0.307	0.251	5.217
U_{DH2N}	0.245	0.032	0.017
U_{DH3N}	0.062	0.219	5.200

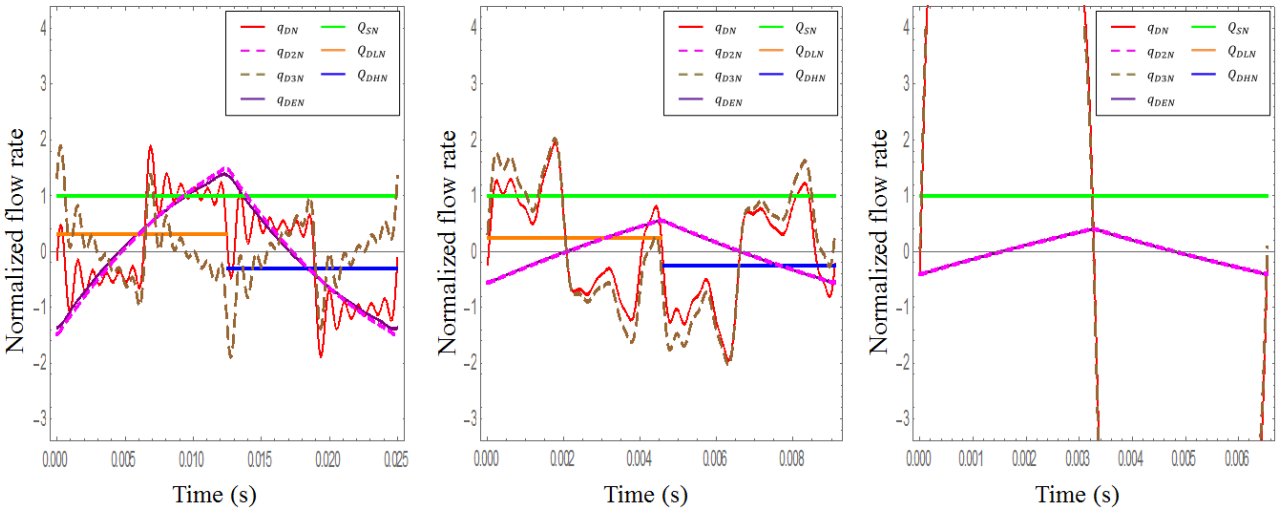

(a) f=40Hz *(b) f=110Hz* *(c) f=153Hz*

Figure 5. Normalized flow response calculated by the proposed method (d=0.5)

The low-order modes of q_D: q_{D2} has a convex upward waveform in the low pressure connection period and a convex downward waveform in the high pressure connection period in the valve switching frequency f = 40Hz. In the valve switching frequency f=110Hz and 153Hz, the unevenness of the waveform decrease and approaches a straight line as compared with f=40Hz. As the degree of convexity increases, U_{DH2N} increases and the vibration regeneration rate ε_D decreases.

The high-order modes of q_D: q_{D3} differs greatly in the valve switching frequency f=40Hz, 110Hz and 153Hz. U_{DH3N} is much smaller than U_{DHN} and U_{DH2N} in the valve switching frequency f=40Hz. On the other hand, U_{DH3N} becomes very large due to resonance, while U_{DH2N} becomes very small in the valve switching frequency f=153Hz.

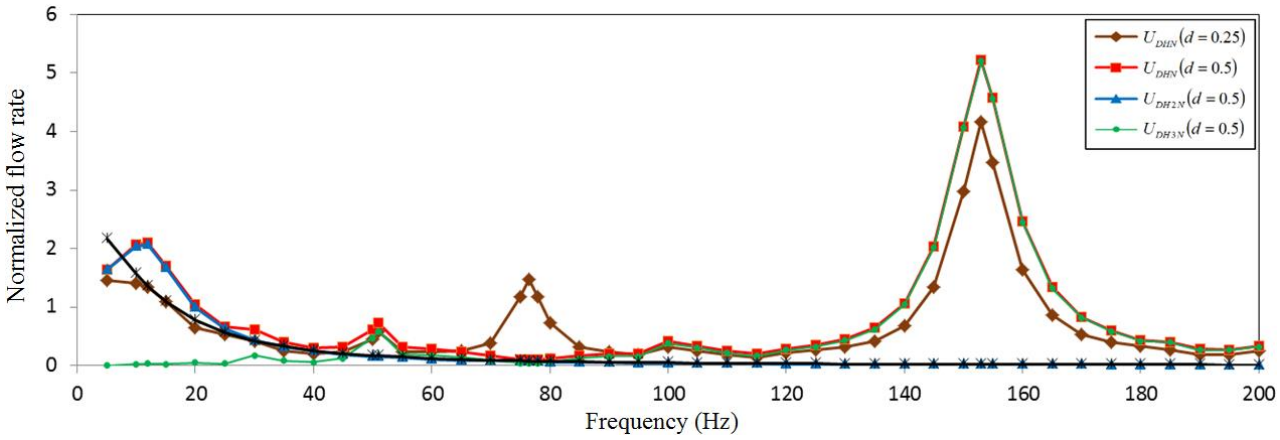

Figure 6. Effects of the valve switching frequency f on U_{DHN} (d=0.25, 0.5) and U_{DH2N}, U_{DH3N} (d=0.5)

Figure 6 shows effects of the valve switching frequency f on U_{DHN} (d=0.25: brown solid, 0.5: red solid) and U_{DH2N} (d=0.5: blue solid), U_{DH3N} (d=0.5: green solid). U_{DH2N} shows a resonance peak in the neighborhood of the natural frequency f_2 and decreases as the valve switching frequency f increases. On the other hand, U_{DH3N} shows a peak at the resonance between the harmonic of the valve switching frequency and the natural frequency f_3 or f_4. Note that there is a second harmonic of the switching frequency at duty ratio d=0.25, and

U_{DHN} (d=0.25) shows a peak at the resonance between the second harmonic of the valve switching frequency and the natural frequency f_3. In the U_{DHN} is the sum of U_{DH2N} and U_{DH3N}, U_{DH2N} is dominant in the region where the valve switching frequency f is small, but U_{DH3N} becomes dominant as the valve switching frequency f increases.

5. CONCLUSION

The energy efficiency of the conventional flow control of hydraulic systems using the pressure loss of throttle valves, which are widely used in construction machinery, is very low. If a switched inertance hydraulic system (SIHS) is used, a significant improvement in the energy regeneration efficiency can be expected. In this study, a flow response calculation method using modal analysis is proposed for a system including a hydraulic cylinder and the mass of the mechanical parts, and the influence of energy regeneration mechanism and its parameters is grasped.

The proposed flow response calculation method is performed by separation into the low-order modes affected by a hydraulic cylinder and the mass of the mechanical parts and the high-order modes affected by the elasticity of oil in the piping.

Also, a new definition of the energy regeneration efficiency is proposed, expressed by the product of the average component and the vibration component. A method to grasp how the two types of mode components influence the energy regeneration efficiency by changing various parameters is proposed.

REFERENCES

[1] Linjama, M., Digital fluid power – state of art, Proceedings of the 12th Scandinavian International Conference on Fluid Power, Vol.3, No.12 （2011）, pp.331–354.

[2] Pan, M., Johnston, N., Plummer, A., Kudzma, S. and Hillis, A., Theoretical and experimental studies of a switched inertance hydraulic system, Proceedings of the Institution of Mechanical Engineers, Part1, Journal of Systems and Control Engineering, Vol.228, No.1 （2014）, pp.12–25.

[3] Pan, M., Johnston, N., Robertson, J., Plummer, A., Hillis, A. and Yang, H., Experimental investigation of a switched inertance hydraulic system with a high-speed rotary valve, Journal of Dynamic Systems, Measurement, and Control, Vol.137, No.12 （2015）, Paper No. 121003.

[4] Scheidl, R., Kogler, H. and Winkler, B., Hydraulic Switching Control – objectives, concepts, challenges and potential applications, Magazine of Hydraulics, Pneumatics, Tribology, Ecology, Sensorics, Mechatronics, No.1 （2013）, pp.7–18.

[5] Yang, H. and Pan, M., Engineering research in fluid power: a review, Journal of Zhejiang University-Science A, Vol.16, Issue6 （2015）, pp.427–442.

[6] Imanishi, E., Nanjo, T., Hirooka, E. and Inoue, Y., Dynamic Simulation of Flexible Multibody System with Hydraulic Drive, Transactions of the Japan Society of Mechanical Engineers, Series C, Vol.69, No.185 （2003）, pp.2336–2343.

[7] Inoue, Y. and Ishii, T., Transient response and stability analysis on hydraulic press, Kobelco Technical Bulletin, Vol.31, No.1 （1981）, pp.32–37.

SIMULATION OF A HYDRAULIC DIRECT-DRIVE SYSTEM FOR A BIPED WALKING ROBOT

Juri Shimizu[1], Takuya Otani[2], Kenji Hashimoto[3], Atsuo Takanishi[2]
[1]The Graduate School of Advanced Science and Engineering, Waseda University, and Hitachi, Ltd.
17 Kikui-cho, Shinjuku-ku, Tokyo, Japan
[1]The Graduate School of Advanced Science and Engineering, Waseda University
[2]The School of Science and Technology, Meiji University
E-mail (juri-shimizu1112@asagi.waseda.jp)

ABSTRACT

A disadvantage of biped robots with electric motor-driven serial links is that a motor and transmission must be installed in each joint, causing the legs to become extremely heavy. Thus, a high-power motor is required at the root of each leg, i.e., at the hip joint. This requirement becomes particularly important as the leg output power is increased. To this end, the use of a hydraulic system has been proposed. This system reduces the power required for the hip joint by installing pressure sources consisting of a heavy motor and a pump outside the legs and by placing only lightweight cylinders at each joint. Previously proposed robots with hydraulic systems have incorporated multiple actuators, where each was controlled by a dedicated proportional valve. However, for biped robots, highly responsive proportional valves are required to ensure that the posture of the robot remains stable. Furthermore, a high supply pressure is necessary for high responsiveness, and thus the energy losses are large. Hence, we propose the use of a hydraulic direct-drive system in which the pump controls the cylinder meter-in flow and a proportional valve controls the meter-out flow. A performance comparison with a conventional system shows that a good position-following capability is achieved, and the motor output can be reduced by 64.9% using the proposed system. A simulation was performed to evaluate whether walking would be possible using the proposed system, and it was found that the system realized walking using a proportional valve with a frequency response of only 20 Hz. These results prove that it is possible to construct a biped robot without incorporating highly responsive servo valves.

KEYWORDS: hydraulics, biped locomotion, humanoid robot, flow-based control

1. INTRODUCTION

The safe and quantitative evaluation of products used by people is necessary. One approach for this is to perform a user evaluation; however, this approach has safety risks and presents problems in terms of reproducibility. Therefore, we, the Waseda University research group, have proposed the application of a biped humanoid robot perform these evaluations. The robot, named WABIAN-2R (WAseda BIpedal humANoid - No. 2 Refined) can execute a stretched knee gait with a pelvis model [1]. The biped robot is shown in Fig. 1. As reported in recent studies, we have been developing a robot that can not only walk, but also hop and run. In such a robot, high power actuators are required. However, it is difficult to install high-power electric motors for human-sized robots owing to space limitations. To resolve this problem, we proposed a method to produce a large torque with pelvic oscillation and leg elasticity [2, 3].

Figure 1. Example of our developed biped robot.

To increase the output of the electrical motor, Urata et al. developed and demonstrated a technique that improves continuous output torque with a liquid cooling system [4]. Other robots mounted two motors in the driving axes [5, 6]. These approaches have resulted in the development of high-speed and high-torque joints in both legs of humanoids, thus achieving high mobility. However, in these conventional methods, it is difficult to place equipment such as motors with the same weight distribution as a human because the motors are directly connected to the axes by mechanical transmission. Therefore, if a hydraulic system can be adopted, the layout of the equipment can be improved.

Hydraulic systems can realize a robot of the same size as a human. For example, Boston Dynamics has developed ATLAS [7], and Hyon et al. demonstrated the capabilities of a hydraulic humanoid robot, called TaeMu [8]. In particular, TaeMu realized a link ratio and weight distribution of legs similar to those of humans. These robots can directly control the torque of each joint by adjusting the actuator pressures using proportional valves. However, in our application, to reproduce a predetermined motion pattern to evaluate products, a system that can directly control the joint angle is required.

The displacement control system is a system that can directly control the actuator stroke [9, 10]. An example of this system being applied to a robot system is Kaminaga's electro-hydrostatic actuator (EHA) [11]. However, the EHA utilizes a through-rod cylinder, which is difficult to mount.

We proposed a hydraulic direct-drive system based on a displacement control system that uses a single-rod cylinder for biped humanoid robots [12]. Excellent energy savings, good velocity tracking ability, and near-perfect position tracking were achieved. The single-rod cylinder is generally more efficient than a hydraulic motor and has better availability and mountability than a through-rod cylinder.

In this paper, we apply the hydraulic direct-drive system to a biped humanoid robot and confirm whether walking can be realized using a pre-calculated walking pattern. The results of a performance comparison with a valve-based control system verify the efficacy of the proposed system.

The remainder of this paper is organized as follows. In section 2, the design of the hydraulic direct-drive system and its theoretical model are introduced. In section 3, the experimental set-up, procedure, and results are described. Finally, the conclusion and the directions for future work are presented in section 4.

2. CONSTRUCTION OF HYDRAULIC DIRECT-DRIVE SYSTEM

In this section, we describe the proposed hydraulic direct-drive system configuration and control concept. Furthermore, we examine the circuit configuration for mounting.

In section 2.1, the design of the proposed hydraulic direct-drive system is described, and in sections 2.2 and 2.3, an operating mode and proposed control method are established.

2.1. Hydraulic Circuit

The single-rod cylinder is superior in terms of mountability and efficiency when used as an actuator for a biped humanoid robot employing a hydraulic system. In this section, a conventional hydraulic circuit configuration for mounting a single-rod cylinder is described, and the features of the proposed hydraulic direct-drive system are described.

2.1.1. Conventional System

Previously proposed robots [7, 8] with hydraulic systems have incorporated multiple single-rod cylinders. Each cylinder was controlled by a dedicated proportional valve. A general valve-based control system using a proportional valve for meter-in and meter-out control is shown in Fig. 2. However, for a biped robot, highly responsive proportional valves are required to ensure that the joints follow the required trajectory. Servo valves are a type of highly responsive proportional valves. However, a servo valve has internal leakage when in the closed position, making it necessary to compensate for this leaking if the posture of the biped robot is to be maintained. Furthermore, a high supply pressure is necessary to realize the high responsiveness, and thus the energy losses are large. Therefore, a hydraulic direct-drive system based on meter-in control using pump-derived output flow and meter-out control using a proportional valve was proposed [12].

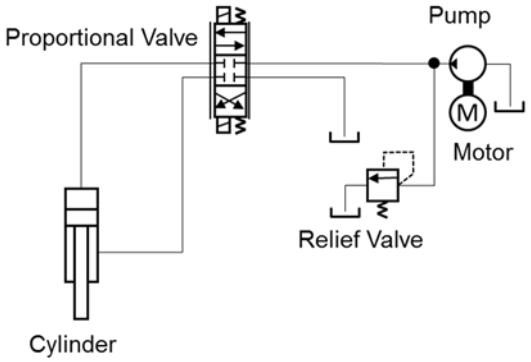

Figure 2. Circuit of conventional system (valve-based control system).

2.1.2. Hydraulic Direct-Drive System

We designed a hydraulic system that independently drives the axis of each joint. For the hydraulic-based drive system, at each axis, we selected an actuator speed control based on the pump output flow for optimizing the demand trajectory.

In addition, we selected a fixed displacement pump because it demonstrates better volumetric efficiency than a variable displacement pump. Furthermore, a displacement control unit is not required in a fixed displacement pump; consequently, it is small and can be mounted easily. The flow rate of the fixed displacement pump can be controlled by regulating the pump's rotational speed. In this study, the pump and a servo motor were connected, and the flow rate was controlled by regulating the rotational speed of the motor. The proposed hydraulic direct-drive system for a single axis is shown in Fig. 3.

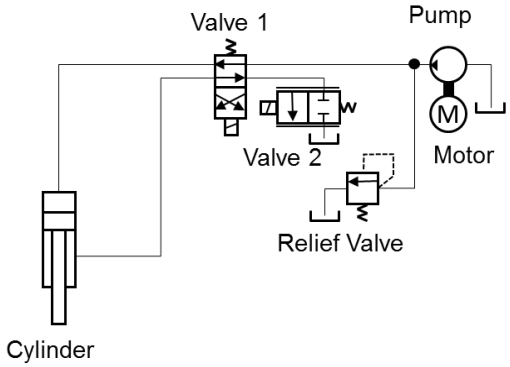

Figure 3. Circuit of hydraulic direct-drive system.

As shown in Fig. 3, the pump and the cylinder are connected through Valve 1, which is a solenoid direction-control valve. The pump outlet port is generally connected to the cap side of the cylinder (without the input signal to Valve 1). The input signal to Valve 1 switches the position of Valve 1 and connects the pump to the rod side of the cylinder. Thus, Valve 1 can control the operating direction of the cylinder.

The tank and the outlet side of the cylinder are connected through Valves 1 and 2. Valve 2 is a solenoid proportional control valve; the opening of Valve 2 can be controlled by an input signal. Valve 2 is used to control the actuator speed in the meter-out mode.

A relief valve is connected to the pump outlet line. It prevents the pump outlet pressure from exceeding the set pressure, thus preventing the pump from being damaged.

2.2. Operating Mode

In the circuit shown in Fig. 3, two flow-control modes were selected depending on the external force acting on the cylinder and the driving direction.

2.2.1. Meter-in Mode

The first flow-control mode was a meter-in flow-control mode with a positive load, in which the driving direction of the cylinder and the direction of the external force were opposite. The meter-in flow-control mode is illustrated in in Fig. 4. As shown in Fig. 4, the chamber of the cylinder connected to the pump has a higher pressure. In this state, the cylinder input flow rate is almost the same as the pump-derived output. Therefore, the pump can control the velocity of the cylinder.

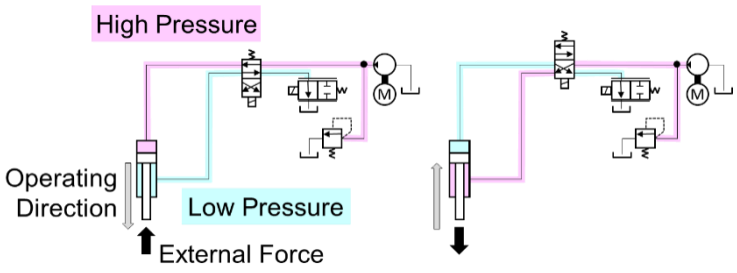

(a) Outstroke direction *(b) Instroke direction*

Figure 4. Meter-in mode.

The demand velocity of the cylinder, V_{dCyl}, is calculated based on the time variation in the demand stroke, L_{dCyl}. Based on the demand velocity of the cylinder, V_{dCyl}, the demand meter-in flow rate Q_{dCyl} of the cylinder is

$$Q_{dCyl\ in} = V_{dCyl}\, A_{Cyl}. \tag{1}$$

A_{Cyl} is the pressure-receiving area of the cylinder and is given by

$$A_{Cyl} = \begin{cases} A_{CylCap} \ (V_{dCyl} > 0 : Outstroke) \\ A_{CylRod} \ (V_{dCyl} < 0 : Instroke) \end{cases}, \quad (2)$$

where A_{CylCap} is the pressure-receiving area of the cap side, and A_{Cylrod} is the pressure-receiving area of the rod side of the cylinder.

In the meter-in flow-control mode, the velocity of the cylinder is controlled by the pump output. The pump-derived output flow Q_{Pump} is generally given by

$$Q_{Pump} = D_P \ \omega \ \eta_{pv} \ , \quad (3)$$

where D_P is the displacement of the pump, ω is the rotational speed of the pump, and η_{pv} is the volumetric efficiency. In this system, the pump was a fixed displacement type, and we controlled its derived output flow Q_{Pump} based on its rotational speed ω. Therefore, the demand pump rotational speed, $\omega_{dPump,}$ for creating the demand velocity of the cylinder, V_{dCyl}, is determined using (1) and (3):

$$\omega_{dPump} = \frac{V_{dCyl} \, A_{Cly}}{D_P \, \eta_{pv}}. \quad (4)$$

2.2.2. Meter-out Mode

The second control mode was a meter-out flow-control mode with a negative load, in which the driving direction of the cylinder and the direction of the external force were the same. The meter-out flow-control mode is illustrated in Fig. 5. The pressure in the chamber of the cylinder connected to Valve 2 is high. In this state, the output flow rate of the cylinder is almost the same as that of Valve 2. Therefore, Valve 2 can control the velocity of the cylinder.

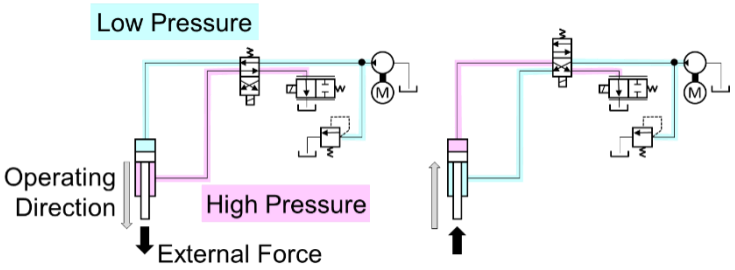

(a) Outstroke direction *(b) Instroke direction*

Figure 5. Meter-out mode.

Based on the demand meter-in flow rate of the cylinder, $Q_{dCyl \ \ in}$, the demand meter-out flow rate of the cylinder, $Q_{dCyl \ out}$, is

$$Q_{dCyl \ out} = \alpha \ Q_{dCyl \ in}, \quad (5)$$

where α is the pressure-receiving area ratio given as follows:

$$\alpha = \begin{cases} \frac{A_{CylRod}}{A_{CylCap}} \ (V_{dCyl} > 0 : Outstroke) \\ \frac{A_{CylCap}}{A_{CylRod}} \ (V_{dCyl} < 0 : Instroke) \end{cases}. \quad (6)$$

In the meter-out flow-control mode, the velocity of the cylinder is controlled by the Valve 2 flow rate, $Q_{Valve \ 2,}$ which is given as:

$$Q_{Valve \ 2} = C_d A_{Valve \ 2} \sqrt{\frac{2 \ (P_{Valve \ 2 \ in} - P_{Valve \ 2 \ out})}{\rho}}, \quad (7)$$

where C_d is the flow coefficient, $A_{Valve \ 2}$ is the valve opening area, $P_{Valve \ 2 \ in}$ and $P_{Valve \ 2 \ out}$ are the pressures at the input port and the output port of Valve 2, respectively, and ρ is the density of the fluid. In this study, petroleum fluid was used. $P_{Valve2 \ out}$ was almost zero, and $P_{Valve2 \ in}$ was almost equal to the cylinder pressure at the meter-out side.

2.3. Control Method

To control the proposed system, feedforward control, implemented based on (1) to (7), was applied, and feedback control was used to compensate for the error of the feedforward control. The block diagram of the position control in the proposed system is shown in Fig. 6. The details of the feedback control are presented below.

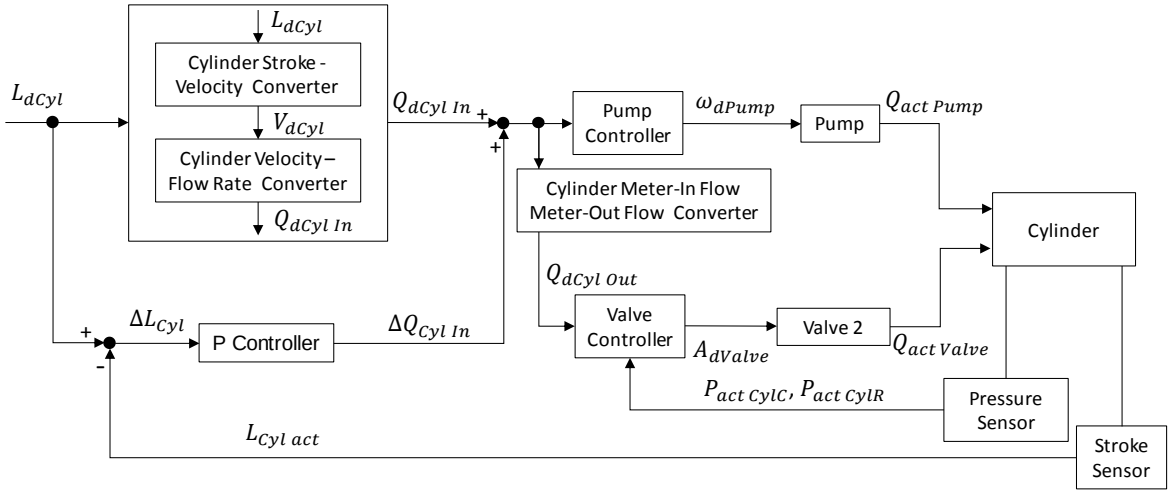

Figure 6. Proposed controller.

In an actual hydraulic system, the required pump-derived output flow rate of the pump is not produced owing to pump leakage or response delay. This flow rate error becomes a factor in calculating the error of the stroke. Therefore, the correction flow rate $\Delta Q_{Cyl\ in}$ is calculated based on the error between the demand value of the cylinder stroke, L_{dCyl}, and the actual value, $L_{Cyl\ \ act}$. The P controller was used to calculate the corrected flow rate $\Delta Q_{Cyl\ in}$. To minimize the target error of the stroke, the gain of the P controller was determined by trial and error. By applying the corrected flow rate $\Delta Q_{Cyl\ in}$, ω_{dPump} is calculated as follows:

$$\omega_{dPump} = \frac{V_{dCyl}\, A_{Cly} + \Delta Q_{Cyl\ in}}{D_P\, \eta_{pv}}. \tag{8}$$

Considering the corrected flow rate $\Delta Q_{Cyl\ in}$, $A_{dValve\ 2}$ is calculated as follows:

$$A_{dValve\ 2} = \frac{\alpha\,(Q_{dCyl\ in} + \Delta Q_{Cyl\ in})}{C_d} \sqrt{\frac{\rho}{2\,P_{act\ Cyl\ low}}}. \tag{9}$$

3. EXPERIMENTS

The performance of the proposed hydraulic direct-drive system was confirmed on a test rig, and walking simulation experiments were conducted to assess the overall function.

3.1. Performance Evaluation

The experiments conducted to verify the performance of the proposed hydraulic direct-drive system are summarized here. The experimental setup is first described in section 3.1.1; then, the experimental procedures are explained in section 3.1.2; the experimental results are aggregated and discussed in section 3.1.3.

3.1.1. Experimental Setup

A test rig was first developed to evaluate the proposed hydraulic system. The hydraulic circuits used in the evaluation are shown in Fig. 7. The circuit of the proposed system (Fig. 7(a)) was compared alongside that of a conventional system (Fig. 7(b)).

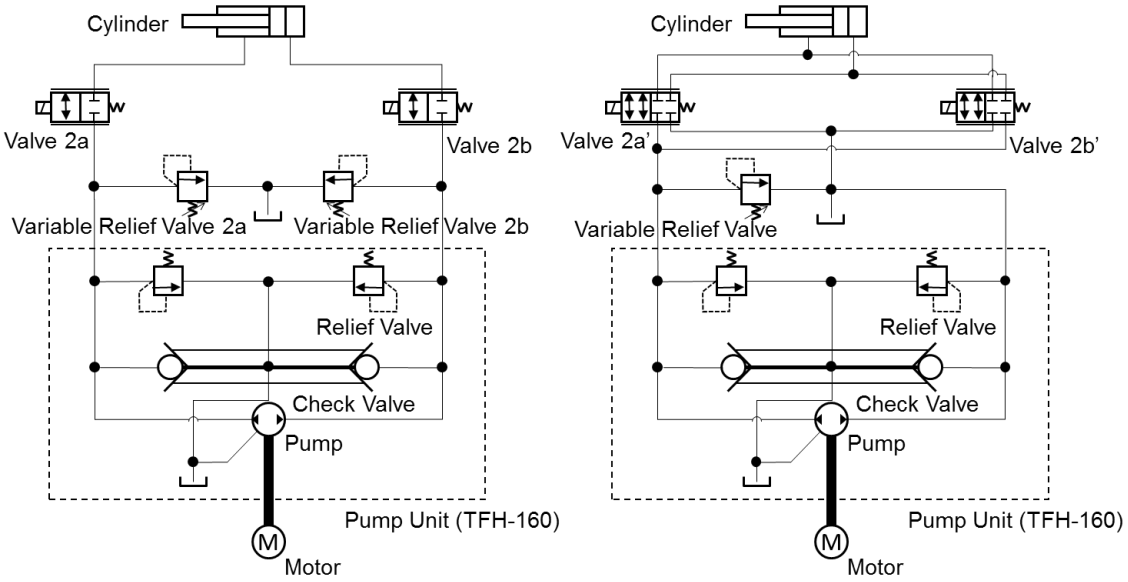

(a) Proposed system (b) Conventional system

Figure 7. Test rig hydraulic circuits.

As shown in Fig. 7(a), the pump unit and the cylinder are connected through Valve 2a and Valve 2b. A pump unit [13] manufactured by Takako Industries is incorporated into the system. This unit includes a pump, a relief valve to protect the pump, and a special check valve unit. The pump has two output ports and can discharge from both ports. The check valve unit has two individual check valves that are interconnected by a rod; this unit therefore connects the low-pressure side of the pump outlet to the tank. Valve 2a and Valve 2b are each one-port solenoid proportional valves. The hydraulic circuit has two variable relief valves that can be used to tune the relief pressure.

As shown in Fig. 7(b), the circuit of a conventional system is similar to that of the proposed system in Fig. 7(a). The pump unit and the cylinder are connected through Valve 2a' and Valve 2b'. The pump unit used in

Table 1. Test hydraulic circuit parameters.

Parameter		Value
Pump displacement (cc/rev)		1.6
Pump relief pressure (MPa)		21
Cylinder stroke (mm)		132
Cylinder piston diameter (mm)		25
Cylinder rod diameter (mm)		16
Variable relief valve set pressure 2a, 2b (MPa)		4.0
Variable relief valve set pressure (MPa)		2.0
Hose inner diameter (mm)		3.6
Hose length (mm)	Pump to Valve 2a, 2b, 2a', 2b'	100
	Valve 2a, 2b, 2a', 2b' to Cylinder	1000
Valve 2a, 2b, 2a', 2b' nominal flow rate (L/min/(MPa))		5/1
Oil kinematic viscosity (mm^2/s)	40 (°C)	14.68
	100 (°C)	3.717
Experimental oil temperature (°C)		25

this system is the same as the one incorporated in the proposed system. Valve 2a' and Valve 2b' are two-port solenoid proportional valves. Although the circuit can be designed with only one proportional valve, two independent valves are used owing to limitations imposed by the experimental equipment. This circuit has one variable relief valve, which can be used to tune relief pressure. The hydraulic parameters of both the conventional circuit and the proposed circuit are listed in Table 1.

To reproduce the mechanical load during robot application, we developed a mechanical loading device connected to a cylinder. The four-bar linkage mechanism was used to secure a wide joint drive range with the cylinder; the configurations are shown in Fig. 8, and the parameters are listed in Table 2.

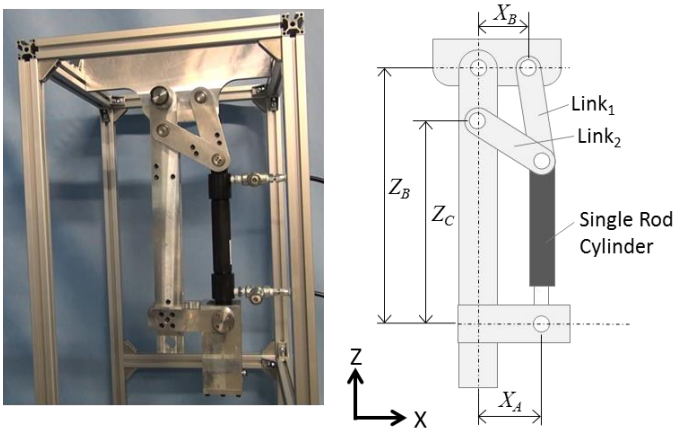

(a) Four-bar linkage mechanism (b) Parameters

Figure 8. Test rig mechanical load.

Table 2. Four-bar linkage mechanism parameters.

Length (mm)		Mass (kg)	
$Link_1$	119.1	Main Frame	4.2
$Link_2$	112.9	Cylinder	2.0
X_A	100.0	$Link_1$	0.6
X_B	68.5	$Link_2$	0.4
Z_B	400.0		
Z_C	342.9		

3.1.2. Experimental Procedure

The trajectory tracking abilities of the conventional valve-based system and the hydraulic direct-drive system for a sinusoidal position input were measured and compared.

A simple feedback control, as shown in Fig. 9, was applied to the conventional system. The P controller was used to control the opening area of Valve 2a' and Valve 2b' in the simple feedback controller. The P gain was set to 5, and the rotational speed of the motor driving the pump was fixed at 2000 rpm. For control of the proposed system, feedforward control and feedback control, which were implemented on the basis of (1) to (9), were applied. The P gain was set to 3.

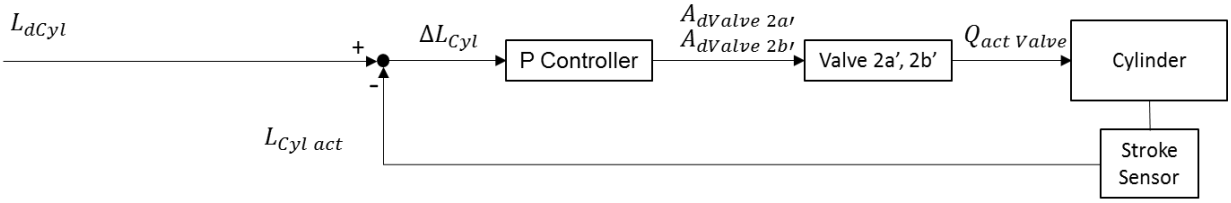

Figure 9. Simple feedback controller for the conventional system.

3.1.3. Experimental Results

The time responses of the proposed and conventional systems to sinusoidal position inputs and the corresponding errors for a stroke amplitude of 50 mm and frequency of 0.5 Hz were measured. Fig. 10 shows various positions of the rig for the frequency response test. The tracking ability of each system for the demand position of the sinusoidal input is shown in Fig. 11(a); Fig. 11(b) shows the errors in the positions of both systems.

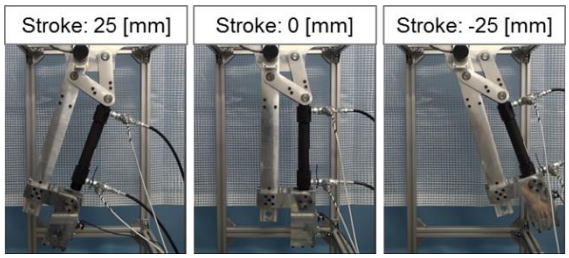

Figure 10. Motion of the test rig during the position frequency response test.

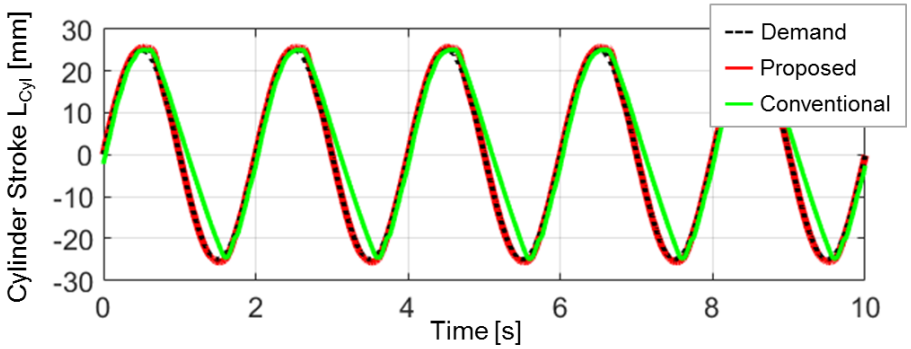

(a) Sinusoidal responses of the proposed and conventional systems compared to the demand

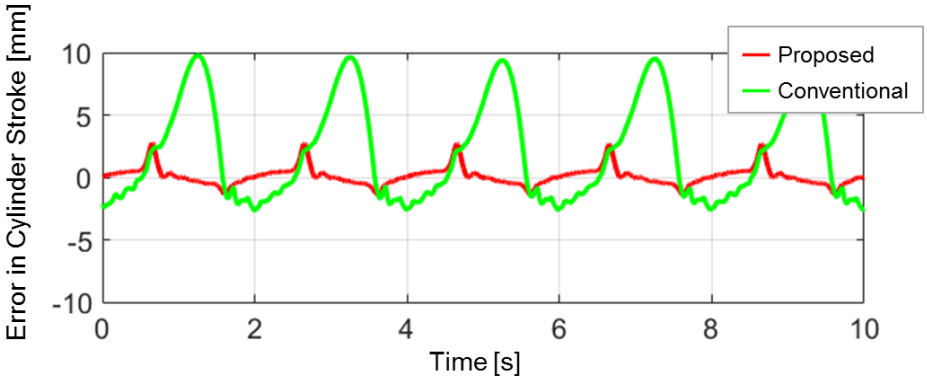

(b) Errors in the responses

Figure 11. Position time response.

The input voltage of Valve 2 is shown in Fig. 12. When extending the cylinder, the maximum input of Valve 2 is 10 V. This indicates that the flow rate is insufficient in the conventional system. The flow rate is insufficient because the error during acceleration of the cylinder increases owing to the initial error that is produced when the direction of the cylinder switches and the switching of Valves 2a' and 2b' is delayed. It can be observed that the proposed hydraulic direct-drive system has a smaller error at the proportional valves compared to the conventional system for the same input response. The demand pump rotational speed is shown in Fig. 13. As shown in Fig. 13, while the rotational speed of the conventional system is 2000 rpm, the maximum speed of the proposed system is 1500 rpm. This result indicates that the proposed system can achieve excellent tracking ability with a lower discharge flow rate compared to the conventional system. This is the effect of compensating for the delay at the time of direction switching of the cylinder by the proposed feedforward control.

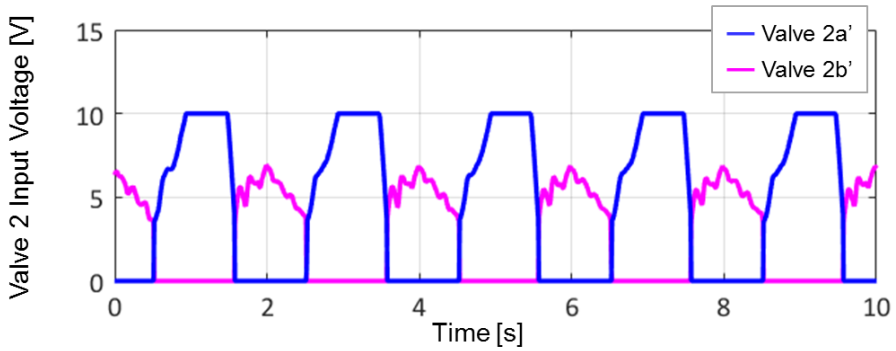

Figure 12. Valve 2 input voltage at conventional system.

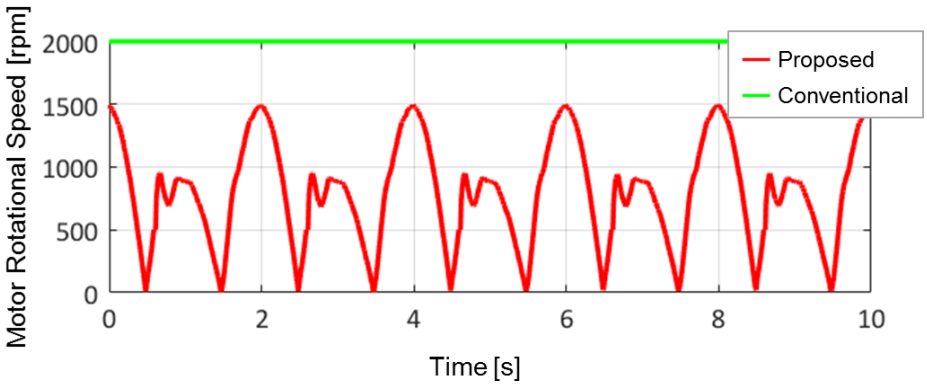

Figure 13. Motor demand rotational speed.

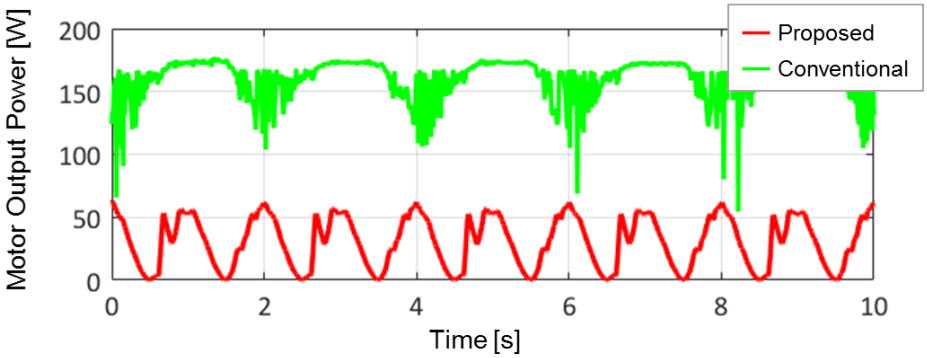

Figure 14. Motor output power.

The results show that the proposed system can achieve better trajectory tracking ability than the conventional system even when using the same responsive valve. Fig. 14 shows the motor output measured

by the motor controller. The maximum output of the proposed system is 61.9 W while that of the conventional system is 176.5 W. Thus, the proposed system can reduce the motor output by 64.9%.

3.2. Walking Simulation

The walking simulations for the proposed hydraulic direct-drive system are examined, and the simulation setup and results are discussed in sections 3.2.1 and 3.2.2, respectively.

We used a physical modeling tool, LMS Imagine.Lab Amesim™ (Siemens K.K.), to evaluate the hydraulic direct-drive system.

3.2.1. Simulation Setup

To evaluate the proposed system, we developed a biped humanoid robot model using the hydraulic direct-drive system. In this model, the proposed hydraulic system was applied to the hip pitch joint, which requires high torque and joint density, and involves a certain difficulty in mounting the drive system. Other joints in the model used the conventional electrical motor and mechanical drive system. The diagrammatic representation of the model is shown in Fig. 15, and the corresponding parameters are listed in Table 3.

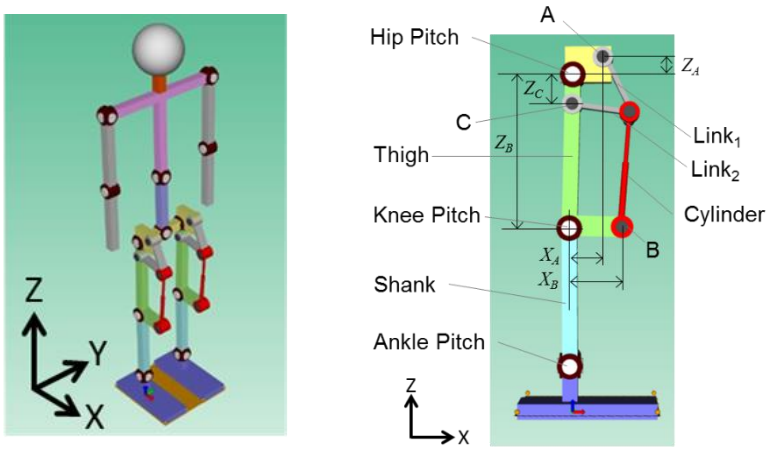

(a) Full body model *(b) Model parameters*

Figure 15. Mechanical model of the biped humanoid robot.

Table 3. Four-bar linkage mechanism parameters.

Length (mm)	Values
$Link_1$	119
$Link_2$	113
X_A	59
Z_A	34
X_B	100
Z_B	300
X_C	0
Z_C	57

The schematic of the constructed hydraulic model is shown in Fig. 16, the various pump efficiencies are shown in Fig. 17, and the hydraulic model and control parameters are listed in Table 4. The Valve 2

response of the proposed system was identified on the basis of the experimental results. The response characteristics of the motor connected to the pump unit were approximated by a second-order lag system, and the parameters were identified from the experimental results presented in section 3.1.

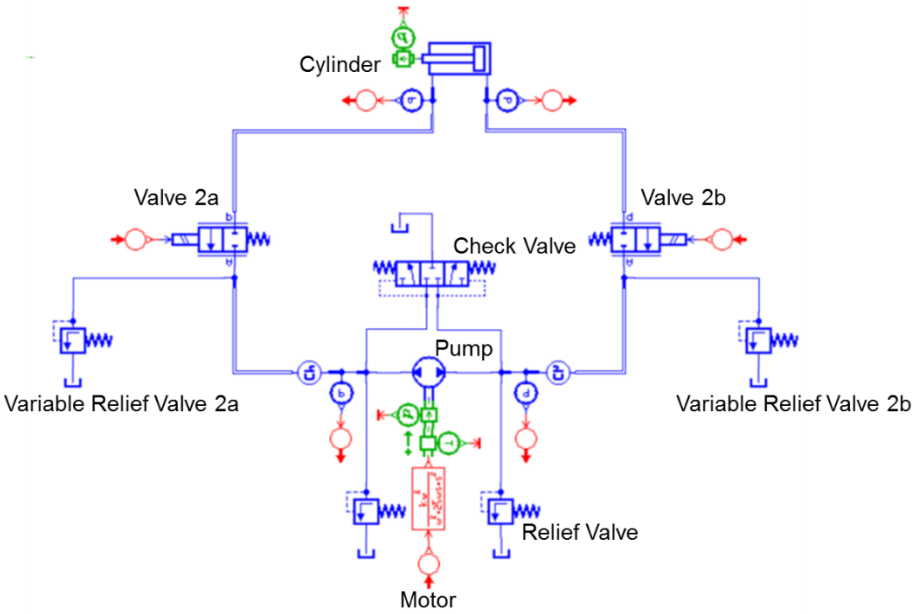

Figure 16. Hydraulic circuit model (LMS AMESim).

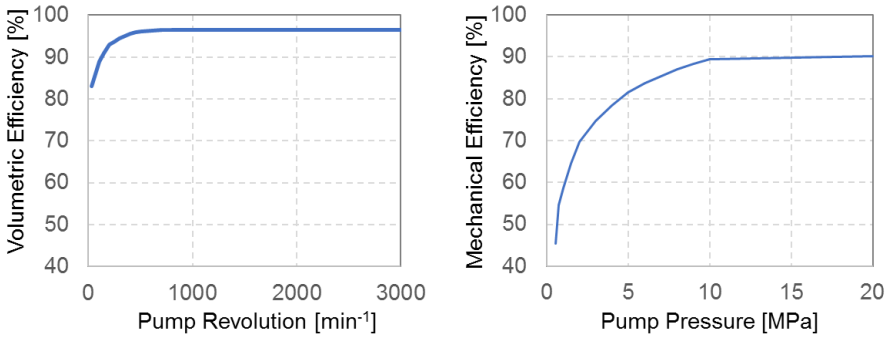

(a) Volumetric efficiency (b) Mechanical efficiency

Figure 17. Pump efficiencies.

Table 4. Four-bar linkage mechanism parameters.

Parameters	Values
Pump displacement (cc/rev)	1.6
Pump relief pressure (MPa)	21
Cylinder stroke (mm)	132
Cylinder piston diameter (mm)	22
Cylinder rod diameter (mm)	10
Valve 1 pressure loss (MPa/(L/min))	0.1/50
Valve 2 maximum area (mm^2)	10
Valve 2 response (Hz)	20
P gain	0.1
D gain	0.001

3.2.2. Simulation Results

The results of the walking simulations are shown in Fig. 18 and Fig. 19. Fig. 18 shows the walking motion of the biped humanoid robot model with the proposed hydraulic system, and Fig. 19 shows the position response of the right-leg cylinder during walking. These results show that the proposed hydraulic direct-drive system can follow the walking demand trajectory of the cylinder under the load of the walking motion.

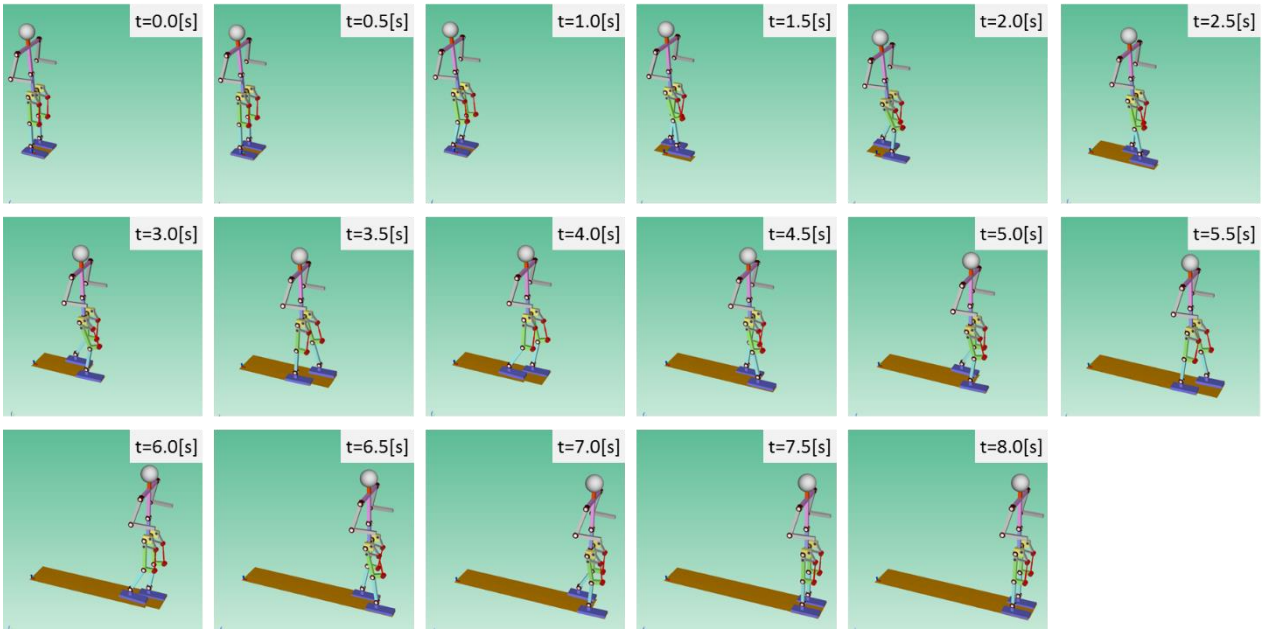

Figure 18. Walking motion of the mechanical model.

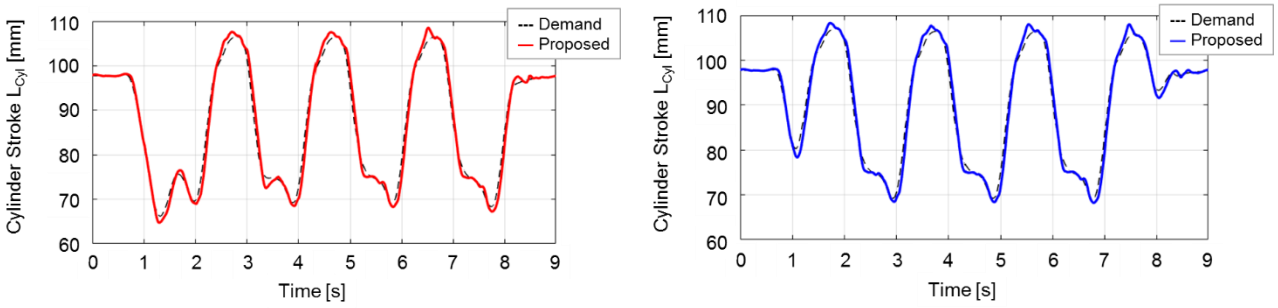

(a) Cylinder of the right leg (b) Cylinder of the left leg

Figure 19. Position time response.

4. CONCLUSION AND FUTURE WORK

In this study, a performance comparison of the hydraulic direct-drive system with the conventional system was conducted to validate the proposed configuration that used a single-rod cylinder. The results showed that good position-following capability was achieved with the proposed system. Furthermore, the motor output could be reduced by 64.9%. The results also showed that the proposed system contributes toward size reduction of the installed motor for biped humanoid robots.

In the simulations, we confirmed that walking along a predetermined path was possible with the proposed system, and the simulation model was thus tuned based on the experiment.

In the future, we intend to optimize the proposed scheme for obtaining suitable gains of the PD controller, and we intend to create a system that can share hydraulic power between the joints using the hydraulic

direct-drive system. We also intend to build a biped robot that incorporates these systems and to perform walking experiments.

5. ACKNOWLEDGMENT

This study was conducted with the support of the Research Institute for Science and Engineering of Waseda University and the Future Robotics Organization of Waseda University, and as a part of the humanoid project at the Humanoid Robotics Institute of Waseda University. This study was also financially supported in part by JSPS KAKENHI Grant No.17H00767. We would like to thank Editage (www.editage.jp) for English language editing.

REFERENCES

[1] Y. Ogura, K. Shimomura, H. Kondo, A. Morishima, T. Okubo, S. Momoki, H. O. Lim & A. Takanishi. 2006. Human-like Walking with Knee Stretched, Heel-contact and Toe-off Motion by a Humanoid robot. Proceedings of the 2006 IEEE/RSJ International Conference on Intelligent Robots and Systems, pp. 3976–3981.

[2] T. Otani, K. Hashimoto, S. Hamamoto, S. Miyamae, M. Sakaguchi, Y. Kawakami, H.O. Lim & A. Takanishi. 2015. Knee Joint Mechanism That Mimics Elastic Characteristics and Bending in Human Running. Proceedings of the 2015 IEEE/RSJ International Conference on Intelligent Robots and Systems, pp. 5156–5161.

[3] T. Otani, K. Hashimoto, S. Miyamae, H. Ueta, M. Sakaguchi, Y. Kawakami, H.O. Lim & A. Takanishi. 2017. Angular Momentum Compensation in Yaw Direction using Upper Body based on Human Running. Proceedings of the. 2017 IEEE International Conference on Robotics and Automation. pp. 4768–4775.

[4] J. Urata, Y. Nakanishi, K. Okuda & M. Inaba. 2010. Design of High Torque and High Speed Leg Module for High Power Humanoid. Proceedings of the 2010 IEEE/RSJ International Conference on Intelligent Robots and Systems, pp. 4497–4502.

[5] Y. Ito, S. Nozawa, J. Urata, T. Nkaoka, K. Kobayashi, Y. Nakanishi, K. Okada & M. Inaba. 2014. Development and Verification of Life-size Humanoid with High-output Actuation System. Proceedings of the 2014 IEEE International Conference on Robotics and Automation, pp. 3433–3438.

[6] I. Park, J. Kim, J. Lee & J. Oh. 2007. Mechanical Design of the Humanoid Robot Platform, HUBO. Advanced Robotics 21(11), pp. 1305–1322.

[7] Atlas | Boston Dynamics, https://www.bostondynamics.com/atlas, accessed 2018/12/15.

[8] S. Hyon, D. Suewaka, Y. Torii & N. Oku. 2017. Design and Experimental Evaluation of a Fast Torque-Controlled Hydraulic Humanoid Robot. IEEE/ASME Transactions on Mechatronics, pp.623-634.

[9] R. Rahmfeld & M. Ivantysynova. 1998. Energy Saving Hydraulic Actuators for Mobile Machines. Proceedings of the First Bratislavian Fluid Power Symposium, pp. 47–57.

[10] J. Zimmerman, E. Busquets & M. Ivantysynova. 2011. 40% Fuel Savings by Displacement Control Leads to Lower Working Temperatures – A Simulation Study and Measurements. Proceedings of the Fifty-Second National Conference on Fluid Power, pp. 693–701.

[11] H. Kaminaga, J. Ono, Y. Nakashima & Y. Nakamura. 2009. Development of Backdrivable Hydraulic Joint Mechanism for Knee Joint of Humanoid Robots. Proceedings of the 2009 IEEE International Conference on Robotics and Automation, pp. 1577–1582.

[12] J. Shimizu, T. Otani, K. Hashimoto & A. Takanishi. 2018. Downsizing the Motors of a Biped Robot Using a Hydraulic Direct Drive System. Proceedings of the 2018 IEEE-RAS International Conference on Humanoid Robots, pp. 580–586.

[13] Takako Industries, INC., http://www.takako-inc.com/, accessed 2018/12/15.

MODEL PREDICTIVE PATH TRACKING CONTROL WITH OFF-AXLE REFERENCE POINT FOR CAR-LIKE ROBOTS

Ilja Stasewitsch, Tobias Blume, Jan Schattenberg, Ludger Frerichs
Institut für mobile Maschinen und Nutzfahrzeuge, Technische Universität Braunschweig
Langer Kamp 19a
38106 Braunschweig
i.stasewitsch@tu-braunschweig.de

ABSTRACT

Two path tracking controls are presented for car-like robots with a reference point which is offside of the robot's pivot point. This offset reference point is called as off-axle reference point. One control method is the linear model predictive path tracking control and the other one is the nonlinear model predictive path tracking control. These controls are implemented and tested in a simulation environment. The nonlinear model predictive control is validated at a test vehicle. In this system a tractor (Fendt 724) is coupling automatically to an implement by using the presented controls.

KEYWORDS: Off-axle path tracking control, Mobile robot control, nonlinear model predictive control, linear model predictive control, Implement coupling, Driver assistant system

1. INTRODUCTION

The latest trend is the development and use of more driver assistant system in off-road machines. We designed in the last years a driver assistant system which is coupling a tractor to an implement by the three-point hitch. This system, which is using a backward-looking stereo vision or a time-of-flight camera, is already descripted in [1] and [2]. The tasks in this system and in general in mobile robotics are path planning, path tracking, localization, mapping and collision avoidance. In this paper we will present the developed model predictive path tracking controls for this system. The control loop therefore is showed in Figure 1. The special feature on this path tracking control is that the reference point is offside of the vehicle's pivot point, called from now on as off-axle reference point. For a mobile robot with Ackermann front steering the vehicle's pivot point is in the rear axle. For path tracking most of the existing control methods were applied in the last three decades in the literature. Table 1 is giving a literature overview for path tracking control. These methods are only covering the special case in which the reference point is the vehicle's pivot point. To the author's knowledge, there are existing two different implemented control methods with off-axle reference point presented by [3], [4]: discrete linear quadratic tracker and LQR control. But because of high performance requirements for our driver assistant system we chose to develop model predictive controls instead of the methods existed in literature. We defined that the control error in the end point of the path has to be less than $\pm 3\ cm$ for the lateral error and less than $2.5°$ for the orientation error. If there would not be any localization error between the tractor and implement, then the path tracking errors could be higher. But according to [5] the localization error in the end point between the tractor and implement is total up to ±2 cm for the lateral error and 1.5° for the orientation error.

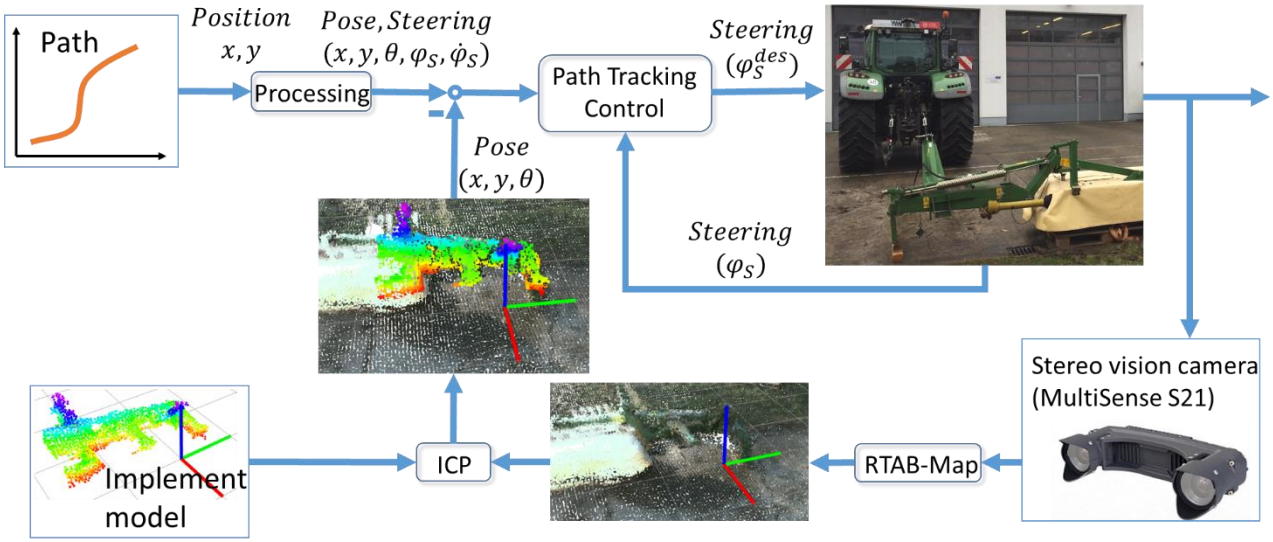

Figure 1. Schematic Overview of the Implemented Closed-Loop Control for the Coupling Driver Assistant System

Firstly, we tried to use a flatness-based path tracking control [6] from a car parking assistant of the automotive industry since this task is similar to the coupling of a tractor and an implement. But this control is for an on-axle reference point and is not satisfied. We presented this control approach in [5] and [7]. To overcome the inadequate control performance the model predictive control were considered as an appropriate method. Because it can use all kind of nonlinear models (no need of a flat output), is doing a predication on the path and can consider limits of the system like the maximal steering angle. In this paper we will present the used linear model predictive path tracking control (LMPPTC) and nonlinear model predictive path tracking control (NMPPTC) with off-axle reference point. We already outlined the NMPPTC in [2], but no results of the control performance as well no comparison of different control methods were shown. Figure 2 is depicting that a path tracking control with off-axle reference point is then necessary if the working tool is offside of the vehicle's pivot point. This is often the case in off-road machines like for agricultural machines, building machines, municipal vehicles or forklift trucks. The paper is structured as followed. In section 2 the control methods and the systems are explained. The results are shown in section 3 and the discussion as well as the conclusion is followed by section 4.

Table 1. Literature Overview for Path Tracking Control Segmented by Control Methods

Method	Exemplary References
PID-Control	[8], [9]
Adaptive Control	[10], [11]
Fuzzy-Logic Control	[12], [13]
Neural Network Based Control	[14], [15]
Robust Control	[16], [17]
State Control	[18], [9],
Flatness-Based Control	[6], [19]
Model Predictive Control	[20], [21]
Sliding Model Control	[22], [23]

Figure 2. Off-Road Machines with Tools offside of the Vehicle's Pivot Point without an Additional Hinge

2. MATERIALS AND METHODS

The Figure 1 and Figure 3 are depicting the developed assistance system. A stereo vision camera (MultiSense S21) is mounted on the roof of the Fendt 724 and is backward-looking. A path between the tractor's three-point hitch and the implement is calculated which is afterwards processed to calculate the pose, the steering angle and the steering rate (see section 2.2). The pose between the tractor and the implement, meaning the localization, is calculated by building up a 3D-map of the environment by using RTAB-Map (see [24]), which is a graph-based SLAM, and the iterative closest point algorithm (ICP) (see [25]). The point cloud model of the implement is taken from the database. The ICP is used to match the implement model into the 3D-Map to obtain the desired position and orientation between the tractor and the implement. The localization error is an error chain of the localization in the map by the RTAB-map and the relative pose between the tractor and the implement by the ICP. A big challenge is according to [2] to find a starting solution of the ICP, so that it can converge in the correct solution. As already mentioned, we have developed the LMPPTC and the NMPPTC (see section 2.3) with off-axle reference point. A kinematic model (see section 2.1) is used in these approaches. The control loops were developed firstly in a simulation and afterwards tested on the test vehicle Fendt 724 (see section 2.4).

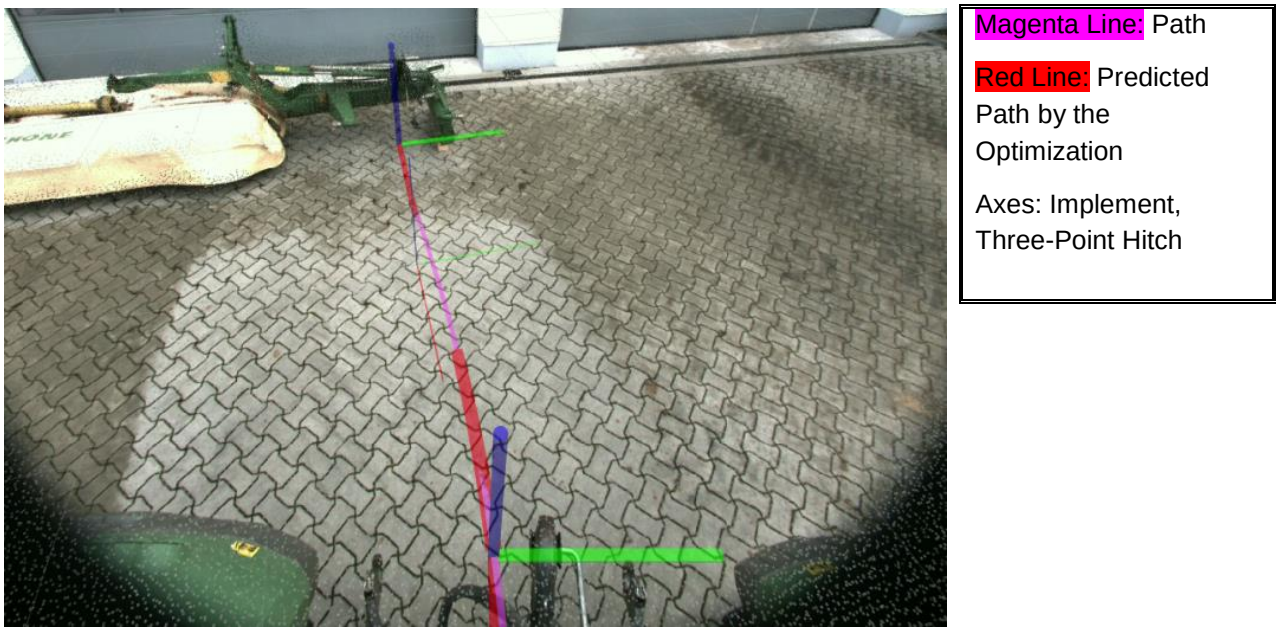

Figure 3. Backward-Looking 2D-Camera Image of the Stereo Vision Camera with Illustration of the Paths and Axes During a Coupling to a Mower

2.1. System Modelling

The design of a model predictive control needs a system model. The considered system in this paper is a robot with an Ackermann steering in the front axle, common called car-like robot in the literature. The system as a kinematic single track model is depicted in the Figure 4. The equation (1) describe the kinematic motion of a robot with an Ackermann steering with off-axle control point:

$$\boldsymbol{f}(\boldsymbol{x},u)=\begin{pmatrix}\dot{x}\\ \dot{y}\\ \dot{\theta}\\ \dot{\varphi}_S\\ \dot{\varphi}_S^{des}\end{pmatrix}=\begin{pmatrix}\frac{v_R}{l_W}\cos\theta-\ v_R\frac{l_O}{l_W}\tan\varphi_S\sin\theta\\ \frac{v_R}{l_W}\cos\theta+\ v_R\frac{l_O}{l_W}\tan\varphi_S\cos\theta\\ \frac{v_R}{l_W}\tan\varphi_S\\ \frac{1}{T_{Steer}}(\varphi_S^{des}-\varphi_S)\\ u\end{pmatrix}. \tag{1}$$

x, y and θ describe the position and the orientation of the reference point in the x-y plane. The steering is modelled in equation (1) as a first-order lag element with φ_S as the steering angle and φ_S^{des} as the desired steering angle. The control input u is the desired steering angular velocity $\dot{\varphi}_S^{des}$, so that the system has an integral behaviour and additionally the rate of the steering rate can be limited and considered by the optimization algorithm. Because only the steering is used as the control variable without the velocity the control is a SIMO system. But the velocity could be controlled by another separated control loop.

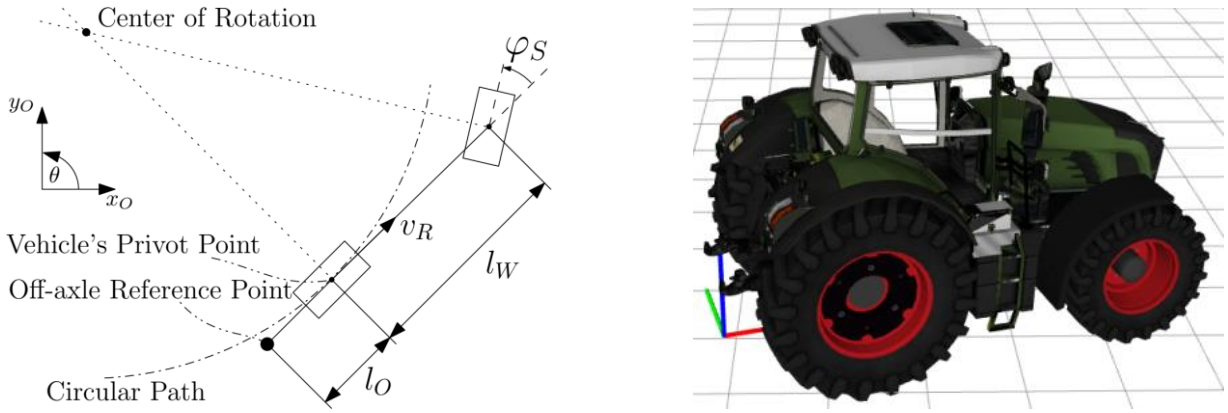

Figure 4. Sketch of the Kinematic Single Track Model with Off-Axle Reference Point Clarified with a Virtual Vehicle

The geometric parameters are listed in Table 2. For the control of the test vehicle it was necessary to model the tractor's steering as a first-order lag element. The parameter $T_{steer}=0.38$ s in equation (1) was determined manually by the step response which is showed in Figure 5. To use the model of the equations (1) in a model predictive control it is necessary to discretize the model. A discretization of equations (1) lead to the following state space representation by using Euler explicit:

$$\boldsymbol{f_{k+1}}(\boldsymbol{x}(k),u(k))=\begin{pmatrix}x(k+1)\\ y(k+1)\\ \theta(k+1)\\ \varphi_S(k+1)\\ \varphi_S^{des}(k+1)\end{pmatrix}=\begin{pmatrix}x(k)+h\left(\frac{v_R}{l_W}\cos\theta(k)-\ v_R\frac{l_O}{l_W}\tan\varphi_S(k)\sin\theta(k)\right)\\ y(k)+h\left(\frac{v_R}{l_W}\sin\theta(k)+\ v_R\frac{l_O}{l_W}\tan\varphi_S(k)\cos\theta\ (k)\right)\\ \theta(k)+h\ \frac{v_R}{l_W}\tan\varphi_S(k)\\ \varphi_S(k)+h\ \frac{1}{T_{Steer}}(\varphi_S^{des}(k)-\varphi_S(k))\\ \varphi_S^{des}(k)+h\,u(k)\end{pmatrix}. \tag{2}$$

Eq. (2) has to be linearized for the LMPPTC, for which the small-angle approximation ($\sin(x)=x$, $\cos(x)=1$) was used:

$$\boldsymbol{f_{k+1}}(\boldsymbol{x}(k), u(k)) = \begin{pmatrix} x(k+1) \\ y(k+1) \\ \theta(k+1) \\ \varphi_S(k+1) \\ \varphi_S^{des}(k+1) \end{pmatrix} = \begin{pmatrix} x(k) + h\left(\frac{v_R}{l_W} - v_R \frac{l_O}{l_W} \varphi_S(k)\theta(k)\right) \\ y(k) + h\left(\frac{v_R}{l_W}\theta(k) + v_R \frac{l_O}{l_W}\varphi_S(k)\right) \\ \theta(k) + h\ \frac{v_R}{l_W}\varphi_S(k) \\ \varphi_S(k) + h\ \frac{1}{T_{Steer}}(\varphi_S^{des}(k) - \varphi_S(k)) \\ \varphi_S^{des}(k) + h\ u(k) \end{pmatrix}. \quad (3)$$

Table 2. Geometric Constant Parameters of the Test Vehicle Fendt 724

Parameter Description	Symbol	Value
Wheelbase	l_W	2.78 m
Offset Length	l_O	-1.17 m
Steering Time Constant	T_{steer}	0.38 s
Velocity at the Rear Axle	v_r	-0.3 … -0.1 m/s

2.2. Path Processing

The mostly path planning algorithms calculate the path for the robot's pivot point. This is the rear axle for the considered system with a Ackermann front steering (see Figure 4), so that the path is given by $x_R(i)$, $y_R(i)$ with i as the path index. The derivation of x_R and y_R can be calculated by

$$x_R'(s) = \frac{dx_R(s)}{ds} \approx \frac{\Delta x_R}{\Delta s}, \qquad y_R'(s) = \frac{dy_R(s)}{ds} \approx \frac{\Delta y_R}{\Delta s}, \quad (3)$$

where the difference of the arc length Δs is defined by

$$\Delta s = \sqrt{\Delta x^2 + \Delta y^2} \text{ with } \Delta x = x(i+1) - x(i) \text{ and } \Delta y = y(i+1) - y(i). \quad (4)$$

The second derivation of x_R and y_R is provided by

$$x_R''(s) \approx \frac{\Delta x_R'}{\Delta s}, \qquad y_R''(s) \approx \frac{\Delta y_R'}{\Delta s}. \quad (5)$$

Through the first and second derivation of the path points x_R', y_R', x_R'', y_R'' the curvature κ can be calculated by

$$\kappa(s) = \frac{x_R'\, y_R'' - x_R''\, y_R'}{\left(x_R'^{\,2} + y_R'^{\,2}\right)^{\frac{3}{2}}}. \quad (6)$$

The steering angle $\varphi_S(s)$ is calculated by the help of the path curvature

$$\varphi_S(s) = \operatorname{atan}(\kappa\ l_W\ ). \quad (7)$$

For the LMPPTC it is necessary to calculate the time derivation of the steering angle velocity $\dot{\varphi}_S(t)$. For this, the derivation of the steering angle according to the arc length has to be determined

$$\varphi_S'(s) = \frac{\mathrm{d}\varphi(s)}{\mathrm{d}s}\frac{\mathrm{d}t}{\mathrm{d}t} \approx \frac{\Delta\varphi(s)}{\Delta s}\frac{\Delta t}{\Delta t} = \frac{\Delta\varphi(s)}{\Delta t}\frac{\Delta t}{\Delta s} \quad (8)$$

With the fixed rear-axle velocity $v_R = \Delta s\ /\ \Delta t$ the steering angle velocity $\dot{\varphi}_S(t)$ can be calculated:

$$\dot{\varphi}_S(t) = \varphi_S'(s) v_R \approx \frac{\Delta\varphi(s)}{\Delta s} v_R. \quad (9)$$

The orientation of the off-axle reference point coincide with the orientation in the rear-axle due to the rigid vehicle's longitudinal axis:

$$\theta(s) = atan2(\Delta y_R, \Delta x_R). \quad (10)$$

The path is calculated for the offset, meaning the off-axle reference point, by

$$x_O = x_R + l_O \sin\theta \qquad y_O = y_R + l_O \cos\theta. \tag{11}$$

The variables $x(s)$, $y(s)$, $\theta(s)$, and $\varphi(s)$ can be used as the time depending variables $x(t)$, $y(t)$, $\theta(t)$ and $\varphi(t)$ for the presented model predictive controls.

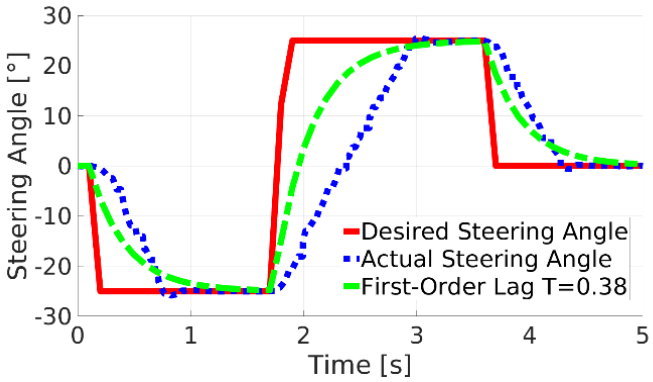

Figure 5. Step Response of the Tractor's Steering and the Steering Model for the Determination of T_{Steer}

2.3. Model Predictive Control

Model predictive control (MPC) is a class of nonlinear control methods, which are generally usable for linear control systems with limits for control and state variables as well as for nonlinear control systems. It is e.g. described detailed in [26]. The functionality of MPC is based on using process models which consists of ordinary differential equation. The model allows the prediction of future behaviour. This possibility is used by MPC by optimizing the output variables online through manipulating the control variables. Linear MPC can be used with linear models or with time-varying models formulated in state space representation. For the LMPPTC a time-varying model is used by linearization of the Equation (2) using the Taylor series. The developed algorithm is based on [20]. Nonlinear MPC is one of few nonlinear control methods. The straightforward design process compared with other nonlinear model based control method allows to handle process models with several or even many inputs and outputs. As a benefit no flat output has to be determined, so that it can handle every model which consists of ordinary differential equation. The drawback is that a global optimum of the optimization cannot be guaranteed due to the nonlinear models in the formulation do not lead to a convex optimization. Calculation within real-time requirements is another challenge and the mathematically not provable stability of this control law is another disadvantage.

2.4. Simulation and Test Vehicle Details

The simulation model is build up in Python with an interface to the Robot Operating System (ROS). The system equations (1) were used with a step size amounting to $h = 5\,ms$. As middleware, ROS communicates with various software packages and is used on the test vehicle Fendt 724 (see [27]). This approach has the benefit that the control can be designed with the simulation model and afterwards be tested easily on the Fendt 724. The ROS node of the simulation model has just to substitute with the test vehicle, but all other ROS nodes can be used without difficulties. The steering and drive are controlled at the Fendt 724 via a CAN interface. As a note, the pose of the reference point is known perfectly in the simulation so that no uncertainties are added to pose. The path in the simulation is a parameterized B-Spline by using the Python library SciPy. For coupling the test vehicle to the implement a G²-spline from [28] was used to get a minimal curvature in the path. The path is transformed into the robot's coordinate system to overcome the problem in the orientation of $\pm 180°$. The LMPPTC was realized in Python and using the modules *numpy* for matrix handling and *quadprog* as the optimization algorithm (see [29]). The online calculation of the matrices and the execution of optimization algorithm is done by multithreading to achieve real-time execution. The C++ library ACADO Toolkit [30] was used for the implementation of the NMPPTC. The library calculates the required matrices for the optimization

offline, which otherwise have to be computed online. This is usually the bottleneck in a nonlinear model predictive control.

3. RESULTS

This section is divided into two parts: simulation results (see section 3.1) and real vehicle's results (see section 3.2). Due to slightly better results of the NMPPTC compared to the LMPPTC in the simulation only the results of the NMPPTC are showed for the test vehicle.

3.1. Simulation Results

The simulation results are used to show the control performance of both control strategies without any further disturbances like localization errors and nonlinearities in the test vehicle steering. The simulation results for the LMPPTC are depicted in Figure 6. The position error is weighted with $q_{xy} = 3$, the orientation error is weighted with $q_\theta = 1$ and the control is unweighted with $R = 0$. The steering angle was limited according the physical limit of the test vehicle: $-35° \leq \varphi_S \leq 35°$. The control input u, so the desired steering angular velocity, is also limited: $-10°/s \leq u \leq 10°/s$. The velocity in the rear-axle v_r is set to $v_r = -0.3\ m/s$, the step size h is set to $h = 0.1\ s$ and the prediction arc length L is set to $L = 1\ m$, so that the prediction steps and control steps are set to

$$n_c = n_p = \frac{L}{v_R\ h} = 30. \tag{12}$$

It can be seen that the control strategy is not violating the limits of the control inputs, except at $1\ m$ driving length at which the limits have to be loosen due to infeasibility in the optimization because the path has a discontinuity at this point. The steering angle is also not violated but it is not necessary for the control. The position tracking error is smaller than 1 cm in the end point. The error is calculated as the smallest Euclidian distance to the path, but the path is discretized with a difference in the arc length of $3\ cm = |v_R|\ h$, so that the path tracking error can be $1.5\ cm$ if even the tracking is perfectly. The positive summary is that the LMPPTC is suitable for the coupling driver assistant system due to the small error in the path tracking.

The simulation results for the NMPPTC are depicted in Figure 7 using the same parameter settings like for the LMPPTC. It is obvious that the path tracking is nearly perfect, only the difference of the simulation step size of $h = 5\ ms$ and the control step size of $h = 0.1\ s$ leads to an oscillating signal in the steering angle. The path tracking error is less than $1.5\ cm$ but taking into account that the path discretization is amounting to $3\ cm$. This control strategy is even more appropriate than the LMPPTC for the driver assistant system according the simulation analysis.

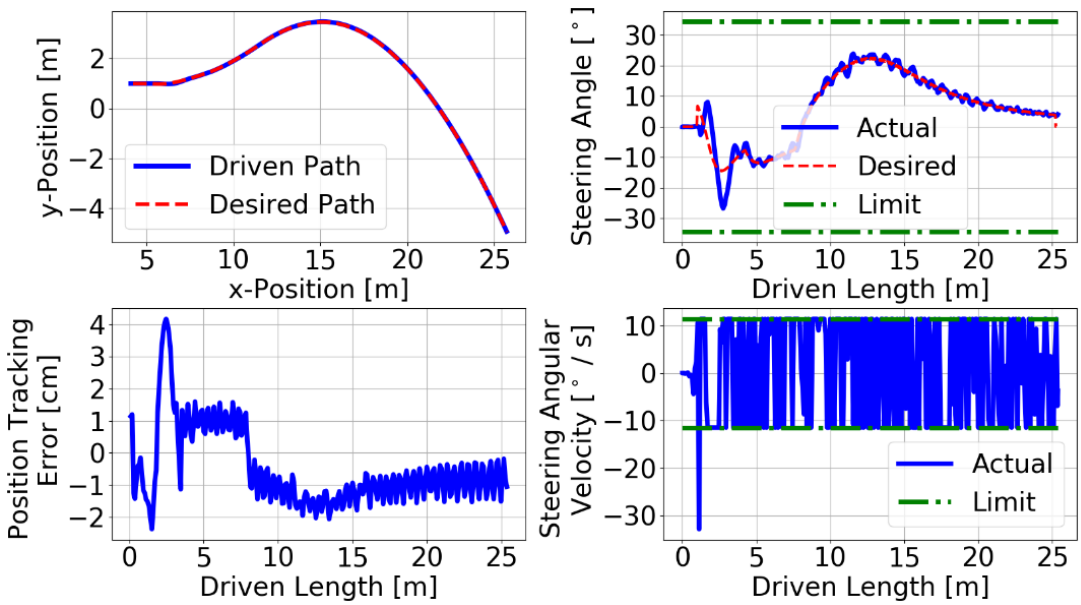

Figure 6. Simulation Results of the Linear Model Predictive Path Tracking Control

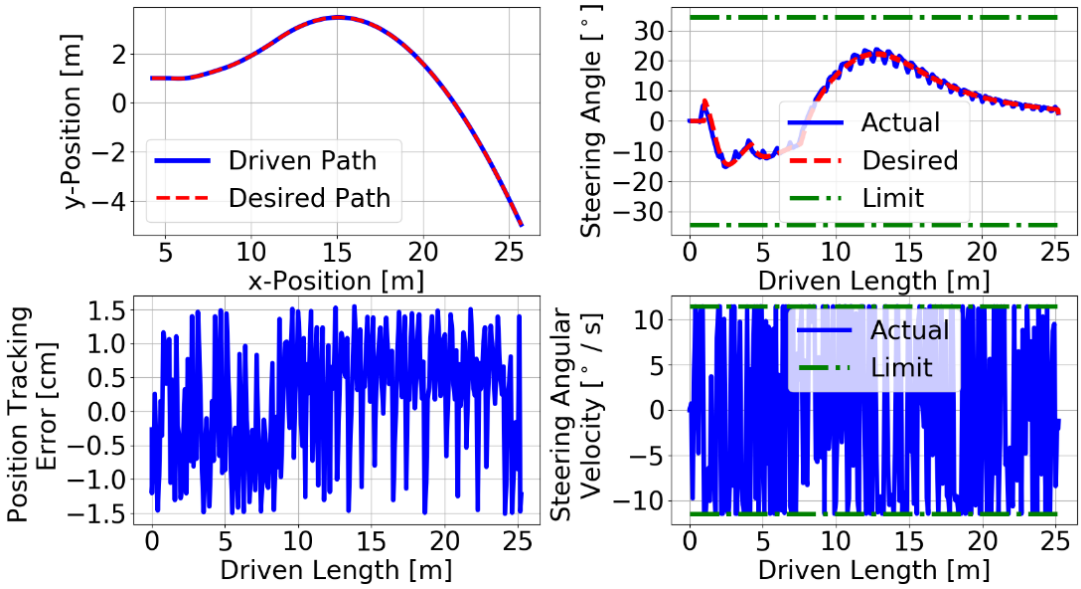

Figure 7. Simulation Results of the Nonlinear Model Predictive Path Tracking Control (NMPPTC)

3.2. Test Vehicle's Results

In Figure 8 an experiment is shown in which the localization between the test vehicle and implement has abrupt changes. In this experiment the velocity of the rear axle is set to $v_R = -0.1$ by contrast to the simulation experiments so that the path discretization is amounting to $1\,cm$. All other parameters are adequate to the simulation result: $L = 1\,m$, $q_{xy} = 3$, $q_\theta = 1$ and $R = 0$. Because of the change in the velocity the prediction steps and control steps are set to $n_c = n_p = 100$. The optimization algorithm does not violate the limitation of the steering angle. The limitation of the desired steering angle velocity is not represented, but is also not violated. The localization discontinues are up to 10 cm. For the path tracking the driven path is oscillating around the desired path. The increased position change in the beginning lead to a high steering angle in the control so that the perspective of the camera changed. This change in perspective again led to a localization error and the controller again uses a high steering angle to eliminate the localization error and the localization error is repeating again. But in spite of these localization position discontinuities the path tracking error is in

the end point less than $2\ cm$ for the distance error and less than $2°$ for the orientation error. Due to the adherence to the maximum permissible errors the coupling was successful.

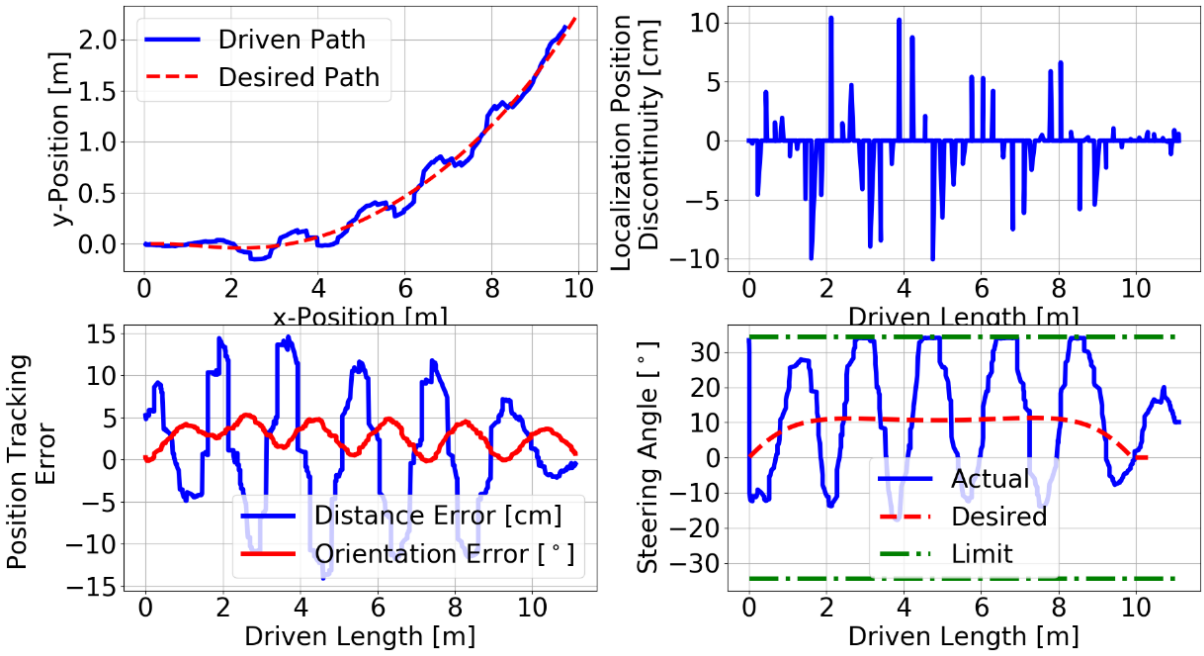

Figure 8. Results of the Nonlinear Model Predictive Path Tracking Control (NMPPTC) with Abrupt Changes in the Localization

In Figure 9 another experiment is presented which was also recorded with the test vehicle. The parameters for this experiment are in agreement with the experiment from Figure 8. The only difference is the starting position of the vehicle, which is on the opposite side of the implement. This perspective of the camera provide a stable localization with only one abrupt change larger than $5\ \mathrm{cm}$ in the beginning of the tracking. The path tracking error is in the end point less than $1\ cm$ for the distance error and less than $2°$ for the orientation error. Due to the adherence to the maximum permissible errors the coupling was successful again.

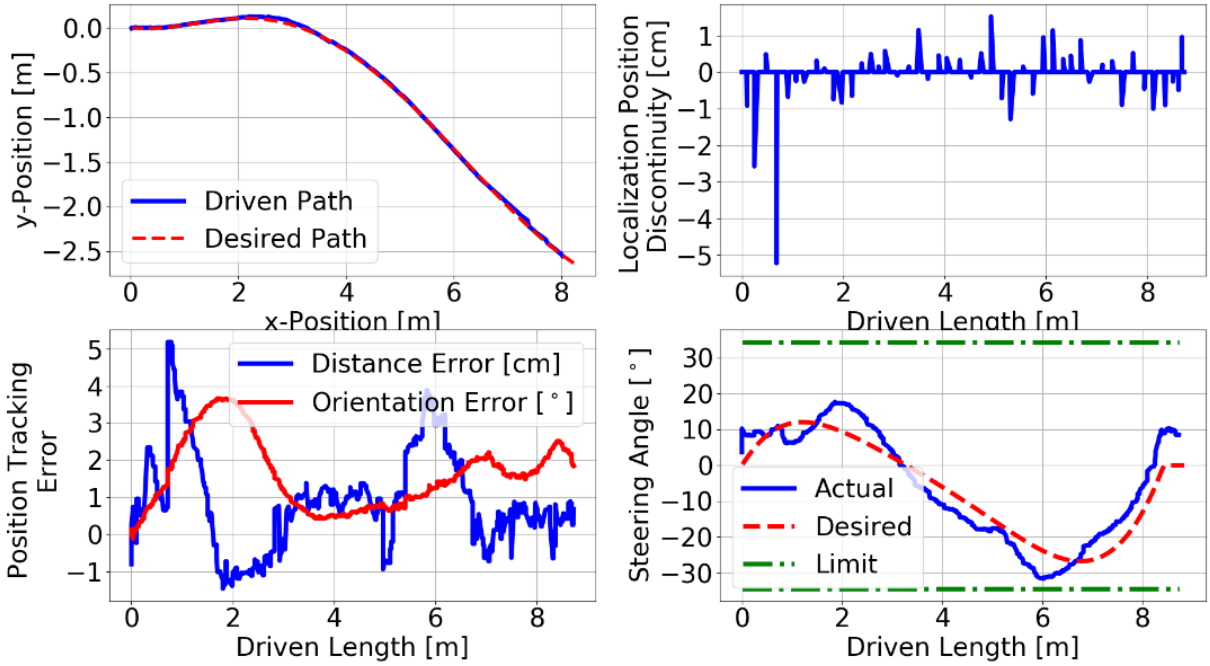

Figure 9. Results of the Nonlinear Model Predictive Path Tracking Control (NMPPTC) with a Stable Localization

4. DISCUSSION AND CONCLUSION

The simulation results and the test vehicle's results are showing that model predictive control is suitable for a path tracking control with off-axle reference point. The presented application, the coupling of a tractor with an implement, demands high requirements to the path tracking. The distance error is defined to be less than $3\ cm$ and the orientation error less than $2.5°$ in the end point. Both control methods, the LMPPTC and the NMPPTC, are suitable regarding to the simulation results for these requirements. The test vehicle's results validate that this requirements are met even with larger localization errors. But the disadvantage of model predictive control is the high computation effort. In this contribution the stability of the controller was not examined and no further technics were applied to ensure that. Other control methods like feedback linearization, sliding-mode control and LQR control can be sufficient and can be applied more likely on embedded systems. Simple PID-controls cannot be used for a negative offset because the linearized system is showing a positive zero, which lead to a non-minimum phase system. But sliding-mode control or LQR control with a feedback linearization could lead to a similar performance. This research gap will be examined.

ACKNOWLEDGMENT

The project was supported by funds of the German Government's Special Purpose Fund held at Landwirtschaftliche Rentenbank.

REFERENCES

[1] Blume, T., Schattenberg, J., & Frerichs, L. (2015). Innovative Assistance Systems based on a Backward-Looking 3D-Time of Flight Camera. In *73rd International Conference on Agricultural Engineering LAND. TECHNIK AgEng* (Vol. 2, No. 15, pp. 5-5).

[2] Blume, T., Stasewitsch, I., Schattenberg, J., & Frerichs, L. (2018). Object recognition and position determination in agriculture using the example of a coupling assistant. *LANDTECHNIK–Agricultural Engineering*, *73*(1).

[3] Bell, T. (1999). Precision robotic control of agricultural vehicles on realistic farm trajectories. Stanford university.

[4] Bell, T. (2000). Automatic tractor guidance using carrier-phase differential GPS. Computers and electronics in agriculture, 25(1-2), 53-66.

[5] Blume, T., Stasewitsch, I., Schattenberg, J., & Frerichs, L. Automated tractor/implement coupling based on a backward-looking 3D-Time-of-Flight Camera. MCG 2016

[6] Müller, B., & Deutscher, J. (2007, July). Orbital tracking control for car parking via control of the clock using a nonlinear reduced order steering-angle observer. In Control Conference (ECC), 2007 European (pp. 1917-1924). IEEE.

[7] Stasewitsch, I., Blume, T., Harms, H., Schattenberg, J., & Frerichs, L. A Low-Speed Flatness-Based Path Tracking Control with the Time-Scaling Concept for Different Types of Steering and Drive for the Robot Operating System. *MCG 2016*

[8] Barton, M. J. (2001). Controller development and implementation for path planning and following in an autonomous urban vehicle. Undergraduate thesis, University of Sydney.

[9] Rajamani, R. (2011). Vehicle dynamics and control. Springer Science & Business Media.

[10] Netto, M. S., Chaib, S., & Mammar, S. (2004, June). Lateral adaptive control for vehicle lane keeping. In American Control Conference, 2004. Proceedings of the 2004 (Vol. 3, pp. 2693-2698). IEEE.

[11] Byrne, R. H., & Abdallah, C. T. (1995). Design of a model reference adaptive controller for vehicle road following. Mathematical and computer modelling, 22(4-7), 343-354.

[12] Sugeno, M., & Murakami, K. (1984). Fuzzy parking control of model car. In Decision and Control, 1984. The 23rd IEEE Conference on (Vol. 23, pp. 902-903). IEEE.

[13] Ollero, A., García-Cerezo, A., & Martínez, J. L. (1994). Fuzzy supervisory path tracking of mobile reports. Control Engineering Practice, 2(2), 313-319.

[14] Watanabe, K., Tang, J., Nakamura, M., Koga, S., & Fukuda, T. (1996). A fuzzy-Gaussian neural network and its application to mobile robot control. IEEE transactions on control systems technology, 4(2), pp. 193-199.

[15] Yoo, S. J., Choi, Y. H., & Park, J. B. (2006). Generalized predictive control based on self-recurrent wavelet neural network for stable path tracking of mobile robots: adaptive learning rates approach. IEEE Transactions on Circuits and Systems , 53(6), pp. 1381-1394.

[16] O'Brien, R. T., Iglesias, P. A., & Urban, T. J. (1996). Vehicle lateral control for automated highway systems. IEEE Transactions on Control Systems Technology, 4(3), 266-273.

[17] Emam, M., & Fakharian, A. (2017). Solving Path Following Problem for Car-Like Robot in the Presence of Sliding Effect via LMI Formulation. Journal of Computer & Robotics, 10(2), 11-22.

[18] Bell, T., O'Connor, M., Jones, V. K., Rekow, A., Elkaim, G., & Parkinson, B. (1998). Realistic autofarming closed-loop tractor control over irregular paths using kinematic GPS. The Journal of Navigation, 51(3), pp. 327-335.

[19] Snider, J. M. (2009). Automatic steering methods for autonomous automobile path tracking. Robotics Institute, Pittsburgh, PA, Tech. Rep. CMU-RITR-09-08.

[20] Kuhne, F., Lages, W. F., & da Silva Jr, J. G. (2004). Model predictive control of a mobile robot using linearization. In Proceedings of mechatronics and robotics (pp. 525-530).

[21] Raffo, G. V., Gomes, G. K., Normey-Rico, J. E., Kelber, C. R., & Becker, L. B. (2009). A predictive controller for autonomous vehicle path tracking. IEEE transactions on intelligent transportation systems, 10(1), 92-102.

[22] Yang, J. M., & Kim, J. H. (1999). Sliding mode control for trajectory tracking of nonholonomic wheeled mobile robots. IEEE Transactions on robotics and automation, 15(3), pp. 578-587.

[23] Solea, R., & Nunes, U. (2007). Trajectory planning and sliding-mode control based trajectory-tracking for cybercars. Integrated Computer-Aided Engineering, 14(1), 33-47.

[24] Labbé, M., & Michaud, F. (2018). RTAB-Map as an Open-Source Lidar and Visual SLAM Library for Large-Scale and Long-Term Online Operation. Journal of Field Robotics. (pp. 1–31). Wiley

[25] Besl, P. J., & McKay, N. D. (1992, April). Method for registration of 3-D shapes. In Sensor Fusion IV: Control Paradigms and Data Structures (Vol. 1611, pp. 586-607). International Society for Optics and Photonics.

[26] Grüne, L., & Pannek, J. (2017). Nonlinear model predictive control. In *Nonlinear Model Predictive Control* (pp. 45-69). Springer, Cham.

[27] Quigley, M., Conley, K., Gerkey, B., Faust, J., Foote, T., Leibs, J. & Ng, A. Y. (2009, May). ROS: an open-source Robot Operating System. In ICRA workshop on open source software (Vol. 3, No. 3.2, p.5).

[28] Bianco, C. G. L., & Piazzi, A. (2000). Optimal trajectory planning with quintic G/sup 2/-splines. In Intelligent Vehicles Symposium, 2000. IV 2000. Proceedings of the IEEE (pp. 620-625). IEEE.

[29]Goldfarb, D., & Idnani, A. (1983). A numerically stable dual method for solving strictly convex quadratic programs. Mathematical programming, 27(1), 1-33.

[30] Houska, B., Ferreau, H. J., & Diehl, M. (2011). ACADO toolkit—An open-source framework for automatic control and dynamic optimization. Optimal Control Applications and Methods, 32(3), 298-312.

DESIGN AND IMPLEMENTATION OF PRESSURE FEEDBACK FOR LOAD-CARRYING APPLICATIONS WITH POSITION CONTROL

Daniel Hagen, Damiano Padovani, Martin Choux
University of Agder, Department of Engineering Sciences
Jon Lilletunsvei 9, 4879 Grimstad, NORWAY
E-mail: daniel.hagen@uia.no

ABSTRACT

This research paper presents the design and implementation of pressure feedback on a hydraulically actuated single-boom crane operated in closed-loop position control. It is well known that systems with pressure compensated proportional valves in combination with over-center valves tend to induce instability, especially when the external load is overrunning (e.g., while lowering a load). However, in some applications pressure oscillations arise also with resistant external loads (e.g., while lifting a load). Hence, a pressure feedback capable of stabilizing the system functioning in both operations using the pressures from both actuator chambers (i.e., piston-side and rod-side) is proposed and compared against the conventional solution using only the rod-side chamber pressure. The investigation demonstrates that the implementation of a proposed "inverse valve dynamic" algorithm is needed in order for the control valve to stabilize the system when introducing the piston-side pressure in the pressure feedback. With this new method, the experimental tests demonstrate a satisfactory reduction of the pressure fluctuations in closed-loop motion control and a good position tracking (the average position error while lowering the load is reduced by almost 90% compared to the original system without pressure feedback). Finally, simulated results show that the proposed pressure feedback allows for potential energy savings of about 50% when lowering the load.

KEYWORDS: Over-center valves, pressure compensated proportional valves, active-damping, pressure feedback, position control, energy saving.

1. INTRODUCTION

The hydraulic circuits of load-carrying applications must contain passive load-holding devices to meet safety regulations. A popular load-carrying solution makes use of pressure-compensated Proportional Directional Control Valves (PDCVs) in combination with Over-Center Valves (OCVs). This is considered state-of-the-art in many industrial fields (e.g., in knuckle-boom cranes for offshore applications) due to the load-independent flow control and reduced system cost. Nevertheless, this approach tends to introduce an oscillatory behavior, or even instability, that undermines both performance and operational safety. Several investigations were carried out to mitigate this issue, especially when dealing with overrunning loads. Optimizing the design parameters [1] is today a common approach that often requires hardware reconfiguration [2] (e.g., adjusting the pilot ratio of the OCV's, increasing the volumes in hydraulic lines related to the OCV pilot pressure and/or the load-sensing pilot pressure of the PDCV's compensator). An alternative is introducing active damping to compensate for oscillations. An overview of active damping focused on hydraulically actuated mobile applications is presented in [3]. This solution is usually referred to as Pressure Feedback (PF) and may involve closed-loop control of the PDCV's spool position [4]. In [5], a high-pass filter is implemented in the PF of a

mobile-crane and demonstrates a clear reduction of the oscillatory behavior. More advanced control strategies using PF are proposed in [6-8] (i.e., adaptive control, frequency-based control and auto tuning). However, according to [9], these methods are complex and less general compared to the approach first described in [4], referred to as the "classical approach". Recently, Pedersen and Andersen demonstrated that there is an optimum range for the high-pass filter parameters that affects both the obtainable damping and the dynamic response [9]. A guideline for adjusting the filter parameters is proposed in [10] for systems with pressure-compensated PDCVs in combination with OCVs. However, the low bandwidth of PDCVs may have essential limitations on the damping effect [9-11], especially when using PDCVs that have a much lower bandwidth compared to servo-valves. Moreover, pressure feedback is typically implemented in combination with open-loop velocity control where the machine operator closes the loop (operator in the control loop). However, in some applications (e.g., automated offshore oil drilling machinery [12]) a fully automated closed-loop position control is applied for more efficient operations. In the offshore environment, these machines are subjected to disturbances such as strong wind and relevant wave motion that may excite resonance modes of the mechanical structure and restrict the dynamic performance of the actuation system. These factors, when combined with the intrinsic oscillatory behavior of the hydraulic system reduce the system productivity. Consequently, there is an on-going trend of replacing hydraulic actuators with electric drives that results in increased energy efficiency and controllability [12-13].

For these reasons, this paper aims to design and implement pressure feedback on a standard valve-controlled actuator equipped with an over-center valve. The main focus is on a pressure feedback algorithm that uses both actuator pressures instead of only the pressure of the rod-side chamber, like [5] and [10-11]; this idea is inspired by a solution successfully implemented on a self-contained electro-hydraulic cylinder with passive load-holding capability that drives a single-boom crane in two quadrant operations [14]. The considered system under investigation is explained in detail in Section 2. A non-linear model is described and validated against experimental data in Section 3.1, and further simplified and linearized in Section 3.2. The linear model is in Section 4 used to analyze the stability of the original system and when implementing the considered pressure feedback methods. In Section 5, the proposed algorithm with pressure feedback is tested on a high-fidelity non-linear model before the final implementation on the experimental test-bed. The last section contains the conclusion.

2. THE CONSIDERED SYSTEM

The considered system is the hydraulically-actuated, single-boom crane visible in Figure 2 that is built specifically for having a flexible structure in the boom with the purpose of inducing pressure oscillations in the hydraulic system depicted in Figure 1. The OCV serves multi-functional purposes such as leak tight load-holding and shock absorption [11]. A state-of-the-art pressure compensated PDCV is connected to a centralized Hydraulic Power Unit (HPU) providing a constant supply pressure (p_S) and a fixed return pressure (p_R) to the actuation system. The motion of the hydraulic cylinder (C) is controlled by the PDCV that receives the control input u_V from the control system.

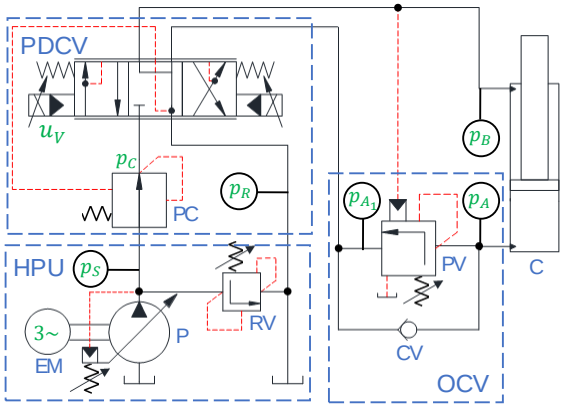

Figure 1. The hydraulic system of the experimental setup.

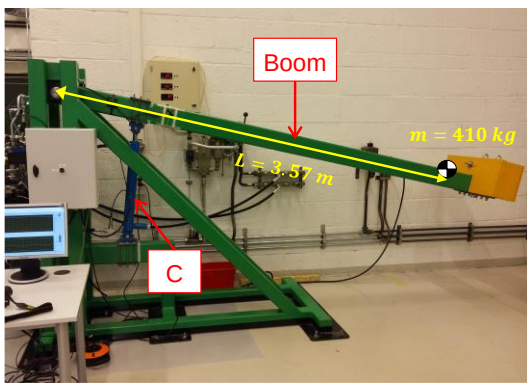

Figure 2. The single-boom crane.

The key components for the experimental setup consist of the following eight elements in addition to the instrumentation: the electric motor (EM) drives the variable-displacement, axial-piston pump (P) with displacement of 75 cm^3/rev. The supply pressure is controlled by the absolute pressure limiter of the pump while a pressure-Relief Valve (RV) is installed for safety. The PDCV, a Danfoss PVG32, consists of two key parts, namely the main spool with integrated closed-loop position control and the Pressure Compensator (PC) that guarantees a load independent flow across the metering edge. The vented OCV, a Sun Hydraulics CWCA with pilot ratio 3:1, contains a by-pass Check Valve (CV) and a pilot-operated Poppet Valve (PV) for controlling the overrunning load when lowering the crane boom. The hydraulic cylinder has piston diameter $D_P = 65\ mm$, rod diameter $D_R = 35\ mm$, and stroke length $h_C = 500\ mm$. Finally, the system is instrumented with sensors for measuring the pressures labeled in Figure 1 as well as the cylinder position (x_C).

3. SYSTEM MODELING AND VALIDATION

This paper makes use of a dynamic model of the valve-controlled system that drives the single-boom crane: the MATLAB-Simulink® environment was chosen to perform the numerical simulations. In this section both a high-fidelity, non-linear model and a simplified linear model are introduced.

3.1. The High-fidelity Model

The mechanical system including the crane boom is modeled using the finite segment method [15-16] (Figure 3), which serves the purpose of representing the relevant flexibility of the structure.

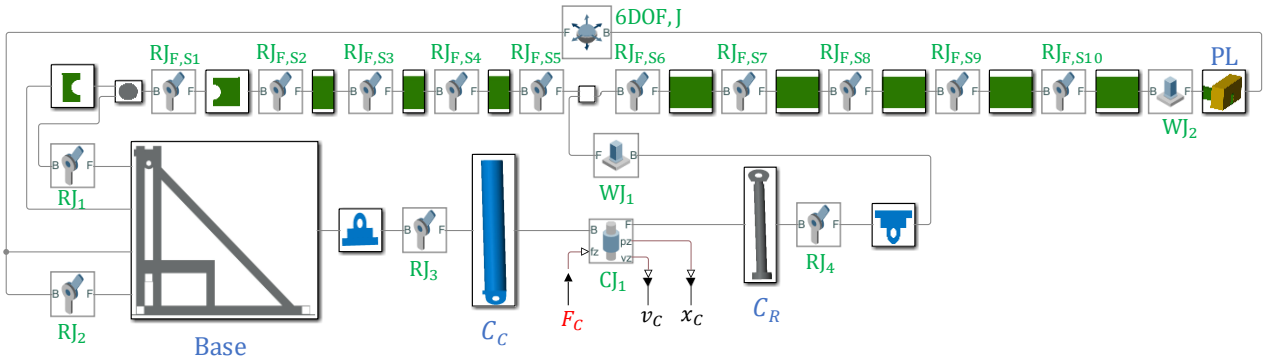

Figure 3. MATLAB-Simulink® multibody model of the flexible boom.

The multibody system (MBS) consists of two revolute joints ($RJ_{1\text{-}2}$) connecting the flexible boom to the base of the crane and two $RJ_{3\text{-}4}$ connecting the cylinder body (C_C) to the base and the rod (C_R) to the boom, respectively. A cylindrical joint (CJ) is applied between C_C and C_R interfacing the hydraulic system through the cylinder piston force (F_C), velocity (v_C) and position (x_C). In the finite segment method, the boom is modeled by a number of smaller boom segments connected together using RJs with an internal torsional spring/damper ($RJ_{F,S1\text{-}10}$) to simulate the bending of the structure. The torsional springs have equivalent stiffness ($k_{eq,i}$) and damping ($C_{eq,i}$) related to the segment number i, as expressed in (1) and (2), where E is the bulk modulus of the boom material, I_Z is the second moment of inertia for the cross section of the boom, $L_{S,i}$ is the length of the segment, and $J_{S,i}$ is the moment of inertia of the segment.

$$k_{eq,i} = \frac{EI_Z}{L_{S,i}} \tag{1}$$

$$C_{eq,i} = \sqrt{2J_{S,i}k_{eq,i}} \tag{2}$$

Concerning the hydraulics, equation (3) elucidates the actuator force transferred to the MBS.

$$F_C = p_A A_A - p_B A_B - F_F \tag{3}$$

The actuator pressures (p_A and p_B) and areas (A_A for the piston-side and A_B for the rod-side) describe the hydraulic force while the friction force (F_F) is given in (4), according to the Stribeck model.

$$F_F = B_{vf}\dot{x} + \tanh(\dot{x}a)\left(F_{Cf} + F_{Sf}e^{-\frac{\dot{x}\cdot\tanh(\dot{x}a)}{\tau_{Sf}}}\right) \tag{4}$$

The different terms identified with experiments are the viscous friction coefficient ($B_{vf} = 1.5 \cdot 10^4$ kg/s), the Coulomb force ($F_{Cf} = 75$ N), the static friction force ($F_{Sf} = 1450$ N), and the static friction force's constant ($\tau_{Sf} = 0.02$ m/s). The hyperbolic tangent is introduced to prevent numerical issues, where the dimensionless tuning parameter is set as $a = 250$.

The well-known pressure build-up equation is then applied to evaluate the pressures labeled in Figure 1 (both the supply pressure $p_S = 180$ bar and the return pressure $p_R = 1.1$ bar are assumed constant). The resulting expressions are given in (5)-(7).

$$\dot{p}_{A1} = \frac{1}{C_{A1}}(Q_{V,In} - Q_{CV} + Q_{PV}), \qquad where\ C_{A1} = \frac{V_{A1,0}}{\beta_{A1}} \tag{5}$$

$$\dot{p}_A = \frac{1}{C_A}(Q_{CV} - A_A v_C - Q_{PV}), \qquad where\ C_A = \frac{A_A x_C + V_{A,0}}{\beta_A} \tag{6}$$

$$\dot{p}_B = \frac{1}{C_B}(Q_{V,Out} + A_B v_C), \qquad where\ C_B = \frac{A_B(h_C - x_C) + V_{B,0}}{\beta_B} \tag{7}$$

The hydraulic capacitances related to the actuator chambers (C_i) are defined recalling the piston position when needed, the cylinder stroke, the volumes of the transmission lines ($V_{i,0}$) that are assumed constant, and the effective fluid's bulk modulus (β_i). This parameter is modeled differently for each capacitance via equation (8).

$$\beta_i = \frac{1}{\frac{1}{\beta_0} - \frac{1}{\kappa_{air}(p_i + p_{atm})\left(\frac{\eta_{air} - 1}{\eta_{air}\left(\frac{p_{atm}}{p_i + p_{atm}}\right)^{\frac{1}{\kappa_{air}}}} - 1\right)}} \tag{8}$$

The terms are the oil's bulk modulus ($\beta_0 = 12000$ bar), the adiabatic air constant ($\kappa_{air} = 1.4$), the pressure in the capacitance (p_i), the atmospheric pressure (p_{atm}) and the volumetric air content of the oil ($\eta_{air} = 0.007$ %). Additionally, the flow rates through the OCV are computed using a simplified approach (9) that involves the valve flow gain ($k_{V,i}$), the cracking pressure ($p_{Cr,i}$), the inlet pressure ($p_{In,i}$), and the outlet pressure ($p_{Out,i}$).

$$Q_i = \begin{cases} 0, & p_{In,i} < p_{Out,i} + p_{Cr,i} \\ k_{V,i}(p_{In,i} - p_{Out,i} - p_{Cr,i}), & p_{In,i} \geq p_{Out,i} + p_{Cr,i} \end{cases} \tag{9}$$

On the contrary, the flow rates through the PDCV are modeled using the orifice equation (10).

$$Q_i = \xi_V C_d A_d \sqrt{\frac{2}{\rho}|\Delta p_i|}\ sign(\Delta p_i) \tag{10}$$

It comprises the valve opening (ξ_V) (i.e., a dimensionless number ranging between -1 and 1 with zero being the center position of the spool), the discharge coefficient (C_d), the maximum flow area (A_d), the fluid density (ρ), and the pressure differential across the spool (Δp_i). The valve opening characteristics, such as the maximum flow areas as well as the spool overlaps (dead-bands) are taken from [17]. The spool position is related to the valve command (u_V) via a second order transfer function ($G_V(s)$ in (11)) that accounts for the valve dynamics. The natural frequency is $\omega_V = 30\ \frac{rad}{s}$ as identified in [18] while the damping ratio is adjusted equal to $\zeta_V = 0.7$ after validation against experimental data.

$$G_V(s) = \frac{\xi_V}{u_V} = \frac{\omega_V^2}{s^2 + 2\omega_V\zeta_V s + \omega_V^2} \tag{11}$$

The PDCV's upstream pressure (p_C) is modeled according to (12); the nominal pressure drop across the spool's metering edge (i.e., the equivalent pressure setting of the compensator $p_0 = 7\ bar$) and the load-sensing pressure (p_{LS}) are introduced. The latter term is selected by a logic function so that $p_{LS} = p_A$ when the spool position is negative, $p_{LS} = p_B$ when the spool position is positive, and $p_{LS} = p_R$ when the spool is centered.

$$p_C = \begin{cases} p_{LS} + p_0, & p_0 \le (p_S - p_{LS}) \\ p_S - p_{LS}, & 0 < (p_S - p_{LS}) < p_0 \\ p_{LS}, & (p_S - p_{LS}) \le 0 \end{cases} \tag{12}$$

The relative opening of the poppet (ξ_{PV}) in the OCV is given in (13), where α_p is the pilot area ratio, $p_{PV,cr}$ is the cracking pressure, and $p_{PV,fo}$ is the extra pressure required to fully open the valve.

$$\xi_{PV} = \frac{\alpha_p \cdot p_B + p_A - p_{PV,cr}}{p_{PV,fo}} \tag{13}$$

The dynamics of the poppet and the dynamics of the pressure compensator are simulated via a first-order transfer function with a time constant $\tau_i = 0.001$ s.

Finally, validation against experimental data was carried out and the results are reported in Figure 4. The comparison shows a good match (except the pressure peak that occurs when the PDCV closes after 20s in Figure 4 (d)) between simulated and measured data, especially, with regards to the oscillatory behavior.

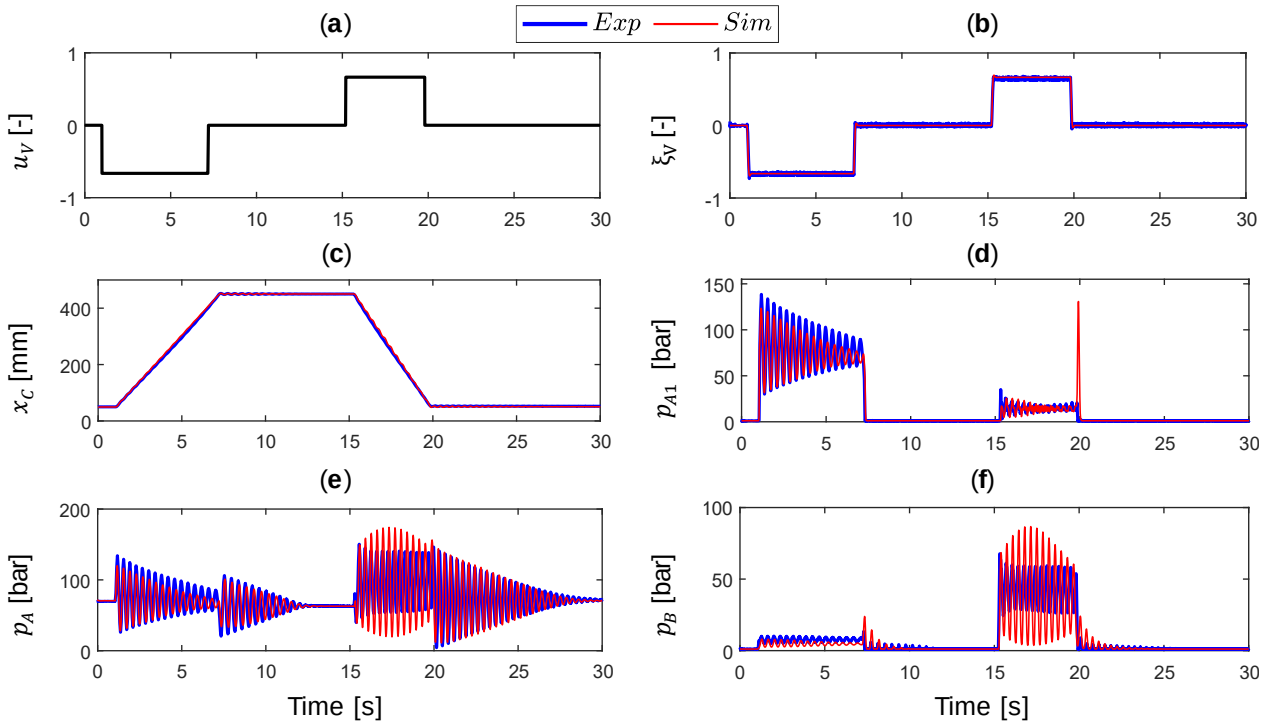

Figure 4. Validation of the non-linear model against experimental data: (a) Input command; (b) PDCV spool position; (c) Cylinder position; (d)-(f) Relevant system pressures.

3.2. The Linear Model

A simplified model emphasizing the cylinder retraction (i.e., the most critical operating condition) was derived for a linear analysis. The flow through the CV elucidated in (5)-(6) is neglected and all capacitances are considered constant and defined by the cylinder position $x_{C,0} = 0.45m$. The resulting force balance on the piston is given in (14).

$$p_A A_A - p_B A_B - B_v v_C = M_{eq}(x_{C,0})\dot{v}_C + G_{eq}(x_{C,0}) \tag{14}$$

The equivalent mass (m_{eq}) is considered as a constant contribution $m_{eq} = M_{eq}(x_{C,0})$. Then, the external load acting on the actuator is the equivalent gravitational term ($G_{eq}(x_{C,0})$) that is assumed as a disturbance.

The general expression (15) is used to find a linear approximation of the PDCV at steady-state (ss).

$$\begin{aligned} \tilde{Q}_i &= \left.\frac{\partial Q_i}{\partial p_i}\right|_{ss} \tilde{p}_i + \left.\frac{\partial Q_i}{\partial u_i}\right|_{ss} \tilde{u}_i = k_{qp,i}\tilde{p}_i + k_{q,i}\tilde{\xi}_i \\ \tilde{p}_i &= p_i - p_i^{ss} \\ \tilde{\xi}_i &= \xi_i - \xi_i^{ss} \end{aligned} \tag{15}$$

The model is linearized around the operating point where the cylinder is almost fully extended and at rest ($v_C = 0\ m/s$) with the PDCV centered ($\xi_V^{ss} = 0$) and the PV closed ($\xi_{PV}^{ss} = 0$). The steady-state values for the pressures (p_i^{ss}) are obtained from experimental data. The flow-pressure gains $k_{qA1,PV}$ and $k_{qA,PV}$ become zero when the PV is considered closed at steady-state. The numerical values for the linearized gains are listed in Table 1. From now on, the "tilde" prescript resulting from the linearization is omitted and, generally, only deviations from the operating point are considered.

Table 1. Parameters used for the linearized model.

$k_{qA,PV}$ $[m^4s/kg]$	$k_{qB,PV}$ $[m^4s/kg]$	$k_{qA1,V_{Out}}$ $[m^4s/kg]$	$k_{q,V_{In}}$ $[m^2/s]$	$k_{q,V_{Out}}$ $[m^2/s]$	$k_{qB,V_{In}}$ $[m^2/s]$	$k_{q,PV}$ $[m^2/s]$
$2.86 \cdot 10^{-8}$	$8.57 \cdot 10^{-8}$	$1.01 \cdot 10^{-10}$	$5.83 \cdot 10^{-4}$	$1.21 \cdot 10^{-4}$	$1.67 \cdot 10^{-11}$	$1.30 \cdot 10^{-3}$
m_{eq} [kg]	μ_C [-]	A_B $[m^2]$	B_v $[Ns/m]$	C_{A1} $[m^3/Pa]$	C_A $[m^3/Pa]$	C_B $[m^3/Pa]$
$1.55 \cdot 10^4$	1.41	$2.4 \cdot 10^{-3}$	$1.5 \cdot 10^4$	$1.52 \cdot 10^{-13}$	$3.78 \cdot 10^{-12}$	$3.59 \cdot 10^{-12}$

A block diagram of the linear model is shown in Figure 5.

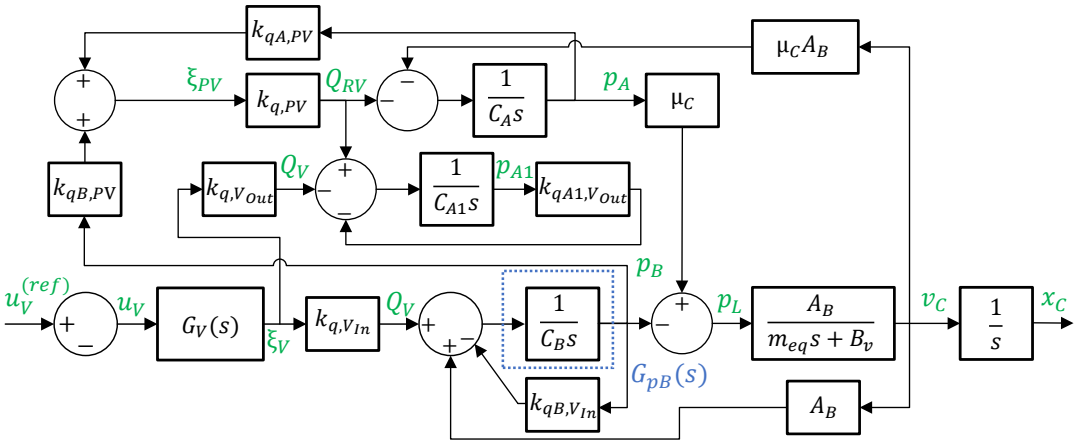

Figure 5. Block diagram of the linearized system model.

Finally, the validation against experimental data is presented for a step command with valve opening $u_V = 10\%$. The results in Figure 6 show a satisfactory agreement between measurements and simulated magnitudes (it should be noted the real system is highly non-linear and the crane has some flexibility). Most importantly, the oscillatory behavior of the pressures is captured at the same amplitude and frequency.

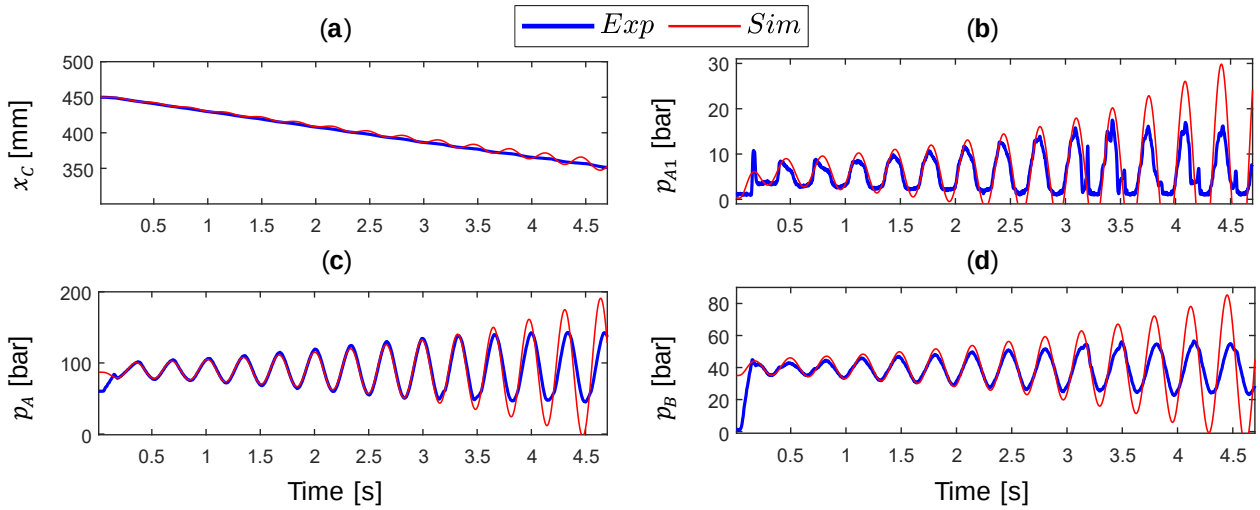

Figure 6. Validation of the linear model against experimental data: (a) Cylinder position; (b)-(d) System pressures.

4. PRESSURE FEEDBACK

Implementing high-pass filtered pressure feedback is proven to increase the system damping for cranes when lowering the load [5]. A first-order high-pass filter (16) is chosen.

$$G_f(s) = \frac{Q_{PF}}{p_i} = \frac{k_f s}{\tau_f s + 1} \tag{16}$$

The two following methods of PF are investigated in this paper.

4.1. The Rod-side Pressure Feedback

First, the rod-side pressure (p_B) is used as feedback element (PF_{pB}) in accordance to the approach chosen in [5], [10] and [11] as shown in Figure 7.

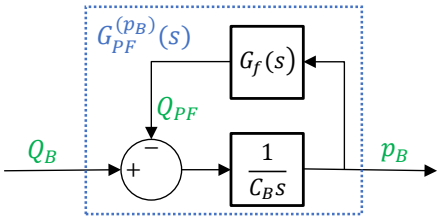

Figure 7. Block diagram of rod-side pressure feedback.

By using the high-passed pressure feedback, the open-loop transfer function $G_{pB}(s)$ of the original system (Figure 5) becomes the compensated open-loop transfer function $G_{PF}^{(p_B)}(s)$ according to (17).

$$G_{PF}^{(p_B)}(s) = \frac{1}{(C_B + k_f)s} \frac{\tau_f s + 1}{\frac{C_B}{C_B + k_f}\tau_f s + 1} \tag{17}$$

For the implementation of this PF on a real application (Figure 8), the non-negligible dynamics of the PDCV should be accounted for when selecting the filter parameters. The inverse of the valve flow gain ($k_{q,V_{In}}$) is, therefore, included to estimate the required valve opening.

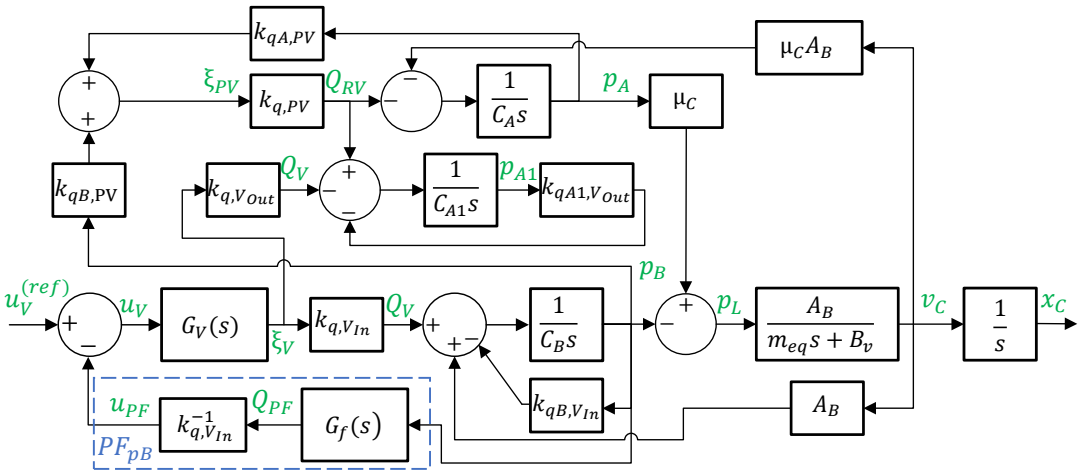

Figure 8. Pressure feedback implemented on the valve side using rod-side pressure.

A state space model (18) is used to generate the transfer function representing the desired system.

$$\begin{bmatrix} \dot{v}_C \\ \dot{v}_C \\ \dot{p}_{A1} \\ \dot{p}_A \\ \dot{p}_B \\ \dot{\xi}_V \\ \ddot{\xi}_V \\ \dot{Q}_{PF} \end{bmatrix} = \begin{bmatrix} 0 & 1 & 0 & 0 & 0 & 0 & 0 & 0 \\ 0 & \frac{-B_v}{m} & 0 & \frac{A_B \mu_C}{m} & \frac{-A_B}{m} & 0 & 0 & 0 \\ 0 & 0 & \frac{-k_{qA1,V}}{C_{A1}} & \frac{k_{q,PV} k_{qA,PV}}{C_{A1}} & \frac{k_{q,PV} k_{qB,PV}}{C_{A1}} & \frac{-k_{q,V_{Out}}}{C_{A1}} & 0 & 0 \\ 0 & \frac{-A_B \mu_C}{C_A} & 0 & \frac{-k_{q,PV} k_{qA,RV}}{C_A} & \frac{-k_{q,PV} k_{qB,PV}}{C_A} & 0 & 0 & 0 \\ 0 & \frac{A_B}{C_B} & 0 & 0 & \frac{-k_{qB,V_{In}}}{C_B} & \frac{k_{q,V_{In}}}{C_B} & 0 & 0 \\ 0 & 0 & 0 & 0 & 0 & 0 & 1 & 0 \\ 0 & 0 & 0 & 0 & 0 & -\omega_V^2 & -2\zeta_V \omega_V & -\omega_V^2 k_{q,V_{In}}^{-1} \\ 0 & \frac{A_B k_f}{C_B \tau_f} & 0 & 0 & 0 & \frac{k_{q,V_{In}} k_f}{C_B \tau_f} & 0 & \frac{-1}{\tau_f} \end{bmatrix} \begin{bmatrix} x_C \\ v_C \\ p_{A1} \\ p_A \\ p_B \\ \xi_V \\ \dot{\xi}_V \\ Q_{PF} \end{bmatrix} + \begin{bmatrix} 0 \\ 0 \\ 0 \\ 0 \\ 0 \\ 0 \\ -\omega_V^2 \\ 0 \end{bmatrix} u_V^{(ref)} \tag{18}$$

Pedersen et al. [9-10] recommend selecting the filter's time constant (τ_f) reasonably high and then adjusting the filter gain (k_f) until sufficient damping is achieved. The high-pass filter time constant should be selected so that $\frac{1}{\tau_f} < \omega_n$, where ω_n is the natural eigenfrequency of the undamped system. According to the absolute stability criteria (19) derived in [11], increasing the rod-side capacitance (C_B) (i.e., increasing the rod-side volume), and/or decreasing the CBV pilot ratio (α_p) can stabilize the system.

$$\frac{C_B}{C_A} > \frac{\alpha_p}{\mu_C} \tag{19}$$

The bore-side capacitance ($C_A \gg C_B$) is chosen as a reference when adjusting the filter gain ($k_f = \lambda_f C_A(x_{C,0})$), where λ_f is a tuning parameter [9-10]. The actuator capacitances depend on the cylinder position (6)-(7), thus to be conservative, k_f is selected when the actuator is close to full extension ($x_{C,0} = 0.45m$) and the volume of the rod-side (V_B) is low. Therefore, $\tau_f = \frac{2}{\omega_n}$ is chosen for $\omega_n = 19.1\, rad/s$, that has been identified from the linear analysis, and $\lambda_f = 2$.

To analyze the stability of the resulting system, Bode plots and a pole-zero plot of the open-loop transfer function in (20) are derived with pressure feedback (PF_{pB}) and also without pressure feedback (PF_{Off}) to have a benchmark. As a side note, the gain $k_{q,V_{In}}^{-1}$ in (18) is selected equal to zero when PF is not desired.

$$G_{x_C}^{(p_B)}(s) = \frac{x_C}{u_V^{(ref)}} = \boldsymbol{C}_{x_C}\left(\boldsymbol{I}s - \boldsymbol{A}^{(p_B)}\right)^{-1}\boldsymbol{B}, \qquad where\ \boldsymbol{C}_{x_C} = [1 \quad 0 \quad 0 \quad 0 \quad 0] \tag{20}$$

Figure 9 (a) shows a clear increase in damping when PF is added. Figure 9 (b) suggests that the system without PF is stable when the cylinder position is below 0.313m. Figure 9 (c) displays that the two positive complex poles of PF_{Off} move to the negative side when adding pressure feedback (PF_{pB}) in the worst-case scenario (i.e., $x_C = 0.45\ m$), resulting therefore in a stable system.

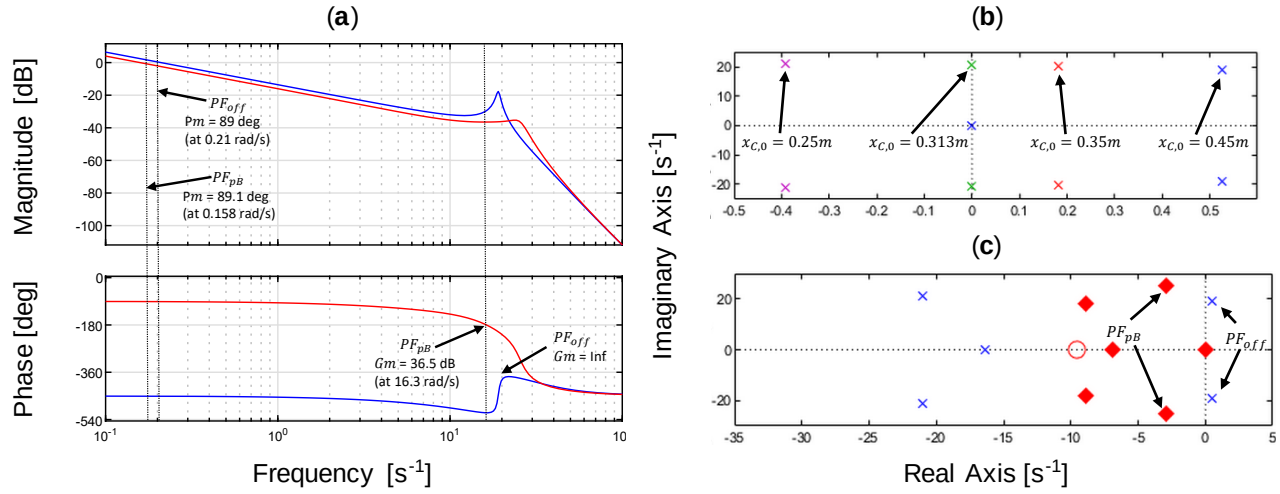

Figure 9. Stability analysis of $G_{x_C}^{(p_B)}(s)$: (a) Bode plots; (b) Plot PF_{Off} at different cylinder positions; (c) Poles and zeros PF_{Off} (blue) and PF_{pB} (red) at $x_{C,0} = 0.45m$.

4.2. The Load Pressure Feedback

A different approach for the pressure feedback based on the "load pressure" (i.e., the difference between the bore chamber pressure multiplied by the area ratio of the cylinder and the rod chamber pressure, $p_L = p_A \mu_C - p_B$) is addressed in order to get rid of the undesired pressure oscillations identified during piston extension (Figure 12). Achieving this result benefits those systems characterized by a flexible mechanical structure like the single-boom crane under investigation.

The row eight of matrix $\boldsymbol{A}$, in (18) is modified according to (21) when including the piston-side chamber pressure.

$$\boldsymbol{A}^{(p_L)} = \begin{bmatrix} \cdots & \cdots & \cdots & \cdots & \cdots & \cdots & \cdots & \cdots \\ 0 & \frac{-k_f A_B \left(\frac{\mu_C^2}{C_A} + \frac{1}{C_B}\right)}{\tau_f} & 0 & \frac{-k_f \mu_C k_{q,PV} k_{qA,RV}}{C_A \tau_f} & \frac{-k_f \mu_C k_{q,PV} k_{qB,PV}}{C_B \tau_f} & \frac{-k_{q,VIn} k_f}{C_B \tau_f} & 0 & \frac{-1}{\tau_f} \end{bmatrix} \tag{21}$$

The open-loop transfer function from valve command to position output ($G_{x_C}^{(p_L)}(s)$) elucidated (22) and the transfer function from valve command to velocity output ($G_{v_C}^{(p_L)}(s)$) elucidated (23) are used to analyze the system stability using load pressure feedback (PF_{pL}, Figure 10). The filter's time constant $\tau_f = \frac{2}{\omega_n}$ and the filter gain tuning parameter $\lambda_f = 0.7$ are used.

$$G_{x_C}^{(p_L)}(s) = \frac{x_C}{u_V^{(ref)}} = \boldsymbol{C}_{x_C}\left(\boldsymbol{I}s - \boldsymbol{A}^{(p_L)}\right)^{-1}\boldsymbol{B}, \quad where\ \boldsymbol{C}_{x_C} = [1 \quad 0 \quad 0 \quad 0 \quad 0] \tag{22}$$

$$G_{v_C}^{(p_L)}(s) = \frac{v_C}{u_V^{(ref)}} = \boldsymbol{C}_{v_C}\left(\boldsymbol{I}s - \boldsymbol{A}^{(p_L)}\right)^{-1}\boldsymbol{B}, \quad where\ \boldsymbol{C}_{v_C} = [0 \quad 1 \quad 0 \quad 0 \quad 0] \tag{23}$$

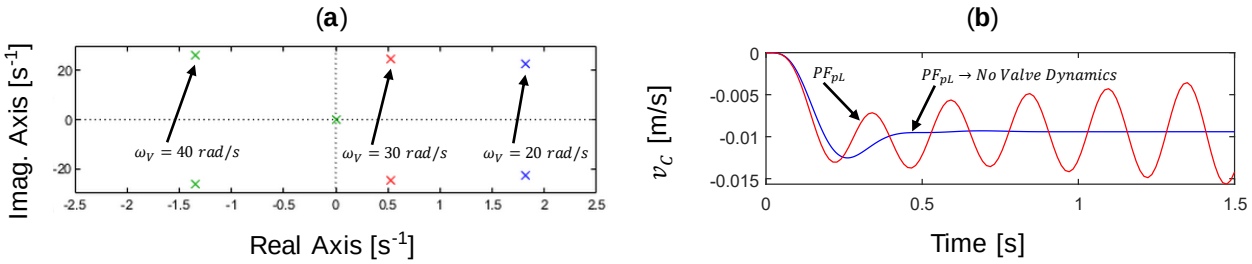

Figure 10. Stability analysis $x_{C,0} = 0.45m$: (a) Pole-zero plot of $G_{x_C}^{(p_L)}(s)$; (b) Step response of $G_{v_C}^{(p_L)}(s)$.

Figure 10 (a) shows that the system with PF_{p_L} is unstable with the considered valve ($\omega_V = 30\ rad/s$); however, increasing the natural eigenfrequency of the valve (e.g., up to $\omega_V = 40\ rad/s$) makes the system stable. Figure 10 (b) compares a step response of $G_{v_C}^{(p_L)}$ with command $u_V = 10\%$ to highlight that the steady-state piston velocity is not achieved when considering the valve dynamics. The latter scenario, as discussed in [9-11], is because of the low bandwidth of PDCVs, and in [9] it is seen that when $\omega_V \geq 3\omega_n$ the effect diminishes. Consequently, the inverse of the valve dynamics ($G_V^{-1}(s)$) must be included in the pressure feedback according to the block diagram in Figure 11.

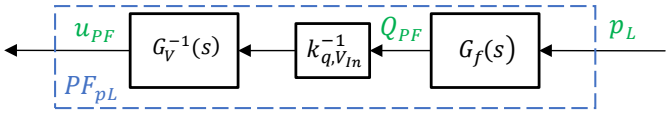

Figure 11. Pressure feedback using the load pressure and including the inverse valve dynamics.

To get a proper transfer function (i.e., the degree of the numerator does not exceed the degree of the denominator), a pseudo transfer function (24) is added assuming $k = 5$.

$$G_V^{-1}(s) = \frac{k^2 s^2 + 2\omega_V \zeta_V k^2 s + \omega_V^2 k^2}{s^2 + 2\omega_V k s + \omega_{n,V}^2 k^2} \tag{24}$$

5. RESULTS

First, the high-fidelity model is used to test the PF based on the rod-side pressure when compared against the original system. Secondly, the load pressure feedback is also evaluated before implementation and testing on the experimental setup. Finally, the proposed pressure feedback is simulated for different OCV's pilot ratios to understand if there is room for potential energy savings.

5.1. The Rod-side Pressure Feedback

To evaluate the performance of this pressure feedback, positive and negative step inputs at 40% of the maximum valve opening are simulated by means of the non-linear dynamic model (Figure 12).

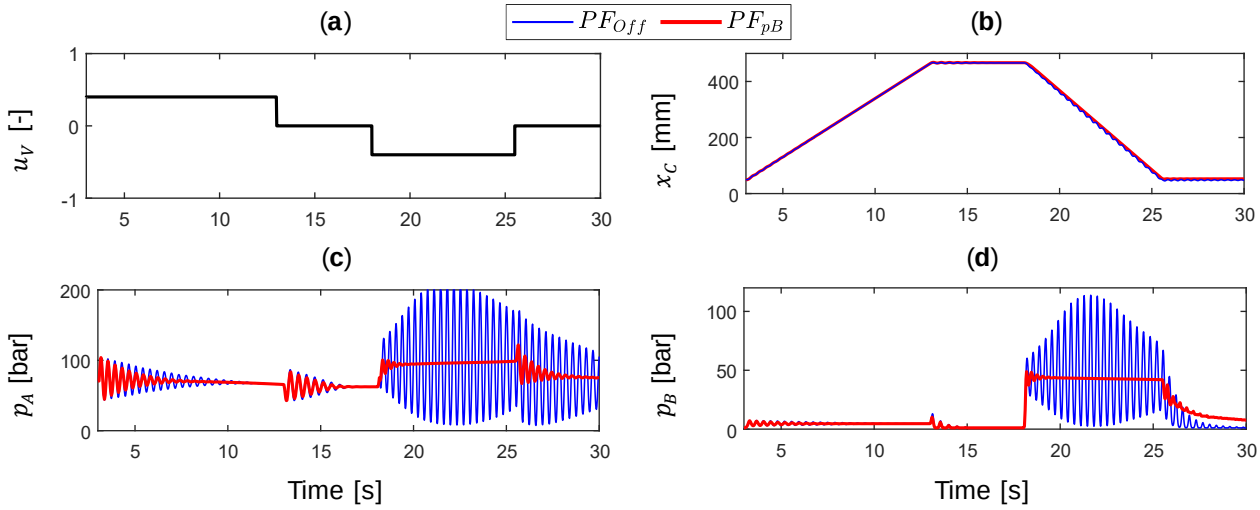

Figure 12. Simulated results with (PF_{pB}) and without (PF_{Off}) pressure feedback: (a) System input; (b) Piston position; (c) Pressure in the bore chamber; (d) Pressure in the rod chamber.

The results in Figure 12 demonstrate a significant improvement when pressure feedback is used since the pressure oscillations are greatly reduced in comparison to the undamped system. This is especially true during piston retraction (i.e., from about 17 to 26 seconds) with an overrunning external load. However, when the cylinder is extending, the pressure feedback based on the rod chamber pressure is not able to mitigate the pressure oscillations (i.e., before 5 seconds). For this reason, the following feedback method involving both actuator pressures is investigated.

5.2. The Load Pressure Feedback

The performance of the proposed pressure feedback (PF_{pL}) is compared in Figure 13 against the conventional feedback approach (PF_{pB}) while simulating a step input.

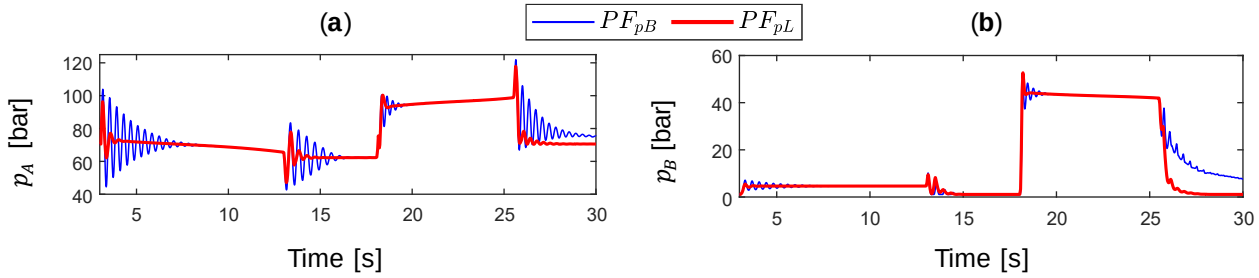

Figure 13. Simulated results of pressure feedback based on rod-side pressure and on load pressure when including $G_V^{-1}(s)$: (a) Pressure in the bore chamber; (b) Pressure in the rod chamber.

The results show a clear improvement of the load pressure feedback in reducing the unwanted pressure oscillations when the piston is extending (i.e., from 0 up to about 12 seconds). In addition, the performance is also improved during piston retraction.

5.3. Experimental Tests – The Closed Loop Position Control

The investigated load pressure feedback is tested experimentally on the considered application and compared to the conventional system that is used as a reference after selecting the filter parameters properly. Figure 14 illustrates the block diagram representing the implemented control algorithm.

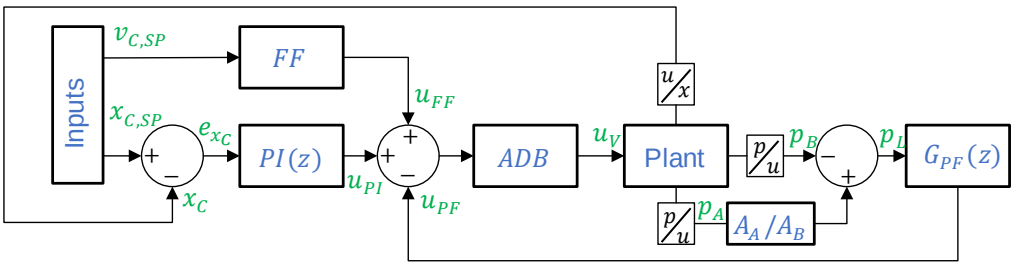

Figure 14. Block diagram of the considered control algorithm.

It consists of a position controller based on a closed-loop PI contribution (u_{PI}) and a feed forward (FF) term elucidated in (25), in addition to the pressure feedback in (26). Anti-dead-band logic is also implemented to compensate for the effective dead-band of the PDCV, as explained in [17].

$$u_{FF} = \frac{A_A v_C}{k_{Q_{max}}} \;\; if \;\; v_C \geq 0; \;\; u_{FF} = \frac{A_B v_C}{k_{Q_{max}}} \; otherwise \tag{25}$$

$$G_{PF}(z) = \frac{u_{PF}}{p_L} = G_V^{-1}(z) k_{q,V_{ln}}^{-1} G_f(z) \tag{26}$$

This controller was first developed in a Simulink® model and then converted to IEC 61131-3 Structured Text code using the Simulink-PLC-Coder®. The generated PLCopen XML file was then uploaded to IndraWorks® and executed on an embedded controller XM22 from Bosch Rexroth that runs at a frequency of 1000 Hz. The Simulink-PLC-Coder® requires discrete blocks, hence all transfer functions in the s-domain were converted to the z-domain.

A setpoint S-curve trajectory with a resulting piston velocity $v_{C,SP} = 20\, mm/s$ was generated and used as input to the position controller (a low velocity is assumed since it is the worst condition due to reduced damping). The measured position error for three different approaches are compared in Figure 15, namely a controller without PF, a control algorithm with PF based on p_B, and a control logic with PF grounded on p_L.

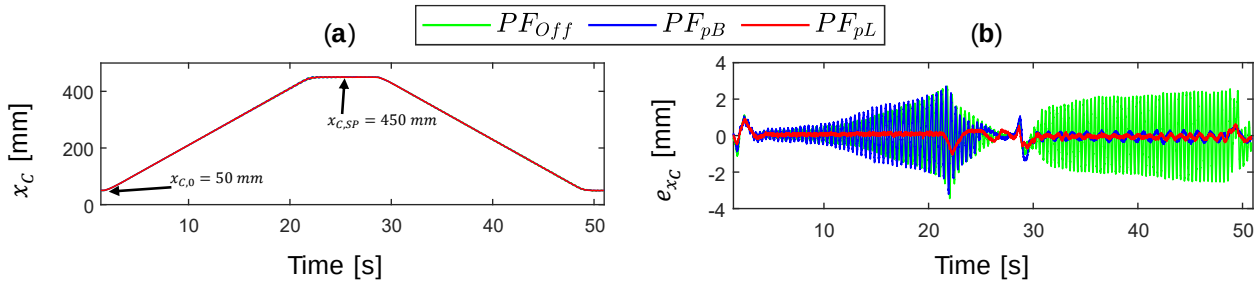

Figure 15. Experimental closed-loop position tracking for different control algorithms.

These experiments demonstrate that adding pressure feedback plays a major role in improving the system performance, even though the induced oscillations make the system with rod-side pressure feedback (PF_{pB}) unstable when the cylinder is extending. Conversely, the system with load pressure feedback (PF_{pL}) stabilizes the system during both piston extension and retraction. This approach results in a much smaller average position error during piston extension (the maximum error is 1.0 mm at about 22 s when the system is decelerating); in comparison to the system without pressure feedback, the improvement in terms of position tracking is close to 2 mm during piston retraction.

The smoother system behavior is clearly reflected in the pressures trends proposed in Figure 16: implementing load pressure feedback removes the oscillatory nature in both quadrants when closed-loop position control is desired.

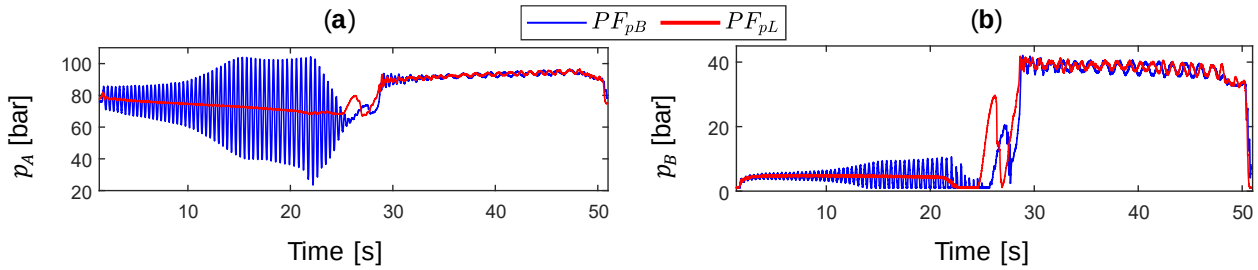

Figure 16. Experimental results comparing PF_{pL} and PF_{pB}: (a) Piston-side pressure; (b) Rod-side pressure.

A similar test for a higher piston velocity ($v_{C,SP} = 120\ mm/s$) that represents the upper limit in terms of velocity requirement for this system is also carried out showing similar behavior (the results are not reported for the sake of brevity).

Lastly, Table 2 provides a synthesis of the system performance for closed-loop position control: the simpler implementation of the rod-side pressure feedback is highlighted (i.e., including the valve dynamics is not strictly necessary) as well as the improved performance of the load pressure feedback (i.e., smoother functioning is achieved in every operation).

Table 2. Performance summary.

Pressure Feedback	$G_V^{-1}(s)$	Lifting	Lowering
Off		-	-
p_B	No	-	+
p_L	Yes	+	+

5.4. The Energy Saving Potential

The OCV's pilot ratio affects both the system stability and the energy efficiency. From the stability criterion given in (19), it is clear that it is not possible to achieve stability for the whole cylinder stroke when standard values of the pilot ratio (i.e., $\alpha_p = 2 \dots 8$) are used [11]. However, implementing pressure feedback can make the system stable. Solving this issue, provides an opportunity to emphasize the system's energy consumption that can potentially be improved by selecting a higher pilot ratio of the OCV. Energy savings can be achieved when lowering the crane if the pressure required to open the OCV is reduced; Figure 17 shows the effects of replacing the reference pilot ratio ($\alpha_p = 3$) with $\alpha_p = 5$ and $\alpha_p = 10$, respectively. The results are derived via the non-linear model simulated in closed-loop position control; the considered scenario is similar to the one discussed in Figure 16 but for a higher piston velocity ($v_{C,SP} = 120\ mm/s$) during piston retraction (i.e., when the OCV regulates).

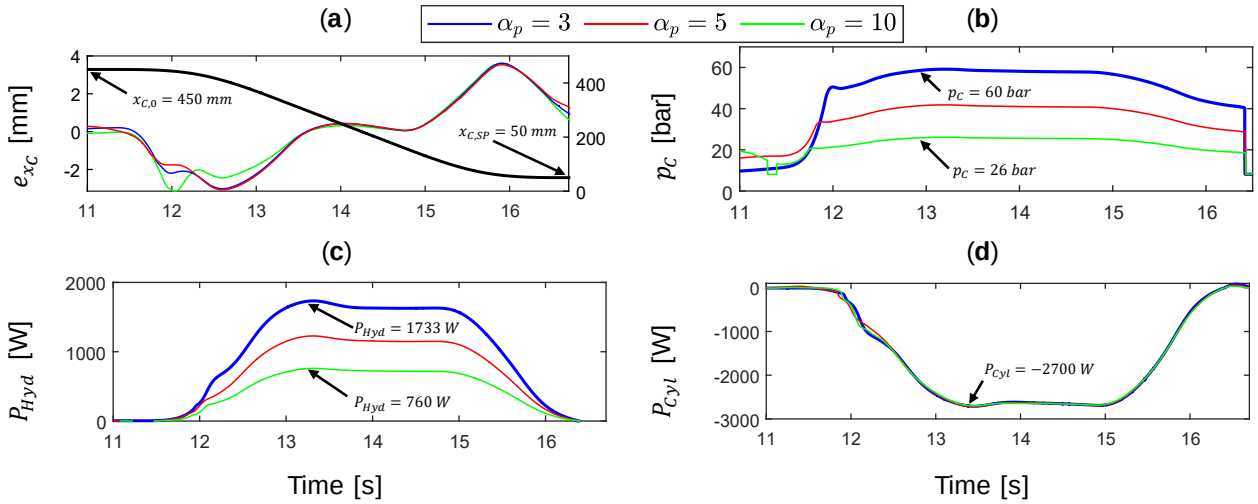

Figure 17. Simulated results with PF_{pL} and different pilot ratios of the OCV: (a) Position error; (b) Rod-side pressure; (c) Consumed hydraulic power; (d) Mechanical power at the actuator.

It can be concluded from Figure 17 (a) that varying the OCV's pilot ratio has little or no effect on the position tracking while the motion remains smooth. This is also confirmed by the trends of the pressure p_C sensed upstream the main spool of the PDCV that are depicted in Figure 17 (b); a lower value of this magnitude translates into energy savings since the required hydraulic power, defined via (27), drops down as visible in Figure 17 (c). In particular, increasing the pilot ratio up to $\alpha_p = 10$ reduces the power consumption to about 50% with respect to the case where $\alpha_p = 3$.

$$P_{Hyd} = p_C Q_B \tag{27}$$

The modifications that enable these energy savings do not affect the system performance because the mechanical power outputted by the actuator expressed in (28), remains about constant for every scenario (Figure 17 (d)).

$$P_{Cyl} = F_C \mathrm{v_C} \tag{28}$$

6. CONCLUSION

The benefits of pressure feedback discussed in the technical literature are often demonstrated on simplified linear models, moreover these references do not show how the pressure feedback algorithm is implemented and tested on real applications using standard directional proportional control valves.

This paper investigates the implementation of pressure feedback on a hydraulically-actuated, single-boom crane operated in closed-loop position control. In comparison to conventional pressure feedback only based on the rod-side chamber pressure, the use of both actuator pressures achieves improved stabilization in both piston extension and retraction. To enable closed-loop stability without compromising the motion performance (i.e., settling time and tracking error), it is necessary to include the piston-side pressure for the considered application. However, adding the piston-side pressure to the pressure feedback induce instability due to the low bandwidth of the directional control valve. One solution presented in this paper is to account for the valve dynamics in the pressure feedback. The experimental results show relevant reduction of the oscillatory behavior of the actuator pressures in closed-loop motion control, the maximum position error during lifting of the payload is reduced from 3.5 mm to 1.0 mm, and the average position error when the payload is lowered is approximately 0.2 mm (in comparison to the system without pressure feedback, this is an improvement of almost 2 mm). Finally, this study demonstrates that the recommended pressure feedback allows the pilot-ratio of the over-center valve to be increased which results in a significant potential for energy savings.

Concerning the future work, the energy saving potential will be experimentally validated and the proposed pressure feedback will be tested on a hydraulic circuit with load-holding valves on both actuator ports in applications where the direction of the external load is changing (i.e., four quadrant operations).

ACKNOWLEDGMENTS

This research received funding from the Norwegian Research Council, SFI Offshore Mechatronics, project number 237896.

REFERENCES

[1] M. R. Hansen and T. O. Andersen, “A Design Procedure for Actuator Control Systems Using Optimization Methods,” in *The 7th Scandinavian International Conference on Fluid Power*, 2001.

[2] P. A. Nordhammer, M. K. Bak, and M. R. Hansen, “A Method for Reliable Motion Control of Pressure Compensated Hydraulic Actuation with Counterbalance Valves,” *Control. Autom. Syst. (ICCAS), 2012 12th Int. Conf.*, 2012.

[3] R. Rahmfeld and M. Ivantysynova, “An overview about active oscillation damping of mobile machine structure,” *Int. J. Fluid Power*, vol. 5, no. 2, 2004.

[4] P. Krus and J.-O. Palmberg, “Damping of mobile systems in machines with high inertia loads,” in *JFPS Int. Symp. Fluid Power*, 1989.

[5] M. R. Hansen and T. O. Andersen, “Improved Functionality and Performance of Mobile Cranes Using Pressure Feedback,” in *Drives and Controls/Power Electronics Conferance*, 2001.

[6] D. Cristofori, A. Vacca, and K. Ariyur, “A Novel Pressure-Feedback Based Adaptive Control Method to Damp Instabilities in Hydraulic Machines,” *SAE Int. J. Commercial Vehicles*, vol. 5, no. 2, 2012.

[7] R. Bianchi, G. F. Ritelli, A. Vacca, and M. Ruggeri, “A Frequency-Based Control Methodology for the Reduction of Payload Oscillations in Hydraulic Load Handling Machines,” in *ASME/BATH 2015 Symposium on Fluid Power and Motion Control*, 2015.

[8] G. F. Ritelli and A. Vacca, “A General Auto-Tuning Method for Active Vibration Damping of Mobile Hydraulic Machines,” in *8th FPNI Ph.D Symposium on Fluid Power*, 2014.

[9] H. C. Pedersen and T. O. Andersen, “Pressure Feedback in Fluid Power Systems - Active Damping Explained and Exemplified,” *IEEE Trans. Control Syst. Technol.*, vol. 26, no. 1, 2018.

[10] H. C. Pedersen, T. O. Andersen, and M. R. Hansen, “Guidelines For Properly Adjusting Pressure Feedback In Systems With Over-Centre Valves,” in *Proceedings of BATH/ASME Symposium on Fluid Power & Motion Control FPMC2016*, 2016.

[11] M. R. Hansen and T. O. Andersen, “Controlling a Negative Loaded Hydraulic Cylinder Using Pressure Feedback,” in *29th IASTED International Conference on Modelling, Identification and Control, MIC*, 2010.

[12] D. Hagen, W. Pawlus, M. K. Ebbesen, and T. O. Andersen, “Feasibility Study of Electromechanical Cylinder Drivetrain for Offshore Mechatronic Systems,” *Model. Identif. Control*, vol. 38, no. 2, 2017.

[13] W. Pawlus, M. Choux, and M. R. Hansen, “Hydraulic vs. Electric: A Review of Actuation Systems in Offshore Drilling Equipment,” *Model. Identif. Control A Nor. Res. Bull.*, vol. 37, no. 1, 2016.

[14] D. Padovani, S. Ketelsen, D. Hagen, and L. Schmidt, “A Self-Contained Electro-Hydraulic Cylinder with Passive Load-Holding Capability,” *Energies, 12(2), 292*, 2019.

[15] R. L. Huston and Y. Wang, “Flexibility Effects in Multibody Systems,” in *Computer-Aided Analysis of Rigid and Flexible Mechanical Systems*, Dordrecht: Springer Netherlands, 1994.

[16] J. K. Sørensen, M. Hansen, Rygaard, and M. K. Ebbesen, “Numerical and Experimental Study of a Novel Concept for Hydraulically Controlled Negative Loads,” *Model. Identif. Control*, 2016.

[17] M. K. Bak and M. R. Hansen, “Model based design optimization of operational reliability in offshore boom cranes,” *Int. J. Fluid Power*, vol. 14, no. 3, 2013.

[18] M. K. Bak and M. R. Hansen, “Modeling , Performance Testing and Parameter Identification of Pressure Compensated Proportional Directional Control Valves,” in *The 7th FPNI PhD Symposium on Fluid Power Modeling*, 2012.

EXPERIMENTAL ANALYSIS OF AN ELECTRO-HYDRAULIC DRIVE FOR AN ELBOW SUPPORT EXOSKELETON

Eva Holl, Rudolf Scheidl
Johannes Kepler University Linz
Linz Austria

ABSTRACT

This paper reports about performance characteristics of a special hydraulic drive for exoskeleton applications. An arm exoskeleton is taken as reference case. The envisaged final control concept is force support for the wearer in load lifting by measuring the active force at the human hand and deriving requested support as desired value for the hydraulic drive operating in in force control mode.

The hydraulic drive combines a speed variable electric motor with a fixed displacement pump to drive a hydraulic cylinder which transmits its force to the elbow joint of the exoskeleton. The investigation of this drive concept serves as a benchmark for other, primarily digital hydraulic concepts which were already started and shall be continued in the future. The essential performance criteria of drives for exoskeletons are low weight and high compactness. Drive efficiency is relevant as far as it serves these criteria by keeping battery and motor lightweight and small. Dynamic response has to be judged with respect to the wearer's expectations for a convenient arm motion.

As simple test rig represents upper and lower arm of an exoskeleton and the flexional degree of freedom of the elbow joint. Of the shelve components are used to form a closed hydraulic system with a low pressure accumulator as hydraulic tank. The performance of the drive system is measured for different loads. Weight of the components and efficiency values are evaluated as performance indicators. The weight of this drive exceeds acceptable limits, is dominated by motor weight but is also raised by the bulky design of several hydraulic components. Measured efficiencies were in the range 24% to 54 %. Recuperated energy is a negligible quantity for the tested loads.

KEYWORDS: Hydraulic drive, exoskeleton actuator, upper limb, elbow joint

1. PURPOSE OF STUDY

Exoskeletons are expected to have a high market potential due to the needs of an aging society and the general trend to assist persons in loading situations [1] predicts some market figures for medical applications which are shown as a trend curve in Figure 1. Industrial applications for work force support are used more often and Otto Bock, a company so far active in the prosthesis and orthesis area, is now offering exoskeletons for industrial use [2]. The range of applications and the corresponding technical requirements are very diverse, but there are at least two central requirements which apply to all kind of exoskeletons: low weight and low space. For an arm exoskeleton [3] specifies an acceptable weight to be in the range of consumer electronic devices, i.e., in the order of one kilogramme. Hydraulic drives have a basic potential to meet these requirements best, but the relatively small power range of exoskeletons and the mentioned

central demands require new components and concepts. Efficient use of energy is important to keep battery and all power conversion components small and to provide a long operation time.

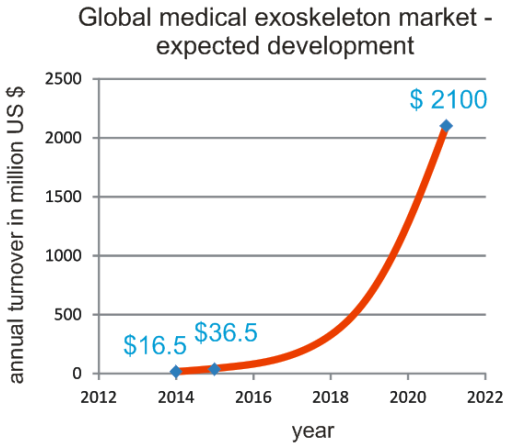

Figure 1. Medical exoskelton market as reported/predicted by [1].

Also in exoskeleton actuation hydraulic drives will face competition with electrical drives. The latter will require some gear to transfer the fast rotary motion into rather low speed motion of the exoskeletal joints. Since electrical motors have a high power density only in case of high speed high gear ratios are required for the adaptation of motor and joint speeds. Probably one of the currently most advanced electromechanical drives for exoskeletons is AnyDrive of Anybotics [4] which has a nominal and peak power of 240 and 720 watts, respectively, and which offers also some compliance, realized by a flexible gear. Its weight is one kilogram. Another electromechanical solution was developed for the exoskeleton Mindwalker of the University of Twente [5 - 7].

A further option, functionally similar to mechanical gears, is a hydraulic gear composed of a constant displacement pump and a hydraulic cylinder. This hydrostatic transmission has no intrinsic losses and can exploit the high force density of hydraulic cylinders to realize the high gear ratio in a compact and light-weight fashion. That, at least is the expectation. Furthermore, the relative ease of realizing damping and fail safe functionality by hydraulic actuators speaks for this actuation concept and has been also the main argument of the authors of [8] to apply this concept for an ankle joint prosthesis drive. A motor pump unit acts on a cylinder for lifting the foot. Controllable damping is enabled by a 3-way bypass valve in the system. During the passive phase the valve is open to enable the fluid flow and in active phase it is closed to avoid losses. This is a nice example for the additional functional features which a hydraulic gear can provide much easier than mechanical gears.

In [9, 10] the use of a digital cylinder for exoskeletons was proposed and studied, respectively, indicating a high potential, provided compact on-off valves are available. A hydraulic piloting concept for valve actuation to reduce the number of solenoids, which are the weight and space determining functional elements of valves, is presented in [11, 12].

The present paper reports about some measurements of an electrohydraulic drive which is composed of a speed variable electric motor, a constant displacement pump, and a differential cylinder, similar to the concept of [8]. The purpose of the experimental setup and the investigations is to obtain reliable performance data about this drive technology using very performant of the shelve components, as a reference for other hydraulic drive concepts, which the workgroup of the second author is developing currently. The load scenario is an elbow joint and the lifting of a dead load. Most important performance characteristics are weight and space, energy consumption, and the dynamical response characteristics. It was expected that the rather small pump is the most performance critical component of the system. Efficiency of hydraulic components drops with lower power and is by far lower in the sub-kilowatts range. This effect is particularly pronounced for pumps and motors; see e.g. [13]. Therefore, pump efficiency for a characteristic load scenario is a key criterion.

2. TEST RIG

The test rig comprises a two body mechanism representing the upper and lower arm exoskeleton but in a standalone fashion not attached to a human body. The arm dimensions correspond to a male adult person. Currently, of the shelve miniature hydraulic components are used as described in Table 1 which lists all used components: The test rig's mechanical structure and hydraulic schematic are given by Figure 2 and Figure 3. The test rig can be controlled in different ways: either by predefined commands for lower arm position (angle ϕ) or by creating a desired lifting force as the adjustable multiple of the arm force applied by a test person at the handle of the lower arm part.

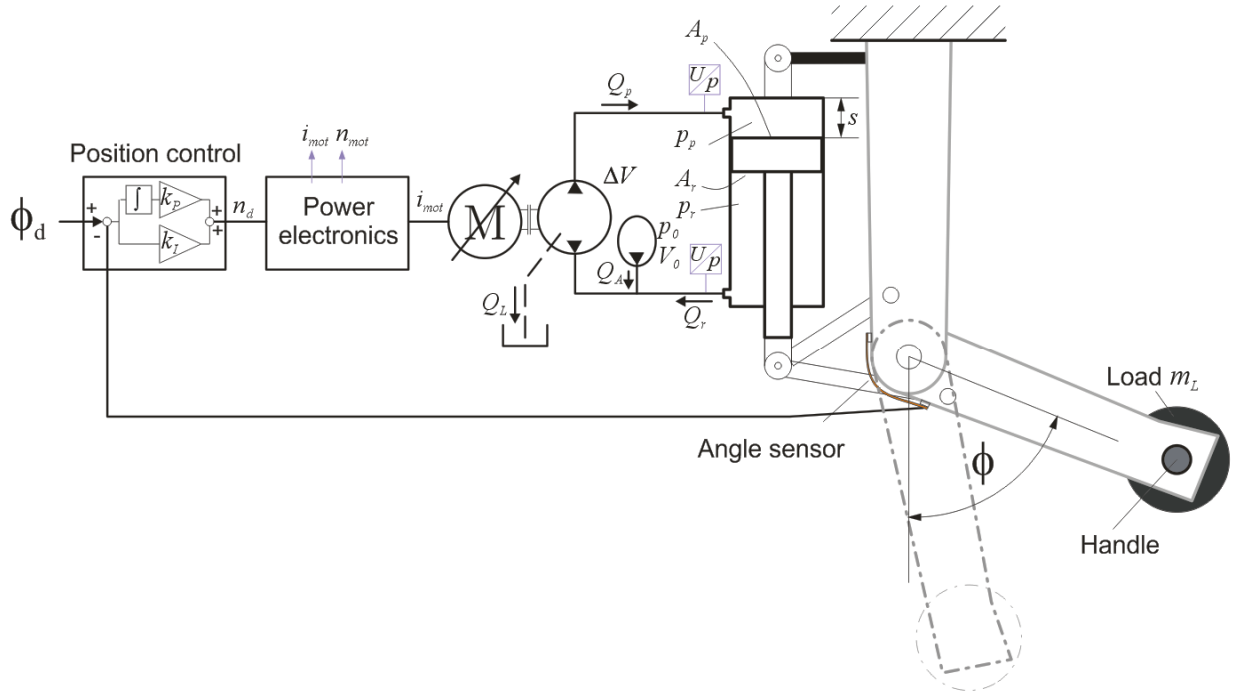

Figure 2: Schematic of the test rig

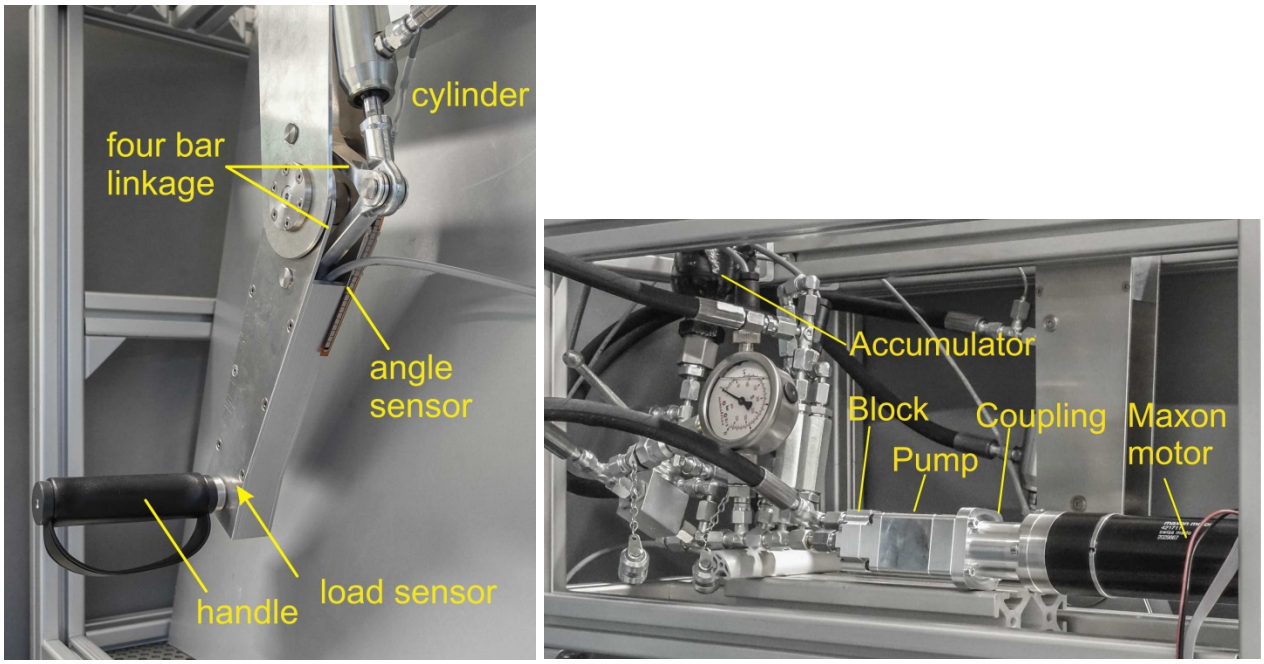

Figure 3: Photos of structural (a) and hydraulic (b) sub-systems.

Table 1. Test rig components

Function	Component type	Data		Further information
Electric motor	MAXON RE50; brushed DC motor and a planetary gear	Idle speed Nom. speed Nom. power Nom. torque Break. torque Best efficiency Speed constant k_{mot} Coil resistance R_{mot} Gear ratio Weight Size	4900 min^{-1} 4620 min^{-1} 200 watts 0.42 Nm 7.37 Nm 94% 102 min^{-1}/V 0.608 Ω 4.3:1 1.1 kg ϕ50 x 108 mm	https://www.maxonmotor.com/
Power electronics/ motor controller	ESCON 50/5	Weight Size Best efficiency	0.204 kg 115x75x24mm 95%	
Coupling	ROTEX GS14	Weight Size	0.06 kg ϕ30 x 35 mm	https://www.ktr.com/en/products/power-transmission-technology/couplings/elastic-jaw-and-pin-bush-couplings/
Pump	TAKAKO TFH – 080	Spec. displacement Weight Size	0.8 cm^3 0.43 kg 40x97 mm	https://www.takako-inc.com/english/products/pump.html
Coupling case	Aluminium component, design and manufacturing	Weight Size	ϕ36.5 x 61.5 mm 0.1 kg	
Hydraulic block	Aluminium component, self made	Weight Size	0.08 kg 40x40x10 mm	
Accumulator	HYDAC 0.16	Size V_0 Prefill pressure p_0 Weight	0.16 liter 10 bar 0.8 kg	https://www.hydac.com/uk-en/start.html
Cylinder	HYTEC CH-71220/50	Piston diameter Rod diameter Weight Size	20 mm 12 mm 0.66 kg ϕ28 x 152 mm	https://www.hytec-hydraulik.com/hydraulics/mini-cylinders.html
Pressure sensors	IFM PU5401	Pressure range Hysteresis	250 bar $< \pm 0.2$ %	
Hoses	Size L6	Total length Weight	1.6 m 0.66 kg	
Angle sensor	SPECTRA SYMBOL FlexSensor	Size	6.35 x112.24 mm	http://www.spectrasymbol.com/product/flex-sensors/

To this end, the arm is equipped with two sensors, a lower arm angle (ϕ) sensor mounted at the elbow joint and a load sensor for the handle force. The latter is realized by strain gauges in the shell structure of the lower arm close to the handle fixation area. The hydraulic differential cylinder is connected by a four bar linkage to the joint. The geometric size of the four bar linkage is optimized w.r.t. to the needed force and its distal space to the arm structure.

The hydraulic concept is obvious from the schematic of Figure 2. The accumulator serves as a closed tank and compensates the flow difference between piston and rod sided lines. Its prefill pressure p_0 has to be large enough to move the arm down against friction forces of the cylinder at a wanted speed. Circuit concepts which enable the full pump pressure also at the rod side could be used instead. These concepts employ piloted check valves to connect the lower pressure line to the low pressure accumulator. Such circuits have been proposed and studied, for instance, in [14]. But, small piloted check valves are not available and the use of purchasable valves increases size and weight of the block and gives a wrong impression of the feasible weight and size of that drive concept.

In the tests reported here only position control was used. Therefore, Figure 2 indicates only this type of control in the schematic. The desired motion is a trapezoidal curve with constant lifting and lowering angular speeds $\dot{\phi}$. A cascaded control structure is applied; a PI controller (controller gains are given in

) does position control and sends a motor speed request to the motor speed controller which is implemented in the power electronic device of the motor. High control performance is not a goal of this study and the used simple control concept turned out to create good enough response, sufficient to assess the performance of the electrohydraulic drive.

Table 2: Controller gains

k_P	120 rpm/rad
k_I	40 rpm/(rad s)

3. MEASUREMENT AND MEASUREMENT RESULTS

Directly measured were elbow angle ϕ, and pressures p_p, p_r, in the piston and rod chambers. Motor current i_{mot} and speed n_{mot} were provided as voltage signals by the motor controller. Actual motor voltage was computed from the voltage formula of DC motors.

$$U_{mot} = \frac{n_{mot}}{k_{mot}} + i_{mot} R_{mot} \tag{1}$$

Motor data k_{mot} and R_{mot} are given in Table 1. The validity of this voltage formula and of the current value provided by the controller were checked by recording the PWM voltage signal directly and the current via a current clamp with a fast oscilloscope for a few short periods. The accumulator is charged/discharged when the arm is lowered/raised. It assists load lifting by a power P_A which is the product of the actual pressure p_r times the accumulator flow rate Q_A. The power formula and the exact and approximate values for Q_A read

$$P_A = Q_A p_r; \quad Q_A = Q_p + Q_L - Q_r \approx \dot{s}\left(A_p - A_r\right). \tag{2}$$

The approximation neglects compressibility and pump leakage. $\dot{s}$ are related to ϕ by the four bar linkage kinematics, described by a function ψ which is not given here in details.

$$s = \psi(\phi); \quad \dot{s} = \frac{d\psi}{d\phi}\dot{\phi}. \tag{3}$$

The circuit drains the pump leakage Q_L to an auxiliary tank since the pump shaft seal cannot stand the maximum accumulator pressures. In practice that leakage must be charged to the accumulator by some auxiliary device which requires extra effort, weight, and space.

Upper level control and data recording were done by a dSpace 1103 system. The following figures show the measured and desired elbow angle ϕ, potential energy of lower arm load, electrical energy sent to the motor, energy contributed by the accumulator, pressures at piston and rod side, and averaged motor voltage, current, and power.

The efficiency of the combined electrical drive and hydraulic pump system computed as the ratio of load potential increase and consumed electric and accumulator energies is

$$\eta_{loadlift} = \frac{m_L g \Delta h}{E_{el} + E_A}; \quad E_{el} = \int_0^{t_{lift}} U_{mot} i_{mot} dt; \quad E_A = \int_0^{t_{lift}} P_A \, dt \tag{4}$$

with the gravity constant g, the load lift height Δh, and the lifting time t_{lift}. For t_{lift} = ~1 sec $\eta_{loadlift}$ for the three different load cases computes to values given by

Table 3: Efficiency of load lifting for three loads

m_L	$\eta_{loadlift}$
1.2 kg	24%
2.2 kg	31%
5.2 kg	54%

Load holding in the upper and lower position requires torque of the electric motor and a corresponding current. Even though the missing back voltage is zero some energy is required due to the coil resistance. For the highest of the three presented load cases that phase requires nearly as much energy as load lifting. For the lowest load the accumulator pressure balances the load; therefore, motor current and voltage are small and power is negligible.

There is practically no energy recuperation. A small portion of negative electric power flow can be seen right after the onset of the load lowering motion for m_L = 5.2 kg (see Figure 4). For larger loads that effect would be more pronounced. But the used power electronics cannot feed energy back to the net but can store only small amounts of energy in its DC link capacitances.

The performed tests use only 60 bars of 200 bars rated for this pump. At such conditions the pump does not have its best efficiency. Thus, better values can be expected for higher loads than those reported. The curves of Figure 4 to Figure 6 show one full load cycle by the elbow angle ϕ, the potential energy of the load, and the work delivered by the electric motor. Table 3 lists the efficiencies of the load lifting process only. If the electric energy consumption of the full cycle is taken as input energy of efficiency evaluation much lower values would result. At the end the total energy has to be provided by the electrical power source. The weight saving or range extension potential of a more efficient use of energy shall be exemplified by an abstract drive with a average efficiencies of η_{lift} in load lifting, a recuperation efficiency of η_{Recup} in load lowering, and load holding without consumption of energy. In the 5.2 kg load case the load potential energy is 19 joule; the investigated drive requires 59 joule in the full cycle with its long load holding phases. With efficiencies of $\eta_{lift} = 60\%$ and $\eta_{Recup} = 50\%$ only 22 joule would be required and only 10.5 joule if $\eta_{lift} = 80\%$ and $\eta_{Recup} = 70\%$.

Pump efficiency was not measured directly. But from the 54% efficiency from the electric input to the motor to the mechanical output at the arm it can be estimated to be approx. 60% in that load scenario.

Even though a very simple control concept was applied the actual elbow angles follow the desired position ϕ_d for the different loads with sufficient accuracy as the time plots in the uppermost diagram of Figure 4 show. At high loads the system exhibits some oscillations. It is very likely that this could be improved with a better controller.

Another criterion for the actuator concept is the achievable drive speed. After the acceleration phase the cylinder stroke velocity is 10 mm/s. This is roughly equivalent to an arm motion of 120°/s. The mean velocity of a typical human hand lift is 113°/s according to Garcia [15]. Including the acceleration phase, within the first second 80° of arm motion is achieved. For lifting the weight from 40° to 120°, that is sufficient. For lowering the weight, the elbow drive needs one second for 85% of the full motion and one more second for the remaining 15%. This is a controller issue and can be improved.

The total weight of the system without accumulator is approx. 3.3 kilograms; the components' weights are shown in Figure 7. The selected accumulator weighs 0.8 kilograms. It is oversized and for the low pressures

required and with the use of fibre reinforced plastic materials a drastic reduction to approximately one fourth would be possible. The same is true for the cylinder which is not designed for low weight. According to [16, 17, 18] reductions in the range of 60% can be expected for accumulators and cylinders. The hosing length and size could be also strongly reduced leading to a strong weight reduction; a total weight of approx. 2.3 kilograms is probably achievable.

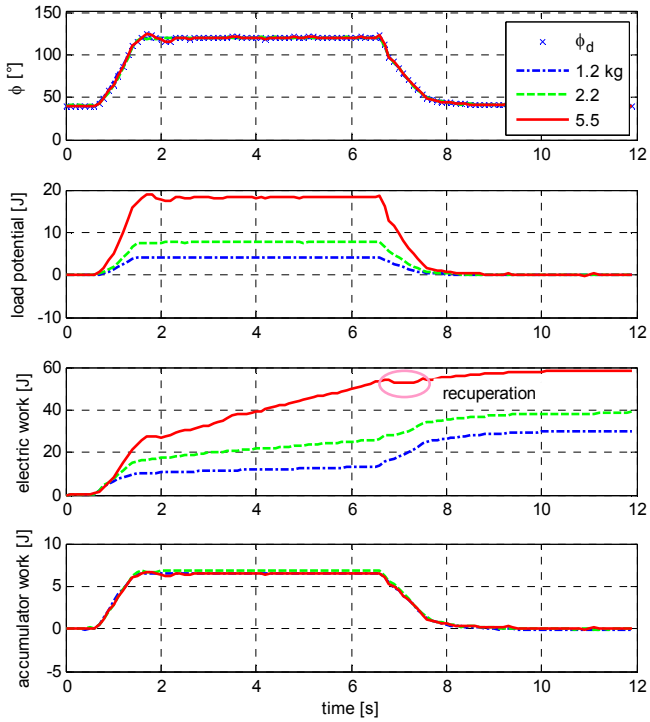

Figure 4: Measured motion and derived energy/work figures for three different loads.

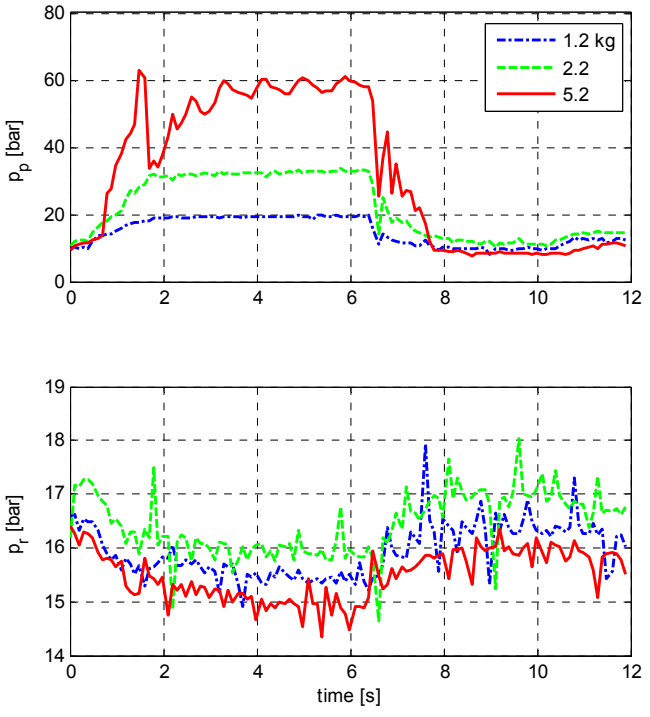

Figure 5: Measured pressures on piston and rod side for three different loads.

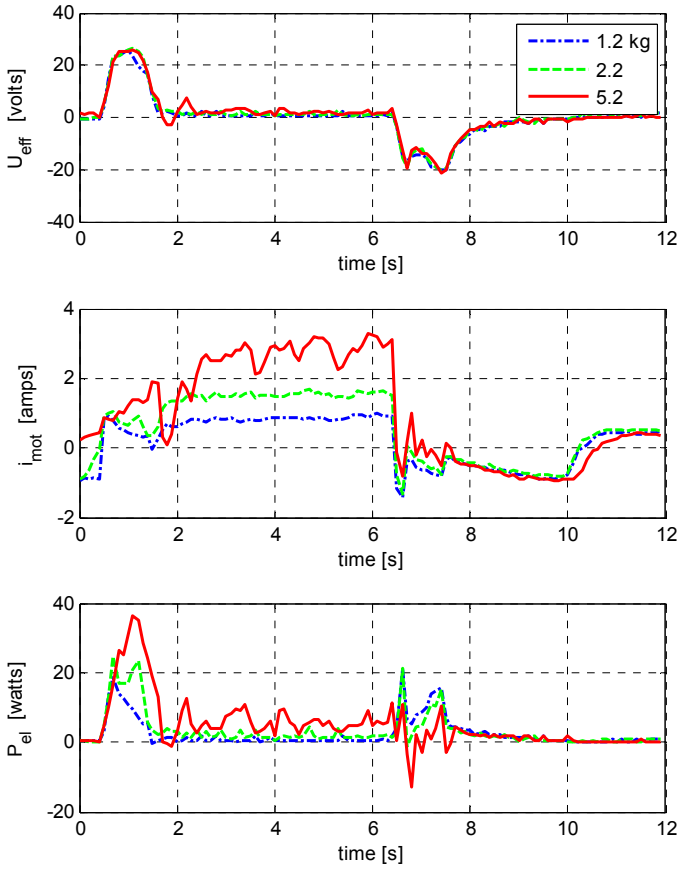

Figure 6: Voltage, current and power of electrical motor for three different loads.

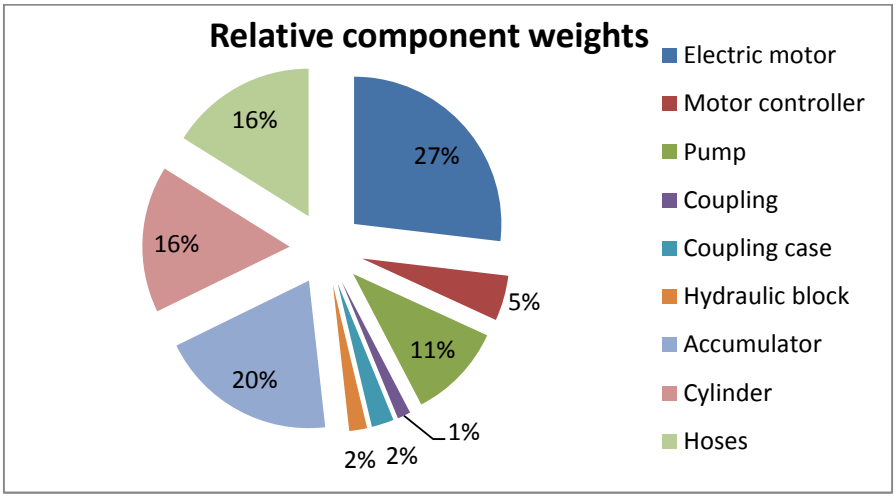

Figure 7: Relative weights of drive components; total weight: 4.1 kg.

The motor is oversized for the load ranges tested. The maximum nominal torque for the maximum measured pressure of approx. 60 bar (see Figure 5) is 0.17 newton meter. Even though the mechanical efficiency puts some factor on it (an estimated range is 1.5 to 2), the maximum torque can be substantially higher, since such motors can be overloaded by at least a factor two for short periods. The maximum pressure of the

pump is 210 bar, the maximum load of the arm would be approx. 20 kilograms. That can be accomplished with the selected motor for a short time.

4. CONCLUSIONS

As stated in Section 1, the investigated electrohydraulic drive system with a speed variable motor serves as a performance reference for digital hydraulic solutions. It is far beyond the one kilogramme seen acceptable for an arm exoskeleton. In that sub-kilowatts range only few pumps and cylinders are marketed and these components are not trimmed for low weight. Also the used electric motor and the power electronics are not optimized w.r.t. weight and size and for the load spectrum of an exoskeleton. However, comparison with AnyDrive [4], which is highly trimmed for exoskeleton use and has a comparable power range (see the performance data in Section 1), shows that there is not much room for improvement of the electric motor which is the heaviest part.

The hydraulic part of this drive concept serves as a simple transmission without additional functionality. As such it must be compared with alternative force transmission technologies, like, for instance, wire cable drives. Useful extra functionality could be powerless load holding, for instance realized with piloted check valves between pump and cylinder. For the load cycles studied in this paper that could roughly halve energy consumption, since the holding phases consume approximately as much energy as load lifting, see Figure 4. But appropriate check valves are currently not available in the required size and optimized w.r.t. low weight.

The main downside of concepts with one speed variable motor per active joint for motion control is the inability of downsizing by power smoothing. Thus, concepts which use a minimum number of electrical drives and hydraulic concepts for motion or force control have a potential to reduce weight, provided the required components, like variable displacement pumps or multi-chamber cylinders are lightweight.

Apart from the pump, all used hydraulic components of the test rig are bulky and heavy in comparison to the arm structure or, even more, to a weight optimized exoskeleton. This is the result of the common design guidelines of such components which are oriented on the heavy duty hydraulics needs of industrial or mobile sectors with quite different power ranges and weight requirements. As a main conclusion, exoskeleton hydraulic components must be separately designed and optimized. Spatial integration of the hydraulic components into the exoskeleton structure is an additional important system design criterion to obtain a small distal space. Auxiliary components which are necessary for a convenient assembly and maintenance, such as couplings and heavy hydraulic fittings, must be saved and replaced my more compact solutions.

NOMENCLATURE

A_P	Piston area	A_r	Rod side area
E_{el}	Consumed electric energy	E_A	Energy coming from accumulator
Q_A	Flow from accumulator	Q_L	Pump leakage flow
Q_P	Pump flow	Q_r	Flow from rod side of cylinder
P_A	Power delivered by accumulator	R_{mot}	Coil resistance of motor
U_{mot}	Motor voltage	V_0	Nominal accumulator volume
g	Gravity constant	i_{mot}	Motor current
k_I	Integral gain of position control	k_{mot}	Speed constant of motor
k_P	Proportional gain of position control	m_L	Load mass
n_d, n_{mot}	Desired and actual motor speeds	p_0	Accumulator prefill pressure
p_P	Pump pressure	p_r	Rod side pressure
s	Piston position	t_{lift}	Time of load lifting process
ΔV	Pump displacement	Δh	Height of load lifting
ϕ, ϕ_d	Elbow angle: actal and desired values	$\eta_{loadlift}$	Efficiency in load lifting
η_{Rcupt}	Efficiency of recuperation process		

REFERENCES

[1] Costello F. 2017. Emerging and enabling technologies. Robotics & Autonomous Systems Innovative UK, Blog, January 5 2017. https://innovateuk.blog.gov.uk/2017/01/05/exoskeletons-and-wearable-robotics/ (visited July 4 2017).

[2] Otto Bock. 2018. https://www.ottobock.com/de/unternehmen/ottobock-industrials/paexo/?gclid=EAIaIQobChMIxO P6ytKI3wIVA5ztCh2-9A7xEAAYASAAEgKwLPD_BwE/ (visited Dec. 12 2018).

[3] Polygerinos P., Wang Z., Galloway K. C., Wood R. J., and Walsh C. J. 2015. Soft robotic glove for combined assistance and at-home rehabilitation. Robotics and Autonomous Systems, vol. 73, pp. 135–143.

[4] Anydrive. 2018. https://www.anybotics.com/anydrive/ (visited Dec. 11 2018).

[5] Wang S., Meijneke C., and van der Kooij H. 2013. Modelling, design, and optimization of Mindwalker series elastic joint. Proceedings of the IEEE International Conference on Rehabilitation Robotics, vol. 2013, pp. 6650381.

[6] Wang S., Wang L., Meijneke C., Asseldonk E. van, Hoellinger T., Cheron G., Ivanenko Y., La Scaleia V., Sylos-Labini F., Molinari M., Tamburella F., Pisotta I., Thorsteinsson F., Ilzkovitz M., Gancet J., Nevatia Y., Hauffe R., Zanow F., and van der Kooij H. 2015. Design and control of the MINDWALKER exoskeleton. IEEE transactions on neural systems and rehabilitation engineering: a publication of the IEEE Engineering in Medicine and Biology Society, vol. 23, no. 2, pp. 277–286.

[7] Gancet J., Ilzkovitz M., Motard E., Nevatia Y., Letier P., de Weerdt D., Cheron G., Hoellinger T., Seetharaman K., Petieau M., Ivanenko Y., Molinari M., Pisotta I., Tamburella F., Labini F. S., d'Avella A., van der Kooij H., Wang L., van der Helm F., Wang S., Zanow F., Hauffe R., and Thorsteinsson F. 2012. MINDWALKER: Going one step further with assistive lower limbs exoskeleton for SCI condition subjects. 4th IEEE RAS EMBS International Conference on Biomedical Robotics and Biomechatronics (BioRob), pp. 1794–1800.

[8] Yu T., Plummer A., Iravani P., Bhatti J., Zahedi S., and Moser D. 2016. The design, analysis and testing of a compact electrohydrostatic powered ankle prosthesis. Proceedings of the ASME/Bath 2016 Symposium on Fluid Power and Motion Control, vol. 2016, paper no. FPMC2016 - 1770, pp. V001T01A034.

[9] Holl E., Scheidl R., and Eshkabilov S. 2017. Simulation Study of a Digital Hydraulic Drive for a Knee Joint Exoskeleton. Proceedings of the 2017 ASME/BATH Symposium on Fluid Power and Motion Control FPMC2017, October 16-20 2017, Sarasota, FL, USA, paper no. FPMC2017 – 4220.

[10] Scheidl R. 2017. Digital Fluid Power for Exoskeleton Actuation – Guidelines, Opportunities, Challenges. Proceedings of the 9th Digital Fluid Power Workshop, Aalborg University. Sept. 7-8 2017, Aalborg, Denmark.

[11] Scheidl R., and Mittlböck S. 2018. A Mathematical Analysis of a Hydraulic Binary Counter for Hydraulic Exoskeleton Actuation. Int. Journal of Hydromechatronics, vol. 1, no. 2.

[12] Scheidl R., and Mittlböck S. 2018. A Hydraulic Piloing Concept of a Digital Cylinder Drive for Exoskeletons. Proceedings of the 2017 ASME/Bath Symposium on Fluid Power and Motion Control - FPMC2018, September 12-14 2018, Bath, UK, paper no. FPMC2018-8875.

[13] Leati E., Poltschak F., and Scheidl R. 2017. An electromagnetically actuated high frequency oscillation pump. Mechatronics 47, pp. 233-245.

[14] Rahmfeld R., and Ivantysynova M. 2001. Displacement controlled linear actuator with differential cylinder - a way to save primary energy in mobile machines. ICFP 2001. Fifth International Conference on Fluid Power Transmission and Control.

[15] García-Alsina J., García A.C., Moranta. M. J., and Pleguezuelos C. E. 2005. Angular position, range of motion and velocity of arm elevation: A study of consistency of performance. Clinical Biomechanics 20, Spain, pp. 932-938.

[16] http://www.hydac.com.br/wp-content/uploads/e_technews_glassfiber-accumulator_150303.pdf (visited April 1, 2019).

[17] http://www.parker.com/portal/site/PARKER/menuitem.bdeb342e104b287234040310237ad1ca/?vgnextoid=feb9b5bbec622110VgnVCM10000032a71dacRCRD&vgnextdiv=687576&producttype=division&channelname=Cylinder+Division+-+Europe&vgnextfmt=FI (visited April 1, 2019).

[18] Stelling O., OTTE B., Petker J. 2014. Composite High Pressure Hydraulic Actuators for Lightweight Applications. Hydraulics & Pneumatics - Proc. 7th National Congress and Exhibition - HPKON 2014. October 22-25, 2014, Istanbul, Turkey.

SICFP19 Sponsors

Bosch Rexroth	
Internet	http://www.boschrexroth.com/
As one of the world's leading suppliers of drive and control technologies, Bosch Rexroth ensures efficient, powerful and safe movement in machines and systems of any size. The company bundles global application experience in the market segments of Mobile Applications, Machinery Applications and Engineering, and Factory Automation. With its intelligent components, customized system solutions and services, Bosch Rexroth is creating the necessary environment for fully connected applications. Bosch Rexroth offers its customers hydraulics, electric drive and control technology, gear technology and linear motion and assembly technology, including software and interfaces to the Internet of Things. With locations in over 80 countries, more than 32 300 associates generated sales revenue of roughly 6.2 billion euros in 2018. Bosch Rexroth Oy Service Business Strategy is to sell solutions of complete systems. Rexroth Oy offers comprehensive consultation, engineering, assembly and after sales service including commissioning and training to customers. Bosch Rexroth Oy has a wide distributor and subcontracting network. Offices are located in Vantaa and Tampere. Total sales in 2018 was 101,7 million eur with 106 employees.	

Freudenberg Sealing Technologies	
Internet	http://www.fst.com

Freudenberg Sealing Technologies (FST) is a longstanding technology expert and market leader for sophisticated and novel applications in sealing technology and electric mobility solutions worldwide. With its unique materials and technology expertise, the company is a proven supplier for demanding products and applications, as well as a development and service partner to customers in the automotive industries and in general industries.

Freudenberg Sealing Technologies generated sales of around € 2.3 billion in 2018, employed some 15,000 people and is part of the global Freudenberg Group.

FST offers its customers a complete line of hydraulic accumulators which include piston, diaphragm and bladder accumulators. Whether your application is stationary or mobile, Freudenberg combines market knowledge, the latest in technology and global support for your next application. We achieve customer-specific solutions including special weight and space-saving accumulators, build with more than six decades of experience with accumulator technology.

Hydac	
Internet	http://www.hydac.fi

The HYDAC group operates worldwide, offering an extensive product range to cover all areas of fluid technology. The products range from components and sub-systems, through to complex controlled and regulated drive units for mobile and industrial machines and systems. In addition we offer our customers a comprehensive package of technical services within the framework of HYDAC Fluid Engineering, for media such as hydraulic oils, lubrication oils, cooling/cutting fluids and water. Our objectives are exclusively to increase machine and system availability and to reduce our customers' operational costs.

The HYDAC group has at its disposal a worldwide network of expertise, high quality standards and customer knowledge and is therefore best placed to fulfil the exacting demands of the international market. The continuous expansion of our global presence with strong local focus enables us to respond to the needs of our customers in almost every part of the world. HYDAC group total sales in 2018 was 1,5 billion EUR and had approximately 9000 employees. Subsidiaries beyond 45 countries.

In Finland Hydac Oy offices are located in Vantaa and Tampere. Total sales in 2018 in Finland was about 40 MEUR by 70 employees.

John Deere	
Internet	http://www.deere.com/

John Deere is the world's leading manufacturer of agricultural and forestry machinery. The company is also a significant manufacturer of construction and landscaping machinery and of engines. Deere & Company was founded in 1837. Throughout its history, the basic values of the company have been integrity, quality, commitment and innovation. The company has production facilities in 16 different countries and employs approximately 60 000 people worldwide. The turnover of the company is in excess of $37 billion.

John Deere Forestry Oy designs and manufactures wheeled cut-to-length forestry machines in Joensuu, Finland. Joensuu factory is the world's largest manufacturer of cut-to-length forest machines. The total area of the factory is approximately 25 000 m². The domestic content of the machines is 80% and approximately 90% of production is exported. John Deere employs more than 700 people in Finland – approximately 400 of them at the Joensuu factory. Joensuu factory's subcontractors employs approximately an additional 1 000 people in Finland. John Deere Forestry Oy has its headquarters in Tampere Finland, which is also the location of product development center and European marketing center.

Parker Hannifin	
Internet	http://www.parker.com

Parker Hannifin is a Fortune 250 global leader in motion and control technologies. For 100 years the company has engineered the success of its customers in a wide range of diversified industrial and aerospace markets.

Parker's engineering expertise and broad range of core technologies uniquely positions the company to help solve the world's greatest engineering challenges. Learn more at www.parker.com or @parkerhannifin.

Ponsse	
Internet	http://www.ponsse.com/en/

Ponsse Plc is one of the world's leading manufacturers of purpose-built forest machines for the forestry professionals taking advantage of the cut-to-length method. Ponsse Plc focuses in the development, production, sales and maintenance of forest machines and related information systems. The extensive PONSSE® product range including e.g. harvesters and forwarders covers the diverse requirements of efficient and sustainable harvesting faced by logging operators around the world. High power hydraulics as well as modern automation and control systems count among the core technologies found in the product offering. Ponsse constantly develops its products and services, keeping a close eye on the new features expected by the forest industry and entrepreneurs. Without exception, our new products are designed on the basis of preferences expressed by our customers. Our mission is to contribute to our customers' success with productive and reliable PONSSE forest machines and services since 1970. It is our promise to be the "Logger's Best Friend".

Ponsse Plc's shares are listed on NASDAG OMX Nordic list and turnover reached 612 MEur in 2018. Currently Ponsse employs more than 1700 employees globally.

Sandvik Group	
Internet	https://www.home.sandvik/en/

Sandvik is a high-tech and global engineering group offering products and services that enhance customer productivity, profitability and safety. We hold world-leading positions in selected areas – tools and tooling systems for metal cutting; equipment and tools, service and technical solutions for the mining industry and rock excavation within the construction industry; products in advanced stainless steels and special alloys as well as products for industrial heating. In 2018, the Group had approximately 42,000 employees and revenues of about 100 billion SEK in more than 160 countries within continuing operations.

Sandvik develops new technologies and innovations in the areas of electrification, automation and digitalization. Approximately 2100 people are employed in Finland. Sandvik employs 1200 people in Tampere, 700 in Turku, 200 in Lahti. Over 95% of the equipment manufactured in Finland is exported. where The Sandvik Tampere site manufactures underground and surface drill rigs, also technology and competence centers, as well as test mine is in Tampere. Loaders and dump trucks for construction and mining industries are manufactured in Turku, where operates competence and electrification centers for Load and Haul operations. The Lahti Plant produces hydraulic hammers and excavator attachments. They also have competence and technology centers for hammers, screens and feeders in Lahti.

SICFP19 ORIENTATION GUIDE

Tampere-talo/
Tampere Hall
Yliopistonkatu 55, PO Box 16
FI-33101 Tampere, Finland
Tel. +358 3 243 4111
www.tampere-talo.fi

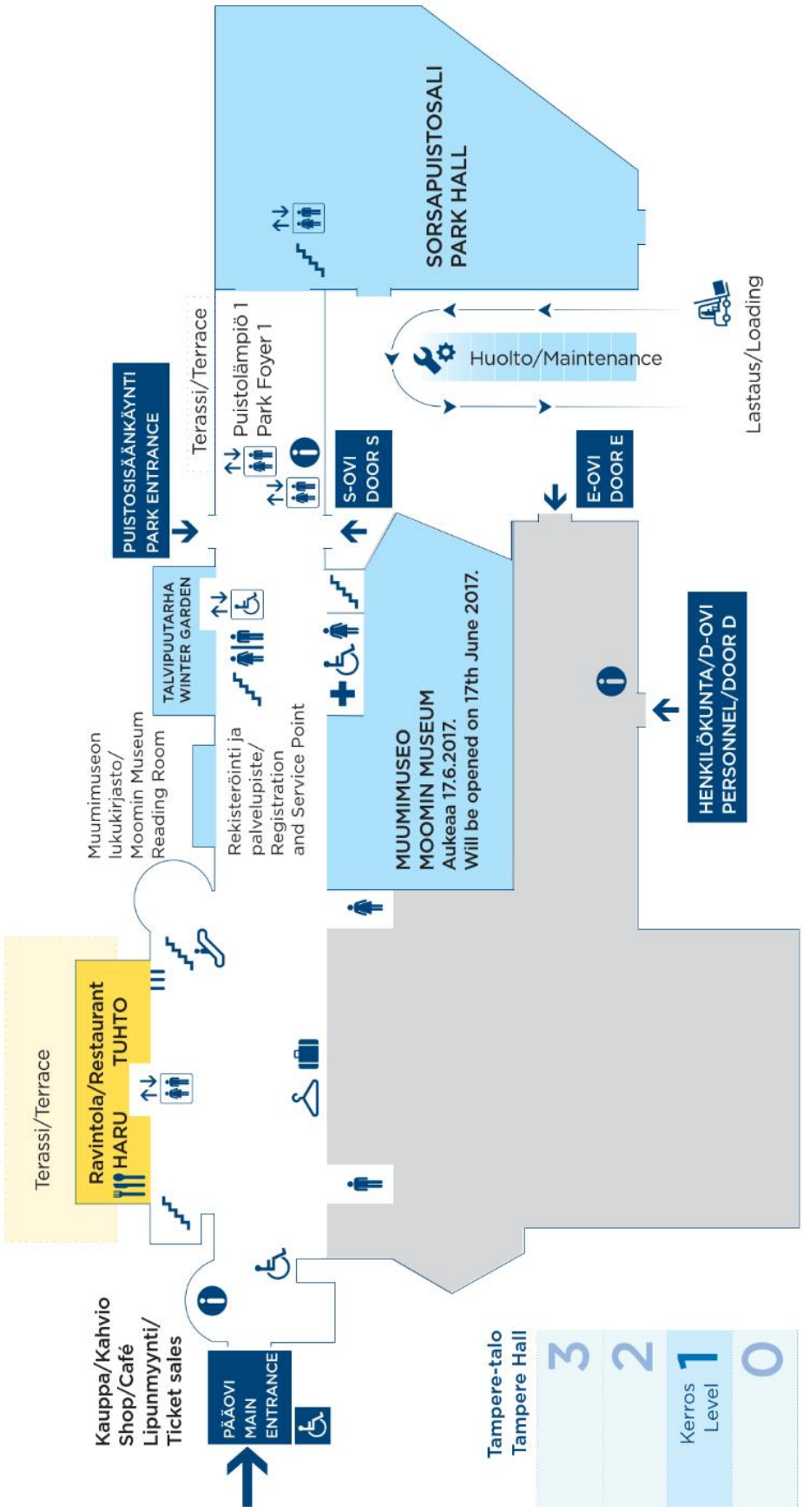

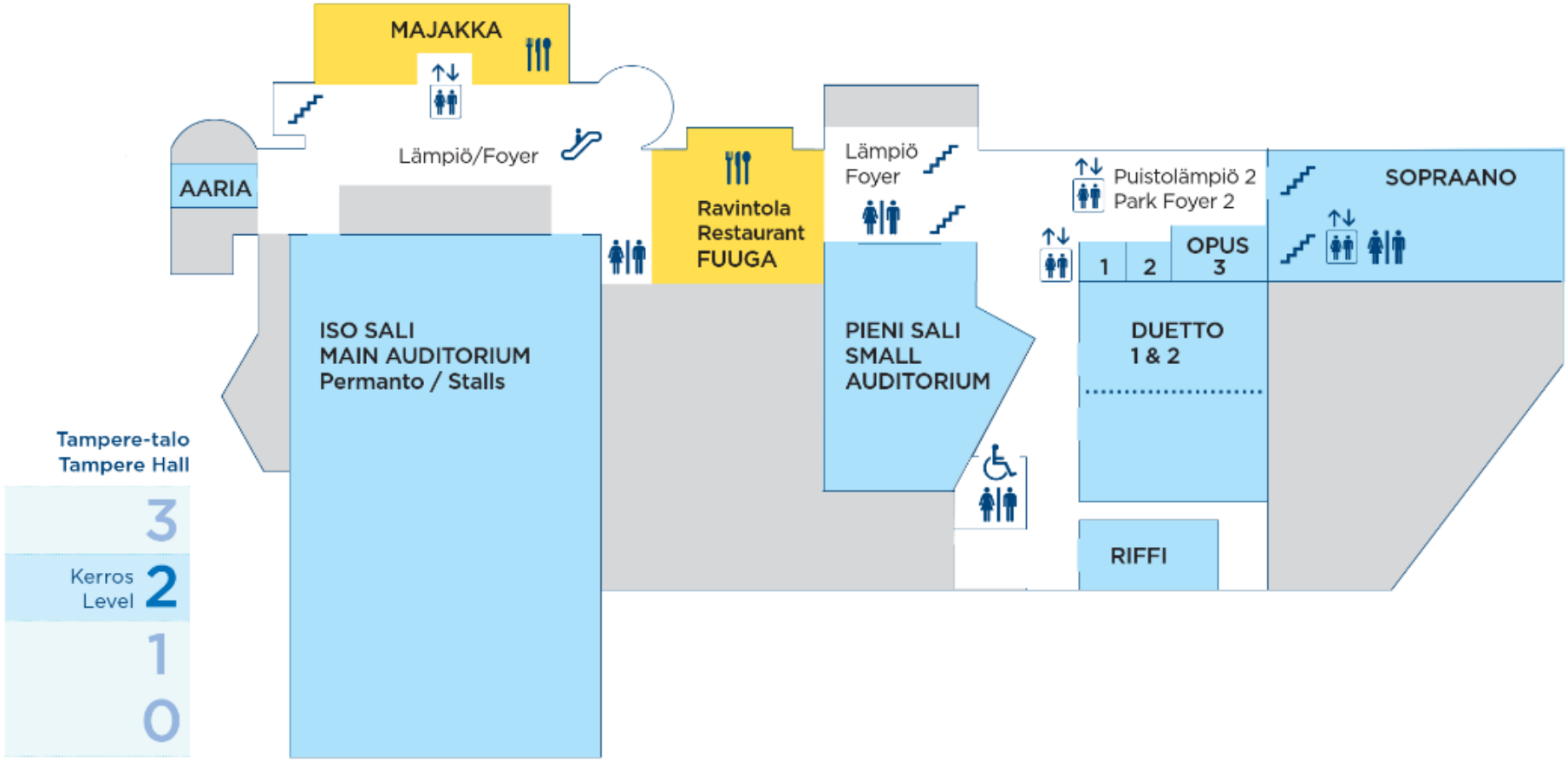
MAJAKKA
Lämpiö/Foyer
AARIA
Ravintola
Restaurant
FUUGA
Lämpiö
Foyer
Puistolämpiö 2
Park Foyer 2
SOPRAANO
1
2
OPUS
3
ISO SALI
MAIN AUDITORIUM
Permanto / Stalls
PIENI SALI
SMALL
AUDITORIUM
DUETTO
1 & 2
RIFFI
Tampere-talo
Tampere Hall
3
Kerros
Level
2
1
0

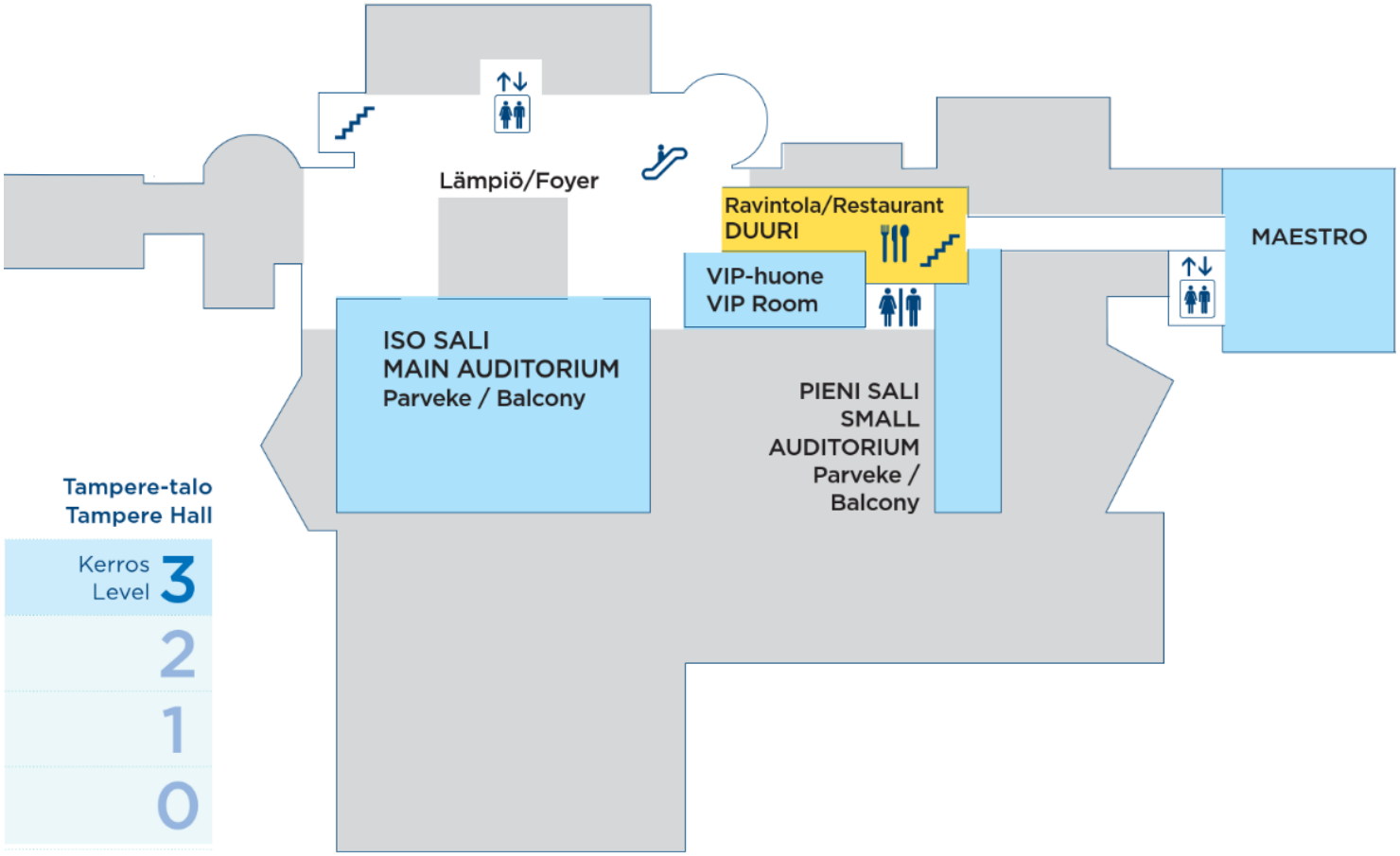
Lämpiö/Foyer
Ravintola/Restaurant
DUURI
VIP-huone
VIP Room
MAESTRO
ISO SALI
MAIN AUDITORIUM
Parveke / Balcony
PIENI SALI
SMALL
AUDITORIUM
Parveke /
Balcony
Tampere-talo
Tampere Hall
Kerros
Level
3
2
1
0

SICFP19 Events & Map Links

1. **Tampere Hall / Tampere-talo,**
   Yliopistonkatu 55, FI-33100 Tampere
   - Get-together 21.5.2019, 17:00 - 20:00
   - Conference 22.5-24.5.2019
   - Gala Dinner 23.5.2019, 19:00 –
   - https://goo.gl/maps/vJoZcuQAw7GgycVG6

2. **Tampere City Hall / Raatihuone**
   Keskustori 10, FI-33210 Tampere
   - Reception by the City of Tampere 22.5.2019 19:00 - 21:00
   - https://goo.gl/maps/1GJ87FkDLasU1pqJ7

3. **Tampere University, Hervanta Campus,**
   Korkeakoulunkatu 6, FI-33720 Tampere
   - Laboratory Tour 24.5.2019, 13:30 - 15:30
   - https://goo.gl/maps/v8ZVPBNqAa65FCr3A

Up to date information and chat from mobile app: